

JCTC

Journal of Chemical Theory and Computation

Special Issue in Honor of Dennis R. Salahub for His 60th Birthday



Dr. Dennis Salahub is presently the Vice-President (Research and International) of the University of Calgary. His mandate of VP (Research), initiated in 2002 when he joined the University of Calgary, was expanded year later to international relations. His decision to take that additional portfolio was not a surprise for those who knew Dennis. His professional life reveals how much he believes in international research collaboration and training and in relationships between people all around the world. This particular conviction has helped him gather many diverse people from many countries into his large group of collaborators.

Dr. Salahub's appointment to the University of Calgary was a return to his home province after a long detour through other horizons. Dennis Salahub was born in Castor, Alberta in 1946. He was a scholar in Edmonton, where he received his undergraduate education and his B.Sc. in 1967. He then moved to the province of Quebec and the Université de Montréal, where he completed his doctorate under the direction of Professor Camille Sandorfy. Knowing about Dennis's further scientific interests in molecular excited states, hydrogen bonds, and biomolecules, it is clear how much he could learn from this great scientist.

After earning his Ph.D. in 1970, Dennis spent several years in postdoctoral studies at Sussex, Waterloo, Johns Hopkins, and finally, General Electric, Schenectady, NY, where he collaborated on pioneering studies with the X_α Scattered Wave method. As Dennis himself¹ will nicely remind us, these were the first successes in chemistry that would later lead to those of the "legitimate" Density Functional Theory.

In 1976, he began his academic career at the Université de Montréal in the Department of Chemistry. He occupied this position until 1999, holding a McConnell Chair from 1990. There, he set up a research program in quantum chemistry, naturally oriented toward DFT. Over the years, his group has improved Density Functional methods and software that extends the range of applications. In the early 1990s, the *deMon* program was developed

in Montreal. New, improved functionals were then elaborated and implemented into the code. From then until now, the DFT-*deMon* has been complemented with other techniques (magnetic properties, reaction fields, molecular mechanics, Born–Oppenheimer molecular dynamics, etc.). Applications were aimed at describing metal clusters, catalysts and their reactivity, and biomolecular processes. Dennis’s group is now currently interested in turning to the description of properties and reactivity in complex environments: transition-metal catalysis, on the one hand, and enzymatic catalysis, on the other.

Dennis’s vision and leadership have been major forces in bringing together students and researchers from diverse countries who have shared their culture, knowledge, and expertises and built numerous international collaborations. We, the three guest editors of this issue, as well as the authors of the dedicated articles have met and work within Dennis’s research group, forming a community that Dennis calls “the deMon family”.

In 1999, Dr. Salahub decided to serve science at another frontline as the Director General of the Steacie Institute for Molecular Sciences at the National Research Council of Canada in Ottawa. He then promoted research projects at NRC in nano-, bio-, and optical sciences and technologies, loyal to his belief that “the fundamental things apply”.²

His return to Alberta as VP (Research) at the University of Calgary started a new period in his career, a new step toward more involvement in “all forms of research in everything from science, engineering, and social sciences to humanities, the arts, medicine, and business”.³ Increasing research funds, creating new multidisciplinary institutes, supporting innovation, promoting collaborative research projects, and international training initiatives are accomplishments in his mandate, which will conclude at the end of June 2007.

During his career, Dr. Salahub has published more than 250 research articles and four books. His scientific recognition is manifested by 300 national and international invited lectures. He expressed his involvement in the scientific community by serving as the program leader of the Centres of Excellence in Molecular and Interfacial Dynamics (CEMAID) from 1991 to 1994 and as a founding member of the Centre de Recherche en Calcul Appliqué (CERCA) in 1991. He has served on NSERC’s Grant Selection Committee and twice on the Reallocation Steering Committee for Chemistry (1997, 2001, Chair). His initiatives have helped to install high-performance computing in Quebec and in Canada.

Dr. Salahub has been the recipient of a CNC-IUPAC Award, the Noranda Award of the Canadian Society for Chemistry, and a Killam Research Fellowship. In 1998, he was named a Fellow of the Royal Society of Canada, and in 2006, he was elected a Fellow of the American Association for the Advancement of Science (AAAS).

Dennis will soon return to intense scientific research. We wish him very fruitful and exciting research, interdisciplinary and involving international collaboration; we know he will excel in the way he has already excelled.

We express our thanks to all who have contributed to this project and, more particularly, to the participating authors. We are delighted to dedicate this special issue to Dr. Dennis R. Salahub in celebration of his 60 years. It has been a privilege to have known and worked with Dennis, and we hope that you will enjoy this tribute to a true scientist and a good friend.

References

- (1) Salahub, D. R. *Theor. Chem. Acc.* **2000**, *103*, 311.
- (2) Steacie Institute motto by D.R.S., a quote from Casablanca by Michael Curtiz (1942), with Humphrey Bogart and Ingrid Bergman.
- (3) From an interview of Dr. Salahub by OnCampus, Calgary.

Annick Goursot,* Jan Andzelm, and Nino Russo

Guest Editors

CT700061E

JCTC

Journal of Chemical Theory and Computation

Quantum Dynamics of Electron Transfer from Bacteriochlorophyll to Pheophytin in Bacterial Reaction Centers[†]

Raffaele Borrelli, Mariangela Di Donato,[‡] and Andrea Peluso*

Dipartimento di Chimica, Università di Salerno, Fisciano (SA), I-84081, Italy

Received December 28, 2006

Abstract: We extend our previous works on the early electron-transfer steps in bacterial photosynthetic reaction centers to the dynamics of electron transfer from the bacteriochlorophyll anion to pheophytin. The approach employed here takes into account the whole set of normal coordinates of the acceptor and donor groups, in order to reliably account both for shifts and mixing of the normal coordinates and for changes in vibrational frequencies upon electron transfer. It is shown that intramolecular modes provide not only a discrete set of states strongly coupled to the initial state but also a quasi-continuum of weakly coupled states, which account for faster dephasing effects. Detuning effects are accounted for by averaging the computed probability over a small range of the electronic energy difference. The computed transition probability is of the same order of magnitude, a few picoseconds, as the observed one.

1. Introduction

Long-range electron transfer (ET) is an important process for energy transduction in living systems. The high structural complexity of the natural energy transducers, for example the photosynthetic reaction centers (PRC), suggests that the efficiency of the energy conversion should result from the interplay of several structural effects.^{1,2} A better understanding of that interplay is desirable not only for scientific purposes but also for technological progress, particularly in the area of supramolecular chemistry involved in the design of molecular machines capable of performing similar operations.^{3–7}

The basic concepts for understanding ET processes in condensed media have been provided by Marcus' theory and its quantum extensions,^{8–11} which have the great merit of having individuated the most important physicochemical factors which affect ET rates: the intramolecular and intermolecular reorganization energies, which depend on the

relative displacements of the equilibrium geometries of the two electronic states, the Gibbs' free energy change upon ET, the Franck–Condon (FC) factors, and the electronic coupling term.

The comprehension of a specific ET mechanism is thus realized in the ability of associating the above quantities, and then ET rates, to the specific physicochemical properties of the single molecular components and of the supramolecular structure of the whole system. A first difficulty arises already at the stage of disentangling all the above quantities from experimental data. That step would require the detailed knowledge of the normal modes of vibration and of their changes upon ET, namely, how they are displaced and/or rotated upon ET, and these data cannot be easily obtained from experimental data.^{12,13}

Because of the lack of specific information about modes which are displaced and/or rotated upon ET, in the past, a single intramolecular mode coupled to a continuum provided by the modes of a thermal bath (the surrounding medium) served as the reference model for the effect of intramolecular vibrations in ET dynamics,¹⁴ but there are reasons to believe that, although fluctuations introduced by the pertinent interactions of the main ET cofactors with the environments are certainly important for ET, the assumption of a single quantum mode could compromise the ability of extracting

[†] Dedicated to Professor Dennis R. Salahub on the occasion of his 60th birthday.

* Corresponding author e-mail: apeluso@unisa.it.

[‡] Present address: Department of Physics and Astronomy, Faculty of Sciences, Free University, 1081 HV Amsterdam, The Netherlands.

from the experimental data all the parameters which control ET.¹² Furthermore, since with only one or even a few discrete modes it is impossible to achieve the degeneracy conditions required for tunneling, those simplified models have led to assign to the classical motion of the surrounding medium a more important role than it might deserve.

Clearly, the possibility of building a more satisfactory model depends on the availability of detailed data concerning the energies and the mutual couplings of the vibronic states involved in ET. Theoretical computations can be of great help in giving reliable estimates of at least a part of the above quantities.¹⁵ In particular, methods based on density functional theory (DFT), a field in which Dennis Salahub has been undoubtedly a pioneer,^{16–19} turned out to be highly reliable in predicting both vibrational frequencies and electronic excitation energies, which are both of primary interest in the analysis of ET rates.

In this paper, we will use the results of DFT computations to characterize the vibronic states of bacteriochlorophyll and bacteriopheophytin, two redox cofactors of the ET chain in bacterial PRCs, and to study the dynamics of the ET process, with the attempt of better clarifying the role of B_A in the ET chain of bacterial PRCs. In fact, the involvement of the monomer bacteriochlorophyll B_A as an intermediate electron acceptor, leading to the formation of the charge separate state $P^+B_A^-$, has been debated for a long time in the literature, probably because the characteristic absorption region for the monomer bacteriochlorophyll, around 800 nm, is highly congested.

The excited state of P^* has a lifetime of ca. 3 ps; within this time interval, spectral features attributable to the formation of the bacteriopheophytin anion (H_A^-) can be identified. Early time-resolved pump–probe measurements, probing the region of the bleaching of the ground-state absorption of P (870 nm) and that of H_A (545 nm) and the appearance of the bacteriopheophytin anion (660 nm), gave no indication of the involvement of an intermediate electron acceptor.²⁰ It was concluded that the presence of B_A served to facilitate the direct electron transfer between P and H_A via a superexchange ET mechanism. Subsequent measurements, probing the spectral region in which the anion of the monomer bacteriochlorophyll is expected to absorb (1020 nm), gave an indication for the formation of the charge-separated state $P^+B_A^-$, which occurs with a time constant of ca. 1 ps.²¹ The results reported in this paper support these experimental findings showing that the $P^+B_A^-$ intermediate rapidly undergoes ET to H_A in ca. 0.5–2 ps, in good agreement with the observed decay time.

2. ET Dynamics

Basic concepts. Our approach to ET dynamics is based on the standard treatment of radiationless processes.²² Here, we rapidly illustrate the basic concepts for the case where ET involves only two molecules, an acceptor A and a donor D . The electronic wavefunctions of this system can be expressed as the superposition of two diabatic states $|AD^- \rangle \equiv |D \rangle$ and $|A^-D \rangle \equiv |A \rangle$, representing electronic states with the negative charge fully localized on one of the two partners.

On the condition that all other states of the systems are well-separated in energy, $|D \rangle$ and $|A \rangle$ form a complete and linearly independent orthonormal basis for the lower-energy electronic states of A and D . Each of the two electronic diabatic states is characterized by a manifold of vibronic states, which can also be grouped in two subsets, denoted $|\overline{D}\rangle$ and $|\overline{A}\rangle$.

In the Born–Oppenheimer approximation, the elements of $|\overline{D}\rangle$ and $|\overline{A}\rangle$ are given by the direct product of the electronic and vibrational wavefunctions:

$$|A, \bar{v}\rangle = |\psi_A\rangle \otimes |\bar{v}_A\rangle, |D, \bar{w}\rangle = |\psi_D\rangle \otimes |\bar{w}_D\rangle \quad (1)$$

where \bar{v} and \bar{w} denote the set of the vibrational quantum numbers associated to each normal mode of vibration.

Any state of the system can then be written as a linear combination of the elements of the two state manifolds:

$$|\Psi(t)\rangle = |\overline{A}\rangle C_A(t) + |\overline{D}\rangle C_D(t) \quad (2)$$

where C_A and C_D are column vectors, whose sizes are given by the dimensions of the vibrational subspaces of $|\overline{A}\rangle$ and $|\overline{D}\rangle$ considered relevant to the problem under consideration.

The expansion coefficients $C(t)$ of eq 2 determine the time evolution of $|\Psi(t)\rangle$ and therefore the dynamics of ET; they are solutions of the time-dependent Schrödinger equation:

$$-i\hbar \begin{pmatrix} \dot{C}_A(t) \\ \dot{C}_D(t) \end{pmatrix} = \begin{pmatrix} \mathbf{H}_{AA} & \mathbf{H}_{AD} \\ \mathbf{H}_{AD}^\dagger & \mathbf{H}_{DD} \end{pmatrix} \begin{pmatrix} C_A \\ C_D \end{pmatrix} \quad (3)$$

with initial conditions specifying the initial state of the system. Each of the four matrix blocks in eq 3 is a matrix whose size depends on the number of vibrational states belonging to $|\overline{A}\rangle$ and $|\overline{D}\rangle$. Since the off-diagonal elements are in general nonvanishing, the elements of $|\overline{A}\rangle$ and $|\overline{D}\rangle$ are not eigenstates of the Hamiltonian operator and change in time.

The matrix elements of the diagonal and extradiagonal blocks of \mathbf{H} are

$$H_{A\bar{w}A\bar{v}} = \langle A\bar{v} | \mathcal{H}^{el} + \mathcal{T}_N | A\bar{w} \rangle = \langle \bar{v}_A | \mathcal{E}_A(R) + \mathcal{T}_N | \bar{w}_A \rangle = E_{A\bar{v}}^{tot} \delta_{\bar{w},\bar{v}} \quad (4)$$

where $\mathcal{E}_A(r)$ is the nuclear potential energy operator of $|\overline{A}\rangle$

$$H_{A\bar{w}D\bar{v}} = \langle A\bar{v} | \mathcal{H}^{el} + \mathcal{T}_N | D\bar{w} \rangle = \langle \bar{v}_A | \lambda(R) + \langle A | \mathcal{T}_N | D \rangle | \bar{w}_D \rangle \quad (5)$$

and

$$\lambda(R) = \langle A | \mathcal{H}^{el} | D \rangle \quad (6)$$

The extradiagonal terms can be further simplified by making the reasonable assumption that

$$\lambda(R) \gg \langle A | \mathcal{T}_N | D \rangle \quad (7)$$

Furthermore, since ET takes place in a small region of nuclear coordinates, see *infra*, the dependence of the electronic coupling term $\lambda(R)$ on the nuclear coordinates can be safely neglected, leading to the well-known result that the off-diagonal terms of the Hamiltonian matrix are

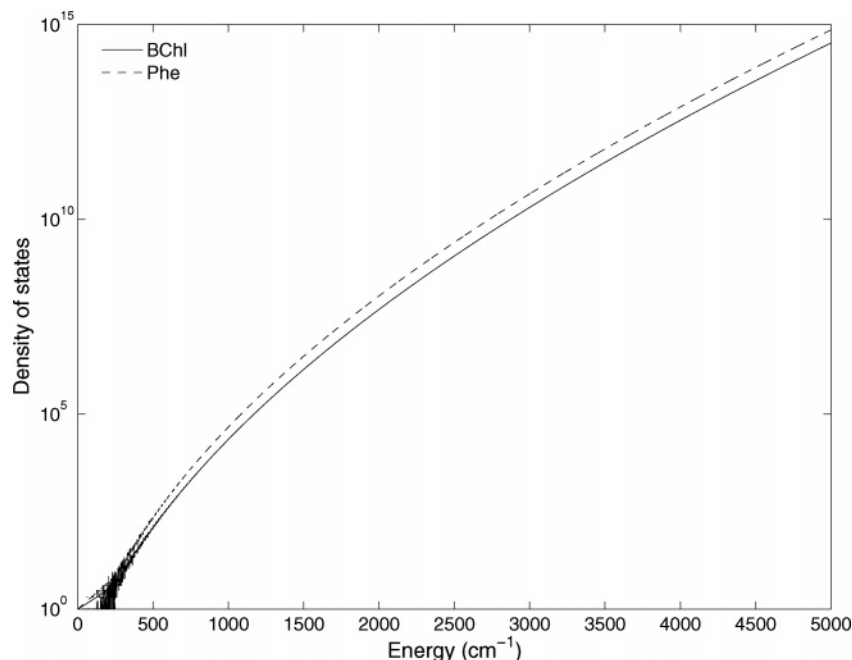


Figure 1. Total density of vibrational states vs energy for the pairs B_A^-/B_A and H_A^-/H_A , computed by using the Beyer–Swinehart algorithm,^{31,32} and the vibrational frequencies computed at DFT level.

proportional to the overlap of the vibrational states of $\overline{|A\rangle}$ and $\overline{|D\rangle}$, the so-called Franck-Cordon integrals:

$$H_{A\overline{w}D\overline{v}} = \lambda \langle \overline{v}_A | \overline{w}_D \rangle \quad (8)$$

ET Active Modes. In a hierarchic order of the different effects which could affect ET dynamics in biosystems, the nuclear modes of vibration of the two molecules which exchange an electron should be considered first. In the present study, we will consider only intramolecular modes and will show that, in the case of ET from B_A^- to H_A , the density of coupled states provided by the intramolecular modes of the two redox partners is sufficient to give transition times for ET in very good agreement with the observed one.

Obviously, for judging the importance of intramolecular modes in the ET process, the whole set of normal modes of the pairs $B_A^-H_A$ and $B_AH_A^-$ have to be properly taken into account in dynamics. The methodology employed here has been specifically designed for using the whole set of normal coordinates of the two redox cofactors;²³ it takes into account all the intramolecular effects which can be important for ET, that is, displacements of the equilibrium coordinates, mixing of the normal modes (Duschinsky effect), and changes in vibrational frequencies. The effects of the surrounding medium are neglected in our dynamic approach. These effects are certainly important, since they account both for energy detuning and for wavefunction dephasing. Detuning is crucial in slow ET, as it happens in intersystem crossing, where the coupling between the vibronic level is so small that tight degeneracy conditions are required.^{24,25} However, in the case of the ET rate being faster than relaxation of the surrounding medium, it is legitimate, at least as a first approximation, to invoke the adiabatic theorem and treat ET keeping fixed all the slower coordinates. If this approximation does not work for the system in hand, one should find either that the computed probability for ET is vanishingly

small or that it becomes vanishingly small by slightly changing the electronic energy difference between the two states. In our case, probabilities for ET computed for different values of the electronic energy difference between the two diabatic states all approach unity, see *infra*, thus confirming the reliability of the adiabatic separation of intramolecular and intermolecular modes for the case in hand. Furthermore, in the case under consideration, the effect of the protein on the electron-transfer rates is negligible; both experimental and theoretical works have shown that the reorganization energy of the protein is relatively small in the case of photosynthetic reaction centers.^{26–30} As concerns dephasing, the use of the whole set of the normal coordinates of the redox molecular pairs allows to partially include the faster dephasing effects, inasmuch as there would be several final states, with different vibrational frequencies, which are populated in the electronic transition. That makes the recurrence times much longer than the transition time, leading to dynamics which are essentially irreversible, see *infra*.

In a discrete state approach to ET dynamics, the selection of the vibronic states to be used in the time evolution is probably the most important problem to deal with. In fact, as shown in Figure 1, the density of the vibrational states increases very rapidly as the internal energy increases. For large molecules, such as bacteriochlorophyll and bacteriopheophytin, the density of vibrational states is about 10^5 at $E_{\text{int}} = 1000 \text{ cm}^{-1}$, computed by using the Beyer–Swinehart algorithm,^{31,32} but when the two molecules are considered together (not shown in Figure 1), it increases up to 10^{40} ! Obviously a selection of the most important state for ET dynamics becomes mandatory.

The assumptions that the nuclear dependence of the electronic coupling term can be neglected allows to easily identify the active modes for the ET process, namely, those modes whose quantum number can change during the

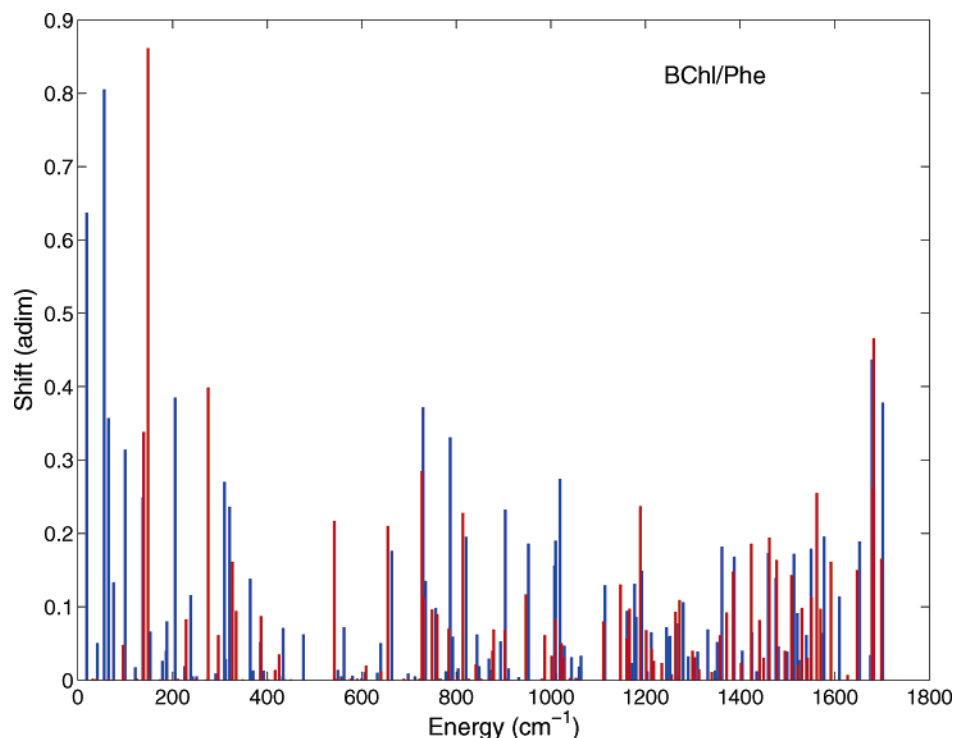


Figure 2. Displaced modes of bacteriochlorophyll (blue) and bacteriopheophytin (red). Absolute values of displacements in adimensional units.

electronic transition. FC integrals between vibronic states with different quantum numbers are vanishingly small whenever changes in population are associated to normal coordinates whose equilibrium positions or directions are the same in the two electronic states. Thus, since the coupling term is proportional to the Franck–Condon integral, eq 8, only displaced or rotated normal modes can give significant FC integrals; all other modes will act as spectators in dynamics since their quantum numbers will be frozen to the initial values.

The displaced and mixed modes can be determined by Duschinsky’s normal mode transformation, a fundamental tool for understanding mechanistic details of both radiative and radiationless photochemical processes in polyatomic molecules.³³ Duschinsky’s transformation allows expression of the normal modes of vibration of an electronic state of a given molecule in terms of the normal modes of another electronic state, a necessary step for the computation of the Franck–Condon integrals, and provides valuable information about modes which change their equilibrium positions and modes which are mixed with each other for the effect of the electronic transition. Displaced and, to a lesser extent, mixed modes determine the shape of the absorption bands and the dynamics of radiationless processes.

Let \mathbf{Q}_A and \mathbf{Q}_D be the normal mode vectors of a molecule in the electronic states $|A\rangle$ and $|D\rangle$, respectively. According to Duschinsky, the two sets of normal coordinates are related by the expression

$$\mathbf{Q}_A = \mathbf{J}\mathbf{Q}_D + \mathbf{K} \quad (9)$$

where \mathbf{J} is a rotation matrix and \mathbf{K} a displacement vector; the former accounts for mixing of the normal modes upon

electronic transition, the latter for changes in the nuclear equilibrium configurations.

If \mathbf{Q}_A and \mathbf{Q}_D are expressed in terms of Cartesian coordinates ξ , which is the most convenient representation for small equilibrium displacements,

$$\mathbf{Q}_\alpha = \mathbf{T}_\alpha^+ \mathbf{m}^{1/2} (\xi - \xi_\alpha^0) \quad \alpha = A, D \quad (10)$$

then

$$\mathbf{J} = \mathbf{T}_A^+ \mathbf{m}^{-1} \mathbf{T}_D, \quad \mathbf{K} = \mathbf{T}_A^+ \mathbf{m}^{-1/2} (\xi_D^0 - \xi_A^0) \quad (11)$$

where \mathbf{m} is the diagonal matrix of the atomic masses and \mathbf{T}_α and ξ_α^0 are the normal mode matrix and the equilibrium position vector of the electronic state $|\alpha\rangle$.

In the case where the two electronic states exhibit large equilibrium geometry differences, the normal mode transformation in the Cartesian representation can differ from eq 9 because of the necessary fulfilling of the Eckart conditions in both electronic states (the so-called axis-switching effect);³⁴ in some cases, the internal coordinate representation can be more convenient than the Cartesian ones; for more details see ref 35.

3. Results

Displaced Modes and Franck–Condon Integrals. The most significant components of the \mathbf{K} vectors and of the \mathbf{J} matrices for B_A^-/B_A and H_A^-/H_A are reported Figure 2 and in Tables 1 and 2, respectively.

Both cofactors possess several modes whose equilibrium positions are significantly displaced upon ET, covering a wide range of wavenumbers, from 25 to 1800 cm^{-1} . Low-frequency modes are important for achieving tight degen-

Table 1. Progressive Normal Mode Number, Wavenumbers (cm^{-1}), and Mixing Coefficients of the Most Mixed^a Normal Modes of the Pair B_A^-/B_A

mode	wavenumber		J^b
	B_A^-	B_A	$B_A^- \rightarrow B_A$
1	19.4	32.5	$-0.78(1) - 0.30(2) - 0.42(4) + 0.29(5)$
2	40.8	49.9	$-0.60(1) + 0.59(2) + 0.43(4) - 0.26(5)$
3	55.7	62.8	$0.74(2) - 0.54(4) + 0.28(5)$
5	75.7	77.6	$0.51(4) - 0.84(5)$
113	1652.5	1657.2	$-0.34(113) + 0.87(114)$
115	1678.7	1690.1	$-0.33(113) + 0.32(114) - 0.50(115) +$
116	1701.4	1724.0	$0.26(113) - 0.81(115) - 0.49(116)$
121	3041.9	3066.6	$-0.32(120) - 0.77(122) + 0.49(125) +$

^a Only mixed modes with maximum coefficient lower than 0.85.

^b Numbers in parentheses refer to the modes of B_A .

Table 2. Progressive Normal Mode Number, Wavenumbers (cm^{-1}), and Mixing Coefficients^a of the Most Mixed Normal Modes of the Pair H_A^-/H_A

mode	frequency		J^b
	H_A^-	H_A	$H_A^- \rightarrow H_A$
1	28.41	32.63	$0.64(1) + 0.68(2) + 0.16(3) - 0.15(4) + 0.23(5) - 0.15(7)$
2	34.45	48.46	$-0.76(1) + 0.57(2) + 0.11(3) - 0.15(4) + 0.22(5)$
3	57.45	67.36	$0.40(2) - 0.14(3) + 0.52(4) - 0.73(5)$
4	67.44	70.02	$-0.14(2) + 0.96(3) - 0.20(5)$
5	74.34	81.45	$0.82(4) + 0.55(5)$
46	794.93	810.15	$0.71(47) - 0.43(48) 0.52(54) - 0.10(57) + 0.11(58)$
48	810.86	834.01	$-0.37(47) - 0.44(48) + 0.20(50) + 0.50(51) + 0.18(54) + 0.56(55)$
49	823.66	839.86	$0.48(47) + 0.50(48) + 0.43(50) + 0.43(51) - 0.27(54) + 0.21(55)$
50	830.85	842.93	$-0.18(47) + 0.52(48) - 0.15(50) + 0.19(51) + 0.74(54) - 0.23(58)$
52	837.68	863.70	$0.64(50) - 0.59(51) + 0.21(54) + 0.16(55) + 0.20(57) - 0.30(60)$
53	851.35	865.04	$0.13(47) + 0.19(48) - 0.32(50) - 0.33(51) + 0.73(55) - 0.40(57)$
54	852.54	867.25	$0.82(52) - 0.56(53)$
55	857.43	882.85	$-0.55(52) - 0.82(53)$
57	875.63	904.07	$+0.21(48) + 0.14(51) + 0.12(54) - 0.29(57) + 0.88(58)$

^a Only mixed modes with maximum coefficient lower than 0.85.

^b Numbers in parentheses refer to the modes of H_A .

eracy between initial and final vibronic states, which is a necessary condition for tunneling. High-frequency modes are also very important because they make it possible to fill up large electronic energy gaps between the initial and final states with a modest increase in vibrational quantum numbers.

As to rotated modes, there are important differences between the two pairs. In B_A^-/B_A , there are three groups of significantly mixed modes, most of which are also displaced. The first group includes the lowest frequency modes, which are also the most displaced modes of the B_A^-/B_A pair; they will be therefore used in dynamic simulations. The other two groups include modes at a higher frequency, whose excitation

lead to energies higher than that of the ground vibronic state of $|B_A^-H_A\rangle$, which we will assume to be the only state populated at $t = 0$. Thus, these groups of rotated modes will not be used in dynamics.

By contrast, H_A exhibits a large number of mixed modes in a wide region of wavenumbers, which can be grouped into four subsets. The first group includes the five lowest-frequency modes; the second one consists of 12 modes spanning the region from 794 to 886 cm^{-1} , cf. Table 2; the last two groups, not reported in Table 2, include eight modes, from 1088 to 1191 cm^{-1} , and 13 modes, falling in the wavenumber range 1327–1509 cm^{-1} . The first group of rotated modes can be potentially useful in dynamics for fine energy tuning; all other modes fall at too high a frequency for this purpose, and since the FC integrals between rotated modes with different quantum numbers are much lower than those obtained from displaced modes, they will be discarded in dynamics.

The FC integrals between the ground vibronic state of $|B_A^-H_A\rangle$ and a selected small fraction (ca. 2×10^{13}) of $|B_A^-H_A\rangle$ are shown in Figure 3, as a function of the vibrational energy of the final states. The vibrational modes of $|B_A^-H_A\rangle$ which have been excited in computation and the maximum number of states for each mode are specified in the caption of Figure 3.

The inset of Figure 3 shows a magnification over a tiny energy region corresponding to the experimental free-energy change upon ET, ca. 1300 cm^{-1} . Since in the model adopted here the coupling between vibronic states is proportional to FC integrals, Figure 3 provides a picture of the relative values of the extra-diagonal row of the Hamiltonian matrix (\mathbf{H}_{AD} of eq 3) as a function of the vibrational energy of the final state. There is a very dense manifold of final vibronic states which are coupled to the initial ground vibronic state; the hole appearing between 800 and 1000 cm^{-1} is an artifact due to our choice of the excitation numbers used in computation, which have been made for favoring the energy region around 1300 cm^{-1} , corresponding to the electronic energy difference between $|B_A^-H_A\rangle$ and $|B_A^-H_A\rangle$. These results would suggest that, provided that small energy fluctuations, much smaller than a thermal quantum $k_B T$ (k_B is the Boltzmann constant), take place, ET from B_A^- to H_A can be mechanistically modeled as a nonradiative transition which mainly involves the intramolecular modes of vibration of the two redox cofactors, without the assistance of the low-frequency modes of the medium, in agreement with the general finding that the rates of most of the ET processes occurring in photosynthetic reaction centers are only moderately temperature-dependent.^{26,27,36–38}

Energy Parameters and Electronic Coupling Elements.

The relative energy of the two electronic states (including the zero-point contribution) has been determined by spectroscopic measurements. The free energy level of the intermediate charge-separated state was found ca. 500 cm^{-1}

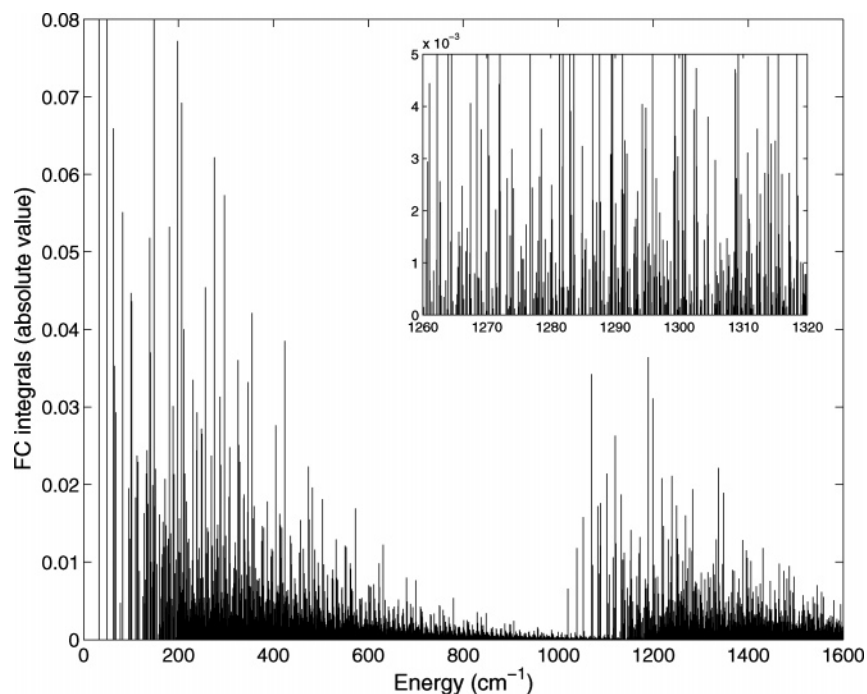


Figure 3. Franck–Condon integrals (absolute value) as a function of the vibrational energy (cm^{-1}) of the final states between the vibronic states of $|B_A^-H_A\rangle$ and a selected large fraction of the manifold of $|B_AH_A^- \rangle$ including the following modes (numbers in parentheses indicate the maximum quantum number allowed in computation): B_A {135.48(3), 146.22(5), 225.01(2), 277.64(2), 297.92(1), 386.37(2), 529.85(2), 659.67(2), 724.18(2), 730.64(2), 761.60(2), 788.83(2), 1281.39(2), 1691.72(2), 1761.78(2)}; H_A , {76.41(2), 86.16(1), 128.06(1), 206.90(2), 318.45(1), 367.50(4), 473.29(6), 1000.67(1), 1083.25(1), 1167.06(1), 1174.46(4), 1447.34(2), 1494.19(3), 1545.19(3), 1643.85(1)}.

below that of P^* , while the energy difference between P^* and the state $P^+H_A^-$ is ca. $1800\text{--}1900\text{ cm}^{-1}$.³⁹

As concerns the electronic coupling element, both the size of the system and the lack of symmetry rule out the possibility of computing that parameter by ab initio configuration interaction computations. It has been shown in the past that, while semiempirical methods do not provide sufficiently accurate estimates for the electronic coupling,^{40,41} the recourse to ab initio Hartree–Fock computations gives values which are in reasonable agreement with those obtained by reasonable fitting of the experimental ET rates.⁴² Reliable estimates of electronic coupling elements can also be obtained from the widely accepted exponential dependence of the electronic coupling element on the distance between the donor and acceptor sites. We have used Hopfield’s expression:⁹

$$H_{lm} = \frac{2.7}{\sqrt{N_a N_b}} \exp(-\beta R_{lm}) \quad \text{in eV} \quad (12)$$

where R is the edge-to-edge distance between two large aromatics of N_a and N_b atoms.

The X-ray structure of the PRC from *Rhodospira sphaeroides*⁴³ indicates that the edge-to-edge distance between B_A and H_A is ca. 4.5 \AA . The parameter β has been estimated by taking as a reference the values of the electronic coupling elements between quinones in bacterial PRC, evaluated as half of the energy difference of the two adiabatic states in a point of the avoided crossing region.⁴⁴ The ab initio multireference configuration interaction value (17 cm^{-1}) yields $\beta = 0.49\text{ \AA}^{-1}$, a value slightly lower than that

suggested by Hopfield (0.72)⁹ but in line with other values reported in the literature.⁴⁵ With that value of β , the coupling factor for ET between B_A^- and H_A is ca. 90 cm^{-1} , in very good agreement with ab initio Hartree–Fock computation.⁴² This point is important because the transition times for ET crucially depend on that parameter.

Transition Probabilities. The Franck–Condon integrals reported in Figure 3 show that there is a dense manifold of vibronic states of $|B_AH_A^- \rangle$ which are coupled to the vibronic ground state of $|B_A^-H_A\rangle$. However, since only a few FC integrals are significantly high, for most of the states of $|B_AH_A^- \rangle$, the coupling term with the initial state is small. We have therefore first investigated the effects of small change in the electronic energy difference (ΔE_{el}) between $|B_A^-H_A\rangle$ and $|B_AH_A^- \rangle$ on the transition probabilities. Several time propagations have been carried out, starting with $\Delta E_{el} = 1300\text{ cm}^{-1}$ and exploring an energy range of $\pm 50\text{ cm}^{-1}$ around this value, without attempting to optimize the active space for each energy point. In all the cases, the transition probabilities for ET approach to unity, thus assuring that the results are not due to the occurrence of a few accidental degeneracies but rather to the existence of a Franck–Condon weighted density of states sufficiently high to promote ET.

The results of some dynamic simulations are displayed in Figure 4, for values of ΔE_{el} in the range $1265\text{--}1315\text{ cm}^{-1}$, by varying each time ΔE_{el} by 5 cm^{-1} . The space of the active modes used in computations is reported in the caption of Figure 4. The transition probabilities reported in Figure 4 are summed over the whole vibrational manifold of $|B_AH_A^- \rangle$. For most values of ΔE_{el} , the initial state irreversibly decays

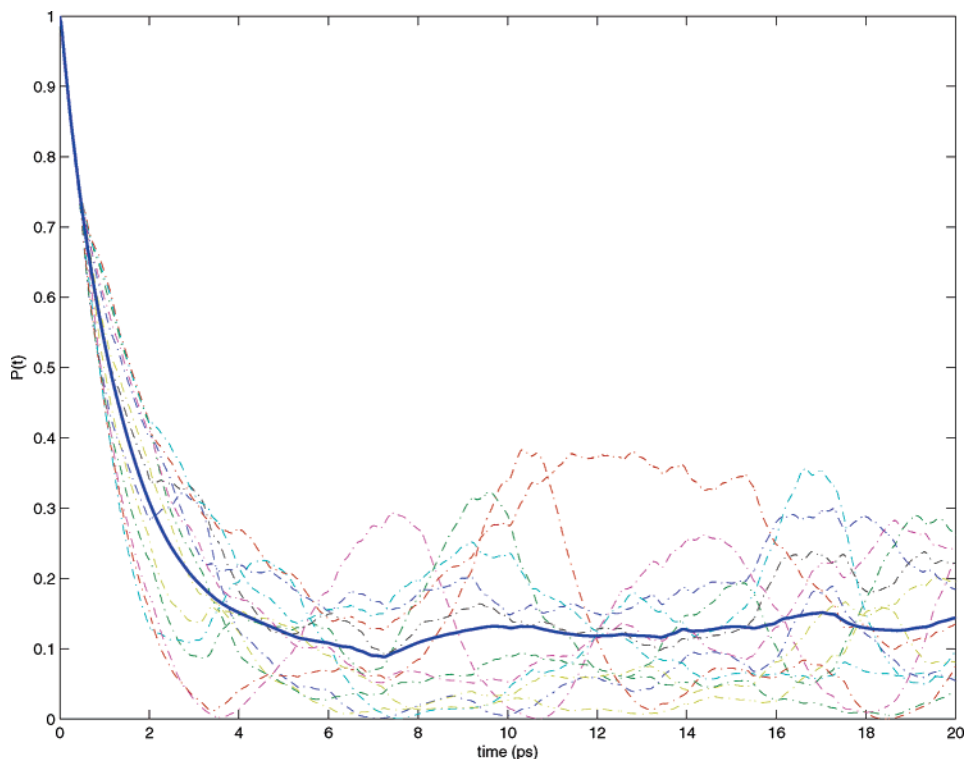


Figure 4. Transition probabilities for ET from B_A to H_A for different values of ΔE_{el} , see text, and their average (thick line). Excited modes (wavelength-maximum excitation): B_A (67.94–2, 77.66–2, 101.51–2, 141.02–2, 206.62–2, 238.65–2, 1020.24–1, 1039.37–1, 1199.50–1, 1282.95–1); H_A^- (139.03–2, 148.44–2, 275.64–2, 326.77–1, 1189.63–1, 1271.98–1).

in the manifold of $|B_A H_A^- \rangle$, within 2–5 ps. In a few cases, the population shows a few damped oscillations which rapidly decay in a few tens of picoseconds. The Boltzmann average of all decay curves (the thick line of Figure 4) has been fitted with an exponential function, from which an average half-transition time of 1 ps has been obtained, in very good agreement with the experimental observation.

4. Conclusion

The results presented in this paper indicate that ET from B_A^- to H_A in photosynthetic reaction centers can be successfully modeled as a nonradiative transition which mainly involves the intramolecular modes of vibration of the two redox cofactors. Thus, a physical model in which the role of the surrounding medium is that of accounting for small energy fluctuations—simulated here by performing an average of the transition probabilities over a tiny interval of ΔE_{el} caused by weak interactions of the two redox partners with their environments—appears to be able to correctly reproduce the rate of ET from chlorophyll to pheophytin in bacterial reaction centers.

The above conclusion of course holds for the specific case of ET considered here, but analyses such as that used here, based on a detailed knowledge of the intramolecular modes of vibration of the two redox cofactors, can be also useful for a better understanding of cases where the embedding medium is known to play a major role.

5. Computational Details

Equilibrium geometries, normal modes, and vibrational frequencies of bacteriochlorophyll and bacteriopheophytin

in their neutral and anionic forms were obtained at the DFT level using the standard B3LYP functional with a 6-31G-(d,p) basis set. In order to obtain reliable estimates of these quantities, we have preferred to compute them for the isolated redox cofactors in the gas phase by using the highest level of computation compatible with the size of the molecules. Of course, quantum mechanics/molecular mechanics methods could be employed for taking into account the effects of the environment, but at the present stage of development, these methods are well-suited only for considering steric effects, which are not expected to play any role in fast ET. Reliable polarizable force fields, which could account for electronic stabilization of ionic states, are not yet available.

The dynamics of ET have been determined by solving the time-dependent Schrödinger equation using a Chebyshev algorithm, with the initial condition that at $t = 0$ only the vibronic ground state of $|B_A H_A^- \rangle$ is populated. As concerns the final states, the vibronic states of $|B_A H_A^- \rangle$ obtained by exciting 19 vibrational normal modes, 13 from chlorophyll and 6 from pheophytin, have been considered in dynamic computations. More than 2×10^8 vibronic states of $|B_A H_A^- \rangle$ have been initially considered. The evaluation of the FC integrals between the vibronic ground state of $|B_A H_A^- \rangle$ and the selected manifold of $|B_A H_A^- \rangle$ has been carried out by using the MOLFC program,⁴⁶ which is based on the recurrence relations reported in ref 47.

The manifold of vibronic states of $|B_A H_A^- \rangle$ has been further pruned by considering only those states whose energy differences with the initially populated state (ΔE_{if}) and couplings V_{if} satisfy the criterion $|V_{if}/\Delta E_{if}| > \epsilon$, where ϵ is a

properly chosen small number (10^{-4} in our case); the resulting vibronic space includes more than 15 000 states.

The modes included in the active space and the number of states for each mode have been selected on the basis of several test computations, which also indicate that there are other modes potentially important for ET. Further investigations and improvements of the model are in progress.

Acknowledgment. A.P. is pleased to dedicate this paper to Dennis Salahub as a token of his esteem and friendship; he will always remember the marvelous days spent in Montreal in Dennis' group. The financial support of the Italian Ministry of University and of the University of Salerno is gratefully acknowledged.

References

- (1) Feher, G.; Allen, J. P.; Okamura, M. Y.; Rees, D. C. *Nature* **1989**, *339*, 111.
- (2) Kuhn, H. *Phys. Rev. A: At., Mol., Opt. Phys.* **1986**, *34*, 3409–3425.
- (3) Gust, D.; Moore, T. A.; Moore, A. L. *Acc. Chem. Res.* **1993**, *26*, 1988.
- (4) Gratzel, M. *Acc. Chem. Res.* **1981**, *14*, 376.
- (5) Ballardini, R.; Balzani, V.; Credi, A.; Gandolfi, M. T.; Venturi, M. *Acc. Chem. Res.* **2001**, *34*, 445.
- (6) Gust, D.; Moore, T. A.; Moore, A. L. *Acc. Chem. Res.* **2001**, *34*, 40–48.
- (7) Kodis, G.; Terazono, Y.; Liddell, P.; Andreasson, J.; Garg, V.; Hamburger, M.; Moore, T. A.; Moore, A. L.; Gust, D. *J. Am. Chem. Soc.* **2006**, *128*, 1818–1827.
- (8) Marcus, R. A. *J. Chem. Phys.* **1956**, *24*, 966–978.
- (9) Hopfield, J. J. *Proc. Natl. Acad. Sci. U.S.A.* **1974**, *71*, 3640–3644.
- (10) Kestner, N. R.; Logan, J.; Jortner, J. *J. Phys. Chem.* **1974**, *78*, 2148–2166.
- (11) Sumi, H.; Marcus, R. A. *J. Chem. Phys.* **1986**, *84*, 4894–4914.
- (12) Markel, F.; Ferris, N.; Gould, I.; Myers, A. *J. Am. Chem. Soc.* **1992**, *114*, 6208–6219.
- (13) Fischer, S. F.; Van Duyne, R. P. *Chem. Phys.* **1977**, *26*, 9–16.
- (14) Schenck, C. C.; Parson, W. W.; Holten, D.; Windsor, M. W.; Sarai, A. *Biophys. J.* **1981**, *36*, 479–489.
- (15) Borrelli, R.; Di Donato, M.; Peluso, A. *Biophys. J.* **2005**, *89*, 830–841.
- (16) Mlynarski, P.; Salahub, D. *Phys. Rev. B: Condens. Matter Mater. Phys.* **1990**, *43*, 1399.
- (17) Jamorski, C.; Casida, M.; Salahub, D. *J. Chem. Phys.* **1996**, *104*, 5134.
- (18) Casida, M.; Jamorski, C.; Casida, K.; Salahub, D. *J. Chem. Phys.* **1998**, *108*, 4439.
- (19) Casida, M.; Salahub, D. *J. Chem. Phys.* **2000**, *113*, 8918.
- (20) Martin, J. L.; Breton, J.; Hoff, A. J.; Migus, A.; Antonetti, A. *Proc. Natl. Acad. Sci. U.S.A.* **1986**, *83*, 957–961.
- (21) Arlt, T.; Schmidt, S.; Kaiser, W.; Lauterwasser, C.; Meyer, M.; Scheer, H.; Zinth, W. *Proc. Natl. Acad. Sci. U.S.A.* **1993**, *90*, 11757–11761.
- (22) Robinson, G. W.; Frosch, R. P. *J. Chem. Phys.* **1963**, *38*, 1187.
- (23) Borrelli, R.; Peluso, A. *J. Chem. Phys.* **2003**, *119*, 8437–8448.
- (24) Landau, L. *Phys. Z. Sowjetunion* **1932**, *2*, 1695.
- (25) Zener, C. *Phys. Rev.* **1929**, *33*, 536.
- (26) Gunner, M. R.; Robertson, D. E.; Dutton, P. L. *J. Phys. Chem.* **1986**, *90*, 3783–3795.
- (27) Gunner, M. R.; Dutton, L. P. *J. Am. Chem. Soc.* **1989**, *111*, 3400–3412.
- (28) Parson, W.; Warshel, A. *J. Phys. Chem. B* **2004**, *108*, 10474–10483.
- (29) Warshel, A.; Chu, Z. T.; Parson, W. W. *Science* **1989**, *246*, 112–116.
- (30) Parson, W. W.; Chu, Z. T.; Warshel, A. *Biophys. J.* **1998**, *74*, 182–191.
- (31) Beyer, T.; Swinehart, D. F. *Commun. Assoc. Comput. Machin.* **1973**, *16*, 379.
- (32) Stein, S. E.; Rabinovitch, B. S. *J. Chem. Phys.* **1973**, *58*, 2438–2445.
- (33) Duschinsky, F. *Acta Physicochim. URSS* **1937**, *7*, 551–566.
- (34) Houghen, J. T.; Watson, J. K. G. *Can. J. Phys.* **1965**, *43*, 298.
- (35) Borrelli, R.; Peluso, A. *J. Chem. Phys.* **2006**, *125*, 194308.
- (36) Woodbury, N. W. T.; Becker, N.; Middendorf, D.; Parson, W. W. *Biochemistry* **1985**, *24*, 7516–7521.
- (37) Kirmaier, C.; Holten, D.; Parson, W. W. *Biochim. Biophys. Acta* **1985**, *810*, 33–48.
- (38) McElroy, J. D.; Mauzerall, D. C.; Feher, G. *Biochim. Biophys. Acta* **1974**, *333*, 261–278.
- (39) Yakovlev, A. G.; Shkuropatov, A. Y.; Shuvalov, V. A. *Biochem.* **2002**, *41*, 2667–2674.
- (40) Warshel, A.; Creighton, S.; Parson, W. W. *J. Phys. Chem.* **1988**, *92*, 2696–2701.
- (41) Plato, M.; Mobius, K.; Michel-Beyerle, M. E.; Bixon, M.; Jortner, J. *J. Am. Chem. Soc.* **1988**, *110*, 7279.
- (42) Zhang, L. Y.; Friesner, R. A. *Proc. Natl. Acad. Sci. U.S.A.* **1998**, *95*, 13603.
- (43) Stowell, M. H. B.; McPhillips, T.; Rees, D. C.; Soltis, S. M.; Abresch, E.; Feher, G. *Science* **1997**, *276*, 812–816; PDB ID: 1AIG.
- (44) Di Donato, M.; Peluso, A.; Villani, G. *J. Phys. Chem. B* **2004**, *108*, 3068–3077.
- (45) Almeida, R.; Marcus, R. A. *J. Phys. Chem.* **1990**, *94*, 2978–2985.
- (46) Borrelli, R.; Peluso, A. *MolFC: A Program for Franck-Condon Integrals Calculation*; Theoretical Chemistry Group, University of Salerno: Salerno, Italy, **2006**. Package available free of charge at <http://www.theochem.unisa.it>.
- (47) Peluso, A.; Santoro, F.; Del Re, G. *Int. J. Quantum Chem.* **1997**, *63*, 233–244.

Theoretical Study of Intramolecular, CH–X (X = N, O, Cl), Hydrogen Bonds in Thiazole Derivatives[†]

Miguel Castro,^{*,‡} Inés Nicolás-Vázquez,^{‡,§} Jesús I. Zavala,[‡] F. Sánchez-Viesca,^{||} and Martha Berros^{||}

Departamento de Física y Química Teórica and Departamento de Química Orgánica, DEPg., Facultad de Química, Universidad Nacional Autónoma de México, México D.F., C.P. 04510, México, and Departamento de Ciencias Químicas, Facultad de Estudios Superiores Cuautitlán, Campo 1, Universidad Nacional Autónoma de México, Cuautitlán Izcalli, C. P. 54740, Edo. de México, México

Received November 14, 2006

Abstract: CH–X (X = N, O, or Cl) hydrogen bonds formed intramolecularly in 2-methyl-4-(2-chloro-4,5-dimethoxyphenyl)thiazole (**1a**), 2-amino-4-(2-chloro-4,5-dimethoxy phenyl)thiazole (**1b**), 2-amino-4-(2,4,5-trimethoxyphenyl)thiazole (**1c**), and 2-methyl-4-(2,4,5-trimethoxyphenyl)thiazole (**1d**) were studied by means of all-electron calculations performed with the B3LYP/6-311++G(d,p) method. Computed ground states, in the gas phase, show the presence of a single H-bond, CH–Cl, in each **1a** and **1b** moiety, and two H-bonds, CH–N and CH–O, for each **1c** and **1d** molecule. H–Cl, H–N, and H–O distances are shorter than the sum of the X and H van der Waals radii. H-bond energies of ≈ 2.0 kcal/mol were estimated for **1a** and **1b** and ≈ 4.0 kcal/mol for **1c** and **1d**. These results agree with those of the theory of atoms in molecules, since bond critical points were found for these H–X bonds. Finally, the chemical shifts in the ¹H NMR were calculated by the GIAO method; in **1a** and **1b** they are merely due to the different topological positions of the H atoms. But in **1c** and **1d** the shifts of H–N and H–O have signatures of H-bond formations.

I. Introduction

Thiazoles,¹ with aryl groups as substituents, may trigger the formation of intramolecular hydrogen bonding, that is favored both by the free rotation around the C–C bond, joining the thiazole and phenyl rings and by the kind of heteroatoms or functional groups attached to the rings. The physicochemical properties of these thiazole derivatives may depend on the type of H-bonds that these compounds can form. In fact,

the use of ¹H NMR and X-ray diffraction methods^{2,3} with this sort of species has suggested the formation of weak intramolecular H-bonds involving aromatic hydrogens. Even more, the results indicate the existence of different rotamers due to the intramolecular H-bonds,^{2,3} suggesting that some aromatic hydrogens in benzene rings show paramagnetic shifts in their ¹H NMR spectra, as an effect of the possible formation of H-bonds. In general, hydrogen bonding became of great interest in the last few decades due to its importance in different biochemical processes.^{4,5} In particular, intramolecular H-bonds are important because they can produce changes in the molecular conformation, affecting consequently the properties of thiazole derivatives.⁶

Conventional H-bonds are usually defined as a Y–H–X interaction, where Y–H is the typical covalent bond being the proton donating moiety and X the accepting center.^{7–11} The formation and binding energy of a conventional H-bond depends on the Lewis acidity of the Y–H bond and on the

[†] Dedicated to Professor Dennis R. Salahub on the occasion of his 60th birthday.

* Corresponding author e-mail: castro@quetzal.pquim.unam.mx.

[‡] Departamento de Física y Química Teórica, Universidad Nacional Autónoma de México.

[§] Departamento de Química Orgánica, Universidad Nacional Autónoma de México.

^{||} Departamento de Ciencias Químicas, Universidad Nacional Autónoma de México.

Lewis basicity of the X moiety; such an acidity-basicity requirement is fulfilled when Y and X are moderate or highly electronegative atoms such as oxygen or fluorine.⁷ More recently, new types of hydrogen bonds have been characterized,^{7–9} and they were recorded as nonconventional hydrogen bonds. One way to achieve the formation of a nonconventional H-bond is when the C–H bond acts as donor. Nonconventional CH–X hydrogen bonds will be addressed in the present research; that is, when the C–H bonds, either from the thiazole or phenyl rings, behave as the Lewis acid, whereas the X proton acceptors are the N atom of the thiazole ring and/or the Cl and O atoms, attached to the phenyl group. Therefore, the objective of this work is to characterize, by means of theoretical calculations, the formation of nonconventional intramolecular H-bonds in the polysubstituted arylthiazole derivatives. We will also show how these results may account for the particular crystal packing of these species. This is accomplished in terms of the calculated geometrical and energetic properties and on the Bader theory¹² of atoms in molecules for a study of electronic densities and Laplacians at bond critical points of the CH–X (X = N, Cl, and O) bonds. The topology of ρ and $\nabla^2\rho$ has proved useful to depict complex H-bonds.¹³ In this work, aside from these parameters the determination of chemical shifts was also addressed. For these purposes, the Density Functional Theory (DFT) methodology was used.¹⁴

II. Computational Methodology

Full optimization, which includes relaxation of geometry and electronic structure of four polysubstituted arylthiazoles derivatives, 2-methyl-4-(2-chloro-4,5-dimethoxyphenyl)thiazole (**Ia**), 2-amino-4-(2-chloro-4,5-dimethoxyphenyl)thiazole (**Ib**), 2-amino-4-(2,4,5-trimethoxyphenyl)thiazole (**Ic**), and 2-methyl-4-(2,4,5-trimethoxyphenyl)thiazole (**Id**), was carried out with the B3LYP/6-311++G(d,p) method.^{15,16} The B3LYP functional has been widely used for the study of weak hydrogen bonds.^{17–24} All-electron calculations were performed with the aid of the Gaussian 98 program.²⁵ In this way the GS (ground-state) geometries of **Ia–Id** were computed. Geometric, energetic, topological, and spectroscopic (chemical shifts) parameters were used for the characterization of these H-bonds. For each compound was computed, using Gaussian-98, the GS wave function, which was further applied for the “atoms in molecules” (AIM) analysis¹² to find bond critical points (BCPs) and associated ring critical points (RCPs). AIM calculations were performed with the aid of the AIM2000 program.²⁶ The BCPs and RCPs were analyzed in terms of electron densities, ρ , and their Laplacians, $\nabla^2\rho$. AIM2000 gives Laplacians that need to be multiplied by -4 to obtain the correct values;²⁷ our reported values are corrected. A vibrational analysis for all species studied in this work was made, finding that the optimized geometries correspond to a minimum on the potential energy surface (PES), since all the computed frequencies were real. The chemical shifts were calculated for these GS structures by means of the gauge invariant atomic orbital (GIAO) method.^{28,29}

III. Results and Discussion

IIIa. Geometrical and Energetic Results. The B3LYP/6-311++G(d,p) GS geometries for the bare **Ia–Id** derivatives are shown in Figure 1. The structures of **Ia** and **Ib** were determined by means of X-ray diffraction;³ they are indicated in Figure 2. Some selected equilibrium bond lengths and bond and dihedral angles are reported in Tables 1–3 of the Supporting Information, where they are compared against their experimental counterparts. The theoretical results show a reasonable agreement with the experiment. For **Ia**, X-rays yields a quasi planar structure with a dihedral $C_7-C_6-C_4-C_5$ angle of 6.54° and Cl–H₁₃ and N₃–H₁₂ contacts of 2.476 and 2.361 Å, respectively. While the theory indicates a less planar geometry, since a bigger value, 25.1° , was obtained for that angle. The calculated Cl–H₁₃ distance, 2.640 Å, differs from the X-ray assignment, while the theoretical result for N₃–H₁₂, 2.385 Å, is close to the X-ray determination. Crystal packing effects account partially for these structural differences. Similarly, X-ray results assign for **Ib** a nonplanar geometry with a $C_7-C_6-C_4-C_5$ angle of 52.27° , while DFT calculations yield a smaller, 25.30° , angle. These differences are also mainly due from crystal packing effects. Indeed, as shown in Figure 2, in the solid phase, each **Ib** unit is strongly bonded to other **Ib** moieties, accounting for the differences of the structural parameters of **Ib** in the gas phase and **Ib** in the crystal. Moreover, the experimentally determined³ Cl–H₁₃ and N₃–H₁₂ distances for **Ib** (2.954 and 2.780 Å, respectively) are significantly longer than the theoretical values, 2.640 and 2.378 Å, and they are also longer than the corresponding experimental values for **Ia**. These features are also a consequence of the more open geometry observed for **Ib**; see the **Ib-Exp** structure in Figure 2.

Another source of discrepancy is the C–H distance, and as determined by X-ray crystallography it is about 0.1 Å shorter than the actual distance to the proton that would be determined by neutron diffraction.³⁰ Correcting, the C–H bond lengths of **Ia** and **Ib**, 1.03 Å, are nearer to the theoretical results, 1.07–1.08 Å. However, for **Ia-Exp**, the corrected Cl–H (2.42 Å) and N–H (2.34 Å) distances still differ noticeably from the theoretical results for bare **Ia**. Whereas the C–H corrections for **Ib-Exp** yield negligible changes for the O–H (2.938 Å) and N–H (2.775 Å) lengths. Overall, neutron diffraction corrections yield small changes for the CH–X (X = N, Cl, and O) distances, which is due to the nonlinearity of these contacts. As will be shown below, CH–X distances and CH–X linearity, or nonlinearity, are very important for determining the formation, or absence, of an intramolecular H-bond. On the other hand, in the literature are reported values of 6.2° up to 58.8° for the $C_7-C_6-C_4-C_5$ angles of 2,4-disubstituted thiazoles;³ the present results fall in this range.

Moving now to **Ic** and **Id**, they have the same value, 2.240 Å, for the O₁₄–H₁₃ distance and similar N₃–H₁₂ separations of 2.340–2.350 Å. Moreover, these compounds are planar since the dihedral $C_5-C_4-C_6-C_7$ angles are close to zero (0.01 – 1.06°); see the structures **Ic** and **Id** in Figure 1. For **Ic** and **Id** there are no experimental geometries reported. Overall, the **Ia–Id** structures suggest the formation of weak

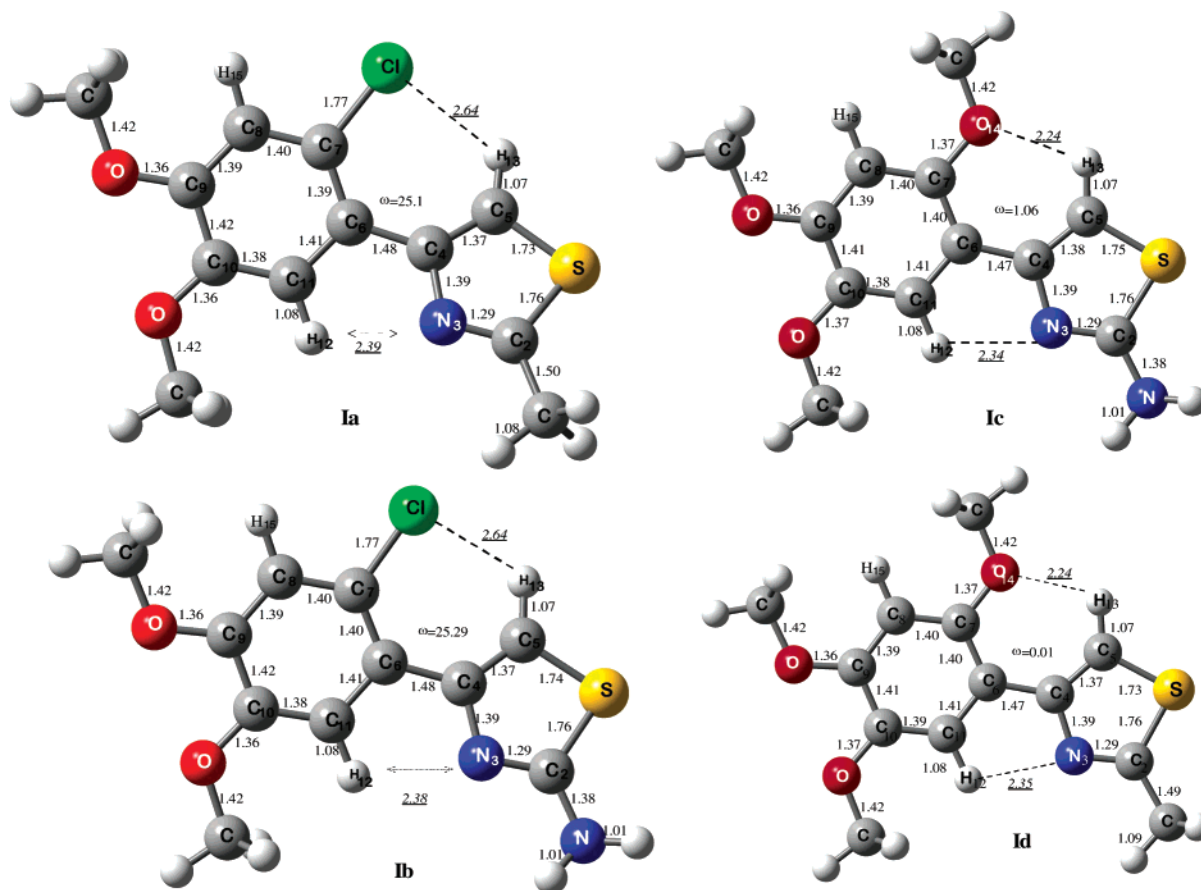


Figure 1. Optimized B3LYP/6-311++G(d,p) geometries for the bare **Ia–Id** derivatives. The CH–Cl, CH–N, and CH–O distances, in Å, are indicated as well as the dihedral angles, $\omega = \text{C}_7\text{C}_6\text{C}_4\text{C}_5$, in deg.

intramolecular H-bonds. Thus, we will continue with the analysis of this type of bonds.

A geometrical criteria for the formation of a CH–X hydrogen bond is that the distance between the proton and the acceptor atoms (H–X) should be shorter than the sum of their van der Waals radii.¹⁰ The theoretical results show $\text{C}_{11}\text{H}_{12}\text{–N}_3$ contacts of 2.378–2.385 Å for **Ia** and **Ib**. Slightly shorter, 2.341–2.349 Å, contacts were obtained for **Ic** and **Id**. In both cases, these CH–N contacts are meaningfully smaller than the sum of the van der Waals radii³¹ of the N (1.5 Å) and H (1.1 Å) atoms, suggesting the intramolecular $\text{C}_{11}\text{H}_{12}\text{–N}_3$ H-bond formation for each **Ia–Id** derivative. In fact, these contacts are even shorter than the reported values, 2.52–2.72 Å, for this kind of CH–N bond.³² Moreover, the calculated $\text{C}_{11}\text{–N}_3$ distances, 2.804 and 2.799 Å, in the $\text{C}_{11}\text{H}_{12}\text{–N}_3$ contacts of **Ia** and **Ib** are relatively close to the X-ray values,³ 2.749 and 2.990 Å; which are smaller than the C–N distance, 3.41 Å, reported for a CH–N H-bond.³⁰ Similarly, the $\text{C}_{11}\text{–N}_3$ distances for **Ic**, 2.786 Å, and **Id**, 2.792 Å, are also smaller than the reported value.³⁰ However, it has been shown that this sort of geometrical criteria, particularly for weak H-bonds, is doubtful.⁷ In fact, as shown below the energetic and topological criteria deny the formation of intramolecular $\text{C}_{11}\text{H}_{12}\text{–N}_3$ bonds in **Ia** and **Ib**. The calculated nonplanar structures of **Ia** and **Ib** are reflected in the absence of these H–N bonds.

On the other hand, the calculated $\text{C}_5\text{H}_{13}\text{–Cl}$ contacts for **Ia** and **Ib**, 2.64 Å, are noticeably smaller than the sum of

the van der Waals radii of the Cl (1.7 Å) and H (1.1 Å) atoms; they are also in agreement with the experimental values, 2.57–2.94 Å, reported for this type of H-bond.³⁰ More recently, Moro et al.³³ described the formation of intramolecular C–H–Cl bonding. In their studied compounds, the H–Cl distances are 2.69 and 2.76 Å; our computed value, 2.64 Å, is close to these experimental findings. The estimated $\text{C}_5\text{–Cl}$ distances, 3.164–3.163 Å, for **Ia** and **Ib**, also are close to the observed values,³³ 3.320(9) and 3.239(11). Moreover, the calculated $\text{C}_5\text{–H}_{13}\text{–Cl}$ angles, 109.4° and 109.3°, for **Ia** and **Ib**, are nearer to the observed range,³³ 117–118°. Thus, these theoretical and experimental results suggest the formation of intramolecular $\text{C}_5\text{H}_{13}\text{–Cl}$ H-bonds in **Ia** and **Ib**.

For the calculated planar structures of the **Ic** and **Id** derivatives, the $\text{C}_5\text{H}_{13}\text{–O}_{14}$ contacts, 2.24 Å, are also noticeably smaller than the sum of the van der Waals radii of the oxygen (1.5 Å) and H atoms (1.1 Å), suggesting the appearance of $\text{C}_5\text{H}_{13}\text{–O}_{14}$ hydrogen bonds in these molecules. Analyzing a database of X-ray structures, Taylor and Kennard³¹ observed that the CH–O interaction is contained in the 2.04–2.39 Å range. From the theoretical point of view, using the B3LYP/6-31G(d,p) method, a value of 2.253 Å was found for the conventional intramolecular O–H bond of hydroxythiophenol.³⁴ The present B3LYP/6-311++G(d,p) results are in favor of the $\text{C}_5\text{H}_{13}\text{–O}_{14}$ intramolecular hydrogen bond formation in each **Ic** and **Id** derivative; this, in addition to the $\text{C}_{11}\text{H}_{12}\text{–N}_3$ bonding, quoted above. Even

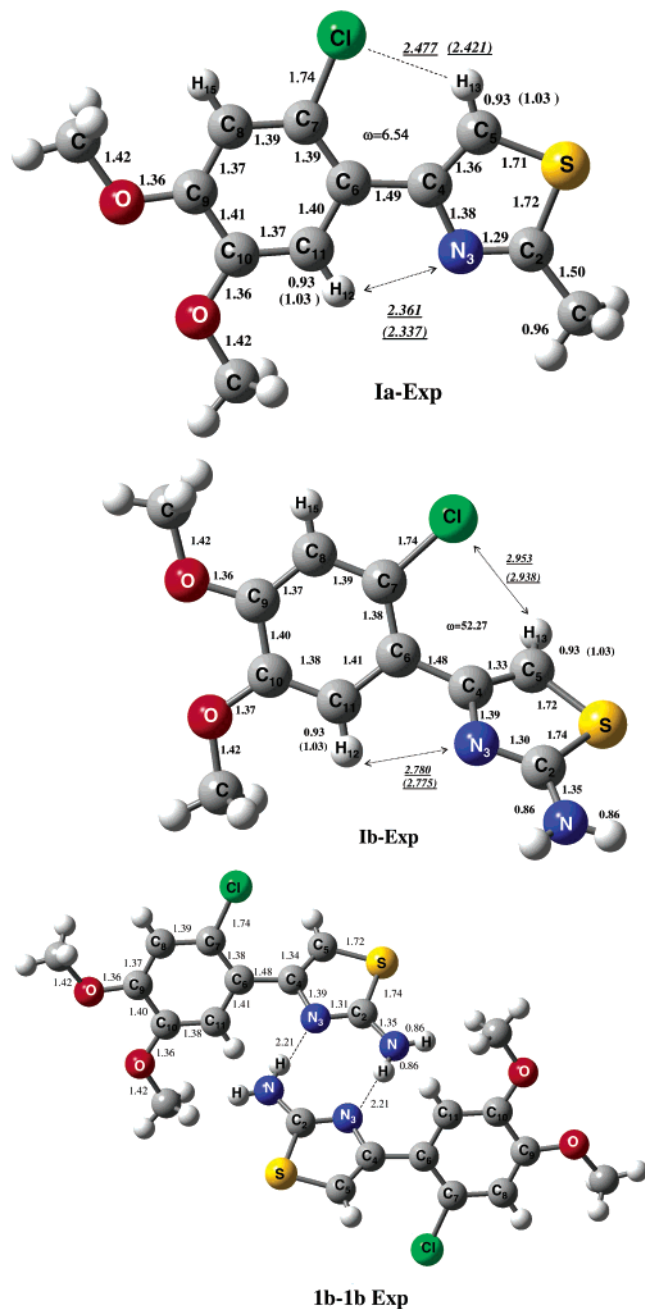


Figure 2. Experimental geometries for the **Ia** (**Ia-Exp**) and **Ib** (**Ib-Exp**) molecules and for the **Ib-Ib** (**Ib-1b-Exp**) dimer. For **Ia** and **Ib** are indicated the neutron diffraction corrections for the C–H bond lengths and for the Cl–H distances.

more, our estimated C_5-O_{14} distances, 2.791 Å for **Ic** and 2.795 Å for **Id**, are shorter than the recommended value, 3.25 Å, for this type of CH–O bonding.⁵

Another property that allows depicting H-bonds is the C–H–X bond angle. Desiraju and Steiner⁷ have found that very strong H-bonds have C–H–X angles of 175–180°, strong H-bonds may have 130–180°, but angles smaller than 130° imply the formation of weak H-bonds. The $C_5-H_{13}-Cl$ bond angles for **Ia** and **Ib** are $\cong 109^\circ$, while smaller $C_{11}-H_{12}-N_3$ angles, of 101° , were computed for these species. Then **Ia** and **Ib** have weak CH–Cl bonds and, presumably, much weaker CH–N bonds.

Ic and **Id** follow the same trend, and they have $C_5-H_{13}-O_{14}$ angles of $\cong 109^\circ$ and $C_{11}-H_{12}-N_3$ angles of $\cong 103^\circ$. Why

then in **Ic** and **Id** $C_{11}H_{12}-N_3$ and $C_5-H_{13}-O_{14}$ bonds are formed, while in **Ia** and **Ib** only $C_5H_{13}-Cl$ bonds are formed? The answer may be due to the fact that, as indicated by the $C_7C_6C_4C_5$ dihedral angle, **Ic** and **Id** are planar species, while this angle indicates a considerable deviation from planarity for **Ia** and **Ib**.

A property that determines the strength of the H-bond formation is the stabilization energy due to this kind of bond. For the intermolecular case, this property is estimated as the energy difference of two states of the AH and B units: the sum of the total energies of two independent AH and B ground states minus the total energy of the AH–B system, i.e., when the moieties are joined by H-bonds. However, in the intramolecular CH–X systems, both donor (CH) and acceptor (N, O, and Cl) fragments are contained within the **Ia–Id** thiazole derivatives, as they cannot be independent moieties. This feature requires the location of a structure where the intramolecular H-bond is absent or diminished. In an attempt to locate such “absent H-bond” structures, we have carried out total energy calculations for each **Ia–Id** derivative, varying the dihedral $C_5C_4C_6C_7$ angles. This rotation is allowed, since, although there is some small degree of π -conjugation between C_4 and C_6 , the C_4-C_6 distance, 1.478 Å, indicates, essentially, a single C–C bond. The PESs for this rotational degree of freedom are shown in Figure 3. It should be pointed that at each selected dihedral angle (it was varied at intervals of 30°), a fully optimization, structural and electronic, was performed. The PESs are symmetrical around 180° . In the first step, the whole PES profile was obtained with the 6-31G(d,p) basis set. Afterward, with the purpose to obtain more accurate results, the important points (GS, 90° , 120° , and 180° points) were computed with the 6-311++G(d,p) basis; the values obtained are also indicated there.

The four **Ia–Id** curves present a similar pattern. The first local maximums, at 90° , are mainly due to the breaking of the small π conjugation between the phenyl and thiazole rings. In addition, these structures have slightly longer C_4-C_6 distances, $\cong 1.49$ Å, than the ground-state geometries. (The C_4-C_6 distance is 1.48 Å for the ground states of **Ia** and **Ib**, and it is 1.47 Å for **Ic** and **Id**, see Figure 1). Absolute maximums at 180° are mainly accounted by the manifestation of heteroatom repulsions, involving relatively high electronegative atoms: N_3-Cl for **Ia** and **Ib** and N_3-O_{14} for **Ic** and **Id**. Additionally, the $H_{12}-H_{13}$ repulsions, in the four cases, also contribute to the energy increase. On the other hand, the minimums at 120° reflect the absence of such heteroatom and $H_{12}-H_{13}$ repulsions as well as the absence of intramolecular H-bond formation, since the N_3-Cl , N_3-O_{14} , and $H_{12}-H_{13}$ and the H–N, Cl–H, and O–H distances are quite big; see Figure 3. We have estimated the stabilization energy, due to intramolecular H-bonding, subtracting the total energy of the corresponding **Ia–Id** GS from the respective value at 120° . For the nonplanar GSs of **Ia** and **Ib** were obtained 2.1 kcal/mol for this property, at the B3LYP/6311++G(d,p) level of theory. While for **Ic** and **Id**, the stabilization energy is $\cong 4.1$ kcal/mol. The quasiplanar geometry of **Ic** and **Id** coupled with the presence of the more electronegative O atoms is mainly responsible for the H-bond

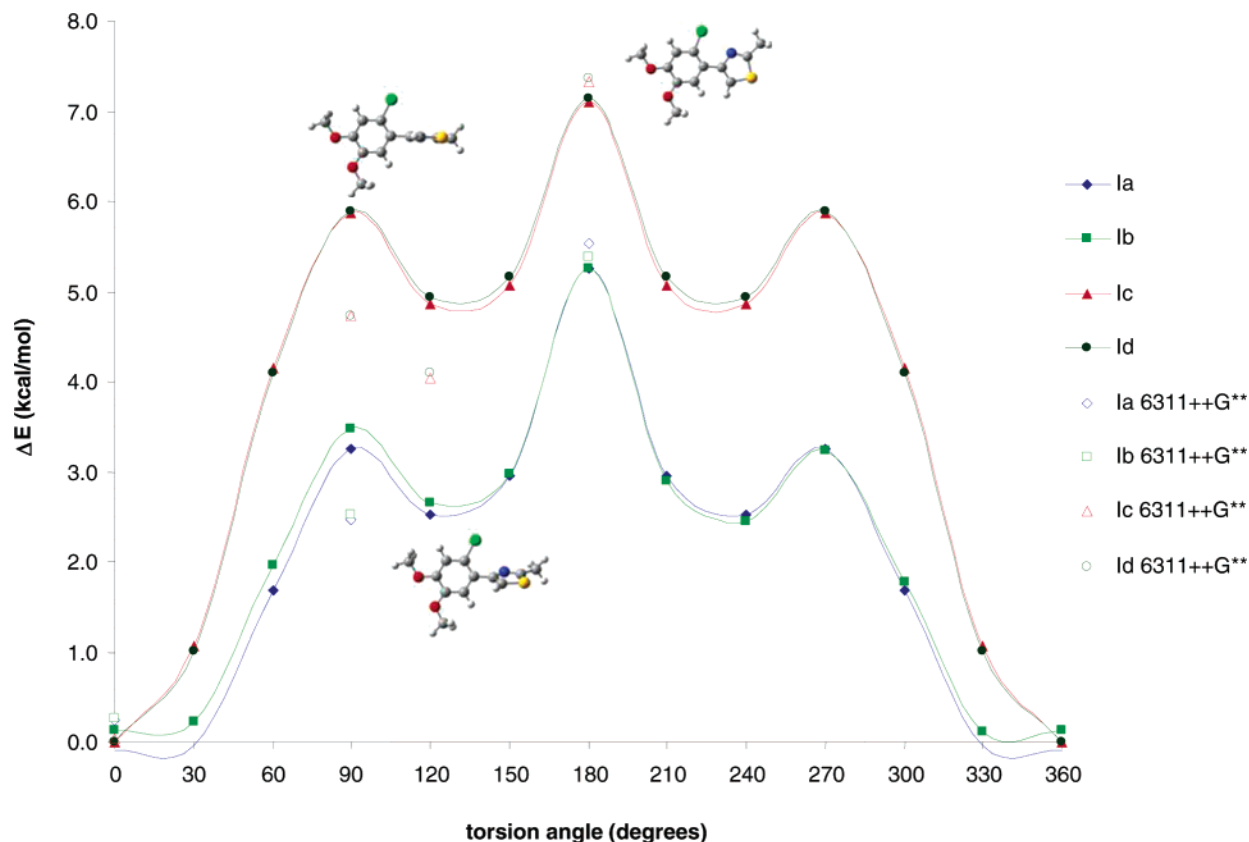


Figure 3. Potential B3LYP/6-31G(d,p) energy surfaces for **Ia**–**Id**. They were obtained through the variation, by steps of 30°, of the $\omega = C_7C_6C_4C_5$ dihedral angle. Also are indicated the B3LYP/6-311++G(d,p) results for the optimized **Ia**–**Id** structures at 90°, 120°, and 180°. In detail are shown the drawings for the corresponding structures at 0°, 90°, 120°, and 180° of the **Ia** molecule.

energy in these species. Then, this energetic criterion suggests the formation of weak intramolecular H-bonds in **Ia** and **Ib**. Below we will show, through the topological behavior of the electronic density, that in **Ia** and **Ib** only are formed intramolecular $C_5H_{13}-Cl$ bonds; while two intramolecular H-bonds, $CH-N$ and $CH-O$, are formed in each **Ic** and **Id** derivative. Indeed, the calculated H-bond energies account for the formation of two weak H-bonds in **Ic** and **Id**. Each $C_{11}H_{12}-N_3$ and $C_5H_{13}-O_{14}$ contact will have, roughly, a H-bond energy of about 2.0 kcal/mol; this value falls within the assigned range, 2–5 kcal/mol, for weak H-bonds.⁷ Moreover, the estimated H-bond energies of **Ia** and **Ib**, 2.0 kcal/mol, suggest the formation of a weak $C_5H_{13}-Cl$ bond. According to Scheiner et al.,³⁵ the magnitude of this attractive weak interaction falls on the borderline, 2–3 kcal/mol, of true H-bonds.

It is important to highlight that the experimental geometry of **Ia** is quasiplanar, since the dihedral $C_7-C_6-C_4-C_5$ angle is 6.54°, while the X-ray structure of **Ib** is nonplanar with a dihedral $C_7-C_6-C_4-C_5$ angle of 52.24°. **Ia** has a methyl group in the C_2 position, and **Ib** has an amine group. This amine group may allow the formation of two intermolecular $NH-N_3$ bonds between two **Ib** molecules; see the structure **Ib-Ib-Exp** in Figure 2. These intermolecular $NH-N_3$ bonds account for the type of crystal structure showed by the **Ib** thiazole derivative, where **Ib** is rotated 52.27°. The intermolecular $NH-N_3$ bonding is the main trigger for the stabilization of such 52° **Ib** conformer or, so-called, rotamer.

The B3LYP/6-311++G(d,p) binding energy of the two intermolecular N_3H-H bonds for the **Ib-Ib** dimer is equal to 8.2 kcal/mol, yielding 4.1 kcal/mol for each intermolecular N_3H-N bond; which is bigger than the stabilization energy, 2.1 kcal/mol, due to the intramolecular $C_5H_{13}-Cl$ binding, obtained for the (gas phase) GS of **Ib**, where the dihedral angle is equal to 25.3°.

IIIb. Atoms in Molecules and Chemical Shifts Results.

We will now address the analysis of the electronic densities, ρ , and Laplacians, $\nabla^2\rho$, of the intramolecular $C_{11}H_{12}-N_3$, $C_5H_{13}-Cl$, and $C_5H_{13}-O$ contacts. For each **Ia**–**Id** ground-state structure was computed, using the code Gaussian-98, the corresponding B3LYP/6-311++G(d,p) wave function. Furthermore, these GS wave functions were used to determine BCPs and RCPs with AIM2000.^{26,36} The obtained topological parameters are reported in Table 1 and in Figure 4 for **Ib**. For **Ia** and **Ib**, the AIM treatment defines clearly BCPs ($\rho = 0.0125 \text{ e au}^{-3}$ and $\nabla^2\rho = +0.0468 \text{ e au}^{-5}$) along the $C_5H_{13}-Cl$ paths; see Figure 4. Note that the values for the Laplacians are positive, as expected for a weak H-bond. Consistently, the six member rings, originated by the $H_{13}-Cl$ bonds, show quite defined RCPs ($\rho = 0.0093 \text{ e au}^{-3}$ and $\nabla^2\rho = +0.0452 \text{ e au}^{-5}$); although, due to the asymmetry, they are somehow deviated from the center. For instance, in the phenyl and thiazole groups, the RCPs are located at the center of the rings. See Figure 4.

On the other hand, the $C_5H_{13}-O_{14}$ and $C_{11}H_{12}-N_3$ paths of **Ic** and **Id** define clearly the appearance of BCPs and

Table 1. Calculated B3LYP/6-311++G(d,p) Density (ρ), in $e\text{ au}^{-3}$, and Laplacians ($\nabla^2\rho$), in $e\text{ au}^{-5}$, for the Bond Critical Points (BCP) and Ring Critical Points (RCP) of the CH–N, CH–Cl, and CH–O Contacts of the **1a**–**1d** Ground States

		ρ_{BCP}	$\nabla^2\rho_{\text{BCP}}$	ρ_{RCP}	$\nabla^2\rho_{\text{RCP}}$
1a	C–H–N				
	C–H–Cl	0.0125	0.0468	0.0093	0.0452
1b	C–H–N				
	C–H–Cl	0.0125	0.0468	0.0093	0.0452
1c	C–H–N	0.0158	0.0692	0.0158	0.0796
	C–H–O	0.0168	0.0684	0.0109	0.0636
1d	C–H–N	0.0157	0.0688	0.0157	0.0784
	C–H–O	0.0168	0.0684	0.0109	0.0632

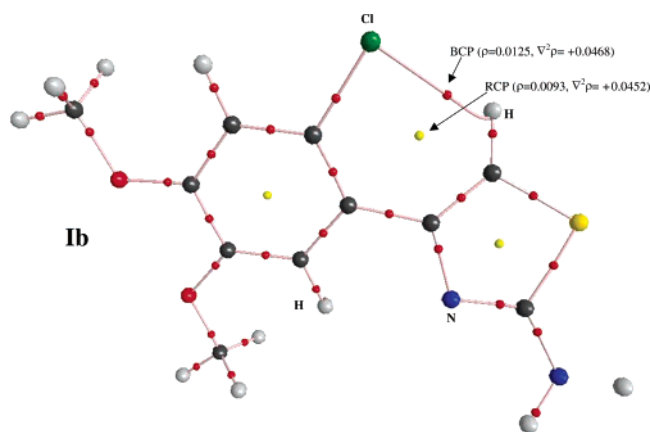


Figure 4. Molecular graph for the GS of **1b**. The B3LYP/6-311++G** density (ρ), in $e\text{ au}^{-3}$, and laplacians ($\nabla^2\rho$), in $e\text{ au}^{-5}$, are indicated for the BCP of the CH–Cl contact and the RCP for the ring.

RCPs; see Table 1. In fact, of the studied species, these compounds show the shorter $\text{C}_5\text{H}_{13}\text{--O}_{14}$ and $\text{C}_{11}\text{H}_{12}\text{--N}_3$ contacts, where the former is the shortest one. The AIM results for the $\text{C}_5\text{H}_{13}\text{--O}_{14}$ BCPs ($\rho = 0.0168\text{ e au}^{-3}$ and $\nabla^2\rho = +0.0684\text{ e au}^{-5}$) and the values for the $\text{C}_{11}\text{H}_{12}\text{--N}_3$ BCPs ($\rho = 0.0157\text{--}0.0158\text{ e au}^{-3}$ and $\nabla^2\rho = +0.0688\text{--}+0.0692\text{ e au}^{-5}$) of **1c** and **1d**, see Table 1, are in agreement with the topological criteria for the existence of H-bonds as given by Koch and Popelier:¹³ $0.002\text{--}0.035\text{ e au}^{-3}$ for the electronic density and $0.024\text{--}0.139\text{ e au}^{-5}$ for the associated Laplacian.

Aside from the AIM evidence of CH–X ($X = \text{Cl}$ and O) bonding, it was found that the highest occupied molecular orbital (HOMO) of **1a** and **1b**, shown in Figure 5, has signatures of bonding interactions for $\text{C}_5\text{--H}_{13}\text{--Cl}$. Also the HOMOs of **1c** and **1d** reveal bonding interactions for $\text{C}_5\text{--H}_{13}\text{--O}$.

The AIM results for the experimental geometry of **1a** reveal the formation of a $\text{C}_5\text{--H}_{13}\text{--Cl}$ intramolecular H-bond and the absence of $\text{C}_{11}\text{--H}_{12}\text{--N}_3$ bonding. This picture is similar to that found for **1a** in the gas phase. **1a** is quasiplanar, both in the gas phase and in the crystal; see Figures 1 and 2. However, for the experimental geometry of **1b** AIM indicates the absence of $\text{C}_5\text{--H}_{13}\text{--Cl}$ and $\text{C}_{11}\text{--H}_{12}\text{--N}_3$ intramolecular H-bonds, which may be due to a large deviation from planarity of **1b** in the crystal. The deviation may be due to

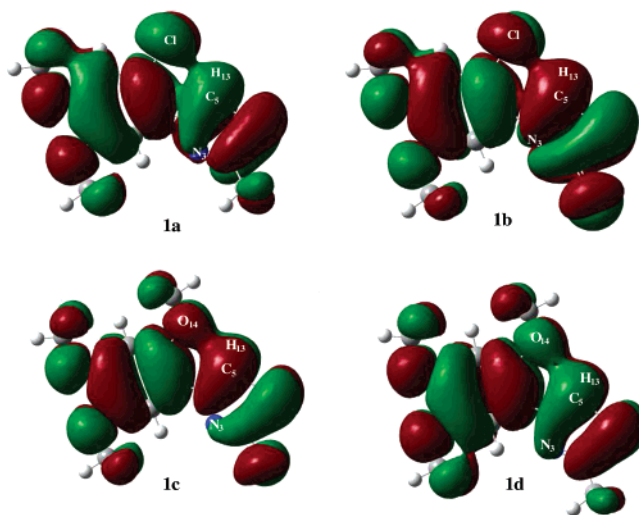
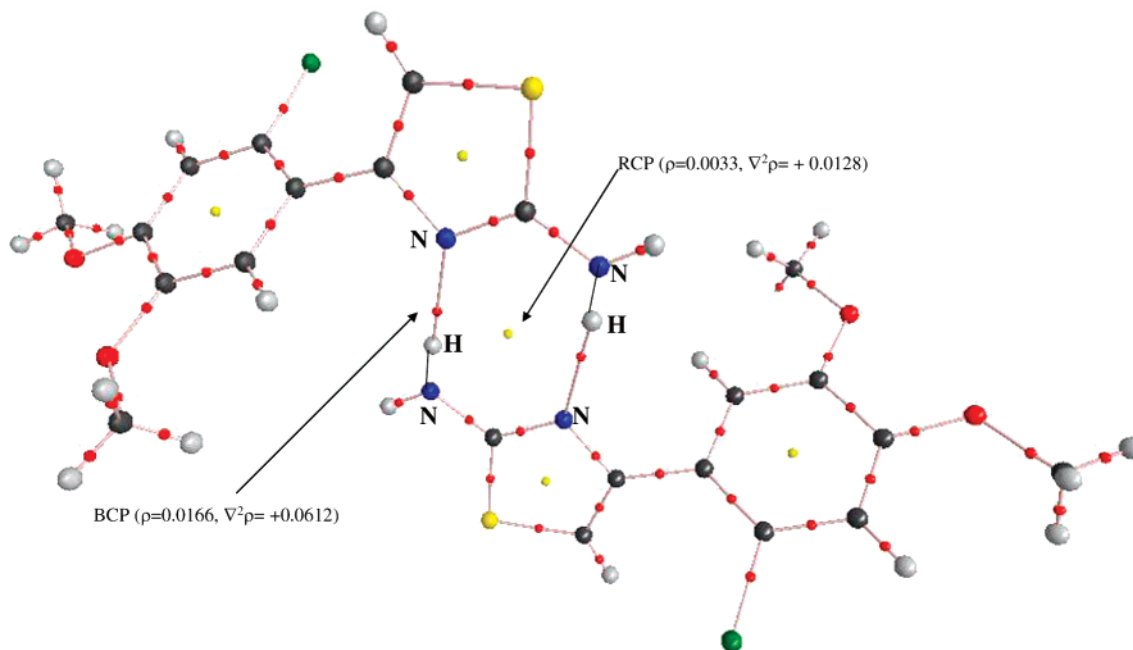


Figure 5. Contour plots of the higher occupied molecular orbitals (HOMO) for the GSs of **1a**–**1d**. The HOMOs contain signatures of C–H–X, ($X = \text{Cl}$ and O) bonding interactions.

the intermolecular H-bonding that may occur among the **1b** units in the crystal. We have also performed AIM calculations for the **1b**–**1b** dimer, labeled as **1b**–**1b**–**Exp** in Figure 2, where the bond lengths and angles are equal to the experimental values. The results indicate the formation of two intermolecular $\text{NH}\text{--N}_3$ bonds between two **1b** units; see Figure 6. As quoted, B3LYP/6-311++G(d,p) indicates a binding energy of 8.2 kcal/mol for **1b**–**1b**, yielding 4.1 kcal/mol for each $\text{N}\text{--H}\text{--N}_3$ bond; which is a bigger value than the binding energy of the $\text{C}_5\text{--H}_{13}\text{--Cl}$ intramolecular H-bond calculated for **1b** in the gas phase, about 2.1 kcal/mol.

Finally, a theoretical study of the chemical shifts in the ^1H NMR was made by the GIAO method at the B3LYP/6-311++G(d,p) electronic level of treatment. This approach also may be useful for a potential identification of H-bonds.^{35,37–39} The calculated chemical shifts, in ppm, for some representative hydrogen atoms of the **1a**–**1d** species are reported in Table 2; in parentheses are indicated the experimental values.² These theoretical results are in close agreement with the values obtained experimentally² by ^1H NMR. For example, the calculated chemical shifts of the H_{12} and H_{13} atoms are overestimated by 0.35–0.52 ppm, while underestimations of 0.22–0.40 ppm were obtained for H_{15} ; see Table 2. For **1a** and **1b** there is no clear correlation between shifts and H-bond formation. For instance, in **1a**, H_{12} and H_{13} have very similar values, 7.92 and 7.98 ppm, respectively, which are bigger, by 1.24–1.30 ppm, than the value for H_{15} . The experiment also indicates similar shifts for H_{12} and H_{13} , bigger than that of H_{15} . However, as shown above, H_{12} does not form an H-bond. Moreover, in **1b**, the shift of H_{12} (not forming a H-bond) is bigger, by 1.25 ppm, than that of H_{15} ; but H_{13} (forming a H-bond) has a smaller difference, 0.82 ppm, from the value of H_{15} . The experiment also yields a smaller difference between the shifts of H_{13} and H_{15} . That is, in **1a** and **1b**, there is not a clear correlation between chemical shifts and H-bonds. In these cases, the shifts are merely due to the different topological positions of the H atoms. A different behavior is observed for **1c** and **1d**, since the H_{12} and H_{13} centers of these moieties, which



Ib-Ib-Exp

Figure 6. Molecular graph for the **Ib-Ib** dimer (**Ib-Ib-Exp**). The calculated B3LYP/6-311++G** density (ρ), in e au⁻³, and laplacianes ($\nabla^2\rho$), in e au⁻⁵, are indicated for the BCPs of the intermolecular N—H—N and N—H—N hydrogen bonds. Note the appearance of the associated RCP.

Table 2. Calculated GIAO B3LYP/6-311++G(d,p) Chemical Shifts, in ppm, for the Benzene H₁₂ and Thiazole H₁₃ Atoms, Involved in the H-Bond Interactions and for the Aromatic H₁₅ Atoms not Forming H-Bonds^a

	H ₁₂	H ₁₃	H ₁₅
Ia	7.92 (7.51)	7.98 (7.63)	6.68 (6.93)
Ib	7.94 (7.42)	7.51 (7.04)	6.69 (6.91)
Ic	8.06 (7.63)	7.59 (7.08)	6.17 (6.57)
Id	8.38 (7.90)	8.25 (7.74)	6.25 (6.63)

^a The experimental values are shown in parentheses.

form clearly H-bonds, have shifts that are significantly bigger, 1.42–1.89 ppm, than that of the H₁₅ atom. In other words, in **Ic** and **Id** the chemical shifts of the H₁₂ and H₁₃ centers have signatures of H-bonds. The magnitude of these shifts is in agreement with the estimated higher H-bond energy, 4.1 kcal/mol for **Ic** and **Id**, and with the topological results from AIM, which show the formation of two, C₅H₁₃—O₁₄ and C₁₁H₁₂—N₃, H-bonds.

Conclusions

The nonconventional CH—X (X = N, O, or Cl) H-bonds formed intramolecularly in the **Ia–Id** thiazoles were studied by means of calculations made with the B3LYP/6-311++G-(d,p) method. The obtained results for the geometrical, energetic, topological, and spectroscopic properties allowed the characterization of these H-bonds. The computed properties for the bare GSs suggest the formation of one H-bond,

CH—Cl, in **Ia** and **Ib**; in these species the CH—N bond is absent, while two H-bonds, CH—N and CH—O, are formed in **Ic** and **Id**. Indeed, the geometrical criteria indicate that the H—Cl distances, 2.64 Å, of **Ia** and **Ib** and the H—N and H—O lengths, 2.34–2.35 and 2.24 Å, respectively, of **Ic** and **Id** are noticeably shorter than the respective sum of the X and H van der Waals radii. Consistently, according to the theory of atoms in molecules, the electronic density shows bond critical points for the CH—X bonds. The weak character of these H-bonds is indicated by the H-bond energies, which are \approx 2.1 kcal/mol for **Ia** and **Ib** and \approx 4.1 kcal/mol for **Ic** and **Id**. Deviation from planarity also is important; **Ia** and **Ib** with nonplanar structures have only one H-bond, CH—Cl, whereas **Ic** and **Id** with quasi-planar geometries have two H-bonds, CH—O and CH—N. Moreover, in the crystal **Ib** is largely deviated from planarity, avoiding the formation of intramolecular CH—X bonds; instead, there are formed two intermolecular NH—N bonds between two **Ib** units. This N—H—N bond is stronger than the C—H—Cl bond of **Ib** in the gas phase. The chemical shifts in the ¹H NMR were also calculated by the GIAO method. In **Ia** and **Ib** they are merely due to the different topological positions of the H atoms. But in **Ic** and **Id** the shifts in H—N and H—O have signatures of H-bond formations.

Acknowledgment. We acknowledge financial support from DGAPA-UNAM under Project PAPIIT: IN-107905. J. I. Zavala appreciates a scholarship from these sources. I. Nicolás-Vázquez deeply thanks CONACyT-México and DGAPA-UNAM (PASPA) for a grant. The access to the supercomputer facilities at DGSCA-UNAM is strongly

appreciated. Dr. Alfredo Vazquez is thanked for valuable discussions. The referee's suggestions are deeply acknowledged.

Supporting Information Available: Selected equilibrium bond lengths and bond and dihedral angles (Tables 1–3). This material is available free of charge via the Internet at <http://pubs.acs.org>.

References

- Joule, J. A.; Mills, K. 1,3-Azoles: imidazoles, thiazoles, and oxazoles: reactions and synthesis. In *Heterocycle chemistry*, 4th ed.; Blackwell Sciences Publishing: Oxford, U.K., 2002; pp 402–425.
- Sánchez-Viesca, F.; Berros, M. *Heterocycles* **2002**, *57*, 1869–1879.
- Bernés, S.; Berros, M. I.; Rodríguez de Barbarín, C.; Sánchez-Viesca, F. *Acta Crystallogr., Sect. C: Cryst. Struct. Commun.* **2002**, *C58*, o151–o153.
- Castellano, R. K.; Diederich, E. A.; Meyer, E. A. *Angew. Chem., Int. Ed. Engl.* **2003**, *42*, 1210–1250.
- Desiraju, G. R. *Acc. Chem. Res.* **2002**, *35*, 565–573.
- Diñçer, M.; Özdemir, N.; Çukurovali, A.; Yilmaz, I. *Acta Crystallogr., Sect. C: Cryst. Struct. Commun.* **2005**, *E61*, o1712–o1714.
- Desiraju, G. R.; Steiner The Hydrogen Bond. In *The weak hydrogen bond in structural chemistry and biology*, 1st ed.; Oxford University Press, Inc.: New York, 1999; pp 1–28.
- Grabowski, S. J. *J. Phys. Org. Chem.* **2004**, *17*, 18–31.
- Grabowski, S. J.; Pfitzner, A.; Zabel, M.; Dubis, A. T.; Palusiak, M. *J. Phys. Chem. B* **2004**, *108*, 1831–1837.
- Domagala, M.; Grabowski, S. J.; Urbaniak, K.; Mlostoń, G. *J. Phys. Chem. A* **2003**, *107*, 2730–2736.
- Dubis, A. T.; Grabowski, S. J.; Romanowska, D. B.; Misiaszek, T.; Leszczynski, J. *J. Phys. Chem. A* **2002**, *106*, 10613–10621.
- Bader, R. F. W. Atoms and the topology of the charge density, Chemical bonds and molecular graphs. In *Atoms in Molecules. A Quantum Theory*, 1st ed.; Oxford University Press: New York, 1990; pp 32–35.
- Koch, U.; Popelier, P. L. A. *J. Phys. Chem.* **1995**, *99*, 9747–9754.
- Bickelhaupt, F. M.; Baerends, E. J. Kohn-Sham Density Functional Theory: Predicting and understanding chemistry. In *Reviews in Computational Chemistry*, 1st ed.; Lipkowitz, K. B., Boyd, D. B., Eds.; Wiley-VCH, John Wiley and Sons, Inc.: New York, 2000; Vol. 15, pp 1–86.
- Becke, A. D. *J. Chem. Phys.* **1993**, *98*, 5648–5652.
- Lee, C.; Yang, W.; Parr, R. G. *Phys. Rev.* **1988**, *B37*, 785–789.
- Calhorda, M. J. *Chem. Commun.* **2000**, 801–809.
- Richardson, T. R.; Gala, S.; Crabtree, R. H.; Siegbahn, P. E. M. *J. Am. Chem. Soc.* **1995**, *117*, 12875–12876.
- Orlova, G.; Scheiner, S. *J. Phys. Chem. A* **1998**, *102*, 260–269.
- Orlova, G.; Scheiner, S. *J. Phys. Chem. A* **1998**, *102*, 4813–4818.
- Adotöledo, D.; Aviyenta, V.; Martin, J. M. L.; Lifshitz, C. *J. Phys. Chem. A* **1998**, *102*, 6357–6365.
- Rablen, P. R.; Lockman, J. W.; Jorgensen, W. L. *J. Phys. Chem. A* **1998**, *102*, 3782–3797.
- Chung, G.; Kwon, O.; Kwon, Y. *J. Phys. Chem. A* **1998**, *102*, 2381–2387.
- Alkorta, I.; Rozas, I.; Elguero, J. *Theor. Chem. Acc.* **1998**, *99*, 116–123.
- Frisch, M. J.; Trucks, G. W.; Schlegel, H. B.; Gill, P. M. W.; Johnson, B. G.; Robb, M. A.; Cheeseman, J. R.; Keith, T. A.; Petersson, G. A.; Montgomery, J. A.; Raghavachari, K.; Al-Laham, M. A.; Zakrzewski, V. G.; Ortiz, J. V.; Foresman, J. B.; Cioslowski, J.; Stefanov, B.; Nanayakkara, A.; Challacombe, M.; Peng, C. Y.; Ayala, P. Y.; Chen, W.; Wong, M. W.; Andres, J. L.; Replogle, E. S.; Gomperts, R.; Martin, R. L.; Fox, D. J.; Binkley, J. S.; Defrees, D. J.; Baker, J.; Stewart, J. J. P.; Head-Gordon, M.; Gonzalez, C.; Pople, J. A. *GAUSSIAN 98 (Revision C.3)*; Gaussian Inc.: Pittsburgh, PA, 1998.
- AIM2000 designed by Friedrich Biegler-König, University of Applied Sciences, Bielefeld, Germany, 2000.
- Popelier, P. Bond characterization. In *Atoms in Molecules. An Introduction*, 1st ed.; Prentice Hall, Pearson Education Limited: Englewood Cliffs, NJ, 2000; pp 150–156, 113.
- Ditchfield, R. *Mol. Phys.* **1974**, *27*, 789–807.
- Wolinski, K.; Hinton, J. F.; Pulay, P. *J. Am. Chem. Soc.* **1990**, *112*, 8251–8260.
- Cotton, F. A.; Daniels, L. M.; Jordan IV, G. T.; Murillo, C. A. *Chem. Commun.* **1997**, 1673–1674.
- Bondi, A. J. *Phys. Chem.* **1964**, *68*, 441–451.
- Taylor, R.; Kennard, O. *J. Am. Chem. Soc.* **1982**, *104*, 5063–5070.
- Moro, A. C.; Watanabe, F. W.; Ananias, S. R.; Mauro, A. E.; Netto, A. V. G.; Lima, A. P. R.; Ferreira, J. G.; Santos, R. H. A. *Inorg. Chem. Commun.* **2006**, *9*, 493–496.
- Chung, G.; Kwon, O.; Kwon, Y. *J. Phys. Chem. A* **1997**, *101*, 9415–9420.
- Scheiner, S.; Gu, Y.; Kar, T. *J. Mol. Struct. (THEOCHEM)* **2000**, *500*, 441–452.
- Rozas, I.; Alkorta, I.; Elguero, J. *J. Phys. Chem. A* **2001**, *105*, 10462–10467.
- Scheiner, S.; Grabowski, S. J.; Kar, T. *J. Phys. Chem. A* **2001**, *105*, 10607–10612.
- Mizuno, K.; Ochi, T.; Shindo, Y. *J. Chem. Phys.* **1998**, *109*, 9502–9507.
- Alkorta, I.; Elguero, J. *New J. Chem.* **1998**, 381–385.

CT600336R

Electronic Structure of Trigonal-Planar Transition-Metal–Imido Complexes: Spin-State Energetics, Spin-Density Profiles, and the Remarkable Performance of the OLYP Functional[†]

Jeanet Conradie^{‡,§} and Abhik Ghosh^{*,‡}

Center for Theoretical and Computational Chemistry, Department of Chemistry, University of Tromsø, N-9037 Tromsø, Norway, and Department of Chemistry, University of the Free State, 9300 Bloemfontein, Republic of South Africa

Received November 16, 2006

Abstract: We have carried out a detailed multifunctional density functional theory study of first-row transition-metal (Cr to Cu) β -diketiminato (“nacnac”) imido and oxo complexes. All the complexes studied exhibit essentially the same d-orbital energy ordering, which is $a_1 (d_{x^2-z^2}) \leq a_2 (d_{xy}) \leq a_1 (d_{y^2}) < b_2 (d_{yz}) < b_1 (d_{xz})$, where the metal–imido vector is identified with the z axis and metal–N₃ plane is identified with the xz plane. A curious aspect of this orbital ordering is that the metal $d_{x^2-z^2}$ orbital, one of whose lobes points directly at the imido nitrogen, is considerably lower in energy than the d_π orbitals. We have determined that the remarkable stability of the d_σ -type orbitals owes largely to the way these orbitals hybridize or “shape-shift” as a result of the absence of ligands trans or equatorial with respect to the imido (or oxo) group. Of the many functionals examined, OLYP and OPBE, based on the Handy–Cohen OPTX exchange functional, appear to provide the best overall description of the spin-state energetics of the various complexes. In particular, these two functionals predict an $S = 3/2$ ground state for Fe(III) nacnac imido complexes and an $S = 0$ ground state for Co(III) nacnac imido complexes, as observed experimentally. In contrast, classic pure functionals such as PW91 predict $S = 1/2$ ground states or at best equienergetic $S = 1/2$ and $S = 3/2$ states for the Fe(III) imido complexes, while hybrid functionals such as B3LYP and O3LYP predict $S = 1$ or 2 ground states for the Co(III) nacnac imido complexes.

Introduction

Multiply bonded metal–ligand units are a subject of enduring interest in chemistry.¹ In part, this interest stems from the relevance of such units as mimics of enzymatic iron–oxo intermediates.^{2,3} In addition, transition-metal oxo, imido,^{4,5} nitrido, phosphinidene and phosphido complexes undergo a variety of synthetically useful atom- and group-transfer reactions.⁶ Not surprisingly, inorganic chemists are continu-

ally driven to create new multiply bonded metal–ligand entities, while theoreticians rush to elucidate their electronic structures. Interestingly, not long ago, middle and late transition-metal oxo and imido complexes were thought to be inevitably unstable and inaccessible, because of energetically costly metal(d_π)–ligand(p_π) antibonding interactions.⁷ However, our conception of the field has changed dramatically in recent years; thus, quite a few low-coordinate middle and late transition-metal imido complexes have been synthesized and structurally characterized.^{5,8–19} Although density functional theory (DFT) calculations have accompanied a number of these synthetic studies, a comprehensive, comparative electronic-structural perspective of the different

[†] Dedicated to Dennis R. Salahub on the occasion of his 60th birthday.

* Corresponding author e-mail: abhik@chem.uit.no.

[‡] University of Tromsø.

[§] University of the Free State.

complexes has yet to emerge, which is what we sought to develop in our laboratory. Accordingly, we will present here a systematic account of DFT calculations, employing a variety of exchange-correlation functionals, on trigonal-planar (β -diketiminato)M(NR) complexes, where M = Cr(III), Mn(III), Fe(III), Fe(IV), Co(III), Ni(III), and Cu(III) and R = alkyl or aryl. Warren and co-workers have synthesized and structurally characterized close experimental analogues of two of these complexes, namely, Co(III) ($S = 0$)²⁰ and Ni(III) ($S = 1/2$).²¹ Some of the specific issues that we sought to address in this study are as follows.

Although DFT calculations have provided a “first-order” electronic description of certain of the above complexes,^{19–21} we remained particularly intrigued by a key aspect of the bonding. Several of these complexes have a low-energy, single or doubly occupied metal($d_{x^2-z^2}$)–imido(p_σ) σ -antibonding molecular orbital (MO) that is significantly lower in energy than the two d_{π} – p_π antibonding MOs. However, there is little comment in the literature as to why a σ -antibonding MO should fill preferentially, relative to the π -antibonding MOs. Is this a special feature of the imido ligand? To investigate, we have compared the above-mentioned imido complexes with a full set of the corresponding oxo species, which have yet to be experimentally observed. We will see that the d-orbital ordering is largely determined by the trigonal-planar stereochemistry of the metal center.

Another aspect of the bonding we will focus on involves the spin-density profiles of the complexes. So far, there is little information in the literature on the spin-density distributions of the Fe(III) and Ni(III) imido complexes, for which DFT calculations have been reported.^{19–21} Here, we provide detailed information, partly via high-quality spin-density plots, on the spin-density profiles of all the open-shell species studied. By indicating how the spin density partitions itself between the metal and the ligands, this information affords a remarkably useful tool for visualizing and quantifying the nature of metal–ligand covalent bonding in open-shell coordination complexes.^{22,23}

Perhaps the key contribution of this study is toward elucidating the spin-state energetics²⁴ of the various trigonal-planar imido complexes. Already, the literature raises a number of intriguing questions. For example, an Fe(III) imido complex apparently exhibits an unusual intermediate-spin $S = 3/2$ ground state,¹⁹ while the analogous Co(III) complex is $S = 0$.²⁰ How much higher in energy are the alternative spin states? We have posed similar questions for the other imido complexes as well. In this connection, our calculations on the hypothetical oxo analogues of the imido complexes have also proved very insightful. As expected, significant differences exist between the energy spacings of the valence MOs of the imido and oxo complexes. We will see that in certain cases analogous imido and oxo complexes are even predicted to exhibit different ground states.

Intimately associated with the question of transition-metal spin-state energetics is the issue of how accurately we can compute them.^{24–26} As far as DFT is concerned, it is fair to say that we are still in the early stages of providing a

comprehensive answer to this question. In our experience, traditional pure functionals such as PW91 tend to favor low-spin, more-covalent states, while hybrid functionals such as B3LYP behave oppositely.^{24,26} In this study, we have carried out full geometry optimizations with two different functionals—PW91 and OLYP—as well as single-point energy calculations with a large variety of functionals, both pure and hybrid. An important conclusion to emerge from this large volume of data is that some of the newer “pure” functionals OLYP and OPBE, based on Handy and Cohen’s OPTX exchange functional,²⁷ may be among the best, from the point of view of transition-metal spin-state energetics.

Methods

All species studied were optimized with the PW91²⁸ and OLYP²⁷ generalized gradient approximations, triple- ζ plus polarization Slater-type orbital basis sets, and a fine mesh for numerical integration of the matrix elements, as implemented in the ADF 2005²⁹ program system. In addition, we also carried out single-point noniterative post-self-consistent field (SCF) calculations with a variety of pure and hybrid functionals, namely, BLYP,^{30,31} BP86,^{32,33} OPBE,^{27,34,35} XLYP,³⁶ B3LYP(VWN5),^{37–39} O3LYP(VWN5),^{27,38} and X3LYP(VWN5).³⁶ Unless otherwise indicated, the VWN functional was used as the local part of all of the above functionals. In general, for all the species studied, the calculated $\langle S^2 \rangle$ values were in excellent agreement with the theoretically expected values.

Results and Discussion

A. A Basic Description of the Bonding. Before discussing the bonding in the imido complexes, it might be useful to start with a qualitative MO picture of an electronically “simpler” β -diketiminato complex, (nacnac)NiL, where nacnac[−] is the anion of 2,4-bis(2,6-dimethylphenylimido)pentane and L is a relatively weak, innocent ligand such as chloride. Such a picture, already available from earlier work in this field,^{19,20,21,40,41} is presented in Figure 1. Under C_{2v} symmetry, the five d orbitals transform as $2a_1$, a_2 , b_1 , and b_2 . Both d_σ orbitals (relative to the metal–L linkage) transform as a_1 and are denoted as a_{1-1} (d_{y^2}) and a_{1-2} ($d_{x^2-z^2}$), where the metal–L axis defines the z direction, while the two d_π orbitals transform as b_1 and b_2 and the d_δ orbital as a_2 . The b_1 -symmetry M(d_π)–imido(p_π) antibonding MO has the highest orbital energy of all the metal d-based MOs, a feature that persists in the metal–imido complexes as well. The high energy of this MO also owes significantly to σ -antibonding interactions with the nacnac ligand, as depicted in Figure 1.

In this work, we have modeled the experimentally known 1-adamantylimido^{19–21} complexes as NMe and NPh complexes; the latter has the advantage of capturing the full C_{2v}

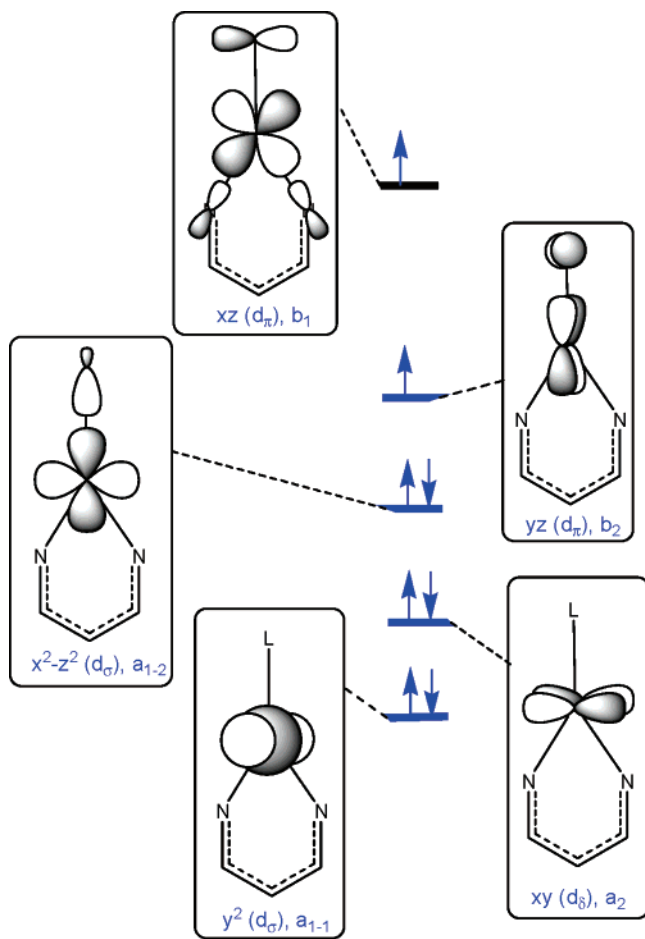
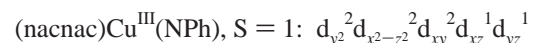
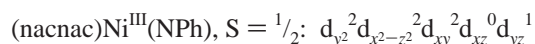
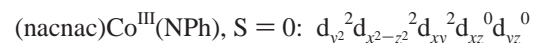
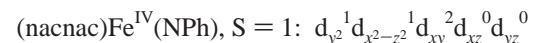
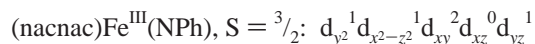
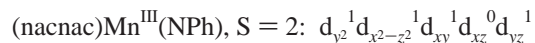
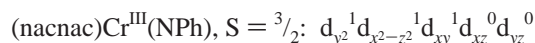


Figure 1. Qualitative MO diagram for a typical β -diketiminato complex, (nacnac)NiL, where L is a relatively weak, innocent ligand such as chloride. The d_σ , d_π , and d_δ descriptions are relative to the M–L bond.

symmetry of the bonding problem. Extensive symmetry-unconstrained optimizations confirmed that the C_s and C_{2v} point group symmetries were appropriate for nearly all the NMe and NPh complexes, respectively. In addition, we found that the phenyl group in the NPh moiety generally exhibits a distinct energetic preference for being coplanar with the metal–N₃ moiety. Figure 2 presents PW91 MO energy-level diagrams for four of the NPh complexes, namely, Fe(III) ($S = 3/2$), Co(III) ($S = 0$), Ni(III) ($S = 1/2$), and Cu(III) ($S = 1$), while Table 1 details the atomic compositions of the five primarily d-type MOs. Note from Figure 2 is that all four compounds exhibit roughly the same energy ordering of the d-based MOs, namely, $a_{1-2} (d_\sigma) \leq a_2 (d_\delta) \leq a_{1-1} (d_\sigma) < b_2 (d_\pi) < b_1 (d_\pi)$ (the orbitals being listed from low to high orbital energy). The qualitative shapes of these MOs are similar across all the compounds studied and are depicted in Figure 3 for (nacnac)Ni^{III}(NPh). Actually, all the compounds examined in this study, including the oxo species, exhibit essentially the same energy ordering of the d-type MOs. This strongly suggests that this orbital ordering (though not the exact energy spacing) is largely determined by the C_{2v} -type trigonal-planar geometry of these complexes, rather than by just the imido ligand.

The various metal–NPh (as well as NMe) complexes studied exhibit the following electronic configurations:



The finding that the orbital ordering in these imido complexes (see Figure 2) is rather similar to that in a much weaker-field complex such as (nacnac)NiCl (Figure 1) is quite remarkable and has not been adequately emphasized in the literature. A key point here is that the d_σ -type a_{1-2} MO, which has a lobe pointing directly at the imido nitrogen, has a much lower orbital energy than either of the two d_π -type MOs. This is understandable in the case of a chloride complex such as (nacnac)NiCl but calls for a closer examination for the imido complexes, in view of the much stronger ligand field strength of imido ligands.

The shape of the a_{1-2} MO, the HOMO-4 in Figure 3, provides a clue to its stability. Its d character is best described as $d_{x^2-z^2}$, z being the direction of the metal–imido axis. Although the $d_{x^2-z^2}$ orbital suffers a head-on antibonding interaction with the imido σ lone pair, the repulsion is less than it would be with a d_z orbital, which would stick out further in the z direction. Second, as shown in Figure 3, the lateral lobes of the $d_{x^2-z^2}$ orbital actually engage in a bonding interaction with the imido group. Third, as shown in Table 1, small amounts of Fe s and p character also play a role in muting the Fe(d_σ)–N(p_σ) antibonding interaction. We propose that it is this unusual orbital topology, resulting from the absence of both equatorial and trans ligands, relative to the imido group, that effectively quenches the σ -antibonding nature of this MO.

Two further points are worth making in this connection. First, the topology of the above-mentioned orbital is somewhat different from that of the d_z -based MO that is also unusually stable and occupied in pseudotetrahedral Fe(III) and Co(III) imido complexes.⁵ In this case, much larger admixtures of p_z character appear to be a key factor that minimizes the metal–ligand antibonding interaction. While details of these calculations have been described elsewhere, Figure 4 presents key DFT results for Fe^{III}(MeBP₃)(NMe) (MeBP₃ is a monoanionic methytrisphosphinoborate model ligand),^{42,43} a model pseudotetrahedral imido complex, including a graphical representation of the d_z -based singly occupied molecular orbital (SOMO). Second, we are aware of another example, $S = 1/2$ Fe(5,5-tropocoronand)(NO), from the nitrosyl literature,⁴⁴ where the muted antibonding interaction between a relatively stereochemically inactive Fe $d_{x^2-z^2}$ orbital and the NO lone pair in the singly occupied

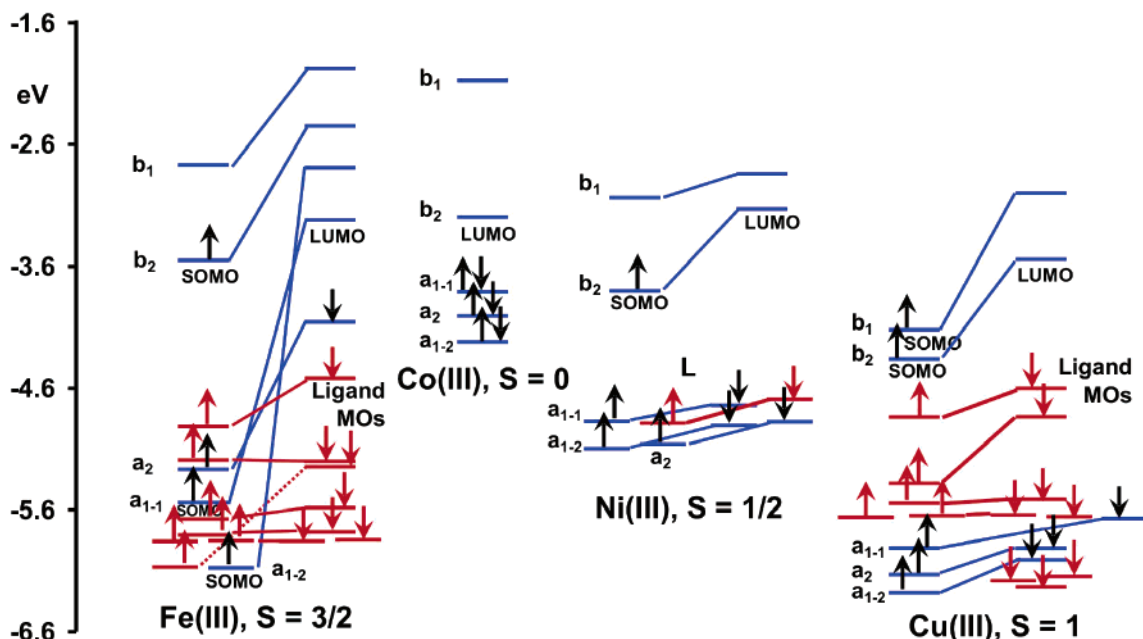


Figure 2. MO energy level diagrams for (nacnac) $M^{III}(\text{NPh})$, $M = \text{Fe, Co, Ni, and Cu}$. Primarily metal-based MOs are indicated in blue and primarily ligand-based MOs in red.

Table 1. Atomic Contributions of the Primarily 3d-Based Majority-Spin MOs for (nacnac) $M^{III}(\text{NPh})$; $M = \text{Fe, Co, Ni, and Cu}$ ^a

metal	S	a_{1-2}	a_2	a_{1-1}	b_2	b_1
Fe(III)	3/2	HOMO-10, (SOMO): 78% Fe (70% $d_{x^2-y^2}$, 5% d_{z^2} , 3% s)	HOMO-3: 83% Fe (d_{xy})	HOMO-4, (SOMO): 62% Fe (50% d_{z^2} , 2% p, 10% s), 9% N_{imido}	HOMO (SOMO): 19% Fe (d_{yz}), 31% N_{imido}	LUMO: 36% Fe (d_{xz}), 38% N_{imido}
Co(III)	0	HOMO-2: 83% Co (63% d_{z^2} , 6% $d_{x^2-y^2}$, 2% p, 12% s), 7% N_{imido}	HOMO-1: 84% Co (d_{xy})	HOMO: 93% Co (86% $d_{x^2-y^2}$, 5% d_{z^2} , 2% p)	LUMO: 40% Co (d_{yz}), 20% N_{imido}	LUMO+1: 43% Co (d_{xz}), 23% N_{imido}
Ni(III)	1/2	HOMO-4: 81% Ni (39% d_{z^2} , 37% $d_{x^2-y^2}$, 3% p, 2% s), 6% N_{imido}	HOMO-3: 86% Ni (d_{xy})	HOMO-1: 92% Ni (54% $d_{x^2-y^2}$, 28% d_{z^2} , 10% s)	HOMO (SOMO): 24% Ni (d_{yz}), 26% N_{imido}	LUMO: 40% Ni (d_{xz}), 30% N_{imido}
Cu(III)	1	HOMO-9: 88% Cu (71% $d_{x^2-y^2}$, 14% d_{z^2} , 3% s)	HOMO-8: 64% Cu (d_{xy})	HOMO-7: 82% Cu (60% d_{z^2} , 16% $d_{x^2-y^2}$, 4% p, 2% s) 6% N_{imido}	HOMO-1 (SOMO): 11% Cu (d_{yz}), 19% N_{imido}	HOMO (SOMO): 32% Cu (d_{xz}), 26% N_{imido}

^a This table accompanies Figure 2.

MO results in a linear NO ligand,^{45,46} which is very uncommon for low-spin $\{\text{FeNO}\}^7$ complexes.⁴⁷ It is thus becoming clear that an increasing number of novel structural and stereochemical phenomena may be attributed to specific d-orbital hybridizations resulting from low-coordinate environments, as opposed to “normal” octahedral ones.

The MO topologies and symmetries, as presented above, allow an appreciation of the variations in the metal– N_{imido} distances and molecular spin-density profiles for the various first-row transition-metal complexes, as discussed in the next two sections.

B. Structural Chemistry. Selected optimized geometry parameters and Mulliken spin populations for NMe, NPh, and oxo complexes are listed in Tables 2 and 3, respectively.

Much of the same information is depicted graphically for NMe and NPh complexes in Figures 5 and 6, respectively. Let us first discuss trends in the metal–imido distance among the middle transition metals (Cr, Mn, and Fe). From $S = 3/2$ Cr(III) to $S = 2$ Mn(III), the metal– N_{imido} distance expands slightly, by a couple of hundredths of an angstrom, reflecting the single d_{π} – p_{π} antibonding interaction in the Mn(III) complexes. The effect is slight because it is superimposed on the tendency of ionic radii to shrink from left to right across a transition series, because of less effective shielding of the inner electrons. Thus, from $S = 2$ Mn(III) to $S = 3/2$ Fe(III), the metal–imido distance shrinks by about 0.03 Å, although both ions feature a single d_{π} – p_{π} antibonding interaction in their respective complexes. The metal– N_{imido}

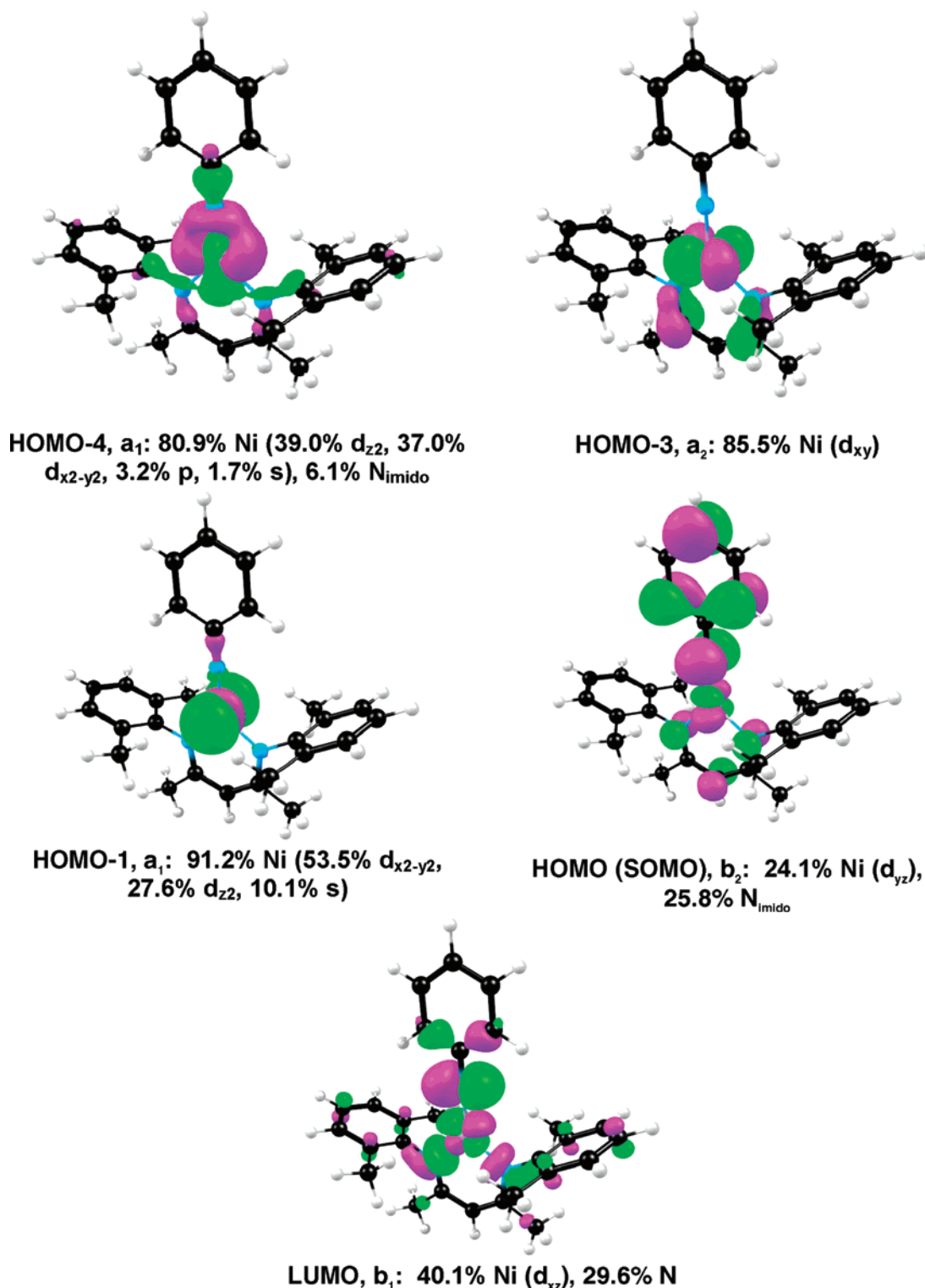


Figure 3. Plots of the primarily 3d-based majority-spin MOs of (nacnac) N^{III} (NPh).

distances in the three different spin states of the Fe(III) complexes nicely illustrate the effect of the number of the number π -antibonding interactions. Thus, from low-spin to intermediate-spin Fe(III), the Fe– N_{imido} distance increases by about 0.03 Å, while going to high-spin Fe(III) increases this distance by at least another 0.05 Å. Unfortunately, no middle transition-metal nacnac imido complex has been isolated and structurally characterized, so these structural trends appear to be largely of predictive value. Holland and

co-workers, however, apparently have generated a three-coordinate $S = 3/2$ Fe(III)–imido complex in solution; however, no experimental metrical parameters are as yet available for this species.^{19,48}

Our optimized Co and Ni imido structures are in excellent agreement with the crystallographic structures of very similar compounds.^{20,21} Thus, the PW91 (1.625 Å) and OLYP (1.627 Å) Co–NMe distances agree well with the Co–NAd (1.624 Å) distance in the experimentally studied cobalt complex.²⁰

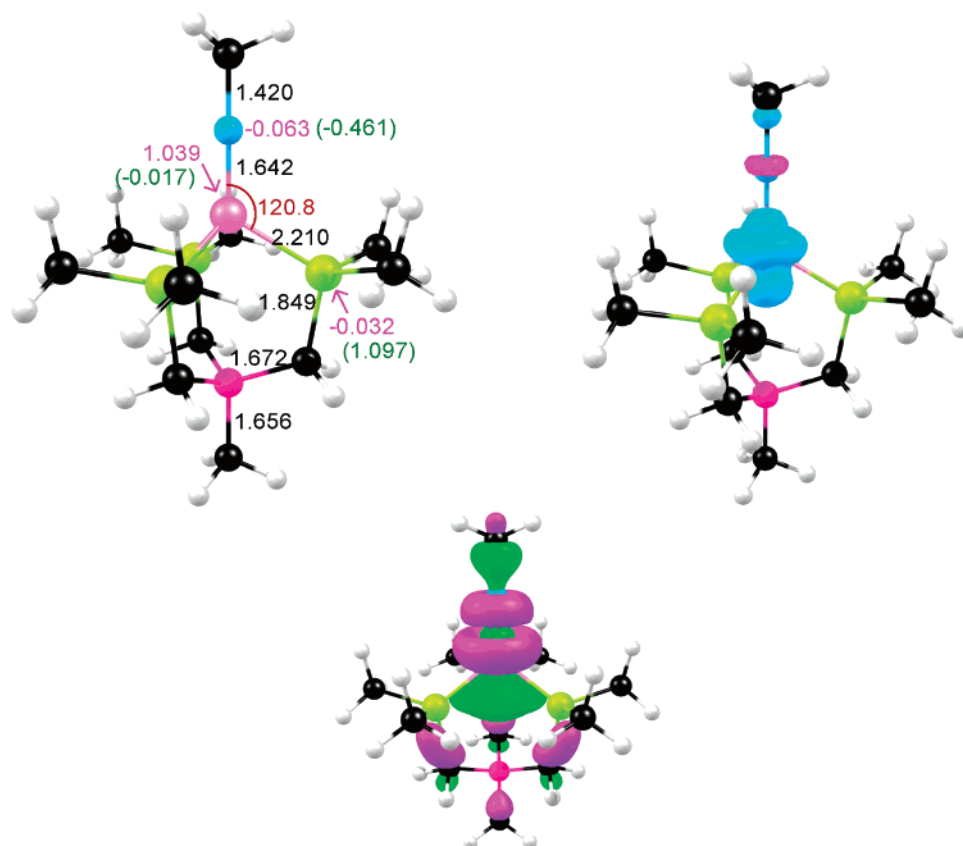


Figure 4. Selected results for Fe^{III}(MeBP₃)(NMe) (*C*_{3v}), a pseudotetrahedral Fe(III) imido complex. Top left: Optimized distances (Å, in black), angles (deg, red), Mulliken spin populations (magenta), and charges (green, in parentheses). Top right: A plot of the spin density, with majority and minority spin densities indicated in cyan and magenta, respectively. Bottom: A plot of the SOMO.

Likewise, the PW91 (1.668 Å) and OLYP (1.675 Å) Ni–NMe distances agree well with an experimental Ni–NAD distance of 1.662 Å.²¹ Note that the optimized Cu–NMe distances (PW91 1.762 Å and OLYP 1.782 Å) are longer still. The increase in the metal–N_{imido} distance from Co(III) to Ni(III) to Cu(III) nicely reflects the increasing number of d_{π} – p_{π} antibonding interactions along the series of metal ions – 0, 1, and 2, respectively.

C. Spin-Density Profiles. Figures 5 and 6 present graphical representations of the spin-density profiles of key NMe and NPh complexes, while Tables 2 and 3 present listings of Mulliken spin populations. The MO descriptions of the complexes given above allow us to readily appreciate the spin-density profiles, as discussed case by case below.

Cr(III). The $d_{y^2}^1 d_{x^2-z^2}^1 d_{xy}^1$ electronic configuration suggests that most of the excess spin density should be localized on the metal. This is indeed the case; however, both PW91 and OLYP calculations indicate a substantial minority spin density on the imido nitrogen. Careful examination of the shapes of the different valence MOs indicates that this excess minority spin density results from a slight spatial offset between the α - and β -spin forms of the d_{π} – p_{π} bonding MOs. Such spatially offset π bonding is actually relatively common in open-shell transition-metal complexes, and we have seen a similar occurrence in a NO complex, Mo(P)(NO)(MeOH) (P = porphyrin), which has a $\{\text{MoNO}\}^5 d_{\pi}^2 d_{\sigma}^2 d_{\delta}^1$ configuration but, nonetheless, exhibits a significant amount of minority spin density on the NO.⁴⁹

Mn(III) and Fe(III). In these cases, note from Figures 5 and 6 that the spin-density profile is highly anisotropic at the imido nitrogen. While a dumbbell of majority spin density reflects single occupancy of the d_{yz} -based b_2 MO, note the dumbbell of minority spin density in the xz plane (once again, reflecting a spatially offset π bonding in the xz plane). As a result, there is only a tiny amount of excess spin density on the imido nitrogens of these complexes.

Fe(IV). Crudely speaking, the spin-density profile of the cationic $S = 1$ Fe(IV) complexes resembles those of the Cr(III) complexes, as expected from the $d_{y^2}^1 d_{x^2-z^2}^1 d_{xy}^2$ electronic configuration of the former. As in the Cr(III) case, a cylindrically symmetric blob of minority spin density resides on the imido nitrogen.

We will not have much occasion to discuss the Mulliken charges shown in Figures 5 and 6. However, note that the Fe, N_{imido}, and N_{nacnac} charges are only slightly higher in the cationic Fe(IV) case than in the Fe(III) case, consistent with the electroneutrality principle.

Ni(III). The $S = 1/2$ Ni(III) spin density mirrors the form of the singly occupied b_2 d_{π} -based orbital. Note that the spin density partitions itself roughly 1:2 between the Ni and the N_{imido}. In other words, as previously noted,²¹ the Ni(III) complexes may be described as having substantial Ni^{II}–NR⁺ character.

Cu(III). The cylindrically symmetric $S = 1$ Cu(III) spin density corresponds faithfully to a pair of singly occupied d_{π} -based orbitals. In this case, the spin density is even more

Table 2. Selected Geometry Parameters (Å, deg) and Mulliken Spin Populations for (nacnac)M(NMe) Complexes Optimized under a C_s Symmetry Constraint

metal ion	charge	S	M–N _{imido}		M–N _{nacnac} ^a		∠(NMN) _{nacnac}	
			PW91	OLYP	PW91	OLYP	PW91	OLYP
Cr(III)	0	3/2	1.686	<i>b</i>	2.016	<i>b</i>	131.5	<i>b</i>
Mn(III)	0	1	1.660	<i>b</i>	1.909	<i>b</i>	130.3	<i>b</i>
Mn(III)	0	2	1.703	1.723	2.010	2.041	131.6	131.2
Fe(III)	0	1/2	1.633	1.639	1.891	1.911	131.4	129.9
Fe(III)	0	3/2	1.673	1.686	1.958	1.955	128.6	129.9
Fe(III)	0	5/2	1.749	1.750	2.016	2.058	109.0	111.8
Fe(IV)	1	1	1.657	1.658	1.881	1.920	129.8	132.4
Fe(IV)	1	2	1.690	1.693	1.913	1.943	108.7	113.7
Co(III)	0	0	1.625	1.627	1.856	1.876	132.3	132.5
Co(III)	0	1	1.666	1.683	1.911	1.943	129.0	131.6
Co(III)	0	2	1.747	1.751	1.965	1.998	111.5	112.7
Ni(III)	0	1/2	1.668	1.675	1.883	1.910	130.9	130.8
Ni(III)	0	3/2	1.745	1.753	1.924	1.956	107.9	109.8
Cu(III)	0	0	1.723	1.738	1.926	1.960	130.5	130.9
Cu(III)	0	1	1.762	1.782	1.951	1.990	130.4	130.4

metal ion	charge	S	S _M		S _{N(imido)}		S _{N(nacnac)} ^a	
			PW91	OLYP	PW91	OLYP	PW91	OLYP
Cr(III)	0	3/2	3.359	<i>b</i>	−0.458	<i>b</i>	−0.065	<i>b</i>
Mn(III)	0	1	2.533	<i>b</i>	−0.335	<i>b</i>	−0.045	<i>b</i>
Mn(III)	0	2	4.018	4.174	−0.067	−0.210	−0.042	−0.037
Fe(III)	0	1/2	1.376	1.550	−0.289	−0.419	−0.017	−0.017
Fe(III)	0	3/2	2.769	2.949	0.135	0.067	−0.025	−0.001
Fe(III)	0	5/2	3.747	3.744	0.964	0.975	0.036	0.037
Fe(IV)	1	1	2.325	2.533	−0.275	−0.499	−0.036	−0.049
Fe(IV)	1	2	3.042	3.266	0.587	0.425	0.057	0.058
Co(III)	0	0						
Co(III)	0	1	1.655	1.648	0.281	0.307	0.016	0.016
Co(III)	0	2	2.543	2.540	1.114	1.141	0.071	0.073
Ni(III)	0	1/2	0.332	0.303	0.598	0.652	0.014	0.005
Ni(III)	0	3/2	1.272	1.287	1.270	1.293	0.105	0.101
Cu(III)	0	0						
Cu(III)	0	1	0.330	0.331	1.361	1.404	0.068	0.063

^a Average bond distance ^b SCF cycles did not converge.

polarized toward the imido nitrogen, split 1:5, in fact, between the Cu and N_{imido}. Thus, once again, we have a highly noninnocent imido ligand, and the complex might well be described as a Cu(I) triplet-nitrene conglomerate.

A comment is in order on the small differences in spin-density profile between the NMe and NPh complexes. The difference is especially pronounced when the *b*₂ d_π-based MO is singly occupied, as in the Ni(III) case. In this case, both the Ni and the imido nitrogens in the NPh complexes carry a smaller amount of spin density, relative to their NMe analogues; the difference is accounted for by the presence of some spin density at the ortho and para carbons of the NPh group.

D. Spin-State Energetics and the Performance of Different Functionals. We now come to what we view as the heart of this study. The energetics of the low-lying spin states of transition-metal complexes is not only a core issue for coordination chemistry but also an important one for computational studies. In particular, this is still a problematic issue for DFT calculations. Classic “pure” functionals such as PW91 typically unduly favor states with lower spin

Table 3. Selected Geometry Parameters (Å, deg) and Mulliken Spin Populations for (nacnac)M(NPh) Complexes Optimized under a C_{2v} Symmetry Constraint

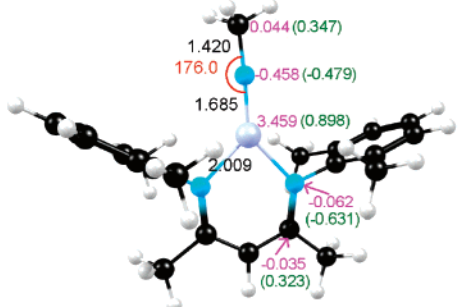
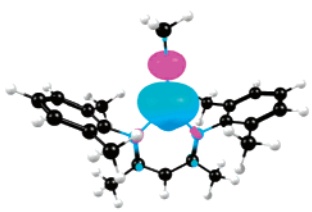
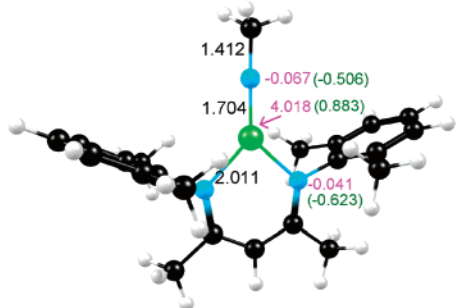

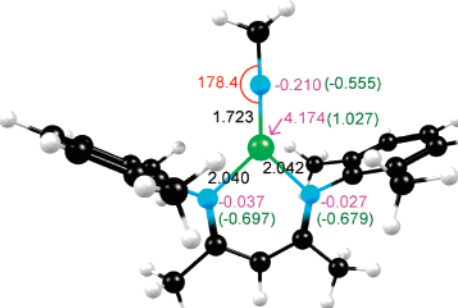
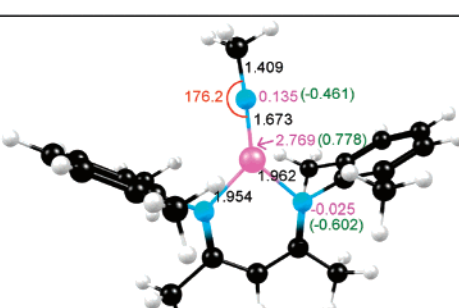
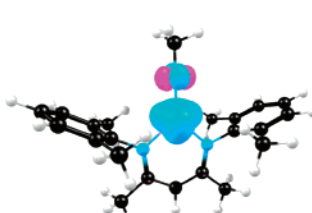
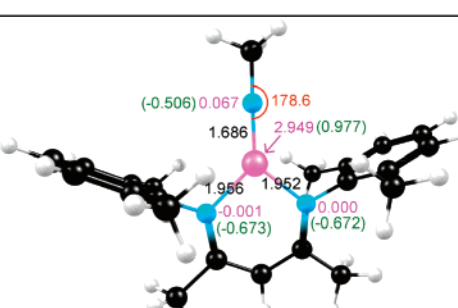
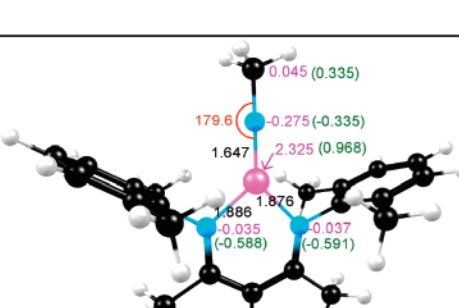
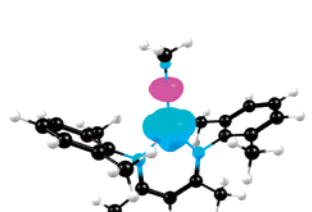
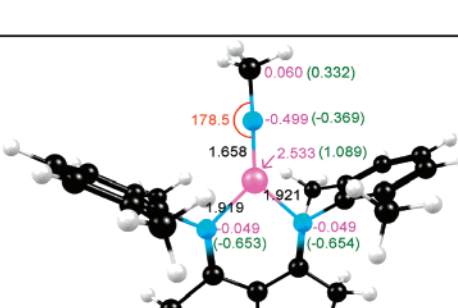
metal ion	charge	S	M–N _{imido}		M–N _{nacnac}		∠(NMN) _{nacnac}	
			PW91	OLYP	PW91	OLYP	PW91	OLYP
Cr(III)	0	3/2	1.710	1.712	2.010	2.004	134.7	133.6
Mn(III)	0	1	1.685	<i>a</i>	1.905	<i>a</i>	133.1	<i>a</i>
Mn(III)	0	2	1.716	1.736	1.995	2.028	133.0	132.3
Fe(III)	0	1/2	1.658	1.671	1.887	1.913	1.333.0	132.5
Fe(III)	0	3/2	1.688	1.700	1.912	1.947	131.8	131.4
Fe(III)	0	5/2	1.753	1.756	2.016	2.064	130.9	131.1
Fe(IV)	1	1	1.674	1.692	1.883	1.907	133.1	132.4
Fe(IV)	1	2	1.712	1.722	1.907	1.936	129.6	129.2
Co(III)	0	0	1.647	1.653	1.852	1.872	133.4	133.2
Co(III)	0	1	1.691	1.700	1.909	1.932	132.9	133.0
Co(III)	0	2	1.743	1.746	1.973	2.018	130.0	130.4
Ni(III)	0	1/2	1.682	1.690	1.875	1.903	132.5	132.5
Ni(III)	0	3/2	1.732	1.743	1.923	1.959	126.7	126.4
Cu(III)	0	0	1.758	1.774	1.940	1.972	131.7	131.7
Cu(III)	0	1	1.769	1.789	1.948	1.985	131.5	131.5

metal ion	charge	S	S _M		S _{N(imido)}		S _{N(nacnac)}	
			PW91	OLYP	PW91	OLYP	PW91	OLYP
Cr(III)	0	3/2	3.517	3.511	−0.414	−0.412	−0.070	−0.070
Mn(III)	0	1	2.600	<i>a</i>	−0.302	<i>a</i>	−0.047	<i>a</i>
Mn(III)	0	2	3.946	4.112	−0.134	−0.280	−0.042	−0.035
Fe(III)	0	1/2	1.450	1.647	−0.273	−0.396	−0.019	−0.020
Fe(III)	0	3/2	2.739	2.873	0.075	−0.034	−0.003	0.002
Fe(III)	0	5/2	3.801	3.786	0.755	0.788	0.015	0.021
Fe(IV)	1	1	2.406	2.617	−0.243	−0.372	−0.018	−0.009
Fe(IV)	1	2	3.314	3.410	0.177	0.106	0.011	0.017
Co(III)	0	0						
Co(III)	0	1	1.556	1.549	0.165	0.164	0.014	0.016
Co(III)	0	2	2.602	2.589	0.895	0.926	0.052	0.053
Ni(III)	0	1/2	0.276	0.263	0.381	0.414	0.017	0.011
Ni(III)	0	3/2	1.378	1.378	1.049	1.078	0.077	0.073
Cu(III)	0	0						
Cu(III)	0	1	0.324	0.304	1.058	1.099	0.072	0.068

^a SCF cycles did not converge.

multiplicities, while hybrid functionals have been documented to behave oppositely. In this study, we have carried out single-point energy calculations on the OLYP optimized geometries of all the NPh and oxo complexes studied. These results afford a wealth of information on (a) trends in spin-state energetics in nacnac imido complexes, (b) the performance of the different functionals, and (c) comparisons of NPh and oxo spin-state energetics. The various energetics results are shown in Tables 5–7. All of these issues are discussed below on a case by case basis.

Mn(III). For Mn(III) imido complexes, the “pure” functionals such as PW91, BLYP, BP, and XLYP indicate nearly isoenergetic *S* = 1 and 2 states. In contrast, the newer “pure” functionals OLYP and OPBE, which include the Handy–Cohen exchange OPTX exchange functional, favor the *S* = 2 state by about 0.7 and 0.5 eV, respectively. The three hybrid functionals examined also favor the *S* = 2 state by a similar margin. The *S* = 0 state is far higher in energy than either the *S* = 1 or 2 state. Overall, the results suggest an *S* = 2 ground state.

PW91			OLYP
 <p>0.044 (0.347) 1.420 176.0 -0.458 (-0.479) 1.685 3.459 (0.898) 2.009 -0.062 (-0.631) -0.035 (0.323)</p>			(nacnac)Cr^{III}(NMe), S = 3/2
 <p>1.412 -0.067 (-0.506) 1.704 4.018 (0.883) 2.011 -0.041 (-0.623)</p>		 <p>178.4 -0.210 (-0.555) 1.723 4.174 (1.027) 2.040 2.042 -0.037 (-0.697) -0.027 (-0.679)</p>	(nacnac)Mn^{III}(NMe), S = 2
 <p>1.409 0.135 (-0.461) 1.673 2.769 (0.778) 1.962 1.954 -0.025 (-0.602)</p>		 <p>(-0.506) 0.067 178.6 2.949 (0.977) 1.686 1.956 1.952 -0.001 (-0.673) 0.000 (-0.672)</p>	(nacnac)Fe^{III}(NMe), S = 3/2
 <p>0.045 (0.335) 179.6 -0.275 (-0.335) 1.647 2.325 (0.968) 1.886 1.876 -0.035 (-0.588) -0.037 (-0.591)</p>		 <p>0.060 (0.332) 178.5 -0.499 (-0.369) 1.658 2.533 (1.089) 1.919 1.921 -0.049 (-0.653) -0.049 (-0.654)</p>	[(nacnac)Fe^{IV}(NMe)]⁺, S = 1

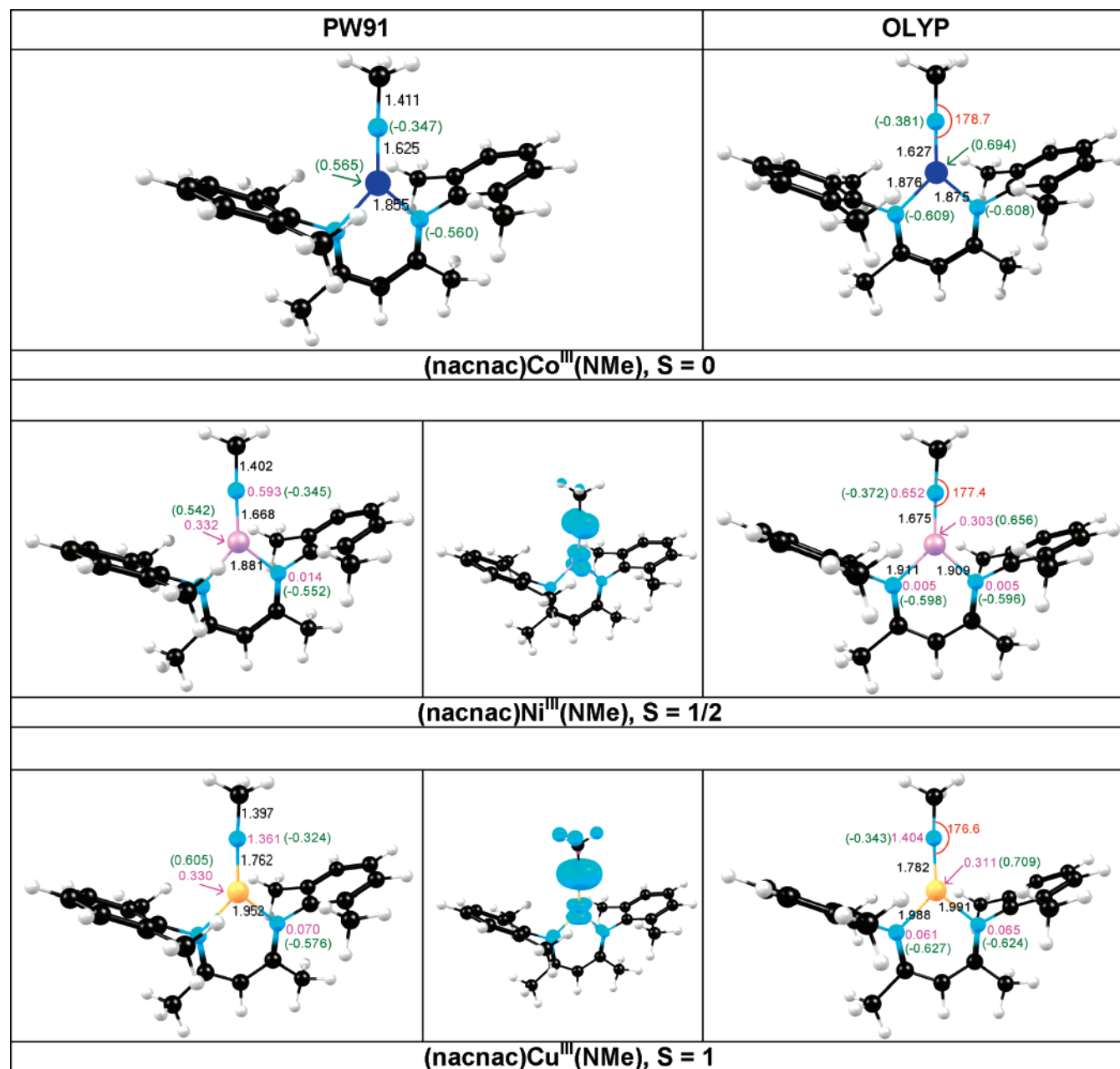


Figure 5. Calculated results for (nacnac)M(NMe) complexes for M = Cr^{III} (S = 3/2), Mn^{III} (S = 2), Fe^{III} (S = 3/2), Fe^{IV} (S = 1), Co (S = 0), Ni (S = 1/2), and Cu (S = 1): PW91- and OLYP-optimized distances (Å, black), Mulliken charges (green), and spin populations (magenta); for the open-shell species, PW91 spin-density plots are also shown, with majority and minority spin densities in cyan and magenta, respectively. Color code for atoms: C (black), H (white), N (magenta), Cr (light blue), Mn (green), Fe (cyan), Co (royal blue), Ni (pink), and Cu (light orange).

Fe(III). For (nacnac)Fe^{III}(NMe), as shown in Table 5, the “classic” PW91 functional predicts an S = 1/2 ground state by a clear margin of energy, in apparent disagreement with an electron paramagnetic resonance and Mössbauer analysis on a closely related species, while the newer Handy–Cohen OLYP functional predicts an S = 3/2 ground state, by a clear margin of energy, apparently consistent with experimental results. For (nacnac)Fe^{III}(NPh), as shown in Tables 5 and 6, the pure functionals such as PW91, BLYP, BP, and XLYP indicate nearly isoenergetic S = 1/2 and 3/2 states and an S = 5/2 state nearly 0.9 eV higher in energy.^{50,51} The OLYP and OPBE functionals predict S = 3/2 ground states, S = 1/2 excited states 0.3–0.4 higher in energy, and S = 5/2 excited states about 0.5 eV higher in energy than the ground states.

In contrast, the hybrid functionals do predict S = 3/2 ground states but switch the ordering of the S = 1/2 and 5/2 states, relative to OLYP and OPBE.

Co(III). For Co(III) imido complexes, all the pure functionals examined clearly predict an S = 0 ground state, consistent with experimental results, while the hybrid functionals predict higher-multiplicity spin states. Thus, at least for the spin-state energetics of the Co(III) imido complexes, the pure functionals appear to be significantly better. Note once again that the newer pure functionals OLYP and OPBE behave somewhat differently from the older ones; thus, the older pure functionals predict substantially higher relative energies for the S = 2 state, compared with OLYP and OPBE.

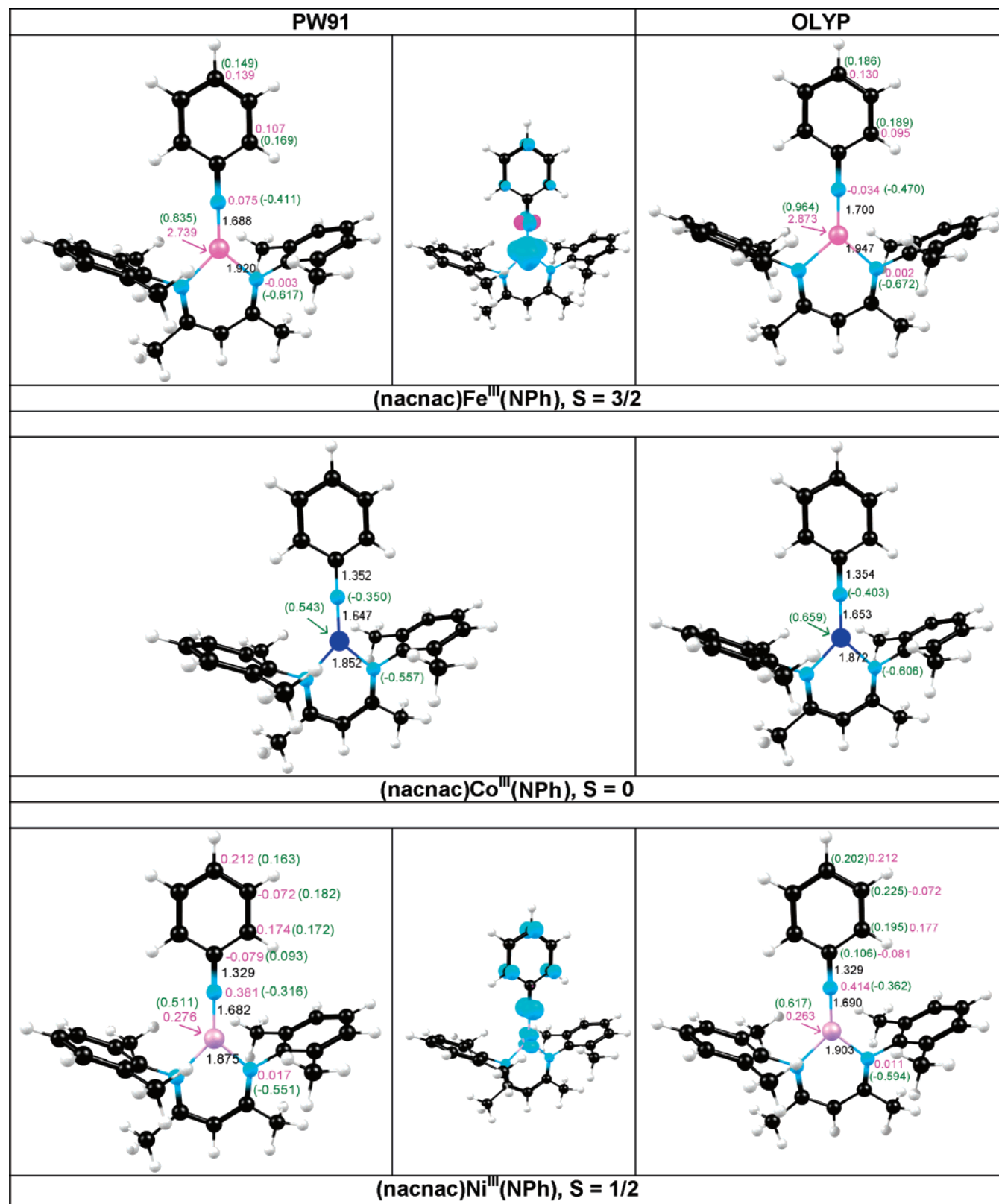


Figure 6. Calculated results for selected (nacnac)*M*(NPh) complexes for *M* = Fe^{III} (*S* = 3/2), Co (*S* = 0), and Ni (*S* = 1/2): PW91- and OLYP-optimized distances (Å, black), Mulliken charges (green), and spin populations (magenta); for the open-shell species, PW91 spin-density plots are also shown, with majority and minority spin densities in cyan and magenta, respectively. Color code for atoms: same as in Figure 5.

Ni(III) and *Cu(III)*. All the functionals examined, whether pure or hybrid, predict *S* = 1/2 and *S* = 1 ground states for the Ni(III) and Cu(III) complexes, respectively, by a clear margin of energy.

The above results afford remarkable insights into the relative performance of the different functionals. In the case of the Fe(III) imido complexes, the classic pure functionals fail to predict an *S* = 3/2 ground state, as observed

Table 4. Selected Geometry Parameters (Å, deg) and Mulliken Spin Populations for (nacnac)M(O) Complexes Optimized under C_{2v} Symmetry Constraints

metal ion	charge	S	M–O		M–N _{nacnac}		$\angle(\text{NMN})_{\text{nacnac}}$	
			PW91	OLYP	PW91	OLYP	PW91	OLYP
Cr(III)	0	$3/2$	1.641	<i>a</i>	1.997	<i>a</i>	135.5	<i>a</i>
Mn(III)	0	1	1.619	1.623	1.984	1.907	133.7	132.9
Mn(III)	0	2	1.659	1.668	1.984	2.009	133.5	132.5
Fe(III)	0	$1/2$	1.600	1.599	1.844	1.854	132.5	131.9
Fe(III)	0	$3/2$	1.634	1.639	1.909	1.917	132.1	131.0
Fe(III)	0	$5/2$	1.682	1.684	2.013	2.038	131.3	130.6
Fe(IV)	1	1	1.610	1.612	1.865	1.880	133.4	132.1
Fe(IV)	1	2	1.647	1.648	1.888	1.914	130.0	129.0
Co(III)	0	0	1.633	1.637	1.842	1.855	134.2	133.6
Co(III)	0	1	1.616	1.616	1.858	1.880	131.8	131.4
Co(III)	0	2	1.666	1.666	1.963	2.002	130.6	130.6
Ni(III)	0	$1/2$	1.667	1.675	1.872	1.894	133.3	133.1
Ni(III)	0	$3/2$	1.654	1.655	1.924	1.962	130.0	130.1
Cu(III)	0	0	1.718	1.727	1.934	1.967	132.9	132.6
Cu(III)	0	1	1.735	1.748	1.948	1.986	132.9	132.4

metal ion	charge	S	S_M		S_O		$S_{N(\text{nacnac})}$	
			PW91	OLYP	PW91	OLYP	PW91	OLYP
Cr(III)	0	$3/2$	3.185	<i>a</i>	−0.170	<i>a</i>	−0.080	<i>a</i>
Mn(III)	0	1	2.202	2.382	−0.005	−0.090	−0.061	−0.073
Mn(III)	0	2	3.822	3.938	0.166	0.076	−0.051	−0.050
Fe(III)	0	$1/2$	0.946	1.029	0.148	0.126	−0.026	−0.037
Fe(III)	0	$3/2$	2.638	2.728	0.404	0.363	−0.010	−0.013
Fe(III)	0	$5/2$	3.913	3.909	0.872	0.893	0.037	0.038
Fe(IV)	1	1	2.161	2.333	0.195	0.181	−0.122	−0.154
Fe(IV)	1	2	3.250	3.373	0.595	0.629	0.024	0.009
Co(III)	0	0						
Co(III)	0	1	1.386	1.412	0.621	0.626	0.015	0.004
Co(III)	0	2	2.707	2.705	1.032	1.053	0.090	0.088
Ni(III)	0	$1/2$	0.409	0.384	0.551	0.618	0.024	0.013
Ni(III)	0	$3/2$	1.478	1.485	1.159	1.179	0.131	0.124
Cu(III)	0	0						
Cu(III)	0	1	0.457	0.425	1.140	1.190	0.139	0.133

^a SCF cycles did not converge.

experimentally, unduly favoring an $S = 1/2$ state instead. In the case of the Co(III) imido complexes, the hybrid functionals fail to yield $S = 0$ ground states, as observed experimentally. That leaves only the newer pure functionals OLYP and OPBE, which yield energetics that, as far as we know, are entirely consistent with experimental results in this field.

In turn, these raise the prospect of a tantalizing scenario. If the OLYP (and OPBE) energetics are really semiquantitatively accurate—and there is a certain leap of faith here—then the OLYP/OPBE columns in Tables 5–7 offer for the first time a good *global* picture of the spin-state energetics of the many different nacnac imido and oxo species studied. Whether or not this is actually the case will become clearer as more experimental data accumulate.

E. Spin-State Energetics of the Oxo Species. We have mentioned above that imido and oxo species exhibit roughly the same orbital energy ordering. However, the orbital energy spacings are significantly different, leading, in a few cases, to different spin-state energetics (Table 7), relative to the imido complexes (Table 6). Some highlights of our results

Table 5. PW91 and OLYP Energies (eV) for Different Spin States of NMe, NPh, and Oxo Complexes^a

metal	S	axial ligand					
		NMe		NPh		oxo	
		PW91	OLYP	PW91	OLYP	PW91	OLYP
Mn(III)	2	0.00	0.00	0.00	0.00	0.00	0.00
	1	−0.02	0.52	0.11	0.73	0.20	0.53
	0	2.49	2.68	1.28	2.92	0.54	0.87
Fe(III)	$3/2$	0.00	0.00	0.00	0.00	0.00	0.00
	$5/2$	0.53	0.46	0.91	0.53	0.78	0.36
	$1/2$	−0.36	0.16	0.00	0.29	0.44	0.73
Fe(IV)	1	0.00	0.00	0.00	0.00	0.00	0.00
	2	0.55	0.25	0.86	0.62	0.43	0.14
Co(III)	0	0.00	0.00	0.00	0.00	0.00	0.00
	1	0.47	0.33	0.37	0.20	−0.36	−0.56
	2	0.90	0.45	1.02	0.53	0.07	−0.48
Ni(III)	$1/2$	0.00	0.00	0.00	0.00	0.00	0.00
	$3/2$	0.67	0.47	1.16	0.88	0.26	−0.06
Cu(III)	1	0.00	0.00	0.00	0.00	0.00	0.00
	0	0.45	0.57	1.28	1.28	0.40	0.66

^a All energies refer to fully optimized structures, and the energy zero levels are indicated in bold.

are as follows. As in the Fe(III) imido case, the Fe^{III}O complexes also exhibit $S = 3/2$ ground states. However, in contrast to the Co(III) imido case, *all* the functionals examined predict open-shell $S = 1$ or $S = 2$ ground states for the Co^{III}O complexes; thus, while all the pure functionals including OLYP and OPBE favor $S = 1$ ground states, the three hybrid functionals examined favor $S = 2$ ground states. In the Ni^{III}O case, both the newer pure functionals (OLYP and OPBE) and the hybrid functionals favor $S = 3/2$ ground states, while the older pure functionals favor $S = 1/2$ states. In the Cu^{III}O case, all the functionals favor an $S = 1$ state, relative to an $S = 0$ excited state, by several tenths of an electronvolt.

By way of a minor digression, we would like to point out that the calculated spin-state energetics of (nacnac)Cu^{III}O species (which might also be viewed as Cu^{II}–O•) may be relevant for the dioxygen activation mechanisms of “non-coupled” dicopper monooxygenases such as peptidyl α -hydroxylating monooxygenase (PHM) and dopamine β -monooxygenase (DBM).⁵² Although no Cu^{III}O species has been experimentally detected, at least two groups have considered the intermediacy of such species for PHM⁵³ and/or DBM.^{54,55} As in this study, both groups predicted triplet ground states for the Cu^{III}O intermediates considered; however, these studies considered four- and five-coordinate Cu^{III}O species, whereas we have been exclusively concerned with trigonal-planar species in this study.

For the time being, the above results for the oxo species cannot be related to experimental results, but they clearly emphasize that the spin-state energetics of otherwise analogous imido and oxo complexes may be quite different, a prediction we look forward to seeing experimentally confirmed.

F. Adiabatic Electron Affinities. Given that the Ni and Cu complexes studied are high-valent species, we wished to obtain a computational “handle” on their reactivity,

Table 6. Multifunctional Single-Point Energies (eV) of Different Electronic States of NPh Complexes at Optimized OLYP Structures^a

metal	S	BLYP	BP	OPBE	XLYP	B3LYP (VWN5)	O3LYP (VWN5)	X3LYP (VWN5)
Mn(III)	2	0.00	0.00	0.00	0.00	0.00	0.00	0.00
	1	0.08	0.14	0.52	0.09	0.73	0.81	0.78
	0	2.39	2.53	2.99	2.40	3.37	3.43	3.45
Fe(III)	3/2	0.00	0.00	0.00	0.00	0.00	0.00	0.00
	5/2	0.86	0.87	0.53	0.85	0.26	0.23	0.22
	1/2	-0.05	0.01	0.40	-0.05	0.40	0.56	0.43
Co(III)	0	0.00	0.00	0.00	0.00	0.00	0.00	0.00
	1	0.38	0.37	0.18	0.36	-0.25	-0.14	-0.29
	2	0.98	1.01	0.54	0.95	-0.24	-0.12	-0.33
Ni(III)	1/2	0.00	0.00	0.00	0.00	0.00	0.00	0.00
	3/2	1.10	1.14	0.90	1.08	0.55	0.60	0.51
Cu(III)	1	0.00	0.00	0.00	0.00	0.00	0.00	0.00
	0	0.60	0.62	0.68	0.61	0.87	0.88	0.90

^a Energy zero levels are indicated in bold. (This table should be read in conjunction with Table 5.)

Table 7. Multifunctional Single-Point Energies (eV) of Different Electronic States of Oxo Complexes at Optimized OLYP Structures^a

metal	S	BLYP	BP	OPBE	XLYP	B3LYP (VWN5)	O3LYP (VWN5)	X3LYP (VWN5)
Mn(III)	2	0.00	0.00	0.00	0.00	0.00	0.00	0.00
	1	0.15	0.21	0.58	0.15	0.82	0.90	0.87
	0	0.67	0.79	1.25	0.69	1.78	1.79	1.87
Fe(III)	3/2	0.00	0.00	0.00	0.00	0.00	0.00	0.00
	5/2	0.77	0.75	0.33	0.76	0.16	0.04	0.11
	1/2	0.41	0.45	0.81	0.42	1.09	1.15	1.14
Fe(IV)	1	0.00	0.00	0.00	0.00	0.00	0.00	0.00
	2	0.45	0.42	0.09	0.45	0.08	-0.07	0.05
Co(III)	0	0.00	0.00	0.00	0.00	0.00	0.00	0.00
	1	-0.30	-0.34	-0.62	-0.30	-0.65	-0.78	-0.68
	2	0.08	0.07	-0.52	0.05	-0.97	-1.07	-1.06
Ni(III)	1/2	0.00	0.00	0.00	0.00	0.00	0.00	0.00
	3/2	0.25	0.26	-0.07	0.24	-0.08	-0.24	-0.11
Cu(III)	1	0.00	0.00	0.00	0.00	0.00	0.00	0.00
	0	0.40	0.42	0.58	0.40	0.64	0.70	0.66

^a Energy zero levels are indicated in bold. (This table should be read in conjunction with Table 5.)

especially via reductive pathways. We have done so, admittedly in a crude manner, by calculating the adiabatic electron affinities (EAs) for several of the NPh and oxo complexes studied, which are listed in Table 8. For certain of the complexes, more than one EA has been reported because of multiple contenders for the ground state of either the neutral or anionic species. Our key conclusions vis-à-vis the EAs are as follows.

First, none of the EAs is exceptionally high. Even for (nacnac)Cu^{III}(NPh), the OLYP EA of 1.65 eV is essentially the same as that of the analogous Ni(III) complex. Thus, we speculated that such a Cu(III) imido complex should be experimentally accessible.⁵⁶ Indeed, while this paper was under review, Warren and co-workers reported a transient (nacnac)Cu^I-nitrene intermediate, albeit with no detailed spectroscopic characterization.

Second, compared to imido complexes, the EAs of the oxo complexes are not remarkably high either. Thus, the oxo species appear to be viable as reactive intermediates. However, being sterically unprotected (say, relative to the

Table 8. Adiabatic Electron Affinities (eV) of the (nacnac)M(L) Complexes Studied

	S for neutral	S for anion	EA	
			PW91	OLYP
(nacnac)Fe(NPh)	3/2	1	1.70	1.21
(nacnac)Co(NPh)	0	1/2	1.77	1.52
(nacnac)Ni(NPh)	1/2	0	1.58	1.31
(nacnac)Ni(NPh)	1/2	1	1.52	1.63
(nacnac)Cu(NPh)	1	1/2	1.93	1.65
(nacnac)Fe(O)	3/2	1	1.24	0.77
(nacnac)Co(O)	1	1/2	1.61	1.14
(nacnac)Co(O)	1	3/2	1.62	1.53
(nacnac)Ni(O)	1/2	1	1.43	1.12
(nacnac)Ni(O)	3/2	1	2.09	1.63
(nacnac)Cu(O)	1	1/2	2.11	1.78

adamantylimido complexes studied experimentally), the oxo complexes are likely to be susceptible to dimerization as well as a variety of other reaction pathways.^{20,57}

Third, not surprisingly, the PW91 and OLYP EAs differ significantly in a number of cases. On the basis of our overall findings, we view the OLYP EAs as significantly more accurate.

Conclusion

In summary, we have carried out a detailed multifunctional study of first-row transition-metal (Cr to Cu) nacnac imido and oxo complexes. In our opinion, two broad themes stand out from a plethora of detailed results.

First, all the imido and oxo species share essentially the same orbital ordering, which is $a_{1-2} (d_{\sigma}) \leq a_2 (d_{\delta}) \leq a_{1-1} (d_{\sigma}) < b_2 (d_{\pi}) < b_1 (d_{\pi})$, which is in fact very similar to the orbital ordering in a simple (i.e., not particularly π -bonding) complex such as (nacnac)NiCl. This indicates that the orbital energy ordering is largely dictated by the trigonal-planar coordination environment rather than by the imido or oxo ligand. The remarkable stability of the d_{σ} orbitals, relative to the metal–imido linkage, owes largely to the way these orbitals can deform or hybridize as a result of the absence of ligands trans or equatorial with respect to the imido (or oxo) group. We believe that this is one of the first careful examinations of the “shape-shifting” nature of metal orbitals in low-coordinate environments.

Second, the pure functionals OLYP and OPBE, based on the Handy–Cohen OPTX exchange functional, appear to provide the best overall description of the spin-state energetics of the complexes examined. In particular, these two functionals correctly predict $S = 3/2$ and 0 ground states for the Fe(III) imido and Co(III) imido complexes, respectively. In contrast, classic pure functionals such as PW91 predict $S = 1/2$ ground states or at best equienergetic $S = 1/2$ and $3/2$ states for the Fe(III) imido complexes, while hybrid functionals predict $S = 1$ or 2 ground states for the Co(III) imido complexes, both of which are inconsistent with experimental results. In other words, there is no reason to suppose that hybrid functionals are inherently better than pure functionals, as is sometimes claimed.²⁶

Acknowledgment. This work was supported by the Research Council of Norway, the South African National Research Foundation (grant number 2054243), and the Central Research Fund of the University of the Free State, South Africa.

Supporting Information Available: Optimized PW91/TZP Cartesian coordinates for the molecules studied (67 pages). This information is available free of charge via the Internet at <http://pubs.acs.org>.

References

- (1) Nugent, W. A.; Mayer, J. M. *Metal–Ligand Multiple Bonds*; Wiley: New York, 1988.
- (2) Holm, R. H. *Chem. Rev.* **1987**, *97*, 1401–1449.
- (3) Shan, X. P.; Que, L., Jr. *Inorg. Biochem.* **2006**, *100*, 421–433.
- (4) Wigley, D. E. *Prog. Inorg. Chem.* **1994**, *42*, 239–482.

- (5) Mehn, M. P.; Peters, J. C. *J. Inorg. Biochem.* **2006**, *100*, 634–643.
- (6) For a representative review, see: Mindiola, D. J. *Acc. Chem. Res.* **2006**, *39*, 813–821.
- (7) Mayer, J. M. *Comm. Inorg. Chem.* **1988**, *8*, 125–135.
- (8) Hay-Motherwell, R. S.; Wilkinson, G.; Hussain-Bates, B.; Hursthouse, M. B. *J. Chem. Soc., Dalton Trans.* **1992**, 3477–3482.
- (9) Hay-Motherwell, R. S.; Wilkinson, G.; Hussain-Bates, B.; Hursthouse, M. B. *Polyhedron* **1999**, *12*, 2009–2012.
- (10) Glueck, D. S.; Wu, J. X.; Hollander, F. J.; Bergman, R. G. *J. Am. Chem. Soc.* **1991**, *113*, 2041–2054.
- (11) Glueck, D. S.; Green, J. C.; Michelman, R. I.; Wright, I. N. *Organometallics* **1992**, *11*, 4221–4225.
- (12) Waterman, R.; Hillhouse, G. L. *Organometallics* **2003**, *22*, 5182–5184.
- (13) Mindiola, D. J.; Hillhouse, G. L. *J. Am. Chem. Soc.* **2002**, *124*, 9976–9977.
- (14) Melenkivitz, R.; Mindiola, D. J.; Hillhouse, G. L. *J. Am. Chem. Soc.* **2002**, *124*, 3846–3847.
- (15) Mindiola, D. J.; Hillhouse, G. L. *J. Am. Chem. Soc.* **2001**, *123*, 4623–4624.
- (16) Jenkins, D. M.; Betley, T. A.; Peters, J. C. *J. Am. Chem. Soc.* **2002**, *124*, 11238–11239.
- (17) Shay, D. T.; Yap, G. P. A.; Zakharov, L. N.; Rheingold, A. L.; Theopold, K. H. *Angew. Chem., Int. Ed.* **2005**, *44*, 1508–1510.
- (18) Hu, X.; Meyer, K. *J. Am. Chem. Soc.* **2004**, *126*, 16322–16323.
- (19) Eckart, N. A.; Vaddadi, S.; Stoian, S.; Lachicotte, R. J.; Cundari, T. R.; Holland, P. L. *Angew. Chem., Int. Ed.* **2006**, *45*, 6868–6871.
- (20) Dai, X.; Kapoor, P.; Warren, T. H. *J. Am. Chem. Soc.* **2004**, *126*, 4798–4799.
- (21) Kogut, E.; Wiencko, H. L.; Cordeau, D. E.; Warren, T. H. *J. Am. Chem. Soc.* **2005**, *127*, 11248–11249.
- (22) For a discussion of the spin-density profiles of various types of heme and nonheme Fe^{III/IV/V}O species, see: Conradie, J.; Tangen, E.; Ghosh, A. *J. Inorg. Biochem.* **2006**, *100*, 707–715.
- (23) For recent findings on iron-oxo spin-density profiles from our laboratory, see: (a) Ghosh, A.; Tangen, E.; Ryeng, H.; Taylor, P. R. *Eur. J. Inorg. Chem.* **2004**, 2442–2445. (b) Wasbotten, I.; Ghosh, A. *Inorg. Chem.* **2006**, *45*, 4910–4913. (c) Conradie, J.; Wasbotten, I. H.; Ghosh, A. *J. Inorg. Biochem.* **2006**, *100*, 502–506.
- (24) For a comparison of ab initio and DFT calculations on transition-metal spin-state energetics, see: Ghosh, A.; Taylor, P. R. *Curr. Opin. Chem. Biol.* **2003**, *91*, 113–124.
- (25) For a series of commentaries on the performance of DFT on transition-metal complexes, see: Ghosh, A. *J. Biol. Inorg. Chem.* **2006**, *11*, 671–673.
- (26) Ghosh, A. *J. Biol. Inorg. Chem.* **2006**, *11*, 712–724.
- (27) Handy, N. C.; Cohen, A. *J. Mol. Phys.* **2001**, *99*, 403–412.

- (28) Perdew, J. P.; Chevary, J. A.; Vosko, S. H.; Jackson, K. A.; Perderson, M. R.; Singh, D. J.; Fiolhais, C. *Phys. Rev. B: Condens. Matter Mater. Phys.* **1992**, *46*, 6671–6687.
- (29) Velde, G. T.; Bickelhaupt, F. M.; Baerends, E. J.; Guerra, C. F.; Van Gisbergen, S. J. A.; Snijders, J. G.; Ziegler, T. J. *J. Comput. Chem.* **2001**, *22*, 931–967.
- (30) Becke, A. D. *Phys. Rev. A: At., Mol., Opt. Phys.* **1998**, *38*, 3098–3100.
- (31) Lee, C.; Yang, W.; Parr, R. G. *Phys. Rev. B: Condens. Matter Mater. Phys.* **1988**, *37*, 785–789.
- (32) Becke, A. D. *Phys. Rev. A: At., Mol., Opt. Phys.* **1988**, *38*, 3098.
- (33) Perdew, J. P. *Phys. Rev. B: Condens. Matter Mater. Phys.* **1986**, *33*, 8822. Erratum: Perdew, J. P. *Phys. Rev. B: Condens. Matter Mater. Phys.* **1986**, *34*, 7406.
- (34) Perdew, J. P.; Burke, K.; Ernzerhof, M. *Phys. Rev. Lett.* **1996**, *77*, 3865–3868.
- (35) Perdew, J. P.; Burke, K.; Ernzerhof, M. *Phys. Rev. Lett.* **1997**, *78*, 1396.
- (36) Xu, X.; Goddard, W. A., III. *Proc. Natl. Acad. Sci. U.S.A.* **2004**, *101*, 2673.
- (37) Stephens, J.; Devlin, F. J.; Chabalowski, C. F.; Frisch, M. J. *J. Phys. Chem.* **1994**, *98*, 11623–11627.
- (38) Watson, M. A.; Handy, N. C.; Cohen, A. J. *J. Chem. Phys.* **2003**, *119*, 6475–6481.
- (39) Hertwig, R. H.; Koch, W. *Chem. Phys. Lett.* **1997**, *268*, 345–351.
- (40) Andres, H.; Bominaar, E. L.; Smith, J. M.; Eckert, N. A.; Holland, P. L.; Munck, E. *J. Am. Chem. Soc.* **2002**, *124*, 3012–3025.
- (41) Holland, P. L.; Cundari, T. R.; Perez, L. L.; Eckert, N. A.; Lachicotte, R. J. *J. Am. Chem. Soc.* **2002**, *124*, 14416–14424.
- (42) This is a simple C_{3v} model of a pseudotetrahedral Fe(III) trisphosphine imido complex reported in: Brown, S. D.; Betley, T. A.; Peters, J. C. *J. Am. Chem. Soc.* **2003**, *125*, 322–323.
- (43) Tangen, E.; Conradie, J.; Ghosh, A. *J. Chem. Theory Comput.* **2007**, *3*, 448–457.
- (44) For a recent review of bonding in NO complexes, see: Ghosh, A. *Acc. Chem. Res.* **2005**, *38*, 943–954.
- (45) Franz, K. J.; Lippard, S. J. *J. Am. Chem. Soc.* **1999**, *121*, 10504–10512.
- (46) Tangen, E.; Conradie, J.; Ghosh, A. *Inorg. Chem.* **2005**, *44*, 8699–8706.
- (47) Unusual d orbital hybridization also provides an explanation for the linearity of the NO group in the $S = 1/2$ $\{FeNO\}^7 [Fe(CN)_4(NO)]^{2-}$ anion: Conradie, J.; Ghosh, A. *J. Inorg. Biochem.* **2006**, *100*, 2069–2073.
- (48) In general, the great majority of the complexes studied conform to exact or approximately C_{2v} symmetry. The high-spin Fe(III) complexes are an exception; in these, the Fe–N_{imido} vector is somewhat bent to one side in the diketiminato plane. However, even in this case, the potential associated with the bending is very soft.
- (49) Tangen, E.; Ghosh, A. *J. Inorg. Biochem.* **2005**, *99*, 959–962.
- (50) We have observed a similar tendency of the PW91 functional to unduly favor low-spin states for a number of iron porphyrin complexes: (a) Ghosh, A.; Gonzalez, E.; Vangenberg, T.; Taylor, P. *J. Porphyrins Phthalocyanines* **2001**, *5*, 345–356. (b) Ghosh, A.; Persson, B. J.; Taylor, P. R. *J. Biol. Inorg. Chem.* **2003**, *8*, 507–511. (c) Ghosh, A.; Taylor, P. R. *J. Chem. Theory Comput.* **2005**, *1*, 597–600.
- (51) There are few studies on the performance of the newer functionals vis-à-vis transition-metal spin-state energetics. However, the following papers, not necessarily concerned with transition metals, provide valuable evaluations of the OPTX-based functionals: (a) Vargas, A.; Zerara, M.; Krausz, E.; Hauser, A.; Daku, L. M. L. *J. Chem. Theory Comput.* **2006**, *2*, 1342–1359. (b) Ramachandran, B. *J. Phys. Chem. A* **2006**, *110*, 396–403. (c) Larkin, J. D.; Bock, C. W.; Schaefer, H. F., III. *J. Phys. Chem. A* **2005**, *109*, 10100–10105. (d) Xu, X.; Goddard, W. A., III. *J. Phys. Chem. A* **2004**, *108*, 8495–8504. (e) Guner, V. A.; Khuong, K. S.; Houk, K. N.; Chuma, A.; Pulay, P. *J. Phys. Chem. A* **2004**, *108*, 2959–2965.
- (52) Klinman, J. P. *Chem. Rev.* **1996**, *96*, 2541–2561.
- (53) Chen, P.; Solomon, E. I. *J. Am. Chem. Soc.* **2004**, *126*, 4991–5000.
- (54) Kamachi, T.; Shiota, Y.; Yoshizawa, K. *Inorg. Chem.* **2005**, *44*, 4226–4236.
- (55) Yoshizawa, K.; Kihara, N.; Kamachi, T.; Shiota, Y. *Inorg. Chem.* **2006**, *44*, 4226–4236.
- (56) Badiei, Y. M.; Krishnaswamy, A.; Melzer, M. M.; Warren, T. H. *J. Am. Chem. Soc.* **2006**, *128*, 15056–15057.
- (57) Spencer, D. J. E.; Reynolds, A. M.; Holland, P. L.; Jazdzewski, B. A.; Duboc-Toia, C.; Le Pape, L.; Yokota, S.; Tachi, Y.; Itoh, S.; Tolman, W. B. *Inorg. Chem.* **2002**, *41*, 6307–6321.

CT600337J

JCTC

Journal of Chemical Theory and Computation

On the Possibility of Electronic DNA Nanobiochips[†]

V. D. Lakhno* and V. B. Sultanov

*Institute of Mathematical Problems of Biology, Russian Academy of Sciences,
142290 Pushchino, Moscow Region, Russia*

Received November 23, 2006

Abstract: We have considered as a theoretical possibility for the development of a nanobiochip the operation principle of which is based on measuring conductance in single-stranded and double-stranded DNA. Calculations have demonstrated that in the majority of cases the conductance of double-stranded nucleotides considerably exceeds that of single-stranded ones. The results obtained are in agreement with recent experiments on measuring the oligonucleotide conductance. It has been shown that an electronic biochip containing 11 nucleotide pairs will recognize $\approx 97\%$ sequences. It has also been demonstrated that the percentage of identifiable sequences will grow with the sequence length.

DNA microarrays, also known as biochips and genechips, have become the latest and most efficient method to analyze thousands of genes simultaneously. Potential applications are countless, including gene expression analysis, studies of genetic disorders, drug development, and even the solution of mathematical problems.^{1,2} Development of the method is concerned with further miniaturization, i.e., increase in the number of spots on the biochip. Progress in this field goes on at about the same rate as which miniaturization in computer technology advances (Moore's law).

The methods for processing information readout from biochips may come up against the limits of miniaturization still earlier than the computer technology (where the circuits of $0.1 \mu\text{m}$ size are presently used) will do, since readings from biochips are currently taken by measuring the intensity of a signal from an individual spot and analyzing changes in its intensity or color. This places a fundamental limitation on the accuracy of the measurements which is determined by the wavelength of the light emitted by a fluorescent marker used in the biochip technology, i.e., $\approx 1 \mu\text{m}$. At present, the technically attainable size of a spot is about $20 \mu\text{m}$.

One way to overcome this limitation is to develop electronic biochips from which one could read detailed

information by measuring the conductance of an individual fragment of a DNA molecule used in biochips. This would enable the biochip technology to break through into the nanometer region since in this case the resolution of the readings would be determined by the characteristic size comparable with the diameter of a DNA molecule, i.e., $\approx 2 \text{ nm}$.

The aim of this work is to study the possibility for the development of a nanobiochip, the operation principle of which is based on measuring the DNA conductance. Theoretically, a nanobiochip based on measuring the conductance will be efficient if the conductance of a single-stranded DNA will differ considerably from that of a DNA duplex obtained as a result of hybridization of the single-stranded DNA with a complementary strand. This paper just deals with elucidation of this problem.

Presently there are a great many approaches to the development of biosensors which could discriminate between a single-stranded DNA and its hybrid with a complementary strand. These approaches include optical,³ electrochemical,^{4–9} and microgravimetric¹⁰ methods. Without going into detail we will just notice that all the approaches have their advantages and drawbacks. The chief drawback of the above methods is that they all require rather a great number of similar sequences on a chip which presents an obstacle for substantial miniaturization.

The model of a nanobiochip considered here is a single-stranded DNA fragment whose ends are attached to elec-

[†] Dedicated to Dennis R. Salahub on the occasion of his 60th birthday.

* Corresponding author e-mail: lak@impb.psn.ru.

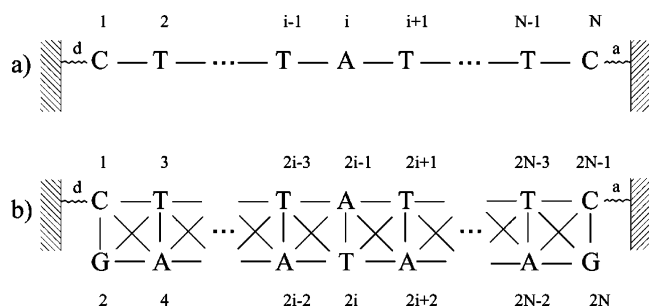


Figure 1. (a) Single-stranded DNA and (b) DNA duplex with all nearest interactions.

Table 1. Matrix Elements of an Electron Transition (in eV) between Neighboring Nucleotides in DNA Duplexes^{11,12 a}

Transitions inside the Strand									
5' → 3'				3' → 5'					
A	C	T	G	A	C	T	G		
A	0.030	0.061	0.105	0.049	A	0.030	0.029	0.086	0.089
C	0.029	0.041	0.1	0.042	C	0.061	0.041	0.076	0.110
T	0.086	0.076	0.158	0.085	T	0.105	0.1	0.158	0.137
G	0.089	0.110	0.137	0.084	G	0.049	0.042	0.085	0.084

Transitions between the Strands									
5' → 5'				3' → 3'					
A	C	T	G	A	C	T	G		
A	0.035	0	0.016	0.021	A	0.062	0	0.016	0.021
C	0	0.0007	0	0	C	0	0	0	0
T	0.016	0	0.002	0	T	0.007	0	0.002	0
G	0.021	0	0.009	0.019	G	0.021	0	0	0.043

oxidation potentials ¹³ (in acetonitrile solution).				transitions inside the site	
A	C	T	G	C-G	A-T
1.69	1.9	1.9	1.24	0.050	0.034

^a Table 1 was reproduced from work.¹⁶

trodes as shown in Figure 1(a). Figure 1(b) presents a nucleotide sequence shown in Figure 1(a) in hybrid with a complementary strand in which charge transfer is determined by matrix elements of the transitions between neighboring nucleotides. The values of matrix elements in the case when charge is carried by holes are given in Table 1.

Our scheme of a nanobiochip where the ends of only one DNA strand are fixed reflects an experimental situation¹⁴ (and references therein). In these works the ends of only the DNA strand attached to electrodes are modified (by thiol group).

The charge transfer can be calculated with an effective tight-binding Hamiltonian \hat{H} with diagonal elements determined by oxidation energies of the bases and off-diagonal

elements equal to the corresponding charge coupling of neighboring bases:¹⁵

$$\hat{H} = \hat{H}^0 + \hat{V}$$

$$\hat{H}^0 = E_d |d\rangle\langle d| + \sum_{i=1}^{2N} E_i |i\rangle\langle i| + E_a |a\rangle\langle a|$$

$$\hat{V} = v_{d,1} |d\rangle\langle 1| + v_{a,2N-1} |2N-1\rangle\langle a| + \hat{V}_M$$

$$\hat{V}_M = \sum_{i \neq j} v_{ij} |i\rangle\langle j|$$

where $v_{d,1}$ and $v_{a,2N-1}$ are the coupling matrix elements between donor (d) and nucleotide (1) and acceptor (a) and nucleotide (2N-1), respectively; \hat{V}_M is the bridge DNA Hamiltonian, where v_{ij} are the matrix elements between neighboring nucleotides; E_d , E_a , and E_i are hole energies on donor, acceptor, and i th nucleotide, respectively. This Hamiltonian takes into account all the links between neighboring nucleotides (including off-diagonal ones). The lack of some off-diagonal links in Table 1 stems from the fact that their value is small, and they cannot be found by quantum-chemical calculations with good accuracy.

To compare the conductances of the single-stranded DNA fragment and the DNA duplex presented in Figure 1 let us consider their ratio f

$$f = \frac{R_{1N}^2}{R_{1,2N-1}^2}$$

where

$$\hat{R} = (E - \hat{H})^{-1}$$

is a resolvent, corresponding to appropriate \hat{H} , R_{ij} are appropriate Green's functions,¹⁵ E is a complex variable, the real part of which is interpreted as a hole energy; and the parameters of electrodes playing the roles of a donor and an acceptor are taken to be $E_a = E_d = E_G$, $v_{d1} = v_{G1}$, and $v_{a,2N-1} = v_{G,2N-1}$. In other words we consider the situation when the energy parameters of electrodes are close to corresponding values of guanines. Notice, that the longer the sequence is used in a biochip, the less important a particular choice of the donor and acceptor parameters is.

The ratio f , which is a function of the sequence, was calculated for all possible nucleotide sequences of length $N = 8, 9, 10, 11$. The number of such sequences is 4^N . The function f was calculated for $E = -0.5$ eV, which was found¹⁶ from the condition of the best agreement of the calculated charge-transfer rates with the experimentally measured ones for some oligonucleotide sequences. The sequences in which f differed from 1 by less than 10% :

Table 2. Results of the Calculations

N	percent $f < 1$	percent of indistinguishable (%)	max(f), sequence	min(f), sequence
8	75.5	7	1.3×10^6 , CAAATGTG	3.5×10^{-7} , CCCCCCG
9	79.9	5.1	7.6×10^7 , ACTTGAACC	1.5×10^{-8} , CCCCCCGG
10	82.4	3.8	1.4×10^{10} , CACGAGGAG	6×10^{-10} , CCCCCCGGG
11	85	2.8	4.2×10^{13} , TGCGCCTTCCC	2.5×10^{-11} , CCCCCCGGGG

$|f-1| < 0.05$ (in the absence of interactions between the strands $f \equiv 1$) were considered to be indistinguishable. The results of the calculations are presented in Table 2. The second column of Table 2 shows that in the majority of cases the conductance of double-stranded nucleotides considerably exceeds that of single-stranded ones. This conclusion is confirmed by experimental data.¹⁴

The third column of Table 2 shows that the percentage of indistinguishable sequences decreases as the sequence length N grows. The results obtained testify to the perspective of the development of nanobiochips whose operation principle is based on the conductance measurement. The accuracy of operation of such biochips will be the higher, the larger will be the sequence length.

As was shown above, the charge-transfer rate in a DNA molecule strongly depends on the type of a nucleotide sequence. However, current theoretical estimations of charge tunneling probabilities in specific double helices of oligonucleotides made with the use of matrix elements of overlap integral of electronic orbitals of neighboring nucleotides in DNA are based only on a significantly idealized (nearly to planar) model of base-pairing. They do not take into account either the significant heterogeneity of nucleotide geometry parameters in a DNA molecule observed in X-ray experiments or the existence of large “propeller” and “buckle” deformations of the planar structure of H-bonding bases. These deformations, as is known, can reach 50°. ^{17–20} In addition DNA thermal fluctuations break the global helix symmetry and may localize the wavefunction (HOMO and/or LOMO) to different areas as a function of time. It was shown ^{21–23} that correct description of the formation of a DNA double helix requires consideration of intrinsic polymorphism of H-bonding of canonical base pairs which arises from a bistable, pyramidal structure of amino-substituted nitrous bases. Calculation of oligonucleotide double strands in the gas phase and in pure water solution have demonstrated the existence of rather large “propeller-like” and “steplike” deformations of H-bonding base pairs in double helix stacking conditions. It is this initial nonplanar structure of canonical DNA base pairs that initiates their noncoplanar packing in the structure of double helix and, hence, is responsible for the dependence of the form of a DNA helix on the nucleotide sequence. Based on these results we can conclude that probabilities of charge transfer in DNA with due regard for real distortions of base pairing in the structure of double helices will greatly differ from those obtained in studies with the idealized model of planar base pairs.

In conclusion we note that the parameters (matrix elements) used by us approximate and point out some physical factors which also can lead to their deviation from our parameter values (i.e., with a specific substrate, environment, etc.). In a real nanobiochip the complementary DNA strand can come in contact with electrodes. To rule out this possibility one should take measurements with several

identical chips in parallel. These difficulties can be overcome in calculations of a specific laboratory nanobiochip. Such studies which we are planning to carry out in the future will more correctly describe the dependence of the electron tunneling rate in a DNA molecule with a nucleotide sequence under study.

References

- (1) Holloway, A. J.; van Laar, K. R.; Tothil, R. W.; David, D. L. *Nature Genet.* **2002**, *32*, 481–489.
- (2) Mantripragada, K. K.; Buckley, P. G.; Diaz de Stahl; Dumanski, J. P. *Trends Genet.* **2004**, *20*, No. 2.
- (3) Piunno, P. A. E.; Krull, U. J.; Hudson, R. H. E.; Damha, M. J.; Cohen, H. *Anal. Chem.* **1995**, *67*, 2635.
- (4) Kelley, S. O.; Barton, J. K.; Jackson, N. M.; Hill, M. G. *Bioconjugate Chem.* **1997**, *8*, 31.
- (5) Wong, E. L. S.; Googing, J. J. *Anal. Chem.* **2003**, *75*, 3845.
- (6) Xu, C.; He, P. G.; Fang, Y. Z. *Anal. Chim. Acta* **2000**, *411*, 31.
- (7) Millan, K. M.; Mikkelsen, S. R. *Anal. Chem.* **1993**, *65*, 2317.
- (8) Hashimoto, K.; Ito, K.; Ishimori, Y. *Anal. Chem.* **1994**, *66*, 3830.
- (9) Wong, E. L. S.; Mearns, F. J.; Gooding, J. J. *Sens. Actuators, B* **2005**, 111–112, 515.
- (10) Su, X. D.; Robelek, R.; Wu, Y. J.; Wang, G. Y.; Knoll, W. *Anal. Chem.* **2004**, *76*, 489.
- (11) Voityuk, A. A.; Rösch, N.; Bixon, M.; Jortner, J. *J. Phys. Chem. B* **2000**, *104*, 9740.
- (12) Jortner, J.; Bixon, M.; Voityuk, A. A.; Rösch, N. *J. Phys. Chem. B* **2002**, *106*, 7599.
- (13) Lewis, F. D.; Wu, Y. *J. Photochem. Photobiol.* **2001**, *2*, 1.
- (14) van Zalinge, H.; Schiffrin, D. J.; Bates, A. D.; Haiss, W.; Ulstrup, J.; Nichols, R. *Chem. Phys. Chem.* **2006**, *7*, 94–98.
- (15) Mujica, V.; Kemp, M.; Ratner, M. A. *J. Chem. Phys.* **1994**, *101*, 6849.
- (16) Lakhno, V. D.; Sultanov, V. B.; Pettitt, B. M. *Chem. Phys. Lett.* **2004**, *400*, 47.
- (17) Wilson, C. C. *Nucleic Acid. Res.* **1987**, *15*, 8577.
- (18) El-Hassen, M. A.; Calladine, C. R. *J. Mol. Biol.* **1996**, *259*, 95.
- (19) Jursa, J.; Kypr, J. *Gen. Physiol. Biophys.* **1993**, *12*, 401.
- (20) Heinemann, U.; Alings, C.; Hahn, M. *Biophys. Chem.* **1994**, *50*, 157.
- (21) Kabanov, A. V.; Komarov, V. M. *Int. J. Quantum Chem.* **2002**, *88*, 579.
- (22) Komarov, V. M. *J. Biol. Phys.* **1999**, *24*, 167.
- (23) Komarov, V. M. *Biophysics* **1998**, *43*, 917.

Metal–Molecule Interactions To Produce Hydrogen: What Do They Have in Common?†

Job Valdespino-Saenz, Alfredo Guevara-García, Marco-Vinicio Vázquez, and Ana Martínez*

Instituto de Investigaciones en Materiales, Universidad Nacional Autónoma de México, Circuito Exterior s/n, C. U., P.O. Box 70-360, Coyoacán 04510, México, D. F. México

Received December 13, 2006

Abstract: The main purpose of this work is to study metal–molecule interactions that can lead to the production of molecular hydrogen. Two systems were chosen for this analysis: yttrium atom and clusters interacting with the simple electron donor ammonia (NH₃) and copper atoms and ions with imidazole. For yttrium with ammonia as well as for copper with imidazole there is a charge-transfer process from the metal to the molecule that promotes the dissociation of the hydrogen atoms.

Introduction

Human population growth has severe consequences for the environment. One negative factor is pollution caused by the emission of several gases related to the widespread use of carbon-containing fuels. The emission of greenhouse gases into the atmosphere is increasing due to a constantly growing world energy demand and the amount of fossil fuels being burned in order to meet that demand. The development of zero emission energy production systems is one of the major goals of many research efforts. The most attractive option with regards to sustainability is the use of molecular hydrogen as a fuel.¹

It is well-known that in order to be sustainable, the hydrogen production process must be water based, with no consumption of raw materials and with zero emissions of greenhouse gases. Electrolysis at low temperature is one of the options, but, for the time being, that is more expensive than the production of hydrogen from natural gas. Making hydrogen using steam has two disadvantages, namely, that the process consumes natural gas, another carbon-based nonrenewable source, and produces carbon dioxide. Recently, the manufacture of hydrogen by electrolysis at high temperature² has been reported. It is a promising idea that could be used in the Icelandic geothermal context; however, the

appropriate heat exchangers necessary for this process are still under development.

Nevertheless, the production of hydrogen from water is not the only available option. There are many chemical interactions that have hydrogen as one of the main products of the reaction. Heterogeneous catalysis is one of several procedures that can be used for this end. For the further development of heterogeneous catalysis, the analysis of the nature of the interaction between small molecules or radicals and transition metals is very important. For this reason, the reactivity of transition metals with numerous molecules and radicals has been the subject of several studies.^{3–17} Many of these studies focused on the reaction of transition-metal atoms and clusters, and it was considered that the understanding of their reactivity with small molecules could shed light upon several mechanisms of surface chemistry and provide details of complicated processes associated with heterogeneous catalysis. By considering only the processes that produce hydrogen, we could arrive at the knowledge necessary for the development of a water independent hydrogen fuel technology.

Concerning the interactions of transition-metal atoms and clusters with molecules that produce hydrogen, there have been several studies reported recently. For example, some groups have studied the dehydrogenation reactions of organic molecules with Nb clusters and cluster cations.^{18–21} In particular, ethene chemistry is well characterized for neutral transition-metal atoms reactions in the gas phase. These reactions with niobium atoms and clusters indicate dehydrogenation of ethene for all clusters, the extent of the

† Dedicated to Dennis R. Salahub on the occasion of his 60th birthday.

* Corresponding author phone: (5255) 56 22 45 96; fax: (5255) 56 16 12 51; e-mail: martina@iim.unam.mx.

reactivity depending on cluster size.²¹ The reactions of Nb clusters with ethane lead to partially or fully dehydrogenated products, involving mechanistic steps that are generally barrierless. On the other hand, the dehydrogenation reaction by a bare Nb atom and a cation²² proceeds by the formation of a molecular hydrogen complex that releases hydrogen without an energy barrier.

Other studies consider different aspects, but they are also related to the formation of molecular hydrogen. For example, DNA bases and their interaction with metal atoms have been studied in order to analyze structural information that could be relevant to the knowledge of metal effects on biological processes.²³ Despite the fact that the subject of these studies is not the production of hydrogen, the results show that for guanine–Cu and uracil–Cu anionic, it is possible to produce the detachment of one electron from the anion and also the removal of one hydrogen atom, with the consequent formation of molecular hydrogen. This could happen because the vertical ionization energy of the anion is close to the dissociation energy of one hydrogen atom. Elsewhere, oxidative additions at the metal centers have been studied due to their importance in organometallic reactions in homogeneous catalysis.²⁴ The first observation of the yttrium imide (YNH) molecule in gas phase was made with laser vaporization of yttrium metal in a molecular beam, using an He/NH₃ mixture as a carrier gas.²⁵ In that study, the interaction of yttrium atoms with ammonia was examined, and it was reported that the reaction proceeds by the formation of a M–NH₃ molecular complex followed by an oxidative addition. The formation of an yttrium imide molecule (YNH) in the gas phase could also produce molecular hydrogen.

Within this framework, the main purpose of this work is to study metal–molecule interactions that can lead to the production of molecular hydrogen. Two systems were chosen for this analysis: yttrium atom and clusters interacting with the simple electron donor ammonia (NH₃) and copper atoms and ions with imidazole. The noncovalent interaction with metal ions present in the latter system is a simple model for a wide variety of nitrogen-containing heterocycles. Both systems contain a transition-metal atom with one unpaired electron. The idea is to find the relationship between the electronic structure and the reactivity of these systems, in search of the production of hydrogen molecules. With this objective, optimized geometries, net atomic charges, and molecular orbitals are reported for Y–NH₃, Y₂–NH₃, and Cu–(imidazole)_N (N = 1–3, neutral and anionic), and several reaction mechanisms are also analyzed.

Aromaticities computed via the HOMA indexes for the imidazole molecules are reported, in order to analyze the aromatic character of these systems. HOMA index can be used to estimate an aromatic character of π -electron systems (molecules, ions, or their fragments).

Computational Details

Density functional theory,^{26–28} as implemented in the suite of programs *Gaussian 03*,²⁹ has been used to carry out all calculations. The hybrid three parameters B3LYP^{30–32} functional and the LANL2DZ^{33–45} basis set were used to perform

complete optimizations of molecular geometries without symmetry constraints. Harmonic frequencies analyses^{36,37} allowed us to verify optimized minima.

Previous studies show that DFT reproduces equilibrium geometries and relative stabilities with hybrid functionals, which partially include the Hartree–Fock exchange energy. The results are in good agreement with those obtained using the Møller–Plesset perturbational theory at second order and basis sets of medium quality, such as 6-31G(d,p), and cc-pVDZ.^{38–40} For this reason, in this work, we are confident of the results obtained with B3LYP.

The number of isomers used in the initial stage of the study provided several initial geometries, which, in turn, allowed us to widely explore the potential energy surface, in search of the global minimum. Notwithstanding the difficulties associated with the localization of the ground states, we cannot exclude the possibility that the global minimum could be missed. Nonetheless, the number of initial geometries examined was large enough to reliably identify the global minima in each system.

To compute vertical electron detachment energies (VEDE) of anionic species and vertical ionization potentials of the neutrals, further single-point calculations were required. Formation energies for neutral and anionic species were calculated using zero-point corrected energies.

Although there is no universally accepted method of assigning electrostatic charges to atoms, and no experimental technique is actually available to measure them directly, in a former study, de Oliveira et al.⁴¹ reported the testing of the quality of charges obtained via the Mulliken and Bader population analysis methods. Those authors found a good agreement between the methods, taking into account the qualitative description of the atomic charges. Thus, in this paper, Mulliken atomic charges are used to discuss the qualitative behavior of the charge-transfer process.

The HOMA (harmonic oscillator model of aromaticity) method⁴² was used as reported by Krygowski.^{43–46} The bond lengths of the optimized structures were employed for the study of aromaticity with this model.

Visualization of the results was carried out using the Molekel^{47–49} and the Ball&Stick⁵⁰ packages.

Results and Discussion

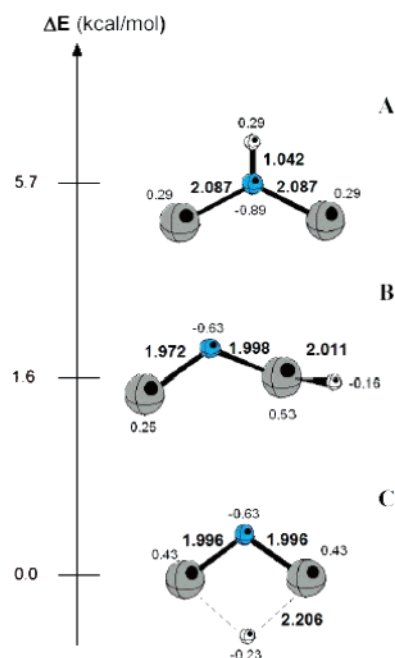
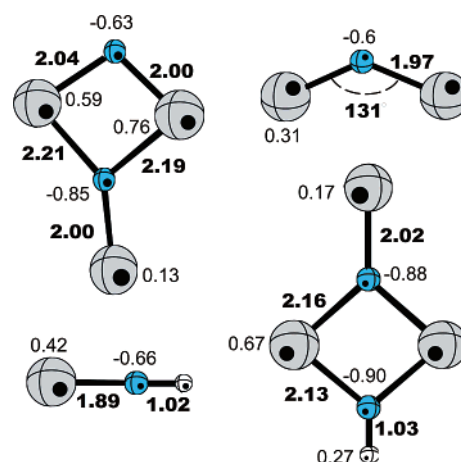
Y and Y₂ with Ammonia. Our study is primarily stimulated by experimental results, obtained some time ago,⁵¹ concerning the reactivity of the yttrium atom toward ammonia, at room temperature, in a fast-flow reactor. The yttrium nitride species from these experiments were detected in ionization but created as neutral. The results gave as very prominent species Y₂N, Y₃N₂, Y₄N₃, Y₅N₄, Y₆N₅, Y₇N₆, and Y₈N₇. Nevertheless, the authors of a previous study reported⁵² that the first step of the reaction is the formation of yttrium imide (YNH) through the oxidative addition of the N–H bond of ammonia and the elimination of molecular hydrogen. With this in mind, in this study, we analyze the interaction of ammonia with yttrium atom and dimer. In Table 1, we report the systems considered in this paper. The selection of these molecules is related to the available experimental informa-

Table 1. Vertical and Adiabatic Ionization Potentials (in eV) of the Systems Considered in This Work for the Interaction of Yttrium with Ammonia^a

	2S+1	calcd vertical IP (eV)	calcd adiabatic IP (eV)	exptl IP (eV)
Y ₂	5	5.07	5.04	4.98
YNH	2	5.95	5.94	5.84
YN	1	6.38	6.37	~6.4
A Y ₂ NH	1	5.41	5.20	5.5
B Y ₂ NH	1	5.64	5.21	5.5
C Y ₂ NH	3	5.16	5.11	5.5
Y ₂ N ² B ₂	2	5.30	5.20	4.4
Y ₂ N ² B ₁	2	4.58	4.46	4.4
Y ₃ N ₂ H	3	4.74		
Y ₃ N ₂	2	4.54	4.50	4.27

^a Experimental available information is also shown (Simard, private communication).

tion, since we used the ionization potentials to validate the results. In Table 1, vertical and adiabatic ionization potentials for the most stable structures are reported. Available experimental results are also shown. Experimentally, ionization potentials are always vertical. It may happen that they correspond to adiabatic when there is a major change in structures, but this is not the case for these systems. As may be observed, theoretical values are in good agreement with experimental results, except for Y₂N (²B₂ electronic state). The reason for this disagreement between experimental and calculated ionization potentials can be that the excitation arise from high lying vibrational states or low lying electronic states. The observed ionization potential value is smaller than the calculated one. This is possible because the Y₂N may be excited by the plasma originating from the laser vaporization source.⁵¹ The calculated vertical IP value for an excited state (17.1 kcal/mol less stable, ²B₁ electronic state) matches quite well with the experimental value (see Table 1). However, for further discussion we will use ²B₂ electronic state, given that it is more stable. Comparing experimental values with theoretical values in Table 1, it is readily apparent that, in most cases, the calculated ionization potential is overestimated. The only theoretical value that is underestimated with respect to the experiment is that for Y₂NH. For this system, other structures were considered for the optimization. In Figure 1, Y₂NH optimized structures are reported. In Table 1, the corresponding IP theoretical values are also reported. As may be observed, the promotion of an hydrogen atom toward the metal atom leads us to a more stable structure (by 4.1 kcal/mol). The ground state is a specie that contains one hydrogen atom interacting with two metal atoms. The hydrogen atomic charge is positive in the Y₂NH (imide), while it is negative for the other structures. The energy difference between these species is very small, and we may consider that we are at the limits of the calculation. Comparing the experimental IP with the theoretical values reported in Table 1 for these isomers, it is apparent that agreement is more or less the same for the three structures. With these results, it is not possible to say that one structure is more stable than the others. Further studies, now in progress, consider the energy barriers and possible transition states necessary to determine whether the hydrogen atom is

**Figure 1.** Relative stability between optimized Y₂NH isomers.**Figure 2.** Optimized geometries for the most stable isomers of the Y_mN_x and Y_mN_xH species. Bond lengths, in Å, and atomic charges, in au, are also shown.

bound to the metal or not. At this point, and for this study, the discussion will continue with Y₂NH (imide), since we would like to compare the results with those obtained for YNH and Y₃N₂H.

Optimized structures of the systems considered in this work are reported in Figures 1 and 2. All species are neutral. The first reaction of ammonia with the yttrium atom has been described as an oxidative addition to produce yttrium imide (YNH).^{17,25} The reported Y–N bond distance is 1.877 Å and 1.926 Å, for experimental and theoretical values, respectively.¹⁷ As can be seen in Figure 1, the optimized bond length (1.89 Å) is in very good agreement with the experimental value. In addition, the error in the calculated ionization energy is minor, and it is possible to say that the difference is small enough for a reliable assignment of YNH stable structure.

In Figures 1 and 2, Y₂N and Y₂NH are observed to have a bent structure, with a bond angle close to 130 degrees.

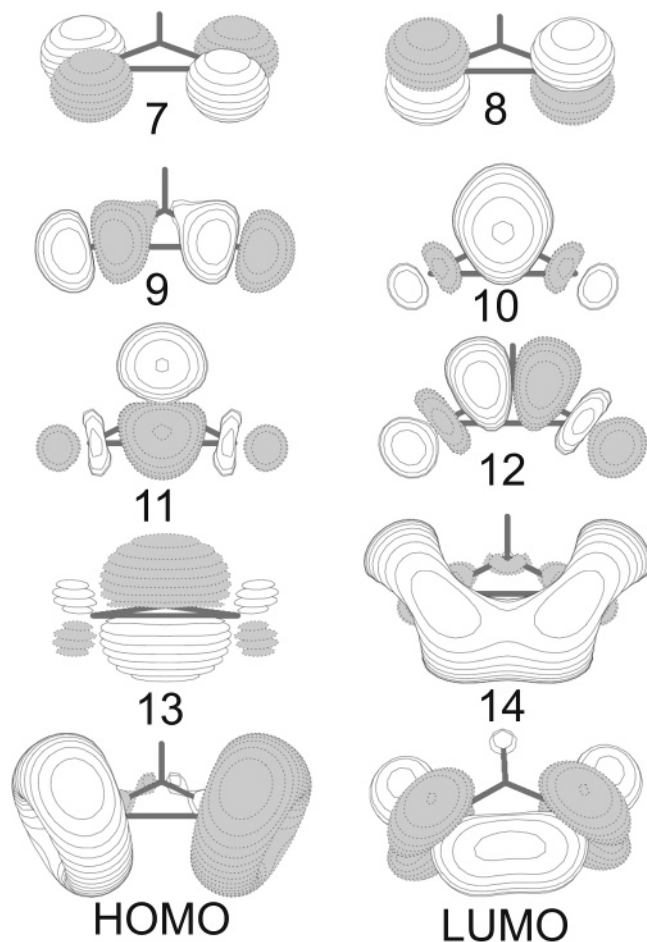


Figure 3. Molecular orbital pictures of Y_2NH .

Y–N bond length is shorter for Y_2N than for Y_2NH (imide). Molecular orbital pictures reported in Figures 3 and 4 (for Y_2NH and Y_2N , respectively) are quite similar. The exception is orbital 11. For Y_2NH , this orbital has an antibonding interaction between N and the metal atoms, and this explains the differences in the bond distances with respect to Y_2N . The bent structure is promoted by the bonding interaction of the yttrium d orbitals in both systems. HOMO are nonbonding orbitals located on the metal atoms, while the LUMO is a metal–metal antibonding orbital. As Figure 2 shows, this bent shape is observed in all of the systems. Moreover, with and without the hydrogen atom, the structures for Y_3N_2 and Y_3N_2H are very similar.

For all species, the analysis of the net atomic charges from the Mulliken population analyses indicates that metal atomic charges are positive, while nitrogen atomic charges are negative, as might be expected. There is a charge-transfer process from the Y atoms to either the NH moiety or the N atom. At the beginning of the reaction, it may be considered that there is a donation of the electron pairs from the ammonia molecule to the metal atoms. For this donation, the vacant orbitals of the yttrium atoms play a fundamental role. After this dative bond is formed, there is a back-donation to the p orbitals of N. The charge-transfer process from the Y atoms to the NH moiety promotes the dissociation of the ammonia molecule. It appears that the reaction

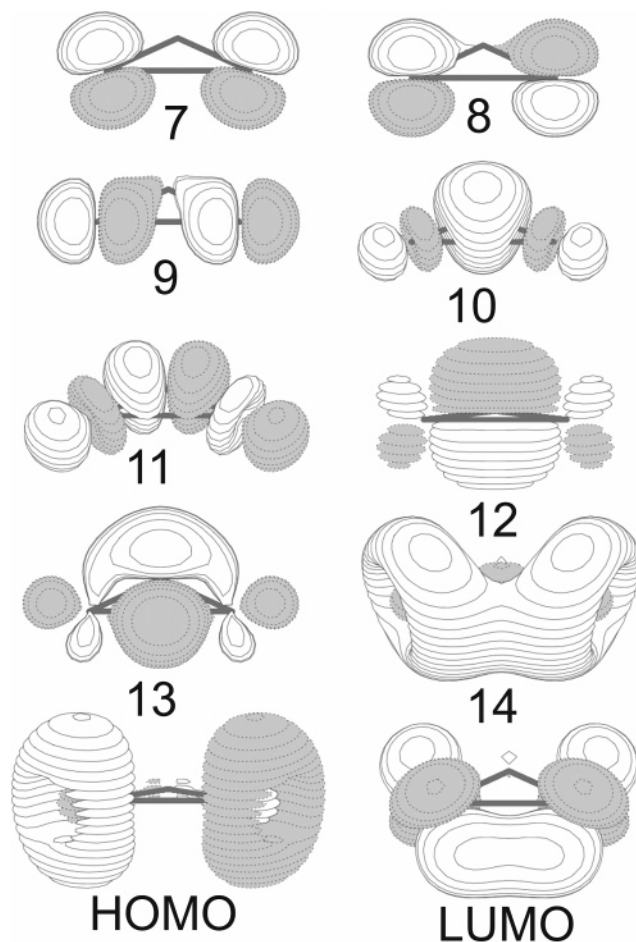


Figure 4. Molecular orbital pictures of Y_2N .

Table 2. Formation Energies (in kcal/mol) for the Reactions Schemes under Study, for the Interaction of Yttrium with Ammonia

	reaction	ΔE (kcal/mol)
A	$2 YNH \rightarrow 2 YN + H_2$	107.4
B	$Y + YNH \rightarrow Y_2NH$	–65.0
C	$Y + YNH \rightarrow Y_2N + H$	–10.7
D	$Y_2NH + YNH \rightarrow Y_3N_2 + H_2$	–69.8
E	$Y_2N + YNH \rightarrow Y_3N_2H$	–90.8
F	$Y_2N + YNH \rightarrow Y_3N_2 + H$	–19.7
G	$Y + Y \rightarrow Y_2$	–25.5
H	$Y + NH_3 \rightarrow YNH + H_2$	–30.6
I	$Y_2 + NH_3 \rightarrow Y_2NH + H_2$	–70.2

mechanism involves a charge-transfer process from the Y to the ammonia.

In order to analyze the reaction for the production of molecular hydrogen, Table 2 reports the binding energies for different reaction paths. For these analyses, only the molecules with experimental determination of the ionization potential were considered. The exception is Y_3N_2H , since the experimental value has not yet been determined, and we use the optimized structure as the product of one of the reactions.

The YNH molecule may perhaps interact with different reactants that could be present in the experiment. The first consideration for the reaction of yttrium imide is the

interaction between two equal molecules (scheme A in Table 2). The reaction produces YN and H₂. As may be observed, this reaction is not energetically feasible, given that the products of the reaction are less stable than the reactants by more than 100 kcal/mol. Yttrium imide could also interact with yttrium atoms, yielding Y₂NH or Y₂N and atomic hydrogen (schemes B and C, Table 2). In both cases, the products are more stable than the reactants. Comparing these two reactions, it is energetically more favorable to produce Y₂NH than Y₂N plus H.

After the formation of YNH, Y₂NH, and Y₂N, these three molecules could join up in such a way that they produce a cluster with three yttrium atoms, nitrogen, and with or without hydrogen, as may be observed in Table 2 (schemes D–F). Y₂NH and YNH react to form Y₃N₂ plus molecular hydrogen (path D). The stabilization energy is close to 70 kcal/mol, so the formation of molecular hydrogen seems to be energetically feasible. On the other hand, YNH interacts with Y₂N, and there are two possible paths for the reaction: the formation of Y₃N₂H (scheme E) or the production of Y₃N₂ and H (scheme F). The experimental ionization potential for Y₃N₂H has not been reported as yet, so we do not know if it is possible to obtain this product in the experiment. Comparing both reactions, we may say that it is energetically more stable to produce Y₃N₂H than Y₃N₂ and H.

It is not only the Y atom that is capable of reacting with ammonia to form H₂, given that Y₂ is also a potential reactant. We may suppose, however, that Y and ammonia are at the beginning of the reaction. The first interaction produces YNH and H₂ and also Y₂. Looking at the values in Table 2, it may be observed that the binding energies are similar for both reactions (−30.6 and −25.5 kcal/mol, for the formation of YNH and Y₂, respectively). After this first interaction, ammonia, Y, Y₂, and YNH could be present in the reactor. The dimer can interact with ammonia to form Y₂NH and H₂; yttrium could react with YNH to form Y₂NH (schemes I and B, respectively), and, once again, the binding energies for these two processes are comparable. In Figure 5, the scheme of the reaction between Y₂ and ammonia is reported. As may be observed, there is a first approximation of the ammonia molecule to one of the metal atoms, followed by the formation of Y₂NH and H₂. The energy differences indicate that both interactions are feasible, since the products are more stable than the reactants. The most probable reaction is the formation of Y₂NH and H₂, because H₂ is a relatively stable molecule. Comparing this reaction with the formation of Y₂NH, starting from Y and YNH (path B), it is possible to say that the stability is fairly similar. If Y, Y₂, and YNH are together in the experiment with ammonia, it is probable that Y₂NH will be formed, with the consequent production of H₂.

From all these reactions, it is possible to conclude that YNH could react with Y₂NH to produce H₂ and that the yttrium dimer is a possible reactant also, producing molecular hydrogen and Y₂NH. These results consider that ammonia is the limiting reactant. If ammonia is in excess, we should consider other interactions with ammonia as we did in a previous study.⁵² In that prior report, experimentally and

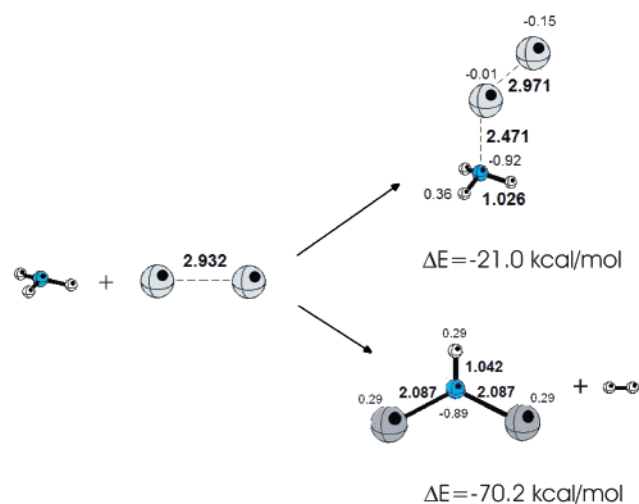
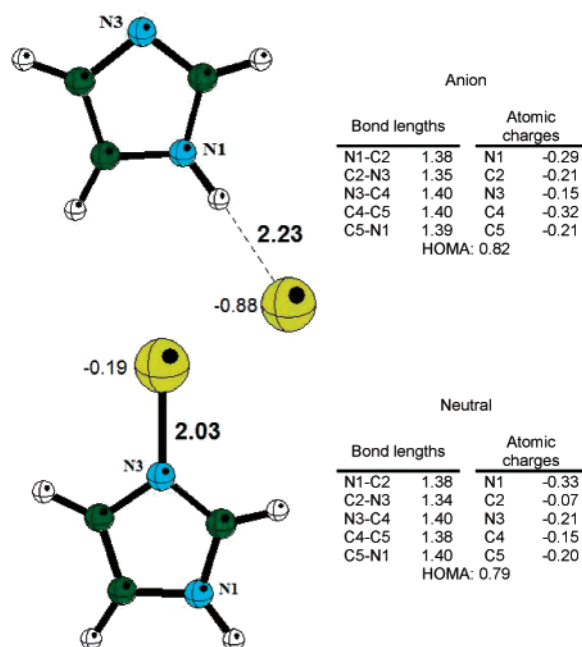


Figure 5. Reaction between NH₃ and Y₂. Two possible paths, one with NH₃ simply adsorbed to Y₂, and the other with H₂ production. Bond lengths are in Å, and atomic charges in au are also shown.

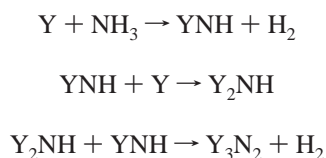
theoretically, we concluded that yttrium imide reacts with ammonia to form a species with the general formula YNH(NH₃)_{*n*}. DFT calculations revealed evidence supporting the dissociative absorption of NH₃ by YNH to form Y(NH₂)₂. This diamide specie can absorb additional NH₃ molecules to form Y(NH₂)₂NH₃, Y(NH₂)₂(NH₃)₂, and Y(NH₂)₂(NH₃)₃. The diamide species are more stable than the imide complexes (YNH(NH₃)_{*n*}) by approximately 30 kcal/mol. These stabilization energies are similar to the energy differences reported in Table 2 for the interactions between Y atoms to form Y₂; however, the formation of the diamide species is energetically less favorable than the formation of Y₂NH (from Y₂ plus NH₃), Y₃N₂ (from Y₂NH plus YNH), and Y₃N₂H (from Y₂N and YNH) (see Table 2). In accordance with that stated up to this point, oxidative addition is the first step of the reaction of the yttrium atom with ammonia to form the imide species. Yttrium atoms could also interact and yttrium dimers will be formed, since the binding energies are similar (−30.6 and −25.5 kcal/mol). If ammonia is the limiting reactant, it is most probable that YNH will react with Y, Y₂NH, and Y₂N, as may be observed in Table 2. If Y₂ is already formed, then the addition of one ammonia molecule to Y₂ to form Y₂NH + H₂ will occur. If the dimer is not formed because ammonia is in excess and the most probable reaction is the formation of YNH, then we may consider that the sequential addition of three further NH₃ molecules to YNH, in order to produce the diamide species, is a possible reaction. Nonetheless, the formation of the diamide species is energetically less favorable, so it is possible to say that, in the presence of YNH, Y, Y₂, and ammonia, the most energetically favorable reactions include the formation of Y₂NH and H₂.

Currently, the optimum reactions for the production of H₂ are with Y₂NH and YNH (path D in Table 2) and Y₂ with ammonia (path I). YNH could also react with ammonia molecules to form the diamide species. To avoid competition with the diamide formation, it is preferable to have ammonia as the limiting reactant. If this is the case, it is possible to control the experiment in order to have only the following

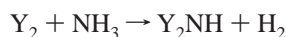
Table 3. Anionic and Neutral C₃H₄N₂Cu Optimized Geometries^a

^a Bond lengths are in Å, atomic charges in au.

reactions that are energetically viable:

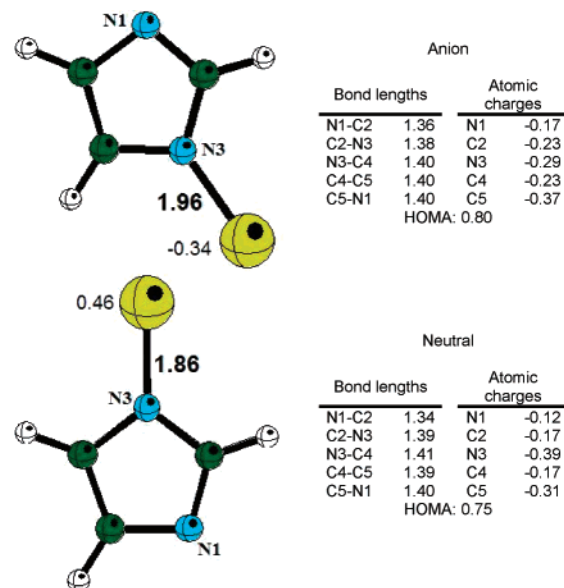


If the production of Y₂ is controlled, then it is possible to obtain molecular hydrogen through the following reaction:



The nature of the relationship between the size of the metal cluster and the reactivity of these clusters with ammonia is still an open question, and further calculations are in progress in an attempt to find an answer.

Cu–(imidazole)_N (N = 1–3). Imidazole has a five-membered planar ring structure. Two p electrons are located on N1; N3 and the three carbon atoms provide one p electron each to form a sextet aromatic π system. Additionally, N3 has a lone pair of electrons in the plane of the molecule. Consequently, imidazole has multiple binding sites and could interact with atoms or molecules as an aromatic π ligand or as a simple σ ligand.⁵³ In this study, the interaction of imidazole molecules with copper atoms is analyzed (neutral and anionic). The study of the anionic species is important because we would like to know if it is possible to obtain molecular hydrogen from these compounds. Given that there is an electronic repulsion between the copper atom and the imidazole molecule in the Cu–imidazole (neutral) system, we may consider that this electronic repulsion will be bigger in the anionic species. Other studies on anions, such as Cu–guanine and Cu–uracil,²³ conjectured that it could be possible to produce the dissociation of one hydrogen atom

Table 4. Anionic and Neutral C₃H₃N₂Cu Optimized Geometries^a

^a Bond lengths are in Å, atomic charges in au.

Table 5. Reactions of Cu–(imidazole)_N Species with H₂ Production^a

reaction	ΔE (kcal/mol)
I 2 C ₃ H ₄ N ₂ Cu → 2 C ₃ H ₃ N ₂ Cu + H ₂	9.3
II 2(C ₃ H ₄ N ₂ Cu) ⁻¹ → 2(C ₃ H ₃ N ₂ Cu) ⁻¹ + H ₂	-12.8
III (C ₃ H ₄ N ₂) ₂ Cu → (C ₃ H ₃ N ₂) ₂ Cu + H ₂	7.0
IV [(C ₃ H ₄ N ₂) ₂ Cu] ⁻¹ → [(C ₃ H ₃ N ₂) ₂ Cu] ⁻¹ + H ₂	-48.9
V (C ₃ H ₄ N ₂) ₃ Cu → (C ₃ H ₄ N ₂) ₂ Cu(C ₃ H ₂ N ₂) + H ₂	14.5
VI [(C ₃ H ₄ N ₂) ₃ Cu] ⁻¹ → [(C ₃ H ₄ N ₂) ₂ Cu(C ₃ H ₂ N ₂)] ⁻¹ + H ₂	-32.9

^a Reaction energies are in kcal/mol.

from these species. According to this thesis, it is necessary that we study the neutral and anionic Cu–(imidazole)_N compounds, in order to ascertain whether the dissociation of hydrogen is energetically favorable.

Table 3 reports the optimized structure of Cu–imidazole (neutral and anionic). Bond lengths and atomic charges are also shown. In a previous work, Wang et al.⁵⁴ reported an experimental and theoretical study of Al and Cu–imidazole, neutral and cationic. They produced Al and Cu–imidazole in laser-vaporization supersonic molecular beams, determined the zero electron kinetic energy (ZEKE) spectrum, and used the second-order Moller–Plesset (MP2) theory to perform a theoretical study. The σ structure was found to be more stable than the π structure. The weakness of this bond between Cu and imidazole is attributed to the antibonding (HOMO) interaction and the electron repulsion between the N lone-pairs and the Cu 4s electrons. Comparing the optimized structures for Cu–imidazole at the MP2 level with the structure that we obtained with B3LYP and LANL2DZ (see Table 3), it may be said that they are in good agreement. The optimized Cu–N bond distance is 1.978 and 2.03 Å, for MP2 and B3LYP, in that order. The electronic state is the same (²A'). This comparison is useful for validating our

Table 6. Anionic (A) and Neutral (B) (C₃H₄N₂)₂Cu Optimized Geometries^a

A. Anion				B. Neutral			
I		Atomic charges		I		Atomic charges	
Bond lengths		N1	-0.14	Bond lengths		N1	-0.09
N1-C2	1.35	C2	-0.20	N1-C2	1.34	C2	-0.21
C2-N3	1.38	N3	-0.31	C2-N3	1.38	N3	-0.24
N3-C4	1.39	C4	-0.21	N3-C4	1.40	C4	-0.32
C4-C5	1.39	C5	-0.31	C4-C5	1.39	C5	-0.32
C5-N1	1.40			C5-N1	1.40		
HOMA: 0.81				HOMA: 0.80			
II		Atomic charges		II		Atomic charges	
Bond lengths		N1	-0.14	Bond lengths		N1	-0.14
N1-C2	1.35	C2	-0.21	C2-N3	1.38	C2	-0.21
C2-N3	1.38	N3	-0.31	N3-C4	1.40	N3	-0.24
N3-C4	1.39	C4	-0.21	C4-C5	1.38	C4	-0.32
C4-C5	1.39	C5	-0.31	C5-N1	1.40	C5	-0.22
C5-N1	1.40			HOMA: 0.79			
HOMA: 0.81							

H-Cu-H-N3 : 118.7°

H-Cu-N1-C2 : 0.0°
N1-H-C2-N3 : -180.0°

^a Bond lengths are in Å, atomic charges in au.**Table 7.** Anionic (A) and Neutral (B) (C₃H₃N₂)₂Cu Optimized Geometries^a

A. Anion				B. Neutral			
I, II		Atomic charges		I, II		Atomic charges	
Bond lengths		N1	-0.34	Bond lengths		N1	-0.36
N1-C2	1.38	C2	-0.23	N1-C2	1.42	C2	-0.13
C2-N3	1.36	N3	-0.16	C2-N3	1.35	N3	-0.10
N3-C4	1.40	C4	-0.36	N3-C4	1.39	C4	-0.27
C4-C5	1.40	C5	-0.22	C4-C5	1.43	C5	-0.16
C5-N1	1.40			C5-N1	1.37		
HOMA: 0.76				HOMA: 0.75			

N1-Cu-N1 : 180.0°
N1-Cu-N1-C2 (I → II) : -128.2°
N1-Cu-N1-C2 (II → I) : 37.8°

N1-Cu-N1 : 180.0°
C2-N1-Cu-C2 : 179.8°

^a Bond lengths are in Å, atomic charges in au.

methodology, since the MP2 calculations agree with the experimental results that they also reported.

After this validation, we can compare the bond distances shown in Table 3 for the neutral and the anionic species. The bond length is shorter for the neutral than for the anionic. The electron repulsion between the N lone-pairs and the Cu 4s electrons is higher in the anion, due to the fact that the extra electron is located on the metal atom. This corresponds with the values for the electron affinity, given that, for copper, it is higher than for the imidazole. The negative metal

atom is moved from the nitrogen atom in the neutral to an hydrogen atom in the anion.

In order to analyze the effect of the dissociation of one hydrogen atom, in Table 4, the optimized structures for (Cu–imidazole)–H compounds (C₃H₄N₂Cu, neutral and anionic) are reported. As may be observed, when the hydrogen atom is removed, the Cu–N bond distance shortens in both systems, neutral and anionic. The electron repulsion is reduced because the metal atom is less negative (for the neutral it becomes positive), and the extra electron of the

Table 8. Anionic (A) and Neutral (B) $(C_3H_4N_2)_3Cu$ Optimized Geometries

A. Anion				B. Neutral			
I, II		Atomic charges		I, II		Atomic charges	
Bond lengths				Bond lengths			
N1-C2	1.36	N1	-0.27	N1-C2	1.36	N1	-0.32
C2-N3	1.39	C2	-0.09	C2-N3	1.37	C2	-0.04
N3-C4	1.40	N3	-0.37	N3-C4	1.40	N3	-0.35
C4-C5	1.38	C4	-0.26	C4-C5	1.38	C4	-0.22
C5-N1	1.41	C5	-0.16	C5-N1	1.41	C5	-0.15
HOMA: 0.73				HOMA: 0.77			

III				III			
Bond lengths		Atomic charges		Bond lengths		Atomic charges	
Bond lengths				Bond lengths			
N1-C2	1.47	N1	-0.27	N1-C2	1.49	N1	-0.24
C2-N3	1.47	C2	-0.30	C2-N3	1.49	C2	-0.31
N3-C4	1.38	N3	-0.27	N3-C4	1.37	N3	-0.24
C4-C5	1.42	C4	-0.39	C4-C5	1.43	C4	-0.34
C5-N1	1.38	C5	-0.39	C5-N1	1.37	C5	-0.34
HOMA: 0.22				HOMA: 0.02			

N1-Cu-N1 :		153.8°	
C2-H-Cu :		113.1°	

N1-Cu-N1 :		151.0°	
N1-Cu-C2 (I→III) :		104.5°	

^a Bond lengths are in Å, atomic charges in au.

Table 9. Anionic (A) and Neutral (B) $(C_3H_4N_2)_2Cu(C_3H_2N_2)$ Optimized Geometries

A. Anion				B. Neutral			
I, II		Atomic charges		I, II		Atomic charges	
Bond lengths				Bond lengths			
N1-C2	1.35	N1	-0.22	N1-C2	1.35	N1	-0.32
C2-N3	1.38	C2	-0.03	C2-N3	1.37	C2	-0.02
N3-C4	1.40	N3	-0.37	N3-C4	1.40	N3	-0.35
C4-C5	1.39	C4	-0.26	C4-C5	1.38	C4	-0.22
C5-N1	1.40	C5	-0.24	C5-N1	1.40	C5	-0.16
HOMA: 0.79				HOMA: 0.80			

III				III			
Bond lengths		Atomic charges		Bond lengths		Atomic charges	
Bond lengths				Bond lengths			
N1-C2	1.40	N1	-0.39	N1-C2	1.36	N1	-0.26
C2-N3	1.40	C2	0.04	C2-N3	1.36	C2	0.08
N3-C4	1.40	N3	-0.45	N3-C4	1.40	N3	-0.26
C4-C5	1.41	C4	-0.37	C4-C5	1.41	C4	-0.35
C5-N1	1.40	C5	-0.38	C5-N1	1.40	C5	-0.35
HOMA: 0.67				HOMA: 0.81			

N1-Cu-N1 :		109.6°	
N1-Cu-C2 (I→III) :		140.9°	

^a Bond lengths are in Å, atomic charges in au.

anion is spread over the imidazole molecule. Therefore, the negative charge is mainly located on the carbon atoms instead of on the nitrogen atoms. Concerning the aromaticity, as the HOMA values indicate in Tables 3 and 4, the imidazole molecule is more aromatic in the anionic than in the neutral. The extra electron is responsible for this behavior.

With these structures we can analyze the reaction for the production of molecular hydrogen, as can be seen in Table 5. Considering the neutral systems, the dehydrogenation reaction to produce H_2 is energetically unfavorable. However, the formation of H_2 from Cu–imidazole anion is favorable (-12.8 kcal/mol).

The results for the species with one copper atom and two imidazole molecules are quite similar, as can be seen in

Tables 6 and 7. For the neutrals, the structures with and without two hydrogen atoms are planar, while, for the anions, the imidazole molecules are not in the same plane. Cu–N bond lengths are almost the same for the neutral and the anion Cu–(imidazole)₂–2H systems ($(C_3H_3N_2)_2Cu$), see Table 7), and these bonds are shorter than the same bonds of the Cu–(imidazole)₂ species. The atomic charge of the copper atom is negative for complexes with full imidazole molecules, as can be seen in Table 6, where the negative metal atom is oriented toward the positive hydrogen atoms. Conversely, copper atoms are positive on the Cu–(imidazole)₂–2H complexes. From this, we can infer that the positive metal atomic charge promotes the bond with the nitrogen atom (negatively charged). The aromaticity of

imidazole molecules on these species is more or less the same. The less aromatic compound is $\text{Cu}-(\text{imidazole})_2-2\text{H}$ neutral. Departing from these structures, we analyzed the dehydrogenation reaction in order to obtain H_2 . The results are reported in Table 5. It may be observed that the reaction for the anionic system is energetically favorable (-48.9 kcal/mol), whereas for the neutral, the products of the reaction are less stable than the reactants, by 7 kcal/mol.

In Tables 8 and 9, the most stable optimized structures of $\text{Cu}-(\text{imidazole})_3$ and $\text{Cu}-(\text{imidazole})_3-2\text{H}$ ($(\text{C}_3\text{H}_3\text{N}_2)_2\text{Cu}-(\text{C}_3\text{H}_2\text{N}_2)$, neutral and anionic) are reported. As can be seen, the results are similar to those for the optimized structures with one and two imidazole molecules. The most stable structures of $\text{Cu}-(\text{imidazole})_3$ (neutral and anionic) contain one isomer of the imidazole having two hydrogen atoms bonded to one carbon atom and nitrogen atoms that have no hydrogens. The interaction of copper and two imidazole molecules takes place on two negatively charged nitrogen atoms and, moreover, forms a "bridge" with two hydrogen atoms of the opposite imidazole molecule. When two hydrogen atoms are detached, the structures are planar and two N-H interactions are formed. The metal atom is connected to the three molecules, from one carbon atom and two nitrogen atoms. HOMA values indicate that the imidazole molecule that contains two hydrogen atoms bonded to a carbon atom is less aromatic, as could be anticipated from the bond distances. When one hydrogen atom is detached, in the neutral molecule, the HOMA values indicate that the aromaticity of the imidazole molecules is the same, while for the anionic it is different. One imidazole molecule situated in the middle is less aromatic than the others. In Table 5, it may be observed that the dehydrogenation reaction is energetically stable for the anion, but not for the neutral, as was found for the species with one and two imidazole molecules.

Comparing the formation energies for the three systems under study, we may say that the most favorable reaction is the one where the copper atom is more positive ($+0.33$ in $\text{Cu}-(\text{imidazole})_2-2\text{H}$). The formation energy is proportional to the positive charge of the copper atom on the dehydrogenated products. It appears that there is a charge-transfer process from the copper atom to the nitrogen atoms of the imidazole molecules. When this charge transfer is large, the interaction energy is similarly large. For the thermodynamically stable production of H_2 from $\text{Cu}-(\text{imidazole})_N$, the species must be anionic.

Conclusions

Two systems were considered for the study of metal-molecule interactions that can lead to the production of molecular hydrogen: yttrium atom and clusters interacting with the simple electron donor ammonia (NH_3) and copper atoms and ions with imidazole.

For yttrium with ammonia, oxidative addition is the first step of the reaction where the imide species is formed; however, yttrium atoms could also interact, forming yttrium dimers as a result. If ammonia is the limiting reactant, it is most probable that YNH will react with Y, Y_2NH , and Y_2N . If Y_2 is already formed, the addition of one ammonia

molecule to Y_2 to form $\text{Y}_2\text{NH} + \text{H}_2$ will occur. If the dimer is not formed, because ammonia is in excess and the most probable reaction then is the formation of YNH, we may consider that the sequential addition of three further NH_3 molecules to YNH, in order to produce the diamide species, is a possible reaction. To avoid competition with the diamide formation, it is preferable to have ammonia as the limiting reactant. From this analysis, it is possible to conclude that the optimum reactions for the production of H_2 are those with Y_2NH and YNH and Y_2 with ammonia.

For copper with imidazole, the dehydrogenation reaction is energetically stable for the anion but not for the neutral. For yttrium with ammonia as well as for copper with imidazole there is a charge-transfer process from the metal to the molecule that promotes the dissociation of the hydrogen atoms. Further studies are required if conclusions are to be drawn regarding the common characteristics necessary in the metal-molecule interactions, in order to produce molecular hydrogen. It is important that we learn more about the energetic barriers, the interaction of copper with ammonia, and also the interaction of yttrium with imidazole, in order to be able to make a complete comparison between these two systems. Calculations are in progress with a view to answering these questions and also in understanding the relationship between the reactivity and the size of the metal clusters.

Acknowledgment. This study was made possible due to funding supplied by DGAPA-PAPIIT, grant no. IN124602-3, and the Consejo Nacional de Ciencia y Tecnología (CONACyT) of Mexico, grant no. 69878, and the resources made available to us by the Instituto de Investigaciones en Materiales (IIM). Conversations with Benoit Simard from the Steacie Institute of Ottawa, Canada were invaluable in clarifying many aspects of this work. The authors would like to acknowledge Sara Jiménez Cortés and María Teresa Vázquez for their technical support and DGSCA/UNAM (México) for providing computer time.

References

- (1) Barbarossa, V.; Brutti, S.; Diamanti, M.; Sau, S.; De Maria, G. *Int. J. Hydrogen Energy* **2006**, *31*, 883–890.
- (2) Sigurvinsson, J.; Mansilla, C.; Arnason, B.; Botemps, A.; Maréchal, A.; Sigfusson, T. I.; Werkoff, F. *Energy Convers. Manage.* **2006**, *47*, 3543–3551.
- (3) Schilling, J. B.; Goddard, W. A., III; Beauchamp, J. L. *J. Am. Chem. Soc.* **1986**, *108*, 582–584.
- (4) Schilling, J. B.; Goddard, W. A., III; Beauchamp, J. L. *J. Am. Chem. Soc.* **1987**, *109*, 5573–5580.
- (5) Elkind, J. L.; Armentrout, P. B. *Inorg. Chem.* **1986**, *25*, 1078–1080. Armentrout, P. B.; Halle, L. F.; Beauchamp, J. L. *J. Chem. Phys.* **1982**, *76*, 2449–2457.
- (6) Knight, L. B., Jr.; Cobranchi, S. T.; Herlong, J.; Kirk, T.; Balasubramanian, K.; Das, K. K. *J. Chem. Phys.* **1990**, *92*, 2721–2732.
- (7) Geusic, M. E.; Morse, M. D.; Smalley, R. E. *J. Chem. Phys.* **1985**, *82*, 590–591.
- (8) Morse, M. D.; Geusic, M. E.; Heath, J. R.; Smalley, R. E. *J. Chem. Phys.* **1985**, *83*, 2293–2304.

- (9) Richtsmier, S. C.; Parks, E. K.; Liu, K.; Pobo, L. G.; Riley, R. E. *J. Chem. Phys.* **1985**, *82*, 3659–3665.
- (10) Whetten, R. L.; Zakin, M. R.; Cox, D. M.; Trevor, D. J.; Kaldor, A. *J. Chem. Phys.* **1986**, *85*, 1697–1698.
- (11) Low, J. J.; Goddard, W. A., III *Organometallics* **1986**, *5*, 609–622.
- (12) Bühl, M.; Kabrede, H. *J. Chem. Theory Comput.* **2006**, *2*, 1282–1290.
- (13) Balasubramanian, K.; Liao, M. Z. *J. Phys. Chem.* **1989**, *93*, 89–94.
- (14) Balasubramanian, K. *Int. J. Quantum Chem. Symp.* **1988**, *22*, 465–476.
- (15) Backwall, J. E.; Bjorkman, E. E.; Petterson, L.; Siegbahn, P. E. M. *J. Am. Chem. Soc.* **1985**, *107*, 7265–7267.
- (16) Das, K. K.; Balasubramanian, K. *J. Chem. Phys.* **1989**, *91*, 2433–2442.
- (17) Das, K. K.; Balasubramanian, K. *J. Chem. Phys.* **1990**, *93*, 6671–6675.
- (18) Zakin, M. R.; Cox, D. M.; Kaldor, A. *J. Phys. Chem.* **1987**, *91*, 5224–5228.
- (19) Zakin, M. R.; Brickman, R. O.; Cox, D. M.; Kaldor, A. *J. Chem. Phys.* **1988**, *88*, 5943–5947.
- (20) Berg, C.; Schindler, T.; Lammers, A.; Niedner-Schatteburg, G.; Bondybey, V. E. *J. Phys. Chem.* **1995**, *99*, 15497–15501.
- (21) Parnis, J. M.; Escobar-Cabrera, E.; Thompson, M. G. K.; Jacula, J. P.; Lafleur, R. D.; Guevara-Garcia, A.; Martínez, A.; Rayner, D. M. *J. Phys. Chem. A* **2005**, *109*, 7046–7056.
- (22) Rivalta, I.; Russo, N.; Sicilia, E. *J. Mol. Struct. (THEOCHEM)* **2006**, *762*, 25–31.
- (23) Martínez, A. *J. Chem. Phys.* **2005**, *123*, 024311(1–9).
- (24) Spessard, G. O.; Miessler, G. L. *Organometallic Chemistry*; Prentice Hall: Upper Saddle River, NJ, 1996; pp 245–299.
- (25) Simard, B.; Jakubec, Z. *J. Chem. Phys.* **1999**, *111*, 1483–1493.
- (26) Kohn, W.; Becke, A. D.; Parr, R. G. *J. Phys. Chem.* **1996**, *100*, 12974–12980.
- (27) Hohenberg, P.; Kohn, W. *Phys. Rev.* **1964**, *136*, B864–B871.
- (28) Kohn, W.; Sham, L. J. *Phys. Rev.* **1965**, *140*, A1133–A1138.
- (29) Frisch, M. J.; Trucks, G. W.; Schlegel, H. B.; Scuseria, G. E.; Robb, M. A.; Cheeseman, J. R.; Montgomery, J. J. A.; Vreven, T.; Kudin, K. N.; Burant, J. C.; Millam, J. M.; Iyengar, S. S.; Tomasi, J.; Barone, V.; Mennucci, B.; Cossi, M.; Scalmani, G.; Rega, N.; Petersson, G. A.; Nakatsuji, H.; Hada, M.; Ehara, M.; Toyota, K.; Fukuda, R.; Hasegawa, J.; Ishida, M.; Nakajima, T.; Honda, Y.; Kitao, O.; Nakai, H.; Klene, M.; Li, X.; Knox, J. E.; Hratchian, H. P.; Cross, J. B.; Bakken, V.; Adamo, C.; Jaramillo, J.; Gomperts, R.; Stratmann, R. E.; Yazyev, O.; Austin, A. J.; Cammi, R.; Pomelli, C.; Ochterski, J. W.; Ayala, P. Y.; Morokuma, K.; Voth, G. A.; Salvador, P.; Dannenberg, J. J.; Zakrzewski, V. G.; Dapprich, S.; Daniels, A. D.; Strain, M. C.; Farkas, O.; Malick, D. K.; Rabuck, A. D.; Raghavachari, K.; Foresman, J. B.; Ortiz, J. V.; Cui, Q.; Baboul, A. G.; Clifford, S.; Cioslowski, J.; Stefanov, B. B.; Liu, G.; Liashenko, A.; Piskorz, P.; Komaromi, I.; Martin, R. L.; Fox, D. J.; Keith, T.; Al-Laham, M. A.; Peng, C. Y.; Nanayakkara, A.; Challacombe, M.; Gill, P. M. W.; Johnson, B.; Chen, W.; Wong, M. W.; Gonzalez, C.; Pople, J. A. Gaussian, Inc.: Wallingford CT, 2004.
- (30) Becke, A. D. *Phys. Rev. A* **1988**, *38*, 3098–3100.
- (31) Mielich, B.; Savin, A.; Stoll, H.; Preuss, H. *Chem. Phys. Lett.* **1989**, *157*, 200–206.
- (32) Lee, C.; Yang, W.; Parr, R. G. *Phys. Rev. B* **1988**, *37*, 785–789.
- (33) Hay, P. J.; Wadt, W. R. *J. Chem. Phys.* **1985**, *82*, 270–283.
- (34) Hay, P. J.; Wadt, W. R. *J. Chem. Phys.* **1985**, *82*, 299–310.
- (35) Wadt, W. R. *J. Chem. Phys.* **1985**, *82*, 284–298.
- (36) Foresman, J. B.; Frisch, A. E. *Exploring Chemistry with Electronic Structure Methods*, 2nd ed.; Gaussian, Inc.: Pittsburgh, PA, 1996; pp 61–90.
- (37) Ochterski, J. W. *Vibrational analysis in Gaussian*; Gaussian, Inc.: Pittsburgh, PA, 1999; p 10.
- (38) Shishkin, O. V.; Gorb, L.; Luzanov, A. V.; Elstner, M.; Suhai, S.; Leszczynski, J. *J. Mol. Struct. (THEOCHEM)* **2003**, *625*, 295–303.
- (39) Møller, C.; Plesset, M. S. *Phys. Rev.* **1934**, *46*, 618–622.
- (40) Saebo, S.; Almlof, J. *Chem. Phys. Lett.* **1989**, *154*, 83–89.
- (41) de Oliveira, A. E.; Guadagnini, P. H.; Haiduke, R. L. A.; Bruns, R. E. *J. Phys. Chem. A* **1999**, *103*, 4918–4924.
- (42) Kruszewski, J.; Krygowski, T. M. *Tetrahedron Lett.* **1972**, *13*, 3839–3842.
- (43) Krygowski, T. M. *J. Chem. Inf. Comput. Sci.* **1993**, *33*, 70–78.
- (44) Krygowski, T. M.; Anulewicz, R.; Kruszewski, J. *Acta Crystallogr., Sect. B: Struct. Sci.* **1983**, *B39*, 732–739.
- (45) Krygowski, T. M.; Cyranski, M. K. *Tetrahedron* **1996**, *52*, 10255–10264.
- (46) Krygowski, T. M.; Cyranski, M. K. *Chem. Rev.* **2001**, *101*, 1385–1420.
- (47) Schaftenaar, G.; Noordik, J. H. *J. Comput.-Aided. Mol. Des.* **2000**, *14*, 123–134 (Molden).
- (48) Flükiger, P.; Lüthi, H. P.; Portmann, S.; Weber, J. 4.3 ed.; Swiss Center for Scientific Computing: Manno, Switzerland, 2000–2002.
- (49) Portmann, S.; Lüthi, H. P. *Chimia* **2000**, *54*, 766–770.
- (50) Müller, N.; Falk, A. 3.75 ed.; Johannes Kepler University: Linz, 2000.
- (51) Simard, B., private communication.
- (52) (a) Simard, B.; Rayner, D. M.; Benichou, E.; Mireles, N.; Tenorio, F. J.; Martínez, A. *J. Phys. Chem. A* **2003**, *107*, 9099–9104. (b) Martínez, A. *J. Phys. Chem. A* **2006**, *110*, 1978–1981.
- (53) Sundberg, R. J.; Martin, R. B. *Chem. Rev.* **1974**, *74*, 471–517.
- (54) Wang, X.; Sup-Lee, J.; Yang, D. S. *J. Phys. Chem. A* **2006**, *110*, 12777–12784.

JCTC

Journal of Chemical Theory and Computation

Density Functional Static Dipole Polarizability and First-Hyperpolarizability Calculations of Na_n ($n = 2, 4, 6, 8$) Clusters Using an Approximate CPKS Method and its Comparison with MP2 Calculations[†]

K. B. Sophy,[‡] Patrizia Calaminici,[§] and Sourav Pal^{*,‡}

Theory Group, Physical Chemistry Division, National Chemical Laboratory, Pune 411 008, India, and Departamento de Química, CINVESTAV, Av. Instituto Politecnico Nacional 2508, A. P. 14-740 Mexico, D. F. 07000, Mexico

Received December 14, 2006

Abstract: We report the static dipole polarizability and first-hyperpolarizability of the sodium atom clusters, Na_n , $n = 2, 4, 6$ and 8 , using our recent implementation of a numerical-analytical approach to the coupled-perturbed Kohn–Sham (CPKS) equations in deMon2k. The calculations are reported for VWN and BP86 exchange–correlation functionals using Sadlej and TZVP-FIP1 basis sets which have been previously optimized for polarizability calculations. All-electron calculations were performed for the optimizations at the VWN/DZVP/A2 and PW86/DZVP/A2 levels. Comparisons are made with Hartree–Fock (HF) and MP2 benchmark calculations.

Introduction

Linear and nonlinear response electric properties, namely, dipole polarizability and dipole first-hyperpolarizabilities, of metal clusters have been of considerable interest over the past decade.¹ The size dependence of the optical properties^{2,3} makes the study of clusters even more interesting for understanding the correlation between the two. Clusters³ are aggregates of atoms or molecules, generally intermediate in size. Clusters of up to 40 atoms are considered to be small sized. The properties of small clusters vary so much with size and shape that their correlation with number of component particles is not simple. For large clusters the properties approach those of the corresponding bulk material. Molecules are characterized by having definite compositions and, in most cases, definite structures. The properties of clusters, on the other hand, depend on the number of atoms in the cluster and so does the most stable structure. Clusters thus differ from conventional molecules because of composition and structure. Clusters could be composed of any number

of particles of the same or different kind and can be further classified as homogeneous or heterogeneous clusters, respectively, and for most of them as the number of atoms increases, the number of stable structures grows rapidly. Clusters have drawn interest for several reasons. There are powerful ways to study them, both experimentally and theoretically. Clusters may give way to make altogether new kinds of materials, to carry out chemical reactions in new ways, and to gain understanding of the intermediate matter, which exist as one goes from molecules to crystals to bulk. All these makes cluster science a fascinating field, which not only enriches the fields around it but also offers tantalizing possibilities for new materials and processes.

Metal clusters, in general, have been studied to a reasonable extent.⁴ However, the presence of a single valence electron makes the alkali metal clusters the simplest metal cluster, and, therefore, it has been used as a prototype system for understanding the size effects in metal clusters. Here, we would concentrate on sodium clusters of up to 8 atoms. Polarizabilities for the sodium clusters have been reported using theory^{5–13,16} as well as experiments.^{14–17} Guan et al. (ref 12 and references therein) have done all-electron density functional calculations for Na_n ($n = 1–6$) clusters using local and gradient-corrected functionals. They have discussed several popular models for studying polarizability of clusters

[†] Dedicated to Dennis R. Salahub on the occasion of his 60th birthday.

* Corresponding author fax: 91-20-25902636; e-mail: s.pal@ncl.res.in.

[‡] National Chemical Laboratory.

[§] CINVESTAV.

spanning the simplest and oldest conducting sphere model for studying the clusters to the free electron model used for studying the bulk alkali metals. Guan et al. have also mentioned about the quantum mechanical jellium sphere approximation differing from the classical sphere model due to the fact that the quantum mechanical density extends beyond the radius of the classical sphere, thus the effective sphere being larger.

In this paper, we will study the correlation of response electric properties with size for the homonuclear alkali metal clusters of sodium using an approximate formalism proposed by us earlier.^{18–20} We study the dipole polarizability and the first-hyperpolarizability of the even number of Na atom clusters using local density approximation (LDA) and generalized gradient approximation (GGA) based exchange-correlation functionals in the presence of an external homogeneous static electric field perturbation. We will also discuss the effect of electron correlation on the polarizabilities. We have done an all-electron calculation for the optimizations as well as for the response properties. Calculations, that consider all the electrons in the cluster, are not very common. This is especially the case for ab initio calculations. There are some all-electron optimizations available using the DFT.^{12,13}

The paper is organized in the following manner. The theoretical methods used and the computational and technical details of our calculations are described in the following section. We will discuss our results in section 3 and summarize our conclusions in section 4. Unless otherwise stated, we use atomic units throughout this paper.

Theoretical Methods and Computational and Technical Details

A. Theory. DFT^{21,22} has been widely used for molecular response property calculations. Response property of molecule is the response of the molecule to some kind of perturbation. For an external perturbation the molecular energy has a dependence on the perturbation and can be expanded as a Taylor series expansion. In the presence of a static electric field perturbation, the energy expansion becomes

$$E(F) = E(0) - \sum_i \mu_i F_i - \frac{1}{2} \sum_{i,j} \alpha_{ij} F_i F_j - \frac{1}{6} \sum_{i,j,k} \beta_{ijk} F_i F_j F_k - \dots \quad (1)$$

where $i, j,$ and k are summation indices each spanning the $x, y,$ and z direction, the first term is the energy of the molecule in the absence of the electric field perturbation, F , the second term, gives the dipole moment, the third term gives the dipole polarizability, the fourth term gives the dipole first-hyperpolarizability, and so on

Alternatively, the field dependent dipole moment in turn can be written as

$$\mu_i(F) = \mu_i + \sum_j \alpha_{ij} F_j + \frac{1}{2} \sum_{j,k} \beta_{ijk} F_j F_k + \dots \quad (2)$$

where $i, j,$ and k are the $x, y,$ and z directions, $\mu_i, \alpha_{ij},$ and β_{ijk} are the component of the permanent dipole moment, dipole

polarizability, and the dipole first-hyperpolarizability, respectively, and so on

These molecular electric response properties can be obtained by explicitly obtaining the derivatives of energy with respect to the perturbation, i.e., analytically using the coupled Kohn–Sham method^{23–28} or by doing a least-squares fit to a polynomial,²⁹ or by using a numerical finite-field method. Choosing the finite field values symmetrically (e.g. 0.001 au, like we have chosen in this work), the next highest contamination in the numerical procedure can be eliminated, thus ensuring more numerical stability of the results. However, the precision in the calculation of energies limits the size of the field value. In the analytical response approach, the CPKS equations need to be solved to obtain the response of the electron density in terms of the derivative of the molecular orbital coefficients. The CPKS matrix equations are basically the derivative of the perturbed KS operator matrix equations with respect to the electric field perturbation, which means that the Hamiltonian has a dependence on the electric field and can be written as

$$H(F) = H_0 + \mu F \quad (3)$$

where the first term is the unperturbed Hamiltonian, and the second term is the perturbation that is linear in field, F . We thus have a linear response term in the Hamiltonian. Solving the CPKS equations, we can obtain the perturbed density matrix. And, due to the variational nature of the DFT we can make use of the $(2n+1)$ rule for the energy derivative³⁰ which is a result of the Hellmann–Feynman theorem.^{31,32} As a consequence, the first-order response of the electron density which is the first-order change in the density can be used to obtain response properties up to the third order. This means that we can evaluate not only the dipole polarizability but also the dipole first-hyperpolarizability using this response of the electron density.

B. Computational and Technical Details. The linear combination of the Gaussian-type orbitals Kohn–Sham density functional theory (LCGTO-KS-DFT) method, as implemented in the program deMon2k,³³ was used to carry out all geometry optimizations and harmonic vibrational frequency calculations. The program uses the formalism of the Kohn–Sham equations³⁴ and analytic energy gradients for the structure optimizations. The exchange-correlation potential was numerically integrated on an adaptive grid.³⁵ The grid accuracy was set to 10^{-5} in all calculations. The Coulomb energy was calculated by the variational fitting procedure proposed by Dunlap, Connolly, and Sabin.^{36,37} For the fitting of the density, the *AUXIS* option with the auxiliary function set A2³⁸ was used in all the optimization calculations and the vibrational analysis calculation following the previous work of Calaminici et al.,¹³ which was found sufficient for the purpose. In order to localize different minima on the potential energy surface (PES), the structures of the studied sodium clusters have been optimized considering as starting points different initial geometries and multiplicities. In order to avoid spin contamination the calculations were performed with the restricted open shell Kohn–Sham (ROKS) method. The ROKS method in deMon2k is the DFT analog of the Rootaan’s open shell equations for HF theory; it means that

all coupled alpha and beta electrons occupy the same space orbital and that the corresponding close shell exchange-correlation potential is given as an average of the alpha and beta exchange-correlation potential. The calculations were performed in the LDA using the exchange-correlation contributions proposed by Vosko, Wilk, and Nusair³⁹ and employing all-electron basis sets.³⁸ The same functional was used for the frequency analysis in order to distinguish between minima and transition state on the potential energy surface (PES). Cluster optimizations were also carried out at the GGA using the same basis and auxiliary function set with the exchange-correlation functional of Perdew and Wang (PW86).^{40,41} A quasi-Newton method in internal redundant coordinates with analytic energy gradients was used for the structure optimization.⁴² The convergence was based on the Cartesian gradient and displacement vectors with a threshold of 10^{-4} and 10^{-3} au, respectively. For the sodium tetramer, the GGA calculation required tougher convergence criteria of 10^{-7} and 10^{-6} due to the fact that at this level of theory the PES of this system is extremely flat. A vibrational analysis was performed in order to discriminate between minima and transition states. The second derivatives were calculated by numerical differentiation (two-point finite difference) of the analytic energy gradients using a displacement of 0.001 au from the optimized geometry for all 3N coordinates. The harmonic frequencies were obtained by diagonalizing the mass-weighted Cartesian force constant matrix. The response property calculations were then freshly carried out for these ground-state Na cluster geometries.

We have used the 1.7 version⁴³ of deMon2k, in which we have incorporated a numerical-analytical CPKS method (a simplified approximation), earlier proposed by us.^{18–20} We use the POLAR keyword in the deMon2k program, which employs a finite field approximation to obtain dipole-based polarizabilities of molecules. This option in deMon2k leads to a series of calculations involving different electric field perturbations (namely, -0.001 and 0.001 , in atomic units) to the Hamiltonian around zero field value. Using these, we construct the derivative KS-operator matrix in the finite field approximation. The choice of the field strengths at an interval of 0.001 au could be justified by simply noting the difference between the calculated β value and the theoretical value of zero for Na_2 . We have used the field value of 0.001 au in our response calculations as the error in our β value of Na_2 was minimum for this interval, the error increased for any value around 0.001 au. A separate module has been introduced by us, into the deMon2k for carrying out the CPKS procedure so as to obtain the response of the electron density in terms of the perturbed coefficient matrix. The CPKS equation to be solved for obtaining the response of the coefficient matrix is

$$U'_{ia} = \frac{\sum_{\mu, \nu} C_{\mu i}^{\dagger} H'_{\mu \nu} C_{\nu a}}{(\epsilon_i - \epsilon_a)} \quad (4)$$

where the C and the ϵ are the coefficient matrix and the eigenvalues of the unperturbed DFT calculation. H' is the derivative KS-operator matrix (which in principle needs to

be constructed analytically for every iteration) constructed using the finite-difference 3-point formula for the first derivative just once for every direction. The U' matrix is related to the derivative coefficient matrix, C' , which we are interested in through the unperturbed coefficient matrix, C , as

$$C' = CU' \quad (5)$$

The CPKS module is thus used to obtain a single-step solution of the CPKS equations for each of the three, x , y , and z , directions by using our method of approximating the derivative KS-operator matrix for each direction and plugging in the equation for U' to obtain the respective derivative coefficient matrices. These are then used to obtain the derivative density matrices which are the response of the electron density in the three directions. We thus have three derivative density matrices. The polarizability is obtained as the trace of the product of the derivative density matrix for a direction a with the dipole moment integrals in direction b , where a and b span the x , y , and z directions, thus giving the corresponding polarizability component. Thus all the components of the polarizability tensor can be obtained using the derivative density matrix. The first hyperpolarizability which is the third derivative of energy with respect to the electric field can also be obtained as per the $(2n+1)$ rule.³⁰ The first-hyperpolarizability can be trivially obtained using the derivative KS-operator matrix in the MO basis and derivative coefficient matrix for all permutations thus obtaining each of the components of the hyperpolarizability tensor. The novelty of our method lies in the simple single-step solution to the CPKS equations which avoids the complicated algebra as well as expensive computational time that would be required to construct the analytic derivative KS-operator matrix involving the derivative of the exchange-correlation term. Also the derivative KS-operator matrix needs to be evaluated for every iteration. Our method circumvents this complication thus saving time and computational effort. It is highly advantageous for response property calculations involving large molecules or large basis sets or both.

We report the mean and anisotropic polarizability and mean first-hyperpolarizability values obtained using the respective tensor components. The mean polarizability was calculated from the polarizability components as

$$\bar{\alpha} = \frac{1}{3} (\alpha_{xx} + \alpha_{yy} + \alpha_{zz}) \quad (6)$$

and the polarizability anisotropy as

$$|\Delta\alpha|^2 = \frac{3\text{tr}\alpha^2 - (\text{tr}\alpha)^2}{2} \quad (\text{general axes}) \quad (7)$$

$$= \frac{1}{2} [(\alpha_{xx} - \alpha_{yy})^2 + (\alpha_{xx} - \alpha_{zz})^2 + (\alpha_{yy} - \alpha_{zz})^2] \quad (\text{principal axes}) \quad (8)$$

The orientationally averaged first-hyperpolarizability were obtained as

$$\beta_i = \frac{1}{3} \sum_k \beta_{ikk} \quad (9)$$

$$\beta = \sqrt{\beta_x^2 + \beta_y^2 + \beta_z^2} \quad (10)$$

It is well-known that a general characteristic required for basis sets to perform well for polarizability calculation is that they should contain diffuse functions.⁴⁴ An economical strategy for constructing these kinds of basis sets is to augment valence basis sets of reasonable good quality with additional polarization functions.^{45–48} We have chosen as valence basis a newly developed triple- ζ basis set (TZVP) which was optimized for gradient corrected DFT calculations.⁴⁹ The basis set was then augmented with three field-induced polarization (FIP) functions, two p and one d, which were derived following the work of Zeiss et al.⁴⁶ They derived the FIP function exponents from an analytic analysis of the field-induced charges in hydrogen orbitals. The exponents of the additional FIP functions have been presented already in ref 13. In order to avoid the contamination of the valence basis set with the diffuse p- and d-type Gaussians of the FIP functions, spherical basis functions are used in all the calculations. We have named the resulting basis set TZVP-FIP1. Our DFT response property calculations were done using the Sadlej⁴⁵ and TZVP-FIP1 basis sets with the *CARTESIAN* option for the orbitals. We did not employ the auxiliary basis for fitting the exchange-correlation functional in our response property calculations; i.e. the *VXCTYPE BASIS* option was used. The calculations were done using the LDA based VWN³⁹ and GGA based BP86^{50,41} functionals in the deMon2k for both the basis sets. This entire set of response calculations was repeated for both sets of Na cluster geometries. In our calculations we have chosen only closed shell Na clusters due to the fact that we have implemented the linear response approach in a numerical-analytical manner in the deMon2k only for closed shell cases. We have therefore used the restricted Kohn–Sham (RKS) scheme of calculation, where the grid accuracy of 10^{-6} au was used for the property calculations. The density convergence was set to 10^{-10} au in the HF and MP2 as well as DFT calculations. The HF and MP2 benchmark calculations were carried out using the GAMESS,⁵¹ and the DFT calculations were done using deMon2k program. The DFT optimized structures were used for the MP2 and the HF calculations. These properties are evaluated using the finite field method available in GAMESS for a finite field value of 0.001 au. The results are discussed in the following section.

Results and Discussion

A. Equilibrium Geometries. We report the ground-state structures of the even number of sodium atom clusters from dimer to octamer obtained using the VWN and PW86 (bond distances in parenthesis) functionals in Figure 1. The equilibrium structures obtained from both functionals are similar and show a general topological agreement with the earlier theoretical reports.^{6,7,52} All-electron type optimizations for the sodium clusters using GGA based functionals are available but scarce.^{12,13} We have carried out all-electron type optimization for both VWN as well as PW86 functionals in the present work.

The dimer bond distance is equal to 3.017 Å with both the optimizations, whereas the experimental value is 3.078

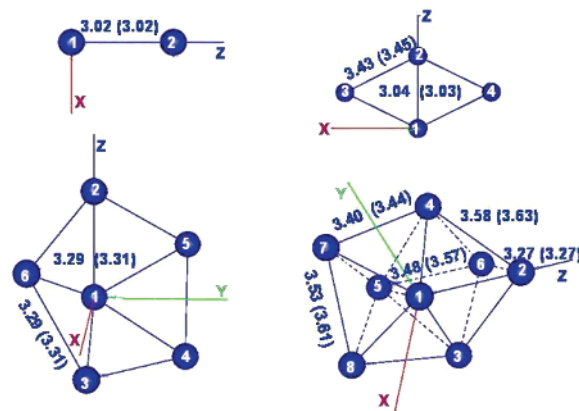


Figure 1. Calculated equilibrium geometries and the orientations used for the calculations of Na_n ($n = 2, 4, 6,$ and 8) clusters using the VWN and PW86 (in parentheses) functionals and A2/DZVP basis. Bond distances in Å.

Table 1. Harmonic Frequencies (in cm^{-1}) for the Normal Modes of Na_n ($n = 2, 4, 6,$ and 8) Clusters in Their Calculated Ground States Using VWN Functional and PW86 Functional with DZVP Basis Set and A2 Auxiliary Basis

cluster	VWN	PW86	expt
Na_2	161	160	159 ^a
Na_4	35, 37, 77, 98, 144, 162	6, 43, 76, 100, 141, 163	
Na_6	31, 31, 55, 75, 77, 91, 91, 102, 102, 142, 147, 147	36, 36, 46, 70, 72, 89, 89, 93, 94, 140, 141, 142	
Na_8	32, 49, 56, 60, 65, 68, 73, 77, 85, 96, 108, 114, 119, 129, 134, 137, 141, 180	31, 49, 50, 57, 60, 64, 68, 69, 72, 74, 101, 101, 106, 121, 127, 130, 130, 131	

^a From ref 54.

Å.⁵³ The geometries for the remaining clusters differ very slightly for the two optimizations. The ground-state structure of Na_4 is a D_{2h} rhombic structure, whereas the one for the Na_6 is a C_{5v} pentagonal pyramid. The equilibrium geometry for the Na_8 is a rather compact dicapped octahedral (DCO) structure.

B. Harmonic Frequencies. We have tabulated the normal modes for both sets of optimized structures of the Na clusters in Table 1. The absence of imaginary frequency was used to confirm that all the optimized structures were minima on the PES. The reported experimental frequency for the dimer is 159 cm^{-1} .⁵⁴ Our calculation for dimer using the VWN and PW86 functionals gave 161 and 160 cm^{-1} values, respectively, which are in good agreement with the experimental value. Earlier calculations of tetramer harmonic frequencies by Dahlseid et al.⁵⁵ at the configuration interaction-singles (CIS) level gave 27, 43, 73, 98, 130, and 150 as the frequencies. The qualitative trend for our harmonic frequencies in Table 1 is similar, except for the first frequency for the tetramer at the PW86 level which is small. It can be seen that the first few frequencies of the clusters are smaller in magnitude. This could be attributed to the extremely flat PES of the clusters which further complicates the distinction between the global and the local minima. This

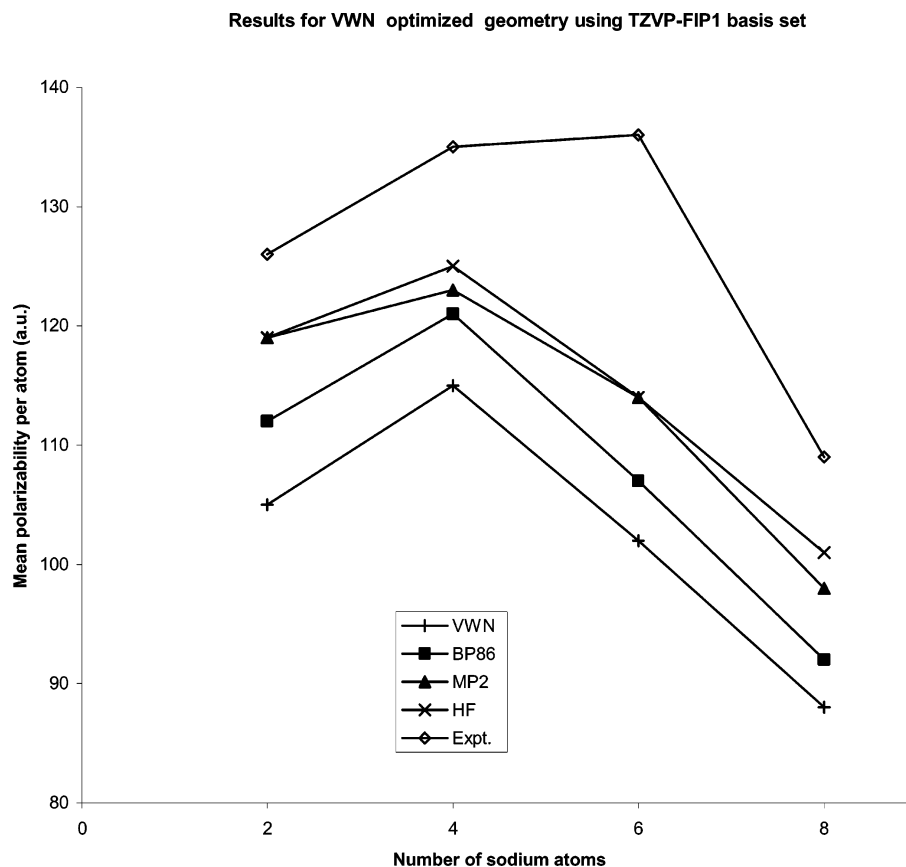


Figure 2. A plot of calculated mean polarizability per atom using the TZVP-FIP1 basis for Na_n ($n = 2, 4, 6,$ and 8) clusters optimized using VWN/A2/DZVP versus number of atoms.

could especially be a serious problem as we go to even larger clusters where the number of stable configurations increases drastically. In our calculations we had to tighten the convergence criterion for the tetramer due to its flat PES to obtain a minimum energy structure.

C. Static Mean Polarizability, Polarizability Anisotropy, and First-Hyperpolarizability. We have calculated the mean polarizability, $\bar{\alpha}$, and polarizability anisotropies, $|\Delta\alpha|$, for the optimized minimum energy structures of Na_2 , Na_4 , Na_6 , and Na_8 , which are even numbered sodium atom clusters. We have also done the calculations for the dipole first-hyperpolarizability. Our calculations have been carried out at the DFT level. MP2 level calculations were done for benchmarking our results. We also carried out calculations at the HF level to put correlation effects in a clearer perspective. Additionally, we have also collected the dipole-based finite field polarizabilities as available in the deMon2k program to compare with our DFT polarizability values. The results are presented in graphical as well as tabular form. The graphs contain plots of mean polarizability per atom in atomic units against the number of atoms and compared with the available experimental values. The experimental values were calculated from the measurement of relative polarizabilities of Knight et al.¹⁴ and the absolute measurement of the atomic polarizability by Molof et al.¹⁷ We will first discuss the polarizability results presented graphically. The DFT response property calculations have been done using the VWN and BP86 functionals. The basis sets used for the calculations are Sadlej and TZVP-FIP1. There are two sets

of Na cluster geometries used for the calculations, one optimized using a VWN functional and the other optimized using the PW86 functional, and both sets are optimized using the DZVP/A2 basis set. Each figure has a plot showing the mean polarizability per atom, $(\bar{\alpha}/n)$; values for all four Na clusters obtained at the VWN, BP86, MP2, and HF level of theory were compared with the experimental values. These are presented in Figures 2–5 corresponding to the combination of the exchange-correlation functional used for the optimization and the basis set used for the polarizability calculation. Comparison of the DFT values from the plots for the two sets of geometries shows that for a given basis set and exchange-correlation functional the results do not show any change except for 1–2 au, which means that the level of optimization of the geometries do not affect the mean polarizability per atom for the DFT calculations. Since the trends for the mean polarizability per atom are similar for both sets of optimized geometries of Na clusters, we will discuss only the general trend pointing out any difference wherever necessary.

A particular trend that can be seen for the mean polarizability per atom values for the VWN, BP86, MP2, and HF calculations in all the plots is that the values from the theoretical calculations for all the Na clusters are less than the experimental values of the mean polarizability per atom, except at two places for the calculations using the Sadlej basis set, one, in Figure 5 for both the HF as well as MP2 values of the Na_2 cluster optimized at the PW86 level and second, in Figure 3 for the MP2 value for the VWN

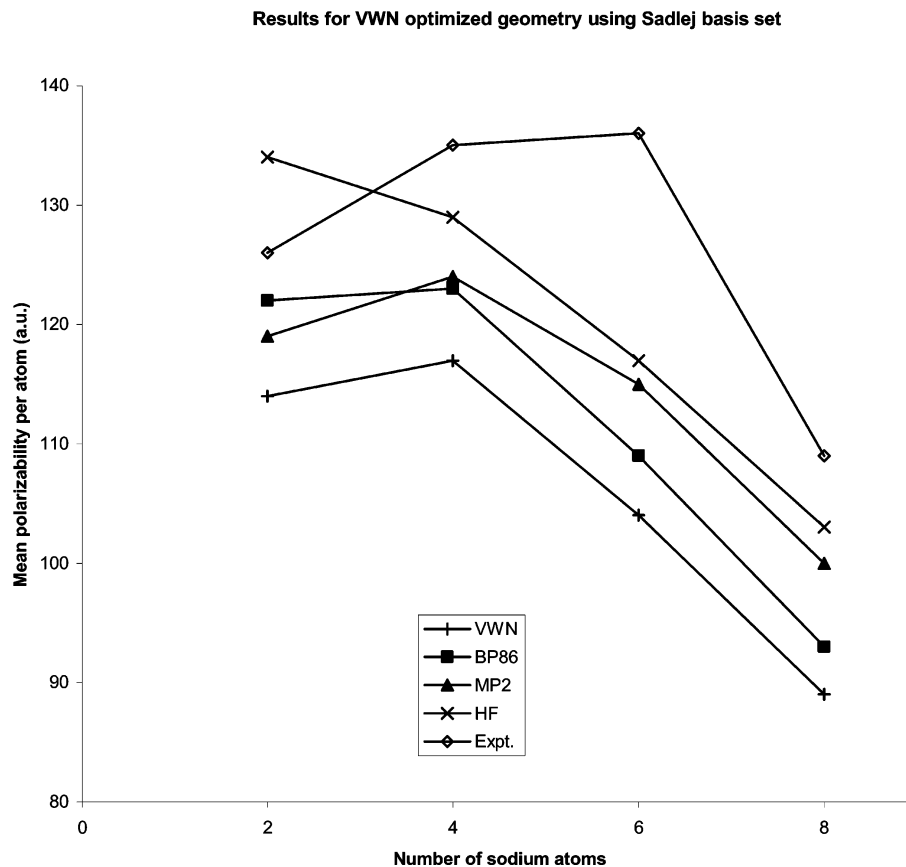


Figure 3. A plot of calculated mean polarizability per atom using the Sadlej basis for Na_n ($n = 2, 4, 6,$ and 8) clusters optimized using VWN/A2/DZVP versus number of atoms.

optimized Na_2 cluster. The value for the Na_2 cluster in both cases is overestimated from that of the experiment by 8 au which is about 6% as seen in both Figures 3 and 5. Also, the values from MP2 and the HF are closest to the experimental values followed by the ones using GGA BP86, the exception being in the case of calculations done using the Sadlej basis for the Na_2 cluster optimized using the VWN functional where the BP86 values are closer to experiment as is evident from Figure 3. The VWN values, in general, show the largest deviation from the experimental values. This is in line with the correlation effects being incorporated in the exchange-correlation functionals used for the DFT and the MP2 theory. For VWN which is a LDA based functional, the density is mapped locally to a homogeneous electron gas picture which exhibits a strong overestimation of the correlation effects as is well-known. However, for the mapping of the response of the density as a consequence of the external electric field perturbation, the VWN functional is unable to show that strong correlation effects which are probably due to less nonlocal effects in the density redistribution. This can be clearly seen in the values of mean polarizability per atom which are farthest from the experimental ones in Figures 2–5. The BP86 nonlocal functional and the ab initio methods, on the other hand, show the nonlocality in the density response although to different extents thus giving relatively higher values in comparison to VWN ones in all the plots. If we observe the trend in the experimental values of the Na clusters, we see that the polarizability per atom values increases from Na_2 to Na_4 to a reasonable extent, then there is a very slight increase from

Na_4 to Na_6 , whereas from Na_6 to Na_8 there is a drastic drop in the value. Qualitatively this trend is more correctly reflected by all four methods for the values from the TZVP-FIP1 basis for both sets of geometries. For the Sadlej basis however, both the HF and MP2 values overshoot the experimental value of 126 au as seen in Figure 5 for the Na_2 cluster optimized at the PW86 level; similarly Figure 3 shows an overestimation of the HF polarizability value for the Na_2 cluster optimized at the VWN level. Also the slight increase in experimental value from Na_4 to Na_6 is seen to be otherwise in all the calculations, independent of the optimization and level of calculation. The maximum deviation from the experimental values is for the Na_6 cluster results, irrespective of the level of theory used. This is the case for every calculation, the highest being 25% for the VWN method in Figure 2. A comparison of the similarity in the plots for the TZVP-FIP1 basis set (i.e., Figures 2 and 4) and the Sadlej basis set (i.e., Figures 3 and 5) for the two sets of optimized geometries show that the level of optimization does not affect the polarizability calculations at the DFT level. This similarity in the plots can also be seen for the MP2 calculations using the TZVP-FIP1 basis set (i.e., Figures 2 and 4); however, this is not the case for the Sadlej basis (Figures 3 and 5). The behavior of the MP2 as well as HF calculations for the two basis sets could be assigned to the fact that the TZVP-FIP1 basis set has been optimized for the polarizability calculation using DFT, whereas the Sadlej basis is an optimized basis for the polarizability calculation using ab initio methods.

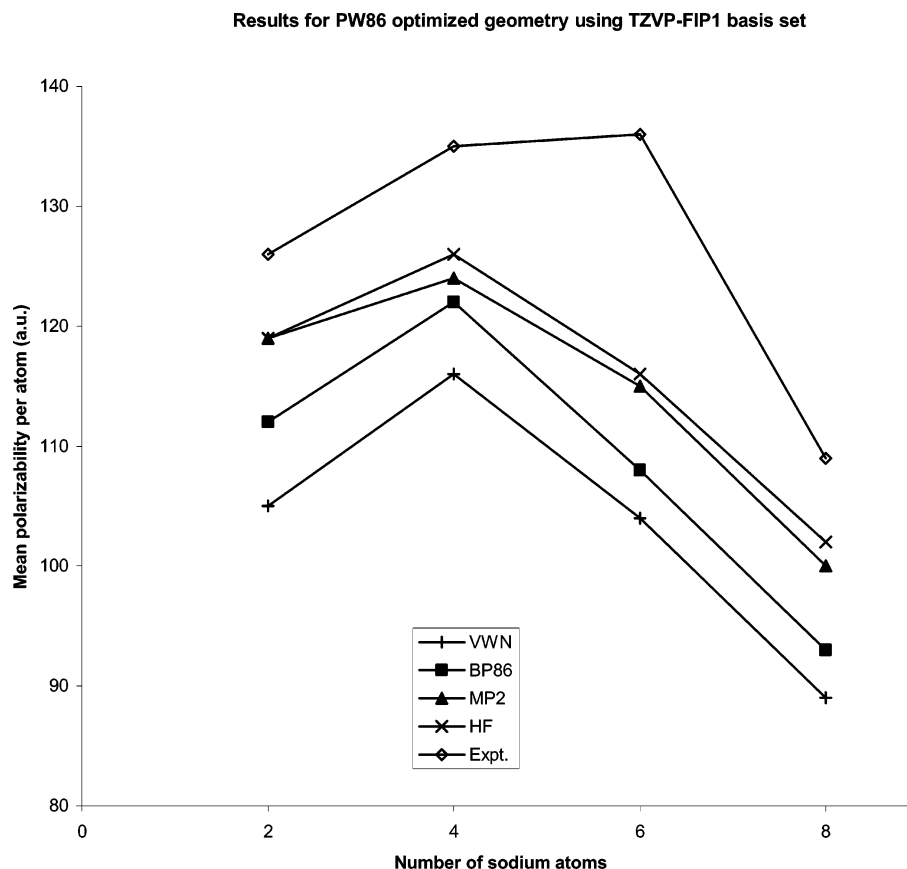


Figure 4. A plot of calculated mean polarizability per atom using the TZVP-FIP1 basis for Na_n ($n = 2, 4, 6,$ and 8) clusters optimized using PW86/A2/DZVP versus number of atoms.

In Table 2, we have compared the experimental and DFT mean polarizability per atom values obtained by Rayane et al.¹⁶ in angstrom units with our DFT calculations for the Na cluster geometries optimized at the PW86-DZVP-A2 level. We have compared our results for the VWN and BP86 functionals obtained using the Sadlej and TZVP-FIP1 basis sets. The comparison has been done with the values reported by Rayane et al.¹⁶ calculated at the PW91 level for the SU and 6-31G basis sets and measured experimentally. Although we have discussed our mean polarizability per atom values above earlier, we would like to have a comparison with other DFT results available. It can be clearly seen that the values reported by Rayane et al. are closer to the experiment as compared to our results. They have argued that the SU basis gives values closer to the experiment in comparison with the 6-31G basis as there is more polarization (d-orbitals) and diffuse functions in the SU basis which are expected to be important for polarizability calculation. On a similar basis, we could assign the marginally better behavior of the Sadlej basis as compared to the TZVP-FIP1 basis, especially for the dimer, to the fact that there is a larger number of polarization functions in the Sadlej basis as compared to the TZVP-FIP1, whereas there are more diffuse functions in the TZVP-FIP1 basis set. Another reason for TZVP-FIP1 not performing better than the Sadlej basis despite being optimized for DFT could be the use of Cartesian basis functions in all our response property calculations. The use of spherical basis functions is advised to avoid contamination of the valence basis set with the diffuse p- and d-type

Gaussians of the FIP functions. This could be explained by taking an example of s- and d-orbitals located on the same center. In the spherical representation of these two orbitals shells, i.e., the orbitals are constructed from a one-dimensional radial function and real spherical harmonics, the overlap matrix elements vanish due to the orthogonality of the spherical harmonics, whereas in the case of Cartesian representation the d shell is overdetermined by a total symmetric component ($d_{xx} + d_{yy} + d_{zz}$) that can mix with the s-orbitals (a similar situation holds for the p- and f-shells). Rayane et al.¹⁶ have also concluded that diffuse functions are less important for static response in the ground-state calculations of clusters. Calculated values of polarizability per atom using the PW91 functional reported by Rayane et al. are in better agreement with the experiments than our values calculated using VWN and BP86. In our calculation we find that the values obtained from the BP86 are closer to the experiment than the VWN ones.

Tables 3–6 present our calculations done for each of the Na clusters, i.e., each cluster calculations are presented in separate tables. We have reported the polarizability anisotropy and the orientationally averaged first hyperpolarizability values obtained using the DFT, HF and MP2 calculations in these tables. The DFT finite field (FF) results of polarizability are also presented in the tables for comparison. We have already discussed the mean polarizability per atom values presented in Figures 2–5. We now turn to the mean polarizability values and the polarizability anisotropy values given in Tables 3–6. As we move across Tables 3–6 for

Results for PW86 optimized geometry using Sadlej basis set

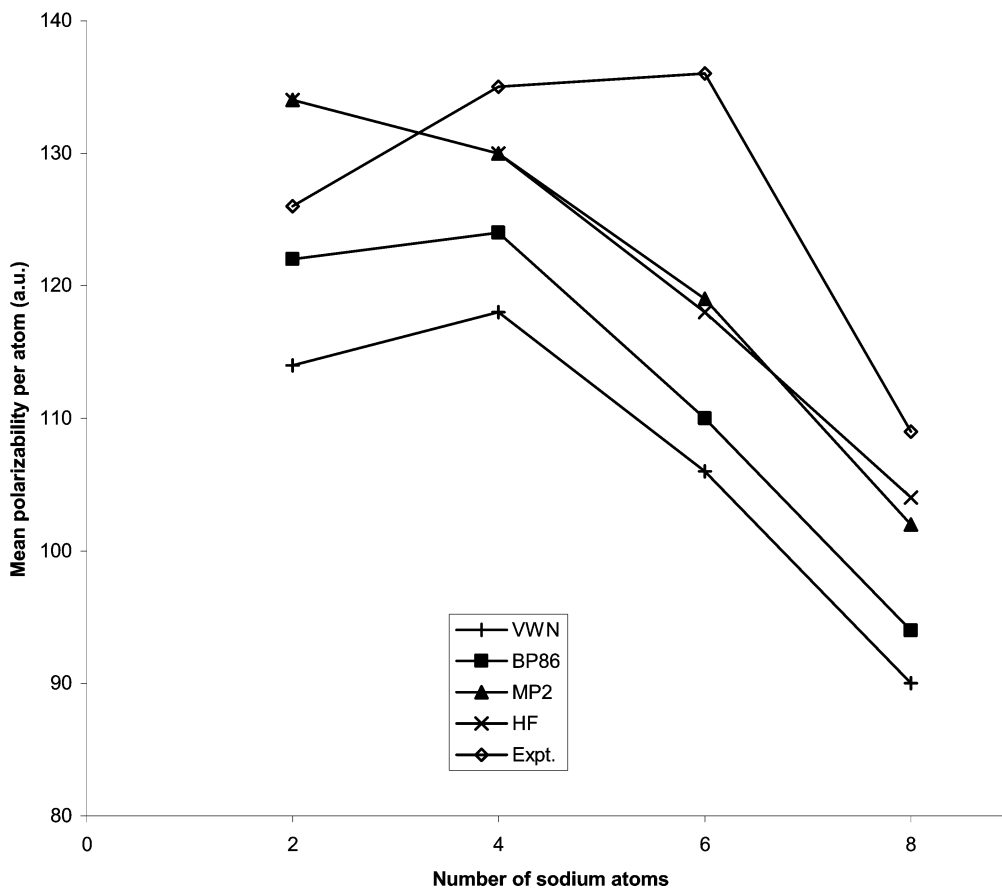


Figure 5. A plot of calculated mean polarizability per atom using the Sadlej basis for Na_n ($n = 2, 4, 6,$ and 8) clusters optimized using PW86/A2/DZVP versus number of atoms.

the clusters Na_2 through Na_8 , we observe that the DFT polarizability anisotropy value increases as we move from the dimer to the tetramer and decreases as we go to the hexamer and octamer. This trend in the values reflects the clear relation between the cluster structure and the polarizability anisotropy values. It is worth noting that as the cluster structure becomes compact like in the case of the octamer the polarizability anisotropy value decreases. The value for the octamer is even less than the value for the dimer which has an open structure. As we go from the tetramer to hexamer, we see that the hexamer being a closed structure as against the planar tetramer, it shows a decrease in the polarizability anisotropy value from that of the tetramer. A comparison of the polarizability anisotropy values for all the clusters among the two basis sets for each of the methods shows that the Sadlej basis gives values lesser than the TZVP-FIP1 basis, except for the case of the hexamer where the trend is reversed. A general trend of the BP86 functional giving slightly higher values for the polarizability anisotropy than the VWN functional can be seen in all the calculations. We could not compare our results with experiments as there is no experimental measurement of polarizability anisotropy available.

The implications from the values of the mean polarizability for the different methods, basis sets, and functionals used would now be discussed. The TZVP-FIP1 basis used in the

Table 2. Calculated Values of Static Mean Polarizabilities per Atom (in \AA^3) for Na_n Clusters ($n = 2, 4, 6,$ and 8) Optimized at the PW86/DZVP/A2 Level in Comparison with Theory and Experiment

clusters	XC	basis	$\bar{\alpha}/n$
Na_2	PW91	SU ^a	19.1
	PW91	6-31G ^a	19.0
	VWN	Sadlej (TZVP-FIP1)	16.9 (15.5)
	BP86	Sadlej (TZVP-FIP1)	18.0 (16.6)
		expt ^a	19.65
Na_4 (rhombus)	PW91	SU ^a	19.6
	PW91	6-31G ^a	19.3
	VWN	Sadlej (TZVP-FIP1)	17.5 (17.2)
	BP86	Sadlej (TZVP-FIP1)	18.4 (18.0)
		expt ^a	20.95
Na_6 (pentagonal pyramid)	PW91	SU ^a	17.4
	PW91	6-31G ^a	17.3
	VWN	Sadlej (TZVP-FIP1)	15.6 (15.4)
	BP86	Sadlej (TZVP-FIP1)	16.3 (16.1)
		expt ^a	18.63
Na_8 (DCO)	PW91	SU ^a	14.9
	PW91	6-31G ^a	14.6
	VWN	Sadlej (TZVP-FIP1)	13.3 (13.3)
	BP86	Sadlej (TZVP-FIP1)	13.9 (13.8)
		expt ^a	16.69

^a From ref 16.

Table 3. Static Mean Polarizability, Polarizability Anisotropy, and Mean First-Hyperpolarizability of Na₂ Cluster Optimized with DZVP/A2 (in Atomic Units)

optimized	basis set	method	$\bar{\alpha}$	$ \Delta\alpha $	$\beta_x = \beta_y$	β_z	β	
VWN	TZVP-FIP1	MP2	237.08		0.0	0.0	0.0	
		VWN	209.48	157.17	0.0	1.0	1.0	
		VWN-FF	209.41	157.47				
		BP86	223.96	169.23	0.0	1.7	1.7	
		BP86-FF	223.63	170.17				
		HF	237.37		0.0	0.0	0.0	
		Sadlej	MP2	268.69		0.0	0.0	0.0
	VWN	227.98	132.07	0.0	1.6	1.6		
	VWN-FF	227.89	132.60					
	BP86	243.02	140.96	0.0	2.5	2.5		
	BP86-FF	242.66	142.31					
	HF	267.12		0.0	0.0	0.0		
	PW86	TZVP-FIP1	MP2	237.08		0.0	0.0	0.0
			VWN	209.48	157.17	0.0	1.0	1.0
VWN-FF			209.41	157.47				
BP86			223.96	169.23	0.0	1.7	1.7	
BP86-FF			223.63	170.17				
HF			237.37		0.0	0.0	0.0	
Sadlej			MP2	268.69		0.0	0.0	0.0
VWN		227.98	132.07	0.0	1.6	1.6		
VWN-FF		227.89	132.60					
BP86		243.02	140.96	0.0	2.5	2.5		
BP86-FF		242.66	142.31					
HF		267.12		0.0	0.0	0.0		
expt				251.90				

^a Experimental values calculated from the measurement of relative polarizabilities of Knight et al.¹⁴ and the absolute measurement of the atomic polarizability by Molof et al.¹⁷

response property calculations is optimized for the gradient-corrected functions and is not correlation consistent. Although it may be too small for ab initio MP2 calculations, we have carried out the MP2 calculations using the TZVP-FIP1 basis set for benchmarking our results. On the other hand, the Sadlej basis is optimized for ab initio polarizability calculations and is a medium-sized basis as compared to the TZVP-FIP1. As the number of atoms in the cluster increases the mean polarizability value increases. Our DFT mean polarizability values deviate from the corresponding finite-field DFT mean polarizabilities by less than 0.4 au for the dimer, 0.6 au for the tetramer, 1.6 au for the hexamer, and by less than 2.8 au for the octamer. Also, the mean polarizability values from the GGA based BP86 functional are closer to the experimental values as compared to the ones using the VWN functional, for both sets of optimized sodium clusters. All this can be clearly observed from the mean polarizability values of the clusters in Tables 3–6.

The following critical observations are made after comparison of the DFT mean polarizability values with the MP2 and HF values. In general, both the HF and the MP2 mean polarizability values are closer to the experimental values as compared to the DFT results. In fact, certain HF values are closer to the experimental results than the MP2 values which is unexpected, as MP2 is a correlated method, whereas HF theory lacks correlation terms in its energy expression. Also, usually DFT is believed to perform better than the HF theory due to incorporation of the correlation effects. We,

however, see that as we go from the TZVP-FIP1 basis to the Sadlej in each of the tables (Tables 3–6), the mean polarizability value increases for the DFT and HF as well as the MP2 method. But what is worth noting is that the HF overshoots the experimental value for the dimer in Table 3 for the Sadlej basis. This can be used to understand the basic problem in the HF theory that as the basis set size increases further the mean polarizability value would go way beyond the experimental value. The results from MP2 theory do not show much improvement either, since MP2 energy does not contain contributions from a singly excited determinant, which are important for dipole based properties. The improvement may start appearing only at the MP4 level. However, MP4 calculations are computationally very expensive. It could be observed that although the DFT values are not closer to the experiments there is a significant increase as we go from the TZVP-FIP1 basis to the Sadlej and as we move from a local to a nonlocal functional. As a consequence, we could expect the mean polarizability values to approach the experimental values as the basis set size increases. The correlation effects due to a proper choice of the exchange-correlation functional may improve the results further. Thus it can be seen that for the response property calculation DFT provides a better choice than even the MP2 ab initio method. It may be noted that the temperature effects which are present in the experiments is missing in the above theories, which makes the comparison of theory with experiment difficult.

We now discuss the hyperpolarizability values from our calculations. Due to the absence of experimental data, we compare the DFT calculations with our HF and MP2 results. The β value for the dimer should be zero; however, we see that in Table 3 there is a negligible value of at most 2.5 au for the DFT calculations. This error shoots up for selections of the electric field strengths other than 0.001 au which was chosen for these calculations. The error for the β values of the dimer could be assigned to the percolation of the inaccuracies into the response density matrix due to the numerical approximation employed for obtaining the derivative KS-operator matrix in our method. For the tetramer in Table 4 the β_x values for the VWN optimized structure varies between 14 and 20 au which is reflected in the β as the components along the other two directions are relatively lesser in magnitude for the Sadlej and the TZVP-FIP1 basis, whereas the β values for the PW86 optimized geometry are close to zero. The β value for the TZVP basis from the BP86 method is closer to the MP2 value of 21.3 au, whereas for the Sadlej basis the β value for the VWN is closer to the corresponding MP2 value of 14.1 au and the value for the BP86 is overestimated for the VWN optimized structure. The HF β values are less than the MP2 and corresponding DFT values. As we move to the PW86 optimized structure results in Table 4, the β values from all methods are negligible. It can be seen that the tetramer has a rhombic planar structure that is symmetric due to which the β values are not very high. The β values are expected to increase as the asymmetry in the structure increases. The dimer and tetramer structures are nearly symmetric which is also reflected from the β values in the tables. As we move from tetramer to hexamer

Table 4. Static Mean Polarizability, Polarizability Anisotropy, and Mean First-Hyperpolarizability of Na₄ Cluster Optimized with DZVP/A2 (in Atomic Units)

optimized	basis set	method	$\bar{\alpha}$	$ \Delta\alpha $	β_x	β_y	β_z	β
VWN	TZVP-FIP1	MP2	490.55		18.8	-1.8	-9.8	21.3
		VWN	459.58	452.84	15.6	-1.2	-9.2	18.2
		VWN-FF	459.42	454.36				
		BP86	482.30	472.29	19.7	6.5	-0.1	20.8
		BP86-FF	481.74	474.52				
		HF	498.39		6.9	-2.0	-7.3	10.2
	Sadlej	MP2	513.92		13.9	-1.4	2.0	14.1
		VWN	469.14	450.20	14.2	2.5	-3.0	14.7
		VWN-FF	469.18	452.38				
		BP86	492.84	468.94	16.6	5.4	-8.2	19.3
		BP86-FF	492.49	472.34				
		HF	515.55		0.3	-1.7	6.4	6.6
		MP2	494.73		0.0	0.6	0.3	0.7
		VWN	463.43	463.43	0.0	-0.9	0.0	0.9
PW86	TZVP-FIP1	VWN-FF	463.33	463.94				
		BP86	486.36	484.22	0.0	-1.2	0.1	1.2
		BP86-FF	485.81	484.48				
		HF	502.04		0.0	-0.6	0.0	0.6
		MP2	518.00		0.0	-0.5	0.1	0.5
		VWN	473.06	458.97	-1.5	-3.2	0.5	3.6
	Sadlej	VWN-FF	473.14	461.23				
		BP86	496.78	478.20	0.0	-0.8	0.1	0.8
		BP86-FF	496.52	481.58				
		HF	519.06		0.0	-0.4	0.0	0.4
		expt		538.62				

^a Experimental values calculated from the measurement of relative polarizabilities of Knight et al.¹⁴ and the absolute measurement of the atomic polarizability by Molof et al.¹⁷

Table 5. Static Mean Polarizability, Polarizability Anisotropy, and Mean First-Hyperpolarizability of Na₆ Cluster Optimized with DZVP/A2 (in Atomic Units)

optimized	basis set	method	$\bar{\alpha}$	$ \Delta\alpha $	β_x	β_y	β_z	β
VWN	TZVP-FIP1	MP2	680.80		-1266.9	-938.4	-773.0	1755.9
		VWN	614.16	374.13	-1621.4	-1200.5	-929.3	2221.2
		VWN-FF	613.87	374.35				
		BP86	640.91	390.11	-2046.4	-1478.9	-1207.3	2798.7
		BP86-FF	639.81	391.03				
		HF	683.24		-1173.7	-869.3	-712.8	1625.2
	Sadlej	MP2	704.06		-1147.9	-854.0	-705.9	1595.4
		VWN	623.65	377.87	-1332.2	-995.6	-819.1	1853.9
		VWN-FF	623.16	377.56				
		BP86	652.04	395.27	-1527.2	-1015.1	-798.6	2000.1
		BP86-FF	650.57	396.02				
		HF	701.13		-1172.3	-873.9	-719.3	1629.5
		MP2	690.85		-1284.2	-983.7	-753.3	1784.5
		VWN	623.61	384.59	-1628.6	-1278.4	-832.6	2231.6
PW86	TZVP-FIP1	VWN-FF	623.20	385.70				
		BP86	650.54	398.93	-2095.9	-1540.6	-1186.7	2859.1
		BP86-FF	649.66	401.80				
		HF	692.82		-1176.9	-901.1	-690.0	1635.0
		MP2	714.07		-1157.4	-888.9	-683.6	1611.5
		VWN	633.17	388.13	-1338.1	-1058.4	-706.9	1846.7
	Sadlej	VWN-FF	632.59	388.44				
		BP86	661.88	405.03	-1481.3	-1091.5	-751.9	1987.7
		BP86-FF	660.27	406.75				
		HF	710.57		-1173.1	-903.8	-694.2	1635.5
		expt		816.62				

^a Experimental values calculated from the measurement of relative polarizabilities of Knight et al.¹⁴ and the absolute measurement of the atomic polarizability by Molof et al.¹⁷

in Table 5, the β values and its components show a dramatic increase in magnitude. The values from the MP2 and HF method are closer to each other. It is clear from Table 5 that both VWN and BP86 results are overestimated in comparison with the MP2 and HF values irrespective of the functional and basis set used for the calculation. This is true for both the optimized structures of the hexamer. All the component β values for the hexamer in Table 5 are negative, and the overestimation of the β values is more for the BP86 functional as compared to the VWN. This could be due to the under binding of the electrons by the two DFT functionals. What is clearly noticeable in Table 6 is the sudden

drop in the β values for the octamer. This could be due to the compact structure of the octamer which is a result of the magic number of 8-electrons present in its valence shell. All the other calculation including MP2 and HF for both the geometries seems to be completely disordered. We could argue that a small change in geometry can lead to a completely unexpected trend in the β values which are highly sensitive both to the correlation effects as well as structural instability. The MP2 and HF β values are comparable for the TZVP-FIP1 and the Sadlej basis for the PW86 optimized structures of the octamer, whereas the VWN and BP86 β values are comparable for the VWN optimized structures of

Table 6. Static Mean Polarizability, Polarizability Anisotropy, and Mean First-Hyperpolarizability of Na₈ Cluster Optimized with DZVP/A2 (in Atomic Units)

optimized	basis set	method	$\bar{\alpha}$	$ \Delta\alpha $	β_x	β_y	β_z	β
VWN	TZVP-FIP1	MP2	787.48		-90.6	-2.8	-4.1	90.7
		VWN	706.50	107.28	-44.5	12.2	20.7	50.6
		VWN-FF	705.51	108.68				
		BP86	736.18	109.78	-10.6	51.4	-9.5	53.3
		BP86-FF	734.04	111.15				
		HF	805.62		-29.3	2.7	25.4	38.9
		MP2	804.63		1.6	-7.0	-4.4	8.2
	Sadlej	VWN	711.19	97.8	-35.4	43.0	-17.7	58.4
		VWN-FF	709.65	100.05				
		BP86	744.20	105.40	-55.3	36.6	9.3	67.0
		BP86-FF	741.45	107.79				
		HF	819.90		-39.9	3.8	35.4	53.5
		MP2	797.96		10.2	-25.7	3.9	27.9
		VWN	715.21	104.11	-43.4	18.8	-15.9	49.9
PW86	TZVP-FIP1	VWN-FF	714.22	104.51				
		BP86	743.64	100.91	13.3	18.8	-0.6	23.0
		BP86-FF	741.50	103.94				
		HF	815.15		-10.2	-17.2	-12.6	23.6
		MP2	815.41		10.7	-26.2	3.5	28.5
		VWN	718.60	93.59	-31.2	32.1	122.3	130.2
		VWN-FF	717.14	93.84				
	Sadlej	BP86	750.63	93.55	-76.9	81.5	208.7	236.9
		BP86-FF	747.93	95.69				
		HF	829.78		-13.2	-21.0	-19.1	31.3
		MP2	868.75					
		HF	829.78					
		MP2	868.75					
		HF	868.75					
Expt.			868.75					

^a Experimental values calculated from the measurement of relative polarizabilities of Knight et al.¹⁴ and the absolute measurement of the atomic polarizability by Molof et al.¹⁷

the octamer. There are no experimental β values available for comparison with our values which could have helped to understand the behavior of β values of the sodium clusters better.

Conclusion

We have reported the polarizability and first-hyperpolarizability components for Na clusters and discussed the results obtained using our numerical-analytic approach to the CPKS method in the DFT in comparison to the benchmark ab initio MP2 and HF calculations. The results were compared to experiments wherever possible. First, we find that our numerical-analytic CPKS method gives reasonably good values of static mean dipole polarizabilities. The polarizability results gave the correct qualitative trend comparable with the experiments. The MP2 and HF values of the polarizabilities as well as the first-hyperpolarizabilities were comparable to each other. This is mainly due to the cancellation of errors in the HF method and the basis set effect which even gave HF values in smaller basis closer to the experiment. The MP2 results do not improve the HF values of property although the DFT values seem to converge toward the experimental values as the basis set is increased. Improvement of the functional can lead to faster convergence of results. However, it needs to be kept in mind that the comparison of the polarizabilities from experiments with theory is not as simple, as the temperature effects present in the experiments are missing in the theories used in this paper. It was found that the Sadlej basis gave marginally better values of polarizability than the TZVP-FIP1 basis set as it contains a greater number of polarization functions required for estimation of the response properties. The correlation effects due to the local and nonlocal nature of the exchange-correlation functionals used was discussed for the polarizabilities. However, we were unable to evaluate the precision of our method for the first-hyperpolarizability calculations

of the sodium clusters due to the unavailability of experimental values. Measurements of these quantities experimentally, especially for the smaller clusters, would help us get more insight into the response electric properties of the Na clusters. Further the basis set effects and correlation effects due to different exchange-correlation functionals, even meta-GGA for that matter, could be the next step to try. The influence of using different auxiliary basis sets for fitting the coulomb potential, on these properties which we did not attempt in this work, could also be studied. Finally, the advantage due to our single step approximation to the CPKS would only enhance the applicability of the DFT for calculation of the response properties for large systems.

Acknowledgment. K.B.S. acknowledges the financial assistance received from the Council of Scientific and Industrial Research (CSIR) during the course of this work. Financial support from the CONACYT project U48775 is gratefully acknowledged by P.C. This study is, in part, a contribution to a Franco-Mexican collaboration financed through ECOS-Nord Action M02P03.

References

- (1) Bonin, K. D.; Kresin, V. V. *Electric-Dipole Polarizabilities of Atoms, Molecules and Clusters*; World Scientific: Singapore, 1997.
- (2) Kreibig, U.; Vollmer, M. *Optical Properties of Metal Clusters*; Springer: Berlin, 1995.
- (3) Berry, R. S.; Haberland H. In *Clusters of Atoms and Molecules: Theory, Experiment and Clusters of Atoms*; Chem. Phys. 52; Haberland, H., Ed.; Springer-Verlag: Berlin, 1994; p 374.
- (4) Alonso, J. A. *Chem. Rev.* **2000**, *100*, 637.
- (5) Manninen, M.; Nieminen, R. M.; Puska, M. J. *Phys. Rev. B* **1986**, *33*, 4289.

- (6) Moullet, I.; Martins, J. L.; Reuse, F.; Buttet, J. *Phys. Rev. B* **1990**, *42*, 11598.
- (7) Moullet, I.; Martins, J. L.; Reuse, F.; Buttet, J. *Phys. Rev. Lett.* **1990**, *65*, 476.
- (8) Urban, M.; Sadlej, A. J. *J. Chem. Phys.* **1995**, *103*, 9692.
- (9) Solov'yov, I. A.; Solov'yov, A. V.; Greiner, W. *Phys. Rev. A* **2002**, *65*, 053203.
- (10) Chandrakumar, K. R. S.; Ghanty, T. K.; Ghosh, S. K. *J. Chem. Phys.* **2004**, *120*, 6487.
- (11) Maroulis, G. *J. Chem. Phys.* **2004**, *121*, 10519.
- (12) Guan, J.; Casida, M. E.; Köster, A. M.; Salahub, D. R. *Phys. Rev. B* **1995**, *52*, 2184.
- (13) Calaminici, P.; Jug, K.; Köster, A. M. *J. Chem. Phys.* **1999**, *111*, 4613.
- (14) Knight, W. D.; Clemenger, K.; de Heer, W. A.; Saunders, W. A. *Phys. Rev. B* **1985**, *31*, 2539.
- (15) de Heer, W. A. *Rev. Mod. Phys.* **1993**, *65*, 611.
- (16) Rayane, D.; Allouche, A. R.; Benichou, E.; Antoine, R.; Aubert-Frecon, M.; Dugourd, Ph.; Broyer, M.; Ristori, C.; Chandezon, F.; Huber, B. A.; Guet, C. *Eur. Phys. J. D* **1999**, *9*, 243.
- (17) Molof, R. W.; Miller, T. M.; Schwartz, H. L.; Benderson, B.; Park, J. T. *J. Chem. Phys.* **1974**, *61*, 1816.
- (18) Sophy, K. B.; Pal, S. *J. Chem. Phys.* **2003**, *118*, 10861.
- (19) Sophy, K. B.; Pal, S. *J. Mol. Struct.: THEOCHEM* **2004**, *676*, 89.
- (20) Pal, S.; Sophy, K. B. In *Lecture Series on Computer and Computational Sciences*; Maroulis, G., Simos, T., Eds.; Brill Academic Publishers: The Netherlands; 2005; Vol. 3, p 142.
- (21) Parr, R. G.; Yang, W. *Density Functional Theory of Atoms and Molecules*; Oxford University Press: Oxford, 1989.
- (22) Dreisler, R. M.; Gross, E. K. U. *Density Functional Theory*; Springer: Berlin, 1990.
- (23) Colwell, S. M.; Murray, C. W.; Handy, N. C.; Amos, R. D. *Chem. Phys. Lett.* **1993**, *210*, 261.
- (24) Lee, A. M.; Colwell, S. M. *J. Chem. Phys.* **1994**, *101*, 9704.
- (25) Kamiya, M.; Sekino, H.; Tsuneda, T.; Hirao, K. *J. Chem. Phys.* **2005**, *122*, 234111.
- (26) Jamorski, C.; Casida, M. E.; Salahub, D. R. *J. Chem. Phys.* **1996**, *104*, 5134.
- (27) Casida, M. E. In *Recent Developments and Applications of Modern Density Functional Theory*; Seminario, M. J., Ed.; Elsevier: Amsterdam, 1996; p 391.
- (28) Ipatov, A.; Fouqueau, A.; del Valle, C. P.; Cordova, F.; Casida, M. E.; Köster, A. M.; Vela, A.; Jamorski, C. *J. Mol. Struct.: THEOCHEM* **2006**, *762*, 179.
- (29) Guan, J.; Duffy, P.; Carter, J. T.; Chong, D. P.; Casida, K. C.; Casida, M. E.; Wrinn, M. *J. Chem. Phys.* **1993**, *98*, 4753.
- (30) Pulay, P. *J. Chem. Phys.* **1983**, *78*, 5043.
- (31) Hellmann, H. *Einführung in die Quantenchemie*; Deuticke: Leipzig, 1937; p 285.
- (32) Feynman, R. P. *Phys. Rev.* **1939**, *56*, 340.
- (33) Köster, A. M.; Calaminici, P.; Flores-Moreno, R.; Geudtner, G.; Goursoot, A.; Heine, T.; Ipatov, A.; Janetzko, F.; Martin del Campo, J.; Patchkovskii, S.; Reveles, S. U.; Salahub, D. R.; Vela, A. The deMon Developers: Mexico, 2006.
- (34) Kohn, W.; Sham, L. J. *Phys. Rev. A* **1965**, *140*, 1133.
- (35) Köster, A. M.; Flores-Moreno, R.; Reveles, J. U. *J. Chem. Phys.* **2004**, *121*, 681.
- (36) Dunlap, B. I.; Connolly, J. W. D.; Sabin, J. R. *J. Chem. Phys.* **1979**, *71*, 4993.
- (37) Mintmire, W.; Dunlap, B. I. *Phys. Rev. A* **1982**, *25*, 88.
- (38) Godbout, N.; Salahub, D. R.; Andzelm, J.; Wimmer, E. *Can. J. Phys.* **1992**, *70*, 560.
- (39) Vosko, S. H.; Wilk, L.; Nusair, M. *Can. J. Phys.* **1980**, *58*, 1200.
- (40) Perdew, J. P.; Wang, Y. *Phys. Rev. B* **1986**, *33*, 8800.
- (41) Perdew, J. P. *Phys. Rev. B* **1986**, *33*, 8822; **1986**, *34*, 7406.
- (42) Reveles, J. U.; Köster, A. M. *J. Comput. Chem.* **2004**, *25*, 1109.
- (43) Köster, A. M.; Calaminici, P.; Flores, R.; Geudtner, G.; Goursoot, A.; Heine, T.; Janetzko, F.; Patchkovskii, S.; Reveles, J. U.; Vela, A.; Salahub, D. R. *deMon2k*; The deMon Developers: Cinvestav, 2004.
- (44) Werner, H. -J.; Meyer, W. *Mol. Phys.* **1976**, *31*, 855.
- (45) Sadlej, A. J. *Collect. Czech. Chem. Commun.* **1988**, *53*, 1995.
- (46) Zeiss, G. D.; Scott, W. R.; Suzuki, N.; Chong, D. P.; Langhoff, S. R. *Mol. Phys.* **1979**, *37*, 1543.
- (47) Jaszu'nski, M.; Roos, B. O. *Mol. Phys.* **1984**, *52*, 1209.
- (48) Roos, B. O.; Sadlej, A. J. *Chem. Phys.* **1985**, *94*, 43.
- (49) Krack, M. private communication.
- (50) Becke, A. D. *Phys. Rev. A* **1988**, *38*, 3098.
- (51) Schmidt, M. W.; Baldridge, K. K.; Boatz, J. A.; Elbert, S. T.; Gordon, M. S.; Jensen, J. H.; Koseki, S.; Matsunaga, N.; Nguyen, K. A.; Su, S. J.; Windus, T. L.; Dupius, M.; Montgomery, J. A. *J. Comput. Chem.* **1993**, *14*, 1347.
- (52) Martins, J. L.; Buttet, J.; Car, R. *Phys. Rev. B* **1985**, *31*, 1804.
- (53) Herzberg, G. *Molecular Spectra and Molecular Structure, I. Spectra of Diatomic Molecules*; Van Nostrand Reinhold: New York, 1950.
- (54) Verma, K. K.; Bahns, J. T.; Rajaei-Rizi, A. R.; Stwalley, W. C.; Zemke, W. T. *J. Chem. Phys.* **1983**, *78*, 3599.
- (55) Dahlseid, T. A.; Kappes, M. M.; Pople, J. A.; Ratner, M. A. *J. Chem. Phys.* **1992**, *96*, 4924.

Peculiarities of the Electronic Structure of Cytochrome P450 Compound I: CASPT2 and DFT Modeling[†]

Mariusz Radoń

Department of Theoretical Chemistry, Jagiellonian University, Ingardena St. 3,
30-060 Cracow, Poland

Ewa Broclawik*

Institute of Catalysis and Surface Chemistry, Polish Academy of Sciences,
Niezapominajek St. 8, 30-239 Cracow, Poland

Received December 14, 2006

Abstract: CASSCF/CASPT2 ab initio formalism has been applied to a thiolate model of cytochrome P450 compound I. A_{2u} ground state of porphyrin radical character was found in agreement with experimental results. A strong mixing of CASSCF reference states in multistate CASPT2 was observed, which is an interesting phenomenon, rare for the ground state near the equilibrium geometry. Details of the CASSCF/CASPT2 procedure (including the construction of the active space) are discussed. Parallel DFT calculations revealed that relative energies and the scheme of spin coupling are qualitatively reproduced by hybrid DFT (B3LYP); however, results from nonhybrid functionals (BLYP, BP86) are significantly different in these aspects.

1. Introduction

Cytochrome P450 (CYP) is a ubiquitous oxygenase of high biological importance. Its elusive active form, so-called compound I (Cpd I), is one of the strongest oxidants in biology.¹ Chloroperoxidase (CPO) is another enzyme forming Cpd I of similar structure in the active site; the common and specific feature of these two systems is the coordination of heme Fe via S of cysteine.

The electronic structure of low-lying states of the Cpd I, crucial for predicting and understanding its reactivity, was extensively studied, however, almost exclusively by means of density functional theory (DFT) and mostly using hybrid functionals (e.g., B3LYP).² In view of these results, low-lying electronic states of Cpd I arise from the coupling between *three unpaired electrons* located on the oxyferylporphyrin active site. Two of them occupy antibonding π^* orbitals of oxyferyll (FeO) moiety and couple to triplet configuration (*uu*). The third unpaired electron (of free-radical nature) couples with the triplet either ferro- or

antiferromagnetically, consequently yielding quartet (*uuu*) or doublet (*uud*) configuration. This coupling is rather weak and may be described in terms of the Heisenberg Hamiltonian $H = -\vec{S}_1\vec{S}_2$. In some calculations the third electron (radical) is located on the highest a_{2u} orbital of the porphyrin ring, whereas in others—on the $3p_\pi \equiv \pi_S$ lone pair of the axial S from cysteine, perpendicular to the Fe–S axis. In other words, two types of states of different radical and thus of different chemical characters exist. The states are conventionally labeled as ${}^2,4A_{2u}$ and ${}^2,4\Pi_S$. Relative energies of these porphyrin- and sulfur-radical states were shown^{2,3} to be strongly dependent on the basis set and the functional used as well as on the environment of the active site considered in the computational model (vacuum, polarizable continuum, or explicit molecules in the nearest neighborhood).

Experimental studies on Cpd I of P450 are difficult due to the elusiveness of the active form; however, recently Kellner et al.⁴ showed using UV–vis spectroscopy that the ground state is of a porphyrin radical nature. The same conclusion was drawn for CPO Cpd I by Rutter et al.⁵ by means of EPR and Moesbauer and by Hosten et al.⁶ using Resonance Raman spectroscopy.

[†] Dedicated to Professor Dennis R. Salahub on the occasion of his 60th birthday.

* Corresponding author e-mail: broclawi@chemia.uj.edu.pl.

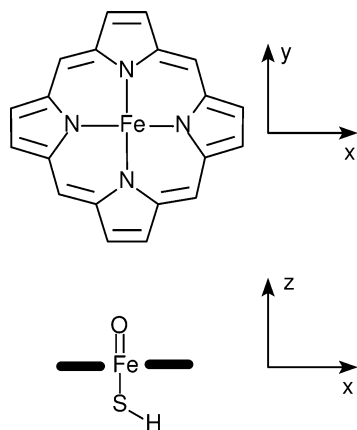


Figure 1. Top and side view of the Cpd I model system used in this study.

In this paper we focus on the description of Cpd I electronic structure by means of various methods: CASSCF/CASPT2,^{7,8} hybrid DFT (B3LYP), and nonhybrid DFT (BLYP, BP86). The CASSCF/CASPT2 method—the main formalism presented—may be useful in resolving doubts arising from DFT methodology. It was chosen as a relatively low-cost and a rather reliable *ab initio* method,⁹ which includes explicitly static and dynamic correlation, and is capable of describing a multiconfigurational nature of antiferromagnetic doublets properly.

2. Methods and Models

All calculations concern the idealized model system of the Cpd I active site [Fe(O)(SH)Por] having C_S symmetry (see Figure 1). This model has been already verified at the B3LYP level¹⁰ as a good mimic of the Cpd I active site (providing similar relative energies as a full-cysteine model). Due to symmetry the states of interest belong to distinct representations of C_S : ${}^2,4\Pi_S \in A'$ while ${}^2,4A_{2u} \in A''$. According to the formal symmetry group (C_S) there are only two representations (A', A''); however, in this work all states are conventionally labeled after the location of free radical. Porphyrin-centered molecular orbitals are traditionally called a_{2u}, a_{1u}, e_g . Actually these orbitals are only slightly perturbed by the lowering of symmetry in our system. Thus A_{2u}, Π_S etc./ a_{2u}, π_S etc. are not formal symmetry irreps but *conventional* labels of states/orbitals.

2.1. DFT Calculations. Unrestricted DFT geometry optimizations were performed with symmetry constrains for ${}^2\Pi_S, {}^4\Pi_S$ (lowest doublet and quartet of A' symmetry) and for ${}^2A_{2u}, {}^4A_{2u}$ (lowest doublet and quartet of A'' symmetry). For the B3LYP functional (using Gaussian03¹¹) two basis sets were tested: one composed of ANO-S (6s4p3d2f)¹² for Fe and cc-pVDZ for other atoms (called below BS1) and the second—6-311G**—for all atoms (BS2). Similar calculations were repeated with BLYP and BP86 functionals (using the ADF suite¹³) in a comparable *n*ZP basis set of ADF: TZP for Fe and DZP for other atoms.

Vacuum geometries were used to estimate environmental effects in the frame of DFT by means of the simplest possible model—self-consistent reaction field (SCRf) of solvent with $\epsilon = 5.6$.³ In this work SCRf calculations serve only to analyze general trends induced by polarizable environment

and are treated rather qualitatively. Due to availability, the PCM model¹⁴ was used in Gaussian03 and COSMO¹⁵ in ADF.

2.2. CASSCF/CASPT2 Calculations. CASSCF/CASPT2 calculations were performed at equilibrium DFT geometries using the Molcas¹⁶ suite in the ANO-S basis set¹² (contracted to 6s4p3d2f for Fe, to 4s3p2d for S, to 3s2p1d for N, C, O, and to 2s1p for H). The imaginary level shift 0.1 au was applied (to justify this choice the influence of level shift was analyzed).

Our primary goal in selecting active orbitals was to describe all of the lowest states appearing in DFT (i.e., ${}^2,4A_{2u}, {}^2,4\Pi_S$). Additionally, two other porphyrin-radical states were of interest: ${}^2,4A_{1u}$. This was motivated by the results of Hosten et al.⁶ suggesting that CPO Cpd I might have an unpaired electron in a_{1u} instead of the a_{2u} orbital of porphyrin.

The following orbitals were active in CASSCF (we postpone the detailed discussion of this choice to section 3.2.3): (1) $\pi_{xz}^*, \pi_{yz}^*, \pi_{xz}, \pi_{yz}, \sigma_{2z}^*, \sigma_{z^2}$ (located mainly on FeO moiety), (2) π_S, σ_S (located mainly of S), and (3) a_{2u}, a_{1u} , and pair of e_g (four frontiers of porphyrin ring). Contours of these orbitals are presented in Figure 2.

While computing the quartets of A'' irrep (${}^4A_{2u}, {}^4\Sigma_S$) one orbital (π_S) was excluded because it was not participating in any state included in the state-average CASSCF and therefore had the tendency to rotate out of the active set (and become inactive).

Our calculation flow consists of State-Average CASSCF (SA-CASSCF) followed by Multi-State CASPT2 (MS-CASPT2).¹⁷ MS-CASPT2 is a generalization of a “normal”, so-called State-Specific CASPT2 (SS-CASPT2) approach. In the MS-CASPT2 method the correlation effects are estimated (up to the second order) for several SA-CASSCF states collectively. The states are coupled via an effective Hamiltonian and allowed to mix. The possibility of mixing can make up for some limitations of the active space, manifesting in inaccurate SS-CASPT2 energies due to deficiencies in CASSCF states.¹⁷ Resulting linear combinations of CASSCF eigenvectors are called *Perturbatively-Modified (PM) states*. We should stress that they are not the final CASPT2 wave functions but only proper combinations of reference states from CASSCF which yield final wave functions after applying the CASPT2 wave operator.

The SA-CASSCF procedure was applied for each irrep and multiplicity to cover the states of interest: ${}^2,4\Pi_S, {}^2,4A_{1u}, {}^2,4A_{2u}$. As will be shown in section 3.2.1, some of them appear in CASSCF at relatively high energies (this is due to not including dynamic correlation yet). In other words, at the CASSCF level there are other states with energies between the lowest and the highest states of interest. For the sake of objectivity, we decided to include all these “intermediate” states in a state-average energy expression: in this way none of the prospective candidates for the ground state is ruled out a priori. According to the expectations, in the final MS-CASPT2, the “intermediate” states turned out to be higher in energy than the states of interest, *except for the* ${}^2,4\Sigma_S$ states—i.e. states analogous to ${}^2,4\Pi_S$ but with a radical in the $3p_\sigma \equiv \sigma_S$ orbital of sulfur. Results for ${}^2,4\Sigma_S$ will be given below as these states play an important role in further analysis.

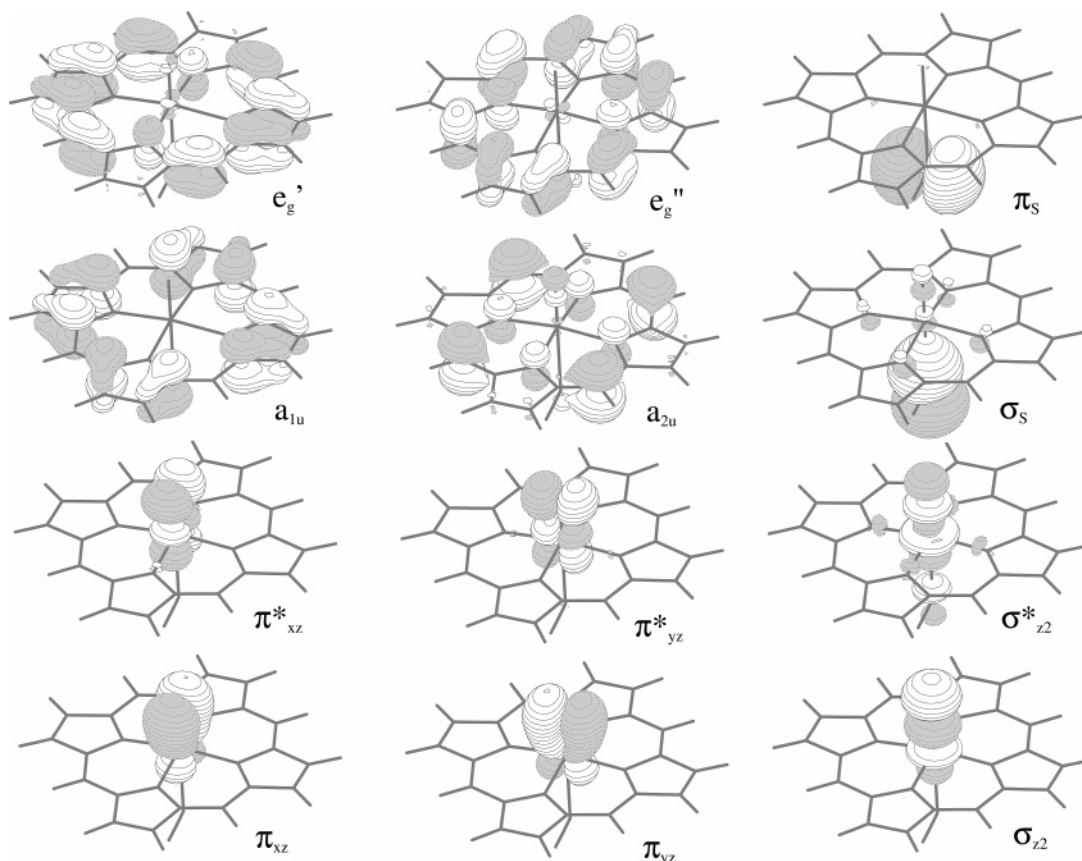


Figure 2. Contour plots of active orbitals.

2.3. Analysis of Properties. The coupling constant J was estimated for CASSCF/CASPT2 states simply as

$$J = \frac{2}{3} (E_d^{\text{CAS}} - E_q^{\text{CAS}}) \quad (1)$$

For Kohn–Sham wave-functions from unrestricted DFT the following formula (derived by Rodriguez and McCusker¹⁸) was employed due to spin contamination:

$$J = 2 \frac{E_d^{\text{DFT}} - E_q^{\text{DFT}}}{\frac{3}{2} \left(\frac{3}{2} + 1 \right) - \langle \hat{S}^2 \rangle_d} \quad (2)$$

In the above formulas $\langle \rangle_d$ is the average value in the doublet state. E_d and E_q are the vertical energies of doublet and quartet (computed for the equilibrium geometry of the lower of them).

Spin distributions for unrestricted Kohn–Sham (UKS) orbitals were further analyzed by means of *natural spin orbitals*, which provide the leading one-electron contributions to spin density: in this analysis the molecular spin density is decomposed into squares of orbitals carrying excessive \uparrow and \downarrow spin. These orbitals are simply eigenvectors of spin density matrix, $P_\uparrow - P_\downarrow$ (diagonalization should be done in orthonormal basis). Corresponding eigenvalues are called *occupation numbers* and may be associated with populations of excessive spin. An occupation number equals to +1 for one \uparrow electron, to -1 for one \downarrow electron, and to some real number between -1 and +1 in a general case. For unrestricted single determinantal methods the resulting

occupations may be nontrivial since coefficients of UKS orbitals for \uparrow and \downarrow spins differ (this is also the reason why it is difficult to analyze excessive spin distribution only by inspecting UKS orbitals). *Natural orbitals*, defined (analogously) as eigenvectors of $P_\uparrow + P_\downarrow$, are complementary tools used to analyze the distribution of unpaired electrons. Contributions from “closed shells” are ≈ 2 , from “virtual orbitals” ≈ 0 and ≈ 1 from orbitals carrying unpaired electrons.

Natural- and natural spin orbitals were computed from unrestricted orbitals using the original authors’ program. Contour plots of orbitals and densities were prepared using Molden¹⁹ and the Grid Viewer from the Molcas¹⁶ suite. Small functionality was added to the Molcas code to enable extracting natural spin orbitals for PM states (used to compute spin densities for PM states).

3. Results and Discussion

3.1. DFT Modeling. B3LYP equilibrium geometries are included in the Supporting Information (see section 6). Adiabatic energies and exchange coupling constants for three examined functionals are given in Table 1.

According to our B3LYP results—being in general agreement with literature studies employing this functional^{2,10}—the ground state is porphyrin radical (A_{2u}), both in vacuum and polar environment. The type of coupling strongly depends on the environment and on the basis set used, which makes a conclusive assignment of multiplicity difficult.^{2,3} Nevertheless, for the hybrid functional the coupling is *weak* in all cases, about 0.1 kcal/mol, i.e., an order of

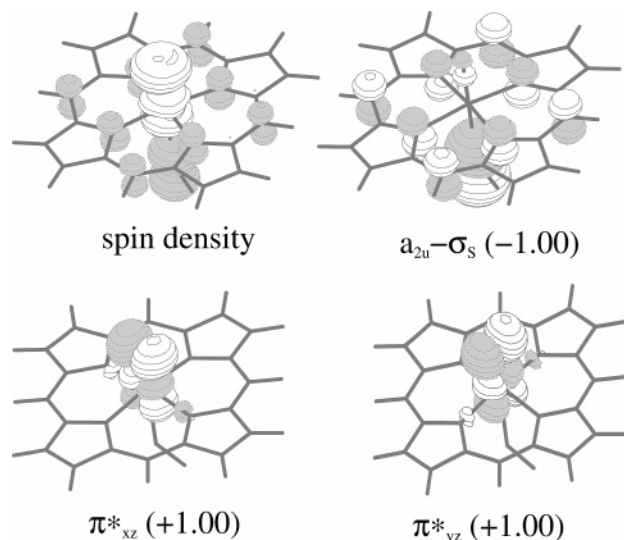


Figure 3. Contour plots of spin density and natural spin orbitals corresponding to three unpaired electrons for the ${}^2A_{2u}$ state, obtained from B3LYP/BS1 KS orbitals.

Table 1. Relative Adiabatic Energies (E_{ad}) and Coupling Constants (J), All in kcal/mol, for Various Functionals in Vacuum and SCRf

	B3LYP/BS1		B3LYP/BS2		BLYP		BP86	
	vac	SCRf	vac	SCRf	vac	SCRf	vac	SCRf
$E_{ad}({}^2A_{2u})$	0.1	0.0	0.0	0.1	1.8	0.1	2.5	0.0
$E_{ad}({}^4A_{2u})$	0.0	0.1	0.0	0.0	3.1	0.0	5.0	0.7
$E_{ad}({}^2\Pi_S)$	3.1	5.3	3.4	6.0	0.0	2.2	0.0	1.3
$E_{ad}({}^4\Pi_S)$	3.3	5.5	3.4	5.8	4.6	5.5	5.5	5.3
$J(A_{2u})$	0.06	-0.16	-0.03	0.05	-2.23	0.04	-3.32	-2.89
$J(\Pi_S)$	-0.12	-0.11	0.06	0.07	-2.49	-1.89	-2.94	-2.43

magnitude smaller than the separation between different types of radicals. In contrast to B3LYP, two nonhybrid functionals examined yield a different pattern of energies: not only the vacuum ground-state radical character is different but also J is much bigger (on the order of 2 kcal/mol, comparable to the separation of porphyrin and sulfur radicals). The influence of the polar environment yields generally the stabilization of ${}^2,{}^4A_{2u}$ states for all potentials; however, this effect is much more clear for B3LYP than for BLYP and BP86.

According to spin distributions depicted in the first plots of Figures 3 and 4 (for doublets, in B3LYP) interacting spins are well separated in space—thus one would expect *weak exchange interaction*. However, in view of Table 1 this physically intuitive picture of weak spin-coupling occurring in two different types of radicals (${}^2\Pi_S$ or ${}^2A_{2u}$) is supported only by the hybrid functional (B3LYP), while nonhybrid ones lead to a qualitatively different description.

Low-spin (doublet) states were carefully analyzed by means of natural spin orbitals. Three such orbitals, with eigenvalues closest to ± 1 , are depicted in Figures 3 and 4. All others have much smaller eigenvalues and are of minor importance for qualitative analysis.

The presented orbitals originate from B3LYP, but their spatial contours are quite similar for all functionals tested. However, eigenvalues (occupation numbers) *do differ sig-*

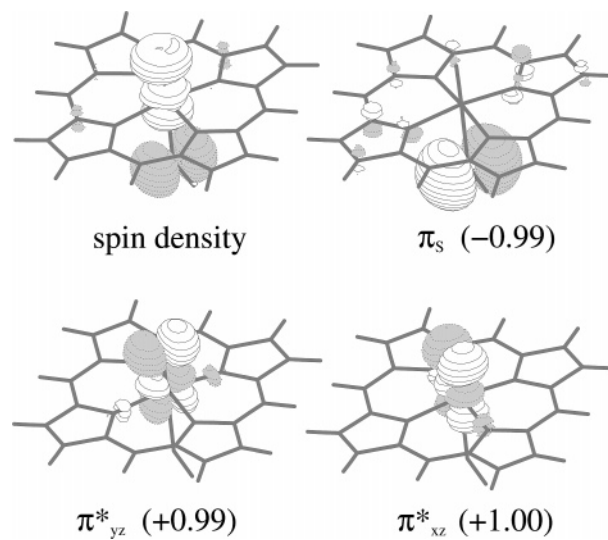


Figure 4. Contour plots of spin density and natural spin orbitals corresponding to three unpaired electrons for the ${}^2\Pi_S$ state, obtained from B3LYP/BS1 KS orbitals.

Table 2. Selected Natural Spin Orbitals (with Occupation Numbers Closest to ± 1) for Doublet States from Various DFT Models

functional	${}^2A_{2u}$			${}^2\Pi_S$		
	π_{xz}^*	π_{yz}^*	$a_{2u} - \sigma_S$	π_{yz}^*	π_{xz}^*	π_S
B3LYP/BS1	1.00	1.00	-1.00	0.99	1.00	-0.99
B3LYP/BS2	1.00	1.00	-1.00	1.00	1.00	-1.00
BLYP	0.68	1.00	-0.68	0.68	1.00	-0.68
BP86	0.52	1.00	-0.52	0.66	1.00	-0.66

Table 3. Selected Natural Orbitals (with Occupation Numbers Closest to 1) for Doublet States from Various DFT Models

functional	${}^2A_{2u}$			${}^2\Pi_S$		
	$a_{2u} - \sigma_S$	π_{yz}^*	$\pi_{xz}^* + \sigma_S$	$\pi_{yz}^* - \pi_S$	π_{xz}^*	$\pi_S + \pi_{yz}^*$
B3LYP/BS1	0.98	1.00	1.02	0.89	1.00	1.11
B3LYP/BS2	0.97	1.00	1.03	0.97	1.00	1.03
BLYP	0.26	1.00	1.74	0.27	1.00	1.73
BP86	0.14	1.00	1.86	0.25	1.00	1.75

nificantly (Table 2): for B3LYP there are three values close to “ideal” +1, +1, -1 describing the antiferromagnetic coupling of $S_1 = 1$ with $S_2 = 1/2$, which supports nicely the three electron model. [In principle, electronic configuration describing this coupling is three-determinantal: $|uud\rangle = (1/\sqrt{6})(2|\uparrow\uparrow\downarrow\rangle - |\uparrow\uparrow\uparrow\rangle - |\downarrow\uparrow\uparrow\rangle)$ and yields natural spin orbitals with eigenvalues $+2/3, +2/3, -1/3$, similar to those indeed found in CASSCF/CASPT2. However, in one-determinantal approximation this type of coupling is best described by $|\uparrow\uparrow\downarrow\rangle$ configuration, having spin orbitals with +1,+1,-1 eigenvalues.] For spin orbitals from BLYP and BP86 only one eigenvalue is close to +1, while all others have much smaller absolute values. A similar observation holds for natural orbitals (Table 3): again, in B3LYP their occupations are close to 1, 1, 1 (three unpaired electrons), while BLYP and BP86 give numbers rather closer to the following: 2 (electronic pair), 1 (single unpaired electron),

Table 4. SS- and MS-CASPT2 Vertical Energies (at B3LYP/BS1 ${}^2A_{2u}$ Geometry) for the States of Interest

relative energy [kcal/mol]			
SS-CASPT2		MS-CASPT2	
${}^2\Pi_S$	0.0	$1^4(A_{2u}, \Sigma_S)$	0.0
${}^4\Sigma_S$	1.0	$1^2(A_{2u}, \Sigma_S)$	0.9
${}^4\Pi_S$	1.3	${}^2\Pi_S$	8.2
${}^2\Sigma_S$	5.4	${}^4\Pi_S$	9.6
${}^2A_{2u}$	8.1	${}^2A_{1u}$	22.9
${}^4A_{2u}$	11.4	${}^4A_{1u}$	25.2
${}^2A_{1u}$	14.6	$2^2(A_{2u}, \Sigma_S)$	27.4
${}^4A_{1u}$	16.9	$2^4(A_{2u}, \Sigma_S)$	28.9

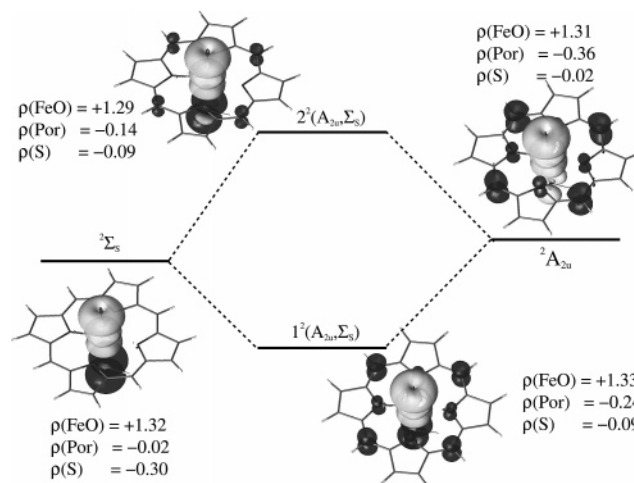
and 0 (vacant orbital). It follows that the “occupation schemes” exhibited by KS determinants from tested nonhybrid potentials are inconsistent with three unpaired electrons model of Cpd I. More precisely, occupation numbers obtained for nonhybrid DFT suggest the important contribution of another doublet configuration—with only one unpaired electron located on FeO. However, CASSCF/CASPT2 does not confirm any such doublet configuration (see below)—in fact the CASSCF/CASPT2 results are quite similar to the B3LYP ones. In the authors’ opinion, the reported difference between functionals is an artifact of BLYP and BP86 arising from a bad description of exchange in these nonhybrid potentials.

3.2. CASSCF/CASPT2 Modeling. 3.2.1. Vertical Energies. In the first step, vertical energies for all states were computed at the ${}^2A_{2u}$ B3LYP/BS1 geometry (below we refer to these energies as “vertical”). Because the CASSCF method does not cover dynamic correlation one should not expect that experimental data can be understood by means of CASSCF energies. Indeed, at this level both porphyrin radical states are lying extremely high: ${}^2A_{2u}$ about 60–70 kcal/mol and ${}^2A_{1u}$ about 50 kcal/mol above the lowest state, which is ${}^2\Pi_S$ (with a quartet of only 3 kcal/mol above). On the other hand, ${}^2A_{2u}$ states are relatively low-lying (about 10 kcal/mol above and the lowest state) and are the lowest doublet and quartet states in A'' irrep, instead of ${}^2A_{2u}$ being the lowest states of this irrep in DFT! SS-CASPT2 corrects this poor result somewhat, because porphyrin-radical states become lowered more than the sulfur-radical ones, but the latter states are still lying lower (compare Table 4).

The interaction between reference states in MS-CASPT2 affects mostly ${}^2A_{2u}$ and ${}^2A_{1u}$ which mix and form PM states (linear combinations) with comparable weights of two interacting components. These PM states are labeled symbolically as $1^{2,4}(A_{2u}, \Sigma_S)$ and $2^{2,4}(A_{2u}, \Sigma_S)$. Other states of interest are almost unaffected by the multistate procedure (preserve their character from CASSCF). Final energies are given in Table 4.

To analyze the nature of resulting PM states, their spin densities were compared with spin densities of the pure CASSCF reference states. Spin densities for doublets (more interesting for visual analysis) are presented in Figure 5.

They illustrate well in which way σ_S -type and a_{2u} -type radicals (observed in CASSCF) form states of mixed nature. This interstate mixing is understandable in view of the DFT

**Figure 5.** Contour plots of spin densities for CASSCF roots (${}^2\Sigma_S$, ${}^2A_{2u}$) and PM states ($1^2(A_{2u}, \Sigma_S)$, $2^2(A_{2u}, \Sigma_S)$). Mulliken spin populations of FeO, S, and a porphyrin ring are also given.

results—in fact, states from DFT previously labeled ${}^2A_{2u}$ contain the important Σ_S contribution (see Figure 3); therefore—to be in agreement with the CASSCF/CASPT2 notation—they should be labeled as ${}^2A_{2u}, \Sigma_S$.

At the MS-CASPT2 level the results become consistent with experiment: the ground state is a combination of A_{2u} and Σ_S having a partial but significant porphyrin-radical nature (compare Figure 5). One should be aware, however, that the extent of MS-CASPT2 mixing may generally depend on the selection of active orbitals and cannot be treated as a routine remedy to cover eventual errors due to poor active space. Some warnings and recommendations regarding this point are raised by Serrano-Andrés et al.²⁰

3.2.2. Multiplicity of the Ground State and the Coupling Constant J . From vertical energies computed so far, the doublet or quartet (A_{2u}, Σ_S) emerges as a ground state. The difference in energy between them is quite small, and the order of states is likely to change during the geometry optimization. Hence, to assign the multiplicity of the ground state one should, in principle, compare adiabatic energies obtained from geometry optimizations in the frame of MS-CASPT2. However, since analytical gradients are not available in CASPT2, this way is not practical. CASSCF equilibrium geometries are often used as approximations to CASPT2 ones—unfortunately this is also impossible in our case because the final wave function of MS-CASPT2 originates not from a single CASSCF root (as in an ordinary, single-state CASPT2) but from their linear combination (PM state). To the best of the authors’ knowledge, no software capable of computing CASSCF gradients for such a combination exists. The third way—and the only possible one here—is to use equilibrium geometries from DFT (B3LYP). As was noted, the correspondence of B3LYP solutions to MS-CASPT2 PM states is rather good, thus the trick might work. Following this idea, the authors recomputed the energies of all states in the proper geometries (for example, ${}^4A''$ states, to which ${}^4A_{2u}$ belongs, were computed for the ${}^4A_{2u}$ B3LYP geometry). Unfortunately, it turned out that for some states “adiabatic energies” computed in such a way

were *higher* than vertical energies for the initial geometry! It means that in our case geometries from B3LYP cannot be treated as good approximations to “true” (i.e., optimal for MS-CASPT2) ones. For this reason, the above estimations of adiabatic energies are not discussed further.

Nevertheless, the question of whether the ground state is $1^2(A_{2u}, \Sigma_S)$ or $1^4(A_{2u}, \Sigma_S)$ remains vital. To approach the answer, we compared the relative energies of the doublet and quartet at equilibrium geometries of the corresponding states from B3LYP. Results for the first geometry were already presented above (with the quartet ground state and $J = +0.61$ kcal/mol). For the second geometry, the ground state turned out to be a doublet with $J = -0.30$ kcal/mol. The absolute energy of this state is the lowest one among all the state energies computed in this work. Thus, according to the highest manageable level we have applied, the ground state is $1^2(A_{2u}, \Sigma_S)$ and coupling is antiferromagnetic. However, this is not a firm conclusion, since for giving a definite answer true equilibrium geometries should be known. Unfortunately, as was noted, those from B3LYP do not even provide reasonable MS-CASPT2 adiabatic energies.

3.2.3. Discussion of the Active Space Selection, Multi-state Methodology, and Level Shift Influence. The selection of active orbitals is a result of our extensive, preliminary research (not reported here). We started from the orbitals which are absolutely necessary for constructing states of interest: π_{xz}^* , π_{yz}^* , π_S , a_{2u} , a_{1u} . Porphyrin’s LUMO (e_g) was added to improve the description of the porphyrin ring.

Due to strong static correlation in moiety, the bonding pair π_{xz} , π_{yz} has to be active as a counterpart of antibonding π_{xz}^* , π_{yz}^* . Similarly, strong correlation is associated with the σ component of the bond, i.e., orbitals σ_z and σ_z^* . If they are not active, then their contributions to second-order energy are much bigger than for any other orbital. In contrast, omitted d orbitals ($3d_{x^2-y^2}$, $3d_{xy}$) have rather small contributions to second-order energy—they are comparable or smaller than contributions of many omitted porphyrin π orbitals, which cannot be active due to size limitations. Furthermore, these two d orbitals do not change occupations in any of the states considered here: $3d_{xy}$ is (approximately) “doubly occupied”, whereas $3d_{x^2-y^2}$ participates in “doubly occupied” and “vacant” molecular orbitals. [Here the terms “vacant” and “doubly occupied” are used to describe the occupation numbers *only in the leading* configuration.] Therefore, one can guess that eventual corrections due to making them active would approximately cancel in relative energies.

The sulfur σ_S orbital was added due to different reasons. Indeed, we have discovered that in CASSCF calculation for $2^4A''$ with *active* a_{2u} and *inactive* σ_S these orbitals exchange ($a_{2u} \rightleftharpoons \sigma_S$), and, as a result, the state which originally was 2^4A_{2u} becomes $2^4\Sigma_S$! The only way we have found to avoid this rotation was to make both orbitals active.

The procedure applied in this study (i.e., SA-CASSCF followed by MS-CASPT2) has some drawbacks. First of all, the orbitals being optimized in the CASSCF level are common for all electronic states involved, and hence they are far from optimal for any of them. Therefore SA-CASSCF performs worse with respect to electronic correlation than single-state CASSCF. Second, as was already noted, within

Table 5. MS-CASPT2 Energies of $1^2, 4(A_{2u}, \Sigma_S)$ and $2^4\Pi_S$ States for Two Choices of the Active Space: 15 in 12 and 11 in 8

	relative energy [kcal/mol]	
	15 in 12	11 in 8
$1^2(A_{2u}, \Sigma_S)$	0.9	0.0
$1^4(A_{2u}, \Sigma_S)$	0.0	1.1
$2^4\Pi_S$	8.2	8.6
$4^4\Pi_S$	9.6	7.8

the applied approach geometry optimization is impossible, either at the SA-CASSCF or the MS-CASPT2 level. From similar reasons accounting for environmental effects is very problematic in SA-CASSCF (because of the optimization of dielectric cavity based on a selected CASSCF state). In spite of these problems and limitations, the multistate approach seems to be the method of choice in our case, since the character of the CASSCF solution is qualitatively incorrect, and the important component (A_{2u}) of the true ground state has very high CASSCF energy. If this high-lying CASSCF state is ignored, then one obtains $2^4\Pi_S$ and $2^4\Sigma_S$ as the lowest states in CASPT2, which the result is obviously wrong.

To estimate and eventually reduce the problem of the worse description of electronic correlation due to the presence of many states in SA-CASSCF optimization, we attempted to reduce the number of CASSCF roots involved in state-average calculations. With this aim we excluded from the previous active space some orbitals which were nearly doubly occupied in the states of interest and hence seemed to be not crucial, i.e., e_g of porphyrin (for all interesting states) and consequently also a_{2u} , σ_S (for Π_S , $A_{1u} \in A'$) or a_{1u} , π_S (for Σ_S , $A_{2u} \in A''$). This reduction results in an “11 in 8” active space (the previous, bigger one is called “15 in 12”). Our experience from an “15 in 12” active space was that the presence of the removed orbitals merely generated many “intermediate” states in CASSCF (i.e., the states lying between the states of interest as mentioned in section 2.2), which states are of no importance for final conclusions. The MS-CASPT2 ground-state candidates $1^2, 4(A_{2u}, \Sigma_S)$ and $2^4\Pi_S$ for both active spaces are compared in Table 5. One can see that the ground-state character and separation between two types of radicals are almost unaffected. Although the multiplicity of the ground state is different than previously, we are not entitled to discuss such a small difference in energies without the geometry optimization. Once again the type of exchange coupling appears to be sensitive to computational parameters. Nevertheless, Table 5 fully supports our previous conclusions regarding the radical character of the ground state. Moreover, the mixing between the CASSCF states still occurs in MS-CASPT2 to a similar extent as previously.

Another question is the dependence of our results on level shift. This was answered by analyzing level shift influence (in range 0.05–0.25 au) on relative MS-CASPT2 energies, relative SS-CASPT2 energies, reference weights, and weights of CASSCF roots in PM states. [Reference weight is the weight of the CASSCF reference function in SS-CASPT2 solution.] Details of this analysis can be found in the Supporting Information (see section 6). It shows that our results are not suffering from an intruder state problem even

for the smallest level shift, and our previous choice of 0.1 au is strongly supported. Although some dependencies on level shift are observed, they are quite understandable (they may be qualitatively explained by considering the influence of level shifting on the fraction of dynamic correlation recovered in CASPT2).

4. Conclusions

In spite of the technical difficulties due to the problem size and the need to compute high-lying A_{2u} states a reasonable active space was found. We note that no successful studies on Cpd I at the CASSCF/CASPT2 level have been reported so far. The computed ground state has an expected porphyrin radical nature in agreement with experimental results. In contrast to predicting radical character, we do not pretend to determine multiplicity of the ground state (and coupling constant J) on the basis of the above results; answering this question would require knowledge of optimal geometries for PM states since we need to compare energies differing by 1 kcal/mol or less.

We note that to obtain proper radical character and energies of the states in CASPT2, high-lying A_{2u} should be included in SA-CASSCF, and multistate treatment in CASPT2 is mandatory. Then, ab initio treatment of P450 or CPO Cpd I is possible, but there are important problems (not rooted solely in the size of the system), which had to be solved. Experience gained from this study might be useful in eventual future research employing bigger active spaces (e.g., having all d orbitals of Fe active).

It follows that the B3LYP ground state is analogous to the one found in CASSCF/MS-CASPT2 (e.g., by its spin density distribution, the electron coupling scheme, and the extent of mixing between sulfur and porphyrin radical). This agreement and observed big role of dynamic correlation—which dramatically changes identities and ordering of CASSCF states—provide a good forecast to use the B3LYP functional for similar systems. This simple method both describes exchange coupling rather well and has a dynamic correlation incorporated already in SCF (in contrast to the CASSCF/CASPT2 approach). However, one should be aware that nonhybrid functionals, with a worse description of exchange, applied to Cpd I may yield results that are qualitatively inconsistent with B3LYP and CASSCF/CASPT2 ones.

Acknowledgment. The computations were performed at the Academic Computer Centre CYFRONET AGH (computational grants no. MNiSW/SGI2800/UJ/133/2006 and MNiSW/SGI3700/UJ/133/2006). This work was partially sponsored by The Polish State Committee for Scientific Research (grant no. 2P04A 042 26). We thank Prof. K. Pierloot and Prof. B. O. Roos for valuable discussions and comments.

Supporting Information Available: B3LYP/BS1 equilibrium geometries and details of analysis of level shift influence on CASSCF/CASPT2 results. This material is available free of charge via the Internet at <http://pubs.acs.org>.

References

(1) Denisov, I. G.; Makris, T. M.; Sligar, S. G.; Schlichting, I. *Chem. Rev.* **2005**, *105*, 2253–2277.

- (2) Shaik, S.; Kumar, D.; de Visser, S. P.; Altun, A.; Thiel, W. *Chem. Rev.* **2005**, *105*, 2279–2328.
- (3) Ogliaro, F.; Cohen, S.; de Visser, S. P.; Shaik, S. *J. Am. Chem. Soc.* **2000**, *122*, 12892–12893.
- (4) Kellner, D. G.; Hung, S.-C.; Weiss, K. E.; Sligar, S. G. *J. Biol. Chem.* **2002**, *277*, 9641–9644.
- (5) Rutter, R.; Hager, L. P.; Dhonau, H.; Hendrich, M.; Valentine, M.; Debrunner, P. *Biochemistry* **1984**, *23*, 6809–6816.
- (6) Hosten, C. M.; Sullivan, A. M.; Palaniappan, V.; Fitzgerald, M. M.; Turner, J. *J. Biol. Chem.* **1994**, *269*, 13966–13978.
- (7) Roos, B. O.; Taylor, P. R.; Siegbahn, P. E. M. *Chem. Phys.* **1980**, *48*, 157–173.
- (8) Andersson, K.; Malmqvist, P.-A.; Roos, B. O. *J. Chem. Phys.* **1991**, *96*, 1218–1226.
- (9) Pierloot, K. *Mol. Phys.* **2003**, *101*, 2083–2094.
- (10) Ogliaro, F.; Cohen, S.; Filatov, M.; Harris, N.; Shaik, S. *Angew. Chem., Int. Ed.* **2000**, *39*, 3851–3855.
- (11) Frisch, M. J.; Trucks, G. W.; Schlegel, H. B.; Scuseria, G. E.; Robb, M. A.; Cheeseman, J. R.; Montgomery, J. A., Jr.; Vreven, T.; Kudin, K. N.; Burant, J. C.; Millam, J. M.; Iyengar, S. S.; Tomasi, J.; Barone, V.; Mennucci, B.; Cossi, M.; Scalmani, G.; Rega, N.; Petersson, G. A.; Nakatsuji, H.; Hada, M.; Ehara, M.; Toyota, K.; Fukuda, R.; Hasegawa, J.; Ishida, M.; Nakajima, T.; Honda, Y.; Kitao, O.; Nakai, H.; Klene, M.; Li, X.; Knox, J. E.; Hratchian, H. P.; Cross, J. B.; Bakken, V.; Adamo, C.; Jaramillo, J.; Gomperts, R.; Stratmann, R. E.; Yazyev, O.; Austin, A. J.; Cammi, R.; Pomelli, C.; Ochterski, J. W.; Ayala, P. Y.; Morokuma, K.; Voth, G. A.; Salvador, P.; Dannenberg, J. J.; Zakrzewski, V. G.; Dapprich, S.; Daniels, A. D.; Strain, M. C.; Farkas, O.; Malick, D. K.; Rabuck, A. D.; Raghavachari, K.; Foresman, J. B.; Ortiz, J. V.; Cui, Q.; Baboul, A. G.; Clifford, S.; Cioslowski, J.; Stefanov, B. B.; Liu, G.; Liashenko, A.; Piskorz, P.; Komaromi, I.; Martin, R. L.; Fox, D. J.; Keith, T.; Al-Laham, M. A.; Peng, C. Y.; Nanayakkara, A.; Challacombe, M.; Gill, P. M. W.; Johnson, B.; Chen, W.; Wong, M. W.; Gonzalez, C.; Pople, J. A. *Gaussian 03, revision C.02*; Gaussian, Inc.: Wallingford, CT, 2004.
- (12) Pierloot, K.; Dumez, B.; Widmark, P.-O.; Roos, B. *Theor. Chim. Acta* **1995**, *90*, 87–114.
- (13) Baerends, E. et al. *ADF2004.01*; SCM, Theoretical Chemistry, Vrije Universiteit: Amsterdam, The Netherlands. <http://www.scm.com> (accessed December 2006).
- (14) Cossi, M.; Rega, N.; Scalmani, G.; Barone, V. *J. Chem. Phys.* **2001**, *114*, 5691–5701.
- (15) Klamt, A. *J. Phys. Chem.* **1995**, *99*, 2224–2235.
- (16) Andersson, K. et al. *MOLCAS Version 5.4*; Lund University: Sweden, 2002.
- (17) Finley, J.; Malmqvist, P.-A.; Roos, B. O.; Serrano-Andres, L. *Chem. Phys. Lett.* **1998**, *288*, 299–306.
- (18) Rodriguez, J. H.; McCusker, J. K. *J. Chem. Phys.* **2002**, *116*, .
- (19) Schaftenaar, G.; Noordik, J. *J. Comput.-Aided Mol. Des.* **2000**, *14*, 123–134.
- (20) Serrano-Andrés, L.; Merchán, M.; Lindh, R. *J. Chem. Phys.* **2005**, *122*, 104107–104116.

JCTC

Journal of Chemical Theory and Computation

Equilibrium Geometries of Noncovalently Bound Intermolecular Complexes Derived from Subsystem Formulation of Density Functional Theory[†]

Marcin Dułak,[‡] Jakub W. Kamiński,^{*,‡,§} and Tomasz A. Wesolowski[‡]

Département de Chimie Physique, Université de Genève, 30, quai Ernest-Ansermet, CH-1211 Genève 4, Switzerland, and Institute of Physical and Theoretical Chemistry, Wrocław University of Technology, Wyb. Wyspiańskiego 27, 50-370 Wrocław, Poland

Received December 18, 2006

Abstract: The subsystem formulation of density functional theory is used to obtain equilibrium geometries and interaction energies for a representative set of noncovalently bound intermolecular complexes. The results are compared with literature benchmark data. The range of applicability of two considered approximations to the exchange-correlation- and nonadditive kinetic energy components of the total energy is determined. Local density approximation, which does not involve any empirical parameters, leads to excellent intermolecular equilibrium distances for hydrogen-bonded complexes (maximal error 0.13 Å for NH₃–NH₃). It is a method of choice for a wide class of weak intermolecular complexes including also dipole-bound and the ones formed by rare gas atoms or saturated hydrocarbons. The range of applicability of the chosen generalized gradient approximation, which was shown in our previous works to lead to good interaction energies in such complexes, where π -electrons are involved in the interaction, remains limited to this group because it improves neither binding energies nor equilibrium geometries in the wide class of complexes for which local density approximation is adequate. An efficient energy minimization procedure, in which optimization of the geometry and the electron density of each subsystem is made simultaneously, is proposed and tested.

1. Introduction

The principal motivation for this work originates in our interest in the *orbital-free embedding* formalism¹ to study environment-induced changes of the electronic structure of an embedded species: localized electronic excitations,^{2,3} hyperfine tensor,⁴ dipole moments,⁵ f -levels,⁶ and the gap between the high- and low spin potential energy surfaces,⁷ for instance. In the orbital-free embedding calculations, all the information about the environment is confined in its electron density, and only the selected subsystem is described at the orbital level.

The quality of such properties of the total system as electron density distribution, total energy, response properties, etc., derived from the orbital-free embedding calculations is determined by the following two factors: the use of approximate density functionals for exchange-correlation- and nonadditive kinetic energy instead of the corresponding exact quantities (see the Methods section below) and the choice of the electron density corresponding to the environment, which is derived from some other methods involving lower computational costs. Whereas the accuracy of the used functionals cannot be controlled in a straightforward manner (their exact forms are known only for some systems), the effect of the choice of the electron density of the environment can be easily verified in practice because the electron density assigned to the environment can be also subject of optimization. The process of minimization of the total energy with respect to both components of the total electron density can

[†] Dedicated to Dennis R. Salahub on the occasion of his 60th birthday.

* Corresponding author e-mail: Jakub.Kaminski@chiphy.unige.ch.

[‡] Université de Genève.

[§] Wrocław University of Technology.

proceed as a series of partial minimization steps (*freeze-and-thaw* cycle), in which both subsystems exchange their roles until minimum is reached.⁸ Of course, both subsystems are treated on equal footing, and the notion of *environment* and *embedded subsystem* loses its meaning at the end of such minimization procedure. Fully variational calculations represent numerical implementation of the subsystem formulation of density functional theory (DFT) introduced by Cortona.⁹

In the multilevel computer simulations applying orbital-free embedding formalism, fully variational calculations can be applied as a complementary tool to assess the adequacy of the electron density chosen to represent the environment. For instance, the effect of relaxation of the electron density of the environment in model systems was reported in several previous publications.^{2-4,6}

This work concerns the source of errors in orbital-free embedding calculations arising from the use of approximate density functionals for exchange-correlation and nonadditive kinetic energies. To this end, the subsystem formulation of DFT is used to minimize the total energy with respect to electron densities of both subsystems in a representative sample of weakly interacting intermolecular complexes. Compared to investigations of the adequacy of the applied density functional reported previously, we focus the analysis not on interaction energies only but on equilibrium geometries.

The effect of the environment on the electronic structure of the embedded subsystem can be seen as the result of two effects: the environment induced changes of the geometry and the direct electronic effects (for a recent representative analysis, see ref 10). In many cases, the geometry of the investigated system is known from either experiment or computational studies applying other methods. It would be, however, desirable to apply the *orbital-free embedding* type of calculations also to optimize the geometry of the embedded subsystem without relying on structural data obtained from other methods.

Studying the applicability of the subsystem formulation of density functional theory to derive equilibrium geometries is made here not only for the outlined pragmatic reasons. Whereas the errors in the total energy originate from the errors in the functionals and their derivatives, the errors in the equilibrium geometry originate only from the fact that the functional derivatives (effective potentials) of the relevant density functionals are not exact. We note that the errors in electron density and all one-electron properties also depend only on the quality of the effective potentials.

Opposite to the Kohn–Sham formulation of DFT, not a single reference system of noninteracting electrons but several such artificial systems are considered in the subsystem formulation of DFT.⁹ As a consequence, different components of the total energy are approximated by means of explicit density functionals than in calculations based on the Kohn–Sham framework. In the subsystem formulation of DFT, the approximated components include exchange-correlation energy and a small part of the kinetic energy (nonadditive kinetic energy). Both local density approximation (LDA) and generalized gradient approximation (GGA)

types of functionals for the kinetic energy component have been used/tested.¹¹ Using LDA functionals for all relevant energy contributions in subsystem formulation of DFT results in a computational method which is entirely parameter-free. In previous computational studies of weakly bound intermolecular complexes, which focused mainly on interaction energies, this approximation proved to be very good for hydrogen-bonded complexes¹² as well as a number of other complexes formed by atoms or nonpolar molecules Ne–Ne, F₂–Ne, N₂–N₂, N₂–Ar, Ar–Ar, and CH₄–CH₄, for instance.¹³ For a large class of weak intermolecular complexes, however, such as diatomic molecules interacting with benzene,¹⁴ benzene dimer,¹⁵ C₃H₆–Ar, C₆H₆–Ar, C₆H₆–CH₄, C₆H₆–C₂H₆, C₃H₈–C₃H₈, C₆H₆–C₂H₄, and C₆H₆–C₂H₂,¹³ LDA leads to unsatisfactory results. As a rule of thumb, LDA fails in obtaining interaction energies if π -systems are involved in the intermolecular interaction.¹⁶ For such a system, a particular combination of gradient dependent functionals of the GGA type proposed and tested for the first time in ref 14 improves the interaction energies qualitatively. Unfortunately, this approximation worsens the interaction energies in the case of systems for which LDA is adequate. We underline that opposite to the LDA case, the GGA functionals are not defined uniquely. In our choice for GGA functionals, motivated by their properties, the nonadditive kinetic energy is approximated using such a GGA functional, which leads to the best associated functional derivative in the case of weakly overlapping pairs of electron densities.¹¹ As far as the exchange-correlation component is concerned, the chosen approximation is the functional of Perdew and Wang,^{17,18} which has the most similar analytic form to the one for the kinetic energy part and satisfies the Lieb-Oxford condition.¹⁹

It is worthwhile to recall that in the original applications of the subsystem formulation of density functional theory to ionic solids, the subsystems corresponded to atoms and the LDA functionals were used together with additional approximations on the symmetry and localization of orbitals for each subsystem.^{9,20} In our adaptation of this formalism to molecular systems, LDA and GGA functionals can be used, and no restrictions are made on symmetry or localization of orbitals in each subsystem.⁸

The above numerical results concerning applicability of LDA and GGA functionals in the subsystem formulation of DFT leave us, therefore, with a number of questions of practical importance such as the following: (i) In which class of systems LDA can be reliably applied to obtain interaction energies? (ii) In which class of systems GGA can be reliably applied to obtain interaction energies? (iii) How good are LDA and GGA equilibrium geometries?

LDA applied in the Kohn–Sham framework to approximate the exchange-correlation energy is known to lead to rather unsatisfactory interaction energies for weakly bound intermolecular complexes. Therefore, the good performance of LDA applied to both exchange-correlation and nonadditive kinetic energy functionals in the subsystem formulation of DFT indicates that errors in the corresponding functionals cancel each other to some extent. This brings up additional intriguing questions of a more fundamental nature: (iv) What

are the physical conditions for such a cancellation to take place? (v) How to construct conjoint gradient-dependent approximations to the exchange-correlation- and nonadditive kinetic energies assuring that such cancellation is maximal?

Moreover, since the overall accuracy of the interaction energy is determined by the errors in two types of quantities, functionals and their functional derivatives, it is important to assess the quality of these quantities independently for each considered approximation.

In this work, we report the results of numerical analysis addressing some of the above practical issues in detail. To this end, the equilibrium geometries are in focus of our analysis. The quality of this property is determined by the functional derivatives of the approximated density functionals. The practical importance of determining the range of applicability of LDA and GGA are obvious. This work complements the recently reported analysis of the interaction energies¹⁶ calculated at equilibrium geometries obtained from benchmark wavefunction based calculations.

As far as accuracy of the kinetic-energy-functional dependent energy component is concerned, the Kohn–Sham results (LDA and GGA) are also discussed in this work. In the applied computational scheme, any differences between Kohn–Sham and subsystem-based calculations can be attributed to this functional (and its derivative).

For some intermolecular complexes of high symmetry, we reported already the equilibrium geometries derived from subsystem based calculations applying the functionals of the LDA and GGA type. The recent numerical implementation of the formalism makes it possible to study systems with more degrees of freedom such as the ones in the Zhao and Truhlar data set comprising equilibrium geometries and interaction energies for a group of representative intermolecular complexes,²¹ obtained by means of a high-level wave function based type of calculations and intended to be used as a benchmark. These authors used the same reference data to assess the performance of various approximations to the exchange-correlation energy functional applied within the Kohn–Sham framework.

The complexes in the test set are divided into the following groups:^{22,23}

- *hydrogen bonded* (HB6/04) $\text{NH}_3\text{--NH}_3$, HF--HF , $\text{H}_2\text{O--H}_2\text{O}$, $\text{NH}_3\text{--H}_2\text{O}$, $\text{HCONH}_2\text{--HCONH}_2$, and HCOOH--HCOOH ,

- *dominated by dipolar interactions* (DI6/04): $\text{H}_2\text{S--H}_2\text{S}$, HCl--HCl , $\text{H}_2\text{S--HCl}$, $\text{CH}_3\text{Cl--HCl}$, $\text{HCN--CH}_3\text{SH}$, and $\text{CH}_3\text{SH--HCl}$,

- *weakly bonded* (WI9/04): He--Ne , He--Ar , Ne--Ne , Ne--Ar , $\text{CH}_4\text{--Ne}$, $\text{C}_6\text{H}_6\text{--Ne}$, $\text{CH}_4\text{--CH}_4$, $\text{C}_2\text{H}_2\text{--C}_2\text{H}_2$, and $\text{C}_2\text{H}_4\text{--C}_2\text{H}_4$. It is worthwhile to underline that the strength of intermolecular interactions varies in a wide range (up to about 16 kcal/mol).

The numerical differences between our results and that in the compared database can be attributed to three factors: (i) the used basis sets, (ii) numerical procedures, and (iii) the approximations to the relevant density functionals. The errors due to the first two factors can be easily controlled and reduced in our implementation of the formalism. The effect of using approximated functionals instead of the exact ones

requires, however, dedicated studies on a case by case basis such as the ones reported in the present work.

2. Methods

2.1. The Subsystem Formulation of Density Functional Theory. In the subsystem formulation of density functional theory,⁹ several sets of one-electron functions are used to construct the electron density of each subsystem. Within each set, the one-electron functions are orthogonal.

In the particular case of two subsystems, considered here, a natural choice of the subsystems corresponds to individual molecules forming the complex. The key quantity in this formulation of DFT is the functional referred to here as Ξ^S , which depends explicitly on two sets of one-electron functions ($\{\phi_i^A\}$, $i = 1, N^A$, $\{\phi_i^B\}$, $i = 1, N^B$) and reads as

$$\Xi^S[\{\phi_i^A\}, \{\phi_i^B\}] = V[\rho_A + \rho_B] + J[\rho_A + \rho_B] + E_{\text{xc}}[\rho_A + \rho_B] + 2 \sum_{i=1}^{N^A} \left\langle \phi_i^A \left| -\frac{1}{2} \nabla^2 \right| \phi_i^A \right\rangle + 2 \sum_{i=1}^{N^B} \left\langle \phi_i^B \left| -\frac{1}{2} \nabla^2 \right| \phi_i^B \right\rangle + T_s^{\text{nad}}[\rho_A, \rho_B] \quad (1)$$

where

$$\rho_A = 2 \sum_{i=1}^{N^A} |\phi_i^A|^2 \quad \rho_B = 2 \sum_{i=1}^{N^B} |\phi_i^B|^2 \quad (2)$$

The density functionals $E_{\text{xc}}[\rho]$, $J[\rho]$, and $V[\rho]$, represent exchange-correlation energy, the Coulomb repulsion, and the energy of the interaction with external field (nuclei), respectively. These functionals are defined in the same way as in the Kohn–Sham formulation of DFT. The bifunctional $T_s^{\text{nad}}[\rho_A, \rho_B] = T_s[\rho_A + \rho_B] - T_s[\rho_A] - T_s[\rho_B]$ is expressed by means of the density functional of the kinetic energy in the reference system of noninteracting electrons ($T_s[\rho]$).²⁴ In practical calculations based on the Kohn–Sham formalism, the numerical value of $T_s[\rho]$ is available at the end of the self-consistent procedure without relying on any approximated functionals. In calculations based on the subsystem formulation of DFT, only the embedded orbitals are available. They are used to calculate the exact values of $T_s[\rho_A]$ and $T_s[\rho_B]$. The numerical value of the total kinetic energy $T_s[\rho_A + \rho_B]$ is constructed using the exact results for $T_s[\rho_A]$ and $T_s[\rho_B]$ and the $T_s^{\text{nad}}[\rho_A, \rho_B]$ term, which is calculated by means of an approximated functional depending explicitly on two electron densities.

The functional $\Xi^S[\{\phi_i^A\}, \{\phi_i^B\}]$ is related to the Hohenberg–Kohn energy functional $E^{\text{HK}}[\rho]$:²⁵

$$\begin{aligned} E^{\text{HK}}[\rho_A + \rho_B] &= \min_{\{\phi_i^A\} \rightarrow \rho_A} \min_{\{\phi_i^B\} \rightarrow \rho_B} \Xi^S[\{\phi_i^A\}, \{\phi_i^B\}] \\ &= \min_{\{\phi_i^A\} \rightarrow \rho_A} \Xi^E[\{\phi_i^A\}, \rho_B] \\ &\leq \Xi^E[\{\phi_i^A\}, \rho_B] \leq \Xi^S[\{\phi_i^A\}, \{\phi_i^B\}] \end{aligned} \quad (3)$$

The equality is reached for the orbitals, obtained in the constrained search definition of $T_s[\rho]$ ²⁴ provided the total

electron density $\rho_A + \rho_B$ is ν -representable, i.e., the $E^{\text{HK}}[\rho_A + \rho_B]$ exists (for a complete discussion of the relation between the universal functionals in Hohenberg–Kohn theorem and their counterparts defined in constrained search see ref 26).

Euler–Lagrange minimization of $\Xi^E[\{\phi_i^A\}, \rho_B]$ with respect to $\{\phi_i^A\}$ leads to one-electron equations¹

$$\left[-\frac{1}{2}\nabla^2 + v_{\text{eff}}^{\text{KSCED}}[\rho_A, \rho_B]\right]\phi_i^A = \epsilon_i^A \phi_i^A \quad i = 1, N^A \quad (4)$$

where

$$v_{\text{eff}}^{\text{KSCED}}[\rho_A, \rho_B](\vec{r}) = v_{\text{eff}}^{\text{KS}}[\rho_A + \rho_B](\vec{r}) + \left.\frac{\delta T_s^{\text{nad}}[\rho, \rho_B]}{\delta \rho(\vec{r})}\right|_{\rho=\rho_A} \quad (5)$$

The label KSCED (Kohn–Sham Equations with Constrained Electron Density) is used here to indicate that the multiplicative potential and the obtained one-electron functions differ from the corresponding quantities in the Kohn–Sham framework.

To facilitate comparisons with other embedding approaches, it is convenient to split $v_{\text{eff}}^{\text{KSCED}}$ into two components: the Kohn–Sham effective potential for the isolated subsystem A (all ρ_B -independent terms) and the remaining part representing the effect of the environment (all ρ_B -dependent terms)

$$v_{\text{eff}}^{\text{KSCED}}[\rho_A, \rho_B](\vec{r}) = v_{\text{eff}}^{\text{KS}}[\rho_A](\vec{r}) + v_{\text{emb}}^{\text{KSCED}}[\rho_A, \rho_B](\vec{r}) \quad (6)$$

where

$$v_{\text{eff}}^{\text{KS}}[\rho_A](\vec{r}) = v_{\text{ext}}^A(\vec{r}) + \int \frac{\rho_A(\vec{r}')}{|\vec{r}' - \vec{r}|} d\vec{r}' + \left.\frac{\delta E_{\text{xc}}[\rho]}{\delta \rho(\vec{r})}\right|_{\rho=\rho_A} \quad (7)$$

and

$$v_{\text{emb}}^{\text{KSCED}}[\rho_A, \rho_B](\vec{r}) = v_{\text{ext}}^B(\vec{r}) + \int \frac{\rho_B(\vec{r}')}{|\vec{r}' - \vec{r}|} d\vec{r}' + \left.\frac{\delta E_{\text{xc}}[\rho]}{\delta \rho(\vec{r})}\right|_{\rho=\rho_A+\rho_B} - \left.\frac{\delta E_{\text{xc}}[\rho]}{\delta \rho(\vec{r})}\right|_{\rho=\rho_A} + \left.\frac{\delta T_s^{\text{nad}}[\rho, \rho_B]}{\delta \rho(\vec{r})}\right|_{\rho=\rho_A} \quad (8)$$

Note that it is sufficient to know the electron density of the environment ρ_B to express the embedding potential given in eq 8. No information about the orbital structure of the environment is needed. For this reason, we refer to calculations using eq 8 as *orbital-free embedding*. The results of embedding calculations depend, however, on the choice made for ρ_B . In this work, ρ_B and ρ_A are treated at the same footing, as in the original subsystem formulation of DFT by Cortona. The two sets of orbitals $\{\phi_i^A\}$ and $\{\phi_i^B\}$ minimizing $\Xi^S[\{\phi_i^A\}, \{\phi_i^B\}]$ satisfy two sets of coupled equations

$$\left[-\frac{1}{2}\nabla^2 + v_{\text{eff}}^{\text{KSCED}}[\rho_A, \rho_B]\right]\phi_i^A = \epsilon_i^A \phi_i^A \quad i = 1, N^A \quad (9)$$

$$\left[-\frac{1}{2}\nabla^2 + v_{\text{eff}}^{\text{KSCED}}[\rho_B, \rho_A]\right]\phi_i^B = \epsilon_i^B \phi_i^B \quad i = 1, N^B \quad (10)$$

where the electron densities and orbitals are related via eq 2.

At a given external field (geometry of nuclei), minimization of the total energy with respect to ρ_A and ρ_B can be obtained in a self-consistent procedure (*freeze-and-thaw*⁸), in which eqs 9 and 10 are solved consecutively until convergence. In this way, the fully variational calculations based on the subsystem formulation of DFT are formulated as a self-consistent series of *orbital-free embedding* calculations.

The orbitals derived from eqs 9 and 10 ($\phi_{i(o)}^A$ and $\phi_{i(o)}^B$) yield the electron densities ρ_A^o and ρ_B^o . By construction, ρ_A^o and ρ_B^o are pure-state noninteracting ν -representable. Therefore,

$$T_s[\rho_A^o] = 2 \sum_{i=1}^{N^A} \left\langle \phi_{i(o)}^A \left| -\frac{1}{2}\nabla^2 \right| \phi_{i(o)}^A \right\rangle \quad (11)$$

$$T_s[\rho_B^o] = 2 \sum_{i=1}^{N^B} \left\langle \phi_{i(o)}^B \left| -\frac{1}{2}\nabla^2 \right| \phi_{i(o)}^B \right\rangle \quad (12)$$

In such a case, the right-hand side of eq 1 evaluated for $\phi_{i(o)}^A$ and $\phi_{i(o)}^B$ equals exactly to $E^{\text{HK}}[\rho_A^o + \rho_B^o]$.

2.2. Approximations for $E_{\text{xc}}[\rho]$ and $T_s^{\text{nad}}[\rho_A, \rho_B]$. In this work, LDA and GGA density functionals are considered. We will use the labels KSCED LDA and KSCED GGA for the corresponding computational methods, in which the total energy of the intermolecular complex is evaluated from eq 1 and the embedded orbitals are obtained from eqs 9 and 10.

In the KSCED LDA calculations, the exchange functional is approximated using the expression for the uniform gas of noninteracting electrons by Dirac,²⁷ the correlation energy is approximated using the Vosko et al.²⁸ parametrization (eq 4.4 in ref 28 referred frequently as “VWN V”) of the Ceperley–Alder²⁹ reference data for correlation energy in the uniform electron gas, and the nonadditive kinetic energy is approximated using the Thomas–Fermi formula for the kinetic energy.^{30,31} Note that the above approximate functionals do not rely on any empirical data.

In the KSCED GGA calculations, the Perdew–Wang (PW91)^{17,18} exchange–correlation functional is used, whereas the nonadditive kinetic energy bifunctional $T_s^{\text{nad}}[\rho_A, \rho_B]$ is approximated according to the formula: $T_s^{\text{nad}}[\rho_A, \rho_B] \approx T_s^{\text{nad(GGA97)}}[\rho_A, \rho_B] = T_s^{\text{LC94}}[\rho_A + \rho_B] - T_s^{\text{LC94}}[\rho_A] - T_s^{\text{LC94}}[\rho_B]$, where $T_s^{\text{LC94}}[\rho]$ denotes the Lembarki–Chermette³² functional of the kinetic energy. The $T_s^{\text{nad(GGA97)}}[\rho_A, \rho_B]$ was shown to provide a good approximation to the nonadditive kinetic energy potential in the case of weakly overlapping densities.^{11,33}

2.3. Energy Minimization. The local minimum at the Born–Oppenheimer potential energy surface corresponds to a minimum of the functional $\Xi^S[\{\phi_i^A\}, \{\phi_i^B\}]$ with respect to several independent quantities: positions of nuclei in each subsystem $\{\mathbf{R}_A\}$ and $\{\mathbf{R}_B\}$ (geometrical degrees of freedom) and two electron densities ρ_A and ρ_B (electronic-structure related degrees of freedom). The electronic energy in the Born–Oppenheimer approximation corresponds to the numerical value of the Hohenberg–Kohn total energy functional $E^{\text{HK}}[\rho_A^o + \rho_B^o]$. All quantities needed to evaluate

Table 1. Considered Optimization Schemes

label	optimized	frozen	treatment of ρ_A and ρ_B
A	$\{\mathbf{R}_A\}, \rho_A, \{\mathbf{R}_B\}, \rho_B$		fully variational ^{8,9}
B	$\{\mathbf{R}_A\}, \rho_A, \rho_B$	$\{\mathbf{R}_B\}$	fully variational ^{8,9}
C	ρ_A, ρ_B	$\{\mathbf{R}_A\}, \{\mathbf{R}_B\}$	fully variational ^{8,9}
D	$\{\mathbf{R}_A\}, \rho_A$	$\{\mathbf{R}_B\}, \rho_B$	partially variational ¹
E	ρ_A	$\{\mathbf{R}_A\}, \{\mathbf{R}_B\}, \rho_B$	partially variational ¹
F	$\{\mathbf{R}_A\}, \{\mathbf{R}_B\}$	ρ_A, ρ_B	nonvariational (frozen) ⁴⁴
G		$\{\mathbf{R}_A\}, \{\mathbf{R}_B\}, \rho_A, \rho_B$	nonvariational (frozen) ⁴⁴

$E^{\text{HK}}[\rho_A^o + \rho_B^o]$ and its gradients with respect to nuclear positions are available at the end of the *freeze-and-thaw* procedure (schemes A–C in Table 1).

If, however, only one component of the electron density (say ρ_A) is subject to optimization (eq 4), whereas ρ_B is not (schemes D and E in Table 1), eq 1 provides the upper bound for the electronic energy in the Born–Oppenheimer approximation

$$E^{\text{HK}}[\rho_A^o(B) + \rho_B] \geq E^{\text{HK}}[\rho_A^o + \rho_B^o] = E^{\text{HK}}[\rho_{AB}^o] \quad (13)$$

where $\rho_A^o(B)$ denotes the electron density obtained from eq 4, in which a given ρ_B is used. On the virtue of the second Hohenberg–Kohn theorem, the equality is reached only if the assumed ρ_B added to $\rho_A^o(B)$ equals the ground-state electron density at this geometry (ρ_{AB}^o). Nevertheless, the orbitals obtained from eq 4 provide all necessary quantities to evaluate the numerical value of $E^{\text{HK}}[\rho_A^o(B) + \rho_B] - E^{\text{HK}}[\rho_B]$ and its gradients with respect to the coordinates of the nuclei in the subsystem A. Therefore, it is possible to optimize the geometry of subsystem A with frozen geometrical and electronic degrees of freedom of the subsystem B (scheme D in Table 1). For an assumed ρ_B its adequacy can be controlled by comparing the results obtained from schemes D and B (or E and C if the geometry is not the subject of investigation).

We notice also that the Gordon–Kim model^{34,35} (schemes F and G in Table 1) represents an extremely simplified optimization scheme, in which changes of ρ_A and ρ_B associated with intersubsystem degrees of freedom are not taken into account. Such a scheme is only applicable in some cases (rare gas dimers, for instance). For molecules, neglecting the complexation induced changes of the electron density is not a universally adequate approximation as reported previously.^{12,13}

Our numerical implementation of eqs 9 and 10 makes it possible to perform the total energy optimization following each of the schemes listed in Table 1.

In this work, we focus on the adequacy of the used approximations to $E_{\text{xc}}[\rho]$ and $T_s^{\text{nad}}[\rho_A, \rho_B]$ functionals for obtaining equilibrium geometries. Therefore, scheme A (full optimization including geometrical and electronic degrees of freedom) is applied. In our previous works, concerning the interaction energies at some representative points at the potential energy surface, scheme C was applied.^{12,13,16} We perform the search for the local minima in the vicinity of the reference equilibrium structures taken from the data set of Zhao and Truhlar. The equilibrium geometries are obtained following an efficient minimization procedure, in which the

structural and electronic degrees of freedom are optimized simultaneously (sequence II in Table 2). For each geometry update either eq 9 or 10 is solved only once. Until the equilibrium energy is reached, the numerical value of $E^{\text{HK}}[\rho_A^o(B) + \rho_B]$ (or $E^{\text{HK}}[\rho_A + \rho_B^o(A)]$) does not correspond to the electronic energy in the Born–Oppenheimer approximation. Obtaining this energy at intermediate geometries would require performing the *freeze-and-thaw* procedure (see sequence I in Table 2). Typically, the *freeze-and-thaw* procedure involves solving the pair of eqs 9 and 10 two or three times. Therefore, sequence II can be expected to reduce the computational effort by about a factor of 5. In this work, we consider also an even more simplified optimization procedure, in which the exchange–correlation and nonadditive kinetic energy functionals are linearized in either ρ_A (eq 9) or in ρ_B (eq 10). The errors associated with the linearization are small, and they disappear by construction at the end of the *freeze-and-thaw* procedure³⁶ (and also at the end of the geometry optimization procedure). The resulting computational savings depend on the number of iterations in the self-consistent procedure to solve eq 4.

2.4. Computational Details. The calculations are carried out using our numerical implementation of the subsystem formulation of DFT (the program deMon2K-KSCED³⁷) based on the program deMon2K.³⁸ For geometry optimization, the following deMon2K-KSCED options and parameters are applied: 10^{-6} au self-consistent field energy convergence criterion, adaptive grid (TOL=5.0E-07 “GUESS” grid³⁹), and the atomic basis set MG3S⁴⁰ used within the monomer-centered expansion scheme (KSCED(m) - see below). The MG3S basis set is chosen based on our recently reported analysis¹⁶ of the effect of changing the basis set on the interaction energies. In principle, two types of basis set expansions can be considered for orbitals corresponding to each subsystem: centered on the monomer or centered on the dimer. The corresponding calculations are labeled as KSCED(m) or KSCED(s), respectively, following the convention of ref 11. For a given choice of the atomic basis sets, the KSCED(s) scheme leads to results closer to the complete basis set limit than the KSCED(m) one. However, if the atomic basis sets are sufficiently large, as the ones chosen for these studies, the two schemes lead to very similar interaction energies.¹⁶ For the calculation of the interaction energies on the optimized geometries, the following deMon2K-KSCED program options are applied: 10^{-6} au self-consistent field energy convergence criterion, the pruned “MEDIUM” (75,302)p⁴¹ grid, and the dimer-centered MG3S basis sets (KSCED(s) type of calculations).

Classical electron–electron interactions (Coulomb) are evaluated using auxiliary fitting functions referred to as GEN-A2*, which are automatically generated for any given orbital basis sets.⁴² Further details concerning the formal framework of the applied computational methods and the numerical implementation can be found in refs 8, 9, and 12.

The energy derivatives with respect to the coordinates of nuclei of the subsystem A are calculated using the deMon2K-KSCED program and passed together with the total energy and the coordinates of the subsystem A to the generic limited-memory quasi-Newton code for unconstrained optimization

Table 2. Complete (Sequence I) or Partial (Sequence II) Optimization of the Total Electron Density in One Update of the Coordinates of All Atoms in the Complex^a

sequence I	sequence II
$\overbrace{\{\mathbf{R}_B^k\}, \{\mathbf{R}_A^i\}, \rho_B \longleftrightarrow \rho_A}^{\text{Eq.9 or 10}}$ <p style="text-align: center;">freeze-and-thaw</p> $\Updownarrow \text{until } \mathbf{R}_A \text{ convergence} \quad i=1, N-1$ $\overbrace{\{\mathbf{R}_B^k\}, \{\mathbf{R}_A^i\}, \rho_A, \rho_B \implies \{\mathbf{R}_A^{i+1}\}}^{\text{L-BFGS}}$	$\overbrace{\{\mathbf{R}_B^k\}, \{\mathbf{R}_A^i\}, \rho_B \implies \rho_A^i}^{\text{Eq.9}}$ $\Updownarrow \text{until } \mathbf{R}_A \text{ convergence} \quad i=1, N-1$ $\overbrace{\{\mathbf{R}_B^k\}, \{\mathbf{R}_A^i\}, \rho_A^i, \rho_B \implies \{\mathbf{R}_A^{i+1}\}}^{\text{L-BFGS}}$
$\overbrace{\{\mathbf{R}_B^k\}, \{\mathbf{R}_A^N\}, \rho_A \longleftrightarrow \rho_B}^{\text{Eq.10 or 9}}$ <p style="text-align: center;">freeze-and-thaw</p> $\Updownarrow \text{until } \mathbf{R}_B \text{ convergence} \quad k=1, M-1$ $\overbrace{\{\mathbf{R}_B^k\}, \{\mathbf{R}_A^N\}, \rho_A, \rho_B \implies \{\mathbf{R}_B^{k+1}\}}^{\text{L-BFGS}}$	$\overbrace{\{\mathbf{R}_B^k\}, \{\mathbf{R}_A^N\}, \rho_A^N \implies \rho_B^k}^{\text{Eq.10}}$ $\Updownarrow \text{until } \mathbf{R}_B \text{ convergence} \quad k=1, M-1$ $\overbrace{\{\mathbf{R}_B^k\}, \{\mathbf{R}_A^N\}, \rho_A^N, \rho_B^k \implies \{\mathbf{R}_B^{k+1}\}}^{\text{L-BFGS}}$

^a The self-consistent procedure to solve eqs 9 and 10 is denoted with *freeze-and-thaw*. The procedure to update of the coordinates in one subsystem using analytic gradients obtained from eq 9 (for subsystem A) or eq 10 (for subsystem B) is denoted with L-BFGS.

L-BFGS⁴³ (Broyden-Fletcher-Goldfarb-Shanno) using a Perl script, which controls the optimization process. The L-BFGS algorithm uses the following two nondefault parameters: EPS = 1.0E-05 (threshold for the norm of the gradient in [hartree/bohr]) and M = 5 (the number of corrections used in the update of the inverse of the Hessian). Such an optimization procedure yields the precision of the intermolecular distances for the given set of molecules on the order of 0.01 Å as tested by performing optimization starting from different geometries. The applied optimization procedure is very efficient in localizing the equilibrium intermolecular distance. For all systems discussed in this study, the equilibrium geometries were obtained by performing multiple optimization runs, each starting from a different geometry of the complex. In the initial geometry, the original structure from the Zhao–Truhlar database was modified by changing the intermolecular distance (by a few Å) as well as by mutual orientation of the monomers. Such a procedure

leads to almost identical final geometries (they lie within 0.01 Å). Unfortunately, such a procedure fails to localize the minimum at flat potential energy surfaces, where some degrees of freedom are associated with very small gradients such as that corresponding to a parallel displacement of one monomer in the benzene dimer.

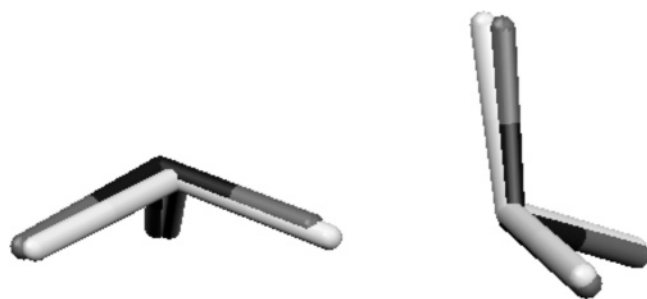
3. Results and Discussion

3.1. Geometries: LDA. Table 3 collects the selected representative parameters describing intermolecular degrees of freedom in the considered complexes derived from KSCED LDA calculations together with the corresponding reference data. The chosen two geometrical parameters are the intermolecular distance *R* between the closest two heavy atoms in two molecules forming the complex and a representative angle describing the relative orientation of the monomers (*φ*). The labels given for the chosen angle allow one to identify it in a straightforward manner. For instance,

Table 3. Key Parameters of the Equilibrium Geometry Obtained from KSCED LDA Calculations^a

compound	Def _R	R	R _{ref}	R - R _{ref}	Def _φ	φ	φ _{ref}
NH ₃ -NH ₃	dNN	3.14	3.27	-0.13	HNN	16	14
HF-HF	dFF	2.87	2.78	0.08	HFF	113	115
H ₂ O-H ₂ O	dOO	2.96	2.94	0.02	HOO	5	4
NH ₃ -H ₂ O	dNO	2.97	2.97	0.01	HON	5	6
HCONH ₂ -HCONH ₂	dNO	2.89	2.88	0.01	ONC	114	116
HCOOH-HCOOH	dOO	2.81	2.70	0.11	OOO	127	125
H ₂ S-H ₂ S	dSS	4.03	4.12	-0.09	HSS	90	84
HCl-HCl	dClCl	3.60	3.79	-0.19	HClCl	47	8
H ₂ S-HCl	dSCl	3.81	3.76	0.05	HCIS	92	88
CH ₃ Cl-HCl	dClCl	3.70	3.61	0.09	CIClC	81	82
HCN-CH ₃ SH	dCS	3.62	3.52	0.10	SNC	170	162
CH ₃ SH-HCl	dSCl	3.70	3.61	0.09	HCIS	14	11
He-Ne	dHeNe	2.81	3.03	-0.22	-	-	-
He-Ar	dHeAr	3.16	3.48	-0.32	-	-	-
Ne-Ne	dNeNe	3.04	3.09	-0.05	-	-	-
Ne-Ar	dNeAr	3.47	3.49	-0.02	-	-	-
CH ₄ -Ne	dCNe	3.44	3.49	-0.05	HNeC	70	71
C ₆ H ₆ -Ne	dCNe	3.66	3.51	0.15	NeCC	79	79
CH ₄ -CH ₄	dCC	3.61	3.61	-0.00	HCC	70	70
C ₂ H ₂ -C ₂ H ₂	dCC	3.22	3.46	-0.23	CCC	122	123
C ₂ H ₄ -C ₂ H ₄	dCC	3.83	3.83	0.00	CCC	80	80

^a *R* (in Å) denotes the distance between the two closest heavy atoms of different monomers, and *φ* (in deg) is a representative angle determining the relative orientation between the monomers. The reference values *R*_{ref} and *φ*_{ref} are taken from ref 22.

**Figure 1.** The optimized geometry (KSCED LDA) of the H₂O-H₂O complex superimposed on the reference equilibrium geometry (dark colors).**Figure 2.** The optimized geometry (KSCED LDA) of NH₃-NH₃ superimposed on the reference equilibrium geometry (dark colors).

the HOO denotes the H-O-O angle in the case of the water dimer.

KSCED LDA performs very well for hydrogen-bonded complexes. This result is illustrated in Figures 1 and 2 showing the optimized geometry superimposed on the

reference one for two representative complexes: H₂O-H₂O, for which KSCED LDA optimized geometry deviates the least from the reference one, and NH₃-NH₃, from which the deviation from the reference is the largest among the hydrogen-bonded complexes. The errors of intermolecular distances *R* are smaller than 0.10 Å for all complexes in this set except for NH₃-NH₃ and HCOOH-HCOOH. The errors in intermolecular distances tend to decrease with increasing binding energy.

In the set of the complexes of dipole character the most important difference with respect to the reference geometry is found for HCl-HCl. In the LDA optimized geometry, two monomers are in a parallel-like orientation, and in the reference one they are almost perpendicular.

For the most weakly bound systems, noticeable errors in the intermolecular distance (0.2–0.3 Å) occur for He-Ne, He-Ar, and C₆H₆-Ne. Most of the intermolecular equilibrium distances in this set are underestimated, which is an opposite tendency found in the other sets.

Analyzing the overall performance of local density approximation shows that it performs very well for hydrogen-bonded complexes, which confirms the results reported elsewhere,¹² and reasonably well for weakly bound complexes. In most cases, local density approximation overestimates intermolecular distances, except for the complexes in the W9/04 set (weakly bound complexes).

Local density approximation applied within the Kohn-Sham framework leads systematically to worse results. In the case of all considered intermolecular complexes, the Kohn-Sham LDA calculations lead to underestimated intermolecular equilibrium distances. For hydrogen-bonded complexes, the errors reach -0.27 Å for NH₃-NH₃. In the case of dipole bound species, the maximal error occurs for H₂S-H₂S (-0.38 Å). Taking into account that the errors of equilibrium geometries are determined by the quality of the exchange-correlation effective potential whereas the differences between Kohn-Sham LDA and KSCED LDA results are due to the errors in the functional derivatives of the T_s^{nadd} , the superiority of KSCED LDA is the result of the compensation of errors in these quantities. For interaction energies, such compensation was reported previously for several systems^{13,14} (see also below).

3.2. Geometries: GGA. KSCED GGA calculations lead to underestimated intermolecular distances for all considered complexes (see Table 4). For hydrogen-bonded complexes, the errors in intermolecular distance are larger than the ones in the KSCED LDA case reaching -0.43 Å for NH₃-NH₃. Figures 3 and 4 show the KSCED GGA optimized geometry superimposed on the reference one for two representative complexes: HCOOH-HCOOH, for which KSCED GGA optimized geometry deviates the least from the reference one, and NH₃-NH₃, for which the deviation from the reference is the largest among the hydrogen-bonded complexes.

For the dipole-bound complexes, the largest difference with respect to the reference geometry is found for HCl-HCl. As in the case of KSCED LDA equilibrium geometry, the two monomers adopt a parallel-like orientation. In this group of complexes, the errors in the intermolecular distances are rather large reaching 0.44 Å for HCl-HCl.

Table 4. Key Parameters of the Equilibrium Geometry Obtained from KSCED GGA Calculations^a

compound	Def _R	R	R _{ref}	R - R _{ref}	Def _φ	φ	φ _{ref}
NH ₃ -NH ₃	dNN	2.83	3.27	-0.43	HNN	40	14
HF-HF	dFF	2.73	2.78	-0.05	HFF	103	115
H ₂ O-H ₂ O	dOO	2.84	2.94	-0.10	HOO	5	4
NH ₃ -H ₂ O	dNO	2.86	2.97	-0.11	HON	6	6
HCONH ₂ -HCONH ₂	dNO	2.77	2.88	-0.11	ONC	115	116
HCOOH-HCOOH	dOO	2.68	2.70	-0.02	OOO	128	125
H ₂ S-H ₂ S	dSS	3.84	4.12	-0.27	HSS	94	84
HCl-HCl	dClCl	3.35	3.79	-0.44	HClCl	46	8
H ₂ S-HCl	dSCl	3.62	3.76	-0.14	HCIS	87	88
CH ₃ Cl-HCl	dClCl	3.49	3.61	-0.12	CIClC	78	82
HCN-CH ₃ SH	dCS	3.21	3.52	-0.31	SNC	146	162
CH ₃ SH-HCl	dSCl	3.47	3.61	-0.14	HCIS	21	11
He-Ne	dHeNe	2.55	3.03	-0.48			
He-Ar	dHeAr	2.97	3.48	-0.51			
Ne-Ne	dNeNe	2.73	3.09	-0.36			
Ne-Ar	dNeAr	3.22	3.49	-0.27			
CH ₄ -Ne	dCNe	3.15	3.49	-0.34	HNeC	70	71
C ₆ H ₆ -Ne	dCNe	3.39	3.51	-0.12	NeCC	78	79
CH ₄ -CH ₄	dCC	3.29	3.61	-0.33	HCC	70	70
C ₂ H ₂ -C ₂ H ₂	dCC	2.95	3.46	-0.51	CCC	120	123
C ₂ H ₄ -C ₂ H ₄	dCC	3.52	3.83	-0.31	CCC	79	80

^a R (in Å) denotes the distance between the two closest heavy atoms of different monomers, and φ (in deg) is a representative angle determining the relative orientation between the monomers. The reference values R_{ref} and φ_{ref} are taken from ref 22.

In the last group of complexes (weakly bound), the errors of the KSCED GGA equilibrium intermolecular distances are very large reaching 0.51 Å.

In view of the fact that the chosen GGA functional significantly worsens the equilibrium geometry for the complexes, for which KSCED LDA leads to rather good results, this approximation does not represent a universal improvement over LDA. Since, however, it leads to significantly better binding energies for (π-stacked systems¹³⁻¹⁵), it can be considered as a pragmatic choice for this type of complexes.

As far as Kohn-Sham calculations are concerned, the PW91 results are significantly and systematically better than the LDA ones. For instance, the errors in the PW91 equilibrium intermolecular distances do not exceed 0.1 Å, whereas the LDA one reaches -0.27 Å for hydrogen-bonded complexes. Opposite to the tendencies discussed previously for LDA, KSCED GGA are not better than Kohn-Sham PW91 ones. The Kohn-Sham equilibrium geometries are slightly (hydrogen-bonded complexes) or noticeably (dipole bound and van der Waals) better quality than the KSCED GGA results. This indicates that the error in the PW91 exchange-correlation potential is not compensated so well with the error in the GGA97 nonadditive kinetic energy potential as it is the case of LDA.

3.3. Binding Energies at Optimized Geometries. Binding energies discussed in this section are calculated at the optimized geometries and are obtained using the dimer centered expansion of the electron density of each subsystem (KSCED(s) type of calculations). The basis set superposition error and the errors resulting from the superposition of numerical grids are taken into account following the proce-

cedure of ref 16, which is also given in the Supporting Information. We start the analysis with the LDA results. For most of the considered hydrogen-bonded complexes, the binding energies are very good. For dipole-bound complexes, the errors in the binding energy are larger. The maximal relative overestimation of the binding energy for HCN-CH₃SH reaches 30%, whereas the binding energy in CH₃Cl-HCl is underestimated by 19%. For van der Waals complexes, KSCED LDA does not perform uniformly. The interactions of helium with other atoms is overestimated significantly. The accuracy of the KSCED LDA binding energies changes from excellent to mediocre along the series, Ne-Ne, Ne-Ar, Ne-CH₄, and Ne-C₆H₆. For complexes involving saturated hydrocarbons, KSCED LDA performs reasonably well underestimating, however, the binding energy.

Results collected in Table 5 indicate clearly that the presence of a multiple bond of one molecule in the vicinity of the other molecule in the complex leads systematically to significant errors in binding energies calculated at the KSCED LDA level. Except for C₂H₂-C₂H₂, they are underestimated by about a factor of 2. This trend is in line with that for interaction energies calculated at reference intermolecular geometries for the same¹⁶ or other complexes involving conjugated π systems.¹³⁻¹⁵

The choice of the GGA functionals (exchange-correlation- and nonadditive kinetic energies) used in this work was shown previously to lead to significant improvements of accuracy of the interaction energies in the cases where KSCED LDA fails: complexes between diatomic molecules and benzene,¹⁴ benzene dimer,¹⁵ and other complexes involving interactions with π bonds.¹³ Results collected in Table 5 show that this choice of gradient-dependent functionals for exchange-correlation- and nonadditive kinetic energies significantly worsens this quantity for all types of complexes considered in this work.

As far as the compensation of errors in the exchange-correlation- and nonadditive kinetic energies are concerned, a similar trend (for LDA, the compensation of errors in the energies occurs systematically, whereas it is less systematic in the GGA case) can be seen as the one for the accuracy of the effective potentials discussed in the previous section. The binding energies derived from Kohn-Sham LDA calculations are significantly worse than their KSCED LDA counterparts. For all the considered complexes, the deviations from the reference data are rather large, reaching 7.75 kcal/mol for HCONH₂-HCONH₂ and 12.01 kcal/mol for HCOOH-HCOOH (the corresponding KSCED LDA errors are 0.09 kcal/mol and 1.72 kcal/mol) for instance. As far as GGA is concerned such systematic trends cannot be identified. On the average, the Kohn-Sham PW91 binding energies are better than KSCED GGA.

3.4. Acceleration Techniques for Geometry Optimization. In this section, we consider two optimization schemes (see Table 2) as well as their two modifications: (i) sequence I', in which the converged freeze-and-thaw cycle is replaced by solving the pair of eqs 9 and 10 only once per geometry update, and (ii) a modified sequence II, in which the functional $E_{xc}[\rho_A + \rho_B] - E_{xc}[\rho_A] + T_s^{\text{nad}}[\rho_A, \rho_B]$ is linear-

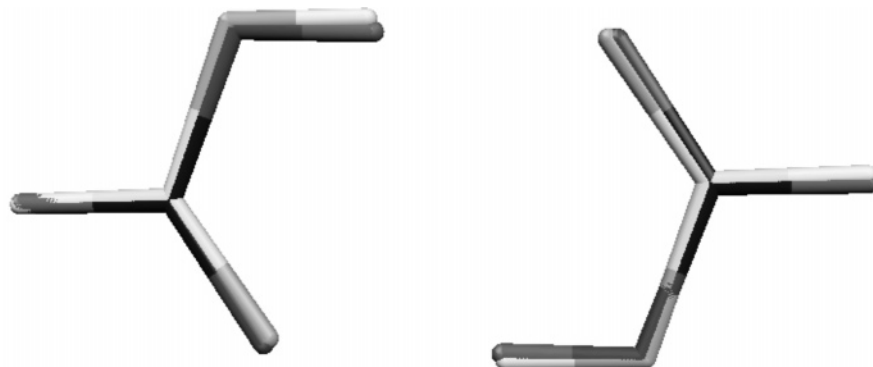


Figure 3. The optimized geometry (KSCED GGA) of the HCOOH–HCOOH complex superimposed on the reference equilibrium geometry (dark colors).

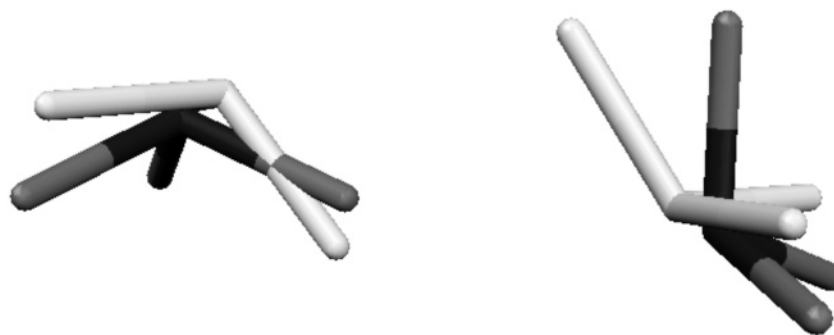


Figure 4. The optimized geometry (KSCED GGA) of NH₃–NH₃ superimposed on the reference equilibrium geometry (dark colors).

Table 5. Binding Energies ($-\Delta E$ in kcal/mol) Calculated at Optimized Geometries^a

compound	$-\Delta E^{\text{LDA}}$		$-\Delta E^{\text{GGA}}$		$-\Delta E^{\text{Ref}}$
NH ₃ –NH ₃	3.99	(27)	5.59	(77)	3.15
HF–HF	4.12	(–10)	5.00	(9)	4.57
H ₂ O–H ₂ O	4.97	(0)	5.94	(20)	4.97
NH ₃ –H ₂ O	6.72	(5)	8.03	(25)	6.41
HCONH ₂ –HCONH ₂	15.03	(1)	17.85	(19)	14.94
HCOOH–HCOOH	14.43	(–11)	17.47	(8)	16.15
H ₂ S–H ₂ S	2.12	(28)	2.76	(66)	1.66
HCl–HCl	2.18	(8)	3.19	(59)	2.01
H ₂ S–HCl	3.44	(3)	4.34	(30)	3.35
CH ₃ Cl–HCl	2.89	(–19)	4.05	(14)	3.55
HCN–CH ₃ SH	4.68	(30)	5.73	(60)	3.59
CH ₃ SH–HCl	4.40	(6)	5.74	(38)	4.16
He–Ne	0.09	(125)	0.46	(1050)	0.04
He–Ar	0.15	(150)	0.47	(683)	0.06
Ne–Ne	0.08	(0)	0.52	(550)	0.08
Ne–Ar	0.12	(–8)	0.54	(315)	0.13
CH ₄ –Ne	0.15	(–32)	0.66	(200)	0.22
C ₆ H ₆ –Ne	0.23	(–51)	0.95	(102)	0.47
CH ₄ –CH ₄	0.44	(–14)	1.03	(102)	0.51
C ₂ H ₂ –C ₂ H ₂	1.84	(37)	2.72	(103)	1.34
C ₂ H ₄ –C ₂ H ₄	1.06	(–25)	2.00	(41)	1.42

^a The relative error $((\Delta E - \Delta E^{\text{Ref}})/\Delta E^{\text{Ref}} \times 100\%)$ is given in parentheses.

ized in ρ_A in the procedure to solve eq 9 in order to accelerate it (for eq 10, $E_{\text{xc}}[\rho_A + \rho_B] - E_{\text{xc}}[\rho_B] + T_s^{\text{nad}}[\rho_A, \rho_B]$ is linearized in ρ_B). By construction, linearization is exact at

the end of the *freeze-and-thaw* cycle. In view of the fact that linearization might lead to noticeable savings in the computer time, it is worthwhile to investigate the effect of linearization applied without converging *freeze-and-thaw* cycle in the intermediate stages. For two intermolecular complexes (H₂O–H₂O, HCl–CH₃SH), performance of the four alternative optimization procedures is analyzed in either the complete or partial optimization of geometry. In the partial optimization case, the geometry of one monomer is optimized keeping the geometry of the other frozen (Scheme B in Table 1). In the geometry optimization, the same convergence criteria and the other optimization parameters as described in the previous section and local density approximation are applied. The starting geometries were prepared by modifying the coordinates taken from ref 21 for one molecule in the complex (the selected intermolecular degrees of freedom are given in Table 6).

In the complete optimization calculations, all four optimization schemes lead to equivalent results. The Cartesian coordinates of corresponding atoms in optimized structures differ by less than 0.01 Å. This scatter of the minimized geometries corresponds to the precision of the optimization procedure itself. The key geometrical parameters obtained in the partial optimization (rigid geometry of one monomer) are collected in Table 6. All simplified schemes lead to the optimized geometries, which do not differ significantly from that derived using the Born–Oppenheimer surface type of optimization (sequence I in Table 2).

Table 6. Key Parameters of the Equilibrium Geometry Obtained Using Four Optimization Procedures Considered in the Text^a

compound/parameter		sequence I	sequence I'	sequence II	sequence II linearized
H ₂ O–H ₂ O	dOO	2.95	2.95	3.02	3.00
	HOO	6	6	6	6
HCl–CH ₃ SH	dSCI	3.66	3.69	3.76	3.77
	HCIS	16	15	19	19

^a Coordinates of only one molecule (A) in the complex (A-B) are optimized. Starting parameters: dOO: 3.38 Å, HOO: 60°, dSCI: 2.65 Å, HCIS: 108°.

The computational costs of the four considered optimization schemes differ significantly. In the case of the H₂O–H₂O dimer, the most expensive one (sequence I) involves 88 geometry updates to converge the coordinates of the first subsystem and solving the pair of eqs 9 and 10 two to three times per geometry update. Sequence I' converges after 91 geometry updates; however, the pair of eqs 9 and 10 is solved only once per geometry update. In sequence II, the number of geometry updates increases to 117 but involves solving eq 9 only once per geometry update. The most effective among the studied optimization schemes is the one in which sequence II is used and eq 9 is solved using linearized functionals. Linearization results in an additional reduction of the time of computations by 20–25% per geometry update. Optimization of geometry using this scheme involves 71 geometry updates.

4. Conclusions

The current study concerns the applicability of the subsystem formulation of density functional theory for studies of equilibrium geometries and binding energies in weakly bound intermolecular complexes. Two types of approximations are considered: (i) local density approximation, which was shown in our previous studies to lead to good binding energies in hydrogen-bonded systems¹² and several weakly bound complexes^{13,16} but fails for such complexes where π -electrons are involved in the interaction,^{13,14,16} and (ii) our choice for gradient dependent approximation, which improves significantly the interaction energies for cases where LDA fails.^{13,14,16} In the present work, a systematic analysis of the accuracy of equilibrium geometries is made, complementing thus the previously obtained results concerning interaction energies and equilibrium geometries in complexes of high-symmetry.

Concerning the applicability of local density approximation in the subsystem formulation of DFT in deriving not only intermolecular energies but also equilibrium geometries, the present work confirms the adequacy of this approximation for hydrogen-bonded complexes (the largest deviation between calculated and reference intermolecular distance amounts to 0.13 Å for NH₃–NH₃), a group of dipole-bound complexes (the largest deviation between calculated and reference intermolecular distance amounts to 0.19 Å for HCl–HCl, for which also the relative orientation is the worst), and even very weak intermolecular complexes involving Ne, Ar, and saturated hydrocarbons. In this group of complexes, the maximal relative errors in the binding energies reach 30%, but they are significantly smaller in most cases. Using local density approximation in the subsystem

formulation of DFT is, however, not recommended if the target of calculations is both the binding energy and equilibrium geometry in complexes involving molecules with conjugated bonds (benzene, ethylene). This trend is in line with our previously reported results. For the weakest bonds involving He, local density approximation leads to the parameters of the potential energy surface, of only qualitative value (binding energies are overestimated by a factor of 2 or 3 in He–Ne and He–Ar dimers, respectively, whereas the equilibrium distances are too short by 0.2–0.3 Å).

As far as the chosen gradient dependent approximation is concerned, it improves neither binding energies nor equilibrium geometries in the group of complexes for which local density approximation is adequate (hydrogen bonds, dipole-bonds, weak complexes involving, Ne, Ar, or saturated hydrocarbons). Its range of applicability is, therefore, limited to such complexes where π -electrons are involved in the interaction in line with our previously reported studies.

Owing to the mathematical structure of the subsystem formulation of density functional theory, performing simultaneous optimization of different types of degrees of freedom (electron density and nuclear coordinates in each subsystem) is straightforward. An efficient optimization scheme is proposed, in which the system reaches the minimum on the Born–Oppenheimer surface only at the end of the procedure reducing thus the computational efforts in the intermediate geometries.

This work represents an intermediate step toward development of first-principles based multilevel simulation techniques for studying electronic structure in condensed matter systems. The orbital-free embedding formalism uses functionals and potentials defined in the Kohn–Sham formulation of density functional theory. However, they are applied for other basic descriptors of the whole investigated system: the embedded orbitals for one part and electron density only for another one. In the present work, we explore the applicability of the simplest approximation—local density approximation—to derive energetic and geometrical properties of weakly interacting systems. A large class of intermolecular interactions was identified, for which LDA provides an adequate approximation to derive both the properties depending on the quality of the density functionals as well as their derivatives. In this class, the balance of approximate terms is such that the errors of the exchange-correlation- and nonadditive kinetic energy functionals cancel to a large extent. Practical applications of KSCED LDA framework in multiscale numerical studies for embedded systems interacting with their environment through interactions belonging to this class are currently carried out in our group.

As far as going beyond LDA in the subsystem formulation of DFT is concerned, the current study indicates clearly that the GGA functionals chosen based on our previous studies provide only a temporary solution for cases where LDA fails. Development of a consistent GGA approximation retaining the strengths of LDA and providing an efficient compensation of errors in gradient-dependent terms is an objective of our current studies.

Acknowledgment. The CPU computer time from the Poznań Supercomputing and Networking Center is greatly acknowledged. This work has been supported by the Swiss National Scientific Foundation.

Supporting Information Available: Optimized geometries, definitions of the labels used for intermolecular degrees of freedom, binding energies, and description of numerical implementation of the formalism. This material is available free of charge via the Internet at <http://pubs.acs.org>.

References

- (1) Wesolowski, T. A.; Warshel, A. *J. Phys. Chem.* **1993**, *97*, 8050.
- (2) Wesolowski, T. A. *J. Am. Chem. Soc.* **2004**, *126*, 11444.
- (3) Neugebauer, J.; Jacob, C. R.; Wesolowski, T. A.; Baerends, E. J. *J. Phys. Chem. A* **2005**, *109*, 7805.
- (4) Neugebauer, J.; Louwse, M. J.; Belanzoni, P.; Wesolowski, T. A.; Baerends, E. J. *J. Chem. Phys.* **2005**, *123*, 114101.
- (5) Jacob, C. R.; Wesolowski, T. A.; Visscher, L. *J. Chem. Phys.* **2005**, *123*, 174104.
- (6) Zbiri, M.; Atanasov, M.; Daul, C.; Garcia-Lastra, J. M.; Wesolowski, T. A. *Chem. Phys. Lett.* **2004**, *397*, 441.
- (7) Leopoldini, M.; Russo, N.; Toscano, M.; Dułak, M.; Wesolowski, T. A. *Chem. Eur. J.* **2006**, *12*, 2532.
- (8) Wesolowski, T. A.; Weber, J. *Chem. Phys. Lett.* **1996**, *248*, 71.
- (9) Cortona, P. *Phys. Rev. B* **1991**, *44*, 8454.
- (10) Neugebauer, J.; Baerends, E. J. *J. Phys. Chem. A* **2006**, 8786.
- (11) Wesolowski, T. A. *J. Chem. Phys.* **1997**, *106*, 8516.
- (12) Kevorkyants, R.; Dułak, M.; Wesolowski, T. A. *J. Chem. Phys.* **2006**, *124*, 024104.
- (13) Wesolowski, T. A.; Tran, F. *J. Chem. Phys.* **2003**, *118*, 2072.
- (14) Wesolowski, T. A.; Ellinger, Y.; Weber, J. *J. Chem. Phys.* **1998**, *108*, 6078.
- (15) Tran, F.; Weber, J.; Wesolowski, T. A. *Helv. Chim. Acta* **2001**, *84*, 1489.
- (16) Dułak, M.; Wesolowski, T. A. *J. Mol. Mod.* **2007**, *13*, in press.
- (17) Perdew, J. P.; Chevary, J. A.; Vosko, S. H.; Jackson, K. A.; Pederson, M. R.; Singh, D. J.; Fiolhais, C. *Phys. Rev. B* **1992**, *46*, 6671.
- (18) Perdew, J. P.; Chevary, J. A.; Vosko, S. H.; Jackson, K. A.; Pederson, M. R.; Singh, D. J.; Fiolhais, C. *Phys. Rev. B* **1993**, *48*, 4978.
- (19) Lieb, E. H.; Oxford, S. *Int. J. Quantum Chem.* **1981**, *19*, 427.
- (20) Cortona, P.; Monteleone, A. V. *J. Phys.: Condens. Matter* **1996**, *8*, 8983.
- (21) Zhao, Y.; Truhlar, D. G. *J. Chem. Theory Comput.* **2005**, *1*, 415.
- (22) Zhao, Y.; Truhlar, D. G. *J. Phys. Chem. A* **2005**, *109*, 5656.
- (23) Zhao, Y.; Truhlar, D. G. *Phys. Chem. Chem. Phys.* **2005**, *7*, 2701.
- (24) Levy, M. *Proc. Natl. Acad. Sci. U.S.A.* **1979**, *76*, 6062.
- (25) Wesolowski, T. A. *One-electron equations for embedded electron density: challenge for theory and practical payoffs in multi-level modelling of soft condensed matter*; volume X of *Computational Chemistry: Reviews of Current Trends*; Leszczynski, J., Ed.; World Scientific: 2006; pp 1–82.
- (26) van Leeuwen, R. *Adv. Quantum Chem.* **2003**, *43*, 25.
- (27) Dirac, P. A. M. *Proc. Cambridge Philos. Soc.* **1930**, *26*, 376.
- (28) Vosko, S. H.; Wilk, L.; Nusair, M. *Can. J. Phys.* **1980**, *58*, 1200.
- (29) Ceperley, D. M.; Alder, B. J. *Phys. Rev. Lett.* **1980**, *45*, 566.
- (30) Thomas, L. H. *Proc. Cambridge Philos. Soc.* **1927**, *23*, 542.
- (31) Fermi, E. *Z. Phys.* **1928**, *48*, 73.
- (32) Lembarki, A.; Chermette, H. *Phys. Rev. A* **1994**, *50*, 5328.
- (33) Wesolowski, T. A.; Chermette, H.; Weber, J. *J. Chem. Phys.* **1996**, *105*, 9182.
- (34) Massey, H. S. W.; Sida, D. W. *Philos. Mag.* **1955**, *46*, 190.
- (35) Gordon, R. G.; Kim, Y. S. *J. Chem. Phys.* **1972**, *56*, 3122.
- (36) Dułak, M.; Wesolowski, T. A. *J. Chem. Theory Comput.* **2006**, *2*, 1538.
- (37) Dułak, M.; Wesolowski, T. A. *Int. J. Quantum Chem.* **2005**, *101*, 543.
- (38) Köster, A. M.; Flores-Moreno, R.; Geudtner, G.; Goursot, A.; Heine, T.; Reveles, J. U.; Vela, A.; Salahub, D. R. deMon 2003; NRC, Canada. <http://www.deMon-software.com/> (accessed Sep 8, 2006).
- (39) Dułak, M.; Wesolowski, T. A. Adaptive grid technique for computer simulations of condensed matter using orbital-free embedding formalism. In *Lecture Series on Computer and Computational Sciences Vol. 3*; Simos, T., Maroulis, G., Eds.; VSP/Brill: 2005; pp 282–288.
- (40) Lynch, B. J.; Zhao, Y.; Truhlar, D. G. *J. Phys. Chem. A* **2003**, *107*, 1384.
- (41) Gill, P. M. W.; Johnson, B. G.; Pople, J. A. *Chem. Phys. Lett.* **1993**, *209*, 506.
- (42) Köster, A. M.; Calaminici, P.; Escalante, S.; Flores-Moreno, R.; Goursot, A.; Patchkovskii, S.; Reveles, J. U.; Salahub, D. R.; Vela, A.; Heine, T. *The deMon User's Guide, Version 1.0.3, 2003–2004*. <http://www.deMon-software.com/> (accessed Sep 8, 2006).
- (43) Liu, D. C.; Nocedal, J. *Math. Program.* **1989**, *45*, 503.
- (44) Kim, Y. S.; Gordon, R. G. *J. Chem. Phys.* **1974**, *61*, 1.

Improved meta-GGA Correlation Functional of the Lap Family[†]

Emil Proynov* and Jing Kong

*Q-Chem Inc., The Design Center, Suite 690, 5001 Baum Boulevard,
Pittsburgh, Pennsylvania 15213*

Received December 19, 2006

Abstract: A new correlation functional of the Lap series is derived based on a more elaborated form of correlation wave vectors. Its validation is carried out within two different codes: deMon-KS3 and Q-Chem 3.0. In deMon the implementation in a post-SCF manner is similar to the preceding BLap3 and Bm τ 1 schemes. In Q-Chem the new functional is programmed self-consistently using the integration by parts procedure for the matrix elements. The post-SCF version of the functional deals with three fitting parameters; the previous Lap3 and τ 1 functionals have four and five parameters, respectively. The SCF implementation requires only two fitting parameters. Preliminary comparative tests are discussed.

1. Introduction

Since the mid 1980s and the early 1990s, the development of new exchange-correlation (XC) functionals is on the frontier of density functional theory (DFT). One of the present authors (E.P.) had the luck to get in the right place at the right time for functional development, by joining the Montreal group of Professor Dennis Salahub in 1991. The early 1990s was a time when generalized-gradient approximation (GGA) was triumphing for several years as a top-notch exchange-correlation theory. In the fall of 1992 Axel Becke in his talk on the Canadian Theoretical Chemistry Symposium in Montreal launched the idea of fusing exact exchange into the GGA machinery. This and his seminal papers on the subject¹ started the era of hybrid functionals. The dramatic increase of accuracy brought about by the hybrid approach shifted for awhile attention away from other possibilities for improvement. The Montreal group was particularly interested in developing such alternatives that would not require the more expensive exact exchange. A paper submitted in the beginning of 1994² showed that some improvement over GGA can be achieved by employing a correlation functional that involves the electron kinetic-energy density (τ) and the Laplacian of the electron density as functional variables. By the time the manuscript referred

to in ref 2 was submitted, functionals of a similar type were known only for exchange.^{3–5} At the Sanibel symposium in 1994 Becke⁶ reported another correlation functional that employs τ and the Laplacian of the density based on different arguments. The interest of the Montreal group on such functionals has persisted, and some further development (BLap3,⁷ Bm τ 1⁸) continued. Extensive validation tests were also reported by this and other groups showing that for some problems (weak hydrogen bonds,^{9–11} reaction barriers,^{12–14} proton affinities,¹⁵ transition-metal compounds^{8,12}) these new functionals may rival the hybrid methods. Other exchange and correlation functionals involving τ were proposed later on by different groups.^{16–19} All these were named ‘meta-GGA’ functionals by Perdew and co-workers^{17,18} In ref 18 it was mentioned that “The current revival of interest in meta-GGAs may be due to Salahub and collaborators”. It became gradually clear that the meta-GGA avenue hides some uncharted potentials. An accurate nonempirical meta-GGA scheme was also developed (the TPSS functional).^{19,22} More recently, accurate multiparameter hybrid-meta-GGA schemes were constructed improving reaction barriers and metal–ligand bonding.^{20,21}

In this work we explore one possibility of improving correlation functionals from the Lap family.^{2,7} These functionals employ the so-called correlation wave vectors. A more elaborated form of these wave vectors is employed here, as described in section 2. The meta-GGA correlation functional

[†] Dedicated to Professor Dennis R. Salahub on the occasion of his 60th birthday.

* Corresponding author e-mail: emil@q-chem.com.

Lap3⁷ is used as a starting point, and the new correlation functional is generated from it in section 3. Some preliminary validation tests are then discussed.

2. Theory

Various methods of deriving correlation functionals within the Kohn–Sham (KS) DFT have been developed to date. A summary of all these is beyond the scope of the present work. We focus here on the approach described in refs 2, 7, and 23. It is based on solving explicitly the adiabatic connection formula separately for each spin–spin component of the correlation energy using spin polarized, λ -dependent pair correlation functions (PCF). These functions depend on the interelectronic distance, the electron density n_σ and possibly its derivatives, and the correlation wave vectors (known also as inverse correlation lengths or scaling factors): $g_{\sigma\sigma}^{(\lambda)}(r_{12}; n_\sigma, n_\sigma', k_\sigma, k_\sigma')$. Once such PCFs are found, the exchange–correlation energy as defined in the KS-DFT scheme can be determined via the adiabatic connection formula^{24,25}

$$E_c^\uparrow = \int_0^1 d\lambda \int d1 d2 \frac{1}{r_{12}} n_\uparrow(1)n_\uparrow(2) [g_{\uparrow\uparrow}^{(\lambda)}(r_{12}) - 1] \quad (1)$$

$$E_{xc}^{\sigma\sigma} = \frac{1}{2} \int_0^1 d\lambda \int d1 d2 \frac{1}{r_{12}} n_\sigma(1)n_\sigma(2) [g_{\sigma\sigma}^{(\lambda)}(r_{12}) - 1] \quad (2)$$

where λ is the coupling strength parameter as defined in the adiabatic connection method. The above formulas presume the following partitioning of the Kohn–Sham exchange–correlation energy density ϵ_{xc} into separate spin–spin components:

$$E_{xc}[n_\uparrow, n_\downarrow] = \int dr n(\mathbf{r}) \epsilon_{xc}(\mathbf{r}), \quad n = n_\uparrow + n_\downarrow \quad (3)$$

$$\epsilon_{xc}(n_\uparrow, n_\downarrow) = \sum_\sigma \epsilon_{xc\sigma}(n_\sigma) + \epsilon_c^\uparrow(n_\uparrow, n_\downarrow) \quad (4)$$

$$\epsilon_{xc\sigma}(n_\sigma) = \epsilon_{xc\sigma}(n_\sigma) + \epsilon_c^{\sigma\sigma}(n_\sigma) \quad (5)$$

The latter expression, together with eq 2, define the exchange-only energy in the KS scheme as the $\lambda \rightarrow 0$ limit of the exchange–correlation energy.

Using pair-correlation functions and/or the associated exchange and correlation holes in real space has been one of the most popular approaches in deriving exchange and correlation functionals.^{3,25–30} Even though an exact first principles derivation of PCFs is prohibitive, some important properties of these are known, such as normalization conditions, cusp conditions and hole curvature, asymptotic behavior, and coordinate scaling properties. This gives a powerful tool in constructing ad hoc real space models based on physical arguments. Related to this is the existence of some degree of universality in the way electrons correlate in different systems, especially at small interelectronic distance.³¹ The behavior of the electrons at small and vanishing interelectronic distance is governed by specific cusp conditions for the PCF.^{32,33} These conditions are λ dependent and spin specific.³³ A family of spin-polarized, λ dependent PCFs that obeys automatically the opposite-spin cusp conditions was proposed in ref 23 (a typo in the way the parameter m enters the PCF is corrected in eq 8 below)

$$g_{\uparrow\uparrow}^{(\lambda)}(\mathbf{R}, r) = 1 - \exp(-k_{\uparrow\uparrow}^2 r^2) [F_1(\lambda) - F_2(\lambda)] \quad (6)$$

$$F_1(\lambda) = m - \Phi_{\uparrow\uparrow}^{(\lambda)}(m + \lambda r) \quad (7)$$

$$F_2(\lambda) = \exp(-k_{\uparrow\uparrow}^2 r^2) \left[m - 1 - \Phi_{\uparrow\uparrow}^{(\lambda)}(m + \lambda r) + (\Phi_{\uparrow\uparrow}^{(\lambda)})^2 \left(1 + \lambda r + \frac{\lambda^2 r^2}{4} \right) \right] \quad (8)$$

where $r = r_{12} = |\mathbf{r}_1 - \mathbf{r}_2|$. For any m and $k_{\uparrow\uparrow}$, this PCF obeys the opposite-spin cusp conditions and has the following nonzero cusp:

$$\lim_{r \rightarrow 0} g_{\uparrow\uparrow}^{(\lambda)}(\mathbf{R}, r) = [\Phi_{\uparrow\uparrow}^{(\lambda)}(k_{\uparrow\uparrow})]^2 > 0 \text{ for any } 0 \geq \lambda \leq 1 \quad (9)$$

Finding a suitable parallel-spin PCF that would obey the respective (more complicated) cusp conditions is difficult because these involve the exchange and the same-spin correlation altogether.³³

The focus of this section is on the correlation wave vectors. The inverse of the wave vector of a given spin–spin component is related to the corresponding correlation length that governs the range of the correlated motion about a given reference electron. Solving the adiabatic connection formula 1 with the above PCF for $m = 2$ yields a correlation energy that is a function solely of the electron density and the wave vector $k_{\uparrow\uparrow}$ (see refs 7 and 23)

$$\epsilon_c^\uparrow = \frac{n_\uparrow n_\downarrow}{n} Q^\uparrow(k_{\uparrow\uparrow}), \quad n = n_\uparrow + n_\downarrow \quad (10)$$

$$Q^\uparrow(k) = -\frac{b_1}{1 + b_2 k} + \frac{b_3}{k} \ln \left(\frac{b_4 + k}{k} \right) + \frac{b_5}{k} - \frac{b_6}{k^2} \quad (11)$$

where b_i are theoretical coefficients yielded by the algebra. The form of the wave vector $k_{\uparrow\uparrow}$ is not uniquely determined to this end and remains to be specified. Different functionals can in fact be generated from eqs 10 and 11 depending on what form of the correlation wave vector $k_{\uparrow\uparrow}$ is used. The same is true for the parallel-spin component of the correlation energy density $\epsilon_c^\sigma(n_\sigma)$ as defined by eq 5. In the Lap3 functional this energy is approximated by an ad hoc modification of eqs 10 and 11 (see ref 7 for details)

$$\epsilon_c^{\sigma\sigma} = \left(1 - \frac{1}{N_\sigma} \right) \frac{1}{2} \frac{n_\sigma^2}{n} Q^{\sigma\sigma}(k_\sigma) \quad (12)$$

$$Q^{\sigma\sigma}(k_\sigma) \approx C_p Q^\uparrow(k_\sigma) \quad (13)$$

where N_σ is the total number of electrons with spin σ entering the Fermi-Amaldi type self-interaction correction (SIC) factor, and C_p is a ‘reduction’ parameter ranging between 0 and 1, that governs the relative share of parallel-spin correlation beyond the Fermi exchange. Again, various energy expressions can be generated using different forms of k_σ . The simplest choice for k_σ that follows from scaling and dimensional arguments and by analogy with the uniform electron gas is (“a rho to one-third” proportionality)

$$k_\sigma(\mathbf{r}) = \alpha_p k_{fs} \quad (14)$$

where α_p is a scaling parameter, and $k_{f\sigma}$ is the spin-polarized local Fermi wave vector:

$$k_{f\sigma}(\mathbf{r}) = a'_x n_\sigma^{1/3}(\mathbf{r}) = a_x [n(\mathbf{r})(1 \pm \xi(\mathbf{r}))]^{1/3},$$

$$\sigma = \uparrow(+), \sigma = \downarrow(-) \quad (15)$$

$a'_x = (6\pi^2)^{1/3}$, $a_x = (3\pi^2/2)^{1/3}$. The spin-polarization parameter ξ is defined as

$$n_\uparrow = \frac{1}{2}n(1 + \xi); \quad n_\downarrow = \frac{1}{2}n(1 - \xi) \quad (16)$$

The local Fermi wave vector is an important characteristic of the uniform electron gas reflecting the range of the Fermi interaction about a reference electron. Within approximation 14, the smaller the electron density, the larger the correlation length increasing as $1/n_\sigma^{1/3}$. More subtle is the problem of how to model the opposite-spin wave vector. To our knowledge, the only known approximation to date is the one proposed by Becke in the context of his 1988 correlation functional²⁷ (we call it here ‘Becke ansatz’). It is based on the plausible assumption that the correlation length for opposite-spin interaction is proportional to the arithmetic mean of the correlation lengths for the two same-spin interactions. With the local form of the wave vectors this leads to

$$k_{\uparrow\downarrow}(\mathbf{r}) = \beta_p \frac{2k_{\uparrow\uparrow}k_{\downarrow\downarrow}}{(k_{\uparrow\uparrow} + k_{\downarrow\downarrow})} \quad (17)$$

where β_p is another scaling parameter. In refs 2 and 7 it was set to $\beta_p = \alpha_p$ for simplicity. The only proof of this ansatz is ‘in the pudding’: it was thoroughly tested in the context of different functionals,^{2,6–8,27} and it normally leads to reasonable results. Using these formulas for the wave vectors in eqs 10–13 yields a correlation functional that depends solely on the electron spin densities (‘gradientless functional’). It is however not a uniform electron gas approximation per se. An important difference is²³ that eqs 10–13 obey the finite scaling bound, which is an exact property of finite systems but not of the uniform electron gas³⁴

$$\lim_{\gamma \rightarrow \infty} E_c[n_\gamma] > -\infty \quad (18)$$

where n_γ is homogeneously scaled electron density $n_\gamma(\mathbf{r}) = \gamma^3 n(\gamma\mathbf{r})$.

The discussed gradientless functional was implemented (without the parallel-spin term) as a one-parameter local XC scheme in combination with the standard local-spin-density (LSD) exchange²³ as well as with a homemade modified local exchange.³⁵ The results for atomization energies and especially for bond lengths were on average better than the standard LSD. One possible reason for this is the fulfillment of the finite scaling bound, eq 18. Also, this functional and the gradientless potential that stems from it are self-interaction free.³⁷ Still, it remains a local functional in the sense that the correlation energy density depends solely on the local value of the electron density at a given reference point and does not ‘feel’ its neighborhood. A question then arises: how about other forms of the correlation wave vectors. Is it possible to generate a nonlocal functional

starting from eqs 10–13? One possibility for this was considered in ref 2 based on the notion of local electron temperature $k_B T_{s\sigma}$ as defined in the local thermodynamic approach of DFT (LTD).^{4,36} In spin polarized form this ‘temperature’ reads

$$k_B T_{s\sigma}(\mathbf{r}) = \frac{2}{3} \frac{t_{s\sigma}(\mathbf{r})}{n_\sigma(\mathbf{r})} \quad (19)$$

where $t_{s\sigma}$ is the electron kinetic energy density by the LTD definition

$$t_{s\sigma} = \tau_\sigma - \frac{1}{8} \nabla^2 n_\sigma \quad (20)$$

and τ_σ is the (‘Laplacian-free’) electron kinetic energy density

$$\tau_\sigma = \frac{1}{2} \sum_i |\nabla \varphi_{i\sigma}|^2 \quad (21)$$

$\varphi_{i\sigma}$ are the KS SCF spin orbitals. Both definitions lead to the same total kinetic energy. With the particular choice of 1/8 for the coefficient multiplying the Laplacian, $t_{s\sigma}$, remains positively defined in most cases (section 4). The local electron temperature was used to model the spherically averaged exchange hole $\bar{h}_{\sigma\sigma}$ employed in the LTD approach:⁵

$$\bar{h}_{\sigma\sigma}(\mathbf{R}, r) \approx n_\sigma(\mathbf{R}) e^{-r^2 k_B T_{s\sigma}(\mathbf{R})} \quad (22)$$

This, together with eqs 19–21 suggests the following LTD ansatz for the parallel-spin correlation wave vectors:²

$$k_\sigma^2 \approx \alpha_e^2 \frac{2}{3} \frac{t_{s\sigma}}{n_\sigma} \quad (23)$$

In the present work we use a slightly different equivalent form of it:

$$k_\sigma^2 \approx \alpha_e^2 \frac{10}{3} \frac{t_{s\sigma}}{n_\sigma}, \quad \alpha_e^2 = \frac{\alpha_e'^2}{5} \quad (24)$$

When α_e and α_p from eq 14 are set equal, formula 24 provides a smooth transformation of the nonlocal wave vector to its local counterpart, eq 14, in the ‘gradientless limit’. This is the limit when all derivatives of the electron density vanish and the kinetic energy density is given by its uniform gas (spin-polarized) expression:

$$t_{s\sigma} = \tau_\sigma = C_{\text{TF}\sigma} n_\sigma^{5/3}, \quad C_{\text{TF}\sigma} = \frac{3}{10} (3\pi^2)^{2/3} 2^{2/3} \quad (25)$$

In the context of the LTD model, the electron correlation length increases (the wave vector k_σ decreases) when the electrons are ‘freezing down’ and their kinetic energy is decreasing.

For the opposite-spin wave vector we use the Becke ansatz in the context of definition 24:

$$k_{\uparrow\downarrow}(\mathbf{r}) = \beta_e \frac{2b_{s\uparrow}b_{s\downarrow}}{(\sqrt{n_\uparrow}b_{s\uparrow} + \sqrt{n_\downarrow}b_{s\downarrow})} \quad (26)$$

$$b_{s\sigma} = \sqrt{\frac{10}{3}t_{s\sigma}} \equiv \frac{1}{6}\sqrt{120\tau_{\sigma} - 15\nabla^2 n_{\sigma}} \quad (27)$$

Using this model for the wave vectors in eqs 10–13 generates a fully nonlocal correlation functional. By fully nonlocal we mean that it is not representable by any finite gradient expansion about either the uniform-gas limit or some other local form of the correlation energy. Using the nonlocal wave vectors, eqs 24 and 26, in the corresponding PCF, eq 6, transforms the latter into a fully nonlocal PCF similar to the PCFs used in the weighted density approximation.³⁸

Having τ as a functional variable has some advantages. It is a fine-tuned real space descriptor of inhomogeneity in atoms and molecules.³⁹ The curvature of the exact exchange hole also depends on τ and the Laplacian of the density, which has been a motivation of using these as functional variables.^{3,6,30} The LTD analogy discussed above is yet another complementary motivation for the same.²

Recently a new functional originating from the same family of PCF, eq 6, was considered⁴⁰ and used to obtain a compact analytical representation of the uniform electron gas correlation energy.⁴⁰ In due course of these derivations it became evident that the correlation wave vectors, as given by eqs 14 and 17, are still missing something. Based on an analytical fit to literature benchmark values of the correlation energy it was shown⁴⁰ that the scaling parameters α_p and β_p should be multiplied by certain functions of the electron density (or equivalently the density parameter $r_s = (3/4\pi n)^{1/3}$):

$$k_{\sigma}(\mathbf{r}) = \alpha_p \alpha_{\text{eff}}(r_s) k_{i\sigma} \quad (28)$$

$$k_{\uparrow}(\mathbf{r}) = \beta_p \beta_{\text{eff}}(r_s) \frac{2k_{\uparrow}k_{\downarrow}}{(k_{\uparrow} + k_{\downarrow})} \quad (29)$$

$$\beta_{\text{eff}}(r_s) = \eta_1 + \eta_2 \exp(-\eta_3 r_s^{1/3}) r_s^{1/4} + \eta_4 \exp(-\eta_5 r_s^{1/3}) r_s^{1/3} \quad (30)$$

$$\alpha_{\text{eff}}(r_s) = \eta_6 + \eta_7 \exp(-\eta_8 r_s^{1/3}) r_s^{2/3} + \eta_9 \exp(-\eta_{10} r_s^{1/3}) r_s^{1/3} \quad (31)$$

The optimal values of the coefficients η_i were obtained in ref 40 based on an interpolation of the uniform electron gas benchmarks data of refs 41–43.

Employing such density dependent screening functions in the local form of the correlation wave vectors was necessary to achieve a good interpolation of the transition between the high-density and the low-density limits of the uniform electron gas.⁴⁰ The present work aims at verifying whether incorporating these screening functions (with some additional scaling) in the nonlocal wave vectors would affect the accuracy of a nonlocal functional that employs them, such as Lap3 for example. One may suspect that for atoms and molecules the corresponding screening functions would be quite different from those suitable for the uniform electron gas. Nevertheless, we believe that even though finite systems like atoms and molecules are different from the uniform electron gas, some similarity may exist in the way electron correlation changes upon a transition from regions of high electron density to regions of low electron density. This is

of course only a hypothesis ('a similarity hypothesis') that can in part be verified by the quality of the results discussed next.

3. Derivation of the tLap Correlation Functional

The new correlation functional is obtained from eqs 10–13 using the following novel form of the correlation wave vectors (compare with eqs 24 and 26)

$$k_{\sigma}^2 = \alpha_e^2 \alpha_{\text{eff}}^2(n) \frac{10}{3} \frac{t_{s\sigma}}{n_{\sigma}} \quad (32)$$

$$k_{\uparrow}(\mathbf{r}) = \beta_e \beta_{\text{eff}}(n) \frac{2b_{s\downarrow} b_{s\uparrow}}{(\sqrt{n_{\downarrow}} b_{s\downarrow} + \sqrt{n_{\uparrow}} b_{s\uparrow})} \quad (33)$$

where the factors $b_{s\sigma}$ are given by eq 27, $\alpha_{\text{eff}}(n)$ and $\beta_{\text{eff}}(n)$ are the density-dependent screening functions, eqs 30 and 31, after changing the variable r_s to n . We have implemented this correlation functional ('tLap' from "tau+Laplacian") in two different codes: in a developing version of Q-Chem 3.0⁴⁷ and in a modified version of the deMon-KS3 code.⁴⁶ The latter is an old noncommercial release of the deMon program.

The new form of the wave vectors induces some modifications of the functional structure. In the original Lap3 functional, one of the theoretical b_i coefficients, namely b_3 in eqs 11 and 13, had to be rescaled in order to optimize reasonably the results. This was thought to be due to the approximate PCF used. Preliminary tests of the tLap functional revealed that this empirical adjustment was actually necessary to compensate for an imprecision of the wave vectors used. In the tLap functional a relaxation of the b_3 coefficient is no longer required. In fact, the optimal results are obtained when this coefficient keeps its theoretical value together with the rest of b_i : $b_1 = 2.763169$; $b_2 = 1.757515$; $b_3 = 1.741397$; $b_4 = 0.568985$; $b_5 = 1.572202$; $b_6 = 1.885389$

Yet another empirical parameter is no longer necessary, the reduction factor C_p in the parallel-spin correlation energy component, eq 13. In the tLap functional it is set to $C_p \equiv 1$, while the balance between opposite-spin and parallel-spin correlation is tuned by the two scaling parameters α_e and β_e in eqs 32 and 33. These are the only two fitting parameters in the tLap functional.

The implementation of the new functional in deMon-KS3 in a post-SCF fashion is similar to the Lap3 and τ_1 functionals. The exchange functional of Becke(88)⁴⁹ is used throughout this work as a partner of tLap ('BtLap' XC scheme). Hence the post-SCF implementation is based on a KS potential that consists of two terms: (i) the Becke(88) exchange potential in a fully SCF manner and (ii) a local correlation potential obtained by differentiating the correlation energy in its gradientless limit, i.e., when eqs 28 and 29 are used for the wave vectors in place of eqs 32 and 33. In this local potential the two scaling parameters are set equal, $\alpha_p = \beta_p$, which gives one fitting parameter in the potential to optimize with respect to geometry estimates. Such a potential composition, even though not fully SCF, yields very good structure parameters, especially concerning weak

Table 1. Molecules Included in the Validation Tests

H ₂ , N ₂ , F ₂ , O ₂ , S ₂ , P ₂ , Cl ₂ , HF, CO, NO, PN, CN, NH, CS, CH, OH, HCl, SiO, NaCl, NaF, HCN, H ₂ O, H ₂ S, CO ₂ , NH ₃ , PH ₃ , N ₂ O, H ₂ O ₂ , SiH ₄ , CH ₄ , C ₂ H ₂ , C ₂ H ₄ , C ₂ H ₆ , H ₂ CO, CH ₃ OH, C ₆ H ₆ , <i>trans</i> -butadiene (C ₄ H ₆), pyrrole (C ₄ H ₅ N), pyridine (C ₅ H ₅ N)

intermolecular and intramolecular hydrogen bonds.⁸ In the case of tLap the corresponding local correlation potential is a bit more complicated due to the presence of the density-dependent screening functions, eqs 30 and 31. Post-SCF implementation of meta-GGA functionals was recently adopted also in the code ADF based on BLYP as a SCF carrier (see ref 14). The improvement brought by the meta-GGA functionals is mostly in the relative energies. A post-SCF implementation allows for the benefit from this in an economic way (“get the most for the least”). Similar is the situation with the CCSD(T) post-Hartree–Fock method for example. Nevertheless, a SCF implementation of the BtLap functional has its merits. Having the true analytical energy gradient is very important for various applications. We present here SCF results with the BtLap functional within the Q-Chem code. In the MO-LCGTO representation the matrix elements of the XC potential ($V_{\mu\nu}^{\text{xc},\sigma}$) are determined by differentiating the XC energy matrix over the density matrix ($P_{\mu\nu}^{\sigma}$)

$$V_{\mu\nu}^{\text{xc},\sigma} = \frac{\partial E_{\text{xc}}}{\partial P_{\mu\nu}^{\sigma}} = \sum_i \frac{\partial f_{\text{xc}}}{\partial g_i} \frac{\partial g_i}{\partial P_{\mu\nu}^{\sigma}} \quad (34)$$

where f_{xc} is the exchange-correlation kernel that is a function of certain variables g_i :

$$E_{\text{xc}} = \int f_{\text{xc}}(g_1, g_2, \dots, g_i, \dots) d\mathbf{r} \quad (35)$$

This is equivalent to the integration by parts standard procedure of evaluating matrix elements of a XC potential without computing explicitly this potential.^{48,50} In the case of tLap, the functional variables to differentiate upon are n_{σ} , τ_{σ} , and $\nabla^2 n_{\sigma}$, $\sigma = \alpha, \beta$.

4. Results and Discussion

Detailed validation tests of the BtLap XC scheme are currently ongoing. Here we report some preliminary results following the wisdom that a careful selection of diverse test examples is more important than their number.⁵² We use in part the test set elaborated previously.^{7,8,51} It includes atomization energies and bond lengths for a variety of bonding situations that have proven to be difficult at least for the GGA functionals. The choice of the examples was based also on the availability of benchmark data. The set of molecules used in the present tests is listed in Table 1.

In addition to this, we include the dimerization energy and geometry of two weakly bound dimers (H₂O)₂ and (HF)₂ as examples of intermolecular hydrogen bonding.^{8,51}

The calculations with deMon-KS3 employ a TZVP2* orbital basis set of Gaussian-type functions that had been optimized specifically for KS-DFT calculations.⁵³ Auxiliary bases from the deMon library were used for fitting the charge density and the XC potential in order to avoid four-center

integrals and to facilitate the energy derivatives. Upon SCF convergence, one final extra-iteration is performed numerically (without fitting) on the grid to obtain more accurately the total energy.

Several different basis sets of Pople were tested within Q-Chem, ranging from 6-311G(d), and 6-311++G(d,p), to 6-311++G(f,d,p) up to the exhaustive G3LARGE available in Q-Chem. For each system we have used the largest basis set that still leads to a converged, stable SCF solution. Both Q-Chem and deMon-KS3 employ atom-centered grid for the numerical integrations. Becke’s relative weight scheme⁵⁴ is used to adjust the weights as the grid points originating from different atoms overlap in space. The radial part of the grid is treated by the Euler-Maclaurin scheme proposed by Murray et al.⁵⁵ and the angular part by Lebedev quadrature.⁵⁶ In Q-Chem the quadrature is pruned by removing angular points from regions where they are not necessary. We use here the pruned grid SG-1,⁵⁷ which has 50 radial and 194 angular points. In some cases a larger grid of 128 radial and 194 angular points was used. It has been shown recently⁵⁸ that auxiliary cubic grids can be used to reduce greatly the cost of the atom-centered grid. The calculations with deMon-KS3 employ an unpruned grid scheme as described in ref 46. The user defined number of grid points was 128 radial points and 194 Lebedev angular points. The optimization of the fitting parameters in tLap is completed so far within the deMon-KS3 code only. With Q-Chem we employ for the time being these parameter values. The optimization was done looping over a subset of 10 molecules (H₂, N₂, O₂, F₂, CO₂, N₂O, CH₄, C₂H₄, C₆H₆, (H₂O)₂) and comparing atomization energies and bond lengths. Atomic correlation energy tests are not used in the present fitting procedure. The following parameter values are obtained: (1) $\alpha_e = 2.53$ – optimizes the share of parallel-spin correlation and (2) $\beta_e = 1.087$ – optimizes the share of opposite-spin correlation. In the post-SCF implementation there is one additional parameter entering only in the local SCF correlation potential: (3) $\alpha_p = \beta_p = 0.786$ – optimizes the geometry performance.

The SCF implementation of the BtLap scheme in Q-Chem is based on eq 34. Special care should be taken to avoid negative values of the kinetic energy density t_s , eq 20, since the wave vectors are ill defined in such cases. We have verified the sign of t_s for each system studied at each grid point and SCF iteration. With no exception t_s as defined by eq 20 remained always positive after the first 4–5 SCF iterations. However, its sign often fluctuates at the beginning of the SCF, which may cause convergence problems. To avoid such situations we do the first 4 SCF iterations using the local correlation potential used in the post-SCF implementation of BtLap.

The atomization energy (E_{at}) is calculated as the difference between the molecular ground-state energy and the sum of ground-state energies of the constituent atoms. One problem here is that the atomic ground state is not unambiguously determined within the standard KS-DFT scheme based on a single KS determinant. Results from different codes may slightly differ depending on how atoms are handled. In both Q-Chem 3.0 and deMon-KS3, the single-determinantal atomic KS state is converged to integer orbital occupancies.

Table 2. Mean Absolute Deviations (kcal/mol) for Atomization Energies (without the ZPE Contribution)

functional	20 diatomics	19 polyatomics	all 39	12 difficult
XC with no HF Mixing				
BP(d) ^a	3.94	15.13	9.39	20.68
BP(Q)	5.97	16.40	10.85	22.37
BLYP(Q)	5.58	5.23	5.41	7.73
OCS1(d) ^b	4.36	3.16	3.78	4.82
BLap3(d) ^a	3.30	8.39	5.78	9.86
Bm τ 1(d) ^a	3.11	4.13	3.61	5.09
BtLap(d)	3.21	3.60	3.41	4.77
BtLap(Q)	3.08	3.81	3.44	5.67
Hybrid XC				
BMK(Q)	2.72	2.49	2.61	2.58
B3LYP(Q)	2.54	1.84	2.20	2.42

^a Result from ref 8. ^b Result from ref 51 where the OCS1 XC scheme of Handy and Cohen^{61,62} was implemented in deMon-KS3.

For open-shell atoms this means having one or several holes within a partly filled shell. The location of these holes is sensitive to the functional used and the way the SCF procedure is conducted. The two codes use different approaches in constructing the KS potential and conducting the SCF procedure. As it was mentioned before, deMon-KS3 uses auxiliary basis fitting. As a result, one may observe some differences in the atomization energies between the two codes. Using fractional orbital occupancies that maintain atomic spherical symmetry is another known way of handling atoms within the standard KS scheme. However, the physical meaning of such ‘spherical atoms’ is not so obvious.

Table 2 contains the calculated atomization energies in terms of mean absolute deviations (MAD) from the experimental values. The post-SCF BtLap results with deMon-KS3 are labeled ‘BtLap(d)’, while the SCF BtLap results with Q-Chem are labeled ‘BtLap(Q)’. Similarly are labeled other XC functionals used with either of the two codes for comparison. The deviations are with respect to experimental values deduced from refs 59 and 60 after removing the temperature and ZPE contributions.

Comparing the BtLap(d) results with BLap3(d), a visible improvement is seen with BtLap(d). To note in particular the decrease of MAD for polyatomics from 8.39 kcal/mol with BLap3(d) to 3.6 kcal/mol with BtLap(d) and the decrease of MAD for the selected 12 ‘difficult’ molecules from 9.86 kcal/mol with BLap3(d) to 4.77 with BtLap(d). The latter are cases where the GGA scheme BP shows MAD bigger than 0.5 eV: O₂, CO₂, N₂O, H₂O₂, CH₄, C₂H₄, C₂H₆, CH₃OH, C₆H₆, C₄H₆, C₄H₅N, C₅H₅N. Among the functionals with no HF mixing in Table 2, BtLap(d) shows the smallest MAD. The MAD of the self-consistent version BtLap(Q) is slightly smaller than that of BtLap(d) for diatomic atomization energies and slightly bigger in the polyatomic case, Table 2. The latter is mainly due to the somewhat bigger MAD for the considered 12 difficult cases. This will be kept in mind during the reoptimization of the two fitting parameters in BtLap(Q). We expect that using the new form of the correlation wave vectors in other similar functionals, as for example Bm τ 1, may bring some relative improvement there as well (work in progress).

Table 3. Mean Absolute Deviations (Å) for Bond Lengths of 36 Molecules (45 Bonds)

functional	diatomics	polyatomics	all
XC with no HF Mixing			
BP(d) ^a	0.0242	0.0136	0.0183
BP(Q)	0.0230	0.0132	0.0176
OCS1(d) ^b	0.0271	0.0231	0.0249
BLYP(Q)	0.0174	0.0112	0.0140
BLap3(d) ^a	0.0189	0.0080	0.0132
Bm τ 1(d) ^a	0.0198	0.0084	0.0128
BtLap(Q)	0.0155	0.0105	0.0127
BtLap(d)	0.0133	0.0084	0.0106
Hybrid XC			
BMK(Q)	0.0112	0.0081	0.0095
B3LYP(Q)	0.0073	0.0046	0.0058

^a Result from ref 8. ^b Result from ref 51.

It is interesting to compare the atomization energies with one and the same GGA scheme, say BP, Becke(88)⁴⁹ exchange plus Perdew(86)^{63,64} correlation, with each of the two codes (Table 2). In deMon-KS3 BP is implemented self-consistently using analytical functional derivatives for the SCF XC-potential but fitting its numerical values using an auxiliary basis set. In Q-Chem the BP XC scheme is implemented using the integration by parts procedure to evaluate the matrix elements of the SCF potential with no auxiliary basis fitting. This leads to some differences in the BP results obtained with the two codes.

We compare also the results with the OCS1 and BLYP functionals, following up the discussion on the same in ref 62. Keeping in mind the different codes and test sets used, the present results seem to confirm that OCS1 yields on average better atomization energies than BLYP. While being not strictly speaking GGA functionals, both OCS1 and BLYP are performing better than BP, at least on the test set used here.

Concerning the two hybrid functionals, B3LYP and BMK, both yield MAD of atomization energies below 3 kcal/mol on this test set, B3LYP doing slightly better than BMK. The latter was particularly optimized for thermochemical kinetics.²⁰ Maintaining at the same time very good performance on atomization energies is a plus for the BMK scheme.

Next we consider the functional performance for bond lengths. The reference bond lengths are from the experimental data in refs 66 and 67 corrected for rovibrational effects⁶⁵ when necessary. The obtained MAD values with different functionals are listed in Table 3. Comparing again BtLap(d) with BLap3(d), some improvement is seen with BtLap(d) yielding MAD close to that of BMK(Q). To keep in mind here that BtLap(d) and BLap3(d) are post-SCF schemes, and these bond lengths are a merit of the respective local correlation potential as explained in the preceding section. The MAD with the SCF version BtLap(Q) are somewhat bigger than that of BtLap(d) due to some more or less systematic elongation of the bond lengths.

The hybrid schemes BMK, and especially B3LYP, yield rather good bond lengths on this test set.

It is seen that the selected set of test examples, even though not large in number, allows for the assessment of the

Table 4. BSSE Corrected Dimerization Energy (kcal/mol) and Distances (Å) in the Water Dimer and HF Dimer

functional	(H ₂ O) ₂		(HF) ₂	
	E _b	R(OO)	E _d	R(FF)
Pure DFT XC with no HF Mixing				
BP(d) ^a	4.69	2.885	4.56	2.705
BP(Q)	4.06	2.900	4.06	2.737
BLYP(Q)	4.08	2.944	4.22	2.774
BLap3(d) ^a	4.63	2.979	4.68	2.793
Bmτ1(d) ^a	4.79	2.982	4.54	2.793
BtLap(d)	4.91	2.941	4.87	2.760
Hybrid XC				
BMK(Q)	4.13	2.936	4.27	2.728
B3LYP(Q)	4.37	2.919	4.53	2.745
experiment ^b	4.7–5.0	2.95–2.97	4.5–4.7	2.74–2.78

^a Reference 8. ^d References 68 and 69 for (H₂O)₂, ref 70 for (HF)₂.

functional performance. We agree with the conclusions of ref 52 that a huge number of tests is not necessary. The situation is similar to the pre-election polls. These can yield reliable predictions and statistics even though only a small fraction of the electorate is questioned. Including cases that are difficult for at least GGA helps the analysis more when they are not immersed in a very large number of other tests.⁴⁰

Our last test example is on the weakly bound water dimer and HF dimer held by a hydrogen bond (Table 4). The BLap3, BP, and Bmτ1 results have been reported previously⁸ and are given here for comparison.

Regarding the water dimer, BtLap(d) and BLap3(d) yield comparable dimerization energies, both within the experimental margin. With an exception of BP(d), the rest of the results included in Table 4 are slightly below the lower end of the experimental range. Turning to the dimerization energy of (HF)₂, the BLap3(d) estimate is within the experimental margin, while the BtLap(d) energy is slightly above it. B3LYP(Q) and BP(d) yield for this dimer an accurate estimate, BMK(Q), BLYP(Q) and BP(Q) hit again somewhat lower. For both dimers the largest margin between the various energy estimates is less than 0.85 kcal/mol. More diverse are the results for the long O–O and F–F distances. These are known as difficult to reproduce characteristics. The BtLap(d) scheme is doing slightly better than BLap3(d) in both cases. Again to keep in mind that these distances are not a merit of the nonlocal tLap correlation functional per se but of the associated local potential in the post-SCF implementation of BtLap(d). The BtLap(Q) SCF version still meets some accuracy problems here, and the results will be reported elsewhere.

The considered hybrid methods have some problems in reproducing the O–O distance in the water dimer, tending to underestimate it: B3LYP by about 0.03 Å from the lower end of the experimental margin, BMK by about 0.015 Å. According to our data, the simpler BLYP scheme seems to perform better than either B3LYP or BMK in this case. B3LYP is doing very well for the F–F distance in the HF dimer, while BMK slightly underestimates it.

Concerning other tests from the set package considered in refs 8 and 51, the calculations are completed with BtLap-

(d), the results being of about the same quality as those with BLap3(d). The optimization of the SCF scheme BtLap(Q) within Q-Chem is work in progress. The improvement over BLap3 achieved with the BtLap functional is mainly in the calculated thermochemical and structural data, Tables 2 and 3.

One final remark about the importance of the correlation energy in KS-DFT: the exchange energy is usually about 10–20 times bigger than the correlation energy. This may produce the illusion that correlation functional is not that important and all we need is a good exchange functional. The present results clearly illustrate among other things that using the same exchange functional with various correlation counterparts leads to a dramatic alteration of the DFT accuracy. Both components of the XC functional are equally important since their separate definition and treatment is only virtual.

5. Conclusions

This work explores a way of improving further correlation functionals of the Lap series that were developed in the 1990s in the research group of Professor Dennis Salahub. Recent study⁴⁰ has shown, based on uniform electron gas tests, that the correlation wave vectors used in this type of functionals are still missing something. Corrections in terms of density dependent screening functions are proposed that yield a new functional starting from the Lap3 formulation. Compared to the latter, noticeable improvement for atomization energies is achieved, while two of the previous fitting parameters inherited from Lap3 are no longer necessary. One explanation for this is that the employed local screening functions seem to provide (after some uniform scaling) a reasonable transition between the high-density and low-density limits even in finite systems. This may suggest that the similarity hypothesis discussed above (which is close in spirit to the short-wavelength hypothesis³¹) has some reasoning. Interpolations of similar kind based on precise analysis of the uniform electron gas in the two density limits and real space cut-offs and splines were the keys in constructing nonempirical GGA and meta-GGA functionals (see ref 19 and references therein). The tLap model uses an alternative approach toward a similar goal in the context of a fully nonlocal functional. It would become nonempirical when the scaling parameters α_e and β_e in eqs 32 and 33 are equal to 1.00. The value of the opposite-spin scaling parameter β_e used now (1.087) is close to its theoretical value of 1.00. A better parallel-spin correlation model is needed to complete the goal.

The screening functions were obtained in ref 40 based on an interpolation to benchmark values of the spin-resolved correlation energy of the uniform electron gas. Two different forms of these functions were reported corresponding to two different benchmark energy data. The form used here conforms to the data of refs 41–43. We have tried also the second form of the screening functions that matches the energy estimates of refs 44 and 45. The two reference energy sources differ in the dependence of the separate spin components of the correlation energy on the density parameter. We were not able to find a suitable parametrization of

the tLap functional that would yield improvement using the second type of screening functions.

The BtLap scheme is implemented in two different codes, Q-Chem 3.0 and deMon-KS3. In spite of the program differences, the results obtained with BtLap(d) /deMon-KS3 and BtLap(Q) /Q-Chem so far agree reasonably. The optimization of the SCF version BtLap(Q) is in progress.

Acknowledgment. We would like to thank NIH for the financial support of this research through Small Business Research Grants R43GM073408 and R43GM065617. E.P. thanks Dennis Salahub for the long years of collaboration, encouragement and friendship.

References

- (1) Becke, A. D. *J. Chem. Phys.* **1993**, *98*, 1372.
- (2) Proynov, E. I.; Vela, A.; Salahub, D. R. *Chem. Phys. Lett.* **1994**, *230*, 419.
- (3) Becke, A. D.; Roussel, M. R. *Phys. Rev. A* **1989**, *39*, 3761.
- (4) Ghosh, S. K.; Berkowitz, M.; Parr, R. G. *Proc. Natl. Acad. Sci. U.S.A.* **1984**, *81*, 8028.
- (5) Parr, R. G.; Yang, W. *Density Functional Theory of Atoms and Molecules*; Oxford University Press: Oxford, 1989; p 118.
- (6) Becke, A. D. *Int. J. Quantum Chem. Symp.* **1994**, *28*, 625.
- (7) Proynov, E. I.; Sirois, S.; Salahub, D. R. *Int. J. Quantum Chem.* **1997**, *64*, 427.
- (8) Proynov, E.; Chermette, H.; Salahub, D. R. *J. Chem. Phys.* **2000**, *113*, 10013.
- (9) Sirois, S.; Proynov, E. I.; Nguyen, D. T.; Salahub, D. R. *J. Chem. Phys.* **1997**, *107*, 6770.
- (10) Sirois, S. Ph.D. Thesis, Université de Montréal, Montreal, 1996.
- (11) Guo, H.; Sirois, S.; Proynov, E. I.; Salahub, D. R. Density Functional Theory and its application to hydrogen bonded systems. In *Theoretical Treatments of Hydrogen Bonding*; Dusan Hadzi, D., Ed.; Wiley: New York, 1997; pp 49–74.
- (12) Salahub, D. R.; Chretien, S.; Milet, A.; Proynov, E. Improving the functionals, extending the applications. In *Transition State Modeling for Catalysis*; Truhlar, D. G., Morokuma, K., Eds.; American Chemical Society: Washington, DC, 1999; ACS Series 721, pp 20–32.
- (13) Grüning, M.; Gritsenko, O. V.; Baerends, E. J. *J. Phys. Chem. A* **2004**, *108*, 4459.
- (14) Grüning, M. Ph.D. Thesis, Vrije Universiteit, Amsterdam, 2003.
- (15) Chandra, A. K.; Goursot, A. *J. Phys. Chem.* **1997**, *100*, 11596.
- (16) Van Voorhis, T.; Scuseria, G. E. *J. Chem. Phys.* **1998**, *109*, 400.
- (17) Perdew, J. P.; Kurth, S.; Zupan, A.; Blaha, P. *Phys. Rev. Lett.* **1999**, *82*, 2544.
- (18) Kurth, S.; Perdew, J. P.; Blaha, P. *Int. J. Quantum Chem.* **1999**, *75*, 889.
- (19) Tao, J.; Perdew, J. P.; Staroverov, V. N.; Scuseria, G. E. *Phys. Rev. Lett.* **2003**, *91*, 146401.
- (20) Boese, A. D.; Martin, J. M. L. *J. Chem. Phys.* **2004**, *121*, 3405.
- (21) Zhao, Y.; Schultz, E.; Truhlar, D. G. *J. Chem. Phys.* **2005**, *123*, 161103.
- (22) Staroverov, V. N.; Scuseria, G. E.; Tao, J.; Perdew, J. P. *Phys. Rev. B* **2004**, *69*, 75102.
- (23) Proynov, E. I.; Salahub, D. R. *Phys. Rev. B* **1994**, *49*, 7874.
- (24) Langreth, D. C.; Perdew, J. P. *Solid State Commun.* **1975**, *17*, 1425.
- (25) Gunnarsson, O. O.; Lundqvist, B. I. *Phys. Rev. B* **1976**, *13*, 4274.
- (26) Perdew, J. P.; Wang, Y. *Phys. Rev. B* **1986**, *33*, 8800.
- (27) Becke, A. D. *J. Chem. Phys.* **1988**, *88*, 1053.
- (28) Lee, C.; Yang, W.; Parr, R. G. *Phys. Rev. B* **1988**, *37*, 785.
- (29) Gritsenko, O. V.; Rubio, A.; Balbás, L. C.; Alonso, J. A. *Phys. Rev. A* **1993**, *47*, 1811.
- (30) Becke, A. D. *J. Chem. Phys.* **2003**, *119*, 2972.
- (31) Burke, K.; Perdew, J. P.; Levy, M. Nonlocal density functionals for exchange and correlation: Theory and applications. In *Modern Density Functional Theory. A Tool for Chemistry*; Seminario, J. M., Politzer, P., Eds.; Elsevier: Amsterdam, The Netherlands, 1995; p 29.
- (32) Thakkar, A.; Smith, V. H. *Chem. Phys. Lett.* **1976**, *42*, 476.
- (33) Rajagopal, A.; Kimball, J.; Banerjee, M. *Phys. Rev. B* **1978**, *18*, 2339.
- (34) Levy, M. *Phys. Rev. A* **1991**, *43*, 4637.
- (35) Proynov, E. I.; Vela, A.; Salahub, D. R. *Phys. Rev. A* **1994**, *50*, 3766.
- (36) Berkowitz, M. *Chem. Phys. Lett.* **1986**, *129*, 486.
- (37) Moscardó, F.; Perez-Jiménes, A. J. *Int. J. Quantum Chem.* **1998**, *67*, 143.
- (38) Gunnarsson, O.; Jones, R. O. *Phys. Scr.* **1980**, *21*, 394.
- (39) Becke, A. D.; Edgecombe, K. E. *J. Chem. Phys.* **1990**, *92*, 539.
- (40) Proynov, E. *J. Mol. Struct. (Theochem)* **2006**, *762*, 139.
- (41) Wang, Y.; Perdew, J. P. *Phys. Rev. B* **1991**, *44*, 13298.
- (42) Perdew, J. P.; Wang, Y. *Phys. Rev. B* **1992**, *46*, 12947.
- (43) Perdew, J. P.; Wang, Y. *Phys. Rev. B* **1992**, *45*, 13244.
- (44) Gori-Giorgi, P.; Perdew, J. P. *Phys. Rev. B* **2002**, *66*, 165118.
- (45) Gori-Giorgi, P.; Perdew, J. P. *Phys. Rev. B* **2004**, *69*, 041103.
- (46) Casida, M. E.; Daul, C. A.; Goursot, A.; Koester, A.; Petterson, L.; Proynov, E.; St-Amant, A.; Salahub, D. R. (principal authors). Duarte, H.; Godbout, N.; Guan, J.; Jamorski, C.; Leboeuf, M.; Malkin, V.; Malkina, O.; Sim, F.; Vela, A. (contributing authors) *deMon Software- deMon-KS3 Module*; University of Montreal: Montreal, QC, 1996.
- (47) Shao, Y.; Fusti-Molnar, L.; Jung, Y.; Kussmann, J.; Ochsenfeld, C.; Brown, S. T.; Gilbert, A. T. B.; Slipchenko, L. V.; Levchenko, S. V.; O'Neill, D. P.; DiStasio, R. A., Jr.; Lochan, R. C.; Wang, T.; Beran, G. J. O.; Besley, N. A.; Herbert, J. M.; Lin, C. Y.; Van Voorhis, T.; Chien, S. H.; Sodt, A.; Steele, R. P.; Rassolov, V. A.; Maslen, P. E.; Korambath, P. P.; Adamson, R. D.; Austin, B.; Baker, J.; Byrd, E. F. C.; Dachsel, H.; Doerksen, R. J.; Dreuw, A.; Dunietz, B. D.; Dutoi, A. D.; Furlani, T. R.; Gwaltney, S. R.; Heyden, A.; Hirata, S.; Hsu, C. P.; Kedziora, G.; Khalliulin, R. Z.; Klunzinger, P.; Lee, A. M.; Lee, M. S.; Liang, W.; Lotan, I.; Nair, N.; Peters, B.; Proynov, E. I.;

- Pieniazek, P. A.; Rhee, Y. M.; Ritchie, J.; Rosta, E.; Sherrill, C. D.; Simmonett, A. C.; Subotnik, J. E.; Woodcock, H. J., III; Zhang, W.; Bell, A. T.; Chakraborty, A. K.; Chipman, D. M.; Keil, F. J.; Warshel, A.; Hehre, W. J.; Schaefer, H. F., III; Kong, J.; Krylov, A. I.; Gill, P. M. W.; Head-Gordon, M. *Phys. Chem. Chem. Phys.* **2006**, *8*, 3172.
- (48) Neumann, R.; Nobes, R. H.; Handy, N. C. *Mol. Phys.* **1996**, *87*, 1.
- (49) Becke, A. D. *Phys. Rev. A* **1988**, *38*, 3098.
- (50) Pople, J. A.; Gill, P. M. W.; Johnson, B. G. *Chem. Phys. Lett.* **1992**, *199*, 557.
- (51) Proynov, E. I.; Thakkar, A. *Int. J. Quantum Chem.* **2006**, *106*, 436.
- (52) Lynch, B. J.; Truhlar, D. G. *J. Phys. Chem. A* **2003**, *107*, 8996.
- (53) Godbout, N.; Salahub, D. R.; Andzelm, J.; Wimmer, E. *Can. J. Chem.* **1992**, *70*, 560.
- (54) Becke, A. D. *J. Chem. Phys.* **1988**, *88*, 2547.
- (55) Murray, C. W.; Handy, N. C.; Lamming, G. J. *Mol. Phys.* **1993**, *4*, 997.
- (56) Lebedev, V. I.; Skorokhodov, A. L. *Russ. Acad. Sci. Dokl. Math.* **1992**, *45*, 587.
- (57) Gill, P. M. W.; Johnson, B. G.; Pople, J. A. *Chem. Phys. Lett.* **1993**, *209*, 506.
- (58) Kong, J.; Brown, S. T.; Fusti-Molnar, L. *J. Chem. Phys.* **2006**, *124*, 094109.
- (59) Curtiss, L. A.; Raghavachari, K.; Redfern, P. C.; Pople, J. A. *J. Chem. Phys.* **1997**, *106*, 1063.
- (60) Kafafi, S. A. *J. Phys. Chem. A* **1998**, *102*, 10404.
- (61) Handy, N. C.; Cohen, A. J. *Mol. Phys.* **2001**, *99*, 403.
- (62) Cohen, A. J.; Handy, N. C. *Mol. Phys.* **2001**, *99*, 607.
- (63) Perdew, J. P. *Phys. Rev. B* **1986**, *33*, 8822.
- (64) Perdew, J. P. *Phys. Rev. B* **1986**, *34*, 7406.
- (65) Bak, K. L.; Gauss, J.; Jørgensen, P.; Olsen, J.; Helgaker, T.; Stanton, J. F. *J. Chem. Phys.* **2001**, *114*, 6548.
- (66) Huber, K. P.; Herzberg, G. *Molecular Spectra and Molecular Structure. IV. Constants of Diatomic Molecules*; Reinhold van Nostrand: New York, 1979; pp 3–220.
- (67) *Structure Data of Free Polyatomic Molecules*; Hellwege, K. H., Hellwege, A. M., Eds.; Landolt-Börnstein, New Series, Group II, Springer: Berlin, Germany, 1979; Vol. 7, pp 3–250.
- (68) Chałsiński, G.; Szczyński, M. M. *Chem. Rev.* **1994**, *94*, 1723.
- (69) van Duijneveldt-van de Rijdt, J. G.; van Duijneveldt, F. B. *J. Chem. Phys.* **1992**, *97*, 5019.
- (70) Quack, M.; Suhm, M. A. *Theor. Chim. Acta* **1996**, *93*, 61.

CT600372T

Interaction between *n*-Alkane Chains: Applicability of the Empirically Corrected Density Functional Theory for Van der Waals Complexes[†]

Annick Goursot,^{*,‡} Tzonka Mineva,[‡] Ruslan Kevorkyants,[‡] and Dahbia Talbi[§]

UMR 5253 CNRS, Institut Gerhardt, Ecole de Chimie de Montpellier, 8 rue de l'Ecole Normale, 34296 Montpellier, Cédex 5, France, and GRAAL, Université Montpellier II, Place Eugène Bataillon, 34095 Montpellier, Cédex 5, France

Received December 20, 2006

Abstract: The geometries, interaction energies, and vibrational frequencies of a series of *n*-alkane dimers up to dodecane have been calculated using density functional theory (DFT) augmented with an empirical dispersion energy term (DFT–D). The results obtained from this method for ethane to hexane dimers are compared with those provided by the MP2 level of theory and the combined Gaussian-3 approach with CCSD(T) being the highest correlation method [G3(CCSD(T))]. Two types of dimer isomers have been studied. The most stable isomers have the two carbon chains in parallel planes, whereas the second ones have the two carbon chains in the same plane. Butane is found to be the shortest carbon chain to form dimers with similar properties, that is, a constant average distance between the monomer carbon skeletons, a similar increment per CH₂ unit for the dimer interaction energy, and comparable dimer symmetric stretching frequencies. The values and trends obtained from the DFT–D approach agree very well with those obtained from MP2 for the geometries and vibrational frequencies and from the G3(CCSD(T)) method for the energies, validating the use of DFT–D for the study of large hydrocarbon complexes.

1. Introduction

Despite some success in the description of short-range weak interactions,^{1,2} application of usual density functional theory (DFT) to van der Waals complexes is not theoretically justified and gives generally erroneous results in many systems involving nonbonding interactions.^{3–7} The incapacity of most of the present exchange-correlation functionals based on the local density approximation (LDA), generalized gradient-corrected approximations (GGA), or more sophisticated meta-GGA to treat properly long-range interactions is now recognized. Therefore, significant progress in making DFT more appropriate for weakly interacting systems has been made in recent years. Long-

range density functional theory, applying to nonoverlapping^{8–10} and also overlapping electron densities,^{7,11} has been proposed and applied to rare-gas dimers and rare-gas atoms interacting with small molecules^{9,10} and arene dimers¹² and to more extended systems.^{13,14} van der Waals interaction energies of small dimer systems have also been calculated using the symmetry-adapted perturbation theory and the time-dependent DFT method.^{15,16} Molecular polarizabilities, from which dispersion interaction energy can be calculated, have been estimated from time-dependent calculations¹⁷ or from the instantaneous dipole moment of the exchange hole.^{18–20} New combinations and parametrizations of GGA^{21,22} or meta-GGA²³ exchange-correlation functionals have also been proposed to allow the incorporation of the long-range part of electron correlation.

Dispersion effects are naturally accounted for in the wave function methods including a sufficiently high-level electron

[†] Dedicated to Professor Dennis R. Salahub on the occasion of his 60th birthday.

* Corresponding author e-mail: goursot@rhodium.enscm.fr.

[‡] Ecole de Chimie de Montpellier.

[§] GRAAL.

correlation, but these methods are relevant only for small-size compounds and must be essentially used for benchmark calculations.

Because van der Waals interaction energies are important for large systems, Wu and Yang²⁴ have proposed an empirical dispersion energy correction (E_{disp}) to the usual DF energy (DFT–D approach), using atomic C_6 coefficients, derived from molecular C_6 coefficients. The idea of using a correction term originates from the works for correcting the Hartree–Fock (HF) method^{25–27} and from Elstner et al.²⁸ for correcting the self-consistent-charge tight-binding method. Whereas the inherent nonlocal character of the Hartree–Fock method provides a correct description of the long-range exchange repulsion intermolecular forces, the DF approaches based on the local density expansion are not strictly applicable, and their performance depends on the particular exchange–correlation functional. The questions of the explicit form of damping functions that assures E_{disp} to be zero at the overlapped electron density region and one at the long distance were treated by Wu and Yang²⁴ and by Zimmerli et al.²⁹ Grimme has concluded that a proper scaling of E_{disp} is needed for each particular density functional.³⁰ Instead of scaling the empirical dispersion energy, Jurečka et al.³¹ adopted a global scaling factor of the atomic van der Waals radii, optimized for a training set of noncovalent complexes. The transferability of this scheme was reported to be very satisfactory on the basis of the interaction energy values obtained for a set of small weak complexes and employing different LDA, GGA, and meta-GGA functionals. More recently, the inclusion of higher-order correction terms, involving C_8 and C_{10} coefficients associated with an adequate damping function, was proposed by Johnson and Becke,²⁰ aiming at a better description of π stacked systems. All the above-mentioned methods are tested on training sets including small-size weakly bound complexes, for comparison with high-level post-Hartree–Fock results.

The goal of this work is to verify the applicability of a computationally efficient technique with a good transferability and acceptable errors to structures and interaction energies of molecular complexes. Such a methodology is necessary for the study of systems involving alkane–alkane, alkane–water hydrophobic, and hydrogen-bonding interactions. Handling large scale systems with DFT methods augmented with a damped empirical dispersion correction (DFT–D) is generally performed with GGA functionals. Variational density fitting and the use of the auxiliary density in the exchange–correlation potential³² calculation allows a substantial speedup. The results presented in this work concern dimers of saturated hydrocarbons.

For small dimers, the DFT–D results are compared with those obtained at the MP2 and the combined G3(CCSD(T)) levels of theory³³ employed to correct the interaction energies for the basis set and correlation limit errors. Results obtained with classical molecular mechanics (MM) are also used for comparison.

2. Methods

2.1. Dispersion Correction. The dispersion term, limited to the dipole–dipole contribution to the dispersion interaction

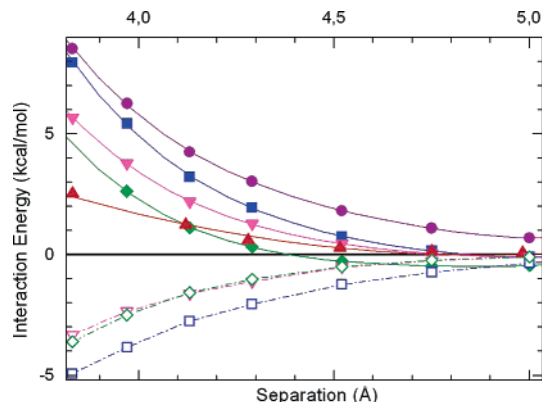


Figure 1. Interaction energy (IE) between two butane molecules in the butane dimer (isomer **a**) calculated using BLYP (●), revPBE-LYP (■), PBE (◆), and TPSS (▼) compared with the HF values (▲): (top) without their correlation interaction contribution and (bottom) correlation-only interaction energy for revPBE-LYP (□), PBE (◇), and TPSS (▽).

energy, $E_{\text{disp}} = -\sum_{i=1}^N \sum_{j=i+1}^{N-1} (C_6^{ij}/r_{ij}^6) f_{\text{damp}}(r_{ij})$ is expressed as the sum of all possible contributions of the i, j atom pair in an N -atomic system with an interatomic distance r_{ij} . In the DF approach including a damped empirical correction for the van der Waals interactions, E_{disp} is simply added to the usual DF energy and the ∇E_{disp} is added to the DF energy gradient. The present E_{disp} expression, limited to the first C_6/R^6 term, contains implicitly most of the physical intermolecular dispersion via the fitting of the atomic C_6 coefficients to molecular C_6 values, obtained from a training set of 44 pairs of molecules including hydrocarbons and other small organic compounds.²⁴

The dispersion coefficients $C_6^{ij} = (2C^i C^j)/(C^i + C^j)$ are computed from the atomic C_6^i , as proposed by Wu and Yang,²⁴ but averaged over the possible hybridization states of the atoms, which are 2.845 and 26.360 au for H and C atoms, respectively. The damping function used is $f_{\text{damp}}(r_{ij}) = 1/(1 + e^{-\alpha(r_{ij}/r_0 - 1)})$ with $\alpha = 23.0$ ²⁴ and with r_0 being the sum of the atomic van der Waals radii.³⁴

The dispersion correction energy, its gradient, and second derivative were implemented in the deMon2K program,³⁵ allowing geometry optimization and vibrational frequency analysis.

We used a nonscaled empirical dispersion term, unlike in previous DFT–D calculations^{30,31} where different scaling factors were adopted depending on the chosen exchange–correlation functionals. In fact, scaling was used previously to correct the erroneous behavior of GGA exchange functionals, which either show an unexpected attractive tendency in the van der Waals region (and thus avoid a double counting of the “dispersion”) or, in contrast, have a too strong repulsion slope in this region. The latter trend is mainly displayed by the Becke exchange functional,³⁶ whereas PW91³⁷ and PBE³⁸ exchange functionals are responsible for the former.

2.2. Choice of the Exchange–Correlation Functionals.

In order to illustrate the above-mentioned problem, we report in Figure 1 the repulsive (top) and correlation (bottom) contributions to the nondispersion-corrected interaction

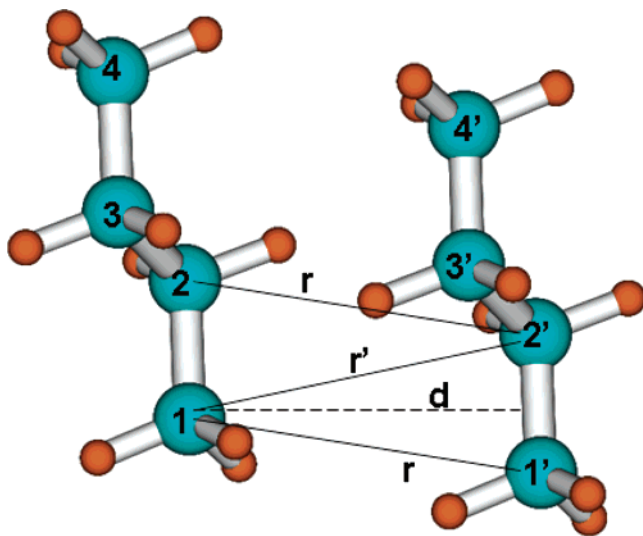


Figure 2. Geometric parameters r , r' , and d , defined using the butane dimer (isomer a).

energy between two butane molecules as a function of their shortest $C\cdots C$ intermolecular distance (r' in Figure 2). For proper comparison of the exchange functionals, the repulsive interaction energies have been calculated by removing the correlation contribution from the total interaction energy (without dispersion). The optimized butane monomer energies were used. These values are compared with the HF interaction energies (using the MP2-optimized structures). As shown in Figure 1 (top), the revised version of PBE, that is, revPBE,³⁹ and TPSS⁴⁰ repulsive curves are close to HF for the long distances, that is, between 4.4 and 5 Å, where they reach zero, ensuring no double counting of “dispersion” effects. In contrast, Becke (B) exchange leads to a much stronger repulsion, whereas PBE is attractive for distances beyond 4.4 Å. Similar conclusions have been reported for the benzene–benzene interaction.¹⁴

As expected, correlation interaction energies are more attractive with decreasing the separation between the butane monomers (Figure 1, bottom). The LYP⁴¹ functional shows a larger correlation interaction than the other two functionals.

Using the PBE exchange and correlation functionals without empirical dispersion correction leads to a small minimum for the butane dimer (−0.8 kcal/mol at a separation of 4.5 Å). A PBE–D calculation leads thus to a much too large stabilization of 4.1 kcal/mol compared with the MP2 and CCSD(T) interaction energy of 2.7 kcal/mol.

As shown in Figure 1, combining the PBE correlation with the revPBE exchange yields a large repulsive interaction in the range of 4–4.4 Å which cannot be compensated by the damped dispersion correction. Combining the “semiempirical” revPBE exchange, adjusted on atomic exchange energies, with the LYP correlation functional, self-interaction (SI)-free by construction, allows a good balance of repulsive and attractive effects between the two subsystems. In fact, the revPBE exchange leads to less SI error than PBE (5 times less for the H atom). The PBE exchange SI error is mostly compensated by the SI error of the PBE correlation itself. Therefore, combining the revPBE exchange with the PBE correlation is much less appropriate than combining it with the LYP correlation.

The calculations reported further are thus obtained using the revPBE-LYP functionals, augmented with the damped empirical dispersion, as described above and which will be referred to as DFT–D.

Finally, the result that the TPSS repulsion curve is very comparable to the HF interaction energy curve validates the construction of an adequate meta-GGA correlation functional, in which dispersion effects could be incorporated, using a strategy adopted by Zhang and Salahub²³ and including alkane van der Waals complexes in the training set.

2.3. Computational Details. The Dunning correlation-consistent cc-pVTZ basis,⁴² associated with automatically generated auxiliary basis functions up to $l = 4$ for fitting the density,³⁵ has been used for all dimers. For the DFT–D calculations, the exchange–correlation potential was computed using the variationally fitted density.³²

The DFT–D results for smaller C_nH_{2n+2} dimers ($n = 2–4, 6, \text{ and } 8$) were compared with the computations carried out with the Moller–Plesset second-order perturbation method (MP2) as implemented in the G03 code,⁴³ using the 6-31g-(d) basis set to optimize geometrical parameters and obtain vibrational properties. Single-point calculations at these geometries have then been performed to obtain energies at the cc-pVTZ level of theory (MP2/cc-pVTZ). It is a general consensus that the MP2 method combined with a relatively small basis set overestimates interaction energies in the van der Waals complexes. For this reason, the interaction energies between alkane moieties were also computed by the combined Gaussian-3 (G3) method:³³ a series of single-point energy calculations at the MP2/6-31g(d) optimized geometry were performed following the G3 algorithm. Instead of the usual QCISD(T) method suggested in the G3 approach, we have adopted the CCSD(T) calculations. These data are referred to as G3(CCSD(T)) in the text.

The obtained minima structures were localized by carrying out full geometrical optimization without imposing any constraint. The true minima on the potential energy surface (PES) for dimers up to octane were confirmed from the vibrational frequency analysis. The vibrational frequencies were obtained analytically with the G03 program and numerically with the deMon program. To minimize the numerical errors in the geometry optimization procedure, which are significant for weakly bound systems, the DFT–D calculations were performed using an adaptive grid with a tolerance equal to 10^{-14} . The tolerance of the energy gradients was equal to 10^{-5} to 10^{-6} hartree and for the energy convergences to 10^{-7} (DFT–D) and 10^{-8} hartree (MP2).

The amount of the basis set superposition error (BSSE) was examined following the counterpoise approach.

The MM results, reported for the series $n = 2–12$ of alkane dimers, have been obtained with the TINKER program,⁴⁴ using the OPLS-AA force field.⁴⁵

3. Results

3.1. Geometries. As it is the case for long alkane chains in surfactants or in lipids, the *n*-alkane dimers with $n \geq 3$ have been considered in a trans conformation. For these dimers, two types of isomers were found, as illustrated in Figure 3 for the octane dimer. The most stable complexes correspond

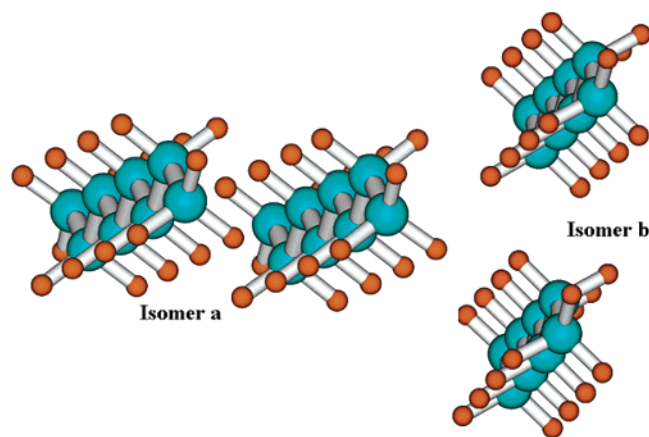


Figure 3. Schematic presentation of isomer **a** (the most stable minimum) and isomer **b** (the second minimum) structures of n -alkane dimers, using the results obtained for the octane dimer.

Table 1. Optimized Intermolecular Distances, r , r' , and d (defined in Figure 2), between the Monomers of the C_nH_{2n+2} Dimers ($n = 1, 12$) Computed at the DFT–D/cc-PVTZ Level^a

n	2	3	4	5	6	7	8	10	12
r^b	4.10 (4.22)	4.18 (4.23)	4.20 (4.24)	4.21 (4.23)	4.21 (4.22)	4.22 (4.22)	4.22 (4.22)	4.23	4.23
r'^b	3.85 (4.30)	4.00 (3.98)	4.12 (4.11)	4.12 (4.10)	4.13 (4.09)	4.13	4.13 (4.10)	4.13	4.13
d^b	3.88 (4.19)	3.98 (3.95)	4.09 (4.08)	4.09 (4.06)	4.09 (4.07)	4.10	4.09 (4.06)	4.09	4.09
r^c		4.48 (4.51)	4.65 (4.69)	4.71 (4.71)	4.71 (4.71)	4.72	4.72	4.73	4.74
r'^c		3.95 (4.04)	4.04 (4.09)	4.07 (4.09)	4.09 (4.10)	4.09	4.10	4.11	4.12
d^c		3.94 (4.02)	3.95 (3.98)	3.95 (3.96)	3.96 (3.96)	3.96	3.96	3.95	3.95

^a The values in parentheses are obtained from the MP2/6-31g(d) method for $n = 2-6$ and 8. ^b Most stable isomer **a** (Figure 3). ^c Second stable isomer **b** (Figure 3).

to two monomers with carbon skeletons in parallel planes (isomer **a**, Figure 3), whereas the less stable isomer **b** (Figure 3) is related to carbon skeletons in the same plane. For the ethane dimer, isomers **a** and **b** correspond to the same structure with the four carbons in one plane.

The geometries of the alkane dimers are defined by the intermolecular $C\cdots C$ distances illustrated in Figure 2 for the butane dimer, isomer **a**. These notations are valid for all alkane isomers. If the carbon atoms are labeled 1, 2, ..., n for one monomer and 1', 2', ..., n' for the second monomer, one finds n distances r , between the carbon pairs i and i' and $n - 1$ distances r' , independently on the number n of carbons in the monomers. As an example, the butane dimer (Figure 2) has four equivalent r distances (1–1', 2–2', 3–3', and 4–4') and three equivalent r' distances (1–2', 2–3', and 3–4'). It is clear from Figure 2 that the relative values of r and r' measure the translational shift of the carbon skeletons, in both isomers. The d parameter measures the distance between the parallel C–C bonds of the two monomers. All the r , r' , and d values, presented in Table 1, have been obtained averaging the corresponding parameters

on the n calculated r and $n - 1$ calculated r' and d values for all dimers. The average values reported in Table 1 have a mean absolute error less than 0.02 Å for DFT–D and 0.05 Å for MP2. Moreover, all ($i, i', i' + 1, i + 1$) dihedral angles (see Figure 2 for illustration) are less than 1°. The propane dimers make an exception with average distances calculated with a mean absolute error of about 0.06 Å, whereas the two dihedral angles as mentioned above deviate from planarity by about 2–3° for MP2 and DFT–D.

The analysis of Table 1 reveals a very good agreement between the geometrical parameters obtained with the two different methodologies, especially for $n \geq 3$, allowing to draw general conclusions without referring to the method. The most stable isomers **a** with the C_n chains in parallel planes have r and r' values more similar than the other isomers **b** and, at the same time, a slightly larger distance d between the chains. Indeed, the $r - r'$ value amounts to about 0.1 Å for isomers **a** and 0.6 Å for isomers **b**, whereas the distance d between the alkane chains decreases by about 0.15 Å from the former to the latter. Finally, both isomers have comparable r' distances between the ($i, i' + 1$) carbon pairs. These results illustrate the fact that the shift of the monomers with respect to each other ($r - r'$) is correlated with the value of the distance d between the chains. Decreasing the electrostatic repulsion between dimer chains is achieved through both their relative shift and their larger separation. At the same time, shorter distances between the chains favor the dispersion attraction. Obviously, a shorter chain–chain distance in isomers **b** does not compensate the much longer r distance, yielding then a weaker dispersion attraction.

It is worth noting that the dimer chains from C_4 to C_{12} behave similarly, with a very nice invariability of the r , r' , and d geometrical parameters. This allows us to anticipate that increasing a monomer chain by one CH_2 unit will increase by the same amount the electrostatic repulsion and the dispersion attraction for chains in parallel planes at about 4.10 Å and at about 3.95 Å in the same plane. The ethane dimer which contains only CH_3 groups and the propane dimer with two CH_2 against four CH_3 groups do not show the same characteristics as the longer alkane dimers, with shorter r , r' , and d values. We can thus conclude that the butane dimer is the first “long” chain alkane dimer, with the same number of CH_2 as CH_3 groups.

Very recent MP2 calculations on n -alkane dimers up to decane, with D_2 fixed symmetry, have been reported, but their detailed geometries were not discussed.⁴⁶ Earlier MP2 studies on the potential energy surfaces of small hydrocarbon dimers (ethane and propane) reported a separation distance of 4.18 Å for the propane dimer.^{47,48} In these works, C_{2v} symmetry was imposed, and the PES was described from the MP2 single-point interaction energies at various intermolecular distances fitted against a Morse potential. The separation distance between propane monomers found in ref 47 agrees well with the r values of 4.18 and 4.23 Å obtained at the DFT–D and MP2 levels, respectively, for the most stable isomer **a**, although a comparison between optimized structures and PES single points is not easy.

The OPLS-AA empirical potential calculations yielded r and r' values equal to 4.11 and 4.00 Å (isomer **a**), and 4.39

Table 2. Calculated Interaction Energies (kcal/mol) of the Most Stable Structures of the Ethane, Propane, and Butane Dimers, Compared with Different Methods

	MP2 ^a (this work)	G3 ^b (CCSD(T)) (this work)	MP2 ^c ref. 47	MP2 ^d ref. 46	MP2 ^e ref. 46	CCSD(T) ^f ref. 46	DFT–D ^g (this work)
C ₂	–1.12	–1.00		–1.04	–1.35	–1.22	–1.28
C ₃	–1.89	–1.86	–1.63	–1.64	–2.08	–1.87	–1.72
C ₄	–2.58	–2.69		–2.44	–2.97	–2.74	–2.66

^a MP2 opt 6-31g(d) basis; energy cc-pVTZ. ^b MP2 opt 6-31g(d) basis; CCSD(T) limit. ^c MP2 opt 6-311+G(d2f,2pd); geometry of monomers fixed. ^d MP2 opt 6-311G(dp); energy cc-pVTZ. ^e MP2 opt 6-311G(dp); MP2 limit. ^f MP2 opt 6-311g(dp); CCSD(T) limit. ^g revPBE-LYP-D opt cc-pVTZ.

and 3.75 Å (isomer **b**), respectively, for the considered series from $n = 3$ to 12. For the ethane dimer, the calculated r and r' values were 4.08 and 3.83 Å, respectively. These results are in relatively good agreement when compared with our DFT–D and MP2 calculations for the isomer **a**, despite an underestimation by 0.12 Å of the distance between the chains. In contrast, the distances found for isomers **b** are neatly underestimated with respect to the quantum chemical methods, with a distance between the chains too short by almost 0.3 Å. However, the relatively good agreement obtained for the largest interactions is encouraging for further use of this force field in combined DFT–D/MM approaches.

3.2. Interaction Energies. A dimer interaction energy (ΔE) has been computed as the difference between the energy of the dimer at the optimized geometry and the sum of the energies of the two monomers at infinity. The structures of the monomers have been fully optimized at all computational levels considered in this work, as described in section 2. Indeed, the BSSE correction has been evaluated for the ethane up to hexane dimers. For both MP2 and DFT–D calculations, its value decreases rapidly with increasing the number of CH₂'s in the monomer and becomes already negligible for the butane dimer for MP2 and the propane dimer for DFT–D.

We have found it interesting to compare first, in detail, the DFT–D results with those obtained with post-Hartree–Fock methods, at different levels of theory for the ethane, propane, and butane dimers, separately. The “long” alkane dimers, including also the butane dimer, will then be discussed further.

3.2.1. C₂ to C₄ Dimers: DFT–D Compared with Post-Hartree–Fock Methods. The results obtained for the C₂, C₃, and C₄ dimers are compared in Table 2 for different methods. First, it is worth noting the overall good agreement between the various approaches, despite differences which are due to the respective approximations of the methods, and that we would like to comment upon.

The dependence of the MP2 electron correlation energy, for small hydrocarbon dimers, on the size of basis functions has been discussed previously^{46,49} and shown to be less pronounced for the longer dimers.⁴⁶ The results reported for propane from ref 47 correspond to a dimer optimization with frozen monomer geometries.

The MP2 basis set limit calculations in ref 46 show a trend to overestimate the dimer stabilization with respect to the ethane to butane reported CCSD(T)(limit) values. The G3-(CCSD(T)) results in this work and the CCSD(T)(limit) from ref 46 show small differences which are probably due to slightly different geometries of the respective dimers and

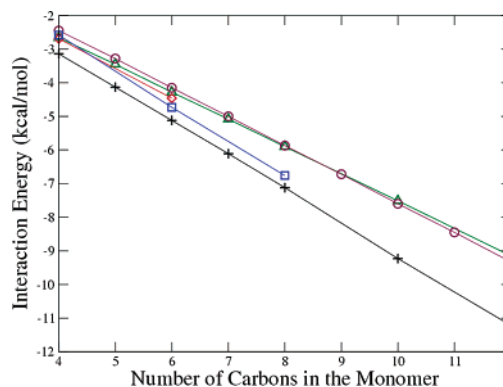


Figure 4. Interaction energy in kilocalories per mole of the isomers **a** of C₄ to C₁₂ alkane dimers, computed with different methods. The symbols denote various computational approaches as follows: (Δ) DFT–D/cc-pVTZ, (\circ) MM–OPLS, (\square) MP2/cc-pVTZ, and (\diamond) G3(CCSD(T)). The DFT–D dispersion interaction energies are denoted with crosses.

the different combined computations for the basis and correlation limits.

The values obtained from DFT–D are in very good agreement with those obtained from the CCSD(T)(limit) results. The evolution of the interaction energy from ethane to butane is also well-reproduced. In all methods, the dimer binding energy changes less from ethane to propane than from propane to butane, confirming that butane dimer can be considered as the first “long” alkane chain dimer.

Finally, let us mention that the isomers **b** of propane and butane dimers have evaluated interaction energies of –1.54 and –2.00 kcal/mol with DFT–D.

3.2.2. C₄ to C₁₂ Dimers: DFT–D Compared with MP2, CCSD(T), and MM Methods. A graphical comparison between the ΔE values obtained from the various methods is presented in Figure 4 for isomers **a** and Figure 5 for isomers **b**. The evolution of ΔE from C₄ to C₁₂ chains shows a very regular linear dependency for both isomers and for all the methods. The same trend can be found from the MP2 interaction energies reported in ref 46 for C₄ to C₁₀. As already mentioned above, starting from butane, the CH₂···CH₂ interactions increase regularly going from C_n to C_{n+1} dimers.

The MP2 values for isomer **a** show a larger dimer stabilization of about 12% than revealed by the DFT–D interaction energies, with the same trend followed by the MP2 basis set limit calculations in ref 46 for the butane to decane series. However, the G3(CCSD(T)) corrections to the MP2 electron correlation in the case of the hexane dimer **a** yield $\Delta E = -4.46$ kcal/mol, agreeing well with the DFT–D

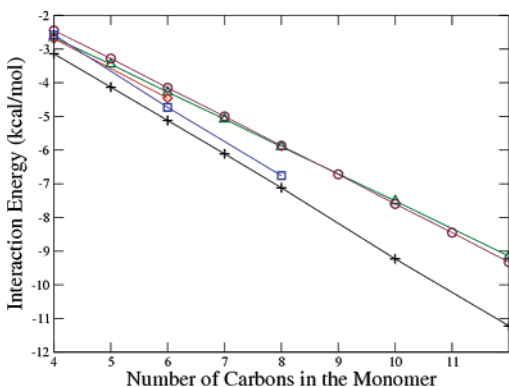


Figure 5. Interaction energy in kilocalories per mole of the isomers **b** of C_4 to C_{12} alkane dimers, computed with different methods. The symbols denote various computational approaches as follows: (Δ) DFT–D/cc-pVTZ, (\circ) MM–OPLS, (\square) MP2/cc-pVTZ, and (\diamond) G3(CCSD(T)). The DFT–D dispersion interaction energies are denoted with crosses.

value of -4.27 kcal/mol, whereas the MP2 value, at the same geometry, is -4.73 kcal/mol. The three methods yield very similar values for the stabilization of the hexane dimer isomer **b**.

It is interesting to note that the MM results are in very good agreement with the quantum mechanical values, especially for the most stable isomers **a**. This method obviously underestimates the energy difference between the two types of structures, that is, isomers **a** and **b**. This result is related with the underestimated MM intermolecular chain distances in isomer **b**, as shown in section 3.1.

For the most stable isomers, the average increase of interaction energy per CH_2 unit is estimated at -0.81 from DFT–D, -0.97 from MP2(limit),⁴⁶ and -0.86 kcal/mol from MM. From the G3(CCSD(T)) results for butane and hexane, a value of 0.88 kcal/mol can be proposed, which confirms the validity of the DFT–D description along with the chain lengthening. The average increase of interaction energy per CH_2 unit is much less for isomer **b**, since it amounts to -0.53 from DFT–D and -0.61 kcal/mol as deduced from the G3–(CCSD(T)) results for butane and hexane dimers **b**.

Since DFT–D geometries correlate well with those provided by MP2 methods which include implicitly the dispersion attraction, one can attempt to evaluate the dispersion increase along with the alkane chain lengthening, comparing the ΔE_{disp} and ΔE values provided by the DFT–D method.

The analysis of these values displayed in Figures 4 and 5 leads to the conclusion that attractive dispersion-like forces have a main contribution in alkane dimer formation. For the considered series of C_4 to C_{12} dimers, ΔE_{disp} is found to be somewhat larger than the total interaction energy. Interestingly, the difference between ΔE_{disp} and ΔE increases only from 0.14 to 0.70 kcal/mol for isomer **b** from C_4 to C_{12} dimers, whereas it changes from 0.48 to 2.07 kcal/mol for isomer **a**, showing that the repulsive electrostatic and electron exchange forces in the total interaction energies appear to have a larger effect for isomer **a** than for isomer **b**. At the same time, the dispersion interaction between the two alkane moieties is stronger in the case of dimers **a**. The two

monomers lying in mutually parallel planes (structure **a**) have $r(i, i')$ distances shorter by nearly 0.5 Å than those lying in the same plane (structure **b**), due to the stronger dispersion-like attraction. Therefore, higher ΔE_{disp} values obtained for isomers **a** correlate with closer contacts between carbon and hydrogen in this isomer in accordance with a conclusion drawn in ref 48 concerning the structure of the most stable minimum on the PES of the propane dimer. This conclusion is also confirmed by the average increase of “dispersion interaction” associated per CH_2 unit from butane to decane, which amounts to -1.0 for isomers **a** and -0.6 kcal/mol for isomers **b**.

The simultaneous increase of both attractive and repulsive intermolecular interactions with increasing the n -alkane size leads thus to a nearly linear relationship of the total interaction energy with n .

It is worth noting that dispersion energy also contributes to the total energies of the individual n -alkane monomers. This contribution varies from -3.7 for butane to -14.8 kcal/mol for dodecane, with a regular decrease of -1.4 kcal/mol per CH_2 unit. The internal E_{disp} value is thus about 50% larger than the dispersion contribution to the dimer binding. This shows that, in the alkane monomers, the damped dispersion at midrange contributes also to the total energies. However, the amount of stabilization provided by the internal dispersion in an alkane molecule is very small with respect to the other energy contributions (0.55% of the correlation energy for n -butane, 0.57% for isobutane, 0.70% for n -octane, and 0.81% for isooctane). This explains why this E_{disp} term cannot compete with some other effects, such as those governing the branched/linear alkane relative stabilities.⁵⁰

The geometries and interaction energies obtained for n -alkane dimers show thus a very good agreement, when a comparison is possible, with the post-Hartree–Fock results. The performance of the revPBE-LYP-D method has also been verified for the two benzene dimers with sandwich (S) and parallel displaced (PD) structures for which the stabilization energy is due solely to dispersion interactions. Optimization of these dimers was performed at the revPBE-LYP-D/cc-pVTZ level and energies corrected for BSSE. The stabilization of the S dimer is 1.0 kcal/mol (distance 3.96 Å), whereas that of the PD dimer is 1.7 kcal/mol (distance 3.67 Å, displacement 0.95 Å). These values agree very well with CCSD(T) results reported with similar bases: 1.1 kcal/mol (S) and 2.0 kcal/mol (PD), with aug-cc-pVDZ,⁵¹ and 0.7 kcal/mol (S) and 1.6 kcal/mol (PD), with cc-pVTZ.⁵² The basis set extension effect on the above DFT–D values is comparable with that displayed by post-Hartree–Fock methods.

3.3. Vibrational Frequencies. Vibrational frequencies, within the harmonic approximation, have been computed at the DFT–D/cc-pVTZ and MP2/6-31g(d) levels of theory for a limited number of dimers, that is, ethane, propane, butane, hexane, and octane dimers (isomers **a**). Each dimer has six low-frequency modes. From the analysis of the six normal vectors, five of the low-frequency modes are assigned to coupled internal rotations of the CH_2 and CH_3 groups. Only one normal vector was found related with the stretching displacements of the n carbon atoms of one monomer with

Table 3. Far-Infrared Intermolecular Stretching Vibrational Frequencies in cm^{-1} for the Most Stable Isomers **a** of $\text{C}_n\text{H}_{2n+2}$ Dimers ($n = 2, 3, 4, 6, \text{ and } 8$) Computed at the DFT–D/cc-pVTZ and MP2/6-31 g(d) Levels

<i>n</i>	2	3	4	6	8
DFT–D	64.5 (sym) 65.2 (asym)	53.9	59.3	58.9	57.9
MP2	46.9 (sym) 48.1 (asym)	51.3	53.9	58.3	56.1

respect to the corresponding ones of the other monomer. Therefore, the frequency of this mode, displayed in Table 3 for the selected dimers, was attributed to the intermolecular stretching vibration of the dimer. For the ethane complex, the intermolecular stretching mode is split into symmetric and asymmetric components following the analysis of the computed normal vectors.

As revealed from the Table 3 results, both DFT–D and MP2 methods yield very comparable intermolecular stretching frequencies, especially for the longer alkanes. The discrepancy for the ethane dimer is a consequence of the different structures found with the two methods (Table 1). The MP2 dimer has a larger intermolecular distance, a smaller interaction energy, and thus a reduced intermolecular stretching frequency with respect to DFT–D. The molecular stretching C–C and C–H and bending CH_2 vibrations in all studied dimers are very close to those obtained for the isolated monomers, thus correlating with the results that the geometry changes of the *n*-alkane moieties in the dimers are negligible. Moreover, the molecular vibrational modes of both moieties are fully degenerate.

4. Conclusions

In this study, we have calculated the interaction energies of two isomers of *trans n*-alkane dimers, from ethane to dodecane, comparing the values and the trends provided by traditional correlated MP2 and CCSD(T) methods and by a DFT approach using the revised PBE exchange and LYP correlation functionals, augmented with an empirical dispersion correction. From the comparison, we have concluded that the DFT–D/cc-pVTZ results are in very good agreement with those obtained from MP2 for the geometries and from CCSD(T)(limit)/cc-pVTZ for the energies, the largest dimer compared being the hexane dimer.

The most stable isomers correspond to two alkane chains with their carbon skeletons in parallel planes, whereas in the other type of isomers, the two carbon skeletons are in the same plane. In both cases, the butane dimer is the first complex among the C_n series for which regular trends for geometric and energetic properties are found to apply. Interestingly, the distance *d* between the two carbon skeletons from C_4 to higher alkanes remains constant, with a value of 4.09 Å for the most stable isomers and 3.96 Å for the second isomers. Both types of dimers have their alkane chains shifted one with respect to the other, allowing then the best $\text{CH}_2 \cdots \text{CH}_2$ adjustment between the chains, in terms of the balance of electrostatic and exchange repulsion and long-range attraction. As a consequence, adding a CH_2 unit to a C_n

dimer, $n > 4$, generates a regular increase of stabilization for the dimer of about -0.8 kcal/mol due to dispersion. In relation with these trends, the symmetric stretching frequencies of the dimers are found constant at about $56\text{--}58$ cm^{-1} , the five other far-infrared modes being coupled group rotations of the two dimer moieties.

The comparison between the results obtained from MP2/G3(CCSD(T)) and revPBE-LYP, augmented with a dispersion correction, demonstrates the applicability of this DFT–D method to describing the properties of molecular clusters containing long alkane chains.

Acknowledgment. The CNRS-Bulgarian Academy of Sciences bilateral project is acknowledged for exchange support. The COST chemistry D26 action is also acknowledged for short-term mission support. The CNRS post-doc program is acknowledged for funding the postdoctoral position of R.K.

References

- (1) Tsuzuki, S.; Lüthi, H. P. Interaction Energies of van der Waals and Hydrogen Bonded Systems Calculated Using Density Functional Theory: Assessing the PW91 Model. *J. Chem. Phys.* **2001**, *114*, 3949.
- (2) Tao, J.; Perdew, J. P. Test of a Nonempirical Density Functional: Short-Range Part of the van der Waals Interaction in Rare-Gas Dimers. *J. Chem. Phys.* **2005**, *122*, 114102.
- (3) Jones, R. O.; Gunnarsson, O. The Density Functional Formalism, Its Applications and Prospects. *Rev. Mod. Phys.* **1989**, *61*, 689.
- (4) Perez-Jorda, J. M.; Becke, A. D. A Density-Functional Study of van der Waals Forces—Rare-Gas Diatomics. *Chem. Phys. Lett.* **1995**, *233*, 134.
- (5) Kohn, W.; Meir, Y.; Makarov, D. E. Van der Waals Energies in Density Functional Theory. *Phys. Rev. Lett.* **1998**, *80*, 4153.
- (6) Müller-Detlef, K.; Hobza, P. Noncovalent Interactions: A Challenge for Experiment and Theory. *Chem. Rev.* **2000**, *100*, 143.
- (7) Dobson, J. F. Prospects for a van der Waals Density Functional. *Int. J. Quantum Chem.* **1998**, *69*, 615.
- (8) Rapcewicz, K.; Ashcroft, N. W. Fluctuation Attraction in Condensed Matter – A Nonlocal Functional Approach. *Phys. Rev. B: Condens. Matter Mater. Phys.* **1991**, *44*, 4032.
- (9) Andersson, Y.; Langreth, D. C.; Lundqvist, B. I. Van der Waals Interactions in Density-Functional Theory. *Phys. Rev. Lett.* **1996**, *76*, 102.
- (10) Wesolowski, T. A.; Tran, F. Gradient-Free and Gradient-Dependent Approximations in the Total Energy Bifunctional for Weakly Overlapping Electron Densities. *J. Chem. Phys.* **2003**, *118*, 2072.
- (11) Rydberg, H.; Lundqvist, B. I.; Langreth, D. C.; Dion, M. Tractable Nonlocal Correlation Density Functionals for Flat Surfaces and Slabs. *Phys. Rev. B: Condens. Matter Mater. Phys.* **2000**, *62*, 6997.
- (12) Sato, T.; Tsuneda, T.; Hirao, K. A Density-Functional Study on π -Aromatic Interaction: Benzene Dimer and Naphthalene Dimer. *J. Chem. Phys.* **2005**, *123*, 104307.

- (13) Rydberg, H.; Dion, M.; Jacobson, N.; Schröder, E.; Hyldgaard, P.; Simak, S. I.; Langreth, D. C.; Lundqvist, B. I. Van der Waals Density Functional for Layered Structures. *Phys. Rev. Lett.* **2003**, *91*, 126402.
- (14) Dion, M.; Rydberg, H.; Schröder, E.; Langreth, D. C.; Lundqvist, B. I. Van der Waals Density Functional for General Geometries. *Phys. Rev. Lett.* **2004**, *92*, 246401.
- (15) Hesselmann, A.; Jansen, G. Intermolecular Dispersion Energies from Time-Dependent Density Functional Theory. *Chem. Phys. Lett.* **2003**, *367*, 778.
- (16) Misquitta, A. J.; Jeziorski, B.; Szalewicz, K. Dispersion Energy from Density-Functional Theory Description of Monomers. *Phys. Rev. Lett.* **2003**, *91*, 033201.
- (17) Osinga, V. P.; van Gisbergen, S. J. A.; Snijders, J. G.; Baerends, E. J. Density Functional Results for Isotropic and Anisotropic Multipole Polarizabilities and C-6, C-7, and C-8 van der Waals Dispersion Coefficients for Molecules. *J. Chem. Phys.* **1997**, *106*, 5091.
- (18) Becke, A. D.; Johnson, E. R. A Density-Functional Model of the Dispersion Interaction. *J. Chem. Phys.* **2005**, *122*, 154104.
- (19) Becke, A. D.; Johnson, E. R. Exchange-Hole Dipole Moment and the Dispersion Interaction: High-Order Dispersion Coefficients. *J. Chem. Phys.* **2006**, *124*, 014104.
- (20) Johnson, E. R.; Becke, A. D. A Post-Hartree-Fock Model of Intermolecular Interactions: Inclusion of Higher-Order Corrections. *J. Chem. Phys.* **2006**, *124*, 174104.
- (21) Kurita, N.; Inoue, H.; Sekino, H. Adjustment of Perdew–Wang Exchange Functional for Describing van der Waals and DNA Base-Stacking Interactions. *Chem. Phys. Lett.* **2003**, *370*, 161.
- (22) Walsh, T. R. Exact Exchange and Wilson–Levy Correlation: A Pragmatic Device for Studying Complex Weakly-Bonded Systems. *Phys. Chem. Chem. Phys.* **2005**, *7*, 443.
- (23) Zhang, Y.; Salahub, D. R. A Reparametrization of a meta-GGA Exchange-Correlation Functional with Improved Description of van der Waals Interactions. *Chem. Phys. Lett.* **2007**, *436*, 394.
- (24) Wu, Q.; Yang, W. Empirical Correction to Density Functional Theory for van der Waals Interactions. *J. Chem. Phys.* **2002**, *116*, 515.
- (25) Ahlrichs, R.; Penco, R.; Scoles, G. Intermolecular Forces in Simple Systems. *Chem. Phys.* **1977**, *19*, 119.
- (26) Hepburn, J.; Scoles, G. A Simple but Reliable Method for the Prediction of Intermolecular Potentials. *Chem. Phys. Lett.* **1975**, *36*, 451.
- (27) Mooij, W. T. M.; van Duijneveldt, F. B.; van Duijneveldt–van de Rijdt, J. G. C. M.; van Eijck, B. P. Transferable *ab Initio* Intermolecular Potentials. I. Derivation from Methanol Dimer and Trimer Calculations. *J. Phys. Chem. A* **1999**, *103*, 9872.
- (28) Elstner, M.; Hobza, P.; Frauenheim, T.; Suhai, S.; Kaxiras, E. Hydrogen Bonding and Stacking Interactions of Nucleic Acid Base Pairs: A Density-Functional-Theory Based Treatment. *J. Chem. Phys.* **2001**, *114*, 5149.
- (29) Zimmerli, U.; Parrinello, M.; Koumotsakos, P. Dispersion Corrections to Density Functionals for Water Aromatic Interactions. *J. Chem. Phys.* **2004**, *120*, 2693.
- (30) Grimme, S. Accurate Description of van der Waals Complexes by Density Functional Theory Including Empirical Corrections. *J. Comput. Chem.* **2004**, *25*, 1463.
- (31) Jurečka, P.; Černý, J.; Hobza, P.; Salahub, D. R. Density Functional Theory Augmented with an Empirical Dispersion Term. Interaction Energies and Geometries of 80 Non-Covalent Complexes Compared with *ab Initio* Quantum Mechanics Calculations. *J. Comput. Chem.* **2007**, *28*, 555.
- (32) Koester, A. M.; Ulises Reveles, J.; del Campo, J. M. Calculation of Exchange-Correlation Potentials with Auxiliary Function Densities. *J. Chem. Phys.* **2004**, *121*, 3417.
- (33) Curtiss, L. A.; Raghavachari, K.; Redfern, P. C.; Rassolov, V.; Pople, J. A. Gaussian-3 (G3) Theory for Molecules Containing First and Second-Row Atoms. *J. Chem. Phys.* **1998**, *109*, 7764.
- (34) Bondi, A. van der Waals Volumes and Radii. *J. Phys. Chem.* **1964**, *68*, 441.
- (35) Koester, A. M.; Calaminici, P.; Flores-Moreno, F.; Geudtner, G.; Goursot, A.; Heine, T.; Janetzko, F.; Patchkovskii, S.; Reveles, J. U.; Vela, A.; Salahub, D. R. *The deMon Developers*; University of Calgary: Calgary, Canada, 2004.
- (36) Becke, A. D. A Multicenter Numerical Integration Scheme for Polyatomic Molecules. *J. Chem. Phys.* **1988**, *88*, 2547.
- (37) Perdew, J. P.; Wang, Y. Accurate and Simple Analytic Representation of the Electron-Gas Correlation Energy. *Phys. Rev. B: Condens. Matter Mater. Phys.* **1992**, *45*, 13244.
- (38) Perdew, J. P.; Burke, K.; Ernzerhof, M. Generalized Gradient Approximation Made Simple. *Phys. Rev. Lett.* **1996**, *77*, 3865; **1997**, *78*, 1396(E).
- (39) Zhang, Y.; Yang, W. Comment on “Generalized Gradient Approximation Made Simple”. *Phys. Rev. Lett.* **1998**, *80*, 890.
- (40) Tao, J. M.; Perdew, J. P.; Staroverov, V. N.; Scuseria, G. E. Climbing the Density Functional Ladder: Non Empirical Meta-Generalized Gradient Approximation Designed for Molecules and Solids. *Phys. Rev. Lett.* **2003**, *91*, 146401.
- (41) Lee, C.; Yang, W.; Parr, R. G. Development of the Colle–Salvetti Correlation-Energy Formula into a Functional of the Electron Density. *Phys. Rev. B: Condens. Matter Mater. Phys.* **1988**, *37*, 785.
- (42) Dunning, T. H., Jr. Gaussian Basis Sets for Use in Correlated Molecular Calculations. I. The Atoms Boron through Neon and Hydrogen. *J. Chem. Phys.* **1989**, *90*, 1007. Woon, D. E.; Dunning, T. H., Jr. Gaussian Basis Sets for Use in Correlated Molecular Calculations. V. Core-Valence Basis Sets for Boron through Neon. *J. Chem. Phys.* **1995**, *103*, 4572.
- (43) Frisch, M. J.; Trucks, G. W.; Schlegel, H. B.; Scuseria, G. E.; Robb, M. A.; Cheeseman, J. R.; Montgomery, J. A., Jr.; Vreven, T.; Kudin, K. N.; Burant, J. C.; Millam, J. M.; Iyengar, S. S.; Tomasi, J.; Barone, V.; Mennucci, B.; Cossi, M.; Scalmani, G.; Rega, N.; Petersson, G. A.; Nakatsuji, H.; Hada, M.; Ehara, M.; Toyota, K.; Fukuda, R.; Hasegawa, J.; Ishida, M.; Nakajima, T.; Honda, Y.; Kitao, O.; Nakai, H.; Klene, M.; Li, X.; Knox, J. E.; Hratchian, H. P.; Cross, J. B.; Adamo, C.; Jaramillo, J.; Gomperts, R.; Stratmann, R. E.; Yazyev, O.; Austin, A. J.; Cammi, R.; Pomelli, C.; Ochterski, J. W.; Ayala, P. Y.; Morokuma, K.; Voth, G. A.; Salvador, P.; Dannenberg, J. J.; Zakrzewski, V. G.; Dapprich, S.; Daniels, A. D.; Strain, M. C. Farkas, O.; Malick, D. K.;

- Rabuck, A. D.; Raghavachari, K.; Foresman, J. B.; Ortiz, J. V.; Cui, Q.; Baboul, A. G.; Clifford, S.; Cioslowski, J.; Stefanov, B. B.; Liu, G.; Liashenko, A.; Piskorz, P.; Komaromi, I.; Martin, R. L.; Fox, D. J.; Keith, T.; Al-Laham, M. A.; Peng, C. Y.; Nanayakkara, A.; Challacombe, M.; Gill, P. M. W.; Johnson, B.; Chen, W.; Wong, M. W.; Gonzalez, C.; Pople, J. A. *Gaussian 03*, revision C.02; Gaussian, Inc.: Pittsburgh, PA, 2003.
- (44) *Tinker 4.0, Software Tools for Molecular Design*; Washington University School of Medicine: St. Louis, MO, 2003.
- (45) Jorgensen, W. L. *Parameters for Organic Molecules, Ions and Nucleic Acids*; Yale University: New Haven, CT, 1997.
- (46) Tsuzuki, S.; Honda, K.; Uchimaru, T.; Mikami, M. Estimated MP2 and CCSD(T) Interaction Energies of *n*-Alkane Dimers at the Basis Set Limit: Comparison of the Methods of Helgaker et al. and Feller. *J. Chem. Phys.* **2006**, *124*, 114304.
- (47) Jalkanen, J.; Mahlanen, R.; Pakkanen, T. A.; Rowley, R. L. *Ab Initio* Potential Energy Surfaces of the Propane Dimer. *J. Chem. Phys.* **2002**, *116*, 1303.
- (48) Jalkanen, J.; Mahlanen, R.; Pakkanen, T. A.; Yang, T.; Rowley, R. L. Interaction Energy Surfaces of Small Hydrocarbon Molecules. *J. Chem. Phys.* **2003**, *118*, 5474.
- (49) Tsuzuki, S.; Uchimaru, T.; Tanabe, K. *THEOCHEM* **1994**, *307*, 107.
- (50) Grimme, S. Seemingly Simple Stereoelectronic Effects in Alkane Isomers and the Implications for Kohn–Sham Density Functional Theory. *Angew. Chem., Int. Ed.* **2006**, *45*, 4460.
- (51) Hobza, P.; Selzle, H. L.; Schlag, E. W. New Structure for the Most Stable Isomer of the Benzene Dimer: A Quantum Chemical Study. *J. Phys. Chem.* **1993**, *97*, 3937.
- (52) Tsuzuki, S.; Honda, K.; Uchimaru, T.; Mikami, M.; Tanabe, K. Origin of Attraction and Directionality of the π/π Interaction: Model Chemistry Calculations of Benzene Dimer Interaction. *J. Am. Chem. Soc.* **2002**, *124*, 104.

CT600373F

Restricted Ensemble-Referenced Kohn–Sham versus Broken Symmetry Approaches in Density Functional Theory: Magnetic Coupling in Cu Binuclear Complexes[†]

Ibério de P. R. Moreira,[‡] Ramon Costa,[§] Michael Filatov,^{||} and Francesc Illas^{*,‡}

Departament de Química Física & CeRQT and Departament de Química Inorgànica & CeRQT, Universitat de Barcelona i Parc Científic de Barcelona, C/ Martí i Franquès 1, E-08028 Barcelona, Spain, and Theoretical Chemistry, Materials Science Centre, University of Groningen, Nijenborgh 4, 9747 AG Groningen, The Netherlands

Received January 8, 2007

Abstract: The performance of density functional theory in estimating the magnetic coupling constant in a series of Cu(II) binuclear complexes is investigated by making use of two open shell formalisms: the broken symmetry and the spin-restricted ensemble-referenced Kohn–Sham methods. The strong dependence of the calculated magnetic coupling constants with respect to the exchange–correlation functional is confirmed and found to be independent of whether spin symmetry is imposed or not. The use of a method which guarantees the spin state does not improve the correlation with the experiment and indeed shows some worsening due to an overestimation of the ferromagnetic interactions. However, with the present exchange–correlation functionals, a rather systematic deviation is found. Therefore, it would be possible to develop improved density functionals which will allow for a rigorous treatment of open shell systems in density functional theory.

1. Introduction

The Kohn–Sham (KS) implementation¹ of density functional theory (DFT)² has no doubt become the standard electronic structure method in computational chemistry as well as computational materials science.^{3–6} Successful applications of DFT in chemistry are very broad covering, among others, molecular structure, thermochemistry, reactivity in organic, inorganic and organometallic chemistry, interpretation of infrared spectra, prediction of nuclear magnetic resonance shielding, core level binding energies,^{7–9} and, more recently, interpretation of optical spectra.¹⁰ Likewise, there are numerous examples of successful applications of DFT in condensed

matter and surface science.³ The prediction of crystal structures, the reconstruction of complex surfaces, the structure of chemisorbed molecules, and the reaction mechanisms of chemical reactions mediated by surfaces can be mentioned in this respect along with the broad field of applications emerging from coupling of DFT with molecular dynamics which in itself generated a new field usually termed *ab initio* simulations.¹¹

The basis of the Kohn–Sham method is the existence of a reference system of noninteracting electrons with the density identical to that of the real physical system. The existence of such a reference system is usually taken for granted although there is a large body of literature dealing with this important problem. In the original KS formulation, the density of the reference system is written as a Slater determinant with identical spatial part for the alpha and beta spin orbitals and for an even number of electrons resulting in a closed shell electronic structure. For stable molecules and nonmagnetic solids having precisely a closed shell electronic structure this is a very reasonable choice which indeed imposes spin symmetry. In the case of radicals and

[†] Dedicated to Dennis R. Salahub on the occasion of his 60th birthday.

* Corresponding author e-mail: francesc.illas@ub.edu.

[‡] Departament de Química Física & CeRQT, Universitat de Barcelona i Parc Científic de Barcelona.

[§] Departament de Química Inorgànica & CeRQT, Universitat de Barcelona i Parc Científic de Barcelona.

^{||} University of Groningen.

other magnetic systems the closed shell *Ansatz* cannot be used and different alternatives have been proposed, with the spin-unrestricted or spin-polarized version of the KS implementation (UKS) being almost universally used in this case.^{12,13}

The UKS implementation is very similar to the Unrestricted Hartree Fock (UHF) method proposed earlier by Pople and Nesbet¹⁴ and by Berthier.¹⁵ For many years, the UHF method was the most common approach to the open shell problem in quantum chemistry, and in the late 1970s and early 1980s it was implemented in almost all semiempirical and *ab initio* Hartree–Fock computational codes. The periodic formulation of the UHF method was also developed and later coded into the CRYSTAL suite of programs.¹⁶ However, many numerical applications of UHF to different systems soon encountered certain problems, mainly related to the so-called spin contamination arising from the fact that the corresponding UHF wave function is not an eigenfunction of the square of the total spin operator. These difficulties led quantum chemists to seek for alternatives to UHF within the different orbitals for different spins scheme; we mention here extended Hartree–Fock^{17–19} and similar formalisms. However, these methods appeared to be very complex and not very accurate because of the lack of the dynamic electron correlation. Hence, the UHF approaches were almost abandoned, and the problems encountered by these methods were solved by making use of the more advanced wave function theory (WFT) methods of electronic structure such as the multiconfigurational self-consistent field (MCSCF), the configuration interaction (CI) methods, or the coupled cluster (CC) approaches.²⁰ Notice, however, that these methods demand a huge increase in the computational complexity and an enormous computational cost. In principle, numerical accuracy up to a predefined threshold can be achieved by these sophisticated wave function based methods. In practice, however, even with the present day available supercomputers, very accurate calculations can be carried out in systems containing a rather limited (~ 10 – 20) number of atoms. Clearly, density functional methods do not face these limitations, because the electron correlation is implicitly introduced through the exchange–correlation functional. However, one must be aware of the possible artifacts arising from the fact that, while the real system of interacting electrons possesses the well-defined spin symmetries, the UKS noninteracting reference system does not.

In the case of radicals or open shell systems with a high spin open shell ground state, the UKS approach is almost free of problems, at least judged from the numerical success evidenced in many applications. The problems remain, however, when the system of interest exhibits a low spin ground state or when the property of interest concerns energy differences involving both high and low spin states. This is the case of biradicals and, also, of a broad class of systems such as di- or polinuclear complexes with open shell transition-metal atoms; the same problem appears when computing various spectral terms of a given atomic or molecular multiplet state. A practical solution to the problem of computing the energy of low spin states for transition-metal dinuclear complexes has been given by Noodleman^{21,22}

in the framework of UHF and of SCF- $X\alpha$ methods. An independent, closely related, method was also proposed by Yamaguchi in the framework of UHF.²³ These practical approaches are all based on the use of broken symmetry (BS) solutions which do not necessarily represent the desired state but the energy of which can be related to the desired spin state through spin symmetry considerations, such as the Slater sum rule as applied by Ziegler, Rauk, and Baerends,²⁴ through projection techniques, such as the methods of Noodleman^{21,22} and Yamaguchi,²³ or through the appropriate mapping approach.^{25,26} In this context it is also worth pointing out the pioneering calculations of Bagus and Bennet²⁷ on the energies of atomic multiplets in the framework of SCF- $X\alpha$.

The broken symmetry approaches provide a way to bypass the problem of dealing with low spin states in the UKS calculations; however, the problem itself still remains. The origin of the problem is in the neglect of spin symmetry requirement in the wave function of the noninteracting reference system employed in the KS self-consistent approach. This problem has attracted the attention of many theoretical groups, and a number of well-defined procedures have been proposed. Thus, new Kohn–Sham procedures within strict spin-restricted formalism have been proposed which result in a proper description of open shell states where the total spin quantum numbers (S and S_z) are well defined, for instance, the spin-Restricted Ensemble-referenced Kohn–Sham (REKS) method of Filatov and Shaik,^{28,29} which is, in its spirit, similar to the well-known CASSCF approach. The CAS-DFT approach³⁰ has been also formulated where the nondynamic electron correlation effects and the proper spin symmetry are introduced through the CASSCF wave function and the dynamic electron correlation is taken over by a suitable correlation functional. The problem of CAS-DFT lies, however, in the double counting of correlation effects, which are implicitly incorporated via the density functional and are explicitly treated by the WFT method. The time dependent DFT formalism^{31–33} does also treat spin symmetry correctly, but its current implementation cannot be applied to the problem of magnetic coupling where the low spin ground state possesses strong multireference character and requires the inclusion of doubly excited configurations for its proper description. Hence, the REKS approach seems to be the most appropriate spin restricted KS method which can be applied to the study of magnetic coupling in this kind of systems.

In the present work, we extend our previous studies about the REKS description of magnetic systems^{34,35} to a new series of large Cu binuclear complexes, which cover a broad range of physical situations, from strongly antiferromagnetic coupling to ferromagnetic interactions. In doing so one must be aware of the strong dependence of the magnitude of the calculated magnetic interaction on the exchange–correlation functional employed in the calculations. In particular, we recall the dramatic effect of the amount of the Fock exchange in the HF/DFT hybrid functionals.^{36–38} Indeed, by tuning this parameter one can obtain almost any a priori desired result. This criticism does not, by any means, pretend to invalidate the high quality research in this field and the meaningful

magneto-structural correlations derived from these calculations. We just want to stress the weakness of the present approaches and, hence, stimulate further research work in the development of new and improved density functionals. In any case, this discussion makes it clear that the predictive capability of DFT approaches with regard to the quantitative prediction of magnetic coupling in this type of systems is limited. Therefore, the aim of the present work is not to reproduce the experimental values but to examine the performance of the REKS approach and, for a series of density functionals, compare the results predicted by this more physically grounded formalism with those obtained by means of a more pragmatic broken symmetry approach.

2. Density Functional Description of Open Shell Electronic States in Magnetic Systems

Many magnetic systems exhibit localized magnetic moments at a given atom—or group of atoms—with unpaired electrons. Hence, an effective magnetic moment, \mathbf{S}_i , which depends on the actual electronic configuration of the magnetic center, can be associated with this center to rationalize the magnetic properties of these systems. Various interactions between these localized magnetic moments are possible which give rise to an interesting magnetic behavior and define the observed magnetic properties. These interactions are usually described with the help of the phenomenological Heisenberg–Dirac–van Vleck (HDVV) Hamiltonian which provides the simplest physical model for the description of magnetic coupling (or exchange coupling) in a broad class of chemical compounds including organic biradicals, inorganic complexes, and ionic solids. This Hamiltonian describes the isotropic interaction between localized magnetic moments \mathbf{S}_i and \mathbf{S}_j as

$$\hat{H}^{\text{HDVV}} = - \sum_{i>j} J_{ij} \hat{\mathbf{S}}_i \cdot \hat{\mathbf{S}}_j \quad (1)$$

where the J_{ij} constant controls the magnitude and type of interaction between \mathbf{S}_i and \mathbf{S}_j localized spin moments. In eq 1, a positive value of J_{ij} corresponds to a ferromagnetic interaction. The HDVV Hamiltonian can be rigorously derived from the effective Hamiltonian theory. This is an effective Hamiltonian which describes the low-energy spectrum arising from the interactions between \mathbf{S}_i and \mathbf{S}_j . These interactions are of quantum mechanical nature, and, in general, they are much stronger than the classical interactions between magnetic dipoles.

For the simplest problem of two electrons in two atomic orbitals, such as in a Cu dinuclear complex, it follows that the lowest energy electronic states are a singlet, S , and a triplet, T . These states are the eigenstates of the HDVV Hamiltonian, and the magnetic coupling constant can be obtained as in eq 2.

$$J = E(S) - E(T) \quad (2)$$

Assuming that the HDVV Hamiltonian effectively describes the low-energy spectrum of these systems, a one-to-one correspondence between the eigenstates of the HDVV Hamiltonian and those of the exact nonrelativistic Hamiltonian must exist. In particular, notice that the lowest

eigenstates of the exact Hamiltonian are also a singlet S and a triplet T . The one-to-one correspondence between the eigenfunctions of the HDVV and those of the exact Hamiltonian follows from the fact that both Hamiltonians commute with the total spin operators.

In practice, however, the eigenfunctions of the exact Hamiltonian are not known, and a suitable approximation is generally used. Within the spin-restricted description of the relevant electronic states, the one-to-one correspondence mentioned above is imposed by construction. In the simplest case of two electrons in two atomic orbitals (i_A and j_B), one can choose a delocalized description and construct two molecular orbitals of g (even) and u (odd) symmetry. The lowest singlet state is multireference in nature and involves a variable mixing of the two resulting closed shell determinants which, for a given set of g and u molecular orbitals, is optimal for the variational two by two configuration interaction *Ansatz*. Alternatively, one can choose to continue using the localized description, and, in this case, several single Slater determinants can be constructed. Thus, one has the ferromagnetic solution, $|\text{FM}\rangle$,

$$|\text{FM}\rangle = | \dots i_A j_B \rangle \quad (3)$$

which corresponds to the $M_S = 1$ (or $M_S = -1$) component of the triplet state T , and two broken symmetry solutions

$$|\text{BS1}\rangle = | \dots \bar{i}_A j_B \rangle \quad (4)$$

and

$$|\text{BS2}\rangle = | \dots \bar{i}_A \bar{j}_B \rangle \quad (5)$$

which can be combined to yield the $M_S = 0$ component of the triplet T or the singlet S thus preserving the space and spin symmetry. In practice, one can choose to work with only one of the two broken symmetry solutions and variationally optimize the orbitals with respect to it. The resulting wave function does not have spin and space symmetry and does not represent any electronic state of the exact Hamiltonian. Nevertheless, one can relate the expectation energy of the broken symmetry solution to that of the singlet state by an appropriate mapping. This is the basis of the broken symmetry approach proposed by Noodleman^{21,22} and Yamaguchi et al.²³ Hence, it is easy to show that

$$J = E(S) - E(T) = \frac{2(E(\text{BS}) - E(\text{FM}))}{1 + \langle i'_A | j'_B \rangle^2} \quad (6)$$

where “ i'_A ” and “ j'_B ” stand for the self-consistent localized orbitals on magnetic centers A and B, and $\langle i'_A | j'_B \rangle$ corresponds to the overlap integral between these magnetic orbitals. It has been shown that this overlap integral is usually less than 0.1,²⁵ and, therefore, the denominator in eq 6 does not significantly deviate from unity.

In the standard Kohn–Sham implementation of density functional theory, the reference state is a single determinant state, and, hence, the only way to get an estimate of the magnetic coupling constant is the computation of the $|\text{FM}\rangle$ and $|\text{BS}\rangle$ single determinant state through eq 6 and neglecting the overlap term. On the other hand, in the spin-

restricted ensemble-referenced Kohn–Sham (REKS) method, employed in the present study, a completely different strategy is used which is based on the ensemble approach to density functional theory. Within the standard Kohn–Sham procedure to DFT, it is tacitly assumed that *any* physical density can be represented by a single Slater determinant constructed from the N lowest eigenfunctions of a certain Hamiltonian which describes a system of noninteracting particles moving in potential V_s (pure state V -representability). However, already in the early works on Kohn–Sham DFT, it was realized that such a representation can not be the most general one, and it was suggested to employ the ensemble density (weighted sum of the densities of several states) to represent the physical density (density of a system of interacting particles).^{39,40} The rigorous proof that any physical density can be represented by an ensemble of densities, as in eq 7, has been provided by Lieb⁴¹ and Englisch and Englisch.⁴²

$$\rho(\mathbf{r}) = \sum_i w_i \rho_i(\mathbf{r}) \quad (7)$$

Within the Kohn–Sham approach, the ensemble representation translates to the fractional occupation numbers of the Kohn–Sham orbitals, that is

$$\rho(\mathbf{r}) = \sum_k n_k |\phi_k(\mathbf{r})|^2 \quad (8)$$

where the occupation numbers n_k vary between 0 and 2. In spite of its formal exactness, the ensemble representation was considered to be of a purely academic interest until its practical validity was demonstrated in the first principles numeric Kohn–Sham simulations of the exact densities for a number of strongly correlated systems carried out by Baerends et al.⁴³ and Ullrich et al.⁴⁴ Together with the theoretical arguments, these results show unambiguously that the ensemble representation is of immediate practical relevance and that it is the only *rigorous* representation for the density of a strongly correlated system of electrons.

The practical implementation of the ensemble approach to DFT was hindered by the absence of approximate density functionals conforming to the ensemble densities. The REKS method²⁹ was designed to fill this gap in computational DFT. The method combines the ensemble representation for the density with certain ideas from wave function theory (WFT) for constructing the energy functional for ensemble densities. Therefore, the method shares some features of the multireference approaches in WFT, and the nomenclature developed for the complete active space (CAS)SCF methods is applicable to REKS as well. Thus, in the REKS(2,2) (two active electrons in two active orbitals) method, the density is represented as an average over densities of two configurations: one with doubly occupied KS orbital $\phi_r(\mathbf{r})$ and another with doubly occupied orbital $\phi_s(\mathbf{r})$, where $\phi_r(\mathbf{r})$ and $\phi_s(\mathbf{r})$ can be the HOMO and the LUMO in the conventional single determinant KS calculation. The inactive core KS orbitals are occupied with 2 electrons each, and the ground state density is given as in eq 9.

$$\rho^{\text{REKS}}(\mathbf{r}) = \left(\sum_k^{\text{core}} 2 |\phi_k(\mathbf{r})|^2 \right) + n_r |\phi_r(\mathbf{r})|^2 + n_s |\phi_s(\mathbf{r})|^2 \quad (9)$$

The total ground state energy for a state with two fractionally occupied KS orbitals is represented as a weighted sum of the KS energies of the individual configurations $E^{\text{KS}}(\dots\phi_r^2\dots)$ and $E^{\text{KS}}(\dots\phi_s^2\dots)$ and a coupling term which is expressed as a linear combination of the KS energies of the singly excited configurations generated within the same (2,2) active space, see eq 10.

$$E^{\text{REKS}(2,2)} = \frac{n_r}{2} E^{\text{KS}}(\dots\phi_r^2\dots) + \frac{n_s}{2} E^{\text{KS}}(\dots\phi_s^2\dots) + f(n_r, n_s) \left[E^{\text{KS}}(\dots\phi_r\phi_s\dots) - \frac{1}{2} E^{\text{KS}}(\dots\phi_r\bar{\phi}_s\dots) - \frac{1}{2} E^{\text{KS}}(\dots\bar{\phi}_r\phi_s\dots) \right] \quad (10)$$

Thus, the energy of the ensemble state is represented as an ensemble of the energies of individual states (microstates) where each microstate is assumed to be pure state V -representable. Each of the microstates can be viewed as a weighted sum of a number of the real physical states, in the same way that a broken spin-symmetry state can be viewed as a sum of the true singlet and triplet states. Therefore, eq 10 is based on model considerations similar to those used in the works of Ziegler et al.²⁴ and von Barth.¹³ Note, however, that the total energy in eq 10 is minimized with respect to the KS orbitals and their fractional occupation numbers. As it has been demonstrated by Staroverov et al.,⁴⁵ within the finite basis set, the optimization of the total energy with respect to the orbitals is equivalent to the optimization with respect to the KS potential. Therefore, this orbital optimization procedure is a valid implementation of the KS scheme for an orbital-dependent density functional.

The factor $f(n_r, n_s)$ in front of the last term in eq 10 can be derived from the following considerations. In the case of (near) degenerate active orbitals $\phi_r(\mathbf{r})$ and $\phi_s(\mathbf{r})$, where the occupation numbers are $n_r \approx n_s \approx 1$, the factor $f(n_r, n_s)$ is given by eq 11, which is the same as in the CASSCF(2,2) energy functional.

$$f(n_r, n_s) = (n_r n_s)^{1/2} \quad (11)$$

In such a case, nearly all the correlation energy taken into account via the functional form (10) corresponds to the nondynamic correlation energy. In the situation where there is a substantial energy gap between $\phi_r(\mathbf{r})$ and $\phi_s(\mathbf{r})$ and one of the occupation numbers is nearly zero and another is nearly two (“normal” single reference case), the factor $f(n_r, n_s)$ should satisfy eq 12 which can be obtained from analysis of the energy functional in DFT with the fractional occupation numbers (DFT-FON) method.⁴⁶

$$f(n_r, n_s) = (n_r n_s) \quad (12)$$

In this regime, the energy functional (10) with the factor (12), no extra correlation energy is taken into account *explicitly*, via the functional form (10), and the double counting of the correlation energy is suppressed.

In the first implementation of the REKS method, a geometric average of the two asymptotes (11) and (12) was taken for the factor $f(n_r, n_s)$ in eq 10; see eq 13

$$f^{\text{REKS}}(n_r, n_s) = (n_r n_s)^{3/4} \quad (13)$$

This choice provides a reasonable account of the nondynamic electron correlation combined with the sufficient suppression of the double counting of the dynamic correlation, as was confirmed in comparisons of the REKS results for “normal” single-reference states with the results from the conventional single-reference KS method.

Recently, another algebraic expression for the factor $f(n_r, n_s)$, which interpolates between the asymptotic regimes (11) and (12), was suggested. This expression, eq 14,

$$f^{\text{REKS(new)}}(n_r, n_s) = [n_r n_s]^{(1-1/2n_r n_s + \delta/1 + \delta)}, \quad \delta = 0.4 \quad (14)$$

satisfies the condition (11) in the vicinity of the orbitally (near) degenerate state and provides a better suppression of the double counting of the dynamic electron correlation in the “normal” state; a detailed description of this new formula and the choice of the parameters in it will be given elsewhere. This is evidenced by the results of the calculations for the planar and the 90°-twisted ethylene carried out with the use of the old formula (13), with the new formula (14) and (for the planar ethylene) with the standard closed-shell single-reference KS approach (RKS). Calculations employing the 6-311(d,p) basis set together with the B3LYP density functional and the geometries optimized with the RKS method for the planar ethylene and with the old REKS method for the twisted ethylene give total energies of $E^{\text{RKS}} = -78.6139345$ au, $E^{\text{REKS}} = -78.6145855$ au, and $E^{\text{REKS(new)}} = -78.6139726$ au for the planar geometry. Thus the new formula (14) provides considerably better elimination of the double counting of the dynamic electron correlation in the “normal” state. The old REKS formula (eq 13) “overshoots” the total energy by 0.408 kcal/mol, whereas with the new formula as in eq 14 the REKS energy differs from the RKS one by 0.024 kcal/mol only. This implies that the effect of the double counting of the dynamic correlation should not be observed in practical calculations. For the orbitally degenerate state of 90°-twisted ethylene, both formulations of REKS, the old and the new one, yield total energies of -78.5064634 au and -78.5064635 au, respectively, which are practically identical. The advantage of the new formula (14) will become obvious later on when discussing the singlet–triplet separations in binuclear metal complexes.

The fractional occupation numbers in REKS are analogous to the natural orbital occupation numbers in conventional wave function multireference methods. Thus, one can analyze the REKS density and energy in similar terms as in conventional WFT. Because of the variational nature of the REKS energy functional, the one-electron properties, including the energy gradient, can be straightforwardly obtained from its density matrix. The feasibility of the REKS method makes it an attractive alternative to conventional multireference methods in WFT, in particular, when large molecular systems, such as those studied in the present work, are considered. Moreover, because the REKS method belongs

to the class of spin-restricted methods, it does not experience difficulties with the spurious spin-contamination which plagues spin-unrestricted (DFT or not) calculations. This however implies that, in the calculation of singlet–triplet energy separations, the triplet state energy should be calculated with the use of the spin-restricted method as well. Thus, the spin-restricted open-shell KS (ROKS) method is employed in the present work for the calculation of these differences in connection with the REKS method.

3. Computational Details

For each one of the different systems described in the next section, we have computed the magnetic coupling constant with the use of both, the broken symmetry UKS and the REKS/ROKS, approaches discussed above. The extended basis sets are employed which consist of the 6-3111+G basis set on Cu and the 6-31G* basis set on the remaining atoms. Several exchange-correlation functionals are examined which start from quite opposite extremes. At one extreme, we have the Hartree–Fock method which uses the exact nonlocal exchange and neglects the electron correlation effects (except for a part of nondynamical correlation introduced through the spin polarization). At the other extreme, there lies the Local Density Approximation (LDA) which employs local exchange and correlation functionals. However, because this approach fails to describe most magnetic systems, it is not considered here. Hence, the pure DFT method chosen in this work is the gradient-corrected BLYP density functional obtained by using the Becke (B) exchange⁴⁷ and the Lee–Yang–Parr (LYP) correlation functional⁴⁸ which is based on the original work of Colle and Salvetti on the correlation factor.^{49,50} Next, we explore a couple of hybrid HF/DFT functionals which incorporate a certain amount of the Fock exchange. These are the BH&HLYP⁵¹ and B3LYP functional⁵² which both use the Becke gradient corrected exchange and the LYP correlation functionals and mix in 50% and 21% of the Fock exchange, respectively.

The broken symmetry UKS and ROKS computations have been carried out using the Gaussian03⁵³ package, and the REKS calculations have been carried out with the CO-LOGNE2005 code.⁵⁴

4. Selected Reference Systems: Structure and Exchange Constants

In order to investigate the effect of spin symmetry requirements on the predicted magnetic coupling constants of real systems as well as to further analyze the performance of the different exchange-correlation functionals, a set of binuclear Cu complexes covering a broad range of J values, ranging from strong ferro- to strong antiferromagnetic couplings, has been chosen. This set of molecules has been selected according to the following criteria: (i) In order to minimize the zero field splitting effects which can be problematic in a nonrelativistic approach, as the one used here, we have exclusively considered binuclear copper(II) complexes; (ii) The simplicity of the molecular structure with a moderate number of atoms (in some systems, the large innocent groups have been substituted by simpler groups); (iii) A wide diversity of bridging ligands; (iv) The crystalline structure

Table 1. Cambridge Structural Database Notation, Chemical Formula, Magnetic Coupling Constant, and References for Experimental Structure and/or Magnetic Data of the Six Compounds Studied in the Present Work

CCDC refcode	chemical formula	J (cm ⁻¹)	ref
YAFZOU	[{Cu(phen)} ₂ (μ-AcO)(μ-OH)](NO ₃) ₂ ·H ₂ O	111	56
XAMBUI	[{Cu(dpt)} ₂ (μ-O ₂ C-(η ⁵ -C ₅ H ₄)Fe(η ⁵ -C ₅ H ₅)) ₂](ClO ₄) ₂	2	57
PATFIA	[{Cu(dmen)} ₂ (μ-OMe){μ-O ₂ C-(η ⁵ -C ₅ H ₄)Fe(η ⁵ -C ₅ H ₅)}](ClO ₄) ₂	-11	58
CAVXUS	[{Cu(petdien)} ₂ (μ-C ₂ O ₄)](PF ₆) ₂	-19	59, 60
CUAQAC02	[{Cu(H ₂ O)} ₂ (μ-AcO) ₄]	-286	61
BISDOW	[{Cu(bpy)(H ₂ O)(NO ₃)} ₂ (μ-C ₂ O ₄)]	-382	62

is well characterized experimentally, even with the positions of H atoms well determined. The resulting set of structures, together with the corresponding standard abbreviations as in the Cambridge Structural Database,⁵⁵ which will be used henceforth, is listed in Table 1. The relevant experimental data has been taken from refs 56–62, and the compounds are sorted in the order of decreasing J values.

In order to avoid mixing structural and electronic effects, the crystallographic structures for which the magnetic parameters have been measured have been used without further optimization. In BISDOW we excluded the nitrate ligands since it has been found that these do not significantly affect the calculated coupling constant values. Following the previous work, all ferrocenecarboxylate ligands in XAMBUI and PATFIA complexes have been replaced by formiate groups.^{57,58}

In the following we provide a short description of the more salient features of each of these compounds.

YAFZOU shows a triplet ground state, and its structure contains a dimeric Cu(II) cation where the metal ions are bridged by a hydroxo and a carboxylate ligands. Two terminal 1,10-phenantrolin ligands configure an essentially square planar coordination geometry for each copper atom. The resulting core geometry leads to a strong ferromagnetic coupling which agrees with the well studied magnetostructural correlation for this kind of heterobridged complexes.^{58,63–65}

XAMBUI contains a centrosymmetric dicopper(II) cation which consists of two [Cu(dpt)] fragments (dpt = dimethylpropylenetriamine) bridged by two ferrocenecarboxylate ligands in *syn,anti* binding, which form a core consisting of a six-membered ring in a chair conformation. Copper atoms are in a square-pyramidal coordination, with parallel basal planes, where each carboxylate group is bonded to a basal position of one copper and one apical position of the other. This disposition makes the magnetic orbitals parallel, which obscures the superexchange pathways, thus resulting in a very weak ferromagnetic coupling.

PATFIA consists of two Cu(II) ions bridged by one methoxo and one ferrocenecarboxylate group. The coordination sphere of each copper ion is completed by one bidentate chelating ligand (dmen = N,N-dimethylethylenediamine), resulting in a slightly distorted square planar environment. In this compound the methyl group of the bridge is close to the Cu–O(CH₃)–Cu core plane, leading to an antiferromagnetic coupling.

CAVXUS contains a binuclear cation where the copper atoms are bridged through an oxalato bis-chelating ligand.

The coordination environment is completed by a tridentate N,N,N',N'',N''-pentaethyldiethylenetriamine (petdien) ligand resulting in a pronounced trigonal bipyramidal (pentacoordinated) character. The deviation from the square planar to the trigonal bipyramidal geometry results in a reduction of the antiferromagnetic coupling, as shown by Kahn and co-workers.⁶⁰

The CUAQAC02 complex is the well-known copper(II) acetate which consists of two copper ions bridged by four acetate groups in a paddle-wheel core. The coordination environment of the metal ions is square-planar pyramid, with a water molecule in the apical position. This system has been studied by many groups either experimentally or theoretically and is one of the best known models for fundamental magnetic studies.⁶⁶

BISDOW consists of a centrosymmetric binuclear neutral molecule where the two copper ions are bridged by an oxalato bis-chelating anion. Coplanar to the bridge there are two terminal 2,2'-bipyridine chelating ligands, providing a basic square planar environment for the copper atoms. In addition, a nitrate anion and a water molecule coordinate each metal center at longer distances, thus completing a 4 + 1+1 coordination mode. The influence of these groups on the magnetic coupling is negligible, especially for the weakest nitrate ligands, at 2.75 Å bond distance.

5. Results and Discussion

The results for the six compounds described above, and summarized in Table 2, confirm previous findings^{25,34–38} reviewed at length recently²⁶ but also add some new, interesting and somehow unexpected features. First, let us concentrate on the predictions of the broken symmetry approach for the different methods described in section 3. The most evident trend is that HF largely underestimates the magnitude of the magnetic coupling constant, whereas a pure DFT method such as the gradient corrected BLYP largely overestimates it. The prediction of the two hybrid methods represents a general improvement although some necessary remarks will be raised in the forthcoming discussion. Except for the very weakly antiferromagnetic PATFIA compound, all methods correctly predict the ferro- or antiferromagnetic character. This is quite an unexpected conclusion, especially for the HF method since, at first sight, one would expect the nature and the extent of electronic correlation effects to be different for the different compounds. However, previous analyses of the electronic correlation effects based on accurate configuration interaction wave functions reveal a common origin of the most important terms,^{67,68} confirming earlier analysis based on perturbation

Table 2. *J* Values (in cm⁻¹) Using Spin Unrestricted and Restricted Formalisms for the Different Binuclear Copper Complexes Studied in This Work

compound [<i>J</i> _{exptl}]	method	broken symmetry <i>J</i> = 2(<i>E</i> (BS) – <i>E</i> (T))	REKS/ROKS <i>J</i> = Δ <i>E</i> _{ST}	
			REKS	REKS (new)
YAFZOU [+111 cm ⁻¹]	HF	+37	+18	+18
	BH&HLYP	+91	+89	+87
	B3LYP	+194	+269	+264
	BLYP	+261	+462	+447
XAMBUI [+2.5 cm ⁻¹]	HF	+0.1	+0.1	+0.04
	BH&HLYP	+0.7	+1.0	+0.75
	B3LYP	+3.9	+7.0	+6.2
PATFIA [–11 cm ⁻¹]	HF	+16	+11	–0.2
	BH&HLYP	+9.0	+78	+32
	B3LYP	–61	+247	+139
CAVXUS [–19 cm ⁻¹]	BLYP	–493	+105	–55
	HF	–1.0	–0.5	–1.1
	BH&HLYP	–5.3	0.3	–3.4
CUAQAC02 [–286 cm ⁻¹]	B3LYP	–21.2	19.6	+3.3
	BLYP	–83.3	+83.1	+27.4
	HF	–39	–12	–20
BISDOW [–382 cm ⁻¹]	BH&HLYP	–132	–47	–91
	B3LYP	–429	–158	–285
	BLYP	–1121	–595	–774
BISDOW [–382 cm ⁻¹]	HF	–49	–17	–30
	BH&HLYP	–160	–68	–135
	B3LYP	–634	–224	–429
BISDOW [–382 cm ⁻¹]	BLYP	–2299	–1164	–1361

theory.⁶⁶ Therefore, one can conclude that for strongly ferro- or antiferromagnetic compounds, even the HF method will predict a qualitatively correct magnetic description although it is not clear that this simple approach will be able to make good predictions about the magneto-structural correlations. For weakly antiferromagnetic compounds such as PATFIA it is likely that HF will make a wrong prediction. Notice, however, that the situation for weakly ferromagnetic compounds is different since HF predicts the right ferromagnetic character of XAMBUI. This is because direct exchange, explicitly accounted for in the HF method, makes a very important contribution to ferromagnetic interactions.

A more quantitative picture can be found by inspecting the correlation between the experimental and calculated values (Figure 1) which, for each exchange-correlation potential, is given below

$$J_{\text{calc}}^{\text{HF}} = 0.165 J_{\text{exp}} + 10.108 \quad \text{with } R^2 = 0.94 \quad (15)$$

$$J_{\text{calc}}^{\text{BH\&H}} = 0.489 J_{\text{exp}} + 14.896 \quad \text{with } R^2 = 0.98 \quad (16)$$

$$J_{\text{calc}}^{\text{B3LYP}} = 1.608 J_{\text{exp}} - 1.193 \quad \text{with } R^2 = 0.99 \quad (17)$$

$$J_{\text{calc}}^{\text{BLYP}} = 4.757 J_{\text{exp}} - 155.08 \quad \text{with } R^2 = 0.91 \quad (18)$$

Equations 16–18 show that all methods including a part of Fock exchange are able to reproduce the experimental trend in a semiquantitative way and, also, that a pure gradient

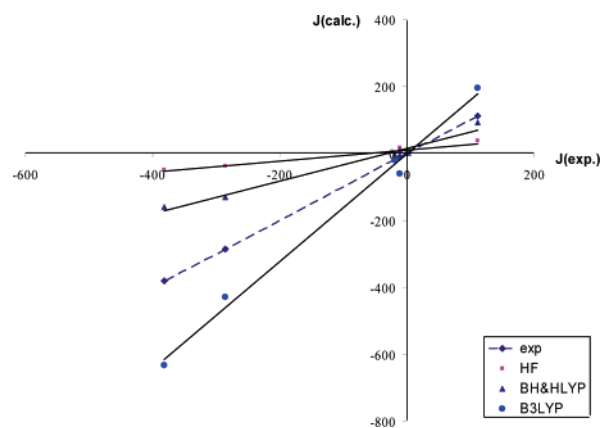


Figure 1. Experimental versus HF, BH&HLYP, and B3LYP calculated broken symmetry values of the magnetic coupling constant of the six compounds studied in the present work. The experimental versus experimental plot is also drawn for reference. Values for the corresponding correlation factors are given in eqs 15–17.

corrected method such as BLYP leads to a global description which is even worse than the one obtained with the HF method. Moreover, the independent term in eqs 16–18 provides a measure of the limitations of each method. Thus, within the broken symmetry approach, HF and BH&HLYP should not be applied to compounds where the magnetic coupling is antiferromagnetic and of the order of 10–15 cm⁻¹ because they will predict a ferromagnetic behavior. The fact that HF and BH&HLYP underestimate the magnitude of the magnetic coupling constant is also clear from the values of the slope of the straight lines in eqs 15 and 16 which is significantly smaller than 1. Notice also that the correlation improves with decreasing the amount of Fock exchange, the 21% included in the B3LYP functional being close to an optimum value, at least for the list of compounds studied in the present work. This can be deduced from the small value of intersect with the *J*_{calc} axis. However, the slope of the linear regression suggests that the broken symmetry B3LYP predicts *J* values which are clearly too large. Assuming, with no theoretical justification,^{26,34,35} that the energy of the broken symmetry solution is an estimate of the energy of the open shell singlet state will lead to a slope of ~0.8, closer to the desired value but still with an average 20% error. Therefore, the good correlation found for hydroxo- and alkoxy-bridged Cu(II) binuclear complexes⁶⁹ and some other binuclear complexes does not seem to hold when the magnetic coupling spans a wide range of values and when the nature of the bridging ligands is also of increased complexity.⁷⁰ Here, it is worth pointing out recent studies on magnetic solids evidencing that the proper choice of Fock exchange is less universal than desired and therefore is dependent on the type of system. In fact, previous calculations have shown that at least for NiO⁷¹ and cuprates^{68,72} the best percentage of Fock exchange is ~35%.

The results obtained from the broken symmetry approach evidence once again the strong dependence of the magnetic coupling constant on the exchange-correlation functional.^{34–38} One can, of course, still argue that the good correlation for the B3LYP results is indicative of the suitability of this

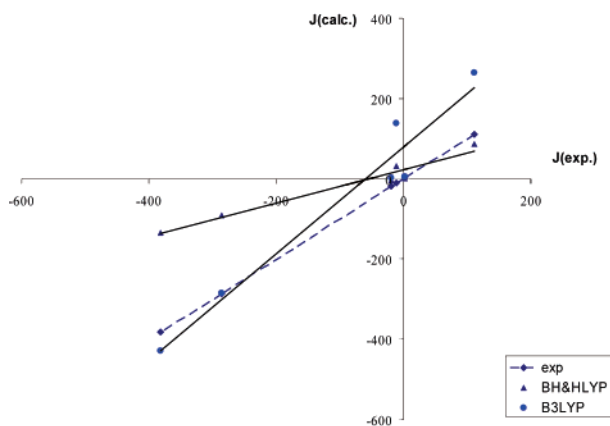


Figure 2. Experimental versus BH&HLYP and B3LYP calculated ROKS/REKS(new) (cf. eq 14) values of the magnetic coupling constant of the six compounds studied in the present work. The experimental versus experimental plot is also drawn for reference. Values for the corresponding correlation factors are given in eqs 19 and 20.

functional to describe magnetic interactions in these systems. This is even more the case if one decides to neglect spin symmetry considerations and take the broken symmetry energy as that of the singlet state and compute J using eq 2 instead of eq 6. This line of reasoning is only based on numerical arguments^{69,70} and lacks fundamental theoretical support.^{34,35} A better assessment of the reliability of the existing exchange-correlation functionals in the description of the magnetic coupling can be made by using a method which does not rely on the broken symmetry approach and, therefore, does allow one to avoid referring to the expectation value of the square of the total spin operator which is not really defined within the framework of DFT since it is a two-electron operator. This is because in DFT, the density, and not the N -electron wave function, is the main mathematical object, and one can claim that the Kohn–Sham determinant is just a construct to get the density. However, in such a case one can only use DFT to get the energy of the ground state without any information about its spin state. This point of view will, of course, restrict the use of DFT to ground state properties only, and prediction of magnetic coupling constants will not be possible. The spin-Restricted Ensemble-referenced Kohn–Sham (REKS) method described in section 2 offers a theoretically well-grounded alternative since it ensures that the final density for the antiferromagnetic state arises from a singlet state. Using the ROKS procedure for the triplet state permits one to compute J as in eq 2, that is using exactly the same mapping that one would use when aiming to compute J from a wave function approach.

Now, let us focus on the results for the magnetic coupling of the compounds in Table 1 as predicted from the ROKS/REKS formalism and using different correlation functionals. As in the case of the broken symmetry results, a more quantitative picture can be found by inspecting the correlation between the experimental and calculated values (Figure 2) which, for the two hybrid exchange correlation potentials, is given by eqs 19 and 20 below.

$$J_{\text{calc}}^{\text{BH\&H}} = 0.415 J_{\text{exp}} + 22.204 \quad \text{with } R^2 = 0.96 \quad (19)$$

$$J_{\text{calc}}^{\text{B3LYP}} = 1.328 J_{\text{exp}} + 79.087 \quad \text{with } R^2 = 0.95 \quad (20)$$

From results in Table 2 and the correlation in eqs 19 and 20 it is clear that the use of a formalism which is rigorously spin restricted does not largely improve the results. This is contrary to what is expected and to what is commonly found when using wave function formalism. The direct conclusion is therefore that the exchange-correlation functionals investigated are not capable of correctly describing open shell systems. This is confirmed by the analysis of the results obtained using the HF exchange potential (and no correlation potential) in the ROKS/REKS formulas. The predicted ROHF/REHF magnetic coupling constants are smaller in absolute value than those predicted using the broken symmetry approach. This is because the broken symmetry approach introduces an uncontrolled amount of dynamic electron correlation through spin polarization,⁷³ and, hence, the UHF broken symmetry results are usually very similar to those obtained through a Complete Active Space Configuration Interaction wave function. However, in the ROKS/REKS formalism the amount of dynamical correlation is minimized to avoid a double counting since this has to be introduced by the correlation functional. Using the REKS formula as in eq 13 or 14 leads to a similar qualitative description (Table 2). A somewhat better correlation between the experimental and the calculated results is obtained using the new REKS formula as in eq 14. Since the BLYP results are always grossly overestimated (by a factor of ~ 3) we will focus in the results corresponding to the BH&HLYP and B3LYP hybrid functionals which are summarized in Figure 2. This plot is qualitatively similar to Figure 1, and the slope of the straight lines (0.415 and 1.328) is very similar to the values in eqs 16 and 17 for the broken symmetry calculations. However, the linear regression lines appear to be somewhat displaced to the left with a concomitant increase in the intercept to the J_{calc} axis. This is a clear indication that when used in rigorous spin restricted formalism the BH&HLYP and B3LYP exchange-correlation functionals tend to grossly overestimate the ferromagnetic component of the magnetic coupling.

A clear conclusion of the above discussion is that, for a given exchange-correlation functional, the scale factor between experimental and either broken symmetry or ROKS/REKS values is almost the same, provided the latter are displaced to the origin of coordinates. A corollary of the conclusion above is that eq 6 must be used when employing the broken symmetry approach, otherwise the scale factor between experimental and calculated values corresponding to a given functional will be method dependent. To summarize, broken symmetry and ROKS/REKS lead to similar descriptions although with the present functionals the latter exhibits a trend to overestimate the ferromagnetic interactions. However, the fact that the deviation is rather systematic opens the possibility for the development of improved functionals which will allow for a rigorous treatment of open shell systems in density functional theory.

6. Conclusions

In this work we have investigated the performance of two different formalisms to describe open shell systems in density functional theory by analyzing the calculated magnitude of the magnetic coupling constant in a series of Cu(II) binuclear complexes. The two open shell formalisms are the broken symmetry approach, where the spin symmetry requirements are neglected, and the restricted ensemble Kohn–Sham method, where the spin symmetry is fully taken into account. The series of compounds includes both ferro- and antiferromagnetic compounds and cover a broad range of values.

The present study confirms the strong dependence of the calculated magnetic coupling constant with respect to the exchange-correlation functional. This is found to be a general conclusion which does not depend on whether spin symmetry is imposed or not. All methods, including HF and gradient corrected functionals, are capable of properly describing the main trends, especially for compounds with large values of the magnetic coupling constants. However, the HF method largely underestimates this property, whereas pure density functional largely overestimates it. The use of hybrid functionals improves both the correlation between calculated and experimental values and the quantitative agreement with the experiment. However, even the hybrid B3LYP functional is shown to be unable to accurately predict magnetic coupling constant in different families of compounds.

The use of a method which guarantees the correct spin state does not improve the correlation with respect to experiment and indeed shows some worsening due to an overestimation of the ferromagnetic interactions. However, for a given exchange-correlation functional, the scale factor between experimental and either broken symmetry or ROKS/REKS values is nearly the same although only if a displacement of the coordinate origin is carried out for the latter. This fact provides further support to the argument about the use of proper mapping to obtain meaningful values of the magnetic coupling constant even if the final results may not be in numerical agreement with experiment due to the above-mentioned dependence of the calculated value on the exchange-correlation functional.

To conclude, the spin unrestricted broken symmetry and spin restricted ROKS/REKS approaches lead to similar descriptions of the magnetic coupling constants. However, in the latter case and with the present exchange-correlation functionals, a rather systematic deviation is found. Therefore, it would be possible to develop improved functionals which will allow for a rigorous treatment of open shell systems in density functional theory. In this sense, a particularly promising approach could be the use of the recently proposed local hybrid functionals⁷⁴ which for the prediction of thermodynamic data have very recently proven to be competitive with other hybrid functional such as B3LYP.⁷⁵ Clearly, the performance of such new functionals in the description of magnetic coupling needs to be explored.

Acknowledgment. Financial support has been provided by the Spanish Ministry of Education and Science—projects CTQ2005-08459-CO2-01, UNBA05-33-001, and the Ramón y Cajal program (I. de P.R.M.)—and, in part, by Generalitat

de Catalunya—projects 2005SGR-00697, 2005 PEIR 0051/69, and Distinció per a la Promoció de la Recerca Universitària de la Generalitat de Catalunya granted to F.I. Part of the computer time was provided by the Centre de Supercomputació de Catalunya (CESCA) through generous grants from Universitat de Barcelona, Fundació Catalana per a la Recerca and BSC.

References

- (1) Kohn, W.; Sham, L. *Phys. Rev.* **1965**, *140*, A1133.
- (2) Hohenberg, P.; Kohn, W. *Phys. Rev.* **1964**, *136*, B864.
- (3) For reviews on DFT methods, see for example: (a) Parr, R. G.; Yang, W.; *Density-Functional Theory of Atoms and Molecules*. In *International Series of Monographs on Chemistry*; Oxford University Press: New York, 1989; Vol. 16. (b) *Density Functional Methods in Chemistry*; Labanowski, J. K., Andzelm, J. W., Eds.; Springer: Heidelberg, 1990. (c) *Modern Density Functional Theory—A Tool For Chemistry in Theoretical and Computational Chemistry*; Seminario, J. M., Politzer, P., Eds.; Elsevier: Amsterdam, 1995; Vol. 2. (d) *Chemical Applications of Density Functional Theory*; Laird, B. B., Ross, R. B., Ziegler, T., Eds.; ACS Symposium Series 629, American Chemical Society: Washington, DC, 1996. (e) *Electronic Density Functional Theory, Recent Progress and New Directions*; Dobson, J. F., Vignale, G., Das, M. P., Eds.; Plenum Press: New York, 1998. (f) Gill, P. In *Encyclopedia of Computational Chemistry*; Schleyer, P. V. R., Allinger, N. L., Clark, T., Gasteiger, J., Kollman, P. A., Schaefer, H. F., III, Schreiner, P. R., Eds.; Wiley: Chichester, U.K., 1998; Vol. 1, p 678.
- (4) Fulde, P. *Electron Correlations in Molecules and Solids*; Springer-Verlag: Berlin and Heidelberg, 1995.
- (5) Koch, W.; Holthausen, M. C. *A Chemist's Guide to Density Functional Theory*; Wiley-VCH Verlag GmbH: Weinheim, 2000.
- (6) Payne, M. C.; Teter, M. P.; Allan, D. C.; Arias, T. A.; Joannopoulos, J. D. *Rev. Mod. Phys.* **1992**, *64*, 1045.
- (7) *Recent Developments and Applications of Modern Density Functional Theory (Theoretical and Computational Chemistry)*; Seminario, J. M., Ed.; Elsevier: Amsterdam, 1996.
- (8) *Density Functional Theory of Molecules, Clusters and Solids (Understanding Chemical Reactivity)*; Ellis, D., Ed.; Springer: Berlin, 2002.
- (9) *Principles and Applications of Density Functional Theory in Inorganic Chemistry I (Structure and Bonding)*; Kaltsoyannis, N., McGrady, J. E., Eds.; Springer: Berlin, 2004.
- (10) *Time-Dependent Density Functional Theory (Lecture Notes in Physics)*; Marques, M. A. L., Ullrich, C. A., Nogueira, F., Rubio, A., Burke, K., Gross, E. K. U., Eds.; Springer: Berlin, 2006.
- (11) Martin, R. M. *Electronic Structure: Basic Theory and Practical Methods*; Cambridge University Press: Cambridge, 2004.
- (12) Gunnarsson, O.; Lundqvist, B. I. *Phys. Rev. B* **1976**, *13*, 4274.
- (13) Von Barth, U. *Phys. Rev. A* **1979**, *20*, 1693.
- (14) Pople, J. A.; Nesbet, R. K. *J. Chem. Phys.* **1954**, *22*, 571.
- (15) Berthier, G. *J. Chim. Phys. Biol.* **1954**, *51*, 363.

- (16) Saunders, V. R.; Dovesi, R.; Roetti, C.; Orlando, R.; Zicovich-Wilson, C. M.; Harrison, N. M.; Doll, K.; Civalieri, B.; Bush, I.; D'Arco, Ph.; Llunell, M. *CRYSTAL2003 User's Manual*; University of Torino: Torino, 2003.
- (17) Löwdin, P. O. *Phys. Rev.* **1955**, *97*, 1509.
- (18) Löwdin, P. O. *Rev. Mod. Phys.* **1960**, *32*, 328.
- (19) Mayer, I.; Ladik, J.; Biczo, G. *Int. J. Quantum Chem.* **1973**, *7*, 583.
- (20) Jensen, F. *Introduction to Computational Chemistry*; John Wiley & Sons: Chichester, 2002.
- (21) Noodleman, L. *J. Chem. Phys.* **1981**, *74*, 5737.
- (22) Noodleman, L.; Davidson, E. R. *Chem. Phys.* **1986**, *109*, 131.
- (23) Yamaguchi, K.; Jensen, F.; Dorigo, A.; Houk, K. N. *Chem. Phys. Lett.* **1988**, *149*, 537.
- (24) Ziegler, T.; Rauk, A.; Baerends, E. J. *Theor. Chim. Acta* **1977**, *43*, 261.
- (25) Caballol, R.; Castell, O.; Illas, F.; Malrieu, J. P.; Moreira, I. de P. R. *J. Phys. Chem. A* **1997**, *101*, 7860.
- (26) Moreira, I. de P. R.; Illas, F. *Phys. Chem. Chem. Phys.* **2006**, *8*, 1645.
- (27) Bagus, P. S.; Bennet, B. I. *Int. J. Quantum Chem.* **1975**, *9*, 143.
- (28) Filatov, M.; Shaik, S. *Chem. Phys. Lett.* **1998**, *288*, 689.
- (29) Filatov, M.; Shaik, S. *Chem. Phys. Lett.* **1999**, *304*, 429.
- (30) Gräfenstein, J.; Cremer, D. *Chem. Phys. Lett.* **2000**, *316*, 569.
- (31) Gross, E. K. U.; Kohn, W. *Adv. Quantum Chem.* **1990**, *21*, 255.
- (32) Cassida, M. In *Recent Advances in Density Functional Methods*; Chong, E. D., Ed.; World Scientific: Singapore, 1995; Vol. I.
- (33) Stratmann, R. E.; Scuseria, G. E.; Frisch, M. J. *J. Chem. Phys.* **1998**, *109*, 8218.
- (34) Illas, F.; Moreira, I. de P. R.; Bofill, J. M.; Filatov, M. *Phys. Rev. B* **2004**, *70*, 132414.
- (35) Illas, F.; Moreira, I. de P. R.; Bofill, J. M.; Filatov, M. *Theor. Chem. Acc.* **2006**, *116*, 587.
- (36) Martin, R. L.; Illas, F. *Phys. Rev. Lett.* **1997**, *79*, 1539.
- (37) Illas, F.; Martin, R. L. *J. Chem. Phys.* **1998**, *108*, 2519.
- (38) Ciofini, I.; Illas, F.; Adamo, C. *J. Chem. Phys.* **2004**, *120*, 3811.
- (39) Gilbert, T. L. *Phys. Rev. B* **1975**, *12*, 2111.
- (40) Valone, S. M. *J. Chem. Phys.* **1980**, *73*, 1344, 4653.
- (41) Lieb, E. H. *Int. J. Quantum Chem.* **1983**, *24*, 243.
- (42) Englisch, H.; Englisch, R. *Phys. Stat. Sol. (B)* **1984**, *123*, 711; *124*, 373.
- (43) Schipper, P. R. T.; Gritsenko, O. V.; Baerends, E. J. *Theor. Chem. Acc.* **1998**, *99*, 329.
- (44) Ullrich, C. A.; Kohn, W. *Phys. Rev. Lett.* **2001**, *87*, 093001.
- (45) Staroverov, V. N.; Scuseria, G. E.; Davidson, E. R. *J. Chem. Phys.* **2006**, *124*, 141103.
- (46) Wang, S. G.; Schwarz, W. H. E. *J. Chem. Phys.* **1996**, *105*, 4641.
- (47) Becke, A. D. *J. Chem. Phys.* **1993**, *98*, 5648.
- (48) Lee, C.; Yang, W.; Parr, R. G. *Phys. Rev. B* **1988**, *37*, 785.
- (49) Colle, R.; Salvetti, O. *Theor. Chim. Acta* **1975**, *37*, 329; **1979**, *53*, 55.
- (50) Colle, R.; Salvetti, O. *J. Chem. Phys.* **1993**, *79*, 1404.
- (51) Becke, A. D. *J. Chem. Phys.* **1993**, *98*, 1372.
- (52) Becke, A. D. *Phys. Rev. A* **1988**, *38*, 3098.
- (53) *Gaussian 03 (Rev. B.04)*; Frisch, M. J.; Trucks, G. W.; Schlegel, H. B.; Scuseria, G. E.; Robb, M. A.; Cheeseman, J. R.; Montgomery, J. A., Jr.; Vreven, T.; Kudin, K. N.; Burant, J. C.; Millam, J. M.; Iyengar, S. S.; Tomasi, J.; Barone, V.; Mennucci, B.; Cossi, M.; Scalmani, G.; Rega, N.; Petersson, G. A.; Nakatsuji, H.; Hada, M.; Ehara, M.; Toyota, K.; Fukuda, R.; Hasegawa, J.; Ishida, M.; Nakajima, T.; Honda, Y.; Kitao, O.; Nakai, H.; Klene, M.; Li, X.; Knox, J. E.; Hratchian, H. P.; Cross, J. B.; Adamo, C.; Jaramillo, J.; Gomperts, R.; Stratmann, R. E.; Yazyev, O.; Austin, A. J.; Cammi, R.; Pomelli, C.; Ochterski, J. W.; Ayala, P. Y.; Morokuma, K.; Voth, G. A.; Salvador, P.; Dannenberg, J. J.; Zakrzewski, V. G.; Dapprich, S.; Daniels, A. D.; Strain, M. C.; Farkas, O.; Malick, D. K.; Rabuck, A. D.; Raghavachari, K.; Foresman, J. B.; Ortiz, J. V.; Cui, Q.; Baboul, A. G.; Clifford, S.; Cioslowski, J.; Stefanov, B. B.; Liu, G.; Liashenko, A.; Piskorz, P.; Komaromi, I.; Martin, R. L.; Fox, D. J.; Keith, T.; Al-Laham, M. A.; Peng, C. Y.; Nanayakkara, A.; Challacombe, M.; Gill, P. M. W.; Johnson, B.; Chen, W.; Wong, M. W.; Gonzalez, C.; Pople, J. A. *Gaussian Inc.*: Pittsburgh, PA, 2003.
- (54) Kraka, E.; Gräfenstein, J.; Filatov, M.; Polo, V.; Wu, A.; He, Y.; Olsson, L.; Konkoli, Z.; He, Z.; Gauss, J.; Reichel, F.; Cremer, D. *COLOGNE2005*; Göteborg University: Göteborg, 2005.
- (55) Allen, F. H. The CSD System: The Cambridge Structural Database: A quarter of a million crystal structures and rising. *Acta Crystallogr., Sect. B: Struct. Sci.* **2002**, *B58*, 380–388. Bruno, I. J.; Cole, J. C.; Edgington, P. R.; Kessler, M.; Macrae, C. F.; McCabe, P.; Pearson, J.; Taylor, R. ConQuest: New software for searching the Cambridge Structural Database and visualizing crystal structures. *Acta Crystallogr., Sect. B: Struct. Sci.* **2002**, *B58*, 389.
- (56) Tokii, T.; Hamamura, N.; Nakashima, M.; Muto, Y. *Bull. Chem. Soc. Jpn.* **1992**, *65*, 1214.
- (57) López, C.; Costa, R.; Illas, F.; Molins, E.; Espinosa, E. *Inorg. Chem.* **2000**, *39*, 4560.
- (58) López, C.; Costa, R.; Illas, F.; de Graaf, C.; Turnbull, M. M.; Landee, C. P.; Espinosa, E.; Mata, I.; Molins, E. *Dalton Trans.* **2005**, 2322.
- (59) Sletten, J. *Acta Chem. Scand. A* **1983**, *37*, 569.
- (60) Julve, M.; Verdaguer, M.; Gleizes, A.; Philoche-Levisalles, M.; Kahn, O. *Inorg. Chem.* **1984**, *23*, 3808.
- (61) de Meester, P.; Fletcher, S. R.; Skapski, A. C. *J. Chem. Soc., Dalton Trans.* **1973**, 2575.
- (62) Castillo, O.; Muga, I.; Luque, A.; Gutierrez-Zorrilla, J. M.; Sertucha, J.; Vitoria, P.; Roman, P. *Polyhedron* **1999**, *18*, 1235.
- (63) Nishida, Y.; Kida, S. *J. Chem. Soc., Dalton Trans.* **1986**, 2633.
- (64) McKee, V.; Zvagulis, M.; Reed, C. A. *Inorg. Chem.* **1985**, *24*, 2914.

- (65) Chou, Y. C.; Huang, S. F.; Koner, R.; Lee, G. H.; Wang, Y.; Mohanta, S.; Wei, H. H. *Inorg. Chem.* **2004**, *43*, 2759.
- (66) de Loth, Ph.; Cassoux, P.; Daudey, P. J.; Malrieu, J. P. *J. Am. Chem. Soc.* **1981**, *103*, 4007.
- (67) Calzado, C. J.; Cabrero, J.; Malrieu, J. P.; Caballol, R. *J. Chem. Phys.* **2002**, *116*, 2728.
- (68) Calzado, C. J.; Cabrero, J.; Malrieu, J. P.; Caballol, R. *J. Chem. Phys.* **2002**, *116*, 3985.
- (69) Ruiz, E.; Alemany, P.; Alvarez, S.; Cano, J. *J. Am. Chem. Soc.* **1997**, *119*, 1297.
- (70) Ruiz, E.; Cano, J.; Alvarez, S.; Alemany, P. *J. Comput. Chem.* **1999**, *20*, 1391.
- (71) Moreira, I. de P. R.; Illas, F.; Martin, R. L. *Phys. Rev. B* **2002**, *65*, 155102.
- (72) Moreira, I. de P. R.; Dovesi, R. *Int. J. Quantum Chem.* **2004**, *99*, 811.
- (73) Cremer, D.; Filatov, M.; Polo, V.; Kraka, E.; Shaik, S. *Int. J. Mol. Sci.* **2002**, *3*, 604.
- (74) Jaramillo, J.; Scuseria, G. E.; Ernzerhof, M. *J. Chem. Phys.* **2003**, *118*, 1068.
- (75) Bahmann, H.; Rodenberg, A.; Arbuznikov, A. V.; Kaupp, M. *J. Chem. Phys.* **2007**, *126*, 11103.

CT7000057

Structure and Electron Delocalization in Al_4^{2-} and Al_4^{4-} [†]

Rafael Islas,^{‡,§} Thomas Heine,^{*,§} and Gabriel Merino^{*,‡}

Facultad de Química, Universidad de Guanajuato, Noria Alta s/n, Guanajuato, Gto, 36050, México, and Institut für Physikalische Chemie und Elektrochemie, TU Dresden, D-01062 Dresden, Germany

Received January 10, 2007

Abstract: Structure, dynamics, and electron delocalization of Al_4^{2-} and Al_4^{4-} based clusters are investigated. Gradient-corrected Density-Functional Born–Oppenheimer Molecular Dynamics simulations indicate that Al_4^{2-} based clusters have a rigid planar Al framework, while the Al_4^{4-} based moieties show large distortions from planarity. The induced magnetic field analysis of these species indicates that both systems have diatropic σ -systems, while the π -system is diatropic for Al_4^{2-} and paratropic for Al_4^{4-} . The total magnetic response is diatropic for Al_4^{2-} , while Al_4^{4-} is “bitropic”: it has typical antiaromatic long-range cones, while the magnetic field in the Al_4^{4-} ring plane is similar to that of aromatic annulenes.

I. Introduction

Aromaticity is the simplest way to explain the stability of unsaturated cyclic hydrocarbons with $(4n + 2)$ electrons delocalized in π -orbitals perpendicular to the ring plane.¹ Even though the introduction of the aromaticity concept in chemistry is quite old, its definition is still controversial. In view of these problems of subjectivity, it is remarkable that aromaticity is useful to rationalize and understand the structure and reactivity of many organic molecules. In 1971, Wade proposed a similar concept to describe delocalized σ -bonding in closed-shell boron deltahedra, which follow a $2n+2$ skeletal electron rule.^{2,3} This concept has been extended by Hirsch to treat spherical clusters by his $2(n+1)^2$ rule,⁴ and various applications to organic and inorganic clusters have been reported.^{5,6} However, stability based on aromaticity had not been confirmed for any metallic moiety until Li et al. published their seminal paper entitled “*Observation of all-metal aromatic molecules*”.⁷

A series of compounds consisting of a square planar Al_4^{2-} , face-capped by an M^+ cation ($\text{M}=\text{Li}, \text{Na}, \text{Cu}$), were produced by laser vaporization, and their electronic spectra were obtained using negative ion photoelectron spectroscopy.

Li et al. found that theoretical vertical detachment energies of the pyramidal structures are in excellent agreement with the experimental spectra, thereby suggesting that C_{4v} structures are the global minima for the MAL_4^- species.

Ab initio calculations show that Al_4^{2-} have two electrons residing in a π -orbital, satisfying the Hückel rule for aromatic compounds. Li et al.⁷ concluded that this π -orbital holds “*the key to understanding the structure and bonding of MAL_4^- species*”. However, electron delocalization in Al_4^{2-} is not so simple. There are two delocalized σ -bonding orbitals (HOMO-1 and HOMO-2) spread across all four aluminum atoms. Therefore, the stability of Al_4^{2-} has been ascribed to its doubly aromatic behavior (π - and σ -aromaticity), which is different from hydrocarbon aromatic molecules.^{7,8} Similar systems inhibiting double aromaticity, Ga_4^{2-} and In_4^{2-} ,⁹ and in valence-isoelectronic Hg_4^{6-} ,¹⁰ have been discussed earlier. Aromaticity and electron delocalization of Al_4^{2-} have been studied in detail.^{11,12} Fowler et al. evaluated the ring current in Al_4^{2-} and MAL_4^- ($\text{M}=\text{Li}, \text{Na}, \text{Cu}$) and concluded that σ -electrons are responsible for the delocalized diatropic current induced by a perpendicular magnetic field.^{13,14} A diatropic (diamagnetic) current results in a shielded applied magnetic field, while a paratropic (paramagnetic) current has opposite direction and deshielding. Based on the analysis of aromatic ring-current shielding calculations (ARCS),¹⁵ Juselius et al. concluded that π -electrons contribute to the diatropic ring current, and thus Al_4^{2-} is both σ - and π -aromatic,¹⁶ while a recent analysis of Havenith and Fowler

[†] Dedicated to Professor Dennis R. Salahub on the occasion of his 60th birthday.

* Corresponding author e-mail: gmerino@quijote.ugto.mx (G.M.) and thomas.heine@chemie.tu-dresden.de (T.H.).

[‡] Universidad de Guanajuato.

[§] TU Dresden.

showed that the contributions of the π -system to the ring current is significantly smaller than that of the σ -system.¹⁷ This is opposite to the magnetic character of annulenes, which is essentially determined by the π -subsystem. Santos et al. have studied both the total and the σ - π separated electron localization function (ELF)^{18,19} of several molecules.²⁰ They found that Al_4^{2-} has a surprisingly high ELF_π bifurcation value of 0.99, which is even higher than the value associated with benzene. At the same time, Al_4^{2-} shows a high bifurcation value of ELF_σ (0.88), which suggests strong σ -delocalization. Further evidence of the σ -delocalization in Al_4^{2-} can be given by the analysis of the individual canonical molecular orbital contributions to NICS (MO-NICS). Within gradient-corrected DFT, the six σ -orbitals contribute more than 50% of the diatropicity of Al_4^{2-} , while the sum of the MO-NICS contributions^{21,22} of the σ -orbitals in both benzene and D_{2h} cyclobutadiene is positive (paratropic).²³ Al_4^{2-} has also been studied employing the gauge-independent magnetic induced currents (GIMIC).²⁴ With GIMIC, integrated current densities can easily be produced, which supplement information from current density maps with integrated information. In addition, it is possible to subtract disturbing effects coming from surrounding Li cations. The GIMIC method clearly shows that the Al_4^{2-} moiety is diatropic, and no paratropic current is observed.

Boldyrev and Kuznetsov obtained a rough evaluation of the resonance energies for Na_2Al_4 .²⁵ The resonance energies are high: 125 kJ mol^{-1} (B3LYP/6-311+G*) and 200 kJ mol^{-1} (CCSD(T)/6-311+G(2df)) compared to 83 kJ mol^{-1} in benzene. However, it should be noted that it is hard to accurately evaluate the resonance energy in this cluster due to two factors: the interaction between Na^+ and Al_4^{2-} and the problem of identifying a reference molecule with an Al–Al double bond. Zhan et al. concluded that in terms of the magnitude of the Dewar resonance energy,⁸ the aromaticity of the Al_4^{2-} is multiple-fold as compared to the usual “1-fold” aromaticity of benzene.⁸ Al_4^{2-} can be represented by 64 potentially resonating Kekulé-like structures; each Kekulé-like structure has three localized chemical bonds, compared to only two Kekulé structures of benzene. Consequently, the resonance energy of Al_4^{2-} ($\sim 304 \text{ kJ mol}^{-1}$ as the upper limit and $\sim 220 \text{ kJ mol}^{-1}$ as the lower limit) is at least 2.5 times that of benzene. Therefore, Al_4^{2-} could be considered as a “3-fold” aromatic system.

In 2003, Kuznetsov et al. proposed that the Al_4^{4-} fragment would be a good candidate to be the first antiaromatic all-metal system: if two additional electrons enter the π -system, Al_4^{4-} will be antiaromatic within Hückel theory.²⁶ They stated that the deviation from an equilateral square ring confirms that the compound is antiaromatic. In the same year, Chen et al. argued that the Al_4Li_3^- species is *aromatic* rather than antiaromatic, due to the predominating effects of σ -aromaticity over π -antiaromaticity.²³ Havenith et al. pointed out the mixed character of Al_4Li_3^- and Al_4Li_4 : It shows a diatropic current in the molecular plane, but a paratropic one out-of-plane.²⁷ This lively discussion has been reviewed by Boldyrev et al.¹² and Tshipis et al.²⁸

In this work, we study Al_4^{2-} and Al_4^{4-} cores in two ways: First, we perform molecular dynamics simulations to

understand the role of the Li counterions. Are they only suppliers of charge, or do they play a more important role for these clusters? Then, cognizant of the difficulties in assigning an aromatic or antiaromatic character to these clusters, we nevertheless try to improve our understanding of electron delocalization of Al_4^{2-} and Al_4^{4-} using the induced magnetic field (\mathbf{B}^{ind}).²⁹ We calculate the contributions of the π - and of the σ -electrons to the magnetic field individually.³⁰ With the full magnetic response of the cluster it is easier to distinguish local effects of the Li ions from those of the Al_4^{n-} clusters, and a more detailed interpretation of the results is possible.

II. Computational Details

Structures were optimized using Becke’s exchange (B),³¹ Lee, Yang and Parr (LYP) correlation,³² and within the hybrid functional (B3LYP) approach, as implemented in Gaussian. All geometrical optimizations were done using the 6-311++G(2df) basis set.^{33,34} The NMR calculations were performed using the PW91 functional and IGLO-III basis set.³⁵ Cartesian shielding tensors were computed using the IGLO method.³⁶ The deMon program³⁷ was used to compute the molecular orbitals and the deMon-NMR package^{38,39} for the shielding tensors. Induced magnetic fields²⁹ were computed by

$$\mathbf{B}^{\text{ind}}(\mathbf{R}) = -\sigma_{\alpha\beta}(\mathbf{R})\mathbf{B}^{\text{ext}} \quad (1)$$

from Cartesian shielding tensors and are in ppm of the units of the external field. Assuming an external magnetic field of $|\mathbf{B}^{\text{ext}}| = 1.0 \text{ T}$, the unit of the induced field is $1.0 \mu\text{T}$, which is equivalent to 1.0 ppm of the shielding tensor. VU⁴⁰ was employed for visualization of the induced field vectors, their contour lines, and isosurfaces. The σ - and π -contributions to the induced magnetic field have been separated using the IGLO method, where localized molecular orbitals (LMOs) have been created using the procedure suggested by Pipek and Mezey.⁴¹ We have chosen a LMO representation⁴² in favor over a canonical MO representation,^{21,22,43} as this approach has been proven to give reliable results for annulenes³⁰ and is computationally advantageous.

Born–Oppenheimer Molecular dynamics simulations have been performed at the PBE³³/DZVP³⁴ level within the NVT (constant number of particles, volume, and temperature) ensemble⁴⁴ using deMon.³⁷ After equilibration, trajectories of up to 25 ps were produced at temperatures of 300 K and 600 K, with a temperature coupling constant $\tau = 0.5 \text{ ps}$ and a time step of 0.5 fs .⁴⁴

III. Results and Discussion

It is not straightforward to separate the magnetic response of planar Al_4^{2-} and Al_4^{4-} clusters into σ - and π -contributions. While for hydrocarbons it is clear that the stabilization of planar rings is due to the π -electrons and Hückel theory is applicable in a simple way, it is well-known that for metal clusters the situation is not so simple: Both, σ - and π -systems, show a large degree of delocalization, which is a result of the small number of electrons in both electronic subsystems and the ring topology, which favors delocalized

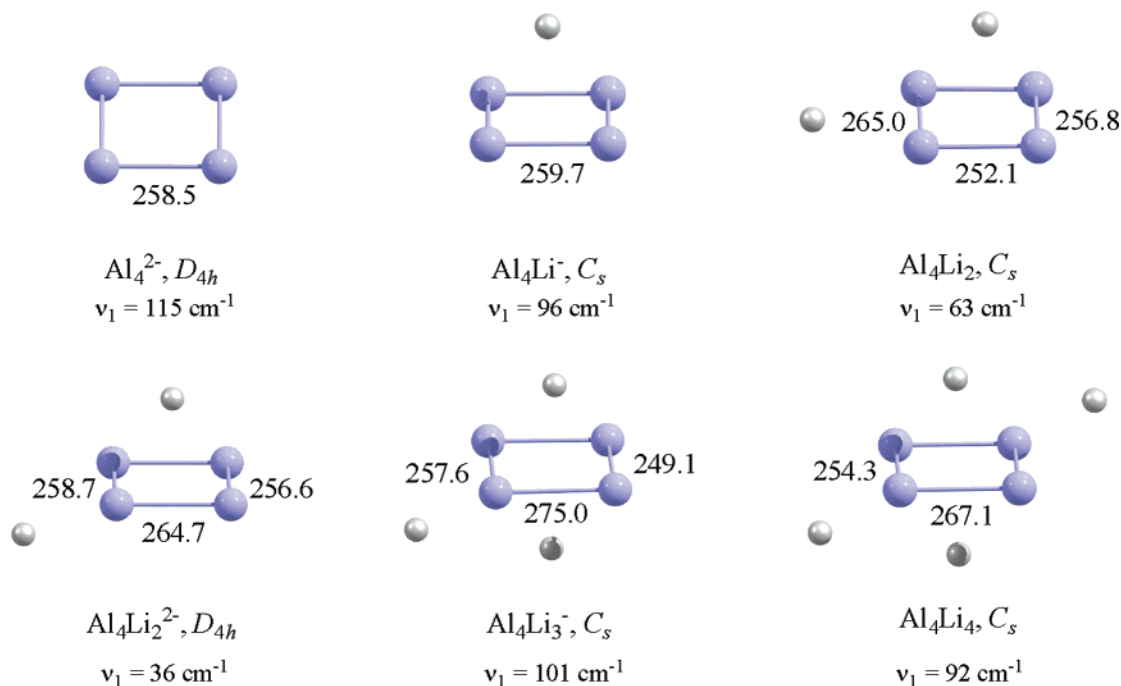


Figure 1. Optimized geometries of the title systems calculated with B3LYP/6-311++G(2df). Bond lengths are given in picometers.

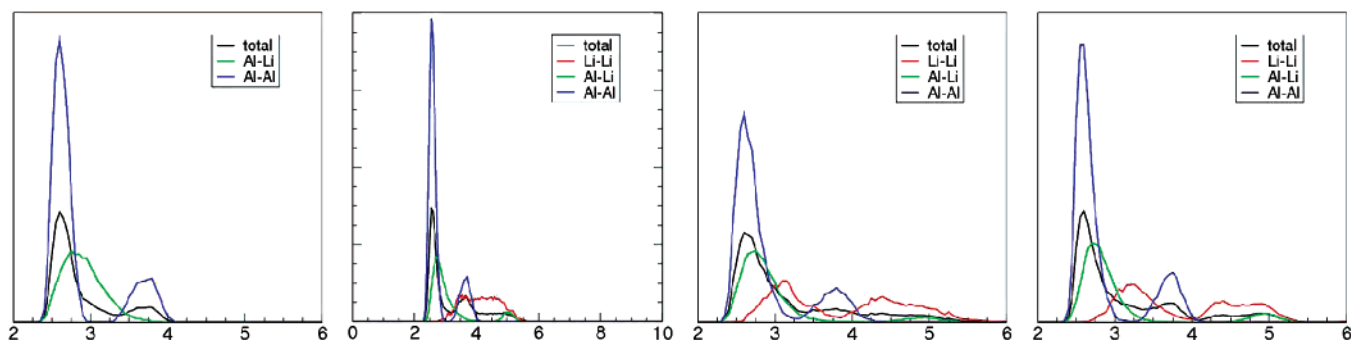


Figure 2. Pair distribution functions, taken from MD trajectories at 300 K of (from left to right) Al_4Li^- , Al_4Li_2 , Al_4Li_3^- , and Al_4Li_4 . Distances are given in Å, and all functions follow identical normalization criteria.

electrons.^{12–14,16,17,26–28,43,45–48} Further, the calculation of highly anionic species often results in technical problems as convergence failures. Therefore, we studied closed-shell clusters with an increasing number of Li^+ counterions, starting from Al_4^{2-} , Al_4Li^- , Al_4Li_2 , Al_4Li_3^- , and Al_4Li_4 .

A. Structure. As can be seen from Figure 1, the geometries depend only slightly on the number of counter charges as long as the formal charge of the Al_4 backbone is maintained. While the bond lengths differ by 7 pm in the dianion (keeping the quadratic form of the metal frame), the bond lengths differs by 35 pm in Al_4Li_3^- , i.e., the ground state of Li_3Al_4^- possesses a distorted rectangular Al_4 framework. Shaik et al. stated that even if there is a distortion from the square structure in Li_3Al_4^- , it is an aromatic system because of the distortive nature of π -electrons.⁴⁹ Juselius et al. used the ARCS method to show that Al_4^{4-} is antiaromatic and concluded that the normally reliable NICS calculations failed in this case.¹⁶ It is a lively discussion. But there still remains a simple question: are the lithium atoms only suppliers of charge, or do they play a more important role for these clusters.

Our molecular dynamics simulations show that the stability of the positions of the lithium atoms depends strongly on the cluster. For Al_4Li^- , the lithium atom sits on top of the ring and does not leave this position during a trajectory of 25 ps at 300 K. It shows, however, large amplitude movements parallel to the ring, partially hopping to the corners and back to the position on top of the ring center. The lowest vibrational frequency of this cluster, 96 cm^{-1} , corresponds to this movement of the lithium atom. The pair distribution function (PDF) (Figure 2) indicates the large fluxionality of the Li ion by the very broad Al–Li signal. The sharp Al–Al signal indicates that within the resolution of the PDF the bond lengths are equalized.

Opposite to simple electrostatic expectations, the second Li cation in Al_4Li_2 is not located at the opposite ring site, forming a bipyramidal cluster, it rather sits on top of an Al–Al bond. The structure of Al_4Li_2 is more fluxional than that of Al_4Li^- , as the electrostatic attraction between ring and cations is weaker and also as both cations repel each other and show collective motions. In particular the Li atom sitting on the bond shows large amplitude motions. This is

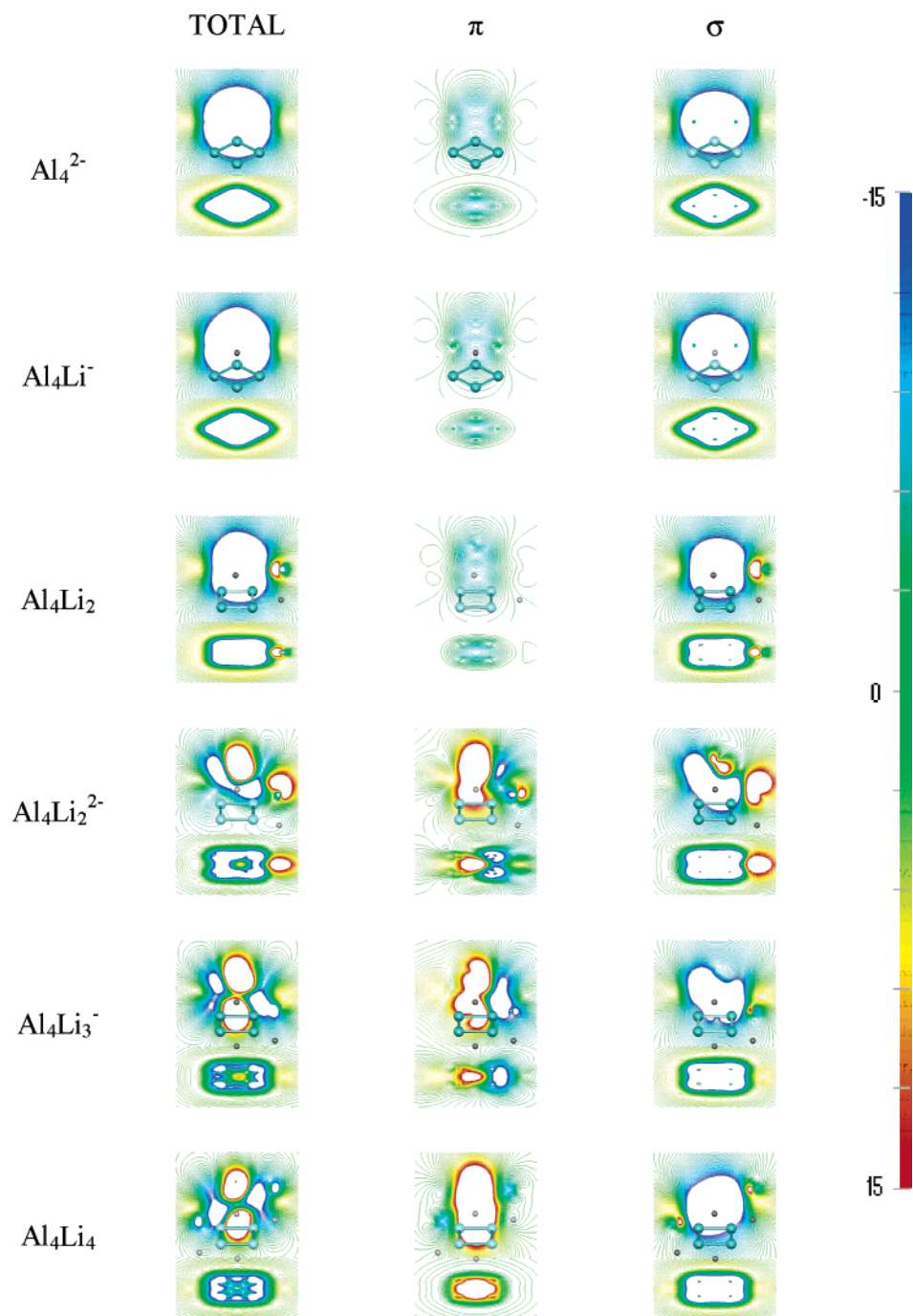


Figure 3. Contour lines of the z -component of \mathbf{B}^{ind} in the molecular plane and perpendicular to the molecular plane through the origin. The scale is given in ppm or μT for an external field of 1 T.

also visible in the PDF, where the Li–Li signal is very broad, similar to that of a liquid.

For Al_4Li_3^- we observe the largest fluxionality. The influence on the Al–Al bond length by the neighboring cations is visible by the much wider Al–Al signal, even though the resolution of the PDF cannot distinguish between different Al–Al bond lengths. During a 25 ps simulation, even at 300 K, Li atoms hop between different sites, which is reflected by the widely spread Li–Li signal. For Al_4Li_4 , the Al–Al distances show a similar distribution as for Al_4Li^- , while the fluxionality of the Li atoms is similar as in Al_4Li_3^- . Also here, Li atoms exchange positions during the simulation.

B. Electron Delocalization. The degree of aromaticity of the Al_4^{2-} and Al_4^{4-} anions has been studied using different theoretical schemes. They include the plotting of ring current densities,^{13,17,47} further quantified by the calculation of GIMIC ring currents above and below the ring,⁴⁶ and an analysis on MO-resolved nucleus-independent chemical shifts.⁴⁸ For Al_4^{2-} , a σ - and π -resolved NICS analysis is available.²³ These results have been summarized in a special issue of *Chemical Reviews* devoted to electron delocalization.^{11,12}

It is agreed that the σ -system contributes strongly to the aromatic character of both Al_4^{2-} and Al_4^{4-} frameworks. There is also no argument that the π -contribution of Al_4^{2-} is diatropic, as there is only a single occupied π -orbital, and

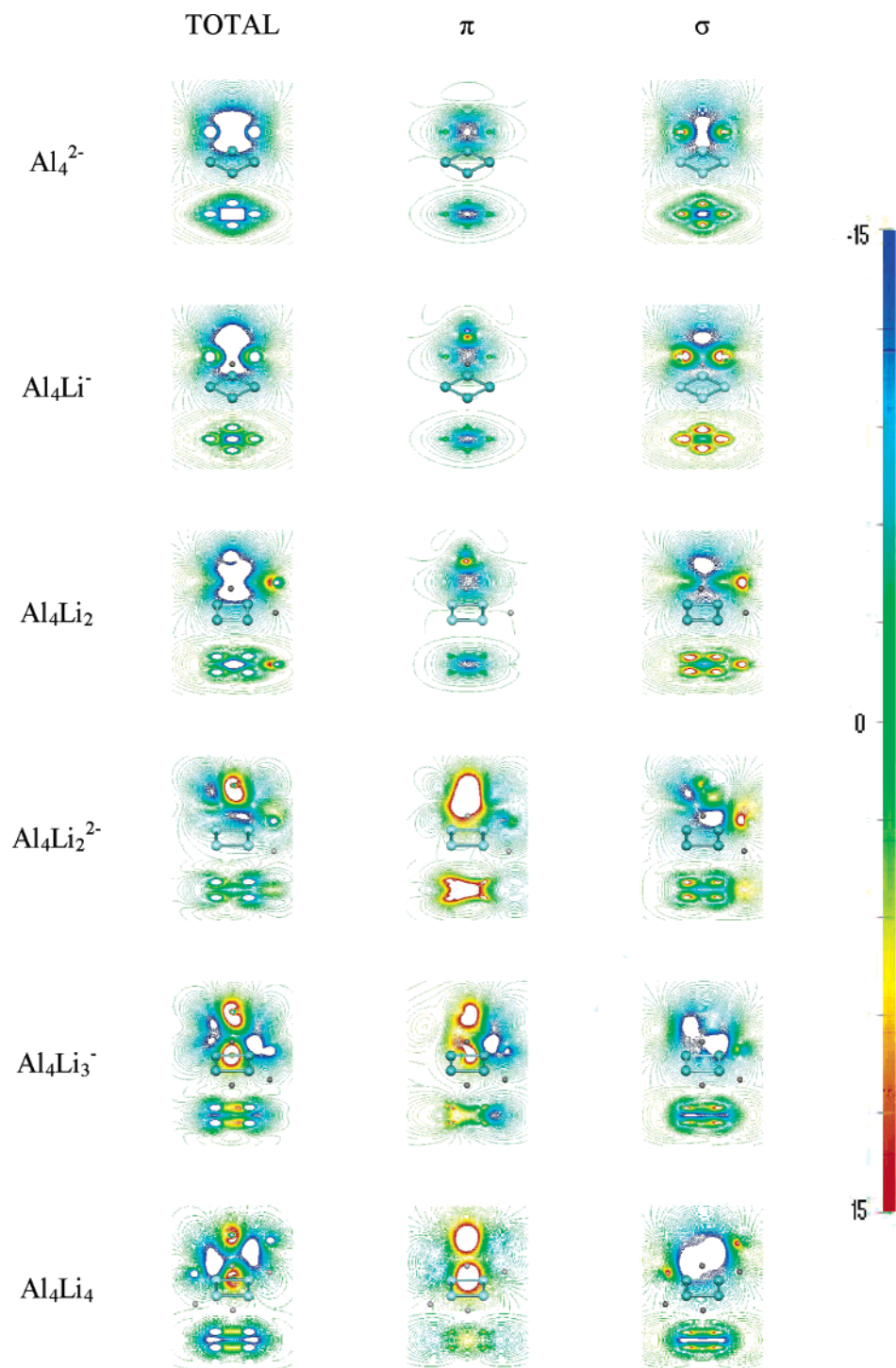


Figure 4. Contour lines of NICS parameter in the molecular plane and perpendicular to the molecular plane through the origin. The scale is given in ppm or μT for an external field of 1 T.

that the π -contribution in Al_4^{4-} species is paratropic. There is, however, disagreement as to whether Al_4^{4-} should be called an aromatic or an antiaromatic molecule.²³ The argument of Boldyrev and Wang states that there is a paratropic π -system which is occupied as in classical antiaromatic hydrocarbons, i.e., C_4H_4 . Furthermore, the π -states of Al_4^{4-} are degenerate, leading to a Jahn–Teller-like distortion similar to for C_4H_4 . The response of Chen and others is that the antiaromatic effect of the π -system is overwhelmed by the aromatic effect of the σ -system.

In agreement, the ring current maps of Havenith et al. show that the current through the π -orbitals is not significant.^{17,27}

We plotted the σ - and π -separated z -components of the induced magnetic fields, which coincide with the NICS_{zz} index at the ring center⁴⁹ (Figure 3), and of $\text{NICS}(\mathbf{r})$ (Figure 4).

In Figure 3, the z -component of the induced magnetic field, applied perpendicular to the ring, is shown for Al_2^{2-} and Al_4^{4-} based species. For the Al_2^{2-} moieties, the total magnetic

response is quite similar to that of aromatic hydrocarbons.³⁰ For Al_4^{4-} , the situation is not that clear. The shielding cones of the molecule on top and bottom, induced by the π -electrons, is comparable to that of cyclobutadiene,³⁰ though smaller in magnitude and perturbed by the Li ions. Closer to the ring plane and at positions far from the ring center, however, the response is aromatic and similar to that of an aromatic hydrocarbon. The same magnetic response applied to C_4H_4 would result in aromatic protons. It is therefore difficult to make a final statement as to whether Al_4^{4-} should be called aromatic or antiaromatic. Evidently, NICS can fail near the ring center. Therefore, the NICS or z -component of B^{ind} isolines or isosurfaces give us important (but still partial) insight into electron delocalization.

It is, however, clear that σ - and π -components of Al_4^{4-} show an opposite response. The σ -system is evidently diatropic and very similar to that of Al_4^{2-} . On the other hand, the π -systems of Al_4^{4-} moieties show a typical antiaromatic response, as in an antiaromatic annulene, e.g., C_4H_4 . In agreement with previous studies,^{17,23,27} for Al_4^{2-} , the contribution of the π -system is small compared to the σ -system.

The advantage of a complete response map over a single magnetic index is obvious: For the Al_4^{4-} species, the z -component of the B^{ind} index will deliver a small number, indicating either a small net para- or diatropicity. The NICS-(1) family of indices, and even the ARCS approach,¹⁵ will sense the paratropic π -system, as no information of the outer ring areas enter. The complete map of the induced magnetic field, however, shows the “bitropic” character of the molecule: there is a diatropic contribution raised by the σ -electrons which dominates in the ring plane and a paratropic part, induced by the π -system around the z -axis. The same effect is visible in ring current maps at different height profile.²⁷ In contrast to many other molecules as hydrocarbons,³⁰ both contributions are significant.

IV. Conclusions

Our calculations show that Al_4^{2-} and Al_4^{4-} based metal clusters cannot be discussed isolated from the counterions: They not only stabilize the Al_4^{n-} anions electrostatically but also have an influence on the chemical structure. Molecular dynamics simulations show that the cations are relatively fixed for Al_4Li^- and Al_4Li_2 but become more floppy for $Al_4Li_3^-$ and Al_4Li_4 . For these molecules, any static structural representation is not realistic.

Magnetically, the induced magnetic field representation agrees with former investigations based on NICS and ring current calculations concerning the character of the σ - and π -systems. For the total response, our computations show that a simple classification of a molecule as “aromatic” or “antiaromatic” is impossible for those systems containing a Al_4^{4-} backbone, at least as long as this term does not have a more strict definition. For this case, the complete map of the induced magnetic field shows the “bitropic” character of the molecule, the diatropic contribution raised by the σ -electrons which dominates in the ring plane, and the paratropic part, induced by the π -system around the z -axis. While the long-range response perpendicular to the molecular planes is typical, though smaller in magnitude, for molecules

with aromatic (Al_4^{2-}) and antiaromatic (Al_4^{4-}) π -systems, respectively, the response in the ring planes is similar to that of aromatic molecules.

Acknowledgment. This work was funded in part by grants from PROMEP-SEP (project UGTO-PTC-079), DIN-PO-UGTO, and the Deutsche Forschungsgemeinschaft (DFG).

Supporting Information Available: Coordinates of the optimized structures, vibrational frequencies, and energies. This material is available free of charge via the Internet at <http://pubs.acs.org>.

References

- (1) Schleyer, P. v. R. *Chem. Rev.* **2001**, *101*, 1115.
- (2) Wade, K. *Chem. Commun.* **1971**, 792.
- (3) Srinivas, G. N.; Anoop, A.; Jemmis, E. D.; Hamilton, T. P.; Lammertsma, K.; Leszczynski, J.; Schaefer, H. F. *J. Am. Chem. Soc.* **2003**, *125*, 16397.
- (4) Hirsch, A.; Chen, Z. F.; Jiao, H. J. *Angew. Chem., Int. Ed.* **2001**, *40*, 2834.
- (5) King, R. B.; Heine, T.; Corminboeuf, C.; Schleyer, P. v. R. *J. Am. Chem. Soc.* **2004**, *126*, 430.
- (6) Chen, Z. F.; King, R. B. *Chem. Rev.* **2005**, *105*, 3613.
- (7) Li, X.; Kuznetsov, A. E.; Zhang, H. F.; Boldyrev, A. I.; Wang, L. S. *Science* **2001**, *291*, 859.
- (8) Zhan, C. G.; Zheng, F.; Dixon, D. A. *J. Am. Chem. Soc.* **2002**, *124*, 14795.
- (9) Kuznetsov, A. E.; Boldyrev, A. I.; Li, X.; Wang, L. S. *J. Am. Chem. Soc.* **2001**, *123*, 8825.
- (10) Kuznetsov, A. E.; Corbett, J. D.; Wang, L. S.; Boldyrev, A. I. *Angew. Chem., Int. Ed. Engl.* **2001**, *40*, 3369.
- (11) Heine, T.; Corminboeuf, C.; Seifert, G. *Chem. Rev.* **2005**, *105*, 3889.
- (12) Boldyrev, A. I.; Wang, L. S. *Chem. Rev.* **2005**, *105*, 3716.
- (13) Fowler, P. W.; Havenith, R. W. A.; Steiner, E. *Chem. Phys. Lett.* **2001**, *342*, 85.
- (14) Fowler, P. W.; Havenith, R. W. A.; Steiner, E. *Chem. Phys. Lett.* **2002**, *359*, 530.
- (15) Juselius, J.; Sundholm, D. *Phys. Chem. Chem. Phys.* **1999**, *1*, 3429.
- (16) Juselius, J.; Straka, M.; Sundholm, D. *J. Phys. Chem. A* **2001**, *105*, 9939.
- (17) Havenith, R. W. A.; Fowler, P. W. *Phys. Chem. Chem. Phys.* **2006**, *8*, 3383.
- (18) Becke, A. D.; Edgecombe, K. E. *J. Chem. Phys.* **1990**, *92*, 5397.
- (19) Silvi, B.; Savin, A. *Nature* **1994**, *371*, 683.
- (20) Santos, J. C.; Tiznado, W.; Contreras, R.; Fuentealba, P. *J. Chem. Phys.* **2004**, *120*, 1670.
- (21) Corminboeuf, C.; Heine, T.; Weber, J. *Phys. Chem. Chem. Phys.* **2003**, *5*, 246.
- (22) Heine, T.; Schleyer, P. v. R.; Corminboeuf, C.; Seifert, G.; Reviakine, R.; Weber, J. *J. Phys. Chem. A* **2003**, *107*, 6470.
- (23) Chen, Z. F.; Corminboeuf, C.; Heine, T.; Bohmann, J.; Schleyer, P. v. R. *J. Am. Chem. Soc.* **2003**, *125*, 13930.

- (24) Juselius, J.; Sundholm, D.; Gauss, J. *J. Chem. Phys.* **2004**, *121*, 3952.
- (25) Boldyrev, A. I.; Kuznetsov, A. E. *Inorg. Chem.* **2002**, *41*, 532.
- (26) Kuznetsov, A. E.; Birch, K. A.; Boldyrev, A. I.; Li, X.; Zhai, H. J.; Wang, L. S. *Science* **2003**, *300*, 622.
- (27) Havenith, R. W. A.; Fowler, P. W.; Steiner, E.; Shetty, S.; Kanhere, D.; Pal, S. *Phys. Chem. Chem. Phys.* **2004**, *6*, 285.
- (28) Tsepis, C. A. *Coord. Chem. Rev.* **2005**, *249*, 2740.
- (29) Merino, G.; Heine, T.; Seifert, G. *Chem. Eur. J.* **2004**, *10*, 4367.
- (30) Heine, T.; Islas, R.; Merino, G. *J. Comp. Chem.* **2007**, *28*, 302.
- (31) Becke, A. D. *J. Chem. Phys.* **1993**, *98*, 5648.
- (32) Lee, C. T.; Yang, W. T.; Parr, R. G. *Phys. Rev. B* **1988**, *37*, 785.
- (33) Perdew, J. P.; Wang, Y. *Phys. Rev. B* **1992**, *45*, 13244.
- (34) Godbout, N.; Salahub, D. R.; Andzelm, J.; Wimmer, E. *Can. J. Chem.* **1992**, *70*, 560.
- (35) Kutzelnigg, W.; Fleischer, U.; Schindler, M. *The IGLO-Method: Ab Initio Calculation and Interpretation of NMR Chemical Shifts and Magnetic Susceptibilities*; Springer-Verlag: Heidelberg, 1990; Vol. 23.
- (36) Kutzelnigg, W. *Isr. J. Chem.* **1980**, *19*, 193.
- (37) Köster, A. M.; Calaminici, P.; del Campo, J. M.; Casida, M. E.; Flores-Moreno, R.; Geudtner, G.; Goursot, A.; Heine, T.; Ipatov, A.; Janetzko, F.; Patchkovskii, S.; Reveles, J. U.; Salahub, D. R.; Vela, A. *deMon*, 2.2.1; Mexico, Ottawa, Calgary, 2005.
- (38) Malkin, V. G.; Malkina, O. L.; Reviakine, R.; Schimmelpennig, B.; Arbuznikov, V.; Kaupp, M. *MAG-ReSpect 1.0*, *MAG-ReSpect 1.0*; 2001.
- (39) Malkin, V. G.; Malkina, O. L.; Salahub, D. R. *Chem. Phys. Lett.* **1993**, *204*, 80.
- (40) Ozell, B.; Camarero, R.; Garon, A.; Guibault, F. *Finite Elem. Des.* **1995**, *19*, 295.
- (41) Pipek, J.; Mezey, P. G. *J. Chem. Phys.* **1989**, *90*, 4916.
- (42) Schleyer, P. v. R.; Jiao, H. J.; Hommes, N. J. R. V.; Malkin, V. G.; Malkina, O. L. *J. Am. Chem. Soc.* **1997**, *119*, 12669.
- (43) Corminboeuf, C.; Heine, T.; Seifert, G.; Schleyer, P. v. R.; Weber, J. *Phys. Chem. Chem. Phys.* **2004**, *6*, 273.
- (44) Berendsen, H. J. C.; Postma, J. P. M.; Van Gunsteren, W. F.; Di Nola, A.; Haak, J. R. *J. Chem. Phys.* **1984**, *81*, 3684.
- (45) Lin, Y. C.; Sundholm, D.; Juselius, J.; Cui, L. F.; Li, X.; Zhai, H. J.; Wang, L. S., *J. Phys. Chem. A* **2006**, *110*, 4244.
- (46) Lin, Y. C.; Juselius, J.; Sundholm, D.; Gauss, J. *J. Chem. Phys.* **2005**, *122*.
- (47) Havenith, R. W. A.; Fowler, P. W.; Steiner, E. *Chem. Eur. J.* **2002**, *8*, 1068.
- (48) Fowler, P. W.; Rogowska, A.; Soncini, A.; Lillington, M.; Olson, L. P. *J. Org. Chem.* **2006**, *71*, 6459.
- (49) Jug, K.; Hiberty, P. C.; Shaik, S. *Chem. Rev.* **2001**, *101*, 1477.

CT700009K

JCTC Journal of Chemical Theory and Computation

Theoretical Study of the Magnetic Properties of an Mn₁₂ Single-Molecule Magnet with a Loop Structure: The Role of the Next-Nearest Neighbor Interactions[†]

Joan Cano,[§] Ruben Costa,[‡] Santiago Alvarez,[‡] and Eliseo Ruiz^{*:‡}

Departament de Química Inorgànica and Centre de Recerca en Química Teòrica, Universitat de Barcelona, Martí i Franquès 1-11, 08028 Spain, and Institució Catalana de Recerca i Estudis Avançats (ICREA)

Received January 12, 2007

Abstract: The magnetic properties of a Mn₁₂ single-molecule magnet with a loop structure are characterized by a computational study based on density functional theory. A study of the two reported crystal structures of such a complex correctly reproduces the experimental spin ground state. We have analyzed the effect of the choice of spin configurations employed for the calculations, as well as the influence of the inclusion of the next-nearest neighbor interactions on the calculated exchange coupling constants. Quantum Monte Carlo simulations performed with the calculated exchange coupling constants show that the best agreement with the experimental susceptibility curve is achieved by using the hybrid B3LYP functional.

Introduction

The synthesis and study of magnetic properties of large polynuclear transition metal clusters is a field to which many research groups have devoted considerable effort during the past years.¹ Some of those polynuclear complexes show a slow relaxation of the magnetization that could eventually lead to applications for information storage at the molecular level.^{2,3} The first single-molecule magnet (SMM) reported was the [Mn₁₂O₁₂(CH₃COO)₁₆(H₂O)₄] complex, usually known as Mn₁₂ or Mn₁₂ acetate, that adopts a compact cluster structure with a central cubane of four Mn^{IV} cations surrounded by a crown of eight Mn^{III} cations.⁴ In order to have a slow relaxation of the magnetization, one needs a high-energy barrier between the states with positive and negative magnetic moments, and also quantum tunneling effects should be avoided.^{5,6} Such a barrier is known to depend directly on the square of the total spin of the molecule and on its magnetic anisotropy parameter *D*, that in the case of the Mn₁₂ acetate are *S* = 10 and *D* = −0.46 cm^{−1}.^{7,8}

Hence, high-spin and large, negative anisotropy-parameter polynuclear complexes are much sought after synthetic targets due to their possible technological applications.

In order to quantify the *S* value of the ground state for a polynuclear complex, we should employ a Heisenberg spin Hamiltonian that can be expressed as

$$\hat{H} = - \sum_{i>j} J_{ij} \hat{S}_i \hat{S}_j + D \left(\hat{S}_z^2 - \frac{1}{3} \hat{S}^2 \right) + E (\hat{S}_x^2 - \hat{S}_y^2) \quad (1)$$

where \hat{S}_i and \hat{S}_j are the spin operators of paramagnetic centers *i* and *j* and \hat{S} and \hat{S}_z are the total spin operator of the molecule and its axial component, respectively. The *J_{ij}* values are the exchange coupling constants for the different pairwise interactions between the paramagnetic centers of the molecule, while *D* and *E* are the axial and rhombic components of the anisotropy, respectively. Spin-orbit coupling effects must be taken into account for the calculation of the zero-field splitting parameters *D* and *E*;^{9–13} otherwise, only the exchange coupling constants can be determined. However, the study of the magnetic properties of such systems from magnetic susceptibility curves presents considerable problems from the experimental point of view due to the large number of states involved. For instance, a Mn₁₂ complex containing six Mn^{II} and six Mn^{III} ions has 7.29 × 10⁸ M_s states. For

[†] Dedicated to Professor Dennis R. Salahub on the occasion of his 60th birthday.

* Corresponding author e-mail: eliseo.ruiz@qi.ub.es.

[‡] Universitat de Barcelona.

[§] ICREA.

such a large number of states, even if symmetry is taken into account, it is impossible to build up the Hamiltonian matrix using a Heisenberg Hamiltonian (eq 1), as required to perform a fitting of the J values, due to the huge amount of memory required. Even in the case that the memory was available and it was possible to diagonalize the matrix, there are many sets of exchange coupling constants that may perfectly fit the experimental data. Thus, from only the experimental magnetic susceptibility data, it is possible to extract the total spin value of the ground state, whereas in inelastic neutron scattering experiments, one obtains the relative energies and spin values of the excited states.¹⁴

On the other hand, theoretical methods based on density functional theory have been employed to analyze the spin states. For instance, we can mention earlier studies devoted to simple molecules¹⁵ and polynuclear metal clusters,¹⁶ but it is only in recent years that each approach has been extensively employed. Such methodology also allows one to obtain all the exchange coupling constants present in polynuclear transition-metal complexes, information that is extremely useful for the future design of new molecular systems with improved magnetic properties.^{13,17–20} For instance, the exchange interactions of the widely experimentally studied Mn₁₂ acetate complex have been calculated using theoretical methods based on density functional theory by different authors.^{13,21–24} In order to calculate the n J_{ij} exchange coupling constants of a polynuclear complex, we must at least perform $n + 1$ energy calculations of different spin configurations that correspond to single-determinant Kohn–Sham solutions.^{25–27} Such spin configurations must be selected in a such way as to make it possible to solve a system of n equations with n unknowns, the J_{ij} values. However, some questions emerge at this point concerning the choice of a few spin configurations for the calculations among thousands of possibilities. Thus, an interesting point is to evaluate the dependence of the calculated J values on the selected set of spin configurations. This problem is directly related with the accuracy of the phenomenological Heisenberg Hamiltonian to describe the magnetic properties in such systems. In principle, if the exchange interactions can be properly described by the Heisenberg Hamiltonian, the calculated J values should be independent of the spin configurations selected. However, different authors have pointed out this problem, and it is usually proposed to calculate more energies than strictly needed and then perform a least-squares fitting to extract the exchange coupling constants until the calculated values converge.^{13,28} Even if we can obtain a set of J values that remain unchanged upon increasing the number of spin configurations, there is still the problem of whether the simple Heisenberg Hamiltonian describes correctly such systems or we need to include some additional terms. In order to solve the limitations of the Heisenberg Hamiltonian employed, some approaches have been adopted, such as the inclusion of the often neglected next-nearest neighbor interactions or to include new three- or four-body spin terms in the Hamiltonian.²⁹ Theoretical methods can be employed to elucidate the importance of such terms. However, from the experimental point of view, it is

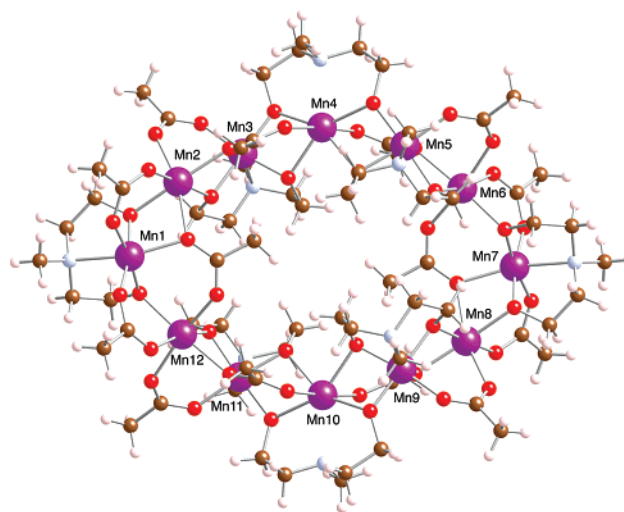


Figure 1. Molecular structure of the Mn₁₂ complex, [Mn^{III}₆-Mn^{II}₆(O₂CMe)₁₄(mda)₈] (mdaH₂ = N-methyldiethanolamine).^{30,31} Mn^{III} and Mn^{II} cations correspond to odd and even numbers, respectively.

a difficult task because of an increased number of fitting parameters, making it harder to obtain a unique fit.

The main goal of this work is to study the magnetic properties of a Mn₁₂ complex with a loop structure (see Figure 1) showing SMM behavior. We have selected this system instead of other SMMs, such as, the first SMM Mn₁₂ complex,⁴ because its cyclic structure makes this system well-suited for an analysis of the role of the next-nearest neighbor interactions. This Mn₁₂ compound was independently reported recently by Rumberger et al.^{30,31} and Foguet-Albiol et al.³² with two very similar crystal structures that show an alternation of Mn^{III} and Mn^{II} cations (see Figure 1). Even if the experimental susceptibility curves are relatively similar, the two groups have proposed different magnetic parameters for the ground state, $S = 8$ and $D = -0.47$ cm⁻¹ and $S = 7$ and $D = -0.26$ cm⁻¹, respectively.

Results and Discussion

Magnetic Properties of the Mn₁₂ Complex. We start our study of the magnetic properties of the Mn₁₂ complex by calculating the exchange coupling constants while neglecting next-nearest neighbor interactions. The analysis of the geometry indicates the presence of six different exchange interactions. Thus, the topology of the interactions is represented in Figure 2, and the Heisenberg Hamiltonian has the following expression:

$$\begin{aligned} \hat{H} = & -J_1[\hat{S}_1\hat{S}_2 + \hat{S}_7\hat{S}_8] - J_2[\hat{S}_2\hat{S}_3 + \hat{S}_8\hat{S}_9] \\ & -J_3[\hat{S}_3\hat{S}_4 + \hat{S}_9\hat{S}_{10}] - J_4[\hat{S}_4\hat{S}_5 + \hat{S}_{10}\hat{S}_{11}] \\ & -J_5[\hat{S}_5\hat{S}_6 + \hat{S}_{11}\hat{S}_{12}] - J_6[\hat{S}_6\hat{S}_7 + \hat{S}_1\hat{S}_{12}] \quad (2) \end{aligned}$$

The J values calculated using the whole molecule from the two available crystal structures are collected in Table 1, together with the values reported by Foguet-Albiol et al.,³² who used simple dinuclear models to describe these interactions. For these calculations, we have used the seven low-lying spin configurations that provide a solvable system of

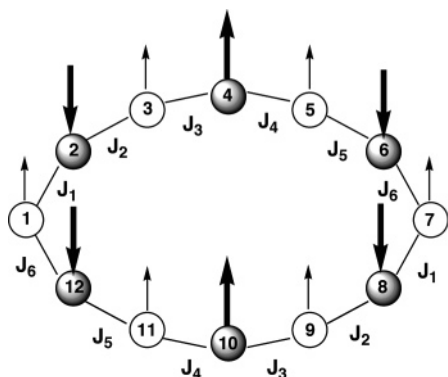


Figure 2. Scheme showing the topology of the exchange interactions in the studied Mn_{12} complex. The arrows indicate the most stable spin configuration that has a total spin $S = 7$ (thin arrows for $S = 2$ Mn^{III} cations; thick arrows for $S = 5/2$ Mn^{II} cations).

equations (see Computational Details section), that is, the minimum needed to obtain the six J values. The analysis of the results allows us to extract the following conclusions: (i) The J_1 , J_2 , and J_5 coupling constants correspond to similar sets of three bridging ligands and consequently present nearly the same weakly antiferromagnetic values. Interactions through a set of one carboxylato and one alkoxo bridges with an additional monodentate carboxylato bridging ligand with long Mn–O bond distances are known to be weakly antiferromagnetic.³³ (ii) The J_3 and J_4 exchange interactions occur through similar bridging ligands and are weakly ferromagnetic, essentially through the two alkoxo bridges since the carboxylato ligands have long bond distances to the metals, especially with the Mn^{III} cation due to the Jahn–Teller effect. (iii) The J_6 coupling constant calculated using the B3LYP functional also corresponds to a weak antiferromagnetic interaction, at difference with the negligible coupling constant obtained by Foguet-Albiol et al. with dinuclear models.³² Only with one of the structures and the Perdew, Burke, and Ernzerhof (PBE) functional do we obtain a very weak J_6 ferromagnetic interaction. We must note that an antiferromagnetic J_6 value is mandatory to obtain a single-

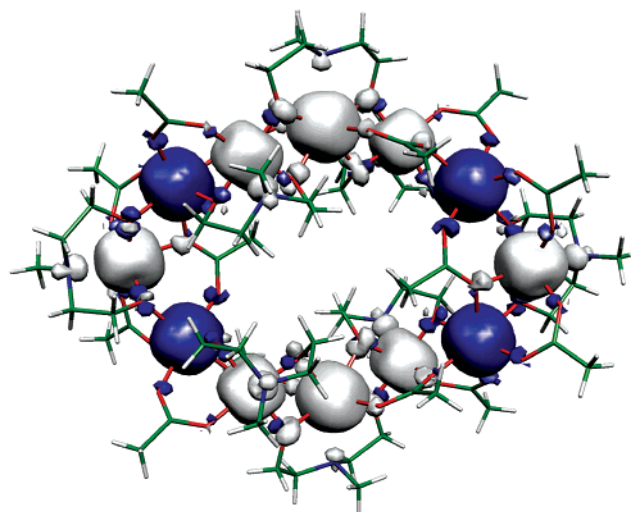


Figure 3. Spin density map for the $S = 7$ single-determinant ground state of the Mn_{12} loop complex, calculated with the B3LYP functional. The isodensity surface represented corresponds to a value of $0.005 \text{ e}^-/\text{bohr}^3$ (white and blue regions indicate positive and negative spin populations, respectively).

determinant ground state with $S = 7$ as found experimentally, whereas an $S = 0$ ground state is predicted for a ferromagnetic J_6 coupling. Hence, our calculated values are consistent with the ground spin configuration with $S = 7$ shown in Figure 2, in agreement with the experimental ground state proposed by Foguet-Albiol et al.³² It must be pointed out, however, that we have estimated energies of the states diagonalizing an approximate half-molecule model that shows the presence of an $S = 8$ state around 10 cm^{-1} above the ground state that could explain why the magnetic susceptibility can as well be fitted using an $S = 8$ ground state as proposed by Rumberger et al.^{30,31}

The B3LYP calculated spin-density values (see Table 1) show a poor spin delocalization, as expected. The PBE functional gives a larger delocalization and, consequently, stronger interactions.^{34,35} In Figure 3, we represent the spin density of the single determinant ground state that reveals

Table 1. Exchange Coupling Constants (in cm^{-1}) for the Mn_{12} Complex, $[\text{Mn}^{\text{III}}_6\text{Mn}^{\text{II}}_6(\text{O}_2\text{CMe})_{14}(\text{mda})_6]$, and Atomic Spin Populations (ρ) Calculated with the PBE (Siesta code) and B3LYP (Gaussian code) Functionals (see Computational Details Section) Using the Two Available Crystal Structures^{30,32 a}

	bridging ligands	Mn...Mn	Mn–X ^b	Mn–X–Mn	PBE	B3LYP ^c	B3LYP-m ^d
J_1	$\mu\text{-O}_2\text{CMe}, \mu\text{-OR}$ $\mu\text{-OCOMe}$	3.206	<i>2.120, 2.183, 2.250</i> 1.976, 1.901, 2.177	103.3, 92.8	–11.4(–6.0)	–4.1(–5.6)	–2.8
J_2	$\mu\text{-O}_2\text{CMe}, \mu\text{-OR}$ $\mu\text{-OCOMe}$	3.149	<i>2.097, 2.195, 2.159</i> 1.949, 1.916, 2.255	103.3, 90.1	–18.3(–14.9)	–8.0(–2.5)	–9.2
J_3	$\mu\text{-O}_2\text{CMe}, 2 \mu\text{-OR}$	3.169	<i>2.245, 2.234, 2.210</i> 2.255, 1.907, 1.882	101.2, 99.6	+6.5 (+10.9)	+4.6 (+6.3)	+7.0
J_4	$\mu\text{-O}_2\text{CMe}, 2 \mu\text{-OR}$	3.183	<i>2.234, 2.204, 2.288</i> 2.198, 1.901, 1.889	101.4, 98.8	+6.6 (+9.2)	+4.6 (+5.4)	+8.0
J_5	$\mu\text{-O}_2\text{CMe}, \mu\text{-OR}$ $\mu\text{-OCOMe}$	3.198	<i>2.201, 2.172, 2.222</i> 1.984, 1.928, 2.198	102.3, 92.6	–8.4 (–5.4)	–2.8 (–5.9)	–5.0
J_6	$2 \mu\text{-O}_2\text{CMe}, \mu\text{-OR}$	3.473	<i>2.200, 2.143, 2.110</i> 1.989, 1.914, 2.177	117.6	–0.9 (+1.2)	–7.0 (–3.5)	+0.04
$\rho(\text{Mn}^{\text{II}})$					4.69	4.82	
$\rho(\text{Mn}^{\text{III}})$					3.80	3.85	

^aGeometrical parameters of the structure published by Rumberger et al.^{30,31} are also given (distances in Å, bond angles in degrees). ^b Values in italics correspond to the Mn^{II} cations. ^c In parentheses are those corresponding to the structure obtained by Foguet-Albiol et al. ^d Values obtained with dinuclear models (ref 18).

Table 2. Exchange Coupling Constants (in cm⁻¹) for [Mn^{II}₆Mn^{II}₆(O₂CMe)₁₄(mda)₈]^{30,31} Calculated with the PBE and B3LYP Functionals Using Different Sets of *n* Spin Configurations^a

<i>n</i>	PBE				
	6	13	16	24	32
<i>J</i> ₁	-11.4	-10.8 (9)	-10.6 (9)	-10.4 (6)	-12.1 (7)
<i>J</i> ₂	-18.3	-15.3 (8)	-15.4 (9)	-16.0 (5)	-16.3 (6)
<i>J</i> ₃	+6.5	+6.6 (5)	+6.4 (5)	+6.5 (4)	+6.4 (5)
<i>J</i> ₄	+6.6	+8.6 (7)	+8.5 (5)	+8.3 (3)	+8.1 (4)
<i>J</i> ₅	-8.4	-7.2 (8)	-7.7 (7)	-8.2 (4)	-8.4 (5)
<i>J</i> ₆	-0.9	-2.9 (10)	-1.8 (8)	-1.2 (4)	-1.8 (4)

<i>n</i>	B3LYP				
	6	13	16	24	32
<i>J</i> ₁	-4.11	-3.9 (3)	-3.8 (3)	-3.8 (2)	-4.4 (3)
<i>J</i> ₂	-7.96	-6.8 (3)	-6.9 (3)	-7.1 (1)	-7.2 (2)
<i>J</i> ₃	+4.60	+4.6 (2)	+4.6 (2)	+4.6 (2)	+4.5 (2)
<i>J</i> ₄	+4.61	+5.4 (2)	+5.3 (2)	+5.2 (1)	+5.1 (2)
<i>J</i> ₅	-2.77	-2.3 (3)	-2.5 (3)	-2.7 (2)	-2.8 (2)
<i>J</i> ₆	-7.03	-7.8 (4)	-7.3 (3)	-7.1 (2)	-7.3 (2)

^a The number in parentheses indicates the standard deviation of the least-squares fitting.

the weak spin delocalization. The spin density at the Mn^{II} cations remains almost spherical. At the bridging ligand mediating ferromagnetic interactions (*J*₃ and *J*₄), spin polarization contributions show up in both positive and negative spin density lobes at the same atom.

Influence of the Choice of Spin Configurations on the Calculated *J* Values. In order to check the influence of the number of configurations employed in the calculations, we have analyzed the results taking up to 32 spin configurations together with the *S* = 7 ground-state spin solution. The fitted *J* values are collected in Table 2. In each case, the configurations correspond to the low-lying cases that provide a solvable system of equations. The analysis of the results gives some insights: (i) The nature and relative strength of the exchange interaction is well-reproduced by both functionals (PBE and B3LYP) independently of the number of spin configurations considered. (ii) The standard deviations are smaller than one wavenumber in all cases, independently of the magnitude of the interaction. (iii) The errors obtained with the PBE functional are slightly larger than those obtained with the hybrid functional. (iv) The inclusion of spin configurations with relatively high energies in the case of *n* = 32 induces rather small variations in the *J* values that are practically converged with a smaller number of spin configurations. (v) For the weakest interaction (*J*₆), the errors obtained with the PBE functional are approximately of the same order of magnitude as the coupling constant, although the sign remains unchanged for all numbers of spin configurations.

Role of the Next-Nearest Neighbor Interactions. As mentioned in the introduction, one of the goals of this work was to study the role of the next-nearest neighbor interactions. Due to the cyclic structure of the complex, it is a good test case to verify such an effect independently of other terms, such as the fourth-order terms that have also been proposed

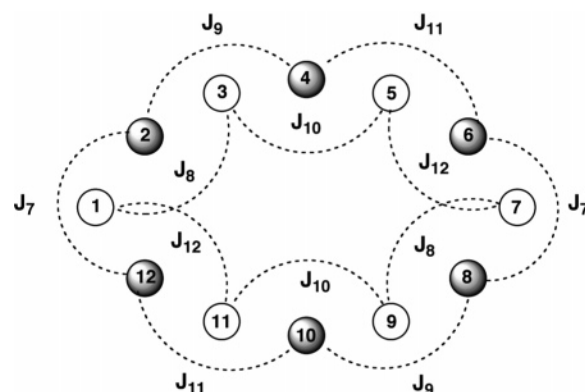


Figure 4. Scheme showing the topology of the next-nearest neighbor exchange interactions in the studied Mn₁₂ complex.

to improve the description of the Hamiltonian. Such next-nearest neighbor interactions are depicted in Figure 4 with the corresponding mathematical expression for the Heisenberg Hamiltonian given in eq 3. With that Hamiltonian, *J*₁–*J*₆ are nearest-neighbor coupling constants and *J*₇–*J*₁₂ correspond to next-nearest neighbor interactions.

$$\begin{aligned}
 \hat{H} = & -J_1[\hat{S}_1\hat{S}_2 + \hat{S}_7\hat{S}_8] - J_2[\hat{S}_2\hat{S}_3 + \hat{S}_8\hat{S}_9] - \\
 & J_3[\hat{S}_3\hat{S}_4 + \hat{S}_9\hat{S}_{10}] - J_4[\hat{S}_4\hat{S}_5 + \hat{S}_{10}\hat{S}_{11}] - J_5[\hat{S}_5\hat{S}_6 + \hat{S}_{11}\hat{S}_{12}] - \\
 & J_6[\hat{S}_6\hat{S}_7 + \hat{S}_{12}\hat{S}_1] - J_7[\hat{S}_1\hat{S}_3 + \hat{S}_7\hat{S}_9] - J_8[\hat{S}_2\hat{S}_4 + \hat{S}_8\hat{S}_{10}] - \\
 & J_9[\hat{S}_3\hat{S}_5 + \hat{S}_9\hat{S}_{11}] - J_{10}[\hat{S}_4\hat{S}_6 + \hat{S}_{10}\hat{S}_{12}] - J_{11}[\hat{S}_5\hat{S}_7 + \hat{S}_{11}\hat{S}_1] - \\
 & J_{12}[\hat{S}_6\hat{S}_8 + \hat{S}_2\hat{S}_{12}] \quad (3)
 \end{aligned}$$

The *J* values calculated including the next-nearest neighbor interactions with different sets of spin configurations are presented in Table 3. The main conclusions that can be extracted from such results are as follows: (i) The inclusion of the next-nearest neighbor interactions does not change significantly the magnitudes of the first neighbor coupling constants but reduces the error by around 1 order of magnitude, becoming smaller than 0.01 cm⁻¹ in the case of the hybrid functional. Such results are reported with three decimals to show the accuracy reached in the fitting procedure even if it is probably beyond their physical accuracy. (ii) The convergence of the *J* values with the number of configurations is faster and smoother than when only first-neighbor interactions are considered. (iii) In the case of the PBE functional, the errors are larger than those obtained with the hybrid functional. (iv) The PBE functional gives a higher value of the *J*₆ coupling constants when next-nearest neighbor interactions are considered, becoming closer to the B3LYP results. (v) Only in the case of *J*₇ is the value of the next-nearest neighbor coupling constant significant, which should be attributed to the presence of a direct interaction through an anti-syn carboxylato bridging ligand³⁶ between the two metals (see Figure 1). (vi) All other next-nearest neighbor interactions show a very weak antiferromagnetic coupling with the exception of *J*₁₂, which is practically negligible.

Quantum Monte Carlo Simulations. In order to verify the applicability of the calculated *J* values, we wish to compare the experimental magnetic susceptibility curve with

Table 3. Exchange Coupling Constants (cm^{-1}) for $[\text{Mn}^{\text{II}}_6\text{Mn}^{\text{II}}_6(\text{O}_2\text{CMe})_{14}(\text{mda})_8]^{30,31}$ Including the Next-Nearest Neighbor Interactions (see Figures 2 and 4) Calculated with the PBE and B3LYP Functionals Using Different Sets of n Spin Configurations^a

n	PBE				
	12	13	16	24	32
J_1	-12.00	-11.98 (10)	-11.96 (10)	-11.94 (8)	-11.95 (5)
J_2	-15.54	-15.50 (9)	-15.46 (9)	-15.51 (9)	-15.60 (5)
J_3	+5.87	+5.88 (8)	+5.88 (10)	+5.90 (9)	+5.83 (5)
J_4	+7.83	+7.80 (8)	+7.82 (9)	+7.94 (8)	+7.90 (5)
J_5	-7.37	-7.46 (10)	-7.37 (7)	-7.40 (7)	-7.34 (4)
J_6	-3.38	-3.28 (10)	-3.22 (8)	-3.21 (9)	-3.29 (4)
J_7	-1.96	-1.95 (7)	-1.90 (6)	-1.90 (6)	-1.94 (2)
J_8	-0.19	-0.05 (13)	-0.02 (11)	-0.02 (8)	-0.10 (5)
J_9	-0.72	-0.76 (6)	-0.74 (7)	-0.78 (6)	-0.77 (4)
J_{10}	-0.35	-0.43 (7)	-0.41 (8)	-0.49 (7)	-0.44 (4)
J_{11}	-0.79	-0.78 (5)	-0.77 (5)	-0.75 (5)	-0.77 (4)
J_{12}	+0.06	+0.06 (8)	+0.13 (5)	+0.16 (6)	+0.18 (4)

n	B3LYP				
	12	13	16	24	32
J_1	-4.321	-4.320 (4)	-4.319 (6)	-4.316 (9)	-4.313 (6)
J_2	-6.858	-6.856 (4)	-6.853 (6)	-6.856 (9)	-6.876 (7)
J_3	+4.283	+4.283 (4)	+4.283 (6)	+4.269 (9)	+4.288 (7)
J_4	+5.071	+5.069 (3)	+5.067 (5)	+5.062 (8)	+5.076 (7)
J_5	-2.425	-2.429 (5)	-2.436 (6)	-2.448 (7)	-2.456 (6)
J_6	-7.917	-7.913 (5)	-7.907 (6)	-7.910 (9)	-7.907 (5)
J_7	-0.710	-0.709 (3)	-0.709 (3)	-0.709 (6)	-0.707 (3)
J_8	-0.015	-0.009 (6)	-0.000 (7)	+0.006 (8)	-0.001 (7)
J_9	-0.340	-0.342 (3)	-0.345 (4)	-0.351 (7)	-0.336 (6)
J_{10}	-0.135	-0.139 (3)	-0.143 (4)	-0.136 (7)	-0.145 (6)
J_{11}	-0.277	-0.276 (2)	-0.274 (3)	-0.273 (5)	-0.267 (5)
J_{12}	+0.000	+0.000 (3)	-0.000 (5)	-0.007 (6)	-0.008 (6)

^a The number in parentheses indicates the standard deviation of the least-squares fitting.

that obtained from those calculated parameters. Since the large size of the Hamiltonian matrix prevents the exact diagonalization or the use of the Lanczos algorithm³⁷ on the whole matrix, we have employed quantum Monte Carlo simulations (see Computational Details) using the calculated J values obtained with the two available crystal structures using only first-neighbor interactions and the largest set of spin configurations (see Table 2). There are two relatively similar experimental curves (see Figure 5) that were obtained by fitting an $S = 8$ ground state^{30,31} (white squares) or an $S = 7$ value (white circles).³² Our results are in good agreement with the experimental data (especially those obtained with the B3LYP functional) for the decay region below 150 K where the PBE functional gives a too fast drop due to the higher J_2 antiferromagnetic value. We have employed a $g = 2$ value for the quantum Monte Carlo simulations. However, using $g = 1.95$ close to the $g = 1.91$ obtained from the fitting by Rumberger et al.,³² our simulation matches almost perfectly the experimental curve.

From the shape of the magnetic susceptibility curves, it is not easy to conclude which is the total spin of the ground state; however, the theoretical results clearly indicate the presence of an $S = 7$ single-determinant ground state with an $S = 9$ excited-state very close in energy.

Conclusions

The exchange coupling constants calculated using methods based on density functional theory provide an accurate

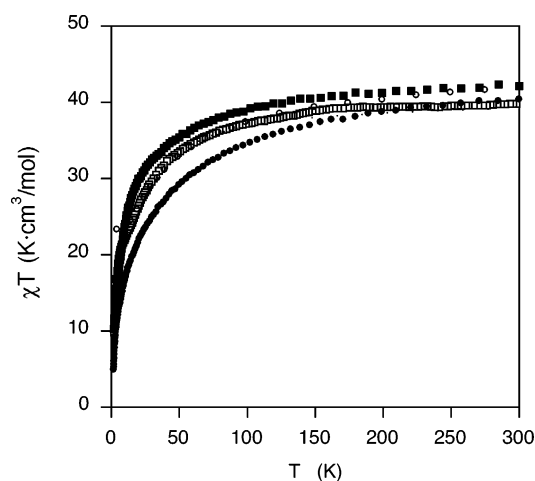


Figure 5. Temperature dependence of the magnetic susceptibility of the Mn_{12} complex, two experimental curves (white squares^{30,31} and circles³²), and from quantum Monte Carlo simulations using the coupling constants calculated with the PBE (black circles) and B3LYP (black squares) functionals (see Computational Details).

description of the available experimental magnetic properties of the studied loop Mn_{12} complex. Thus, the calculated exchange coupling constants using the hybrid B3LYP functional for the two experimental crystal structures predict an $S = 7$ single-determinant ground state in good agreement with the $S = 7$ and 8 values proposed experimentally.

The use of numerical calculations with the PBE functional gives fair results in general, although the weakest exchange coupling constant (J_6) calculated for one of the crystal structures has a wrong positive sign. The use of quantum Monte Carlo simulations indicates that the calculated exchange coupling constants using the B3LYP functional and a Gaussian basis set reproduce nicely the experimental curve with a better agreement than the PBE functional combined with a numerical basis set.

We have also analyzed the effect of the choice of the spin configurations for the calculation of the exchange coupling constants showing that the values obtained are practically independent of the number of spin configurations employed. The calculated errors are similar for all the interactions independently of their value, and such errors are larger for the numerical PBE results than for the B3LYP method using Gaussian functions as a basis set. The inclusion of next-nearest neighbor interactions reduces the errors in the exchange coupling constants by about one order of magnitude, while the values corresponding to the first-neighbor coupling constants remain practically unchanged. The convergence of the calculated J values with the number of spin configurations is faster and smoother than when only first-neighbor interactions are considered. The next-nearest neighbor interactions correspond usually to very weak antiferromagnetic coupling with the exception of J_7 , which corresponds to an interaction through a syn-anti carboxylato bridging ligand between the two metals.

Computational Details

In our calculations, we have employed the experimental structures³² due to the large dependence of the magnetic

Table 4. Spin Configurations Employed in the Calculations Sorted by Energy, with Exception of the First 12 Configurations That Were Selected to Have a Solvable System of Equations, with Their Total Spin Value^a

	atoms with down spin	S		atoms with down spin	S
sd0	Mn2, Mn4, Mn8, Mn10	7	sd17	Mn2, Mn4, Mn7, Mn10	8
sd1	Mn2, Mn4, Mn9, Mn11	9	sd18	Mn1, Mn4, Mn7, Mn9, Mn11, Mn12	1
sd2	Mn2, Mn4, Mn7, Mn8, Mn10	3	sd19	Mn2, Mn3, Mn5, Mn6, Mn7, Mn10	0
sd3	Mn2, Mn4, Mn9, Mn11, Mn12	4	sd20	Mn4, Mn10	17
sd4	Mn2, Mn4, Mn7, Mn9, Mn10	4	sd21	Mn1, Mn2, Mn4, Mn7, Mn10	4
sd5	Mn2, Mn4, Mn6, Mn7, Mn9, Mn11	0	sd22	Mn3, Mn9	19
sd6	Mn2, Mn4, Mn10	12	sd23	Mn2, Mn8	17
sd7	Mn3, Mn5, Mn6, Mn7, Mn10	5	sd24	Mn2, Mn4, Mn7, Mn10, Mn12	3
sd8	Mn2, Mn4, Mn6, Mn8, Mn10	2	sd25	Mn1, Mn4, Mn6, Mn7, Mn10	4
sd9	Mn2, Mn4, Mn8	12	sd26	Mn2, Mn3, Mn5, Mn7, Mn10	5
sd10	Mn2, Mn4, Mn5, Mn8, Mn10	3	sd27	Mn1, Mn4, Mn7, Mn10	9
sd11	Mn2, Mn3, Mn4, Mn8, Mn10	3	sd28	Mn2, Mn3	18
sd12	Mn2, Mn4, Mn7, Mn9	9	sd29	Mn5, Mn11	19
sd13	Mn2, Mn4, Mn7, Mn9, Mn11	5	sd30	–	27
sd14	Mn2, Mn5, Mn6, Mn7, Mn10	4	sd31	Mn1, Mn7	19
sd15	Mn2, Mn4, Mn7, Mn9, Mn11, Mn12	0	sd32	Mn6, Mn12	17
sd16	Mn2, Mn3, Mn5, Mn8, Mn10	4			

^a Mn^{III} and Mn^{II} cations correspond to odd and even numbers, respectively.

properties with structural parameters, and very small variations in the geometry such as those induced by packing forces can produce large changes in the calculated exchange coupling constants.^{18,38} The calculations with the B3LYP functional³⁹ were performed with the NWChem code (version 4.7)^{40,41} and a guess function generated with the Jaguar 6.0 code.⁴² The triple- ζ all-electron Gaussian basis set proposed by Schaefer et al. was employed.⁴³ The NWChem calculations were carried out in parallel using 256 processors in a JS21 cluster at the Barcelona Supercomputer Center.

The SIESTA program (Spanish Initiative for Electronic Simulations with Thousands of Atoms)^{44–47} was employed with the GGA exchange-correlation functional proposed by Perdew, Burke, and Ernzerhof (PBE).⁴⁸ We have selected values of 50 meV for the energy shift and 200 Ry for mesh cutoff that provide a good compromise between accuracy and computer time needed to calculate the exchange coupling constants.^{49,50} Only external electrons are included in the calculations, the cores being replaced by norm-conserving scalar relativistic pseudopotentials factorized in the Kleinman–Bylander form.⁵¹ These pseudopotentials are generated following the approach proposed by Trouiller and Martins⁵² from the ground-state atomic configurations for all the atoms except for Mn, for which the Mn^{II} configuration [Ne]3s²-3p⁶4s⁰3d⁵ was employed. The core radii for the s, p, and d components of the Mn atoms are 1.4, 1.9, and 1.5, respectively, and we have included partial-core corrections for a better description of the core regions.⁵³ The cutoff radii were 1.15 for oxygen, nitrogen, and hydrogen atoms; 1.25 for carbon; and 1.6 for chlorine atoms.

The spin configurations adopted for the [Mn^{III}₆Mn^{II}₆(O₂-CMe)₁₄(mda)₈] complex in order to obtain the exchange coupling constants are collected in Table 4.

Due to the impossibility to perform the exact diagonalization of the Hamiltonian matrix because of its huge size, we have employed quantum Monte Carlo simulations that allow the treatment of quantum spin systems.⁵⁴ Among them, we have employed the decoupled cell Monte Carlo method proposed by Homma et al.^{55,56} The basic idea of such simulations is to perform the exact diagonalization only for a small subsystem, the decoupled cell. The conditional probability of a spin placed in the center of the subsystem

being up or down is obtained from these exact diagonalization procedures, then it is possible to construct a Markov chain of a quantum system by using the Metropolis algorithm as in the classical Monte Carlo approach. In this case, we have employed a cell considering five atoms including, in such a way, the interactions of the central atom with first and next-nearest neighbors. In general, the quality of such quantum methods will depend on the size of the cell employed in the calculation of the probabilities, being hypothetically exact when the whole system is considered. We have employed successfully these kinds of simulations previously in single-molecule magnets, for instance, in an Fe₈ complex.⁵⁷ The simulations reproduce correctly the results of the exact diagonalization of the Hamiltonian down to relatively low temperatures.

Acknowledgment. The research reported here was supported by the Dirección General de Investigación del Ministerio de Educación y Ciencia and Comissió Interdepartamental de Ciència i Tecnologia (CIRIT) through grants CTQ2005-08123-C02-02/BQU and 2005SGR-00036, respectively. The authors thankfully acknowledge the computer resources, technical expertise, and assistance provided by the Barcelona Supercomputing Center (Centro Nacional de Supercomputación). R.C. thanks the Ministerio de Educación y Ciencia for a Mobility Program grant to cover his stay in Barcelona.

References

- (1) Miller, J. S.; Drillon, M. *Magnetism: Molecules to Materials*; Wiley-VCH: Weinheim, Germany, 2001–2005; Vol. 1–5.
- (2) Aromí, G.; Brechin, E. *Struct. Bonding* **2006**, *122*, 1.
- (3) Christou, G. *Polyhedron* **2005**, *24*, 2065.
- (4) Caneschi, A.; Gatteschi, D.; Sessoli, R.; Barra, A. L.; Brunel, L. C.; Guillot, M. *J. Am. Chem. Soc.* **1991**, *113*, 5873.
- (5) Friedman, J. R.; Sarachik, M. P.; Tejada, J.; Ziolo, R. *Phys. Rev. Lett.* **1996**, *76*, 3830.
- (6) Thomas, L.; Lioni, F.; Ballou, R.; Sessoli, R.; Gatteschi, D.; Barbara, B. *Nature (London, U.K.)* **1996**, *383*, 145.
- (7) Sessoli, R.; Gatteschi, D. *Angew. Chem., Int. Ed.* **2003**, *42*, 246.
- (8) Gatteschi, D.; Sessoli, R.; Villain, J. *Molecular Nanomagnets*; Oxford University Press: Oxford, U. K., 2006.

- (9) Pederson, M. R.; Khanna, S. N. *Phys. Rev. B: Condens. Matter Mater. Phys.* **1999**, *60*, 9566.
- (10) Kortus, J.; Pederson, M. R.; Baruah, T.; Bernstein, N.; Hellberg, C. S. *Polyhedron* **2003**, *22*, 1871.
- (11) Pederson, M. R.; Bernstein, N.; Kortus, J. *Phys. Rev. Lett.* **2002**, *89*, 097202/1.
- (12) Pederson, M. R.; Porezag, D. V.; Kortus, J.; Khanna, S. N. *J. Appl. Phys.* **2000**, *87*, 5487.
- (13) Ruiz, E. *Struct. Bonding* **2004**, *113*, 71.
- (14) Gatteschi, D. *J. Phys. Chem. B* **2001**, *104*, 9780.
- (15) Goursot, A.; Malrieu, J. P.; Salahub, D. R. *Theor. Chim. Acta* **1995**, *91*, 225.
- (16) Castro, M.; Salahub, D. R. *Phys. Rev. B: Condens. Matter Mater. Phys.* **1993**, *47*, 10955.
- (17) Postnikov, A. V.; Kortus, J.; Pederson, M. R. *Phys. Status Solidi B* **2006**, *243*, 2533.
- (18) Ruiz, E.; Alemany, P.; Alvarez, S.; Cano, J. *J. Am. Chem. Soc.* **1997**, *119*, 1297.
- (19) Ruiz, E.; Alvarez, S.; Rodríguez-Fortea, A.; Alemany, P.; Pouillon, Y.; Massobrio, C. Electronic Structure and Magnetic Behavior in Polynuclear Transition-Metal Compounds. In *Magnetism: Molecules to Materials*; Miller, J. S., Drillon, M., Eds.; Wiley-VCH: Weinheim, Germany, 2001; Vol. 2, pp 227–279.
- (20) Ruiz, E.; Cano, J.; Alvarez, S.; Caneschi, A.; Gatteschi, D. *J. Am. Chem. Soc.* **2003**, *125*, 6791.
- (21) Boukhvalov, D. W.; Al-Saqer, M.; Kurmaev, E. Z.; Moewes, A.; Galakhov, V. R.; Finkelstein, L. D.; Chiuzaibaian, S.; Neumann, M.; Dobrovitski, V. V.; Katsnelson, M. I.; Lichtenstein, A. I.; Harmon, B. N.; Endo, K.; North, J. M.; Dalal, N. S. *Phys. Rev. B: Condens. Matter Mater. Phys.* **2007**, *75*, 014419.
- (22) Boukhvalov, D. W.; Lichtenstein, A. I.; Dobrovitski, V. V.; Katsnelson, M. I.; Harmon, B. N.; Mazurenko, V. V.; Anisimov, V. I. *Phys. Rev. B: Condens. Matter Mater. Phys.* **2002**, *65*, 184435.
- (23) Park, K.; Pederson, M. R. *Phys. Rev. B: Condens. Matter Mater. Phys.* **2004**, *70*, 054414.
- (24) Park, K.; Pederson, M. R.; Hellberg, C. S. *Phys. Rev. B: Condens. Matter Mater. Phys.* **2004**, *69*, 014416.
- (25) Ruiz, E.; Cano, J.; Alvarez, S.; Alemany, P. *J. Comput. Chem.* **1999**, *20*, 1391.
- (26) Ruiz, E.; Rodríguez-Fortea, A.; Cano, J.; Alvarez, S.; Alemany, P. *J. Comput. Chem.* **2003**, *24*, 982.
- (27) Ruiz, E.; Alvarez, S.; Cano, J.; Polo, V. *J. Chem. Phys.* **2005**, *123*, 164110.
- (28) Bencini, A.; Totti, F. *Int. J. Quantum Chem.* **2005**, *101*, 819.
- (29) Moreira, I. d. P. R.; Calzado, C. J.; Malrieu, J. P.; Illas, F. *Phys. Rev. Lett.* **2006**, *97*, 087003.
- (30) Rumberger, E. M.; Zakharov, L. N.; Rheingold, A. L.; Hendrickson, D. N. *Inorg. Chem.* **2004**, *43*, 6531.
- (31) Rumberger, E. M.; Zakharov, L. N.; Rheingold, A. L.; Hendrickson, D. N. *Inorg. Chem.* **2005**, *44*, 2742.
- (32) Foguet-Albiol, D.; O'Brien, T. A.; Wernsdorfer, W.; Moulton, B.; Zaworotko, M. J.; Abboud, K. A.; Christou, G. *Angew. Chem., Int. Ed.* **2005**, *44*, 897.
- (33) Que, L.; True, A. E. *Prog. Inorg. Chem.* **1990**, *38*, 97.
- (34) Cano, J.; Ruiz, E.; Alvarez, S.; Verdaguier, M. *Comments Inorg. Chem.* **1998**, *20*, 27.
- (35) Ruiz, E.; Cirera, J.; Alvarez, S. *Coord. Chem. Rev.* **2005**, *249*, 2649.
- (36) Rodríguez-Fortea, A.; Alemany, P.; Alvarez, S.; Ruiz, E. *Chem.—Eur. J.* **2001**, *7*, 627.
- (37) Rajaraman, G.; Ruiz, E.; Cano, J.; Alvarez, S. *Chem. Phys. Lett.* **2005**, *415*, 6.
- (38) Ruiz, E.; Cano, J.; Alvarez, S.; Alemany, P. *J. Am. Chem. Soc.* **1998**, *120*, 11122.
- (39) Becke, A. D. *J. Chem. Phys.* **1993**, *98*, 5648.
- (40) Kendall, R. A.; Apra, E.; Bernholdt, D. E.; Bylaska, E. J.; Dupuis, M.; Fann, G. I.; Harrison, R. J.; Ju, J. L.; Nichols, J. A.; Nieplocha, J.; Straatsma, T. P.; Windus, T. L.; Wong, A. T. *Comput. Phys. Commun.* **2000**, *128*, 260.
- (41) Aprà, E.; Windus, T. L.; Straatsma, T. P.; Bylaska, E. J.; de Jong, W.; Hirata, S.; Valiev, M.; Hackler, M.; Pollack, L.; Kowalski, K.; Harrison, R.; Dupuis, M.; Smith, D. M. A.; Nieplocha, J. V. T.; Krishnan, M.; Auer, A. A.; Brown, E.; Cisneros, G.; Fann, G.; Fruchtl, H.; Garza, J.; Hirao, K.; Kendall, R.; Nichols, J.; Tsemekhman, K.; Wolinski, K.; Anchell, J.; Bernholdt, D.; Borowski, P.; Clark, T.; Clerc, D.; Dachsel, H.; Deegan, M.; Dylla, K.; Elwood, D.; Glendening, E.; Gutowski, M.; Hess, A.; Jaffe, J.; Johnson, B.; Ju, J.; Kobayashi, R.; Kutteh, R.; Lin, Z.; Littlefield, R.; Long, X.; Meng, B.; Nakajima, T.; Niu, S.; Rosing, M.; Sandrone, G.; Stave, M.; Taylor, H.; Thomas, G.; van Lenthe, J.; Wong, A.; Zhang, Z. *NWChem, A Computational Chemistry Package for Parallel Computers*, Version 4.7; Pacific Northwest National Laboratory: Richland, WA, 2005.
- (42) *Jaguar 6.0*; Schrödinger, Inc.: Portland, OR, 2005.
- (43) Schaefer, A.; Huber, C.; Ahlrichs, R. *J. Chem. Phys.* **1994**, *100*, 5829.
- (44) Artacho, E.; Gale, J. D.; García, A.; Junquera, J.; Martin, R. M.; Ordejón, P.; Sánchez-Portal, D.; Soler, J. M. *SIESTA*, v.1.3; Siesta: Madrid, Spain, 2001.
- (45) Soler, J. M.; Artacho, E.; Gale, J. D.; García, A.; Junquera, J.; Ordejón, P.; Sánchez-Portal, D. *J. Phys.: Condens. Matter* **2002**, *14*, 2745.
- (46) Artacho, E.; Sánchez-Portal, D.; Ordejón, P.; García, A.; Soler, J. M. *Phys. Status Solidi A* **1999**, *215*, 809.
- (47) Sánchez-Portal, D.; Ordejón, P.; Artacho, E.; Soler, J. M. *Int. J. Quantum Chem.* **1997**, *65*, 453.
- (48) Perdew, J.; Burke, K.; Ernzerhof, M. *Phys. Rev. Lett.* **1996**, *77*, 3865.
- (49) Massobrio, C.; Ruiz, E. *Monatsh. Chem.* **2003**, *134*, 317.
- (50) Ruiz, E.; Rodríguez-Fortea, A.; Tercero, J.; Cauchy, T.; Massobrio, C. *J. Chem. Phys.* **2005**, *123*, 074102.
- (51) Kleinman, L.; Bylander, D. M. *Phys. Rev. Lett.* **1982**, *48*, 1425.
- (52) Trouiller, N.; Martins, J. L. *Phys. Rev. B: Condens. Matter Mater. Phys.* **1991**, *43*, 1993.
- (53) Louie, S. G.; Froyen, S.; Cohen, M. L. *Phys. Rev. B: Condens. Matter Mater. Phys.* **1982**, *26*, 1982.
- (54) Suzuki, M. *Quantum Monte Carlo Methods*; Springer-Verlag: Berlin 1987; Springer Series in Solid-State Science Vol. 74.
- (55) Homma, S.; Matsuda, H.; Ogita, N. *Prog. Theor. Phys.* **1986**, *75*, 1058.
- (56) Homma, S. The Decoupled Cell Method of Quantum Monte Carlo Calculation. In *Quantum Monte Carlo Methods in Condensed Matter Physics*; Suzuki, M., Ed.; World Scientific Publishing Co. Pte. Ltd.: Singapore, 1993; pp 163–177.
- (57) Ruiz, E.; Cano, J.; Alvarez, S. *Chem.—Eur. J.* **2005**, *11*, 4767.

JCTC Journal of Chemical Theory and Computation

DFT Method Estimation of Standard Redox Potential of Metal Ions and Metal Complexes[†]

Yoshiki Shimodaira,[‡] Toshiko Miura,[§] Akihiko Kudo,[‡] and Hisayoshi Kobayashi^{*,§}

Department of Applied Chemistry, Faculty of Science, Science University of Tokyo, 1-3 Kagurazaka, Shinjuku-ku, Tokyo 162-8601, Japan, and Department of Chemistry and Materials Technology, Kyoto Institute of Technology, Matsugasaki, Kyoto 606-8585, Japan

Received January 13, 2007

Abstract: The DFT method calculation was carried out to evaluate standard redox potential (SRP) for metal-to-metal cation and metal-to-metal complex systems. With the Born–Haber cycle, standard redox potential was composed of the cohesive energy, ionization energy, and solvation energy. The ligand exchange energy was added in case of metal complex. The solvent effects were incorporated by the self-consistent reaction field theory at the level of the polarized continuum model (PCM). At the highest level of calculations, the geometry optimization and harmonic frequency analysis were evaluated under the PCM. Utilizing experimental values of the cohesive energy of metals, the standard deviations between the calculated and experimental SRP values were 0.20–0.27 V depending on the calculation levels and basis sets used. For three Ag complexes with CN[−], S₂O₃^{2−}, and NH₃ ligands, the discrepancy was within 0.3 V.

Introduction

Although the standard redox potential (SRP) determining the equilibrium between bulk metal and metal ion or metal complex is the most fundamental quantity in electrochemistry, computational chemistry approach has not been carried out so far. The SRP corresponds to a process in which a metal ion begins to be deposited on the solid metal electrode soaking in acid solution and to be reduced. However, it is easily anticipated that many factors relating adsorption and coordination of solvent molecules to metal surfaces and to metal ions influence the process in a complicated manner. In recent years, quantum chemical methodology for the solution chemistry has developed.^{1–3} Techniques managing solvent as continuum models have been established and incorporated in many molecular orbital (MO) and density functional theory (DFT) method programs. It means that new approaches on electrochemistry become possible. A straightforward application is evaluation of solvation free energy,

and many papers have been published so far.^{4–8} Baik and Friesner estimated the redox potentials for organic molecules and metal complexes.⁹ Undsemaa and Tamm calculated the redox potentials for oxidation number change of transition-metal ions.¹⁰ They also presented the structure of hydration spheres.

In this study, we try to evaluate the SRP for 21 metal ions (metal aqueous complexes) such as Li⁺, K⁺, Ca²⁺, Na⁺, Mg²⁺, Al³⁺, Ti²⁺, Mn²⁺, Zn²⁺, Cr³⁺, Fe²⁺, Co²⁺, Ni²⁺, Fe³⁺, Cu²⁺, Cu⁺, Ag⁺, Pd²⁺, Pt²⁺, Au³⁺, and Au⁺ in the increasing order of experimental SRP values¹¹ and three Ag complexes with nonaqueous ligands, [Ag(NH₃)₂]⁺, [Ag(CN)₂][−], and [Ag(S₂O₃)₂]^{3−}, based on the DFT calculations. The redox potentials for the oxidation number change of a transition-metal complex, such as [Fe(CN)]^{3−} + e[−] → [Fe(CN)]^{4−}, have been reported by other researches.^{9,10} Those calculations require only the isolated complexes. However, for silver complexes, the oxidation number becomes zero when reduced. So some device is necessary, and our approach is applicable for this case.

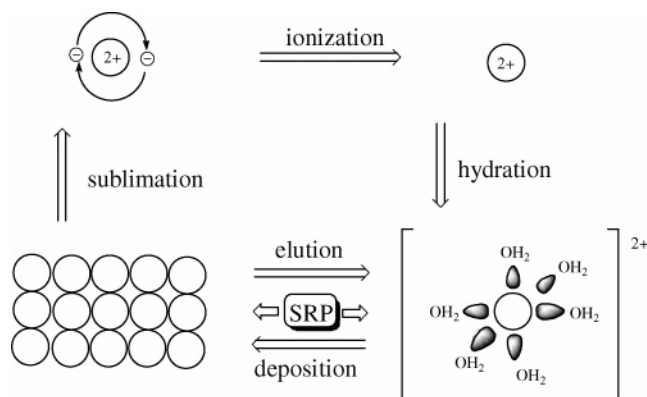
To get an image of change of states easily, we consider the opposite direction of the process, i.e., the process from solid metal to hydrated metal ion. This process is partitioned into the three processes utilizing the Born–Haber cycle

[†] Dedicated to Professor Dennis R. Salahub on the occasion of his 60th birthday.

* Corresponding author e-mail: kobayashi@chem.kit.ac.jp.

[‡] Science University of Tokyo.

[§] Kyoto Institute of Technology.

Scheme 1. Born–Haber Cycle and SRP Process

(Scheme 1): (1) sublimation or cohesion to atoms from solid, (2) ionization of atoms, and (3) formation of a hydrated complex from the bare ion and water molecules. For the case of the metal-to-metal complex, (4) the ligand exchange process is added. The SRPs are estimated as the sum of energy changes for the three or four processes. The usefulness of our approach has been demonstrated in a preliminary report.¹²

Method of Calculation and Models

Equation 1 shows the energy change from bulk metal to hydrated metal ion shown in Scheme 1.

$$\Delta\epsilon = \epsilon_{\text{cohe}}^{\text{expt}} + \epsilon_{\text{ion}} + \epsilon_{\text{hydra}} (+ \epsilon_{\text{li-ex}}) \quad (1)$$

The first term on the right-hand side $\epsilon_{\text{cohe}}^{\text{expt}}$ is the sublimation process from solid to gas. This quantity is equivalent to the cohesive energy, which could be evaluated as an energy difference between a bulk solid and an isolated atom if band calculation is carried out. Since the other processes are able to be evaluated within a molecular model, and the purpose of the present work is not to evaluate the cohesive energy precisely, experimental values of the cohesive energy are employed.¹³ The second term ϵ_{ion} and the third term ϵ_{hydra} on the right-hand side are ionization energy and hydration energy, respectively. The present method is also applied to Ag complexes with nonaqueous ligands. Then the fourth term $\epsilon_{\text{li-ex}}$ representing the ligand exchange energy is added.

There are two approaches to estimate the ionization energy. One is to calculate the energy difference between a neutral atom and its cation (so-called ΔSCF method), as shown in eq 2a, using the same functional and basis set as the rest of the calculation (e.g., hydration energy). In another approach, experimental values of the ionization energy are employed as shown in eq 2b. These are referred to as theoretical and experimental estimation of ionization energies.

$$\epsilon_{\text{ion}} = \epsilon[\text{M}^{n+}] - \epsilon[\text{M}^0] \quad (2a)$$

$$\epsilon_{\text{ion}} = \epsilon_{\text{ion}}^{\text{expt}} \quad (2b)$$

$$\epsilon_{\text{hydra}} = \epsilon[\text{M}(\text{OH}_2)_6^{n+}] - \epsilon[\text{M}^{n+}] - \epsilon[6\text{H}_2\text{O}] \quad (3)$$

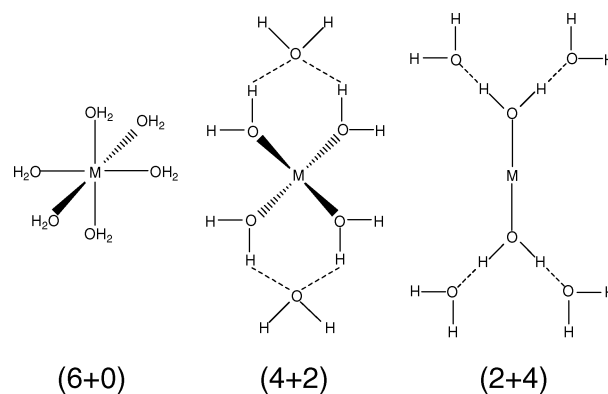


Figure 1. Schematic illustration of three aqueous metal complexes. Six coordination octahedral structure, four coordination tetrahedral structure with two water molecules in the second coordination shell, and two coordination linear structure with four water molecules in the second coordination shell. Their coordination modes are abbreviated as (6 + 0), (4 + 2), and (2 + 4), respectively.

The hydration energy is expressed in eq 3. In this calculation, six water molecules are arranged around the metal cation, and the hydration energy is the difference between the energy of an aqueous metal complex and the sum of energies of a bare cation and an aqueous cluster composed of six water molecules. Three types of coordination modes of aqueous complexes are considered as shown in Figure 1: (1) six coordination octahedral structure, (2) four coordination tetrahedral structure with two water molecules in the second coordination shell, and (3) two coordination linear structure with four water molecules in the second coordination shell. Their coordination modes are abbreviated as (6 + 0), (4 + 2), and (2 + 4), respectively. The two or four water molecules in the second coordination shell have no realistic evidence. However the use of (4 + 2) and (2 + 4) modes rather than (4 + 0) and (2 + 0) modes can restrict the reference system to $6\text{H}_2\text{O}$ only. For individual metals, the most stable configuration is determined by optimizing the three coordination modes of an aqueous complex in gas-phase and then by recalculating their total energies in solution.

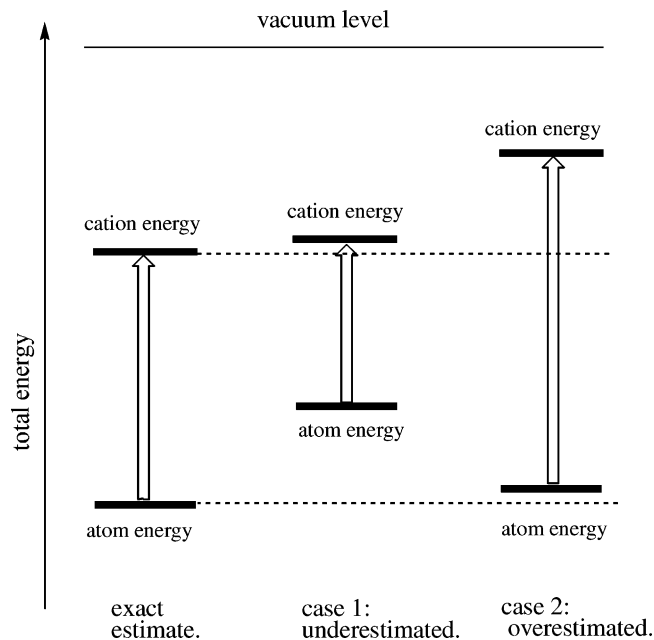
$$\Delta\epsilon = \epsilon_{\text{cohe}}^{\text{expt}} + \epsilon_{\text{ion}} + \epsilon_{\text{hydra}}$$

$$= \epsilon_{\text{cohe}}^{\text{expt}} + (\epsilon[\text{M}^{n+}] - \epsilon[\text{M}^0]) + (\epsilon[\text{M}(\text{OH}_2)_6^{n+}] - \epsilon[\text{M}^{n+}] - \epsilon[6\text{H}_2\text{O}]) \quad (4a)$$

$$= \epsilon_{\text{cohe}}^{\text{expt}} - \epsilon[\text{M}^0] + \epsilon[\text{M}(\text{OH}_2)_6^{n+}] - \epsilon[6\text{H}_2\text{O}]$$

$$\Delta\epsilon = \epsilon_{\text{cohe}}^{\text{expt}} + \epsilon_{\text{ion}}^{\text{expt}} + \epsilon[\text{M}(\text{OH}_2)_6^{n+}] - \epsilon[\text{M}^{n+}] - \epsilon[6\text{H}_2\text{O}] \quad (4b)$$

The total energy change is expressed in eqs 4a or 4b, depending on the estimation of the ionization energy. In the theoretical estimation scheme (eq 4a), the energy of the metal ion appears twice in the opposite sign, and these terms are canceled. Only the energy of the metal atom is left in the final equation. On the other hand, only the energy of the

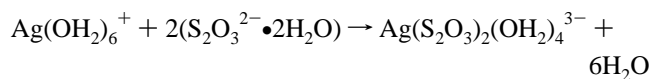
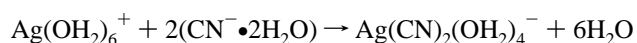
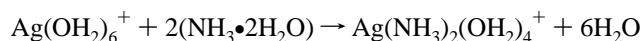
Scheme 2. Origin of Errors in Ionization Energy Calculation

metal cation appears in eq 4b. We adopt both the estimation schemes mixed. This reasoning is discussed below.

One origin of numerical errors comes from the inaccuracy in the total energies of metal atom and cation. This situation is illustrated in Scheme 2. Because of the variational principle, the energy levels for atoms and cations are never calculated deeper than their exact energy levels. It means that the errors are classified into two cases. In case 1, underestimation of the ionization energy suggests that the energy of atom is evaluated more poorly (higher in energy). In case 2, overestimation of the ionization energy suggests that the energy of cation is evaluated too much upward. The cation energy and atom energy are relatively more reliable in case 1 and case 2, respectively, and therefore the adoption of the experimental estimation scheme for case 1 (since it depends on the cation energy only) and the adoption of theoretical estimation schemes for case 2 (since it depends on the atom energy only) reduce the numerical errors.

Electronic configurations and spin multiplicities for the ground state of atoms are referred to in a book by Karplus and Porter.¹⁴ For transition metals, spin multiplicities for cations are estimated by considering that the outer s electrons are removed first and then the d electrons. For the electronic configurations of metal atoms and cations, the electron populations among the three p orbitals and the five d orbitals should be equal if the spherical symmetry is conserved. In the present work, no restriction is imposed. So the obtained electron density does not satisfy exactly the spherical symmetry, but their energies are adopted intact.

For Ag complexes with nonaqueous ligands, the ligand exchange reactions are written individually by the following chemical equations, in terms of the hydrated complex and the hydrated ligand molecules or ions.



The ligand exchange energy is evaluated by eq 5, where $n = 0, 1,$ and 2 for $L = \text{NH}_3, \text{CN}^-,$ and $\text{S}_2\text{O}_3^{2-},$ respectively. Equations 4a and 4b are modified to eqs 6a and 6b.

$$\epsilon_{\text{li-ex}} = \epsilon[\text{AgL}_2(\text{OH}_2)_4^{(1-2n)}] + \epsilon[6\text{H}_2\text{O}] - \epsilon[\text{Ag}(\text{OH}_2)_6^+] - 2\epsilon[L^{n-} \cdot 2\text{H}_2\text{O}] \quad (5)$$

$$\Delta\epsilon = \epsilon_{\text{cohe}}^{\text{expt}} + \epsilon_{\text{ion}} + \epsilon_{\text{hydra}} + \epsilon_{\text{li-ex}} = \epsilon_{\text{cohe}}^{\text{expt}} - \epsilon[\text{M}^0] + \epsilon[\text{M}(\text{OH}_2)_6^{n+}] - \epsilon[6\text{H}_2\text{O}] + \epsilon_{\text{li-ex}} \quad (6a)$$

$$\Delta\epsilon = \epsilon_{\text{cohe}}^{\text{expt}} + \epsilon_{\text{ion}}^{\text{expt}} + \epsilon[\text{M}(\text{OH}_2)_6^{n+}] - \epsilon[\text{M}^{n+}] - \epsilon[6\text{H}_2\text{O}] + \epsilon_{\text{li-ex}} \quad (6b)$$

The solvent effects are taken into consideration in an indirect manner, that is, by the self-consistent reaction field method at the level of the polarized continuum model (PCM).¹⁻³ All the species except for the isolated metal atom M^0 and the metal ion M^{n+} appearing in eqs 2a to 6b are evaluated in solution.

There are three levels of calculation. The lowest level is that optimization is carried out in gas-phase and the optimized geometry is used for the PCM calculation without further optimization. We refer to this level of calculation as method-Hv. “H” means enthalpy, which is equal to the SCF energy if the change of volume is ignored. “v” represents that the geometry is optimized in “vacuum”.

In the second level of calculation, the geometry is optimized under the PCM, and the corresponding label is method-Hp. “p” represents PCM. In the highest level of calculation, the geometry optimization is the same as the second level, i.e., under the PCM, and furthermore the harmonic frequency is calculated under the PCM to consider the zero point energy and the vibrational contribution of entropy. Small correction from translation and rotation contribution is estimated by the classical approximation. With the PCM, the harmonic frequency is evaluated by the calculus of finite difference of the energy gradient since the analytical second energy derivative is not available. This level of calculation is labeled as method-G, where “G” means the Gibbs free energy. In method-G, the thermal correction is also considered for free atoms and cations. We have the gas-phase results too, but we will not show them since they are far from experimental results. In the present model, electrons released from atoms are assumed to go away from the system, and the charging-up effects of electrodes are not considered.

According to the text book of physical chemistry or electrochemistry, the SRP or the standard hydrogen electrode (SHE) potential E_{SHE} is related to the free energy change $\Delta\epsilon$ by eq 7, where $\Delta\epsilon$ is represented in “eV” unit, and ν is the number of electrons transferred to cation. The absolute potential value for hydrogen electrode (4.43 V) is taken from the paper by Reiss and Heller.¹⁵

$$E_{\text{SHE}} = \left(\frac{\Delta\epsilon}{\nu|e|} - 4.43 \right) \quad (7)$$

All the calculation is carried out with Gaussian 03 program package.¹⁶ The Becke three-parameter Lee–Yang–Parr hybrid functionals are employed.^{17–20} Two types of basis sets are used, i.e., all-electron 6-311G(d,p) and the Los Alamos model core potential (MCP).^{21,22} Both basis sets have their limits of application. The all-electron 6-311G(d,p) basis is not applicable to the second and third row transition elements, and we treated 16 ions, Li⁺, K⁺, Ca²⁺, Na⁺, Mg²⁺, Al³⁺, Ti²⁺, Mn²⁺, Zn²⁺, Cr³⁺, Fe²⁺, Co²⁺, Ni²⁺, Fe³⁺, Cu²⁺, and Cu⁺ with this basis set. On the other hand, the MCP basis is not applicable to Li⁺, Na⁺, Mg²⁺, and Al³⁺ ions because of no valence electrons, and we applied the MCP basis to the following 17 ions, K⁺, Ca²⁺, Ti²⁺, Mn²⁺, Zn²⁺, Cr³⁺, Fe²⁺, Co²⁺, Ni²⁺, Fe³⁺, Cu²⁺, Cu⁺, Ag⁺, Pd²⁺, Pt²⁺, Au³⁺, and Au⁺. Several ions are dealt with by the both basis sets and could be compared to each other.

Results and Discussion

1. Isolated Ligand Systems. The optimized structures of water cluster 6H₂O, and three ligand–water clusters 2(NH₃•2H₂O), 2(CN[−]•2H₂O), and S₂O₃^{2−}•2H₂O are shown in Figure 2. All four structures are optimized in gas-phase or under the PCM depending on the methods. Except for 2(S₂O₃^{2−}•2H₂O), the whole structures 6H₂O, 2(NH₃•2H₂O), and 2(CN[−]•2H₂O) are optimized, and their energies are used. However, the whole structure 2(S₂O₃^{2−}•2H₂O) could not be optimized. It separates into the two subunits S₂O₃^{2−}•2H₂O probably due to the strong electrostatic repulsion between them, even in the PCM calculation. Then the optimization is carried out with the single subunit, and the energy is doubled to estimate that for 2(S₂O₃^{2−}•2H₂O).

2. SRPs for 21 Metal Ions. For 21 metal ions examined, three configurations of aqueous complexes are optimized in gas-phase, and then the energies of configurations are recalculated under the PCM. The most stable configuration is selected, and its energy is used to evaluate the SRP with methods-Hv. For methods-Hp and -G, the structure is optimized again under the PCM. Table 1 shows the spin multiplicity for atom and cation, the experimental values of cohesive energy and ionization energy, the most stable configuration of aqueous complex, and the experimental SRP value. The spin multiplicity and stable configuration are common to all the calculations. We consulted three experimental SRP values referred to as refs 7a–c. References 7a and 7b are almost the same, but that from ref 7c deviates from the former two to some degree. So the value from ref 7b is adopted as the reference experimental SRP value and cited in Table 1.

Table 2 shows the results of all-electron calculation for the 16 metals. It contains the hydration energy, (calculated) ionization energy, and SRP values with their deviations from the experimental value (Δ SRP), for the three methods. For Mn²⁺, Zn²⁺, Cr³⁺, Fe²⁺, Co²⁺, Ni²⁺, Cu²⁺, and Cu⁺, the ionization energies are underestimated, and the experimental ionization energy is employed. For other ions, the calculated ionization energy is employed. The largest discrepancy is

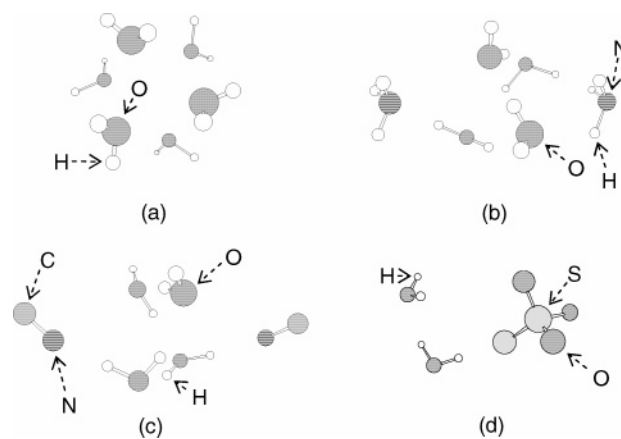


Figure 2. Optimized structures for water cluster and three ligand–water clusters with the lowest total energies: (a) 6H₂O, (b) 2(NH₃•2H₂O), (c) 2(CN[−]•2H₂O), and (d) S₂O₃^{2−}•2H₂O.

Table 1. Name of Ion, Multiplicity of Atom and Ion, Experimental Cohesive Energy, Experimental Ionization Energy, Most Stable Configuration, and Experimental SRP Value

ion name	multiplicity ^a	cohesive energy ^b	ioniza. energy ^c	configuration ^d	exptl SRP value ^e
Li ⁺	2→1	1.63	5.392	4 + 2	−3.045
K ⁺	2→1	0.934	4.341	4 + 2	−2.925
Ca ²⁺	1→1	1.84	17.984	6 + 0	−2.84
Na ⁺	2→1	1.113	5.139	4 + 2	−2.714
Mg ²⁺	1→1	1.51	22.681	6 + 0	−2.356
Al ³⁺	2→1	3.39	53.261	6 + 0	−1.676
Ti ²⁺	3→3	4.85	20.40	6 + 0	−1.63
Mn ²⁺	6→6	2.92	23.075	6 + 0	−1.18
Zn ²⁺	1→1	1.35	27.358	6 + 0	−0.7626
Cr ³⁺	7→4	4.10	54.226	6 + 0	(−0.740) ^f
Fe ²⁺	5→5	4.28	24.05	6 + 0	−0.440
Co ²⁺	4→4	4.39	24.96	6 + 0	−0.277
Ni ²⁺	3→3	4.44	25.803	6 + 0	−0.257
Fe ³⁺	5→6	4.28	54.701	6 + 0	(−0.037) ^g
Cu ²⁺	2→2	3.49	28.018	6 + 0	0.340
Cu ⁺	2→1	3.49	7.726	2 + 4	0.520
Ag ⁺	2→1	2.95	7.576	2 + 4	0.7991
Pd ²⁺	1→1	3.89	27.77	4 + 2	0.915
Pt ²⁺	3→1	5.84	27.563	4 + 2	1.188
Au ³⁺	2→1	3.81	9.225	4 + 2	1.52
Au ⁺	2→1	3.81	9.225	2 + 4	1.83

^a “M–N” means that the spin multiplicity for atom is *M* and that of cation is *N*. ^b Cohesive energy is taken from ref 9, and the unit is eV. ^c Experimental ionization energy taken from ref 7c, and the unit is eV. ^d Configuration symbols “6 + 0”, “4 + 2”, and “2 + 4” mean that number of H₂O molecules in the first coordination shell is 6, 4, and 2, respectively. ^e Cited from ref 7b. Unit is V. ^f Estimated from the two reaction, Cr²⁺ + 2e[−] = Cr and Cr³⁺ + e[−] = Cr²⁺. ^g Estimated from the two reaction, Fe²⁺ + 2e[−] = Fe and Fe³⁺ + e[−] = Fe²⁺.

found for Cu⁺ throughout the three methods. The next ones are Al³⁺, K⁺, Li⁺ and Co²⁺, and their relative magnitude of deviation is changing depending on the methods. Raising the calculation level to method-Hp and method-G, the magnitude of discrepancy are almost the same. The standard deviation for the 16 metals is 0.20–0.22 V.

Table 3 shows the results of MCP calculation such as the hydration energy, ionization energy, and SRP with Δ SRP

Table 2. Name of Ion, Hydration Energy, Ionization Energy, SRP Values, and their Differences from Experimental Values Calculated with an All-Electron Basis Set^a

ion	hydra. energy	ioniza. energy ^b	method-Hv		method-Hp		method-G	
			SRP	Δ SRP	SRP	Δ SRP	SRP	Δ SRP
Li ⁺	-6.12	5.62	-3.31	-0.26	-3.36	-0.31	-3.23	-0.19
K ⁺	-3.65	4.50	-2.65	0.27	-2.74	0.18	-2.67	0.25
Ca ²⁺	-16.88	18.24	-2.83	0.01	-2.88	-0.04	-3.00	-0.16
Na ⁺	-4.78	5.42	-2.68	0.04	-2.80	-0.08	-2.70	0.01
Mg ²⁺	-20.51	23.19	-2.34	0.02	-2.38	-0.03	-2.38	-0.03
Al ³⁺	-48.02	53.92	-1.33	0.34	-1.39	0.29	-1.29	0.39
Ti ²⁺	-19.41	20.50	-1.46	0.17	-1.52	0.11	-1.59	0.04
Mn ²⁺	-19.50	23.06	-1.18	-0.00	-1.23	-0.05	-1.28	-0.10
Zn ²⁺	-21.45	27.13	-0.80	-0.04	-0.84	-0.08	-0.81	-0.05
Cr ³⁺	-46.96	53.96	-0.64	0.10	-0.70	0.05	-0.64	0.10
Fe ²⁺	-20.51	24.00	-0.52	-0.08	-0.57	-0.13	-0.58	-0.14
Co ²⁺	-21.54	24.87	-0.52	-0.25	-0.58	-0.30	-0.54	-0.26
Ni ²⁺	-22.07	25.66	-0.34	-0.08	-0.39	-0.13	-0.32	-0.06
Fe ³⁺	-45.90	55.39	0.16	0.20	0.11	0.14	0.14	0.18
Cu ²⁺	-22.00	26.36	0.32	-0.02	0.28	-0.06	0.29	-0.05
Cu ⁺	-6.75	7.18	0.04	-0.48	-0.17	-0.69	-0.11	-0.63
StDev				0.20		0.22		0.22

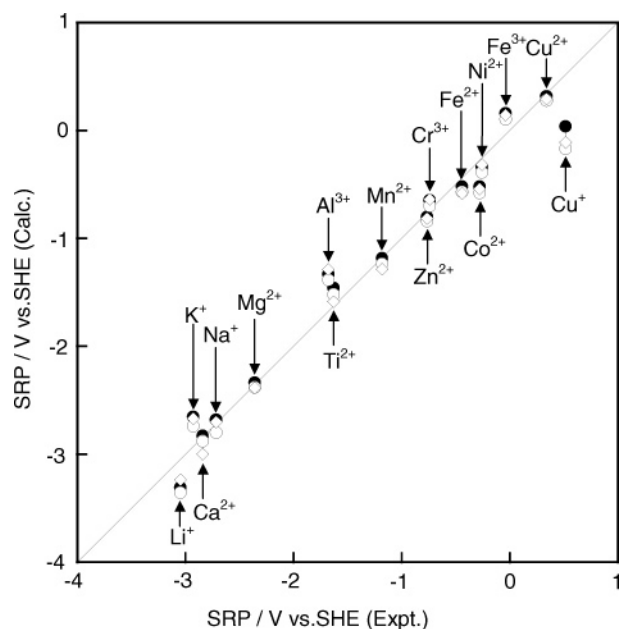
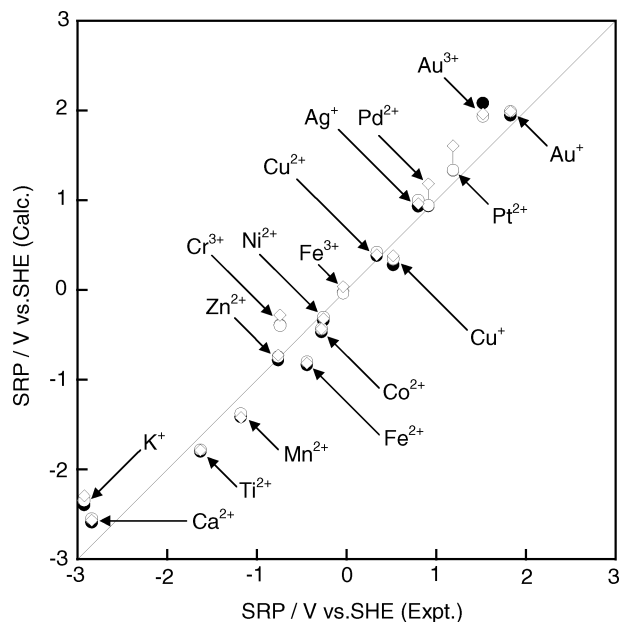
^a Units for hydration and ionization energies are in eV, and units for SRP and Δ SRP are in V. ^b For Mn²⁺, Zn²⁺, Cr³⁺, Fe²⁺, Co²⁺, Ni²⁺, Cu²⁺, and Cu⁺, calculated ionization energies (italicized) underestimate experimental ionization energy, and the SRP (and also Δ SRP) is evaluated using the experimental ionization energy.

Table 3. Name of Ion, Hydration Energy, Ionization Energy, SRP Values, and their Differences from Experimental Values Calculated with the MCP Basis Set^a

ion	hydra. energy	ioniza. energy ^b	method-Hv		method-Hp		method-G	
			SRP	Δ SRP	SRP	Δ SRP	SRP	Δ SRP
K ⁺	-3.34	4.44	-2.39	0.53	-2.34	0.59	-2.29	0.63
Ca ²⁺	-16.36	18.21	-2.59	0.26	-2.55	0.32	-2.57	0.27
Ti ²⁺	-20.15	20.57	-1.80	-0.17	-1.78	-0.15	-1.78	-0.15
Mn ²⁺	-20.06	23.18	-1.41	-0.23	-1.38	-0.19	-1.42	-0.24
Zn ²⁺	-21.40	26.38	-0.78	-0.02	-0.74	0.02	-0.72	0.04
Cr ³⁺	-48.72	56.74	-0.39	0.35	-0.39	0.35	-0.28	0.46
Fe ²⁺	-21.13	23.89	-0.83	-0.39	-0.80	-0.36	-0.82	-0.38
Co ²⁺	-22.11	25.65	-0.47	-0.19	-0.43	-0.16	-0.43	-0.16
Ni ²⁺	-22.63	26.37	-0.34	-0.08	-0.30	-0.05	-0.32	-0.06
Fe ³⁺	-47.17	56.09	-0.03	0.01	-0.04	-0.00	0.04	0.07
Cu ²⁺	-22.46	28.60	0.39	0.05	0.42	0.08	0.39	0.05
Cu ⁺	-6.61	7.83	0.28	-0.24	0.35	-0.17	0.38	-0.14
Ag ⁺	-5.34	7.75	0.93	0.13	1.00	0.20	0.96	0.16
Pd ²⁺	-23.93	30.78	0.94	0.02	0.94	0.03	1.18	0.27
Pt ²⁺	-24.74	30.43	1.34	0.15	1.34	0.15	1.61	0.42
Au ³⁺	-50.30	66.03	2.09	0.57	1.93	0.41	1.96	0.44
Au ⁺	-6.86	9.42	1.94	0.11	1.99	0.16	1.99	0.16
StDev				0.23		0.23		0.27

^a Units for hydration and ionization energies are in eV, and units for SRP and Δ SRP are in V. ^b For Zn²⁺ and Fe²⁺, calculated ionization energies (italicized) underestimate experimental ionization energy, and the SRP (and also Δ SRP) is evaluated using the experimental ionization energy.

values evaluated by the three methods for the 17 metals. For Zn²⁺ and Fe²⁺, the ionization energies are underestimated, and the experimental ionization energies are used. Throughout the three methods, the largest discrepancy is seen for

**Figure 3.** Correlation between three levels of calculated SRP and experimental SRP for 16 metal ions calculated with all-electron basis. Full circle, open circle, and open square represent values by methods-Hv, -Hp, and -G, respectively.**Figure 4.** Correlation between three levels of calculated SRP and experimental SRP for 17 metal ions calculated with MCP basis. Full circle, open circle, and open square represent values by methods-Hv, -Hp, and -G, respectively.

Au³⁺, K⁺, and next Fe²⁺ and Cr³⁺. In method-G, the agreement becomes worse even for Pt²⁺. Thus the standard deviations are 0.23, 0.23, and 0.27 V for methods-Hv, -Hp, and -G, respectively.

Figures 3 and 4 show correlation relation between the calculated SRPs and the experimental SRP's. In the order of methods-Hv, -Hp, and -G, the computational cost increases, and the accuracy of calculated results is expected to be improved. Although the discrepancy is decreased for some ions, the overall consistency is not improved. Baik and

Table 4. Energy Components To Evaluate SRP for Ag Complexes^{a,b}

ligand	2(L ⁿ⁻ •2H ₂ O)	AgL ₂ (OH ₂) ₄ ⁽¹⁻²ⁿ⁾	ε _{li-ex}	SRP (calc)	SRP (expt)
NH ₃ ; n = 0	-418.9058	-564.5968	-0.571	0.361	0.373
CN ⁻ ; n = 1	-491.6624	-637.3890	-1.538	-0.607	-0.310
S ₂ O ₃ ²⁻ ; n = 2	-797.7425	-943.4578	-1.157	-0.225	-0.017

^a Units for 2(Lⁿ⁻•2H₂O) and AgL₂(OH₂)₄⁽¹⁻²ⁿ⁾ are hartree (au), the unit for ε_{li-ex} is eV, and those for SRP(calc) and SRP(expt) are V. ^b Aqueous complex, Ag(OH₂)₆⁺, and water cluster, 6H₂O, are those used in the present work and common to three systems. Their energies are -604.3313 au and -458.6612 au, respectively. The sum of cohesive, ionization, and hydration energies for Ag, ε_{cohe}^{expt} + ε_{ion} + ε_{hydra}, is taken from Table 3 and 5.36 eV.

Friesner also stated on this point.⁹ In their words, there is another source of entropy such as reorientation of solvents, which is not taken into account by the vibrational analysis of solute. Unfortunately, cancellation of errors occurs, and the three methods afford the almost same results for the all-electron calculation, and methods-Hv and -Hp give better results than method-G for the MCP calculation.

3. SRPs for Three Ag Complexes. The ligand exchange reactions are dealt with at the level of method-Hv. The energies of aqueous complex and water cluster are same as those used in the previous section. The structures of three Ag complexes, Ag(NH₃)₂(OH₂)₄⁺, Ag(CN)₂(OH₂)₄⁻, and Ag(S₂O₃)₂(OH₂)₄³⁻, where nonaqueous ligands occupy the trans position, are optimized in gas-phase, and then the energies are re-evaluated with the PCM. Several configurations for the ligand-water complexes are examined with the PCM, and the most stable configuration with the lowest energy is adopted as the reference, which is shown in Figure 2(b)-(d).

Table 4 shows the energies for ligand-water complex and Ag complex. Using these energies and the energies of aqueous complex and water cluster, the ligand exchange energy, ε_{li-ex}, is evaluated. Adding ε_{li-ex} to the sum of cohesive, ionization, and hydration energies, ε_{cohe}^{expt} + ε_{ion} + ε_{hydra}, taken from Tables 1 and 3, the SRP is obtained after converting the energy to the electrochemical potential according to eq 7. For [Ag(CN)₂(OH₂)₄]⁻ and [Ag(S₂O₃)₂(OH₂)₄]³⁻, the discrepancy is smaller than 0.3 V, and an excellent agreement is obtained for [Ag(NH₃)₂(OH₂)₄]⁺.

Conclusion

In this work, for the first time we presented the theoretical estimation of SRP concerning the process from bulk metal to metal ion and metal complex. The 21 metal ions and three Ag complexes were examined. Throughout the three levels of calculations, Cu⁺ and Al³⁺ ions and K⁺ and Au³⁺ ions indicated the worst agreement with the experimental data for the all-electron and MCP basis sets, respectively. The ill-tempered nature of Cu⁺ was much improved for the MCP calculation. These ill-tempered ions increased the standard deviation and lowered the whole quality of calculations, although the agreement was given within 0.2 V, i.e., 4.6 kcal/mol for 11 and 10 ions with the all-electron and MCP basis

sets, respectively, in method-Hv. Except for method-G with the MCP basis set, the standard deviations were in the range of 0.20–0.23, and these are fairly good values. Although there is room to be improved, such as accurate evaluation of ionization energy and entropy contribution, it is a kind of surprise that we have reproduced the SRP by the DFT calculation based on a very simple idea, i.e., the Born-Harber cycle. In future works, detailed parts of the PCM parameter such as volume size should be optimized as well as a more careful selection of the exchange correlation functionals.

Acknowledgment. This work was supported by the grants from the Ministry of Education, Culture, Sports, Science and Technology of Japan (No. 17560684). The authors are grateful for their undergraduate students, Takuya Nakagawa, Toshitaka Tanaka, and Fumiaki Matsumiya, for their efforts for computer operation and graphical drawing.

References

- (1) (a) Miertus, S.; Scrocco, E.; Tomasi, J. *Chem. Phys.* **1981**, *55*, 117. (b) Miertus, S.; Tomasi, J. *Chem. Phys.* **1982**, *65*, 239.
- (2) Friedrichs, M.; Zhou, R.; Edinger, S. R.; Friesner, R. A. *J. Phys. Chem. B* **1999**, *103*, 3057.
- (3) Cossi, M.; Scalmani, G.; Rega, N.; Barone, V. *J. Chem. Phys.* **2002**, *117*, 43.
- (4) Edinger, S. R.; Cortis, C.; Shenkin, P. S.; Friesner, R. A. *J. Phys. Chem. B* **1997**, *101*, 1190.
- (5) Kubicki, J. D. *J. Phys. Chem. A* **2001**, *105*, 8756.
- (6) Liptak, M. D.; Gross, K. C.; Seybold, P. G.; Feldgus, S.; Shields, G. C. *J. Am. Chem. Soc.* **2002**, *124*, 6421.
- (7) Han, W.-G.; Liu, T.; Lovell, T.; Noodleman, L. *Inorg. Chem.* **2006**, *45*, 8533.
- (8) Abreu, A. H. D.; Guimarães, L.; Duarte, H. A. *J. Phys. Chem. A* **2006**, *110*, 7713.
- (9) Baik, M.-H.; Friesner, R. A. *J. Phys. Chem. A* **2002**, *106*, 7407.
- (10) Undsemaa, M.; Tamm, T. *J. Phys. Chem. A* **2003**, *107*, 9997.
- (11) (a) Bard, A. J.; Faulkner, L. R. In *Electrochemical Methods, Fundamentals and Applications*, 2nd ed.; John Wiley & Sons: U.S.A., 2001; pp 808–810. (b) In *Kagaku-binran*; Kiso-hen, II, Eds.; Chemical Society of Japan: Maruzen, Japan, 1984; pp 466–468. (c) In *CRC Handbook of Chemistry and Physics*, 66th ed.; Weast, R. C., Eds.; CRC Press: U.S.A., 1986; pp D-151–158.
- (12) Kobayashi, H.; Miura, T.; Shimodaira, Y.; Kudo, A. *Chem. Lett.* **2004**, *33*, 1176.
- (13) Kittel, C., In *Introduction to Solid State Physics*, 8th ed.; John Wiley & Sons: U.S.A., 2005; p 50.
- (14) Karplus, M.; Porter, R. N. In *Atoms and Molecules*; W. A. Benjamin: U.S.A., 1970; pp 202–207.
- (15) Reiss, H.; Heller, A. *J. Phys. Chem.* **1985**, *89*, 4207.
- (16) Frisch, M. J.; Trucks, G. W.; Schlegel, H. B.; Scuseria, G. E.; Robb, M. A.; Cheeseman, J. R.; Montgomery, J. A., Jr.; Vreven, T.; Kudin, K. N.; Burant, J. C.; Millam, J. M.; Iyengar, S. S.; Tomasi, J.; Barone, V.; Mennucci, B.; Cossi, M.; Scalmani, G.; Rega, N.; Petersson, G. A.; Nakatsuji, H.;

Hada, M.; Ehara, M.; Toyota, K.; Fukuda, R.; Hasegawa, J.; Ishida, M.; Nakajima, T.; Honda, Y.; Kitao, O.; Nakai, H.; Klene, M.; Li, X.; Knox, J. E.; Hratchian, H. P.; Cross, J. B.; Adamo, C.; Jaramillo, J.; Gomperts, R.; Stratmann, R. E.; Yazyev, O.; Austin, A. J.; Cammi, R.; Pomelli, C.; Ochterski, J. W.; Ayala, P. Y.; Morokuma, K.; Voth, G. A.; Salvador, P.; Dannenberg, J. J.; Zakrzewski, V. G.; Dapprich, S.; Daniels, A. D.; Strain, M. C.; Farkas, O.; Malick, D. K.; Rabuck, A. D.; Raghavachari, K.; Foresman, J. B.; Ortiz, J. V.; Cui, Q.; Baboul, A. G.; Clifford, S.; Cioslowski, J.; Stefanov, B. B.; Liu, G.; Liashenko, A.; Piskorz, P.; Komaromi, I.; Martin, R. L.; Fox, D. J.; Keith, T.; Al-Laham, M. A.; Peng, C. Y.; Nanayakkara, A.; Challacombe, M.; Gill, P. M. W.; Johnson, B.; Chen, W.; Wong, M. W.; Gonzalez, C.; Pople, J. A. *Gaussian 03, Revision B.03*; Gaussian, Inc.: Pittsburgh, PA, 2003.

- (17) Becke, A. D. *Phys. Rev. A* **1988**, *38*, 3098.
- (18) Lee, C.; Yang, W.; Parr, R. G. *Phys. Rev. B* **1988**, *37*, 785.
- (19) Becke, A. D. *J. Chem. Phys.* **1993**, *98*, 1372.
- (20) Gill, P. M. W.; Johnson, B. G.; Pople, J. A. *Int. J. Quantum Chem. Symp.* **1992**, *26*, 319.
- (21) Hay, P. J.; Wadt, W. R. *J. Chem. Phys.* **1985**, *82*, 270; **1985**, *82*, 299.
- (22) Dunning, T. H. J.; Hay, P. J. In *Modern Theoretical Chemistry*; Schaefer, H. F., III, Ed.; Plenum Press: New York, 1976; pp 1–35.

CT700015T

High-Density Limit of Two-Electron Systems: Results from the Extended Overhauser Approach†

Paola Gori-Giorgi* and Andreas Savin

Laboratoire de Chimie Théorique, CNRS UMR7616, Université Pierre et Marie Curie, 4 Place Jussieu, F-75252 Paris, France

Received January 15, 2007

Abstract: The “extended Overhauser model” [Overhauser, A. W. *Can. J. Phys.* **1995**, *73*, 683] for the calculation of the spherically and system-averaged pair density (APD) has been recently combined with the Kohn–Sham equations to yield realistic APD and correlation energies. In this work we test this approach in the high-density (weakly correlated) limit of the He isoelectronic series and of the Hooke’s atom isoelectronic series. Unlike many of the commonly used energy functionals, the Overhauser approach yields accurate correlation energies for both series.

1. Introduction

Kohn–Sham (KS) Density Functional Theory^{1–3} (DFT) is nowadays one of the most popular methods for electronic structure calculations both in chemistry and solid-state physics, thanks to its combination of low computational cost and reasonable performances. The accuracy of a KS-DFT result is limited by the approximate nature of the exchange–correlation energy density functional $E_{xc}[n]$. Simple approximations (local-density approximation and generalized gradient corrections) for $E_{xc}[n]$ provide practical estimates of thermodynamical, structural, and spectroscopic properties of atoms, molecules, and solids. However, with the current approximations, KS-DFT is still lacking in several aspects, in particular it fails to handle near-degeneracy correlation effects (rearrangement of electrons within partially filled shells) and to recover long-range van der Waals interaction energies. The inaccuracy of KS-DFT stems from our lack of knowledge of $E_{xc}[n]$, and much effort is put nowadays in finding new approximations to this term (for recent reviews, see, e.g., refs 2–4). A popular trend in the development of new KS $E_{xc}[n]$ is the use of the exact exchange functional $E_x[n]$ (in terms of the KS orbitals) and thus the search for an approximate, compatible, correlation functional $E_c[n]$.

An exact expression for $E_c[n]$ is the coupling-constant integral^{5–8}

$$E_c[n] = \int_0^{\lambda_{\text{phys}}} d\lambda \int_0^\infty dr_{12} 4\pi r_{12}^2 f_c^\lambda(r_{12}) \frac{\partial w^\lambda(r_{12})}{\partial \lambda} \quad (1)$$

where the interaction between the electrons is adiabatically turned on from $w^{\lambda=0}(r_{12}) = 0$ to the Coulomb repulsion $w^{\lambda=\lambda_{\text{phys}}}(r_{12}) = 1/r_{12}$ by varying a real parameter λ (typical examples are $w^\lambda(r_{12}) = \lambda/r_{12}$, with $\lambda_{\text{phys}} = 1$, or $w^\lambda(r_{12}) = \text{erf}(\lambda r_{12})/r_{12}$, with $\lambda_{\text{phys}} = \infty$). The one-electron density $n(\mathbf{r})$ is (ideally) kept independent of λ and equal to the one of the physical system by means of a suitable external potential $v^\lambda(\mathbf{r})$. In eq 1 the correlation part of the spherically and system-averaged pair density (intracule density) $f_c^\lambda(r_{12})$ is defined as follows. For each λ , take the square of the many-electron wavefunction Ψ^λ ground state of the Hamiltonian H^λ

$$H^\lambda = - \sum_{i=1}^N \frac{\nabla_i^2}{2} + \frac{1}{2} \sum_{i \neq j=1}^N w^\lambda(|\mathbf{r}_i - \mathbf{r}_j|) + \sum_{i=1}^N v^\lambda(\mathbf{r}_i) \quad (2)$$

and integrate it over all variables except the scalar electron–electron distance $r_{12} = |\mathbf{r}_1 - \mathbf{r}_2|$

$$f_c^\lambda(r_{12}) = \frac{N(N-1)}{2} \sum_{\sigma_1 \dots \sigma_N} \int |\Psi^\lambda(\mathbf{r}_{12}, \mathbf{R}, \mathbf{r}_3, \dots, \mathbf{r}_N)|^2 \frac{d\Omega_{\mathbf{r}_{12}}}{4\pi} d\mathbf{R} d\mathbf{r}_3 \dots d\mathbf{r}_N \quad (3)$$

where $\mathbf{R} = (\mathbf{r}_1 + \mathbf{r}_2)/2$. The correlation part $f_c^\lambda(r_{12})$ is then defined as $f_c^\lambda(r_{12}) = f^\lambda(r_{12}) - f_{\text{KS}}(r_{12})$, where the intracule

† Dedicated to Professor Dennis R. Salahub on the occasion of his 60th birthday.

* Corresponding author e-mail: gori@lct.jussieu.fr.

density of the KS system is $f_{\text{KS}}(r_{12}) = f^{\lambda=0}(r_{12})$ (and yields the Hartree plus the exchange energy).

The traditional DFT approach to the construction of approximate $E_c[n]$ is based on the idea of universality. For example, the familiar local-density approximation (LDA) consists of transferring, in each point of space, the pair density from the uniform electron gas to obtain an approximation for $f_c^\lambda(r_{12})$ in eq 1. In a couple of recent papers,^{9–11} we have started to explore a different way of constructing $E_c[n]$, based on an “average pair density functional theory” (APDFT), which was inspired by the seminal work of Overhauser¹² and its subsequent extensions.^{13–16} In this approach, we solve a set of radial (one-dimensional) Schrödinger-like equations that give, in principle, the exact $f^\lambda(r_{12})$ along the DFT adiabatic connection. In practice, this formalism contains an unknown effective electron–electron interaction that needs to be approximated. The APDFT equations must be solved for each system and combined self-consistently with the KS equations.¹¹ Preliminary applications of this approach, combined with a simple approximation⁹ for the effective electron–electron interaction that enters in the formalism, gave accurate intracule densities $f(r_{12})$ and correlation energies $E_c[n]$ for the He isoelectronic series.^{9,11}

Katriel et al.¹⁷ have recently tested most of the currently available correlation energy functionals in the high-density (weakly correlated) limit of the He and of the Hooke’s atom isoelectronic series, finding that, while several functionals are accurate for the He sequence, none is satisfactory for the Hooke’s atom series. Motivated by their findings, in this work we compute the correlation energy and the intracule density in the high-density limit of the two series via the APDFT approach,^{9–11} finding accurate results in both cases.

The paper is organized as follows. In the next section, section 2, we recall the basic equations that define the high-density limit of the He and Hooke’s atom sequences, to which we apply, in sections 3 and 4, the formalism of refs 9–11 to compute the intracule density and the correlation energy. In section 5 we also analyze the failure of LDA in this limit from the point of view of $f(r_{12})$. The last section, section 6, is devoted to conclusions.

2. The High-Density Limit of the He and Hooke’s Atom Isoelectronic Series

The two Hamiltonians analyzed in this paper read

$$H = -\frac{\nabla_1^2}{2} - \frac{\nabla_2^2}{2} + v(r_1) + v(r_2) + \frac{1}{r_{12}}$$

$$v(r) = \begin{cases} -\frac{Z}{r} & \text{He series} \\ \frac{1}{2}kr^2 & \text{Hooke’s atom series} \end{cases} \quad (4)$$

We are interested in the high-density (weakly correlated) limit, which corresponds to $Z \rightarrow \infty$ and $k \rightarrow \infty$. By switching to scaled coordinates $\mathbf{s} = \mathbf{r}/\alpha$, with $\alpha = Z^{-1}$ (He series) and

$\alpha = k^{-1/4}$ (Hooke’s series), both Hamiltonians have the form

$$H = \frac{1}{\alpha^2} \left(-\frac{\nabla_{s_1}^2}{2} - \frac{\nabla_{s_2}^2}{2} + \tilde{v}(s_1) + \tilde{v}(s_2) + \frac{\alpha}{s_{12}} \right) \equiv \frac{1}{\alpha^2} (\tilde{H}_0 + \alpha \tilde{H}_1) \quad (5)$$

where $\tilde{v}(s) = -1/s$ for the He series, and $\tilde{v}(s) = s^2/2$ for the Hooke’s atom series. We thus study perturbatively the system described by $\tilde{H}_0 + \alpha \tilde{H}_1$.

The order zero of the one-electron density $n(r)$ and of the intracule density $f(r_{12})$, in scaled units, is simply

$$n^{(0)}(s) = \begin{cases} \frac{2}{\pi} e^{-2s} & \text{(He)} \\ \frac{2}{\pi^{3/2}} e^{-s^2} & \text{(Hooke)} \end{cases} \quad (6)$$

$$f^{(0)}(s_{12}) = \begin{cases} \frac{1}{24\pi} (3 + 6s_{12} + 4s_{12}^2) e^{-2s_{12}} & \text{(He)} \\ \frac{1}{(2\pi)^{3/2}} e^{-s_{12}^2/2} & \text{(Hooke)} \end{cases} \quad (7)$$

These functions are correctly normalized, so that if we switch back to coordinates \mathbf{r} we have $n^{(0)}(r) = \alpha^{-3} n^{(0)}(s = \alpha^{-1}r)$, etc.

The first-order correction to the scaled density, $n(s) = n^{(0)}(s) + \alpha n^{(1)}(s) + \dots$ is given by

$$n^{(1)}(s) = 2n^{(0)}(s)\chi(s) \quad (8)$$

where¹⁸

$$\chi(s) = -\frac{23}{32} - \frac{e^{-2s}}{4} - \frac{3}{8}\gamma + \frac{3}{16} \frac{1 - e^{-2s}}{s} + \frac{5}{8}s + \frac{3}{8} \text{Ei}(-2s) - \frac{3}{8} \ln(s) \quad (9)$$

for the He isoelectronic series, with $\gamma = 0.577216 \dots$,

$$\text{Ei}(-x) = -\int_x^\infty \frac{e^{-t}}{t} dt \quad (10)$$

and^{19,20}

$$\chi(s) = \frac{\text{erf}(s)}{s} - \frac{\sqrt{2}(1 + \ln 2)}{\sqrt{\pi}} - \frac{1}{s\sqrt{\pi}} \int_0^\infty dx (e^{-(x-s)^2} - e^{-(x+s)^2}) \times \left[e^{x^2/2} \text{erfc}\left(\frac{x}{\sqrt{2}}\right) + \sqrt{2}x \int_0^{x/\sqrt{2}} dt e^{t^2} \text{erfc}(t) \right] \quad (11)$$

for the Hooke’s atom isoelectronic series.

By definition, the Kohn–Sham Hamiltonian describes a noninteracting system that has the same density of the physical, interacting system. Thus, the first-order change in the electron density of eq 8 corresponds to a first-order change in the KS system. Therefore, we write the scaled intracule $f(s_{12})$ up to orders α as

$$f(s_{12}) = f^{(0)}(s_{12}) + \alpha [f_{\text{KS}}^{(1)}(s_{12}) + f_c^{(1)}(s_{12})] + O(\alpha^2) \quad (12)$$

where we have separated the first-order correction into a Kohn–Sham part and a correlation part. The KS part $f_{\text{KS}}^{(1)}$ is

entirely determined by the first-order density $n^{(1)}$ of eq 8

$$f_{\text{KS}}^{(1)}(s_{12}) = \int ds n^{(0)}(s + s_{12})n^{(0)}(s)\chi(s) \quad (13)$$

and is reported in Appendix A in analytic form for the He isoelectronic series, while it is obtained numerically for the case of the Hooke's series.

The total first-order intracule $f^{(1)} = f_{\text{KS}}^{(1)} + f_c^{(1)}$ is known analytically in the case of the Hooke's series^{19,20}

$$f^{(1)}(s_{12}) = \frac{2e^{-s_{12}^{2/4}}}{(2\pi)^{3/4}} \left[1 - \frac{1 + \ln 2}{\sqrt{2\pi}} + \frac{1}{s_{12}} - \frac{e^{s_{12}^{2/2}}}{s_{12}} \operatorname{erfc}\left(\frac{s_{12}}{\sqrt{2}}\right) + \sqrt{2} \int_0^{s_{12}/\sqrt{2}} e^{t^2} \operatorname{erfc}(t) dt \right] \quad (14)$$

3. Effective Equations for $f(r_{12})$ in the High-Density Limit

3.1. Formalism. We are interested in calculating $f_c^{(1)}$ and the corresponding second-order correlation energy $E_c^{(2)}$ with the method of refs 9–11, in which the intracule density $f(r_{12})$ of the physical system is obtained from a set of effective equations, which for two-electron systems reduce to

$$[-\nabla_{r_{12}}^2 + w_{\text{eff}}(r_{12})]\psi(r_{12}) = \epsilon\psi(r_{12}) \quad (15)$$

with $f(r_{12}) = |\psi(r_{12})|^2$. Equation 15 can be derived by considering^{10,11} a set of Hamiltonians characterized by a real parameter ξ

$$H^\xi = -\sum_{i=1}^N \frac{\nabla_i^2}{2} + \frac{1}{2} \sum_{i \neq j=1}^N w^\xi(|\mathbf{r}_i - \mathbf{r}_j|) + \xi \sum_{i=1}^N v_{ne}(\mathbf{r}_i), \quad f^\xi(r_{12}) = f(r_{12}) \forall \xi \quad (16)$$

that describe a set of systems in which the external potential is turned off as $\xi \rightarrow 0$, and the intracule density is kept fixed, equal to the one of the physical system, by means of a suitable electron–electron interaction $w^\xi(r_{12})$. In the case $N = 2$, when $\xi = 0$ we have a translationally invariant system (the center-of-mass degree of freedom is described by a plane wave) of two fermions in a relative bound state (similar to the case of positronium but with a different interaction). This relative bound state is such that the square of the wavefunction for the relative coordinate r_{12} is equal to $f(r_{12})$ of the starting physical system and is thus described by eq 15.^{10,11} For more than two electrons, in the case of a confined system (atom, molecule), the limit $\xi \rightarrow 0$ in eq 16 describes a cluster of fermions, and eq 15 becomes an approximation^{10,11,21} for the internal degrees of freedom of the cluster.

Here we focus on the high-density limit of the Hamiltonians of eq 5, and we thus stick to the case $N = 2$. In general, the effective electron–electron interaction $w_{\text{eff}}(r_{12})$ in eq 15 is not known and must be approximated. In the case of the He series, we have found^{9–11} that a simple approximation based on the original idea of Overhauser^{12,13} gives very accurate results for $2 \leq Z \leq 10$. In what follows we analyze the performance of the same approximation in the very $Z \rightarrow \infty$ limit, and we extend our study to the $k \rightarrow \infty$ limit of the Hooke's atom series. Of course, in the special case of the Hooke's series, the Hamiltonian (5) is exactly separable into

center-of-mass and relative coordinates, so that the exact $w_{\text{eff}}(r_{12})$ is directly available. However, the point here is to check whether the same approximate $w_{\text{eff}}(r_{12})$ that accurately describes the He series is capable of yielding also good results for the Hooke's series, since this seems to be not the case for the currently available correlation energy functionals.¹⁷

The construction of an approximation for the e–e effective potential w_{eff} starts with the decomposition^{9–11}

$$w_{\text{eff}}(r_{12}) = w_{\text{eff}}^{\text{KS}}(r_{12}) + w_{\text{eff}}^c(r_{12}) \quad (17)$$

where $w_{\text{eff}}^{\text{KS}} = \nabla^2 \sqrt{f_{\text{KS}}}/\sqrt{f_{\text{KS}}}$ is the potential that generates the Kohn–Sham f_{KS} via eq 15, and $w_{\text{eff}}^c(r_{12})$ is a correlation potential that needs to be approximated. In the usual DFT language, eq 17 implies that we are treating exchange exactly.

In scaled units \mathbf{s} , using standard perturbation theory we obtain the equation for the first-order contribution to f [see eq 12] that separates into the Kohn–Sham and the correlation parts

$$[-\nabla^2 + w_{\text{eff}}^{\text{KS}(0)} - \epsilon^{(0)}] \psi_{\text{KS}}^{(1)} = [\epsilon_{\text{KS}}^{(1)} - w_{\text{eff}}^{\text{KS}(1)}] \psi^{(0)} \quad (18)$$

$$[-\nabla^2 + w_{\text{eff}}^{\text{KS}(0)} - \epsilon^{(0)}] \psi_c^{(1)} = [\epsilon_c^{(1)} - w_{\text{eff}}^{c(1)}] \psi^{(0)} \quad (19)$$

where $\psi^{(0)} = \sqrt{f^{(0)}}$, $f_{\text{KS}}^{(1)} = 2\psi^{(0)}\psi_{\text{KS}}^{(1)}$, $f_c^{(1)} = 2\psi^{(0)}\psi_c^{(1)}$, and

$$w_{\text{eff}}^{\text{KS}(0)}(s_{12}) = \frac{2(8s_{12}^4 - 8s_{12}^3 - 38s_{12}^2 - 36s_{12} - 9)}{(4s_{12}^2 + 6s_{12} + 3)^2} - 1 \quad (\text{He series}) \quad (20)$$

$$w_{\text{eff}}^{\text{KS}(0)}(s_{12}) = \frac{s_{12}^2}{4} \quad (\text{Hooke's series}) \quad (21)$$

In eq 18, $f_{\text{KS}}^{(1)}$ is exactly known for both series, so that we can also obtain $w_{\text{eff}}^{\text{KS}(1)}$ by inversion.

We thus concentrate on the correlation part, since we want to test approximations for w_{eff}^c . Defining $u_c(x) = x\psi_c^{(1)}(x)$ and $u_0(x) = x\psi^{(0)}(x)$, we have

$$\left[\frac{d^2}{dx^2} - w_{\text{eff}}^{\text{KS}(0)} + \epsilon^{(0)} \right] u_c = [w_{\text{eff}}^{c(1)} - \epsilon_c^{(1)}] u_0 \quad (22)$$

Following the method of refs 18 and 22–25 we look for a solution of the kind $u_c(x) = u_0(x)y(x)$. The function $y(x)$ is then given by

$$y(x) = \int_0^x \frac{dx'}{u_0^2(x')} \int_0^{x'} u_0^2(x'') [w_{\text{eff}}^{c(1)}(x'') - \epsilon_c^{(1)}] dx'' + C_2 \quad (23)$$

The constant C_2 is fixed by requiring the proper normalization

$$\int_0^\infty f_c^{(1)}(x) x^2 dx = 0 \Rightarrow \int_0^\infty y(x) u_0^2(x) dx = 0 \quad (24)$$

The other integration constant has been fixed in eq 23 by setting equal to zero an unphysical term $C_1 \int_0^\infty u_0^{-2}(x') dx'$ that would make $u_c(x)$ diverge for large x .

3.2. Testing Approximations: The Overhauser Potential. In refs 9–11 an approximation for w_{eff}^c was built as an average “Overhauser-type” potential^{12,13}

$$w_{\text{eff}}^c(r_{12}) \approx \left(\frac{1}{r_{12}} + \frac{r_{12}^2}{2\bar{r}_s^3} - \frac{3}{2\bar{r}_s} \right) \theta(\bar{r}_s - r_{12}) \quad (25)$$

where $\theta(x)$ is the Heaviside step function, and \bar{r}_s is related to the average density or, better, to the dimension of the system. For two-electron atoms it was simply estimated as⁹

$$\bar{r}_s = \left(\frac{4\pi}{3} \bar{n} \right)^{-1/3} \quad (26)$$

where

$$\bar{n} = \frac{1}{N} \int d\mathbf{r} n(\mathbf{r})^2 \quad (27)$$

The idea beyond this approximation is the following. The e–e correlation potential $w_{\text{eff}}^c(r_{12})$ changes the Kohn–Sham f into the physical one and must thus keep the information on the one-electron density (which is the same in the two systems) while turning on the e–e interaction $1/r_{12}$. In eqs 25–27 this information is approximately kept via the average density \bar{n} .

In scaled units, the Overhauser potential to first order in α , to be used in eq 19, becomes

$$w_{\text{eff}}^{c(1)}(s_{12}) \approx \left(\frac{1}{s_{12}} + \frac{s_{12}^2}{2\bar{s}_s^3} - \frac{3}{2\bar{s}_s} \right) \theta(\bar{s}_s - s_{12}) \quad (28)$$

where, if we adopt the prescription of eqs 26 and 27, $\bar{s}_s = 3^{1/3} + O(\alpha)$ for the He series and $\bar{s}_s = (3\sqrt{\pi})^{1/3} + O(\alpha)$ for the Hooke’s atom series.

Equation 23 with the potential of eq 28 can be evaluated analytically as a function of s_{12} and \bar{s}_s for both series, although the final expressions are cumbersome and will not be reported here. The resulting $f_c^{(1)}$ for the He series is shown in Figure 1, together with the corresponding scaled quantity, $Z^{-2}f_c(s/Z)$, for some finite Z . [Since $f_c^{(1)}(s) = \lim_{Z \rightarrow \infty} Z f_c(s)$, and $f_c(s) = Z^{-3}f_c(s/Z)$, the quantity to be compared with $f_c^{(1)}(s)$ is $Z^{-2}f_c(s/Z)$.] For finite Z we show both the “exact” result²⁶ and the approximate result⁹ obtained

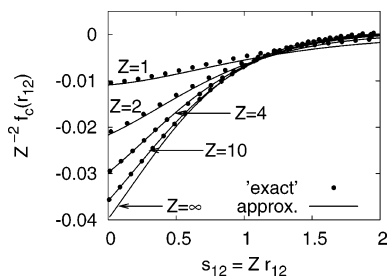


Figure 1. The correlation part of the intracule density, $f_c = f - f_{\text{KS}}$, divided by Z^2 , as a function of the scaled variable $s_{12} = Z r_{12}$ for the He isoelectronic series. The “exact” results are obtained from the accurate wavefunctions of ref 26. Approximate results at finite Z using the “Overhauser model” are taken from ref 9. The $Z = \infty$ result corresponds to eq 23 with the potential of eq 28.

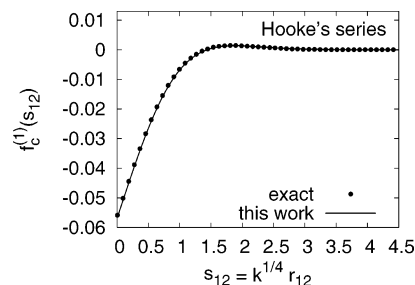


Figure 2. The correlation part of the first-order intracule, $f_c^{(1)}(s_{12})$ [see eq 12], for the Hooke’s series. The exact values are compared with the results from the Overhauser-type approximation of eq 28.

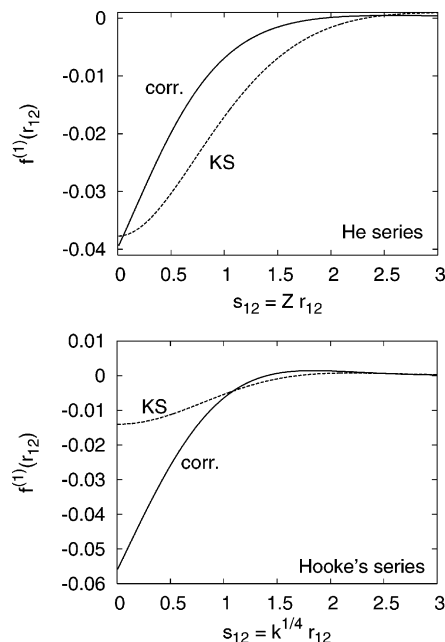


Figure 3. The decomposition of the first-order intracule density $f^{(1)}(s_{12})$ [see eq 12]: the Kohn–Sham part and the correlation part.

with the Overhauser-type potential of eqs 25–27. We see that the Z dependence of the short-range part of f_c is very well captured by this simple approximation. Figure 1 also suggests that the $Z \rightarrow \infty$ limit of the short-range part of f_c is well described by this approach. In Figure 2 we show the result for $f_c^{(1)}$ in the case of the Hooke’s series from the Overhauser potential compared to the exact one, finding very accurate agreement.

The KS and the correlation components of $f^{(1)}$ are shown in Figure 3 for both series. We see that in the case of the He series the KS and the correlation parts have roughly the same depth, while in the case of the Hooke’s series the correlation part is much deeper than the KS one. This is due to the fact that the KS part gives the change in the e–e distance probability distribution only due to the first-order change in the one-electron density. In the case of the Hooke’s series the first-order change in the density is much smaller, since the harmonic confining external potential is stronger than the Coulombic one. Indeed, the function $\chi(s)$ of eq 8 in the case of the He series is about twice the one for the Hooke’s atom series.

4. Adiabatic Connection and Correlation Energy

The APD $f_c^{(1)}(s_{12})$ gives the correlation contribution to second order to the expectation $\langle V_{ee} \rangle$ of the Coulomb electron–electron repulsion operator, $V_{ee} = 1/r_{12}$

$$\langle V_{ee} \rangle = \frac{1}{\alpha^2} [\alpha \langle V_{ee} \rangle^{(1)} + \alpha^2 \langle V_{ee} \rangle^{(2)} + O(\alpha^3)] \quad (29)$$

where

$$\langle V_{ee} \rangle^{(2)} = \langle V_{ee} \rangle_{\text{KS}}^{(2)} + \langle V_{ee} \rangle_c^{(2)}$$

and

$$\langle V_{ee} \rangle_c^{(2)} = \int_0^\infty 4\pi s_{12} f_c^{(1)}(s_{12}) ds_{12} \quad (30)$$

Our $f_c^{(1)}$ from the Overhauser potential give $\langle V_{ee} \rangle_c^{(2)} = -0.10256$ Ha for the He sequence (to be compared with the exact²⁷ value, -0.09333 Ha) and $\langle V_{ee} \rangle_c^{(2)} = -0.10377$ Ha for the Hooke's series (to be compared with the exact^{19,20} value, -0.09941 Ha). The error is thus 9 mH for the He series and 4 mH for the Hooke's series.

The correlation energy can then be obtained via the adiabatic connection formula of eq 1, which for $E_c^{(2)}$ reads

$$E_c^{(2)} = \int_0^{\lambda_{\text{phys}}} d\lambda \int_0^\infty ds_{12} 4\pi s_{12}^2 f_c^{(1)}(s_{12}) \frac{\partial w^\lambda(s_{12})}{\partial \lambda} \quad (31)$$

where $f_c^{(1)}$ is the first-order correlated part of f for the system with interaction $\alpha w^\lambda(s_{12})$. If we were able to calculate the exact $f_c^{(1)}$ for any w^λ , the resulting $E_c^{(2)}$ from eq 31 would be independent of the choice of w^λ . However, when we deal with approximations, we can obtain better results with some choices rather than others.

As in ref 9, we build an Overhauser-type potential along the adiabatic connection as

$$w_{\text{eff}}^{c,\lambda}(s_{12}; \bar{s}_s) = w^\lambda(s_{12}) - \int_{|\mathbf{s}| \leq \bar{s}_s} \bar{n} w^\lambda(|\mathbf{s} - \mathbf{s}_{12}|) d\mathbf{s} \quad (32)$$

where, in scaled units, if we stick with the choice of eqs 26 and 27, $\bar{n} = (4\pi)^{-1}$ for the He series and $\bar{n} = (4\pi^{3/2})^{-1}$ for the Hooke's series. The idea behind eq 32 is that the average density \bar{n} (and thus the average \bar{s}_s) is kept fixed to mimic the fact that the one-electron density does not change along the adiabatic connection while we turn on the e–e interaction.

4.1. Linear Adiabatic Connection. If we set $w^\lambda(s_{12}) = \lambda/s_{12}$, eq 32 simply gives the Overhauser potential of eq 28 with a multiplying factor λ in front. From eq 23, we see that this corresponds to $E_c^{(2)} = \langle V_{ee} \rangle_c^{(2)}/2$, as in the exact case. I.e., the simple approximation of eq 32 has the correct scaling behavior in the $\alpha \rightarrow 0$ limit. Our result for $E_c^{(2)}$ with the linear adiabatic connection thus gives an error of 4.5 mH for the He series and 2 mH for the Hooke's series.

4.2. The “erf” Adiabatic Connection. A choice for w^λ that separates short- and long-range effects is the “erf” adiabatic connection,^{9,28–33} $w^\lambda(s_{12}) = \text{erf}(\lambda s_{12})/s_{12}$, for which eq 31 becomes

$$E_c^{(2)} = \int_0^\infty d\lambda \int_0^\infty ds_{12} 4\pi s_{12}^2 f_c^{(1)}(s_{12}) \frac{2}{\sqrt{\pi}} e^{-\lambda^2 s_{12}^2} \quad (33)$$

The Overhauser-type potential corresponding to this interaction is reported in the appendix of ref 9. For the He isoelectronic series with $2 \leq Z \leq 10$, the Overhauser-type approximation combined with the “erf” adiabatic connection gives⁹ correlation energies with errors within 4 mH, better than the linear adiabatic connection that gives errors within 10 mH.

In the weakly correlated limit, instead, we obtained, via eq 33, $E_c^{(2)} = -0.041$ Ha for the He series and $E_c^{(2)} = -0.046$ Ha for the Hooke's series. The errors with respect to the exact values, 6 mH and 4 mH, respectively, are thus slightly worse than those obtained with the linear adiabatic connection.

5. The LDA Failure in the High-Density Limit: An Analysis from the Intracule Density

As a further element of comparison, we also computed the first-order $f_c^{(1)}(s_{12})$ within the local-density approximation (LDA)

$$f_c^{(1)\text{LDA}}(s_{12}) = \lim_{\alpha \rightarrow 0} \frac{1}{\alpha} \int \frac{n^{(0)}(\mathbf{s})^2}{2} g_c(\tilde{k}_F(\mathbf{s})s_{12}; \alpha \tilde{r}_s(\mathbf{s})) d\mathbf{s} \quad (34)$$

where $g_c(r_{12}; r_s)$ is the pair-correlation function of the uniform electron gas³⁴ of density $n = (4\pi r_s^3/3)^{-1}$, and

$$\tilde{k}_F(\mathbf{s}) = [3\pi^2 n^{(0)}(\mathbf{s})]^{1/3}, \quad \tilde{r}_s(\mathbf{s}) = \left[\frac{4\pi n^{(0)}(\mathbf{s})}{3} \right]^{-1/3} \quad (35)$$

With these definitions, the density parameter r_s of the uniform electron gas is locally proportional to α . We have numerically evaluated the right-hand-side of eq 34 at smaller and smaller α (i.e., at larger and larger Z and k), for $0 \leq s_{12} \leq 5$. As α decreases, the results tend to a well-defined curve, shown in Figures 4 and 5, together with the result from the Overhauser model (He series) and the exact result (Hooke's series).

Since, as shown by eq 34, the $\alpha \rightarrow 0$ limit corresponds to the $r_s \rightarrow 0$ limit of the uniform electron gas pair-correlation function g_c , to better understand the LDA result for f_c we now analyze more in detail the high-density behavior of g_c . This analysis extends and completes the one done in ref 35. When $r_s \rightarrow 0$, the short-range part of g_c scales as

$$g_c(x, r_s \rightarrow 0) = r_s g_c^{(1)}(x) + O(r_s^2 \ln r_s), \quad x = r_{12}/r_s \quad (36)$$

where the function $g_c^{(1)}(x)$ does not depend explicitly on r_s and has been computed by Rassolov et al.^{36,37} It is accurately recovered by the model g_c of ref 34 that we have used in the evaluation of eq 34. The scaled variable x is locally proportional to the scaled variable s_{12} [see eq 35]. Equation 36 thus shows that the short-range part (corresponding to values of the scaled variable x not too large) of g_c in the $r_s \rightarrow 0$ limit has a scaling similar to the one of the He and

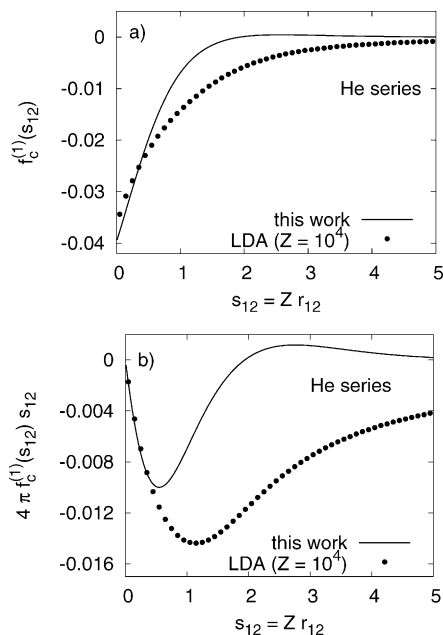


Figure 4. The correlated part of the intracule density, $f_c^{(1)}(s_{12})$, of order $\alpha = 1/Z$ for the He series [see eq 12]: the present calculation is compared with the LDA approximation (panel a). Panel b shows the same quantities multiplied by $4\pi s_{12}$: the integral under each curve gives the correlation part of the second-order contribution to the expectation value $\langle V_{ee} \rangle$, which diverges in the case of LDA.

Hooke's series in the $\alpha \rightarrow 0$ limit. This is also reflected by a good performance of LDA for $s_{12} \approx 1$, as shown by Figures 4 and 5.

However, the high-density electron gas is an extended system with important long-range correlations that are not present in finite systems like atoms and molecules. In fact, the scaling of eq 36 is not valid when $x \gg 1$: it has been shown that the long-range part of g_c scales as^{34,38,39}

$$g_c(x \gg 1, r_s) \rightarrow r_s^2 h(v) \quad (37)$$

where v is another scaled variable, $v = \sqrt{r_s} x$, which is thus locally proportional to $\sqrt{\alpha} s_{12}$. The function $h(v)$ has the following asymptotic behaviors

$$h(v \ll 1) \propto v^{-2}, \quad h(v \gg 1) \propto v^{-4} \quad (38)$$

which are also correctly included in the model g_c of ref 34. When $r_s \rightarrow 0$ (i.e., $\alpha \rightarrow 0$), even for very large x the scaled variable v is small, so that the long-range ($x \gg 1$) behavior of g_c is more and more dominated by the small v part of $h(v)$, i.e., it behaves more and more like v^{-2} rather than like v^{-4} . It is this increasing dominance of the "short-range component of the long-range part" that causes the $\propto \log(r_s)$ behavior in the correlation energy per electron of the high-density electron gas and thus the divergence of the LDA correlation energy in the large- Z and large- k limit of the He and Hooke's atom sequences (see, e.g., ref 40). In fact, when $Z \rightarrow \infty$ (or $k \rightarrow \infty$), the high-density long-range behavior of g_c affects the long-range part of $f_c^{\text{LDA}}(s_{12})$ in eq 34.

The small- v behavior $\propto v^{-2}$ of the function $h(v)$ is related to the $1/r_{12}$ divergence of the Coulomb potential at small

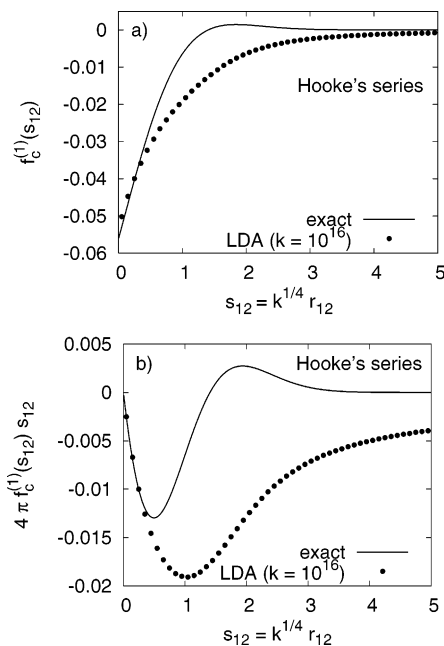


Figure 5. The correlated part of the intracule density, $f_c^{(1)}(s_{12})$, of order $\alpha = k^{-1/4}$ for the Hooke's atom series [see eq 12]: the exact result is compared with the LDA approximation (panel a). Panel b shows the same quantities multiplied by $4\pi s_{12}$: the integral under each curve gives the correlation part of the second-order contribution to the expectation value $\langle V_{ee} \rangle$, which diverges in the case of LDA.

r_{12} . For this reason, the $\propto \log(r_s)$ high-density behavior of the correlation energy is still present in a uniform electron gas with screened (or short-range only) Coulomb interaction (e.g.,⁴¹ $\text{erfc}(\lambda r_{12})/r_{12}$), while it is absent in an electron gas with long-range-only interaction (e.g.,^{42,43} $\text{erf}(\lambda r_{12})/r_{12}$).

6. Conclusions

We have computed the intracule density and the correlation energy for the high-density (weakly correlated) limit of the He and Hooke's atom isoelectronic series via an approach^{9–11,21} based on an "average pair density functional theory" (APDFT) and inspired by the seminal work of Overhauser.^{12–16} Unlike the currently available correlation energy functionals analyzed in ref 17, the APDFT approach gives accurate results for both series. In its present formulation, the APDFT approach works well for two-electron systems and for the uniform electron gas. Its extension to many-electron systems of nonuniform density is a big challenge, and we are presently exploring several different paths to achieve this ambitious goal.¹¹

We have also analyzed the LDA failure in the same weakly correlated limit of the He and Hooke's atom series, in terms of the long-range part of the intracule density. The results of Katriel et al.¹⁷ show that higher-order functionals such as PBE⁴⁴ and TPSS⁴⁵ can reasonably fix the LDA problems in the case of the He isoelectronic series but are much less satisfactory for the Hooke's atom sequence, yielding a wrong scaling in the $k \rightarrow \infty$ limit (PBE) or a correct scaling with an error of about 40% on the asymptotic value of the correlation energy (TPSS). As stressed by Katriel et al.,¹⁷ these differences in performances for the two series raise

serious doubts on the universality of currently available correlation energy functionals. The accuracy of the results obtained via the APDFT approach for both series suggests that the effort toward its generalization to many-electron systems of nonuniform density could be really worthwhile.

Appendix: $f_{\text{KS}}^{(1)}(r_{12})$ for the He Isoelectronic Series

For the He isoelectronic series eq 13 corresponds to

$$f_{\text{KS}}^{(1)}(x) = \frac{1}{864\pi x} \{ 4e^{-4x}[-41 + 3x(1 + 9x)] + 81e^{2x}(x-1)[\text{Ei}(-6x) - \text{Ei}(-4x)] + e^{-2x}[164 + 27(3 + x(9 + 4x(3 + 2x)))] [\text{Ei}(-2x) - \gamma - \log(x)] + 3x[-163 + 6x(15 + x(7 + 10x)) - 27\log(4/3)] - 162\log(2) + 81\log(3) \} \quad (39)$$

where γ and the function Ei have been defined after eq 9.

References

- (1) Kohn, W. *Rev. Mod. Phys.* **1999**, *71*, 1253.
- (2) Mattsson, A. E. *Science* **2002**, *298*, 759.
- (3) *A Primer in Density Functional Theory*; Fiolhais, C., Nogueira, F., Marques, M., Eds.; Springer-Verlag: Berlin, 2003.
- (4) Perdew, J. P.; Ruzsinszky, A.; Tao, J.; Staroverov, V. N.; Scuseria, G. E.; Csonka, G. I. *J. Chem. Phys.* **2005**, *123*, 062201.
- (5) Harris, J.; Jones, R. *J. Phys. F* **1974**, *4*, 1170.
- (6) Langreth, D. C.; Perdew, J. P. *Solid State Commun.* **1975**, *17*, 1425.
- (7) Gunnarsson, O.; Lundqvist, B. I. *Phys. Rev. B* **1976**, *13*, 4274.
- (8) Yang, W. *J. Chem. Phys.* **1998**, *109*, 10107.
- (9) Gori-Giorgi, P.; Savin, A. *Phys. Rev. A* **2005**, *71*, 032513.
- (10) Gori-Giorgi, P.; Savin, A. *Philos. Mag.* **2006**, *86*, 2643.
- (11) Gori-Giorgi, P.; Savin, A. submitted to *Int. J. Mod. Phys. B* arXiv:cond-mat/0611324. arXiv.org ePrint archive. <http://arxiv.org/abs/cond-mat/0611324> (accessed Nov 13, 2006).
- (12) Overhauser, A. W. *Can. J. Phys.* **1995**, *73*, 683.
- (13) Gori-Giorgi, P.; Perdew, J. P. *Phys. Rev. B* **2001**, *64*, 155102.
- (14) Davoudi, B.; Polini, M.; Asgari, R.; Tosi, M. P. *Phys. Rev. B* **2002**, *66*, 075110.
- (15) Corona, M.; Gori-Giorgi, P.; Perdew, J. P. *Phys. Rev. B* **2004**, *69*, 045108.
- (16) Nagy, I.; Diez Muino, R.; Juaristi, J. I.; Echenique, P. M. *Phys. Rev. B* **2004**, *69*, 233105.
- (17) Katriel, J.; Roy, S.; Springborg, M. *J. Chem. Phys.* **2006**, *124*, 234111.
- (18) Schwartz, C. *Ann. Phys. (N.Y.)* **1959**, *6*, 156.
- (19) White, R. J.; Byers Brown, W. *J. Chem. Phys.* **1970**, *53*, 3869.
- (20) Cioslowski, J.; Pernal, K. *J. Chem. Phys.* **2000**, *113*, 8434.
- (21) Nagy, Á. *J. Chem. Phys.* **2006**, *125*, 184104.
- (22) Dalgarno, A.; Lewis, J. T. *Proc. Roy. Soc. (London)* **1955**, *A233*, 70.
- (23) Dalgarno, A. *Proc. Roy. Soc. (London)* **1956**, *A69*, 784.
- (24) Dalgarno, A.; Stewart, A. L. *Proc. Roy. Soc. (London)* **1956**, *A238*, 276.
- (25) Young, W. H.; March, N. H. *Phys. Rev.* **1958**, *109*, 1854.
- (26) Freund, D. E.; Huxtable, B. D.; Morgan, J. D., III *Phys. Rev. A* **1984**, *29*, 980. We used an improved version (provided to us by C. Umrigar) of the accurate variational wavefunctions described in this work to obtain one-electron densities $n(r)$ and functions $f(r_{12})$. See, also: Umrigar, C. J.; Gonze, X. *Phys. Rev. A* **1994**, *50*, 3827.
- (27) See, e.g.: Huang, C.-J.; Umrigar, C. J. *Phys. Rev. A* **1997**, *56*, 290.
- (28) Savin, A.; Colonna, F.; Pollet, R. *Int. J. Quantum Chem.* **2003**, *93*, 166 and references therein.
- (29) Savin, A. In *Recent Developments and Applications of Modern Density Functional Theory*; Seminario, J. M., Ed.; Elsevier: Amsterdam, 1996; p 327.
- (30) Leininger, T.; Stoll, H.; Werner, H.-J.; Savin, A. *Chem. Phys. Lett.* **1997**, *275*, 151.
- (31) Pollet, R.; Savin, A.; Leininger, T.; Stoll, H. *J. Chem. Phys.* **2002**, *116*, 1250.
- (32) Pollet, R.; Colonna, F.; Leininger, T.; Stoll, H.; Werner, H.-J.; Savin, A. *Int. J. Quantum Chem.* **2003**, *91*, 84.
- (33) Toulouse, J.; Colonna, F.; Savin, A. *Phys. Rev. A* **2004**, *70*, 062505.
- (34) Gori-Giorgi, P.; Perdew, J. P. *Phys. Rev. B* **2002**, *66*, 165118.
- (35) Burke, K.; Angulo, J. C.; Perdew, J. P. *Phys. Rev. A* **1994**, *50*, 297.
- (36) Rassolov, V. A.; Pople, J. A.; Ratner, M. A. *Phys. Rev. B* **1999**, *59*, 15625.
- (37) Rassolov, V. A.; Pople, J. A.; Ratner, M. A. *Phys. Rev. B* **2000**, *62*, 2232.
- (38) Wang, Y.; Perdew, J. P. *Phys. Rev. B* **1991**, *44*, 13298.
- (39) Perdew, J. P.; Wang, Y. *Phys. Rev. B* **1992**, *46*, 12947.
- (40) Perdew, J. P.; McMullen, E. R.; Zunger, A. *Phys. Rev. A* **1981**, *23*, 2785.
- (41) Zecca, L.; Gori-Giorgi, P.; Moroni, S.; Bachelet, G. B. *Phys. Rev. B* **2004**, *70*, 205127.
- (42) Paziani, S.; Moroni, S.; Gori-Giorgi, P.; Bachelet, G. B. *Phys. Rev. B* **2006**, *73*, 155111.
- (43) Toulouse, J.; Gori-Giorgi, P.; Savin, A. *Int. J. Quantum Chem.* **2006**, *106*, 2026.
- (44) Perdew, J. P.; Burke, K.; Ernzerhof, M. *Phys. Rev. Lett.* **1996**, *77*, 3865.
- (45) Tao, J.; Perdew, J. P.; Staroverov, V. N.; Scuseria, G. E. *Phys. Rev. Lett.* **2003**, *91*, 146401.

CT700019H

Radical-Induced Damage in 3'dTMP — Insights into a Mechanism for DNA Strand Cleavage†

Ru bo Zhang,^{‡,§} Feng xin Gao,[‡] and Leif A. Eriksson^{*,§}

The Institute for Chemical Physics and School of Science, Beijing Institute of Technology, Beijing 100081, China, and Department of Natural Sciences and Örebro Life Science Center, Örebro University, 701 82 Örebro, Sweden

Received December 13, 2006

Abstract: DNA strand scission and base release in 3'dTMP, induced by H and OH radical addition to thymine, is studied at the DFT B3LYP/6-31+G(d,p) level in the gas phase and in solution. In particular the mechanism of H atom transfer subsequent to radical formation, from C2' on the sugar to the C6 site on the base, is explored. Bulk solvation is found to lower the barrier by up to 5 kcal mol⁻¹ and the reaction energy by up to 12 kcal mol⁻¹ for the hydroxyl radical adducts. The strengths of the N1–C1'(N1-glycosidic bond) and C3'–O(P) bonds are calculated, showing that homolytic bond breaking processes are largely favored in both cases. The barrier for C3'–O(P) bond rupture is approximately 18.2 kcal mol⁻¹, and its breakage is preferred by 10–15 kcal mol⁻¹ over that of N1-glycosidic bond cleavage in both the gas phase and solvents, which is consistent with the changes in C3'–O(P) and N1–C1' bond lengths during the H transfer reactions. Mulliken spin densities, NPA charges, and vertical electron affinities are calculated to clarify the reactive properties of the intramolecular H-transfer radicals.

1. Introduction

Radical attack on DNA is one of the main reasons for DNA damage.¹ Electron paramagnetic resonance (EPR) spectroscopy in conjunction with spin-trapping carried out in aqueous solution has shown that H, OH, and alkoxy radicals can attack the C5–C6 double bond of the pyrimidine base moieties via addition or the sugar moiety via hydrogen abstraction, in nucleosides, nucleotides, and DNA.^{2–4} Thyl radical attack on the C6-position of pyrimidine nucleosides has also been reported.⁵ The chemical behavior of phenyl radicals toward DNA and its components has been extensively investigated.⁶ Much theoretical work has been devoted to unveil the effects and mechanisms of radiation in DNA lesion formation. In the case of thymidine, the hydroxyl radical may either add to the C5=C6 double bond or abstract a hydrogen atom from the C5 methyl group, with addition to C5 being the major

pathway.⁷ For H atom addition, formation of the 5,6-dihydro-6-thymyl radical is preferred over the corresponding 5-thymyl radical, although the relative energy difference between the two products is only 3.1 kcal/mol.⁸ A competing set of reactions is posed by H atom abstraction by the OH radical from the sugar moiety. These depend on the C–H bond strength and lead to alteration of the sugar moiety and subsequent rearrangements that in turn have been suggested to generate base release or strand break.^{9,10}

It is generally accepted that nucleobase-radical adducts contribute to strand break.^{11–13} The exact mechanism is, however, uncertain to date. Electron spin resonance (ESR) results have indicated this to be a slow process,¹⁴ with the rate-limiting step suggested to involve intra- or internucleotide hydrogen atom abstraction from a sugar group (paths A and C, shown schematically in Scheme 1).¹⁵ This process has also been proposed to proceed by way of initial protonation of the radical adduct, followed by dehydration to form the radical cation, intramolecular H-transfer, and strand scission (path B of Scheme 1).¹⁶ The mechanism involving intranucleotide hydrogen atom abstraction as well as protonation/dehydration pathway has been

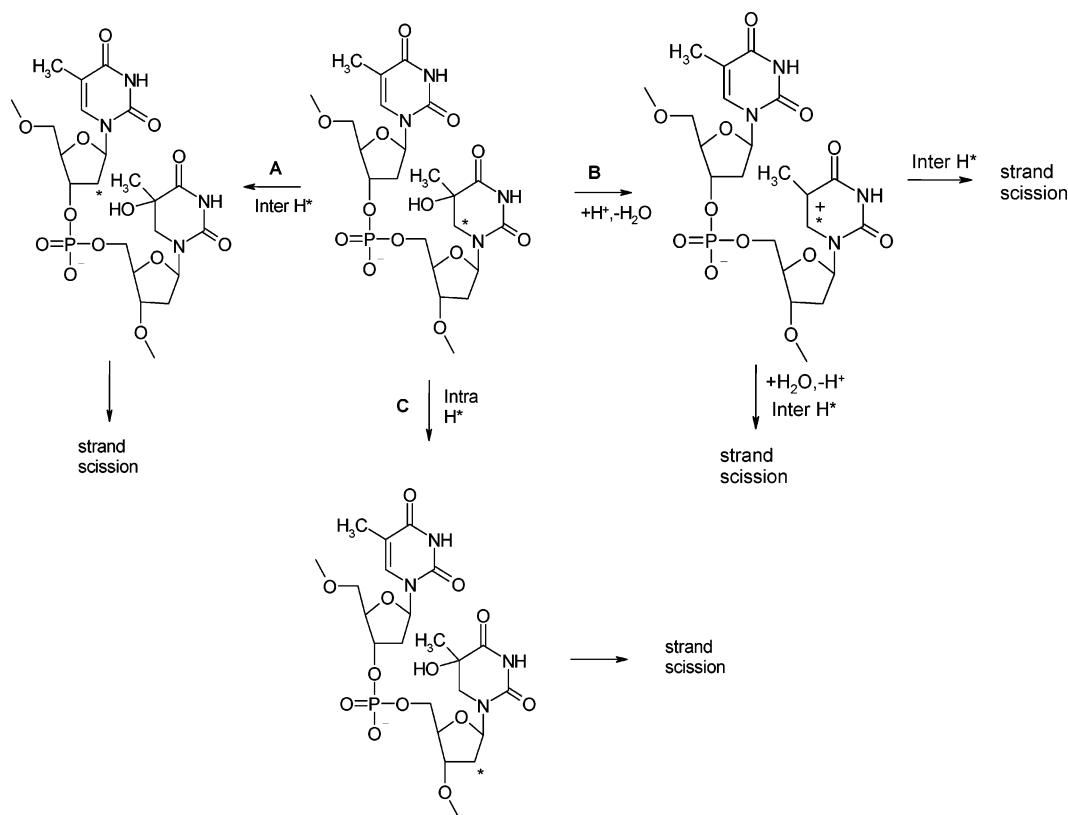
† Dedicated to Dennis R. Salahub on the occasion of his 60th birthday.

* Corresponding author e-mail: leif.eriksson@nat.oru.se.

‡ Beijing Institute of Technology.

§ Örebro University.

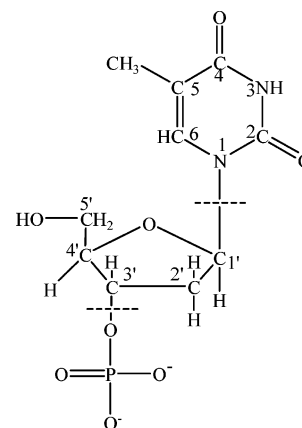
Scheme 1



proposed to be less important in the biopolymer, due to the stability of the nucleobase-radical adduct.¹⁷ It is evident that the above processes often are quenched in the presence of oxygen molecules although they have been reported to occur in hypoxic cells.¹¹

The OH and H radical adducts of the pyrimidines at either C5 or C6 have both oxidizing and reducing capabilities.¹⁸ N1-glycosidic bond rupture was proposed to be caused by the cationic C6 lesion, arising as a result of one-electron removal of the 5,6-dihydro-6-thymyl radical,¹⁹ whereas the capture of an additional electron by the cytosine N3–H atom radical adduct led to the automatic rupture of the C3'–O(P) bond.²⁰ The electron detachment energy of 5'dAMP-H anionic radicals, which results through OH radical induced H abstraction from the sugar, was calculated to explore the effects of DNA damage.²¹ The work reported herein primarily refers to deoxythymidine 3'-monophosphate (3'dTMP, cf. Chart 1), which is employed to model the 3'-terminal of the DNA strand. Given the complex and asymmetric local environment, both 'back' and 'front' attacks at the C5 site of the base by OH and H radicals are considered. In particular, the processes of carbon-centered H-atom transfer from C2' on the sugar moiety to C6 on the radical-modified thymine base are explored in detail. The bond dissociation energy (BDE) of the C3'–O(P) and C1'–N1 (glycosidic) bonds and the activation barriers are calculated in order to investigate possible cleavage modes in DNA under radical stress. In addition, the direct effects of electronic attack on the H-transfer barrier, both without and including additional H/OH radical addition to thymine, are investigated.

Chart 1



2. Methodology

All geometries were optimized at the hybrid Hartree–Fock–density functional theory B3LYP level,^{22,23} in conjunction with the 6-31+G(d,p) basis set. Frequency calculations were performed at the same level of theory, to confirm the correct nature of the stationary points. From the frequency calculations, zero-point energies (ZPE) were extracted and added to the electronic energies, as applicable. Natural bond orbital (NBO) theory²⁴ and natural population analysis (NPA) were used to determine atomic charges. Bulk solvation effects were considered using the integral equation formalism of the polarized continuum model (IEF-PCM)²⁵ with dielectric constants $\epsilon = 4.3$ and $\epsilon = 78.4$, respectively, to model the extreme cases of a hydrophobic environment and of aqueous solution. Vertical electron affinities (VEA) were determined

Table 1. ZPE-Corrected Reaction Energies and Activation Barriers (in kcal/mol) for the H-Atom Transfer Reactions at the B3LYP/6-31+G(d,p) Level

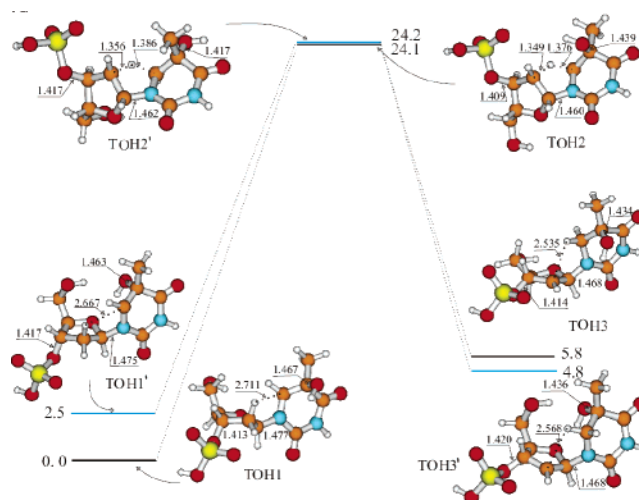
reactions	TH1'→ TH3'	TH1→ TH3	TOH1'→ TOH3'	TOH1→ TOH3
transition barrier				
vacuum	23.9	25.1	21.7	24.1
$\epsilon = 4.3$	24.6	25.0	21.0	19.7
$\epsilon = 78.4$	25.3	24.2	19.0	23.1
reaction energy				
vacuum	4.6	6.3	2.3	5.8
$\epsilon = 4.3$	4.5	5.2	1.7	-6.2
$\epsilon = 78.4$	3.4	4.7	0.8	-4.8

as the energy difference of the parent compound and its reduced form, evaluated at the optimized geometry of the parent compound. Bond dissociation energies (BDE) for the fragmentation reactions were obtained by evaluating the ZPE-corrected energy difference between the optimized fragments and the complex. No basis set superposition effects (BSSE) were considered in these calculations, based on the sizes of the systems in question and the fact that such corrections can be expected to be much smaller than the evaluated energy differences to change any of the conclusions drawn from the computed data. All calculations were performed using the Gaussian 03 package.²⁶ Atomic labeling used in the text and tables throughout refers to Chart 1. The DNA strand was truncated by hydrogen atoms at the C5'OH and the C3'-OP(O)₂-OH ends, and the phosphate was kept negatively charged to ensure an appropriate environment. The use of a negatively charged phosphate group proved to be of importance to the results obtained, as will be discussed below.

3. Results and Discussions

3.1. H Atom Transfer Initiated by H Radical or Free Electron Addition. As previously noted, H atom addition in 3'dTMP occurs primarily on the pyrimidine C5 atom. Two cases are considered herein—H atom attack from the back ('primed') and front ('unprimed') at the C5 site of the base, TH1' and TH1, respectively (cf. Chart 1). The energy difference between the two radical adducts is 1.7 kcal mol⁻¹ in favor of the 'front' adduct TH1, due to more favorable interaction between the phosphate group and the sugar and between the C5'OH group and the radical site. The radical centers are, as expected, localized at C6 in both cases (C6 spin densities 0.752 e in TH1 and 0.736 e in TH1'). Among the H atoms of the deoxyribose moiety, H2' is the one closest to the radical center C6, at a distance of 2.855 Å in TH1 and 2.677 Å in TH1'. H2' abstraction by the C6 radical center has been attributed to be responsible for strand breaks²⁷ and is the primary reaction studied herein.

The activation barrier for H2' atom transfer to C6 is 23.9 kcal mol⁻¹ in TH1'→TH3'; 1–2 kcal mol⁻¹ lower than for the TH1→TH3 case. Since the two transition states TH2 and TH2' have almost the same energy (see Table 1), the barrier difference is attributed to the different stability of the reactants TH1 and TH1'. In TH2', the C2'–H2' distance is

**Figure 1.** Energy profiles and selected geometrical parameters of the stationary structures along the H atom abstraction reaction TOH1(·)→TOH3(·), obtained at the ZPE-corrected UB3LYP/6-31+G(d,p) level.

1.355 Å, 0.03 Å shorter than H2'–C6. The spin density is mainly localized on C2' (0.676 e), C3' (-0.136 e), and C6 (0.532 e), clearly illustrating the spin transfer associated with these reactions. H2' has a spin density of -0.084 e in TH2', compared to -0.002 e in TH1' and TH3'. The situation is highly analogous in the 'front' transition state TH2. The H atom transfer produces a sugar-centered radical localized on C2', which forms a potential basis for subsequent reactions such as electron transfer, H atom transfer along the deoxyribose moiety, and/or addition of O₂. The C1'–N bond length is shortened in both TH3 and TH3', as compared with the reactant species, whereas C3'–O(P) becomes slightly elongated.

To elucidate the influence of electron addition on the sugar-to-base H atom transfer, the H2' abstraction reaction was also studied following the reduction of 3'dTMP, rather than addition of hydrogen or hydroxyl radicals. The unpaired spin in the 3'dTMP electronic adduct is mainly localized to C6 (0.58 e), compared with the spin density of approximately 0.74–0.75 e on C6 in TH1 and TH1'. The activation barrier in the gas phase is 29.3 kcal mol⁻¹, and the overall reaction energy is endothermic by 21.0 kcal mol⁻¹. Compared with the above H atom-induced abstraction reaction, it shows that an additional proton added to C5 is favorable for the reaction by reducing the barrier by ~4 kcal mol⁻¹ and contributes to a drastic lowering of the reaction energy, from 21.0 to 6.3 kcal mol⁻¹. The results emphasize the fact that the local field can play an important role on mediating these reactions.

3.2. H Atom Transfer Initiated by OH Radical Addition. In analogy with the C5–H adducts described above, the role of hydroxyl radical addition to C5 on C6–H2' abstraction was investigated. The C5–O(H), N1–C1', and C3'–O(P) bond lengths are essentially identical in the two cases ('front' adduct TOH1 and 'back' adduct TOH1', respectively), as are the C6···H2' distances (cf. Figure 1). As shown in Figure 1, TOH1' is less stable than TOH1 by 2.5 kcal mol⁻¹, which can be correlated to a slightly weaker

repulsion between the thymine-OH group and the sugar moiety in TOH1.

The gas-phase activation barrier for H2' atom transfer to C6 is 21.7 kcal mol⁻¹ for TOH1'→TOH3', which is 2.6 kcal mol⁻¹ lower than in the TOH1→TOH3 case. The distances between H2' and C2' (C6) are 1.356 (1.386) Å, respectively, in TOH2' and slightly shorter in TOH2. The N1–C1' bond length is shortened somewhat during the H atom transfer, although the N1–C1' and C3'–O(P) bond differences when going from reactant to product are smaller in the case of the C5–OH adducts compared to the above C5–H systems. The reaction energy is endothermic by 2.3 kcal mol⁻¹ for TOH1'→TOH3' and 5.8 kcal mol⁻¹ for TOH1→TOH3. The spin transfer from C6 in TOH1 and TOH1', to the radical center localized on C2' in TOH3 and TOH3', is very similar to the H-adduct cases.

3.3. Effects of Bulk Solvation on the Reactive Profiles.

The role of bulk solvation on the reaction profiles was explored through the use of a surrounding dielectric medium with $\epsilon = 4.3$ and 78.4 to simulate extreme cases in the local surroundings of DNA. In Table 1, the energetics derived from the density functional theory self-consistent reaction field (DFT-SCRf) calculations are listed. Several features can be observed from the reaction profiles after accounting for the implicit solvent effects generated by the nonaqueous and aqueous medium. First of all, the barriers for the TH1'→TH3' and TH1→TH3 reactions are nearly unchanged, showing that bulk solvation does not influence the reaction rates. For the TOH1'→TOH3' reaction, the barrier is lowered to 19.0 kcal mol⁻¹ in aqueous medium. Almost the same barrier height is found for TOH1→TOH3 reaction in the nonaqueous medium.

Regarding the overall reaction energies, bulk solvation effects throughout contribute favorably to the H atom transfer. The OH radical-induced reactions are preferred over H radical-induced ones by up to 10 kcal mol⁻¹. In aqueous medium, the reaction energy of TOH1'→TOH3' is essentially thermoneutral, whereas the bulk solvation effects are even more favorable to the TOH1→TOH3 reaction; these now become exothermic by 4.8 kcal mol⁻¹ in aqueous medium and 6.2 kcal mol⁻¹ in the nonaqueous medium. Thus, the H atom transfer reaction is strongly dependent on radical species, direction of attack ('back' or 'front' of base plane), and surrounding medium.

In addition, the radical intermediates have very diverse properties.¹⁸ Depending on the local surroundings, the species can capture one electron and become closed-shell dianions (the phosphate groups already carry a negative charge) or donate an electron to a suitable acceptor. For the possibility of the former, Gutowski et al. considered anionic resonance states as a path to valence bound anionic states.²⁰ The electron affinities of separate DNA bases are well characterized and understood.²⁸ Herein, we have calculated the vertical electron affinities (VEA) of the OH– or H–3'dTMP anion radicals, within the present theoretical level. According to the data given in Table 2, the gas-phase VEAs are consistently negative, showing that the closed-shell dianion species become unstable in the gas phase. Bulk solvation already at $\epsilon = 4.3$ contributes to the stability of the dianion and renders

Table 2. Vertical Electron Affinities (in eV)

	TH1'	TH1	TH3'	TH3
vacuum	–1.6	–1.7	–2.1	–2.1
$\epsilon = 4.3$	1.3	1.3	1.2	1.2
	TOH1'	TOH1	TOH3'	TOH3
vacuum	–1.0	–1.1	–2.0	–2.0
$\epsilon = 4.3$	2.0	2.1	1.3	1.0

all the VEAs positive. In addition, in solution the reactant VEAs are always greater than those of the products.

NBO charges are calculated on the different products as well as their corresponding closed-shell electron adduct species in vacuum and nonaqueous solution ($\epsilon=4.3$). The results are listed in Table 3. For the radical adducts, which are anionic due to the unprotonated oxygen in the phosphate groups, the negative charges are mainly localized on the phosphate (–1.22 e⁻) and radical-modified thymine (–0.260 to –0.278 e⁻). The sugar groups carry a positive charge (0.479–0.499 e⁻). Upon the capture of an excess electron, the negative charge on the phosphate groups remains essentially unaltered (–1.31 e⁻), whereas for the modified thymine, the negative charge is increased to up to –0.534 e⁻. The most significant changes are assigned to the sugar groups, where the negative charge increases by about 0.67 e⁻. The captured electron will hence mainly be localized to the sugar group. Bulk solvation tends to move the negative charge in the electron adduct from the base to the sugar but does not effect the charge on the phosphate.

Another interesting result is that the N1-glycosidic bond automatically decomposes upon reduction. In, for example, the closed-shell TH3 anion adduct, NBO charge analysis shows that the altered base behaves as the leaving group with –0.936 e⁻ charge, a slight positive charge is found on the sugar, and a nearly unchanged negative charge (–1.3 e⁻) remains on the phosphate. The data show that ~0.4 e⁻ are transferred from the sugar to the altered base upon the N1-glycosidic bond breakage. The data differ from the findings of Gutowski et al.,²⁰ where instead the C3'–O(P) bond is ruptured. The reason for this discrepancy is the fact that Gutowski employed a neutral (protonated) phosphate, which hence allows this group to function as an unphysical electron sink. The importance of using negatively charged phosphates in the determination of sugar C'–H bond dissociation energies has recently been emphasized in a very careful study by Guo and co-workers.²⁹ It was very clearly shown, that using neutral (protonated) phosphates gave a much different ordering in relative C'–H bond strengths of the sugar moiety, as compared to the results when anionic phosphates were employed. As opposed to the former, the latter systems were able to account fully for the experimental findings for these systems. In the current model, we note that the charged phosphate leads to a repulsive effect between the negative charges and spontaneous base release.

The energetics are markedly different from that seen in the corresponding 5'dTMP model, previously investigated in our group.³⁰ In that case, the barriers to H transfer were 5–10 kcal/mol higher for the different anionic radical

Table 3. NPA Charge Distribution on Base (B), Sugar (S), and Phosphate Group (P) of the Radical Anions and Their Vertical and Adiabatic Closed-Shell Electron Adducts in Vacuum and in Nonaqueous Solution (in Parentheses)

	radical anion			electron adduct ^a			electron adduct ^b		
	B	S	P	B	S	P	B	S	P
TH3'	-0.26	0.48	-1.22	-0.53	-0.18	-1.29	-0.94	0.22	-1.28
TH3	-0.26	0.48	-1.22	(-0.39)	(-0.30)	(-1.31)	(-0.93)	(0.23)	(-1.30)
TOH3'	-0.28	0.50	-1.22	-0.53	-0.17	-1.30	-0.94	0.22	-1.28
TOH3	-0.26	0.48	-1.22	(-0.38)	(-0.30)	(-1.32)	(-0.93)	(0.23)	(-1.30)
				(-0.41)	(-0.27)	(-1.32)	(-0.94)	(0.23)	(-1.30)
				-0.51	-0.21	-1.29	-0.95	0.23	-1.28
				(-0.38)	(-0.31)	(-1.31)	(-0.94)	(0.24)	(-1.30)

^a Vertical electron addition to radical anion. ^b Adiabatic species, leading to spontaneous base release.

adducts; the lowest barrier was there obtained for the TH1'→TH3 system, at 27.0 kcal mol⁻¹. Upon addition of an excess electron to those system, spontaneous base release did not occur, but a drastic reduction in H transfer barrier was observed, especially for the H radical adducts (to between 5 and 15 kcal mol⁻¹). Subsequent to H transfer, the barrier to C1'–N1 bond rupture was only a few kcal mol⁻¹. Base release will, hence, eventually be the observed lesion also in the reduced radical adducts, although the 5'dTMP systems appear to be considerably less reactive than the current 3'dTMP ones. This can be understood from the closer proximity to the lesion in 3'dTMP than in 5'dTMP.

3.4. Free Radical Induced Bond Scission. Upon the formation of the C2'-centered radical (i.e., without the additional reduction), the unpaired electron can be transferred to the neighboring atoms, C1' and C3'. The C–C bond lengths on the sugar moiety provide some indications for this. For example, the C1'–C2' and C2'–C3' bond lengths are respectively 1.529 and 1.543 Å in TH1'. After H2' is transferred to the C6 site of the base, the two bonds become shorter and of equal lengths. Delocalization of the unpaired electron to the neighboring carbon atoms hence occur, which in turn influence N1–C1' or C3'–O(P) bond dissociation. It is thus of interest to explore the thermodynamic properties of potential bond dissociation induced by the radical adduct formation. In this section, we discuss bond dissociation energies (BDE) toward strand scission and base release, presented in Table 4.

Homolytic dissociation of the N1-glycosidic bond leading to the formation of a neutral base (B) radical and a negatively charged closed shell sugar–phosphate (SP) moiety was found to be highly favored over heterolysis, with BDE values ranging from 29.1 to 32.2 kcal mol⁻¹ in gas phase. Both homolytic and heterolytic base release leads to the formation of a C1'=C2' double bond in the sugar ring. Bulk solvation ($\epsilon=4.3$) contributes to a lowering of the homolytic BDE by 2–8 kcal mol⁻¹. Even larger effects are noted for the heterolytic process, due to the negatively charged base formed. The BDE values of TH3' and TH3 are lower than those of TOH3' and TOH3 for the homolytic process but larger in the case of heterolysis.

Rupture of C3'–O(P) is also explored and can be compared to the dissociation of the N1-glycosidic bond; again both homolysis and heterolysis are calculated, the latter

Table 4. ZPE-Corrected Gas-Phase Bond Dissociation Energies (in kcal mol⁻¹) for Base Release or Strand Break^d

	N1–C1'	TH3'	TH3	TOH3'	TOH3
homolysis	29.1	29.1	29.1	32.2	31.1
	(22.2)	(22.7)	(22.7)	(24.0)	(29.2)
heterolysis ^a	55.5	55.5	55.5	51.3	50.2
	(45.5)	(45.9)	(45.9)	(42.6)	(47.8)
heterolysis ^b	335.8	335.8	335.8	255.4	254.4
	(217.3)	(217.7)	(217.7)	(142.3)	(147.5)
	C3'–O(P)	TH3'	TH3	TOH3'	TOH3
homolysis	19.1	19.3	19.3	18.1	20.0
	(9.4)	(10.1)	(10.1)	(8.6)	(15.2)
heterolysis ^c	262.0	259.7	259.7	261.8	265.4
	(97.9)	(97.4)	(97.4)	(101.2)	(104.5)

^a Base (B) is closed-shell anion; sugar–phosphate (SP) moiety neutral doublet. ^b B is closed-shell cation; SP doublet dianion. ^c SB is neutral doublet; P singlet dianion. ^d Values in nonaqueous medium ($\epsilon=4.3$) given in parentheses.

associated with HPO₄²⁻ as the leaving group. Also in this case homolytic dissociation is favored, with BDE values ranging from 18.1 to 20.0 kcal mol⁻¹, whereas the heterolytic processes require far more energy. Bulk solvation plays a significant role in reducing the BDE values, by 5–10 kcal mol⁻¹ for homolytic dissociation and around 160.0 kcal mol⁻¹ for heterolysis (due to the dianionic phosphate formed).

From the computed data, it is clear that homolytic dissociation is the primary reaction under H and OH radical stress and that cleavage of C3'–O(P) is dominant over that of the N1-glycosidic bond, assuming that the systems are not influenced by additional electron capture. Further implications are given by the structural changes. The N1–C1' bond lengths are all contracted, whereas the C3'–O(P) ones become slightly longer during the TH1(') → TH3(') and TOH1(') → TOH3(') reactions, which also indicates that cleavage of C3'–O(P) is expected to be the dominant process over N1-glycosidic bond rupture upon radical formation.

In order to obtain a reliable bond scission profile in vacuum, the potential energetic surface (PES) was scanned from TOH3' to the decomposed species by varying C3'...O(P) and C1'...N1 distances with a step-length of 0.1 Å, respectively, and optimizing the remaining coordinates. The energies for the C3'O(P) and C1'N1 bonds scans are

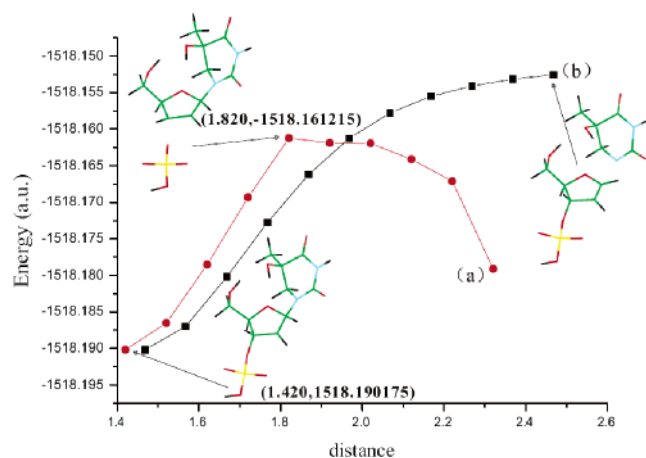


Figure 2. The decomposition curves for the C3'–O(P) and C1'–N1 bonds of TOH3', obtained at the B3LYP/6-31+G-(d,p) level (without ZPE corrections): (a) the C3'–O(P) bond dissociation and (b) the C1'–N1 bond dissociation.

displayed in Figure 2. For the C3'–O(P) bond PES, there is a quasi-saddle point at the C3'...O(P) distance of 1.820 Å with an energy at the B3LYP/6-31+G(d,p) level of approximately 18.2 kcal mol⁻¹ relative to the TOH3' starting point, comparable to the value needed for the decomposition of the N1-glycosidic bond of the dT electron adduct³¹ and less than the energy required for the initial C2'–H transfer. For the elongation of the C1'–N1 bond, the energy is continuously increasing during the 1.0 Å increase in bond length. The results show that the C3'–O(P) bond is facile to be decomposed, while the N1-glycosidic bond remains stable under radical stress, which is consistent with the BDE calculations.

In a very recent paper, the heterolytic process of the N9-glycosidic bond cleavage in 2'-deoxyguanosine promoted by cations, especially by dicationic systems, was reported.³² The BDE values obtained were 44.3 (singly protonated), 58.0 (Cu⁺), -29.2 (Cu²⁺), and -36.2 (doubly protonated) kcal mol⁻¹, respectively. All results taken together illustrate that the decomposition modes are strongly dependent on the local DNA environment (electron attachment, proton transfer, metal ion or radical stress) and on the stability of the decomposed species. We also emphasize again that the usage of appropriately charged models appears to be essential.

4. Conclusions

In the present work, hybrid DFT methods have been employed to investigate the potential DNA-scission processes induced by H and OH radical addition to the C5 site of thymine in 3'dTMP. Geometries, unpaired electron spin densities, NPA charges, and reaction energies were obtained at the B3LYP/6-31+G(d,p) level in the gas phase, followed by energy calculations performed at the same level in solution ($\epsilon=4.3$ and 78.4) using IEF-PCM to model bulk solvation. The barriers of subsequent C2'–H abstraction by the C6 radical site range from 21.7 to 25.1 kcal mol⁻¹ in the gas phase and 19.0 to 25.3 kcal mol⁻¹ in aqueous solution. Bulk solvation contributes more markedly by reducing the reaction energies, especially for the OH radical adducts.

Vertical electron affinities were determined and showed that the capture of an excess electron by the radical systems is favored by solvation also in nonaqueous medium. NPA charges show that the negative charges of the radical adducts are situated on the radical-modified base and the phosphate fragments, respectively. Addition of an excess electron has significant consequences to the system. The additional electron is initially localized on the sugar fragment. However, all electron adducts were found to result in base release upon structural relaxation, with concomitant transfer of the added electron to be entirely localized on the leaving base.

Analysis of bond dissociation energies (BDE) of the N1–C1' (N1-glycosidic bond) and C3'–O(P) bonds of the radical products TH3(•) and TOH3(•) were performed. A homolytic process is supported for both cases and C3'–O(P) bond rupture seems more favorable than the rupture of the N1-glycosidic bond. The C3'–O(P) bond is facile to be decomposed with a barrier of 18.2 kcal mol⁻¹, while the N1-glycosidic bond is still stable under the radical stress. The change in N1–C1' and C3'–O(P) bond lengths before and after the reactions support the above conclusion. The nonaqueous bulk solvation contributes to the bond rupture through a drastic decrease of the homolytic BDE value by up to 15 kcal mol⁻¹.

Acknowledgment. The Swedish Science Research Council (VR) and the National Natural Science Foundation of China (Grant No. 20643007) are gratefully acknowledged for financial support. We also acknowledge generous grants of computing time at the National supercomputing facilities in Linköping (NSC).

References

- (1) von Sonntag, C.; Schuchman, H.-P. Ionizing radiation damage to DNA. In *Encyclopedia of Molecular Biology and Molecular Medicine*; Meyers, R. A., Ed.; VCH Weinheim: 1996; Vol. 3, pp 354–365.
- (2) Halliwell, B.; Gutteridge, J. M. C. *Free Radicals in Biology and Medicine*; Oxford University Press: Oxford, U.K., 1999.
- (3) Stein, G.; Weiss, J. Chemical effects of ionizing radiations. *Nature* **1948**, *161*, 650.
- (4) Commoner, B.; Townsend, J.; Pake, G. E. Free Radicals in Biological Materials. *Nature* **1954**, *174*, 689.
- (5) Nauser, T.; Schöneich, C. Thiyl Radical Reaction with Thymine: Absolute Rate Constant for Hydrogen Abstraction and Comparison to Benzylic C–H Bonds. *Chem. Res. Toxicol.* **2003**, *16*, 1056.
- (6) Ramírez-Arizmendi, L. E.; Heidbrink, J. L.; Guler, L. P.; Kenttämaa, H. I. Reactivity of Substituted Charged Phenyl Radicals toward Components of Nucleic Acids. *J. Am. Chem. Soc.* **2003**, *125*, 2272.
- (7) von Sonntag, C. *The Chemical Basis of Radiation Biology*; Taylor & Francis: London, U.K., 1987.
- (8) Wetmore, S. D.; Boyd, R. J.; Eriksson, L. A. Theoretical Investigation of Adenine Radicals Generated in Irradiated DNA Components. *J. Phys. Chem. B* **1998**, *102*, 10602.

- (9) Drew, H. R.; Wing, R. M.; Takano, T.; Broka, C.; Tanaka, S.; Itakura, K.; Dickerson, R. E. Structure of a B-DNA Dodecamer: Conformation and Dynamics. *Proc. Natl. Acad. Sci. U.S.A.* **1981**, *78*, 2179.
- (10) Balasubramanian, B.; Pogozelski, W. K.; Tullius, T. D. Failure of egg cylinder elongation and mesoderm induction in mouse embryos lacking the tumor suppressor smad2. *Proc. Natl. Acad. Sci. U.S.A.* **1998**, *95*, 9738.
- (11) Lemaire, D. G. E.; Bothe, E.; Schulte-Frohlinde, D. Yields of Radiation-induced Main Chain Scission of Poly U in Aqueous Solution: Strand Break Formation Via Base Radicals. *Int. J. Radiat. Biol.* **1984**, *45*, 351.
- (12) Symons, M. C. R. Application of electron spin resonance spectroscopy to the study of the effects of ionising radiation on DNA and DNA complexes. *J. Chem. Soc., Faraday Trans.* **1987**, *83*, 1.
- (13) Becker, D.; Sevilla, M. D. In *Advances in Radiation Biology, Volume 17, DNA and Chromatin Damage Caused by Radiation*; Lett, J. T., Sinclair, W. K., Eds.; Academic Press: New York, 1987.
- (14) Bothe, E.; Qureshi, G. A.; Schulte-Frohlinde, D. Rate of OH radical induced strand break formation in single stranded DNA under anoxic conditions. An investigation in aqueous solutions using conductivity methods. *Z. Naturforsch.* **1983**, *38C*, 1030.
- (15) (a) Karam, L. R.; Dizdaroglu, M.; Simic, M. G. Intramolecular H Atom Abstraction from the Sugar Moiety by Thymine Radicals in Oligo- and Polydeoxynucleotides. *Radiat. Res.* **1988**, *116*, 210. (b) Deeble, D. J.; von Sonntag, C. Radiolysis of Poly(U) in Aqueous Solution. The Role of Primary Sugar and Base Radicals in the Release of Undamaged Uracil. *Int. J. Radiat. Biol.* **1984**, *46*, 247.
- (16) (a) Hildenbrand, K.; Behrens, G.; Schulte-Frohlinde, D.; Herak, J. N. Comparison of the reaction of OH and of SO₄⁻ radicals with pyrimidine nucleosides. An electron spin resonance study in aqueous solution. *J. Chem. Soc., Perkin Trans. 2* **1989**, 283. (b) Schulte-Frohlinde, D.; Hildenbrand, K. In *Free Radicals in Synthesis and Biology*; Minisci, F., Ed.; 1989; p 335. (c) Schulte-Frohlinde, D.; Opitz, J.; Gomer H.; Bothe, E. Model studies for the direct effect of high-energy irradiation on DNA. Mechanism of strand break formation induced by laser photoionization of poly U in aqueous solution. *Int. J. Radiat. Biol.* **1985**, *48*, 397. (d) Wagner, J. R.; van Lier, J. E.; Johnston, L. J. Quinone sensitized electron transfer photooxidation of nucleic acids: chemistry of thymine and thymidine radical cations in aqueous solution. *Photochem. Photobiol.* **1990**, *52*, 333. (e) Krishna, C. M.; Decarroz, C.; Wagner, J. R.; Cadet J.; Riesz, P. Menadione sensitized photooxidation of nucleic acid and protein constituents. An ESR and spin-trapping study. *Photochem. Photobiol.* **1987**, *46*, 175.
- (17) Barvian, M. R.; Barkley, R. M.; Greenberg, M. M. Reactivity of 5,6-Dihydro-5-hydroxythymidin-6-yl Generated via Photoinduced Single Electron Transfer and the Role of Cyclohexa-1,4-diene in the Photodeoxygenation Process. *J. Am. Chem. Soc.* **1995**, *117*, 4894.
- (18) Colson, A.-O.; Sevilla, M. D. Ab Initio Molecular Orbital Calculations of Radicals Formed by H• and •OH Addition to the DNA Bases: Electron Affinities and Ionization Potentials. *J. Phys. Chem.* **1995**, *99*, 13033.
- (19) Zhang, Q.; Wang, Y. Independent Generation of the 5-Hydroxy-5,6-dihydrothymidin-6-yl Radical and Its Reactivity in Dinucleoside Monophosphates. *J. Am. Chem. Soc.* **2004**, *126*, 13287.
- (20) Dabkowska, I.; Rak, J.; Gutowski, M. DNA strand breaks induced by concerted interaction of H radicals and low-energy electrons-A computational study on the nucleotide of cytosine. *Eur. Phys. J. D* **2005**, *35*, 429.
- (21) Hou, R.; Gu, J.; Xie, Y.; Yi, X.; Schaefer, H. F., III. The 2'-Deoxyadenosine-5'-phosphate Anion, the Analogous Radical, and the Different Hydrogen-Abstracted Radical Anions: Molecular Structures and Effects on DNA Damage. *J. Phys. Chem. B* **2005**, *109*, 22053.
- (22) Becke, A. D. Density-functional thermochemistry. III. The role of exact exchange. *J. Chem. Phys.* **1993**, *98*, 5648.
- (23) Lee, C.; Yang, W.; Parr, R. G. Development of the Colle-Salvetti correlation-energy formula into a functional of the electron density. *Phys. Rev. B* **1988**, *37*, 785.
- (24) Reed, A. E.; Curtiss, L. A.; Weinhold, F. Intermolecular interactions from a natural bond orbital, donor-acceptor viewpoint. *Chem. Rev.* **1988**, *88*, 899.
- (25) Tomasi, J.; Persico, M. Molecular Interactions in Solution: An Overview of Methods Based on Continuous Distributions of the Solvent. *Chem. Rev.* **1994**, *94*, 2027.
- (26) Frisch, M. J.; Trucks, G. W.; Schlegel, H. B.; Scuseria, G. E.; Robb, M. A.; Cheeseman, J. R.; Montgomery, J. A., Jr.; Vreven, T.; Kudin, K. N.; Burant, J. C.; Millam, J. M.; Iyengar, S. S.; Tomasi, J.; Barone, V.; Mennucci, B.; Cossi, M.; Scalmani, G.; Rega, N.; Petersson, G. A.; Nakatsuji, H.; Hada, M.; Ehara, M.; Toyota, K.; Fukuda, R.; Hasegawa, J.; Ishida, M.; Nakajima, T.; Honda, Y.; Kitao, O.; Nakai, H.; Klene, M.; Li, X.; Knox, J. E.; Hratchian, H. P.; Cross, J. B.; Adamo, C.; Jaramillo, J.; Gomperts, R.; Stratmann, R. E.; Yazyev, O.; Austin, A. J.; Cammi, R.; Pomelli, C.; Ochterski, J. W.; Ayala, P. Y.; Morokuma, K.; Voth, G. A.; Salvador, P.; Dannenberg, J. J.; Zakrzewski, V. G.; Dapprich, S.; Daniels, A. D.; Strain, M. C.; Farkas, O.; Malick, D. K.; Rabuck, A. D.; Raghavachari, K.; Foresman, J. B.; Ortiz, J. V.; Cui, Q.; Baboul, A. G.; Clifford, S.; Cioslowski, J.; Stefanov, B. B.; Liu, G.; Liashenko, A.; Piskorz, P.; Komaromi, I.; Martin, R. L.; Fox, D. J.; Keith, T.; Al-Laham, M. A.; Peng, C. Y.; Nanayakkara, A.; Challacombe, M.; Gill, P. M. W.; Johnson, B.; Chen, W.; Wong, M. W.; Gonzalez, C.; Pople, J. A. *Gaussian 03, Revision B.04*; Gaussian, Inc.: Pittsburgh, PA, 2003.
- (27) Pardo, L.; Banfelder, J. T.; Osman, R. Ab initio LCAO-MO-SCF study of bonding in the simplest phosphorus ylide. *J. Am. Chem. Soc.* **1992**, *114*, 2382.
- (28) (a) Oyler, N. A.; Adamowicz, L. Electron attachment to uracil: theoretical ab initio study. *J. Phys. Chem.* **1993**, *97*, 11122. (b) Hendricks, J. H.; Lyapustina, S. A.; de Clercq, H. L.; Bowen, K. H. The dipole bound-to-covalent anion transformation in uracil. *J. Chem. Phys.* **1998**, *108*, 8. (c) Wetmore, S. D.; Boyd, R. J.; Eriksson, L. A. Electron affinities and ionization potentials of nucleotide bases. *Chem. Phys. Lett.* **2000**, *322*, 129. (d) Wesolowski, S. S.; Leininger, M. L.; Pentchev, P. N.; Schaefer, H. F., III. Electron Affinities of the DNA and RNA Bases. *J. Am. Chem. Soc.* **2001**, *123*, 4023.

- (29) Li, M.-J.; Liu, L.; Wei, K.; Fu, Y.; Guo, Q.-X. Significant Effects of Phosphorylation on Relative Stabilities of DNA and RNA Sugar Radicals: Remarkably High Susceptibility of H-2' Abstraction in RNA. *J. Phys. Chem. B* **2006**, *110*, 13582.
- (30) Zhang, R. B.; Eriksson, L. A. The Role of Nucleobase Carboradical and Carbanion on DNA Lesions: A Theoretical Study. *J. Phys. Chem. B* **2006**, *110*, 23583.
- (31) Gu, J.; Xie, Y.; Schaefer, H. F., III. Glycosidic Bond Cleavage of Pyrimidine Nucleosides by Low-Energy Electrons: A Theoretical Rationale. *J. Am. Chem. Soc.* **2005**, *127*, 1053.
- (32) Ríos-Font, R.; Bertrán, J.; Rodríguez-Santiago, L.; Sodupe, M. Effects of Ionization, Metal Cationization and Protonation on 2'-Deoxyguanosine: Changes on Sugar Puckering and Stability of the N-Glycosidic Bond. *J. Phys. Chem. B* **2006**, *110*, 5767.

CT6003593

CO₂ Activation by Nb⁺ and NbO⁺ in the Gas Phase. A Case of Two-State Reactivity Process[†]

S. Di Tommaso, T. Marino, F. Rondinelli, N. Russo, and M. Toscano*

Dipartimento di Chimica and Centro di Calcolo ad Alte Prestazioni per Elaborazioni Parallele e Distribuite—Centro d'Eccellenza MIUR, Universita' della Calabria, I-87030 Arcavacata di Rende (CS), Italy

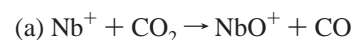
Received January 13, 2007

Abstract: Gas-phase carbon dioxide activation by Nb⁺ and NbO⁺ was studied at the density functional level of theory using the hybrid exchange correlation functional B3LYP. Three reaction profiles corresponding to the quintet, triplet, and singlet multiplicities were investigated in order to ascertain the presence of some spin inversion during the CO₂ reduction. Carbon dioxide activation mediated by metal cations was found to be an exothermic spin-forbidden process resulting from a crossing between quintet and triplet energetic profiles. The endothermic reaction of NbO⁺ with carbon dioxide was a barrierless process involving spin inversion. Geometries of minima along potential energy surfaces and reaction heats were in agreement with those from experimental studies carried out by using a guided ion beam tandem mass spectrometer.

1. Introduction

The possibility of activating carbon dioxide, the main greenhouse gas, has received considerable attention in previous years.^{1–5} As it is not possible to reduce significantly CO₂ emissions from anthropic sources, the interest in its chemical fixation⁶ and utilization as a starting material of chemically useful compounds is increased. However, only nature can effectively regenerate organic molecules from carbon dioxide by using it as a one-carbon building block.⁷ In previous years, chemical processes based on the use of metal species as catalysts for carbon dioxide reduction were investigated, both experimentally and theoretically.^{8–11} By using a guided ion beam mass spectrometer, Sievers and Armentrout elucidated the reaction mechanisms of bare zirconium¹² and niobium¹³ cations and those of their respective monoxide and dioxide cations with CO₂. Details of the zirconium-ion-assisted CO₂ reduction potential energy surface were obtained by density functional theory.¹⁴ Experimental data highlight the importance of analyzing the electronic terms and symmetry of metal cations involved in ground and excited states' energetic profiles. In this paper,

we studied, at the same level of theory used for the activation of carbon dioxide by zirconium,¹² the following reactions:



Our main aim was to elucidate the reaction mechanisms and determine the activation barriers useful to give insight into kinetic aspects. In particular, analysis of potential energy surfaces (PES), vibrational characterization of stationary and saddle points of each reaction pathway, and determination of exothermicity and endothermicity and bond dissociation energies were carried out in our work.

2. Computational Methods

All calculations were performed using the Gaussian 03 package.¹⁵ Full optimizations were carried out for all molecular structures involved in the reaction mechanisms by means of B3LYP/DFT methods^{16,17} in connection with the 6-311+G** basis set^{18,19} for nonmetal atoms and the LANL2DZ pseudopotential²⁰ for niobium ions. Energetic values include zero-point energy corrections obtained from the vibrational analysis.

[†] Dedicated to Professor Dennis R. Salahub on the occasion of his 60th birthday.

* Corresponding author fax: +39-0984-493390; email: m.toscano@unical.it.

Transition states were confirmed applying the intrinsic reaction-coordinated procedure implemented in the Gaussian 03 package.^{21,22}

The most stable electronic states of bare niobium and metal monoxide and dioxide monocations as well as those of all other species were carefully searched by the Alter keyword that ensures that the orbitals selected for occupation in the wavefunction are those of lowest energy. Wave function stability was tested by the Stable calculation method.^{23–25}

3. Results and Discussion

3.1. Determination of Metal Species Electronic States.

A reaction profile involves crossings of different spin surfaces along the reaction coordinate, then it is described as a two-state reactivity pathway.²⁶ Such a type of mechanism requires the determination of the correct reactivity scale for metal cations' ground and excited states, or in other words the exactness of electronic states' ordering and splitting. According to our calculations, the electronic configuration of the Nb⁺ ground state (⁵D) was found to be 4d⁴, while among its excited states, ³P was the lowest in energy with a 4d⁴ configuration too. The energy gap between the ground and first excited states was evaluated to be 17.25 kcal/mol, in good agreement with the experimental energy separation of 15.91 kcal/mol reported by Sievers and Armentrout.¹³

Nb⁺ in its lowest singlet state (¹S with configuration 4d⁴) lies at 23.72 kcal/mol above the ⁵D quintet.

Photoelectronic studies carried out by Dyke and co-workers²⁷ by ionizing the NbO molecule in its ground state (⁴Σ⁻) hypothesized ³Σ⁻ as the ground state of the NbO⁺ cation.

Our computations confirmed this suggestion deriving from a 2σ²1π⁴1δ² electronic configuration.

NbO⁺ singlet (¹A') and quintet (⁵Σ_u) excited electronic states were found to lie at 4.84 and 53.04 kcal/mol above the ground state, respectively.

Neither experimental nor theoretical information exists for the NbO₂⁺ ground state. Our B3LYP study indicated that the lowest-energy configuration of the niobium dioxide monocation has the singlet multiplicity (¹A₁) like its isoivalent ZrO₂ neutral molecule.^{13,28} Triplet (³B₂) and quintet (⁵B₂) excited states were found at 1.7 and 5.15 eV above the ground state, respectively.

On the basis of these results, it appears clear that the processes (a and b) to be investigated are, in principle, spin-forbidden reactions. Furthermore, the participation of the highest excited states is very unlikely; thus, the energetic profile for these multiplicities was not reported. However, energetic data were included in the tables.

3.2. Path a: Activation of CO₂ by Nb⁺. The most stable structure of the first adduct along the potential energy profile concerning path a (see Figure 1) was obtained by considering all known different coordination modes (η_o^1 , η_{o,o^2} , η_{c,o^2} , and η_c^1) of CO₂ to a transition metal atom.²⁹ Full optimizations of these starting geometries did not always give stable molecular systems as the data of Table 1 demonstrate. In particular, we have observed that the η_{c,o^2} structure in its quintet spin state collapsed in η_o^1 , while singlet η_c^1 evolved in η_{c,o^2} . The triplet η_{c,o^2} , singlet η_{o,o^2} , and quintet η_c^1

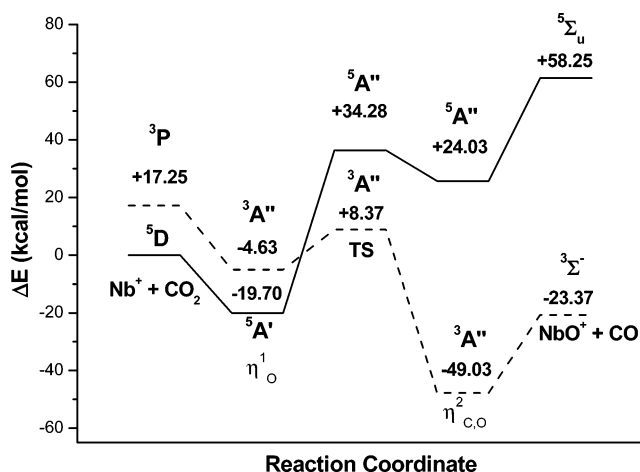


Figure 1. Potential energy surfaces relating to the Nb⁺ + CO₂ reaction for quintet and triplet spin states.

Table 1. Absolute (*E* in au) Energies for Different NbCO₂⁺ Isomers

coordination modes	quintet	triplet	singlet
	<i>E</i>	<i>E</i>	<i>E</i>
η_o^1	-244.576 973	-244.552 958	244.541 046
η_{o,o^2}	-244.521 936	-244.521 655	no coordination
η_{c,o^2}	in η_o^1	no coordination	-244.527461
η_c^1	no coordination	-244.515227	in η_{c,o^2}

optimizations led to weak adducts in which CO₂ was practically not coordinated to the cation.

For all examined multiplicities, the most stable coordination of niobium to carbon dioxide was found to be the η_o^1 one. Quintet η_o^1 constitutes the deepest minimum lying at 19.70 kcal/mol below the reactants asymptote. Irrespective of multiplicity, the η_o^1 compounds always present a linear structure (see Figure 2) with similar geometrical parameters except for the Nb⁺–O bond length.

Absolute and relative energies for compounds lying on the path a PES are listed in Table 2.

For both spin states, the first step consists in the evolution of the η_o^1 adduct in the η_{c,o^2} complex through a transition state (TS).

The three-center transition state on the quintet PES (⁵A'') lies at 34.28 kcal/mol above the energetic zero and is characterized by an imaginary vibrational frequency of 432 cm⁻¹ that corresponds to the stretching of the incoming Nb⁺–C bond coupled with the bending of the C–Nb⁺–O₁ angle.

The analogous transition state on the triplet surface (³A'') is located at 8.36 kcal/mol above the reactants asymptote in their electronic state of quintet. The imaginary frequency of 218 cm⁻¹ appears to be associated only with the bending of Nb⁺–O₁–C because the Nb⁺–C distance is too long to observe its stretching in the computed IR spectrum.

From a structural point of view, the two transition states are quite different, as can be argued from parameters reported in Figure 2. A crossing between the two potential energy profiles suggests that a spin inversion occurs; thus, after the formation of the η_o^1 molecular complex, the triplet multiplicity path becomes energetically favored.

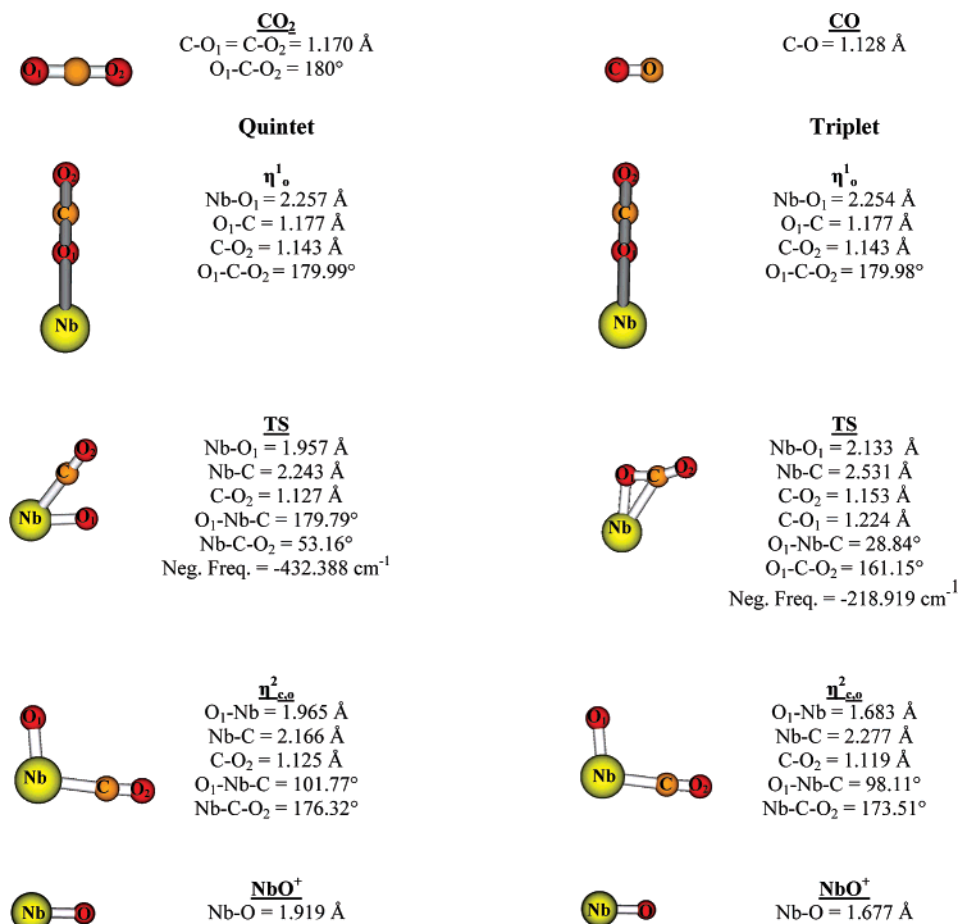


Figure 2. Optimized structures and geometrical parameters of compounds relating to path a.

Table 2. Absolute (E in au) and Relative (ΔE in kcal/mol) Energies for the Compounds Having Quintet, Triplet, and Singlet Multiplicities Involved in Path a^a

species	quintet		triplet		singlet	
	E	ΔE	E	ΔE	E	ΔE
Nb ⁺ + CO ₂	-244.545 584	0	-244.518 091	17.25	-244.507 775	23.72
η_o^1	-244.576 973	-19.70	-244.552 958	-4.63	-244.541 046	2.85
TS	-244.490 952	34.28	-244.532 249	8.37	-244.524 269	13.36
$\eta_{c,o}^2$	-244.507 294	24.03	-244.623 721	-49.03	-244.617 693	-45.25
NbO ⁺ + CO	-244.452 742	58.25	-244.582 829	-23.37	-244.573 845	-17.73

^a ΔE values of excited states are referred to reactants' energy in their state of quintet.

Table 3. Absolute (E in au) and Relative (ΔE in kcal/mol) Energies for the Compounds Having Quintet, Triplet, and Singlet Multiplicities Involved in Paths b.1 and b.2

species	quintet		triplet		singlet	
	E	ΔE	E	ΔE	E	ΔE
NbO ⁺ + CO ₂	-319.743 959	81.62	-319.874 046	0	-319.865 062	5.64
ONbCO ₂ ⁺	-319.784 405	56.25	-319.907 404	-20.93	-319.897 074	-14.45
NbO ₂ ⁺ + CO	-319.633 760	150.77	-319.783 502	+56.81	-319.857 197	10.57
NbCO ₂ ⁺ + O	-319.597 173	182.29	-319.713 600	+100.67	-319.707 572	104.46

In fact, travelling on the quintet PES, after TS, we found that the O-Nb⁺-CO $\eta_{c,o}^2$ species is quite unstable (24.03 kcal/mol above reactants) and practically unreachable because of the presence of an activation barrier of about 54 kcal/mol.

Consequently, the NbO⁺ and CO products, placed 58.25 kcal/mol above the reactants asymptote, cannot be obtained through this reaction channel.

Different features can be recognized in triplet energy surface. If we take into account the two-state reactivity

phenomenon, the second molecular intermediate $\eta_{c,o}^2$ (³A'') is formed starting from the quintet η_o^1 by overcoming an activation barrier of 28.06 kcal/mol. The $\eta_{c,o}^2$ (³A'') species lies at 49.03 kcal/mol below the quintet reactants asymptote, while the products are placed at -23.37 kcal/mol on the PES.

If the overlap of potential energy surfaces is considered, the reduction of CO₂ by Nb⁺ appears to be an exothermic process with a reaction heat of 23.37 kcal/mol and a rate-determining step that implies the clearing of an activation barrier of 28.06 kcal/mol. Furthermore, according to the spin

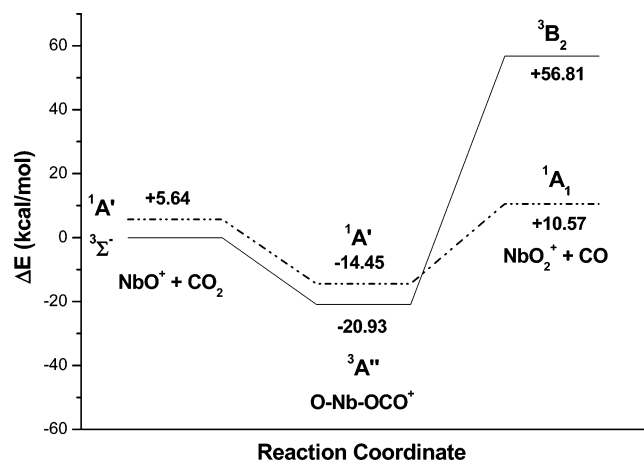


Figure 3. Energetic profiles relating to the interaction between NbO^+ and CO_2 : path b.1.

inversion occurrence, the overall mechanism is that of a spin-forbidden two-state reaction.

3.3. Path b: Activation of CO_2 by NbO^+ . Experimental data achieved by Sievers and Armentrout¹³ suggest that NbO^+ produced by path a, as elucidated above, reacts with carbon dioxide, giving rise to $\text{NbO}_2^+ + \text{CO}$ or $\text{NbCO}_2^+ + \text{O}$ products through two different channels of path b that we named b.1 and b.2.

Molecular structures involved in both these channels were optimized by considering quintet, singlet, and triplet spin states. As shown in Table 3, quintet stationary points have higher energy than the corresponding species with different multiplicities; thus, the relative PES was not further considered. Furthermore, it is also possible to note that irrespective of the considered multiplicity the formation of NbCO_2^+ and atomic oxygen requires a huge quantity of energy, making meaningless the discussion about the b.2 path. However, it is worthwhile that both b.1 and b.2 profiles proceed through

a barrierless mechanism since the molecular adduct resulting from the interaction between NbO^+ and CO_2 evolves into the products without involving any transient structure. Besides, both b.1 and b.2 reaction paths are endothermic processes, as highlighted from relative energies listed in Table 3.

The triplet and singlet b.1 paths for the formation of $\text{NbO}_2^+ + \text{CO}$ were reported in Figure 3. Optimized structures and geometrical parameters of species involved are shown in Figure 4.

The molecular adduct $\text{O-Nb}^+-\text{OCO}$ with a triplet spin state is 20.93 kcal/mol more stable than the reactants, while products with the same multiplicity are located at very high energy (56.81 kcal/mol above the NbO^+ and CO_2 asymptote). The triplet pathway is therefore very endergonic.

On the contrary, on the singlet PES, the species $\text{O-Nb}^+-\text{OCO}$ and the final products lie 14.45 and 10.57 kcal/mol below and above the reference, respectively.

A look to both potential energy surfaces shows that the formation of NbO_2^+ and CO is characterized by a spin inversion. The crossing occurs after the molecular adduct and entails that the reaction be a spin-forbidden process with reactants having a triplet multiplicity and products in the singlet spin state. The global process is endothermic for 10.57 kcal/mol.

4. Conclusions

Gas-phase interactions of Nb^+ and NbO^+ with carbon dioxide were examined at the density functional level of theory, by using B3LYP/6-311+G**/LANL2DZ theoretical protocol. Triplet, quintet, and singlet multiplicities were analyzed for both pathways and for different reaction channels.

The singlet energy surface for the interaction of Nb^+ with CO_2 was found to be greatly disfavored because of the high energy of all stationary points. Between triplet and quintet

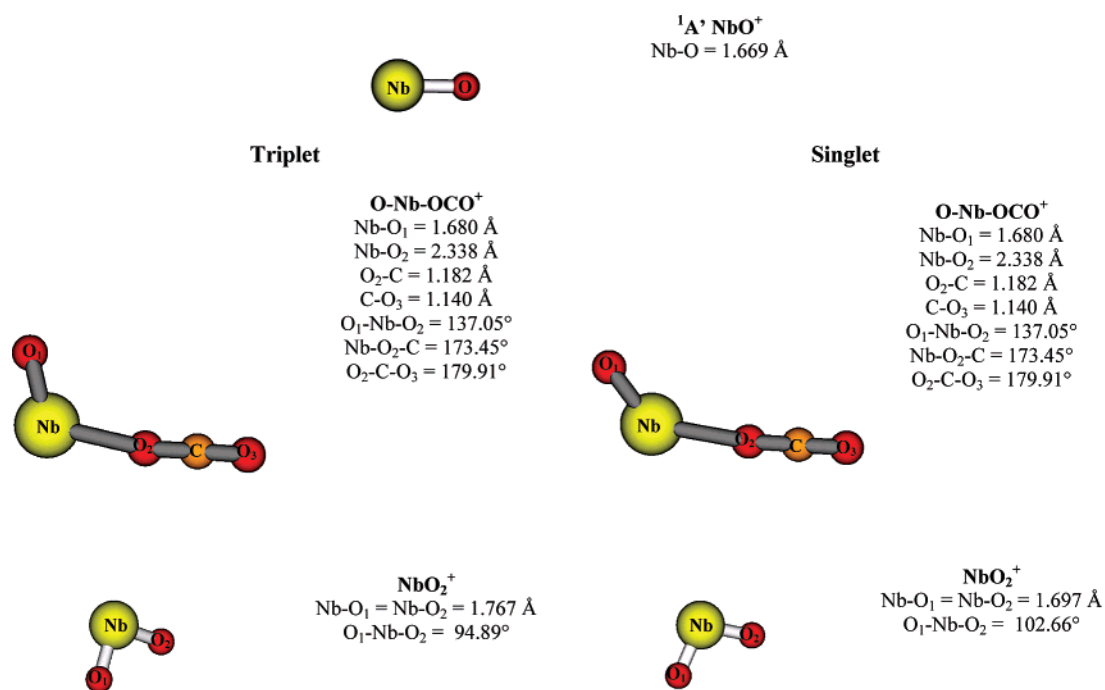


Figure 4. Optimized structures and geometrical parameters of compounds involved in path b.1.

potential energy profiles, a crossing occurs that causes a spin inversion at the transition-state level. Thus, CO₂ activation catalyzed by Nb⁺ can be described as a two-state-reactivity process with a reaction heat of 23.37 kcal/mol.

In brief, the coordination of the niobium cation in its quintet ground state to CO₂ gives rise to the linear ⁵A' η_o¹ adduct that, through a transition state having triplet multiplicity, evolves in the ³A'' η_{c,o}² compound, which in turn dissociates into the ³Σ⁻ NbO⁺ and CO products.

The spin-forbidden profile is in agreement with the information derived by Sievers and Armentrout's mass spectrometry measurements.

The analysis of both possible reaction paths relating to NbO⁺ and CO₂ interaction indicates that the most favored channel involves the abstraction of carbon dioxide oxygen by a monoxide cation.

The quintet potential energy profile as well as the path concerning the formation of NbCO₂⁺ and O products are energetically unlikely.

The global reaction path for the formation of NbO₂⁺ and CO derives from the overlap of triplet and singlet profiles showing a crossing following the formation of the ONb-OCO⁺ molecular adduct, which causes a spin inversion. No transition state was observed for this process.

In our work, particular attention has received the determination of the electronic terms for metal compounds involved in all of the pathways, as some of them are unknown theoretically or experimentally. For the niobium cation, the comparison of our data with experimental ones indicates that the used level of theory is suitable enough to predict the exact ordering of triplet and quintet states other than the energetic gap between them.

Acknowledgment. We gratefully acknowledge the Dipartimento di Chimica, Università della Calabria for financial aid.

References

- Behr, A. *Carbon Dioxide Activation by Metal Complexes*; VCH: New York, 1998.
- Louie, J.; Gibby, J. E.; Farnworth, M. V.; Tekavec, T. N. *J. Am. Chem. Soc.* **2002**, *124*, 15188.
- Gibson, D. H. *Chem. Rev.* **1996**, *96*, 651.
- Niemelä, M.; Nokkosmäki, M. *Catal. Today* **2005**, *100*, 269.
- Solymosi, F. J. *J. Mol. Catal.* **1991**, *65*, 337.
- Lu, X. B.; Wang, Y. *Angew. Chem., Int. Ed.* **2004**, *43*, 3574.
- Brändén, C. I.; Schneider, G. *Carbon Dioxide Fixation and Reduction in Biological and Model Systems*; Oxford University Press: New York, 1994.
- Avila, Y.; Barrault, J.; Pronier, S.; Kappenstein C. *Appl. Catal., A* **1995**, *132*, 97.
- Fujita, T.; Nishiyama, Y.; Ohtsuka, Y.; Asami, K.; Kusakabe, K. I. *Appl. Catal., A* **1995**, *126*, 245.
- Otorbaev, D. K. *Chem. Phys.* **1995**, *196*, 543.
- Sahibzada, M.; Chadwick, D.; Metcalfe, I. S. *Catal. Today* **1996**, *29*, 367.
- Sievers, M. R.; Armentrout, P. B. *Int. J. Mass Spectrom.* **1999**, *185*, 117.
- Sievers, M. R.; Armentrout, P. B. *Int. J. Mass Spectrom.* **1998**, *179*, 115.
- Rondinelli, F.; Russo, N.; Toscano, M. *Theor. Chem. Acc.* **2006**, *115*, 434.
- Frisch, M. J.; Trucks, G. W.; Schlegel, H. B.; Scuseria, G. E.; Robb, M. A.; Cheeseman, J. R.; Montgomery, J. A., Jr.; Vreven, T.; Kudin, K. N.; Burant, J. C.; Millam, J. M.; Iyengar, S. S.; Tomasi, J.; Barone, V.; Mennucci, B.; Cossi, M.; Scalmani, G.; Rega, N.; Petersson, G. A.; Nakatsuji, H.; Hada, M.; Ehara, M.; Toyota, K.; Fukuda, R.; Hasegawa, J.; Ispida, M.; Nakajima, T.; Honda, Y.; Kitao, O.; Nakai, H.; Klene, M.; Li, X.; Knox, J. E.; Hratchian, H. P.; Cross, J. B.; Adamo, C.; Jaramillo, J.; Gomperts, R.; Stratmann, R. E.; Yazyev, O.; Austin, A. J.; Cammi, R.; Pomelli, C.; Ochterski, J. W.; Ayala, P. Y.; Morokuma, K.; Voth, G. A.; Salvador, P.; Dannenberg, J. J.; Zakrzewski, V. G.; Dapprich, S.; Daniels, A. D.; Strani, M. C.; Farkas, O.; Malick, D. K.; Rabuck, A. D.; Raghavachari, K.; Foresman, J. B.; Ortiz, J. V.; Cui, Q.; Baboul, A. G.; Clifford, S.; Cioslowski, J.; Stefanov, B. B.; Liu, G.; Liashenko, A.; Piskorz, P.; Komaromi, V.; Martin, R. L.; Fox, D. J.; Keith, T.; Al-Laham, M. A.; Peng, C. Y.; Nanayakkara, A.; Challacombe, M.; Gill, P. M. W.; Johnson, B.; Chen, W.; Wong, M. W.; Gonzalez, C.; Pople, J. A. *Gaussian 03*; Gaussian, Inc: Wallingford, CT, 2004.
- Lee, C.; Yang, W.; Parr, R. G. *Phys. Rev. B: Condens. Matter Mater. Phys.* **1998**, *37*, 785.
- Colle, R.; Solvetti, D. *Theor. Chim. Acta* **1975**, *37*, 329.
- McLean, A. D.; Chandler, G. S. *J. Chem. Phys.* **1980**, *72*, 5639.
- Krishnan, R.; Binkley, J. S.; Seeger, R.; Pople, J. A. *J. Chem. Phys.* **1980**, *72*, 650.
- Hay, P. J.; Wadt, W. R. *J. Chem. Phys.* **1985**, *82*, 284.
- Gonzalez, C.; Schlegel, H. B. *J. Chem. Phys.* **1989**, *90*, 2154.
- Gonzalez, C.; Schlegel, H. B. *J. Phys. Chem.* **1990**, *94*, 5523.
- Seeger, R.; Pople, J. A. *J. Chem. Phys.* **1977**, *66*, 3045.
- Bauernschmitt, R.; Ahlrichs, R. *J. Chem. Phys.* **1996**, *104*, 9047.
- Schlegel, H. B.; Mc Douall, J. J. *Computational Advances in Organic Chemistry*; Ogretir, C., Csizmadia, J. G., Eds.; Kluwer Academic: The Netherlands, 1991.
- Schröder, D.; Shaik, S.; Schwarz, H. *Acc. Chem. Res.* **2000**, *33*, 139.
- Dyke, J. M.; Ellis, A. M.; Fehér, M.; Morris, A.; Paul, A. J.; Stevens, J. C. H. *J. Chem. Soc., Faraday Trans.* **1987**, *283*, 1555.
- Siegbahn, P. E. M. *J. Phys. Chem.* **1993**, *97*, 9096.
- Schaftenaar, G.; Noordik, J. H. *J. Comput.-Aided Mol. Des.* **2000**, *14*, 123.

CT700014K

Lewis Acid and Substituent Effects on the Molecular Mechanism for the Nazarov Reaction of Penta-1,4-dien-3-one and Derivatives. A Topological Analysis Based on the Combined Use of Electron Localization Function and Catastrophe Theory[†]

Victor Polo and Juan Andrés*

Departamento de Química Física y Analítica, Universidad Jaime I, Apartado 224, 12080, Castellón, Spain

Received February 5, 2007

Abstract: The joint use of the topological analysis provided by the electron localization function (ELF) and catastrophe theory (CT), at the B3LYP/6-31G(d) calculation level, allows us to examine the Lewis acid (protonation H⁺ and presence of BH₃) and the role of an electron donor substituent (–OCH₃) at α and β positions along the course of the molecular mechanism for the Nazarov rearrangement of penta-1,4-dien-3-one and eight derivatives. The progress of the reaction is monitored by the changes of the ELF structural stability domains (SSDs), each change being controlled by a turning point derived from CT. These SSDs and the corresponding turning points are associated with a sequence of elementary chemical steps. Along the cyclization path of penta-1,4-diene-3-one, four SSDs as well as three turning points (cusp1–fold1–cusp2) have been characterized. The first and second SSDs correspond to a polarization of the C–O bond and electronic redistribution among the C–C bonds, respectively, and they can be associated with the formation of an oxyallyl structure. The third and fourth SSDs can be assigned to the ring closure process. Protonation of the oxygen atom shifts the reactive directly into the second SSD, greatly reducing the activation and reaction energies. The electronic effects due to Lewis acids and electron donor substituents have been rationalized in terms of calculations of mesomeric structures from ELF basin populations. The combination of Lewis acids together with α and β –OCH₃ substitutions renders a cooperative and competitive effect on activation and reaction free energies, respectively.

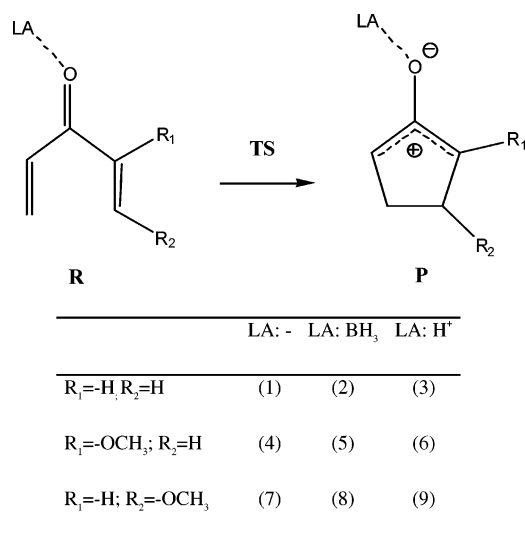
1. Introduction

One of the fundamental issues of the theoretical descriptions of chemical reactivity stands on the complete understanding of reaction mechanisms. The rearrangements among electron pairs along the pathway connecting the reactives to the products can be perturbed in multiple ways; that is, catalysts can accelerate the reaction toward a desired product. The

analysis of the electron density enables the extraction of information from the wave function in a form that is readily interpretable with reference to physicochemical properties of a molecule. Modern techniques for the analysis of chemical bonding have been developed recently on the basis of properties of the topological analysis of the electron density, as the atoms in molecules of Bader¹ or the electron localization function (ELF),² developed for the study of electron pairing by Silvi and Savin.³ Topological analysis of ELF enables the chemist to condense the information succinctly to interpret diverse bonding situations, such as the recently defined bond shift,⁴ (homo-) aromaticity,⁵ or the

[†] Dedicated to Professor Dennis R. Salahub on the occasion of his 60th birthday.

* Corresponding author phone: (+34) 964-728071; fax: (+34) 964-728066; e-mail: andres@qfa.uji.es.

Scheme 1. Reactions Studied in This Work

nature of the bridge bond in propellanes.⁶ A further development was introduced by the bonding evolution theory (BET)⁷ which combined the ELF and Thom's catastrophe theory (CT)⁸ for the analysis of the creation/annihilation of ELF basins. According to BET, the rigorous definition of electron pairing provided by ELF⁹ and the identification and characterization of turning points along the reaction pathway can be associated into well-defined chemical events (bond breaking/forming processes, creation/annihilation of lone pairs, etc.); therefore, an innovative understanding of the corresponding molecular mechanism associated with chemical rearrangements can be reached. In this regard, several papers have been presented to map out chemical reactions.¹⁰ Although this analysis relies on a "static" description of the reaction path, Adamo and co-workers¹¹ have investigated using *ab initio* molecular dynamics bond breaking and formation processes, and they found that the ELF topology yielded equivalent results to the "static" description.

Electrocyclizations are powerful transformations in organic synthesis.¹² One type of electrocyclic reaction is a 4π -electron process known as the Nazarov cyclization^{13–15} involving the conversion of a divinyl ketone to an oxallyl five-membered ring (see Scheme 1). Traditionally, harsh reaction conditions with strong acids or high temperatures were needed. Recently, the potential applications of the Nazarov reaction in synthesis have grown enormously by the use of Lewis acids as catalysts, complexation with chiral metals for asymmetric synthesis,¹⁶ and the wide variety of substrates as well as procedures that allow carrying out of the "interrupted" Nazarov reaction.¹⁷

In the Nazarov reaction, the key step is the cyclization of a 4π -electron system through a conrotatory (under thermal conditions) electrocyclic process to form a five-membered ring. Although the mechanism of the Nazarov reaction is well-known at an experimental¹⁵ as well as theoretical level,¹⁸ our understanding is far from complete. It is well-known that three electronic factors control the progress of the cyclization, namely, (a) protonation of the oxygen or complexation to a mild Lewis acid (LA) catalyzes the cyclization,¹⁹ (b) α -electron-donating substituents accelerate the reaction,²⁰ and (c) β -electron-donating substituents ac-

celerate the retro-Nazarov ring cleavage.²¹ The current work is devoted to investigate how and where the bond breaking/forming processes and the corresponding electronic distributions take place along the molecular mechanisms of the Nazarov reaction of diallyl ketones to obtain five-membered rings from the perspective of the ELF and CT analysis, taking into account the $a-c$ factors described above. A set of 3×3 reactions have been calculated (see Scheme 1) considering the protonation, H⁺, of the oxygen atom of the C₁-O₆ group and the presence of BH₃, as strong and moderate LAs, respectively, and methoxy (-OCH₃) as an electron-donating group in the α (at C₂ atom) and β (at C₃ atom) positions. The effect of the LA on the cyclization of penta-1,4-diene-3-one is shown in reactions 1–3; the LA combined to an α - or β -methoxy group in reactions 4–6 and 7–9, respectively.

The structure of the article is arranged as follows: the computational methods are presented in section 2. The results and discussion section is divided in four parts. First, in order to understand the electronic structure of penta-1,4-diene-3-one and its oxallyl ring, the weights of the Lewis resonance structures will be determined on the basis of ELF basin populations. Second, the reaction mechanism for the cyclization process for the neutral and protonated species, reactions 1 and 3, respectively, will be discussed by means of the combined use of ELF and CT analysis. Third, the electron-donating capability of the α and β -OCH₃ groups will be shown by means of trends of ELF basin populations for the stationary points of reactions 1, 4, and 7. Fourth, the electronic effects due to LA and -OCH₃ substitution will be related to the calculated activation and reaction free energies. A brief concluding remarks section closes the article.

2. Theoretical Methods

The geometry optimizations and electronic structure calculations were carried out by the Gaussian 03 program.²² Structures were optimized using the B3LYP hybrid exchange-correlation potential²³ together with the 6-31G(d) basis set.²⁴ For the sake of comparison, reaction 7 is calculated using the 6-31+G(d) basis set, because the oxallyl ring structure cannot be found without diffuse functions. Stationary points on the potential energy surface were characterized by harmonic analysis using the same theoretical level as used in the optimization. The B3LYP activation energy is in good agreement with experimental data and previous works using *ab initio*^{18a–d} or DFT methods.^{18e,f} In the present work, reactives are connected to the transition structure (TS) by means of intrinsic reaction coordinate (IRC) calculations, using the method proposed by Fukui²⁵ and developed by Gonzalez and Schlegel.²⁶ A step size of 0.1 amu^{1/2} bohr and the calcfc option as implemented in Gaussian 03 were employed for the IRC calculations.

The topological analysis of the ELF function, $\eta(r)$, has been proved to be a useful tool to investigate the electronic structure and chemical reactivity of molecular systems.²⁷ An exploration of the mathematical properties of $\eta(r)$ enables a partition of the molecular position space in basins of attractors, which present a one-to-one correspondence with chemical local objects such as bonds and lone pairs. These

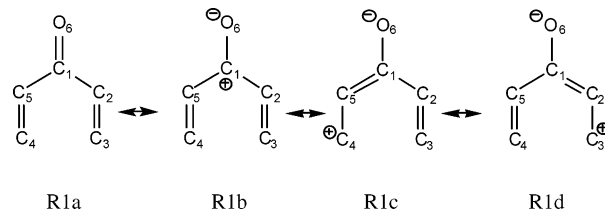
basins are either core basins, $C(X)$, or valence basins, $V(X, \dots)$, belonging to the outermost shell and characterized by their coordination number with core basins, which is called the synaptic order.²⁸ From a quantitative point of view, the electron density method can be integrated over the basins to provide the basin populations, \bar{N} . Along the reaction pathway, the change of the nuclear coordinates can lead to different topologies of the ELF. Thus, the reaction path is divided into subsets with the same ELF topology, and they are called structural stability domains (SSDs). Two consecutive SSDs are connected by a turning or bifurcation point which is characterized by a zero value of the Hessian matrix of the ELF. Each catastrophe transforms the overall topology in such a way that the Poincaré–Hopf relation is fulfilled. Three types of bifurcation catastrophes have been found so far in the study of chemical reactivity: (i) the fold catastrophe, corresponding to the creation or the annihilation of two critical points of different parity; for example, a wandering point gives rise to an attractor (index 0) and a saddle point of index 1; (ii) the cusp catastrophe, which transforms one critical point into three (and vice versa) such as in the formation or the breaking of a covalent bond; and (iii) the elliptic umbilic in which the index of a critical point changes by two. More information about the ELF and CT analysis of the chemical reactivity can be found elsewhere.⁷ Technically, the Kohn–Sham orbitals were obtained for each point of the calculated IRC path, and the ELF analysis was carried out using a cubical grid of a step size smaller than 0.1 bohr, employing the TopMod package of programs.²⁹ The graphical representation was obtained using the MOLEKEL program.³⁰

3. Results and Discussion

3.1. Calculation of Lewis Resonance Structures for Penta-1,4-diene-3-one and Its Oxyallyl Ring. The analysis based on the ELF topology allows quantification of the resonance structures proposed in Denmark's pioneering study of substituent effects in the Nazarov reaction,²⁰ even for the neutral species. Hence, for penta-1,4-diene-3-one (R1), the ELF shows two lone pairs represented by $V_{1,2}(O_6)$ basins with an integrated population of 2.62 e each. The C–O bond is strongly polarized toward the O atom, and its population is 2.35 e. This type of bond corresponds to a charge-shift type due to the different electronegativity of the atoms, where some amount of the bond electron density is shifted toward the oxygen lone pairs. Single (double) C–C bonds are represented by one (two) disynaptic basin(s) between the corresponding atoms with typical populations for this type of basin. The product, the oxyallyl ring (P1), presents a larger population on the two O_6 lone pairs, 2.82 e each, and a smaller C–O bond population, 2.05 e. The C_1 – C_2 and C_1 – C_5 basins present a population intermediate between a single and double bond, 2.70 e. The C–C bonds adjacent to C_1 – C_2 and C_1 – C_5 are slightly more populated than single bonds.

The basin populations of reactives and products correspond to a superposition of Lewis resonance structures R1a–R1d and P1a–P1b as depicted in Schemes 2 and 3, respectively. Structure R1a has three double bonds and all atoms remain neutral, whereas R1b–R1d are zwitterionic structures, the

Scheme 2. Proposed Lewis Resonance Forms for Penta-1,4-diene-3-one (R1)



Scheme 3. Proposed Lewis Resonance Forms for the Oxyallyl Ring (P1)

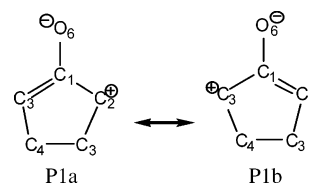


Table 1. Basin Populations (\bar{N}) and Number of Electrons Per Basin for Each Lewis Resonance Form of (a) R1 and (b) P1

	(a) R1					
	ELF		Lewis structures			
	\bar{N}	$\bar{N}_{\text{scaled}}^a$	R1a	R1b	R1c	R1d
$V(C_3, C_4)$	2.21	2.35	2	2	4	2
$V(C_4, C_5)$	2.21	2.35	2	2	2	4
$V(C_4, O_6)$	2.35	2.50	4	2	2	2
$V(O_6)$	5.23	5.56	4	6	6	6
$V(C_2, C_3)$	3.41	3.62	4	4	2	4
$V(C_1, C_5)$	3.41	3.62	4	4	4	2
	(b) P1					
	ELF		Lewis structures			
	\bar{N}	$\bar{N}_{\text{scaled}}^b$	P1a	P1b		
$V(C_1, C_2)$	2.71	2.89	2	4		
$V(C_1, C_5)$	2.71	2.89	4	2		
$V(C_1, O_6)$	2.05	2.19	2	2		
$V(O_6)$	5.64	6.02	6	6		

^a Scale factor of $20/(\sum \bar{N}) = 1.06$. ^b Scale factor of $14/(\sum \bar{N}) = 1.03$.

negative and positive charge being located on the oxygen atom and on the C_1 , C_3 , and C_4 carbon atoms, respectively. The corresponding ELF basin populations and the number of electrons for each resonance structure are gathered in Table 1a and b, respectively. Fitting the resonance weights to the basin populations yields the following results: $w_{R1a} = 0.24$, $w_{R1b} = 0.40$, $w_{R1c} = 0.18$, and $w_{R1d} = 0.18$. Although the carbocation is delocalized between C_1 , C_3 , and C_4 , the weight of R1b equals the sum of R1c and R1d. The oxyallyl ring P1 can be reasonably described by the superposition of just two distinct resonance forms P1a and P1b with equal weights.

3.2. A Combined Used of the ELF and Catastrophe Theory Analysis of the Protonation Effect in Nazarov's Cyclization. The reaction paths connecting R–TS–P calculated using the IRC method for reactions 1 and 3 are shown in Figure 1.³¹ Below the potential energy profile, a schematic representation of the change of topology of ELF basins using Lewis type structures is depicted. Reaction 1 presents four

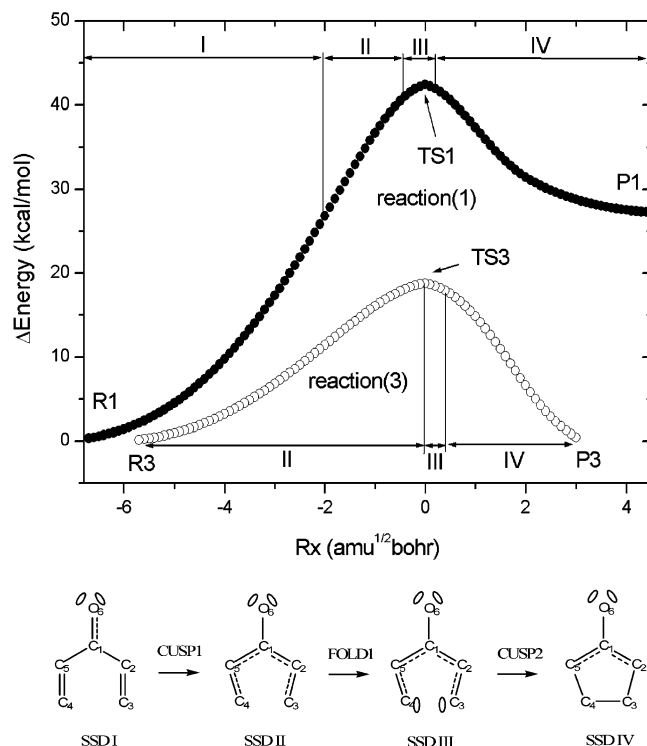


Figure 1. B3LYP/6-31G(d) calculated energy profiles for the Nazarov cyclizations 1 and 3 (energy values relative to the respective reactive) calculated by means of the IRC method, with a step size of 0.1 ($\text{amu}^{1/2} \text{ bohr}$). Below the graph, a schematic representation of the Lewis resonance forms for each SSD is depicted from the perspective of the ELF analysis (full lines and ellipses representing disynaptic and monosynaptic basins, respectively, while dotted lines indicate a large basin population).

SSDs (I–IV) connected by cusp1, fold1, and cusp2 turning points, respectively. A snapshot of the ELF for each SSD is displayed in Figure 2. The protonated reaction (reaction 3) presents neither the first SSD nor the cusp1 turning point, the other ELF topological features being identical to those of reaction 1. The populations for valence basins at the first and last points of each SSD of reactions 1 and 3 are gathered in Tables 2 and 3. In addition, the distance $r_{\text{C}_3-\text{C}_4}$ and the increment of energy along each SSD are also included.

The first SSD (I) of the reaction path of reaction 1 is characterized by the absence of transference of electronic charge between the ELF basins. However, there are substantial geometrical changes due to the conrotatory movement of both CH_2 terminal units. This SSD is the most costly energetically (25.83 kcal/mol), and a polarization of the C_1-O_6 bond is appreciated by the increment of 0.13 e of the basins associated with the lone pairs of the O_6 atom. The second SSD (II) of reaction 1 starts by the transformation of the degenerate disynaptic $V_{1,2}(\text{C}_{i=2,4}, \text{C}_{j=3,5})$ into a unique $V(\text{C}_{i=2,4}, \text{C}_{j=3,4})$ basin by means of a cusp-type turning point, cusp2. The rotation of the CH_2 units along the first SSD leads to the merge of the two basins corresponding to the terminal double bonds into a single one. Reaction 3 starts in this SSD; the protonation of O_6 creates a $V(\text{O}_6, \text{H})$ basin of 1.77 e; besides, the population of the lone pair of O_6 is 4.14 e, and the $\bar{N}[V(\text{C}_1, \text{O}_6)]$ basin is decreased to 1.77 e. There

are also substantial changes on the C–C bond basins; whereas $V(\text{C}_{i=1,1}, \text{C}_{j=2,5})$ and $V(\text{C}_1, \text{C}_5)$ increase the population to 2.38 e, $V(\text{C}_{i=2,3}, \text{C}_{j=3,4})$ is connected by one disynaptic basin with a population of 3.23 e. Hence, the ELF topology of R3 is equivalent to the corresponding one at the second SSD of reaction 1. Along the second step, there is a noticeable charge-transfer process from the new basin $V(\text{C}_{i=2,4}, \text{C}_{j=3,5})$, -0.23 e (reaction 1) and -0.55 e (reaction 3), to the $V(\text{C}_{i=1,1}, \text{C}_{j=2,5})$ basins, 0.20 e (reaction 1) and 0.27 e (reaction 3), and $V(\text{O}_6)$, 0.14 e (reaction 1) and 0.20 e (reaction 3). This electronic rearrangement is accompanied by an increment of the energy of 14.66 and 18.83 kcal/mol, for reactions 1 and 3, respectively.

The third SSD (III) begins shortly before the TS1 is reached, at $R_x = -0.30 \text{ amu}^{1/2} \text{ bohr}$, and at the same point as TS3. According to Thom's catastrophe theory, it is a fold-type turning point, fold1, where two monosynaptic basins on the terminal carbons are created [$V(\text{C}_3)$ and $V(\text{C}_4)$]. Hence, terminal carbons are now connected by two monosynaptic basins, and this type of interaction between atoms has been termed as a "proto-covalent" bond, and it takes place immediately before (or after) the formation (breaking) of a covalent bond. It is interesting to remark that TS1 and TS3 belong to different SSDs; thus, examination of the TS instead of the progress along the reaction path could be misleading. The only transference of electron density among ELF basins occurs from $V(\text{C}_{i=2,4}, \text{C}_{j=3,5})$ to the newly created $V(\text{C}_{i=3,4})$.

The last step starts at $R_x = +0.20$ (reaction 1) and $+0.50$ (reaction 3) $\text{amu}^{1/2} \text{ bohr}$, and it corresponds to the creation of a disynaptic basin $V(\text{C}_3, \text{C}_4)$ from the monosynaptic basins $V(\text{C}_3)$ and $V(\text{C}_4)$ by means of a cusp-type turning point; in other words, the ring is closed by the formation of a covalent bond between the terminal atoms. Along the fourth SSD (IV), there is an energy stabilization of 15.03 and 6.28 kcal/mol for reactions 1 and 3, respectively, and the new basin commences with a low population (0.93 e), and it increases until a population typical of a single C–C bond is reached, 1.83 e (reaction 1) and 1.84 e (reaction 3).

In summary, although the cyclization from the penta-1,3-diene-4-one to the corresponding oxyallyl ring takes place along one TS, the individual electronic rearrangements do not take place simultaneously but along four well-defined SSDs of the ELF separated by cusp1–fold1–cusp2 turning points. The reaction starts by the formation of the oxyallyl structure, while the ring closure takes place in the last part of the reaction. The presence of a LA, cases 2 and 3, stabilizes the negative partial charge of O_6 and shifts electron density from the terminal double bonds to the single bonds and from the C_1-O_6 bond to O_6 lone pairs. As a consequence of these electronic rearrangements, the reaction path of 3, H^+ protonation, begins directly at the second SSD avoiding the first (and energetically very costly) SSD of reaction 1. In SSD II, there is an electronic transfer process from terminal C–C bonds to C_1-C_2 and C_1-C_5 . The third step starts in the vicinities of the TS, and it is characterized by the proto-covalent bond between terminal C atoms. Finally, the ring-closure process takes place by the formation of the covalent bond C_3-C_4 .

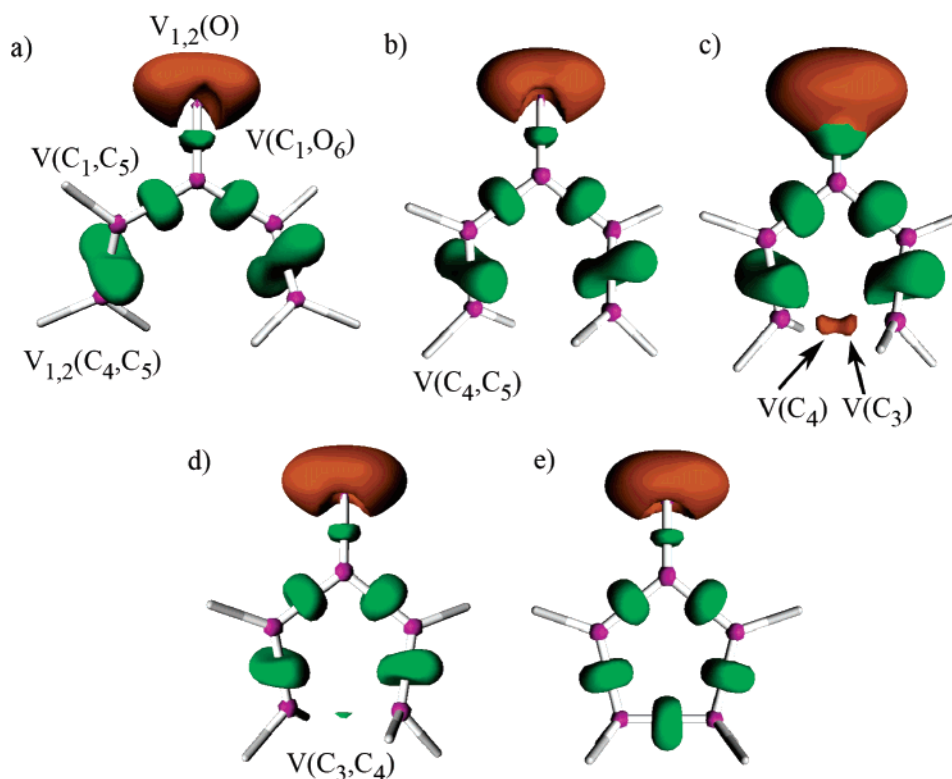


Figure 2. Snapshots of ELF localization domains ($\eta = 0.8$ isosurface, except 0.75 for c) for (a) reactive (SSD I), (b) $R_x = -0.40$ (SSD II), (c) TS (SSD III), (d) $R_x = -0.20$ (SSD IV), and (e) product (SSD IV). Basin color legend: purple for core, orange for monosynaptic, and green for disynaptic. Hydrogenated basins are omitted for clarity.

Table 2. R_x (in $\text{amu}^{1/2} \text{ bohr}$), Increments of Energy within Each SSD ΔE^a (in kcal/mol), $r_{C_3-C_4}$ Distance (in Å), and Integrated Electron Populations for Valence ELF Basins of Reaction 1 Calculated for the Initial and Final Points of Each SSD Identified on the Energy Reaction Profile Using the ELF Analysis

SSD	I		II		III			IV	
	R								
R_x	R	-2.0	-1.9	-0.4	-0.3	TS(0.0)	0.1	0.2	P
$r_{C_3-C_4}$	3.229	2.319	2.302	2.035	2.018	1-949	1.916	1.898	1.541
ΔE	25.83		14.66		1.74			-15.03	
$V(C_1, C_2)$	2.21	2.29	2.31	2.51	2.53	2.56	2.61	2.64	2.74
$V(C_1, O_6)$	2.35	2.29	2.28	2.16	2.14	2.15	2.14	2.12	2.05
$V(O_6)$	2.62/2.62	2.68/2.68	2.68/2.68	2.75/2.75	2.76/2.76	2.75/2.75	2.76/2.76	2.77/2.77	2.82/2.82
$V(C_3, C_4)$								0.93	1.83
$V(C_3)$					0.22	0.36	0.44		
$V(C_4)$					0.22	0.36	0.44		
$V_{1,2}(C_{2,4}, C_{3,5})$	1.63/1.78	1.63/1.65	3.27	3.04	2.82	2.65	2.55	2.51	2.12
$V(H_1, C_{3,4})$	2.1	2.11	2.12	2.11	2.09	2.05	2.04	2.03	1.95
$V(H_6, C_{3,4})$	2.09	2.11	2.11	2.1	2.1	2.1	2.1	2.09	1.97

^a For each SSD, $\Delta E = E(\text{final}) - E(\text{initial})$.

3.3. ELF Analysis of $-\text{OCH}_3$ Substituent Effects on the Nazarov Cyclization. The ELF analysis of the reaction path for reactions 4 and 7, with an $-\text{OCH}_3$ in α and β positions, respectively, shows the same sequence of SSDs and turning points as the unsubstituted reaction (reaction 1). The corresponding stationary points (R, TS, and P) of these three reactions (1, 4, and 7) have the same ELF topology. Therefore, a comparative analysis of their differences on the basin populations, and their trends, can be carried out in order to understand the $-\text{OCH}_3$ effect on the electronic rearrangements of Nazarov cyclization. The data of ELF populations for R, TS, and P of reactions 1, 4, and 7 are gathered in Table 4.

A comparative analysis of the progress of these reactions (4 and 7) with respect to the parent model (reaction 1) points out a similar behavior. However, there are two main differences between reactions 4 and 1: first, there is a larger increment of $\bar{N}[V(C_1, C_5)]$ for reaction 4 than in reaction 1; second, there is a transfer of electron charge from the lone pairs of O_7 to the C_2-O_7 bond. Hence, $V(O_7)$ decreases its population, R4 (4.59 e), TS4 (4.41 e), and P4 (4.03 e), while $\bar{N}[V(C_2, O_7)]$ increases for R4 (1.50 e), TS4 (1.63 e), and P4 (1.89 e). Both differences may be interpreted in terms of the resonance Lewis structures discussed in section 3.1. Whether for P1 both Lewis structures, a and b, have equal weight, for P4, the weight of the corresponding P4a is larger

Table 3. Rx (in amu^{1/2} bohr), SSD Increment of Energy ΔE^a (in kcal/mol), $r_{C_3-C_4}$ Distance, and Integrated Electron Populations for Valence ELF Basins of Reaction 3 Calculated for the Initial and Final Points of Each SSD Identified on the Energy Reaction Profile Using the ELF Analysis

SSD	II		III		IV	
	R	TS (0.0)	0.1	0.5	0.6	P
Rx						
$r_{C_3-C_4}$	3.183	2.108	2.074	2.003	1.985	1.536
ΔE	18.83		6.28		6.28	
V(C ₁ ,C ₂)	2.38	2.65	2.66	2.69	2.69	2.71
V(C ₁ ,O ₆)	1.77	1.65	1.65	1.64	1.65	1.61
V(O ₆)	4.14	4.34	4.35	4.38	4.38	2.16/2.31
V(O ₆ ,H)	1.77	1.71	1.7	1.69	1.68	1.64
V(C ₃ ,C ₄)					0.69	1.84
V(C ₃)			0.19	0.31		
V(C ₄)			0.19	0.31		
V1(C _{2,4} ,C _{3,5})	3.23	2.68	2.61	2.49	2.46	2.09
V(H ₁ ,C _{3,4})	2.1	2.13	2.13	2.14	2.15	2.16
V(H ₆ ,C _{3,4})	2.09	2.22	2.08	2.04	2.03	1.92

^a For each SSD $\Delta E = E(\text{final}) - E(\text{initial})$.

than P4b due to the electron donation of the $-OCH_3$ group. A transfer of electronic charge from the O₇ lone pairs to the C₂–C₇ bond around 0.40 e is sensed, stabilizing the cation at the C₂ atom. Hence, the analysis of ELF is in full agreement with Denmark's model, giving a quantitative measure of the electron-donating effect.

The ELF basin population trends observed on the stationary points of reaction 7 are more similar to those of reaction 1 than in the case of reaction 4. However, analysis of the behavior of $\bar{N}[V(C_3, O_7)]$ and $\bar{N}[V(O_7)]$ basins for R7–TS7–P7 structures shows a transfer of electronic charge of 0.22 e (approximately) from V(C₃,O₇) to V(O₇) basins. Therefore, the $-OCH_3$ electron-donating effect at the C2 and C3 positions go in opposite directions. However, the magnitude of the electron donation from the lone pairs of O₇ to the C₃–O₇ bond in reaction 7 is smaller than in reaction 4, and the role of this electronic transfer into the basins participating on the cyclization process cannot be clearly distinguished. Therefore, the electron-donating effect of the β $-OCH_3$ group should stabilize R7 and TS7 (less) with respect to P7,

Table 4. ELF Integrated Populations (in Electrons) for the Most Representative Basins of Reactive (R), Transition Structure (TS), and Product (P) for Reactions 1, 4, and 7

	R1	TS1	P1	R4	TS4	P4	R7	TS7	P7
V(C ₁ ,C ₂)	2.21	2.58	2.67	2.26	2.51	2.62	2.26	2.81	2.79
V(C ₂ ,C ₃)	1.63/1.78	2.64	2.12	1.77/1.87	2.72	2.17	1.76/1.84	2.51	2.18
V(C ₃ ,C ₄)			1.83			1.88			1.83
V(C ₃)		0.37			0.24			0.59	
V(C ₄)		0.36			0.5			0.45	
V(C ₄ ,C ₅)	1.63/1.78	2.65	2.12	1.68/1.78	2.66	2.04	1.79/1.67	2.55	2.12
V(C ₅ ,C ₁)	2.21	2.56	2.74	2.22	2.88	3.2	2.22	2.52	2.62
V(C ₁ ,O ₆)	2.35	2.15	2.05	2.34	2.14	1.95	2.25	2.14	2.07
V1,2(O ₆)	2.62/2.62	2.75/2.75	2.82/2.82	2.61/2.65	2.79/2.7	2.99/2.79	2.7/2.64	2.8/2.75	2.85/2.77
V(C ₂ ,O ₇)				1.5	1.63	1.89			
V(C ₃ ,O ₇)							1.53	1.41	1.31
V(O ₇ ,C)				1.41	1.42	1.49	1.38	1.34	1.32
V(O ₇)				2.45/2.14	4.41	4.03	4.57	2.41/2.31	2.47/2.40

which also agrees with Denmark's model predicting that β -electron-donating groups should stabilize the pentadiene cation, discouraging cyclization. Comparison between TS1 and TS7 reveals a larger $\bar{N}[V(C_1, C_2)]$ for the latter, 0.23 e, suggesting a more efficient electronic charge process from V(C₂,C₃) to V(C₁,C₂) due to the presence of the $-OCH_3$ group. Also, the populations of V(C₃) and V(C₄) basins at TS7 are not identical, indicating that the bond formation is not a pure homolytical process.

3.4. Does the Presence of Lewis Acid and α, β $-OCH_3$ Substitution Yield a Cooperative or a Competitive Effect?

Once the changes on the electronic structure due to LA-protonation (H^+) and presence of BH_3 —and α, β methoxy substitution have been analyzed using the ELF analysis, we will relate these observations to the thermochemical data calculated at the B3LYP/6-31G(d) level, namely, the activation free energy, ΔG_{act} [$\Delta G_{act} = G(TS) - G(R)$], and reaction free energy, ΔG_{reac} [$\Delta G_{reac} = G(P) - G(R)$] calculated at 298 K and 1 atm. In addition, the combined effect of the LA and α or β $-OCH_3$ substitution will be considered. In Table 5, ΔG_{act} and ΔG_{reac} for reactions 1–9 are collected.

As it was discussed previously, the Lewis acid, BH_3 or protonation (H^+), interacts with one of the lone pairs of O₆, forming a dative bond or an O–H bond, respectively.³² Therefore, the effect of the Lewis acid can be viewed as a relative stabilization of the transition structure and the product with respect to the reactive. Therefore, both ΔG_{act} and ΔG_{reac} will be reduced to 32.60 and 13.55 kcal/mol in reaction 2 and 19.02 and -2.95 kcal/mol in reaction 3, respectively. The calculated ΔG_{act} and ΔG_{reac} for reaction 4 are 36.77 and 8.82 kcal/mol, respectively. This result is in agreement with both experimentally and computationally acknowledged conclusions¹³ that the rate acceleration effect is due to α $-OCH_3$ substitution in the Nazarov cyclization. Interestingly, the ELF analysis predicts a stabilization of the transition structure and the product due to α $-OCH_3$ substitution, similar to the effect of the LA. Hence, both effects take place on different structures, and they can work in a cooperative way as it is observed from the calculations of ΔG_{act} and ΔG_{reac} for reactions 5, 26.80 and -2.68 kcal/mol, and 6, 11.15 and -26.26 kcal/mol, respectively.

Table 5. Activation and Reaction Free Energies Calculated at 298 K and 1 atm (ΔG_{act} and ΔG_{reac}) Obtained at the B3LYP/6-31G(d) Calculation Level

reaction	R ₁	R ₂	LA	ΔG_{act}	ΔG_{reac}
1	-H	-H		42.83	27.64
2	-H	-H	BH ₃	32.60	13.55
3	-H	-H	H ⁺	19.02	-2.95
4	-OCH ₃	-H		36.77	8.82
5 ^a	-OCH ₃	-H	BH ₃	26.80	-2.68
6	-OCH ₃	-H	H ⁺	11.15	-26.26
7	-H	-OCH ₃		43.41	38.11
8	-H	-OCH ₃	BH ₃	34.68	28.27
9	-H	-OCH ₃	H ⁺	27.76	24.70

^a Reaction 7 was calculated using the 6-31+G(d) basis set.

Experimental and theoretical calculations have shown the acceleration of the retro-Nazarov cyclization with electron-donor substituents in carbon β .²¹ The B3LYP calculated ΔG_{act} and ΔG_{reac} of reaction 7 are 43.41 and 38.11 kcal/mol, respectively. The ELF analysis reveals that the electron-donating effect of β -OCH₃ substitution stabilizes the reactive and the TS (less) while the LA also stabilizes the TS and the product. Therefore, both effects are competitive on the reactive structure yielding smaller ΔG_{act} but similar ΔG_{reac} values for reactions 8, and 28.27 kcal/mol, and 9, 27.76 and 24.70 kcal/mol, respectively.

4. Conclusions

The forming/breaking bond processes and electronic rearrangements along the reaction path associated with the Nazarov cyclizations of penta-1,4-diene-3-one and derivatives have been studied in the framework provided by the topological analysis of the ELF together with CT. The presence of a Lewis acid (protonation H⁺ and BH₃) as well as an electron-donor substituent (-OCH₃) at α and β positions is taken into account using nine different reaction models. The main conclusions can be summarized as follows:

(i) The weights of the Lewis resonance structures have been calculated from ELF basin populations for penta-1,4-diene-3-one (R1) and its corresponding oxyallyl ring (P1).

(ii) The cyclization of R1 takes place following four different structural SSDs (I–IV) connected by three turning points (cusp1–fold1–cusp2). The first and most energetically demanding step for R1, reaction 1, corresponds to a polarization of the C–O bond, while the second step is associated with the electronic rearrangement among carbon–carbon bonds. The transition structure is located at the third SSD where the terminal carbon–carbon bond is not yet formed, and finally the ring closure process takes place.

(iii) The protonation of the ketone implies a modification of the ELF topology of the reactive (R3). Hence, the ELF topology of R3 corresponds to the second SSD of reaction 1, and the energetically expensive first SSD is avoided. The protonation of O₆ plays a decisive catalytic role, and it can be associated with the relative stabilization of the TS and product with respect to the reactive due to their larger zwitterionic character.

(iv) The analysis of ELF basin populations of reactives, transition structures, and products of reactions 1, 4, and 7

reveals the electron-donor capability of the -OCH₃ substituent at α and β positions, C₂ and C₃ carbon atoms, respectively. The basin corresponding to the lone pairs of O₇ can donate up to 0.58 e to the V(C_{i=2,3}-O₇) bonding basin, depending on the electronic demands of the rearrangements taking place along the reaction path. The electron-donating effect goes in opposite directions for reactions 4 and 7.

(v) The variation of activation and reaction free energies observed for the combined effects of a Lewis acid (H⁺, BH₃) and the α or β -OCH₃ substituents has been rationalized in terms of stabilization of the stationary points for reactions 1–9 due to the previously described electronic effects. The presence of Lewis acids and the presence of the α -OCH₃ substituent is cooperative, reducing greatly the activation free energy and yielding a clearly exergonic reaction. On the other hand, LA and β -OCH₃ act in a competitive way, decreasing the acceleration of the cyclization process.

Acknowledgment. This work was supported by the Ministerio de Ciencia y Tecnología (MCyT), DGICYT, BQU2003-04168-C03-03, and CTQ2006-15447-C02-01; Generalitat Valenciana, Projects GRUPOS03/176 and ACOMP06/122; and the Universitat Jaume I-Fundacio Bancaixa, Project P1.1B2004-20. V.P. thanks support by the Juan de la Cierva fellowship from the MCyT. The authors also are grateful to the Servei d'Informatica, Universitat Jaume I for a generous allotment of computer time. Dr. Luis Domingo is acknowledged for his comments on the manuscript.

Supporting Information Available: Optimized B3LYP/6-31G(d) or 6-31+G(d) for reaction 7; geometries, total energies (au), lowest frequency (cm⁻¹), zero-point energy correction, enthalpy, and free energy for the reactive, transition structure, product of reactions 1–9 are provided. This material is available free of charge via the Internet at <http://acs.pubs.org>.

References

- (1) (a) Bader, R. F. W. *Acc. Chem. Res.* **1985**, *18*, 9–15. (b) Bader, R. F. W. *Atoms in Molecules. A Quantum Theory*; Clarendon Press: Oxford U. K., 1990.
- (2) Becke, A. D.; Edgecombe, K. E. *J. Chem. Phys.* **1990**, *92*, 5397–5403.
- (3) Silvi, B.; Savin, A. *Nature* **1994**, *371*, 683–686.
- (4) Shaik, S.; Danovich, D.; Silvi, B.; Lauvergnat, D. L.; Hiberty, P. C. *Chem.-Eur. J.* **2005**, *11*, 6358–6371.
- (5) (a) Lepetit, C.; Silvi, B.; Chauvin, R. *J. Phys. Chem. A* **2003**, *107*, 464–473. (b) Santos, J. C.; Andres, J.; Aizman, A.; Fuentealba, P. *J. Chem. Theory Comput.* **2005**, *1*, 83–86. (c) Poater, J.; Duran, M.; Sola, M.; Silvi, B. *Chem. Rev.* **2005**, *105*, 3911–3947.
- (6) Polo, V.; Andres, J.; Silvi, B. *J. Comput. Chem.* **2007**, *28*, 857–863.
- (7) Krokidis, X.; Noury, S.; Silvi, B. *J. Phys. Chem. A* **1997**, *101*, 7277–7282.
- (8) (a) Thom, R. *Structural Stability and Morphogenesis: An Outline of a General Theory of Models*; Benjamin: Reading, PA, 1975. (b) Poston, T.; Stewart, L. *Catastrophe Theory and its Applications*; Dover Publications, Inc.: Mineola, New York, 1996.

- (9) Silvi, B. *J. Phys. Chem. A* **2003**, *107*, 3081–3085.
- (10) (a) Berski, S.; Andres, J.; Silvi, B.; Domingo, L. R. *J. Phys. Chem. A* **2003**, *107*, 6014–6024. (b) Polo, V.; Andres, J.; Castillo, R.; Berski, S.; Silvi, B. *Chem.—Eur. J.* **2004**, *10*, 5165–5172. (c) Santos, J. C.; Andrés, J.; Aizman, A.; Fuentealba, P.; Polo, V. *J. Phys. Chem. A* **2005**, *16*, 3687–3693. (d) Santos, J. C.; Polo, V.; Andres, J. *Chem. Phys. Lett.* **2005**, *406*, 393–397. (e) Polo, V.; Andres, J. *J. Comput. Chem.* **2005**, *26*, 1427–1437. (f) Berski, S.; Andrés, J.; Silvi, B.; Domingo, L. R. *J. Phys. Chem. A* **2006**, *110*, 13939–13947.
- (11) (a) Joubert, L.; Adamo, C. *J. Chem. Phys.* **2005**, *123*, 211103. (b) Joubert, L.; Pavone, M.; Barone, V.; Adamo, C. *J. Chem. Theory Comput.* **2006**, *2*, 1220–1227.
- (12) (a) Marvell, E. N. *Thermal Electrocyclic Reactions*; Academic Press: New York, 1980; Vol. 43. (b) Ansari, F. L.; Qureshi, R.; Qureshi, M. L. *Electrocyclic Reactions*; Wiley: Weinheim, Germany, 1999. (c) Woodward, R. B.; Hoffmann, R. *The Conservation of Orbital Symmetry*; Verlag Chemie: Weinheim, Germany, 1970.
- (13) Nazarov, I. N.; Zaretskaya, I. I. *Izv. Akad. Nauk. SSSR, Ser. Khim.* **1941**, 221–224.
- (14) See the reviews: (a) Denmark, S. E. Nazarov and Related Cationic Cyclizations. In *Comprehensive Organic Synthesis*; Trost, B. M., Fleming, I., Paquette L. A., Eds.; Pergamon: Oxford, U. K., 1991; Vol. 5, pp 751–784. (b) Habermas, K. L.; Denmark, S. E.; Jones, T. K. The Nazarov Cyclization. In *Organic Reactions*; Paquette, L. A., Ed.; Wiley: New York, 1994; Vol. 45, pp 1–158.
- (15) (a) Frontier, A. J.; Collison, C. *Tetrahedron* **2005**, *61*, 7577–7606. (b) Pellissier, H. *Tetrahedron* **2005**, *61*, 6479–6517.
- (16) Liang, G. X.; Trauner, D. *J. Am. Chem. Soc.* **2004**, *126*, 9544–9545.
- (17) (a) Wang, Y.; Arif, A. M.; West, F. G. *J. Am. Chem. Soc.* **1999**, *121*, 876–877. (b) Giese, S.; Kastrup, L.; Stiens, D.; West, F. G. *Angew. Chem., Int. Ed.* **2000**, *39*, 1970.
- (18) (a) Smith, D. A.; Ulmer, C. W. *J. Org. Chem.* **1991**, *56*, 4444–4447. (b) Smith, D. A.; Ulmer, C. W. *Tetrahedron Lett.* **1991**, *32*, 725–728. (c) Smith, D. A.; Ulmer, C. W. *J. Org. Chem.* **1993**, *58*, 4118–4121. (d) Smith, D. A.; Ulmer, C. W. *J. Org. Chem.* **1997**, *62*, 5110–5115. (e) Faza, A. N.; Lopez, C. S.; Alvarez, R.; de Lera, I. R. *Chem.—Eur. J.* **2004**, *10*, 4324–4333. (f) Cavalli, A.; Masetti, M.; Recanatini, M.; Prandi, C.; Guarna, A.; Occhiato, E. G. *Chem.—Eur. J.* **2006**, *12*, 2836–2845.
- (19) Even reagent-free Nazarov cyclizations have been proposed: Douelle, F.; Tal, L.; Greaney, M. F. *Chem. Commun.* **2005**, *5*, 660–662.
- (20) (a) Denmark, S. E.; Habermas, K. L.; Hite, G. A. *Helv. Chim. Acta* **1988**, *71*, 168–194. (b) Tius, M. A. *Acc. Chem. Res.* **2003**, *36*, 284–290.
- (21) (a) Harmata, M.; Lee, D. R. *J. Am. Chem. Soc.* **2002**, *124*, 14328–14329. (b) Harmata, M.; Schreiner, P. R.; Lee, D. R.; Kirchhoefer, P. L. *J. Am. Chem. Soc.* **2004**, *126*, 10954–10957.
- (22) Frisch, M. J.; Trucks, G. W.; Schlegel, H. B.; Scuseria, G. E.; Robb, M. A.; Cheeseman, J. R.; Montgomery, J. A., Jr.; Vreven, T.; Kudin, K. N.; Burant, J. C.; Millam, J. M.; Iyengar, S. S.; Tomasi, J.; Barone, V.; Mennucci, B.; Cossi, M.; Scalmani, G.; Rega, N.; Petersson, G. A.; Nakatsuji, H.; Hada, M.; Ehara, M.; Toyota, K.; Fukuda, R.; Hasegawa, J.; Ishida, M.; Nakajima, T.; Honda, Y.; Kitao, O.; Nakai, H.; Klene, M.; Li, X.; Knox, J. E.; Hratchian, H. P.; Cross, J. B.; Bakken, V.; Adamo, C.; Jaramillo, J.; Gomperts, R.; Stratmann, R. E.; Yazyev, O.; Austin, A. J.; Cammi, R.; Pomelli, C.; Ochterski, J. W.; Ayala, P. Y.; Morokuma, K.; Voth, G. A.; Salvador, P.; Dannenberg, J. J.; Zakrzewski, V. G.; Dapprich, S.; Daniels, A. D.; Strain, M. C.; Farkas, O.; Malick, D. K.; Rabuck, A. D.; Raghavachari, K.; Foresman, J. B.; Ortiz, J. V.; Cui, Q.; Baboul, A. G.; Clifford, S.; Cioslowski, J.; Stefanov, B. B.; Liu, G.; Liashenko, A.; Piskorz, P.; Komaromi, I.; Martin, R. L.; Fox, D. J.; Keith, T.; Al-Laham, M. A.; Peng, C. Y.; Nanayakkara, A.; Challacombe, M.; Gill, P. M. W.; Johnson, B.; Chen, W.; Wong, M. W.; Gonzalez, C.; Pople, J. A. *Gaussian 03*, revision C.02; Gaussian, Inc.: Wallingford, CT, 2004.
- (23) (a) Becke, A. D. *Phys. Rev. A: At., Mol., Opt. Phys.* **1988**, *38*, 3098–3100. (b) Becke, A. D. *J. Chem. Phys.* **1993**, *98*, 1372–1377. (c) Lee, C. T.; Yang, W. T.; Parr, R. G. *Phys. Rev. B: Condens. Matter Mater. Phys.* **1988**, *37*, 785–789.
- (24) Hariharan, P. C.; Pople, J. A. *Theor. Chim. Acta* **1973**, *28*, 213–222.
- (25) (a) Fukui, K. *J. Phys. Chem.* **1970**, *74*, 4161. (b) Fukui, K. *Acc. Chem. Res.* **1981**, *14*, 363–368.
- (26) Gonzalez, C.; Schlegel, H. B. *J. Phys. Chem.* **1990**, *94*, 5523–5527.
- (27) (a) Savin, A.; Becke, A. D.; Flad, J.; Nesper, R.; Preuss, H.; Vonscherner, H. G. *Angew. Chem., Int. Ed.* **1991**, *30*, 409–412. (b) Savin, A.; Jepsen, O.; Flad, J.; Andersen, O. K.; Preuss, H.; Vonscherner, H. G. *Angew. Chem., Int. Ed.* **1992**, *31*, 187–188. (c) Savin, A.; Nesper, R.; Wengert, S.; Fassler, T. F. *Angew. Chem., Int. Ed.* **1997**, *36*, 1809.
- (28) Silvi, B. *J. Mol. Struct.* **2002**, *614*, 3–10.
- (29) Noury, S.; Krokidis, X.; Fuster, F.; Silvi, B. *Comput. Chem.* **1999**, *23*, 597–604.
- (30) Flükiger, P.; Lüthi, H. P.; Portmann, S.; Weber, J. *MOLEKEL 4.0*; J. Swiss Center for Scientific Computing: Manno, Switzerland, 2000.
- (31) The same study along the IRC path was carried out for reaction 2 yielding an intermediate situation between 1 and 3; for the sake of clarity, the analysis of 2 is not discussed here.
- (32) In the case of methoxy substitution at C₂, the BH₃ can interact with both oxygen atoms. The trans conformation with respect to the C₂ carbon atom has been chosen to analyze the Lewis acid effect on the keto group.

JCTC Journal of Chemical Theory and Computation

Toward a Separate Reproduction of the Contributions to the Hartree–Fock and DFT Intermolecular Interaction Energies by Polarizable Molecular Mechanics with the SIBFA Potential[†]

Jean-Philip Piquemal,^{*,‡} Hilaire Chevreau,[‡] and Nohad Gresh^{*,§}

Laboratoire de Chimie Théorique, UMR 7616, Université P. & M. Curie, Case courrier 137, 4, place Jussieu, F. 75252 Paris, Cedex 05, France, and Laboratoire de Pharmacochimie Moléculaire et Structurale, U648 INSERM, IFR Biomédicale, 45, Rue des Saints-Pères, 75006, Paris, France

Received January 14, 2007

Abstract: Following recent refinements of the SIBFA intermolecular potential to the multipolar electrostatic contribution by inclusion of an explicit ‘penetration’ component, the short-range repulsion term is augmented with a S^2/R^2 component. The SIBFA potential, and the behaviors of its individual contributions encompassing polarization and charge transfer, were evaluated in a diversity of hydrogen-bonded complexes as well as in a model stacked complex by comparisons with results from ab initio quantum-chemical (QC) computations with energy decomposition. Close agreements between SIBFA and QC results are found on both the interaction energies and their contributions. Extensions to computations at the DFT level are also presented.

Introduction

In Anisotropic Polarizable Molecular Mechanics (APMM) procedures,^{1–8} representation of the electrostatic contribution of the interaction energy with distributed multipoles constitutes an essential asset. Following the developments pioneered by Stone (see ref 9 and references herein) and Claverie,¹⁰ the multipoles are extracted from the quantum-chemical (QC) wave function of the molecule considered and stored in a library. The electrostatic interaction energy between two interacting molecules is then computed as a sum of multipole–multipole interactions. This enables to faithfully reproduce the anisotropic features of the Coulomb contribution of a corresponding ab initio supermolecule computation.^{11,13–15} However, the Coulomb component embodies, in addition to the multipolar component, attractive effects due to charge penetration.^{16,17} The corresponding

energy term, denoted as E_{pen} , is not explicitly represented in virtually all APMM procedures. Instead, on account of its overlap-dependent character, it is lumped together with the short-range repulsion contribution. The first explicit introduction of E_{pen} was done in the framework of the Effective Fragment Potential (EFP) method.¹⁶ It was recently introduced¹⁷ as well in the SIBFA (Sum of Interactions Between Fragments Ab initio computed)^{1,2} procedure and in the GEM (Gaussian Electrostatic Model) approach⁴ using different formalisms. The use of energy-decomposition procedures in the ab initio supermolecular approach unravels the weights of the individual component of the Hartree–Fock (or DFT) interaction energy, ΔE_{HF} (or ΔE_{DFT}) between two, or several, interacting molecules and their distance and angular dependencies.^{11,13,15,18}

It was found using SIBFA that the multipolar contribution E_{MTP} augmented with by E_{pen} , denoted as E_{MTP^*} , could closely reproduce the numerical values of the ab initio Coulomb contribution E_c for diverse representative complexes, such as neutral or ionic H-bonded, or stacking as well as cation–ligand complexes.¹⁷ The Frozen Core term, E_{FC} , from an ab initio energy-decomposition procedure is the sum of the Coulomb, E_c , and the short-range exchange, E_{exch} , contribu-

[†] Dedicated to Professor Dennis R. Salahub on the occasion of his 60th birthday.

* Corresponding author e-mail: jpp@lct.jussieu.fr (J.-P.P.) and nohad.gresh@univ-paris5.fr (N.G.).

[‡] Université P. & M. Curie.

[§] U648 INSERM, IFR Biomédicale.

tions. In this work and by analogy to perturbation theory we will term it E_1 . The corresponding term in SIBFA is $E_{MTP} + E_{pen} + E_{rep}$. Since the first two terms should match $E_c(\text{HF})$, E_{rep} should now match as closely as possible E_{exch} , rather than it be calibrated to match the actual $E_{FC}(\text{HF}) - E_{MTP}(\text{SIBFA})$ difference. While this could on principle be attained by simply rescaling the multiplicative factor of E_{rep} , we sought for further refinements in its formulation. Such comparisons are carried out parallel to the corresponding comparisons between E_{MTP^*} and E_c . In ‘classical’ molecular mechanics using point charges to compute electrostatics, the repulsion contribution is generally computed as a sum of ‘isotropic’ $1/R^n$ terms. In the context of APMM, it would be desirable to have a representation of E_{exch} that accounts as closely as possible for both its distance and its angular dependencies. Apart from SIBFA, only a few APMM procedures endow E_{rep} with angular features³ and with dependencies upon the electronic populations of the interacting atoms:^{19,20} that is, the more electron-rich a given atom, the larger its contribution to the repulsion. However to our knowledge, there are scarce reports that do confront the angular dependencies of E_{rep} to those of E_{exch} . Examples of such reports were published using the SIBFA procedure for both hydrogen-bonded²¹ and cation–ligand complexes.²² Since the initial inception of this procedure, and following the early proposals by Murrell et al.,²³ a dependence of E_{rep} upon a functional, S^2 , of the square of the overlap between the interacting molecules was sought for. Thus E_{rep} was expressed under the form of a sum of bond–bond, bond–lone pair, and lone pair–lone pair overlaps interactions.²⁴ Denoting by R the distance between the centroids of the simulated localized orbitals, further developments resorted to a S^2/R formula instead of an S^2 one and explicitly introduced the effects of the hybridization of the orbitals localized on the bonds, not just those localized on the lone pairs.²² In the present work, we will seek to confer more flexibility to such a representation. Again following the work by Murrell and Teixeira-Dias,²³ we will include an additional term, with an actual S^2/R^2 dependency.²⁵ This introduction occurs at the cost of only a minor calibration effort, since the amplitude of each of the S^2/R and the S^2/R^2 terms is governed by only two parameters, namely a multiplicative coefficient and the exponent of the exponential. As in our preceding papers, the values of the effective radii of each involved atom depend on its chemical nature and hybridization, are identical for both S^2 components, and are transferable. The present work constitutes a generalization²⁵ of the one recently published by us²⁶ which bore on the refinements of Zn(II) representation in this context. The formulation of the two second-order contributions, polarization (E_{pol}) and charge-transfer (E_{ct}), is the same as in our previous papers.²⁶ The organization of the paper is the following.

A further refinement of the expression of E_{pen} is briefly introduced, that now embodies the effects of penetration on the charge–quadrupole component of E_{MTP} , in addition to those exerted on the charge–charge and charge–dipole components. The formulation of E_{rep^*} is then presented. Calibration of both E_{MTP^*} and E_{rep^*} is subsequently done on a training set constituted by the water dimer in the same

five configurations as investigated in our previous paper.¹⁷ This is followed by tests on water clusters. Water boxes in an energy-minimized icelike arrangement are considered for $n = 12, 16,$ and 20 molecules, and, for $n = 16$, an arrangement extracted from a Monte Carlo simulation on a large box of 64 molecules is also considered. Three nonstandard H-bonded chains ($n = 12$) are next considered to probe the behavior of E_{pol} in polarizable potentials against their QC counterpart: these involve bifurcated and transverse bifurcated arrangements as introduced by Giese and York²⁷ as well as helical as some of us have suggested in a recent paper (Piquemal et al., submitted for publication). We then present several tests of the accuracy of E_{MTP^*} and E_{rep} in first-order, and E_{pol} and E_{ct} in second-order, by comparing their distance and/or angular dependencies to those of their respective counterparts E_c , E_{exch} , E_{pol} , and E_{ct} . These tests bear on the following hydrogen-bonded complexes: a neutral H-bond complex, the formamide dimer; an anionic H-bond acceptor, formate, with a neutral H-bond donor, water; a cationic H-bond donor, methylammonium, with a neutral acceptor, water; and an ionic complex, formate–methylammonium. It was finally essential to assess if the refinements in the representation of H-bonded complexes would translate into an improved representation of stacked complexes, such that as many polar atoms of one monomer would ‘overlap’ those of the other monomer. This was done on the complex between two parallel formamide molecules upon performing rotation of the second monomer around the z -axis. To conclude, we present an extension of this work to interaction energies computed at the correlated DFT level for water using a large basis set. In this context, we also investigate ten hydrogen-bonded complexes that were recently studied in detail by van Duijneveldt et al. to benchmark several molecular mechanics potentials against high level QC computations.²⁸

The present work builds up on several previous studies in which SIBFA, ab initio HF, and MP2 as well as DFT calculations were performed in parallel. Several of these were done in close collaboration with Professor Salahub’s group and were instrumental in the continued evolution and refinements of this procedure: from bimolecular or small complexes,²¹ to intramolecular interactions in di- and oligopeptides,^{29,30} and to critical assessment of the handling of cooperativity effects in peptide H-bonded networks³¹ and anisotropy in dimerization energies of protein–protein recognition motives.³²

Procedure

Ab Initio Calculations. At the Hartree–Fock level, the energy decomposition calculations have been carried using the RVS¹¹ decomposition scheme at Hartree Fock level, as implemented in GAMESS.³³ The basis sets retained for these computations are the CEP 4-31G(2d)³⁴ and DZVP2.³⁵ The SIBFA DZVP2 results required for the SIBFA version dedicated to open shell cation interactions³⁶ will be discussed if different from the CEP 4-31G(2d) version. The CEP 4-31G(2d) pseudopotential has been shown to provide ΔE values close to those computed with the 6-311G** in models of zinc metalloprotein complexes with inhibitors.¹ At the

DFT level, the chosen functional was B3LYP^{37,38} coupled to the aug-cc-PVTZ basis set.³⁹ All energy decomposition computations at this level have been carried out with a modified version of the CSOV¹⁸ energy decomposition scheme implemented in a modified version of HONDO 95.3¹³ enabling the computations of the electrostatic interaction energies in complexes with more than two molecules. Distributed polarizabilities are extracted from a procedure originally due to Garmer and Stevens⁴⁰ and implemented at the HF and DFT level in our “in house” version of HONDO 95.3. Jaguar 6.0⁴¹ has also been used to calculate the DFT total interaction energies in water oligomers.

Extended Formulation for E_{MTP^*} . E_{MTP^*} is calculated using distributed multipoles, up to quadrupoles and derived from the ab initio wave function of the molecule considered. They are distributed on its atoms and the barycenters of its chemical bonds following a procedure due to Vigne-Maeder and Claverie.¹⁰

E_{MTP^*} was computed¹⁷ as a sum of six terms:

$$E_{\text{MTP}^*} = E_{\text{mono-mono}^*} + E_{\text{mono-dip}^*} + E_{\text{mono-quad}} + E_{\text{dip-dip}} + E_{\text{dip-quad}} + E_{\text{quad-quad}} \quad (1)$$

To take into account the short-range electrostatic penetration effect, we have in ref 17 modified two terms of the classical E_{MTP} , which are both related to monopole interaction ($E_{\text{mono-mono}^*}$ and $E_{\text{mono-dip}^*}$). Even though these modifications gave accurate results, we have extended here the correction to the monopole–quadrupole term.

The expression is grounded on the ab initio formulation of the Coulomb electrostatic interaction energy, E_c (see refs 13 and 14 and references herein for details)

$$E_c = -2 \sum_i \sum_v Z_v \int (|\varphi_i(1)|^2 / r_{1v}) d\tau_1 - 2 \sum_j \sum_\mu Z_\mu \int (|\varphi_j(1)|^2 / r_{2\mu}) d\tau_2 + 4 \sum_i \sum_j \int (|\varphi_i(1)|^2 |\varphi_j(2)|^2 / r_{12}) d\tau_1 d\tau_2 + \sum_\mu \sum_\nu Z_\mu Z_\nu / r_{\mu\nu} \quad (2)$$

where μ and φ_i are the nuclei and the unperturbed molecular orbitals of monomer A and ν and φ_j , those of monomer B.

The monopole–monopole energy for two interacting centers i and j is given by

$$E_{\text{mono-mono}^*} = [Z_i Z_j - \{Z_i(Z_j - q_j)(1 - \exp(-\alpha_j \cdot r)) + Z_j(Z_i - q_i)(1 - \exp(-\alpha_i \cdot r))\} + (Z_i - q_i)(Z_j - q_j)(1 - \exp(-\beta_i \cdot r))(1 - \exp(-\beta_j \cdot r))] \cdot (1/r) \quad (3)$$

where Z_i and Z_j are the number of valence electrons of the two atoms concerned. In the case of the monopoles located on bonds Z is equal to zero. α_i and β_i are parameters depending on effective van der Waals radii r_{vdw} and are given by

$$\alpha_i = \gamma / r_{\text{vdw}i} \quad \text{and} \quad \beta_i = \delta / r_{\text{vdw}i} \quad (4)$$

where γ and δ are parameters depending on the basis set/methodology used for reference ab initio calculations. For

bond monopoles the r_{vdw} values are taken equal to the arithmetic mean between those of the atoms forming the bond.

The monopole–dipole energy term is given by

$$E_{\text{mono-dip}^*} = -\mu_j \cdot \xi^* \quad (5)$$

with

$$\xi^* = \{Z_i - (Z_i - q_i)(1 - \exp(-\eta r))\} \cdot \mathbf{r}_{ij} / r_{ij}^3 \quad (6)$$

and

$$\eta = \chi / ((r_{\text{vdw}i} + r_{\text{vdw}j}) / 2) \quad (7)$$

where χ is a parameter depending on the basis set/methodology used for reference ab initio calculations. At this point, this formulation includes a correction for terms varying like R^{-1} (monopole–monopole correction), for terms varying like R^{-2} (monopole–dipole correction) but does not include correction for terms varying like R^{-3} (dipole–dipole and monopole–quadrupole).

The standard monopole–quadrupole interaction is given by

$$E_{\text{mono-quad}} = E_{\text{mono-quad1}} + E_{\text{mono-quad2}} \quad (8)$$

with

$$E_{\text{mono-quad}} = q(Q_a / 2r^3)[3(\mathbf{a} \cdot \mathbf{r}/r)^2 - 1] \quad (9)$$

where $E_{\text{mono-quad1}}$ and $E_{\text{mono-quad2}}$ are respectively the interaction energy of a monopole interacting with an axial quadrupole (the two axial quadrupoles representing the true quadrupole are different for $E_{\text{mono-quad1}}$ and $E_{\text{mono-quad2}}$). \mathbf{a} defines the unit vector defining the axis, \mathbf{r} is the vector along r , directed from the monopole to axial quadrupole, and Q_a is the corresponding quadrupole magnitude with direction \mathbf{a} .

The energy can be refined by modifying the monopole q

$$E_{\text{mono-quad}^*} = E_{\text{mq1}^*} + E_{\text{mq2}^*} \quad (10)$$

with

$$E_{\text{mq1}^*} = \{Z_i - (Z_i - q_i)(1 - \exp(-\varphi r))\} (Q_a / 2r^3)[3(\mathbf{a} \cdot \mathbf{u})^2 - 1] \quad (11)$$

and

$$\varphi = \Omega / ((r_{\text{vdw}i} + r_{\text{vdw}j}) / 2) \quad (12)$$

where Ω is a parameter depending on the basis set/methodology used for reference ab initio calculations.

Thus E_{MTP^*} is given by

$$E_{\text{MTP}^*} = E_{\text{mono-mono}^*} + E_{\text{mono-dip}^*} + E_{\text{mono-quad}^*} + E_{\text{dip-dip}} + E_{\text{dip-quad}} + E_{\text{quad-quad}} \quad (13)$$

where γ , δ , χ , and φ were fit so that E_{MTP^*} reproduces E_c on the linear and bifurcated water dimers reported in this study.

Formulation of the Short-Range Repulsion Intermolecular Interaction Energy. Initially, E_{MTP} , lacking the attractive penetration component E_{pen} , was systematically less

attractive than E_c . Thus we had chosen a S^2/R formulation of E_{rep} in order to include E_{pen} in the repulsion since a similar dependency upon in S^2/R is observed for both exchange-repulsion and penetration.^{16,42} E_{rep} was calibrated so that the actual sum of $E_{\text{MTP}} + E_{\text{rep}}$, namely $E_1(\text{SIBFA})$, matches the corresponding sum of $E_c + E_{\text{exch}}$, namely $E_1(\text{RVS})$. Since E_{MTP^*} should now match E_c , E_{rep} should correspondingly match E_{exch} . This has led us to accordingly search for an improved reformulation of E_{rep} , while still retaining a molecular orbital (MO) overlaplike formulation.

$E_{\text{rep}}(\text{SIBFA})$ is now formulated as a sum of bond–bond, bond–lone pair, and lone pair–lone pair interactions under the form of an $S^2/R + S^2/R^2$ formulation. \mathbf{S} denotes the overlap between localized MOs of the interacting partners expressed under the form of sums of Slater hybrid orbitals around the pair of atoms making up the bonds and as hybrids around the lone pair bearing-heteroatoms. The localized MOs are represented by centers along the chemical bonds and the lone pairs of heteroatoms.

In the case of two interacting molecules A with bonds AB and lone pairs L_α and C with bonds CD and lone pairs L_γ , E_{rep} has the form

$$E_{\text{rep}} = C_1 \left(\sum_{\text{AB}} \sum_{\text{CD}} \text{rep}(\text{AB}, \text{CD}) + \sum_{\text{AB}} \sum_{L_\gamma} \text{rep}(\text{AB}, L_\gamma) + \sum_{L_\alpha} \sum_{\text{CD}} \text{rep}(L_\alpha, \text{CD}) + \sum_{L_\alpha} \sum_{L_\gamma} \text{rep}(L_\alpha, L_\gamma) \right) \quad (14)$$

Each term of this equation depends upon a functional, \mathbf{S} , of the overlap as

$$\text{rep}(\text{AB}, \text{CD}) = N_{\text{occ}}(\text{AB}) N_{\text{occ}}(\text{CD}) \mathbf{S}^{**2}(\text{AB}, \text{CD}) / (D_{\text{AB}, \text{CD}})^n \quad (15)$$

where $n = 1$ or 2 , and $N_{\text{occ}}(\text{AB})$ and $N_{\text{occ}}(\text{CD})$ are the occupation numbers of bonds AB and CD. N_{occ} is equal to 2 for doubly occupied bonds and lone pairs and to 1 for π type orbitals. $D_{\text{AB}, \text{CD}}$ denotes the distance between the barycenters of bonds AB and CD.

The expression for the overlap term \mathbf{S} was detailed in a preceding paper.²² The formulation of \mathbf{S} includes exponentials of the distance between pair of atoms belonging to the interacting bonds or lone pairs. Such distances are divided by the geometric mean of the effective radii of these atoms. As for E_{MTP^*} such radii are atom-type dependent. For any given atom type such as $\text{O}(\text{sp}^2)$, $\text{O}(\text{sp})$, etc., they are also determined on the basis of isodensity contour maps around a representative isolated molecule to which they belong. Dependencies of these radii upon the electronic populations of the interacting atoms are considered following an expression described in ref 43.

Polarization and Charge-Transfer Terms

The formulation and calibration of E_{pol} and E_{ct} are identical to those given in ref 26 for all computations done at the HF level, while new parameters have been calibrated for the DFT computations. E_2 corresponds to the sum of polarization and charge-transfer energies.

Note on Polarization Energies. In the tables, two values of the ab initio E_{pol} energies are given. The first corresponds

to the nonantisymmetrized but fully relaxed Kitaura–Morokuma⁴⁴ value and the second to antisymmetrized RVS values. The fully relaxed SIBFA E_{pol} can be compared to the $E_{\text{pol}}(\text{KM})$ as only the first iteration of the SIBFA polarization contribution is compared to $E_{\text{pol}}(\text{RVS})$. The $E_{\text{pol}}(\text{RVS})$ values are given in parentheses in the table as well as the values of $E_{\text{pol}}(\text{SIBFA})$ prior to iterating (for details, see Piquemal et al., submitted for publication).

Results and Discussion

Calibration and Tests on Five Model Water Dimers. We have in ref 17 compared the evolutions of E_{MTP^*} and of E_c in the five water dimers represented in Figure 1a–e. We have observed that when augmented with E_{pen} , E_{MTP^*} could closely match E_c in the range of relevant O–H, O–O, and H–H distances, even in unphysical configurations, such as complexes 1d and 1e. We now compare (Figure 1a–e) the behaviors of E_{rep^*} to those of E_{exch} .

The calibration of E_{rep} bore on the effective radii of O and H and the exponents α_1 and α_2 and multiplicative constants C_1 and C_2 of the S^2/R and of the S^2/R^2 terms. They were given in ref 26. It was done in order for E_{rep^*} to reproduce the numerical values of E_{exch} in the linear and bifurcated water dimers (complexes 1a and 1c) upon performing variations of the H–O distance. Extension to complexes other than 1a and 1c, such as 1b, 1d, and 1e, have to our knowledge little or no precedents in the development and evaluation of APMM procedures. Such comparisons should be allowed for evaluation if bond–bond, bond–lone pair, and lone pair–lone pair interactions are correctly expressed and balanced within E_{rep} . We note in particular the predominance of lone pair–lone pair repulsion in configuration d and that of bond–bond repulsion in configuration e, while bond–lone pair repulsion should be the dominant repulsive contribution in a and c. To what an extent will these varying weights enable the reproduction of the numerical values of E_{exch} and its radial behaviors?

Figure 1a–e shows close agreements throughout the range of relevant H–O distances (>1.7 Å) as well as O–O and H–H distances (>2.7 and >1.5 Å respectively). Thus, for complexes 1a, 1b, and 1c, the errors amount to 0.17, 0.07, and 0.11 kcal/mol, respectively, at equilibrium distance. For complexes 1d and 1e, they amount to 0.08 and 0.10 kcal/mol at the representative H–H and O–O distances of 2.3 and 2.8 Å, respectively.

The values of $\Delta E(\text{SIBFA})$ and $\Delta E(\text{RVS})$ and their respective contributions at equilibrium distances for complexes 1a–c and for complexes 1d and 1e are reported in Table 1. It shows that the close agreements between $\Delta E(\text{SIBFA})$ and $\Delta E(\text{RVS})$ are due to corresponding agreements at the level of the individual contributions.

Water Clusters. An essential objective of APMM procedures is the simulation of very large complexes that are not amenable to QC procedures. It is necessary to ensure that the agreement found at the level of bimolecular complexes will be preserved in multimolecular complexes. A critical issue relates to whether E_{pol} and E_{ct} from SIBFA can reproduce the nonadditive behaviors of their RVS counterparts. We have previously addressed the issues of

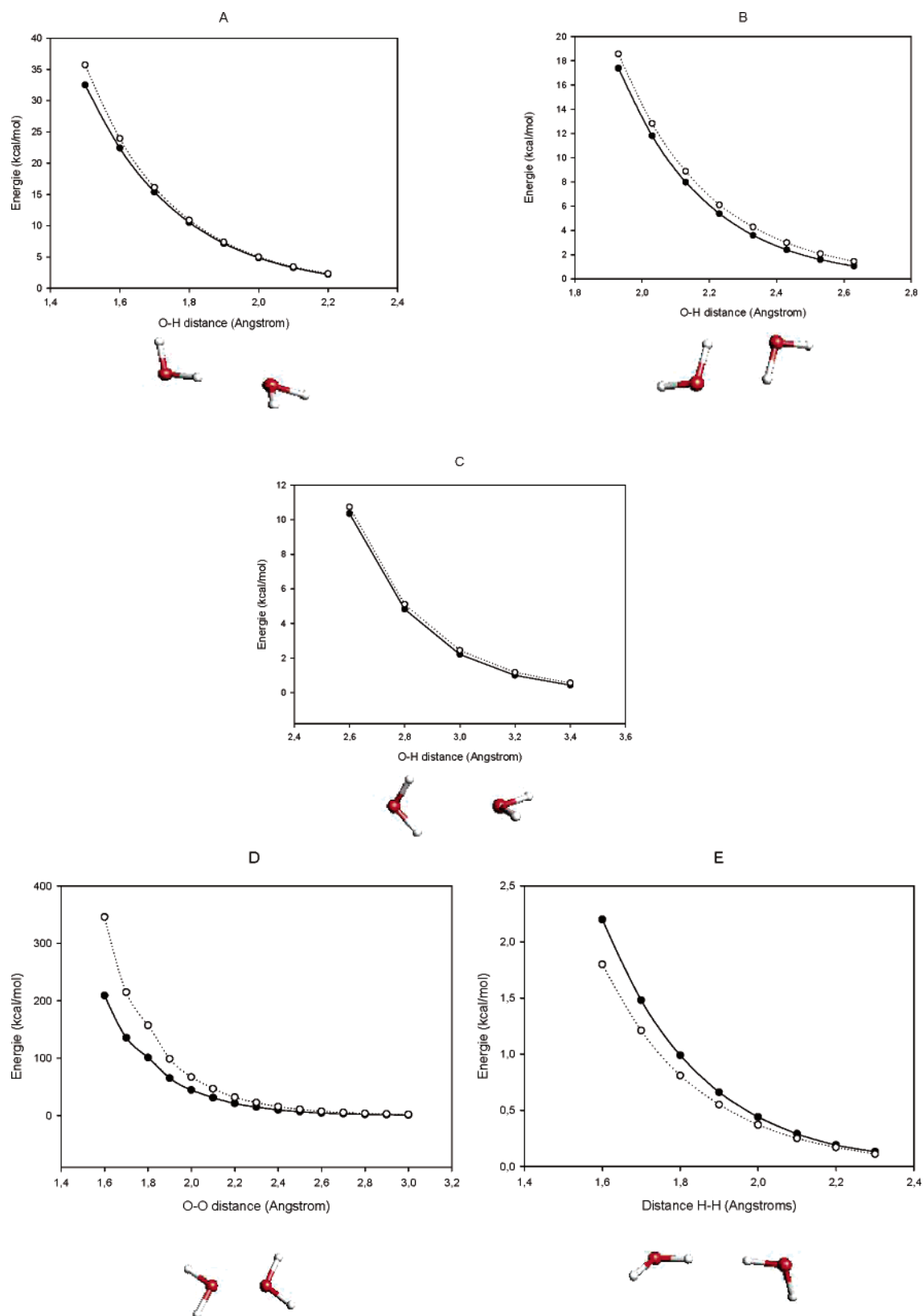


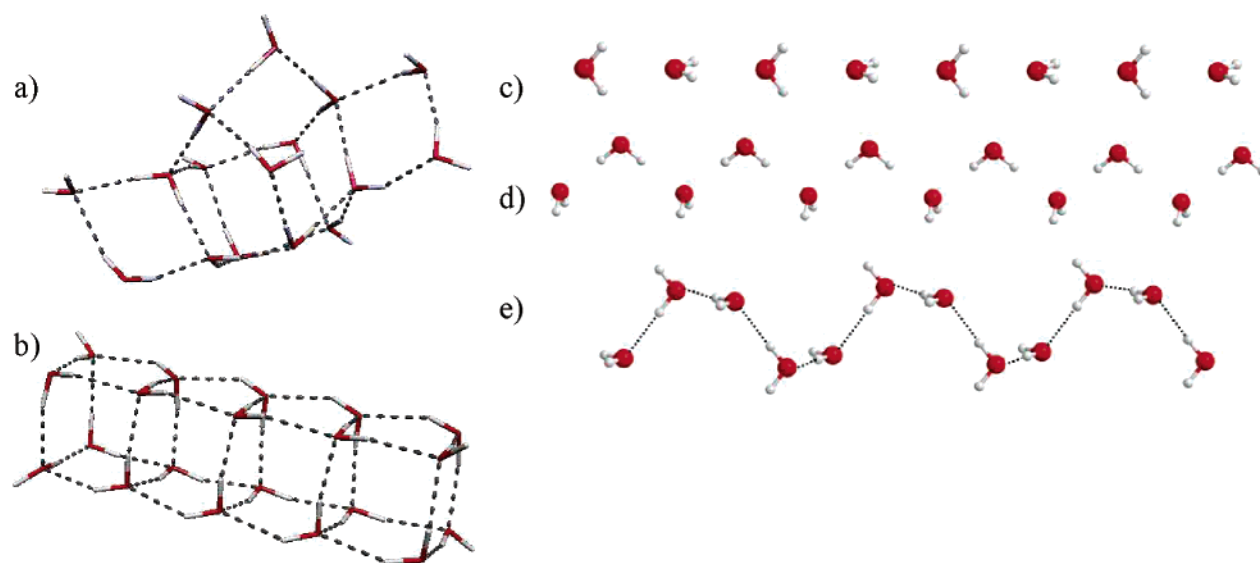
Figure 1. Distance variations of the exchange repulsion component (E_{exch}) (kcal/mol) versus modified SIBFA component (E_{rep}^*) for five water dimers at the Hartree–Fock level.

cooperativity in water aggregates^{43,45} and peptide H-bonded networks³¹ and of anticooperativity in polyligated Zn(II) complexes.⁴⁶ We here present results on water aggregates in three-dimensional cubic arrangements with $n = 12$, 16, and 20 water molecules (shown in Figure 2a for $n = 20$)

which were previously investigated in the framework of the density fitting based GEM force field.⁴ Single-point RVS analyses were performed for each of the three energy-minimized structures. We have also performed a similar SIBFA vs RVS comparison in a small aggregate ($n = 16$)

Table 1. RVS and SIBFA Interaction Energies (kcal/mol) for the Water Dimers at the Equilibrium Point or Standard Orientation

energy (kcal/mol)	E_c	E_{exc}	E_1	E_{pol}	E_{ct}	E_2	ΔE
linear dimer (SIBFA)	-5.98	3.42	-2.56	-0.70	-0.60	-1.30	-3.87
linear dimer (RVS)	-5.81	3.26	-2.54	-0.67	-0.63	-1.30	-4.04
cyclic dimer (SIBFA)	-5.42	2.87	-2.55	-0.34	-0.26	-0.60	-3.16
cyclic dimer (RVS)	-4.79	2.19	-2.40	-0.31	-0.29	-0.60	-3.23
bifurcated dimer (SIBFA)	-3.48	1.17	-2.31	-0.20	-0.15	-0.35	-2.67
bifurcated dimer (RVS)	-3.17	1.00	-2.17	-0.21	-0.19	-0.40	-2.78
H-H dimer (SIBFA)(2.3)	1.84	0.17	2.03	-0.06	0.00	-0.06	1.96
H-H dimer (RVS)	2.11	0.13	2.24	-0.12	-0.12	-0.24	1.88
O-O dimer (SIBFA)(2.8)	1.91	2.41	4.32	-0.31	0.0	-0.31	4.02
O-O dimer (RVS)	2.83	1.96	4.79	-0.38	-0.12	-0.50	4.12

**Figure 2.** Representation of water aggregates [a, b]) and of sequentially H-bonded 12 water chains [c)–e]): a), a water aggregate in an energy-minimized ice box with $n = 20$ water molecules; b), a water aggregate with $n = 16$ waters, as extracted from a Monte Carlo simulation on a water box with 64 molecules; c), a bifurcated arrangement; d), a transverse bifurcated; and e), a helical arrangement.**Table 2.** RVS and SIBFA Interaction Energies (kcal/mol) in Four 12–20 Water Clusters

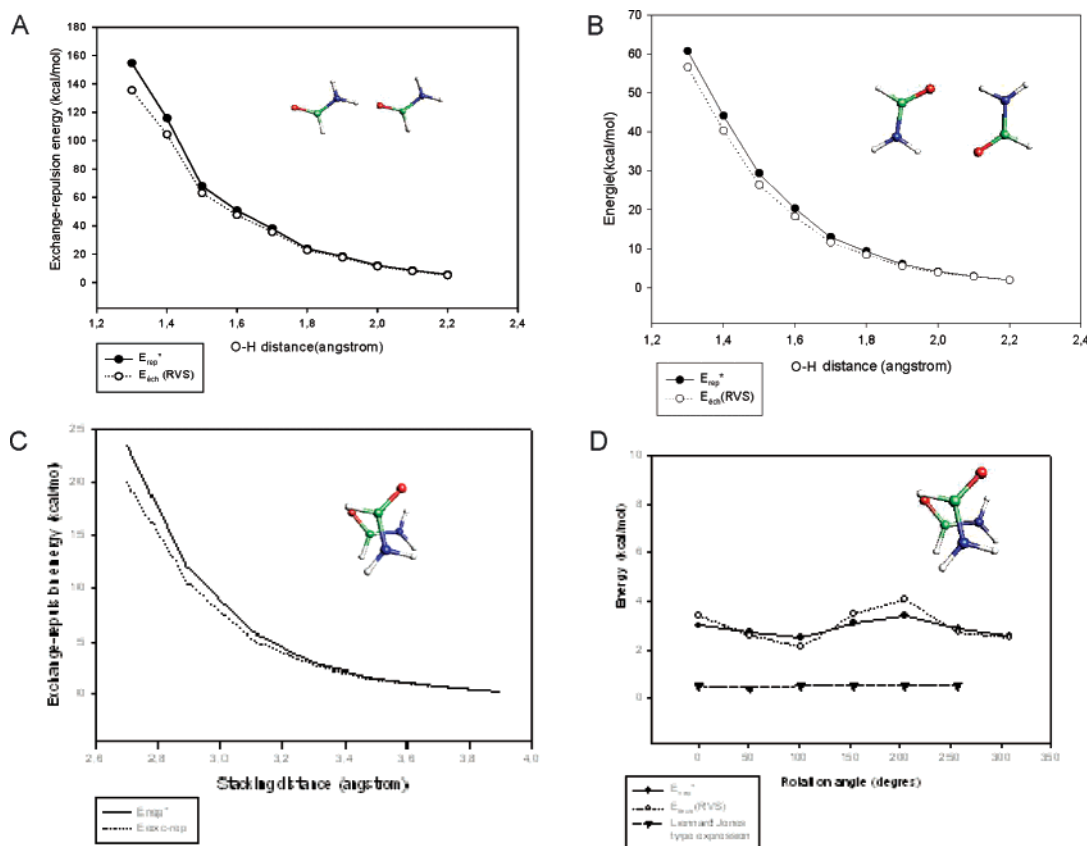
no. of waters	12		16		16 (MC)		20	
	SIBFA*	RVS	SIBFA*	RVS	SIBFA*	RVS	SIBFA*	RVS
E_{MTP^*}/E_c	-167.6	-168.5	-230.9	-231.4	-179.5	-179.8	-293.2	-294.3
E_{rep^*}/E_{exc}	151.9	151.4	207.9	207.5	149.8	149.9	263.6	263.2
E_1	-15.8	-17.1	-23.1	-23.9	-29.7	-29.9	-30.6	-31.1
E_{pol^*}/E_{pol} RVS	-30.6	-34.7	-42.0	-47.8	-32.7	-35.5		
E_{pol}/E_{pol}	-41.3	-44.7	-56.5	-61.7	-44.1	-45.1	-71.3	-78.6
E_{ct}	-22.1	-23.1	-30.2	-31.3	-22.6	-23.1	-37.3	-39.4
$\Delta E(SIBFA)/\Delta E(RVS)$	-79.2	-80.1	-109.8	-110.4	-96.4	-94.8	-139.2	-139.1

extracted from an ongoing Monte Carlo (MC) simulation performed on a water box of $n = 64$ molecules (Figure 2b). Thus we wished to evaluate not only the overall accuracy of $\Delta E(SIBFA)$ as compared to $\Delta E(RVS)$ but also the extent of related agreements of the individual contributions. The results are reported in Table 2. A striking feature of the three cubic arrangements relates to E_{pol} , whose numerical values outweigh those of the summed first-order contribution E_1 . This is because the large stabilizing values of E_{MTP^*} are opposed by those of E_{rep} , a reflection of the shortening of

the O–O H-bonding distances (in the 2.72–2.90 Å range for $n = 20$) due to cooperativity. In fact, even E_{ct} has larger stabilizing values than E_1 in these three cubiclike structures. The weights of the second-order terms increase with respect to E_1 upon increasing n . E_{pol} also has a greater stabilizing role than E_1 in the MC structure, while E_{ct} is smaller in magnitude than it, a reflection of the relative lengthening of intermolecular O–O distances. For all four complexes, $\Delta E(SIBFA)$ reproduces very closely $\Delta E(RVS)$, the relative error being contained within 2%. The individual contribu-

Table 3. RVS and SIBFA Interaction Energies (kcal/mol) for Water Chains: Bifurcated Chain (BC), Transverse Hydrogen-Bonded Chain (t-HBC), and Longitudinal Hydrogen-Bonded Chain (l-HBC)

energies (kcal/mol)	E_c	E_{exch}	E_1	E_{pol}	E_{ct}	E_2	ΔE
HBC SIBFA	-81.6	54.0	-27.6	-18.2 (-14.0)	-9.5	-27.7	-55.4
HBC RVS	-81.2	54.3	-26.8	-17.3 (-14.5)	-9.8	-24.3	-53.1
t-HBC SIBFA	-58.8	29.9	-28.8	-9.0 (-7.2)	-3.6	-12.6	-41.4
t-HBC RVS	-53.5	27.3	-26.3	-9.8 (-8.2)	-3.5		-39.2
l-HBC SIBFA	-60.9	54.0	-6.9	-3.9 (-3.6)	-7.5	-11.4	-18.3
l-HBC RVS	-60.5	55.1	-5.4	-5.5 (-4.7)	-7.7		-17.8

**Figure 3.** Formamide dimers. *In-plane H-bonded.* a) linear monodentate and b) bridged. Compared evolutions (in kcal/mol) of E_{exch} (RVS) and E_{rep} (SIBFA) as a function of the H–O distance. *Stacked.* Compared evolutions (in kcal/mol) of E_{exch} (RVS) and E_{rep} (SIBFA) as a function of c) interplanar separation and d) rotations around the z-axis at fixed interplanar separation of 3.3 Å.

tions, E_{MTP}^* and E_{rep} within E_1 and E_{pol} and E_{ct} in second-order, match their RVS counterparts. As commented in previous papers^{43,45,46} there is a good correspondence, on the one hand, between E_{pol}^* (SIBFA) which is computed with the field due to the sole permanent multipoles and E_{pol} (RVS) and, on the other hand, E_{pol} (SIBFA) embodying the effect of induced dipoles on the field⁴³ and E_{pol} (KM) that results from the Kitaura–Morokuma (KM) analysis⁴⁴ (for details, see Piquemal et al., submitted for publication).

Water Chains. Further tests on the ability of polarizable potentials to account for nonadditive effects were put forth by Giese and York²⁷ and Chelli and Procacci.^{47,48} They bore on two kinds of H-bonded chains of water molecules, namely bifurcated and transverse (Figure 2c,d). The possible issues of overpolarization (due to the absence of exchange-polarization in some potentials) as opposed to underpolarization (due to the lack of an explicit charge-transfer

contribution) were addressed by these authors. In another chain (Figure 2e), denoted as longitudinal helical, that was recently considered by Chelli and Procacci (Piquemal et al., *J. Phys. Chem. B*, in press), each nonterminal water acts simultaneously as a single H-bond donor and as a single H-bond acceptor (Figure 3c). Such a complex was designed in order to amplify the polarization response. We have recently evaluated the ability of both SIBFA and two Chemical Potential Equalization procedures designed by these authors⁴⁸ to give correct E_{pol} values from QC calculations as well as for the average water dipole moment in these chains (Piquemal et al., submitted for publication). As a continuation of this work, we give in Table 3 the results of SIBFA versus RVS analyses on these three dodecamer chains. As in ref 27, O–O H-bond distances are set to 2.97 Å and $n = 12$ water molecules. The analyses were also done at O–O H-bond distances of 2.48 and 3.50 Å and with

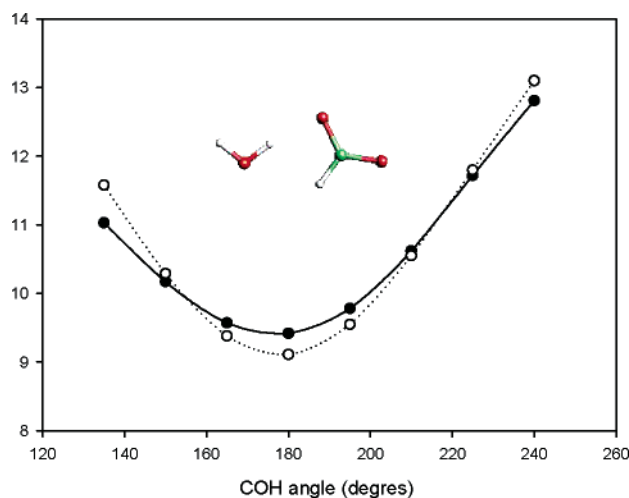


Figure 4. Compared in-plane angular evolutions (in kcal/mol) of $E_{\text{exch}}(\text{RVS})$ and $E_{\text{rep}}(\text{SIBFA})$ (dashed line) in a formate–water complex, as a function of the $\theta = \text{C}–\text{O}–\text{H}$ angle. The $\text{H}–\text{O}$ distance is fixed at 1.8 Å.

shorter chains (unpublished). The results from Table 3 confirm the ability of SIBFA to correctly reproduce $\Delta E(\text{RVS})$ and its individual contributions in these three chains.

CEP 4-31G(2d) vs DZVP2: Pseudopotential versus All Electrons Basis Set. The same agreement with *ab initio* is obtained at both level of basis set. Nevertheless, a difference can be noticed concerning the repartition of the penetration correction. While its monopole–quadrupole component is negligible with the CEP 4-31G(2d) basis set, this is no longer true for the full electron calculation where the correction monopole–quadrupole correction is required to obtain the same level of agreement with RVS computations (not shown).

Other H-Bonded Complexes. Formamide Dimer. The study by *ab initio* SCF methods, of the formamide dimer as a model for the H-bond between peptide units, was pioneered by Dreyfus and Pullman.⁴⁹ Such a complex had also lent itself to a study by one of the very first energy-decomposition approaches. Figure 3a,b bears on the linear and on the bridged formamide dimers, respectively. They represent the evolution of $E_{\text{rep}}(\text{SIBFA})$ compared to $E_{\text{exch}}(\text{RVS})$ as a function of the $\text{N}–\text{O}$ distance of approach. These two figures illustrate that the parallelism between $\Delta E(\text{SIBFA})$ and $\Delta E(\text{RVS})$ reflects that between their individual first-order contributions as well as (not shown) second-order ones.

The results concerning the bridged formamide dimer are given in Table 1 of the Supporting Information.

Formate–Water. In order to evaluate the extent to which E_{rep} can account for the anisotropy features of E_{exch} , we have considered a complex between formate and a water molecule acting as an H-bond donor. In this complex, the distance between the donated H and one anionic O is fixed at 1.8 Å, the $\text{O}–\text{H}–\text{O}$ angle is fixed at 180°, and stepwise in-plane variations of the $\theta = \text{C}–\text{O}–\text{H}$ angle are done (see Figure 4). This figure shows both $E_{\text{rep}}(\text{SIBFA})$ and $E_{\text{exch}}(\text{RVS})$ to have a marked angular behavior, with a maximum at θ at approximately 120°, $E_{\text{rep}}(\text{SIBFA})$ having a shape that parallels that of E_{exch} . Such an angular behavior can only obtain thanks to the explicit introduction of localized lone pairs in

SIBFA. By contrast, a simplified representation of E_{rep} under the form of atom–atom terms with $1/R^{12}$ dependence gives rise to a flat behavior (not shown). This is explained by the fact in the whole zone of water variations away from the other anionic O, the closest water–formate distance is that between the donated water H and the acceptor anionic O. Such a distance is constant, while, due to the $1/R^{12}$ dependence, the other atoms on both monomers affect only negligibly the behavior of E_{rep} with such a representation.

In Table 2 of the Supporting Information are reported the RVS and SIBFA interaction energies concerning the bridged formate–water complex at equilibrium distance ($d_{\text{O}–\text{H}} = 1.9$ Å), confirming again the agreement of SIBFA and RVS results at the level of both the total energies and their individual contributions.

Methylammonium–Water. The methylammonium–water complex was previously investigated in three distinct arrangements, the cation approaching water along the external bisector of the HOH angle: (a) in the prolongation of one NH bond; (b) through the external bisector of one HNH angle; and (c) in the prolongation of the CN bond.²¹ Concerning the first-order contributions, however, $E_1(\text{SIBFA})$ was then identified to $E_1(\text{RVS})$ without further identification of E_{MTP^*} to E_{c} and of E_{rep} to E_{exch} . The results with the present refinements are reported as Supporting Information (Table 3) concerning complexes *a–c* at their optimized O–N distances. Good agreements are noticed for the three structures.

Formate–Methylammonium. The formate–methylammonium complex had, similarly, been investigated in ref 21 in two binding modes: (a) bidentate (denoted as ‘B’), in which two ammonium protons interact each with one anionic oxygen, the two $\text{H}–\text{O}$ distances being equal and the HNH plane being coplanar to the formate plane; and (b) monodentate (denoted as ‘M’), in which one ammonium H binds externally to one anionic O. The $\text{N}–\text{H}–\text{O}$ angle is 180, one HNH plane involving this H is coplanar with the formate plane, and similar to the formate–water complex, stepwise 15 deg variations are done on the $\theta = \text{H}–\text{O}–\text{C}$ angle. Results for the bidentate complex are reported as Supporting Information (see Table 4) at the optimized O–N distances of ‘B’ and ‘M’ complexes. A close agreement is found between SIBFA and RVS. Figure 5 confirms this point and shows the importance of a good description of the anisotropy of the exchange–repulsion in the rotations performed in the monodentate mode.

Stacked Formamide Complex. An ubiquitous determinant in molecular recognition concerns stacking interactions with aromatic or conjugated groups. Numerous examples are provided by structural biology, supramolecular chemistry, and solid-state X-ray crystallography.^{50–52} An important issue relates to the computation of the van der Waals contribution to the total binding energy, since it is a major contributor to stabilization, yet its accurate evaluation requests beyond-HF calculations and the use of very extended basis sets. We concentrate here on a model complex of two stacked formamide molecules (see Figure 3c,d). This complex has been previously investigated by Sponer and Hobza.^{53,54} These

Table 4. CSOV/B3LYP and SIBFA* Energies for Selected Dimers and Water Cluster: aug-cc-pVTZ Basis Set^a

energies (kcal/mol)	E_c	E_{exch}	E_1	E_{pol}	E_{ct}	E_2	ΔE
linear dimer	-7.68	6.21	-1.44	-1.37	-1.61	-2.98	-4.42
(CSOV)	-7.78	6.30	-1.47	-1.31	-1.58	-2.90	-4.40
cyclic dimer	-5.27	2.90	-2.37	-0.30	-0.45	-0.75	-3.12
(CSOV)	-4.83	2.69	-2.15	-0.42	-0.56	-0.98	-3.13
bifurcated dimer	-4.32	2.30	-2.02	-0.28	-0.44	-0.73	-2.75
(CSOV)	-4.34	2.67	-1.67	-0.38	-0.41	-0.79	-2.46
H–H dimer (2.2)	2.06	0.26	2.32	-0.08	0.00	-0.08	2.25
(CSOV)	2.1	0.26	2.36	-0.23	-0.27	-0.50	1.87
H–H dimer (2.5)	1.48	0.10	1.58	-0.04	0.00	-0.04	1.38
(CSOV)	1.52	0.10	1.63	-0.12	-0.12	-0.24	1.39
O–O dimer (2.8)	1.86	2.23	4.10	-0.26	-0.15	-0.42	3.68
(CSOV)	1.53	2.57	4.10	-0.40	0.00	-0.40	3.68
cluster 16 H ₂ O	-184.0	149.2 (154.5)	-34.8 (-29.5)	-45.9	-41.0	-86.9	-121.7 (-116.3)
ab initio	-186.4	166.5	-19.8	-45.1	NC	NC	-114.0
cluster 20 H ₂ O	-298.2	262.1 (272.3)	-36.0 (-26.1)	-72.3	-75.8	-148.1	-184.1 (-174.0)
ab initio	-309.4	292.2	-17.2	-78.6	NC	NC	-168.1

^a The values of the ab initio polarization energies are given at the HF/CEP 4-31G(2d) level. The ΔE (DFT) values are BSSE corrected. For the exchange-repulsion contribution, results given in parentheses correspond to SIBFA calculations performed using lone pairs positions as described in ref 4.

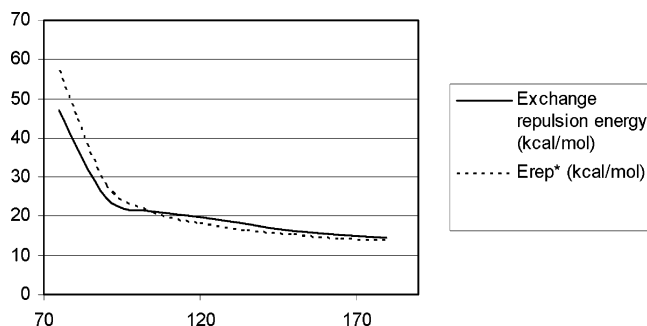


Figure 5. Compared in-plane angular evolutions (in kcal/mol) of E_{exch} (RVS) and E_{rep} (SIBFA) in a formate–monomethylammonium complex, as a function of the $\theta = \text{C–O–H}$ angle. The H–O distance is fixed at 1.7 Å.

authors have evaluated the effects on the binding energies of correlation (at both MP2 and CCSD(T) levels) and of different basis sets, up to the cc- and aug-cc-pVDZ/cc-pVDZ ones. The two extreme arrangements, parallel as well as antiparallel, were considered. These studies were undertaken in view of subsequent detailed analyses of stacking interactions in nucleic acid bases, which, similar to formamide, encompass C=O, C–N, and –NH functional groups. This was exemplified in a recent study of stacked cytosine dimers.⁵⁵ In the present study, and prior to similar subsequent extensions, we wish to first evaluate the extent to which each of the individual SIBFA contributions can reproduce the distance and the orientation dependencies of its HF counterpart. For that purpose, we start from a position where each monomer overlaps maximally with the other. This is done by giving to each atom of the second monomer the same x and y coordinates as the corresponding atom of the first. ΔE (SIBFA) is then optimized by varying the z coordinate of the second formamide kept parallel to the first. At the optimized value of z (3.3 Å), clockwise rotation of the second formamide is done around the z -axis. Such arrangements are chosen in order to once more critically evaluate E_{rep} (SIBFA). Indeed, the onset of bond–bond, bond–lone pair, and lone

pair–lone pair interactions is maximized, so that this contribution could only reproduce the behavior and numerical values of E_{exch} (RVS) if all three components are properly and consistently formulated and weighted. An additional requisite is that the π lone pairs on the C, N, and O atoms be properly represented. For that purpose, we have proposed in ref 26, a representation of the π system as bent sp hybrids.²⁵ Their localizations with respect to the atom bearing them as well as their partial occupation numbers were determined by using a Zn(II) cation as a probe over the formamide plane above the C, N, and O atoms and performing parallel SIBFA and RVS computations to optimize the fit of E_{rep} (SIBFA) to E_{exch} (RVS). Here, we justify this choice by drawing electron density maps (see Figure 1 of the Supporting Information). In these figures, the outermost contour corresponds to a density of 0.001 au which has been shown to be a measure of the van der Waals radius⁵⁶ in a way that can be directly measured (in Å). As can be seen, the density expansion is greater in the molecular plane than in the plane perpendicular to it and containing the π system. Figure 3c,d compares the evolutions of E_{rep} (SIBFA) and E_{exch} (RVS) as a function of, respectively, the interplanar distance z and of the rotation angle around the z -axis.

E_{rep} (SIBFA) shows the same directional features as E_{exch} (RVS) but slightly underestimates (see Figure 3d). By contrast, a $1/R^{12}$ expression gives rise to a flat behavior.

As can be seen in Figure 6, the agreement of E_{MTP}^* (SIBFA), here at the DZVP2 level, can be further improved upon inclusion of E_{pen} compared to previous calculations at the same level.¹⁷ Again, the extra monopole–quadrupole correction is required to obtain such results.

To conclude on the stacked formamide dimers, a very good agreement can be evidenced upon comparing the evolution of ΔE (SIBFA) to that of ΔE (RVS) for rotations around the z -axis (see Figure 7). This demonstrates that the anisotropic character of SIBFA can faithfully mirror that of the ab initio computations for stacked complexes.

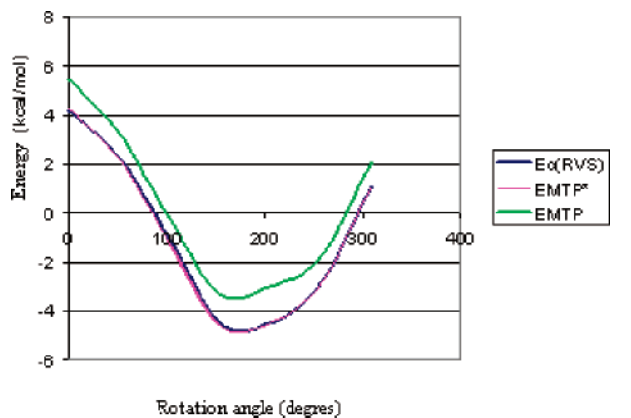


Figure 6. Stacked formamide dimer. DZVP2 computations. Variations (in kcal/mol) of $E_c(\text{RVS})$ and E_{MTP^*} (SIBFA) as a function of angle of rotation around the z-axis.

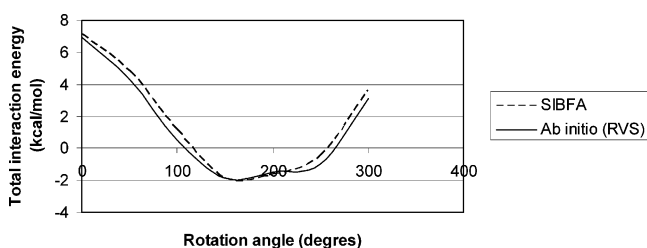


Figure 7. Stacked formamide dimer. Compared evolutions (in kcal/mol) of $\Delta E(\text{SIBFA})$ and $\Delta E(\text{RVS})$ for rotations around the z-axis.

Inclusion of Electron Correlation. Our approach to handling the effects of electron correlations in APMM procedures is the following: (a) concerning E_{MTP^*} and E_{pol} , by deriving distributed multipoles and polarizabilities from DFT computations, and (b) concerning E_{rep} and E_{ct} , by recalibrating the multiplicative constants so that these contributions reproduce their counterparts from CSOV^{13,18} analyses of bimolecular complexes computed at the DFT level. There remains the problem of dispersion since present functionals cannot provide the energy gain due to dispersion effects, namely the actual van der Waals term.⁵⁷ Even standard MP2 computations need to be augmented by CCSD(T) computations.^{58,59} Initially regarding SIBFA, the calibration of the dispersion contribution E_{disp} was performed in a “HF + dispersion” approximation so that $\Delta E + E_{\text{disp}}$ matches in model bimolecular complexes high-level MP2, CCSDT, or Symmetry-Adapted Perturbation Analyses (SAPT)¹² interaction energies. In this work, we propose to use a “DFT + E_{disp} ” approach.

DFT Computations. Toward reproduction of DFT calculations, it is essential to first evaluate the extent to which SIBFA can reproduce first the individual components of CSOV not only in the five water dimers presented above but also in more difficult configurations. Indeed, in 2002, van Duijneveldt et al.²⁸ have reinvestigated using molecular mechanics ten water dimers originally due to Tschumper et al.⁶⁰ and occurring as stationary points on the water dimer surface obtained at high level QC (CCSD(T)/large basis set + diffuse functions). Energy-decomposition analysis enabled the evaluation of the relative merits of several polarizable

potentials concerning the representation of the individual QC energy contributions. Recently, some of us proposed a new-generation force field based on density fitting termed GEM (Gaussian Electrostatic Model)^{4,65} able to address accurately such a difficult issue. In the present study, these ten complexes are reinvestigated in light of the refinements to the SIBFA first-order contributions that now include correlated multipoles and polarizabilities. The choice of aug-cc-pVTZ is consistent with both van Duijneveldt et al. and the GEM studies. It also enables the evaluation of the SIBFA potential as compared to reference calculations performed using large basis sets with diffuse functions.

The results for the first five dimers (the linear configuration being also included in Tschumper’s et al.⁶⁰ training set) are reported in Table 4 and appear in good agreement with the CSOV results. Figures 8 and 9 show the behavior of the energy components for scans of the intermolecular O–H distance in the linear dimer configuration. A good agreement of all the different SIBFA components is obtained with their ab initio counterparts even below the equilibrium position ($d_{\text{O}\cdots\text{H}} = 1.95 \text{ \AA}$). This also confirms the GEM-0 results⁴ that showed the capabilities of the charge-transfer expression to account for the QC charge-transfer energy gain observed upon going from HF to DFT.¹³

At such a difficult level including diffuse functions, more configurations are needed to test the potential energy surface. Therefore, we have performed calculations following van Duijneveldt et al.²⁸ recommendations. As can be seen in Figure 10 which bears on all 14 dimer configurations tested in this work a good correlation is obtained with ab initio (0.989). Compared to CSOV, the mean error of the SIBFA total interaction energy on the additional nine dimers^{28,60} is 0.22 kcal/mol. This error appears larger than the one observed with the more sophisticated GEM-0 force field.⁴ Nevertheless, it demonstrated that SIBFA can meet the requirements suggested by van Duijneveldt et al.²⁸ concerning molecular dynamics potentials, namely that they should be able to reproduce ab initio total interaction energies with errors about 1 kJ in order to stay below kT at room temperature. It is interesting to quote that most of the errors are, following the numbering of ref 28, concentrated in dimers 6–10 (the worst agreement being on dimer 9 with an error of 0.6 kcal/mol) which are only weakly attractive and highly stabilized by the introduction of diffuse functions at the ab initio level.⁶⁰ We have also tested this correlated SIBFA potential on water clusters (16 and 20 molecules, see Table 4) for which ab initio data are available from ref 4. While the DFT-derived E_{MTP^*} shows robustness compared to CSOV, a deviation is observed for E_{rep^*} with an error about 10% compared to reference data. To understand the origin of these discrepancies we have changed the positions of the water lone pairs (initially derived at the HF level) according to the position of the centroids of the Boys localized orbitals⁶¹ obtained at the B3LYP/aug-cc-pVTZ that were retained in the GEM-0 approach.⁴ Indeed, the errors are decreasing (see Table 4) when a consistent location is chosen. It is important to point out that we had also recomputed the exchange-repulsion energies of the 14 water dimers with this new location and noticed no improvement. This underlines the difficulty of a

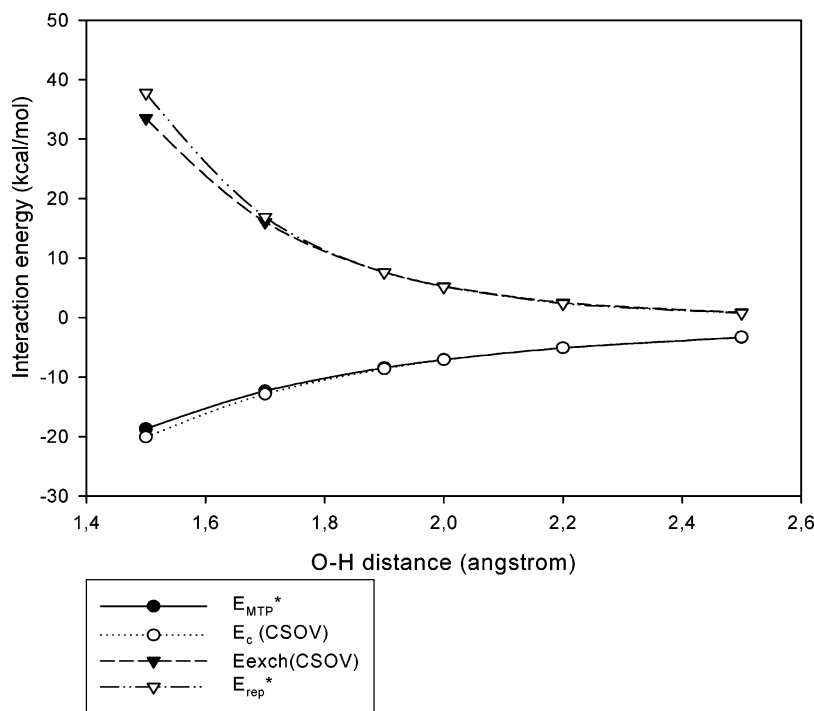


Figure 8. Linear water dimer. Variations (in kcal/mol), as a function of intermolecular distance, of E_c (RVS) and E_{exch} (RVS) calculated at the B3LYP/aug-cc-pVTZ/CSOV level and corresponding variations from modified SIBFA contributions E_{MTP}^* and E_{rep}^* .

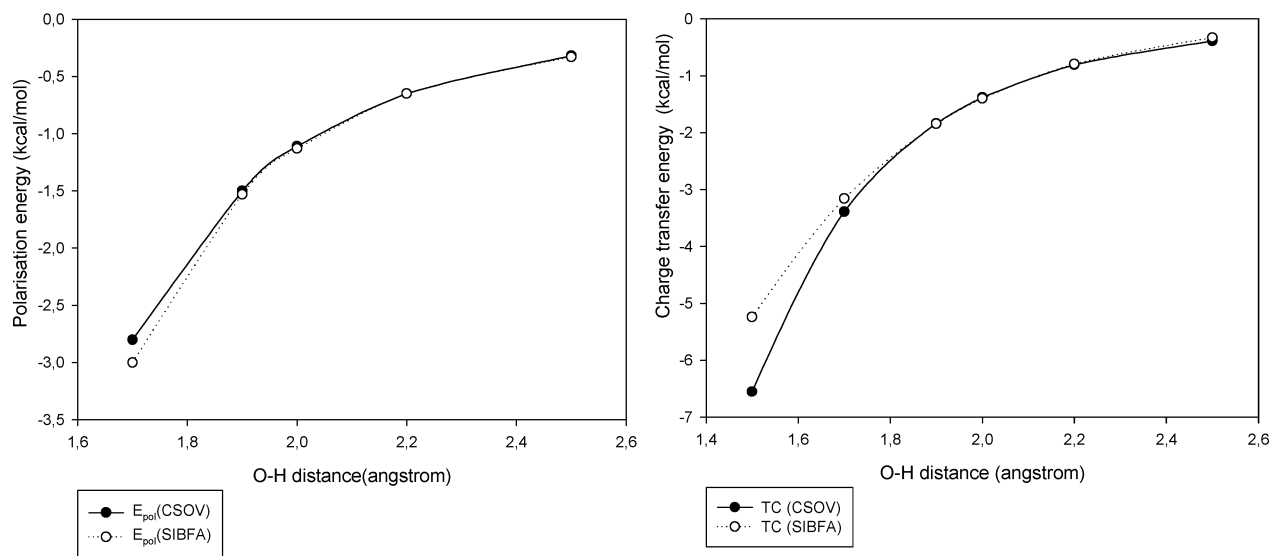


Figure 9. Linear water dimer. Variations (in kcal/mol), as a function of intermolecular distance, of E_{pol} (RVS) and E_{ct} (RVS) calculated at the B3LYP/aug-cc-pVTZ/CSOV level and corresponding variations from modified SIBFA contributions E_{pol} and E_{ct} .

choice of a limited training set of geometries. To conclude on the total energies, we have observed a good agreement with ab initio in the two structures even if some error in compensation between components occurs.

Inclusion of Dispersion: DFT+ disp Approximation vs CCSD(T). We present here some preliminary results using a “DFT+dispersion” approximation. We have modified by a factor of 70% the multiplication coefficient of the dispersion energy contribution, E_{disp} , as formulated in ref 43 so that it matches the values given in ref 28 for the ten water dimers computed at the CCSD(T)/aug-cc-pVTZ level. We observed an average error of 0.22 kcal/mol on the

total training set. Figure 11 reports, concerning the linear water dimer, the evolution of the SIBFA(B3LYP/aug-cc-pVTZ)+ E_{disp} interaction energies along with those of the CCSD(T)/aug-cc-pVTZ ones. Starting from an O–H distance of 1.85–2.5 Å, we observed that SIBFA reproduces CCSD(T) computations with an average error limited to 0.2 kcal (0.1 kcal at the equilibrium geometry, $d_{OH} = 1.95$ Å). More detailed explorations of these approximations, supplemented by extensive CCSD(T) calculations, are currently under investigation and will be reported subsequently.

Perspectives. The development of polarizable molecular potentials is the object of intense efforts, as attested since

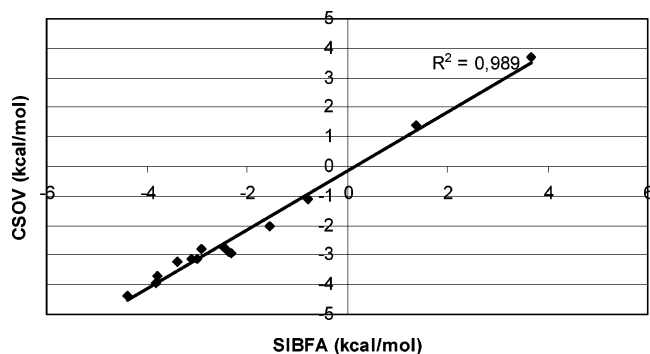


Figure 10. Correlation line between SIBFA and CSOV total interaction energies for fourteen water dimers.

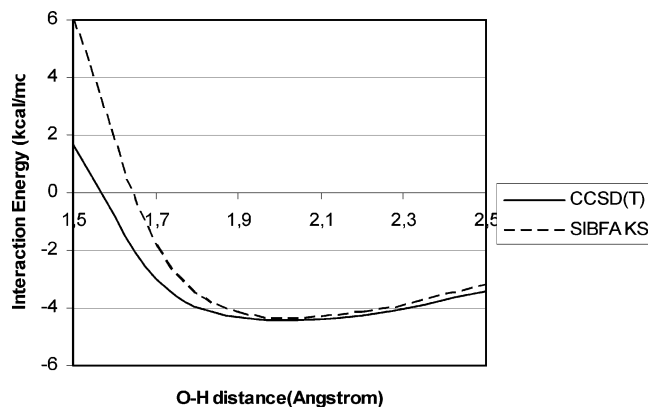


Figure 11. Linear water dimer. Evolution of the SIBFA-(B3LYP/aug-cc-pVTZ)+ E_{disp} interaction energies along with that of the CCSD(T)/aug-cc-pVTZ ones.

2001 by review papers published on a nearly yearly basis.^{2,62,63} We indicate here some ongoing developments and enrichments of the SIBFA potential.

From APMM toward APMD. The analytical gradients of most of the energy contributions have been coded and checked, while the coding of the remaining gradients is underway. This has enabled preliminary molecular dynamics (MD) simulations to be done in the framework of the SIBFA potential. Extension of this approach including Particle Mesh Ewald^{6,67–70} procedures to handle long-range interactions is underway. This should allow for a further advance, namely from APMM toward APMD.

Toward Third-Generation Molecular Mechanics Potentials. A GEM methodology (Gaussian Electrostatic Model)^{4,66} was recently developed and is able to provide total intermolecular interactions energies⁴ and to handle long-range electrostatic thanks to a generalized PME procedure.⁶⁶ In GEM, fitted Gaussian densities are derived from first-order density matrices and used to compute in the framework of quantum chemistry the intermolecular Coulomb and overlap integrals, the latter then enabling an accurate evaluation of the exchange-repulsion interactions. In a series of test cases including water dimers and oligomers, E_c and E_{exch} from CSOV analysis were reproduced by their GEM counterpart with relative errors <1% and a considerable time gain compared to ab initio. It was, furthermore, shown by Piquemal et al.⁴ that E_{pol} and E_{ct} could be computed *in the framework of the SIBFA procedure* upon resorting to the

GEM potentials and screened fields as an alternative to those derived from the distributed multipoles. Thus, a molecular mechanics procedure initially formulated and calibrated on the basis of QC can now resort concerning its electrostatic and overlap-depending terms to analytical integrals formulated in the context of ab initio QC. Such a methodology can be considered as a representative of future third-generation molecular mechanics potentials. The recent integration of QM and GEM by Cisneros et al.⁷⁰ constitutes an incentive for the next level of integration, that is, toward a QM/GEM/SIBFA procedure.

Conclusions

Along with the developments published in refs 17 and 26, we have elaborated on further refinements of the two first-order contributions, E_{MTP} and E_{rep} , of the SIBFA procedure. This enables term-to-term identifications of both first- and second-order contributions to their counterparts from RVS/KM/CSOV analyses of the HF/DFT intermolecular interaction energy. $\Delta E(\text{SIBFA})$ has been validated by comparisons with $\Delta E(\text{RVS})$ in several bi- and multimolecular H-bonded complexes, in arrangements significantly different from those used in the calibration. These tests were carried out on each of the four SIBFA contributions against their RVS counterparts. They bore on water clusters and water chains, formamide dimers, and complexes involving one or two ionic molecules. A striking result found in the water clusters related to the predominant weight of the second-order contributions E_{pol} and E_{ct} , particularly for the cubiclike arrangements and for the larger values of n . This was fully supported by the RVS analysis, and very close numerical agreements were found for both the total interaction energies and each of its four contributions. Close numerical agreements were also found in three dodecameric water chains which had been originally designed to probe the nonadditivity response of E_{pol} as a function of the H-bonding geometry. The anisotropic behavior of $\Delta E(\text{SIBFA})$ and of its contributions were also probed in two illustrative examples namely a formate–water complex and a stacked formamide dimer. In the latter the number of bond–bond, bond–lone pair, and lone pair–lone pair interactions is maximized, and all three terms need to be properly expressed and weighted. The correct reproduction of E_{exch} by E_{rep} throughout the angular rotations proved the correctness of the formulation of E_{rep} .

We showed that it was also possible to account for the effects of correlation on ΔE , by deriving the distributed multipoles and polarizabilities obtained at the DFT level. This approach was validated by several tests on 14 water dimers as well as on two water aggregates. A final extension consisted of the reintroduction of the ‘dispersion’ contribution. With correlated multipoles and polarizabilities, it was possible to only refit E_{disp} so that it reproduces the difference between CCSD(T) and DFT computations at equilibrium distance. This procedure is being presently generalized and adapted to the GEM^{4,66} procedure (Piquemal, et al., manuscript in preparation).

As underlined in refs 2, 4, and 26 the present results illustrate the necessity for APMM procedures to be separate, anisotropic, nonadditive, and transferable. Each of these

facets was addressed here. With these refinements, the SIBFA procedure was recently applied in studies of inhibitor binding to the Zn-metalloenzyme phosphomannoisomerase⁷¹ and to the C-terminal Zn-finger of the HIV-1 nucleocapsid (Miller-Jenkins et al., submitted for publication). Extensions are underway to drug binding to kinases.

Acknowledgment. The authors are grateful to Dr. Claude Giessner-Prettre for stimulating discussions. One of us (J.-P. Piquemal) would like to thank Thomas A. Darden (NIEHS) for a postdoctoral position where part of this work was initiated. We also wish to thank CINES (Montpellier, France), CRIHAN (Rouen, France), and CCRE (UPMC, France) for the generous allocation of computer time. We wish to thank Drs. Riccardo Chelli and Piero Procacci (University of Florence, Italy) for providing us with the coordinates of the longitudinal helical hydrogen-bonded chain dodecamer.

Supporting Information Available: RVS and SIBFA interaction energies (Tables 1–4) and density maps (Figure 1). This material is available free of charge via the Internet at <http://pubs.acs.org>.

References

- (1) Antony, J.; Piquemal, J.-P.; Gresh, N. *J. Comput. Chem.* **2005**, *26*, 1131.
- (2) Gresh, N. *Curr. Pharm. Des.* **2006**, *12*, 2121.
- (3) Millot, C.; Stone, A. *J. Mol. Phys.* **1992**, *77*, 439.
- (4) Piquemal, J.-P.; Cisneros, G. A.; Reinhardt, P.; Gresh, N.; Darden, T. A. *J. Chem. Phys.* **2006**, *124*, 104101.
- (5) Ren, P.; Ponder, J. W. *J. Phys. Chem. B* **2003**, *107*, 5933.
- (6) Piquemal, J.-P.; Perera, L.; Cisneros, G. A.; Ren, P.; Pedersen, L. G.; Darden, T. A. *J. Chem. Phys.* **2006**, *125*, 054511.
- (7) Gordon, M. S.; Freitag, M.; Bandyopadhyay, P.; Jensen, J. H.; Kairys, V.; Stevens, W. J. *J. Phys. Chem. A* **2001**, *105*, 293.
- (8) Hagberg, D.; Karlstrom, G.; Roos, B. O.; Gagliardi, L. *J. Am. Chem. Soc.* **2005**, *127*, 14250.
- (9) Stone, A. J. *J. Chem. Theory Comput.* **2005**, *1*, 1128.
- (10) Vigne-Maeder, F.; Claverie, P. *J. Chem. Phys.* **1988**, *88*, 4934.
- (11) Stevens, W. J.; Fink, W. H. *Chem. Phys. Lett.* **1987**, *139*, 15.
- (12) Jeziorski, S. B.; Moszynski, R.; Szalewicz, K. *Chem. Rev.* **1994**, *94*, 1887.
- (13) Piquemal, J.-P.; Marquez, A.; Parisel, O.; Giessner-Prettre, C. *J. Comput. Chem.* **2005**, *26*, 1052.
- (14) Cisneros, G. A.; Piquemal, J.-P.; Darden, T. A. *J. Chem. Phys.* **2005**, *123*, 044109.
- (15) te Velde, G.; Bickelhaupt, F. M.; Baerends, E. J.; Fonseca Guerra, C.; van Gisbergen, S. J. A.; Snijders, J. G.; Ziegler, T. *J. Comput. Chem.* **2001**, *22*, 931.
- (16) Freitag, M. A.; Gordon, M. S.; Jensen, J. H.; Stevens, W. J. *J. Chem. Phys.* **2003**, *112*, 7300.
- (17) Piquemal, J.-P.; Gresh, N.; Giessner-Prettre, C. *J. Phys. Chem. A* **2003**, *107*, 10353.
- (18) Bagus, P. S.; Illas, F. *J. Chem. Phys.* **1992**, *96*, 8962.
- (19) Claverie, P. In *Intermolecular interactions: from diatomics to biopolymers*; Pullman, B., Ed.; Wiley: 1978; pp 69–305.
- (20) Hermida-Ramon, J.; Brdarski, S.; Karlstrom, G.; Berg, U. *J. Comput. Chem.* **2003**, *24*, 161.
- (21) Gresh, N.; Leboeuf, M.; Salahub, D. R. In *Modeling the Hydrogen Bond*; ACS Symposium Series, 1994; Vol. 569, pp 82–112.
- (22) Gresh, N. *J. Comput. Chem.* **1995**, *16*, 856.
- (23) Murrell, J. N.; Teixeira-Dias, J. J. N. *Mol. Phys.* **1970**, *19*, 521.
- (24) Gresh, N.; Claverie, P.; Pullman, A. *Int. J. Quantum Chem.* **1986**, *29*, 101.
- (25) Piquemal, J.-P. Ph.D. Thesis, Université Pierre et Marie Curie, Paris, France, 2004.
- (26) Gresh, N.; Piquemal, J.-P.; Krauss, M. *J. Comput. Chem.* **2005**, *26*, 1052.
- (27) Giese, T. J.; York, D. M. *J. Chem. Phys.* **2005**, *123*, 164108.
- (28) van Duijneveldt-van de Ridt, J. G. C. M.; Mooij, W. T. M.; van Duijneveldt, F. B. *Phys. Chem. Chem. Phys.* **2003**, *5*, 1169.
- (29) Gresh, N.; Tiraboschi, G.; Salahub, D. R. *Biopolymers* **1998**, *45*, 405.
- (30) Gresh, N.; Kafafi, S. A.; Truchon, J. F.; Salahub, D. R. *J. Comput. Chem.* **2004**, *25*, 823.
- (31) Guo, H.; Gresh, N.; Roques, B. P.; Salahub, D. R. *J. Phys. Chem. B* **2000**, *104*, 9746.
- (32) Gresh, N.; Guo, H.; Salahub, D. R.; Roques, B. P.; Kafafi, S. A. *J. Am. Chem. Soc.* **1999**, *121*, 7885.
- (33) Gordon, M. S.; Schmidt, M. W. Advances in electronic structure theory: GAMESS a decade later. In *Theory and Applications of Computational Chemistry, the first forty years*; Dykstra, C. E., Frenking, G., Kim, K. S., Scuseria, G. E., Eds.; Elsevier: Amsterdam, 2005.
- (34) Stevens, W. J.; Basch, H.; Krauss, M. *J. Chem. Phys.* **1984**, *81*, 6026.
- (35) Godbout, N.; Salahub, D. R.; Andzelm, J.; Wimmer, E. *Can. J. Chem.* **1992**, *70*, 560.
- (36) Piquemal, J.-P.; Williams-Hubbard, B.; Fey, N.; Deeth, R. J.; Gresh, N.; Giessner-Prettre, C. *J. Comput. Chem.* **2003**, *24*, 1963.
- (37) Becke, A. D. *Phys. Rev. A* **1988**, *38*, 3098.
- (38) Lee, C.; Yang, W.; Parr, R. G. *Phys. Rev. B* **1988**, *37*, 785.
- (39) Dunning, T. H., Jr. *J. Chem. Phys.*, **1989**, *90*, 1007.
- (40) Garmer, D. R.; Stevens, W. J. *J. Chem. Phys.* **1989**, *93*, 8263.
- (41) JAGUAR, Version 6.0; Schrödinger, LLC: New York, 2005.
- (42) Claverie, P. Ph.D. Thesis, Université Pierre et Marie Curie, Paris, France, 1973.
- (43) Gresh, N. *J. Phys. Chem. A* **1997**, *101*, 8680.
- (44) Kitaura, K.; Morokuma, K. *Int. J. Quantum Chem.* **1976**, *10*, 325.
- (45) Masella, M.; Gresh, N.; Flament, J.-P. *J. Chem. Soc. Faraday Trans.* **1998**, *94*, 2745.

- (46) Tiraboschi, G.; Gresh, N.; Giessner-Prettre, C.; Pedersen, L. G.; Deerfield, D. W. *J. Comput. Chem.* **2000**, *21*, 1011.
- (47) Chelli, R.; Schettino, V.; Procacci, P. *J. Chem. Phys.* **2005**, *122*, 234107.
- (48) Chelli, R.; Procacci, P. *J. Chem. Phys.* **2002**, *117*, 9175.
- (49) Dreyfus, M.; Pullman, A. *Theor. Chim. Acta* **1970**, *19*, 20.
- (50) Burley, S. K.; Petsko, G. A. *Science* **1985**, *229*, 23.
- (51) Fyfe, M. C. T.; Stoddart, J. F. *Acc. Chem. Rev.* **1997**, *10*, 3393.
- (52) Claessens, C. G.; Stoddart, J. F. *J. Phys. Org. Chem.* **1997**, *10*, 254.
- (53) Hobza, P.; Sponer, J. *J. Mol. Struct. (THEOCHEM)* **1996**, *388*, 115.
- (54) Sponer, J.; Hobza, P. *Chem. Phys. Lett.* **1997**, *267*, 263.
- (55) Jurecka, P.; Sponer, J.; Hobza, P. *J. Phys. Chem. B* **2004**, *108*, 5466.
- (56) Gillespie, R. J.; Popelier, L. A. In *Chemical bonding and molecular geometry*; Oxford University Press: New York, 2001.
- (57) Guo, H.; Salahub, D. R. *Angew. Chem.* **1998**, *37*, 2985.
- (58) Jurecka, P.; Sponer, J.; Cerny, J.; Hobza, P. *Phys. Chem. Chem. Phys.* **2006**, *8*, 1985.
- (59) Zierkiewicz, W.; Michalska, D.; Cerny, J.; Hobza, P. *Mol. Phys.* **2006**, *104*, 2317.
- (60) Tschumper, G. S.; Leininger, M. L.; Hoffman, B. C.; Valeev, E. F.; Quack, M.; Schaefer, H. F., III. *J. Chem. Phys.* **2002**, *116*, 690.
- (61) Foster, J. M.; Boys, S. F. *Rev. Mod. Phys.* **1960**, *32*, 300.
- (62) Halgren, T. A.; Damm, W. *Curr. Opin. Struct. Biol.* **2001**, *11*, 236.
- (63) Rick, S. W.; Stuart, S. J. *Rev. Comput. Chem.* **2002**, *18*, 89.
- (64) Ponder, J. W.; Case, D. A. *Adv. Protein Chem.* **2003**, *66*, 27.
- (65) McKerell, J. *J. Comput. Chem.* **2004**, *25*, 1584.
- (66) Cisneros, G. A.; Piquemal, J.-P.; Darden, T. A. *J. Chem. Phys.* **2006**, *125*, 184101.
- (67) Darden, T. A.; York, D. M.; Pedersen, L. G. *J. Chem. Phys.* **1993**, *98*, 10089.
- (68) Essmann, U.; Perera, L.; Bertkowitz, M. L.; Darden, T. A.; Lee, H.; Pedersen, L. G. *J. Chem. Phys.* **1995**, *103*, 8577.
- (69) Sagui, C.; Pedersen, L. G.; Darden, T. A. *J. Chem. Phys.* **2004**, *120*, 1630791.
- (70) Cisneros, G. A.; Piquemal, J.-P.; Darden, T. A. *J. Phys. Chem. B* **2006**, *110*, 13682.
- (71) Roux, C.; Gresh, N.; Perera, L.; Piquemal, J.-P.; Salmon, L. *J. Comput. Chem.* **2007**, *28*, 938.

CT7000182

JCTC

Journal of Chemical Theory and Computation

New Investigations of Geometric, Electronic, and Spectroscopic Properties of Tetrapyrrolic Macrocycles by a TD–DFT Approach. Carbon, Nitrogen, and Chalcogen (O, S, Se) Peripheral Substitution Effects on Ni(II) Porphyrinato Complexes[†]

Ivan Infante[‡] and Francesco Lej^{*,§}

Faculty of Sciences, Section of Theoretical Chemistry, Vrije Universiteit Amsterdam, De Boelelaan 1083, 1081 HV, Amsterdam, The Netherlands, and LaMI, Dipartimento di Chimica and LaSCAMM, INSTM Sezione Basilicata, Università della Basilicata, Via N. Sauro 85, 85100 Potenza, Italy

Received December 13, 2006

Abstract: The electronic structure of five complexes [M(oXHpz)] [M = Ni²⁺; oXHpz²⁻ = 2,3,7,8-, 12,13,17,18-octakis-substituted (X = CH₂, NH, O, S, Se)-5,10,15,20-tetraazaporphyrinate dianion] has been investigated using a density functional approach. All the geometries have been obtained minimizing the total intramolecular energy using a nonlocal hybrid functional (B3LYP) at the 6-31g* level. The electronic configuration of Ni²⁺ is (d_{x²-y²})⁰(d_{xy})²(d_{xz},d_{yz})⁴(d_{z²})². Optimized geometries exhibit a planar conformation and are all above the threshold for ruffling, which is described by a Ni–N_p bond distance of 1.85–1.87 Å for sterically unhindered porphyrazines. Indeed, the smallest bond distance is 1.880 Å for Ni(oOHPz). Peripheral substituents yield modifications to the “core” of the macrocycle and to the energy levels, changing σ and π interactions. Furthermore, within a time-dependent density functional theory approach, excited states of Ni(oXHpz) [X = CH₂, NH, O, S, Se,] complexes have been studied and compared with available experimental UV–vis spectra.

Introduction

In the past few years, a new challenge for theoretical chemistry has been the possibility to study big systems using massive computational resources. Such large complexes can be now analyzed with full quantum mechanical approaches, like density functional theory, without big loss of accuracy and wasting of time. Furthermore, the contemporary increasing in new techniques to synthesize porphyrazines¹ has provided a new chance to improve the knowledge of these compounds. Indeed, a high growing interest in studying these compounds has been developed be-

cause of their high flexibility; rich coordination chemistry; and excellent chemical, thermal, and photochemical stability.^{2–21} These new molecules are characterized by a highly delocalized electronic structure in which the four pyrrole moieties are linked to each other by four aza bridges.

Recently, a new branch of compounds has been developed, in which tie-ether groups are covalently attached at the β positions of the pyrrole moieties.^{22–25} These alkyl(sulfanyl)-porphyrazines have interesting spectroscopic and chemical behavior. In particular, transition metal tie-ether porphyrazines present new in- and out-of-plane peripheral coordination chemistry and have the capability to form liquid crystals and Langmuir–Blodgett films.^{26–32} In addition to this, the synthesis of both asymmetric “free-base” and metal ion porphyrazine has become of great interest owing to the formation of a push–pull tetrapyrrolic system lacking a

[†] Dedicated to Professor Dennis R. Salahub on the occasion of his 60th birthday.

* Corresponding author e-mail: lej@unibas.it.

[‡] Vrije Universiteit Amsterdam.

[§] Università della Basilicata.

symmetry center, which allows these complexes to produce the best performing nonlinear optical materials.^{33–35}

One of the main characteristics of porphyrazines, central-coordinated by a nickel ion, is the possibility to easily interchange the peripheral zone of the molecule with different substituents. For example, the syntheses of Ni(oEtpz), Ni(oNH₂pz), and Ni(oSCH₃pz) have been recently performed, and the closeness on the periodic table of the atoms directly connected to the pyrrole moieties has induced us to explore in more detail the spectroscopic trend along the same row (C, N, O) and the same group (O, S, Se).

The acronym we used to describe the M(oXHpz) porphyrinato complexes follows these rules: M stands for the metal center in its 2+ oxidation state (Ni²⁺ in this case); o stands for 2,3,7,8,12,13,17,18-octakis-substituted; XH indicates the type of substituents linked to the peripheral pyrroles (X = CH₂, NH, O, S, Se); pz indicates the 5,10,15,20-tetraazaporphyrinate moiety. The whole oXHpz²⁻ is described in its dianionic form.

In this paper, we have studied the electronic structure of Ni(oXHpz) (X = CH₂, NH, O, S, Se) complexes providing deep investigation of the ground and excited states.

In section 2, we have given insights on the methodological approach to compute the properties of the compounds of interest. We elucidated all molecular and electronic properties on the basis of density functional theory.

In section 3, we have analyzed the characteristics of the geometrical structures using peripherally unhindered porphyrazines, in which the terminal atom is simply linked to a hydrogen atom.

In section 4, we have performed an analysis of the soft vibrational modes. We have based our approach on past papers,^{36–39} in which it has been shown that possible deformations out of the plane of porphyrin-like molecules can be determined by the peripheral substituents or by the dimension of the “core size”. These effects are very interesting because they might provide the modification of redox potential and UV–vis spectra.^{40,41} Therefore, we have investigated, analyzing the low vibrational modes, the same characteristics on a peripherally unhindered porphyrinato complex.

Furthermore, as it can be seen in section 5, the effect of introducing different atoms linked to the four pyrrole moieties is also interesting in the modification of the electronic structure and of the bonding properties. Therefore, we performed calculation using the Ziegler–Rauk fragment decomposition scheme^{42,43} to determine the characteristics of the interaction between nickel ions and the porphyrinato framework. In this scheme, we separate the ionic contribution^{44–46} (electrostatic plus Pauli term) and the orbital interactions contribution (σ and π interactions), which is decomposed according to the irreducible representation of the molecular point group.

In section 6, we have coped with the spectroscopic behavior of these porphyrinato complexes. The spectroscopic behavior of the Ni(oEtpz) complex has been recently investigated in two works. The first explores the nature of the UV–vis bands performing an assignment of the electronic transitions.⁴⁷ The spectrum has been shown to be

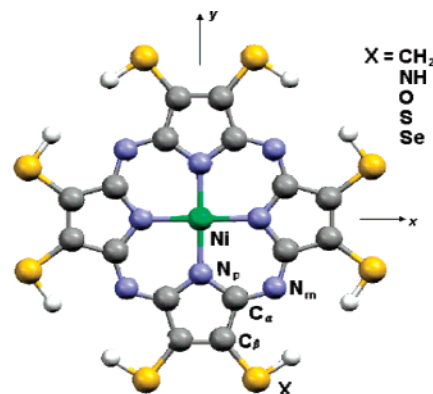


Figure 1. Atom labeling scheme for Ni(oXHpz) [X = CH₂, NH, O, S, Se].

composed by a Q band lying in the visible region and a Soret band, which is characterized by a main band (N) and two shoulders, in the near UV–vis region. It is possible to note a rather small presence in the literature of theoretical works which discuss the issue of the efficacy of different exchange–correlation (xc) functionals on the description of large molecules’ excited states such as porphyrazine-like complexes.⁴⁸ Furthermore, a deep analysis of the assignment of the transition using different xc functionals (pure and hybrid) has been taken out,⁴⁹ in order to figure out how the choice of the functional can produce modification in the nature of the transitions and consequently a different assignment of the electronic excitations.

In order to determine from a theoretical point of view the excited states and the oscillator strengths of Ni(oXHpz) [X = CH₂, NH, O, S, Se] complexes, we carried out calculations using time-dependent density functional theory (TD–DFT) (vide infra). This recent method scales with a N^3 factor; therefore, it provides good results with a low computational effort compared to the correlated post-Hartree–Fock procedures. As a first approach (section 6.1), we investigated the effect on the excited states and oscillator strengths induced by the distortion from the planarity of the nickel porphyrinato complexes. Indeed, the more computationally intensive and the more distorted Ni(oSCH₃pz) complex should be taken in consideration because of its larger resemblance with the experimental Ni(oSEtpz) (Et = ethyl) data. In order to avoid too time-consuming calculations, we have underlined the differences with the unhindered Ni(oSHpz) compound, taking the unhindered complex as a reference throughout the paper. In the successive sections (6.2 and 6.3), we analyzed the effect of the peripheral substitution on the transitions and the assignment of these highly delocalized complexes. Section 7 concludes the paper.

2. Computational Details

The electronic structure of Ni(oXHpz) (X = CH₂, NH, O, S, Se) complexes, sketched in Figure 1 together with the reference frame orientation, has been investigated using the Kohn–Sham density functional approach.⁵⁰ Geometrical parameters (bond angles and bond distances), low-frequency modes, bonding energies, and excited states have been computed performing a full optimization with strict convergence criteria [4.5×10^{-4} for the maximum force and 3.0

Table 1. Geometrical Parameters for Ni(oXHpz) [X = CH₂, NH, O, S, Se] Complexes Calculated at B3LYP/6-31g* Level

bond distance (Å)	X = CH ₃	X = NH	X = O	X = S	X = Se
Ni–N _p	1.888	1.880	1.873	1.888	1.890
N _p –C _α	1.375	1.377	1.374	1.375	1.377
C _α –C _β	1.455	1.450	1.450	1.455	1.452
C _β –C _β	1.368	1.370	1.366	1.368	1.364
C _α –N _m	1.319	1.324	1.324	1.319	1.319
C _β –X	1.495	1.393	1.348	1.753	1.878
bond angle (deg)	X = CH ₃	X = NH	X = O	X = S	X = Se
C _α –N _m –C _α	121.4	120.4	119.9	121.4	121.3
C _α –N _p –C _α	105.5	105.1	104.9	105.5	105.6
C _β –C _α –N _p	110.9	111.1	111.3	110.9	110.6
C _β –C _β –C _α	106.4	106.3	106.2	106.4	106.6
C _α –C _β –X	125.7	124.4	124.1	125.7	127.0
C _β –C _β –X	127.9	129.2	129.6	127.9	126.4

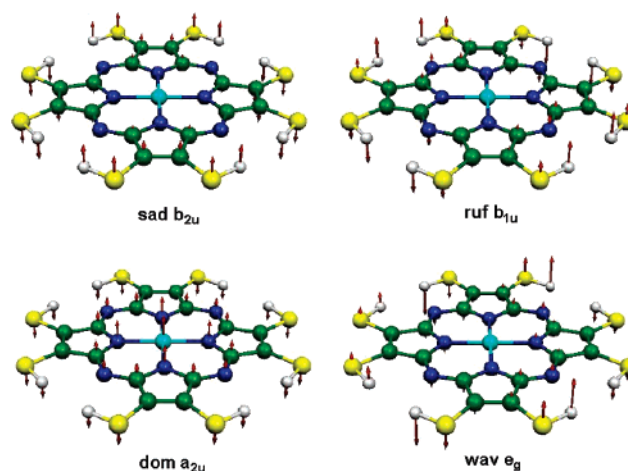
× 10^{−4} for the root-mean square (RMS) of the force] and using as the xc potential the Becke's three-parameter nonlocal hybrid functional (B3LYP)⁵¹ at the 6-31g* basis-set level by the Gaussian 98 package.⁵²

All extrema, detected evaluating the matrix of second-derivative energy, have been successively analyzed with the ADF2000 program^{53–55} to elucidate the bonding interactions between the metal (Ni²⁺) and the macrocyclic fragment (oXHpz^{2−}) using a Ziegler and Rauk approach.^{42,43} In this case, due to technical problems, the xc functional chosen is the GGA Becke–Perdew (BP86).⁵⁶ The basis set on metal is an uncontracted triple- ζ Slater-type orbital type augmented by a single- ζ polarization function. A double- ζ plus a single- ζ polarization function has been used for C, N, H, O, S, and Se. The cores of all atoms have been kept frozen.¹⁸

TD–DFT^{57,58} based on the iterative Davidson procedure⁵⁹ has been used to determine the excitation energies and oscillator strengths. Transition to the E_u and A_{2u} states are dipole-allowed, and only the former has been analyzed because the oscillator strengths of the latter are too small and not important to the interpretation of the main characteristics of the available experimental spectra (vide infra). In order to evaluate the excitation energies, we have used the Gaussian 98 package using again a B3LYP/6-31g* approach.

3. Molecular Structure

Optimizations using B3LYP/6-31g* yield a good agreement between theory and experiment for the Co(oSHpz) complex;²² therefore, our studies on Ni(oXHpz) complexes are based on the same approach. Besides, no comparison with experimental geometry is possible lacking, until now, any experimental crystal structure for nickel complexes. Geometrical parameters are described in Table 1. Possible out-of-plane deformations of the macrocycle can be due to two factors: (1) a small ionic radii of the metal, which can contract the “core” (i.e., the M–N_p bond distance in this case) and yield a distortion of the planarity and (2) the presence of bulky peripheral substituents. In our study, we consider porphyrazines without peripheral hindrance; that is,

**Figure 2.** Drawing of the low vibrational out-of-plane modes of Ni(oXHpz) [X = CH₂, NH, O, S, Se] complexes. Arrows' lengths are proportional to the displacement of the eigenvectors.

only hydrogen atoms are linked to the chalcogen atoms (O, S, and Se; Figure 1). Vibrational analysis on optimized structures shows minima with *D*_{4h} symmetry for all Ni(oXHpz) [X = CH₂, O, S, Se] molecules, whereas the Ni(oNH₂pz) complex belongs to the *D*_{2d} point group owing to the rotation of the amine terminal groups to a most stable position. In the latter case, the *D*_{2d} symmetry is not given by the modification from the planarity but only from the position of the hydrogen atoms in the NH₂ molecule; therefore, the “core” stays planar and the periphery as well. As observed previously, the nonplanar distortions of metalloporphyrins can be classified according to irreducible representations of the *D*_{4h} point group [*D*_{2d} for the Ni(oNH₂pz) molecule] of a square-planar porphyrin macrocycle. Extending the same approach to porphyrazines, which have the same porphyrin-like skeleton but with four aza bridges between two adjacent pyrroles, we can classify the lowest-frequency modes in four possible ways: ruf (b_{1u}), sad (b_{2u}), dom (a_{2u}), and wav (e_g) (Figure 2)—as regards the *D*_{2d} symmetry, we have ruf (a₁), sad (a₂), dom (b₂), and wav (e). In Table 2, the lowest-frequency vibrations are described using a B3LYP/6-31g* approach. No imaginary frequencies are present in the case of planar structures; therefore, all complexes are above the threshold of the ruffling mode, which is described by a Ni–N_p bond distance of 1.85–1.87 Å for sterically unhindered porphyrazines.⁴⁰ Indeed, peripheral substitutions with different atoms modify the “core” dimension inducing the shortest Ni–N_p bond distance (1.873 Å) for the Ni(oOHPz) complex and the longest one (1.890 Å) for the Ni(oSeHpz) complex.

The different contraction of the “core” induces modifications on the geometrical parameters of the four pyrroles of the macrocycle. In particular, the smallest “core” size for the Ni(oOHPz) complex determines a lowering of the C_α–N_m–C_α bond angle (119.9°) and a stretching of the C_α–N_m bond distance (1.324 Å) with respect to the other three molecules [121.3–121.4° (C_α–N_m–C_α bond angle) and 1.319 Å (C_α–N_m bond distance)], which have about the same “core” size.

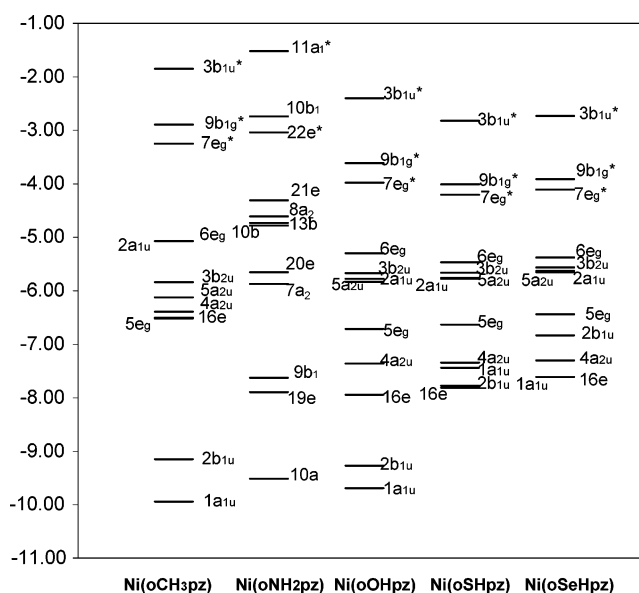
Table 2. Low Vibrational Modes (cm^{-1}), Force Constants ($\text{mdyn}/\text{\AA}$), and Reduced Masses (amu) of Ni(oXHpz) [X = CH₂, O, S, Se] (D_{4h}) and Ni(oNH₂pz) (D_{2d}) Complexes Determined at the B3LYP/6-31g* Level

modes	irreducible representation		Ni(oCH ₃ pz)	Ni(oNH ₂ pz)	Ni(oOHpz)	Ni(oSHpz)	Ni(oSeHpz)
saddling	b _{2u}	ν	27	29 (a ₂)	32	15	10
		k	0.0019	0.0030	0.0061	0.0021	0.0020
		μ	4.2614	5.9069	10.1932	16.4733	46.7589
ruffling	b _{1u}	ν	32	46 (a ₁)	48	26	21
		k	0.0024	0.0070	0.0101	0.0043	0.0101
		μ	4.0267	5.6105	7.4574	10.4722	61.3682
doming	a _{2u}	ν	58	59 (b ₂)	55	47	42
		k	0.0092	0.0144	0.0237	0.0273	0.0082
		μ	4.6309	7.0858	13.1603	21.0660	7.8892
waving	e _g	ν	62	83 (e)	84	49	33
		k	0.0024	0.0206	0.0344	0.0150	0.0197
		μ	1.0410	5.0920	8.1184	10.6974	31.3409

4. Analysis of the Low-Frequency Modes

Peripheral unhindered porphyrazines show modes with very low frequencies; thus, we can imagine that the presence of terminal bulky substituents might induce several different modifications from planarity owing to the steric effects between adjacent peripheral tails. The decreasing trend of the frequencies of sad, ruf, dom, and wav modes along the series (O > S > Se) and the increasing trend along the series (C < N < O) might be determined analyzing the force constants and the reduced masses related to these modes (Table 2). We remember that the vibrational frequencies (harmonic approximation) are represented in the following form: $\nu = 1.3 \times 10^{-3} \sqrt{k/\mu}$, where ν is expressed in cm^{-1} , k is in $\text{millidynes per angstrom}$, and μ is in atomic mass units. From Figure 2, we can note that the sad, ruf, and wav modes are mainly characterized by the vibration of the peripheral atoms. In this way, for the Ni(oOHpz) complex, we obtain the highest force constants (Table 2), probably due to the less polarizable behavior of the oxygen atoms with respect to the sulfur and selenium ones, and intermediate reduced masses, due to the lower atomic weight of the oxygen atoms. The combination of these two factors determines the highest values for the frequencies of the low-frequency modes for Ni(oOHpz). The vibrational gap between the Ni(oSHpz) and the Ni(oSeHpz) complexes are less pronounced, because, in particular for ruf and wav modes, the force constants are smaller in Ni(oSHpz), while the reduced masses are larger for Ni(oSeHpz). In these cases, the reduced masses have a larger impact than the force constants and the molecule with terminal selenium atoms shows the lowest vibrational frequencies. On the contrary, along the CH₃, NH₂, and OH series, the increasing trend can be attributed to the increase of the force constants, because of reduced masses of the same order for the C, N, and O atoms (between 4 and 13 amu).

Different behavior is computed for the doming mode, which is characterized by the out of plane displacement of the “core” atoms (Ni and Np). Also in this case, the Ni(oSeHpz) complex has the lowest frequency (42 cm^{-1}), but this effect is given by a very low force constant and not by the reduced mass (see Table 2 for further details).

**Figure 3.** Energy-level diagrams for Ni(oXHpz) [X = CH₂, NH, O, S, Se] complexes at the BP/TZ2P level. All virtual MOs are indicated by a (*) near the labels.

5. Electronic Structure: Ground State

In this paragraph, we used the BP/TZ2P approach to analyze energy levels (Figure 3).

In the previous paragraph, we have seen that the Ni(oNH₂pz) complex belongs to the D_{2d} point group. This modification of the molecular symmetry is due to the position of the terminal amine groups, which assume their most stable position providing a hydrogen bond between two adjacent NH₂ groups maintaining the σ_h plane. In spite of this lowering of symmetry from D_{4h} , we can observe that the complex is planar and the internal Nipz skeleton (i.e., without the hydrogen atoms linked to the terminal nitrogen atoms) is virtually D_{4h} . Thus, we can compare the molecular orbitals (MOs) obtained for the Ni(oXHpz) [X = CH₂, O, S, Se] complexes with the Ni(oNH₂pz) ones. In this way, we can have the following most important correspondence: 3b_{1u} (D_{4h}) → 14a₁ (D_{2d}); 9b_{1g} → 11b₁; 7e_g → 23e; 6e_g → 22e; 3b_{2u} → 9a₂; 5a_{2u} → 13b₂; 4a_{2u} → 12b₂; 2a_{1u} → 10b₁; 2b_{1u} → 12a₁; and so on.

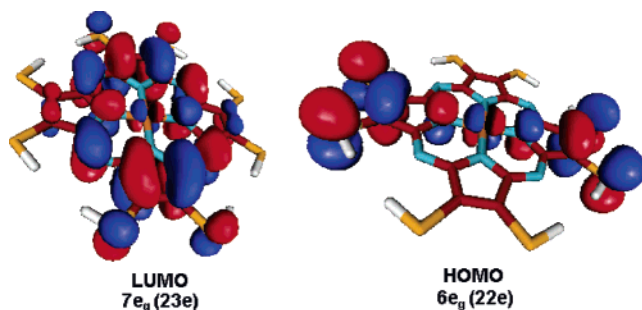


Figure 4. HOMO and LUMO MOs have similar shape for all Ni(oXHpz) complexes. Envelope surfaces at a Ψ value corresponding to $0.02 (1/\text{bohr}^3)^{1/2}$.

As illustrated in Figure 3, peripheral substitution with sulfur atoms yields the lowest highest occupied molecular orbital (HOMO) and lowest unoccupied molecular orbital (LUMO) energies. In all Ni(oXHpz) complexes, the HOMO ($6e_g$) and LUMO ($7e_g$) belong to the same irreducible representation and are characterized by an antibonding π interaction between the d_{xz} (or d_{yz}) atomic orbital and the p_z atomic orbital of nitrogen atoms (Figure 4; see also, Table 3).

The charge rearrangement described by the Mulliken gross population gives only a qualitative understanding of the transfer of electrons between the metal and the ring. In order to analyze from a quantitative point of view the bonding energy, we used the Ziegler and Rauk decomposition scheme described previously.^{42,43} The results are reported in Table 4. For a better description of the system, we chose the metal fragment in the +2 oxidation state (Ni^{2+}) with the following electronic configuration of the valence orbitals: $(d_{x^2-y^2})^0(d_{xy})^2-(d_{yz})^4(d_z)^2$; while the macrocycle fragment is chosen in the ionic (-2) state (oXHpz^{2-}).

5.1. Steric Interaction. The Pauli repulsion term, ΔE^{Pauli} , follows the trend of Ni–N_p bond distances of Ni(oXHpz) complexes, with the most destabilizing term for Ni(oOHpz) being +10.20 eV (Ni–N_p bond distance of 1.873 Å) and with the smallest contribution for Ni(oSeHpz) being +9.51 eV (Ni–N_p bond distance of 1.890 Å). This trend can be explained on the basis of the increase of Pauli repulsion between two closed-shell fragments along with the contraction of the core size.

Amine terminal groups give the most negative electrostatic contribution, ΔE^{elstat} , to nickel porphyrines [–28.59 eV, against –28.20 eV (X = CH₃), –27.74 (X = O), –25.73 eV (X = S), and –25.03 eV (X = Se)].

In general, the steric interaction ($\Delta E^{\text{Pauli}} + \Delta E^{\text{elstat}}$) is stabilizing due to the large attractive term, and it follows the trend Ni(oNH₂pz) > Ni(oCH₃pz) > Ni(oOHpz) > Ni(oSHpz) > Ni(oSeHpz).

5.2. Orbital Interaction. The orbital interaction term, ΔE^{oi} , can be decomposed in the irreducible representations belonging to the D_{4h} or D_{2d} point group.

As regards the D_{4h} complexes, the metal does not participate to the a_{2g} , a_{1u} , b_{1u} , and b_{2u} MOs; therefore, their contribution is based only on polarization effects due to the mixing between occupied and unoccupied orbitals of the macrocycle fragment. We aggregated these irreducible

representations in a single term denoted ΔE^{nb} , where the subscript nb stands for “nonbonding”. The effect is not large though not negligible: –1.54 eV (X = O), –1.56 eV (X = S), –1.57 eV (X = Se), and –1.62 eV (X = CH₂).

The $\Delta E^{\text{A}_{1g}}$ term is almost similar in all Ni(oXHpz) complexes, –2.34 eV (X = O, S), –2.35 eV (X = CH₂), and –2.38 eV (X = Se), reflecting an analogous σ donation from the ligand orbitals to the 4s atomic orbital (AO) of the metal.

The $\Delta E^{\text{B}_{1g}}$ term is the largest contribution to the orbital σ interaction with a transfer of about one electron to the empty $3d_{x^2-y^2}$ of the nickel atom. Terminal substitution with selenium atoms gives the most stabilizing term [–8.88 eV (X = Se), against –8.81 eV (X = CH₂), –8.60 eV (X = O), –8.63 eV (X = S)].

The $\Delta E^{\text{A}_{2u}}$ term gives a little contribution to the π orbital interaction, because the $4p_z$ AO does not have a good match with occupied ligand orbitals. The stabilization is between –0.95 eV (X = O, CH₂) and –1.04 eV (X = S, Se).

The ΔE^{E_u} term is characterized by a strong σ donation from the macrocycle to the $4p_\sigma$ AOs of the metal. In particular, the Ni(oSeHpz) and Ni(oSHpz) complexes show also a polarization effect on the ligand orbitals; therefore, their stabilizations, of –3.78 and –3.57 eV, respectively, are stronger than those of the Ni(oOHpz) and Ni(oCH₃pz) complexes where this polarization is absent.

The $\Delta E^{\text{B}_{2g}}$ term gives substantially a nonbonding contribution with a small back-donation from the $3d_{xy}$ AO to the lowest empty ring orbital. The effect is small and similar for all Ni(oXHpz) complexes (between 0.71 and 0.74 eV).

The ΔE^{E_g} term is by far the largest contribution to the π interaction. It is mainly characterized by a π back-donation of almost 0.2 electrons from the d_π AOs of the metal to the ligand virtual orbitals. Previous calculations on the Co(OSMepz) complex,⁶⁰ where the polarization prevails over a marginal π back-donation, show how the substitution of the metal center can affect the charge rearrangement between the metal and the tetrapyrrole moiety.

The total orbital contribution prevails over the ionic contribution in all four Ni(oXHpz) complexes. The molecule substituted peripherally with selenium atoms presents the most negative energy: –20.41 eV, followed by Ni(oCH₃pz) [–20.09 eV] \cong Ni(oNH₂pz) [–20.04 eV] > Ni(oSHpz) [–19.86 eV] > Ni(oOHpz) [–19.64 eV].

As concerns the Ni(oNH₂pz) complex (D_{2d}), the metal contribution is present in all irreducible representations with the exception of the a_2 one. However, this nonbonding contribution is small (1.28) even if not marginal.

Owing to the lowering of symmetry from D_{4h} to D_{2d} , in the ΔE^{A_1} (D_{2d}) term, we can aggregate a bonding $\Delta E^{\text{A}_{1g}}$ (D_{4h}) and a nonbonding $\Delta E^{\text{B}_{1u}}$ (D_{4h}) contribution. The Ni(oNH₂pz) molecule yields a value (2.43 eV), which is on the same order as those of the other complexes, which are in the range of 2.39–2.51 eV.

The ΔE^{B_1} term can be compared with the sum of $\Delta E^{\text{B}_{1g}} + \Delta E^{\text{A}_{1u}}$ ones. Also, in this case, the value (8.91 eV) is intermediate with respect to the contributions of the other complexes (in the range between 8.85 and 9.12 eV).

Table 3. Atomic Orbital Contributions (%) for Each Irreducible Representation of Ni(oXHpz) [X = CH₃, O, S, Se] (*D_{4h}*) and Ni(oNH₂pz) (*D_{2d}*) Complexes at BP/TZ2P Level

Γ	Ni	L	CH ₃	Ni	L	O	Ni	L	S	Ni	L	Se	Γ	Ni	L	NH ₂
Unoccupied Orbitals																
4b _{2u}	0	92	8	0	98	2	0	98	2	0	98	2	10a ₂	0	98	2
17e _u	0	4	96	0	8	92	0	8	92	0	8	92	24e	0	8	92
3b _{1u}	0	92	8	0	92	8	0	88	12	0	90	10	14a ₁	0	94	6
9b _{1g}	55	41	4	55	44	1	54	44	2	54	42	4	11b ₁	55	44	1
7e _g	4	93	3	4	90	6	4	85	11	4	86	10	23e	4	89	7
Occupied Orbitals																
6e _g	52	44	4	28	50	22	17	49	44	17	35	48	22e	24	61	15
3b _{2u}	0	88	12	0	66	34	0	41	59	0	35	65	9a ₂	0	81	19
5a _{2u}	0	86	14	1	60	39	1	35	64	1	29	70	13b ₂	1	55	44
2a _{1u}	0	95	5	0	86	14	0	69	31	0	62	38	10b ₁	0	92	8
11a _{1g}	97	3	0	97	3	0	97	3	0	97	3	0	13a ₁	97	3	0
5e _g	35	54	11	57	25	18	57	15	28	50	13	37	21e	58	47	5
2b _{1u}	0	80	20	0	30	70	0	18	82	0	16	84	10a ₁	2	31	67
4e _g	5	91	4	7	74	19	6	24	70	12	20	68	20e	5	54	41
4a _{2u}	0	99	1	2	98	0	2	98	0	2	98	0	12b ₂	1	98	1
1a _{1u}	0	12	88	0	23	77	0	41	59	0	46	54	9b ₁	2	16	82
16e _u	0	99	1	0	99	1	0	99	1	0	99	1	19e	0	99	1
2b _{2u}	0	66	34	0	63	37	0	66	34	0	69	31	8a ₂	0	64	36
3a _{2u}	0	30	70	0	50	50	1	67	32	0	72	28	11b ₂	0	32	68

Table 4. Bonding Decomposition Energy (eV) between Ni²⁺ (M) and oXpz²⁻ (L) Fragments for Ni(oXHpz) [X = CH₂, NH, O, S, Se] Complexes According to the Ziegler and Rauk Approach

	Ni(oOHPz)	Ni(oSHPz)	Ni(oSeHPz)	Ni(oCH ₃ pz)		Ni(oNH ₂ pz)
Pauli	+10.20	+9.61	+9.51	+9.89	Pauli	+9.96
Elstat	-28.50	-25.77	-25.54	-29.34	Elstat	-28.59
total s.i.	-17.54	-16.12	-15.52	-18.31	total s.i.	-18.63
A _{1g}	-2.30	-2.30	-2.38	-2.35	A ₁	-2.43
B _{1g}	-8.60	-8.63	-8.88	-8.81	A ₂	-1.28
B _{2g}	-0.75	-0.72	-0.73	-0.75	B ₁	-8.91
E _g	-2.13	-2.13	-2.13	-2.05	B ₂	-1.78
A _{2u}	-1.03	-0.95	-0.95	-1.04	E	-5.65
E _u	-3.29	-3.57	-3.78	-3.47	total o.i.	-20.04
nb	-1.54	-1.56	-1.57	-1.62	total o.i.+s.i.	-38.67
total o.i.	-19.64	-19.86	-20.41	-20.09		
total o.i.+s. i	-37.18	-35.98	-35.93	-38.39		

The ΔE^{B_2} term is related to the sum of $\Delta E^{B_{2g}} + \Delta E^{A_{2u}}$ ones. The Ni(oNH₂pz) complex provides an orbital interaction (1.78 eV), which is similar to those obtained with the other complexes (between 1.67 and 1.79 eV).

The ΔE^E terms can be compared with the sum between ΔE^{E_g} and ΔE^{E_u} terms of the *D_{4h}* complexes. The total ΔE^E contribution (5.65 eV) is on the same order as those of the other porphyrinato molecules (between 5.42 and 5.92 eV).

5.3. Total Bonding Energy. The total bonding energy ($\Delta E^{si} + \Delta E^{oi}$) indicates that the Ni(oNH₂pz) complex has the strongest Ni²⁺/oXpz²⁻ interaction, and it is due to the large stabilization energy given by the electrostatic term. In conclusion, the ΔE^{oi} terms are substantially similar for all Ni(oXHpz) complexes. Within the whole set of substituents, its change remains in the range of only 0.8 eV, with respect to the 2.8 eV of the ionic term. Therefore, the total bonding energy is controlled mainly by the steric term, which is the largest for the Ni(oNH₂pz) complex.

6. Electronic Structure: Excited States

The analysis of excitation energies has been performed using the recent TD-DFT approach. This method provides similar results with respect to the post-Hartree-Fock techniques but with a lower computational effort. In particular, Stratmann and co-workers⁶⁰ have shown a good agreement between the experimental data and the calculated ones obtained at the B3LYP/6-31g* level on the free-base porphyrin. Furthermore, we recently analyzed⁴⁹ the effect of different xc potentials (B3LYP, BP, BLYP, LB94, and SAOP) on the assignment of the experimental spectrum of the Ni(oEtpz) complex. In that case, the computed RMS, relative to the difference between the calculated and the experimental data, indicates a sufficiently good description provided by the B3LYP/6-31g* approach. The choice of the B3LYP xc functional is not based on a better performance compared to other functionals but on consistency with the rest of the paper. Indeed, despite the overall low RMS, B3LYP does not

describe well the Q region of the spectrum. As regards the choice of the basis set, in a previous paper, it was pinpointed that the excitation energies are substantially unchanged using a basis set as large as 6-311+g**.⁶¹ Therefore, in order to examine the excited states of the Ni(oXHpz) complexes, the B3LYP/6-31g**/B3LYP/6-31g* method has been chosen. All Ni(oXHpz) molecules present a D_{4h} symmetry, with the exception of Ni(oNH₂pz) (D_{2d}); therefore, the dipole-allowed transitions belong to the A_{2u} and E_u irreducible representations [B_2 , E for the Ni(oNH₂pz) complex]. The A_{2u} (B_2) excitations have negligible intensity: the oscillator strengths are on the average 10^3 times less intense than the E_u (E) ones, therefore we will discuss only the E_u (E) transitions. We have also compared our theoretical results with available experimental data.^{47,62}

6.1. The Planar Ni(oSHpz) and the Saddled Ni(oSHpz) and Ni(oSCH₃pz) Complexes. The first complex analyzed is the Ni(oSHpz) molecule. Indeed, the excited states of the Ni(oHpz) and Ni(oCH₃pz) complexes have been recently discussed,⁴⁹ and we used their assignment for determining those of the Ni(oXHpz) ones. The TD-DFT results on the Ni(oSHpz) complex are compared with the experimental spectrum collected for the nickel octa(ethyl)sulfanyl porphirazinato [Ni(oSEtpz)] complex in the CHCl₃ solvent (Figure 5).

In the visible region is present a main band, denoted as the Q band,⁶³ which lies at 1.84 eV (673 nm), and it is characterized also by a less intense shoulder (sh₁) at 2.01 eV (616 nm). The second band lies at 2.56 eV (484 nm), and it is denoted as an “extra band”. The last band is the Soret band, which lies in the UV region and can be split into several components: the most intense one, that which we denote as the N band, lies at 3.98 eV (311 nm). Furthermore, the spectrum shows significant broadening due to the presence of intermolecular interactions even at a low concentration (1.09×10^{-6} M). As it will be seen soon, the oscillator strengths calculated at the D_{4h} molecular symmetry are too low or too high in intensity with respect to the experimental spectrum. Indeed, the Ni(oSHpz) molecular structure, on which we performed our calculations, is planar, whereas the experimental Ni(oSEtpz) complex might be distorted. Hence, we carried out geometry optimizations on two of the most probable modifications from the planarity of the Ni(oSCH₃pz) complex (this complex differs from the unhindered one because we have added methyl groups on the terminal sulfur atoms, and it resembles closely the experimental complex)—the saddled (C_{2v}) and the ruffled (C_{2v}) conformations—and both are more stable than the planar one. The choice of these two isomers is based on the results of the section 4, in which we have pointed out that the two lowest-frequency modes are the sad and the ruf vibrational modes. The first one (sad) has been found more stable of 4.6 kcal/mol than the ruffled one. Therefore, we performed TD-DFT calculations on the saddled Ni(oSHpz) complex (in order to take account of the distortion effects on the excitation energies and oscillator strengths) and on the saddled Ni(oSCH₃pz) complex (in order to analyze the methyl substitution effect on the sulfur atoms) (Figure 6). Symmetry lowering from the planar D_{4h} to the distorted C_{2v}

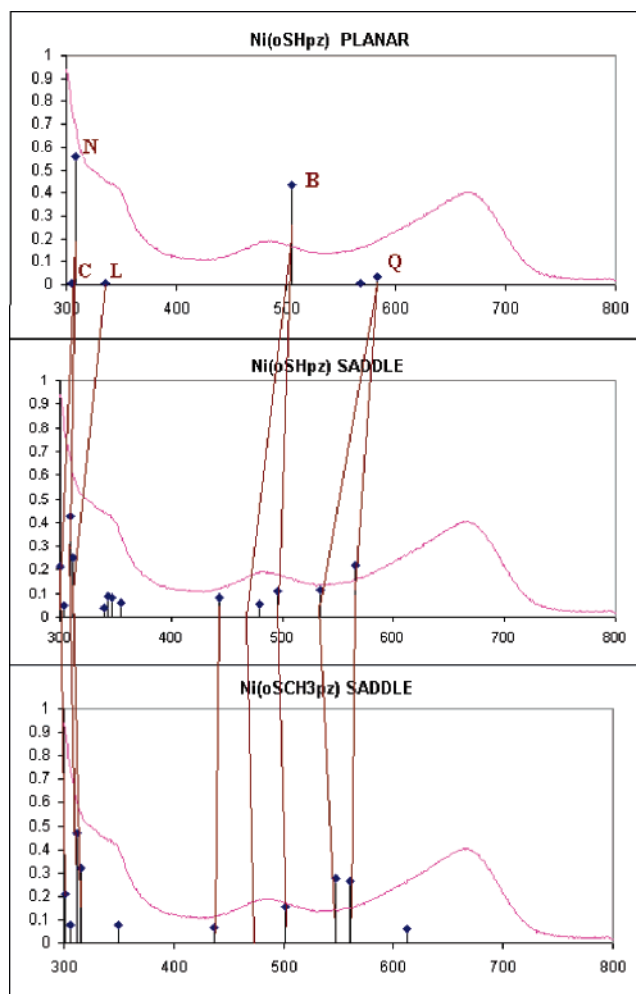


Figure 5. Vertical bold lines indicating the most important calculated singlet–singlet excited states with oscillator strengths higher than 2.5×10^{-2} . The experimental spectrum of the Ni(oSEtpz) complex recorded in a CH₃Cl solution is indicated by a continuum line (—). All the calculations have been performed at the B3LYP/6-31g* level for the Ni(oSHpz) (D_{4h} , C_{2v}) and Ni(oSCH₃pz) (C_{2v}).

increases the number of dipole-allowed transitions, though they show low intensities. In order to achieve a straightforward interpretation of the experimental spectrum, we have chosen the most important excited states. Indeed, we selected only those transitions which show an oscillator strength above a chosen threshold (2.5×10^{-2}). We remember that within the C_{2v} symmetry the dipole-allowed transitions belong to the A_1 , B_1 , and B_2 irreducible representations. The A_1 excitations have negligible intensity; therefore, we studied only the B_1 and B_2 transitions. See Figure 5 and Table 5 for further details.

Q Band. The calculated Q band of the planar Ni(oSHpz) complex is characterized mainly by three ligand-to-ligand charge transfer (LLCT) transitions: $2a_{1u} \rightarrow 7e_g$ (0.2084), $5a_{2u} \rightarrow 7e_g$ (0.2037), and $3b_{2u} \rightarrow 7e_g$ (0.0562). The numbers between parentheses are the squared coefficients of the single Slater determinants. These excitations have opposite transition dipole moments, and they tend to cancel out each other. The weights of these two contributions are almost the same; therefore, the total oscillator strength is small ($f = 0.0318$).

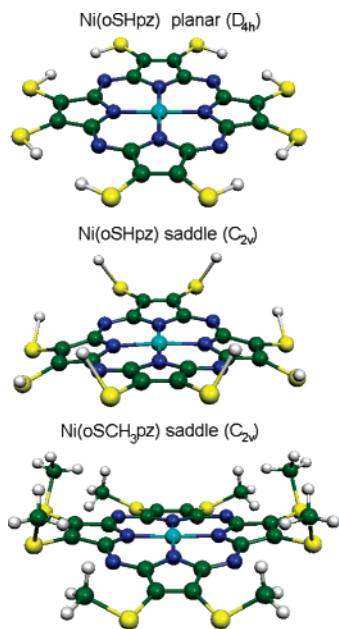


Figure 6. Conformations of Ni(oSXpz) [$X = \text{H}, \text{CH}_3$] complexes on which we performed TD-DFT calculations at the B3LYP/6-31g* level.

The 1E_u excited states is downward-shifted toward lower energies with respect to the Ni(oCH₃pz) complex: from 2.48 eV (500 nm) to 2.13 eV (582 nm) at the B3LYP level (Figure 7). This effect is due to the decrease of both $5a_{2u}/7e_g$ and $3b_{2u}/7e_g$ gaps determined by the substitution of the peripheral CH₃ groups [Ni(oCH₃pz)] of the complex with the sulfur atoms [Ni(oSHpz)], as can be seen in Figure 3 [this figure represents the MO's energy levels calculated at the BP/TZ2P level: even if the absolute energy values are different, the trends between the Ni(oXHpz) complexes are similar to those obtained with the B3LYP/6-31g* approach]. In spite of a strong energy overestimation of the Q band for both the complexes, the difference between the excitation energies of the two peaks (82 nm) is in excellent agreement with the experimental one (83 nm).

The intensities of the computed Q bands are rather low with respect to the experiment (1.84 eV, 672 nm). Anyway, we can observe that in the case of the Ni(oSHpz) molecular distortion from the planar conformation to the saddled one an increase is provided of the oscillator strengths of these two bands, which lie closer to the experimental one. We remember that the structural deformation lowers the symmetry from D_{4h} to C_{2v} ; therefore, the 1E_u excited state (Q band) is split in two into the 1B_1 and 1B_2 excitations. Indeed, also the composition of the Q band is slightly changed due to the geometry modification, and the 1B_1 and 1B_2 excitations are mainly formed by the $18a_2 \rightarrow 23b_2$ ($27a_1 \rightarrow 23b_1$) and $18a_2 \rightarrow 23b_1$ ($27a_1 \rightarrow 23b_2$) transitions, respectively, which correspond to the $3b_{2u} \rightarrow 7e_g$ and $2a_{1u} \rightarrow 7e_g$ ones in the planar D_{4h} . In the 1B_1 excitation, the weight of the $26a_1 \rightarrow 23b_1$ transition (which corresponds to the $5a_{2u} \rightarrow 7e_g$) is substantially smaller than the $18a_2 \rightarrow 23b_2$ ($f = 0.2867$); therefore, in spite of the opposite transition dipole moments, the oscillator strengths remains quite large ($f = 0.2186$). An analogous behavior is valid also for the 1B_2 excited state ($f = 0.1131$), which is characterized mainly

by the $27a_1 \rightarrow 23b_2$ ($f = 0.4032$) transition. As concerns the excitation energies, the Q band is determined by a slight blue shift: from 586 nm (1E_u) to 566 nm (1B_1) and 535 nm (1B_2).

The further addition of methyl groups on the terminal sulfur atoms provides similar excitation energies (561 and 548 nm, respectively) for the 1B_1 and 1B_2 excited states and intense oscillator strengths ($f = 0.2627$ and 0.2749) in good agreement with the experimental Q band.

B Band. The extra band (2.45 eV; 506 nm) is composed mainly of the $5a_{2u} \rightarrow 7e_g$ (0.2371), $2a_{1u} \rightarrow 7e_g$ (0.1421), and $4a_{2u} \rightarrow 7e_g$ (0.0371) LLCT transitions. Previously,⁶⁴ this extra band was denoted as the W band because it was interpreted as a new band stemming from the substitution of the peripheral CH₃ groups with the sulfur atoms. From our point of view, on the basis of the composition of this excited state, we suggest that this band correspond to the B band of the [Ni(oCH₃pz)] complex, which is shifted to lower energies owing to the decrease of the $4a_{2u}/7e_g$ and $5a_{2u}/7e_g$ gaps. In this way, the Soret band of the Ni(oCH₃pz) molecule, composed by the three B, N, and L bands, which are enveloped in one wide band, is now decomposed and separated in different bands.

Moreover, the intensity of the computed B band seems to be too large for the experiment. In order to understand this last behavior, we analyzed the saddled Ni(oSHpz) complex, which provides an excitation energy of the B band similar to that obtained with the planar one. Indeed, the 2E_u (D_{4h} , planar) excited state (506 nm) is split into the more intense 2B_1 excitation (496 nm, $f = 0.1091$) and the less intense 2B_2 one (478 nm, $f = 0.0137$). The reduction of the oscillator strengths from $f = 0.4329$ (D_{4h}) is mainly due to the different contribution of the single Slater determinants involved in the transition. For instance, the composition of the 2B_1 excited state corresponds to the planar 2E_u one, but it is also mixed with a strong contribution from $25a_1 \rightarrow 23b_1$ (0.1098), which is present only in the saddled geometry. This transition quenches the oscillator strengths, which passes from 0.4329 (D_{4h}) to 0.1091 (C_{2v}). Furthermore, the 2B_1 excited state is characterized by the $25a_1 \rightarrow 23b_2$ (0.4191) transition and by marginal contributions from other transitions. In this way, this excitation has a small intensity. The distorted structure yields other allowed transition in the region between 430 and 500 nm, which can give important contributions to the experimental B band. In particular, two of them lie at 479 nm ($f = 0.0562$) and 443 nm ($f = 0.0810$).

The addition of the methyl groups in the Ni(oSCH₃pz) complex does not influence both the excitation energy (2B_1 502 nm and 2B_2 468 nm) and the oscillator strength (2B_1 0.1537 and 2B_2 0.0244) of the B band with respect to the saddled Ni(oSHpz) molecule. Furthermore, the two satellite peaks in the 430–500 nm region have negligible intensity and should be not crucial to the interpretation of the Ni(oSCH₃pz) spectrum.

N Band. The N band is the most intense of the entire spectrum. This characteristic is confirmed also by the strong oscillator strength ($f = 0.5578$). Besides, this 3E_u excited state lies at the same energy (309 nm) with respect to that obtained in the Ni(oCH₃pz) complex (310 nm). This excited

Table 5. Computed Vertical Excitation Energies (eV) and Oscillator Strengths of Different Ni(oSXpz) [X=H, CH₃] Complexes at B3LYP/6-31g* Level

		composition	exp.	excitation energies eV (nm)	oscillator strength
SH	1 ¹ E _u	0.2037(5a _{2u} →7e _g); 0.0562(3b _{2u} →7e _g); 0.2084(2a _{1u} →7e _g)		2.13	0.0318
planar	(Q)			(582)	
SH	1 ¹ B ₁	0.0580(27a ₁ →23b ₁); 0.2867(18a ₂ →23b ₂); 0.0209(24a ₁ →23b ₁)		2.19	0.2186
saddle				(566)	
	1 ¹ B ₂	0.4032(27a ₁ →23b ₂); 0.0161(18a ₂ →23b ₁); 0.0236(24a ₁ →23b ₂)	1.84	2.32	0.1131
			(672)	(534)	
SCH ₃	1 ¹ B ₁	0.0369(27a ₁ →23b ₁); 0.3026(18a ₂ →23b ₂); 0.0271(24a ₁ →23b ₁)		2.21	0.2627
saddle				(561)	
	1 ¹ B ₂	0.2537(27a ₁ →23b ₂); 0.1327(18a ₂ →23b ₁); 0.0268(24a ₁ →23b ₂)		2.26	0.2749
				(548)	
SH	2 ¹ E _u	0.2371(5a _{2u} →7e _g); 0.1421(2a _{1u} →7e _g); 0.0371(4a _{2u} →7e _g)		2.45	0.4329
planar	(B)			(506)	
SH	2 ¹ B ₁	0.3128(26a ₁ →23b ₁); 0.0157(18a ₂ →23b ₂); 0.1098(25a ₁ →23b ₁)		2.50	0.1091
saddle				(496)	
	2 ¹ B ₂	0.0289(26a ₁ →23b ₂); 0.1327(18a ₂ →23b ₁); 0.4191(25a ₁ →23b ₂)	2.56	2.59	0.0137
			(484)	(478)	
SCH ₃	2 ¹ B ₁	0.3904(26a ₁ →23b ₁); 0.0314(18a ₂ →23b ₂); 0.0155(25a ₁ →23b ₁)		2.47	0.1537
saddle				(502)	
	2 ¹ B ₂	0.4046(26a ₁ →23b ₂); 0.0137(25a ₁ →23b ₂)		2.65	0.0244
				(468)	
SH	3 ¹ E _u	0.2475(4a _{2u} →7e _g); 0.1404(2b _{1u} →7e _g); 0.0119(6e _g →3b _{1u}); 0.0361(1a _{1u} →7e _g)		4.01	0.5578
planar	(N)			(309)	
SH	3 ¹ B ₁	0.2170(24a ₁ →23b ₁); 0.1227(22b ₁ →28a ₁); 0.0288(16a ₂ →23b ₂)		3.93	0.3569
saddle				(315)	
	3 ¹ B ₂	0.0711(24a ₁ →23b ₂); 0.1660(22b ₁ →28a ₁); 0.1056(23a ₁ →23b ₂)	3.98	4.08	0.1555
			(311)	(304)	
SCH ₃	3 ¹ B ₁	0.1970(24a ₁ →23b ₁); 0.1427(22b ₁ →19a ₂); 0.0279(16a ₂ →23b ₂)		3.97	0.4713
saddle				(312)	
	3 ¹ B ₂	0.0626(24a ₁ →23b ₂); 0.1546(22b ₁ →28a ₁); 0.1184(23a ₁ →23b ₂)		4.12	0.2089
				(301)	
SH	4 ¹ E _u	0.4478(6e _g →3b _{1u}); 0.0160(4a _{2u} →7e _g)		3.69	0.0036
planar	(L)			(336)	
SH	4 ¹ B ₁	0.2922(24a ₁ →23b ₁); 0.0614(22b ₁ →19a ₂)		3.85	0.3325
saddle				(322)	
	4 ¹ B ₂	0.0644(24a ₁ →23b ₂); 0.3015(22b ₁ →28a ₁)	3.59	3.95	0.0111
			(345)	(314)	
SCH ₃	4 ¹ B ₁	0.2730(24a ₁ →23b ₁); 0.0814(22b ₁ →19a ₂)		3.82	0.3179
saddle				(324)	
	4 ¹ B ₂	0.0666(24a ₁ →23b ₂); 0.3123(22b ₁ →28a ₁)		3.92	0.0073
				(316)	
SH	5 ¹ E _u	0.3465(2b _{1u} →7e _g); 0.0952(4a _{2u} →7e _g); 0.0177(1a _{1u} →7e _g)		4.07	0.0047
planar	(C)			(304)	
SH	5 ¹ B ₁	0.3211(23a ₁ →23b ₁); 0.0812(22b ₁ →19a ₂)		4.00	0.0699
saddle				(310)	
	5 ¹ B ₂	0.0994(23a ₁ →23b ₂); 0.3041(22b ₁ →28a ₁)		4.11	0.0085
				(301)	
SCH ₃	5 ¹ B ₁	0.3228(23a ₁ →23b ₁); 0.0915(22b ₁ →19a ₂)		4.05	0.0752
saddle				(306)	
	5 ¹ B ₂	0.1004(23a ₁ →23b ₂); 0.2996(22b ₁ →28a ₁)		4.12	0.0112
				(301)	

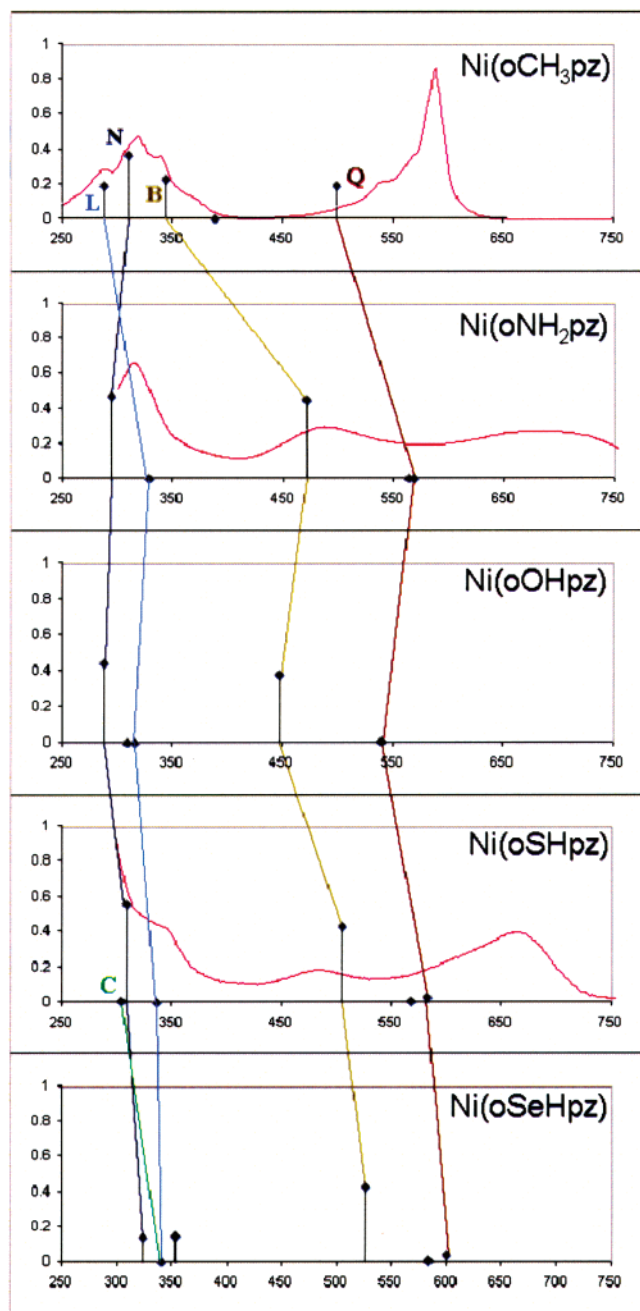


Figure 7. Vertical bold lines indicating the most important singlet-singlet excited states computed for the planar Ni(oXHpz) [X = CH₂, NH, O, S, Se] complexes at the B3LYP/6-31g* level. The available experimental spectra of the Ni(oEtpz),⁹ Ni(oNMe₂pz),³² and Ni(oSEtpz) complexes are indicated with continuum lines (—).

state is formed by the $4a_{2u} \rightarrow 7e_g$ (0.2475) and $1a_{1u} \rightarrow 7e_g$ (0.0361) transitions mixed with the $2b_{1u} \rightarrow 7e_g$ (0.1404) and $6e_g \rightarrow 3b_{1u}$ (0.0119) ones. Also in this case, transitions are mainly LLCTs with a small MLCT contribution provided by the $6e_g \rightarrow 3b_{1u}$ excitation. Indeed, the $6e_g$ MO is partially localized on the nickel ion (17%).

The saddled Ni(oSHpz) geometry induces a splitting of the 3^1E_u excited state into the 3^1B_1 and 3^1B_2 . The former has a strong oscillator strength ($f = 0.3569$) and lies at 313 nm, while the latter is less intense ($f = 0.1555$) and is shifted to lower wavelengths (304 nm). The composition of these

two bands is almost the same (only the weight of the single transition is changed) and corresponds to the N band in the case of the planar conformation (see Table 5).

The effect of the methyl groups on the sulfur atoms is not relevant. Indeed, the 3^1B_1 and 3^1B_2 excited states are determined by similar excitation energies (3^1B_1 312 nm; 3^1B_2 301 nm) and oscillator strengths ($3^1B_1 f = 0.4713$; $3^1B_2 f = 0.2089$).

L Band. In the Ni(oCH₃pz) complex, the 4^1E_u excited state relative to the sh₃ shoulder is characterized mainly by the $6e_g \rightarrow 3b_{1u}$ MLCT transition and lies at higher energy than the N band. According to the labeling of Weiss et al.,⁶⁵ the sh₃ peak can be indicated using the L letter because at the B3LYP level this excited state is electronic in origin. Peripheral substitution with sulfur atoms determines a lowering of the $3b_{1u}$ MO energy and leaves the $6e_g$ MO energy substantially unaltered. Therefore, there is a decrease of the $6e_g/3b_{1u}$ gap, giving an excitation energy downward-shifted to lower energy (3.69 eV, 336 nm).

As in the previously described bands, also the 4^1E_u excited state is split into two transitions (4^1B_1 and 4^1B_2) owing to the lowering of the molecular symmetry from D_{4h} to C_{2v} . The 4^1B_1 excitation lies at 322 nm ($f = 0.3325$) and is more intense than the correspondent 4^1B_2 one (325 nm, $f = 0.0111$). The composition of these two bands presents a significant contribution from the $22b_1 \rightarrow 28a_1$ MLCT transition, which is equivalent to the $6e_g \rightarrow 3b_{1u}$ one of the planar complex.

The effect of adding the methyl terminal does not yield important variations with respect to the Ni(oSHpz) complex. For instance, the 4^1B_1 and 4^1B_2 excited states show similar excitation energies (4^1B_1 324 nm; 4^1B_2 316 nm) and oscillator strengths ($4^1B_1 f = 0.3179$; $4^1B_2 f = 0.0073$).

C Band. Another interesting feature is based on the presence of one more transitions, denoted as the C band according to Weiss et al. labeling.⁶⁵ This excited state is mainly due to the $2b_{1u} \rightarrow 7e_g$ transition, and it falls to 4.07 eV (304 nm) with a low oscillator strength, that is, at a higher energy than the N band. When we perform the distortion from the planarity, the 5^1E_u excited state is split into the 5^1B_1 ($f = 0.0699$) and 5^1B_2 ($f = 0.0085$) transitions. In particular, the 5^1B_1 excitation has an oscillator strength smaller, on an order of 10, than the B band; thus, it can give a significant contribution to the widening of the Soret band. It is characterized mainly by the $23a_1 \rightarrow 23b_1$ excitation, which corresponds to the $2b_{1u} \rightarrow 7e_g$ transition in the planar case.

Adding of the methyl groups on the sulfur atoms promotes the formation of 5^1B_1 and 5^1B_2 excited states, which have similar excitation energies (5^1B_1 306 nm; 5^1B_2 301 nm) and oscillator strengths ($5^1B_1 f = 0.0752$; $5^1B_2 f = 0.0112$).

6.2. The CH₃, NH₂, and OH Peripheral Substitution Effect on the Trend of the Main Excited States. As we have seen in the previous section, the excitation energies of the main bands (Q, B, N, L, and C) calculated in the case of the planar Ni(oSHpz) conformation lie at similar energies to those obtained on the saddled Ni(oSCH₃pz) complex. Thus, in order to analyze the trend of the main excited states induced by the peripheral substitution, we performed calcula-

Table 6. Computed Vertical Excitation Energies (eV) and Oscillator Strengths of Different Ni(oXHpz) [X = CH₂, O, S, Se] (*D_{4h}*) and Ni(oNH₂pz) (*D_{2d}*) Complexes at the B3LYP/6-31g* Level

state		composition	exp.	excitation energies eV (nm)	oscillator strength
1 ¹ E _u (Q)	CH ₃	0.0676(5a _{2u} →7e _g); 0.0144(4a _{2u} →7e _g); 0.0369(1a _{1u} →7e _g)	2.11 (587)	2.48 (500)	0.1934
	NH ₂	0.1514(13b ₂ →23e); 0.1939(9a ₂ →23e); 0.1205(10b ₁ →23e)	wide band	2.18 (568)	0.0013
	OH	0.2362(5a _{2u} →7e _g); 0.0100(4a _{2u} →7e _g); 0.2201(2a _{1u} →7e _g); 0.0254(3b _{2u} →7e _g)		2.30 (539)	0.0096
	SH	0.2037(5a _{2u} →7e _g); 0.0562(3b _{2u} →7e _g); 0.2084(2a _{1u} →7e _g);	1.84 (672)	2.13 (582)	0.0318
	SeH	0.0650(5a _{2u} →7e _g); 0.2012(3b _{2u} →7e _g); 0.2101(2a _{1u} →7e _g);		2.06 (602)	0.0357
2 ¹ E _u (B)	CH ₃	0.2746(5a _{2u} →7e _g); 0.1745(4a _{2u} →7e _g)	3.66 (339)	3.60 (344)	0.2297
	NH ₂	0.1492(13b ₂ →23e); 0.1916(10b ₁ →23e); 0.0510(12b ₂ →23e)	2.53 (489)	2.63 (471)	0.4460
	OH	0.1880(5a _{2u} →7e _g); 0.1486(2a _{1u} →7e _g); 0.0564(4a _{2u} →7e _g)		2.77 (447)	0.3761
	SH	0.2371(5a _{2u} →7e _g); 0.1421(2a _{1u} →7e _g); 0.0371(4a _{2u} →7e _g)	2.56 (484)	2.45 (506)	0.4329
	SeH	0.2433(5a _{2u} →7e _g); 0.1443(2a _{1u} →7e _g); 0.0264(4a _{2u} →7e _g)		2.36 (525)	0.4299
3 ¹ E _u (N)	CH ₃	0.2209(4a _{2u} →7e _g); 0.0961(5a _{2u} →7e _g); 0.0576(6e _g →3b _{1u}); 0.0144(1a _{1u} →7e _g)	3.92 (316)	4.09 (303)	0.3689
	NH ₂	0.3418(12b ₂ →23e); 0.0145(22e→3b _{1u})	3.91 (317)	4.22 (294)	0.4715
	OH	0.2209(4a _{2u} →7e _g); 0.0576(6e _g →3b _{1u})		4.30 (288)	0.4420
	SH	0.2475(4a _{2u} →7e _g); 0.1404(2b _{1u} →7e _g); 0.0119(6e _g →3b _{1u}); 0.0361(1a _{1u} →7e _g)	3.98 (311)	4.01 (309)	0.5578
	SeH	0.1690(4a _{2u} →7e _g); 0.0371(6e _g →3b _{1u}); 0.2749(1a _{1u} →7e _g)		3.82 (324)	0.1391
4 ¹ E _u (L)	CH ₃	0.4225(6e _g →3b _{1u}); 0.0324(5a _{2u} →7e _g)	4.27 (290)	4.31 (288)	0.1933
	NH ₂	0.4527(22e→3b _{1u}); 0.0171(12b ₂ →23e)		3.77 (329)	0.0020
	OH	0.4319(6e _g →3b _{1u}); 0.0200(4a _{2u} →7e _g)		3.93 (315)	0.0006
	SH	0.4478(6e _g →3b _{1u}); 0.0160(4a _{2u} →7e _g)	3.59 (345)	3.69 (336)	0.0036
	SeH	0.4320(6e _g →3b _{1u}); 0.0330(4a _{2u} →7e _g)		3.64 (340)	0.0023
5 ¹ E _u (C)	CH ₃	Over 4.30 eV			
	NH ₂	Over 4.30 eV			
	OH	Over 4.30 eV			
	SH	0.3465(2b _{1u} →7e _g); 0.0952(4a _{2u} →7e _g); 0.0177(1a _{1u} →7e _g)		4.07 (304)	0.0047
	SeH	0.4844(2b _{1u} →7e _g)		3.51 (353)	0.1455

tions on the less crowded planar complexes. We remember that the Ni(oNH₂pz) complex belongs to the D_{2d} point group, whereas the Ni(oOHpz) and Ni(oCH₃pz) have D_{4h} symmetry. Furthermore, we can perform a comparison between the calculated data and the experimental ones owing to the presence of spectra collected on the Ni(oEtpz)⁴⁷ and Ni(oNH₂pz)⁶² complexes. See Figure 7 and Table 6 for further details.

Along the CH₃ and NH₂ series, the Q band is downward-shifted to lower energies from 2.48 eV (500 nm) to 2.18 eV (569 nm). This effect is mainly due to the strong contraction of the 13b₂/23e and 9a₂/23e gaps induced by the peripheral introduction of amine groups (see also Figure 3). We remember that the 13b₂, 9a₂, and 23e (D_{2d}) correlate respectively to 5a_{2u}, 3b_{2u}, and 7e_g (D_{4h}). The shift of the Q band is also visible in the experimental spectra, in which the Q band is red-shifted by about 100 nm. As regards the Ni(oOHpz) complex, the Q band is situated at lower energy (2.30 eV, 539 nm) than the respective one of the Ni(oCH₃pz) molecule but is slightly blue-shifted (~20 nm) with respect to the Ni(oNH₂pz) complex.

The B band involves the same transitions of the Q band but with a stronger contribution from the 4a_{2u} → 7e_g excitation. Also in this case, the contraction of the 13b₂/23e gap provides a red shift of about 130 nm. This effect is observable in the experimental spectra: the B band lies in the visible region of the Ni(oNH₂pz) spectrum, whereas it represents a shoulder of the Soret band in the Ni(oCH₃pz) spectrum. The experimental displacement of these two bands (~150 nm) is therefore well-described by the calculations (130 nm). Furthermore, the Ni(oOHpz) complex promotes the B band at 2.77 eV (447 nm), that is, at lower energy than the Ni(oCH₃pz) but at higher energy than the Ni(oNH₂pz) complex.

The N band is composed mainly of the 4a_{2u} → 7e_g (12b₂ → 23e) transition, and its relative gap does not change significantly along the CH₃, NH₂, and OH series (see Figure 3). Calculations suggest a small blue shift of the N band, but this effect is not visible in the experimental spectra owing to the presence of wide bands, which do not allow to pinpoint the shift on the order of 10–20 nm.

As concerns the L band, we can observe a red shift of 41 nm along the C and N series owing to the contraction of the 22e/14a₁ (6e_g/3b_{1u}) gap. This effect determines a displacement of this band, which passes from the left (higher energy) to the right (lower energy) of the N band. This characteristic is also found for the complex with terminal oxygen atoms, but the shifting is less intense (~28 nm).

6.3. The OH, SH, and SeH Peripheral Substitution Effect on the Trend of the Main Excited States. No experimental UV–vis spectra are available for the Ni(oOHpz) and Ni(oSeHpz) molecules; hence, our analysis is based on the possible changes in the energy and in the oscillator strengths of the excited states owing to the peripheral substitution with different chalcogen atoms (Figure 7).

The ¹E_u excited states, related to the Q band, show a decrease of the excitation energy along the chalcogen series: from 2.30 eV (539 nm) (X = O) to 2.06 eV (602

nm) (X = Se). This stems from the monotonic contraction of the 5a_{2u}/7e_g and 3b_{2u}/7e_g gaps (Figure 3). Also, the oscillator strengths are similar, with the exception of the Q transition of Ni(oOHpz), which is less intense than the corresponding one of the Ni(oSHpz) and Ni(oSeHpz) complexes. The other excited states show a similar trend for the B, L, N, and C bands. In particular, the C band, which lies at much higher energy than the N band along the CH₃, NH₂, and OH series (over 4.30 eV; 288 nm), is significantly shifted toward lower energy: 4.07 eV (304 nm) for Ni(oSHpz) and 3.51 eV (353 nm). This effect is due to the different behavior of the 2b_{1u} MO in the Ni(oXHpz) [X = O, S, Se] complexes. Indeed, as can be seen in the ground-state section and in Figure 3, the 2b_{1u} MO is upward-shifted to less negative energies, providing a strong decrease of the 2b_{1u}/7e_g gaps along the chalcogen series. This effect determines a lowering of the excitation energy. This characteristic is particularly important for the interpretation of the differences between the experimental Soret bands of the Ni(oNMe₂pz) and Ni(oSEtpz) compounds. Indeed, in Figure 7 we can observe a larger intensity for the complex with terminal sulfur atoms. From our calculations, the N and the L bands of the Ni(oNH₂pz) and Ni(oSHpz) molecules lie at almost the same excitation energies and oscillator strengths. Therefore, the higher intensity of the Ni(oSHpz) Soret band can be attributed to the presence of the C band, which adds its contribution to the total intensity of the Soret band.

7. Conclusions

Density functional calculations allow characterization of the molecular and electronic structure of the ground state of Ni(oXHpz) [X = O, S, Se, CH₂] complexes. The peripheral substitution has an effect on the MO energy levels. In particular, the molecules with a methyl terminal group present the highest HOMO and LUMO energies and the most negative bonding energy between the metal ion and the macrocycle fragment, while the molecules with sulfur atoms have the lowest HOMO and LUMO energies, and the molecules with selenium atoms present the highest bonding energy.

The peripheral substituents cause modifications to the “core” properties of the macrocycle, changing σ and π interactions between the metal ion and the dianion fragment. Peripherally unhindered Ni(oXHpz) complexes are all planar because Ni–N_p distances are all above the threshold for ruffling. The largest contribution to the bonding energy is the total orbital interactions, which is larger than the ionic contribution throughout the series of all the complexes. The orbital interactions are based mainly on a σ donation from the nitrogen lone pairs to the d_{x²-y²} orbital of the metal. Furthermore, there is a consistent flow of charge from σ macrocyclic orbitals to Ni-4p _{σ} (e_u); the π interactions are weaker but also important: a back-donation from Ni-3d _{π} (e_g) to the empty π “cage” orbitals is present.

TD–DFT calculations allow analysis of the excited states of Ni(oXHpz), and we have compared theoretical results with available experimental spectra [Ni(oEtpz), Ni(oSEtpz), and Ni(N Me₂pz)]. On the basis of the calculated and the experimental data, we can conclude that the Ni(oCH₃pz)

spectrum shows two main bands: the Q band and the broad Soret band, which is composed of three secondary peaks, denoted as B, N, and L. The peripheral substitution with chalcogen, carbon, and nitrogen atoms determines the decomposition of the Soret band into separate peaks: for example, the B band is shifted to lower energies, while the N and L peaks yield one single band. Moreover, the C band, which lies at energies over 4.30 eV (288 nm) along the C, N, O series, is downward-shifted to lower energies due to the terminal substitution with sulfur and selenium atoms. In the Ni(oSHpz) complex, the C peak is close to the N and L peaks to form the Soret band, as observed in the experimental Ni(oSEtpz) spectrum. According to the calculations, in an eventual Ni(oSeHpz) UV-vis spectrum, the C band should lie as a separate band between the Soret and B bands.

Experimental and theoretical chemical “perturbation” of the reference molecule Ni(oCH3pz) by peripheral substitution allows one to track and follow the modification of the computed and measured spectra giving a more firmly grounded interpretation of the properties of this interesting class of molecules.

The same approach we have seen before can be used to analyze the properties determined of the metal substitution with the first row of transition elements. These properties can allow us then to point out the reactivity of these compounds.

Acknowledgment. Financial support through MIUR grants within “legge 488 – cluster 14 po.5 e cluster 16 po.8” and from the Laboratorio per la Sintesi e la Caratterizzazione dei Materiali Molecolari (LASCAMM) of INSTM Sezione Basilicata is gratefully acknowledged. Thanks are expressed to Prof. Ricciardi for collecting the UV-vis spectrum for Ni(oSEtpz).

References

- Hoffman, B. M.; Barrett, A. G. M. Heteroatom-Functionalized Porphyrazines and Multimetallic Complexes and Polymers Derived Therefrom. U.S. Patent 5,912,341, 1999.
- Andersen, K.; Anderson, M.; Anderson, O. P.; Baum, S.; Baumann, T. F.; Beall, L. S.; Broderick, W. E.; Cook, A. S.; Eichhorn, D. M.; Goldberg, D.; Hope, H.; Jarrell, W.; Lange, S. J.; McCubbin, Q. J.; Mani, N. S.; Miller, T.; Montalban, A. G.; Rodriguez-Morgade, M. S.; Lee, S.; Nie, H.; Olmstead, M. M.; Sabat, M.; Sibert, J. W.; Stern, C.; White, A. J. P.; Williams, D. B. G.; Williams, D. J.; Barrett, A. G. M.; Hoffman, B. M. *J. Heterocycl. Chem.* **1998**, *35* (5), 1013–1042.
- Bahr, G.; Schleiter, G. *Chem. Ber.* **1957**, *90*, 438.
- Deng, K. M.; Ding, Z. N.; Ellis, D. E.; Michel, S. L. J.; Hoffman, B. M. *Inorg. Chem.* **2001**, *40* (6), 1110–1115.
- Ehrlich, L. A.; Skrdla, P. J.; Jarrell, W. K.; Sibert, J. W.; Armstrong, N. R.; Saavedra, S. S.; Barrett, A. G. M.; Hoffman, B. M. *Inorg. Chem.* **2000**, *39* (18), 3963–3969.
- Fitzgerald, J.; Haggerty, B. S.; Rheingold, A. N.; May, L. *Inorg. Chem.* **1992**, *31*, 2006.
- Fuchter, M. J.; Beall, L. S.; Baum, S. M.; Montalban, A. G.; Sakellariou, E. G.; Mani, N. S.; Miller, T.; Vesper, B. J.; White, A. J. P.; Williams, D. J.; Barrett, A. G. M.; Hoffman, B. M. *Tetrahedron* **2005**, *61* (25), 6115–6130.
- Ghosh, A.; Fitzgerald, J.; Gassman, P. G.; Almolof, J. *Inorg. Chem.* **1994**, *33*, 6057.
- Hochmuth, D. H.; Michel, S. L. J.; White, A. J. P.; Williams, D. J.; Barrett, A. G. M.; Hoffman, B. M. *Eur. J. Inorg. Chem.* **2000**, *4*, 593–596.
- Kandaz, M.; Michel, S. L. J.; Hoffman, B. M. *J. Porphyrins Phthalocyanines* **2003**, *7* (9–10), 700–712.
- Lee, S. W.; White, A. J. P.; Williams, D. J.; Barrett, A. G. M.; Hoffman, B. M. *J. Org. Chem.* **2001**, *66* (2), 461–465.
- Michel, S. L. J.; Barrett, A. G. M.; Hoffman, B. M. *Inorg. Chem.* **2003**, *42* (3), 814–820.
- Michel, S. L. J.; Hoffman, B. M.; Baum, S. M.; Barrett, A. G. M. Peripherally Functionalized Porphyrazines: Novel Metallomacrocycles with Broad, Untapped Potential. *Prog. Inorg. Chem.* **2001**, *50*, 473–590.
- Montalban, A. G.; Jarrell, W.; Riguet, E.; McCubbin, Q. J.; Anderson, M. E.; White, A. J. P.; Williams, D. J.; Barrett, A. G. M.; Hoffman, B. M. *J. Org. Chem.* **2000**, *65* (8), 2472–2478.
- Montalban, A. G.; Meunier, H. G.; Ostler, R. B.; Barrett, A. G. M.; Hoffman, B. M.; Rumbles, G. *J. Phys. Chem. A* **1999**, *103* (22), 4352–4358.
- Schramm, C. J.; Hoffman, B. M. *Inorg. Chem.* **1980**, *19*, 383.
- Velázquez, C. S.; Fox, G. A.; Broderick, E.; Andersen, K. A.; Anderson, O. P.; Barrett, A. G. M.; Hoffman, B. M. *J. Am. Chem. Soc.* **1992**, *114*, 7416.
- Vesper, B. J.; Lee, S.; Hammer, N. D.; Elseth, K. M.; Barrett, A. G. M.; Hoffman, B. M.; Radosevich, J. A. *J. Photochem. Photobiol., B* **2006**, *82* (3), 180–186.
- Vesper, B. J.; Lee, S. W.; Barrett, A. G. M.; Hoffman, B. M. *Abstr. Pap.—Am. Chem. Soc.* **2001**, *222*, U563–U563.
- Yaping, N.; Fitzgerald, J.; Carroll, P.; Wayland, B. B. *Inorg. Chem.* **1994**, *33*, 2029.
- Zhao, M.; Stern, C.; Barrett, A. G. M.; Hoffman, B. M. *Angew. Chem., Int. Ed.* **2003**, *42* (4), 462+.
- Ricciardi, G.; Bencini, A.; Ciofini, I.; Rosa, A. *Inorg. Chem.* **1999**, *38*, 1422.
- Ricciardi, G.; Belviso, S.; Bencini, A.; Bavoso, A.; Lelj, F. *J. Chem. Soc., Dalton Trans.* **1998**, 1985.
- Ricciardi, G.; Bencini, A.; Bavoso, A.; Rosa, A.; Lelj, F. *J. Chem. Soc., Dalton Trans.* **1996**, 3243.
- Ricciardi, G.; Bencini, A.; Bavoso, A.; Rosa, A.; Lelj, F. *J. Chem. Soc., Dalton Trans.* **1996**, 2799.
- Bonosi, F.; Ricciardi, G.; Lelj, F.; Martini, G. *Thin Solid Films* **1994**, *243*, 310.
- Bonosi, F.; Ricciardi, G.; Lelj, F.; Martini, G. *J. Phys. Chem.* **1994**, *98*, 10613.
- Bonosi, F.; Ricciardi, G.; Lelj, F.; Martini, G. *J. Phys. Chem.* **1993**, *97*, 9181.
- Lelj, F.; Morelli, G.; Ricciardi, G.; Roviello, A.; Sirigu, A. *Liq. Cryst.* **1992**, *12* (6), 941.
- Morelli, G.; Ricciardi, G.; Roviello, A. *Chem. Phys. Lett.* **1991**, *185*, 468.
- Ricciardi, G.; Lelj, F.; Bonosi, F. *Thin Solid Films* **1994**, *243*, 310.

- (32) Ricciardi, G.; Lelj, F.; Bonosi, F. *J. Phys. Chem* **1993**, *215*, 541.
- (33) Belviso, S.; Ricciardi, G.; Lelj, F.; Scolaro, L. M.; Bencini, A.; Carbonera, C. *J. Chem. Soc., Dalton Trans.* **2001**, 1143.
- (34) LeCours, S. M.; Guan, H. W.; Di Magno, S. G.; Wang, C. H.; Therien, M. J. *J. Am. Chem. Soc.* **1996**, *118*, 1497.
- (35) Priyadarshy, S.; Therien, M. J.; Beratan, D. N. *J. Am. Chem. Soc.* **1996**, *118*, 1504.
- (36) Scheidt, W. R. *The Porphyrin Handbook*; Kadish, K. M., Smith, K. M., Guillard, R., Eds.; PUBLISHER: New York, 2000; Vol. 3, pp 49–112.
- (37) Scheidt, W. R.; Lee, Y. J. *Struct. Bonding (Berlin, Ger.)* **1987**, *64*, 2.
- (38) Shelnut, J. A. *The Porphyrin Handbook*; Kadish, K. M., Smith, K. M., Guillard, R., Eds.; PUBLISHER: New York, 2000; Vol. 7, pp 167–223.
- (39) Shelnut, J. A.; Song, X. Z.; Ma, J. G.; Jia, S. L.; Jentzen, W.; Medforth, C. J. *Chem. Soc. Rev.* **1998**, *27*, 31.
- (40) Ghosh, A.; Vangberg, T. *J. Am. Chem. Soc.* **1999**, *121*, 12154.
- (41) Gouterman, M. *J. Chem. Phys.* **1959**, *30*, 1139.
- (42) Ziegler, T.; Rauk, A. *Theor. Chim. Acta* **1977**, *46*, 1.
- (43) Ziegler, T.; Rauk, A. *Inorg. Chem.* **1979**, *18*, 1558.
- (44) Ziegler, T.; Tschinke, V.; Becke, A. *J. Am. Chem. Soc.* **1987**, *109*, 1351.
- (45) Ziegler, T.; Tschinke, V.; Ursenbach, C. *J. Am. Chem. Soc.* **1987**, *109*, 4825.
- (46) Ziegler, T.; Tschinke, V.; Versluis, L.; Baerends, E. J. *Polyhedron* **1988**, *7*, 1625.
- (47) Rosa, A.; Ricciardi, G.; Baerends, E. J.; van Gisbergen, S. J. A. *J. Phys. Chem. A* **2001**, *105*, 3311.
- (48) van Gisbergen, S. J. A.; Rosa, A.; Ricciardi, G. *J. Chem. Phys.* **1999**, *111*, 2499.
- (49) Infante, I.; Lelj, F. *Chem. Phys. Lett.* **2003**, *367*, 308.
- (50) Parr, R. G.; Yang, W. *Density Functional Theory of Atoms and Molecules*; PUBLISHER: New York, 1989.
- (51) Becke, A. D. *J. Chem. Phys.* **1993**, *398*, 5648.
- (52) Frisch, M. J.; Trucks, G. W.; Schlegel, H. B.; Scuseria, G. E.; Robb, M. A.; Cheeseman, J. R.; Zakrzewski, V. G.; Montgomery, J. A.; Stratmann, R. E.; Burant, J. C.; Dapprich, S.; Millam, J. M.; Daniels, A. D.; Kudin, K. N.; Strain, M. C.; Farkas, O.; Tomasi, J.; Barone, V.; Cossi, M.; Cammi, R.; Mennucci, B.; Pomelli, C.; Adamo, C.; Clifford, S.; Ochterski, J.; Petersson, G. A.; Ayala, P. Y.; Cui, Q.; Morokuma, K.; Malick, D. K.; Rabuck, A. D.; Raghavachari, K.; Foresman, J. B.; Cioslowski, J.; Ortiz, J. V.; Stefanov, B. B.; Liu, G.; Liashenko, A.; Piskorz, P.; Komaromi, I.; Gomperts, R.; Martin, R. L.; Fox, D. J.; Keith, T.; Al-Laham, M. A.; Peng, C. Y.; Nanayakkara, A.; Gonzalez, C.; Challacombe, M.; Gill, P. M. W.; Johnson, B. G.; Chen, W.; Wong, M. W.; Andres, J. L.; Head-Gordon, M.; Replogle, E. S.; Pople, J. A. *Gaussian 98*; Gaussian, Inc.: Pittsburgh, PA, 1998.
- (53) Baerends, E. J.; Ellis, D. E.; Ros, P. *Chem. Phys.* **1973**, *2*, 42.
- (54) Fonseca Guerra, C.; Snijders, J. G.; te Velde, G.; Baerends, E. J. *Theor. Chem. Acc.* **1998**, *99*, 391.
- (55) te Velde, G.; Baerends, E. J. *J. Comput. Phys.* **1992**, *99*, 84.
- (56) Perdew, J. P. *Phys. Rev. B: Condens. Matter Mater. Phys.* **1986**, *33*, 8822.
- (57) Casida, M. E. *Recent Developments and Applications of Modern Density Func.*; Elsevier: Amsterdam, 1996; Vol. 4.
- (58) Casida, M. E.; Chong, D. P. *Recent Advances in Density Functional Methods*; World Scientific: Singapore, 1995; Vol. 1, p 155.
- (59) Davidson, E. R. *J. Comput. Phys.* **1975**, *17*, 87.
- (60) Stratmann, R. E.; Scuseria, G. E.; Frisch, M. J. *J. Chem. Phys.* **1998**, *109*, 8218.
- (61) Nguyen, K. A.; Day, P. N.; Pachter, R. *J. Chem. Phys.* **1999**, *110*, 9135.
- (62) Goldberg, D. P.; Montalban, A. G.; White, A. J. P.; Williams, D. J.; Barrett, A. G. M.; Hoffman, B. M. *Inorg. Chem.* **1998**, *37*, 2873.
- (63) Gouterman, M. *Porphyrins*; Dolphin, D., Ed.; Academic: New York, 1978; Vol. II.
- (64) Guo, L.; Ellis, D. E.; Hoffman, B. M.; Ishikawa, Y. *Inorg. Chem.* **1996**, *35*, 5304.
- (65) Weiss, C.; Kobayashi, H. M. G. *J. Mol. Spectrosc.* **1965**, *16*, 415.

Vibronic Quasi-Free Rotation Effects in Biphenyl-Like Molecules. TD–DFT Study of Bifluorene[†]

Rémy Fortrie[‡] and Henry Chermette^{*,§}

Université de Lyon, École Normale Supérieure de Lyon, Laboratoire de Chimie, UMR 5182 du CNRS, 46 Allée d'Italie, F-69364 Lyon Cedex 07, France, and Université Lyon 1 and CNRS UMR 5180 du CNRS Sciences Analytiques, Chimie Physique Théorique, Bat. Paul Dirac (210), 43 Boulevard du 11 Novembre 1918, F-69622 Villeurbanne Cedex, France

Received December 19, 2006

Abstract: In this paper, we investigate the vibronic shape of the lowest UV–visible absorption band of biphenyl-like systems, using the bifluorene molecule as a workhorse. The molecule is here regarded as a one-dimensional two-level system, whose ground and excited states are simulated with time-dependent density functional theory and semiempirical methods. The vibrational Schrödinger equation is then numerically solved along the torsional coordinate, and the vibronic shape of the absorption band is modeled. Comparisons with the harmonic approximation, with or without the Franck–Condon approximation, are performed. This study confirms that a vibronic effect is most likely responsible for the strong dissymmetry of the lowest UV–visible absorption band of biphenyl-like systems and that, for such systems, the experimental data should be extracted using the whole absorption band, instead of a Gaussian fit on the first part of the band, as it is often done when a superposition between several electronic transitions is suspected.

1. Introduction

Biphenyl-like molecules belong to a class of systems that are susceptible, if steric effects do not hinder π – π couplings, to easily undergo quasi-free rotation between fragments.^{1–3} They also have the particularity of exhibiting a quasi-planar structure in their electronic ground state and a quasi-orthogonal structure in their first excited state.⁴ Additionally, they often exhibit a significantly asymmetric lowest UV–vis absorption band, whose origin is questionable. This asymmetry can indeed be interpreted as the result of the superposition of a few electronic transitions, or as the result of a vibronic effect. This article focuses on the analysis of the origin of this asymmetry, using the bifluorene molecule as a workhorse.

Fluorene-based molecules and oligomers have indeed previously been shown to exhibit very promising nonlinear optical properties.^{5–8} As a consequence, this family of compounds is of great interest for new technologies, and several experimental and theoretical investigations have already been dedicated to them.^{9–13} A part of these studies consists in comparing the information resulting from both approaches. Such comparisons are however not obvious, and even if some effort has already been done for rationalizing them,^{14,15} some assumptions and questions remain unjustified or unanswered.

In this article, we focus our attention on the linear optical properties of the smallest fluorene oligomer. The experimental UV–visible absorption spectrum of one of its derivatives, bi-9,9-dihexylfluorene, has already been measured¹² and modeled on the basis of an electronic approach.^{8,12} Both of the previous papers focus on the lowest absorption band of the bi-9,9-dihexylfluorene molecule. The way this band is integrated is not detailed in the first paper, and in the second paper, it has been assumed that it only

[†] Dedicated to Professor Dennis R. Salahub on the occasion of his 60th birthday.

* Corresponding author phone: +33 4 72 44 84 27; fax: +33 4 72 44 53 99; e-mail: henry.chermette@univ-lyon1.fr.

[‡] École Normale Supérieure de Lyon.

[§] Université Lyon 1.

Table 1. Electronic Excitation Spectra of the Bifluorene Molecule in the Gas Phase (A/B Indicates that the Geometry Optimization has been Performed at Level B and the Excitation Spectrum Calculation at Level A)^a

excited state	CNDO/s//AM1 ⁵		ZINDO//AM1		TD-B3LYP		TD-PW91	
	ΔE	<i>f</i>	ΔE	<i>f</i>	ΔE	<i>f</i>	ΔE	<i>f</i>
1	33 822	<u>1.59</u>	29778	<u>1.39</u>	30 663	<u>1.33</u>	26 735	<u>1.06</u>
2	34 334	0.01	33 237	0.01	35 346	0.00	28 928	0.00
3	34 832	0.02	33 359	0.01	35 675	0.00	30 532	0.00
4	35 543	0.00	33 908	0.00	36 051	0.00	31 049	0.00
5	35 700	0.04	34 786	0.00	37 844	0.00	32 365	0.00
6	37 809	0.03	34 960	0.00	37 918	0.00	32 482	0.01
7	40 541	0.00	39 482	0.06	38 260	0.03	34 149	0.00
8	42 961	0.05	41 472	0.02	40 830	0.00	34 165	0.00
9	45 782	0.02	42 129	0.01	41 081	0.00	35 232	0.04
10	45 805	0.15	42 956	0.08	42 139	0.05	35 291	0.03
11	46 224	0.08	42 979	<u>0.73</u>	42 483	0.03	35 702	0.00
12	46 555	0.00	44 151	0.12	42 813	0.18	36 384	0.28
13	46 834	0.39	44 196	<u>1.47</u>	43 460	0.02	36 760	0.01
14	47 018	0.17	44 498	<u>1.16</u>	43 765	0.00	37 216	0.11
15	47 982	0.31	45 791	0.01	44 823	0.00	37 724	0.02
16	48 322	<u>0.64</u>	46 003	0.18	45 415	0.02	38 028	0.01
17	48 687	0.04	46 133	0.00	45 453	0.01	38 056	0.00
18	48 798	<u>1.74</u>	46 868	0.00	46 047	0.00	38 516	0.00
19	49 051	0.02	46 983	0.05	46 499	0.00	38 700	0.00
20	49 335	0.04	47 871	0.00	46 979	0.01	39 663	0.00

^a ΔE represents the excitation wavenumber in cm^{-1} and *f* the oscillator strength. Oscillator strengths larger than 0.50 are underlined. The basis set used at TD-B3LYP and TD-PW91 levels is 6-31G*.

consists of a single electronic transition, even if it is rather large and asymmetric.

The present work completes these previous studies. First, we show, on the basis of electronic excitation spectra calculations, that the single excitation assumption is relevant. Second, we confirm, on the basis of a vibronic analysis, that the asymmetric shape of the absorption band is compatible with a vibrational origin. At first glance, these results may seem of weak importance. However, depending on the origin of the asymmetry, the way the experimental transition wavenumbers and oscillator strengths are extracted and interpreted differ, which has of course some consequences on the conclusions which might be drawn using these data. For example, a trend in the oscillator strengths extracted from the experimental absorption spectra of a series of molecules could be observed, where in fact no particular trend exists, but where the absorption bands were not integrated in a proper way.

This article does neither aim to precisely reproduce the experimental data through theoretical calculations nor pretend to reproduce the complete vibronic absorption spectra of the compound of interest. We are here only concerned with getting arguments on the proper way of using experimental absorption spectra for comparison to theoretical data.

2. Electronic Excitation Spectra

In this section, we investigate the electronic absorption spectrum of the bifluorene molecule in the gas phase thanks to several electronic excitation spectra calculation methods. In each case, the molecular geometry is fully optimized, and the existence of an energy minimum is confirmed thanks to a vibrational analysis. The default thresholds and integration

grid of the software have been used and no particular numerical difficulty has been encountered. Concerning semiempirical methods, AM1^{16–18} is used for optimizing the geometry, while CNDO/s^{5,19,20} and ZINDO^{16,21,22} are used for modeling the electronic absorption spectrum. Additionally, time-dependent density functional theory (TD-DFT) calculations are performed, first using a generalized gradient approximation functional, PW91,^{16,23–25} and then a hybrid functional, B3LYP,^{16,26} that has previously been shown relevant for treating such problems.^{27,28} The basis set used is 6-31G*. Results are gathered in Table 1.

As can be seen, whatever the method, the lowest absorption band remains isolated. No overlap with any other intense electronic transition is expected. The closest transition whose oscillator strength is larger than 0.5 is indeed at least 13 200 cm^{-1} (ZINDO//AM1 value) higher in energy than the lowest absorption band, which is much larger than the width of the experimentally observed absorption band (Figure 1).

This result confirms the idea of a vibronic origin for the dissymmetry of the absorption band. Such a phenomenon is not unusual. For example, Brédas et al. recently investigated the dissymmetric shape of the ionization band of the bifluorene molecule on the basis of a harmonic approximation.²⁹ The shape that they obtained is very similar to that observed for the absorption band we are interested in. A significant difference exists however: the tail theoretically obtained for the ionization band is pretty short if compared with that experimentally observed for the absorption band.

This difference suggests that at least one of the vibrational modes of the bifluorene molecule which are affected by the electronic transition is strongly anharmonic. A good candidate is the quasi-free rotation mode corresponding to the

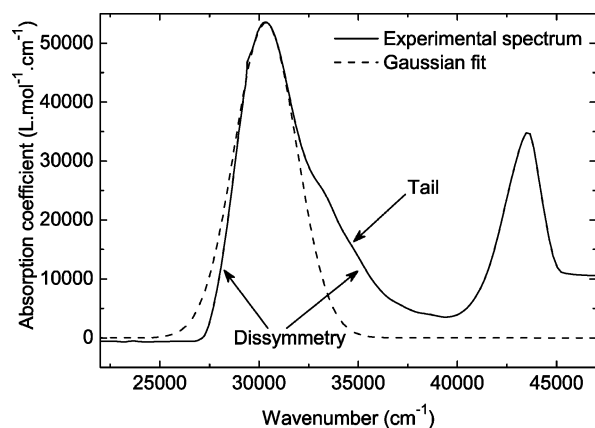


Figure 1. Experimental UV–visible absorption spectrum of bi(9,9-dihexylfluorene) in chloroform at 298 K¹² (solid line) and Gaussian approximation of the lowest absorption band fitted on the top of the band (dashed line). The parameters of the Gaussian function ($A \times \exp\{-[(x-x_c)/w]^2\}$) are $x_c = 30\,303\text{ cm}^{-1}$, $A = 53\,563\text{ L mol}^{-1}\text{ cm}^{-1}$, and $w = 2277\text{ cm}^{-1}$.

respective rotation of both fluorene units. In the following sections, we investigate the consequences of the presence of such a particular vibrational mode on the shape of the lowest electronic absorption band of the bifluorene molecule.

At this point, it has to be emphasized that, from a certain point of view, the problem has here been addressed in an extreme way. Indeed, only two possibilities have been considered: either an electronic or a vibrational origin. Intermediate cases exist however. Some electronic transitions that are forbidden at the optimized geometry of the electronic ground state can indeed give rise to significant contributions if they become allowed in the vicinity of this geometry.²⁷ These effects are not investigated hereafter. However, since they allow the expression of electronic transitions whose transition electric dipole moments are orthogonal to the fluorene–fluorene axis or which consist of antisymmetric combinations of transitions occurring within the π systems of the fluorene units or the benzene rings, the consequences on the UV–visible absorption spectrum are expected to be either very small or located at much higher energies than that of the absorption band of interest. This assessment would of course require confirmation by calculations similar to those performed by Dierkens and Grimme,²⁷ which is not to be performed within the framework of this article.

3. Vibronic Spectrum

As previously mentioned, the goal of this paper is not to precisely reproduce the complete vibronic structure of the absorption spectrum of interest, but to get arguments about the way experimental data have to be extracted and used. As a consequence, and since we are here investigating the impact of the presence of the previously mentioned quasi-free rotation mode on the shape of the absorption spectrum, we will, in the next paragraphs, pay attention only to this particular motion of the molecular system. In other words, the bifluorene molecule is hereafter regarded as a one-dimensional system whose coordinate corresponds to the dihedral angle between both fluorene units ($C_a C_b C_c C_d$ dihedral angle as represented in Figure 2).

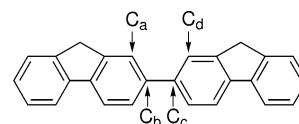


Figure 2. Bifluorene molecule. C_a , C_b , C_c , and C_d define the dihedral angle used as a coordinate for describing its internal quasi-free rotation degree of freedom.

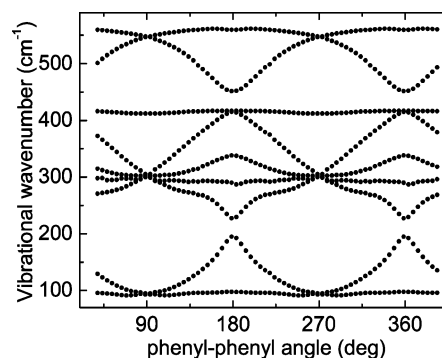


Figure 3. Wavenumbers of the softest orthogonally projected vibrational modes of the biphenyle molecule along its torsional coordinate at the B3LYP/6-31G* level of theory.

This assumption is particularly severe. First, because other vibrational modes are coupled with this torsional coordinate. This can be deduced from Figure 3, where the vibrational modes of the biphenyle molecule have been orthogonally projected with respect to its torsional coordinate. Second, because these other vibrational modes, that we are here neglecting, may also, at least partially, be responsible for the dissymmetry of the absorption band. This contribution is however expected, on the basis of previous studies²⁹ and on the basis of the following Franck–Condon modeling, to be weaker than the one we are here investigating.

Checking the validity of this model might be achieved by solving the vibrational Schrödinger equation of the molecular system over its 126-dimensional potential energy surface. Such a modeling is however heavily computationally demanding and then too far from the purpose of this article.

3.1. Ground State. The following levels of theory are here used for characterizing the ground state of the bifluorene molecule: AM1, B3LYP/6-31G*, B3LYP/6-311++G**,³⁰ and PW91/6-31G*. The previously defined torsional coordinate is sampled every 5°, starting from the fully optimized geometry. For each sample, the dihedral coordinate is frozen and all other geometric parameters are fully optimized. The corresponding energy curves are reported in Figure 4. It can be seen that the shape of the curve is independent of the level of theory and that only the sizes of the energy barriers vary, which is consistent with previous results concerning other biphenyl-like molecules.³¹ It can also be seen that using additional polarization and diffuse functions does not drastically change the shape of the energy curve, and only the 6-31G* basis set is then used further in this article. Note finally that, if all methods give a similar description of the ground state potential energy curve around planar geometries (0 and 180°), there is no clear agreement around orthogonal geometries (90 and 270°), which has significant consequences on the corresponding simulated vibronic absorption spectra, as shown further in this article.

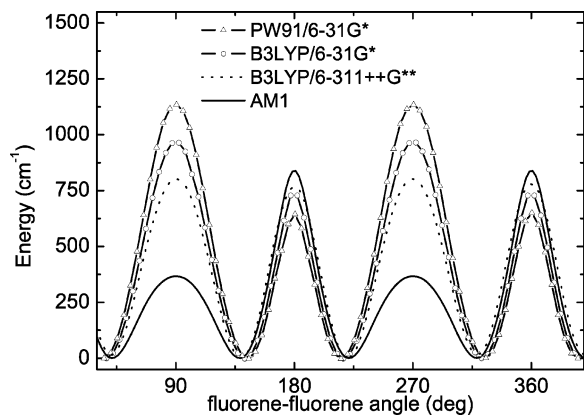


Figure 4. Ground-state energy curves of the bifluorene molecule along its torsional coordinate at the following levels of theory: AM1, B3LYP/6-31G*, PW91/6-31G*, and B3LYP/6-311++G**.³⁰

3.2. Excitation Spectrum. The excitation spectrum of the bifluorene molecule is computed vertically along the torsional coordinate. The following levels of theory are used: ZINDO//AM1, TD-B3LYP/6-31G*, and TD-PW91/6-31G*. The TD-B3LYP/6-31G* excitation spectrum is plotted in Figure 5a. Other excitation spectra are not plotted but are used further in the article.

As a matter of fact, all vibrational modes are also coupled in any excited state of the bifluorene molecule. The same assumptions are however used here that have been used for the ground state. Additionally, only the vertical excitation spectrum is used. This implies that any relaxation of the excited state is neglected. This assumption is acceptable with respect to the vibronic structure of the absorption band if the relaxation energy is quasi-uniform over the torsional coordinate, which we will assume here.

The fact that, from the electronic ground state, among the 20 first possible electronic excitations, only that with the lowest transition energy is probable (Table 1) remains valid whatever the value of the torsional angle between fluorene units. The orthogonal region exhibits however a particularity: at 90 and 270°, the absorbent excited state crosses a transparent state, and they simultaneously exchange their roles. This implies that, over a very short range of angle values, both states are absorbent. However, since, in this region, both states are pseudo-degenerated, they can be rotated into two new absorbent and transparent states, without any major change of the electronic excitation spectrum. Only the first excited state is then hereafter considered.

Both ground-state and excited-state energy curves have been sampled over 72 angle values (every 5°). They are here now fitted using a Fourier's series decomposition, up to the 35th order (Figure 5b).

Vibrational eigenstates are then, for both electronic states of interest, obtained by solving the one-dimensional vibrational Schrödinger equation (eq 1), where θ represents the dihedral angle between both fluorene units, as previously described, I is the quarter of the inertial momentum of the whole molecular system with respect to the line defined by the carbon atoms of both fluorene units that are bonded together (C_b and C_c), $V(\theta)$ is the potential energy function,

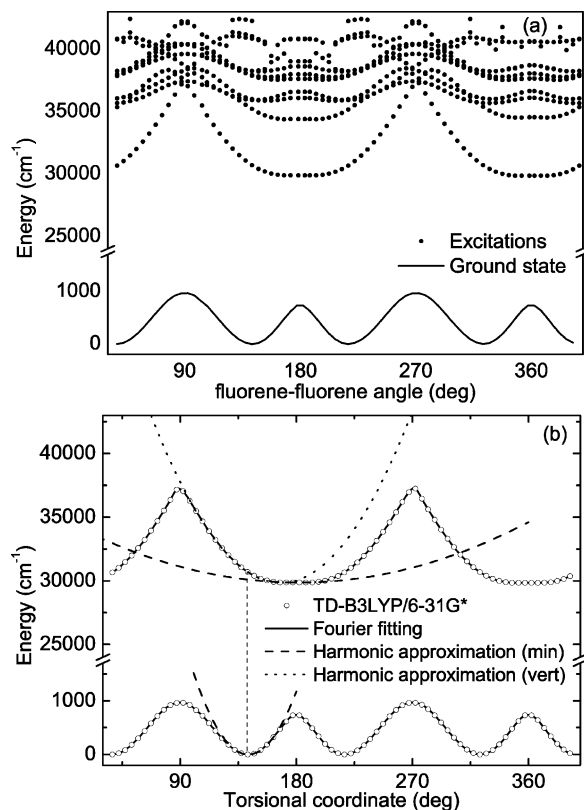


Figure 5. (a) Excitation spectrum of the bifluorene molecule along the fluorene–fluorene dihedral angle at the TD-B3LYP/6-31G* level. Solid line: ground state. Points: existing excitations, whatever the value of the corresponding transition probability. (b) Potential-energy curves associated with the ground state and with the first excited state of the bifluorene molecule along the fluorene–fluorene dihedral angle at the TD-B3LYP/6-31G* level. Empty points: sampling. Solid lines: fits obtained by Fourier decomposition up to the 35th harmonic. Dashed lines: harmonic approximations around energy minima (min). Dotted line: harmonic approximation of the first excited state vertically above the energy minimum of the ground state (vert).

$\phi(\theta)$ and E are the wave function and the energy of the system and \hbar is the reduced Planck constant.

$$-\frac{\hbar^2}{2I} \frac{d^2 \phi(\theta)}{d\theta^2} + V(\theta) \phi(\theta) = E \phi(\theta) \quad (1)$$

Since to each point of the ground-state energy curve corresponds a relaxed geometry of the molecular system, the value of I slightly depends on θ . The variation is however only about 0.8%, and the average value of 1.804×10^{-45} kg m² is hereafter considered (B3LYP/6-31* value). The solutions are developed on a plane waves basis set truncated at the 600th harmonic (1201 basis functions), which corresponds here to a cutoff of 55 863 cm⁻¹. Vibrational eigenstates are graphically represented on Figures 6 and 7, where it can in particular be seen that the vibrational eigenstates are well-converged.

3.3. Oscillator Strengths. The electronic part of the transition electric dipole moment between the electronic ground and excited states strongly varies along the torsional

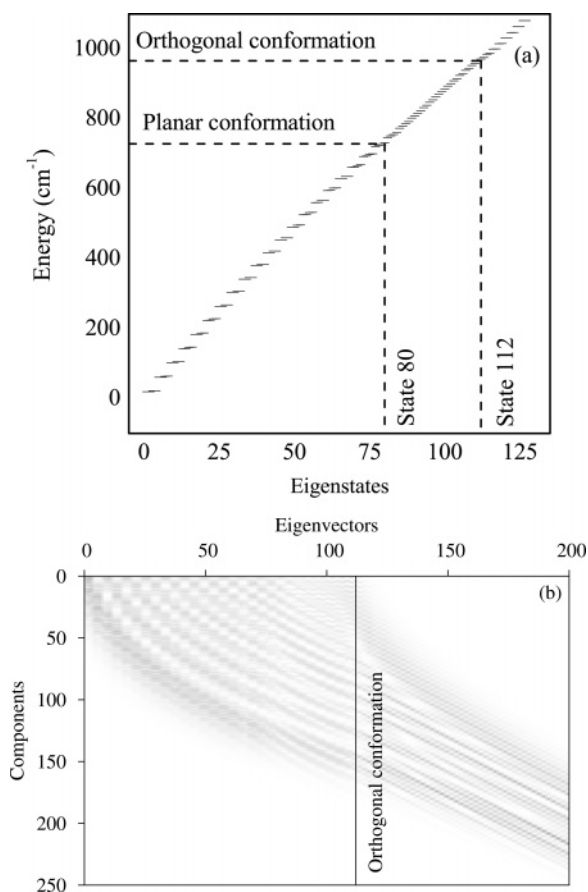


Figure 6. Vibrational eigenstates associated with the electronic ground state. (a) Eigenvalues of the vibrational Hamiltonian operator. (b) Absolute values of the components of the corresponding eigenvectors (continuous grayscale between 0:white and 1:black).

coordinate (Figure 8). As a consequence, transition electric dipole moments between vibronic states, $\langle \psi_{0,v} | \hat{\mu} | \psi_{1,v'} \rangle$, where 0 and 1 refer to the electronic ground and excited states, respectively, and v and v' refer to the vibrational eigenstates, are numerically calculated without further approximation.

3.4. Vibronic Spectrum. A weight is finally attributed to each vibronic transition, depending on the population of the initial vibronic state at the temperature T of interest. We here assume that these populations follow a Boltzmann distribution and each weight is then equal to $\exp(-E_v/k_B T)$, where E_v is the energy of the initial vibronic state and k_B is the Boltzmann constant. The complete vibronic absorption spectrum then consists of the sum of the contributions of all weighted vibronic transitions.

4. Results

In Figure 9 are represented the resulting vibronic absorption spectra. Individual vibronic transitions have been convoluted with Gaussian functions (fwhm: 1000 cm^{-1}). As can be seen on this figure, the absorption band is dissymmetric and becomes larger and weaker when the temperature increases. This behavior is a typical vibronic effect and is also observed within the framework of a more usual harmonic approach (Figure 10).³² In this figure, for making comparison easier, the spectra corresponding to the harmonic approximation

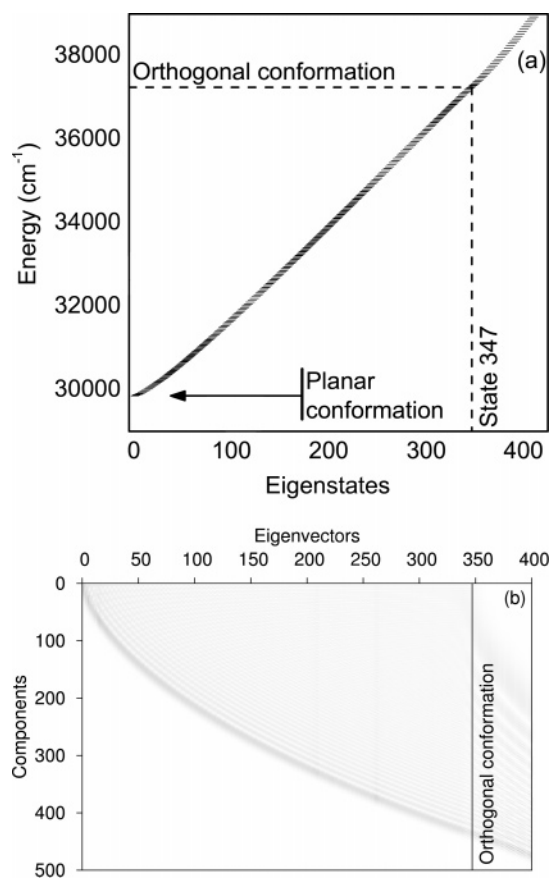


Figure 7. Vibrational eigenstates associated with the electronic excited state. (a) Eigenvalues of the vibrational Hamiltonian operator. (b) Absolute values of the components of the corresponding eigenvectors (continuous grayscale between 0:white and 1:black).

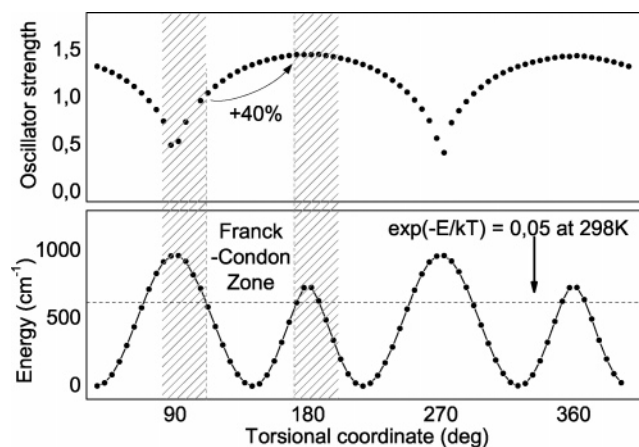


Figure 8. (Top) Oscillator strength corresponding to the electronic part of the transition electric dipole moment between the electronic ground and excited states along the torsional coordinate (B3LYP/6-31G*). (Bottom) Potential-energy curve associated with the electronic ground state (B3LYP/6-31G*). The variation of the oscillator strength over the Franck-Condon zone associated with a limiting Boltzmann factor of 0.05 at 298 K is also represented.

have been shifted and vertically scaled in such a way that the maxima of all curves match up.

As can be seen looking at both scaling factors, using the harmonic approximation leads to a slight overestimation of

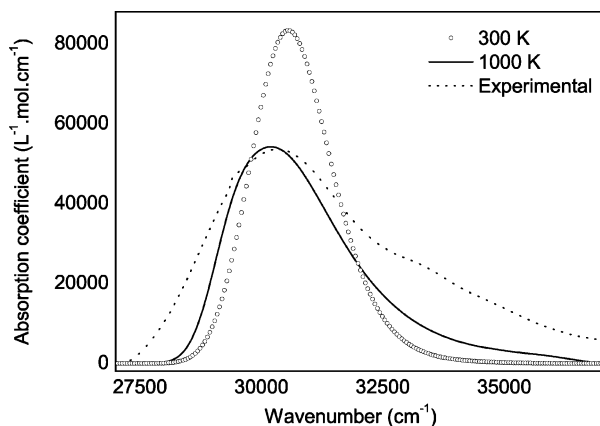


Figure 9. Vibronic absorption spectrum of the bifluorene molecule (TD-B3LYP/6-31G*). Individual vibronic transitions have been convoluted with Gaussian functions (fwhm: 1000 cm^{-1}). No scaling or shifting factor has been applied.

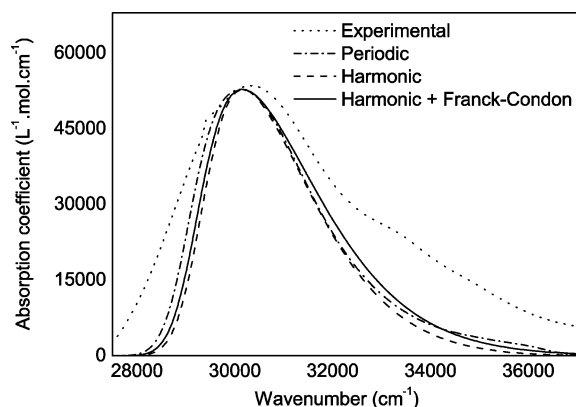


Figure 10. TD-B3LYP/6-31G* vibronic absorption spectra of the bifluorene molecule using different vibrational models: periodic or harmonic, with or without the Franck–Condon approximation.³² Harmonic frequencies, 41.6 cm^{-1} for the ground state and 56.7 cm^{-1} for the excited state, have been obtained by derivation of the electronic potentials, with respect to the torsional angle, for the conformation corresponding to the energy minimum of the ground state (Figure 5). Harmonic and Franck–Condon approximations: shift = 25 cm^{-1} , vertical scaling factor = 89.9%. Harmonic approximation only: shift = 125 cm^{-1} , vertical scaling factor = 83.8%.

the maximum absorption coefficient. It can also be seen that the harmonic approximation fails in correctly describing both the low- and high-energy parts of the absorption band. The low-energy part is too tight and the high-energy part is too wide within the Franck–Condon approximation and falls too short without. In other words, the harmonic approximations are here inadequate for accurately describing the dissymmetry and a long high-energy tail of the absorption band. There are two reasons for this. First, the harmonic approximation simply underestimates the molecular population around orthogonal conformations, and molecules with such conformations are precisely responsible for the existence of the long high-energy tail. Second, as can be seen in Figure 5, the harmonic approximation does not correctly reproduce the potential energy curve of the excited state around planar

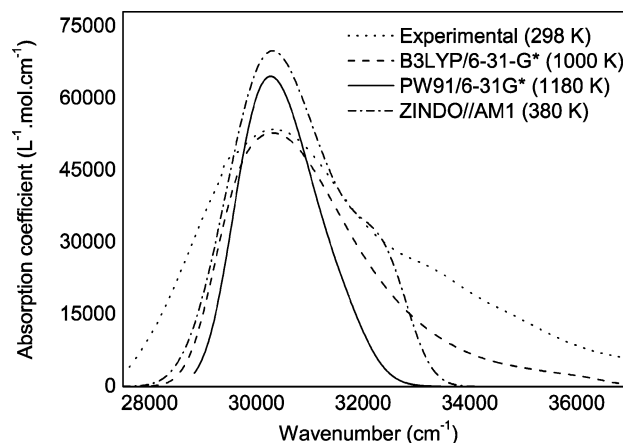


Figure 11. Vibronic absorption band modeled at different levels of theory: ZINDO//AM1 (380 K, shift = 553 cm^{-1}), and TD-PW91/6-31G* (1180 K, shift = 3833 cm^{-1}), and TD-B3LYP/6-31G* (1000 K, shift = 178 cm^{-1}).

conformations, and transitions occurring in these regions are precisely responsible for the low-energy part of the absorption band.

The reader would have noticed that the temperature for which the vibronic spectra are compared is rather high (1000 K) if compared with usual experimental temperatures (300 K). However, this temperature strongly depends on the quality of the description of the potential energy curves of both electronic states, which strongly depends on the quality of the theoretical method.

First, the electronic eigenstates have been calculated for a gas-phase bifluorene, whereas experimental data have been measured in chloroform. This has two consequences: (i) Molecular polarizabilities should be multiplied by a local field factor for any comparison with macroscopic experimental data. (ii) Chloroform is known to generate solvatochromism effects, which are here not taken into account.³³

Second, we are here modeling the bifluorene, but experimental data concern the bi(9,9-dihexylfluorene). Whereas, electronically, replacing hexyl groups by hydrogen atoms almost has no consequence since the lowest electronic transition mainly involves the π system, it has dynamic consequences which are known to strongly affect, at least, the potential energy barriers of the electronic ground state.³⁰ In other words, because of the approximations contained in the sterically simplified model, the theoretical energy barrier is too high, which leads to too high temperatures necessary for modeling the dissymmetry of the spectra. It is then not surprising that the temperature value which corresponds to a particularly strong dissymmetry is experimentally unrealistic.

In order to confirm the vibronic origin of the dissymmetry of the absorption band, two other theoretical methods have been used for modeling the vibronic absorption spectrum: TD-PW91/6-31G* and ZINDO//AM1 (Figure 11). Since the high-energy tail results from the molecules whose conformations are close to the orthogonal one, and since the energy of this particular conformation strongly depends on the theoretical method, the ZINDO//AM1 and TD-PW91/6-31G* spectra have been calculated at 380 and 1180 K, respectively,

so that the Boltzmann factor corresponding to the orthogonal conformation is identical for all methods and we can easily compare the resulting spectra.

At first glance, it appears that both tails are much shorter than with the TD-B3LYP/6-31G* method. This simply comes from the fact that the energy difference between the planar and orthogonal conformations in the excited state is much smaller for ZINDO//AM1 (3357 cm⁻¹) and TD-PW91/6-31G* (3822 cm⁻¹) than for TD-B3LYP/6-31G* (7449 cm⁻¹). Deciding which value is correct is of weak importance and beyond the scope of this article. What is important here is that all three methods give rise to a strongly dissymmetric absorption band with a relatively long high-energy tail. Of course, each method gives rise to a slightly different shape. On the one hand, the TD-PW91/6-31G* method leads to a less dissymmetric and then less convincing shape, but on the other hand, the ZINDO//AM1 method gives rise to a high-energy shoulder, which is similar to that of the experimental spectrum. Anyway, as previously mentioned, it is here very difficult to decide which method gives the best result, and the reality is most probably something in between.

5. Conclusion

In conclusion, we have shown in this paper that the strong dissymmetry and the high-energy tail of the lowest electronic absorption band of the bifluorene molecule are most probably related to a vibronic effect rather than to the overlap of several electronic transitions. This can be generalized to bigger molecular systems, so that by extension, and even if no vibronic analysis has yet been performed, it is reasonable to postulate that the dissymmetric shape of the lowest electronic absorption band of other oligofluorenes is essentially due to vibronic effects.

From the results obtained within this article, it can be deduced that the electronic properties of the transitions involved in the lowest electronic absorption band of oligofluorenes should be extracted using the whole absorption band instead of a single Gaussian function fitted on the first part of the band. This legitimizes, in particular, the way these data have been extracted in a previous paper.⁸

The simple model presented in this article gave some interesting and useful information for extracting electronic data from experimental spectra. The next challenge is now of course to completely model the vibronic absorption spectra of the bifluorene molecule. However, as mentioned above, achieving such a modeling is a difficult task since the molecular system of interest contains 126 internal degrees of freedom. Moreover, the intermediate level of theory used in the present work is known to give a good physical description of common molecular systems but to poorly perform as far as numerical values concerning the electronic transitions are concerned. A more adequate level of theory, like TD-CAM-B3LYP/6-311++G**, for example, where CAM stands for Coulomb-attenuated model,^{34,35} would be necessary for such a more precise modeling, making this task still more challenging.

Acknowledgment. H.C. would like to express his greatest appreciation to Dennis R. Salahub for his pioneering

contributions to the development of density functional theory codes and applications to difficult problems in physical chemistry. He is also grateful to him for a long-standing collaboration. The authors are pleased to dedicate this paper to him for his 60th birthday. The authors also thank Dr. Chantal Andraud for providing them with the original file of the CNDO/s//AM1 one-photon absorption spectrum of bifluorene.

References

- (1) Tachikawa, H.; Kawabata, H. *J. Phys. Chem. B* **2003**, *107*, 1113–1119.
- (2) Nori-shargh, D.; Asadzadeh, S.; Ghjanizadeh, F.-R.; Deyhimi, F.; Mohammadpour, M.; Jameh-Bozorgchi, S. *J. Mol. Struct.* **2005**, *717*, 41–51.
- (3) Mantas, A.; Deretey, E.; Ferretti, F. H.; Estrada, M.; Csizmadia, I. G. *J. Mol. Struct.* **2000**, *504*, 77–103.
- (4) Baca, A.; Rossetti, R.; Brus, L. E. *J. Chem. Phys.* **1979**, *70*, 5575–5581.
- (5) Andraud, A.; Anémian, R.; Collet, A.; Nunzi, J.-M.; Morel, Y.; Baldeck, P. L. *J. Opt. A: Pure Appl. Opt.* **2000**, *2*, 284–288.
- (6) Barsu, C.; Anémian, R.; Andraud, C.; Stephan, O.; Baldeck, P. L. *Mol. Cryst. Liq. Cryst.* **2005**, *446*, 175–182.
- (7) Barsu, C.; Andraud, C.; Amari, N.; Spagnoli, S.; Baldeck, P. L. *J. Nonlinear Opt. Phys. Mater.* **2006**, *14*, 311–318.
- (8) Fortrie, R.; Anémian, R.; Stephan, O.; Mulatier, J.-C.; Baldeck, P. L.; Andraud, C.; Chermette, H. *J. Phys. Chem. C* **2007**, *111*, 2270–2279.
- (9) Reinhardt, B. A. *Photo. Sci. News* **1998**, *4*, 21–34.
- (10) Cho, B. R.; Son, K. H.; Lee, S. H.; Song, Y. S.; Lee, Y. K.; Jeon, S. J.; Choi, J. H.; Lee, H.; Cho, M. H. *J. Am. Chem. Soc.* **2001**, *123*, 10039–10045.
- (11) Kannan, R.; He, G. S.; Yuan, L. X.; Xu, F. M.; Prasad, P. N.; Dombroskie, A. G.; Reinhardt, B. A.; Baur, J. W.; Vaia, R. A.; Tan, L. S. *Chem. Mater.* **2001**, *13*, 1896–1904.
- (12) Morel, Y.; Irimia, A.; Najechalski, P.; Kervella, Y.; Stephan, O.; Baldeck, P. L.; Andraud, C. *J. Chem. Phys.* **2001**, *114*, 5391–5396.
- (13) Belfield, K. D.; Hagan, D. J.; Van Stryland, E. W.; Schafer, K. J.; Negres, R. A. *Org. Lett.* **1999**, *1*, 1575–1578.
- (14) Fortrie, R.; Chermette, H. *C. R. Chim.* **2005**, *8*, 1226–1231.
- (15) Fortrie, R.; Chermette, H. *J. Chem. Phys.* **2006**, *124*, 204104.
- (16) Frisch, M. J.; Trucks, G. W.; Schlegel, H. B.; Scuseria, G. E.; Robb, M. A.; Cheeseman, J. R.; Montgomery, J. A., Jr.; Vreven, T.; Kudin, K. N.; Burant, J. C.; Millam, J. M.; Iyengar, S. S.; Tomasi, J.; Barone, V.; Mennucci, B.; Cossi, M.; Scalmani, G.; Rega, N.; Petersson, G. A.; Nakatsuji, H.; Hada, M.; Ehara, M.; Toyota, K.; Fukuda, R.; Hasegawa, J.; Ishida, M.; Nakajima, T.; Honda, Y.; Kitao, O.; Nakai, H.; Klene, M.; Li, X.; Knox, J. E.; Hratchian, H. P.; Cross, J. B.; Bakken, V.; Adamo, C.; Jaramillo, J.; Gomperts, R.; Stratmann, R. E.; Yazyev, O.; Austin, A. J.; Cammi, R.; Pomelli, C.; Ochterski, J. W.; Ayala, P. Y.; Morokuma, K.; Voth, G. A.; Salvador, P.; Dannenberg, J. J.; Zakrzewski, V. G.; Dapprich, S.; Daniels, A. D.; Strain, M. C.; Farkas, O.; Malick, D. K.; Rabuck, A. D.; Raghavachari, K.; Foresman, J. B.; Ortiz, J. V.; Cui, Q.; Baboul, A. G.; Clifford, S.; Cioslowski, J.; Stefanov, B. B.; Liu, G.; Liashenko, A.;

- Piskorz, P.; Komaromi, I.; Martin, R. L.; Fox, D. J.; Keith, T.; Al-Laham, M. A.; Peng, C. Y.; Nanayakkara, A.; Challacombe, M.; Gill, P. M. W.; Johnson, B.; Chen, W.; Wong, M. W.; Gonzalez, C.; Pople, J. A. *Gaussian 03*, revision B.05; Gaussian, Inc.: Wallingford, CT, 2003.
- (17) Dewar, M. J. S.; Thiel, W. *J. Am. Chem. Soc.* **1977**, *99*, 2338–2339.
- (18) Dewar, M. J. S.; Zoebisch, E. G.; Healy, E. F.; Stewart, J. J. P. *J. Am. Chem. Soc.* **1985**, *107*, 3902–3909.
- (19) Baumann, H. *QCPE Bull.* **1977**, *11*, 333.
- (20) Ziegler, L.; Albrecht, A. C. *J. Chem. Phys.* **1974**, *60*, 3558–3561.
- (21) Zerner, M. C.; Correa de Mello, P.; Hehenberger, M. *Int. J. Quantum Chem.* **1982**, *21*, 251–257.
- (22) Zerner, M. C. In *Rev. Comp. Chem.*; Zerner, M. C., Lipkowitz, K. B., Boyd, D. B., Eds.; VCH Publishing: New York, 1991; Vol. 2, pp 313–365.
- (23) Perdew, J. P. In *Electronic Structure of Solids '91*; Ziesche, P., Eschrig, H., Eds.; Akademie Verlag: Berlin, 1991; Vol. 91, Chapter 11.
- (24) Perdew, J. P.; Chevary, J. A.; Vosko, S. H.; Jackson, K. A.; Pederson, M. R.; Singh, D. J.; Fiolhais, C. *Phys. Rev. B: Condens. Matter Mater. Phys.* **1992**, *46*, 6671–6687.; *Phys. Rev. B: Condens. Matter Mater. Phys.* **1993**, *48*, 4978–4978.
- (25) Perdew, J. P.; Burke, K.; Wang, Y. *Phys. Rev. B: Condens. Matter Mater. Phys.* **1996**, *54*, 16533–16539.
- (26) Becke, A. D. *J. Chem. Phys.* **1993**, *98*, 5648–5652.
- (27) Dierkens, M.; Grimme, S. *J. Chem. Phys.* **2004**, *120*, 3544–3554.
- (28) Sánchez-Carrera, R. S.; Coropceanu, V.; da Silva Filho, D. A.; Fiedlein, R.; Osikowicz, W.; Murdey, R.; Suess, C.; Salaneck, W. R.; Brédas, J.-L. *J. Phys. Chem. B* **2006**, *110*, 18904–18911.
- (29) Coropceanu, V.; André, J.-M.; Malagoli, M.; Brédas, J.-L. *Theor. Chem. Acc.* **2003**, *110*, 59–69.
- (30) Marcon, V.; van der Vegt, N.; Wegner, G.; Raos, G. *J. Phys. Chem. B* **2006**, *110*, 5253–5261.
- (31) Sancho-Carcía, J. C. *J. Chem. Phys.* **2006**, *124*, 124112.
- (32) Wilson, E. B., Jr.; Decius, J. C.; Cross, P. C. *Molecular Vibrations*; Dover Publications: Mineola, NY, 1980; p 14.
- (33) Machado, C.; Machado, V. G. *J. Chem. Educ.* **2001**, *78*, 649–651.
- (34) Yanai, T.; Tew, D. P.; Handy, N. C. *Chem. Phys. Lett.* **2004**, *393*, 51–57.
- (35) Baev, A.; Salek, P.; Gel'mukhanov, F.; Ågren, H. *J. Phys. Chem. B* **2006**, *110*, 5379–5385.

CT600369B

Absorption Spectra of the Potential Photodynamic Therapy Photosensitizers Texaphyrins Complexes: A Theoretical Analysis[†]

Angelo Domenico Quartarolo,[‡] Nino Russo,^{*,‡} Emilia Sicilia,[‡] and Francesco Lej[§]

Dipartimento di Chimica and Centro di Calcolo ad Alte Prestazioni per Elaborazioni Parallele e Distribuite-Centro d'Eccellenza MURST, Università della Calabria, I-87030 Arcavacata di Rende, Italy, and Dipartimento di Chimica, Università degli Studi della Basilicata, Via Nazario Sauro, 85, 85100 Potenza

Received December 22, 2006

Abstract: A systematic study of a class of divalent transition-metal texaphyrin complexes (M-Tex⁺, M = Mn, Fe, Co, Ni, Cu, Zn), recently proposed as active photosensitizers in photodynamic therapy (PDT), was undertaken for the ground and excited electronic states. Geometry optimizations were performed by using the PBE0 exchange-correlation functional coupled with the 6-31G(d) basis set, while electronic excitation energies were evaluated by means of time-dependent density functional response theory (TD-DFT) at the PBE0/6-31+G(d) // PBE0/6-31G(d) level of theory. Solvent effects on excitation energies were taken into account in two ways: by considering solvent molecules explicitly coordinated to the metal center and as bulk effects, within the conductor-like polarizable continuum model (C-PCM). The influence of the metal cation on the so-called Q-band, localized in the near-red visible region of the spectrum, was carefully examined since it plays a basic role in the drug design of new photodynamic therapy photosensitizers. The differences between experimental and computed excitation energies were found to be within 0.3 eV.

1. Introduction

Texaphyrins are a class of expanded porphyrin macrocycles formed by three tripyrrolyldimethene units connected to a phenylenediamine through two imine-type linkages (see Chart 1).^{1–3} The main structural feature of texaphyrins is the increased cavity size, about 20% larger than porphyrins, that allows a better fit of the nearly coplanar nitrogen donors, to the metal cation. Metallotexaphyrins (M-Tex) for nearly the full series of lanthanide(III),^{4,5} Cd(II),^{1,6} Y(III) and In(III),⁷ and for Mn(II) to Zn(II)^{8,9} as well as a metal free aromatic form¹⁰ were synthesized during the past few years. The synthesis was carried out by treating the “sp²-texaphyrin”, a nonaromatic form, with metal salt and air, through

an oxidation-metalation reaction mechanism. Gadolinium(III)-Tex²⁺ and lutetium(III)-Tex²⁺, in a water soluble form, are in late-stage clinical trials for application as an adjuvant in X-ray radiation therapy and photodynamic therapy (PDT), respectively.^{11,12}

Photodynamic therapy is a noninvasive medical technique for the treatment of different types of diseases in oncology and ophthalmology.^{13–15} The basic principle is the combination of a photosensitizing drug capable of absorbing within the body's therapeutic window (620–850 nm), a light source (e.g., laser) of appropriate wavelength and molecular oxygen. The photosensitizer, which shows preferably high accumulation in cancer cells and low dark toxicity, is injected into human body tissue and then irradiated by visible light. After irradiation the light-activated molecule undergoes different reactions, and it can decay from singlet to triplet excited state, through a radiationless transition (intersystem spin crossing). The rate of the latter step is enhanced by the presence in the

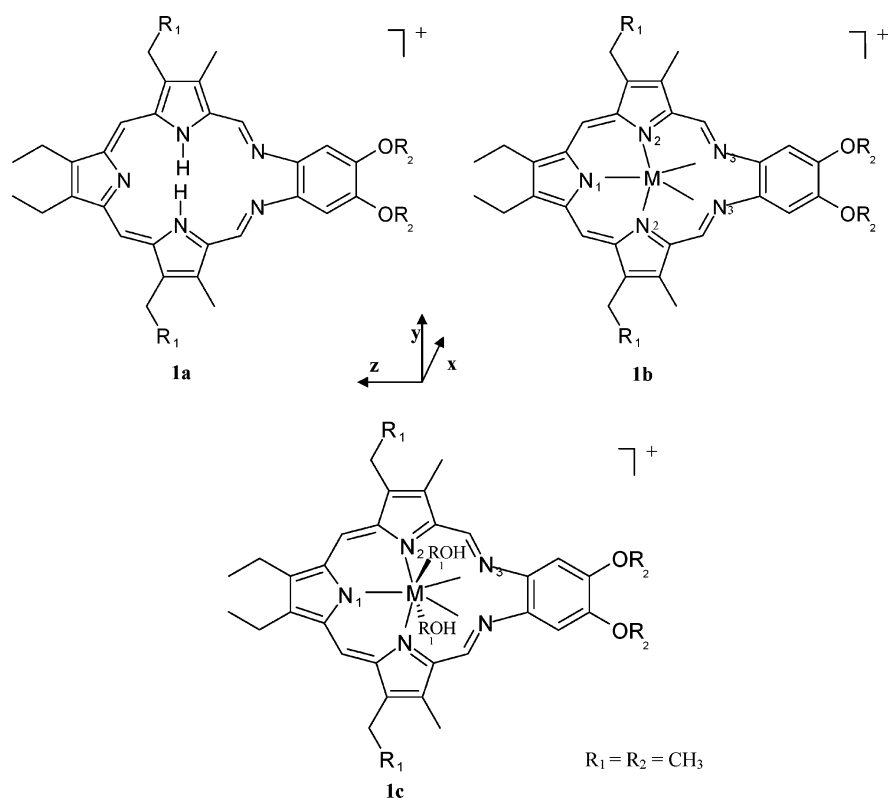
[†] Dedicated to Professor Dennis R. Salahub on the occasion of his 60th birthday.

* Corresponding author: e-mail: nrusso@unical.it.

[‡] Università della Calabria.

[§] Università degli Studi della Basilicata.

Chart 1



molecule of an atom with a high atomic number (heavy atom effect). The key cytotoxic agent is represented by singlet molecular oxygen $^1\text{O}_2$ ($^1\Delta_g$) generated by an energy transfer reaction from the photosensitizer triplet state to the ground state of molecular oxygen $^3\text{O}_2$ ($^3\Sigma_g$).^{16,17} Triplet state energy should match, for a good efficiency, the first excitation energy of molecular oxygen, that is 0.98 eV (1300 nm). The interest in using metallotexaphyrins in PDT is due to their spectral absorbance features. In fact, they exhibit Q-type electronic transitions between 650 and 810 nm and are thus red-shifted by more than 100 nm with respect to porphyrins. This property is related to the increased number of π electrons (22 π -electron system) that causes a greater electron delocalization on the aromatic ring. It is desirable in PDT to have Q-bands in the near-red region of the spectra, since light transmittance into human body changes exponentially with the increasing wavelength of the incident radiation. At present, in literature exist few theoretical works regarding metallotexaphyrins. To our knowledge, a B3LYP density functional study using relativistic ab initio pseudopotentials, was carried out by Cao and Dolg¹⁸ for lanthanide(III) texaphyrins [Ln-Tex(3+), Ln = La, Gd, Lu] and more recently for actinide(III) motexafins [An-Tex(3+), An = Ac, Cm, Lr] by Cao et al.¹⁹ Moreover, a theoretical study for the interpretation of the magnetic circular dichroism spectra (MCD) of texaphyrins was performed by Waluk and Michl.²⁰ The present work deals with a density functional investigation of electronic properties of first-row transition-metal complexes of texaphyrin in organic soluble form (see Chart 1) as well as the evaluation of the electronic excitation energies by means of time-dependent density functional theory (TD-DFT).²¹ Our aim is to give new insights from theory in interpreting spectroscopic properties of metallotexaphyrins

and to contribute to better characterize this novel class of photosensitizers potentially useful in PDT. To account for the interaction with the local environment solvent effects were included both explicitly by considering two methanol solvent molecules directly bound to the metal center and implicitly by using a continuum solvation model.

2. Computational Details

All calculations were carried out at the density functional level of theory with the GAUSSIAN03 program package.²² The hybrid functional approach PBE0^{23,24} was employed for geometry optimization, vibrational frequency analysis, and electronic excitation energy evaluation. The PBE0 exchange-correlation functional is based on the generalized gradient functional of Perdew-Burke-Ernzerhof (PBE)²⁵ with an a priori fixed amount of 25% of Hartree-Fock exchange energy. Restricted formalism was applied for closed shell systems (free base texaphyrin and zinc complex) and an unrestricted one for open shell systems. In the latter case spin contamination, monitored by the expectation value of \hat{S}^2 , was found to be negligible. All molecular structures were fully optimized imposing a C_2 symmetry axis, joining the metal center with the pyrrolic nitrogen atom N₁. For the geometry optimization, a split valence plus polarization basis set 6-31G(d)^{26,27} for H, C, N, and O atoms and a double- ζ quality LANL basis and corresponding pseudopotential for metal atoms (Mn, Fe, Ni, Co, Cu, and Zn) were employed.^{28,29} Vibrational frequency analysis was used to confirm the character of minima of optimized structures. Electronic excitation energies and oscillator strengths were computed within the adiabatic approximation of time-dependent density functional theory (TD-DFT)³⁰ as implemented in Gaussian03. The 6-31+G(d) basis set, which adds

a diffuse function to the 6-31G(d) one for all atoms except hydrogen, was used along with the same pseudopotentials and the corresponding valence basis sets for the metal centers. The influence of scalar relativistic effects of first-row transition metals on excitation energies was evaluated by using the Zn-Tex⁺ complex as a test molecule. For this purpose the Stuttgart relativistic small- and large-core pseudopotentials ECP28SDF and ECP10MWB^{31,32} were used for the zinc atom. In order to characterize the electronic spectra of the examined complexes, the same level of theory used in previous works, which demonstrated as the influence on optical transitions of the basis set choice is minimal and the hybrid functional PBE0 gives usually an accuracy, comparable to refined post-Hartree–Fock approaches at a lower computational cost, of about 0.3 eV for the transition energies.^{33–36} Bulk solvent effects (methanol, $\epsilon = 32.6$) were taken into account within the conductor-like polarizable continuum model (C-PCM).^{37–39} Single-point calculations on the optimized geometries were carried out by the nonequilibrium implementation of C-PCM.^{40–43} The electronic spectra were simulated by means of the SWizard program package.⁴⁴ Here the absorption profile is calculated as a sum of Gaussian functions using the formula

$$\epsilon(\omega) = 2.174 * 10^8 \sum_I \frac{f_I}{\Delta_{1/2}} \exp\left(-2.773 \frac{(\omega - \omega_I)^2}{\Delta_{1/2}^2}\right)$$

where ϵ is the molar absorbance in units of mol⁻¹ cm⁻¹ L, the index sum runs over the number of computed excitation energies ω_I (expressed in cm⁻¹) with corresponding oscillator strengths $\times c4_I$, and $\Delta_{1/2}$ is the half-weight bandwidth assumed constant and equal to 3000 cm⁻¹.

3. Results and Discussion

3.1. Ground-State Spin Multiplicity. Our first task was to determine the ground and lowest excited electronic states for M-Tex⁺ complexes, with and without methanol molecules coordinated to the metal center. As pointed out above, an efficient PDT drug should activate molecular oxygen (³O₂) through an energy transfer, so a preliminary condition to be satisfied is that the electronic gap between ground and first excited states must be greater than or equal to 0.98 eV. For metalloporphyrins-like systems the electronic ground state is influenced by several factors like the ligand size and geometry. For each complex we have considered different spin multiplicities on the basis of the electronic configuration of the divalent metal cation (e.g., ⁶A, ⁴A, and ²A electronic states for Mn (d⁵) complex). The total and relative energies of the two most stable electronic states of each complex are reported in Table 1. As it can be noted, the electronic ground state for every complex, both isolated and coordinated with two solvent molecules, corresponds to a high-spin multiplicity state. For the Mn-Tex⁺ complex doublet, quartet, and sextet states were considered. In this case the ground state for the isolated system was found to be a sextet state, whereas the doublet and quartet states lie 4.01 and 4.38 eV higher in energy than the ground state, respectively. On the other hand, for Mn-Tex(CH₃OH)₂⁺ we found for the first excited state an opposite situation: the ⁴A electronic state is lower in

Table 1. Total (hartrees) and Relative Energies (eV) for All Complexes for Bare Systems and with Two Methanol Molecules Coordinated to the Metal Atom

molecule	molecular symmetry	electronic state	total energy (hartrees)	ΔE (eV)
Isolated Systems				
Mn-Tex ⁺	C ₂	² A	-1844.3437	4.01
Mn-Tex ⁺	C ₂	⁴ A	-1844.3302	4.38
Mn-Tex ⁺	C ₂	⁶ A	-1844.4912	0.00
Fe-Tex ⁺	C ₂	³ A	-1863.9198	1.16
Fe-Tex ⁺	C ₂	⁵ A	-1863.9626	0.00
Co-Tex ⁺	C ₂	² A	-1885.5405	0.99
Co-Tex ⁺	C ₂	⁴ A	-1885.5770	0.00
Ni-Tex ⁺	C ₂	¹ A	-1909.7602	1.56
Ni-Tex ⁺	C ₂	³ A	-1909.8184	0.00
Cu-Tex ⁺	C ₂	⁴ A	-1936.5941	1.14
Cu-Tex ⁺	C ₂	² A	-1936.6022	0.00
Zn-Tex ⁺	C ₂	³ A	-1805.9484	1.32
Zn-Tex ⁺	C ₂	¹ A	-1805.9970	0.00
Complexes Coordinating Two Methanol Molecules				
Mn-Tex(MeOH) ₂ ⁺	C ₂	² A	-2075.6041	2.74
Mn-Tex(MeOH) ₂ ⁺	C ₂	⁴ A	-2075.6432	1.68
Mn-Tex(MeOH) ₂ ⁺	C ₂	⁶ A	-2075.7049	0.00
Fe-Tex(MeOH) ₂ ⁺	C ₂	³ A	-2095.1434	0.99
Fe-Tex(MeOH) ₂ ⁺	C ₂	⁵ A	-2095.1797	0.00
Co-Tex(MeOH) ₂ ⁺	C ₂	² A	-2116.7665	0.84
Co-Tex(MeOH) ₂ ⁺	C ₂	⁴ A	-2116.7974	0.00
Ni-Tex(MeOH) ₂ ⁺	C ₂	¹ A	-2140.9590	1.39
Ni-Tex(MeOH) ₂ ⁺	C ₂	³ A	-2141.0101	0.00
Cu-Tex(MeOH) ₂ ⁺	C ₂	⁴ A	-2167.7654	1.16
Cu-Tex(MeOH) ₂ ⁺	C ₂	² A	-2167.8080	0.00
Zn-Tex(MeOH) ₂ ⁺	C ₂	³ A	-2037.1671	1.32
Zn-Tex(MeOH) ₂ ⁺	C ₂	¹ A	-2037.2157	0.00

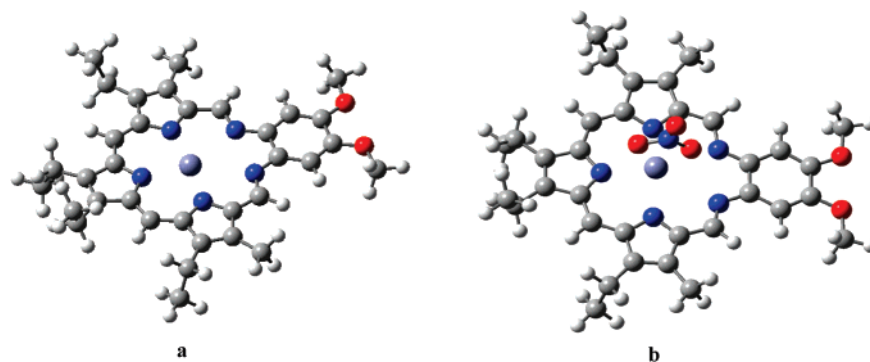
energy than the ²A state (1.68 vs 2.74 eV) with respect to the ⁶A ground state. For the remaining M-Tex⁺ bare systems, the lowest state lies in the range between 1.14 eV (Cu-Tex) and 1.32 eV (Zn-Tex). For the explicitly solvated systems the electronic gap is lower and ranges from 0.84 eV (Co-Tex(CH₃OH)₂⁺) to 1.39 eV (Ni-Tex(CH₃OH)₂⁺). Overall, for the isolated systems all M-Tex⁺ fulfill the ground-excited energetic gap condition (i.e., > 0.98 eV). For systems coordinating two solvent molecules this condition holds for Mn-, Fe-, Ni-, Cu-, and Zn-Tex complexes. These results are in agreement with the experimental measurements of the magnetic moments for each paramagnetic complex,⁹ which gives rise to a high-spin configuration state as confirmed by applying the so-called ‘spin-only formula’. The only exception is represented by the Fe-Tex⁺ complex that exists as a dimer, with two Fe(III) atoms bridged by an oxygen (in a formally trivalent oxidation state).

3.2. Ground-State Geometrical Structures. The geometrical structures of metallotetrapyrins are formally characterized by five possible coordination sites: three pyrrolic (N₁ and N₂ in Chart 1, structure **1a**) and two imine-nitrogen atoms (N₃ in the same chart). The position of the metal center with respect to the mean plane ($\Delta N5$) formed by the five nitrogen atoms is strongly influenced by the presence, in the crystal structure, of counterions (like Cl⁻, NO₃⁻) and/or solvent molecules (MeOH), directly bound to the metal.

Table 2. Selected Bond Lengths (Å) for M(II)-Texaphyrin Complexes^a

complex	M–N ₁	M–N ₂	M–N ₃	M–O _{MeOH}
Mn-Tex ⁺	2.326 (2.383)	2.179 (2.230)	2.553 (2.539)	/
Mn-Tex(MeOH) ₂ ⁺	2.348 (2.409)	2.225 (2.236)	2.554 (2.470)	2.265 (2.217)
Fe-Tex ⁺ ^b	2.300	2.137	2.586	/
Fe-Tex(MeOH) ₂ ⁺ ^b	2.280 (2.321)	2.206 (2.201)	2.580 (2.498)	2.169
Co-Tex ⁺	2.103	2.090	2.815	/
Co-Tex(MeOH) ₂ ⁺	2.247 (2.335)	2.177 (2.176)	2.635 (2.524)	2.146 (2.116)
Ni-Tex ⁺	2.046	2.073	2.896	/
Ni-Tex(MeOH) ₂ ⁺	2.119	2.129	2.805	2.111
Cu-Tex ⁺	2.032	2.049	2.923	/
Cu-Tex(MeOH) ₂ ⁺	2.032	2.057	3.049	2.174
Zn-Tex ⁺	2.165 (2.066)	2.113 (2.127)	2.758 (2.912)	/
Zn-Tex(MeOH) ₂ ⁺	2.108 (2.139)	2.152 (2.138)	2.866 (2.790)	2.160 (2.137)

^a In parentheses are reported averaged experimental values obtained from X-ray structures. ^b Experimental data are relative to μ -oxo Fe(III) texaphyrin dimer

**Figure 1.** Optimized molecular structures for the Zn-Tex⁺ bare complex (a) and in the presence of the counterion NO₃[−] (b).

Structural data, obtained from single-crystal X-ray analysis are available for all M-Tex⁺, in organic soluble form, with the exception of Ni- and Cu-Tex⁺ complexes,⁹ so a direct comparison between experimental and computed geometrical data is possible. Selected optimized metal–nitrogen (M–N) and metal–oxygen (M–O) bond lengths are reported in Table 2. Figure 1 shows the resulting optimized structure of Zn-Tex⁺ and Zn-Tex-NO₃. Owing to the symmetry constraint C₂ axis imposed to the nuclear framework, we can distinguish three kinds of metal–nitrogen bonds (M–N₁, M–N₂, M–N₃); the experimental data, given in parentheses, are referred to as the relative bond lengths averaged around the ideal C₂ axis. For the bare systems, the distance M–N₁ (central pyrrolic nitrogen) ranges from 2.030 to 2.326 Å, decreasing slightly on going from Mn- to Cu-Tex⁺ and thereafter increases for Zn-Tex⁺. A similar trend is found for the M–N₂ distance, which changes from 2.049 to 2.225 Å. The metal–imine nitrogen bond length (M–N₃) increases from Fe- to Cu-Tex⁺, as a geometric consequence of the reduced M–N(pyrrolic) distance. For the Mn-Tex⁺ complex the difference between the experimental and the computed metal–nitrogen distance is about 0.05 Å for both M–N₁ and M–N₂ and 0.01 Å for M–N₃. The experimental value of the distance of the metal from the N5 mean plane is 0.37 Å. This value is due to the presence of the counterion Cl[−], directly bound to the metal, that allows an out-of-plane movement of the metal, giving rise to an increased M–N₁ and M–N₂ distances. In all calculated structures the metal results are always coplanar with nitrogen atoms, also by relaxing completely the geometry during optimization.

Similar considerations are valid for the Zn-Tex⁺ complex where the presence in the experimental structure of a NO₃[−] anion, coordinated to the metal, gives rise to a shift of 0.38 Å for the metal relative to the N5 mean plane. The major discrepancy with experimental data concerns the M–N₃ bond length, whose difference was found to be 0.076 Å; by reoptimizing the structure including the NO₃[−] anion, we obtained a good agreement with the experimental counterpart being the difference of 0.01 Å. As a general rule and by excluding the presence of counterions, we found a pentacoordinated geometry for Mn-Tex⁺ and a tricoordinated one for the other complexes in agreement with experimental findings.⁹

3.3. Gas-Phase Electronic Spectra. The electronic spectra of metallotexaphyrins, like those of metalloporphyrins, are composed of two main absorption bands: one at higher wavelengths, in the visible region, called the Q-band, and the other, at lower wavelengths and more intense, called the B- or Soret band. The electronic spectra of porphyrin-like chromophores were first theoretically rationalized by means of the Gouterman four-orbital model.^{45–46} The electronic bands were interpreted in terms of electronic transitions, involving the two highest occupied molecular orbitals (denoted HOMO and HOMO-1) and the two lowest unoccupied orbitals (LUMO and LUMO+1). On the basis of the proposed theoretical model the Q-band is mainly due to two electronic transitions, named Q_x and Q_y. The Q_x transition arises from the HOMO → LUMO (in brief notation 0–0) electronic excitation (around 60% on average) with a contribution from the HOMO-1 → LUMO+1 (1–1 notation)

Table 3. Excitation Energies in eV (in Parentheses in nm), Oscillator Strengths f , Configurations, and Experimental Data for M-Tex⁺ Bare Systems in vacuo and Solution

state	vacuum				solution (C-PCM)			
	ΔE	$\times c4$	λ_{\max}	main configuration ^a	ΔE	$\times c4$	λ_{\max}	expt ^b ΔE
FB-Tex								
1 ¹ B	1.98 (625.1)	0.0661	2.03	70%(0-0) + 28%(1-1)	1.96 (633.4)	0.1083	2.01	1.72
2 ¹ A	2.07 (598.8)	0.0982	(609.8)	64%(1-0) + 37%(0-1)	2.05 (605.5)	0.1761	(617.3)	(721)
Mn-Tex ⁺								
1 B	1.92 (646.0)	0.0766	2.00	20%(0-0) + 30%(1-1)	1.93 (642.5)	0.1357	2.00	1.71
			(621.1)	19%(0-0) + 31%(1-1)			(621.1)	(727)
2 A	2.06 (601.9)	0.0826		28%(0-1) + 28%(1-0)	2.06 (602.8)	0.1411		
				9%(0-1) + 35%(1-0)				
Fe-Tex ⁺								
1 B	1.95 (635.5)	0.0541	2.00	16%(0-0) + 30%(1-1)	1.96 (631.6)	0.1188	2.01	1.73
			(621.1)	34%(0-0) + 3%(1-1)			(617.3)	(717)
2 A	2.05 (605.6)	0.0799		32%(0-1) + 30%(1-0)	2.06 (601.7)	0.1298		
				5%(0-1) + 32%(1-0)				
Co-Tex ⁺								
1 A	1.96 (632.3)	0.0584	2.01	22%(0-0) + 36%(1-1)	1.96 (632.7)	0.1292	2.01	1.74
			(617.3)	37%(0-0)			(617.3)	(713)
2 B	2.05 (604.4)	0.0726		35%(0-1) + 27%(1-0)	2.05 (604.1)	0.1473		
				8%(0-1) + 31%(1-0)				
Ni-Tex								
1 B	1.97 (628.3)	0.0657	2.03	27%(0-0) + 25%(1-1)	1.96 (631.5)	0.1142	2.02	1.76
			609.8	22%(0-1) + 32%(1-2)			(613.5)	(704)
2 A	2.07 (598.8)	0.0924		15%(1-0) + 33%(0-1)	2.07 (598.9)	0.1486		
				22%(0-2) + 32%(1-1)				
Cu-Tex ⁺								
1 B	1.99 (622.2)	0.0593	2.03	27%(0-0) + 19%(1-1)	1.97 (630.1)	0.1013	2.02	/
			(609.8)	35%(0-1)			(613.5)	
2 A	2.07 (597.7)	0.0909		15%(0-1) + 33%(1-0)	2.06 (601.8)	0.1560		
				22%(0-2) + 32%(1-1)				
Zn-Tex ⁺								
1 ¹ B	1.95 (636.0)	0.0774	2.01	74%(0-0) + 21%(1-1)	1.96 (633.8)	0.1367	2.01	1.76
2 ¹ A	2.07 (600.0)	0.0883	(617.3)	65%(1-0) + 37%(0-1)	2.07 (599.2)	0.1400	(617.3)	(704)

^a By convention, in parentheses the first number, n , is referred to as the occupied orbital contribution from HOMO- n , and the second, m , to the virtual one LUMO+ m . ^b See Table 4, footnote *a*.

of about 40%, whereas the Q_y transition is composed of the HOMO-1 → LUMO (1-0) and HOMO → LUMO+1 (0-1) electronic excitations. In the following we will refer as 'main configuration' to the orbital composition of each vertical excitation energy. Experimental spectroscopic data in solution are available for Mn(II)-, Fe(II)- in monomer form, Co(II)-, Ni(II)-, and Zn(II)-Tex⁺ complexes, so a direct comparison with the computed values is possible. For these compounds the absorption wavelengths of maximum intensity relative to the Q-like band fall in the range between 1.71 eV (727 nm) and 1.76 eV (704 nm), decreasing as a function of the identity of the metal center by 23 nm in going from the Mn- to the Zn-Tex⁺ complex. In order to decouple the effect of the metal and the solvent on the excitations energies, we analyzed first the electronic spectra for bare systems in comparison with the metal-free texaphyrin in monoprotonated form FB-Tex (Chart 1, compound **1a**). Computed vertical excitation energies giving rise to the Q-like band are collected in Table 3 together with the maximum absorption excitation energies obtained from the convolution of the theoretical data by the overlapping of Gaussian

functions. From this table we can infer that for each molecule there are only two excitation energies that contribute to the Q-band. For instance, for the closed-shell Zn-Tex⁺, the first excitation energy is at 1.95 eV ($f = 0.0774$) and arises mainly from HOMO → LUMO (74%) and HOMO-1 → LUMO+1 (21%) electronic excitations. Therefore, on the basis of the Gouterman scheme it can be assigned to the Q_x-type transition. The second excitation energy is at 2.07 eV ($f = 0.0883$), and its main configuration is composed by HOMO-1 → LUMO (65%) and HOMO → LUMO+1 (37%) electronic transitions. This means that this is the Q_y transition. In both cases the transitions have a $\pi \rightarrow \pi^*$ type character, as can be deduced from the plot of the frontier molecular orbitals in Figure 2. Similar results are obtained for the free-metal form of texaphyrin, which presents the first excitation energy at 1.98 eV (Q_x-transition) and the second one at 2.07 eV (Q_y-transition). On the other hand, to describe the transitions for the open shell systems, we have to consider the α - and β -electron excitations. For instance, for the Fe-Tex⁺ complex we found the first excitation energy at 1.95 eV ($f = 0.041$), whose main configuration is

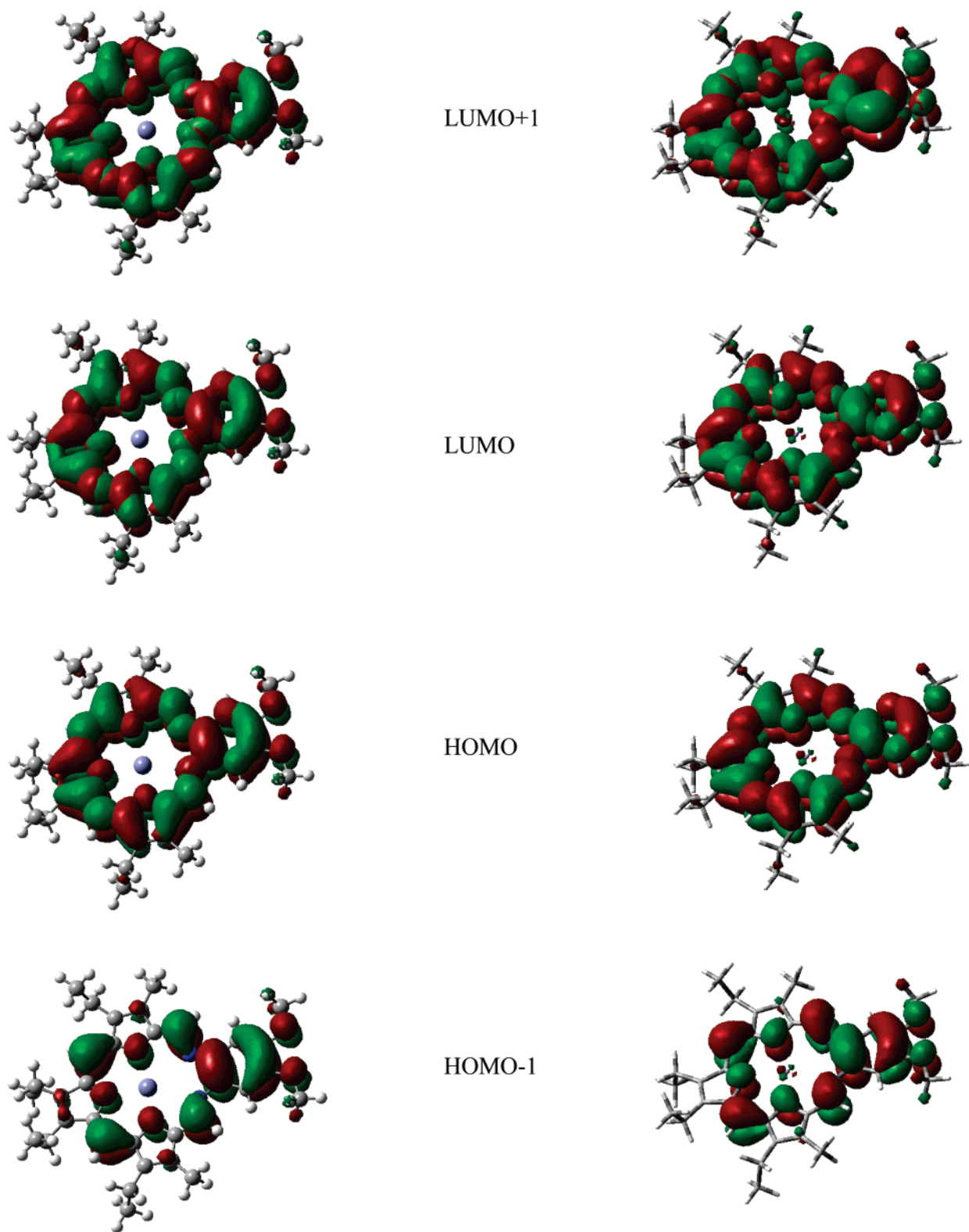


Figure 2. Molecular orbital plot of the four 'Gouterman orbitals' for Zn-Tex⁺ (on the left) and Mn-Tex⁺ (alpha orbitals).

composed of the alpha HOMO \rightarrow LUMO and HOMO $-1 \rightarrow$ LUMO+1 electronic transitions, contributing respectively for 16% and 30%, and the beta HOMO \rightarrow LUMO transition for 34%. The second excitation energy is at 2.05 eV ($f = 0.0799$) and is composed of HOMO-1 \rightarrow LUMO and HOMO \rightarrow LUMO+1 for both alpha and beta electronic transitions. For the other complexes the previously described Gouterman scheme is obeyed with some exceptions that, in any case,

do not introduce significant changes. Since the experimental data are relative to the maximum absorption wavelengths λ_{\max} for the Q- and B-band, it seems more appropriate to compare these data with those obtained from the simulation of the spectra and in particular with the computed maximum absorption wavelengths for the Q-band (Table 3). As can be inferred, all values relative to E_{\max} for the Q-band are overestimated in energy with respect to the experimental

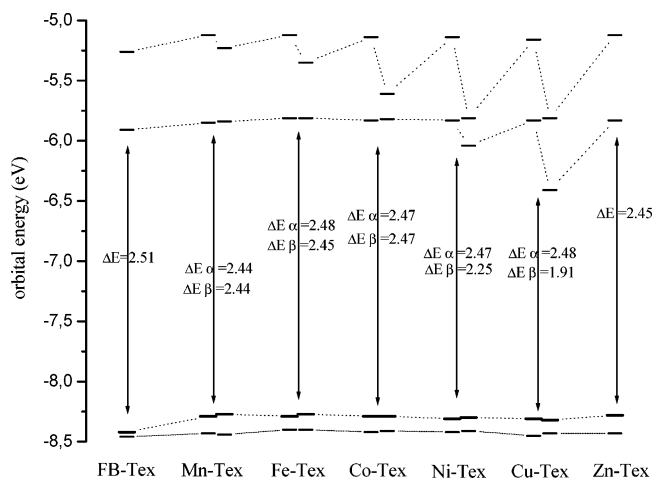


Figure 3. Energy molecular diagram for the four 'Gouterman orbitals' of M-Tex⁺.

ones, and the difference ranges from 0.25 eV for Zn-Tex⁺ to 0.29 eV for Mn-Tex⁺. As found in previous works based on the same level of theory (PBE0/6-31G**//PBE0/6-31+G*), the theoretical error is not larger than 0.3 eV for transition metals containing systems. The influence of the metal on the Q-band relative to the free-metal texaphyrin is in general slight, with the maximum difference of 11 nm for Mn-Tex⁺ and Fe-Tex⁺. As mentioned above, for the experimental spectra the maximum absorption wavelength λ_{\max} for the Q-band is blue-shifted in going from the Mn- to the Zn-Tex⁺ complex. In our case this trend is qualitatively followed except for the zinc complex. It is also worth noting that for Cu-Tex⁺ there are no spectroscopic data since the compound was not well characterized by diffraction analysis. Therefore, we cannot decide whether the breakdown of this trend, at the theoretical level, occurs for the Cu-Tex⁺ or the Zn-Tex⁺ complex. Some hints for the theoretical analysis could come also from the orbital energy diagram in Figure 3, which reports the energetic behavior of the four Gouterman orbitals across the series of the complexes. The first point to note is the regular aspect of the diagram for the energetic gap HOMO–LUMO, which does not show drastic changes along the series. As a consequence, the influence of the metal is confirmed to be small on the excitation energies. An exception could be represented by the β -gap for Cu-Tex⁺ that, however, does not contribute to the transition (see Table 2). The free-metal texaphyrin has the highest gap (2.51 eV), whereas for the unique closed shell Zn-Tex⁺ system a value of 2.45 eV is calculated corresponding to an increased excitation energy E_{\max} . The Zn-Tex⁺ complex has no metal contribution to the frontier orbitals, as deduced from the molecular orbitals plot in Figure 2. For the other systems we have to consider the α and β energetic levels: while the α HOMO–LUMO gap changes little going from Mn- to Cu-Tex⁺ (0.04 eV), the β gap decreases by about 0.5 eV.

4. Solvent Effects

The basic interest in metallotexaphyrins lies in their use as photosensitizers in photodynamic therapy (PDT), so they should be thermodynamically stable in a biological environment in which water is the main component and preserve

their spectroscopic features in this medium. A theoretical analysis accounting for solvent effects on the spectroscopic properties of the photosensitizer can give more insights for a better description of the overall mechanism. The class of metallotexaphyrins under study is soluble in methanol solvent, though water-soluble analogues have been synthesized for Mn(II), Co(II), and Fe(III). The iron complex was characterized by diffraction analysis as a μ -oxo dimer. The water-soluble metal complexes bear an alcohol ($R_1 = -CH_2-CH_2OH$) and a polyethylene glycol [$R_2 = CH_2CH_2O)_3CH_3$] as side-chain substituents that increase their hydrophilic properties. The experimental maximum absorption wavelength in the Q-band region for the water-soluble Mn(II)-Tex⁺ falls at 730 nm, and the wavelength difference with the methanol-soluble form amounts only to 3 nm. For that reason we can argue that the influence of the solubilizing substituents is negligible on the Q-band spectral properties. Therefore, the methanol-soluble complexes can represent an appropriate theoretical model for the study of solvent effects also for biological media. The influence of methanol molecules can be considered implicitly by using a continuum solvent model or explicitly by adding a few solvent molecules to the complex. The latter approach seems reasonable since the metal center tends to complete its coordination sphere as also experimentally found. At the same time, the reaction field generated by the interaction with the bulk solvent could change the electronic distribution and therefore the photochemical properties. In recent works, the coupling of continuum solvent models with explicit treatment of solvent molecules was used to well reproduced UV–vis electronic spectra. As a first step we applied the conductor-like polarizable continuum model (C-PCM) to the optimized M(II)-Tex⁺ structures, as single-point TD-DFT calculations, without adding solvent molecules. From the results reported in Table 3, it is worth noting that the excitation energies are only slightly affected by the reaction field for almost all of the compounds, the difference being within 0.01 eV in the absolute value for the M-Tex⁺s. The oscillator strength for every excitation energy results to be increased for all the compounds with respect to the vacuum state. Regarding the maximum absorption wavelengths λ_{\max} , the FB-Tex, Ni-Tex⁺, and Cu-Tex⁺ are red-shifted, improving the accordance with the experimental data, whereas for the other complexes the λ_{\max} result is unchanged.

4.1. Supramolecular Model. In the supramolecular approach two methanol molecules were added, directly bound to the metal center, as suggested from the crystallographic structures of Mn-, Co-, and Zn-Tex⁺, and the structures were fully optimized in C_2 symmetry. The determination of the most stable electronic state and the gap between the ground and first excited state was discussed previously in section 3.1. The distances between the metal and the oxygen atoms, as listed in Table 2 (M–O), show a good agreement with the experimental bond lengths, with a difference within 0.048 Å. For these structures we reported in Table 4 the vertical excitation energies, the oscillator strengths, and the main configuration computed in vacuo and including also the bulk solvent effects (C-PCM). In both cases the behavior follows again the four-orbitals Gouterman's model. For Mn-, Co-,

Table 4. Excitation Energies in eV (in Parentheses in nm), Oscillator Strengths f , Configurations, and Experimental Data for M-Tex⁺ Complexes with Two Methanol Molecules, in vacuo and Solution

state	vacuum			solution (methanol C-PCM)			expt ^b ΔE
	ΔE	$\times c4$	main configuration ^a	ΔE	$\times c4$	main configuration ^a	
Mn-Tex ⁺							
1 B	1.97 (630.9)	0.0780	28%(0-0) + 29%(1-1) 38%(0-0)	α 1.96 (633.0)	0.1207	27%(0-0) + 28%(1-1) 40%(0-0)	1.71 (727)
2 A	2.11 (586.8)	0.0575	29%(1-0) + 23%(0-1) 35%(1-0) + 12%(0-1)	α 2.09 (592.5)	0.1105	23%(0-1) + 32%(1-0) β 37%(1-0) + 8%(0-1)	
Fe-Tex ⁺							
1 B	1.97 (629.1)	0.0502	29%(0-0) + 5%(1-1) + 6%(3-0) 6%(0-0) + 8%(1-0) + 5%(2-1) + 6%(5-0)	α 1.96 (630.7)	0.0953	34%(0-0) + 3%(1-1) + 5%(3-0) β 5%(0-0) + 14%(1-0) + 38% (2-1)	1.73 (717)
2 B	2.01 (616.3)	0.0372	7%(0-0) + 57%(1-1) 8%(0-0) + 21%(1-0) + 10%(2-1)	α 2.00 (618.8)	0.0444	4%(0-0) + 58%(1-1) β 4%(0-0) + 21%(1-0) + 16%(2-1)	
3 A	2.13 (582.6)	0.0648	32%(1-0) + 14%(0-1) 4%(1-1) + 18%(0-1) + 32%(2-0)	α 2.11 (588.6)	0.1219	35%(1-0) + 10%(0-1) β 13%(0-1) + 8%(1-1) + 35%(2-0)	
Co-Tex ⁺							
1 B	1.99 (621.9)	0.0812	37%(0-0) + 8%(1-1) 37%(0-0) + 13%(1-1)	α 1.97 (628.4)	0.1312	40%(0-0) + 2%(1-1) β 34%(0-0) + 18%(1-1)	1.74 (713)
2 A	2.09 (592.6)	0.0848	34%(1-0) + 13%(0-1) 33%(1-0) + 21%(0-1)	α 2.09 (592.4)	0.1260	36%(1-0) + 11%(0-1) β 35%(1-0) + 19%(0-1)	
Ni-Tex ⁺							
1 B	2.02 (615.0)	0.0822	35%(0-0) + 12%(1-1) 39%(0-0) + 9%(1-1)	α 2.00 (621.5)	0.1327	36%(0-0) + 11%(1-1) β 41%(0-0) + 7%(1-1)	1.76 (704)
2 A	2.10 (589.6)	0.0708	34%(1-0) + 13%(0-1) 32%(1-0) + 22%(0-1)	α 2.10 (590.7)	0.1178	36%(0-1) + 11%(0-1) β 34%(0-1) + 20%(0-1)	
Cu-Tex ⁺							
1 B	1.96 (633.2)	0.0726	19%(0-0) + 28%(1-1) 21%(0-0) + 28%(1-2)	α 1.94 (638.6)	0.1068	39%(0-0) + 3%(1-1) β 36%(0-0) + 15%(1-1)	/
2 A	2.10 (589.5)	0.0745	34%(1-0) + 13%(0-1) 31%(1-0) + 22%(0-1)	α 2.07 (597.6)	0.1450	37%(1-0) + 9%(0-1) β 33%(1-0) + 21%(0-1)	
Zn-Tex ⁺							
1 B	1.97 (629.6)	0.0849	74%(0-0) + 21%(1-1)	1.96 (632.9)	0.1304	77%(0-0) + 18%(1-1)	1.76 (704)
2 A	2.11 (587.2)	0.0582	65%(1-0) + 36%(0-1)	2.09 (594.4)	0.1176	70%(1-0) + 31%(0-1)	

^a By convention, in parentheses the first number, n , is referred to as the occupied orbital contribution from HOMO- n , and the second, m , to the virtual ones LUMO+ m . ^b See Table 3, footnote a.

Ni-, and Zn-Tex⁺, in vacuo, only two excitation energies contribute to the Q-band. On the basis of the main configuration for these compounds we can assign these two excitations to a Q_x-type transition for the lowest excitation energy and to a Q_y-type transition for the next excitation energy, according to what was outlined for the electronic spectra of M-Tex⁺ bare systems (section 3.2). For the Fe-Tex⁺ complex, we found a different behavior regarding the number of excitation energies and their main configuration. Indeed, we found three excitation energies contributing to the Q-like band, with the main configuration that includes also orbital contributions to the electronic transitions other than the four Gouterman's orbitals. The introduction of the bulk solvent effects, through the C-PCM method, in the case of complexes coordinating to solvent molecules results in a slight decrease of the excitation energies (maximum deviation of 0.03 eV for Cu-Tex⁺) and an increase of the relative oscillator strengths. An overall picture of the simulated electronic spectra of Zn-Tex⁺, with and without explicit solvent molecules, and of the theoretical trend for the maximum intensity excitation energies (in eV) of all the compounds are given in Figures 4 and 5, respectively. In

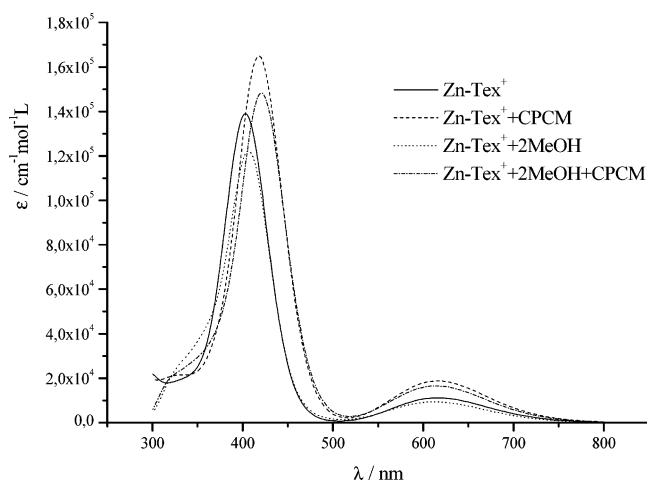


Figure 4. Simulated electronic spectra for the Zn-Tex⁺ complex both in the gas phase and methanol solution (C-PCM), with and without explicit solvent molecules.

the latter case the mean deviation from the experimental data is found to be +0.3 eV, both for the vacuum and implicit solvation models.

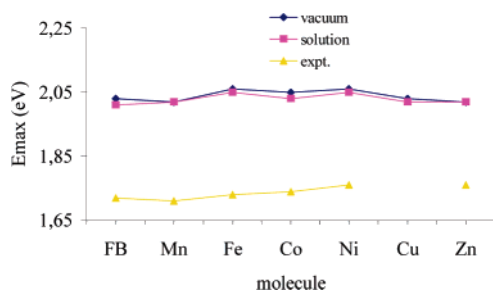


Figure 5. Theoretical and experimental trend of λ_{\max} in the Q-band region for M-Tex⁺ with two methanol molecules, in vacuo and in solution.

As suggested by one of the referees of this work we verified whether the scalar relativistic contributions can account for this error using relativistic pseudopotentials (see Computational Details section) for test calculations on the Zn-Tex⁺ complex. The results clearly show that no significant change for the excitation energies occurs with respect to the chosen pseudopotential (LANL2DZ). In fact, using both relativistic ECPs^{31,32} with 10 and 28 core electrons excitation energies of the Q-band are at 1.95 eV (Q_i) and 2.07 eV (Q_v).

5. Conclusions and Remarks

In the present work we studied the ground-state geometries and electronic absorption spectra of late first-row metal texaphyrin at the density functional level of theory both in vacuo and in methanol solution. Ground-state properties like geometrical parameters and vertical electronic excitations, were computed, analyzed, and compared with available experimental data. Owing to the use of these compounds in photodynamic therapy, particular attention was devoted to two spectral aspects, important for the design of an ideal photosensitizer: (a) determination of the energetic gap between ground and first excited states and (b) computation of the Q-band maximum absorption wavelengths and corresponding molecular orbital contribution to the electronic transitions. The influence of the solvent on the excitation energies was investigated by using polarizable dielectric continuum model (C-PCM) and including explicit solvent molecules as axial ligands to the metal center. In both cases the excitation energies are overestimated by about 0.3 eV in comparison with experimental data. About the energetic behavior, all compounds with two solvent molecules, except Co-Tex⁺, have an energetic gap between the ground and the first excited state greater than 0.98 eV and fulfill one of the requirements for their application as a photosensitizer in PDT. Hopefully this theoretical investigation of the electronic and spectroscopic properties of a class of metallotexaphyrins could give some hints for the design of more efficient agents in photodynamic therapy.

Acknowledgment. Financial support from the Università degli Studi della Calabria and Regione Calabria (POR Calabria 2000/2006, misura 3.16, progetto PROSICA) is gratefully acknowledged.

References

- Sessler, J. L.; Murai, T.; Lynch, V.; Cyr, M. *J. Am. Chem. Soc.* **1988**, *110*, 5586–5588.
- Sessler, J. L.; Hemmi, G.; Mody, T. D.; Murai, T.; Burrell, A.; Young, S. W. *Acc. Chem. Res.* **1994**, *27*, 43–50.
- Sessler, J. L. et al. *Coord. Chem. Rev.* **2003**, *240*, 17–55.
- Sessler, J. L.; Mody, T. D.; Hemmi, G.; Lynch, V. *Inorg. Chem.* **1993**, *32*, 3157–3187.
- Guldi, D. M.; Mody, T. D.; Gerasimchuk, N.; Magda, D.; Sessler, J. L. *J. Am. Chem. Soc.* **2000**, *122*, 8289–8298.
- Maiya, B. G.; Harman, A.; Sessler, J. L.; Hemmi, G.; Murai, T.; Mallouk, T. E. *J. Phys. Chem.* **1989**, *93*, 8111–8115.
- Sessler, J. L.; Tvermoes, N. A.; Guldi, D. M.; Mody, T. D.; Allen, W. E. *J. Phys. Chem. A* **1999**, *103*, 787–794.
- Shimanovich, R.; Hannah, S.; Lynch, V.; Gerasimchuk, N.; Mody, T. D.; Magda, D.; Sessler, J. L.; Groves, J. T. *J. Am. Chem. Soc.* **2001**, *123*, 3613–3614.
- Hannah, S.; Lynch, V.; Guldi, D. M.; Gerasimchuk, N.; MacDonald, C. L. B.; Magda, D.; Sessler, J. L. *J. Am. Chem. Soc.* **2002**, *124*, 8416–8427.
- Hannah, S.; Lynch, V.; Gerasimchuk, N.; Magda, D.; Sessler, J. L. *Org. Lett.* **2001**, *3*, No. 24, 3911–3914.
- Rosenthal, D. I.; Nurenberg, P.; Becerra, C. R.; Frenkel, E. P.; Carbone, D. P.; Lum, B. L.; Miller, R.; Engel, J.; Young, S.; Miles, D.; Renschler, M. F. *Clin. Cancer Res.* **1999**, *5*, 739–745.
- Viala, J.; Vanel, D.; Meingan, P.; Lartigau, E.; Carde, P. *Radiology* **1999**, *212*, 755–759.
- MacDonald, I. J.; Dougherty, T. J. *J. Porphyrins Phthalocyanines* **2001**, *5*, 105–129.
- Van Tenten, Y.; Schuitmaker, H. J.; De Wolf, A.; Willekens, B.; Vrensen, G. F. J. M.; Tassignon, M. J. *Exp. Eye Res.* **2001**, *72*, 41–48.
- Dolmans, D. E. J. G. J.; Fukumura, D.; Jain, R. K. *Nat. Rev. Cancer* **2003**, *3*, 380–387.
- DeRosa, M. C.; Crutchley, R. J. *Coord. Chem. Rev.* **2002**, *233–234*, 351–371.
- Schweitzer, C.; Schmidt, R. *Chem. Rev.* **2003**, *103*, 1685–1757.
- Cao, X.; Dolg, M. *Mol. Phys.* **2003**, *101*, 2427–2435.
- Cao, X.; Li, Q.; Moritz, A.; Xie, Z.; Dolg, M.; Chen, X.; Fang, W. *Inorg. Chem.* **2006**, *45*, 3444–3451.
- Waluk, J.; Michl, J. *Org. Chem.* **1991**, *56*, 2729–2735.
- Casida, M. E.; Time-Dependent Density Functional Response Theory for Molecules. In *Recent Advances in Density Functional Methods*, 1st ed.; Chong, D. P., Ed.; World Scientific: Singapore, Singapore, 1995; Vol. 1, pp 155–192.
- Frisch, M. J.; Trucks, G. W.; Schlegel, H. B.; Scuseria, G. E.; Robb, M. A.; Cheeseman, J. R.; Montgomery, J. A., Jr.; Vreven, T.; Kudin, K. N.; Burant, J. C.; Millam, J. M.; Scalmani, G.; Rega, N.; Petersson, G. A.; Nakatsuji, H.; Hada, M.; Ehara, M.; Toyota, K.; Fukuda, R.; Hasegawa, J.; Ishida, M.; Nakajima, T.; Honda, Y.; Kitao, O.; Nakai, H.; Klene, M.; Li, X.; Knox, J. E.; Hratchian, H. P.; Cross, J. B.; Bakken, V.; Adamo, C.; Jaramillo, J.; Gomperts, R.; Stratmann, R. E.; Yazyev, O.; Austin, A. J.; Cammi, R.; Pomelli, C.; Ochtersky, J. W.; Ayala, P. Y.; Morokuma, K.;

- Voth, G. A.; Salvador, P.; Dannenberg, J. J.; Zakrzewski, V. G.; Dapprich, S.; Daniels, A. D.; Strain, M. C.; Farkas, O.; Malick, D. K.; Rabuck, A. D.; Raghavachari, K.; Foresman, J. B.; Ortiz, J. V.; Cui, Q.; Baboul, A. G.; Clifford, S.; Cioslowski, J.; Stefanov, B. B.; Liu, G.; Liashenko, A.; Piskorz, P.; Komaromi, I.; Martin, R. L.; Fox, D. J.; Keith, T.; Al-Laham, M. A.; Peng, C. Y.; Nanayakkara, A.; Challacombe, M.; Gill, P. M. W.; Johnson, B.; Chen, W.; Wong, M. W.; Gonzalez, C.; Pople, J. A. *Gaussian03, revision B.05*; Gaussian, Inc.: Wallingford, CT, 2004.
- (23) Ernzerhof, M.; Scuseria, G. E. *J. Chem. Phys.* **1999**, *110*, 5029–5036.
- (24) Adamo, C.; Barone, V. *J. Chem. Phys.* **1999**, *110*, 6158–6170.
- (25) Perdew, J. P.; Burke, K.; Ernzerhof, M. *Phys. Rev. Lett.* **1996**, *77*, 3865–3868.
- (26) Hariharan, P. C.; Pople, J. A. *Theor. Chim. Acta* **1973**, *28*, 213.
- (27) Gill, P. M. W.; Johnson, B. G.; Pople, J. A.; Frisch, M. J. *Chem. Phys. Lett.* **1992**, *197*, 499.
- (28) Hay, P. J.; Wadt, W. R. *J. Chem. Phys.* **1995**, *82*, 270–283.
- (29) Francel, M. M.; Petro, W. J.; Hehre, W. J.; Binkley, J. S.; Gordon, M. H.; DeFree, D. J.; Pople, J. A. *J. Chem. Phys.* **1982**, *77*, 3654–3665.
- (30) Stratmann, R. E.; Scuseria, G. E.; Frisch, M. J. *J. Chem. Phys.* **1998**, *109*, 8218–8224.
- (31) Dolg, M.; Wedig, U.; Stoll, H.; Preuss, H. *J. Chem. Phys.* **1987**, *86*, 866–872.
- (32) Schautz, F.; Flad, H. J.; Dolg, M. *Theor. Chem. Acc.* **1998**, *99*, 231–240.
- (33) Petit, L.; Quartarolo, A. D.; Adamo, C.; Russo, N. *J. Phys. Chem. B* **2006**, *110*, 2398–2404.
- (34) Quartarolo, A. D.; Russo, N.; Sicilia, E. *Chem. Eur. J.* **2006**, *12*, 16797–16803.
- (35) Petit, L.; Adamo, C.; Russo, N. *J. Phys. Chem. B* **2005**, *109*, 12214–12221.
- (36) Petit, L.; Maldivi, P.; Adamo, C. *J. Chem. Theory Comput.* **2005**, *1*, 953–962.
- (37) Tomasi, J.; Persico, M. *Chem. Rev.* **1994**, *94*, 2027–2094.
- (38) Tomasi, J.; Mennucci, B.; Cammi, R. *Chem. Rev.* **2005**, *105*, 2999–3093.
- (39) Barone, V.; Cossi, M. *J. Phys. Chem. A* **1998**, *102*, 1995–2001.
- (40) Cossi, M.; Barone, V. *J. Chem. Phys.* **2001**, *115*, 4708–4717.
- (41) Scalmani, G.; Frisch, M. J.; Mennucci, B.; Tomasi, J.; Cammi, R.; Barone, V. *J. Chem. Phys.* **2005**, *124*, 94107–94121.
- (42) Santoro, F.; Barone, V.; Gustavsson, T.; Impropa, R. *J. Am. Chem. Soc.* **2006**, *128*, 16312–16322.
- (43) Impropa, R.; Barone, V.; Santoro, F. *Angew. Chem., Int. Ed.* **2007**, *46*, 405–408.
- (44) Gorelsky, S. I. *SWizard program*; York University: Toronto, Canada, 1998. <http://www.sg-chem.net/> (accessed Sep 2006).
- (45) Gouterman, M. *J. Mol. Spectrosc.* **1961**, *6*, 138–163.
- (46) Gouterman, M.; Wagniere, G. H.; Snyder, L. C. *J. Mol. Spectrosc.* **1963**, *11*, 108–127.

CT600376H

Optical Properties of Phthalocyanine and Naphthalocyanine Compounds[†]

Jan Andzelm,* Adam M. Rawlett, Joshua A. Orlicki, and James F. Snyder

U.S. Army Research Laboratory, Aberdeen Proving Ground, Maryland 21005-5069

Kim K. Baldridge

University of Zurich, 190 Winterthurerstrasse, Zurich CH-8057, Switzerland

Received January 14, 2007

Abstract: Phthalocyanines, naphthalocyanines, and their derivatives are frequently used as light modulating materials. These compounds, with their stable planar square structure and highly delocalized π -electron system, are being used in numerous technological applications, such as pigments in chemical sensors, and more recently as photosensitizers for photodynamic therapy. The nonlinear optical properties (NLO) of these compounds are of particular importance. Using density functional method (DFT), we calculated the optical properties of phthalocyanine and naphthalocyanine complexes with Si as a central atom. We examined the effect of hydrophilic axial substituents and the size of polycyclic aromatic hydrocarbons surrounding the porphyrazine-Si kernel on the optical properties of title molecules. Both UV–vis and RSA spectra are calculated and are compared with available experimental results. The time-dependent DFT (TDDFT) with the B3LYP functional predicts that the characteristic UV–vis absorption maxima are blue-shifted; however, the relative error is almost constant for phthalocyanine and naphthalocyanine compounds. The TDDFT triplet–triplet absorption spectra of Si-phthalocyanine and Si-naphthalocyanine complexes reproduce experimental data well.

1. Introduction

Phthalocyanines (Pcs), naphthalocyanines (Ncs), and their derivatives have been studied extensively since the beginning of the previous century and have been utilized as dyes and pigments because of their intense blue or green color.¹ In recent years, they have also been used in photocopiers and printers,² photovoltaic cells,³ gas sensors,⁴ nonlinear optical limiting devices,⁵ photodynamic therapy agents,⁶ and many other applications. These chromophores display interesting properties, such as high thermal and chemical stability, efficient light absorption in the red visible wavelengths, and both semi- and photoconducting characteristics. These properties are the result of the stable macrocyclic conjugated network of π -electrons leading to high electrical polarizability

and rapid nonlinear response of the charge density to the applied intense electromagnetic fields.⁷ The large nonlinear absorption in the visible spectrum, together with the ultrafast response time and easy processability,⁸ make the optical modulation abilities of this class of chromophores of key importance for many applications.

Optical modulation with Pcs was first reported in 1989 for chloroaluminumphthalocyanine,⁹ and since then many other Pcs and Ncs with these properties have been identified.¹⁰ This variety of chromophores is attributable to the versatility of the synthetic organic chemistry for such molecules. Through synthetic means, one can alter the physical properties (e.g., steric and electronic) of the system by selecting specific coordinating central atoms, attaching various moieties to the exterior ring system, and substituting the ligands on the coordinating central atom.^{10–12}

The optical modulation properties of chromophores can be explained by a reverse saturable absorption (RSA)

[†] Dedicated to Professor Dennis R. Salahub on the occasion of his 60th birthday.

* Corresponding author e-mail: jandzelm@arl.army.mil.

mechanism.¹¹ RSA is essentially a sequential two-photon absorption leading to population of excited triplet states of a material by way of first reaching the excited singlet state. The optimal RSA material would have an excited triplet–triplet cross-section much larger than the cross-section of the ground to first excited singlet–singlet transitions. The intersystem crossing from the lowest singlet excited-state to the lowest triplet excited-state must also be allowed, and the excited-state must have a reasonably long lifetime.¹¹ A practical optical device would require a high concentration of soluble RSA material in the optical beam potentially leading to undesired intermolecular interactions (aggregation). This phenomenon may be alleviated through the use of chromophores with axial substituents that disrupt the favored crystal packing of the unsubstituted chromophore. The use of water as a solvent leads to stacking Pcs, which significantly affects the optical spectra and degrades their optical modulating capabilities.^{13,14} Various axial substituents have been used to minimize the intermolecular stacking of chromophores in water. Huang et al.¹⁵ have used long axial poly(ethylene glycol) (PEG) chains, while Dominguez et al.¹⁶ have synthesized the polyethyleneoxide-capped Pcs.

In this paper we investigate optical absorption as a function of axial substituents in Pcs and Ncs, with silicon as the central atom. In the case of SiPc, hydrophilic substituents such as poly(ethylene oxide) (PEG) oligomers are chosen because they promote water solubility of the system.^{13,15} In the case of SiNc, we select the SINC molecule¹² and also propose other substituents for Ncs. Both visible (UV–vis) and nonlinear (RSA) absorption are studied using quantum chemistry methods. The calculated spectra are compared with the published experimental measurements of the ground-state absorption spectra^{12,13,15–19} and the transient absorption spectra due to the triplet–triplet excitations.^{20–23}

Molecular systems under investigation, particularly in the stacking conformation of the molecules, can involve more than 200 atoms. This requires use of the computationally efficient quantum techniques such as density functional theory (DFT) or semiempirical methods that are computationally less demanding than traditional *ab initio* methods. The need for efficient calculations of optical spectra is paramount, as recently synthesized optically active complexes may involve very large binuclear conjugated-Pc structures,²⁴ dendritic phthalocyanines,¹³ or conjugated carotenoid pigments.²⁵ Therefore, developing fast DFT methods as pioneered by Dunlap,²⁶ Baerends,²⁷ and Salahub²⁸ is of critical importance for successful study of Pc and Nc compounds. These methods approximate electron density and therefore can be used only with the local or gradient corrected Hamiltonian. Therefore, we also use the GGA DFT method in addition to the B3LYP method that is commonly used in calculations for chromophores.

Calculations of absorption spectra were accomplished in the present work using the time-dependent density functional theory (TDDFT)^{29,30} method. This method has been previously shown to provide reasonable predictions for phthalocyanines and metallophthalocyanines structures and UV–vis absorption.^{31–37} While the TD-DFT study of UV–vis spectra requires calculation of singlet–singlet excitations (S–

S), predicting RSA requires calculation of triplet–triplet (T–T) absorption and ultimately excited singlet–triplet cross-section. In this paper we will refer to T–T absorption spectrum as a RSA spectrum. A few investigations have explored excited triplet states for zinc phthalocyanine³² and zinc porphyrin^{23,38} as well as meso-diaryloctaalkyl porphyrins.³⁹ The most relevant for this work is experimental study of the T–T transitions in the SINC molecule^{12,20} and also in silicon phthalocyanines with axial siloxy ligands.^{21,22}

Understanding the mechanism of UV–vis excitations is facilitated by considering the two primary excitation peaks of porphyrins: the Q band in visible range and the B (or Soret) band in the UV region, as has been explained by the “four-orbital model” first introduced in 1963 by Gouterman.⁴⁰ According to this model, the Q band originates from electron excitations out of the HOMO and into the LUMO and LUMO+1, while the B band is from transitions from HOMO-1 to LUMO and LUMO+1. Subsequent studies proposed a more detailed explanation involving more than “four orbitals” because the quasi-degeneracy of orbitals close to the HOMO is removed.⁴¹ The character of UV–vis spectra was studied in detail for porphyrin, porphyrazine,⁴² and metallophthalocyanine³² complexes.

2. Computational Methods

The structures of all molecular systems were calculated using the Dmol,⁴³ GAMESS,⁴⁴ and Gaussian03⁴⁵ software. Initially, structures were optimized using the PBE⁴⁶ DFT functional with the double numerical basis set, DNP,⁴⁷ using DMol. In order to validate the completeness of the basis set, several structures were also investigated using the 6-31G(d), 6-311G(d), 6-311G(d,p), and 6-311+G(d) basis sets.⁴⁸ The excited states were calculated with the hybrid DFT functional B3LYP⁴⁹ within the TDDFT methodology as implemented in the Gaussian03 program.⁵⁰ The UV–vis spectrum was predicted from singlet–singlet excitations, while the RSA spectrum was calculated from the triplet–triplet transitions. The open-shell DFT calculations for the triplets were carried out using the unrestricted Kohn–Sham spin-density approach. The $\langle S^2 \rangle$ values for all triplet states are below 2.04, indicating low spin contamination, a typical feature of the open-shell DFT calculations.⁵¹ The B3LYP Hamiltonian was proven to provide accurate structures and reasonable UV–vis spectra for a variety of chromophores.^{23,31–37,52–54} We have also used the gradient corrected functional PBE because it allows for computationally efficient implementation that is of key importance for this study of large chromophores.^{26–28} In order to improve the efficiency of calculations, we have also imposed the symmetry of the chosen structures and applied fitting functions in the case of gradient corrected DFT functional. We have used the PBE functional to calculate structures of molecular systems. The RSA spectrum was calculated using the singlet ground state and the first triplet excited-state geometries, and we will refer to these levels of calculations as vertical and adiabatic spectra, respectively. The UV–vis spectra were compared with results of the configuration interaction method using single excitations (CIS) within the semiempirical ZINDO/INDO2 method.⁵⁵ It was recently reported for several metal-phthalocyanine

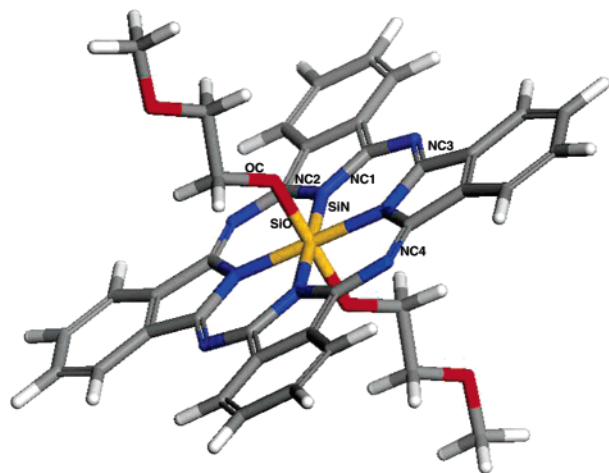


Figure 1. Structure of SiPc-(PEG₇₅)₂.

complexes that the Q-band absorption peaks predicted by ZINDO are in better agreement with the experimental results as compared to the TDDFT calculations.⁵⁶ The ZINDO method was also successfully used to compare electronic properties of zinc phthalocyanine and helicenocyanine.⁵⁷ Considerations of atomic populations were performed using the Hirshfeld population analysis (HPA)⁵⁸ and the popular, Mulliken population analysis (MPA).⁵⁹ Conceptual advantage of HPA over that of MPA was recently discussed by Roy et al.⁶⁰

3. Results

Structures and spectra of SiPc complexes with axially bonded PEG polymers were studied first and compared with the recent experimental measurements. Subsequently results for the SiNc compound with various axial substituents on the central Si atom were investigated. The complete sets of Cartesian coordinates are available upon request.

3.1. Structures and Spectra of SiPc-PEG. The SiPc-PEG complexes are of central interest in this paper because of their solubility in water and their desirable UV–vis and RSA properties. The axial site substitution prevents cofacial aggregation: this was found by attaching PEG polymer¹⁵ or the dendritic fragments to the silicon-containing Pc.¹⁶ This axial modification did not affect the characteristic Q-absorption maximum that was found to be at range of 676–685 nm.^{13,15,16} We have confirmed that the DFT method predicts the sharp Q band regardless of the length or conformations of the PEG polymer attached to central atom in the SiPc-PEG complex.⁶¹ No significant differences in the SiPc ring structure were noted, and the UV–vis spectra show quite similar location of the main Q and B excitation bands.⁶¹

In this paper, we studied the structure and excited states of the SiPc-PEG compound using various levels of theory. A simple SiPc-(PEG₇₅)₂ structure (Figure 1) was chosen because other conformations exhibit similar optical properties. The structure was optimized for a singlet and a triplet state assuming the *C*_{2h} symmetry of the complex. Table 1 shows several structural parameters of the SiPc-(PEG₇₅)₂ complex as a function of methodology used. Across all methods investigated, we note that the structural parameters are within 0.01 Å and 3 deg for bonds and angles,

respectively. Choosing the DFT functional appears to affect the results more than the choice of basis set. The hybrid functional B3LYP predicts contraction of the Pc ring (i.e., shorter SiN, NC, and N=C bonds), while the most widely used gradient-corrected functional, PBE, predicts expansion of the PC ring. The axially inserted PEG appears to be closer to the silicon atom using the hybrid functional than predicted with the GGA functional, a feature predicted regardless of the basis set used. The SiOC angle is 130 deg on average. Improving the basis set causes only a small change (increase) in the SiOC angle. Compared with experimental data⁶² we find an exceptionally good performance of the B3LYP/6-31G(d) approach for the N–C distances of the phthalocyanine planar ring. The discrepancy of 0.04 Å in SiO distances can be attributed to a different ligand connected with oxygen atoms used in our calculations, compared to the one used in the experiment. Since the selected geometry parameters in Table 1 do not include a hydrogen atom, it is sufficient to use single polarization function located only on heavy atoms. Using diffuse functions insignificantly affects the geometry of the planar phthalocyanine ring for the singlet and triplet excited states.

The excitation of one electron from HOMO (*a_u*) to LUMO (*a_g*) gives rise to a ³A_u excited-state within the *C*_{2h} symmetry. The most noticeable structural changes upon going from ground-state singlet, *S*₀, to first triplet state, *T*₁ (Table 1), are the distortions of N–C bonds and enlargement of the SiO bond distance. Energetically, *T*₁ is located 0.94 eV above *S*₀. This adiabatic transition calculated at the B3LYP/6-31G(d) level appears to be converged because the *S*₀ → *T*₁ splitting at the B3LYP/6-311+G(d,p) level is 0.98 eV. The vertical transition calculated at the B3LYP/6-31G(d) level is 1.01 eV, indicating that the effect of structure optimization is more pronounced than the improvements in basis set. The calculated excitation energy of about 1.0 eV compares well with the 1.13–1.14 eV determined from the phosphorescence spectra in chloronaphthalene as reported by Ricciardi et al.³²

Table 2 summarizes computational predictions of the UV–vis and RSA spectra as a function of the methods employed. The choice of structure and method appears to have a more pronounced effect on spectra than in the case of geometry prediction. The Q and RSA band are more sensitive than the B band. We found that using the PBE- or B3LYP-optimized structure affects the spectra slightly, at most by 10 nm. A similar effect can be seen with the increase of the basis set. A better description of hydrogen atoms, through the use of the p polarization function, seems unimportant, confirming that the main absorption bands originate from the $\pi \rightarrow \pi$ transitions of the phthalocyanine core. The use of singlet-optimized structures in calculating triplet excited states can red-shift the RSA band by up to 20 nm. Comparison with experimental data confirms the well-known significant blue-shift of the UV–vis spectrum.^{15,53,54,56} The Q and B bands are shifted by about 70 and 20 nm, respectively. The triplet–triplet absorption spectrum is composed of three major excitations centered around 500 nm. This is very close to a maximum of broad absorption centered at ~495 nm found from transient absorption spectra attributed to the triplet absorption band.^{21,22}

Table 1. Comparison of Structural Parameters of SiPc-(PEG₇₅)₂ for Various Levels of DFT Theory and Basis Set^b

	X-ray data ^a	singlet PBE/DNP	B3LYP/		triplet PBE/DNP	B3LYP/	
			6-31G(d)	6-311+G(d,p)		6-31G(d)	6-311+G(d,p)
SiN	1.92	1.944	1.943	1.943	1.940	1.939	1.939
NC1	1.375	1.383	1.378	1.377	1.372	1.363	1.361
NC2	1.375	1.383	1.378	1.377	1.404	1.404	1.402
NC3	1.321	1.324	1.321	1.319	1.331	1.329	1.327
NC4	1.321	1.324	1.321	1.319	1.321	1.318	1.315
SiO	1.68	1.729	1.724	1.723	1.736	1.731	1.730
CO		1.414	1.406	1.408	1.413	1.405	1.407
SiOC		128.4	130.0	130.9	127.7	129.5	130.4

^a For SiPc(OSiMe₃)₂ from ref 62. ^b See Figure 1 for the definition of structural parameters. Distances are in Å, angles are in deg.

Table 2. Comparison of Main UV–Vis Excitation Energies (in nm) and Oscillator Strengths (*f*) for SiPc-(PEG₇₅)₂^e

	Q		B	
	Singlet–Singlet Transitions			
experiment ^a	677		354	
B3LYP/6-31G(d) ^b	604(0.37)	592(0.37)	335(0.32)	334(0.44)
B3LYP/6-31G(d)	613(0.37)	600(0.36)	338(0.50)	336(0.54)
B3LYP/6-31G(d,p)	612(0.37)	600(0.36)	337(0.64)	335(0.55)
B3LYP/6-311G(d)	618(0.38)	605(0.37)	338(0.58)	337(0.53)
	Triplet–Triplet Transitions			
experiment ^c	495			
B3LYP/6-31G(d) ^b	595(0.10)	515(0.24)	492(0.30)	463(0.25)
B3LYP/6-311G(d) ^b	598(0.08)	517(0.22)	497(0.21)	469(0.32)
B3LYP/6-31G(d) ^d	619(0.12)	526(0.24)	509(0.21)	478(0.31)
B3LYP/6-311G(d) ^d	622(0.14)	526(0.24)	516(0.11)	488(0.20)
B3LYP/6-31G(d)	605(0.10)	522(0.18)	499(0.29)	468(0.26)
B3LYP/6-311G(d)	607(0.11)	522(0.25)	504(0.19)	
B3LYP/6-31G(d,p)	605(0.10)	522(0.15)	499(0.27)	469(0.28)

^a For SiPc-(PEG₅₅₀)₂ from ref 15. ^b Using B3LYP/6-311+G(d) optimized structure. ^c A broad absorption centered at ~495 nm is assigned to the triplet absorption for SiPc-(X)₂ where X are various axially bonded siloxy ligands.^{21,22} ^d PBE/DNP singlet optimized structure was used. ^e The PBE/DNP structure was used unless specified otherwise.

The character of the investigated singlet–singlet transitions was found to follow approximately the Goutermann's assignments, as observed by the data shown in Table 3. The Q band arises from π transitions from occupied to unoccupied orbitals. The largest contribution to Q excitations comes from HOMO to LUMO and LUMO+1 excitations. These π orbitals are localized in the plane of a phthalocyanine ring. There is also a small contribution from lower occupied orbitals HOMO-6 (*b_u*). This orbital has a significant contribution from π orbitals of PEG's oxygen atom. The B band excitations can be interpreted as excitations from several levels below HOMO to LUMO and LUMO+1 levels. The low lying levels such as HOMO-6 to HOMO-13, both of *b_u* symmetry, have significant contributions from π orbitals of PEG's oxygen atom. Level HOMO-8 (*a_u*) has only a small ligand contribution, and the HOMO-11 (*b_g*) is localized far from the center of the Pc structure. It is interesting that none of the major orbitals contributing to the Q or the B band are significantly affected by the central silicon atom.

The character of transitions in the triplet–triplet spectrum is also presented in Table 3. The π spin orbitals close to the

Table 3. B3LYP/6-31G(d) Calculated Major Excitation Energies (ΔE in nm)^a and Oscillator Strengths (*f*) for the SiPc-(PEG₇₅)₂ Complex at C_{2h} Symmetry

ΔE	<i>f</i>	transition	weight ^b	symmetry
		Singlet→Singlet		
		604		
		H→L	0.603	A _u
		H-6→L+1	0.232	
		592		
		H→L+1	0.606	B _u
		H-6→L	0.240	
		335		
		H-6→L	0.503	B _u
		H-13→L	0.292	
		H-11→L	0.216	
		334		
		H-11→L	0.587	B _u
		H-8→L	0.227	
		H-6→L	0.176	
		333		
		H-6→L+1	0.463	A _u
		H-8→L+1	0.358	
		H-13→L+1	0.311	
		322		
		H-13→L	0.616	B _u
		H-6→L	0.218	
		320		
		H-13→L+1	0.564	A _u
		H-6→L+1	0.277	
		313		
		H→L+4	0.655	A _u
		H-11→L+1	0.134	
		Triplet→Triplet		
		595		
		H→L+1 (α)	0.687	B _u
		H-9→L (β)	0.532	
		515		
		H-7→L (β)	0.820	A _u
		H→L+2 (α)	0.358	
		492		
		H-9→L (β)	0.662	B _u
		H→L+5 (α)	0.570	
		463		
		H→L+5 (α)	0.790	B _u
		H-9→L (β)	0.457	

^a Transitions with oscillator strength (*f*) of 0.1 or larger are shown. ^b The absolute values of weights for major transitions are presented.

HOMO levels in both spin manifolds (α and β) are localized within the phthalocyanine plane. However the HOMO-7 and HOMO-9 β spin orbitals have some contribution from the oxygen atom of the PEG ligand. Apparently, the ligand effect on the RSA spectrum is not significant, which was also observed in studies of silicon phthalocyanines various axially bonded siloxy ligands.^{21,22}

3.2. Structures and Spectra of SiNc. Structures of SiNc, SiNc-(OSi(CH₃)₃)₂, and SiNc-(OH)₂ complexes have been optimized using the PBE/DNP level of theory (Figure 2;

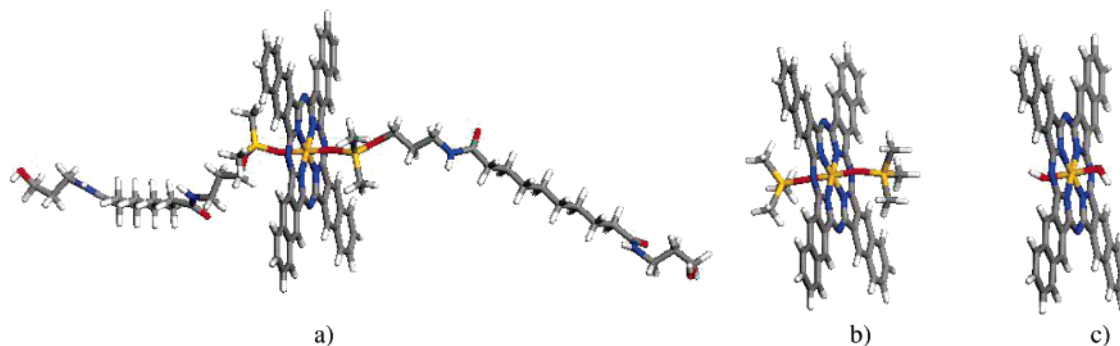


Figure 2. Structure of (a) SINC, (b) SiNc-(OSi(CH₃)₃)₂, and (c) SiNc-(OH)₂.

Table 4. Comparison of Main UV–Vis Excitation Energies (ΔE in nm) and Oscillator Strengths (f) for SINC, SiNc-(OSi(CH₃)₃)₂, and SiNc-(OH)₂ Obtained at the B3LYP/6-31G(d)//PBE/DNP Level

band	SINC ^a	SiNc-(OSi(CH ₃) ₃) ₂	SiNc-(OH) ₂	SiNc-(OH) ₂ ^b
Q	717(0.51)	711(0.53)	713(0.56)	722(0.57)
	715(0.50)	709(0.53)	708(0.55)	717(0.56)
B	431(0.20)	429(0.26)	430(0.20)	433(0.15)
	429(0.17)	428(0.25)	429(0.25)	432(0.23)
	348(0.35)	346(0.39)	348(0.44)	350(0.43)
	347(0.36)	345(0.40)	347(0.36)	349(0.37)
	327(0.51)	326(0.56)	329(0.49)	330(0.52)
	326(0.53)	325(0.57)	328(0.55)	329(0.42)

^a Experimental data for SINC molecule are 778 and 335 nm for the Q and B excitation, respectively.¹² ^b Spectra calculated at the B3LYP/6-311G(d)//PBE/DNP level.

geometry is available as Supporting Information). In the case of SiNc-(OH)₂, both the *C*₁ and *C*_{2h} symmetries were applied. The main structural difference occurs in the dihedral angle involving the position of the hydroxyl group above the SiNc ring. The energy difference between the two structures is about 0.6 kcal/mol, thus, quite insignificant. Table 4 lists B3LYP/6-31G(d)//PBE/DNP primary excitation energies for the SiNc system when various axial substituents are considered. Increasing the basis set to 6-311G(d) causes a minor red shift in the spectra, the largest shift occurring for the Q band at about 8 nm. The three spectra are almost identical, indicating that the nearest environment of the SiNc ring determines the optical properties. The primary geometrical features of the complexes, such as Si–N, are all within 0.01 Å. The central Si–O distance for SINC and SiNc-(OSi(CH₃)₃)₂ are within 0.01 Å, while the Si–O bond length in the case of the SiNc-(OH)₂ complex is slightly longer, at 0.02 Å.

According to the HPA (MPA), the net charge on the central Si atom is 0.435 (2.068), 0.433 (1.792), and 0.412 (1.788) for SINC, SiNc-(OSi(CH₃)₃)₂, and SiNc-(OH)₂ complexes, respectively. Both population analysis schemes indicate a similar electronic environment of the central Si atom for all SiNc complexes considered in this paper.

Experimental data¹² involving SINC dissolved in dimethylformamide (DMF) shows a Q band centered at 778 nm, followed by a transparent region (500–600 nm) and a B (Soret) band located near 335 nm. The characteristic UV–vis absorption maxima of the Q band, Λ_{\max} , for SiNc-(OH)₂

and SiNc[OSi(n-C₆H₁₃)₃]₂ compounds were reported at about 772 nm.⁶³ Spectra calculated at the B3LYP/631G(d) level confirm quite well the experimental position of the B band and the extent of the transparent region (Table 4). However, the Q band is significantly blue-shifted, compared to the experimental data.

All results discussed to this point were obtained in the gas phase and therefore cannot be directly compared with the experimental data. The effect of the solvent, also being systematically analyzed by this group,⁶¹ can be estimated by including explicit water molecules in the calculations for the SiPc-(PEG₇₅)₂ compound. In that case, one observes a small red-shift in the Q band of about 13 nm. A similar effect was recently reported in calculations on the aqueous environment of porphyrazine⁶⁴ using the continuum C-PCM method of solvation. Since the DMF solvent has a dielectric constant of about half that of water, we can expect a much smaller solvent effect in the case of SINC.

Calculations of spectra for the SINC molecule, consisting of 207 atoms, require significant computational resources, particularly if, in addition to UV–vis spectra, calculation of RSA spectra arising from triplet–triplet excitations is performed. It was already noticed that the semiempirical method ZINDO^{55–57} provides a nonexpensive alternative to the calculation of optical properties. Applying the ZINDO method with INDO/2 parametrization we calculated two main excitations at 772 and 768 nm that can be assigned to the Q band. The calculated B band is composed of four major excitations in the range of 353–329 nm. It is apparent that the ZINDO-calculated Q and B bands coincide with experimentally known spectra.

The character of transitions for the major excitation energies of SiNc-(OSi(CH₃)₃)₂ are presented in Table 5. Similarly to the SiPc-(PEG₇₅)₂ transitions, (Table 3) the Q band arises from π excitations, mainly from HOMO to LUMO and LUMO+1. These π orbitals are localized in the plane of a naphthalocyanine ring. There is also a small contribution from the lower occupied orbitals HOMO-8. This orbital has significant contribution from the π orbitals of the ligand's oxygen atom. The B band excitations can be interpreted as excitations from several levels below HOMO to LUMO and LUMO+1 levels. The low lying levels such as HOMO-6 to HOMO-11 have significant contributions from the π orbitals of the ligand's oxygen atom.

The character of transitions in the triplet–triplet spectrum

Table 5. B3LYP/6-31G(d) Calculated Major Excitation Energies (ΔE in nm)^a and Oscillator Strengths (f) for SiNc-(OSi(CH₃)₃)₂

ΔE	f	transition	weight ^b
Singlet→Singlet			
711	0.528	H→L	0.609
		H-8→L+1	0.127
709	0.527	H→L+1	0.610
		H-8→L	0.128
429	0.258	H-1→L	0.564
		H→L+4	0.298
428	0.256	H-1→L+1	0.579
		H→L+5	0.284
346	0.395	H-8→L	0.472
		H-7→L+1	0.345
346	0.391	H-8→L+1	0.480
		H-8→L	0.292
326	0.563	H-10→L	0.382
		H-6→L+1	0.307
325	0.570	H-8→L	0.262
		H-10→L+1	0.363
325	0.570	H-6→L	0.288
		H-8→L+1	0.280
325	0.570	H-11→L+1	0.244
Triplet→Triplet			
693	0.307	H→L (β)	0.885
656	0.128	H→L+5 (α)	0.595
		H-2→L (β)	0.581
587	0.335	H-4→L (β)	0.703
		H→L +5 (α)	0.493
573	0.505	H-4→L (β)	0.562
		H→L+5 (α)	0.505

^a Transitions with oscillator strength (f) of 0.1 or larger are shown.

^b The absolute values of weights for major transitions are presented.

is also analyzed in Table 5. The π spin orbitals close to the HOMO levels in both spin manifolds are localized within the naphthalocyanine ring. However the HOMO-4 β spin orbital has some contribution from the oxygen atom of the ligand's oxygen atom. The main RSA bands of the triplet-triplet spectra calculated here at 573 and 587 nm are very close to these found in laser-induced transient absorptions in the SINC compound.²⁰ It was reported that the triplet-triplet absorption spectrum has a maximum between 590 and 595 nm.²⁰

4. Concluding Remarks

In this paper we have calculated optical properties of phthalocyanine and naphthalocyanine complexes with Si as a central atom. The calculated singlet-singlet excitations were compared with experimentally determined UV-vis spectra.^{15-19,22} The triplet-triplet excitations can be induced by pulsed laser excitations, and they are known to decay with time.²⁰⁻²² A good RSA molecule should exhibit strong $T_1 \rightarrow T_N$ excitations in the transparent region of the spectrum that is bracketed by the B band in the blue region and the Q band in the red region of the UV-vis spectrum.¹¹ By comparing the relative positions of major excitations from the UV-vis and RSA spectra, we can confirm that both silicon-phthalocyanine and -naphthalocyanine compounds

studied in this paper are strong RSA molecules. They offer a transparency in the preferable visual region while exhibiting a strong triplet-triplet absorption band centered between the major Q and B bands of the UV-vis spectrum.

The TDDFT with the B3LYP functional and the 6-31G(d) basis set predicts that the characteristic UV-vis absorption maxima of the Q band, Λ_{\max} , are blue-shifted by about 70 nm, compared to the experimental data.^{53,54,56} The TDDFT method better predicts the position of the B band, with the major peaks appearing at about 330 nm, which is in good agreement with the experiment. Also, the TDDFT-calculated triplet-triplet absorption spectra of Si-phthalocyanine and Si-naphthalocyanine complexes reproduces experimental data very well.²⁰⁻²² The main peaks of the B and RSA bands are calculated within 20 nm of experimental data.

We found that using PBE-optimized geometry, followed by absorption spectra calculations with B3LYP, may result in a small blue-shift of the Q and RSA band by, at most, 10 nm. This is a useful finding because geometry calculations at the GGA level can be performed more efficiently than they can be with a hybrid functional.^{26-28,43} In agreement with earlier reports,^{56,57} we also found that using the ZINDO approach at the DFT-optimized geometry results in the large red-shift of the Q-band position and significant improvement of calculated results as compared with experimental data.

The effect of using triplet-optimized structures in predicting $T_1 \rightarrow T_N$ excitations was also investigated. The vertical $S_0 \rightarrow T_1$ splitting was calculated at 1.01 and 0.81 eV for SiPc-(PEG₇₅)₂ and SiNc-(OSi(CH₃)₃)₂, respectively. The adiabatic splitting was not much different at 0.98 and 0.77 eV, respectively. The calculated values compare reasonably well with reported experimental data of 1.13 and 0.93 eV for the phthalocyanine³² and naphthalocyanine²⁰ complexes, respectively. The position of main peaks in the RSA spectrum changed by about 20 nm by using the adiabatic vs vertical approach.

In agreement with experimental reports, the TDDFT/B3LYP approach confirms the small effect on spectra of axial substituents for silicon-phthalocyanine and naphthalocyanine compounds.^{15,22} The major effect on spectra occurs with increased linear benzoannulation of porphyrazine. It is well-known that the Q and RSA bands become red-shifted in going from the Pc to Nc compounds.^{17-19,23,63} The HOMO level is destabilized, and, consequently, the band gap decreases.⁶⁵ Present calculations clearly reproduce this effect, with the band gap decreasing from about 1.4 to 1.1 eV, respectively. The TDDFT/B3LYP calculations lead to an almost constant error in Λ_{\max} of about 70 and 60 nm for the silicon-phthalocyanine and naphthalocyanine compounds.

Results of this investigation improve our understanding of the role of axial substituents for phthalocyanine and naphthalocyanine compounds and provide validation for the TDDFT approach that can be used for prediction of optical properties of larger Nc compounds. Additional, such studies can aid in synthetic possibilities for naphthalocyanine complexes having desirable optical properties.

Acknowledgment. The authors are indebted to Andrew G. Mott, Robert C. Hoffman, Timothy M. Pritchett, and

Michael J. Ferry for intellectual discussions and insight into this research. Computational resources of ARL and ASC MSRC are gratefully acknowledged. K.K.B. is grateful to the Swiss National Science Foundation for support of this research.

Supporting Information Available: Tables of optimized atomic coordinates for the SiNc species. This material is available free of charge via the Internet at <http://pubs.acs.org>.

References

- Erk, P.; Hengelsberg, In *The Porphyrin Handbook*; Kadish, K. M., Smith, K. M., Guillard, R., Eds.; Elsevier Science: Amsterdam, 2003; Vol. 19, pp 105–150.
- Gregory, P. *Porphyrins Phthalocyanines* **2000**, *4*, 432.
- Eichhorn, H. J. *Porphyrins Phthalocyanines* **2000**, *4*, 88.
- Sadaoka, Y.; Gopel, T. A.; Jones, W. *Sens. Actuators, B* **1990**, *1*, 148.
- Flom, S. R. In *The Porphyrin Handbook*; Kadish, K. M., Smith, K. M., Guillard, R., Eds.; Elsevier Science: Amsterdam, 2003; Vol. 19, pp 179–190.
- Hasrar, H.; van Lier, J. E. *Chem. Rev.* **1999**, *99*, 2379.
- Sheehy, B.; Di Mauro, L. F. *Ann. Rev. Phys. Chem.* **1996**, *47*, 463–494.
- Mckeown, N. B. *Phthalocyanine Materials: Synthesis, Structure and Function*; Cambridge University Press: 1998.
- Coulter, D. R.; Miskowski, V. M.; Perry, J. W.; Wei, T. H.; Stryland, E. W. V.; Hagan, D. J. In *Materials for Optical Switches, Isolators and Limiters; Proceedings of SPIE*; 1989; Vol. 1105, pp 42–52.
- Torre, G.; Vazquez, P.; Agullo-Lopez, F.; Torres, T. *Chem. Rev.* **2004**, *104*, 3723–3750.
- Perry, J. W. In *Nonlinear Optics of Organic Molecules and Polymers*; Nalwa, H. S., Miyata, S., Eds.; CRC Press: Boca Raton, FL, 1997; pp 813–840.
- Wang, N. Q.; Cai, Y. M.; Heflin, J. R.; Wu, J. W.; Rodenberger, D. C.; Garito, A. F. In *Sol-Gel Optics; Proceedings of SPIE*; 1990; Vol. 1328, pp 100–107.
- Ngai, T.; Zhang, G.; Li, X.; Ng, D. K. P.; Wu, C. *Langmuir* **2001**, *17*, 1381–1383.
- Shirk, J. S.; Pong, R. G. S.; Flom, S. R.; Heckmann, H.; Hanack, M. *J. Phys. Chem. A* **2000**, *104*, 1438–1449.
- Huang, J.-D.; Wang, S.; Lo, P.-C.; Fong, W.-P.; Ko, W.-H.; Ng, D. K. P. *New. J. Chem.* **2004**, *28*, 348–354.
- Dominguez, D. D.; Snow, A. W.; Shirk, J. S.; Pong, G. S. *J. Porphyrins Phthalocyanines* **2001**, *5*, 582–592.
- Pop, D.; Winter, B.; Freyer, W.; Hertel, I. V.; Widdra, W. *J. Phys. Chem. B* **2003**, *107*, 11643–11647.
- Pop, D.; Winter, B.; Freyer, W.; Widdra, W. J.; Hertel, I. V. *J. Phys. Chem. B* **2004**, *108*, 9158–9167.
- Pop, D.; Winter, B.; Freyer, W.; Widdra, W. J.; Hertel, I. V. *J. Phys. Chem. B* **2005**, *109*, 7826–7833.
- Firey, P. A.; Ford, W. E.; Sounik, J. R.; Kenney, M. E.; Rodgers, M. A. J. *J. Am. Chem. Soc.* **1988**, *110*, 7626–7630.
- Pelliccioli, A. P.; Henbest, K.; Kwag, G.; Carvagno, T. R.; Kenney, M. E.; Rodgers, A. J. *J. Phys. Chem. A* **2001**, *105*, 1757–1766.
- Anula, H. M.; Berlin, J. C.; Wu, H.; Li, Y.-S.; Peng, X.; Kenney, M. E.; Rodgers, M. A. J. *J. Phys. Chem. A* **2006**, *110*, 5215–5223.
- Rogers, J. E.; Nguyen, K. A.; Hufnagle, D. C.; McLean, D. G.; Su, W.; Gossett, K. M.; Burke, A. R.; Vinogradov, S. A.; Pachter, R.; Fleitz, P. A. *J. Phys. Chem. A* **2003**, *107*, 11331–11339.
- Calvete, M. J. F.; Dini, D.; Flom, R. S.; Hanack, M.; Pong, R. G. S.; Shirk, J. S. *Eur. J. Org. Chem.* **2005**, 3499–3509.
- Marino-Ochoa, E.; Palacios, R.; Kodis, G.; Macpherson, A.; Gillbro, T.; Gust, D.; Moore, T. A.; Moore, A. L. *Photochem. Photobiol.* **2002**, *76*, 116–121.
- Dunlap, B. I.; Connolly, J. W. D.; Sabin, J. R. *J. Chem. Phys.* **1979**, *71*, 3396–3402.
- Baerends, E. J.; Ellis, D. E.; Ros, P. *Chem. Phys.* **1973**, *2*, 41–51.
- Salahub, D. R.; Fournier, R.; Mlynarski, P.; Papai, I.; St-Amant, A.; Ushio, J. In *Density Functional Methods in Chemistry*; Labanowski, J., Andzelm, J., Eds.; Springer-Verlag: New York, 1991; pp 77–100.
- Gross, E. K. U.; Kohn, W. *Adv. Quantum Chem.* **1990**, *21*, 255.
- Casida, M. E.; Jamorski, C.; Casida, K. C.; Salahub, D. R. *J. Chem. Phys.* **1998**, *108*, 4439–4449.
- Nguyen, K. A.; Day, P. N.; Pachter, R. *J. Chem. Phys.* **1999**, *110*, 9135–9144.
- Ricciardi, G.; Rosa, A.; Baerends, E. J. *J. Phys. Chem. A* **2001**, *105*, 5242–5254.
- Liao, M.-S.; Watts, J. D.; Huang, M.-J. *Inorg. Chem.* **2004**, *44*, 1941–1949.
- Wu, D.-S.; Cheng, W.-D.; Li, X.-D.; Lan, Y.-Z.; Chen, D.-G.; Zhang, Y.-C.; Zhang, H.; Gong, Y.-J. *J. Phys. Chem. A* **2004**, *118*, 1837–1843.
- Liao, M.-S.; Watts, J. D.; Huang, M.-J.; Gorun, S. M.; Kar, T.; Scheiner, S. J. *Chem. Theory. Comput.* **2005**, *1*, 1201–1210.
- Zhang, Y.; Zhang, X.; Liu, Z.; Bian, Y.; Jiang, J. *J. Phys. Chem. A* **2005**, *109*, 6363–6370.
- Gunaratne, T. C.; Gusev, A. V.; Peng, X.; Rosa, A.; Ricciardi, G.; Baerends, E. J.; Rizzoli, C.; Kenney, M. E.; Rodgers, M. A. J. *J. Phys. Chem. A* **2005**, *109*, 2078–2089.
- Nguyen, K. A.; Day, P. N.; Pachter, R. *J. Phys. Chem. A* **2000**, *104*, 4748–4754.
- Kyrychenko, A.; Andreasson, J.; Martensson, J.; Albinsson, B. *J. Phys. Chem. B* **2002**, *106*, 12613–12622.
- Gouterman, M.; Wagniere, G. H.; Snyder, L. C. *J. Mol. Spectrosc.* **1963**, *11*, 108.
- Toyota, K.; Hasegawa, J.; Nakatsuji, H. *J. Phys. Chem. A* **1997**, *101*, 446–451.
- Baerends, E. J.; Ricciardi, G.; Rosa, A.; van Gisbergen, S. J. A. *Coord. Chem. Rev.* **2002**, *230*, 5–27.
- Delley, B. *J. Chem. Phys.* **2000**, *113*, 7756–7764.
- Schmidt, M. W.; Baldridge, K. K.; Boatz, J. A.; Elbert, S. T.; Gordon, M. S.; Jensen, J. H.; Koseki, S.; Matsunaga, N.; Nguyen, K. A.; Su, S.; Windus, T. L.; Dupuis, M.; Montgomery, J. A. *J. Comput. Chem.* **1993**, *14*, 1347–1363.

- (45) Frisch, M. J.; Trucks, G. W.; Schlegel, H. B.; Scuseria, G. E.; Robb, M. A.; Cheeseman, J. R.; Montgomery, J. A., Jr.; Vreven, T.; Kudin, K. N.; Burant, J. C.; Millam, J. M.; Iyengar, S. S.; Tomasi, J.; Barone, V.; Mennucci, B.; Cossi, M.; Scalmani, G.; Rega, N.; Petersson, G. A.; Nakatsuji, H.; Hada, M.; Ehara, M.; Toyota, K.; Fukuda, R.; Hasegawa, J.; Ishida, M.; Nakajima, T.; Honda, Y.; Kitao, O.; Nakai, H.; Klene, M.; Li, X.; Knox, J. E.; Hratchian, H. P.; Cross, J. B.; Bakken, V.; Adamo, C.; Jaramillo, J.; Gomperts, R.; Stratmann, R. E.; Yazyev, O.; Austin, A. J.; Cammi, R.; Pomelli, C.; Ochterski, J. W.; Ayala, P. Y.; Morokuma, K.; Voth, G. A.; Salvador, P.; Dannenberg, J. J.; Zakrzewski, V. G.; Dapprich, S.; Daniels, A. D.; Strain, M. C.; Farkas, O.; Malick, D. K.; Rabuck, A. D.; Raghavachari, K.; Foresman, J. B.; Ortiz, J. V.; Cui, Q.; Baboul, A. G.; Clifford, S.; Cioslowski, J.; Stefanov, B. B.; Liu, G.; Liashenko, A.; Piskorz, P.; Komaromi, I.; Martin, R. L.; Fox, D. J.; Keith, T.; Al-Laham, M. A.; Peng, C. Y.; Nanayakkara, A.; Challacombe, M.; Gill, P. M. W.; Johnson, B.; Chen, W.; Wong, M. W.; Gonzalez, C.; Pople, J. A. *Gaussian 03, Revision C.02*; Gaussian, Inc.: Wallingford, CT, 2004.
- (46) Perdew, J. P.; Burke, K.; Ernzerhof, M. *Phys. Rev. Lett.* **1996**, *77*, 3865–3868; **1997**, *78*, 1396–1396.
- (47) Delley, B. *J. Chem. Phys.* **1990**, *92*, 508–517.
- (48) Francl, M. M.; Petro, W. J.; Hehre, W. J.; Binkley, J. S.; Gordon, M. S.; DeFrees, D. J.; Pople, J. A. *J. Chem. Phys.* **1982**, *77*, 3654–3665.
- (49) Becke, A. D. *J. Chem. Phys.* **1993**, *98*, 5648–5652.
- (50) Stratmann, R. E.; Scuseria, G. E.; Frisch, M. J. *J. Chem. Phys.* **1998**, *109*, 8128–8224.
- (51) Baker, J.; Scheiner, A.; Andzelm, J. *Chem. Phys. Lett.* **1993**, *216*, 380.
- (52) Petit, L.; Quartarolo, A.; Adamo, C.; Russo, N. *J. Phys. Chem. B* **2006**, *110*, 2398–2404.
- (53) Infante, I.; Lelj, F. *Chem. Phys. Lett.* **2003**, *367*, 308–318.
- (54) Dreuw, A.; Head-Gordon, M. *Chem. Rev.* **2005**, *105*, 4009–4037.
- (55) Ridley, J.; Zerner, M. *Theor. Chim. Acta* **1973**, *32*, 111–134.
- (56) Zhou, X.; Ren, A.-M.; Feng, J.-K.; Liu, X.-J. *Can. J. Chem.* **2004**, *82*, 19–26.
- (57) Chen, L. X.; Shaw, G. B.; Tiede, D. M.; Zuo, X.; Zapol, P.; Redfern, P. C.; Curtiss, L. A.; Sooksimuang, T.; Mandal, B. K. *J. Phys. Chem. B* **2005**, *109*, 16598–16609.
- (58) Hirshfeld, F. L. *Theor. Chim. Acta B* **1977**, *44*, 129.
- (59) Mulliken, R. S. *J. Chem. Phys.* **1955**, *23*, 1833.
- (60) Roy, R. K.; Bagaria, P.; Naik, S.; Kavala, V.; Patel, B. K. *J. Phys. Chem. A* **2006**, *110*, 2181–2187.
- (61) To be published in the ARL Technical Report.
- (62) Mooney, J. R.; Choy, C. K.; Knox, K.; Kenney, M. E. *J. Am. Chem. Soc.* **1975**, *97*, 3033–3038.
- (63) Wheeler, B. L.; Nagasubramanian, G.; Bard, A. J.; Schechtman, L. A.; Dininny, D. R.; Kenney, M. E. *J. Am. Chem. Soc.* **1984**, *106*, 7404–7410.
- (64) Petit, L.; Quartarolo, A.; Adamo, C.; Russo, N. *J. Phys. Chem. B* **2006**, *110*, 2398–2404.
- (65) Orti, E.; Piqueras Cresp, R.; Bredas, J. L. *Chem. Mater.* **1990**, *2*, 110–116.

CT700017B

Dissociative Adsorption of Hydrogen and Oxygen on Palladium Clusters: A Comparison with the (111) Infinite Surface[†]

Jérôme Roques,[‡] Corinne Lacaze-Dufaure,[§] and Claude Mijoule^{*§}

Université Paris-Sud 11 Institut de Physique Nucléaire 15, rue Georges Clemenceau, Bat 100, bureau M 249, 91406 Orsay, Cedex, France, and Centre Interuniversitaire de Recherche et d'Ingénierie des Matériaux (C.I.R.I.M.A.T), 118 route de Narbonne, 31077 Toulouse, Cedex 4, France

Received December 19, 2006

Abstract: We report a density-functional study of some properties of the dissociative interaction of hydrogen and oxygen molecules on small palladium clusters ($n = 5, 7,$ and 10). The calculated physisorption and chemisorption energies are compared with those of the infinite (111) palladium surface. First, adsorption of atomic hydrogen and oxygen is investigated on the Pd₅, Pd₇, and Pd₁₀ clusters. Second, the interaction between H₂ (O₂) and the small Pd₅ cluster is examined and compared to the process occurring on an infinite (111) surface. Finally, the simultaneous adsorption of two hydrogen (oxygen) atoms is analyzed in detail. As shown in a previous work, the binding energy of the first hydrogen (oxygen) atom does not depend significantly on the cluster size, and small two-layer clusters ($n \leq 10$) can be used to determine with accuracy the interaction of atomic adsorbates with an infinite (111) palladium surface. In this study, we show that the dissociative chemisorption of H₂ and more especially of O₂ on a small palladium cluster may lead to erroneous binding energy: the cluster's size may prevent an accurate description of the adsorbate–adsorbate interaction as a function of their distance. It is demonstrated that a good choice of both the size and the shape of the cluster is preponderant for a good description of the dissociative adsorption of H₂ and O₂ on an infinite (111) surface.

I. Introduction

Because of their importance in the field of catalysis, the interaction of hydrogen and oxygen species with palladium surfaces is of prime interest. In the past, the adsorption of atomic and molecular hydrogen on the (111) palladium surface was largely investigated by experimental approaches.^{1–7} These studies examined atomic hydrogen chemisorption, and it was found that the most favorable adsorption site on the Pd(111) surface is the threefold hollow surface site above

the third-layer metal atoms (fcc site).^{1,4,6} Mitsui et al. determined an energetic barrier of 0.09 eV for the diffusion of an individual H atom on the Pd(111) surface.⁶ The adsorption of H₂ was also investigated.^{1,3,5} Christmann et al. and Conrad et al. concluded to a dissociative adsorption of H₂ on Pd(111) with an initial adsorption energy of 0.90 eV.^{1,3} Resch et al. also predicted, at low initial beam energies, an indirect dissociation pathway via a molecular precursor state, and the activation energy for the dissociation was estimated to be around 0.05 eV.⁵ At higher beam energies a direct activated dissociative process was observed.⁵ More recently, Mitsui et al. showed by tunneling microscopy observations that aggregates of at least three hydrogen vacancies are required for efficient H₂ dissociation on Pd(111).⁷

The adsorption of atomic hydrogen on the (111) palladium surface was also theoretically investigated using clusterlike

[†] Dedicated to Professor Dennis R. Salahub on the occasion of his 60th birthday.

^{*} Corresponding author fax: 33 5 62 88 56 00; e-mail: Claude.Mijoule@ensiacet.fr.

[‡] Université Paris-Sud 11 Institut de Physique Nucléaire 15.

[§] Centre Interuniversitaire de Recherche et d'Ingénierie des Matériaux (C.I.R.I.M.A.T).

approaches^{3,8–11} and slab approaches^{12–19} in the framework of the density functional theory. All these studies pointed out that the H atoms adsorb preferentially on threefold hollow sites, and the fcc site was determined as the more stable adsorption site.^{10,12–19} The adsorption of the H₂ molecule on small Pd_{*n*} (*n* = 1–6) clusters was also studied by DFT calculations,^{20–22} and several local minima were found. They correspond to H₂ physisorption and other dissociative adsorption modes on the Pd_{*n*} clusters. Periodic calculations showed the H₂ molecule dissociation on the Pd(111) surface.^{23,24} Both activated and nonactivated pathways were found.²³ When the dissociation process is activated, the activation energy remains small (~0.05 eV), in agreement with the experimental evidence.

Concerning oxygen species, experimental studies were first carried out on the adsorption of atomic oxygen on the Pd(111) surface.^{25–28} The threefold adsorption sites are found to be the most stable ones (fcc or hcp sites favored, depending on the authors),^{25,27,28} and the Pd(111) surface relaxation upon O adsorption is found negligible.²⁸ The activation barrier for the diffusion of O atoms on the Pd(111) surface is small.²⁵ Experimental data are also available for O₂ adsorption/desorption and dissociation on Pd(111).^{25,26,29,30} Experiments predict a complex adsorption mechanism consisting of a physisorbed and up to three molecular precursor states. At temperatures below 200 K, several molecular O₂ precursors adsorbed on the surface were characterized. Thus the O₂ adsorption process does not proceed in a single step but through a sequence of several well-defined peroxy molecular precursors followed by the dissociation to atomic oxygen at around 200 K.^{26,29,30} Guo et al. measured the desorption temperature and desorption energy E_d of three molecular precursors ($T = 125$ K and $E_d = 0.33$ eV; $T = 150$ K and $E_d = 0.40$ eV; $T = 200$ K and $E_d = 0.53$ eV).²⁶ An activation energy of 2.38 eV was measured for the associative desorption of the O atoms at 800 K.^{25,26} Nolan et al. used EELS and molecular beam techniques to investigate O₂ adsorption on Pd(111) at high energy beam.²⁹ They found a direct molecular chemisorption mechanism at 77 K. Sjövall et al. showed at low coverage that O₂ dissociation is always precursor mediated.³⁰ At low energies, they characterized a physisorbed state prior to the molecular chemisorption. At high beam energies, direct activated adsorption into a chemisorbed molecular precursor state was observed, in agreement with the study of Nolan et al. The adsorption of atomic oxygen was also theoretically investigated on small Pd_{*n*} clusters^{10,31} and on the Pd(111) surface using slab approaches.^{32,33} The fcc adsorption site is predicted to be the most stable site for O adsorption on Pd(111), with an adsorption energy difference between the fcc and hcp sites of 0.2 eV.^{32,33}

In the case of O₂ on Pd(111), several adsorption pathways depending on the initial adsorption position of O₂ on the surface were explored.^{31,32,34–36} Honkala et al. and Eichler et al. found three O₂ molecular states adsorbed on the surface^{32,35} and related them to experimental evidence^{26,29,30} using their vibrational frequencies: the superoxo state was attributed to the top-bridge-top (first O-position of the mass center-second O) adsorption geometry and the peroxy-I to

the top-fcc(or hcp)-bridge adsorption geometries that presented degenerated O₂ adsorption energies. None of the calculated O₂/Pd(111) configuration could be related to the third precursor state (peroxy-II) which was experimentally identified.

In the present paper, we first consider the adsorption and diffusion of atomic hydrogen and atomic oxygen on Pd_{*n*} (*n* = 5, 7, 10) clusters (section III). The interaction of H₂ and O₂ molecules with the small Pd₅ clusters is therefore investigated (section IV). It is followed by the study of successive adsorption of two hydrogen or oxygen atoms to examine the chemisorbed H–H and O–O interactions on the (111) surface (section V). We compare our results with results from periodic calculations or experimental investigations for the infinite (111) surface.

II. Method of Calculation

Our calculations are based on the density-functional theory and performed in the framework of the LCGTO-MCP-LSD method incorporated in the deMon program package release 3.3.^{37–38} The Vosko-Wilk-Nusair local potential³⁹ is used, and the nonlocal gradient-based corrections of Perdew^{40–42} are added for the exchange and correlation terms. We use a 16-electron relativistic model core potential⁴³ for the palladium atoms. The valence 4p, 4d, and 5s electrons are treated explicitly with a (2211/2111/121) orbital basis set. A corresponding (3,4;3,4) auxiliary basis set is used for the fits of the charge density and the exchange-correlation potential. The H and O atoms are described by the (41/1*) and (5211/411/1) orbital basis sets and the corresponding (4,2;4,2) and (5,2;5,2) auxiliary basis sets, respectively.

Small Pd_{*n*} clusters (*n* = 5, 7, 10) are used in this study to investigate the adsorption of H₂ and O₂ as well as the chemisorbed H–H and O–O interactions on the (111) surface. In order to compare our results with those of an infinite (111) surface, the Pd–Pd interatomic distances are frozen at the experimental bulk value, $d(\text{Pd–Pd}) = 2.75$ Å. The calculations are done with spin polarized wave functions. It is shown that the most stable spin states for each system have a multiplicity of $m = 1$ for Pd_{*n*}, H₂, and Pd_{*n*}H₂; $m = 2$ for Pd_{*n*}H; and $m = 3$ for O, O₂, Pd_{*n*}O, and Pd_{*n*}O₂. In order to describe the electron transfer during the adsorption process, a Mulliken population analysis is done for each system.

III. Atomic Adsorption on Small Two-Layer Pd_{*n*} Clusters

In a first step, we study the chemisorption process of atomic hydrogen and oxygen on the surface of the clusters. The effects of the size of the cluster and of the nature of the adsorption site are reported together with the equilibrium Pd–O bond lengths and the activation energies for the diffusion on the surface.

The size effects are studied by using small two-layer Pd_{*n*} clusters (*n* = 5, 7, 10). These clusters are shown in Figure 1. Three different adsorption sites are studied labeled “h” and “f” for the adsorption on threefold hollow hcp and fcc sites, respectively, and “b” for the adsorption on bridge sites (see Figure 1). In each case, the adsorbate-cluster surface

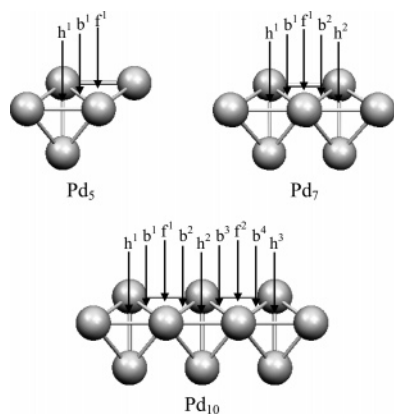


Figure 1. Small palladium clusters used for the study of adsorption of atomic and molecular species on threefold hcp (h), threefold fcc (f), and bridge (b) sites.

Table 1. H Adsorption on hcp, fcc, and Bridge Sites of the Pd₅, Pd₇, and Pd₁₀ Clustersⁱ

	site	E_{ads}	$d(\text{Pd}-\text{H})$	$q(\text{H})$
Pd ₅ H	h ¹	-2.96	1.79	-0.12
Pd ₅ H	b ¹	-2.73	1.71	-0.07
Pd ₅ H	f ¹	-2.94	1.79	-0.13
Pd ₇ H	h ¹ or h ²	-2.91	1.80	-0.13
Pd ₇ H	b ¹ or b ²	-2.68	1.72	-0.09
Pd ₇ H	f ¹	-2.83	1.79	-0.13
Pd ₁₀ H	h ¹ or h ³	-2.87	1.80	-0.12
Pd ₁₀ H	h ²	-2.86	1.79	-0.15
Pd ₁₀ H	b ¹ or b ⁴	-2.70	1.71	-0.07
Pd ₁₀ H	b ² or b ³	-2.73	1.71	-0.08
Pd ₁₀ H	f ¹ or f ²	-2.84	1.79	-0.14
experimental		-2.68 ^a		
other computa-	hcp	-3.8 to -3.4 ^b		
tions	hcp	-2.82 ^c		
	fcc/hcp/bridge	-2.65/-2.59/-2.45 ^d		
	fcc/hcp/bridge	-2.69/-2.60/-2.60 ^e		
	fcc/hcp/bridge	-2.73/-2.67/-2.55 ^f		
	fcc/hcp/bridge	-2.79/-2.74/-2.61 ^g		
	fcc/hcp/bridge	-2.73/-2.69/-2.58 ^h		
	fcc/hcp/bridge	-2.57/-2.49/-2.35 ⁱ		

^a Reference 2. ^b Reference 9 (cluster approach). ^c Reference 11 (cluster approach). ^d Reference 12 (periodic computations). ^e Reference 13 (periodic computations). ^f Reference 14 (periodic computations). ^g Reference 15 (periodic computations). ^h Reference 18 (periodic computations). ⁱ Reference 19 (periodic computations). ^j E_{ads} is the adsorption energy (in eV), $d(\text{Pd}-\text{H})$ is the distance between the hydrogen atom and the nearest Pd neighbor (in Å), and $q(\text{H})$ is the hydrogen Mulliken net charge.

distance is optimized. Adsorption energies E_{ads} are calculated by using the equation

$$E_{\text{ads}} = E(\text{Pd}_n\text{X}) - [E(\text{X}) + E(\text{Pd}_n)] \quad (1)$$

where $\text{X} = \text{H}$ or O , and $E(\text{X})$, $E(\text{Pd}_n)$, and $E(\text{Pd}_n\text{X})$ are the DFT total energies of X , Pd_n , and Pd_nX systems. Adsorption energies of atomic hydrogen on Pd_n are given in Table 1; the most favorable structures correspond to the H adsorption on fcc or hcp sites without any significant energy gap between both sites ($\Delta E_{\text{ads}} = 0.02-0.08$ eV). The adsorption on a bridge site is less favorable and corresponds to a diffusion barrier between two adjacent threefold sites. The

Table 2. O Adsorption on hcp, fcc, and Bridge Sites of the Pd₅, Pd₇, and Pd₁₀ Clusters^c

	site	E_{ads}	$d(\text{Pd}-\text{O})$	$q(\text{O})$
Pd ₅ O	h ¹	-3.67	2.11	-0.53
Pd ₅ O	b ¹	-3.50	2.03	-0.50
Pd ₅ O	f ¹	-3.96	2.11	-0.55
Pd ₇ O	h ¹ or h ²	-3.77	2.11	-0.54
Pd ₇ O	b ¹ or b ²	-3.38	2.04	-0.52
Pd ₇ O	f ¹	-3.79	2.11	-0.50
Pd ₁₀ O	h ¹ or h ³	-3.79	2.11	-0.58
Pd ₁₀ O	h ²	-3.74	2.12	-0.48
Pd ₁₀ O	b ¹ or b ⁴	-3.36	2.03	-0.50
Pd ₁₀ O	b ² or b ³	-3.29	2.05	-0.48
Pd ₁₀ O	f ¹ or f ²	-3.66	2.10	-0.50
other computa-	hollow/bridge	-3.51/-3.34 ^a		
tions	hcp/fcc/bridge	-3.41/-3.60/-3.05 ^b		

^a Reference 31 (periodic computations). ^b Reference 32 (periodic computations). ^c E_{ads} is the adsorption energy (in eV), $d(\text{Pd}-\text{O})$ is the distance between the oxygen atom and the nearest Pd neighbor (in Å), and $q(\text{O})$ is the oxygen Mulliken net charge.

activation energy is of the order of 0.25 eV showing that one hydrogen atom can easily diffuse over an (111) palladium surface. All calculated adsorption energies depend weakly on the size of the cluster showing that the H-surface interaction is localized. Furthermore the cluster-H distances remain almost constant for the same types of adsorption sites, ~ 0.82 Å (fcc and hcp) and ~ 1.02 Å (bridge) as well as the hydrogen net charge which is of $0.12-0.15 e^-$ for adsorption on fcc or hcp sites and $0.08 e^-$ on bridge sites. In the case of atomic oxygen adsorption (Table 2) the most favorable structures correspond also to the adsorption on fcc and hcp sites. The adsorption on a bridge site is about 0.2–0.5 eV higher in energy. The cluster-O distances are almost unchanged for the same types of adsorption sites, ~ 1.39 Å (fcc and hcp) and ~ 1.50 Å (bridge). The electronic transfer from the cluster to the adsorbate is significant. The oxygen net charge is around $0.50-0.55 e^-$ for adsorption on fcc or hcp sites and $0.50 e^-$ on bridge ones. The diffusion barrier between two adjacent hollow sites is of the order 0.20–0.50 eV. As for hydrogen, various properties of O adsorption are nearly size independent, showing that the O–Pd surface interaction is localized.

IV. Molecular Adsorption on Small Two-Layer Pd_n Clusters

Here we turn our attention to the study of the molecular interaction of H₂ and O₂ with a small two-layer Pd₅ cluster, and we discuss the meaning of differences between a cluster-like approach and periodic calculations or experimental investigations on the infinite Pd(111) surface. To do this, we chose to investigate the adsorption process of H₂ and O₂ following the pathway corresponding to an initial fcc-hcp orientation of the diatomic molecule over the cluster's surface (Figure 2). We restrain our study to a two-dimensional potential where both variables are the X–X bond length r and the Pd surface–X₂ distance z . Thus the adsorption energies are given by

$$E_{\text{ads}}(r,z) = E(\text{Pd}_n\text{X}_2)(r,z) - [E(\text{Pd}_n) + E(\text{X}_2)] \quad (3)$$

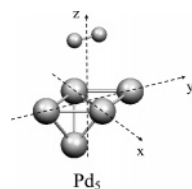


Figure 2. Initial adsorption position of H₂ and O₂ on the Pd₅ cluster.

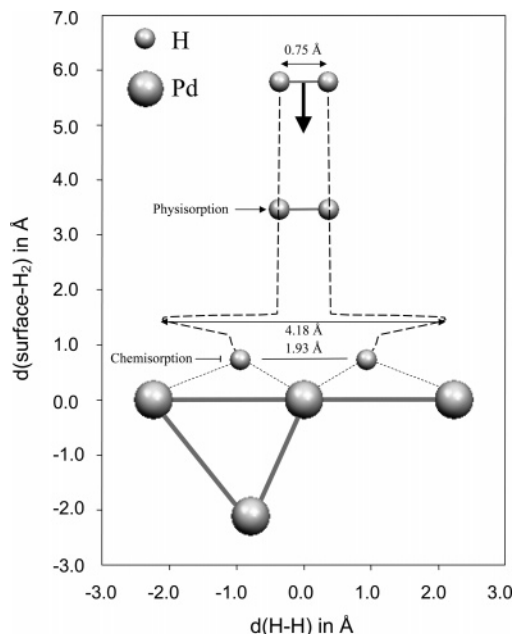


Figure 3. H–H equilibrium distances (Å) as a function of the surface-H₂ distances (Å) for the adsorption pathway displayed in Figure 2. Large circles are Pd atoms and small ones, H atoms.

where X₂ is H₂ or O₂, and then $E(X_2)$ is the total energy of the X₂ molecule in the gas phase. The diatomic molecule center of mass is positioned over a bridge site, while both adsorbate atoms are respectively over an fcc and hcp adsorption site (Figure 2). Such an approach is chosen because for example previous theoretical studies concerning the dissociative adsorption of H₂ on Pd(100) surfaces showed that a rotation of the hydrogen molecule out of a plane parallel to the surface increases the energy.⁴⁵ Thus the diatomic molecule axis is kept parallel to the cluster surface and perpendicular to the Pd–Pd bond (Figure 2). The molecule is moved toward the cluster's surface following the z-axis, and the H–H bond length is optimized for each surface–adsorbate distance. The corresponding adsorption pathways are displayed in Figures 3 and 4.

IV.1. H₂ Adsorption on Pd₅. Figure 3 shows the variation of the H–H bond length r when H₂ is moved toward the cluster surface. All the properties associated with the precursor state, transition state, and chemisorbed state are summarized in Table 3. When $z = 3.42$ Å, the H₂ molecule stabilizes in a precursor state. In this state, no electron transfer between the cluster and the adsorbate is observed, and r remains equal to 0.75 Å (Figure 3, Table 3). The H–H Mayer bond order is equal to 1, and no chemical bond is formed between the adsorbate and the substrate. Therefore, this

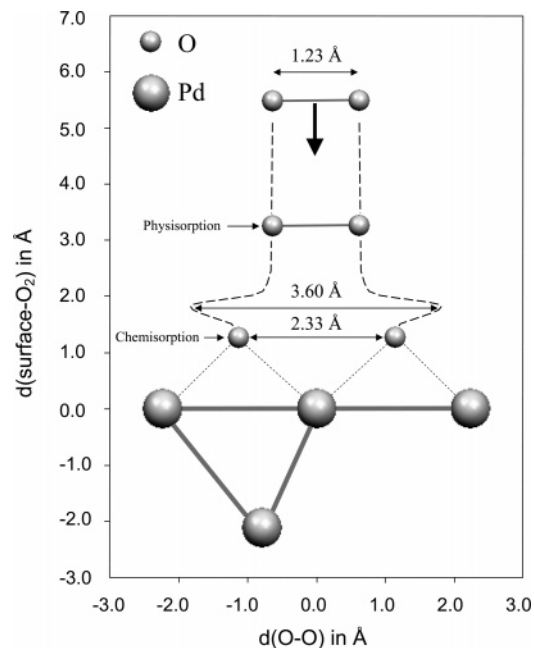


Figure 4. O–O equilibrium distances (Å) in function of the surface-O₂ distances (Å) for the adsorption pathway displayed in Figure 2. Large circles are Pd atoms and small ones, O atoms.

Table 3. Various Parameters of the Adsorption Process of H₂ and O₂ on the Pd₅ Cluster

	H ₂			O ₂		
	phys.	TS	chem.	phys.	TS	chem.
r (Å)	0.75	0.90	1.93	1.23	1.25	2.33
z (Å)	3.42	1.45	0.84	3.20	1.95	1.39
BO(X–X)	1.0	1.0	0.10	2.0	2.0	1.20
$q(X)$ (au)	0.0	0.0	–0.13	0.0	0.0	–0.72
energy (eV)	–0.06	0.15	–0.91	–0.42	0.31	–0.29

precursor state can be identified as the physisorption of H₂ on the cluster surface. The physisorption energy E_{phys} is small and equal to –0.06 eV on Pd₅ (see Table 3). When H₂ continues to move toward the cluster surface, a transition state is observed whose energy is equal to +0.15 eV on Pd₅ (Table 3). It corresponds to an activation energy of 0.21 eV. The (H–H) bond length r increases slightly to 0.90 Å, and the bond order remains equal to 1. No charge transfer is observed between the molecule and the cluster. At $z_{\text{J}} = 1.59$ Å a sharp transition is observed. z_{J} corresponds to the edge of the jellium which would represent the metal in a simple metal-like description; it is equal to the distance between two (111) planes. Thus H₂ is dissociated when placed in a region of high electronic density. Each H atom is screened by the electron density of the cluster. The electrostatic repulsion leads to a H–H distance of 4.18 Å. Finally, when z continues to decrease, the H–Pd_{*n*} interaction increases, and the H atoms locate on the hcp and fcc sites leading to a decreasing of r . At the chemisorption sites, the H atoms are slightly bound (BO = 0.10), but the electrorepulsion is also significant so that the H–H distance reaches 1.93 Å while the hcp–fcc distance is only 1.59 Å.

IV.2. O₂ Adsorption on Pd₅. As in the case of H₂ adsorption, from the unlike O₂ adsorption pathways studied by Honkala et al.,³² we chose to investigate the adsorption pathway corresponding to an fcc-hcp O₂ initial adsorption position (results in Table 3). For the same reasons as H₂ adsorption on Pd₅, we have constrained the O₂ dynamic adsorption process to 2D cuts of the 6D PES. The molecular axis is kept parallel to the cluster surface and perpendicular to the Pd–Pd bond (Figure 2). The adsorbate is moved toward the Pd₅ surface following the *z*-axis, and the O–O bond length is optimized for each value of *z*. The adsorption pathway is displayed in Figure 4. As it was the case for H₂, we first observed a physisorbed state located at *z* = 3.2 Å, with an energy of –0.42 eV. In this state, no electron transfer is observed between the cluster and the molecule. The O₂ molecule still has the same conformation as that in the gas phase, *d*(O–O) = 1.23 Å (Figure 4), the O–O bond order is still equal to 2, and no chemical bond is observed between the adsorbate and the substrate. On the other side, the physisorption energy of O₂ is much larger than that of H₂ showing that the electronic cloud of O₂ is strongly polarized by the presence of the palladium surface. At *z* = 1.95 Å, a transition state is determined with an energy of 0.31 eV leading to an activation energy for the dissociated chemisorption of 0.73 eV. At this point, the O₂ species is still molecular, the O–O length increasing very slightly to 1.25 Å. At *z*₁ = 1.59 Å a sharp transition is observed. Thus O₂ is dissociated, and the electrostatic repulsion leads to a O–O distance of 3.6 Å. Finally, when *z* continues to decrease, the O–Pd_{*n*} interaction increases, and the O atoms locate on the hcp and fcc sites leading to a decreasing of *r*. At the chemisorption site, the O atoms are always relatively bounded (BO = 1.20), but the electrorepulsion is large (*q*(O) = –0.72 au) so that the O–O distance reaches 2.33 Å (in place of 1.59 Å for the hcp-fcc distance). Finally, we can notice that, for this pathway, no molecular chemisorbed precursor is observed on the surface and that this reactional pathway is activated. It is in good agreement with the periodic calculations of Honkala et al.³² Furthermore, comparison of physisorption and chemisorption energies show that the O₂ molecule may dissociate on Pd₅. Honkala et al.³² found that the adsorption of two oxygen atoms constrained on two adjacent adsorption sites (fcc-hcp) is endothermic. Our results show that the O₂ adsorption process on the small Pd₅ cluster is different relatively to an infinite (111) surface for low coverage.

V. Interaction between Chemisorbed Atoms on Small Two-Layer Pd_{*n*} Clusters

In this part, we study the interaction between two adsorbed atoms (hydrogen or oxygen) on the Pd₅, Pd₇, and Pd₁₀ clusters (Figure 1). The first atom being adsorbed in the most stable position, i.e., the hcp site, the second one is allowed to migrate on other threefold sites (hcp or fcc). The range of the atom–atom interaction is then discussed and compared to the reference state where the two atoms are not in interaction. The pathway of the hcp-fcc dissociative adsorption was analyzed more particularly. In fact, it is known that the most stable end configuration of the dissociation is the

Table 4. Chemisorption Energy of Two Hydrogen Atoms Coadsorbed on Various (111) Sites^c

	sites	<i>E</i>		<i>q</i> (H)		BO(H–H)
		<i>E</i> _{ads}	Δ <i>E</i> _{ads}	H ¹	H ²	
Pd ₅ H ₂	h ¹ /f ¹	–0.91	+0.09	–0.12	–0.13	0.10
	Inf	–1.02				
Pd ₇ H ₂	h ¹ /f ¹	–0.72	+0.12	–0.14	–0.12	0.10
Pd ₇ H ₂	h ¹ /h ²	–0.69	+0.23	–0.13	–0.13	0.00
	Inf	–0.92				
Pd ₁₀ H ₂	h ¹ /f ¹	–0.59	+0.22	–0.12	–0.13	0.10
Pd ₁₀ H ₂	h ¹ /h ²	–0.54	+0.29	–0.13	–0.14	0.00
Pd ₁₀ H ₂	h ¹ /f ²	–0.56	+0.25	–0.12	–0.13	0.00
Pd ₁₀ H ₂	h ¹ /h ³	–0.65	+0.19	–0.13	–0.13	0.00
	Inf	–0.82				
other work ^a	hcp/hcp	–0.73				
other work ^b	hcp/fcc	–0.69				
	hcp/hcp	–0.89				
	fcc/fcc	–0.99				

^a Reference 12 (periodic computations – coverage = 1). ^b Reference 23 (periodic computations). ^c *E*_{ads}(eV) is the H¹ plus H² adsorption energy, *q*(H) is the Mulliken net charge located on each H atom, and BO is the H–H bond order. The different adsorption sites are illustrated in Figure 1.

fcc–fcc one's (see ref 23), but only the hcp-fcc configuration is available on the three studied clusters.

V.1. Hydrogen–Hydrogen Interactions. Hydrogen–hydrogen interactions when chemisorbed on Pd₅, Pd₇, and Pd₁₀ are summarized in Table 4. The first atom is chemisorbed on the h¹ site, while the second one is chemisorbed on other three-hollow sites f¹ (5, 7, 10), h² (7, 10), and f² and h³ (10). Chemisorption energies as well as charge transfer and bond orders between the two atoms are reported. In each case the adsorption energy is compared to that of two atoms occupying the same sites without interaction (Δ*E*_{ads} in Table 4) and to the more stable chemisorption configuration where both atoms are chemisorbed on hcp sites, without interaction (labeled Inf in Table 4). Concerning the nearest neighbor adsorption sites, i.e., h¹/f¹ the adsorption energy decreases smoothly with the size of the cluster showing that the size effects are not negligible. Nevertheless, in each case, the chemisorption is dissociative which is not the case for the infinite surface.³² Chemisorption on these sites shows that a significant electrostatic repulsion arises between both atoms due to the electron transfer from the cluster to the H atoms (*q*(H) = –0.13 e). On the other hand, electrostatic repulsion is partially compensated by a small chemical binding energy, the bond order of the H–H bond being equal to 0.10. The h¹/h² interaction (Pd₇, Pd₁₀) is not more stable than the h¹/f¹ configuration. In that case the net charges of the H atoms are the same, but the electrostatic repulsion is smaller due to a larger H–H distance. On the other hand, there is no more attractive chemical binding between both atoms. Finally, the h¹/h³ configuration is the more stable on the Pd₁₀ cluster, but there is always a repulsive energy of the order of 0.17 eV.

V.2. Oxygen–Oxygen Interactions. Oxygen–oxygen interactions when chemisorbed on Pd₅, Pd₇, and Pd₁₀ are summarized in Table 5. As for hydrogen adsorption, the first atom is chemisorbed on the h¹ site, while the second one is

Table 5. Chemisorption Energy of Two Oxygen Atoms Coadsorbed on Various (111) Sites^b

	sites	E		q(O)		BO(O–O)
		E _{ads}	ΔE _{ads}	O ¹	O ²	
Pd ₅ O ₂	h ¹ /f ¹	–0.25	+1.64	–0.74	–0.70	1.20
	Inf	–2.18				
Pd ₇ O ₂	h ¹ /f ¹	–0.34	+1.58	–0.73	–0.62	1.13
Pd ₇ O ₂	h ¹ /h ²	–1.30	+0.70	–0.61	–0.61	0.03
	Inf	–2.0				
Pd ₁₀ O ₂	h ¹ /f ¹	–0.29	+1.42	–0.72	–0.66	1.17
Pd ₁₀ O ₂	h ¹ /h ²	–1.42	+0.37	–0.65	–0.52	0.04
Pd ₁₀ O ₂	h ¹ /f ²	–1.48	+0.22	–0.61	–0.50	0.00
Pd ₁₀ O ₂	h ¹ /h ³	–1.75	+0.09	–0.61	–0.61	0.00
	Inf	–1.84				
other work		–2.39 ^a				

^a Reference 2 (experimental). ^b E_{ads}(eV) is the O¹ plus O² adsorption energy, q(O) is the Mulliken net charge located on each O atom, and BO is the O–O bond order. The different adsorption sites are illustrated in Figure 1.

Table 6. Cluster Size Effects on the Dissociative Chemisorption Energy, Transition State Energy, and Physisorption Energy of H₂ and O₂^b

	E _{chem}		E _{TS}		E _{phys}	
	H	O	H	O	H	O
Pd ₅	–0.91	–0.29	+0.15	+0.31	–0.06	–0.42
Pd ₇	–0.72	–0.34	+0.30	+0.33	–0.08	–0.39
Pd ₁₀	–0.59	–0.29	+0.31	+0.35	–0.08	–0.66
other work ^a	–0.694		+0.019			

^a Reference 23 (periodic computations). ^b All values are in eV.

chemisorbed on the other threefold sites: f¹ (5, 7, 10), h² (7, 10), f², and h³ (10). Chemisorption energies as well as charge transfer and bond orders between the two atoms are also reported. Concerning the nearest neighbor adsorption sites, i.e., h¹/f¹ the adsorption energy decreases significantly with the size of the cluster showing that the size effects are not negligible. In each case, the chemisorption is not dissociative, the physisorption energy being lower in energy (see Table 6). Chemisorption on these sites show that a strong electrostatic repulsion arises between both atoms due to the electron transfer from the cluster to the O atoms (q(O) = –0.72 e). On the other hand, electrostatic repulsion is significantly compensated by a non-negligible chemical binding energy, the O–O bond order being equal to 1.20. Nevertheless the chemisorption energy becomes six times smaller compared to the case where the two O atoms chemisorb without interaction. Contrarily to the case of hydrogen adsorption, the h¹/h² configuration for oxygen adsorption on Pd₇ and Pd₁₀ is much more stable than the h¹/f¹. In that case the net charges of the O atoms are slightly lower, and the electrostatic repulsion is smaller due to a larger O–O distance. The chemical binding between both atoms becomes very small. Finally, the h¹/h³ configuration is the more stable on the Pd₁₀ cluster, with a repulsive energy decreasing to 0.09 eV.

VI. Conclusion

We present first-principle calculations of some properties of the dissociative interaction of hydrogen and oxygen molecules on Pd₅, Pd₇, and Pd₁₀ palladium clusters.

In the first part of our work, we studied the adsorption of a single hydrogen and oxygen atom. In both cases, we find that there is no cluster size effect on the H (O) adsorption energies which are equal on the three clusters when we compare the same types of adsorption sites. The hcp and fcc threefold hollow sites are found to be the most stable without a significant energy gap. The calculation of the energy barriers shows that both atoms can diffuse over a (111) palladium surface.

In the second part, we investigated the adsorption of H₂ and O₂ on the small two-layer Pd₅ cluster. Our results show that H₂ adsorbs dissociatively on the Pd₅ cluster with an electron transfer from the surface toward each hydrogen atom of about 0.13 e[–]. Due to this small negative charge carried by each hydrogen atom there is a weak electrostatic repulsive effect between both hydrogen atoms. It induces a weak destabilization of the adsorption energies relatively to a single adsorption. For oxygen adsorption, our calculations show that O₂ cannot adsorb dissociatively on the Pd₅ cluster because the only two available threefold sites are too close. When O₂ adsorbs on the cluster's surface, there is an electron transfer toward each oxygen atom of about 0.75 e[–] which induces a strong O–O repulsive effect due to the short distance between them. Due to this electrostatic effect, the physisorbed state on Pd₅ is found to be more stable than the chemisorbed one.

In the last part of this work we investigated the coadsorption H–H or O–O on various three-hollow sites. Due to the adsorbate–adsorbate electrostatic repulsive interactions, there is a size effect which depends on the number of threefold hollow sites available on the cluster surface. This effect is stronger for oxygen than for hydrogen because the electron transfer toward oxygen atoms is greater than on hydrogen atoms.

This study clearly shows that the dissociative chemisorption of H₂ and more especially of O₂ on a small palladium cluster may lead to erroneous binding energies due to the cluster shape: the close threefold hollow sites on the cluster's surface may prevent an accurate description of the adsorbate–adsorbate interactions as a function of their distance. However, a good choice of both the size and the shape of the cluster can lead to a good description of the dissociative adsorption process of H₂ and O₂ on an infinite (111) palladium surface.

References

- (1) Conrad, H.; Ertl, G.; Latta, E. E. *Surf. Sci.* **1974**, *41*, 435–446.
- (2) Eberhardt, W.; Louie, S. G.; Plummer, E. W. *Phys. Rev. B* **1983**, *28*, 465–477.
- (3) Christmann, K. *Surf. Sci. Rep.* **1988**, *9*, 1.
- (4) Felter, T. E.; Sowa, E. C.; Van, Hove, M. A. *Phys. Rev. B* **1989**, *40*, 891–899.
- (5) Resch, C. H.; Berger, H. F.; Rendulic, K. D.; Bertel, E. *Surf. Sci.* **1994**, *316*, L1105–L1109.
- (6) Mitsui, T.; Rose, M. K.; Fomin, E.; Ogletree, D. F.; Salmeron, M. *Surf. Sci.* **2003**, *540*, 5–11.
- (7) Mitsui, T.; Rose, M. K.; Fomin, E.; Ogletree, D. F.; Salmeron, M. *Nature* **2003**, *422*, 705–707.

- (8) Baykara, N. A.; Andzelm, J.; Salahub, D. R.; Baykara, S. *Z. Int. J. Quantum Chem.* **1986**, *29*, 1025–1032.
- (9) Rochefort, A.; Andzelm, J.; Russo, N.; Salahub, D. R. *J. Am. Chem. Soc.* **1990**, *112*, 8239–8247.
- (10) Roques, J.; Lacaze-Dufaure, C.; Mijoule, C. *Surf. Sci.* **2001**, *479*, 231–240.
- (11) Bertin, V.; Cruz, A.; Del, Angel, G.; Castro, M.; Poulain, E. *Int. J. Quantum Chem.* **2005**, *102*, 1092–1105.
- (12) Dong, W.; Kresse, G.; Furthmüller, J.; Hafner, J. *Phys. Rev. B* **1996**, *54*, 2157–2166.
- (13) Paul, J. F.; Sautet, P. *Surf. Sci.* **1996**, *356*, L403–L409.
- (14) Dong, W.; Ledentu, V.; Sautet, P.; Eichler, A.; Hafner, J. *Surf. Sci.* **1998**, *411*, 123–136.
- (15) Lovvik, O. M.; Olsen, R. A. *Phys. Rev. B* **1998**, *58*, 10890–10898.
- (16) Pallassana, V.; Neurock, M.; Hansen, L. B.; Hammer, B.; Norskov, J. K. *Phys. Rev. B* **1999**, *60*, 6146–6154.
- (17) Nobuhara, K.; Nakanishi, H.; Kasai, H.; Okiji, A. *J. Appl. Phys.* **2000**, *88*, 6897–6901.
- (18) Watson, G. W.; Welles, R. P. K.; Willock, D. J.; Hurchings, G. J. *J. Phys. Chem. B* **2001**, *105*, 4889–4894.
- (19) Faglioni, F.; Goddard, W. A. *J. Chem. Phys.* **2005**, *122*, 14704–14718.
- (20) Efremenko, I.; German, E. D.; Sheintuch, M. *J. Phys. Chem. A* **2000**, *104*, 8089–8096.
- (21) Wang, Y.; Cao, Z.; Zhang, Q. *Chem. Phys. Lett.* **2003**, *376*, 96–102.
- (22) German, E. D.; Efremenko, I.; Sheintuch, M. *J. Phys. Chem. A* **2001**, *105*, 11312–11326.
- (23) Dong, W.; Hafner, J. *Phys. Rev. B* **1997**, *56*, 15396–15403.
- (24) Nobuhara, K.; Kasai, H.; Dino, W. A.; Nakanishi, H. *Surf. Sci.* **2004**, *566–568*, 703–707.
- (25) Conrad, H.; Ertl, G.; Küppers, J.; Latta, E. E. *Surf. Sci.* **1977**, *65*, 245–260.
- (26) Guo, X.; Hoffman, A.; Yates, J. T., Jr. *J. Chem. Phys.* **1989**, *90*, 5787–5792.
- (27) Steltenpohl, A.; Memmel, N. *Surf. Sci.* **1999**, *443*, 13–18.
- (28) Seitsonen, A. P.; Kim, Y. D.; Schwegmann, S.; Over, H. *Surf. Sci.* **2000**, *468*, 176–186.
- (29) Nolan, P. D.; Lutz, B. R.; Tanaka, P. L.; Mullins, C. B. *Surf. Sci.* **1998**, *419*, L107–L113.
- (30) Sjovall, P.; Uvdal, P. *Chem. Phys. Lett.* **1998**, *282*, 355–360.
- (31) Wan, X.; Yoshizawa, K.; Ohashi, N.; Endou, A.; Takami, S.; Kubo, M.; Miyamoto, A.; Imamura, A. *Scr. Mater.* **2001**, *44*, 1919–1923.
- (32) Honkala, K.; Laasonen, K. *J. Chem. Phys.* **2001**, *115*, 2297–2302.
- (33) Torodova, M.; Reuter, K.; Scheffler, M. *J. Phys. Chem. B* **2004**, *108*, 14477–14483.
- (34) Huber, B.; Häkkinen, H.; Landman, U.; Moseler, M. *Comput. Mater. Sci.* **2006**, *35*, 371–374.
- (35) Eichler, A.; Mittendorfer, F.; Hafner, J. *Phys. Rev. B* **2000**, *62*, 4744–4755.
- (36) Kuittinen, R-L.; Laasonen, K. *Chem. Phys.* **2005**, *314*, 19–24.
- (37) St-Amant, A.; Salahub, D. R. *Chem. Phys. Lett.* **1990**, *169*, 387–392.
- (38) St-Amant, A. Thèse de l'Université de Montréal, 1991.
- (39) Vosko, S. H.; Wilk, L.; Nusair, M. *Can. J. Phys.* **1980**, *58*, 1200–1211.
- (40) Perdew, J. P. *Phys. Rev. Lett.* **1985**, *55*, 1665–1668.
- (41) Perdew, J. P. *Phys. Rev. B* **1986**, *33*, 8822.
- (42) Perdew, J. P.; Wang, Y. *Phys. Rev. B* **1986**, *33*, 8800–8802.
- (43) Andzelm, J.; Radzio, E.; Salahub, D. R. *J. Chem. Phys.* **1985**, *83*, 4573–4580.
- (44) Mijoule, C.; Russier, V. *Surf. Sci.* **1991**, *254*, 329–340.
- (45) Eichler, A.; Kresse, G.; Hafner, J. *Surf. Sci.* **1998**, *397*, 116.

CT600370G

Backbone Importance for Protein–Protein Binding[†]

Irina S. Moreira, Pedro A. Fernandes, and Maria J. Ramos*

REQUIMTE/Departamento de Química, Faculdade de Ciências da Universidade do Porto, Rua do Campo Alegre 687, 4169-007 Porto, Portugal

Received December 28, 2006

Abstract: Although a number of studies have focused on the physical and chemical properties of protein–protein interfaces of complexes to determine their unique features, the importance of the backbone hydrogen bonds to protein–protein binding has been neglected due to the difficulty of quantitatively measuring their contribution to the free binding energy. In this study we are presenting a computational approach that allows the estimation of the contribution to the free binding energy of the CO and NH groups of the backbone of various proteic complexes. A correlation between the quantitative calculated free binding energy contribution of the CO and NH backbone groups of the interfacial residues and the qualitative values expected for this kind of interaction was achieved. The contribution of the backbone to the $\Delta\Delta G_{\text{binding}}$ is significant. The average $\Delta\Delta G_{\text{binding}}$ contribution of the intermolecular hydrogen bonds of the backbone is 1.77 kcal/mol, which is very similar to the average contribution of the different side chains to the $\Delta\Delta G_{\text{binding}}$, with a value of 1.75 kcal/mol. Therefore, the application of this computational approach as well as an alanine scanning mutagenesis study is essential to a more detailed comprehensive knowledge of proteic complex formation.

Introduction

Crystallographic structures of proteins cocrystallized with various ligands, together with structural and thermodynamic studies, made possible the identification of the structural binding epitopes (amino acid residues which are in contact with the other binding partner).^{1–3} These studies have been completed with experimental and computational alanine-scanning mutagenesis of protein–protein interfacial residues that allowed the definition of the functional binding epitopes (contact residues that make energetic contributions to binding).^{4–7}

Although a number of studies have focused on the physical and chemical properties of protein–protein interfaces of complexes to determine their unique features, the importance of the backbone hydrogen bonds to protein–protein binding has been neglected due to the difficulty of quantitatively measuring their contribution to the free binding energy.^{8,9} Protein backbone is an important contributor to interfaces

because it represents in average of about one-fifth of the interface area. These hydrogen bonds contribute significantly to the stability of a protein structure, because they are the major contributors to the electrostatic interactions between proteins.¹⁰ However, hydrogen bonds are extremely important not only for stability but also because they affect other physicochemical properties of a molecule such as solubility, partitioning, distribution, permeability, and specificity that are crucial for drug development.¹¹ Hydrogen bonds are essential in determining binding specificity because they contribute favorably to the free energy of binding, but unfulfilled hydrogen bonds donor/acceptor could substantially destabilize the binding. Such a contrast in energetics contributes to a high selectivity in matching the hydrogen bonds between proteins and confers binding specificity.

The hydrogen bond is viewed as an interaction that has covalent, electrostatic, and van der Waals character and an energy that ranges from 0.25 to roughly 40 kcal/mol. The atoms involved in the hydrogen bond determine the strength of this electrostatic interaction, with the hydrogen bonds that contribute more to the binding normally made between atoms buried in the interior of the protein.⁶ Intermolecular hydrogen

[†] Dedicated to Professor Dennis R. Salahub on the occasion of his 60th birthday.

* Corresponding author e-mail: mjramos@fc.up.pt.

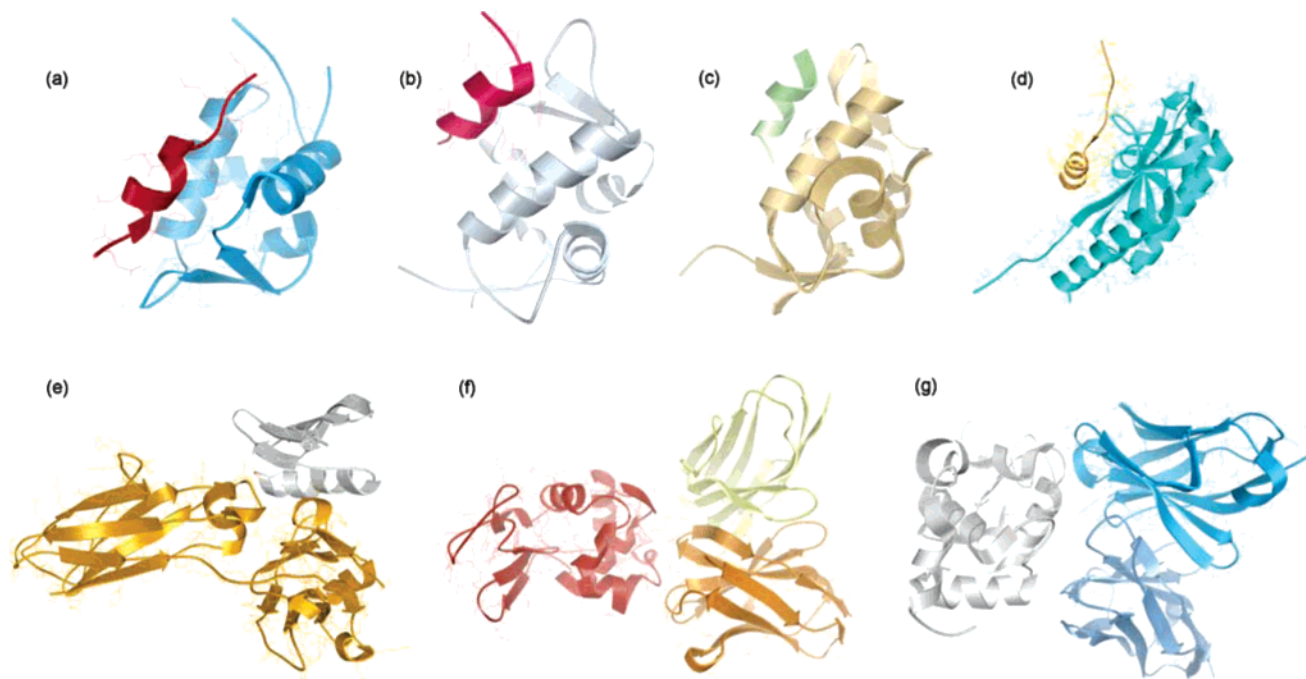
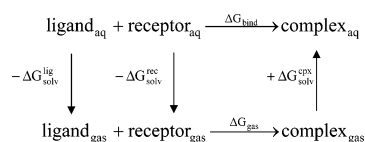


Figure 1. Molecular representation of the complexes formed between (a) the hMDM2 and the P53 protein (1YCR); (b) the xMDM2 and the P53 protein (1YCR); (c) the hMDM2 and an optimized P53 protein (1T4F); (d) a cell division protein ZipA and a cell division protein FtsZ (1F47); (e) a human immunoglobulin IgG complexed with the C2 fragment of streptococcal protein G (1FCC); (f) the lysozyme HEL and the antibody FvD1.3 (1VFB); and (g) the hen egg-white lysozyme (HEL) and the antibody HyHEL-10 (1C08).

Scheme 1. Thermodynamic Cycle Used To Calculate the Complexation Free Energy



bonds are generally weaker and have a larger diversity than the intramolecular ones. The lower quality of the interface hydrogen bond interactions can be attributed to the more hydrophilic side chains buried in the binding protein–protein interface than in the folded monomer interior.¹¹

Besides being very important from a conceptual point of view, understanding the role of the protein backbone is fundamental to understand, control, and manipulate protein complexes. As these complexes are involved in countless biological processes it is important for rational drug design to measure not only the contribution of the amino acid side chains but also the contribution of the protein backbone. Therefore, we have developed a computational method that allows the measurement of the free binding energy contribution of the different NH and CO atoms. This method was applied to seven protein–protein complexes that have a diverse molecular profile possessing a variety of functions and sizes.

Materials and Methods

1. Model Setup. The starting crystallographic structures for the simulations were the complexes formed between the hMDM2 and the P53 protein,¹² between the xMDM2 and

the P53 protein,¹² between the hMDM2 and an optimized P53 protein,¹³ between a cell division protein ZipA and a cell division protein FtsZ,¹⁴ between a human immunoglobulin IgG complexed with the C2 fragment of streptococcal protein G,¹⁵ between the lysozyme HEL and the antibody FvD1.3,¹⁶ and between the hen egg-white lysozyme (HEL) and the antibody HyHEL-10¹⁷ (all represented in Figure 1). They were taken from the RCSB Protein Data Bank with PDB entries 1YCR, 1YCR, 1T4F, 1F47, 1FCC, 1VFB, and 1C08 and with resolutions of 2.60 Å, 2.30 Å, 1.90 Å, 1.95 Å, 3.50 Å, 1.80 Å, and 2.30 Å, respectively. The systems comprised a total of 98, 99, 97, 159, 262, 352, and 350 amino acid residues. All residues were included in their physiological protonation states (charged Glu, Asp, Lys, and Arg, all other residues neutral). In the molecular simulations the solvent was modeled through a modified Generalized Born solvation model¹⁸ being the structure first minimized with 1000 steps of steepest decent followed by 1000 steps of conjugated gradient to release the bad contacts in the crystallographic structure. Subsequently, molecular dynamics (MD) simulations of 5, 4, 4, 4, 5, 3, and 3 ns, respectively, were performed starting from the minimized structure. All molecular mechanics simulations presented in this work were carried out using the sander module, implemented in the Amber8¹⁹ simulations package, with the *Cornell* force field.²⁰ Bond lengths involving hydrogens were constrained using the SHAKE algorithm,²¹ and the equations of motion were integrated with a 2 fs time-step being the nonbonded interactions truncated with a 16 Å cutoff. The temperature of the system was regulated by the Langevin thermostat.^{22–24}

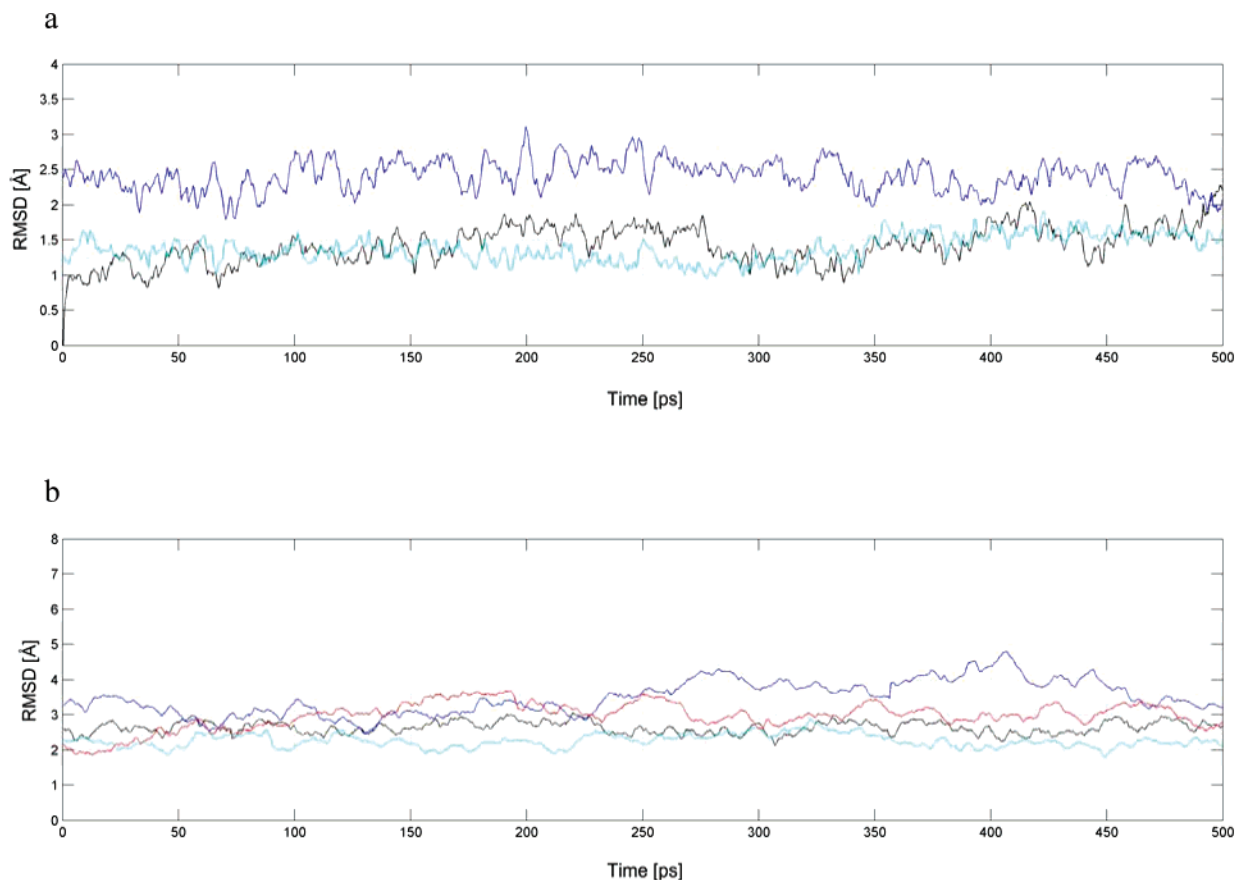


Figure 2. rmsd plots for the protein backbone of the complex formed between (a) (in black) the hMDM2 and the P53 protein (1YCR); (in blue) the xMDM2 and the P53 protein (1YCQ); and (in cyan) the hMDM2 and an optimized P53 protein (1T4F) and (b) (in black) a cell division protein ZipA and a cell division protein FtsZ (1F47); (in blue) a human immunoglobulin IgG complexed with the C2 fragment of streptococcal protein G (1FCC); (in cyan) the lysozyme HEL and the antibody FvD1.3 (1VFB); and (in red) the antibody HyHEL-10 (1C08) relative to its initial structure.

In force field Hamiltonians hydrogen bonds are due primarily to partial electrostatic charges, and therefore the energetic is determined by the values of the partial charges. To understand the importance of the backbone hydrogen bonds we have measured the free binding differences generated upon deletion of the charge of the amide (NH) and carbonyl (CO) groups. To ensure electroneutrality we have distributed the remaining partial charge proportionally by the remaining atoms of the corresponding residue. This procedure was made taking into account the proportions of the different atoms to the final charge of the amino-acid residue. For the binding free energy calculations, 25 snapshots of the complexes were extracted every 20 ps for the last 500 ps of the run.

2. Hydrogen Bonds at the Backbone of the Interfacial Residues. The complexation free energy can be calculated using the thermodynamic cycle shown in Scheme 1 where ΔG_{gas} is the interaction free energy between the ligand and the receptor in the gas phase. $\Delta G_{\text{sol}}^{\text{lig}}$, $\Delta G_{\text{sol}}^{\text{rec}}$, and $\Delta G_{\text{sol}}^{\text{cpx}}$ are the solvation free energies of the ligand, the receptor, and the complex, respectively. The binding free energy difference between the mutant (complex generated upon deletion of the amide and carbonyl groups) and wild type complexes is defined as

$$\Delta\Delta G_{\text{binding}} = \Delta G_{\text{binding-mutant}} - \Delta G_{\text{binding-wild type}} \quad (1)$$

The binding free energy of two molecules is the difference between the free energy of the complex and the respective monomers (the receptor and the ligand).

$$\Delta G_{\text{binding-molecule}} = G_{\text{complex}} - (G_{\text{receptor}} + G_{\text{ligand}}) \quad (2)$$

The free energy of the complex and respective monomers can be calculated by summing the internal energy (bond, angle, and dihedral), the electrostatic and the van der Waals interactions, the free energy of polar solvation, the free energy of nonpolar solvation, and the entropic contribution for the molecule free energy:

$$G_{\text{molecule}} = E_{\text{internal}} + E_{\text{electrostatic}} + E_{\text{vdw}} + G_{\text{polar solvation}} + G_{\text{nonpolar solvation}} - TS \quad (3)$$

The first three terms were calculated using the Cornell force field²⁰ with no cutoff. The electrostatic solvation free energy was calculated by solving the Poisson–Boltzmann equation with the software Delphi v.4,^{25,26} using the same methodology of previous works which has been shown in an earlier work to constitute a good compromise between accuracy and computing time.²⁷ Albeit the use of an internal dielectric value of 2 or 4 did not influence the results significantly, for the energy calculations we have used an internal dielectric constant value of 3 due to the polar nature of the groups in question. The nonpolar contribution to

Table 1. Results of the Study of the Free Binding Energy Contribution of the Different NH and CO Atoms^a

PDB files	protein	residue	$\Delta\Delta G_{\text{binding}}$	PDB files	protein	residue	$\Delta\Delta G_{\text{binding}}$
1YCR	P53	Thr18	-0.27	1YCR	P53	Trp23	-1.29
		Phe19	-0.29			His24	-0.47
		Ser20	0.26			Leu25	-0.84
		Asp21	-0.05			Leu26	-0.16
		Leu22	0.09				
1YCR	hMDM2	Leu54	1.27	1YCR	hMDM2	Tyr67	0.08
		Leu57	-0.01			Gln72	-1.12
		Ile61	0.09			Val93	-0.31
		Met62	0.10			Ile99	0.28
1YCQ	P53	Thr18	-0.52	1YCQ	P53	Trp23	-0.28
		Phe19	-0.35			His24	-0.18
		Ser20	-0.1			Leu25	0.20
		Asp21	-0.15			Leu26	0.34
		Leu22	-0.12				
1YCQ	xMDM2	Ile50	1.62	1YCQ	xMDM2	Tyr63	0.15
		Leu53	0.05			Gln68	-1.40
		Ile57	0.36			Val89	-0.49
		Met58	0.27			His90	0.16
1T4F	P53	Phe19	-0.37	1T4F	P53	Tyr22	-0.51
		Met20	-0.11			Trp23	-1.50
		Asp21	-0.27			Glu24	-0.44
1T4F	xMDM2	Leu54	0.15	1T4F	xMDM2	Tyr67	0.04
		Leu57	0.15			Gln72	-0.72
		Ile61	0.41			Val93	-0.48
		Met62	0.30			Ile99	-0.05
1F47	FtsZ	Asp370	-0.22	1F47	FtsZ	Phe377	0.23
		Tyr371	0.49			Leu378	-0.06
		Leu372	-0.43			Arg379	0.21
		Asp373	-1.66			Lys380	-0.14
		Ile374	1.75				
1F47	ZipA	Val194	0.15	1F47	ZipA	Lys250	-0.26
		Ile196	0.06			Thr253	-0.05
		Asp225	-0.09			Thr267	0.37
		Met226	-0.14			Ile268	0.01
		Ile228	0.12			Phe269	0.04
		Asn247	-1.08			Met270	-0.01
		Met248	-0.38			Gln271	0.01
		Val249	-1.48				
		Thr25	-0.28			Asp40	0.85
		Glu27	1.36			Glu42	0.07
1FCC	protein G (C2 fragment)	Lys28	-0.18	1FCC	protein G (C2 fragment)	Trp43	-0.44
		Lys31	0.22			Thr44	0.29
		Asn35	-0.51			Tyr45	-0.14
		Ile253	2.98			Asn434	-1.48
		Ser254	5.07			His435	-0.84
1FCC	IgG1	Glu380	0.28	1FCC	IgG1	Tyr436	-0.70
		Ser426	0.07			Thr437	0.02
		Met428	0.01			Gln438	-0.09
		His433	-0.58				
		His30	-0.13			Thr53	-0.10
1VFB	antibody FvD1.3 VL	Tyr32	-0.25	1VFB	antibody FvD1.3 VL	Trp92	-1.20
		Tyr49	-0.26			Ser93	-0.48
		Tyr50	-0.65				
		Thr30	0.27			Glu98	0.59
1VFB	antibody FvD1.3 VH	Tyr32	-0.35	1VFB	antibody FvD1.3 VH	Arg99	-0.13
		Trp52	0.09			Asp100	-0.73
		Asn56	0.20			Tyr101	-0.49
		Asp58	-0.05				
		Asp18	0.82			Asp119	0.02
1VFB	HEL	Asn19	-0.1	1VFB	HEL	Val120	0.8
		Tyr23	0.66			Gln121	0.41
		Ser24	3.69			Ile124	-0.15
		Lys116	-1.42			Arg125	-0.54
		Thr118	-0.81			Leu129	-0.13
1C08	HyHEL-10 VL	Asn31Ala	0.13	1C08	HyHEL-10 VL	Asp32Ala	-0.57
		Asn32Ala	-0.18			Tyr50Ala	-0.41
		Tyr50Ala	-0.06			Tyr53Ala	-0.32
		Gln53Ala	-0.34			Tyr58Ala	-0.07
		Tyr96Ala	-0.45			Asp101Ala	-0.01
1C08	HEL	His15Ala	0.36	1C08	HEL	Asn93Ala	0.12
		Tyr20Ala	-0.50			Lys96Ala	-0.40
		Arg21Ala	0.08			Lys97Ala	-1.76
		Trp63Ala	0.17			Ile98Ala	0.84
		Arg73Ala	-0.62			Ser100Ala	-0.45
		Leu75Ala	0.29			Asp101Ala	0.20
		Thr89Ala	-0.22				

^a All the energies are in kcal/mol.

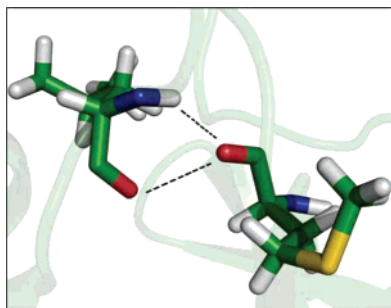


Figure 3. Molecular representation of the interactions established between the Met248 of the ZipA protein and the Leu372 of the binding partner in the 1F47 complex.

solvation free energy due to van der Waals interactions between the solute and the solvent and cavity formation was modeled as a term that is dependent on the solvent accessible surface area of the molecule. It was estimated using an empirical relation, $\Delta G_{\text{nonpolar}} = \sigma A + \beta$, where A is the solvent-accessible surface area that was estimated using the Molsurf program, which is based on the idea primarily developed by Michael Connolly.²⁸ σ and β are empirical constants, and the values used were $0.00542 \text{ kcal } \text{\AA}^{-2} \text{ mol}^{-1}$ and $0.92 \text{ kcal mol}^{-1}$, respectively. The entropy term, obtained as the sum of translational, rotational, and vibrational components, was not calculated, because it was assumed that its contribution to $\Delta\Delta G_{\text{binding}}$ is negligible.²⁹

Results

To obtain reliable estimates of the relative binding energy it was important to ensure that equilibration was achieved. In Figure 2a,b we have plotted the root-mean-square deviations (rmsd) for the backbone atoms of the seven complexes

(1YCR, 1YCQ, 1T4F, 1F47, 1FCC, 1VFB, and 1C08) for the production MD simulation (the last 500 ps). As we can see the MD simulations are very stable with rmsd values lower than 2.0, 3.0, 2.0, 3.0, 4.0, 2.5, and 3.5 for the complexes 1YCR, 1YCQ, 1T4F, 1F47, 1FCC, 1VFB, and 1C08, respectively.

Table 1 summarizes the results of the study of the free binding energy contribution of the different NH and CO atoms applied to the seven complexes mentioned in the Methods section that have a diverse molecular profile possessing a variety of functions and sizes.

Although experimental results play an indispensable role in validating the simulation method as we have mentioned before, the experimental determination of the contribution of the backbone hydrogen interaction is extremely difficult. Thus, the validation of the theoretical method against experimental data can only be qualitative.

We have carefully analyzed all the seven MD simulations, and we have observed 11 hydrogen bonds that were extremely stable during the whole simulation. In the 1YCR complex we observed the hydrogen bond established between the HE1 atom of the Trp23 and the O atom of the Leu54 residue of the hMDM2 protein; in the 1YCQ complex the hydrogen bond established between the HE1 atom of the Trp23 and the O atom of the Ile50 residue of the hMDM2 protein; in the 1F47 the ionic hydrogen bond established between the NH group of the Leu373 and the carboxylate group of the Asp303 residue of the binding partner and the ionic hydrogen bond between the carboxylate group of the Met248 of the ZipA protein and Leu372 of the binding partner; in the 1FCC complex the ionic hydrogen bond established between the NH group of the Ile253 and Ser254 and the carboxylate group of the Glu27 residue of the binding

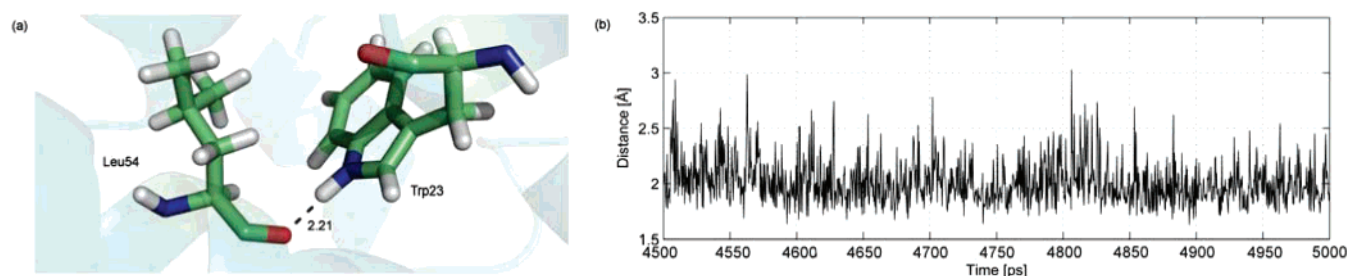


Figure 4. (a) Molecular representation of the hydrogen bond established between the HE1 atom of the Trp23 and the O atom of the Leu54 residue of the hMDM2 protein (snapshot of the production MD simulation) and (b) distance between the HE1 atom of the Trp23 and the O atom of the Leu54 residue of hMDM2 as a function of the production MD simulation time.

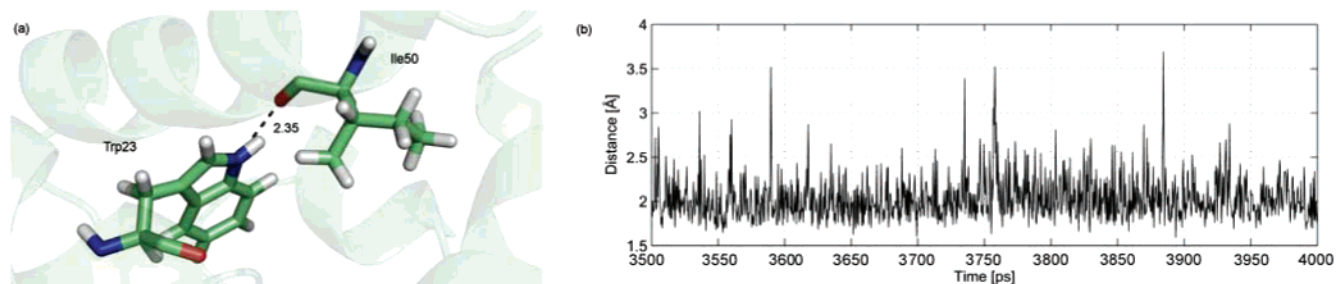


Figure 5. (a) Molecular representation of the hydrogen bond established between the HE1 atom of the Trp23 and the O atom of the Ile50 residue of the xMDM2 protein (snapshot of the production MD simulation) and (b) distance between the HE1 atom of the Trp23 and the O atom of the Ile50 residue of xMDM2 as a function of the production MD simulation time.

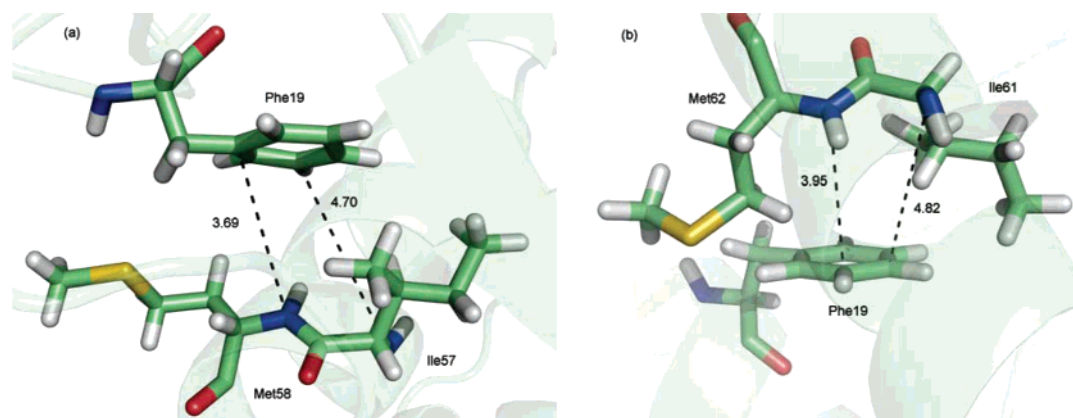


Figure 6. Molecular representation of the NH- π hydrogen bonds established between the phenyl ring of Phe19 and (a) Ile57 and Met58 of the hMDM2 protein and (b) Ile61 and Met62 of the xMDM2 protein. Figures were made from snapshots of the production MD simulation.

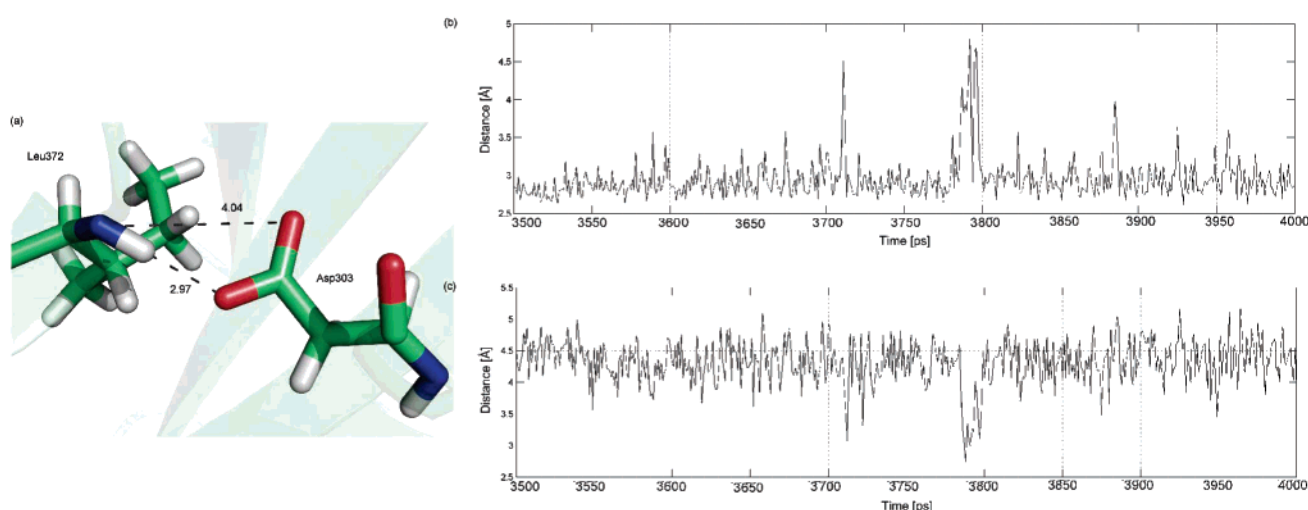


Figure 7. (a) Molecular representation of the hydrogen bond established between the N atom of the Leu372 and the O atom of the Asp303 residue of the binding partner (snapshot of the production MD simulation). (b) Distance between the N atom of Leu372 and the OD1 atom of the O atom of Asp303. (c) Distance between the N atom of Leu372 and the OD2 atom of the O atom of Asp303 as a function of the last 500 ps MD simulation time.

partner; and in the 1VFB the ionic hydrogen bond between the NH group of the Ser24 and the carboxylate group of the Asp100 residue of the binding partner. We have also observed stable NH- π hydrogen bonds established between the phenyl ring of Phe19 and Ile57 and Met58 of the hMDM2 protein as well as between the phenyl ring of Phe19 and Ile61 and Met62 of the xMDM2 protein.

By observation of Table 1 we can conclude that all the stable hydrogen bonds were detected with our computational approach with one exception only: the ionic hydrogen bond between the carboxylate group of the Met248 of the ZipA protein and Leu372 of the binding partner. In Figure 3 it is illustrated in this interaction, and as we can observe both the carboxylate and the amino group of Leu372 are close to the carboxylate group of the Met248. This fact has probably led to a repulsive interaction which justifies the nondetection by the computational approach.

A structural justification was found for every relevant energetic value obtained and shown in Table 1. An excellent

correlation between the quantitative calculated free binding energy contribution of the CO and NH backbone groups of the interfacial residues and the qualitative values expected for the corresponding type of interaction was also encountered. The average $\Delta\Delta G_{\text{binding}}$ contribution of the intermolecular hydrogen bonds of the backbone is 1.77 kcal/mol, which is very similar to the average contribution of the side chain to the $\Delta\Delta G_{\text{binding}}$, with a value of 1.75 kcal/mol. If we do not consider the NH- π hydrogen bonds, then this value raises to 2.73 kcal/mol.

Complex hMDM2:P53. For the first complex we have to emphasize the contribution of the NH and CO groups of the residue Leu54, which upon charge deletion generates a $\Delta\Delta G_{\text{binding}}$ of 1.27 kcal/mol. As it can be observed in Figure 4a the HE1 atom of the hot spot Trp23 establishes a hydrogen bond with the O atom of the residue Leu54 of the hMDM2 protein. This is the only intermolecular bond established in this complex, and in Figure 4b it is plotted as the distance

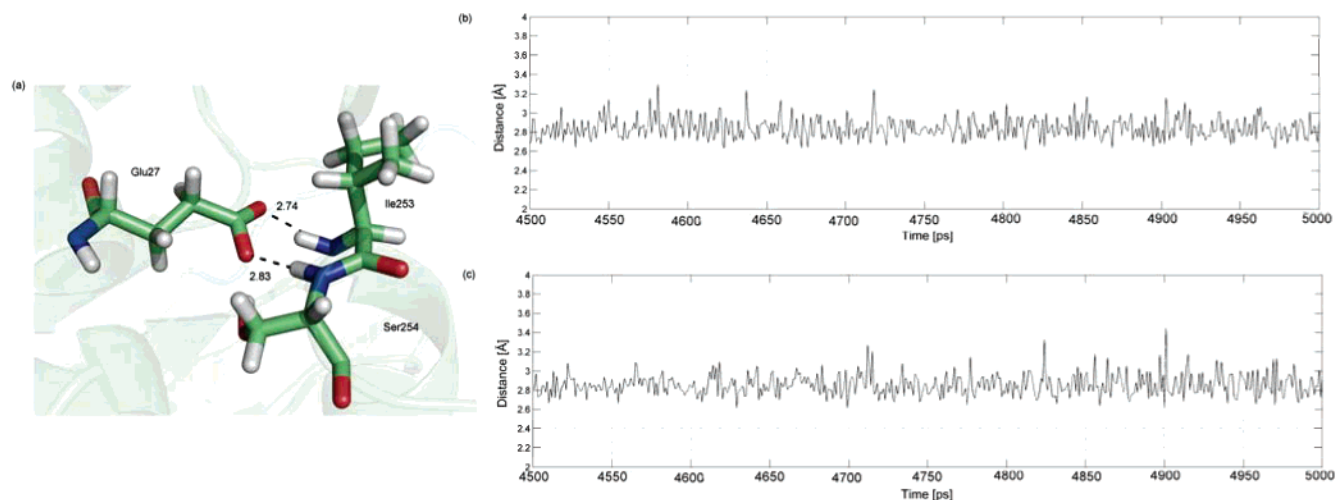


Figure 8. (a) Molecular representation of the hydrogen bond established between the NH group of the Ile253 and Ser254 and the carboxylate group of the Glu27 residue of the binding partner (snapshot of the production MD simulation). (b) Distance between the NH atom of the Ile253 residue and the OD2 atom of the carboxylate group of Glu27. (c) Distance between the NH atom of the Ser254 residue and the OD1 atom of the carboxylate group of Glu27 as a function of the last 500 ps MD simulation time.

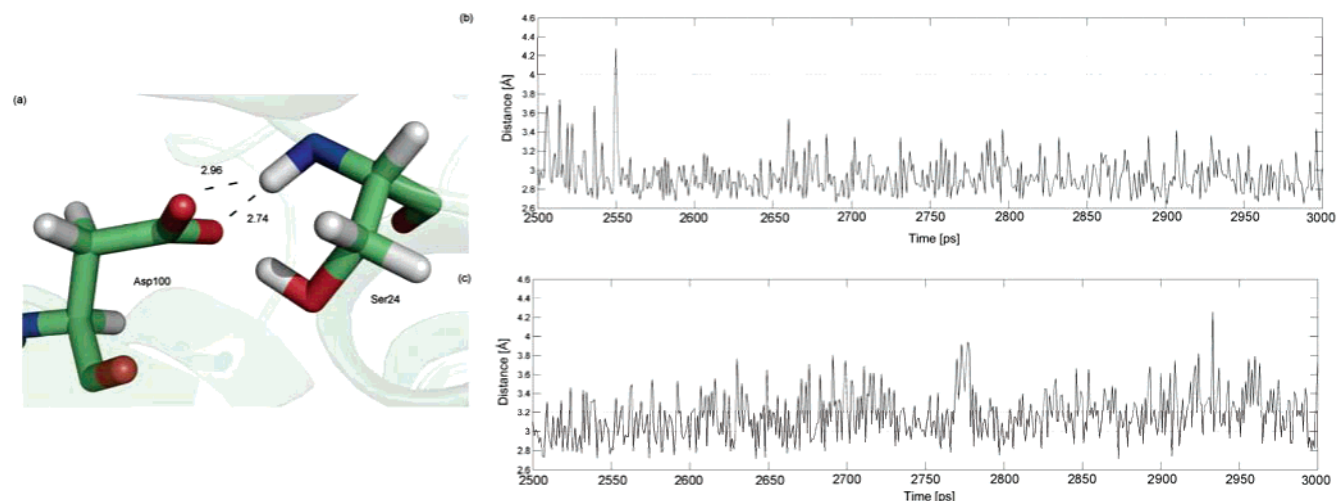


Figure 9. (a) Molecular representation of the hydrogen bond established between the N atom of the Ser24 and the carboxylate atom of the Asp100 residue of the binding partner (snapshot of the production MD simulation). (b) Distance between the N atom of Ser24 and the OD1 atom of the carboxylate group of Asp100. (c) Distance between the N atom of Ser 24 and the OD2 atom of the carboxylate group of Asp100 as a function of the last 500 ps MD simulation time.

between the two interacting atoms in function of time for the last 500 ps of the MD simulation.

Complex xMDM2:P53 and Complex hMDM2:Optimizedp53. For the complex between the P53 and xMDM2 protein (1YCQ), Ile50 is the residue that presents the highest $\Delta\Delta G_{\text{binding}}$ value (1.62 kcal/mol), because it establishes a hydrogen bond with the HE1 atom of the Trp23 residue represented in Figure 5a. This interaction is very important for complex binding with a value kept constant and under 2.0 Å during the MD simulation, as it can be perceived in Figure 5b.

We can also notice that Ile57 and Met58 present a $\Delta\Delta G_{\text{binding}}$ value of 0.36 and 0.27 kcal/mol. These values can be explained by the presence of NH- π hydrogen bonds established between those residues and the phenyl ring of Phe19 and are represented in Figure 6a. In the third complex the NH- π hydrogen bonds established between the Ile61 and

Met62 residues and Phe19 with energies of 0.41 and 0.30 kcal/mol were detected (Figure 6b). When the plane formed by the amide group is roughly perpendicular to the aromatic ring and the amino group points toward the aromatic cycle, the interaction is called amino- π hydrogen bond. Even though the energetic contribution of an amino- π hydrogen bond is usually three times lower than the conventional hydrogen bond, it still contributes significantly to complex binding. It is especially important for a correct ligand orientation.³³

Complex ZipA:FtsZ. In the fourth complex formed between a cell division protein ZipA and a cell division protein FtsZ (1F47) only a hydrogen bond was detected. It is formed between the N atom of the Leu373 and the O atom of the Asp303 residue of the binding partner and generates energy of 1.75 kcal/mol (Figure 7a). In Figure 7b,c we have plotted the distance between the N atom of Leu372 and the OD1 and OD2 atoms of the Asp303, respectively, as a

function of the last 500 ps MD simulation time. We can see by observation of Figure 7b,c that the OD1 atom has a higher contribution to the formation of a hydrogen bond as it is essentially at a 3.0 Å distance (in average 1.5 Å closer than the OD2 atom).

Complex IgG:ProteinG. For the complex formed between a human immunoglobulin IgG complexed with the C2 fragment of streptococcal protein G (1FCC) a superior absolute value of the $\Delta\Delta G_{\text{binding}}$ for the two hydrogen bonds was detected. These two bonds are formed between the OD2 group of the Glu27 residue and the NH group of the Ile253 residues and between the OD1 group of the Glu27 amino acid and the NH group of Ser254 of the C2 fragment of protein G. These bonds represented in Figure 8a generate an energy of 2.98 and 5.07 kcal/mol, respectively. By observation of Figure 8b,c we can notice that they are very stable keeping constant over the MD simulation and with an average length under 2.8 Å. The higher magnitude of the hydrogen bonds in the 1FCC complex is related to the fact that this is an ionic hydrogen bridge between two N backbone atoms and the side chain of a hot spot. In a previous work⁴ we have demonstrated that alanine mutation of Glu27 generates a $\Delta\Delta G_{\text{binding}}$ of 10.27 kcal/mol. With this new computational approach, as these two hydrogen bonds produce a $\Delta\Delta G_{\text{binding}}$ of 8.05 kcal/mol we can understand the relevant interactions that make these residues so fundamental to binding in the 1FCC complex.

Complex HEL:FvD1.3. For the sixth complex formed between the lysozyme HEL and the antibody FvD1.3 (1VFB) only a hydrogen bond was detected with an energy of 3.69 kcal/mol. This bond represented in Figure 9a is formed between the N atom of Ser24 of the HEL lysozyme and the carboxylate group of the Asp100 residue of the antibody FvD1.3.

Once again the fact that the distance between the atoms is constant and less than 3.0 Å value stresses that these bonds are important for complex formation. For the complex formed between hen egg-white lysozyme (HEL) and the antibody HyHEL-10 (1C08) we have not found any hydrogen bond formation.

Conclusion

Hydrogen bonds are due primarily to partial electrostatic charges, and therefore the energetic is determined by the values of the partial charges. To understand the importance of the backbone hydrogen bonds we have measured the free binding differences generated upon deletion of the charge of the amide and carbonyl groups. To ensure electroneutrality we have distributed the remaining partial charge by the remaining atoms, which were made taking into account the proportions of the different atoms to the final charge of the amino-acid residue. This method was applied to seven structures that have a diverse molecular profile possessing a variety of functions and sizes, and a structural justification was found for every relevant energetic value obtained. An excellent correlation between the quantitative calculated free binding energy contribution of the CO and NH backbone groups of the interfacial residues and the qualitative values expected for this kind of interaction was also demonstrated.

The average $\Delta\Delta G_{\text{binding}}$ of the backbone atoms was -0.05 kcal/mol, but the average contribution of the hydrogen bonds was 1.77 kcal/mol. If we do not consider the NH- π hydrogen bonds, the average value raises to 2.73 kcal/mol. Thus, the contribution of the backbone to the $\Delta\Delta G_{\text{binding}}$ is significant. The average $\Delta\Delta G_{\text{binding}}$ contribution of the intermolecular hydrogen bonds of the backbone is very similar to the average contribution of the side chain to the $\Delta\Delta G_{\text{binding}}$, with a value of 1.75 kcal/mol.

As the backbone seems to establish really important interactions to the binding, it is not only advisable but also essential to apply this computational approach when studying a proteic complex because it clearly increases the comprehension of the protein-protein complex binding.

References

- (1) Moreira, I. S.; Fernandes, P. A.; Ramos, M. J. Hot spots – a detailed review of protein-protein interface determinant amino acid residues. *Proteins* **2007**, in press.
- (2) Jones, S.; Thornton, J. M. Principles of protein-protein interactions. *Proc. Natl Acad. Sci. U.S.A.* **1996**, *93*, 13.
- (3) Bogan, A. A.; Thorn, K. S. Anatomy of hot spots in protein interfaces. *J. Mol. Biol.* **1998**, *280*, 1.
- (4) Moreira, I. S.; Fernandes, P. A.; Ramos, M. J. Unraveling the importance of protein-protein interaction: application of a computational alanine scanning mutagenesis to the study of the IgG1: Streptococcal Protein G (C2 Fragment) complex. *J. Phys. Chem. B* **2006**, *110*, 10962.
- (5) Moreira, I. S.; Fernandes, P. A.; Ramos, M. J. Hot spots computational identification- application to the complex formed between the hen egg-white lysozyme (HEL) and the antibody HyHEL-10. *Int. J. Quantum Chem.* **2007**, *107*, 299.
- (6) Moreira, I. S.; Fernandes, P. A.; Ramos, M. J. Unravelling Hot Spots-a comprehensive computational mutagenesis study. *Theor. Chem. Acc.* **2007**, *117*, 99.
- (7) Moreira, I. S.; Fernandes, P. A.; Ramos, M. J. Computational Alanine Scanning Mutagenesis – an improved methodological approach. *J. Comput. Chem.* **2007**, *28*, 644.
- (8) Xu, D.; Tsai, C. J.; Nussinov, R. Hydrogen bonds and salt bridges across protein-protein interfaces. *Protein. Eng.* **1997**, *10*, 999.
- (9) Biot, C.; Buisine, E.; Kwasigroch, J. M.; Wintiens, R.; Rooman, M. Probing the energetic and structural role of amino acid/nucleobase cation- π interactions in protein-ligand complexes. **2002**, *277*, 40816.
- (10) Kumar, S.; Nussinov, R. Close-range electrostatic interactions in proteins. *Chem. Biol. Chem.* **2002**, *3*, 604.
- (11) Sarkhel, S.; Desiraju, G. R. N-H...O, O-H...O, and C-H...O hydrogen bonds in protein-ligand complexes: strong and weak interactions in molecular recognition. *Proteins* **2004**, *54*, 247.
- (12) Kussie, P. H.; Gorina, S.; Marechal, V.; Elenbaas, B.; Moreau, J.; Levine, A. J.; Pavletich, N. P. Structure of the MDM2 oncoprotein bound to the p53 tumor suppressor transactivation domain. *Science* **1996**, *274*, 948.
- (13) Grasberger, B. L.; Schubert, C.; Koblish, H. K.; Carver, T. E.; Franks, C. F.; Zhao, S. Y.; Lu, T.; LaFrance, L. V.; Parks, D. J. Discovery and cocrystal structure of benzodiazepinone HDM2 antagonists that activate p53 in cells. *J. Med. Chem.* **2005**, *48*, 909.

- (14) Mosyak, L.; Zhang, Y.; Glasfeld, E.; Haney, S.; Stahl, M.; Seehra, J.; Somers, W. S. The bacterial cell-division protein ZipA and its interaction with an FtsZ fragment revealed by X-ray crystallography. *EMBO J.* **2002**, *19*, 3179.
- (15) Sauer-Eriksson, A. E.; Kleywegt, G. J.; Uhlen, M.; Jones, T. A. Crystal structure of the C2 fragment of streptococcal protein G in complex with the Fc domain of human IgG. *Structure* **1995**, *3*, 265.
- (16) Bhat, T. N.; Bentley, G. A.; Boulot, G.; Greene, M. I.; Tello, D.; Dall'Acqua, W.; Souchon, H.; Schwarz, F. P.; Mariuzza, R. A.; Poljak, R. J. Bound water molecules and conformational stabilization help mediate an antigen-antibody association. *Proc. Natl. Acad. Sci. U.S.A.* **1994**, *9*, 1089.
- (17) Kondo, H.; Shiroishi, M.; Matsushimai, M.; Tsumoto, K.; Kumagai, I. Crystal structure of anti-hen egg white lysozyme antibody (HyHEL-10) Fv-antigen complex. Local structural changes in the protein antigen and water-mediated interactions of Fv-antigen and light chain-heavy chain interfaces. *J. Biol. Chem.* **1999**, *274*, 27623.
- (18) Tsui, V.; Case, D. A. Theory and applications of the generalized Born solvation model in macromolecular simulations. *Biopolymers (Nucl. Acid Sci.)* **2001**, *56*, 275.
- (19) Case, D. A.; Darden, T. A.; Cheatham, T. E., III; Simmerling, C. L.; Wang, J.; Duke, R. E.; Luo, R.; Merz, H. M.; Wang, B.; Pearlman, D. A.; Crowley, M.; Brozell, S.; Tsui, V.; Gohlke, H.; Mongan, J.; Hornak, V.; Cui, G.; Beroza, P.; Schafmeister, C.; Caldwell, J. W.; Ross, W. S.; Kollman, P. A. *AMBER 8*; University of California: San Francisco, CA, 2004.
- (20) Cornell, W. D.; Cieplak, P.; Bayly, C. I.; Gould, I. R.; Merz, K. M., Jr.; Ferguson, D. M.; Spellmeyer, D. C.; Fox, T.; Caldwell, J. W.; Kollman, P. A. A second generation force field for the simulation of proteins, nucleic acids, and organic molecules. *J. Am. Chem. Soc.* **1995**, *117*, 5179.
- (21) Ryckaert, J. P.; Ciccotti, G.; Berendsen, H. J. Numerical integration of the cartesian equations of motion of a system with constraints: molecular dynamics of n-alkanes. *J. Comput. Phys.* **1977**, *23*, 327.
- (22) Pastor, R. W.; Brooks, B. R.; Szabo, A. An analysis of the accuracy of Langevin and molecular dynamics algorithms. *Mol. Phys.* **1988**, *65*, 1409.
- (23) Loncharich, R. J.; Brooks, B. R.; Pastor, R. W. Langevin dynamics of peptides: The frictional dependence of isomerization rates of N-acetylananyl-N'-methylamide. *Biopolymers* **1992**, *32*, 523.
- (24) Izaguirre, J. A.; Catarello, D. P.; Wozniak, J. M.; Skeel, R. D. Langevin stabilization of molecular dynamics. *J. Chem. Phys.* **2001**, *114*, 2090.
- (25) Rocchia, W.; Sridharan, S.; Nicholls, A.; Alexov, E.; Chiabrera, A.; Honig, B. Rapid grid-based construction of the molecular surface for both molecules and geometric objects: applications to the finite difference Poisson-Boltzmann method. *J. Comput. Chem.* **2002**, *23*, 128.
- (26) Rocchia, W.; Alexov, E.; Honig, B. Extending the applicability of the nonlinear Poisson-Boltzmann equation: multiple dielectric constants and multivalent ions. *J. Phys. Chem. B* **2001**, *105*, 6507.
- (27) Moreira, I. S.; Fernandes, P. A.; Ramos, M. J. Accuracy of the numerical solution of the Poisson-Boltzmann equation. *J. Mol. Struct. (Theochem)* **2005**, *729*, 11.
- (28) Connolly, M. L. Analytical molecular surface calculation. *J. Appl. Crystallogr.* **1983**, *16*, 548.
- (29) Massova, M.; Kollman, P. A. Computational alanine scanning to probe protein-protein interactions: a novel approach to evaluate binding free energies. *J. Am. Chem. Soc.* **1999**, *121*, 36.

CT6003824

Density Functional Study of 2-[(R-Phenyl)amine]-1,4-naphthalenediones[†]

Z. Gómez-Sandoval,[‡] P. Calaminici,[‡] A. M. Köster,^{*,‡} B. Lotina-Hennsen,[§]
B. King-Díaz,[§] N. Macías-Ruvalcaba,[§] M. Aguilar-Martínez,[§] and M. Jiménez-Estrada^{||}

Departamento de Química, CINVESTAV, Avenida Instituto Politécnico Nacional 2508, A.P. 14-740 México D.F. 07000, México, Facultad de Química, Departamentos de Bioquímica y Físicoquímica, Universidad Nacional Autónoma de México, Ciudad Universitaria, México D.F. 04510, México, and Instituto de Química, Universidad Nacional Autónoma de México, Ciudad Universitaria, México D.F. 04510, México.

Received November 12, 2006

Abstract: The molecular and electronic structures of a series of 2-[(R-phenyl)amine]-1,4-naphthalenediones (R = m-Me, p-Me, m-Et, p-CF₃, p-Hex, p-Et, m-F, m-Cl, p-OMe, p-COMe, p-Bu, m-COOH, p-Cl, p-COOH, p-Br, m-NO₂, m-CN, and p-NO₂) and their anions are investigated in the framework of density functional theory. The calculations are of all-electron type using a double zeta valence polarization basis set optimized for density functional theory methods. The theoretical study shows that all compounds are nonplanar. The nonplanarity can be rationalized in terms of occupied π orbitals. A linear correlation between the measured half-wave potentials and the calculated gas-phase electron affinities is found. It holds for local as well as generalized gradient corrected functionals. Structural parameters, harmonic vibrational frequencies, and adiabatic and vertical electron affinities as well as orbital and spin density plots of the studied compounds are presented.

I. Introduction

The quinone moiety appears in a wide range of natural compounds including the electron transport chain of bacteria, mitochondria, and chloroplasts.¹ Interruption of the electron transport chain is an attractive avenue toward green, i.e., ecological less disastrous, herbicides. Therefore, many studies have focused on the chemistry and toxicology of quinone compounds. The biological activity of quinones² is based on their redox system which permits the formation of anion radicals (Q^{•-}) and dianions (Q²⁻) under mild conditions.³ These species are capable of interaction with cellular compounds such as oxygen, deoxyribo nucleic acid (DNA),

and proteins, modifying their biological activities.⁴ The ability of quinones to accept electrons depends on their chemical structure⁵ and the microenvironment of the reaction.⁶ The biological activity of quinones can be modified by substituting the quinone system.^{7,8} Such substitutions do not alter the general characteristic of the quinone redox system but change in a systematic way its electrochemical behavior. In fact, the use of a heteroatom which allows a gradual modulation between the quinone and a substituted phenyl has been suggested in the literature.^{9,10} In this sense, 1,4-naphthoquinone compounds and their derivatives have been widely studied due to their pharmacological use as agents against tuberculosis,¹¹ malaria,¹² bacterial infections,¹³ and neoplasia growth,¹⁴ as larvicides,¹⁵ molluscicides,¹⁵ herbicides,¹⁶ and fungicides.¹⁷

Numerically the substituent effects can be described by molecular properties that are sensitive to the substituent.^{18,19} Because a number of naturally occurring quinones play an important role in electron transport the quinone-hydroxy quinone redox couples are intensive studied. The measured

[†] Dedicated to Professor Dennis R. Salahub on the occasion of his 60th birthday.

* Corresponding author e-mail: akoster@cinvestav.mx.

[‡] CINVESTAV.

[§] Departamentos de Bioquímica y Físicoquímica, Universidad Nacional Autónoma de México.

^{||} Instituto de Química, Universidad Nacional Autónoma de México.

half-wave potentials are sensitive to the substituent pattern and are, therefore, well suited for a numerical description of substituent effects. With this in mind a group of 2-[(R-phenyl)amine]-1,4-naphthalenediones (PANs) have been investigated in our laboratory,²⁰ recently. The half-wave potentials (HWPs) of these compounds were measured by cyclic voltametry in acetonitrile at room temperature. As supporting electrolyte 0.1 M tetraethylammonium tetrafluoroborate was used. Under these conditions ion pairing is minor with anion radicals,^{21,22} and, therefore, solvent effects for the first electron-transfer reaction are negligible.²³ As a consequence, the measured HWPs for the first one-electron transfer, corresponding to the formation of the radical anions, can be directly compared with theoretical gas-phase studies.

Quantitative structure–activity relationship (QSAR) analysis between the herbicide activity and various molecular properties of the studied PAN compounds²⁰ reveal that the HWPs for the first one-electron transfer and detailed geometrical structure data are main ingredients for the prediction of the biological activity of PAN derivatives.²⁴ Therefore, the reliable theoretical prediction of these molecular properties enables the rational design of new herbicides based on this compound class.

With this goal in mind, the results of a density functional theory (DFT) study of a series of PAN derivatives (neutral and anionic) are presented. Optimized structure parameters, harmonic vibrational frequencies, and orbital and spin density plots as well as calculated adiabatic and vertical electron affinities are presented. The relation between the geometric and electronic structure is discussed in details. It is shown that Hückels π counting rule²⁵ can be used to rationalize the geometric structure of the neutral and anionic PAN derivatives.

The article is organized as follows. In section II the computational method is described. In section III the obtained results are analyzed. Finally, in section IV, the conclusions are summarized.

II. Computational Details

Full geometry optimizations, without symmetry constraints, for the following 19 neutral and anionic compounds, H PAN, m-Me PAN, p-Me PAN, m-Et PAN, p-CF₃PAN, p-Hex PAN, p-Et PAN, m-F PAN, m-Cl PAN, p-OMe PAN, p-COMe PAN, p-Bu PAN, m-COOH PAN, p-Cl PAN, p-COOH PAN, p-Br PAN, m-NO₂ PAN, m-CN PAN, and p-NO₂ PAN, were performed. The structures of some selected dianionic compounds such as H, p-Cl, m-Cl, p-Me, and m-Me PAN, were optimized, too.

The optimizations were performed within the density functional theory framework as implemented in the program deMon2k.²⁶ Local and gradient corrected exchange-correlation functionals were used. For the local calculations the Dirac exchange²⁷ in combination with the correlation functional proposed by Vosko, Wilk, and Nusair (VWN)²⁸ was employed. The gradient corrected calculations were performed with the generalized gradient approximation (GGA) for the exchange proposed by Becke²⁹ and the correlation approximation of Lee, Yang and Parr (BLYP).³⁰ The calculations were of all-electron type using a DFT optimized

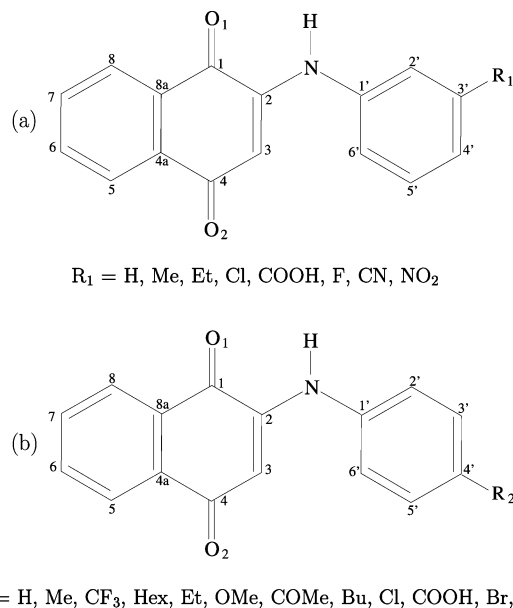


Figure 1. Structure and atomic labels of *meta*- (a) and *para*- (b) substituted PAN derivatives.

double ζ split valence plus polarization basis set (DZVP), and an A2 auxiliary function set³¹ for the variational fitting of the Coulomb potential.³²

A quasi-Newton Levenberg-Marquard method, employing internal redundant coordinates with analytic energy gradients, was used for the structure optimization.³³ The convergence was based on the Cartesian gradient and displacement vectors with thresholds of 10^{-4} and 10^{-3} au, respectively. In order to verify that the optimized structures are minima on the potential energy surface (PES) harmonic frequencies were calculated for selected compounds. The second derivatives were obtained by numerical differentiation (two-points finite difference) of the analytic energy gradients using a displacement of 0.001 au from the optimized geometry for all 3N coordinates. The harmonic frequencies were then obtained by diagonalizing the mass-weighted Cartesian force constant matrix.

III. Results and Discussion

III-A. Structural Analysis. The structures and atomic labels of the studied PAN compounds are shown in Figure 1a,b. R₁ and R₂ represent the substituents in the *meta* and *para* positions, respectively. The optimized VWN geometries are listed in Tables 1–3. Because the DZVP basis set is parametrized for the local VWN functional the optimized structure parameters are usually reliable within 1–2 pm and 1–2 degrees for organic compounds.³⁴ Our DFT calculations show that all neutral PANs are nonplanar independently from the functional used in the optimization. This result is in disagreement with a previous theoretical study³⁵ in which planarity was enforced by the optimization strategy. If this restriction is released,³⁶ then nonplanar structures are also obtained with the theoretical approach in ref 35.

The C₂–N–C₁–C_{6'} dihedral angle (Table 1) for the neutral PANs is found in a range between 14 and 20 degrees. These results were obtained from the optimization of several different initial geometries with varying start values for the

Table 1. Structure Data of the Optimized Neutral PANs^a

geometrical parameter							geometrical parameter						
p-Me	p-CF ₃	p-Hex	p-Et	p-OMe	p-COME		p-Me	p-CF ₃	p-Hex	p-Et	p-OMe	p-COME	
C ₁ -O ₁	1.238	1.238	1.238	1.238	1.239	1.238	O ₁ -C ₁ -C ₂	118.6	118.3	118.6	118.6	118.6	118.3
C ₁ -C ₂	1.496	1.497	1.496	1.496	1.494	1.497	C ₁ -C ₂ -C ₃	120.6	120.5	120.6	120.6	120.6	120.5
C ₂ -C ₃	1.374	1.370	1.374	1.373	1.375	1.370	C ₁ -C ₂ -N	109.6	109.3	109.7	109.6	109.6	109.4
C ₃ -C ₄	1.439	1.443	1.439	1.439	1.437	1.443	C ₂ -N-H	109.4	109.1	109.4	109.4	109.4	109.1
C ₄ -O ₂	1.242	1.240	1.242	1.242	1.243	1.240	C ₂ -N-C _{1'}	132.1	132.2	132.1	132.1	132.0	132.5
C ₄ -C _{4a}	1.488	1.487	1.488	1.488	1.488	1.486	C ₂ -C ₃ -C ₄	121.8	121.7	121.8	121.8	121.8	121.8
C _{4a} -C ₅	1.390	1.390	1.390	1.390	1.391	1.390	H-N-C _{1'}	118.5	118.7	118.5	118.5	118.6	118.4
C ₅ -C ₆	1.393	1.393	1.392	1.392	1.392	1.392	C ₁ -C ₂ -C _{3'}	120.8	120.8	120.7	120.7	121.1	120.7
C ₆ -C ₇	1.398	1.398	1.398	1.398	1.398	1.398	C ₁ -C _{6'} -C _{5'}	120.0	120.0	119.9	119.9	120.7	119.8
C ₇ -C ₈	1.389	1.389	1.389	1.389	1.389	1.389	C _{8a} -C ₁ -C ₂	118.5	118.6	118.5	118.5	118.4	118.6
C ₈ -C _{8a}	1.397	1.397	1.397	1.397	1.397	1.396	C ₂ -N-C ₁ -C _{2'}	-163.4	-165.3	163.4	163.5	162.9	166.6
C _{4a} -C _{8a}	1.403	1.403	1.403	1.403	1.403	1.403	O ₁ -C ₁ -C ₂ -N	-0.6	-0.6	0.5	0.4	0.3	0.7
C ₂ -N	1.349	1.353	1.349	1.349	1.349	1.353	H-N-C ₂ -C ₁	3.2	3.4	-3.3	-3.2	-2.9	-3.5
N-H	1.041	1.042	1.040	1.041	1.041	1.042	C ₁ -C ₂ -C ₃ -C ₄	1.5	1.8	-1.5	-1.6	-1.3	-1.9
N-C _{1'}	1.386	1.381	1.386	1.386	1.387	1.380	C ₂ -C ₃ -C ₄ -C _{4a}	0.4	0.3	-0.5	-0.4	-0.5	-0.2
C ₁ '-C _{2'}	1.403	1.405	1.404	1.404	1.407	1.409	C ₂ -C ₁ -C _{8a} -C ₈	-179.0	-178.8	178.9	178.9	179.0	178.8
C ₂ '-C _{3'}	1.386	1.383	1.386	1.386	1.380	1.379	C _{8a} -C ₁ -C ₂ -N	179.8	179.6	-179.6	-179.7	-179.8	-179.5
C ₃ '-C _{4'}	1.400	1.395	1.400	1.400	1.402	1.402	C ₁ -C ₂ -N-C _{1'}	-176.6	-175.6	176.4	176.5	176.5	175.5
C ₄ -R	1.494	1.490	1.495	1.496	1.352	1.480	O ₁ -C ₂ -C ₄ -O ₂	-173.3	-176.5	176.4	176.2	176.6	176.6
C ₁ '-C _{6'}	1.402	1.404	1.402	1.402	1.399	1.404	C ₂ -N-C ₁ -C _{6'}	19.7	17.6	-19.9	-19.6	-19.8	-15.9
C ₆ '-C _{5'}	1.390	1.388	1.390	1.390	1.392	1.387	O ₁ -H(N)	1.926	1.910	1.927	1.927	1.925	1.912
C ₅ '-C _{4'}	1.398	1.393	1.397	1.397	1.397	1.399							

geometrical parameter							geometrical parameter						
p-Bu	p-Cl	p-COOH	p-Br	p-NO ₂	PAN		p-Bu	p-Cl	p-COOH	p-Br	p-NO ₂	PAN	
C ₁ -O ₁	1.238	1.238	1.238	1.238	1.238	1.238	O ₁ -C ₁ -C ₂	118.6	118.4	118.3	118.4	118.2	118.5
C ₁ -C ₂	1.496	1.496	1.497	1.496	1.498	1.496	C ₁ -C ₂ -C ₃	120.6	120.6	120.5	120.6	120.6	120.5
C ₂ -C ₃	1.374	1.372	1.370	1.372	1.368	1.373	C ₁ -C ₂ -N	109.6	109.5	109.3	109.5	109.2	109.5
C ₃ -C ₄	1.439	1.441	1.443	1.441	1.446	1.440	C ₂ -N-H	109.4	109.2	109.1	109.2	108.8	109.4
C ₄ -O ₂	1.242	1.241	1.240	1.241	1.239	1.242	C ₂ -N-C _{1'}	132.1	132.0	132.5	132.1	132.6	132.2
C ₄ -C _{4a}	1.488	1.487	1.486	1.487	1.485	1.488	C ₂ -C ₃ -C ₄	121.8	120.6	121.7	121.8	121.7	121.8
C _{4a} -C ₅	1.390	1.390	1.390	1.390	1.390	1.390	H-N-C _{1'}	118.4	118.7	118.4	118.7	118.6	118.4
C ₅ -C ₆	1.392	1.393	1.393	1.393	1.393	1.393	C ₁ '-C ₂ -C _{3'}	120.7	121.1	120.6	121.2	120.8	120.8
C ₆ -C ₇	1.398	1.398	1.398	1.398	1.398	1.398	C ₁ '-C _{6'} -C _{5'}	119.9	120.4	120.0	120.5	120.0	120.1
C ₇ -C ₈	1.389	1.389	1.389	1.389	1.389	1.389	C _{8a} -C ₁ -C ₂	118.5	118.5	118.6	118.5	118.6	118.5
C ₈ -C _{8a}	1.397	1.397	1.397	1.397	1.397	1.397	C ₂ -N-C ₁ -C _{2'}	-162.9	163.9	166.3	164.7	167.5	163.4
C _{4a} -C _{8a}	1.403	1.403	1.403	1.403	1.403	1.403	O ₁ -C ₁ -C ₂ -N	-0.3	0.5	0.6	0.6	0.7	0.6
C ₂ -N	1.349	1.351	1.353	1.351	1.356	1.350	H-N-C ₂ -C ₁	3.0	-3.2	-3.5	-3.3	-3.6	-3.4
N-H	1.041	1.041	1.042	1.041	1.043	1.041	C ₁ -C ₂ -C ₃ -C ₄	1.5	-1.6	-1.9	-1.7	-2.0	-1.7
N-C _{1'}	1.387	1.384	1.380	1.383	1.376	1.386	C ₂ -C ₃ -C ₄ -C _{4a}	0.3	-0.4	-0.2	-0.3	-0.2	-0.4
C ₁ '-C _{2'}	1.404	1.404	1.408	1.404	1.409	1.404	C ₂ -C ₁ -C _{8a} -C ₈	-179.2	178.9	178.7	178.8	178.7	178.8
C ₂ '-C _{3'}	1.385	1.385	1.380	1.386	1.380	1.387	C _{8a} -C ₁ -C ₂ -N	180.0	-179.6	-179.6	-179.5	-179.4	-179.5
C ₃ '-C _{4'}	1.400	1.394	1.400	1.393	1.394	1.396	C ₁ -C ₂ -N-C _{1'}	-176.8	175.9	175.4	175.6	174.6	176.5
C ₄ -R	1.495	1.732	1.468	1.887	1.447	1.098	O ₁ -C ₂ -C ₄ -O ₂	-176.5	176.6	176.5	176.5	176.5	176.5
C ₁ '-C _{6'}	1.401	1.402	1.405	1.403	1.406	1.402	C ₂ -N-C ₁ -C _{6'}	19.1	-18.8	-16.5	-18.2	-14.8	-19.4
C ₆ '-C _{5'}	1.390	1.389	1.386	1.390	1.385	1.391	O ₁ -H(N)	1.926	1.917	1.911	1.916	1.900	1.923
C ₅ '-C _{4'}	1.397	1.392	1.398	1.390	1.391	1.393							

geometrical parameter								geometrical parameter							
m-Me	m-Et	m-Cl	m-COOH	m-F	m-NO ₂	m-CN		m-Me	m-Et	m-Cl	m-COOH	m-F	m-NO ₂	m-CN	
C ₁ -O ₁	1.238	1.238	1.238	1.237	1.238	1.237	1.238	O ₁ -C ₁ -C ₂	118.5	118.5	118.4	118.4	118.4	118.2	118.2
C ₁ -C ₂	1.496	1.496	1.497	1.497	1.497	1.498	1.498	C ₁ -C ₂ -C ₃	120.5	120.5	120.6	120.5	120.6	120.5	120.5
C ₂ -C ₃	1.373	1.373	1.371	1.371	1.371	1.369	1.370	C ₁ -C ₂ -N	109.6	109.6	109.5	109.5	109.5	109.3	109.3
C ₃ -C ₄	1.439	1.439	1.442	1.442	1.442	1.444	1.443	C ₂ -N-H	109.4	109.4	109.3	109.5	109.3	109.2	109.1
C ₄ -O ₂	1.242	1.242	1.241	1.241	1.241	1.240	1.240	C ₂ -N-C _{1'}	132.2	132.3	132.0	132.0	131.9	131.9	132.0
C ₄ -C _{4a}	1.488	1.488	1.487	1.487	1.487	1.486	1.486	C ₂ -C ₃ -C ₄	121.8	121.8	121.8	121.8	121.8	121.7	121.7
C _{4a} -C ₅	1.390	1.390	1.390	1.390	1.390	1.390	1.390	H-N-C _{1'}	118.4	118.3	118.7	118.5	118.8	118.9	118.8
C ₅ -C ₆	1.393	1.393	1.393	1.393	1.393	1.393	1.393	C ₁ '-C ₂ -C _{3'}	121.8	121.7	120.0	120.5	119.3	119.4	120.5
C ₆ -C ₇	1.398	1.398	1.398	1.398	1.398	1.398	1.398	C ₁ '-C _{6'} -C _{5'}	119.3	119.4	119.7	120.4	120.0	120.6	120.4
C ₇ -C ₈	1.390	1.389	1.390	1.390	1.389	1.390	1.389	C _{8a} -C ₁ -C ₂	118.5	118.5	118.5	118.5	118.5	118.6	118.6
C ₈ -C _{8a}	1.397	1.397	1.397	1.397	1.397	1.396	1.397	C ₂ -N-C ₁ -C _{2'}	-163.5	164.1	-163.5	-163.6	162.6	-164.0	164.3
C _{4a} -C _{8a}	1.403	1.403	1.403	1.403	1.403	1.403	1.403	O ₁ -C ₁ -C ₂ -N	-0.7	0.7	-0.7	-0.7	0.7	-0.7	0.7
C ₂ -N	1.350	1.350	1.351	1.351	1.352	1.353	1.353	H-N-C ₂ -C ₁	3.4	-3.3	3.5	3.7	-3.5	3.6	-3.4
N-H	1.040	1.040	1.041	1.041	1.041	1.041	1.041	C ₁ -C ₂ -C ₃ -C ₄	1.7	-1.7	1.8	1.8	-1.8	1.8	-1.8
N-C _{1'}	1.386	1.386	1.384	1.385	1.385	1.382	1.382	C ₂ -C ₃ -C ₄ -C _{4a}	0.4	-0.4	0.3	0.3	-0.4	0.3	-0.3
C ₁ '-C _{2'}	1.403	1.403	1.403	1.399	1.403	1.400	1.400	C ₂ -C ₁ -C _{8a} -C ₈	-178.8	178.8	-178.8	-178.8	178.8	-178.8	178.8
C ₂ '-C _{3'}	1.391	1.390	1.386	1.390	1.383	1.384	1.396	C _{8a} -C ₁ -C ₂ -N	179.4	-179.4	179.5	179.5	-179.5	179.6	-179.5
C ₃ '-C _{4'}	1.401	1.401	1.394	1.399	1.390	1.391	1.404	C ₁ -C ₂ -N-C _{1'}	-176.6	176.3	-176.0	-175.8	176.3	-175.8	175.6
C ₄ -R	1.495	1.498	1.733	1.476</											

Table 2. Structure Data of the Optimized Anionic PANs^a

geometrical parameter	p-Me	p-CF ₃	p-Hex	p-Et	p-OMe	p-COMe	geometrical parameter	p-Me	p-CF ₃	p-Hex	p-Et	p-OMe	p-COMe
C ₁ -O ₁	1.278	1.276	1.278	1.278	1.278	1.273	O ₁ -C ₁ -C ₂	118.9	118.9	118.9	118.9	118.8	119.1
C ₁ -C ₂	1.457	1.456	1.457	1.457	1.457	1.458	C ₁ -C ₂ -C ₃	121.9	122.0	121.9	121.9	121.9	121.9
C ₂ -C ₃	1.389	1.387	1.388	1.388	1.388	1.388	C ₁ -C ₂ -N	108.7	108.4	108.7	108.7	108.8	108.5
C ₃ -C ₄	1.431	1.431	1.431	1.431	1.431	1.431	C ₂ -N-H	105.5	105.0	105.5	105.4	105.6	105.3
C ₄ -O ₂	1.265	1.264	1.265	1.265	1.266	1.263	C ₂ -N-C _{1'}	133.8	134.2	133.8	133.8	133.3	134.5
C _{4a} -C _{4a}	1.470	1.470	1.470	1.470	1.470	1.472	C ₂ -C ₃ -C ₄	121.9	122.1	122.2	122.2	122.3	122.1
C _{4a} -C ₅	1.399	1.399	1.399	1.399	1.399	1.399	H-N-C _{1'}	120.3	120.4	120.4	120.4	120.5	119.9
C ₅ -C ₆	1.387	1.387	1.387	1.387	1.387	1.387	C _{1'} -C ₂ -C _{3'}	121.5	121.5	121.4	121.4	121.8	121.4
C ₆ -C ₇	1.409	1.408	1.409	1.409	1.409	1.407	C _{1'} -C _{6'} -C _{5'}	120.6	120.6	120.5	120.5	121.2	120.4
C ₇ -C ₈	1.384	1.384	1.384	1.384	1.384	1.385	C _{8a} -C ₁ -C ₂	117.2	117.2	117.2	117.2	117.1	117.2
C ₈ -C _{8a}	1.407	1.406	1.407	1.407	1.407	1.405	C ₂ -N-C _{1'} -C _{2'}	-175.1	-177.1	175.2	175.2	-173.9	176.1
C _{4a} -C _{8a}	1.420	1.418	1.420	1.420	1.420	1.417	O ₁ -C ₁ -C ₂ -N	0.4	0.4	-0.5	-0.5	0.5	-0.3
C ₂ -N	1.374	1.377	1.375	1.374	1.373	1.375	H-N-C ₂ -C ₁	2.2	2.3	-2.2	-2.1	2.0	-2.4
N-H	1.051	1.055	1.052	1.052	1.051	1.053	C ₁ -C ₂ -C ₃ -C ₄	1.5	1.7	-1.6	-1.6	1.6	-1.6
N-C _{1'}	1.365	1.356	1.364	1.364	1.368	1.356	C ₂ -C ₃ -C ₄ -C _{4a}	-0.1	-0.3	0.3	0.2	-0.2	0.3
C _{1'} -C _{2'}	1.413	1.418	1.413	1.414	1.414	1.420	C ₂ -C ₁ -C _{8a} -C ₈	-179.3	-179.3	179.5	179.3	-179.3	179.3
C _{2'} -C _{3'}	1.385	1.379	1.385	1.385	1.382	1.374	C _{8a} -C ₁ -C ₂ -N	-179.3	-179.3	179.1	179.3	-179.2	179.5
C _{3'} -C _{4'}	1.402	1.402	1.402	1.402	1.400	1.411	C ₁ -C ₂ -N-C _{1'}	-170.5	-170.1	170.0	170.5	-169.6	172.0
C ₄ -R	1.496	1.474	1.497	1.498	1.371	1.457	O ₁ -C ₂ -C ₄ -O ₂	-177.8	-177.8	177.6	177.6	-177.6	177.7
C _{1'} -C _{6'}	1.410	1.415	1.411	1.410	1.406	1.415	C ₂ -N-C _{1'} -C _{6'}	7.0	4.6	-6.8	-6.9	7.9	-5.4
C _{6'} -C _{5'}	1.390	1.384	1.390	1.390	1.395	1.383	O ₁ -H(N)	1.822	1.800	1.821	1.820	1.824	1.816
C _{5'} -C _{4'}	1.398	1.398	1.398	1.398	1.394	1.407							

geometrical parameter	p-Bu	p-Cl	p-COOH	p-Br	p-NO ₂	PAN	geometrical parameter	p-Bu	p-Cl	p-COOH	p-Br	p-NO ₂	PAN
C ₁ -O ₁	1.278	1.277	1.274	1.277	1.268	1.278	O ₁ -C ₁ -C ₂	118.9	118.8	119.1	118.8	119.2	118.9
C ₁ -C ₂	1.457	1.456	1.458	1.456	1.462	1.457	C ₁ -C ₂ -C ₃	121.9	122.0	122.0	122.0	121.8	121.9
C ₂ -C ₃	1.388	1.387	1.388	1.387	1.387	1.388	C ₁ -C ₂ -N	108.8	108.6	108.4	108.6	108.5	108.7
C ₃ -C ₄	1.431	1.431	1.431	1.431	1.431	1.431	C ₂ -N-H	105.5	105.2	105.2	105.2	105.7	105.4
C ₄ -O ₂	1.265	1.264	1.263	1.264	1.260	1.265	C ₂ -N-C _{1'}	133.7	133.7	134.6	133.6	134.6	134.0
C _{4a} -C _{4a}	1.470	1.470	1.471	1.470	1.474	1.470	C ₂ -C ₃ -C ₄	122.2	122.1	122.1	122.1	122.0	122.2
C _{4a} -C ₅	1.399	1.399	1.399	1.399	1.398	1.399	H-N-C _{1'}	120.3	120.6	120.0	120.6	119.5	120.2
C ₅ -C ₆	1.388	1.387	1.387	1.387	1.388	1.387	C _{1'} -C ₂ -C _{3'}	121.4	121.8	121.4	121.9	121.4	121.5
C ₆ -C ₇	1.409	1.408	1.407	1.408	1.406	1.409	C _{1'} -C _{6'} -C _{5'}	120.5	120.9	120.5	121.1	120.5	120.6
C ₇ -C ₈	1.384	1.384	1.384	1.384	1.385	1.384	C _{8a} -C ₁ -C ₂	117.2	117.2	117.2	117.1	117.3	117.2
C ₈ -C _{8a}	1.407	1.407	1.405	1.407	1.404	1.407	C ₂ -N-C _{1'} -C _{2'}	175.1	175.8	176.4	175.8	-175.3	-175.6
C _{4a} -C _{8a}	1.420	1.419	1.417	1.419	1.414	1.420	O ₁ -C ₁ -C ₂ -N	-0.4	-0.5	-0.2	-0.4	0.0	0.3
C ₂ -N	1.375	1.376	1.376	1.376	1.371	1.375	H-N-C ₂ -C ₁	-2.4	-2.2	-2.5	-2.3	2.5	2.3
N-H	1.051	1.053	1.054	1.053	1.052	1.051	C ₁ -C ₂ -C ₃ -C ₄	-1.6	-1.7	-1.6	-1.8	1.5	1.7
N-C _{1'}	1.364	1.361	1.355	1.360	1.358	1.364	C ₂ -C ₃ -C ₄ -C _{4a}	0.2	0.3	0.2	0.3	-0.1	-0.2
C _{1'} -C _{2'}	1.413	1.414	1.420	1.415	1.419	1.414	C ₂ -C ₁ -C _{8a} -C ₈	179.2	179.3	179.3	179.3	-179.3	-179.3
C _{2'} -C _{3'}	1.385	1.385	1.375	1.385	1.376	1.386	C _{8a} -C ₁ -C ₂ -N	179.4	179.3	179.4	179.3	-179.6	-179.4
C _{3'} -C _{4'}	1.402	1.395	1.408	1.394	1.403	1.399	C ₁ -C ₂ -N-C _{1'}	170.0	169.2	171.7	169.1	-172.9	-169.9
C ₄ -R	1.497	1.748	1.447	1.902	1.419	1.098	O ₁ -C ₂ -C ₄ -O ₂	177.6	177.5	177.8	177.5	-177.7	-177.7
C _{1'} -C _{6'}	1.411	1.412	1.416	1.412	1.416	1.411	C ₂ -N-C _{1'} -C _{6'}	-7.2	-5.9	-5.1	-6.0	6.3	5.9
C _{6'} -C _{5'}	1.390	1.390	1.382	1.390	1.381	1.390	O ₁ -H(N)	1.823	1.810	1.809	1.810	1.824	1.821
C _{5'} -C _{4'}	1.398	1.391	1.405	1.390	1.400	1.395							

geometrical parameter	m-Me	m-Et	m-Cl	m-COOH	m-F	m-NO ₂	m-CN	geometrical parameter	m-Me	m-Et	m-Cl	m-COOH	m-F	m-NO ₂	m-CN
C ₁ -O ₁	1.278	1.277	1.277	1.275	1.277	1.265	1.276	O ₁ -C ₁ -C ₂	118.9	118.9	118.9	118.9	118.9	118.9	118.8
C ₁ -C ₂	1.457	1.457	1.456	1.458	1.456	1.466	1.456	C ₁ -C ₂ -C ₃	121.9	121.9	122.0	121.9	121.9	121.5	122.1
C ₂ -C ₃	1.388	1.388	1.387	1.387	1.387	1.384	1.387	C ₁ -C ₂ -N	108.7	108.7	108.6	108.7	108.6	109.2	108.5
C ₃ -C ₄	1.431	1.431	1.431	1.431	1.431	1.432	1.431	C ₂ -N-H	105.4	105.5	105.2	105.6	105.2	107.1	105.2
C ₄ -O ₂	1.265	1.265	1.264	1.264	1.265	1.259	1.264	C ₂ -N-C _{1'}	134.0	133.9	133.6	133.4	133.8	132.7	133.3
C _{4a} -C _{4a}	1.470	1.470	1.470	1.471	1.470	1.474	1.471	C ₂ -C ₃ -C ₄	122.3	122.2	122.1	122.2	122.2	122.2	122.1
C _{4a} -C ₅	1.399	1.399	1.399	1.399	1.399	1.397	1.399	H-N-C _{1'}	120.2	120.2	120.6	120.4	120.5	119.8	120.7
C ₅ -C ₆	1.387	1.387	1.387	1.387	1.387	1.388	1.387	C _{1'} -C ₂ -C _{3'}	122.4	122.4	120.4	121.3	120.0	120.3	121.1
C ₆ -C ₇	1.408	1.409	1.408	1.408	1.408	1.406	1.408	C _{1'} -C _{6'} -C _{5'}	120.0	120.1	120.4	120.8	120.6	120.4	121.0
C ₇ -C ₈	1.384	1.384	1.384	1.384	1.384	1.385	1.384	C _{8a} -C ₁ -C ₂	117.2	117.1	117.1	117.2	117.2	117.5	117.2
C ₈ -C _{8a}	1.407	1.407	1.406	1.406	1.407	1.404	1.406	C ₂ -N-C _{1'} -C _{2'}	175.6	175.3	175.8	175.4	175.5	171.9	176.2
C _{4a} -C _{8a}	1.420	1.420	1.419	1.418	1.419	1.414	1.418	O ₁ -C ₁ -C ₂ -N	-0.3	-0.3	-0.3	-0.3	-0.3	-0.1	-0.4
C ₂ -N	1.375	1.375	1.377	1.375	1.377	1.368	1.377	H-N-C ₂ -C ₁	-2.3	-2.4	-2.5	-2.6	-2.5	-3.1	-2.7
N-H	1.051	1.051	1.053	1.051	1.052	1.046	1.053	C ₁ -C ₂ -C ₃ -C ₄	-1.6	-1.7	-1.8	-2.0	-1.7	-2.3	-2.0
N-C _{1'}	1.364	1.364	1.360	1.363	1.361	1.371	1.359	C ₂ -C ₃ -C ₄ -C _{4a}	0.2	0.1	0.2	0.3	0.3	0.4	0.4
C _{1'} -C _{2'}	1.413	1.414	1.415	1.408	1.414	1.404	1.410	C ₂ -C ₁ -C _{8a} -C ₈	179.3	179.2	179.2	179.2	179.3	179.0	179.2
C _{2'} -C _{3'}	1.388	1.388	1.382	1.392	1.379	1.388	1.395	C _{8a} -C ₁ -C ₂ -N	179.5	179.5	179.4	179.3	179.4	179.6	179.3
C _{3'} -C _{4'}	1.403	1.403	1.394	1.404	1.391	1.401	1.409	C ₁ -C ₂ -N-C _{1'}	170.0	170.1	168.7	168.1	169.5	169.1	167.2
C ₄ -R	1.499	1.501	1.750	1.465	1.354	1.439	1.424	O ₁ -C ₂ -C ₄ -O ₂	177.6	177.7	177.6	177.5	177.6	177.0	177.5
C _{1'} -C _{6'}	1.410	1.410	1.412	1.414	1.413	1.413	1.415	C ₂ -N-C _{1'} -C _{6'}	-5.7	-6.5	-5.7	-6.3	-6.0	-10.1	-5.5
C _{6'} -C _{5'}	1.390	1.391	1.388	1.392	1.389	1.393	1.389	O ₁ -H(N)	1.821	1.823	1.811	1.824	1.813	1.868	1.808
C _{5'} -C _{4'}	1.394	1.393	1.396	1.390	1.396	1.389	1.391								

^a Bond lengths are reported in Å and angles are given in degrees.

Table 3. Structure Data of the Optimized PAN Dianions^a

geometrical parameter	PAN	p-Cl	m-Cl	p-Me	m-Me
C ₁ -O ₁	1.312	1.310	1.310	1.311	1.311
C ₁ -C ₂	1.435	1.435	1.435	1.435	1.436
C ₂ -C ₃	1.411	1.411	1.411	1.411	1.411
C ₃ -C ₄	1.420	1.422	1.421	1.422	1.422
C ₄ -O ₂	1.287	1.286	1.286	1.287	1.287
C ₄ -C _{4a}	1.464	1.465	1.465	1.464	1.464
C _{4a} -C ₅	1.403	1.403	1.403	1.403	1.403
C ₅ -C ₆	1.389	1.389	1.389	1.389	1.389
C ₆ -C ₇	1.419	1.418	1.418	1.419	1.419
C ₇ -C ₈	1.383	1.383	1.383	1.383	1.383
C ₈ -C _{8a}	1.415	1.415	1.414	1.415	1.415
C _{4a} -C _{8a}	1.444	1.442	1.441	1.444	1.443
C ₂ -N	1.389	1.388	1.388	1.388	1.388
N-H	1.078	1.080	1.081	1.077	1.077
N-C _{1'}	1.345	1.344	1.342	1.346	1.345
C _{1'} -C _{2'}	1.429	1.430	1.433	1.428	1.429
C _{2'} -C _{3'}	1.384	1.383	1.377	1.384	1.385
C _{3'} -C _{4'}	1.407	1.400	1.399	1.408	1.410
C _{4'} -R	1.765	1.496			
C _{3'} -R			1.772		1.501
C _{1'} -C _{6'}	1.426	1.427	1.427	1.425	1.425
C _{6'} -C _{5'}	1.387	1.387	1.384	1.388	1.387
C _{5'} -C _{4'}	1.405	1.399	1.408	1.406	1.404
O ₁ -C ₁ -C ₂	119.2	119.2	119.2	119.2	119.2
C ₁ -C ₂ -C ₃	123.5	123.5	123.5	123.5	123.4
C ₁ -C ₂ -N	107.1	107.0	106.9	107.1	107.1
C ₂ -N-H	101.3	101.2	101.1	101.4	101.3
C ₂ -N-C _{1'}	135.9	135.8	135.8	135.8	136.2
C ₂ -C ₃ -C ₄	122.8	122.6	122.7	122.7	122.8
H-N-C _{1'}	122.4	122.6	122.8	122.3	122.2
C _{1'} -C ₂ -C _{3'}	122.1	122.3	120.5	122.0	122.9
C _{1'} -C _{6'} -C _{5'}	121.2	121.5	121.1	121.1	120.7
C _{8a} -C ₁ -C ₂	115.5	115.6	115.6	115.5	115.6
C ₂ -N-C _{1'} -C _{2'}	-179.3	179.2	178.7	-179.8	178.8
O ₁ -C ₁ -C ₂ -N	0.9	-0.9	-0.7	0.9	-0.6
H-N-C ₂ -C ₁	1.3	-1.1	-1.2	1.1	-0.9
C ₁ -C ₂ -C ₃ -C ₄	1.0	-1.0	-0.9	1.1	-0.8
C ₂ -C ₃ -C ₄ -C _{4a}	-0.3	0.2	0.2	-0.2	0.2
C ₂ -C ₁ -C _{8a} -C ₈	-179.9	179.9	179.9	-179.9	180.0
C _{8a} -C ₁ -C ₂ -N	-178.7	178.7	178.9	-178.7	178.9
C ₁ -C ₂ -N-C _{1'}	-171.2	171.4	172.3	-170.7	173.6
O ₁ -C ₂ -C ₄ -O ₂	-178.4	178.5	178.6	-178.5	178.8
C ₂ -N-C _{1'} -C _{6'}	1.5	-1.6	-2.0	1.4	-1.5
O ₁ -H(N)	1.686	1.678	1.673	1.689	1.689

^a Bond lengths are reported in Å and angles are given in degrees.

C₂-N-C_{1'}-C_{6'} dihedral angle. Only the global minima are reported in Table 1. Positive signs of the C₂-N-C_{1'}-C_{6'} dihedral angle indicate that the carbon atoms C_{2'} and C_{3'} are located behind the paper plane in Figure 1. In all compounds the energy differences between the minima with positive and negative C₂-N-C_{1'}-C_{6'} dihedral angles are small. For the PAN system we scanned the PES along the C₂-N-C_{1'}-C_{6'} dihedral angle. The rotation barrier is below 0.5 kcal/mol which explains the floppy behavior of this coordinate in structure optimizations.

The m-F PAN shows the largest deviation from planarity (20.1 degrees), while the p-NO₂ PAN shows the smallest

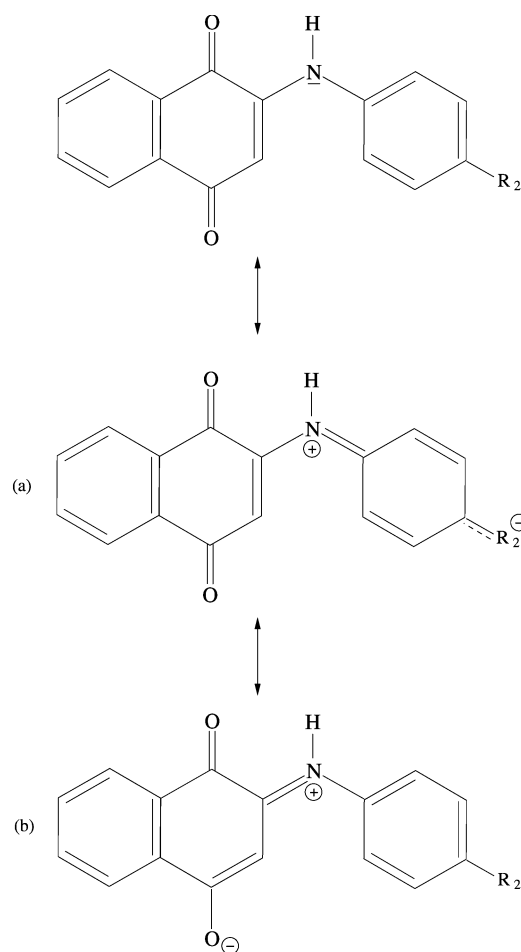


Figure 2. Resonance structures for *para*-substituted phenyl substituents. In (a) R₂ is the dominating electron acceptor, whereas in (b) the quinone oxygen O₂ dominates.

(14.8 degrees). The absolute value of the dihedral angle increases with the electron donor capacity of the *para* substituent along the series p-NO₂ < p-CF₃ < p-Br < H < p-Et < p-Me < p-MeO. This behavior can be straightforwardly explained by the resonance structures depicted in Figure 2 and discussed later on.

When an electron is added to the neutral PANs and the corresponding radical anion is formed, the C₂-N-C_{1'}-C_{6'} dihedral angles decrease by 10 degrees or more as Table 2 shows. The m-NO₂ anion possesses the largest C₂-N-C_{1'}-C_{6'} dihedral angle (10.1 degrees), while the p-CF₃ anion has the smallest dihedral angle (4.6 degrees). If a second electron is added to form the corresponding dianion, then the PANs become practical planar with C₂-N-C_{1'}-C_{6'} dihedral angles of around 1 degree or less. As examples the optimized structure parameters of the H, p-Cl, m-Cl, p-Me, and m-Me PAN dianions are listed in Table 3.

Another structural detail was observed in the naphthoquinone moiety. At first glance one might expect that this moiety is perfectly planar. However, we found a small rumpling in the neutral and anionic systems in the C₁-C₂-C₃-C₄ dihedral angles (see Tables 1 and 2). Because these values are in the range of 2 degrees and, thus, closed to the numerical accuracy of deMon2k we first attributed them to noise in the numerical integration of the exchange-correlation potential. However, the rumpling remained even when

Table 4. Frequencies [cm^{-1}] of Selected Neutral PANs

molecule	frequencies (cm^{-1})										
PAN	14.7	48.5	80.8	91.6	121.7	150.7	196.7	211.6	237.6	259.9	
	293.2	381.1	392.5	405.6	430.4	452.7	457.1	476.5	507.6	550.7	
	578.7	604.0	654.2	658.7	688.1	708.3	711.4	712.4	728.7	757.5	
	770.7	797.8	799.5	814.7	842.9	862.0	877.3	891.9	933.1	953.8	
	963.6	985.3	1006.7	1019.4	1034.1	1037.9	1085.2	1090.7	1121.4	1135.0	
	1136.4	1162.5	1205.1	1228.6	1247.3	1276.8	1313.4	1337.9	1363.4	1414.8	
	1430.7	1457.4	1470.5	1490.9	1496.9	1546.2	1616.3	1626.3	1640.5	1648.5	
	1658.5	1679.3	1710.7	3094.3	3102.4	3105.6	3109.1	3110.1	3117.4	3121.2	
	3122.6	3143.4	3153.4	3288.3							
	p-CF ₃	13.0	29.1	32.0	56.0	67.0	108.2	121.8	145.3	162.8	170.3
		205.3	226.0	254.6	290.7	355.4	381.2	383.2	389.6	402.3	405.1
436.6		452.9	471.2	479.1	498.1	556.8	566.6	574.5	605.2	620.7	
656.5		663.6	708.5	711.2	715.0	728.4	754.7	760.8	767.0	789.5	
797.3		800.0	816.7	837.5	863.6	891.1	937.5	946.0	960.9	983.2	
1006.1		1013.7	1037.2	1073.6	1087.9	1104.7	1113.2	1135.4	1139.9	1161.5	
1182.6		1207.0	1223.2	1244.5	1278.5	1297.2	1323.5	1336.6	1367.7	1409.5	
1431.3		1450.5	1470.8	1491.8	1508.3	1567.9	1616.8	1624.2	1639.2	1654.5	
1670.7		1684.1	1712.1	3109.0	3111.6	3117.2	3123.8	3124.9	3130.2	3133.9	
3153.2		3171.5	3277.4								
m-F		23.5	34.5	81.5	83.9	123.4	152.6	197.0	200.2	211.0	240.3
	258.2	279.9	381.8	392.8	409.2	431.3	442.7	452.6	464.1	489.2	
	512.4	551.7	577.2	596.1	655.6	656.8	664.0	708.7	712.9	716.5	
	720.3	759.2	763.1	767.5	792.8	797.8	823.8	835.8	849.9	890.5	
	909.7	949.9	959.9	981.8	1007.1	1018.6	1036.9	1069.6	1088.8	1111.8	
	1132.4	1143.8	1154.3	1205.8	1237.4	1266.3	1273.8	1309.3	1342.4	1363.8	
	1417.1	1431.4	1447.9	1472.5	1490.4	1511.8	1552.3	1618.2	1632.5	1639.6	
	1653.7	1665.5	1680.8	1712.5	3107.6	3113.6	3116.2	3125.2	3130.6	3133.0	
	3149.4	3156.5	3169.1	3294.6							

improving the grid accuracy. A closer look at the experimental available crystallographic data^{37,38} revealed that this rumpling is in fact in agreement with experiments. Similar deviations from planarity are found in crystallographic data of other aromatic compounds, too.³⁹ The aromaticity is usually not substantially effected by these deviations from planarity.⁴⁰

Because the nitrogen atom modulates the charge transfer between the quinone and the *para*- or *meta*-substituted phenyl ring it is interesting to analyze the bonding in the quinone ring with respect to the phenyl substituent. Along the series p-NO₂ < p-CF₃ < p-Br < H < p-Et < p-Me < p-OMe the electron-donor capacity of the phenyl substituent increases. As a result we observe elongation of the N-C_{1'} bond (from 1.376 Å to 1.387 Å), contraction of the C₂-N bond (from 1.356 Å to 1.349 Å), elongation of the C₂-C₃ bond (from 1.368 Å to 1.375 Å), contraction of the C₃-C₄ bond (from 1.446 Å to 1.437 Å), and elongation of the C₄-O₂ bond (from 1.239 Å to 1.243 Å) in the neutral PANs. These bond length changes can be explained by the two possible resonance structures for the *para*-substituted PANs depicted in Figure 2. If the R₂ electron acceptor strength is larger than that of the quinone oxygen, O₂, then the weight of resonance structure (a) in Figure 2 increases. As a result the N-C_{1'} bond is contracted due to its double bond character in the (a) resonance structure. On the other hand, if the quinone oxygen O₂ is the dominant electron acceptor in the system, then the weight of resonance structure (b) in Figure 2 will be increased. In this situation the C₂-N bond is

shortened due to its double bond character in resonance structure (b).

The other bond length changes are direct consequences of the preference of one or the other resonance structure in Figure 2. Besides these changes in the covalent bonds a slight elongation of the O₁...H(N) distance is also noticed (Table 1). In the corresponding *meta*-substituted compounds a similar trend can be found in the series m-NO₂ > m-CN > mF > m-Cl > m-Et > m-Me. However, the distortions are smaller as in the *para*-substituted systems because no equivalent resonance structures can be formulated. In the anionic systems the same general trend can be observed (see Table 2). The only exception is in the C₃-C₄ bond which is around 1.43 Å long independently from the substitution. In all cases, going from the neutral to the radical anion to the dianion (PAN → PAN^{•-} → PAN²⁻) a gradual contraction of the O₁...H(N) distance occurs. This is due to the increased density at the quinone oxygen O₁ that strengthen the hydrogen bridge.

III-B. Vibrational Analysis. In order to characterize the optimized structures and to simulate the infrared (IR) spectra a harmonic frequency analysis was performed for selected molecules using the VWN optimized structures. The results for the neutral and anionic H, p-CF₃, and m-F PAN are listed in Tables 4 and 5, respectively. Similar results were obtained for other structures.

As can be seen from Tables 4 and 5 all calculated frequencies are positive, and, therefore, the optimized structures are minima on the PES. A closer inspection of

Table 5. Frequencies [cm^{-1}] of Selected Anionic PANs

molecule	frequencies (cm^{-1})										
PAN	24.7	40.7	84.4	101.2	137.1	166.5	199.1	228.6	245.4	255.2	
	286.5	371.3	387.1	407.4	430.3	459.6	470.4	481.4	497.5	551.5	
	577.1	606.9	641.0	654.7	672.8	685.3	707.3	714.8	719.4	735.2	
	765.2	773.7	798.2	817.9	822.6	836.1	848.7	866.8	908.0	919.7	
	934.8	948.4	1003.1	1016.5	1025.6	1034.4	1074.3	1080.5	1104.2	1122.1	
	1128.4	1158.0	1190.0	1215.8	1230.7	1279.0	1290.8	1310.7	1381.5	1404.7	
	1417.8	1453.5	1460.6	1475.0	1491.3	1550.7	1554.2	1569.5	1584.4	1600.7	
	1634.0	1646.3	1664.6	3077.1	3087.2	3089.2	3090.8	3099.6	3104.0	3111.8	
	3115.4	3133.2	3139.7	3159.1							
	p-CF ₃	11.2	20.8	30.7	59.8	72.9	114.4	135.8	142.4	169.0	173.1
		206.6	224.2	252.0	287.9	364.1	373.1	382.9	391.6	398.0	414.4
431.7		459.5	471.6	482.8	495.1	560.6	565.3	568.1	594.0	619.1	
640.3		662.7	686.8	708.0	717.0	717.8	739.3	745.8	762.8	770.1	
776.1		799.3	834.3	848.3	855.9	883.9	917.3	929.6	938.6	954.4	
1007.1		1020.0	1026.6	1050.8	1078.0	1089.4	1095.3	1107.7	1130.1	1147.7	
1154.9		1191.8	1211.7	1230.1	1278.6	1288.3	1301.1	1353.1	1392.0	1395.9	
1420.6		1456.0	1467.6	1481.7	1501.4	1555.0	1562.4	1571.9	1594.6	1598.1	
1639.4		1646.2	1668.5	3081.7	3091.8	3095.0	3102.4	3106.3	3113.8	3116.8	
3123.4		3143.7	3174.1								
m-F		24.2	33.6	76.8	96.6	141.8	165.6	198.2	207.3	220.9	237.0
	260.6	277.2	371.3	394.0	406.8	434.0	442.6	458.7	472.4	497.3	
	510.5	550.5	581.3	589.3	642.8	652.5	662.3	686.7	690.8	708.9	
	716.7	740.4	753.2	766.1	768.6	793.8	805.5	836.0	850.6	866.1	
	894.3	934.9	936.5	949.5	995.6	1015.4	1023.9	1058.7	1078.1	1102.3	
	1115.3	1136.8	1148.8	1191.8	1230.0	1243.8	1263.8	1288.9	1313.6	1375.2	
	1406.6	1418.2	1446.7	1461.0	1482.9	1500.5	1553.4	1556.1	1571.3	1589.0	
	1605.7	1637.5	1645.9	1669.5	3078.9	3090.6	3095.9	3100.6	3107.8	3117.7	
	3122.9	3134.0	3143.1	3168.6							

these tables reveals that the low frequencies of these systems are small. The first two vibrational modes of the neutral PAN (14.7 and 48.5 cm^{-1}) are rotations around the $\text{C}_1\text{--C}_2\text{--N--C}_1'$ and $\text{C}_2\text{--N--C}_1'\text{--C}_6'$ dihedral angles. The following two frequencies (80.8 and 91.6 cm^{-1}) are deformation modes in the naphthoquinone moiety that couple with the above-described two dihedral angles. In the substituted PANs the situation is very similar. A main difference is the coupling of the internal rotations of substituent groups, like the CF_3 , to the low lying frequencies of the $\text{C}_1\text{--C}_2\text{--N--C}_1'$ and $\text{C}_2\text{--N--C}_1'\text{--C}_6'$ dihedral angles. In the corresponding anionic systems this coupling is usually reduced.

In Figure 3 the simulated infrared spectrum (IR) of the PAN molecule is depicted. For the simulation the harmonic frequencies were broadened by 5 cm^{-1} . Five significant groups of signals can be distinguished. The finger print bands (modes 58 and 59 in Table 4; labeled with **A** in Figure 3) appear at around 1350 cm^{-1} . At 1546 cm^{-1} (mode 66 in Table 4; labeled with **B** in Figure 3) the in-plane $\text{N--H}\cdots\text{O}$ deformation band appears. The C=C valence bands (modes 67, 69, 70, and 71 in Table 4; labeled with **C** in Figure 3) dominate the IR spectrum of the PAN. The two shoulders at higher wave numbers (modes 72 and 73 in Table 4; labeled **D** in Figure 3) correspond to the two C=O valence bands (C=O_2 at 1680 cm^{-1} and C=O_1 at 1710 cm^{-1}). The N--H stretch band (mode 84 in Table 4; labeled **E** in Figure 3) appears in our simulation at 3288 cm^{-1} . This is in fair

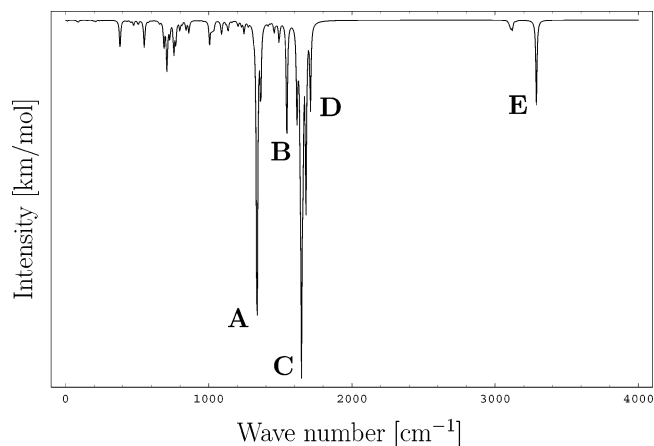


Figure 3. Simulated IR spectrum for the PAN molecule. A broadening of 5 cm^{-1} was applied. See the text for the discussion of the marked bands.

agreement with the experimental observation⁴¹ where a sharp band at 3310 cm^{-1} was assigned to the N--H stretch vibration.

III-C. Electronic Structure Analysis. At first glance the nonplanarity of the neutral PAN derivatives might be assigned to steric interactions. However, this is contradictory to our finding that anionic systems are more planar and that the dianions are almost perfectly planar. Therefore, the electronic structure should be mainly responsible for these structural changes. For this reason we investigated the π orbital occupation of the unsubstituted PAN. In order to

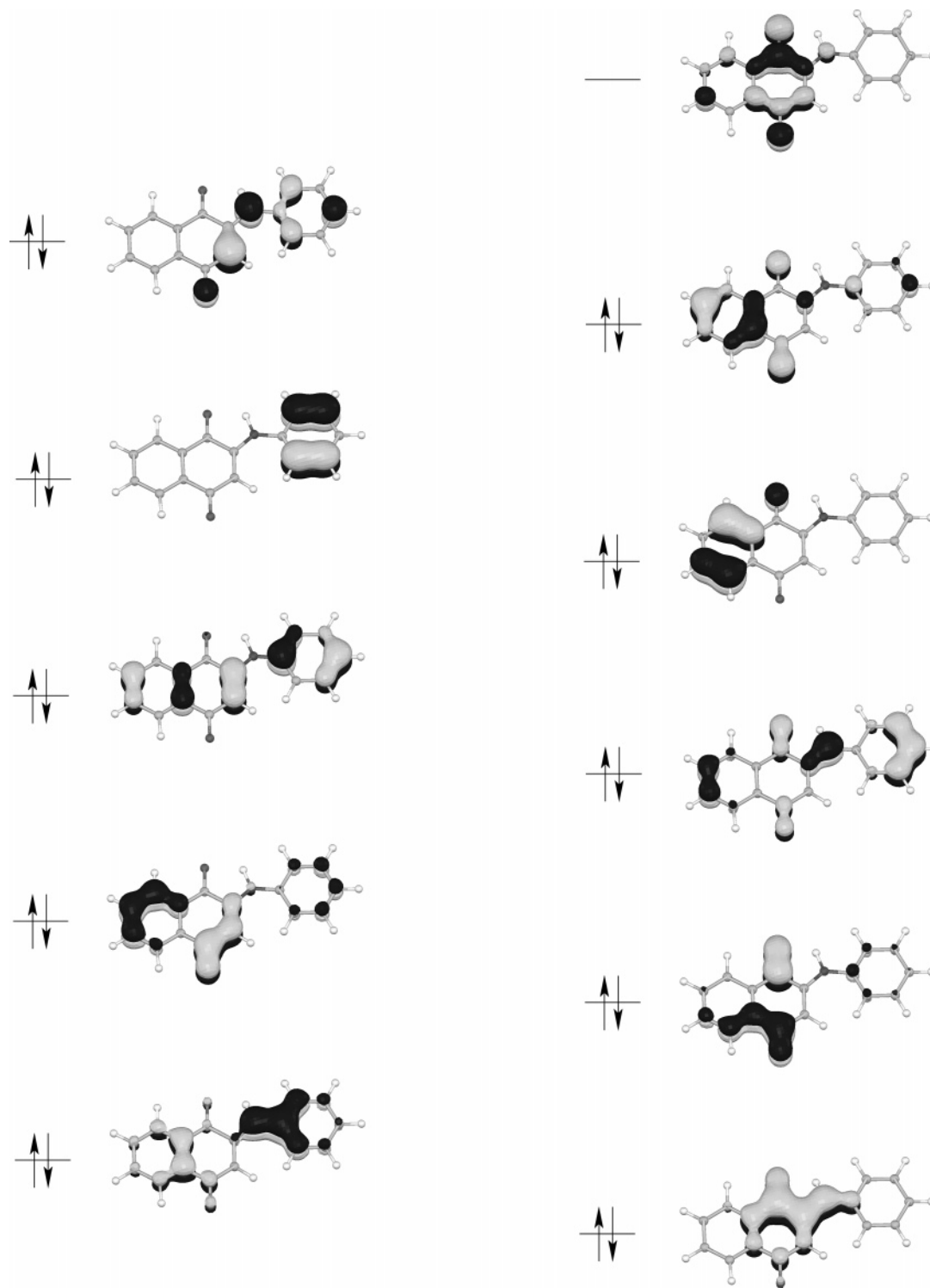


Figure 4. The occupied π orbitals of the PAN molecule in ascending ordering. The LUMO is depicted, too.

simplify the analysis we enforced planarity of the PAN molecule in these calculations. The occupied π orbitals and the lowest unoccupied molecular orbital (LUMO) are graphically displayed in Figure 4. This figure shows that the PAN molecule has ten double occupied π orbitals. The highest occupied π orbital represents the second highest occupied molecular orbital. The LUMO is a π orbital, too. In the PAN systems the planar structure distorts and breaks the conjugation over the whole system. Subsystems with 6 and 14 π electrons are generated, each of them aromatic by itself

according to Hückel's rule. The formation of these subsystems manifests itself in the C_2-N and $N-C_{1'}$ bond lengths. In the neutral PAN systems the C_2-N bond is always shorter than the $N-C_{1'}$ bond. As a consequence resonance structure (b) in Figure 2 is dominant in all neutral PAN systems. Formal counting of the electron pairs in this resonance structure reveals immediately the 6 and 14 π electron subsystems. Such forming of aromatic subsystems has been observed in polycyclic hydrocarbons, too.⁴² If the PAN compound is reduced to form the corresponding

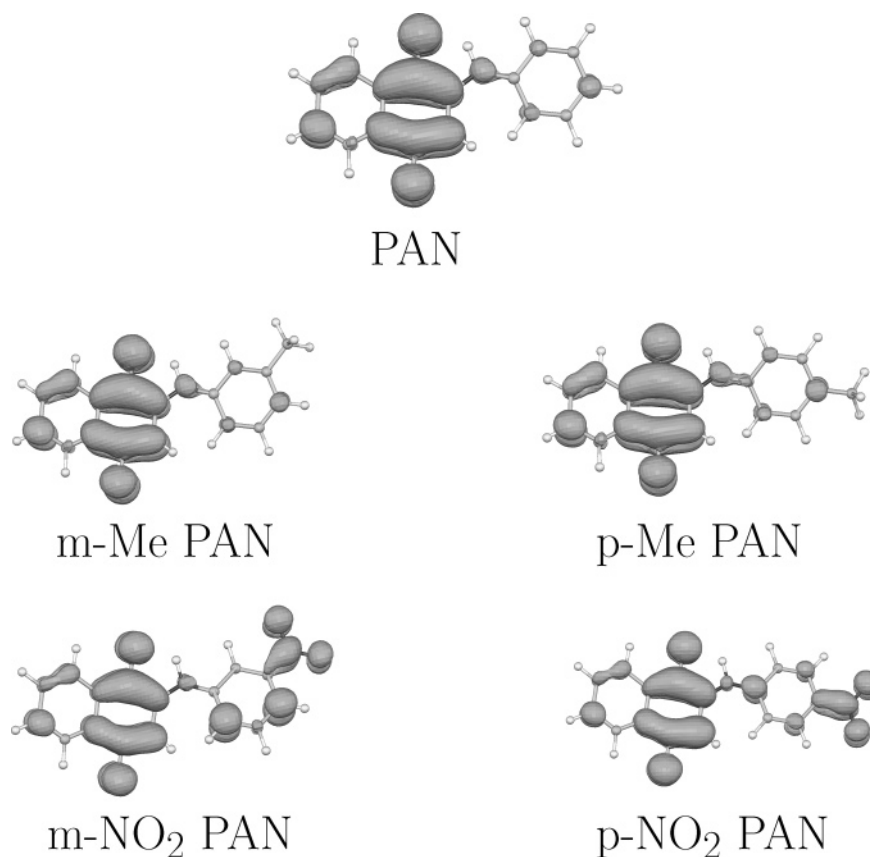


Figure 5. Spin density plots for selected PAN anions.

dianionic system, then the two additional electrons occupy the LUMO π orbital. As can be seen from Figure 4 the LUMO is mainly located in the naphthoquinone moiety. Therefore, the two extra electrons are added to this subsystem. In order to keep it aromatic an electron pair must be expelled. The electron pair flip from the C₂–N to the N–C₁' bond by going from resonance structure (b) to (a) in Figure 2 will, therefore, stabilize anionic systems. In fact, in all dianionic PAN systems the N–C₁' bond is shorter than the C₂–N bond. The increased double bond character of the N–C₁' bond then forces the molecule to planarity.

In Figure 5 spin density plots for H, m-Me, p-Me, m-NO₂, and p-NO₂ PAN anions are depicted. As these plots show the anionic radical electron is mainly localized in the π system of the quinone fragment. The spin density distribution in this moiety is very similar for all five anions independently from the substitution pattern. In m-NO₂ and p-NO₂ PAN anions a substantial part of the spin density is located at the nitro group. An interesting detail represents the spin density distribution in the phenyl group. Usually, spin densities are found in ortho and para positions of this group. However, in the m-NO₂ and p-NO₂ PAN anions this pattern is modified. Therefore, we can conclude that strong electron acceptor substituents modify the spin density distribution in the phenyl ring but not in the naphthoquinone moiety.

III-D. Correlation of Electron Affinities with Half-Wave Potentials. The vertical and adiabatic electron affinities (VEAs and AEAs) were calculated with the local and gradient corrected functionals described in the Computational section. The obtained results for VEAs and AEAs are listed in Table 6 together with the experimental half-wave poten-

Table 6. Calculated Vertical and Adiabatic Electron Affinities [eV] with the VWN and BLYP Functional^a

molecule	VWN		BLYP		HWP
	vertical	adiabatic	vertical	adiabatic	
p-NO ₂ PAN	2.59	2.73	2.13	2.34	-1067
m-NO ₂ PAN	2.45	2.56	1.99	2.21	-1104
p-COMe PAN	2.27	2.43	1.81	2.03	-1126
m-CN PAN	2.25	2.41	1.79	2.00	-1133
p-COOH PAN	2.23	2.41	1.78	2.01	-917
p-CF ₃ PAN	2.19	2.38	1.72	1.99	-1147
m-COOH PAN	2.07	2.25	1.61	1.85	-880
p-Br PAN	2.06	2.23	1.61	1.83	-1176
m-Cl PAN	2.05	2.23	1.59	1.83	-1145
p-Cl PAN	2.03	2.21	1.58	1.81	-1173
m-F PAN	2.01	2.19	1.56	1.80	-1163
H-PAN	1.90	2.07	1.45	1.67	-1209
m-Et PAN	1.87	2.04	1.42	1.64	-1216
m-Me PAN	1.87	2.04	1.42	1.64	-1213
p-Hex PAN	1.86	2.03	1.41	1.63	-1215
p-Bu PAN	1.86	2.03	1.41	1.64	-1217
p-Et PAN	1.86	2.03	1.41	1.63	-1218
p-Me PAN	1.85	2.02	1.40	1.62	-1216
p-OMe PAN	1.80	1.97	1.35	1.57	-1236

^a The experimental values of the half-wave potential [mV] are reported, too.

tials. In Table 6 the molecules are ordered according to their decreasing electron affinities. No qualitative difference between the VWN and GGA trend is observed. Table 6 shows that the electrochemical results obtained for p-COOH PAN (-917 mV) and m-COOH PAN (-880 mV) are very

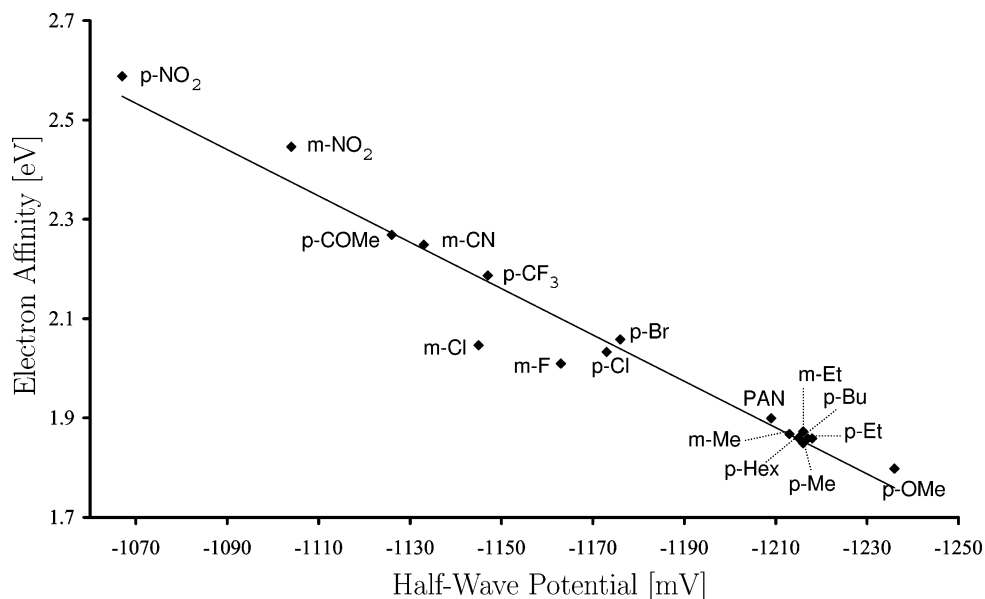


Figure 6. Correlation between the calculated (vertical VWN) electron affinities and the experimental half-wave potentials of the studied PAN systems.

different from those of the other PANs. However, the calculated electron affinities for these two compounds fit very well into the observed trends. Thus, we conclude that for these two compounds side reactions like autoprotonation or dimerization may have occurred under the experimental conditions.⁴³ This is in accordance with the more complex cyclic voltammograms observed for these two compounds. In order to gain more insight into the redox behavior of the PANs, the experimental HWPs for the first one-electron transfer (potential range -880 to -1236 mV), corresponding to the formation of the radical anions, were correlated with the calculated (gas-phase) electron affinities.

For obvious reasons the p-COOH and m-COOH PANs were excluded from this correlation. A linear correlation between the VEAs and the HWPs is obtained, independently from the theoretical level of calculation. Similar linear correlations between gas-phase electron affinities and half-wave potentials measured in acetonitrile have been found for other quinones, too.⁴⁴

The correlation coefficient is around 0.98 which indicates that the one-electron transfers in the cyclic voltammogram can be described by the Nernst equation and that the free energy of the reaction



is proportional to the half-wave potential $E_{1/2}$.⁴⁵ Under this condition the following relationship between the gas-phase electron affinity $EA_{(g)}$ and the half-wave potential $E_{1/2}$

$$EA_{(g)} = kE_{1/2} + C$$

holds if the solvation energy differences between the neutral and anionic PAN systems is similar for all compounds and temperature effects are negligible. This explains the observation in the literature²³ that the solvent has no effect on the first redox potential of some quinone systems. In Figure 6 the VEAs, calculated at the local level, are plotted against the experimental HWPs. The COOH substituted systems are

omitted. We notice a group of 6 PAN compounds with alkyl substituents very close together with low VEAs and high HWPs. An even lower VEA has the p-OMe substituted PAN. As expected, the highest electron affinities are found for strong electron acceptors like p-NO₂. All together the observed trend can be qualitatively explained by the electronic properties of the substituents.

IV. Conclusions

Density functional theory calculations have been performed for the 2-[(R-phenyl)amine]-1,4-naphthalenedione (PAN) molecule and 18 of its derivatives. Neutral, anionic, and selected dianionic PAN systems were studied with local and gradient corrected functionals. The theoretical results show that all neutral compounds are nonplanar. The nonplanarity of the neutral systems is triggered by the electronic structure of the compounds. As an example the electronic structure of the neutral PAN molecule was analyzed in detail. This system possesses 20 π electrons. The distortion from planarity breaks the conjugation and forms two aromatic subsystems with 6 and 14 π electrons. This result in a stabilization of the full system. The same effect was observed for all studied PAN derivatives.

On the other hand, the PAN dianion with 22 π electron cannot be broken down into two aromatic subsystems. As a consequence the dianions are planar and fully conjugated. This structural difference between the neutral and dianionic PAN molecule also shows that steric effects are not the driving force for the distortion from planarity.

From the theoretical study of the neutral and anionic PAN molecules a very good linear correlation between the calculated electron affinity and the experimental half-wave potential was found. An exception represent the two carbo-acid substituted compounds (m-COOH PAN and p-COOH PAN). Our investigation suggests that the measured half-wave potentials of these two compounds are strongly influenced by side reactions. It was shown that solvation energy differences and

temperature effects are negligible for the studied compounds. Therefore, the linear relationship between the electron affinities and the half-wave potentials directly reflects the reversibility of the electron transfer in these systems.

Acknowledgment. This work was financially supported by the CONACYT projects 36037-E, 40379-F, and U48775. Z.G.S. gratefully acknowledge a CONACYT Ph.D. fellowship (93252) and financial support from the Universidad de Colima.

References

- (1) Bentley, R.; Campbell, I. M. *Biological Reactions of Quinones*, in *The Chemistry of the Quinonoid Compounds*; Patai, S., Ed.; John Wiley and Sons: New York, 1974; Chapter 13, pp 683–736.
- (2) Monks, T. J.; Hanzlik, R. P.; Cohen, G. M.; Ross, D.; Graham, D. G. *Toxicol. Appl. Pharmacol.* **1992**, *112*, 2.
- (3) Bishop, N. I. *The Possible Role of Plastoquinone (Q-254) in the Electron Transport System of Photosynthesis*, in *Quinones in Electron Transport*; Wolstenholme, G. E. W., O'Connor, C. M., Eds.; Churchill: London, 1961; pp 385–404.
- (4) Brunmark, A.; Cadenas, E. *Free Radical Biol. Med.* **1988**, *7*, 435.
- (5) Zuman, P. *Substituents Effects in Organic Polarography*; Plenum Press: New York, 1967.
- (6) Trebst, A. Plastoquinone in photosynthetic electron flow in chloroplasts. In *Coenzyme Q*; Wiley: 1985.
- (7) Huntington, J. L.; Davis, D. G. *J. Electron. Soc.* **1971**, *118*, 57.
- (8) Li, C. Y.; Caspar, M. L.; Dixon, D. W. *Electrochim. Acta* **1980**, *25*, 1135. Qureshi, G. A.; Ireland, N. *Bull. Soc. Chim. Belg.* **1981**, *90*, 223.
- (9) Stradins, J.; Glezer, V.; Turovska, B.; Markava, E.; Freimanis, J. *Electrochim. Acta* **1991**, *36*, 1219. Glezer, V.; Turovska, B.; Stradins, J.; Freimanis, J. *Electrochim. Acta* **1990**, *35*, 1933.
- (10) Illescas, B.; Martin, N.; Segura, J. L.; Seoane, C.; Orti, E.; Viruela, P. M.; Viruela, R. *J. Org. Chem.* **1995**, *60*, 5643.
- (11) Oeriu, I.; Benesch, H. *Bull. Soc. Chim. Biol.* **1962**, *44*, 91. Oeriu, I. *Biokhimiya* **1963**, *28*, 380.
- (12) Prescott, B. *J. Med. Chem.* **1969**, *12*, 181.
- (13) Silver, R. F.; Holmes, H. L. *Can. J. Chem.* **1968**, *46*, 1859.
- (14) Hodnett, E. M.; Wongwiechintana, C.; Dunn, W. J.; Marrs, P. *J. Med. Chem.* **1983**, *26*, 570.
- (15) Lopez, J. N. C.; Johnson, A. W.; Grove, J. F.; Bulhoes, M. *S. Cienc. Cult. (Sao Paulo)* **1977**, *29*, 1145.
- (16) U.S. Rubber Co., British Patent 862 489, 1959. Takeda Chemical Industry Co. Ltd., Japanese Patent 18 520, 1963. Ube Industries Ltd., Japanese Patent 126 725, 1979. Shell Internationale Research Maatschappij B.V., British Patent 1 314 881, 1973.
- (17) Clark, N. G. *Pestic. Sci.* **1985**, *16*, 23.
- (18) Krygowski, T. M.; Stępień, B. T. *Chem. Rev.* **2005**, *105*, 3482.
- (19) Exner, O.; Böhm, S. *Curr. Org. Chem.* **2006**, *10*, 763.
- (20) King-Díaz, B.; Macías-Ruvalcaba, N. A.; Aguilar-Martínez, M.; Calaminici, P.; Köster, A. M.; Gómez-Sandoval, Z.; Reveles, J. U.; Lotina-Hennsen, B. *J. Photochem. Photobiol. B* **2006**, *83*, 105.
- (21) Peover, M. E. *Trans. Faraday Soc.* **1962**, *58*, 2370.
- (22) Rüssel, C.; Jaenicke, W. *J. Electroanal. Chem.* **1986**, *199*, 139.
- (23) Sasaki, K.; Kashimura, T.; Ohura, M.; Ohsaki, Y.; Ohta, N. *J. Electrochem. Soc.* **1990**, *137*, 2437.
- (24) Gómez-Sandoval, Z. *σ - π Energy Separation in Density Functional Theory: Implementation and Application*, Ph.D. Thesis, Cinvestav, Mexico-City, 2005.
- (25) Jug, K.; Hiberty, P. C.; Shaik, S. *Chem. Rev.* **2001**, *101*, 1477.
- (26) Köster, A. M.; Calaminici, P.; Flores-Moreno, R.; Geudtner, G.; Goursot, A.; Heine, T.; Janetzko, F.; Patchkovskii, S.; Reveles, J. U.; Vela, A.; Salahub, D. R. *deMon2k*; The deMon Developers: 2005.
- (27) Dirac, P. A. M. *Proc. Camb. Phil. Soc.* **1930**, *26*, 376.
- (28) Vosko, S. H.; Wilk, L.; Nusair, M. *Can. J. Phys.* **1980**, *58*, 1200.
- (29) Becke, A. D. *Phys. Rev. A* **1988**, *38*, 3098.
- (30) Lee, C.; Yang, W.; Parr, R. G. *Phys. Rev. B* **1988**, *37*, 785.
- (31) Godbout, N.; Salahub, D. R.; Andzelm, J.; Wimmer, E. *Can. J. Phys.* **1992**, *70*, 560.
- (32) Dunlap, B. I.; Connolly, J. W. D.; Sabin, J. R. *J. Chem. Phys.* **1979**, *71*, 4993.
- (33) Reveles, J. U.; Köster, A. M. *J. Comput. Chem.* **2004**, *25*, 1109.
- (34) Köster, A. M.; Reveles, J. U.; del Campo, J. M. *J. Chem. Phys.* **2004**, *121*, 3417.
- (35) Aguilar-Martínez, M.; Cuevas, G.; Jiménez-Estrada, M.; González, I.; Lotina-Hennsen, B.; Macías-Ruvalcaba, N. *J. Org. Chem.* **1999**, *64*, 3684.
- (36) Aguilar-Martínez, M.; Bautista-Martínez, J. A.; Macías-Ruvalcaba, N.; González, I.; Tovar, E.; Marín del Alizal, T.; Collera, O.; Cuevas, G. *J. Org. Chem.* **2001**, *66*, 8349.
- (37) van Bolhuis, F.; Kiers, C. *Acta Crystallogr., Sect. B: Struct. Sci.* **1978**, *34*, 1015.
- (38) Gaultier, J.; Hauw, C. *Acta Crystallogr.* **1965**, *18*, 179.
- (39) Krygowski, T. M.; Cyrański, M. K. *Chem. Rev.* **2001**, *101*, 1385.
- (40) Bodwell, G. J.; Bridson, J. N.; Cyrański, M. K.; Kennedy, J. W. J.; Krygowski, T. M.; Mannion, M. R.; Miller, D. O. *J. Org. Chem.* **2003**, *68*, 2089.
- (41) Matsunaga, Y.; Miyajima, N.; Togashi, A. *Bull. Chem. Soc. Jpn.* **1977**, *50*, 2234.
- (42) Behrens, S.; Köster, A. M.; Jug, K. *J. Org. Chem.* **1994**, *59*, 2546.
- (43) González, F.; Aceves, J. M.; Miranda, R.; Gonzáles, I. *J. Electroanal. Chem.* **1991**, *310*, 293.
- (44) Frontana, C.; Vázquez-Mayagoitia, A.; Garza, J.; Vargas, R.; González, I. *J. Phys. Chem. A* **2006**, *110*, 9411.
- (45) Bard, A. J.; Faulkner, L. R. *Electrochemical Methods*, 2nd ed.; Wiley: New York, 2001.

Density Functional Study of the Structure and Properties of Cu_9 and Cu_9^- †

Patrizia Calaminici,* Andreas M. Köster, and Zeferino Gómez-Sandoval

Departamento de Química, CINVESTAV, Av. Instituto Politécnico Nacional 2508, AP 14-740, México D.F. 07000, México

Received December 12, 2006

Abstract: This work presents a study of the structure of neutral and anionic copper cluster nonamers with density functional theory calculations. The structure optimization and frequency analysis were performed at the local density approximation (LDA) level of theory with the exchange correlation functional by Vosko, Wilk, and Nusair (VWN). Improved calculations for the structure stability were based on the generalized gradient approximation (GGA) where the exchange correlation functional of Perdew and Wang (PW) was used. For both neutral and anionic clusters, new isomers are found that are more stable than those already presented in the literature. Adiabatic and vertical electron affinities are calculated and compared with the experimental value reported for Cu_9 . The calculated values are in good agreement with the available experimental data. An analysis of the most relevant molecular orbitals (MOs) of the low-lying neutral and anionic copper cluster nonamers is reported, too.

1. Introduction

The study of clusters and metal compounds has become an increasingly interesting topic in the last years.^{1–10} This is due to their role as precursors of bulk material. In this sense the knowledge of their properties furnishes information how the transition from an atom or molecule to the solid state may occur. Due to the experimental and theoretical techniques developed in the last years these systems are now better characterized. There is a considerable number of different theoretical and experimental works on copper clusters. Although it is not the purpose of the present work to review all of them, we would like to address the reader to the following literature on copper clusters and references therein.^{11–56} Copper clusters with up to 5 atoms were studied about 10 years ago¹⁵ with the density functional program deMon.⁵⁷ In the meantime using a new density functional program⁵⁸ a systematic study of larger copper clusters was performed in order to gain insight into the structure growth. At the same time experiments became available⁵⁹ which allow a reasonable comparison between experimental and

theoretical data. In a recent work we developed a structural concept of copper clusters presenting the structures of small copper clusters with up to 10 atoms.³³ The stability of the structures was tested by a frequency analysis. Based on these results, structures of the corresponding cations and anions were also determined. Further analysis of the clusters furnished information on their binding energies, ionization potentials, and electron affinities. Finally, the energies for the fragmentation of cationic clusters into smaller cationic clusters and neutral atoms or dimers were presented.³³ The search for stable structures of larger clusters is very difficult because of the increasing number of possible arrangements for isomers. In our previous work we used the strategy of capping of smaller clusters or solid-state fragments in order to determine the energetic lowest structures for Cu_9 and Cu_{10} . The global minimum for Cu_9 was found in a C_s symmetry, and it was derived from the Cu_7 bipyramid by double capping of two adjacent upper triangles. For Cu_9^- we found a C_{2v} structure as global minimum which had no topological equivalent for the neutral cluster.³³ We found that the scaled electron affinities for copper clusters up to the octamer are in fair to good agreement with the experimental vertical detachment energies. However, for Cu_9 and Cu_{10} we found that the theoretical and experimental values differ by more

† Dedicated to Dennis R. Salahub on the occasion of his 60th birthday.

* Corresponding author e-mail: pcalamin@cinvestav.mx.

Table 1. Point Group (PG), Relative LDA and GGA Energies [kcal/mol], Structure Parameters [Å], and Frequencies [cm⁻¹] of Neutral Copper Cluster Nonamers^a

cluster	PG	LDA	GGA	structure parameters				frequencies															
1) Cu ₉	C _s	1.95	0.0	r ₁₂ = 2.35	r ₁₃ = 2.37	59	75	83	107	113	121												
				r ₁₄ = 2.39	r ₁₅ = 2.37							125	128	133	138	155	161						
				r ₁₆ = 2.39	r ₁₇ = 2.39							184	192	201	203	221	232						
				r ₂₄ = 2.40	r ₂₆ = 2.40							240	246	270									
				r ₂₉ = 2.41	r ₃₄ = 2.38																		
				r ₃₅ = 2.48	r ₃₇ = 2.38																		
				r ₃₈ = 2.39	r ₄₆ = 3.12																		
				r ₄₈ = 2.38	r ₄₉ = 2.40																		
				r ₅₆ = 2.38	r ₅₈ = 2.39																		
				r ₆₈ = 2.38	r ₆₉ = 2.40																		
				r ₁₂ = 2.36	r ₁₃ = 2.36							72	73	80	110	118	122						
				r ₁₄ = 2.36	r ₁₅ = 2.36													128	129	132	138	140	147
				r ₁₆ = 2.41	r ₁₇ = 2.47													165	167	190	200	215	222
				r ₁₈ = 2.41	r ₂₃ = 2.49													250	254	283			
r ₂₇ = 2.42	r ₃₇ = 2.42																						
r ₃₈ = 2.42	r ₄₅ = 2.49																						
r ₄₈ = 2.41	r ₄₉ = 2.42																						
r ₅₆ = 2.42	r ₅₉ = 2.42																						
r ₆₇ = 2.40	r ₆₉ = 2.40																						
r ₅₆ = 2.42	r ₅₉ = 2.42																						
r ₇₈ = 2.40	r ₇₉ = 2.40																						
3) Cu ₉	C _{2v}	3.23	1.61	r ₁₂ = 2.37	r ₁₅ = 2.38	57	62	68	93	98	121												
				r ₁₆ = 2.41	r ₁₉ = 2.44													122	136	149	152	154	164
				r ₂₉ = 2.44	r ₃₆ = 2.40													165	179	185	202	217	250
				r ₅₆ = 2.37	r ₆₈ = 2.44							256	256	263									
4) Cu ₉	C _{3v}	7.70	13.12	r ₁₂ = 2.35	r ₁₄ = 2.39	78	84	87	92	92	99												
				r ₁₇ = 2.43	r ₁₈ = 2.43							106	108	134	136	161	179						
				r ₂₆ = 2.39	r ₂₉ = 2.43							180	191	195	195	216	242						
				r ₃₅ = 2.39	r ₃₉ = 2.43							260	269	270									
				r ₈₅ = 2.37	r ₈₉ = 2.38																		
5) Cu ₉	C _{2v}	24.39	23.30	r ₁₂ = 2.49	r ₁₅ = 2.49	69	79	82	107	112	114												
				r ₁₆ = 2.34	r ₁₈ = 2.34							122	126	145	150	150	153						
				r ₃₈ = 2.41	r ₄₈ = 2.41							175	180	186	192	222	236						
				r ₅₆ = 2.41	r ₇₈ = 2.46							253	255	255									
				r ₁₂ = 2.48	r ₁₃ = 2.48							52	53	70	98	101	105						
r ₁₄ = 2.48	r ₂₄ = 2.36	109	120	131	135	138	170																
r ₂₆ = 2.36	r ₂₉ = 2.36	173	188	195	212	226	235																
r ₃₄ = 2.36	r ₃₅ = 3.89	238	259	260																			
r ₃₇ = 2.32	r ₃₈ = 2.48																						
r ₄₈ = 2.48	r ₄₉ = 2.36																						

^a The cluster structures and atom numbers are given in Figure 1.

than 0.5 eV. From these results we could not exclude that lower minima may exist on the anionic potential energy surface (PES) of these systems. Very recently a new and very robust algorithm⁶⁰ for structure optimization was developed and implemented in the new density functional code deMon2k.⁶² It was shown that this algorithm provides reliable geometrical parameters even for very large systems.⁶⁰ In this work we present the results of a more extended investigation of the ground-state structure of Cu₉⁻ and Cu₉. The electron affinity is recalculated considering the new ground-state structures presented here. The calculated value of the vertical electron affinity shows now an excellent agreement with the experimental vertical detachment energy measured for the copper nonamer. An analysis of the most relevant molecular orbitals (MOs) of the neutral and anionic copper nonamer low-lying structures is presented, too.

2. Computational Details

The linear combination of Gaussian-type orbitals Kohn–Sham density functional theory (LCGTO-KS-DFT) method⁶¹ as implemented in the program deMon2k⁶² was used to carry out all geometry optimizations and harmonic vibrational frequency calculations. The exchange–correlation potential was numerically integrated on an adaptive grid.⁶³ The grid accuracy was set to 10⁻⁵ in all calculations. The Coulomb energy was calculated by the variational fitting procedure proposed by Dunlap, Connolly, and Sabin.^{64,65} For the fitting of the density the auxiliary function set A2⁶⁶ was used in all calculations. In order to localize different minima on the potential energy surface (PES) of the neutral and anionic copper nonamer, the structures of both clusters have been optimized considering as starting points different initial

Table 2. Point Group (PG), Relative LDA and GGA Energies [kcal/mol], Structure Parameters [Å], and Frequencies [cm⁻¹] of Anionic Copper Cluster Nonamers^a

cluster	PG	LDA	GGA	structure parameters				frequencies			
1) Cu ₉ ⁻	C _s	0.0	0.0	r ₁₂ = 2.41	r ₁₃ = 2.37	62	76	80	102	103	113
				r ₁₄ = 2.43	r ₁₅ = 2.37	116	117	121	139	155	168
				r ₁₆ = 2.43	r ₁₇ = 2.50	179	193	193	201	227	239
				r ₂₄ = 2.33	r ₂₆ = 2.33	243	247	257			
				r ₂₉ = 2.46	r ₃₄ = 2.36						
				r ₃₅ = 2.41	r ₃₇ = 2.39						
				r ₃₈ = 2.45	r ₄₆ = 2.90						
				r ₄₈ = 2.33	r ₄₉ = 2.42						
				r ₅₆ = 2.36	r ₅₈ = 2.45						
				r ₆₈ = 2.33	r ₆₉ = 2.42						
2) Cu ₉ ⁻	C _{2v}	3.00	0.11	r ₁₂ = 2.40	r ₁₃ = 2.41	15	67	91	93	110	110
				r ₁₄ = 2.36	r ₂₄ = 2.40	123	127	127	131	154	160
				r ₂₆ = 2.40	r ₂₉ = 2.37	189	192	201	208	226	230
				r ₃₄ = 2.39	r ₃₅ = 2.39	240	245	256			
				r ₃₇ = 2.36	r ₃₈ = 2.42						
				r ₄₈ = 2.36	r ₄₉ = 2.41						
				r ₁₂ = 2.50	r ₁₄ = 2.38	52	61	77	96	110	117
				r ₁₈ = 2.33	r ₂₃ = 2.38	121	126	127	135	145	172
				r ₂₇ = 2.39	r ₂₉ = 2.36	173	176	193	202	224	232
				r ₃₄ = 2.50	r ₃₅ = 2.43	249	257	257			
r ₅₄ = 2.36	r ₈₉ = 2.45										
4) Cu ₉ ⁻	C _s	2.53	2.55	r ₁₂ = 2.35	r ₁₄ = 2.55	53	70	80	86	110	121
				r ₁₅ = 2.35	r ₁₈ = 2.48	123	132	134	140	150	152
				r ₅₆ = 2.39	r ₆₇ = 2.43	169	184	192	201	213	246
				r ₆₇ = 2.43	r ₆₈ = 2.36	250	253	263			
				r ₁₂ = 2.41	r ₁₃ = 2.41	65	76	82	82	112	121
				r ₁₄ = 2.41	r ₁₅ = 2.41	129	130	132	139	140	144
				r ₄₈ = 2.39	r ₇₁ = 2.48	159	168	191	194	220	224
				r ₇₂ = 2.40	r ₆₈ = 2.40	246	247	254			
				r ₁₂ = 2.46	r ₁₃ = 2.46	74	78	83	115	117	118
				r ₁₄ = 2.46	r ₁₅ = 2.46	120	131	137	143	150	153
r ₄₈ = 2.42	r ₇₁ = 2.57	176	186	192	196	218	234				
r ₇₂ = 2.39	r ₆₈ = 2.42	242	245	247							
7) Cu ₉ ⁻	C _{3v}	19.14	15.68	r ₁₂ = 2.33	r ₁₃ = 2.33	54	55	83	94	94	98
				r ₁₄ = 2.46	r ₂₄ = 2.46	102	102	133	133	148	161
				r ₃₅ = 2.46	r ₃₆ = 2.46	182	182	197	198	217	252
				r ₃₈ = 2.43	r ₃₉ = 2.43	252	253	271			
				r ₈₁ = 2.43	r ₉₂ = 2.43						
				r ₁₂ = 2.43	r ₁₃ = 2.47	42	51	76	100	101	102
				r ₁₄ = 2.47	r ₂₄ = 2.34	107	110	121	143	143	163
				r ₂₉ = 2.50	r ₃₇ = 2.31	172	182	208	210	228	235
				r ₃₈ = 2.47	r ₄₆ = 3.34	237	242	254			
				r ₅₆ = 2.35	r ₅₇ = 2.31						
9) Cu ₉ ⁻	C _s	19.83	17.99	r ₁₂ = 2.37	r ₁₃ = 2.39	22	67	92	99	101	115
				r ₁₄ = 2.43	r ₂₄ = 2.40	125	126	132	139	141	154
				r ₂₉ = 2.40	r ₃₇ = 2.36	177	185	203	207	209	228
				r ₃₈ = 2.41	r ₉₄ = 2.38	229	238	259			
				r ₉₆ = 2.38	r ₉₈ = 2.40						

^a The cluster structures and atom numbers are given in Figure 2.

geometries and multiplicities. In order to avoid spin contamination the restricted open shell Kohn–Sham (ROKS) method was employed. The calculations were performed with the local density approximation (LDA) using the exchange–correlation contributions proposed by Vosko, Wilk, and Nusair⁶⁷ and employing all-electron basis sets.⁶⁶ The same functional was used for the frequency analysis. We already showed that LDA studies on copper clusters with the double- ζ plus valence polarization (DZVP) basis set and the

A2 auxiliary function set⁶⁶ give reliable geometries in structure optimizations.^{15,32,33} Single point energies were then calculated at the optimized structures using the same basis and auxiliary function set with the exchange–correlation functional of Perdew and Wang (PW).^{68,69} A quasi-Newton method in internal redundant coordinates with analytic energy gradients was used for the structure optimization.⁶⁰ The convergence was based on the Cartesian gradient and displacement vectors with a threshold of 10⁻⁴ and 10⁻³ au,

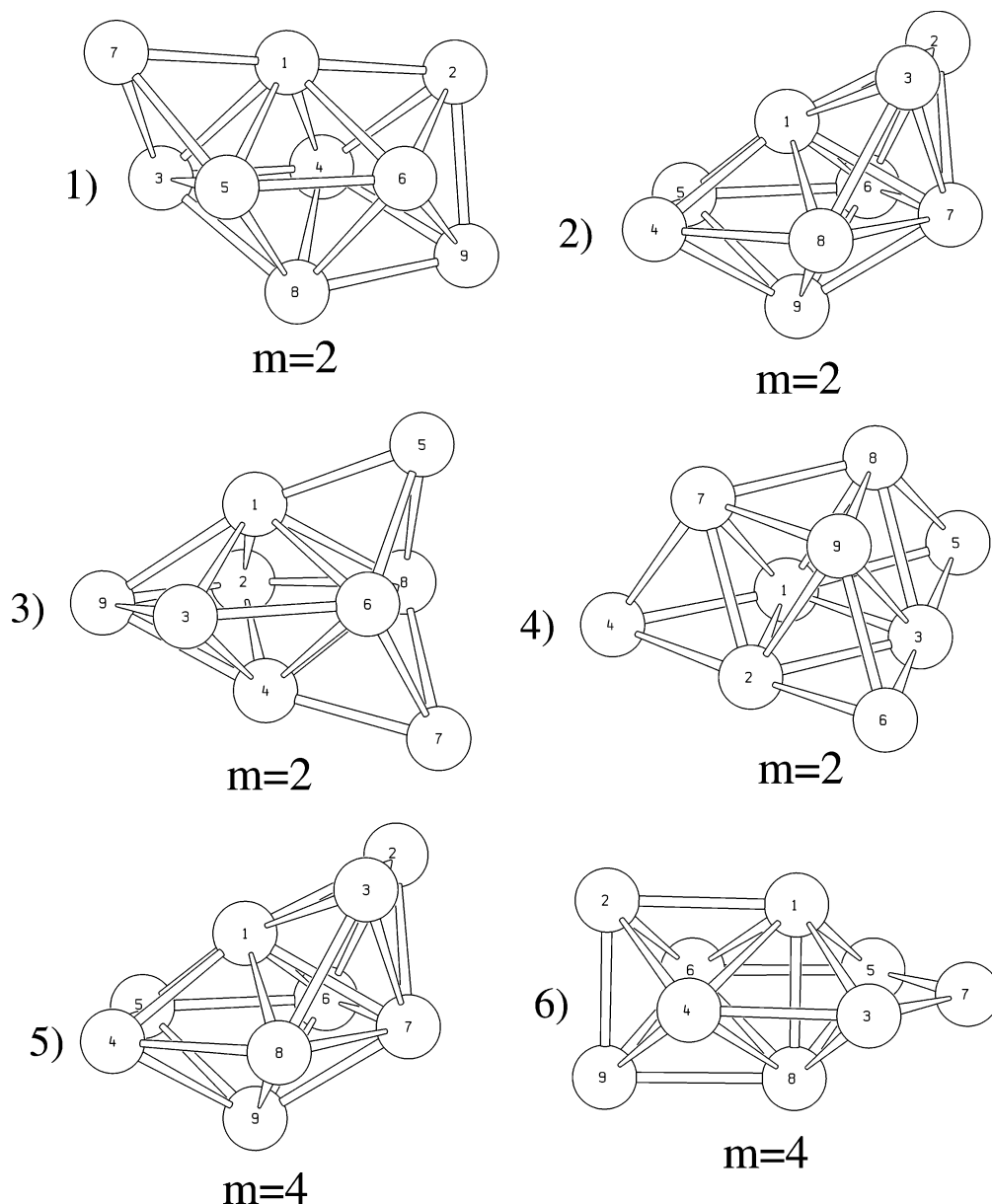


Figure 1. Structures and multiplicities of the neutral copper cluster nonamers.

respectively. A vibrational analysis was performed in order to discriminate between minima and transition states. The second derivatives were calculated by numerical differentiation (two-point finite difference) of the analytic energy gradients using a displacement of 0.001 au from the optimized geometry for all $3N$ coordinates. The harmonic frequencies were obtained by diagonalizing the mass-weighted Cartesian force constant matrix.

3. Results and Discussion

The optimized structure parameters (in Å), relative energies (in kcal/mol), and vibrational frequencies (in cm^{-1}) of the ground-state structure and low-lying minima of neutral and anionic copper nonamers are listed in Tables 1 and 2, respectively. The corresponding cluster structures are depicted in Figures 1 and 2, respectively. In these figures the spin multiplicities for each structure are indicated, too. For Cu_9 and Cu_9^- we investigated several initial structures

including the one obtained by capping of the Cu_8 ground-state structure reported in our previous work,³³ the ones derived from the Cu_7 bipyramid by double capping of two adjacent upper triangles and by double capping of adjacent upper and lower triangles, and a C_{3v} isomer obtained by relaxation of a crystal fragment. For the neutral Cu_9 cluster the multiplicities 2, 4, and 6 are studied for all investigated isomers, whereas for the charged Cu_9^- cluster the multiplicities 1, 3, and 5 are considered. In the case of the neutral copper nonamer six minima structures are found (Figure 1). For Cu_9 , a C_s structure in multiplicity 2 (structure 1 of Figure 1) is found as ground state. This structure results from the capping of the ground-state Cu_8 structure reported in ref 33. To the best of our knowledge this structure has never been reported so far in the literature. At the PW86/DZVP/A2 level of theory the next isomer is only 0.69 kcal/mol above this ground state. It is a doublet with C_s symmetry that can be obtained from the Cu_7 bipyramid by the double capping of

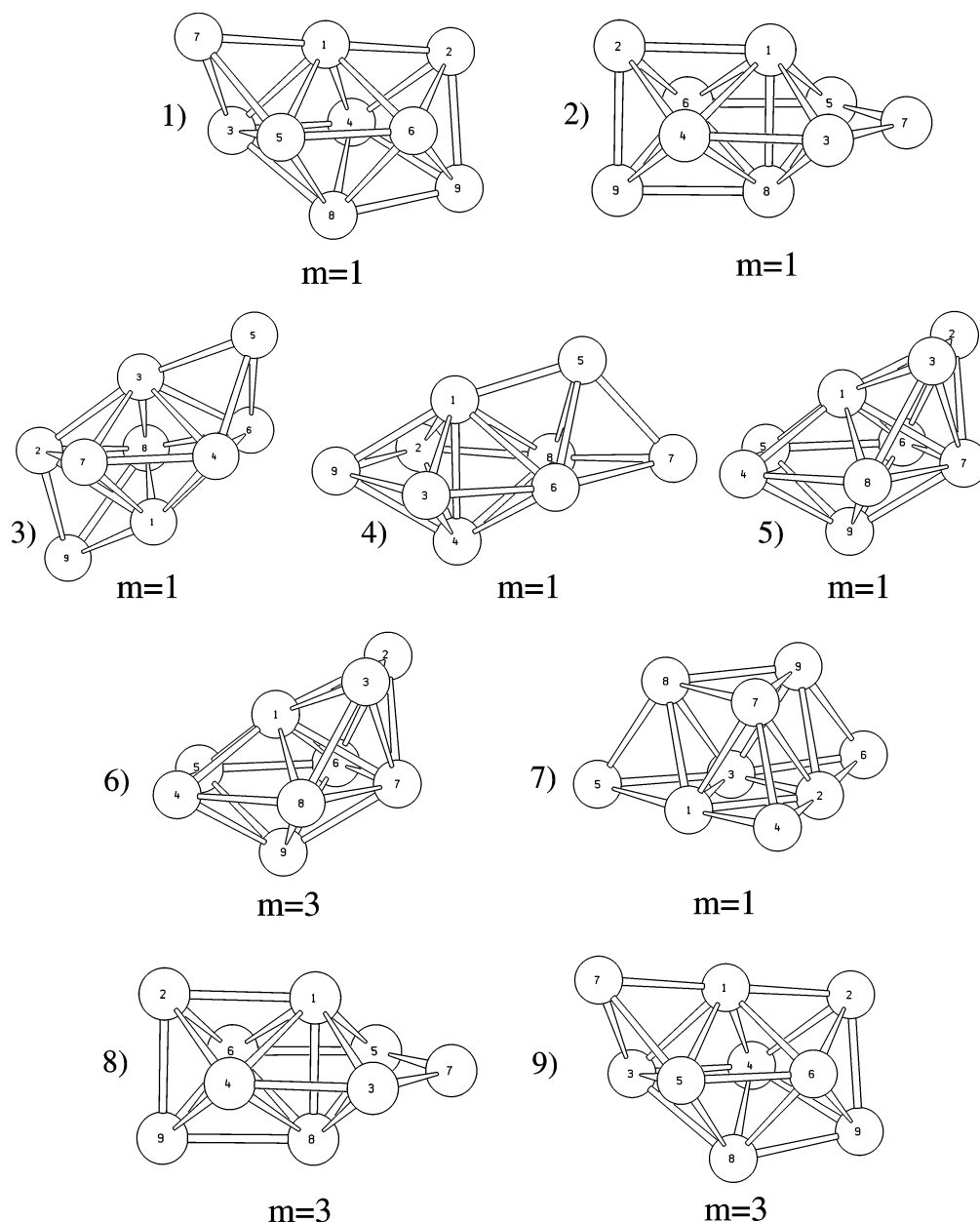


Figure 2. Structures and multiplicities of the anionic copper cluster nonamers.

two adjacent upper triangles (structure 2 of Figure 1). This structure was proposed as the global minimum in our previous work.³³ A C_{2v} isomer on the doublet potential energy surface (PES) obtained from the Cu_7 bipyramid by the double capping of adjacent upper and lower triangles follows 1.61 kcal/mol (structure 3 of Figure 1) above the ground-state C_s structure. The relaxation of a crystal fragment results in a C_{3v} low-lying isomer on the doublet PES (structure 4 of Figure 1), 13.12 kcal/mol above the ground-state structure. The average bond distance of this isomer is still considerably shorter than the copper bulk distance of 2.56 Å. The minima found on the quartet PES are lying much higher in energy as can be seen from Table 1.

Similar to the neutral copper nonamer, we found as a ground-state structure for the anionic copper nonamer the isomer obtained by single capping of the ground-state Cu_8 structure in lower multiplicity (structure 1 of Figure 2). Again, we notice that, as in the case of the neutral Cu_9 cluster,

this structure has never been reported in the literature as a possible ground-state structure for this system. A singlet minimum in C_s symmetry obtained from the Cu_7 bipyramid by double capping of two adjacent upper triangles (structure 2 of Figure 2) lies only 0.11 kcal/mol above the ground state (see Table 2). This minimum was reported as the ground-state structure for Cu_9^- in our previous work.³³ Seven other different local minima are found above the ground state within an energy range of less than 20.00 kcal/mol (see Table 2 and Figure 2). This result shows the variety of energetically low-lying isomers on the PES for this kind of clusters.

Higher spin neutral and anionic copper nonamer structures are not reported, because these structures are much higher in energy as the ones reported in Figure 1 and 2. Tables 1 and 2 show that the order of several Cu_9 and Cu_9^- isomers exchanges if the local density approximation is used. Therefore, the GGA corrections are very important for the

Table 3. Adiabatic and Vertical Electron Affinities (EA) of the Anionic Copper Cluster Nonamer at the LDA Level^a

cluster	adiabatic		vertical		exp. ^b
	EA	scaled EA	EA	scaled EA	
Cu ₉ ⁻	2.58	2.14	2.67	2.22	2.40 ± 0.05 ^b

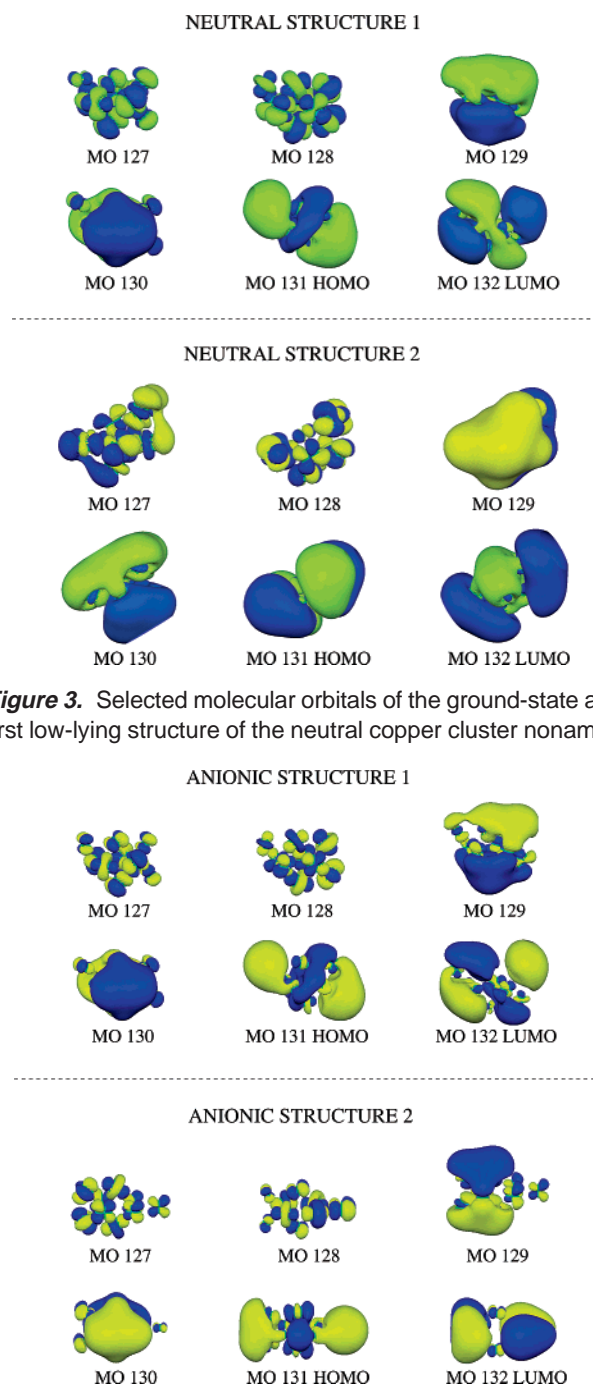
^a All values are in eV. ^b Vertical detachment energy.

correct prediction of the global minimum and for the relative stability order of these systems.

In order to characterize the optimized structures of the neutral and anionic copper clusters and to give clues for further desirable experimental investigations, the harmonic vibrational frequencies have been calculated. The calculated harmonic frequencies for all minima are listed in Tables 1 and 2, respectively. From the assigned ground-state structures of Cu₉ and Cu₉⁻ the adiabatic and vertical electron affinities are calculated. The obtained results are compared with the available experimental data⁷⁰ and are presented in Table 3. Scaled values are also obtained using a scaling factor of 0.831 that results from the adjustment of the atomic electron affinity as described in ref 33. As Table 3 shows, the obtained new results for the electron affinity are in good to fair agreement with the reported experimental value. This result indicates that here the newly reported ground-state structures for the neutral and anionic copper nonamer are the ones most likely observed in the vertical detachment experiments. Because of the very small energy separation to the previously assigned ground states in ref 33 the reported binding energies are almost not effected. Experimental investigations which provide vibrational resolved photoelectron spectra for small copper clusters would be highly desirable in order to give a final answer concerning the ground-state structure of these systems.

The shell model of metal clusters is based on fully delocalized molecular orbitals for the cluster electrons.^{71–75} Investigations have shown that clusters with 2, 8, or 18 electrons have special properties, like a high stability independent of the kind of metal. These so-called magic numbers are directly related to the cluster growth and the electronic structure. In the shell model the valence electrons of the cluster are placed in shells of *s*, *p*, and *d* character of the overall system like in the particle-in-a-box model. In this context clusters of metal atoms with only one valence electron in an *s* orbital are of particular interest, because their structure can be ascribed to the influence of these valence electrons.

With the intention of clarifying whether the molecular orbitals furnish information on the nonamer copper cluster structures the most relevant molecular orbitals (MOs) for the two low-lying structures of Cu₉ and Cu₉⁻ are calculated. The resulting MOs are depicted in Figures 3 and 4, respectively. As Figures 3 and 4 show the lower MOs for the neutral and anionic ground-state structures show a local bonding or antibonding situation of the 3*d* orbitals of the individual copper atoms. In contrast, the MOs closed to the highest occupied (HOMO) and lowest unoccupied (LUMO) molecular orbital gap possess shapes according to the shell model (see Figures 3 and 4) and mainly formed by the 4*s* valence electrons.^{71–75} The HOMO is of d_{z²} type for both

**Figure 3.** Selected molecular orbitals of the ground-state and first low-lying structure of the neutral copper cluster nonamer.**Figure 4.** Selected molecular orbitals of the ground-state and first low-lying structure of the anionic copper cluster nonamer.

the neutral and anionic, ground-state structures, as Figures 3 and 4 show. The HOMO of the first low-lying neutral structure (structure 2 of Figures 1 and 3) is a d-type orbital similar to the one found in a previous theoretical work.⁷⁶ A more detailed analysis reveals that the mixing between the 3*d* and 4*s* atomic orbitals is slightly larger in the anionic clusters.

4. Conclusions

In this work we have reported LCGTO-DFT local and GGA first principle all-electron calculations for the structural and spectroscopic properties of neutral and anionic copper nonamers. Several topological structures on different PES

were investigated for the neutral cluster as well as for the ionic system. We believe that this work represents the most extended study ever reported for the neutral and the anionic copper nonamer cluster. New ground-state structures have been found for both neutral and anionic systems. All found minima were characterized by a vibrational analysis in order to guide future experiments, which we hope will be forthcoming. The inclusion of gradient corrections is important for the relative stability energy of different low-lying isomers. Adiabatic and vertical electron affinity have been reported. The obtained results are in good agreement with the available experimental data. This indicates that the newly suggested ground-state structures for Cu₉ and Cu₉⁻ are most likely the ones observed in the vertical detachment experiments. Experimental vibrational resolved photoelectron spectra would be very important in order to assign unequivocally the ground-state structures of these systems. The analysis of the MOs shows that the orbitals at the HOMO–LUMO gap possess shapes according to the shell model.

Acknowledgment. Financial support from the CONACYT project U48775 is gratefully acknowledged.

References

- (1) Kreibitz, U.; Vollmer, M. *Optical Properties of Metal Clusters*; Springer: Berlin, Germany, 1995.
- (2) Bonin, K. D.; Kresin, V. V. *Electric-Dipole Polarizabilities of Atoms, Molecules and Clusters*; World Scientific: Singapore, 1997; Chapter 3, pp 64–81.
- (3) Green, S. M. E.; Alex, S.; Fleischer, N. L.; Millam, E. L.; Marcy, T. P.; Leopold, D. G. Negative ion photoelectron spectroscopy of the group 5 metal trimer monoxides V₃O, Nb₃O, and Ta₃O. *J. Chem. Phys.* **2001**, *114*, 2653.
- (4) Martínez, A.; Köster, A. M.; Calaminici, P.; Salahub, D. R. Bonding in Nb₃O, Nb₃S and Nb₃Se: A topological analysis of the electrostatic potential. *J. Chem. Phys.* **2001**, *114*, 819.
- (5) Chrétien, S.; Salahub, D. R. Kohn-Sham density-functional study of low-lying states of the iron clusters Fe_n⁺/Fe_n/Fe_n⁻ (n=1–4). *Phys. Rev. B* **2002**, *66*, 155425.
- (6) Gutsev, G. L.; Bauschlicher, C. W., Jr. Electron affinities, ionization energies, and fragmentation energies of Fe_n clusters (n=2–6): A density functional theory study. *J. Phys. Chem. A* **2003**, *107*, 7013.
- (7) Calaminici, P.; Köster, A. M. Structures and vibrations of V₃O and V₃O⁻: A density functional study. *Int. J. Quantum Chem.* **2003**, *91*, 317.
- (8) Calaminici, P.; Köster, A. M.; Salahub, D. R. Negative ion photoelectron spectra simulation of V₃O from a density functional study. *J. Chem. Phys.* **2003**, *118*, 4913.
- (9) Calaminici, P.; Flores–Moreno, R.; Köster, A. M. Structures and vibrations of Nb₃O and Nb₃O⁻: A density functional study. *J. Chem. Phys.* **2004**, *121*, 3558.
- (10) Calaminici, P. Polarizability of Fe_n (n ≤ 4) clusters: an all-electron density functional study. *Chem. Phys. Lett.* **2004**, *387*, 253.
- (11) Koutecký, J.; Fantucci, P. Theoretical Aspects of Metal Atom Clusters. *Chem. Rev.* **1986**, *86*, 539.
- (12) Morse, M. D. Clusters of Transition-Metal Atoms. *Chem. Rev.* **1986**, *86*, 1049, and references therein.
- (13) Flad, J.; Igel-Mann, G.; Preuss, H.; Stoll, H. A Combination Of Pseudopotentials And Density Functionals - Results for Cu_n, Cu_n⁺, Ag_n, and Ag_n⁺ Clusters. *Chem. Phys.* **1984**, *90*, 257.
- (14) Amos, A. T.; Brook, P. A.; Moir, S. A. Extended Hückel Calculations On Copper Clusters. *J. Phys. Chem.* **1988**, *92*, 733.
- (15) Calaminici, P.; Köster, A. M.; Russo, N.; Salahub, D. R. A Density Functional Study of Small Copper Clusters Cu_n (n≤5). *J. Chem. Phys.* **1996**, *105*, 9546.
- (16) Jackson, K. A. First-Principles Study of the Structural and Electronic-Properties of Cu Clusters. *Phys. Rev. B* **1993**, *47*, 9715.
- (17) Tatewaki, H.; Miyoshi, E.; Nakamura, T. Electronic-Structure of Small Copper Clusters. *J. Chem. Phys.* **1982**, *76*, 5073.
- (18) Miyoshi, E.; Tatewaki, H.; Nakamura, T. Electronic-Structure of Small Copper Clusters. *Int. J. Quantum Chem.* **1983**, *23*, 1201.
- (19) Bachmann, C.; Demuynck, J.; Veillard, A. *Faraday Symp. Chem. Soc.* **1980**, *14*, 170.
- (20) Richtsmeier, S. C.; Dixon, D. A.; Gole, J. L. Structure of Group 1B Metal-Clusters, M_n, n=4–6. *J. Phys. Chem.* **1982**, *86*, 3937.
- (21) Bauschlicher, C. W.; Langhoff, S. R.; Patridge, H. Theoretical-Study of the Homonuclear Tetramers and Pentamers of the Group-1B Metals (Cu, Ag, and Au). *J. Chem. Phys.* **1990**, *93*, 8133.
- (22) Post, D.; Baerends, E. J. On the Hartree-Fock and X-Alpha Descriptions of Small Copper Cluster Electronic-Structures. *Chem. Phys. Lett.* **1982**, *86*, 176.
- (23) Taneda, A.; Esfarjani, K.; Hasahi, Y.; Kawazoe, Y. *Similarities and Differences Between Atomic Nuclei and Cluster*; Abe, Y., Arai, I., Lee, S. M., Yabana, Y., Eds.; AIP Conference Proceedings No. 416, American Institute of Physics: New York, United States, 1997; p 471.
- (24) Lammers, U.; Borstel, G. Electronic and Geometrical Structure of Noble-Metal Clusters. *Phys. Rev. B* **1993**, *49*, 17360.
- (25) Walch, S. P.; Laskowski, B. C. Calculated Ground-State Potential Surface and Excitation-Energies for the Copper Trimer. *J. Chem. Phys.* **1986**, *84*, 2734.
- (26) Langhoff, S. R.; Bauschlicher, C. W.; Walch, S. P.; Laskowski, B. C. Ab-Initio Study of the Ground-State Surface of Cu₃. *J. Chem. Phys.* **1986**, *85*, 7211.
- (27) Akeby, H.; Panas, I.; Pettersson, L. G. M.; Siegbahn, P.; Wahlgren, U. Electronic and Geometric Structure of the Cu_n Cluster Anion (n≤10). *J. Phys. Chem.* **1993**, *94*, 9715.
- (28) Massobrio, C.; Pasquarello, A.; Car, R. Structural and Electronic-Properties of Small Copper Clusters - A First Principle Study. *Chem. Phys. Lett.* **1995**, *238*, 215.
- (29) Massobrio, C.; Pasquarello, A.; Car, R. First Principles Study of Photoelectron-Spectra of Cu_n⁻ Clusters. *Phys. Rev. Lett.* **1995**, *75*, 2104.
- (30) Massobrio, C.; Pasquarello, A.; Dal Corso, A. Structural and electronic properties of small Cu-n clusters using generalized-gradient approximations within density functional theory. *J. Chem. Phys.* **1998**, *109*, 6626.

- (31) Crispin, X.; Bureau, C.; Geskin, V.; Lazzaroni, R.; Breás, J.-L. Local density functional study of copper clusters: A comparison between real clusters, model surface clusters, and the actual metal surface. *Eur. J. Inorg. Chem.* **1999**, 349.
- (32) Calaminici, P.; Köster, A. M.; Vela, A.; Jug, K. Comparison of Static Polarizabilities of Cu_n , Na_n and Li_n . *J. Chem. Phys.* **2000**, *113*, 2199.
- (33) Jug, K.; Zimmermann, B.; Calaminici, P.; Köster, A. M. Structure and Stability of Small Copper Clusters Cu_n ($n \leq 10$). *J. Chem. Phys.* **2002**, *116*, 4497.
- (34) Jaque, P.; Toro-Labbé, A. The formation of neutral copper clusters from experimental binding energies and reactivity descriptors. *J. Phys. Chem. B* **2004**, *108*, 2568.
- (35) Parent, D. C.; Anderson, S. L. Chemistry of Metal and Semimetal Cluster Ions. *Chem. Rev.* **1992**, *92*, 1541.
- (36) Jarrold, M. F.; Creegan, K. M. Photodissociation of Copper Clusters, Cu_n^+ ($n = 3-8$), in the 370–710 nm Wavelength Region. *Int. J. Mass Spectrom. Ion Processes* **1990**, *102*, 161.
- (37) Powers, D. E.; Hansen, S. G.; Geusic, M. E.; Michalopoulos, D. L.; Smalley, R. E. Supersonic Copper Clusters. *J. Phys. Chem.* **1983**, *78*, 2866.
- (38) Knickelbein, M. B. Electronic Shell Structure in the Ionization-Potentials of Copper Clusters. *Chem. Phys. Lett.* **1992**, *192*, 129.
- (39) Leopold, D. G.; Ho, J.; Lineberger, W. C. Photoelectron-Spectroscopy of Mass-Selected Metal Cluster Anions. I. Cu_1-10 . *J. Chem. Phys.* **1987**, *86*, 1715.
- (40) Taylor, K. J.; Pettiette-Hall, C. L.; Cheshnovsky, O.; Smalley, R. E. Ultraviolet Photoelectron-Spectra of Coniaged Metal-Clusters. *J. Chem. Phys.* **1992**, *96*, 3319.
- (41) Begemann, W.; Hector, R.; Liu, Y. Y.; Tiggersbäumker, J.; Meiwes-Broer, K. H.; Lutz, H. O. Sputtered Metal and Silicon Cluster Ions - Collision-Induced Fragmentation and Neutralization. *Z. Phys. D: At., Mol. Clusters* **1989**, *12*, 229.
- (42) Begemann, W.; Meiwes-Broer, K. H.; Lutz, H. O. Unimolecular Decomposition of Sputtered Al^+ , Cn^+ and Si^+ Clusters. *Phys. Rev. Lett.* **1986**, *56*, 2248.
- (43) Hilpert, K.; Gingerich, K. A. Atomization Enthalpies of the Molecules Cu_3 , Ag_3 and Au_3 . *Ber. Bunsenges, Phys. Chem.* **1980**, *84*, 739.
- (44) Moskovits, M.; Hulse, J. E. Ultraviolet-Visible Spectra of Diatomic, Triatomic, and Higher Nickel Clusters. *J. Chem. Phys.* **1977**, *66*, 3988.
- (45) Morse, M. D.; Hopkins, J. P.; Langridge-Smith, P. R. R.; Smalley, R. E. Spectroscopic Studies of the Jet-Cooled Copper Trimer. *J. Chem. Phys.* **1983**, *79*, 5316.
- (46) Ozin, G. A.; Mitchell, S. A.; Macintosh, D. F.; Mattar, S. M.; Garcia-Prieto, J. Copper Atoms and Copper Clusters in Solid Xenon - Special Atom and Dimer Sites and Covalently Bound Clusters with 3 to 5 Atoms. *J. Phys. Chem.* **1983**, *87*, 4651.
- (47) DiLella, D. P.; Raylor, K. V.; Moskovits, M. Tricopper - A Fluxional Molecule. *J. Phys. Chem.* **1983**, *87*, 525.
- (48) Howard, J. A.; Preston, K. F.; Sutcliffe, R.; Mile, B. Electron-Spin Resonance-Spectrum of Matrix-Isolated Cu_3 . *J. Phys. Chem.* **1983**, *87*, 536.
- (49) Howard, J. A.; Sutcliffe, R.; Tse, J. S.; Mile, B. Electron-Spin Resonance-Spectrum of Cu_5 , A trigonal Bipyramidal Copper Cluster. *Chem. Phys. Lett.* **1983**, *94*, 561.
- (50) Ingólfsson, O.; Takeo, H.; Nonose, S. Energy-resolved collision-induced dissociation of Al_n^+ clusters ($n=2-11$) in the center of mass energy range from few hundred meV to 10. *J. Chem. Phys.* **1999**, *110*, 4382.
- (51) Pettiette, C. L.; Yang, S. H.; Craycraft, M. J.; Conceicao, J.; Laaksonen, R. T.; Cheshnovsky, O.; Smalley, R. E. Ultraviolet Photoelectron-Spectroscopy of Copper Clusters. *J. Chem. Phys.* **1988**, *88*, 5377.
- (52) Cha, C. Y.; Ganteför, G.; Eberhardt, W. Photoelectron-Spectroscopy of Cu_n^- Clusters - Comparison With Jellium Model Predictions. *J. Chem. Phys.* **1993**, *99*, 6308.
- (53) Howard, J. A.; Sutcliffe, R.; Miles, B. Cryochemical Studies .7. Electron-Spin Resonance-Spectrum of Ag_5 . *J. Phys. Chem.* **1983**, *87*, 2268.
- (54) Howard, J. A.; Sutcliffe, R.; Mile, B. The Geometric and Electronic-Structures of Small Metal-Clusters of Group-1B Metals. *Surf. Sci.* **1985**, *156*, 214.
- (55) Cheshnovsky, O.; Taylor, K. J.; Conceicao, J.; Smalley, R. E. Ultraviolet Photoelectron-Spectra of Mass-Selected Copper Clusters - Evolution of the 3d Band. *Phys. Rev. Lett.* **1990**, *64*, 1785.
- (56) Yang, M.; Jackson, K. A.; Koehler, C.; Frauenheim, T.; Jellinek, J. Structure and shape variations in intermediate-size copper clusters. *J. Chem. Phys.* **2006**, *124*, 024308.
- (57) *deMon Software, deMon-KS Version 3.4*; Casida, M. E.; Daul, C.; Goursot, A.; Köster, A. M.; Pettersson, L. G. M.; Proynov, E.; St-Amant, A.; Salahub, D. R.; Duarte, H.; Guan, J.; Jamorski, C.; Leboeuf, M.; Malkin, V.; Malkina, O.; Sim, F.; Vela, A. Montréal, Canada, 1996.
- (58) *AllChem*; Köster, A. M.; Krack, M.; Leboeuf, M.; Zimmermann, B. Universität Hannover, 1998.
- (59) Krückeberg, S.; Schweikhard, L.; Ziegler, J.; Dietrich, G.; Lützenkirchen, K.; Walther, C. Decay pathways and dissociation energies of copper clusters, Cu_n^+ ($2 \leq n \leq 25$), Cu_n^{2+} ($15 \leq n \leq 25$). *J. Chem. Phys.* **2001**, *114*, 2955.
- (60) Reveles, J. U.; Köster, A. M. Geometry optimization in density functional methods. *J. Comput. Chem.* **2004**, *25*, 1109.
- (61) Kohn, W.; Sham, L. J. Self-Consistent Equations Including Exchange and Correlation Effects. *Phys. Rev. A* **1965**, *140*, 1133.
- (62) Köster, A. M.; Calaminici, P.; Casida, M. E.; Flores-Moreno, R.; Geudtner, G.; Goursot, A.; Heine, T.; Ipatov, A.; Janetzko, F.; Martin del Campo, J.; Patchkovskii, S.; Reveles, J. U.; Salahub, D. R.; Vela, A. the deMon Developers, Mexico, 2006.
- (63) Köster, A. M.; Flores-Moreno, R.; Reveles, J. U. Efficient and reliable numerical integration of exchange-correlation energies and potentials. *J. Chem. Phys.* **2004**, *121*, 681.
- (64) Dunlap, B. I.; Connolly, J. W. D.; Sabin, J. R. First-Row Diatomic-Molecule and Local Density Models. *J. Chem. Phys.* **1979**, *71*, 4993.
- (65) Mintmire, J. W.; Dunlap, B. I. Fitting the Coulomb Potential Variationally in Linear-Combination-of-Atomic-Orbitals Density-Functional calculations. *Phys. Rev. A* **1982**, *25*, 88.
- (66) Godbout, N.; Salahub, D. R.; Andzelm, J.; Wimmer, E. Optimization of Gaussian-Type Basis-Sets for Local Spin-Density Functional Calculations. 1. Boron Through Neon, Optimization Technique and Validation. *Can. J. Phys.* **1992**, *70*, 560.

- (67) Vosko, S. H.; Wilk, L.; Nusair, M. Accurate Spin-Dependent Electron Liquid Correlation Energies for Local Spin-Density Calculations - A Critical Analysis. *Can. J. Phys.* **1980**, *58*, 1200.
- (68) Perdew, J. P.; Wang, Y. Accurate and Simple Density Functional for the Electronic Exchange Energy - Generalized Gradient Approximation. *Phys. Rev. B* **1986**, *33*, 8800.
- (69) Perdew, J. P. Density-Functional Approximation for the Correlation-Energy of the Inhomogeneous Electron-Gas. *Phys. Rev. B* **1986**, *33*, 8822; **1986**, *34*, 7406.
- (70) Ho, J.; Ervin, K. M.; Lineberger, W. C. Photoelectron-Spectroscopy of Metal Cluster Anions - Cu_n, Ag_n and Au_n. *J. Chem. Phys.* **1990**, *93*, 6987.
- (71) de Heer, W. A. The Physics of Simple Metal-Clusters - Experimental Aspects and Simple-Models. *Rev. Mod. Phys.* **1993**, *65*, 611.
- (72) Knight, W. D.; Clemenger, K.; de Heer, W. A.; Sanders, W. A.; Chou, M. Y.; Cohen, M. L. Electronic Shell Structure and Abundances of Sodium Clusters. *Phys. Rev. Lett.* **1984**, *24*, 2141.
- (73) Cohen, M. L.; Knight, W. D. The Physics of Metal-Clusters. *Phys. Today* **1990**, *43*, 42.
- (74) Ekardt, W.; Penzar, Z. Self-Consistent Sommerfeld Droplet as a Simple-Model for an accurate Prediction of the Electronic-Properties of Small metal particles. *Phys. Rev. B* **1988**, *38*, 4273.
- (75) Khanna, S. N.; Jena, P. Atomic Clusters - Building-Blocks for a Class of Solids. *Phys. Rev. B* **1995**, *51*, 13705.
- (76) Jug, K.; Zimmermann, B.; Köster, A. M. Growth pattern and bonding of copper clusters. *Int. J. Quantum. Chem.* **2002**, *90*, 594.

CT600358A

Quantum Chemical Description of Oxygen Activation Process on Co, Mn, and Mo Porphyrins[†]

D. Rutkowska-Zbik, R. Tokarz-Sobieraj, and M. Witko*

Institute of Catalysis and Surface Chemistry, Polish Academy of Sciences, ul. Niezapominajek 8, 30-239 Kraków, Poland

Received December 15, 2006

Abstract: The aim of the present theoretical study is to examine the dioxygen activation process occurring at the metalloporphyrin complexes as the first step of the selective oxidation of hydrocarbons, with the stress put on how this may be affected by the type of the central metal. In order to do so, the properties of the porphyrin complexes of Mn, Mo, and Co are discussed by means of quantum chemical calculations within Density Functional Theory (DFT). As a first step, the dioxygen binding by the above-mentioned systems is considered, followed by the study of the interactions of one and two hydrogen atoms with different types of the adsorbed O₂ molecule onto the porphyrin complex. Finally, the stability of the formed oxo species is discussed.

1. Introduction

Molecular oxygen is a stable paramagnetic molecule with two unpaired electrons; therefore, its reactions with organic substrates, that are usually diamagnetic, are spin-forbidden. Consequently, there is an interest to activate dioxygen so that the oxidation reaction is possible. Among numerous possibilities, the activation of the molecular oxygen may be caused by bonding it to the appropriate center, which usually is a transition-metal atom, e.g., in a coordination compound. Within the last years one of the most popular complexes used to activate the dioxygen molecule became metalloporphyrins. In this class of compounds, a metal ion is equatorially coordinated by the porphyrinato ligand, which may be substituted by different groups (see Figure 1).

The interest in metalloporphyrins is due to the presence of their analogues in different proteins where they serve as dioxygen binding sites as well as active centers of numerous enzymes responsible for bio-oxidation. Their ability to maintain oxidation of organic molecules is the origin of metalloporphyrin-based catalysts for hydrocarbons oxidation in mild conditions.¹ One of the most important advantages of the metalloporphyrins is the possibility of changing their geometric and, at the same time, electronic structure in order

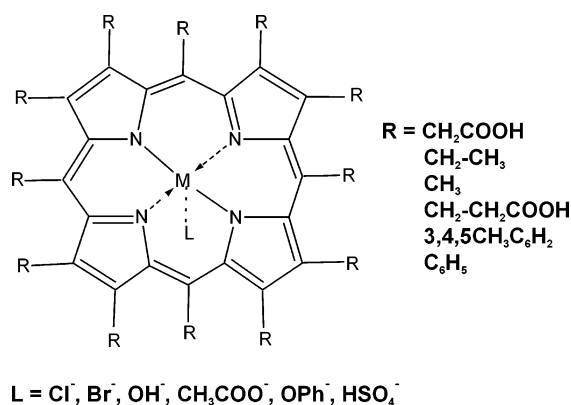


Figure 1. The geometric structure of metalloporphyrins.

to tune their catalytic properties. This is usually done by modulating the character of the porphyrinato ligand substituents (from electron-donating to electron-withdrawing), by changing the central metal ion (its type and oxidation state), or, finally, by modifying the axial ligand that is bound in the trans position with respect to the dioxygen binding site. Such a dependence may be rationalized in the following way. The catalytic oxidation by porphyrins with dioxygen comprises binding of the O₂ molecule to the metal center. The metal-bound dioxygen species may form different geometric structures (side-on and end-on) and may be transformed into other reactive species (hydroperoxo and oxo)—see Figure 2. The possibility of the existence of different forms of so-

[†] Dedicated to Professor Dennis R. Salahub on the occasion of his 60th birthday.

* Corresponding author phone: +48-12-6395101; fax: +48-12-4251923; e-mail: ncwitko@cyf-kr.edu.pl.

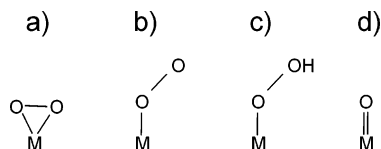
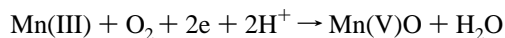


Figure 2. Selected catalytically active forms of oxygen: (a) side-on, (b) end-on, (c) hydroperoxo, and (d) oxo.

called “active oxygen species” as well as their electronic properties and, what follows, their reactivity depend on the character of bonding defined by the type of the central metal as well as on the type of the surrounding ligands. That is why the influence of the metal center on the dioxygen binding appears to be of primary importance.

In order to study the influence of the metal type on the dioxygen activation process the porphyrin complexes of Mn, Co, and Mo are chosen. The selection of these metals results from the fact that their compounds fall into three distinct classes while regarding their catalytic behavior.

On the one hand, the manganese porphyrins are known as moieties that mimic the processes known for the cytochrome P450, which is the cycle of binding and activation of the molecular oxygen, the subsequent process being hydrogen adsorption, and finally the formation of the reactive oxo-complex. The above-mentioned processes are postulated for the manganese-based porphyrin catalysts based on electrochemical experiments; however, instead of the single hydrogen atom binding subsequent proton and electron addition processes were postulated:²



Consequently, a variety of different forms (dioxygen, hydroperoxo, and oxo complexes) may be formed. As catalysts, they are very active in epoxidation and hydroxylation of hydrocarbons under mild conditions.¹

On the other hand, the experimental evidence suggests that the cobalt porphyrins do not form the oxo species, and thus their catalytic activity is attributed mainly to the dioxygen-bound forms of these complexes as well as to their hydroperoxo derivatives.¹ The dioxygen derivatives of these compounds are formed during the catalytic oxidation of hydrocarbons with dioxygen as the oxidant, whereas the presence of hydroperoxo forms of cobalt porphyrins is claimed during the oxidation reactions with either hydrogen peroxide (H_2O_2) or hydroperoxides (ROOH) as oxidants. Similarly to the manganese porphyrins, the cobalt porphyrins are successfully applied for oxidation of hydrocarbons.¹

Finally, the molybdenum porphyrins are known due to their catalytic and photochemical behavior.³ The experimental evidence clearly indicates that molybdenum may coordinate all considered “reactive oxygen species” (i.e., dioxygen, hydroperoxide ligand, and oxo group).^{1,4,5} In addition, in the coordination compounds, the molybdenum ions are known as being able to form multiple oxygen groups.⁷ The molybdenum complexes are used as stereoselective catalysts for epoxidation of olefins,^{7,8} but the nature of oxidizing species is not clearly established. In particular, the requirement of the olefin activation through its coordination to the



Figure 3. Model of the porphyrin molecule.

metal center prior to the oxygen transfer step is still a matter of controversy.

Up to our knowledge, the theoretical studies of the dioxygen activation processes on metalloporphyrins are limited mostly to the modeling of reactions occurring on the iron porphyrin, especially on the iron heme (see e.g., refs 9 and 10 and references therein). This is due to the fact that this process is observed in the cytochrome P450, as mentioned above, and is of great physiological importance. The similar studies for manganese, cobalt, and molybdenum porphyrins are not known. Regarding the geometry and electronic structure of the complexes which may be formed during this process, very little data have been published so far. The literature provides one with the theoretical study of the six-coordinate dioxygen complex of cobalt porphyrin with imidazole as the axial ligand.¹¹ According to this study, the oxygen molecule is bound end-on to the metal center. Moreover, the electronic structure of the five-coordinate manganese porphyrin adduct with the O_2 species is also known,¹² but the studies were performed for manganese(II) and not for manganese(III) as in the present study. For that complex, the end-on structure is more stable than the side-on one. Finally, selected examples of the oxomanganese porphyrin complexes were already the subject of the theoretical studies. Most of them consider the six-coordinate complexes.^{13–15} Very recently, the five-coordinate $[\text{MnPO}]^+$ system has been characterized with the DFT-UB3LYP/BSI method,¹⁶ but its spin state (triplet) was not correctly predicted as compared with the experiment (singlet).

Taking into account all data published so far, our study would be the first not only to model the process of dioxygen activation via subsequent two hydrogen atoms adsorption but also to present the structure and properties of the formed five-coordinate Mn, Co, and Mo porphyrin complexes with the studied ligands.

Therefore, the interest of the present studies is focused on the behavior of Mn, Co, and Mo compounds in dioxygen binding and activation processes in order to examine which parameters of the metal ions are responsible for their catalytic activity. Moreover, the aim is to check the ability of the studied porphyrins to activate the molecular oxygen via hydrogen binding.

2. Methods

Model. As a geometrical model taken into theoretical simulations, the MP complex (where $\text{M} = \text{Co}, \text{Mn}, \text{Mo}$, and $\text{P} = \text{porphyrinato ligand}$) is chosen where all peripheral substituents of the macrocyclic ring are replaced by hydrogen atoms (see Figure 3). Such a choice assures that the examined effect is purely due to the chemical character of the central metal ion, which is chosen on its typical (for coordination compounds) formal valence state, i.e., Co^{2+} , Mn^{3+} , Mo^{4+} . As a result, the studied MP complex is differently charged

Table 1. Electronic Parameters (Charges Q and Sum of Bond Orders) of the Initial MP Complexes ($M = \text{Co}, \text{Mn}, \text{Mo}$)

MP	CoP MULT 2	MnP MULT 5	MoP MULT 5
$Q(M)$	0.56	1.00	1.23
bond orders $\Sigma M-N$	2.72	2.64	2.40

depending on the system, and total charges are equal to 0, 1, and 2 for CoP, MnP, and MoP, respectively.

Computational Method. The calculations are performed by means of ab initio quantum chemical Density Functional Theory method within GGA-RPBE functional,^{17,18} as implemented in StoBe computer code.¹⁹ In this approach, the Kohn–Sham orbitals are described by extended all-electron basis sets of contracted Gaussians.²⁰ All electron basis sets of DZVP quality are applied for all atoms, except for Mo atom, where the model core potential is used.²¹

The energy self-consistency convergence criteria is 10^{-6} au, whereas the energy gradient convergence for the geometry optimization is 10^{-4} au.

The studied systems are discussed in terms of electronic (Mayer bond indices,²² Mulliken charges²³) and geometric (bond lengths, and valence angles) parameters. In addition, each system is characterized by binding energies of the studied oxygen species.

Since the preliminary calculations show that the relaxation of the porphyrin ring is negligible upon binding of a small ligand O_2 (maximum displacement of atoms is ca. 0.03 Å), in the present calculations the optimization comprises only the metal ion and the adsorbed species.

In each case the calculations are performed for different spin states, which are possible for a given system to occur. Nevertheless, in this paper it is decided to include only the results for the systems of the multiplicities that are characterized by the lowest total energies.

3. Results and Discussion

The discussion of the results is organized as follows. First, the calculations of the four-coordinate porphyrin complexes of Co, Mn, and Mo are presented. Second, the dioxygen binding process by the above-mentioned systems is considered. The analysis of the O_2 binding energies allowed one to define the preference of each of the metalloporphyrins to form either end-on or side-on structures. Next, the interaction of the atomic hydrogen with the O_2 molecule bound to the porphyrin complex is taken into account and followed by the investigations of the bonding of second hydrogen atom leading to the formation of the hydroperoxo and oxo species, respectively. Finally, the properties of the different ($\text{Co}=\text{O}$, $\text{Mn}=\text{O}$, $\text{Mo}=\text{O}$) oxo species are discussed.

The Four-Coordinate MP Complexes. Table 1 collects electronic parameters of all studied four-coordinate MP complexes. The ground-state of both MnP and MoP complexes is found to be high-spin (multiplicity equal to 5), whereas the CoP complex is low-spin (multiplicity equal to 2).

In the studied complexes the metal ions always lie in the plane of the macrocyclic ligand. The interesting point,

Table 2. Binding Energies of the O_2 Molecule at the MP Complexes ($M = \text{Co}, \text{Mn}, \text{Mo}$)

$E_B(\text{O}_2)$ [eV]	CoP	MnP	MoP
side-on	1.56	-0.08	-2.55
end-on	-0.28	0.30	-1.84

however, is that in the case of the lower-spin molybdenum systems, the Mo position is significantly out of plane. The displacement of the Mo ion is calculated to be 0.49 Å and 0.28 Å for the systems of multiplicities equal to 1 and 3, respectively.

The bond order indices show that the covalent character of metal–nitrogen bond slightly changes in order $\text{Co}-\text{N} > \text{Mn}-\text{N} > \text{Mo}-\text{N}$, nevertheless the differences are almost negligible (the largest is 0.08 per $M-N$ bond).

In agreement with chemical intuition, in the studied four-coordinate complexes the charge on the metal sites scales with their formal valence state (Co^{2+} , Mn^{3+} , Mo^{4+}). The Co ion exposes the smallest positive charge (+0.56), larger quantifies the Mn atom (+1.00), whereas the largest (+1.23) charge characterizes the Mo site. Since the charge accumulated on the central metal may be the measure of the electrophilicity of an active center of a catalyst, the performed calculations suggest that the cobalt porphyrin would be characterized by the least electrophilic center, while molybdenum porphyrin would possess the most electrophilic one among the studied complexes.

Dioxygen Binding. As mentioned before, dioxygen may be bound to the metal center forming either end-on or side-on complexes. In order to investigate the structure of metal–dioxygen bond in the studied compounds the geometry optimization is performed taking as a starting point two distinct geometries: side-on and end-on. The possibility of the existence of each of these structures and, further, its stability may be deduced from the binding energy of the O_2 molecule to the MP complex. This is calculated as a difference between the total energy of the $\text{MP}-\text{O}_2$ complex and a sum of the total energies of the MP and O_2 fragments:

$$E_B(\text{O}_2) = E(\text{MP}-\text{O}_2) - [E(\text{MP}) + E(\text{O}_2)]$$

Table 2 summarizes the binding energies and clearly shows the differences among the studied systems. The cobalt porphyrin would only form the end-on type complex; the negative dioxygen binding energy indicates the thermodynamically stable bond. The formation of the thermodynamically unstable, side-on form of the CoPO_2 system would cost as much as 1.56 eV. The manganese porphyrin, in contrast, would bind dioxygen exclusively in the side-on type of geometry. These predictions are in line with the experimental evidence for the end-on CoPO_2 and side-on MnPO_2 geometries.^{24,25} It is worth mentioning that the formation of the end-on form of the manganese complex (thermodynamically unstable) would be less energetically demanding ($E_B(\text{O}_2) = 0.30$ eV) than the formation of the side-on derivative of the cobalt porphyrin (neither thermodynamically stable, $E_B(\text{O}_2) = 1.56$ eV). Finally, the negative binding energies of O_2 in the side-on and end-on complexes of the molybdenum porphyrin indicate that both these forms of the $\text{Mo}-\text{O}_2$ group

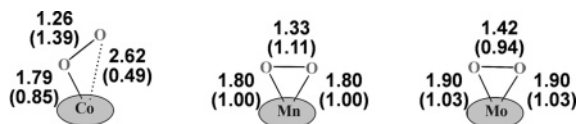


Figure 4. Bond lengths in [Å] and Mayer bond orders indices (in parentheses) for the bound O₂ molecule at the MP system (M = Co, Mn, Mo).

may exist; however, the formation of the side-on complex is favored by 0.71 eV over the end-on form.

The comparison of the resulting energies of the M–O₂ bonds indicates that the bond with the manganese ion is the weakest among the studied metal-dioxygen ones. The molybdenum porphyrin, irrespective of the geometry of the M–O₂ group, binds dioxygen the strongest.

In the following, only the systems characterized by the lowest total energies will be characterized. These are end-on CoP–O₂, side-on MnP–O₂, and side-on MoP–O₂ whose parameters (bond lengths and bond order indices) of the newly formed bonds are presented in Figure 4.

The analysis of the resulting dioxygen complexes reveals that only in the case of the molybdenum porphyrin the binding of the O₂ molecule results in a movement of the Mo ion up out of plane (the Mo displacement is ca. 0.50 Å). The in-plane positions of both, manganese and cobalt ions, are intact upon the dioxygen binding. In each studied complex the O₂ binding leads to the formation of the single metal–oxygen bonds (with bond lengths ca. 1.80 Å), what may be also seen from the M–O bond order (ca. 1.00). In case of both side-on complexes, one notices that the M–O bonds are symmetric, i.e., both have the same length and strength (see Figure 4).

In all cases, the binding of the O₂ molecule to the investigated metalloporphyrins results in the elongation of the O–O bonds (1.22 Å in the isolated molecule). The effect, relatively small for the cobalt porphyrin (elongation by 0.04 Å), is more pronounced in the side-on Mn and Mo complexes, where the bond lengths expand by 0.11 Å and 0.20 Å, respectively. Together with the elongation of the O–O bonds, their weakening is observed, which is reflected by the decrease of the respective bond orders as compared to the isolated O₂ molecule (B.O. = 1.87). These are in line with the trend observed for the elongation of the O–O bonds in the studied compounds; the weakening of this bond is the smallest (Δ B.O. = 0.48) in the cobalt porphyrin, larger in the manganese complex (Δ B.O. = 0.76), and the largest in the molybdenum porphyrin (Δ B.O. = 0.93).

The O₂ binding leads to the rearrangements of the electrons in the studied complexes, which may be quantified by the changes of the charges accumulated on the fragments of the molecules. Table 3 collects the Mulliken charges of the metal and the adsorbed oxygen atoms of the MP–O₂ complexes. The analysis of the charge redistribution after the dioxygen binding allows for finding a number of common points in the studied systems.

First, the binding of the oxygen molecule at the porphyrins induces the electron transfer onto the oxygen species. The bound oxygen molecule becomes negatively charged, thus nucleophilic. It has the highest nucleophilic character while

bound to the molybdenum complex ($q(\text{O}_2) = -0.34$), smaller in the manganese porphyrin ($q(\text{O}_2) = -0.24$), and the smallest in the cobalt complex ($q(\text{O}_2) = -0.14$). It is worth noticing that in the latter case almost the whole negative charge acquired by dioxygen is localized on the outer oxygen atom (Ob).

Second, the analysis of the charge transfers induced by the dioxygen adsorption reveals the important role of the porphyrinato ligand as a source of the electrons in the studied systems. In the case of the Co and Mn compounds the electrons from the porphyrin ring are distributed over the adsorbed oxygen molecule and the metal ions, which leads to the reduction of the metal centers. The largest transfer from the porphyrin ring (0.55e) is observed for the Mn complex, where 0.31e goes to the manganese ion and 0.24e to the adsorbed oxygen molecule. The formation of the end-on species at the Co porphyrin causes the transfer of 0.16e from the porphyrinato ligand onto the cobalt ion and 0.14e onto the oxygen species. The formation of the side-on oxygen species at the Mo porphyrin engages 0.23e from the porphyrin ring and 0.11e from the molybdenum ion, which are directed onto the oxygen molecule.

Finally, spin density analysis performed for the studied systems reveals that the Mn and Mo complexes form the paramagnetic structures with two unpaired electrons located mostly on the metal ions (spin density 2.51 and 1.97, respectively) and partially on the oxygen atoms (each of them is characterized by the spin density equals 0.19 in the case of the Mn porphyrin and 0.17 in the case of the Mo complex). The cobalt porphyrin forms the complex with one unpaired electron located mainly on the dioxygen ligand (spin density 0.99).

While comparing the results of our studies on the dioxygen-bound structures a question arises about parameters of the metal ions which determine their distant behavior in the reaction with dioxygen. The answer to this question is not clear. In this study three different metal ions are studied, each of them being on a different oxidation state (and thus having different charge) but possessing the same coordination environment. It seems that these are the coordination properties of the metal itself that have the largest effect on the coordination mode of the molecular oxygen. For instance, the molybdenum ion, which prefers higher coordination numbers, binds O₂ preferentially as the side-on group, because this way of binding allows it to form a six-coordinate complex rather than a five-coordinate one. This supposition is based on our experience as well as on the experimental evidence^{8–10} which suggests that the Mo ion, irrespective of its oxidation state, prefers the formation of the side-on complexes with the O₂ ligand.

Binding of the First Hydrogen Atom. As the next step, the interaction of the hydrogen atom with the molecular oxygen bound to the investigated porphyrin complexes is discussed. Table 4 and Figure 5 summarize the calculated energetic, electronic, and geometric parameters for the studied systems.

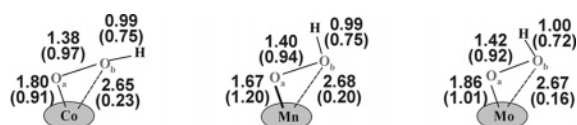
The energies of H binding show that the hydrogen atom becomes stabilized on the oxygen species bound to the porphyrin complex independent of the type of the metal

Table 3. Mulliken Charges on Metal and Oxygen Atoms in the Studied MPO₂ Complexes

MP	CoP–O ₂ end-on MULT 2	MnP–O ₂ side-on MULT 3	MoP–O ₂ side-on MULT 3
Q(M)	0.40	0.69	1.34
Q(O ₂) (Oa; Ob)	–0.14 (–0.02; –0.12)	–0.24 (–0.12; –0.12)	–0.34 (–0.17; –0.17)

Table 4. Binding Energies (*E*) in [eV] and Charges (*Q*) Connected with the H Binding at the MPO₂ Complexes (M = Co, Mn, Mo)

MP	CoP–OOH MULT 1	MnP–OOH MULT 2	MoP–OOH MULT 2
<i>E</i> _B (H)	–2.78	–2.76	–2.37
<i>E</i> _B (OOH)	–0.93	–0.71	–2.79
<i>E</i> _B (OH)	–2.19	–0.56	0.51
Q(M)	0.44	0.72	1.45
Q(Oa)	–0.24	–0.18	–0.27
Q(Ob); Q(H)	–0.33; 0.44	–0.31; 0.46	–0.34; 0.49
Q(OH)	0.11	0.15	0.15

**Figure 5.** Bond lengths in [Å] and Mayer bond orders indices (in parentheses) after H binding at the MPO₂ systems (M = Co, Mn, Mo).

center (Co, Mn, Mo) and of the geometry of oxygen (side-on, end-on). The energies of the hydrogen binding are similar for the Co and Mn complexes (–2.78 eV and –2.76 eV, respectively) and are higher than for the Mo porphyrin (–2.37 eV).

In the studied porphyrins, the hydrogen atom forms the hydroperoxo group bound to the metal site. The stability of the formed OOH species may be indicated by its binding energy, calculated as a difference between the total energy of the MP–OOH complex and a sum of the total energies of MP and OOH fragments:

$$E_B(\text{OOH}) = E(\text{MP} - \text{OOH}) - [E(\text{MP}) + E(\text{OOH})]$$

The obtained data show that the OOH fragment is stabilized in all studied systems. It is thus thermodynamically not favored to transfer this group to a reactant. In addition, it should be noted that whereas the OOH binding energies are comparable for cobalt and manganese complexes (–0.93 eV and –0.71 eV, respectively), its value is quite high in the case of the molybdenum system (–2.79 eV).

One may also consider the binding of the hydrogen atom as a formation of the OH group bound to the oxo site (M=O). In this respect, the obtained Ob–H bond lengths of 1.00 Å and bond orders of ca. 0.7 are typical for the OH groups. The OH fragments are slightly positively charged, and the charges on OH groups are almost identical in all three systems (ca. 0.15). The stability of the formed OH groups is judged from the OH binding energy calculated according to the formula:

$$E_B(\text{OH}) = E(\text{MP} - \text{O} - \text{OH}) - [E(\text{MP} = \text{O}) + E(\text{OH})]$$

Computed in this way, the OH binding energy is the largest for the CoP porphyrin (–2.19 eV) and smaller for the MnP system (–0.56 eV). In the MoP moiety this is characterized by the positive value (0.51) that suggests the metastable bond.

The changes in geometries induced by the binding of the first hydrogen atom may be described as follows. In the side-on structures (the Mn and Mo systems) the binding of H leads to the breaking of one of the metal–oxygen bonds (between the metal and the Ob atom). Now, only one oxygen atom is connected with the metal center. In the studied systems the OH groups remain bonded with the complexes by the O–O bond, rather than the metal–OH bond. In all structures the metal–OH bond length is equal to 2.7 Å and the bond order amounts to 0.2, whereas the O–OH bonds are characterized by bond orders ca. 0.95 and bond lengths close to 1.4 Å.

The bond between the metal and the second oxygen atom (Oa - not directly connected with hydrogen) does not change significantly in the case of the Co and Mo porphyrins with comparison to the initial structures (see Figures 4 and 5). These are still the single metal–oxygen bonds, characterized by bond orders close to 1. In the case of the manganese system, the formation of the OH group leads to the shortening (from 1.80 Å to 1.67 Å) and the strengthening (the bond orders change from 1.00 to 1.20) of the metal–second oxygen bond. The metal–oxygen bond acquires slowly the character of a double bond.

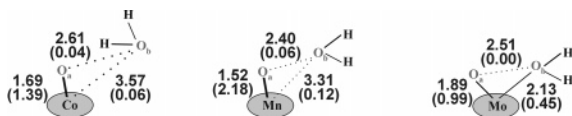
Moreover, the adsorption of hydrogen leads to the further elongation and weakening of the O–O bonds in the Co and Mn porphyrins. The O–O distance increases to ca. 1.40 Å, and the bond orders decrease to ca. 0.95. Only in the case of the Mo system the O–O bond parameters almost do not change after the hydrogen adsorption. The bond length and Mayer bond order indices for MoP system are comparable with their values before adsorption (see Figures 4 and 5).

The delivery of the hydrogen atom results in the oxidation of the metal ions; the largest effect is seen for the Mo porphyrin, where the charge on the metal ion changes from 1.34 before to 1.40 after the hydrogen binding. In the case of the Co and Mn porphyrins, the charge on Co and Mn increases by 0.04 and 0.03 respectively, as compared to the initial complexes with the adsorbed oxygen molecule (see Table 3). In all studied systems, the adsorption of hydrogen leads to the accumulation of the negative charge on both adsorbed oxygen atoms. The charge at the atom connected with hydrogen (Ob) is almost twice as large as compared with the initial complex with the adsorbed oxygen molecule.

The spin density analysis performed for the studied systems reveals that two of the investigated complexes (with manganese and molybdenum ions) are characterized by one unpaired electron in the system. In both cases this is mainly

Table 5. Binding Energies [eV] and Charges (Q) Describing Binding of the Second Hydrogen Atom at the MPO₂H Complexes (M = Co, Mn, Mo)

MP	CoP-OO ₂ H MULT 2	MnP-OO ₂ H MULT 1	MoP-OO ₂ H MULT 1
$E_B(\text{H}^{2\text{nd}})$	-3.02		-2.63
$E_B(\text{H}_2\text{O})$	-0.15	0.00	3.00
Q(M)	0.44	0.64	1.22
Q(Oa)	-0.42	-0.15	-0.36
Q(O _b); Q(H); Q(H)	-0.88; 0.48; 0.39	-0.78; 0.44; 0.44	-0.81; 0.47; 0.47
Q(H ₂ O)	-0.01	0.10	0.13

**Figure 6.** Bond lengths in [Å] and Mayer bond orders indices (in parentheses) after the second H binding at the MPO₂H system (M = Co, Mn, Mo).

located on the central metal ions (spin density equals to 1.04 and 1.27 on Mn and Mo, respectively).

Binding of the Second Hydrogen Atom. In the next step, the adsorption of the second hydrogen atom is studied. Table 5 and Figure 6 show the details of electronic and geometric structure of the formed systems.

The presence of the second hydrogen further differentiates the studied systems; however, a number of similarities may also be found. In all complexes the binding energy of the second hydrogen atom is larger by ca. 0.2 eV than the binding energy of the first hydrogen. The delivery of the second hydrogen promotes a cleavage of the O–O bond; in all complexes the O–O bond length becomes larger than 2.3 Å, and no interaction between the oxygen atoms is observed (bond order indices are close to 0). At the same time, the formation of the water molecule interacting with the porphyrin system is observed. The same as previously, the stability of the formed water species may be indicated by the H₂O binding energy calculated as follows:

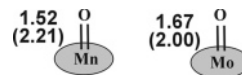
$$E_B(\text{H}_2\text{O}) = E(\text{MP}-\text{OOH}_2) - [E(\text{MP}=\text{O}) + E(\text{H}_2\text{O})]$$

In the case of the CoP porphyrin the formed water molecule is still bonded to the complex (binding energy -0.15 eV). One of the hydrogen atoms from the water group interacts with the oxygen atom, Oa, bonded to the Co ion by a hydrogen bond. The charge on the Co ion does not change after the binding of the second hydrogen atom. The additional electron is located mainly at both oxygen atoms increasing their nucleophilic character. The Co–Oa bond becomes shorter (by 0.11 Å) and stronger (bond order increases by 0.49) than in the complex with only one hydrogen atom. The analysis of the spin density reveals that the unpaired electron present in this system is delocalized between Co and Oa atoms.

The water molecule formed in the MnP system is not bound to the complex. The water binding energy in the investigated structure is calculated to be 0.0 eV. As a consequence, the bond between the manganese ion and the

Table 6. Energies [eV] and Atomic Charges Characterizing the MPO Species (M = Mn, Mo)

MP	MnP=O MULT 1	MoP=O MULT 3
$E_B(\text{O})$	-3.43	-6.63
Q(M)	0.64	1.51
Q(Oa)	-0.15	-0.35

**Figure 7.** Bond lengths in [Å] and Mayer bond order indices (in parentheses) for the MP = O species (M = Mn, Mo).

second oxygen atom acquires the character of the double bond, with bond length (1.52 Å) and bond orders (2.18), which are typical for this type of bond.

In the case of the MoP porphyrin the water binding energy is positive (3.0 eV) suggesting its metastable position, but, surprisingly, the distance between the water molecule and the Mo–Oa group is smaller (2.13 Å) than in the other complexes (where it is larger than 3 Å). Moreover, the Mo–Ob bond order which characterizes the bond strength between Mo and oxygen from the water molecule is not negligible (0.45). As a result, the bond between the molybdenum atom and the second oxygen atom (Oa) almost does not change with comparison to the similar bond in the complex with the hydroperoxo group (bond length is equal to 1.9 Å and bond order to 0.99).

Oxo Complexes. The analysis of the energies of OH and H₂O binding in the studied systems suggests that the oxo species may be formed only by the manganese and the molybdenum complexes, as indicated by the positive values of the respective binding energies (see Tables 4 and 5). This finding leads to the conclusion that the negative binding energies of the OH and H₂O species may be the reason for which the cobalt oxo porphyrins are, up to our knowledge, not observed experimentally. That is why only the manganese and molybdenum oxo systems are discussed in the following.

In the case of the manganese porphyrin, the oxygen–metal bond starts to acquire the double bond character just due to the first hydrogen binding ($R = 1.67$ Å, B.O. = 1.20). After the binding of the second hydrogen and the subsequent formation of the water species (that desorbs from the complex) the parameters characterizing the metal–oxygen bond are almost identical with the parameters calculated for the isolated oxo species ($R = 1.52$ Å, B.O. = 2.18 vs $R = 1.52$ Å, B.O. = 2.21, for the MnP–OOH₂ complex and the isolated oxo species, respectively). The same, the electronic parameters such as charges on the metal (0.64) and the oxygen atom (-0.15) are identical with the ones found for the isolated oxo species (see Table 6 and Figure 7).

In the case of the MoP system, for both MoPOOH and MoPOOH₂ systems, the bond between the molybdenum and Oa oxygen atom should be described as the single rather than the double bond. This is indicated by the relatively long Mo–O distance (1.89 Å) and low bond order (0.99). One should mention that the additional calculations performed for the isolated oxo molybdenum compound clearly show

that the double bond is characterized by the bond of 1.67 Å and bond order equal to 2.00.

The complementary information on the studied oxo complexes is delivered by the binding energy of the oxo atom. In the MoP complex, the oxo species binding energy is twice as large as the binding energy of the oxo species in the manganese complex (−6.63 eV vs −3.43 eV, respectively). As a result, the transfer of the oxygen atom toward an organic molecule would be easier from the MnPO species than from the MoPO one.

4. Conclusions

The results of the performed calculations indicate that different catalytically active forms of oxygen (side-on, end-on, hydroperoxo, or oxo) may be formed on the studied porphyrin complexes depending on the type of the central metal. In this respect, the influence of the metal center is clearly visible. It is unclear, however, which are the properties of the metal ion that are responsible for the observed differences. According to our knowledge, these may include such “intrinsic” parameters as electronic configuration or charge as well as “external” ones such as environment (ligands which coordinate to the metal ion). Although in order to better understand their influence, more calculations are needed, and we hope that our study will shed some light on this issue.

It is seen that in the case of the cobalt porphyrin, the active forms of the catalyst would include the end-on complex with dioxygen as well as its hydroperoxo form. Here, the formation of the oxo-group in the described manner would not occur, because the formed water molecule will not easily dissociate from the CoP=O complex, thus disabling its reactivity.

For the manganese complex, on the opposite, there exists a possibility of the formation of the side-on, hydroperoxo, and oxo types of ligands. All of them may be catalytically active and may contribute to the experimentally observed high reactivity of the manganese porphyrins in homogeneous systems.

Finally, the largest variety of the active oxygen species exists in the case of the molybdenum systems. Here, all studied forms that are side-on, end-on, hydroperoxo, and oxo are possible to occur. What is striking, however, is that after the formation of the oxo-complex, the molybdenum tends to increase its coordination number becoming more hindered, and thus its reactivity may be lowered.

Acknowledgment. Financial support from the Polish Ministry of Scientific Research and Information Technology with grant no. N204 034 31/0795 (years 2006–2008) is acknowledged. The authors acknowledge the computational time at the Academic Computer Center CYFRONET AGH (grant no. KBN/SPP/PAN/019/2001).

References

(1) Suslick, K. S.; Meunier, B.; Robert, A.; Prati, G.; Bernadou, J. In *The Porphyrin Handbook*; Kadish, K. M., Smith, K. M., Guilard R., Eds.; Academic Press: 2000; Vol. 4 pp 30–38, 134–135.

- (2) Albin, V.; Bedioui, F. *Electrochem. Commun.* **2003**, *5*, 129–132.
- (3) Matsuda, Y.; Murakami, Y. *Coord. Chem. Rev.* **1988**, *92*, 157–192.
- (4) Ledon, H. J.; Durbut, P.; Varescon, F. *J. Am. Chem. Soc.* **1981**, *103*, 3601–3603.
- (5) Chong, A. O.; Sharpless, K. B. *J. Org. Chem.* **1977**, *42*, 1587–1590.
- (6) Sheldon, R. A.; Kochi, J. K. *Adv. Catal.* **1976**, *25*, 272–413.
- (7) Mimoun, H. J. *J. Mol. Catal.* **1980**, *7*, 1.
- (8) Jorgensen, K. A.; Hoffman, R. *Acta Chem. Scand. B* **1986**, *40*, 411–419.
- (9) Rydberg, P.; Sigfridsson, E.; Ryde, U. *J. Biol. Inorg. Chem.* **2004**, *9*, 203–223.
- (10) Bach, R. D.; Dmitrenko, O. *J. Am. Chem. Soc.* **2006**, *128*, 1474–1488.
- (11) Degtyarenko, I.; Nieminen, R. M.; Rovira, C. *Biophys. J.* **2006**, *91*, 2024–2034.
- (12) Rutkowska-Zbik, D.; Witko, M. *J. Mol. Catal. A: Chem.* **2006**, *258*, 376–380.
- (13) Ghosh, A.; Gonzalez, E. *Isr. J. Chem.* **2000**, *40*, 1–8.
- (14) de Visser, S. P.; Oligaro, F.; Gross, Z.; Shaik, S. *Chem. Eur. J.* **2003**, *7*, 4954–4960.
- (15) De Angelis, F.; Jin, N.; Car, R.; Groves, J. T. *Inorg. Chem.* **2006**, *45*, 4268–4276.
- (16) Koizumi, K.; Shoji, M.; Nishiyama, Y.; Maruno, Y.; Kitagawa, Y.; Soda, K.; Yamanaka, S.; Okumura, M.; Yamaguchi, Y. *Int. J. Quantum Chem.* **2004**, *100*, 943–956.
- (17) Perdew, J. P.; Burke, K.; Ernzerhof, M. *Phys. Rev. Lett.* **1996**, *77*, 3865–3868.
- (18) Hammer, B.; Hansen, L. B.; Norskov, J. K. *Phys. Rev. B* **1999**, *59*, 7413–7421.
- (19) Hermann, K.; Pettersson, L. G. M.; Casida, M. E.; Daul, C.; Goursot, A.; Koester, A.; Proynov, E.; St-Amant, A.; Salahub, D. R. Contributing authors: Carravetta, V.; Duarte, H.; Friedrich, C.; Godbout, N.; Guan, J.; Jamorski, C.; Leboeuf, M.; Leetmaa, M.; Nyberg, M.; Pedocchi, L.; Sim, F.; Triguero, L.; Vela, A. *StoBe-deMon version 2.1*; StoBe Software: 2005.
- (20) Godbout, N.; Salahub, D. R.; Andzelm, J.; Wimmer, E. *Can. J. Phys.* **1992**, *70*, 560–571.
- (21) Andzelm, J.; Radzio, E.; Salahub, D. R. *J. Chem. Phys.* **1985**, *83*, 4573–4580.
- (22) Mayer, I. *Chem. Phys. Lett.* **1983**, *97*, 270–274.
- (23) Mulliken, R. S. *J. Chem. Phys.* **1955**, *23*, 1833–1840.
- (24) Jones, R. D.; Summerville, D. A.; Basolo, F. *Chem. Rev.* **1979**, *79*, 139–179.
- (25) VanAtta, R. B.; Strouse, C. E.; Hansen, L. K.; Valentine, J. S. *J. Am. Chem. Soc.* **1987**, *109*, 1425–1434.

Trends in Energies and Geometric Structures of Neutral and Charged Aluminum Clusters[†]

René Fournier*

Department of Chemistry, York University, 4700 Keele Street, Toronto,
Ontario M3J 1P3, Canada

Received December 21, 2006

Abstract: The minimum energy geometric structures of Al_n , Al_n^- , and Al_n^+ ($4 \leq n \leq 15$) are predicted from the results of “Tabu Search” (TS) global optimizations performed directly on the BPW91/LANL2DZ potential energy surface. In 24 of the 36 cases investigated, the TS delivered a lower energy structure than previously reported, in one case (Al_{12}^+) it failed to find the global minimum, and in the remaining 11 cases TS confirmed previous structures. All clusters (with $4 \leq n \leq 15$) have the lowest spin state as their ground state except Al_4 (triplet), Al_4^+ (quartet), Al_7^- (triplet), and maybe Al_5^+ (singlet and triplet are degenerate). The 20-electron Al_7^+ and 40-electron Al_{13}^- clusters are relatively stable compared to other clusters, on several criteria; to a lesser degree, Al_7 , Al_{12} , and Al_{13}^+ are also stable.

I. Introduction

Structure determination of clusters is a tough, and still mostly unsolved, problem for both theory and experiment. There are two main sources of difficulty for theory. First, there is a huge number of local minima. With Lennard-Jones (LJ) potential interatomic interactions, the number of local minima of n -atom clusters¹ for $n > 6$ is roughly on the order of $2.7^{(n-5.7)}$. Second, there is a lack of guiding principles in most cases, C_n fullerenes being a notable exception. In order to make meaningful comparisons of calculated properties to experiments, which are often done on clusters in a size range from $n = 2$ up to $n = 30$ and sometimes more, one must attempt global optimization on energy surfaces with very many local minima. A common approach is to first find the lowest energy structures on a model energy surface which could be, for instance, an empirical potential function or a tight-binding energy method. With a simple model, tens of thousands of energy evaluations are possible, and a good global optimization technique like genetic algorithm² is likely to find the global minimum (GM) of the model energy surface and, in the process, will generate many candidates for the GM of higher level theory energy surfaces. Problems arise when the energy model is unreliable and has low-energy structures that are qualitatively different from those of a better

theory. This is, of course, very difficult to know beforehand. Another strategy, which we take here, is to perform the global search directly on the energy surface of a first-principles method, in this case Kohn–Sham Density Functional Theory (KS-DFT) with a generalized gradient approximation (GGA) to exchange–correlation. The problem with this approach is that the high cost of KS-DFT will typically prevent calculating more than a few thousand energies, and this is probably less than the number of local minima at $n \geq 12$.

We have developed a meta-algorithm, called Tabu Search in Descriptor Space (TSDS), to do global optimization efficiently for certain types of clusters. Descriptions can be found for Tabu Search algorithms in general³ and specifically for TSDS optimization of clusters.⁴ Briefly, the key ideas of TSDS are as follows: (i) the only structures that are ever considered are *near* local minima, (ii) each of those structures has its energy evaluated only once or a few times at most, and (iii) a small number (typically 4–7) of structural descriptors such as mean coordination and moments of inertia are used by the algorithm to gradually “learn”, as the search progresses, about regions of descriptor space where local minima are deeper and the chance of finding the GM higher. The user supplied descriptors constitute a crude form of expert knowledge, and, if they are well chosen, they help the algorithm avoid large portions of the energy surface in the later stages of the search. For instance TSDS would consider any structure at the beginning of a search, but, for

[†] Dedicated to Professor Dennis R. Salahub on the occasion of his 60th birthday.

* Corresponding author e-mail: renef@yorku.ca.

most metal clusters, it would avoid structures that have a very low mean atomic coordination (or, equivalently, a very high surface area) toward the end of the search. Yet the search is only weakly biased by the choice of descriptors because the correlation between low energy and specific values of descriptors is not assumed or predefined, it is gradually learned during the search.

We tested the performance of TSDS on model systems such as LJ clusters.⁴ We also made limited use of an early version of TSDS for minimization of Li_n and Be_n cluster structures on first-principles energy surfaces.^{5,6} Reported here are results of systematically applying TSDS to a series of Al_n neutral and charged clusters. We chose the Al_n series because it has been extensively studied and because KS-DFT calculations are relatively fast for Al_n . Experimental results were published for ionization energies (IE),⁷ electron affinities (EA),⁸ and fragmentation channels.⁹ There is also indirect evidence about Al cluster structure coming from experimental studies of relative abundances and reactivity of charged Al clusters.^{10,11} A thorough theoretical study of Al_n , Al_n^+ , Al_n^- ($2 \leq n \leq 15$) was done by Rao and Jena.¹² They used the BPW91/LANL2DZ method (described in the next section) and searched for the GM by doing several local optimizations starting with initial structures that were obtained by global optimization on a simpler model energy surface, or from published results on other clusters, or by an educated guess. They did a detailed comparison of their calculated electronic properties to experiment and generally found good agreement. We chose to use the same energy method because it looks adequate for Al clusters and because repeating the search for GM on the same energy surface but with TSDS would show to what degree the global optimization method matters for structure determination and prediction of cluster properties. There have been many other theoretical studies of aluminum clusters as well.^{13–19} This makes aluminum one of the best characterized series of metal clusters to date and a good testing ground for computational methods.

II. Computational Details

Energy minimizations were all done by Tabu Search in Descriptor Space (TSDS) global optimization with a local spin density functional (SVWN5 Gaussian keyword), followed by many local optimizations with the BPW91 functional, and then by characterizing the lowest energy minimum by calculation of energy second derivatives and vibrational frequencies. All energies were evaluated by KS-DFT with the exchange-correlation functional of Becke, Perdew, and Wang (referred to as “BPW91”) and a LANL2DZ basis set, and the Gaussian03 software was used.²⁰ This is the same method for energy evaluation as used in a previous study,¹² and indeed the energies we get for atoms and other small species where geometries are identical agree to within 10^{-5} au.

No method can ever guarantee to find the GM, but so far our experience^{4–6} indicates that TSDS can find good approximate solutions to GM problems at a relatively small computational cost. In this study, the number of energy evaluations done in the TSDS part were only 120 for $n = 5$,

550 for $n = 10$, and 800 for $n = 15$, and the number of local optimizations, each of which requires many energy evaluations, varied between 10 and 20. The total number of energy evaluations was on the order of 3000 or less for the largest clusters ($n = 13–15$), and roughly half of the computational effort went into doing local optimizations.

III. Results and Discussion

A. Geometric Structures. The GM are displayed in Figure 1, and their energies are listed in Table 1. The neutral and anionic clusters often have the same, or similar, structures. Cationic clusters are very different, and they often adopt much more open structures. One of the most surprising results is that we found many structures with energy lower than previously reported¹² even for very small clusters. They are, with energy lowering, shown in parentheses: Al_4^+ (−0.02 eV), Al_5^- (−0.01 eV), Al_6 (−0.33 eV), Al_6^+ (−0.28 eV), Al_6^- (−0.13 eV), Al_7^- (−0.04 eV), Al_8 (−0.32 eV), Al_8^+ (−0.10 eV). For Al_5^+ we found not only the same triplet GM as Rao and Jena but also a singlet which is the structure we show in Figure 1. This singlet is essentially degenerate with the triplet, the energy difference is less than 0.001 eV. One might have thought that global optimization can be done by trial-and-error for $n \leq 8$, because there are only 8 minima on the LJ energy surface at $n = 8$. Theoretical studies, including our own, have often paid scant attention to the global minimum problem when clusters with 8 or fewer atoms are concerned. But atoms of most elements have interactions that are much more complicated than a Lennard-Jones potential. The number of local minima is most likely larger in Al_n than LJ_n clusters, especially considering that more than one energy surface (spin state) must sometimes be searched. Note that there is a lot of variety among structures in Figure 1, and many of them are distorted, or have low symmetry, or display big variations among coordinations of the different atoms. Those types of structures are normally not minima, or at least not low-lying minima, on the energy surfaces of pairwise additive potentials or embedded atom method (EAM) and similar models. Of the 36 GM shown in Figure 1, 24 constitute an improved (lower energy) structure relative to previous work.¹² The energy lowering is at least 0.01 eV in every case, it is smaller than 0.10 eV in 9 of the 24 cases, and it is larger than 0.30 eV in 6 cases. The energy lowering is 0.19 eV on average. In one case, Al_{12}^+ , TSDS missed the GM and found instead a structure that is 0.10 eV higher than that of Rao and Jena¹² (an icosahedron with a missing peripheral atom).

Generally, the structures that we found (Figure 1) differ in two ways from those reported previously.¹² First, there are more differences among the neutral, cation, and anion of a given n in our set of results. It is understandable because differences in the electronic structures of the neutral and charged clusters are implicitly taken into account at every stage of each TSDS optimization, whereas it comes into play only in the second step of a two-step approach to global optimization. Second, there are many more instances of atoms having a coordination of less than 4 in our structures, even at large n , and those atoms are often part of a quasi-

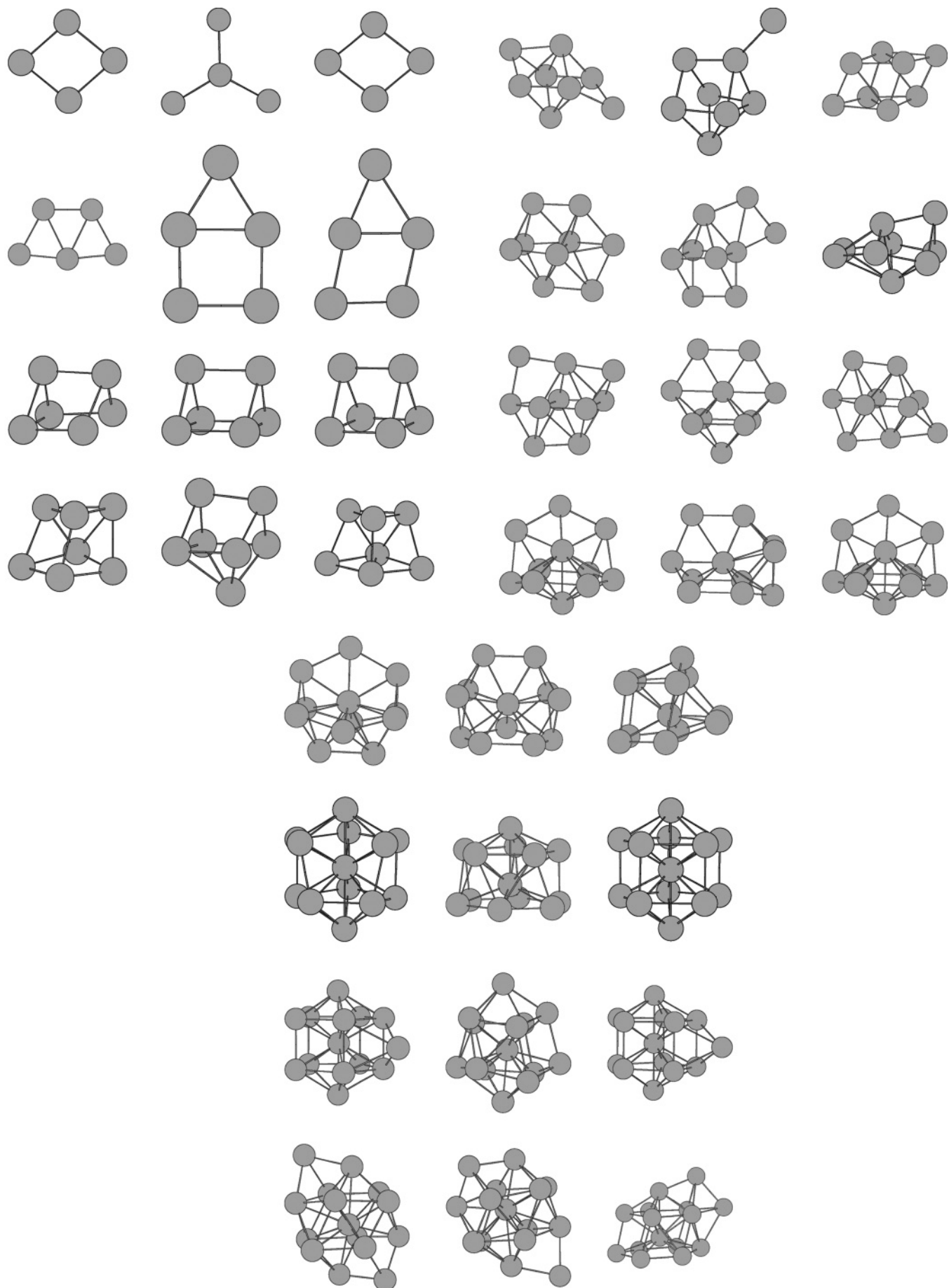


Figure 1. Ground-state geometries found by TSDS optimization on the BPW91/LANL2DZ energy surface for neutral, cationic, and anionic aluminum clusters.

Table 1. Total BPW91/LANL2DZ Energies (au) of Al_n , Al_n^+ , and Al_n^- in their Lowest Energy Structure and Spin State and Vertical Ionization Energy (VIE) of the Neutral in eV

n	$E(0)$	$E(+)$	$E(-)$	VIE
4	-7.956638	-7.718496	-8.034917	6.70
5	-9.980356	-9.737493	-10.056436	6.73
6	-12.002416	-11.763381	-12.089263	6.62
7	-14.047646	-13.831830	-14.123844	6.19
8	-6.065227	-5.832956	-16.147627	6.55
9	-18.080750	-17.856885	-18.180257	6.51
10	-20.114445	-19.891054	-20.206009	6.39
11	-22.141527	-21.930017	-22.244191	6.29
12	-24.190858	-23.963704	-24.277649	6.36
13	-26.227981	-6.017113	-26.340839	6.35
14	-28.258926	-28.050969	-28.343463	6.17
15	-30.275220	-30.072363	-30.371095	5.87

planar 4-atom diamond, or 5-atom rhombus, unit. This is seen in Al_{15}^+ , Al_{12} , Al_{11} , Al_{11}^+ , Al_{11}^- , and Al_8^+ .

We will now compare the structures of Figure 1 to the GM found in other theoretical studies. The GM predicted by a Voter-Chen version of the embedded atom model (EAM) potential in the size range 4–15¹⁴ are *all different* from our GM structures. Another study based on a different empirical potential (Murrell-Motttram 2 + 3-body potential)¹⁵ predicts GM structures similar to those of the Voter-Chen EAM potential for $n = 4-7$ and $n = 11-14$. Again, *none* of those structures agree with the BPW91 GM (Figure 1). Both potentials predict structures that are more compact and have higher symmetry than those of Figure 1. The only resemblance are for Al_{13} and Al_{14} : the empirical potentials predict them to be an icosahedron and a capped icosahedron, and BPW91 predicts them to be a decahedron and a capped decahedron. Empirical potentials for metals are often fitted to bulk properties and tend to favor cluster structures that have high, or even maximal, coordination. But KS-DFT calculations show that there are important changes in local electronic structure as atomic coordination changes,¹³ and it is hard to model these things, and the associated changes in bond energies, with an empirical function. The characteristic density of states of metallic aluminum is almost fully developed only when the number of atoms in Al clusters reaches 25.¹³ It is doubtful that empirical potentials can give accurate energies and structures in clusters smaller than that.

Our structures agree much better with other first-principles studies. Jones used DFT with a local spin density (LSD) exchange-correlation functional and plane wave basis and did simulated annealing to search the GM of Al_n , $n = 3-10$.¹⁶ The structures he found for $n = 4-6, 9$ are similar to ours. However, what we find as the GM of Al_6 (trigonal prism, singlet) is a higher energy isomer on the LSD potential surface, it is 0.35 eV above the GM (a D_{3d} trigonal antiprism).¹⁶ Jones found many low-lying minima having comparable energies at $n = 8-10$, in qualitative agreement with us (Figure 4). Given the large number of isomers, and different functionals, it is remarkable that we find the same GM for Al_9 as Jones.¹⁶ Akola et al. also used LSD with a plane wave basis and searched the potential surface of Al_n ($n = 3-7$) by molecular dynamics followed by local

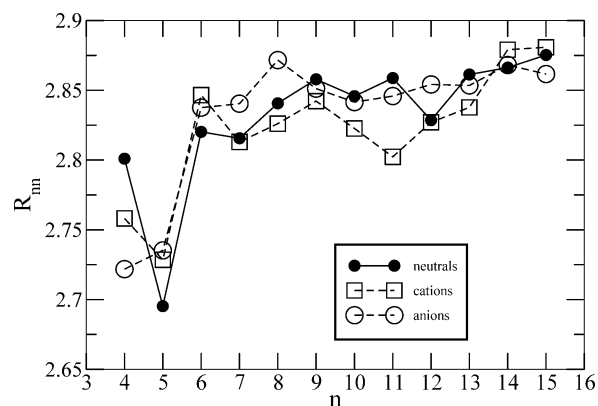


Figure 2. Average of nearest-neighbor distances (Å) in neutral and charged aluminum clusters.

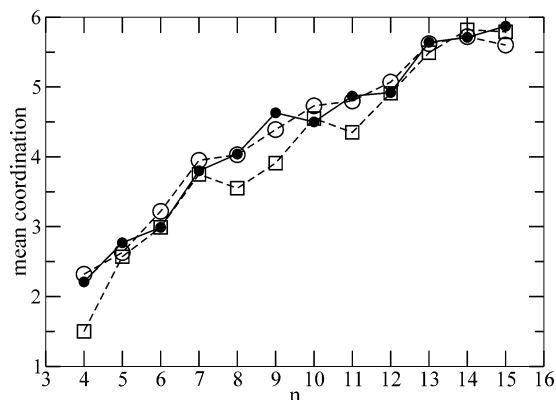


Figure 3. Mean atomic coordination in neutral and charged aluminum clusters.

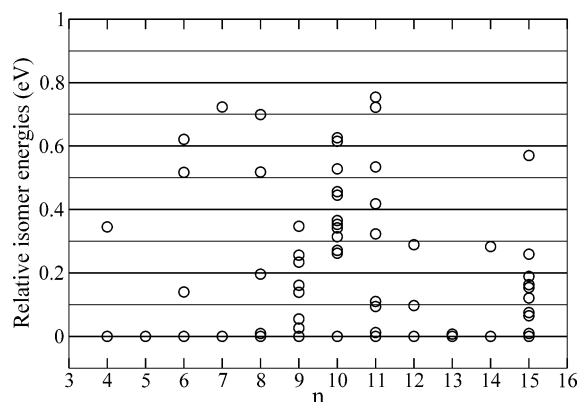


Figure 4. Relative energies of isomers of Al_n .

optimization (conjugate gradient method) on many plausible candidates.¹⁸ For larger clusters, ($n = 12-23$) they used a potential derived from effective medium theory to generate plausible candidates and then carried local optimizations on those by LSD. It is hard to make a comparison because most of their GM structures are not shown, but their predicted GM are apparently quite different from ours. First, the symmetry group of their small clusters match our structures for $n = 4, 5$ but not $n = 6, 7$. Second, they describe the GM of $n = 12-23$ clusters as being “icosahedral-based structures”, but only one of our GM (Al_{15}) is based on the icosahedron. Sun et al. used the B3LYP hybrid functional to study Al_n and Al_nO , $n = 2-10$.¹⁷ They do not describe their GM search method except to say that different initial

Table 2. Lowest Vibrational Frequency (cm^{-1}) of Al_n , Al_n^+ , and Al_n^- in their Lowest Energy Structure and Spin State

n	0	+	-	n	0	+	-
4	74	42	104	10	55	45	59
5	45	30	16	11	24	38	41
6	32	31	38	12	32	45	32
7	50	52	38	13	26	0	36
8	38	31	57	14	17	25	21
9	28	28	14	15	38	28	50

structures were considered. Their predicted GM for the neutrals $n = 4-10$ agree remarkably well with our GM, except $n = 6$ where they predict a distorted octahedron. There also appears to be small differences in bond lengths for $n = 7$ and 8 . Agreement between their GM structures and ours is not very good for anions and cations, but Al_9^- and Al_{10}^- look almost identical. Although they differ in details, there is a resemblance between the B3LYP GM of Sun et al. and our BPW91 GM for Al_n^+ and Al_n^- : in general, structures are not very compact, they have low symmetry, and in many cases there are Al atoms with a low coordination.

The evolution of average nearest-neighbor distance (R_{mn}) (Figure 2) and mean coordination (Figure 3) with cluster size in Al_n are like those given by Rao and Jena¹² but with small differences. The cations have shorter R_{mn} than the neutrals for $n = 4, 8-11$, and this is accompanied by smaller mean coordination (except for $n = 10$). As expected, the curves for neutral and charged clusters in Figures 2 and 3 get close at larger n . The mean coordination of atoms is smaller in Al_n clusters than in Li_n at all sizes.⁵ It is smaller than in Be_n up to $n = 10$ roughly, then it becomes comparable to Be_n .⁶ As n increases, the hybridization in Al clusters gradually evolves from s^2p^1 to s^1p^2 , and the metal character of Al_n develops.¹² As a result, with increasing n , Al_n clusters gradually adopt more compact structures and mean coordinations that are close to maximal and typical of clusters of simpler metals like Li_n and Ag_n .

In our studies of Li^5 and Be^6 clusters, we noted a correlation between the shape (oblate, prolate, quasi-spherical) of the GM found by first-principles and the predicted optimal shape in the ellipsoidal jellium model (EJM). No such correlation is found here for Al_n clusters, no matter whether we take the number of itinerant electron per atom to be 1 or 3. For example, the shape parameter $\eta = (2I_b - I_a - I_c)/I_a$, where $I_a \geq I_b \geq I_c$ are the three moments of inertia of a cluster, equals -0.11 for Al_9 which shows that it is oblate, but the EJM predicts a prolate optimal structure for both 9 and 27 electrons.

Second energy derivatives and vibrational frequencies (Table 2) confirm that all structures in Figure 1 are minima, except maybe Al_{13}^+ for which the lowest frequency is essentially zero and surely lower than the numerical accuracy of the calculations. The highest frequencies for each cluster (not shown in Table 2) cover a range from 260 cm^{-1} in Al_4 to 370 cm^{-1} in Al_5 . With the exception of $n = 5$, the highest frequency goes up from a 273 cm^{-1} average for the three $n = 4$ species, to 291 cm^{-1} ($n = 6$), and to 304 cm^{-1} ($n = 7$). The $n = 5$ species have unusually high vibrational frequencies which must be a result of their quasi-planarity and

Table 3. Most Intense IR Active Vibrational Modes and All Vibrational Frequencies of Al_7^+ and Al_{13}^- with Most IR Intense Shown in Boldface

cluster	frequencies (cm^{-1})
Al_n	$n = 11$: 296; $n = 12$: 331; $n = 13$: 319, 343; $n = 14$: 150, 342
Al_n^+	$n = 4$: 264; $n = 5$: 359; $n = 8$: 144, 322; $n = 9$: 211, 312; $n = 10$: 331, 336; $n = 11$: 278, 279, 296, 298, 315; $n = 12$: 313; $n = 13$: 311, 315; $n = 14$: 313, 324, 338; $n = 15$: 332, 347
Al_n^-	$n = 13$: 168, 169, 176
Al_7^+	52, 58, 107, 176, 177, 181, 232 , 240, 241, 249 , 250 , 259 , 290, 291, 291
Al_{13}^-	35, 60, 61, 68, 68, 115, 115, 128, 129, 129, 168 , 169 , 176 , 189, 192, 202, 202, 204, 205, 209, 209, 215, 240, 250, 250, 267, 267, 269, 269, 292, 315, 317, 336

presence of triangles in the structure: the highest frequency of each species is 370 cm^{-1} (Al_5), 359 cm^{-1} (Al_5^+), and 351 cm^{-1} (Al_5^-). There is a jump from 304 cm^{-1} ($n = 7$) to 338 cm^{-1} at $n = 8$, and thereafter the highest frequencies remain roughly constant and inside the range $322-366 \text{ cm}^{-1}$ for the 24 species with $n > 7$. This is a manifestation of the fact that the change in hybridization (and bonding nature of orbitals) is almost complete by $n = 8$.¹² Note that the first interior atoms show up at larger size, roughly $n = 12$, and that has no clear effect on vibrational frequencies. Table 3 shows the frequencies of modes for which the calculated IR intensity is larger than 10 km/mol . Those are often, but not always, the highest frequency modes. We also list all frequencies for the more stable cluster ions Al_7^+ and Al_{13}^- at the bottom of Table 3.

So far we discussed only the lowest energy minima (GM), but typical TSDS runs end with 10–20 local optimizations that produce anywhere between 1 and 20 distinct minima. In TSDS, diversity in geometric structures is explicitly encouraged. This not only prevents the algorithm from converging too quickly to a single low-energy structure that may not be the GM but also increases the chances of discovering the second, third, ..., most stable isomers. This is a good feature of TSDS because, when comparing to experiments, it is important to look at energy minima that are slightly above the lowest one and get a sense for possible cluster isomers. The energies of Al_n isomers found by TSDS that are within 1.0 eV of the GM but differ from each other by at least 0.01 eV are displayed in Figure 4. Considering that our calculated relative energies are probably not more accurate than 0.2 eV , and room temperature is roughly 0.025 eV , the presence of different cluster isomers is very likely for most cluster sizes except $n = 4, 5, 7, 10, 13, 14$. We will not discuss the structures and properties of isomers other than the GM here as it would be tedious. But those isomers would have to be examined carefully if one had to assign a spectrum for structural determination of specific cluster species.

Local optimization of the neutral Al_n clusters with the SVWN5 exchange-correlation functional yielded the same global minima as with the BPW91 functional except for a few things. The GM of Al_6 in SVWN5 is a edge-capped square pyramid with C_s symmetry. The GM of Al_{12} in

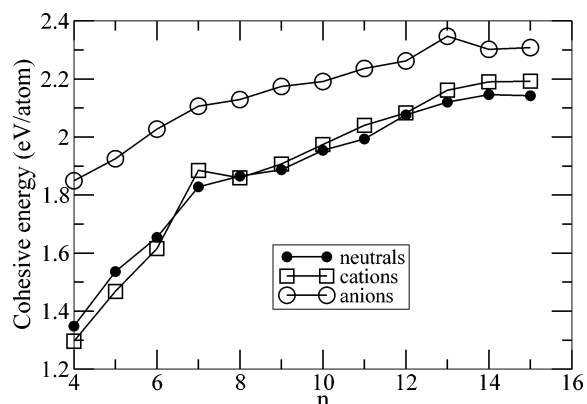


Figure 5. Cohesive energies of neutral and charged aluminum clusters.

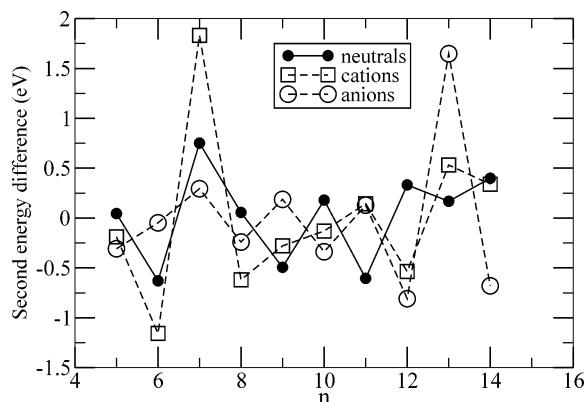


Figure 6. Second energy difference, $\Delta E(n) = E(n+1) + E(n-1) - 2E(n)$, of neutral and charged aluminum clusters.

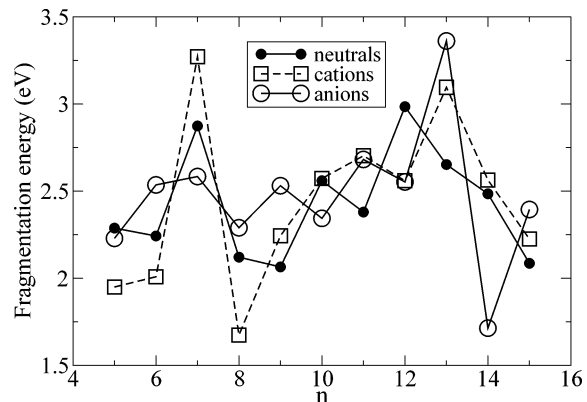
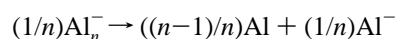
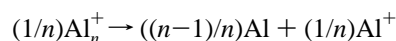


Figure 7. Fragmentation energy of neutral and charged aluminum clusters for the lowest energy fragmentation channel (see text).

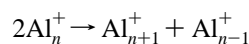
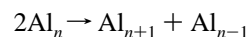
SVWN5 is different from BPW91 but is similar to it: it has a central atom with a coordination of 11 and some atoms with low coordination (two atoms with coordination of 4). The GM of Al_7 , Al_{13} , and Al_{15} obtained by SVWN5 are topologically equivalent to the BPW91 GM of Figure 1 but with fairly large distortions. The GM we find for the other neutral clusters are virtually identical in SVWN5 and BPW91, but one should bear in mind that GM are obtained by local optimization, with either SVWN5 or BPW91, of

the same set of initial structures generated by TS/DS/SVWN5 global optimization. A search done entirely with BPW91 (TS/DS with BPW91 followed by local optimization with BPW91) might yield different BPW91 structures having lower energy. Still, similarities between the two sets of neutral cluster GM structures found here, and similarities to the GM found in previous KS-DFT studies, indicate that the structures and relative isomer energies do not depend strongly on the choice exchange-correlation functional.

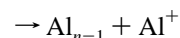
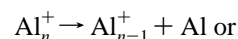
B. Binding Energies. Trends in energies as a function of cluster size are shown in Figures 5–7. The quantities plotted are energies of the following reactions. The cohesive energy is for



the second energy difference corresponds to



and the fragmentation energy along the energetically most favored dissociation channel corresponds to



The cohesive energies of neutrals and cations are always close, with cations having a lower cohesive energy at $n < 7$ and higher cohesive energy at $n \geq 7$. The difference is pronounced for Al_7 and Al_7^+ because the latter has a closed electronic shell (20 electrons) in the jellium model. Dissociating Al_n^+ into $(n-1)$ Al atoms and Al^+ concentrates the positive charge onto a single atomic cation which is energetically more costly as n gets larger, and this is why the cations curve eventually crosses above the neutrals curve. Cohesive energies of anion clusters are higher still because the atomic anion Al^- is relatively unstable. Otherwise, these curves are typical of cluster cohesive energies except for conspicuous peaks at Al_7^+ and Al_{13}^- . The second energy differences, and fragmentation energies, also indicate that Al_7^+ (20 electrons) and Al_{13}^- (40 electrons) are particularly stable. This has been noted before,¹² of course, and is well understood in terms of the closed electronic shells of the jellium. Interestingly, all three species (neutral, cation, anion) are relatively stable at $n = 7$ and $n = 13$ by the criterion set by Figure 6. If these energies were known but the structures were not, it would be tempting to explain the stability at $n = 7$ and 13 by closing of atomic shells²¹ with a pentagonal

bipyramid (PBP, $n = 7$) and icosahedron ($n = 13$). But as Figure 1 shows, none of the $n = 7$ species is a PBP, and none of the 13-atom species is an icosahedron (Al_{13} and Al_{13}^- are decahedra). A better explanation may be that stability is associated not only with closed electronic shells ($N_e = 20, 40$) but also, to a lesser extent, with numbers of electrons just above and below the shell closing numbers. If this view is correct, simultaneous stability of the neutral, anion, and cation of a given size can happen only for clusters of elements having more than one itinerant electron per atom. It should occur for $N_e = 20, 40, 58^7$ or the combinations M_n ($M =$ valence of the element, $n =$ number of atoms in the cluster): $2_{10}, 2_{20}, 2_{26}, 3_7, 3_{13}, 3_{19}, 4_5,$ and 4_{10} .

There is an even–odd oscillation in the energy differences of Figure 6, but it is not perfect and it is not as pronounced as for s -valent metals like Li or Ag. Species with even number of electrons are more stable only for $n \geq 8$ in the neutrals series, $n \geq 6$ for anions, and $n = 10$ breaks the expected pattern in the cations series. The favored fragmentation channel according to our calculations is always $(n-1) + 1$ for neutrals and $(n-1)^- + 1$ for anions. For cations we find the lowest dissociation energy pathway for $n = 5-9$ yields Al^+ and Al_{n-1} except at $n = 8$ and find that the products are Al and Al_{n-1}^+ for $n = 8$ and $n > 9$. Note that the exception ($n = 8$) produces the stable cluster ion Al_7^+ . This is in line with a suggestion by Martínez and Vela¹⁹ that the favored fragmentation route is generally the one giving the hardest fragments, i.e., the fragments with the largest HOMO–LUMO gap. However, hardness is not the only thing that matters. Spreading the positive charge over larger clusters decreases the Coulombic energy, and that is why the preferred dissociation products are Al and Al_{n-1}^+ at $n = 9-15$ and most likely also for $n > 15$. These favored fragmentation channels agree with those of Rao and Jena¹² except Al_9^+ for which they find the lowest dissociation energy leads to Al_8^+ (see the “relaxed” column in their Table 3).

C. Electronic Structure and Electronic Properties. The trends seen in experimental vertical ionization energies (VIEs)⁷ are well reproduced in our calculations (Table 1). The range of VIEs is 6.55–5.75 eV in experiment and 6.73–5.87 eV in our calculations. On average, calculated VIEs are higher by roughly 0.15 eV. Experimental VIEs are nearly constant and equal to 6.45 eV inside the group ($n = 4, 5, 6, 8, 9, 13$), they are all close to 6.20 eV for ($n = 7, 10, 11, 12$), and the two VIEs for $n = 14, 15$ are close to 5.75 eV. Calculated VIEs follow this trend, but they are comparatively too low for Al_7 and Al_{13} (by 0.2 eV) and too high for Al_{14} (by 0.25 eV).

Our calculated adiabatic electron detachment energies (ADEs) are compared to those of previous theoretical work and to two experiments in Table 4. Our GM geometries (and energies) differ from those of Rao and Jena¹² for the neutral or the anion in all cases except $n = 4$ and $n = 14$. Yet, our ADEs do not agree with experiment better or worse than the ADEs of Rao and Jena. Note that the discrepancies between the two sets of experimental results are bigger than 0.3 eV in most cases, but discrepancies between the two sets of calculations are smaller than 0.3 eV in most cases.

Table 4. Adiabatic Electron Detachment Energy from Al_n^- (eV)

n	PW	theory ¹²	expt 1 ¹¹	expt 2 ⁸
4	2.13	2.13	1.74	2.20 ± 0.05
5	2.07	2.06	1.82	2.25 ± 0.05
6	2.36	2.56	2.09	2.63 ± 0.06
7	2.07	2.04	1.96	2.43 ± 0.06
8	2.24	2.56	2.22	2.35 ± 0.08
9	2.71	2.54	2.47	2.85 ± 0.08
10	2.49	2.64	2.47	2.70 ± 0.07
11	2.79	2.64	2.53	2.87 ± 0.06
12	2.36	2.31	2.53	2.75 ± 0.07
13	3.07	3.38	2.86	3.62 ± 0.06
14	2.30	2.30	2.47	2.60 ± 0.08
15	2.61	2.70	2.53	2.90 ± 0.08

The HOMO–LUMO gaps (eV) for the neutral clusters are, in order of increasing size, as follows: 0.30 ($n = 4$), 0.85, 0.74, 0.81, 0.97 ($n = 8$), 0.67, 0.82, 0.63, 1.04 ($n = 12$), 0.74, 0.94, and 0.63 ($n = 15$). The variations are not strong, but the highest gap ($n = 12$) does correspond to a relatively stable cluster. The two magic clusters have the largest gap as expected, 1.57 eV (Al_7^+) and 1.45 eV (Al_{13}^-).

Like Rao and Jena, we find that most Al clusters with $n > 3$ have ground states with the lowest possible multiplicity. However, Rao and Jena found many more exceptions to that trend, that is, clusters that have the next lowest possible multiplicity in their ground state. They are $\text{Al}_4, \text{Al}_4^+, \text{Al}_5^+, \text{Al}_6, \text{Al}_8,$ and Al_{10} . By contrast, the only high-spin clusters that we found are $\text{Al}_4, \text{Al}_4^+,$ and Al_7^- . We must add, however, that the energy difference between high-spin and low-spin energy minima are sometimes very small. They are, in eV, as follows: Al_4 (−0.29), Al_4^+ (−0.08), Al_5^+ (0.00), Al_6 (+0.01), Al_7^- (−0.08), and Al_8 (+0.31). Stern-Gerlach experiments by Cox et al.²² showed that spin multiplicities of neutral Al clusters are 2 for odd n and 3 for even n up to $n < 9$. Here, improving the theoretical geometric structures (of Al_6 and Al_8) seemingly worsens agreement with experiment. It may be that the BPW91 level of theory and TSDBS geometry optimization are still not up to the task of predicting magnetism in small Al clusters or that low-lying isomers complicate the interpretation of magnetic properties so that magnetic moments are of little use for structure assignments.

IV. Conclusion

Global optimization of Al cluster geometries was done with the same energy method (BPW91/LANL2DZ) as in a previous work. Detailed comparison of our results with that previous work gives two main conclusions. First, without guiding principles it is very difficult to find the GM of clusters, even for small clusters ($n \leq 8$). Finding the GM (or good approximations) requires an efficient and unbiased search algorithm coupled with an accurate energy function. Here we found 24 structures that improve upon previously published structures. We want to point out that the way in which the GM were searched in the earlier work¹² is not at all unusual: many theoretical studies have used this approach. Second, it is very difficult to learn about the

geometric structure of metal clusters by comparing experimental and theoretical data about their electronic properties (magnetic moments, ionization energies, electron detachment energies). That is because the jellium model works rather well: electronic properties are largely controlled by the number of electrons, not by the positions of the nuclei. Here, the GM we found for Al_n , Al_n^+ , and Al_n^- differ significantly from previous work,¹² but our calculated properties (preferred fragmentation channels, ionization energies, electron detachment energies, magnetic moments) do not differ much. Theoretically our results are better, but they do not agree with experiment better, and uncertainties (experimental and computational) blur any conclusion we could make about specific structure assignments.

Comparison of structures to other first-principles studies that used different basis sets and functionals^{16,17} show many similarities in the predicted GM structures but differences in details. On the other hand, GM structures predicted using empirical potentials^{14,15} are completely at odds with our results. They are more compact and more symmetrical than first-principles structures and that is probably due to the inability of those empirical potentials to model the change in sp hybridization as a function of atom coordination. For aluminum clusters, the GM of empirical potentials differ too much from those of KS-DFT to be useful as an initial guess for searching KS-DFT energy surfaces.

It will be very difficult to elucidate with confidence the structure of larger ($n > 7$) Al clusters by comparison of the calculated properties of different theoretical isomers to measured properties, for three reasons. First, as we already said, our calculated properties agree no better with experiment than those of Rao and Jena¹² although our GM structures are very different and theoretically better. Second, as Figure 4 shows, there are often many cluster isomers for a given size, and finding all those isomers and computing reliably their properties is a challenge. Third, calculating relative isomer energies with quantitative accuracy²³ (0.01 eV/atom or better) requires computational methods that are impractical and much more costly than what we used here. Structure elucidation for all but the smallest Al clusters will probably require rich and accurate experimental data that are sensitive to geometry (vibrational or well resolved photoelectron spectra for instance), in combination with a computational study that includes an extensive search for the GM and low-lying energy isomers by a first-principles method and a calculation of relative energies and cluster properties with the best possible level of theory.²⁴

Finally, our results confirm that Al_7^+ and Al_{13}^- have special stability and larger HOMO–LUMO gaps as a result of their electron count (20 and 40) matching a shell closing in the jellium model. However, the jellium model does not help understand the evolution of geometries with size.

Acknowledgment. This work was supported by the Natural Sciences and Engineering Research Council of Canada.

References

- (1) Chekmarev, S. F. *Phys. Rev. E* **2001**, *64*, 036703–036703–9. Tsai, C. J.; Jordan, K. D. *J. Phys. Chem.* **1993**, *97*, 11227–11237.
- (2) Roberts, C.; Johnston, R. L.; Wilson, N. T. *Theor. Chem. Acc.* **2000**, *104*, 123–130.
- (3) Gendreau, M. In *Handbook of Metaheuristics*; Glover, F., Kochenberger, G. A., Eds.; Kluwer: Dordrecht, The Netherlands, 2003; pp 37–54.
- (4) Chen, J.; Fournier, R. *Theor. Chem. Acc.* **2004**, *112*, 7–15.
- (5) Fournier, R.; Cheng, J.; Wong, A. *J. Chem. Phys.* **2003**, *119*, 9444–9454.
- (6) Sun, Y.; Fournier, R. *Comput. Lett.* **2005**, *1*, 210–219.
- (7) Schriver, K. E.; Persson, J. I.; Honea, E. C.; Whetten, R. L. *Phys. Rev. Lett.* **1990**, *64*, 2539–2542.
- (8) Li, X.; Wu, H.; Wang, X.-B.; Wang, L.-S. *Phys. Rev. Lett.* **1998**, *81*, 1909–1912.
- (9) Jarrold, M. F.; Bower, E. J.; Kraus, J. S. *J. Chem. Phys.* **1987**, *86*, 3876–3885. Hanley, L.; Ruatta, S. A.; Anderson, S. L. *J. Chem. Phys.* **1987**, *87*, 260–268. Saunders, W. A.; Fayet, P.; Wöste, L. *Phys. Rev. A* **1989**, *39*, 4400–4405.
- (10) Leuchtner, R. E.; Harms, A. C.; Castleman, A. W., Jr. *J. Chem. Phys.* **1991**, *94*, 1093–1101.
- (11) Taylor, K. J.; Pettiette, C. L.; Graycraft, M. J.; Chesnovsky, O.; Smalley, R. E. *Chem. Phys. Lett.* **1988**, *152*, 347–352.
- (12) Rao, B. K.; Jena, P. *J. Chem. Phys.* **1999**, *111*, 1890–1904.
- (13) Salahub, D. R.; Messmer, R. P. *Phys. Rev. B* **1977**, *16*, 2526–2536.
- (14) Sebetci, A.; Güvenç, Z. B. *Modell. Simul. Mater. Sci. Eng.* **2005**, *13*, 683–698.
- (15) Lloyd, L. D.; Johnston, R. L. *Chem. Phys.* **1998**, *236*, 107–121.
- (16) Jones, R. O. *J. Chem. Phys.* **1993**, *99*, 1194–1206.
- (17) Sun, J.; Lu, W. C.; Wang, H.; Li, Z.-S.; Sun, C.-C. *J. Phys. Chem. A* **2006**, *110*, 2729–2738.
- (18) Akola, J.; Häkkinen, H.; Manninen, M. *Phys. Rev. B* **1998**, *58*, 3601–3604.
- (19) Martínez, A.; Vela, A. *Phys. Rev. B* **1994**, *49*, 17464–17467.
- (20) Frisch, M. J.; Trucks, G. W.; Schlegel, H. B.; Scuseria, G. E.; Robb, M. A.; Cheeseman, J. R.; Montgomery, J. A., Jr.; Vreven, T.; Kudin, K. N.; Burant, J. C.; Millam, J. M.; Iyengar, S. S.; Tomasi, J.; Barone, V.; Mennucci, B.; Cossi, M.; Scalmani, G.; Rega, N.; Petersson, G. A.; Nakatsuji, H.; Hada, M.; Ehara, M.; Toyota, K.; Fukuda, R.; Hasegawa, J.; Ishida, M.; Nakajima, T.; Honda, Y.; Kitao, O.; Nakai, H.; Klene, M.; Li, X.; Knox, J. E.; Hratchian, H. P.; Cross, J. B.; Bakken, V.; Adamo, C.; Jaramillo, J.; Gomperts, R.; Stratmann, R. E.; Yazyev, O.; Austin, A. J.; Cammi, R.; Pomelli, C.; Ochterski, J. W.; Ayala, P. Y.; Morokuma, K.; Voth, G. A.; Salvador, P.; Dannenberg, J. J.; Zakrzewski, V. G.; Dapprich, S.; Daniels, A. D.; Strain, M. C.; Farkas, O.; Malick, D. K.; Rabuck, A. D.; Raghavachari, K.; Foresman, J. B.; Ortiz, J. V.; Cui, Q.; Baboul, A. G.; Clifford, S.; Cioslowski, J.; Stefanov, B. B.; Liu, G.; Liashenko, A.; Piskorz, P.; Komaromi, I.; Martin, R. L.; Fox, D. J.; Keith, T.; Al-Laham, M. A.; Peng, C. Y.; Nanayakkara, A.; Challacombe, M.; Gill, P. M. W.; Johnson, B.; Chen, W.; Wong, M. W.; Gonzalez, C.; Pople, J. A. *Gaussian 03, Revision C.02*; Gaussian, Inc.: Wallingford, CT, 2004.

- (21) Martin, T. P. *Phys. Rep.* **1996**, 273, 199–241.
- (22) Cox, D. M.; Trevor, D. J.; Whetten, R. L.; Rohlfing, E. A.; Kaldor, A. *J. Chem. Phys.* **1986**, 84, 4651–4656.
- (23) Schultz, N. E.; Staszewska, G.; Staszewski, P.; Truhlar, D. G. *J. Phys. Chem. B* **2004**, 108, 4850–4861.
- (24) Martínez, A.; Sansores, L. E.; Salcedo, R.; Tenorio, F. J.; Ortiz, J. V. *J. Phys. Chem.* **2002** 106, 10630–10635. Wu, H.; Li, X.; Wang, X.; Ding, C. F.; Wang, L. S. *J. Chem. Phys.* **1998**, 109, 449–458.

CT6003752

Structural and Thermodynamic Analysis of the First Mononuclear Aqueous Aluminum Citrate Complex Using DFT Calculations[†]

Antonio Luiz Oliveira de Noronha, Luciana Guimarães, and Hélio Anderson Duarte*

Grupo de Pesquisa em Química Inorgânica Teórica – GPQIT, Departamento de Química-ICEx-UFMG, 31.270-901 Belo Horizonte, MG, Brazil

Received January 13, 2007

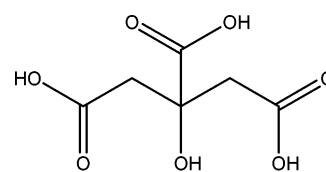
Abstract: Structural and thermodynamic properties of the mononuclear Al/citrate complexes have been theoretically investigated aiming to understand the coordination mechanism at an atomic level. GGA-DFT/PCM calculations have been performed for the different conformations and tautomers arising from the Al^{3+} and citric acid (H_3L) interaction in aqueous solution. The Gibbs reaction energies were estimated based on the reaction of the trigonal planar $\text{Al}(\text{OH})_3$ and H_3L to form different Al–citrate complexes. The estimated Gibbs free reaction energies for the $[\text{AlL}]$, $[\text{AlHL}]^+$, and $[\text{Al}(\text{OH})\text{L}]^-$ species are in good agreement with the experimental values. In these species, the Al^{3+} center is coordinated by two carboxylic and the tertiary hydroxyl groups of the citrate. Conversely to what has been proposed based on the experiments, the present theoretical calculations indicate that the citric acid hydroxyl group remains protonated upon the coordination of Al^{3+} . In fact, our model turns out to be more consistent with the relative $\text{p}K_a$ values of citrate protonation groups and with the hydrolysis constant of the H_2O bound to Al^{3+} leading to better agreement with the available experimental data.

Introduction

Aluminum is present in a wide range of areas in every day life and is the major constituent of soil. Aluminum, and its chemical speciation in the presence of different ligands, has attracted a great deal of attention^{1–6} due to its importance in many processes related to environment, biology, and materials. The Al(III) ion in aqueous solution is a rather complex system⁷ due to the formation of many hydrolysis species with different stoichiometries. Furthermore, in the presence of ligands, such as organic acids, Al(III) is coordinated forming many different species. The role of these species in the environment and biological processes is still an open question and has deserved a great deal of attention in the past few years.^{8–14}

Citrate acid (H_3L)—structure 1—is a very versatile molecule with three carboxylic groups and one tertiary hydroxyl

group which makes this molecule able to coordinate many different metal ions in aqueous solution.



Structure 1

It is an important organic ligand in nature derived from root exudates, decomposing organic matter, and other sources, influencing drastically the hydrolysis of Al^{3+} and, consequently, its speciation in the environment.¹⁵ Citric acid is also the main small molecule in the blood plasma able to coordinate the Al^{3+} . It has been found to contribute for decreasing the toxicity of metal ions in living organisms¹⁶ probably due to its capacity of coordinating metal ions. The structural and thermodynamic knowledge of Al–citrate complexes has fundamental importance and, therefore, has been the subject of many investigations. Thermodynamic

[†] Dedicated to Professor Dennis R. Salahub on the occasion of his 60th birthday.

* Corresponding author phone: ++55-31-3499-5748; fax: ++55-31-3499-5700; e-mail: duarte@ufmg.br.

properties as the equilibrium constants of the different Al/citrate species have been studied using potentiometric measurements.^{17,18} It has been shown that mononuclear species are predominant in the blood plasma concerning kinetic and thermodynamic points of view. The AIL complex is the predominant species in the 2–4 pH range followed by deprotonation to form $[\text{Al}(\text{OH})\text{L}]^{-1}$ which predominates in the 4–6 pH range. The citrate ability to form chelates explains the strong complexes formed with Al^{3+} ion.

It is expected that the metal ion, Al^{3+} , will be coordinated through the stronger electron donor groups, i.e., the citrate carboxylic groups. If only these carboxylic groups are involved in the Al^{3+} coordination, 7-member rings will be formed. However, it is well-known that 7-member rings are not favorable due to bond strengths. Therefore, it has been suggested that the citric acid acts as a tridentate ligand involving carboxylic and hydroxyl groups to form more stable 5- or 6-member rings, depending on which carboxylic groups are involved. In fact, X-ray structure determination¹⁹ has shown that the Al^{3+} is coordinated through the hydroxyl group in the $[(\text{NH}_4)_5\{\text{Al}(\text{C}_6\text{H}_4\text{O}_7)_2\} \cdot 2\text{H}_2\text{O}]$ complex. This mechanism seems to be reasonable even though the carboxylic groups are a much stronger electron donor than the hydroxyl group. The citric acid in aqueous solution presents only three $\text{p}K_{\text{a,s}}$ (3.13, 4.76, 6.40)²⁰ which are associated with the carboxylic groups. How do we explain that the hydroxyl group is involved in the metal ion coordination? The answer has been shown to be very trivial: the hydroxyl group is deprotonated! However, in aqueous solution, this seems to be contradictory since the hydroxyl group has not been observed to be deprotonated in the aqueous pH range. As a comparison, the *tert*-butyl alcohol $\text{p}K_{\text{a}}$ is about 19.

Recently, Aquino et al.²¹ have performed density functional (DFT) investigation for the aluminum(III)–citrate system. They have calculated many different conformations of AIL complexes. The solvent effect has been taken into account using the polarizable continuum method (PCM). The free energy of the complex formation is not in agreement with the experimental value with an error of more than 40 $\text{kcal} \cdot \text{mol}^{-1}$. However, in the literature, there are many examples in which complex formation free energies are predicted with reasonable accuracy (less than 6 kcal/mol) using the DFT-GGA/PCM approach.^{22–31}

The apparent disagreement between the experimental observations and the proposed structures motivated us to revisit the Al/citrate system, focusing in its first mononuclear complex formation. Experimental techniques can provide normally global information on the thermodynamic stability of different species. The goal of this work is to provide a detailed picture of Al/citrate chemical speciation aiming to contribute to the understanding of this complex system at an atomic level.

Computational Aspects

All possible conformations and tautomers arising from the interaction of Al^{3+} with citric acid (H_3L) were calculated using the LCGTO-KS-DFT method (Linear Combination of Gaussian Type Orbital–Kohn–Sham–Density functional)

implemented in the deMon program.³² The following exchange correlation (XC) functionals based on the generalized gradient approximation were employed: BP86, with the Becke³³ expression for the exchange and the Perdew^{34,35} expression for correlation and the PBE XC functional that employs the expressions developed by Perdew, Burke, and Ernzerhof.³⁶ The DZVP and TZVP basis sets explicitly optimized for DFT³⁷ and the Ahlrichs basis sets (A-PVTZ)³⁸ have been used.

Auxiliary basis sets, automatically generated (A2*), were used for fitting the charge density. An adaptive grid^{39,40} with a tolerance of 10^{-6} was employed in the numerical integrations of the exchange–correlation energy and potential.

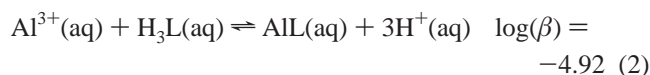
All complexes were fully optimized in the gas phase, without symmetry restrictions using the standard scheme Broyden–Fletcher–Goldfarb–Shanno (BFGS).⁴¹ Harmonic vibrational analyses were performed, and the Hessian matrix was evaluated numerically from the analytical gradients of the potential energy surface (PES). Positive frequencies ensure that a minimum was found in the PES. All geometry optimization and harmonic frequency calculations have been carried out in the gas phase with the deMon program. Thermodynamic properties were obtained following the canonical formalism⁴² at 298 K. Nonspecific solvent effects were obtained from the United Atoms Hartree–Fock/Polarizable Continuum model (UAHF/PCM).^{43,44} As described by Saracino,⁴⁵ in all UAHF/PCM calculations, the cavity radii were obtained by single point calculations at the HF/6-31G(d,p) level, using the DFT optimized geometries. The solvation free energies were obtained using the Gaussian 98 program suite.⁴⁶

It is worth separating the reaction free energy in aqueous solution as the sum of three parts: electronic plus nuclear repulsion energy (ΔE^{ele}), thermal contribution (ΔG^{T}), and solvation free energy (ΔG^{solv}), as given in eq 1. The thermal contribution is estimated using the ideal gas model, the calculated harmonic vibrational frequencies to estimate the zero point energy correction (ZPE), and the correction due to the thermal population of vibrational levels.

$$\Delta G_{\text{aq}}^{\text{tot}} = \Delta E^{\text{ele}} + \Delta G^{\text{T}} + \Delta G^{\text{solv}} \quad (1)$$

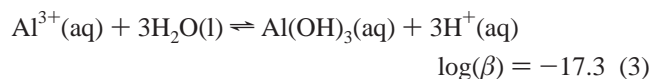
Results and Discussion

The Al^{3+} ion interacts with citric acid (H_3L) to form species 1:1 and 1:2 metal:ligand proportion. The predominant species in acid solution is the 1:1 species as it has been shown by Öhman.¹⁸ The AIL species formation is usually described from the interaction of $\text{Al}^{3+}(\text{aq})$ and citric acid (H_3L) according to eq 2.¹⁸

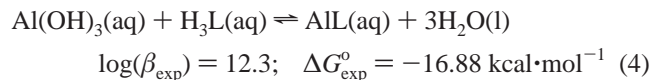


Theoretical estimation of the stability constants of complexes in solution is still a challenging task mostly due to the difficulty in estimating the solvation free energy variation, ΔG^{solv} , term of eq 1. In fact, solvation free energies variation of reactants with neutral charges are better described by the UAHF/PCM approach as it has been shown elsewhere.^{26,27,31} On the other hand, $\text{Al}(\text{OH})_3(\text{aq})$ is

formed according to eq 3.¹⁸



Therefore it is possible to rewrite eq 2 using eq 3 leading to the reaction equation in which all reactants are neutral, as described by eq 4.



This strategy has been shown to be very useful in order to obtain reaction equations that are more adequate to be described by the DFT/PCM approach.^{27,31} Nevertheless, each of the reactants has to be correctly modeled in solution in order to predict the reaction Gibbs free energy of the AlL formation described by eq 4. It is also important to note that the $\Delta G_{\text{exp}}^{\circ}$, shown in eq 4, has larger error bars due to error propagation. Furthermore, stability constants of species that are present only in a small amount—as it is the case of the $\text{Al}(\text{OH})_3$ species—estimated from potentiometric measurements are normally associated with larger error bars.

Al(OH)₃(aq). The $\text{Al}(\text{OH})_3(\text{aq})$ species has a trigonal planar geometry as it is expected. However, in solution, one can argue that the best model for this species could be any one of the $[\text{Al}(\text{OH})_3(\text{H}_2\text{O})]$, $[\text{Al}(\text{OH})_3(\text{H}_2\text{O})_2]$, and $[\text{Al}(\text{OH})_3(\text{H}_2\text{O})_3]$ structures. This is reasonable since in solution water molecules can act as ligands in the first solvation shell. Our results showed no tendency for the water molecule to be at the coordination sphere of the aluminum center in the $\text{Al}(\text{OH})_3$ species. The hexacoordinated species is not a minimum in the potential energy surface, and the water molecules are not bonded to the aluminum. The coordination of one water molecule in $[\text{Al}(\text{OH})_3]$, forming tetrahedral $[\text{Al}(\text{OH})_3(\text{H}_2\text{O})]$, is not favorable by 3 kcal·mol⁻¹. The inclusion of two water molecules, forming $[\text{Al}(\text{OH})_3(\text{H}_2\text{O})_2]$, has a Gibbs free energy of about 12 kcal·mol⁻¹. A detailed observation of estimated Gibbs free energy shows that the electronic energy, ΔE^{ele} , is favorable for $[\text{Al}(\text{OH})_3(\text{H}_2\text{O})]$ formation; however, the thermal, ΔG^{T} , and solvation, ΔG^{solv} , contributions are very positive, making the system nonstable. This is coherent once the water molecules become more labile with the rise in temperature and will not participate as a ligand in the first coordination sphere. Actually, Ikeda et al.⁴⁷ showed from Car–Parrinello molecular dynamics that the trigonal planar $\text{Al}(\text{OH})_3$ is formed in solution.

Recently, Rudolph et al.⁴⁸ measured the Raman spectra of the aqueous Al(III) and compared it with ab initio calculations at the 6-31+G*/MP2 level. They suggested that a complete second shell of solvation with 12 water molecules is necessary in order to reproduce the Raman spectra of Al(III) in solution. One could argue that this approach could also be suitable for the $\text{Al}(\text{OH})_3$ in solution stabilizing water molecules in the first solvation shell. According to Asthagiri et al.,⁴⁹ and we concur, this approach lacks a statistical mechanical foundation. The water molecules in the second solvation shell are normally placed maximizing the hydrogen bonds through full geometry optimization. This invariably leads to artifacts which do not represent the average of the

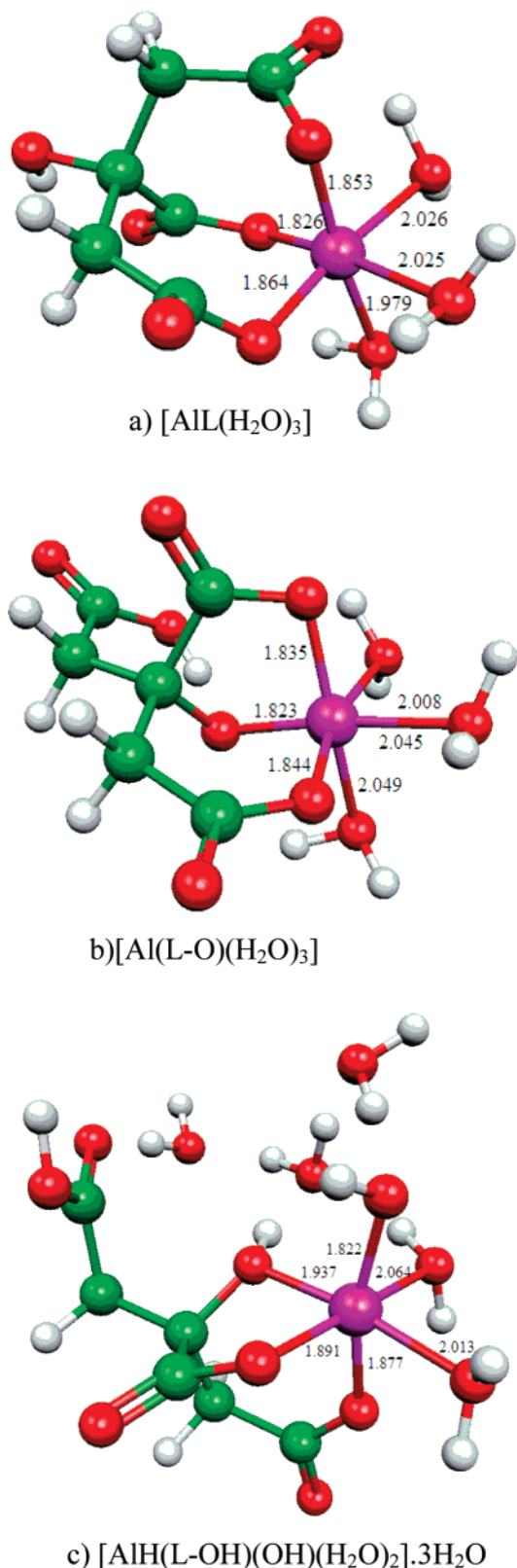


Figure 1. PBE/TZVP optimized geometries representative of the AlL complex. Bond distances are in Å.

configurational space of water molecules located in this second solvation shell.

AlL(aq). Citric acid has 4 possible donors; however, due to the steric hindrance this molecule can only act as a tridentate ligand. In a 1:1 Al: citrate complex, the coordination number of the metal center still remains to be determined.

Table 1. Reaction Free Energies for the Formation of Al(III)/Citrate Species Using Different Levels of Theory^{a,b}

reactions	basis sets	ΔE^{ele}	ΔG^{T^c}	ΔG^{solv}	ΔG^{tot^d}	$\log(\beta)$
Al(OH) ₃ + H ₃ L → [Al(L)(H ₂ O) ₃]	BP86/DZVP	-38.99	18.72	17.97	-2.30	1.7
	BP86/ A-PVTZ	-38.74			-2.05	1.5
	BP86/TZVP	-36.82			-0.13	0.1
	PBE/DZVP	-42.00			-5.31	3.9
	PBE/ A-PVTZ	-41.62			-4.68	3.4
	PBE/TZVP	-39.12			-2.43	1.8
Al(OH) ₃ + H ₃ L → [Al(L-O)(H ₂ O) ₃]	BP86/DZVP	-34.32	18.00	10.86	-5.46	4.0
	BP86/ A-PVTZ	-34.26			-5.40	4.0
	BP86/TZVP	-28.57			0.29	-0.2
	PBE/DZVP	-35.88			-7.02	5.1
	PBE/ A-PVTZ	-37.37			-8.51	6.2
	PBE/TZVP	-34.32			-5.46	4.0
Al(OH) ₃ + H ₃ L + 3H ₂ O ^e → [AlH(L-OH)(OH)(H ₂ O) ₂].3H ₂ O	BP86/DZVP	-55.81	53.80	-3.23	-12.37	9.1
	BP86/ A-PVTZ	-55.08			-11.60	8.5
	BP86/TZVP	-52.10			-8.66	6.4
	PBE/DZVP	-84.35			-33.79	24.7
	PBE/ A-PVTZ	-62.78			-19.34	14.2
	PBE/TZVP	-57.90			-14.46	10.6
experimental					-16.88	12.3

^a All energies are in kcal·mol⁻¹. ^b Medium used in PCM model is water ($\epsilon = 78.4$). ^c Thermal contribution at 298 K including the zero point energy (ZPE). ^d $\Delta G^{\text{tot}} = \Delta E^{\text{ele}} + \Delta G^{\text{T}} + \Delta G^{\text{solv}} - nRT \ln[\text{H}_2\text{O}]$. ^e The presence of water molecules in the reactants are corrected with the expression $-nRT \ln[\text{H}_2\text{O}]$, where n represents the number of water molecules.^{28,52}

The water can act as a ligand to fulfill the available coordination sites of Al³⁺ in the complex. Citric acid can also coordinate the aluminum ion in different ways. The most favorable complexes with 6- and 5-member rings which bind the Al³⁺ through the carboxylic and the hydroxyl groups have been investigated. The 7-member rings formed when the three carboxylic groups are involved in the metal coordination have also been calculated. The available coordination sites of the aluminum center have been fulfilled with water molecules acting as ligands. The tetrahedral and bipyramid structures with one and two water molecules, respectively, are at least 14 kcal·mol⁻¹ higher in energy than the octahedral species.

Figure 1 shows the optimized geometry structures possible to describe the AlL complex in solution. The first structure (Figure 1a) involves the three acidic carboxylic groups forming 7-member rings. Although with the presence of less favorable 7-member rings, it seems reasonable since the carboxylic groups are much more acidic than the tertiary hydroxyl group of the citrate.

The second structure (Figure 1b) is the one normally proposed as the most reasonable since it has 5- and 6-member rings involving the deprotonated hydroxyl group. In order to keep the neutrality, the acidic carboxylic group that is not coordinating the metal center is protonated. This structure has been proposed based on X-ray evidence that 5- and 6-member rings are formed involving the hydroxyl group.¹⁹ Matzapetakis et al. suggested the formula [(NH₄)₅{Al-(C₆H₄O₇)₂}.2H₂O] with the citrate fully deprotonated (i.e., the hydroxyl group is also deprotonated). However, analyzing carefully the preparation and the crystal structure one observes that the formula [(NH₄)₃{Al(C₆H₅O₇)₂}.2NH₄OH] is also consistent, which would have the citrate hydroxyl group protonated. It is important to note that, according to the authors, the pH was adjusted to 8 with NH₄OH(aq) during the preparation. In aqueous solution, it is unlikely that the

citrate tertiary hydroxyl group will be deprotonated under the coordination with Al³⁺ once this group has a pK_a of about 19 (*tert*-butyl alcohol). Furthermore, there is a great deal of evidence that the -OH group can bridge different centers as it is observed in the gibbsite. Recently, the proposed mechanism for As(OH)₃ adsorption on the gibbsite involves the -OH bridging As/Al centers.⁵⁰ Therefore, it is reasonable to propose a structure in which the hydroxyl group remains protonated, and either the free carboxylic group or one of the water molecules bound to Al³⁺ center is deprotonated. A zwitterion is formed, with a positive charge on the Al³⁺ center and a negative charge on the carboxylic group not involved in the Al center coordination. The zwitterion is formed normally in aqueous solution increasing the dipole moment and enhancing the interaction with the polar solvent. Then, the optimization of this structure at the gas phase leads, invariably, to a nonzwitterionic form, i.e., the hydrogen migrates from the hydroxyl group to the carboxylic group. In order to avoid this migration and stabilize the zwitterionic form, three water molecules were placed around the citrate hydroxyl group. The fully optimized structure is shown in Figure 1c. It is interesting to observe that the free carboxylic group turns out to be protonated due to a proton migration from one of the water molecules bound to the Al³⁺ center. This is consistent with the relative pK_a of the different groups involved. The first [Al(H₂O)₆]³⁺ pK_a is about 5.52, and the third citrate pK_a is about 6.40, consequently, the structure shown in Figure 1c is reasonable. However, the structure with the free carboxylic group deprotonated cannot be disregarded. Actually, both can be present in the medium, and they cannot be distinguished through potentiometric measurements.

Gibbs Free Energy Estimate. The estimated Gibbs free energy of the reaction described by eq 4, leading to different structures of the Al³⁺ coordination by citric acid, is shown

in Table 1. The reaction free energy has been separated in each contribution according to eq 1.

The estimate of equilibrium constants of reactions in a condensed medium is a very difficult task. It has been pointed out by De Abreu et al.²⁵ that the DFT calculated thermal contribution is insensitive to the choice of the XC functional and basis sets. They showed that the difference is not larger than 1 kcal·mol⁻¹. Therefore, we decided to calculate this contribution at the level of BP86/DZVP. The UAHF/PCM method has limitations as with any other method based on the continuum models for estimating solvation energy. Specific interaction of the solvent with the solute is not taken into account in this type of model. However, in the literature, there is enough evidence that these specific interactions are canceled when the reaction involves similar reactants and products.^{24,45,51} It has been speculated that a great part of the success of estimating equilibrium constant values is due to a good synergism between the level of theory, basis sets, and the continuum method leading to error compensation.²⁵

According to Table 1, [AlH(L-OH)(OH)(H₂O)₂] is the most favorable species. Other structures investigated are at least 6 kcal·mol⁻¹ higher in energy. The favorable solvation energy observed for the reaction forming [AlH(L-OH)(OH)(H₂O)₂] (Figure 1c) is a consequence of the charge separation in the structure enhancing the solvation. The Gibbs free energy of this reaction (eq 4) is -14.46 kcal·mol⁻¹ at the PBE/TZVP/PCM level of theory, only 2.42 kcal·mol⁻¹ larger than the experimental value. The scheme PBE/TZVP/PCM has been shown to provide pK_a values and hydrolysis constants for Fe³⁺ and Fe²⁺ in good agreement with experimental values.^{28,29} The error bars are about 4 kcal·mol⁻¹ which is reasonable if one takes into account that the ionic strength of the solution is neglected and the error bars of the experimental free energies quoted from experimental equilibrium constants are normally about 1 logarithmic unit, that is, about 1.4 kcal·mol⁻¹. These results support the [AlH(L-OH)(OH)(H₂O)₂] model for the AIL complex in which the hydroxyl group remains protonated, while one water molecule bound to the Al³⁺ center is hydrolyzed. This is in agreement with the relative pK_a of the different groups present in citric acid, the first [Al(H₂O)₆]³⁺ pK_a, and with the perception that 5- and 6-membered rings are more stable.

One could argue that other 1:1 Al/citrate complexes have been observed from potentiometric experiments and that they are derived from this neutral AIL species. Actually, two species are observed: [AlHL]⁺ and [Al(OH)L]⁻.¹⁸ The protonated species probably has its carboxylic group protonated, and only water molecules occupy the available coordination sites of the Al³⁺ center since this species is predominant in a pH less than 3. The [Al(OH)L]⁻ predominates in pH above 4, and, consequently, the citrate free carboxylic group should be deprotonated. This is consistent with the third pK_a of citric acid which is about 6.4. In order to verify if these models are adequate to describe these species in solution, we have estimated the formation constants of these two species using, as a starting point, the neutral [AlH(L-OH)(OH)(H₂O)₂] species. Figure 2 shows the optimized structures of [AlH(L-OH)(H₂O)₃]⁺ and [Al(L-OH)(OH)(H₂O)₂]⁻ species. The Gibbs free energy of the [AlH-

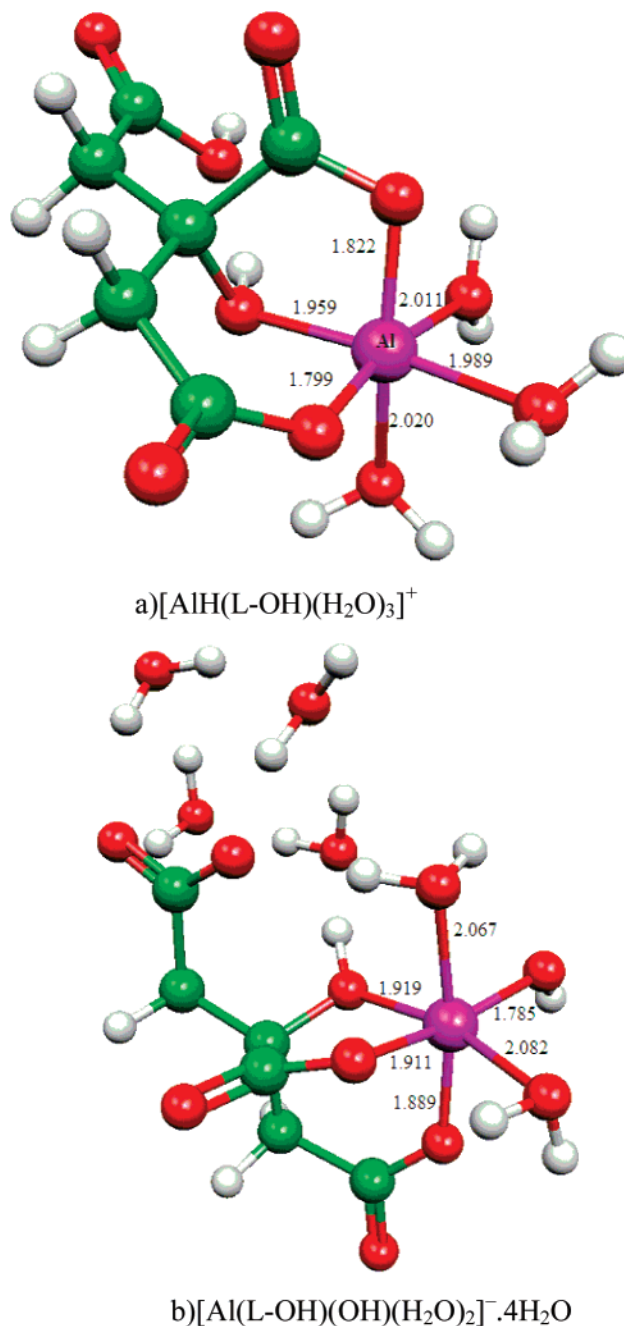


Figure 2. PBE/TZVP optimized structures of the protonated and deprotonated [Al(L-OH)(H₃O)₃]⁺ complex. Bond distances are in Å.

(L-OH)(H₂O)₃]⁺ formation is in very good agreement with the available experimental data, with an error of only 1.1 and 1.6 kcal·mol⁻¹ at the PBE/TZVP/PCM and PB86/TZVP/PCM levels of theory, respectively. The positive charged complexes are usually well described by the continuum model which impact the final results. The [AlH(L-OH)(H₂O)₃]⁺ optimized structure is shown in Figure 2a. The Al-OH₂ bond distances are about 2.0 Å, and the Al-O(carboxyl) is about 1.8 Å. The predicted Al-O(hydroxyl) distance is 1.959 Å which is close to the observed value of 1.937 Å for the [AlH(L-OH)(OH)(H₂O)₂] complex. For the [Al(L-OH)(OH)(H₂O)₂]⁻ species, the Gibbs free energy is about -21.46 and -14.71 kcal·mol⁻¹ at PBE/TZVP/PCM and PB86/TZVP/PCM, respectively. These values must be compared

Table 2. Reaction Free Energies for the Formation of Al(III)/Citrate Charged Species Using Different Levels of Theory^{a,b,e}

reaction	basis set	ΔG^{ele}	ΔG^{Tc}	ΔG^{solv}	$\Delta G^{\text{tot } d}$	$\log(\beta)$
Al(OH) ₃ + H ₃ L + H ₃ O ⁺ → [Al(L-OH)(H ₂ O) ₃] ⁺ + H ₂ O	BP86/DZVP	-85.91	2.26	59.10	-22.17	16.3
	BP86/A-PVTZ	-85.88			-22.14	16.2
	BP86/TZVP	-85.20			-21.46	15.7
	PBE/DZVP	-88.62			-24.88	18.2
	PBE/A-PVTZ	-88.55			-24.81	18.2
	PBE/TZVP	-84.70			-20.96	15.4
experimental					-19.90	14.6
Al(OH) ₃ + H ₃ L + 4H ₂ O → [Al(L-OH)(OH)(H ₂ O) ₂] ⁻ ·3H ₂ O + H ₃ O ⁺	BP86/DZVP	50.61	65.74	-135.32	-21.35	15.7
	BP86/A-PVTZ	47.23			-24.73	18.1
	BP86/TZVP	57.25			-14.71	10.8
	PBE/DZVP	42.80			-29.16	21.4
	PBE/A-PVTZ	38.30			-33.66	24.7
	PBE/TZVP	50.50			-21.46	15.7
experimental					-12.0	8.8

^a All energies are in kcal·mol⁻¹. ^b Medium used in PCM model is water ($\epsilon = 78.4$). ^c Thermal contribution at 298 K, calculated at the BP86/DZVP level. ^d $\Delta G^{\text{tot}} = \Delta E^{\text{ele}} + \Delta G^{\text{T}} + \Delta G^{\text{sol}} - \pm nRT \ln[\text{H}_2\text{O}]$. ^e The presence of water molecules in the reactants or products are corrected with the expression $\pm nRT \ln[\text{H}_2\text{O}]$, where n represents the number of water molecules.^{28,52}

with the experimental estimated value of -12.00 kcal·mol⁻¹. The larger errors (about 9 and 3 kcal·mol⁻¹ for PBE/TZVP/PCM and BP86/TZVP/PCM, respectively) are due to the difficulty in treating negatively charged complexes. The free solvation energy of negative charged systems is difficult to estimate through the PCM model. Furthermore, the electronic energy is more sensitive to basis set quality since more diffuse basis functions are necessary to treat anions adequately. These limitations will impact the total free energy of the reaction. However, it is possible to see from Table 2 that the observed trends are consistent. In general the PBE/TZVP/PCM method provides total free energies in better agreement with available experimental data. The exception is the negatively charged species for which the BP86/TZVP/PCM predicted value is in better agreement with the experimental data. The [Al(L-OH)(OH)(H₂O)₂]⁻ optimized structure is shown in Figure 2b. The Al-O(hydroxyl) distance is about 1.919 Å, and it did not change very much with the deprotonation of the species. The Al-OH₂ bond distances are also about 2.07 Å, as expected. The Al-OH bond distance is about 1.785 Å.

Even though equilibrium constant estimates in aqueous solution are still challenging for theoretical chemistry, insights about the chemical speciation mechanism have been provided for several complexes systems based on DFT calculations and continuum methods with remarkable success.^{22-25,27-29} In the present work, the Gibbs free energies of the Al³⁺ coordination by citric acid forming mononuclear complexes in aqueous solution have been estimated. Conversely to what has been proposed based on the experiments, the present theoretical calculations predict that the citric acid hydroxyl group is not deprotonated even when it is involved in the coordination of the Al³⁺. This is consistent with the relative citric acid pK_a values and the Al³⁺ hydrolysis constant. Other 1:1 Al/citrate complexes with a different degree of protonation have also been calculated, and the reaction free energies have been estimated. The model in which the hydroxyl group remains protonated while involved in the coordination of the metal center leads to a better agreement with the available experimental data.

Final Remarks

The Al³⁺ hydrolysis is already a complex system with many hydroxylated species.⁷ In the presence of citric acid, stable and metastable complexes are formed, and mononuclear complexes at low citrate concentrations are predominant.¹⁸ It has been suggested that the citrate ligand is completely deprotonated including its tertiary hydroxyl group.¹⁹ In our point of view, this is not consistent with acidic properties of this molecule and the Al³⁺ in solution. The hydroxyl group deprotonation is only possible at very high pH or in stringent conditions. However, the hydroxyl group has been unambiguously proven to be involved in the coordination of Al³⁺. Our results indicate the hydroxyl group remains protonated while coordinating the Al³⁺ center. This model is coherent with the potentiometric measurements since the degree of protonation of the species is not changed. In fact, the calculations indicate that the citrate carboxylic group and the H₂O bound to Al³⁺ are more acidic than the citrate -OH group, as it is expected. This might have important consequences in understanding the chemical speciation of the Al³⁺/citrate system at high pH when polynuclear species are present.

Acknowledgment. We would like to thank the following Brazilian Research Agencies for support: Conselho Nacional para o Desenvolvimento Científico e Tecnológico (CNPq), Coordenação de Aperfeiçoamento de Pessoal de Ensino Superior (CAPES), and Fundação de Amparo à Pesquisa do Estado de Minas Gerais (FAPEMIG). The PRONEX-FAPEMIG (EDT 2403/03) is also gratefully acknowledged.

References

- (1) Huh, J. W.; Choi, M. M.; Lee, J. H.; Yang, S. J.; Kim, M. J.; Choi, J.; Lee, K. H.; Lee, J. E.; Cho, S. W. Activation of monoamine oxidase isotypes by prolonged intake of aluminum in rat brain. *J. Inorg. Biochem.* **2005**, *99*, 2088–2091.
- (2) Zhang, F. P.; Ji, M.; Xu, Q.; Yang, L.; Bi, S. P. Linear scan voltammetric indirect determination of Al-III by the catalytic cathodic response of norepinephrine at the hanging mercury drop electrode. *J. Inorg. Biochem.* **2005**, *99*, 1756–1761.

- (3) Esteves, M. A.; Cachudo, A.; Chaves, S.; Santos, M. A. New silica-immobilized hydroxypyrimidinone as sorbent of hard metal ions from aqueous fluids. *J. Inorg. Biochem.* **2005**, *99*, 1762–1768.
- (4) Drabek, O.; Mladkova, L.; Boruvka, L.; Szakova, J.; Nikodem, A.; Nemecek, K. Comparison of water-soluble and exchangeable forms of Al in acid forest soils. *J. Inorg. Biochem.* **2005**, *99*, 1788–1795.
- (5) Boruvka, L.; Mladkova, L.; Drabek, O. Factors controlling spatial distribution of soil acidification and Al forms in forest soils. *J. Inorg. Biochem.* **2005**, *99*, 1796–1806.
- (6) Missel, J. R.; Schetinger, M. R.; Gioda, C. R.; Bohrer, D. N.; Pacholski, I. L.; Zanatta, N.; Martins, M. A.; Bonacorso, H.; Morsch, V. M. Chelating effect of novel pyrimidines in a model of aluminum intoxication. *J. Inorg. Biochem.* **2005**, *99*, 1853–1857.
- (7) Casey, W. H. Large aqueous aluminum hydroxide molecules. *Chem. Rev.* **2006**, *106*, 1–16.
- (8) Pokrovsky, O. S.; Dupre, B.; Schott, J. Fe-Al-organic colloids control of trace elements in peat soil solutions: Results of ultrafiltration and dialysis. *Aquat. Geochem.* **2005**, *11*, 241–278.
- (9) Jelic, R. M.; Joksovic, L. G.; Djurdjevic, P. T. Potentiometric study of the effect of sodium dodecylsulfate and dioxane on the hydrolysis of the aluminum(III) ion. *J. Solution Chem.* **2005**, *34*, 1235–1261.
- (10) Swaddle, T. W.; Rosenqvist, J.; Yu, P.; Bylaska, E.; Phillips, B. L.; Casey, W. H. Kinetic evidence for five-coordination in $\text{AlOH(aq)}(2+)$ ion. *Science* **2005**, *308*, 1450–1453.
- (11) Hiradate, S. Speciation of aluminum in soil environments. *Soil Sci. Plant Nutr.* **2004**, *50*, 303–314.
- (12) Lakatos, A.; Bertani, R.; Kiss, T.; Venzo, A.; Casarin, M.; Benetollo, F.; Ganis, P.; Favretto, D. Al-III ion complexes of saccharic acid and mucic acid: A solution and solid-state study. *Chem.-Eur. J.* **2004**, *10*, 1281–1290.
- (13) Phillips, B. L.; Lee, A.; Casey, W. H. Rates of oxygen exchange between the $\text{Al}_2\text{O}_8\text{Al}_{28}(\text{OH})(56)(\text{H}_2\text{O})(26)(18+)$ (aq) (Al-30) molecule and aqueous solution. *Geochim. Cosmochim. Acta* **2003**, *67*, 2725–2733.
- (14) Silwood, C. J. L.; Grootveld, M. Evaluation of the speciation status of aluminium(III) ions in isolated osteoarthritic knee-joint synovial fluid. *Biochim. Biophys. Acta* **2005**, *1725*, 327–339.
- (15) Kuan, W. H.; Wang, M. K.; Huang, P. M.; Wu, C. W.; Chang, C. M.; Wang, S. L. Effect of citric acid on aluminum hydrolytic speciation. *Water Res.* **2005**, *39*, 3457–3466.
- (16) Driscoll, C. T.; Baker, J. P.; Bisogni, J. J.; Schofield, C. L. Effect Of Aluminum Speciation On Fish In Dilute Acidified Waters. *Nature* **1980**, *284*, 161–164.
- (17) Ohman, L. O.; Sjoberg, S. Equilibrium And Structural Studies Of Silicon(IV) And Aluminum(III) In Aqueous-Solution. 9. A Potentiometric Study Of Mono-Nuclear And Poly-Nuclear Aluminum(III) Citrates. *J. Chem. Soc., Dalton Trans.* **1983**, 2513–2517.
- (18) Ohman, L. O. Equilibrium And Structural Studies Of Silicon(IV) And Aluminum(III) In Aqueous-Solution. 17. Stable And Metastable Complexes In The System $\text{H}^+ - \text{Al}^{3+} - \text{Citric Acid}$. *Inorg. Chem.* **1988**, *27*, 2565–2570.
- (19) Matzapetakis, M.; Raptopoulou, C. P.; Terzis, A.; Lakatos, A.; Kiss, T. Salifoglou, A. Synthesis, structural characterization, and solution behavior of the first mononuclear, aqueous aluminum citrate complex. *Inorg. Chem.* **1999**, *38*, 618–619.
- (20) Lide, D. R. In *Handbook of Chemical and Physics*; CRC Press: New York, 2004; Vol. 1, Chapter 8, pp 8–50.
- (21) Aquino, A. J. A.; Tunega, D.; Haberhauer, G.; Gerzabek, M. H.; Lischka, H. A density-functional investigation of aluminium(III)-citrate complexes. *Phys. Chem. Chem. Phys.* **2001**, *3*, 1979–1985.
- (22) Li, J.; Fisher, C. L.; Chen, J. L.; Bashford, D.; Noodleman, L. Calculation of redox potentials and pK(a) values of hydrated transition metal cations by a combined density functional and continuum dielectric theory. *Inorg. Chem.* **1996**, *35*, 4694–4702.
- (23) Liptak, M. D.; Gross, K. C.; Seybold, P. G.; Feldgus, S.; Shields, G. C. Absolute pK(a) determinations for substituted phenols. *J. Am. Chem. Soc.* **2002**, *124*, 6421–6427.
- (24) Liptak, M. D.; Shields, G. C. Accurate pK(a) calculations for carboxylic acids using Complete Basis Set and Gaussian-n models combined with CPCM continuum solvation methods. *J. Am. Chem. Soc.* **2001**, *123*, 7314–7319.
- (25) De Abreu, H. A.; De Almeida, W. B.; Duarte, H. A. pK(a) calculation of poliprotic acid: histamine. *Chem. Phys. Lett.* **2004**, *383*, 47–52.
- (26) de Noronha, A. L. O.; Duarte, H. A. DFT study of the V(IV)/V(V) oxidation mechanism in the presence of N-hydroxyacetamide. *J. Inorg. Biochem.* **2005**, *99*, 1708–1716.
- (27) Duarte, H. A.; Paniago, E. B.; Carvalho, S.; De Almeida, W. B. Interaction of N-hydroxyacetamide with vanadate: A density functional study. *J. Inorg. Biochem.* **1998**, *72*, 71–77.
- (28) De Abreu, H. A.; Guimaraes, L.; Duarte, H. A. Density-functional theory study of iron(III) hydrolysis in aqueous solution. *J. Phys. Chem. A* **2006**, *110*, 7713–7718.
- (29) Guimaraes, L.; De Abreu, H. A.; Duarte, H. A. Fe(II) hydrolysis in aqueous solution: A DFT Study. *Chem. Phys.* **2007**, *333*, 10–17.
- (30) Kubicki, J. D. Self-consistent reaction field calculations of aqueous Al^{3+} , Fe^{3+} , and Si^{4+} : Calculated aqueous-phase deprotonation energies correlated with experimental $\ln(K_a)$ and pK(a). *J. Phys. Chem. A* **2001**, *105*, 8756–8762.
- (31) Santos, J. M. D.; Carvalho, S.; Panjago, E. B.; Duarte, H. A. Potentiometric, spectrophotometric and density functional study of the interaction of N-hydroxyacetamide with oxovanadium(IV): the influence of ligand to the V(IV)/V(V) oxi-reduction reaction. *J. Inorg. Biochem.* **2003**, *95*, 14–24.
- (32) Koester, A. M.; Flores, R.; Geudtner, G.; Goursot, A.; Heine, T.; Patchkovskii, S.; Reveles, J. U.; Vela, A.; Salahub, D. *Program deMon 2004-Version 1.1.0 exp*; Aug 2004, Ottawa, Canada, 2004.
- (33) Becke, A. D. Completely Numerical-Calculations On Diatomic-Molecules In The Local-Density Approximation. *Phys. Rev. A* **1986**, *33*, 2786–2788.
- (34) Perdew, J. P. Density-Functional Approximation For The Correlation-Energy Of The Inhomogeneous Electron-Gas. *Phys. Rev. B* **1986**, *33*, 8822–8824.

- (35) Perdew, J. P.; Yue, W. Accurate And Simple Density Functional For The Electronic Exchange Energy-Generalized Gradient Approximation. *Phys. Rev. B* **1986**, *33*, 8800–8802.
- (36) Perdew, J. P.; Burke, K.; Ernzerhof, M. Generalized gradient approximation made simple. *Phys. Rev. Lett.* **1996**, *77*, 3865–3868.
- (37) Godbout, N.; Salahub, D. R.; Andzelm, J.; Wimmer, E. Optimization Of Gaussian-Type Basis-Sets For Local Spin-Density Functional Calculations. I. Boron Through Neon, Optimization Technique And Validation. *Can. J. Chem.* **1992**, *70*, 560–571.
- (38) Schafer, A.; Horn, H.; Ahlrichs, R. Fully Optimized Contracted Gaussian-Basis Sets For Atoms Li To Kr. *J. Chem. Phys.* **1992**, *97*, 2571–2577.
- (39) Krack, M.; Koster, A. M. An adaptive numerical integrator for molecular integrals. *J. Chem. Phys.* **1998**, *108*, 3226–3234.
- (40) Koester, A. M.; Flores-Moreno, R.; Reveles, J. U. Efficient and reliable numerical integration of exchange-correlation energies and potentials. *J. Chem. Phys.* **2004**, *121*, 681–690.
- (41) Schlegel, H. B. Optimization of Equilibrium Geometries and Transition Structures. In *Ab Initio Methods in Quantum Chemistry-I: Advances in Chemical Physics*; Lawley, K. P., Ed.; Wiley: New York, 1987; Vol. 67, pp 249–286.
- (42) McQuarrie, D. A. In *Statistical Thermodynamics*; University Science Books: CA, 1973; Vol. 1, Chapter 8, pp 129–141.
- (43) Cossi, M.; Barone, V.; Cammi, R.; Tomasi, J. Ab initio study of solvated molecules: A new implementation of the polarizable continuum model. *Chem. Phys. Lett.* **1996**, *255*, 327–335.
- (44) Tomasi, J.; Persico, M. Molecular-Interactions In Solution-An Overview Of Methods Based On Continuous Distributions Of The Solvent. *Chem. Rev.* **1994**, *94*, 2027–2094.
- (45) Saracino, G. A. A.; Impropa, R.; Barone, V. Absolute pK(a) determination for carboxylic acids using density functional theory and the polarizable continuum model. *Chem. Phys. Lett.* **2003**, *373*, 411–415.
- (46) Frisch, M. J.; Trucks, G. W.; Schlegel, H. B.; Scuseria, G. E.; Robb, M. A.; Cheeseman, J. R.; Zakrzewski, V. G.; Montgomery, J.; Stratmann, R. E.; Burant, J. C.; Dapprich, S.; Millam, J. M.; Daniels, A. D.; Kudin, K. N.; Strain, M. C.; Farkar, O.; Tomasi, J.; Barone, V.; Cossi, M.; Cammi, R.; Mennucci, B.; Pomelli, C.; Adamo, C.; Clifford, S.; Ochterski, J.; Petersson, G. A.; Ayala, P. Y.; Cui, Q.; Morokuma, K.; Malick, D. K.; Rabuck, A. D.; Raghavachari, K.; Foresman, J. B.; Cioslowski, J.; Ortiz, J. V.; Stefanov, B. B.; Liu, G.; Liashenko, A.; Piskorz, P.; Komaromi, I.; Gomperts, R.; Martin, R. L.; Fox, D. J.; Keith, T.; Al-Laham, M. A.; Peng, C. Y.; Nanayakkara, A.; Gonzalez, C.; Challacombe, M.; Gill, P. M. W.; Johnson, B.; Chen, W.; Wong, M. W.; Andres, J. L.; Gonzalez, C.; Head-Gordon, M.; Replogle, E. S.; Pople, J. A. *Gaussian 98, Revision A.6*; Pittsburgh, PA, 1998.
- (47) Ikeda, T.; Hirata, M.; Kimura, T. Hydrolysis of Al³⁺ from constrained molecular dynamics. *J. Chem. Phys.* **2006**, *124*, in press.
- (48) Rudolph, W. W.; Mason, R.; Pye, C. C. Aluminium(III) hydration in aqueous solution. A Raman spectroscopic investigation and an ab initio molecular orbital study of aluminium(III) water clusters. *Phys. Chem. Chem. Phys.* **2000**, *2*, 5030–5040.
- (49) Asthagiri, D.; Pratt, L. R.; Paulaitis, M. E.; Rempe, S. B. Hydration structure and free energy of biomolecularly specific aqueous dications, including Zn²⁺ and first transition row metals. *J. Am. Chem. Soc.* **2004**, *126*, 1285–1289.
- (50) Oliveira, A. F.; Ladeira, A. C. Q.; Ciminelli, V. S. T.; Heine, T.; Duarte, H. A. Structural model of arsenic(III) adsorbed on gibbsite based on DFT calculations. *J. Mol. Struct. (Theochem)* **2006**, *762*, 17–23.
- (51) Toth, A. M.; Liptak, M. D.; Phillips, D. L.; Shields, G. C. Accurate relative pK(a) calculations for carboxylic acids using complete basis set and Gaussian-n models combined with continuum solvation methods. *J. Chem. Phys.* **2001**, *114*, 4595–4606.
- (52) Pliego, J. R. Thermodynamic cycles and the calculation of pK(a). *Chem. Phys. Lett.* **2003**, *367*, 145–149.

CT700016F

Global Potential Energy Surfaces with Correct Permutation Symmetry by Multiconfiguration Molecular Mechanics

Oksana Tishchenko* and Donald G. Truhlar*

Chemistry Department and Supercomputing Institute, University of Minnesota,
Minneapolis, Minnesota 55455-0431

Received October 25, 2006

Abstract: In the framework of the previously developed multiconfiguration molecular mechanics (MCMM) method, we present a new algorithm for constructing global potential energy surfaces that are invariant with respect to the exchange of identical nuclei. We illustrate the new algorithm by its application to the $\text{HOH}'' + \text{H}' \rightarrow \text{OH} + \text{H}'\text{H}''$, $\text{OH}' + \text{HH}''$, $\text{OH}'' + \text{HH}'$, $\text{HOH}' + \text{H}''$, and $\text{H}''\text{OH}' + \text{H}$ reactions. As part of the MCMM methodology, the new scheme can be used to generate multidimensional global PESs for both small and large systems where a few reaction pathways need to be treated as symmetrically equivalent.

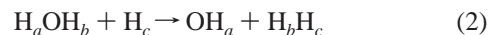
I. Introduction

Multiconfiguration molecular mechanics provides an efficient and systematic scheme for extending molecular mechanics^{1–23} potentials to allow the fitting of potential energy surfaces for reactive systems.^{24–29} This is accomplished by using molecular mechanics to model the diagonal matrix elements³⁰ of the electronic Hamiltonian in a diabatic basis and using electronic structure calculations of the adiabatic electronic ground state to obtain the off-diagonal couplings. In applications so far, we have considered fitting a potential energy surface in a single reaction swath, which consists of those geometries in the valley around a single minimum energy path plus the region on the concave side of that reaction path that is necessary for a semiclassical treatment of large-curvature tunneling.^{31–36} This requires input data only in the reaction swath itself and allows the calculation of accurate rate constants by generalized transition state theory and in particular by variational transition state theory with multidimensional tunneling.^{37–42} To obtain potential energy surfaces more suitable for general dynamics calculations, such as trajectory calculations,^{43–46} one can add additional data far from the minimum-energy reaction paths, for example, by the “Grow” algorithm of Collins.⁴⁷

In some cases, it is desired to model more than one reaction path. Consider for example the reaction



For calculating thermal rate constants by generalized transition state theory, there is no loss of accuracy in labeling the atoms



and treating the path connecting these labeled asymptotes as the only low-energy one because reactive flux via the reaction swath associated with the path leading to $\text{OH}_b + \text{H}_a\text{H}_c$ can be included by a symmetry factor, i.e., by multiplying the rate constant for path (2) by two. However, trajectory calculations, which might be carried out to study high-energy processes or state-selective properties can access geometries where H_a and H_b are equally distant from H_c . The fitted potential energy surface should be invariant to permutations of identical nuclei when geometries connecting specific reaction swaths are energetically accessible. Huang et al.⁴⁸ have recently presented a permutationally invariant fitting basis for enforcing identical particle symmetry in fits of potential energy surfaces. Collins et al.⁴⁷ have used an alternative strategy where all permutationally equivalent geometries are included in the data to be fit. A key element of the present approach is that we use symmetrized diabatic

* Corresponding author e-mail: truhlar@umn.edu (D.G.T.) and oksana@t1.chem.umn.edu (O.T.).

states. This allows us to include the permutation symmetry of selected identical nuclei without increasing the order of the electronic Hamiltonian matrix.

In the present article, we present a general method for enforcing permutation symmetry in MCMM calculations, and we demonstrate it by making a global potential energy surface for the model reaction $\text{H}_2\text{O} + \text{H}$. We illustrate this surface by showing the geometric characteristics of the fit at various molecular geometries. The method is designed for cases where it is sufficient to treat a few exchangeable atoms (typically a few hydrogens) in a symmetrical way and not for treating thousands of hydrogen atoms (e.g., in a protein) symmetrically, which is seldom necessary.

II. Theory

In MCMM, the reactive system is defined using n valence bond (or diabatic) configurations that correspond to reactants, products, and (possibly) stable or metastable intermediates. Each valence bond configuration corresponds to a definite arrangement of bonds. In the present work, we only consider two configurations: $n = 1$, corresponding to the reactant arrangement of bonds, and $n = 2$, corresponding to the product. Near potential energy minima, the diabatic configurations are assumed to be well described by available molecular mechanics potentials $V_{mn}(\mathbf{q})$, where \mathbf{q} denotes a set of redundant or nonredundant internal valence coordinates (bond stretches, bond angle bends, and torsions). At an arbitrary geometry, the potential energy V can be expressed in terms of these V_{mn} by solving the secular equation

$$\begin{vmatrix} V_{11} - V & V_{12} \\ V_{12} & V_{22} - V \end{vmatrix} = 0 \quad (3)$$

where V_{12} is the resonance integral (or diabatic coupling), and V is the lowest eigenvalue of the matrix \mathbf{V} . If analytic gradients and Hessians with respect to nuclear coordinates are available for both V_{nn} and $V_{m'n'}$, then the analytic gradient and Hessian of V are readily available by applying the chain rule to the analytic solution of eq 3.

We consider a reactive system with m identical nuclei (i.e., nuclei with the same atomic number, e.g., hydrogen atoms). First, we define two sets of permutation operators. The first set is the group $\{\mathbf{P}^{(i)} (i = 1, \dots, m!)\}$ of nuclear permutation operators that interchange Cartesian coordinates $\mathbf{x}^{(k)}$ of identical nuclei and generate the permutationally equivalent geometries $\mathbf{x}^{(k,i)}$; this is the symmetric group^{49,50} of degree m and order $m!$ and corresponds to the complete nuclear permutation (CNP) group⁵¹ of a molecule. In the case of a system with three hydrogen atoms such as reaction 1 of H_2O with H , there are $m! = 6$ permutationally equivalent molecular geometries, and the group $\mathbf{P}^{(i)}$ has the following elements: the identity operator, three transposition operators, and two cyclic permutation operators: $\{E, (12), (23), (13), (123), (132)\}$.^{49,51} The second set, $\{\mathbf{P}^{\text{MM}(j)} (j = 1, \dots, m!)\}$, consists of the operators that operate on the molecular mechanics atom types and connectivity patterns at identical nuclei centers while leaving their Cartesian coordinates unchanged. The result of the application of each of the $\mathbf{P}^{\text{MM}(i)}$ to a valence bond structure n in which the atoms are labeled

(e.g., $\text{H}_a\text{OH}_b + \text{H}_c$) is a change in the valence bond connectivity pattern of the nuclei so that $j = 1, \dots, m!$ generates all possible connectivity patterns with the same numbers and kinds of bonds (e.g., $\text{H}_a\text{OH}_c + \text{H}_b$). There is a one-to-one correspondence between the elements of the group $\mathbf{P}^{(i)}$ and applying the elements of the set $\mathbf{P}^{\text{MM}(j)}$, and this correspondence may be used to assign the labels j .

Note that the permutations $\mathbf{P}^{\text{MM}(j)}$ usually change the energy of the system. For example, applying $\mathbf{P}^{\text{MM}(2)}$ to the labeled asymptotic form on the left side of eq 2 results in the same-energy structure ($\text{H}_b\text{OH}_a + \text{H}_c$), whereas applying $\mathbf{P}^{\text{MM}(3)}$ to the same structure yields $\text{H}_a\text{OH}_c + \text{H}_b$ which would generally have higher MM energy unless the OH_b and OH_c distances are the same. Let σ_n , which is called the symmetry factor, be the number of times the lowest-energy MM configuration occurs among the $m!$ symmetrically equivalent MM configurations at a general geometry. Note that there may be high-symmetry geometries where the lowest-energy MM configurations occur more than σ_n times, but σ_n is independent of geometry and corresponds to a general geometry. For example, for studying reaction 1, $n = 1$ is the $\text{H}\cdots\text{H}_2\text{O}$ configuration, and $n = 2$ is the $\text{OH}\cdots\text{H}_2$ configuration, and each has $\sigma_n = 2$, although the lowest-energy configuration occurs 6 times for C_{3v} and D_{3h} geometries.

The requirement that V be invariant with respect to the permutation of identical nuclei suggests that both the diagonal and off-diagonal matrix elements, V_{nn} and $V_{m'n'}$, need to be invariant under such permutations. In MCMM, the diagonal matrix elements are expressed in terms of the predetermined analytical MM functions, and the off-diagonal elements $V_{m'n'}$ are obtained via Shepard interpolation^{47,52–57} using accurate (quantum mechanical (QM)) data at a selected number of molecular geometries. In the interpolation, the data are weighted by a weight function so that data at nearby points are weighted more heavily than those at distant points. The resonance integrals $V_{m'n'}$ depend on both MM and QM energies and derivatives (gradients and Hessians). We will present the algorithm for symmetrizing both V_{nn} and $V_{m'n'}$ in detail below, after a paragraph about the various internal coordinates that are used.

Internal coordinates will appear in the algorithm in three different contexts, and these sets need not necessarily be the same; in fact they ordinarily are not the same. In particular, there are (a) $2m!$ sets of internal coordinates \mathbf{q} used to evaluate MM energies and their derivatives: $m!$ sets for valence bond configuration $n = 1$ and another $m!$ sets for valence bond configuration $n = 2$, (b) a set of internal coordinates \mathbf{r} used in Shepard interpolation, and (c) a set of internal coordinates \mathbf{s} used to calculate the weight function. The number of coordinates in set \mathbf{r} is greater than or equal to $3N_A - 6$, where N_A is the number of atoms in the system, and the number of coordinates in set \mathbf{s} is arbitrary and is called Γ . The compositions of the sets \mathbf{q} are completely determined by the molecular mechanics method (based on the valence bond connectivity patterns), but sets \mathbf{r} and \mathbf{s} are introduced in MCMM. It is worthwhile to explicitly mention that the coordinates \mathbf{q} depend on i . Thus, for example, for $i = 1$ and $n = 2$, we have the $\text{O}-\text{H}_a$ and H_b-H_c bond

distances, and we have O–H_b, O–H_c, H_a–H_b, and H_a–H_c as nonbonded coordinates. In contrast for $i = 2$ we have O–H_b and H_a–H_c as bond distances and O–H_a, O–H_c, H_b–H_a, and H_b–H_c as nonbonded coordinates. This is not reflected in the notation because it would be cumbersome. For symmetrized calculations, both sets (set b called **r** and set c called **s**) should include all permutationally equivalent coordinates that involve the identical nuclei that need to be treated as permutationally equivalent. As described in the original MCMM paper,²⁴ Shepard interpolation is carried out in internal coordinates rather than in Cartesians in order to circumvent the problem of choosing a consistent orientation of Cartesian coordinates at the various interpolation nodes. In the symmetrized application presented below, we use all (six) internuclear distances (and no bond angles or torsions) for this Shepard interpolation step. For evaluating the weight function W , which is explained below, we would in general use the internuclear distances that undergo significant changes during the reaction of interest and, in addition, all permutationally equivalent distances. In the application presented below, we used the set of all internuclear distances for the weights.

The procedure for constructing a PES that is invariant with respect to the exchange of identical nuclei using MCMM involves the following steps:

(i) Read electronic structure information (accurate energies $V^{(k)}$, gradients $\mathbf{G}^{(k)}$, and Hessians $\mathbf{F}^{(k)}$) in Cartesian coordinates for $k = 1, 2, \dots, N$ training geometries $\mathbf{x}^{(k)}$, and for each of these data points generate $m!$ symmetrically equivalent data sets: $\{\mathbf{x}^{(k,i)}, \mathbf{G}^{(k,i)}, \mathbf{F}^{(k,i)}\}$, where

$$\mathbf{x}^{(k,i)} = \mathbf{P}^{(i)} \mathbf{x}^{(k)} \quad (4)$$

$$\mathbf{G}^{(k,i)} \equiv \frac{\partial}{\partial \mathbf{x}} V = \mathbf{P}^{(i)} \mathbf{G}^{(k)} \quad (5)$$

$$\mathbf{F}^{(k,i)} \equiv \frac{\partial^2}{\partial \mathbf{x}^2} V = \mathbf{P}^{(i)} \mathbf{F}^{(k)} \mathbf{P}^{(i)} \quad (6)$$

Notice that $\mathbf{x}^{(k,1)} = \mathbf{x}^{(k)}$, $\mathbf{G}^{(k,1)} = \mathbf{G}^{(k)}$, $\mathbf{F}^{(k,1)} = \mathbf{F}^{(k)}$, and $\mathbf{P}^{(1)}$ corresponds to E , $\mathbf{P}^{(2)}$ corresponds to (12), etc. Notice also that eq 5 corresponds to permuting rows in the gradient vector, and eq 6 corresponds to permuting rows and columns in the Hessian matrix. The potential energy is a scalar and independent of i ; we can call the accurate energy $V^{(k)}$, $V^{(k,1)}$, or $V^{(k,i)}$.

(ii) Define a set of $m!$ MM energies, gradients, and Hessians at point (k) by

$$V_{\text{MM},n}^{(k,j)} \equiv V_{mn}^{(j)}(\mathbf{x}^{(k)}) \quad (7)$$

$$\mathbf{G}_{\text{MM},n}^{(k,j)} \equiv \left. \frac{\partial}{\partial \mathbf{x}} V_{mn}^{(j)} \right|_{\mathbf{x}=\mathbf{x}^{(k)}} \quad (8)$$

and

$$\mathbf{F}_{\text{MM},n}^{(k,j)} \equiv \left. \frac{\partial^2}{\partial \mathbf{x}^2} V_{mn}^{(j)} \right|_{\mathbf{x}=\mathbf{x}^{(k)}} \quad (9)$$

for $n = 1, 2; k = 1, 2, \dots, N; j = 1, 2, \dots, m!$. This set

corresponds to the $m!$ different MM connectivity patterns generated by applying each $\mathbf{P}^{\text{MM}(j)}$ to a valence bond configuration n at each geometry $(\mathbf{x}^{(k,1)})$. The MM energy, gradient, and Hessian on the right sides of eqs 7–9, respectively, are evaluated in the present article using the MM3 force field^{5–7} modified as described in a previous paper,²⁹ although the algorithm is general and can also be applied with other force fields, e.g., with CHARMM.^{18,21} In our work the Cartesian derivatives of eqs 8 and 9 are evaluated from the molecular mechanics force fields by the TINKER program.⁵⁸ (TINKER evaluates the derivatives in the internal coordinate set \mathbf{q} and then transforms them to Cartesian coordinates.)

(iii) Define a symmetrized MM potential and its gradient and Hessian at point k (where a tilde denotes a symmetrization) by

$$\tilde{V}_n^{(k)} = -\Delta \ln \left(\frac{1}{\sigma_n} \sum_j^{m!} e^{-V_{\text{MM},n}^{(k,j)}/\Delta} \right) \quad (10)$$

where Δ is a parameter

$$\tilde{\mathbf{G}}_n^{(k)} \equiv \frac{\partial}{\partial \mathbf{x}} \tilde{V}_n^{(k)} = \frac{\sum_j^{m!} \mathbf{G}_{\text{MM},n}^{(k,j)} e^{-V_{\text{MM},n}^{(k,j)}/\Delta}}{\sum_j^{m!} e^{-V_{\text{MM},n}^{(k,j)}/\Delta}} \quad (11)$$

and

$$\tilde{\mathbf{F}}_n^{(k)} \equiv \frac{\partial^2}{\partial \mathbf{x}^2} \tilde{V}_n^{(k)} = \frac{\sum_j^{m!} (\mathbf{F}_{\text{MM},n}^{(k,j)} - (1/\Delta) \mathbf{G}_{\text{MM},n}^{(k,j)} \mathbf{G}_{\text{MM},n}^{(k,j)\top}) e^{-V_{\text{MM},n}^{(k,j)}/\Delta}}{\sum_j^{m!} e^{-V_{\text{MM},n}^{(k,j)}/\Delta}} + (1/\Delta) \tilde{\mathbf{G}}_n^{(k)} \tilde{\mathbf{G}}_n^{(k)\top} \sum_j^{m!} e^{-V_{\text{MM},n}^{(k,j)}/\Delta} \quad (12)$$

Notice that the symmetrized MM potential is dominated by the σ_n lowest-energy MM configurations among the $m!$ permutations of the labels on the identical atoms. The parameter Δ controls the rate of switching between different dominant configurations in regions that separate the low-energy regions corresponding to the differently permuted coordinates.

We now have the accurate potential, its gradient, and Hessian (eqs 4–6), and the symmetrized MM potential, gradient, and Hessian (eqs 10–12) at each of the N training points. Note that $V^{(k)}$, $\tilde{V}_n^{(k)}$, $\tilde{\mathbf{G}}_n^{(k)}$, and $\tilde{\mathbf{F}}_n^{(k)}$ are independent of i , but $\mathbf{G}^{(k,i)}$ and $\mathbf{F}^{(k,i)}$ depend on i . (Because of the dependence of these quantities on i , the Shepard interpolation must involve $m!N$ terms, rather than N terms, as in the unsymmetrical case.)

(iv) Generate $m!$ values of $\tilde{\mathbf{G}}_n^{(k,i)}$ and $\tilde{\mathbf{F}}_n^{(k,i)}$ from each $\tilde{\mathbf{G}}_n^{(k)}$ and $\tilde{\mathbf{F}}_n^{(k)}$ by applying $\mathbf{P}^{(i)}$, as in step (i).

(v) Then we transform $\mathbf{G}^{(k,i)}$, $\mathbf{F}^{(k,i)}$, $\tilde{\mathbf{G}}_n^{(k,i)}$, and $\tilde{\mathbf{F}}_n^{(k,i)}$ to the set of internal coordinates \mathbf{r} by the Wilson B matrix and C tensor, as described elsewhere.^{24,59,60} This yields

$$\mathbf{g}^{(k,i)} \equiv \frac{\partial}{\partial \mathbf{r}} V \Big|_{\mathbf{r}=\mathbf{r}^{(k,i)}} \quad (13)$$

$$\mathbf{f}^{(k,i)} \equiv \frac{\partial^2}{\partial \mathbf{r}^2} V \Big|_{\mathbf{r}=\mathbf{r}^{(k,i)}} \quad (14)$$

$$\tilde{\mathbf{g}}_n^{(k,i)} \equiv \frac{\partial}{\partial \mathbf{r}} \tilde{V}_n \Big|_{\mathbf{r}=\mathbf{r}^{(k,i)}} \quad (15)$$

$$\tilde{\mathbf{f}}_n^{(k,i)} \equiv \frac{\partial^2}{\partial \mathbf{r}^2} \tilde{V}_n \Big|_{\mathbf{r}=\mathbf{r}^{(k,i)}} \quad (16)$$

Throughout this paper, we will use capital \mathbf{G} and \mathbf{F} to denote the gradients and Hessians with respect to Cartesian coordinates and lower case \mathbf{g} and \mathbf{f} to denote the corresponding derivatives with respect to internal coordinates.

(vi) Next we define two Taylor series for each data point (k,i) by

$$V(\mathbf{r};k) \approx V^{(k,i)} + \mathbf{g}^{(k,i)\top} \Delta \mathbf{r} + \frac{1}{2} \Delta \mathbf{r}^{(k,i)\top} \mathbf{f}^{(k,i)} \Delta \mathbf{r}^{(k,i)} \quad (17)$$

and

$$\tilde{V}_n(\mathbf{r};k) \approx \tilde{V}_n^{(k,i)} + \tilde{\mathbf{g}}_n^{(k,i)\top} \Delta \mathbf{r} + \frac{1}{2} \Delta \mathbf{r}^{(k,i)\top} \tilde{\mathbf{f}}_n^{(k,i)} \Delta \mathbf{r}^{(k,i)} \quad (18)$$

where $V(\mathbf{r};k)$, $\mathbf{g}^{(k,i)}$, $\mathbf{f}^{(k,i)}$, $\tilde{V}_n(\mathbf{r};k)$, $\tilde{\mathbf{g}}_n^{(k,i)}$, and $\tilde{\mathbf{f}}_n^{(k,i)}$ are the QM potential, gradient, and Hessian and the symmetrized MM potential, gradient, and Hessian in the internal coordinates, and

$$\Delta \mathbf{r}^{(k,i)} = \mathbf{r}(\mathbf{x}) - \mathbf{r}(\mathbf{x}^{(k,i)}) \quad (19)$$

where $\mathbf{r}(\mathbf{x}^{(k,i)})$ is the value of \mathbf{r} at point (k,i) . The Taylor series coefficients, denoted as D , \mathbf{b} , and \mathbf{C} , needed for the $m!N$ -term interpolation are then calculated by substituting $V^{(k)}$, $\tilde{V}_n^{(k)}$, $\mathbf{g}^{(k,i)}$, $\mathbf{f}^{(k,i)}$, $\tilde{\mathbf{g}}_n^{(k,i)}$, and $\tilde{\mathbf{f}}_n^{(k,i)}$ (for $n = 1, 2$) into eqs 20–23 of ref 24, with the only difference being that (k) in these equations is now replaced by (k,i) :

$$D^{(k,i)} = (\tilde{V}_1^{(k,i)} - V^{(k,i)})(\tilde{V}_2^{(k,i)} - V^{(k,i)}) \quad (20)$$

$$\mathbf{b}^{(k,i)} = \frac{\tilde{\mathbf{g}}_1^{(k,i)} - \mathbf{g}^{(k,i)}}{\tilde{V}_1^{(k,i)} - V^{(k,i)}} + \frac{\tilde{\mathbf{g}}_2^{(k,i)} - \mathbf{g}^{(k,i)}}{\tilde{V}_2^{(k,i)} - V^{(k,i)}} \quad (21)$$

$$\begin{aligned} \mathbf{C}^{(k,i)} = & (1/D^{(k,i)}) [(\tilde{\mathbf{g}}_1^{(k,i)} - \mathbf{g}^{(k,i)})(\tilde{\mathbf{g}}_2^{(k,i)} - \mathbf{g}^{(k,i)})^\top + \\ & (\tilde{\mathbf{g}}_2^{(k,i)} - \mathbf{g}^{(k,i)})(\tilde{\mathbf{g}}_1^{(k,i)} - \mathbf{g}^{(k,i)})^\top] + \frac{\tilde{\mathbf{f}}_1^{(k,i)} - \mathbf{f}^{(k,i)}}{\tilde{V}_1^{(k,i)} - V^{(k,i)}} + \frac{\tilde{\mathbf{f}}_2^{(k,i)} - \mathbf{f}^{(k,i)}}{\tilde{V}_2^{(k,i)} - V^{(k,i)}} \end{aligned} \quad (22)$$

(vii) Then eq 18 (or equivalently eq 13) of ref 24, with (k,i) replacing (k) gives the Taylor series of $(V_{12})^2$ for each

(k,i) at an arbitrary geometry $\mathbf{r} = \mathbf{r}(\mathbf{x})$ along with its gradient and Hessian in the internal coordinates \mathbf{r} :

$$[V_{12}(\mathbf{r}, k, i)]^2 = D^{(k,i)} \left(1 + \mathbf{b}^{(k,i)\top} \Delta \mathbf{r}^{(k,i)} + \frac{1}{2} \Delta \mathbf{r}^{(k,i)\top} \mathbf{C}^{(k,i)} \Delta \mathbf{r}^{(k,i)} \right) \quad (23)$$

This step uses the Taylor series reversion of Chang and Miller.⁶¹ (Notice that there is a typo in eq 13 of ref 24, namely that all $\Delta \mathbf{q}$ in that equation should have been $\Delta \mathbf{q}^{(k)}$. Furthermore the internal coordinates used in that equation are the set called \mathbf{r} in the present work. Therefore, $\Delta \mathbf{q}^{(k)}$ has now become $\Delta \mathbf{r}^{(k,i)}$.)

This step is carried out as follows: The input geometry in Cartesian coordinates \mathbf{x} is transformed to internal coordinates \mathbf{r} using the full nonlinear expressions that define the internal coordinates in terms of the Cartesians. The internal displacement coordinates are then calculated by eq 19. We then construct Taylor series expansions around each data point (k,i) by combining $\Delta \mathbf{r}^{(k,i)}$ with the constants $D^{(k,i)}$, $\mathbf{b}^{(k,i)}$, and $\mathbf{C}^{(k,i)}$ calculated in step (vi), as in eq 18 of ref 24. Note that substituting eqs 20–23 of ref 24 into eq 18 of ref 24 yields eq 13 of ref 24. Then, as in ref 24 but taking into account all symmetrically equivalent data points, we calculate the generalized distances and weights and carry out Shepard interpolation for V_{12} as in eq 14 of ref 24 but with $m!N$ terms in the sum

$$V_{12}^S(\mathbf{r}) = \sum_{k=1}^N \sum_{i=1}^{m!} W_{ki}(\mathbf{r}) V_{12}^S(\mathbf{r}, k, i) \quad (24)$$

where W_{ki} are normalized weights discussed below (see also Supporting Information), and V_{12}^S is defined by

$$V_{12}^S(\mathbf{r}, k, i) = \sqrt{V_{12}(\mathbf{r}, k, i)^2 u(\mathbf{r}, k, i)} \quad (25)$$

where $V_{12}(\mathbf{r}, k, i)^2$ is given in eq 23, and

$$u(\mathbf{r}, k, i) = \begin{cases} \exp(-\delta/V_{12}(\mathbf{r}, k, i)^2); & V_{12}(\mathbf{r}, k, i)^2 > 0 \\ 0; & \text{otherwise} \end{cases} \quad (26)$$

The derivatives of V_{12}^S of eq 24 are calculated as in eqs 24–29 and 36–41 of ref 24 but summing over k and i , not just k . These derivatives are given in the Supporting Information.

(viii) The derivatives of V_{12}^S are then transformed from the internal coordinates to Cartesian coordinates by using the transformation matrices saved in step (vii), in the same fashion as in the formalism²⁴ for nonsymmetrized potential energy surfaces.

(ix) Define matrix \mathbf{V} at the input geometry \mathbf{x} by

$$\mathbf{V}(\mathbf{x}) = \begin{pmatrix} \tilde{V}_n(\mathbf{x}) & V_{12}^S(\mathbf{x}) \\ V_{12}^S(\mathbf{x}) & \tilde{V}_n(\mathbf{x}) \end{pmatrix} \quad (27)$$

The lowest-energy eigenvalue of this matrix is the MCMM potential energy function. The diagonal matrix elements $\tilde{V}_n(\mathbf{x})$ and their derivatives $\tilde{\mathbf{G}}_n(\mathbf{x})$ and $\tilde{\mathbf{F}}_n(\mathbf{x})$ are obtained as follows: First we define

$$V_{MM,n}^{(j)} \equiv V_{nn}^{(j)}(\mathbf{x}) \quad j = 1, \dots, m! \quad (28)$$

$$\mathbf{G}_{\text{MM},n}^{(j)} \equiv \frac{\partial}{\partial \mathbf{x}} V_{mn}^{(j)} \quad j = 1, \dots, m! \quad (29)$$

and

$$\mathbf{F}_{\text{MM},n}^{(j)} \equiv \frac{\partial^2}{\partial \mathbf{x}^2} V_{mn}^{(j)} \quad j = 1, \dots, m! \quad (30)$$

where, as before, each value of j corresponds to one of the $m!$ connectivity patterns. Then, $\tilde{V}_n(\mathbf{x})$, $\tilde{\mathbf{G}}_n(\mathbf{x})$, and $\tilde{\mathbf{F}}_n(\mathbf{x})$ are calculated as

$$\tilde{V}_n(\mathbf{x}) = -\Delta \ln \left(\frac{1}{\sigma_n} \sum_j^{m!} e^{-V_{\text{MM},n}^{(j)}(\mathbf{x})/\Delta} \right) \quad (31)$$

$$\tilde{\mathbf{G}}_n(\mathbf{x}) = \frac{\sum_j^{m!} \mathbf{G}_{\text{MM},n}^{(j)}(\mathbf{x}) e^{-V_{\text{MM},n}^{(j)}(\mathbf{x})/\Delta}}{\sum_j^{m!} e^{-V_{\text{MM},n}^{(j)}(\mathbf{x})/\Delta}} \quad (32)$$

and

$$\tilde{\mathbf{F}}_n(\mathbf{x}) = \frac{\sum_j^{m!} (\mathbf{F}_{\text{MM},n}^{(j)}(\mathbf{x}) - (1/\Delta) \mathbf{G}_{\text{MM},n}^{(j)}(\mathbf{x}) \mathbf{G}_{\text{MM},n}^{(j)\text{T}}(\mathbf{x})) e^{-V_n^{(j)}(\mathbf{x})/\Delta}}{\sum_j^{m!} e^{-V_{\text{MM},n}^{(j)}(\mathbf{x})/\Delta}} + \frac{(1/\Delta) \tilde{\mathbf{G}}_n \tilde{\mathbf{G}}_n^{\text{T}} \sum_j^{m!} e^{-V_{\text{MM},n}^{(j)}(\mathbf{x})/\Delta}}{\sum_j^{m!} e^{-V_{\text{MM},n}^{(j)}(\mathbf{x})/\Delta}} \quad (33)$$

where $V_{\text{MM},n}^{(j)}(\mathbf{x})$, $\mathbf{G}_{\text{MM},n}^{(j)}(\mathbf{x})$, and $\mathbf{F}_{\text{MM},n}^{(j)}(\mathbf{x})$ are sets of $m!$ MM energies, gradients, and Hessians at the geometry \mathbf{x} .

(x) Find the eigenvalue V of eq 27 and its derivatives in Cartesian coordinates. The lowest eigenvalue of eq 27 is given by

$$V(\mathbf{x}) = \frac{1}{2} (\tilde{V}_1(\mathbf{x}) + \tilde{V}_2(\mathbf{x})) - \frac{(\tilde{V}_1(\mathbf{x}) - \tilde{V}_2(\mathbf{x}))^2 + 4(V_{12}^S(\mathbf{x}))^2}{4}^{1/2} \quad (34)$$

where \tilde{V}_n are the symmetrized uninterpolated MM potentials given by eq 31, and V_{12}^S is the resonance integral obtained via the $m!N$ -term Shepard interpolation, eq 24. The gradient and Hessian components of V with respect to Cartesian coordinates are given by

$$G_i = \frac{\partial V}{\partial x_i} = \frac{1}{2} \left(\tilde{G}_{1i} + \tilde{G}_{2i} - \left(\frac{4V_{12}^S \left(\frac{\partial V_{12}^S}{\partial x_i} \right) + (\tilde{V}_1 - \tilde{V}_2)(\tilde{G}_{1i} - \tilde{G}_{2i})}{((\tilde{V}_1 - \tilde{V}_2)^2 + 4(V_{12}^S)^2)^{1/2}} \right) \right) \quad (35)$$

and

$$F_{ij} = \frac{\partial^2 V}{\partial x_i \partial x_j} = \frac{1}{2} \left(\tilde{F}_{1ij} + \tilde{F}_{2ij} + \frac{(4V_{12}^S (\partial V_{12}^S / \partial x_i) + (\tilde{V}_1 - \tilde{V}_2)(\tilde{G}_{1i} - \tilde{G}_{2i}))}{((\tilde{V}_1 - \tilde{V}_2)^2 + 4(V_{12}^S)^2)^{3/2}} \times \left(4V_{12}^S \left(\frac{\partial V_{12}^S}{\partial x_j} \right) + (\tilde{V}_1 - \tilde{V}_2)(\tilde{G}_{1j} - \tilde{G}_{2j}) \right) - \frac{4 \left(\frac{\partial V_{12}^S}{\partial x_i} \right) \left(\frac{\partial V_{12}^S}{\partial x_j} \right) + (\tilde{G}_{1i} - \tilde{G}_{2i})(\tilde{G}_{1j} - \tilde{G}_{2j})}{((\tilde{V}_1 - \tilde{V}_2)^2 + 4(V_{12}^S)^2)^{1/2}} - \frac{4V_{12}^S \left(\frac{\partial^2 V_{12}^S}{\partial x_i \partial x_j} \right) + (\tilde{V}_1 - \tilde{V}_2)(\tilde{F}_{1ij} - \tilde{F}_{2ij})}{((\tilde{V}_1 - \tilde{V}_2)^2 + 4(V_{12}^S)^2)^{1/2}} \right) \quad (36)$$

Note that steps (i)–(vi) are performed once at the beginning. Then steps (vii)–(x) are carried out every time that the dynamics algorithm needs the energy, gradient, and/or Hessian.

In the present article, the weight function $w(\mathbf{s})$ is evaluated as in eq 34 of ref 24, but taking into account all symmetrically equivalent data points. For doing so, we first transform the Cartesian coordinates of the data points (k, i) and the Cartesian coordinates of a geometry \mathbf{x} (where one needs to evaluate the potential) to the set of the internal coordinates \mathbf{s} . The unnormalized weights are then calculated as

$$w_{ki}(\mathbf{s}) = \frac{1}{d_{ki}(\mathbf{s})^4} \frac{1}{\sum_{k=1}^{(N+2)} \sum_{i=1}^{m!} \frac{1}{d_{ki}(\mathbf{s})^4}} \quad (37)$$

where d_{ki} is the generalized distance between \mathbf{s} and $\mathbf{s}^{(k,i)}$ defined as

$$d_{ki}(\mathbf{s}) = \sqrt{\sum_{\gamma=1}^{\Gamma m!} (s_{\gamma} - s_{\gamma}^{(k,i)})^2} \quad (38)$$

where $\mathbf{s} \equiv \{s_1, s_2, \dots, s_{\gamma}, \dots, s_{\Gamma}\}$. Note that the sum in eq 37 runs over $m!(N+2)$ data points where the $2m!$ extra data points correspond to the permutationally equivalent MM minima for the valence bond configurations $n=1$ and $n=2$. By way of contrast, the sum in eq 24 includes only $Nm!$ terms because we set V_{12} equal to zero at MM minima because we assume that the potential near these points is well described by molecular mechanics. The omission of the extra $2m!$ terms in eq 24 combined with their inclusion in the denominator of eq 37 is equivalent to setting V_{12}^S and its gradient and Hessian equal to zero at the MM minima.

For the present symmetrized application, $\Gamma = 6$ because a four-body system has six internuclear distances. (This value is just accidentally the same as $m!$ in the present case.) In

Table 1. Force Field Parameters for Reaction 1^a

	van der Waals parameters					Morse parameters		
	atomic H	H in H ₂	H in H ₂ O	O in OH	O in H ₂ O	H–H in H ₂	O–H in OH	O–H in H ₂ O
r_m , Å	1.32	1.20	1.32	1.62	1.82			
ϵ , kcal/mol	0.008	0.016	0.008	0.059	0.036			
r_e , Å						0.7414 ^b	0.9707 ^b	0.9470 ^b
f , mdyne/Å						5.75 ^c	6.5	7.45
D_e , kcal/mol						104.2 ^d	120.0 ^e	150.0 ^e

^a The van der Waals energy was calculated using the modified²⁹ Exp-6 potential with the values for A , B , and C as the original MM3⁵ parametrization and the value for D of 0.01 for the symmetrized PES and 0.005 for nonsymmetrized PES. For the bond stretching terms we used the Morse potential. For the angle bending potential in water we used the same functional form and the same parameters as in the original MM3 force field (these parameters are not shown in this table). ^b Reference 62. ^c Reference 63. ^d For the bond stretching term in H₂, D_e was set to be equal to D_{298}^0 of ref 63. ^e For OH stretches, the values used for D_e are larger than the actual equilibrium dissociation energies, which does not cause a problem because in MCM the energy of reaction is evaluated by electronic structure calculations, not by molecular mechanics.

Table 2. Three Geometries Used in Shepard Interpolation^a

structure	$r(\text{OH}_a)$	$r(\text{OH}_b)$	$r(\text{OH}_c)$	$r(\text{H}_b\text{H}_c)$	$\angle\text{H}_a\text{OH}_b$	$\angle\text{H}_a\text{OH}_c$	$\angle\text{H}_b\text{OH}_c$	$\angle\text{H}_c\text{H}_b\text{O}$
SP-I	0.965	1.322		0.824	99.7			164.7
SP-II	1.122	0.992	0.992		102.3	102.3	103.4	
Min-I	1.017	1.017	1.017		102.6	102.6	102.6	

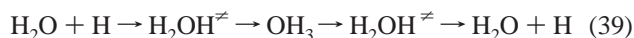
^a Bond distances are in Å and bond angles are in degrees.

most of the previous applications,^{24–29} we used $\Gamma = 3$. The present article also includes, for comparison, some unsymmetrized calculations, and for those calculations we used $\Gamma = 2$.

III. Application and Discussion of Results

The two MM configurations used to represent asymptotic regions are H₂O + H (I) and OH + H₂ (II). The MM parameters^{5,29,62,63} are given in Table 1 (note that there are no standard MM3 parameters for radicals).

For the present application, we used 3 training geometries. In particular, we place QM energies, gradients, and Hessians (a) at geometry of the saddle point, HOHH[‡], of reaction 1 (SP-I), (b) at the saddle point (SP-II, denoted H₂OH[‡] in eq 39) of the exchange reaction,



and (c) at the minimum (Min-I) that corresponds to an ammonia-like radical OH₃. The geometries of these three Shepard points are given in Table 2. We will denote the potential constructed using three QM Hessians as MCM(3). Fifteen other QM Hessians are obtained by symmetry without additional electronic structure calculations and are also used in interpolation. The parameter Δ was set equal to 0.04 E_h ($1 E_h = 1$ hartree).

For the electronic structure calculations we use the hybrid density functional MPWB1K⁶⁴ in conjunction with the 6-31+G(d,p)⁶⁵ basis set; the geometries listed in Table 2 correspond to optimized structures at this level. Even though MPWB1K/6-31+G(d,p) significantly overestimates the barrier height for the exchange reaction (specifically, it gives 29.6 kcal/mol for the zero-point-exclusive barrier of reaction 2 as compared to ~21 kcal/mol for the best estimate⁵⁷), it is sufficient to demonstrate the symmetry properties of the fit. (One should use more sophisticated electronic structure levels to generate QM energies and derivatives when one carries out dynamics calculations.) Geometrically, the intermediate

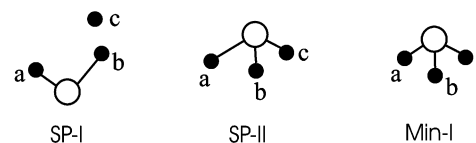


Figure 1. Atom labels for the unique data points (SP-I, SP-II, and Min-I) used in Shepard interpolation.

structure Min-I is rather close to the saddle point for this reaction being separated from the reactant well by a small barrier of 0.7 kcal/mol in MPWB1K/6-31+G(d,p) calculations and 0.3–0.8 kcal/mol in higher-level⁵⁷ calculations. The forward and reverse zero-point-exclusive barriers for the abstraction reaction (1) are 5.0 and 18.6 kcal/mol with MPWB1K/6-31+G(d,p) (cf. the best estimates⁶⁶ of 5.1 kcal/mol and 21.2 kcal/mol, respectively).

Figure 2 shows two-dimensional cuts through the six-dimensional PESs as functions of the two symmetrically equivalent $r(\text{OH})$ distances. The minimum corresponds to the C_{3v} ammonia-like structure OH₃ (Min-I). The top and bottom panels display the symmetrized PES and a nonsymmetrized PES, respectively. The nonsymmetrized PES was calculated with $N = 2$ (QM Hessians are only placed at the saddle point of the O–H_a dissociation channel and at the Min-I geometry) and with $\Gamma = 3$ ($\{\text{O–H}_a; \text{O–H}_b; \text{O–H}_c\}$). This nonsymmetrized surface is called MCM(2). The set of coordinates \mathbf{r} for MCM(2) includes these three coordinates plus the three H–O–H angles. Figure 2 shows that the symmetrized PES has the same shape in the two dissociation valleys, whereas the nonsymmetrized PES does not.

The upper panels of Figure 3 illustrate the symmetrized MCM(3) surface near the saddle point SP-I of the abstraction reaction. These plots are made for the atomic labeling illustrated by the SP-I structure shown in Figure 1 and also for the labeling with H_a and H_b permuted. As one can see from these plots, the interpolated PES is invariant with respect to the exchange of the coordinates of the two

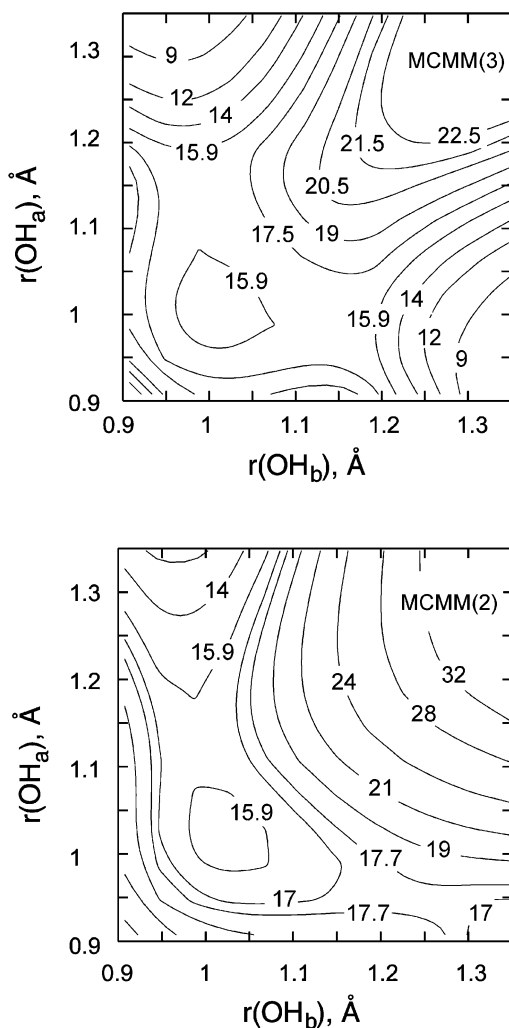


Figure 2. Cuts through interpolated PESs plotted as functions of the OH_a and OH_b distances showing the exchange reaction (eq 39) for the symmetrized PES (top) and nonsymmetrized PES (bottom). All remaining internal coordinates are fixed at their values at the Min-I structure (see Table 2). Contour labels are in kcal/mol. The zero of energy corresponds to the $\text{OH} + \text{H}_2$ asymptote. The symmetrized PES shown in the upper panel is constructed using 3 QM Hessians (MCM(3)) and the unsymmetrized PES shown in the lower panel is constructed using 2 QM Hessians (MCM(2)), as explained in section 3.

hydrogen atoms. This is contrasted with the case of a nonsymmetrized PES that is shown in the lower panels of this figure. This nonsymmetrized PES is constructed from one QM Hessian and is called MCM(1). As in previous MCM applications,^{24–29} the \mathbf{r} coordinates are the natural vibrational coordinates for Shepard interpolation, and the \mathbf{s} coordinates are the set of two distances that undergo significant changes ($\{\text{O}-\text{H}_b, \text{H}_b-\text{H}_c\}$). The lower right panel of Figure 3 shows that the potential is qualitatively incorrect at geometries corresponding to the reaction channel with the interchanged H_a and H_b .

It is essential to note that while the MCM method was originally developed to describe a potential in a localized region of a reaction swath of a particular reaction channel, the new formalism presented above is designed to describe (semi)global PESs that are suitable for study multiple reaction

channels. We used a minimum of three QM Hessians (MCM(3)) for the symmetrized PES and only one or two “reaction-specific” QM Hessians to describe the reaction channel of interest using the nonsymmetrized MCM formalism. The potential shown in the upper panels of Figures 2 and 3 corresponds to a single PES obtained using three QM Hessians, whereas the cuts shown in the lower panels of these figures correspond to the two “different” nonsymmetrized surfaces (one constructed using the QM Hessians at SP-II and Min-I (Figure 1) and the other using the QM Hessian at SP-I (Figure 2)).

IV. Further Discussion and Comments

An accurate PES has been previously developed to describe both the abstraction and exchange reaction channels of reaction 1 by Collins et al.⁵⁶ who pioneered Shepard interpolation as a general scheme to construct (semi)global PESs using a finite number of ab initio energies, gradients, and Hessians.⁴⁷ To generate a PES sufficiently accurate for quantum scattering calculations, these authors used Shepard interpolation of the Taylor expansions of the potential energy at 1000 geometries. Thus that interpolation used 333 times more electronic structure Hessians than the present one. Although the goal of the present work is different, a key point is to note that in the MCM approach, where one interpolates the resonance integral V_{12} and uses previously calibrated MM potentials (along with the user-supplied parameters in reactions where the reactants or products or both are radicals), one generally needs far less electronic structure input data points as compared to the methods where one directly interpolates the potential energy.

Because actual evaluations of the diagonal and off-diagonal elements of the matrix \mathbf{V} and their derivatives are performed in internal rather than in Cartesian coordinates, the MCM PESs are invariant under the operation of inversion,⁵¹ and the symmetrized PES for the $\text{H}_2\text{O} + \text{H}$ system is thus invariant under the operations of the complete nuclear permutation-inversion (CNPI) group.⁵¹ The latter is the direct product of the CNP group and the inversion group and has a very large order when the number of identical atoms in a system is large. In practice, however, one is rarely interested in all possible reactions of the atoms comprising a reactive system, but rather one identifies a few low-energy reaction paths. This implies that only a few identical nuclei in a system need to be treated as symmetrically equivalent, while the other nuclei of the same kind can be considered as distinguishable. (For example, one might treat several protons in the active site of an enzyme symmetrically, but hydrogens far from the reactive site are effectively distinguishable over normal time scales.) The new MCM scheme can therefore be applied to medium and large systems (e.g., using the recently presented²⁸ strategy for evaluation of the resonance integral V_{12} via hybrid QM/MM calculations) just as one would apply the older nonsymmetrized MCM formalism, provided that one uses an appropriate set of internal coordinates for coordinate sets \mathbf{r} and \mathbf{s} (see section III) so that all nuclear centers that need to be considered as indistinguishable are treated symmetrically in Shepard interpolation and in the calculation of the weight function.

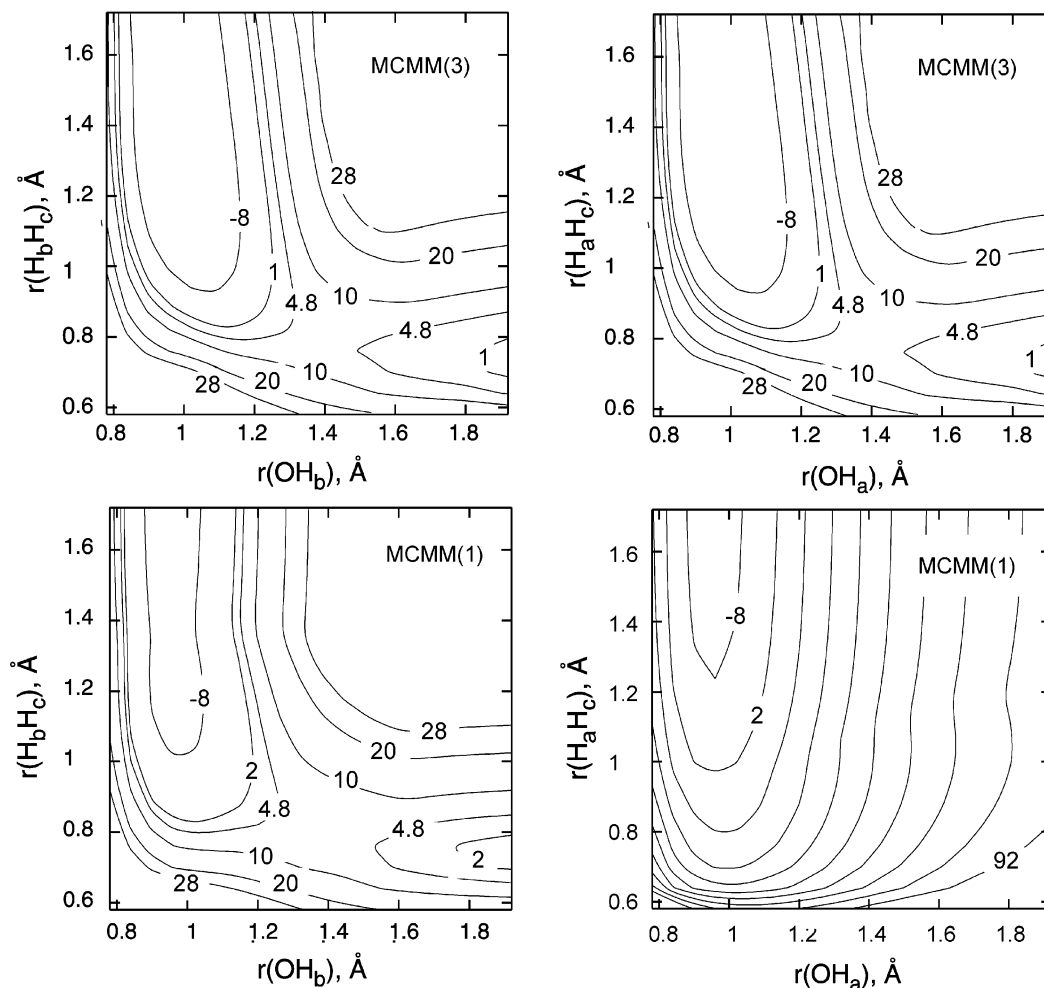


Figure 3. Cuts through interpolated PESs as functions of the OH and HH distances showing the abstraction reaction channel 1: symmetrized PES (upper left and right panels) and nonsymmetrized PES (lower left and right panels). Contour labels are in kcal/mol. Contours on the lower right plot are shown in increment of 10 kcal/mol starting from -8 kcal/mol. The zero of energy corresponds to the $\text{OH} + \text{H}_2$ asymptote. The numbers in parentheses indicate the number of QM Hessians. The cuts shown on the left and right sides of the lower panel correspond to a nonsymmetrized MCMM(1) PES.

While the MM evaluations of the energies and energy derivatives at each geometry are now performed $m!$ times (corresponding to all possible connectivity patterns of the identical nuclei), no extra computational cost is required to generate symmetrically equivalent sets of the gradient vectors and Hessian matrices at Shepard points at the QM level (which is the most computationally demanding part of the MCMM method).

In a broader context, MCMM^{24,25,27–29,67–69} may be considered as a way to extend molecular mechanics to chemical reactions. There are many computational methods in the literature that are designed to do this in one way or another.^{26,61,70–107} Some of these are closely related to MCMM, whereas others are quite different. Furthermore, these methods were introduced to accomplish a variety of different objectives. For example, the empirical valence bond (EVB) method of Warshel and Weiss³⁰ was introduced to transfer potential energy surfaces between environments by adding solvent effects to the diagonal Hamiltonian matrix elements. Either MCMM or EVB can be applied to reactions with more than one reaction pathway by adding additional valence bond structures (e.g., one could use a Hamiltonian

matrix of order seven with three $\text{OH} + \text{H}_2$ structures, three $\text{H}_2\text{O} + \text{H}$ structures, and one OH_3 structure). This has some advantages, but it also has disadvantages, mainly that it leads to a larger matrix to be diagonalized. This in turn means that one must approximate more than one off-diagonal matrix element and that one can no longer take advantage of the simple form of the solution of the 2×2 Hamiltonian used here for obtaining analytic gradients and Hessians.

V. Concluding Remarks

We have presented an algorithm for using multiconfigurational molecular mechanics to fit potential energy surfaces in a way that is manifestly symmetric under the permutation of identical nuclei, while retaining the simple structure of a Hamiltonian matrix of order 2. The algorithm allows us to represent potential energy surfaces in symmetry-equivalent reaction valleys as well as the ridge regions connecting them, and it leads to convenient formulas for analytic gradients and Hessians. The new method was illustrated by an application to the reaction of H_2O with H , for which we obtain a qualitatively correct semiglobal potential energy surface.

Acknowledgment. This work was supported by the United States Department of Energy, Office of Basic Sciences, under grant no. DE-FG02-86ER13579.

Supporting Information Available: Derivatives of V_{12}^S of eq 24 with respect to internal coordinates. This material is available free of charge via the Internet at <http://pubs.acs.org>.

References

- (1) Olson, W. K.; Flory, P. J. *Biopolymers* **1972**, *11*, 25.
- (2) Allinger, N. C. *J. Am. Chem. Soc.* **1977**, *99*, 8127.
- (3) Burkert, U.; Allinger, N. L. *Molecular Mechanics*; American Chemical Society: Washington, 1984.
- (4) van Gunsteren, W. F.; Berendsen, H. J. C.; Geurtsen, R. G.; Zwinderman, H. R. *J. Ann. N. Y. Acad. Sci.* **1986**, *482*, 287.
- (5) Allinger, N. C.; Yuh, Y. H.; Lii, J.-H. *J. Am. Chem. Soc.* **1989**, *111*, 8551.
- (6) Lii, J.-H.; Allinger, N. L. *J. Am. Chem. Soc.* **1989**, *111*, 8566.
- (7) Lii, J.-H.; Allinger, N. L. *J. Am. Chem. Soc.* **1989**, *111*, 8576.
- (8) Cummins, P. L.; Gready, J. E. *Chem. Phys. Lett.* **1990**, *173*, 355.
- (9) Tzuruki, S.; Tanabe, K. *J. Chem. Soc., Perkin Trans. 2* **1991**, 181.
- (10) Casewit, C. J.; Colwell, K. S.; Rappe, A. K. *J. Am. Chem. Soc.* **1992**, *114*, 10035. Casewit, C. J.; Colwell, K. S.; Rappe, A. K. *J. Am. Chem. Soc.* **1992**, *114*, 10046.
- (11) Hagler, A. T.; Ewig, C. S. *Comput. Phys. Commun.* **1994**, *84*, 131.
- (12) Pearlman, D. A.; Case, D. A.; Caldwell, J. W.; Ross, W. S.; Cheatham, T. E., III; DeBolt, S.; Ferguson, D.; Seibel, G.; Kollman, P. *Comput. Phys. Commun.* **1995**, *91*, 1.
- (13) Rappe, A. K.; Colwell, K. S.; Casewit, C. J. *Inorg. Chem.* **1993**, *32*, 3438.
- (14) Cornell, W. D.; Cieplak, P.; Bayly, C. I.; Gould, I. R.; Merz, K. M., Jr.; Ferguson, D. M.; Spellmeyer, D. C.; Fox, T.; Caldwell, J. W.; Kollman, P. A. *J. Am. Chem. Soc.* **1995**, *117*, 5179.
- (15) Norrby, P.-O.; Waernmark, K.; Aekermarck, B.; Moberg, C. *J. Comput. Chem.* **1995**, *16*, 620.
- (16) Jorgensen, W. L.; Maxwell, D. S.; Tirado-Rives, J. *J. Am. Chem. Soc.* **1996**, *118*, 11225.
- (17) Halgren, T. A. *J. Comput. Chem.* **1996**, *17*, 490.
- (18) MacKerell, A. D., Jr.; Bashford, D.; Bellott, M.; Dunbrack, R. L.; Evanseck, J. D.; Field, M. J.; Fischer, S.; Gao, J.; Guo, H.; Ha, S.; Joseph-McCarthy, D.; Kuchnir, L.; Kuczera, K.; Lau, F. T. K.; Mattos, C.; Michnick, S.; Ngo, T.; Nguyen, D. T.; Prodhom, B.; Reiher, W. E., III; Roux, B.; Schlenkrich, M.; Smith, J. C.; Stote, R.; Straub, J.; Watanabe, M.; Wiorkiewicz-Kuczera, J.; Yin, D.; Karplus, M. *J. Phys. Chem. B* **1998**, *102*, 3586.
- (19) Ponder, J. W.; Case, D. A. *Adv. Protein Chem.* **2003**, *66*, 27.
- (20) Patel, S.; Brooks, C. L., III *Mol. Simul.* **2006**, *32*, 231.
- (21) MacKerell, A. D., Jr. *J. Comput. Chem.* **2004**, *25*, 1584.
- (22) Jorgensen, W. L.; Tirado-Rives, J. *Proc. Natl. Acad. Sci. U.S.A.* **2005**, *102*, 6665.
- (23) Marques, H. M.; Cukrowski, I. *Phys. Chem. Chem. Phys.* **2003**, *5*, 5499.
- (24) Kim, Y.; Corchado, J. C.; Villa, J.; Xing, X.; Truhlar, D. G. *J. Chem. Phys.* **2000**, *112*, 2718.
- (25) Albu, T. V.; Corchado, J. C.; Truhlar, D. G. *J. Phys. Chem. A* **2001**, *105*, 8465.
- (26) Truhlar, D. G. *J. Phys. Chem. A* **2002**, *106*, 5048.
- (27) Lin, H.; Pu, J.; Albu, T. V.; Truhlar, D. G. *J. Phys. Chem. A* **2004**, *108*, 4112.
- (28) Lin, H.; Zhao, Y.; Tishchenko, O.; Truhlar, D. G. *J. Chem. Theor. Comput.* **2006**, *2*, 1237.
- (29) Tishchenko, O.; Truhlar, D. G. *J. Phys. Chem. A* **2006**, *110*, 13530.
- (30) Warshel, A.; Weiss, R. M. *J. Am. Chem. Soc.* **1980**, *102*, 6218.
- (31) Garrett, B. C.; Truhlar, D. G.; Wagner, A. F.; Dunning, T. H., Jr. *J. Chem. Phys.* **1983**, *78*, 4400.
- (32) Bondi, D. K.; Connor, J. N. L.; Garrett, B. C.; Truhlar, D. G. *J. Chem. Phys.* **1983**, *78*, 5981.
- (33) Garrett, B. C.; Abusalbi, N.; Kouri, D. J.; Truhlar, D. G. *J. Chem. Phys.* **1985**, *83*, 2252.
- (34) Truhlar, D. G.; Brown, F. B.; Steckler, R.; Isaacson, A. D. In *The Theory of Chemical Reaction Dynamics*; Clary, D. C., Ed.; NATO ASI Series C170; D. Reidel: Dordrecht, The Netherlands, 1986; p 285.
- (35) Truhlar, D. G.; Gordon, M. S. *Science* **1990**, *249*, 491.
- (36) Fernandez-Ramos, A.; Truhlar, D. G. *J. Chem. Phys.* **2001**, *114*, 1491.
- (37) Truhlar, D. G.; Garrett, B. C. *Acc. Chem. Res.* **1980**, *440*, 13.
- (38) Truhlar, D. G.; Isaacson, A. D.; Skodje, R. T.; Garrett, B. C. *J. Phys. Chem.* **1982**, *86*, 2252; **1983**, *87*, 4554(E).
- (39) Pechukas, P. *Ber. Bunsenges. Physik. Chem.* **1982**, *86*, 372.
- (40) Truhlar, D. G.; Isaacson, A. D.; Garrett, B. C. In *Theory of Chemical Reaction Dynamics*; Baer, M., Ed.; CRC Press: Boca Raton, FL, 1985; Vol. 4, p 65.
- (41) Allison, T. C.; Truhlar, D. G. In *Modern Methods for Multidimensional Dynamics Computations in Chemistry*; Thompson, D. L., Ed.; World Scientific: Singapore, 1998; p 618.
- (42) Garrett, B. C.; Truhlar, D. G. In *Theory and Applications of Computational Chemistry: The First Forty Years*; Dykstra, C. E., Frenking, G., Kim, K., Scuseria, G., Eds.; Elsevier: Amsterdam, 2005; p 67.
- (43) Truhlar, D. G.; Muckerman, J. T. In *Atom-Molecule Collision Theory: A Guide for the Experimentalist*; Bernstein, R. B., Ed.; Plenum Press: New York, 1979; p 505.
- (44) Raff, L. M.; Thompson, D. L. In *Theory of Chemical Reaction Dynamics*; Baer, M., Ed.; CRC Press: Boca Raton, FL, 1985; Vol. 3, p 1.
- (45) Mayne, H. R. In *Dynamics of Molecules and Chemical Reactions*; Wyatt, R. E., Zhang, J. Z. H., Eds.; Marcel Dekker: New York, 1996; p 589.
- (46) Schatz, G. C.; Horst, M. T.; Takayanagi, T. In *Modern Methods for Multidimensional Dynamics Calculations in Chemistry*; Thompson, D. C., Ed.; World Scientific: Singapore, 1998; p 1. Tully, J. C. In *Modern Methods for Multidimensional Dynamics Calculations in Chemistry*;

- Thompson, D. C., Ed.; World Scientific: Singapore, 1998; p 34. Stanton, R. V.; Miller, J. L.; Kollman, P. A. In *Modern Methods for Multidimensional Dynamics Calculations in Chemistry*; Thompson, D. C., Ed.; World Scientific: Singapore, 1998; p 355. Jumpter, B. G.; Tuzon, R. E.; Noid, D. W. In *Modern Methods for Multidimensional Dynamics Calculations in Chemistry*; Thompson, D. C., Ed.; World Scientific: Singapore, 1998; p 401.
- (47) Collins, M. A. *Theor. Chem. Acc.* **2002**, *108*, 313.
- (48) Huang, X.; Braams, B.; Bowman, J. M. *J. Chem. Phys.* **2005**, *122*, 44308.
- (49) Rutherford, D. E. *Substitutional Analysis*; Edinburgh University Press: London, 1948.
- (50) Hamermesh, M. *Group Theory*; Addison-Wesley: Reading, MA, 1962; pp 8ff.
- (51) Bunker, P. R.; Jensen, P. *Molecular Symmetry and Spectroscopy*; NRC Research Press: Ottawa, 1998.
- (52) Ischtwan, J.; Collins, M. A.; Watanabe, N.; Hirao, K. *J. Chem. Phys.* **1994**, *100*, 8080.
- (53) Nguyen, K. A.; Rossi, I.; Truhlar, D. G. *J. Phys. Chem.* **1995**, *103*, 5522.
- (54) Bettens, R. P. A.; Collins, M. A. *J. Chem. Phys.* **1999**, *111*, 816.
- (55) Taketsugu, T.; Watanabe, N.; Hirao, K. *J. Chem. Phys.* **1999**, *111*, 3410.
- (56) Zhang, D. Z.; Collins, M. A.; Lee, Soo-Y. *Science* **2000**, *290*, 961.
- (57) Yang, M.; Zhang, D. H.; Collins, M. A.; Lee, S.-Y. *J. Chem. Phys.* **2001**, *115*, 174.
- (58) Ponder, J. W. *TINKER-Version 4.2*; Washington University: St. Louis, MO, 2004.
- (59) Jackels, C. F.; Gu, Z.; Truhlar, D. G. *J. Chem. Phys.* **1995**, *102*, 3188.
- (60) Chuang, Y. Y.; Truhlar, D. G. *J. Phys. Chem A* **1998**, *102*, 242.
- (61) Chang, Y. T.; Miller, W. H. *J. Phys. Chem.* **1990**, *94*, 5884.
- (62) Herzberg, G. *Molecular Spectra and Molecular Structure. I. Spectra of Diatomic Molecules*; Van Nostrand Reinhold Company: New York, 1950.
- (63) *Handbook of Chemistry and Physics*, 87th ed.; Lide, D. R., Ed.; CRC Press: New York, 2006; pp 9–84.
- (64) Zhao, Y.; Truhlar, D. G. *J. Phys. Chem. A* **2004**, *108*, 6908.
- (65) Hehre, W. J.; Radom, L.; Schleyer, P. v. R.; Pople, J. A. *Ab Initio Molecular Orbital Theory*; Wiley: New York, 1986.
- (66) Zhao, Y.; Lynch, B. J.; Truhlar, D. G. *J. Phys. Chem A* **2004**, *108*, 2715.
- (67) Kim, K. H.; Kim, Y. *Bull. Korean Chem. Soc.* **2003**, *24*, 763.
- (68) Kim, K. H.; Kim, Y. *J. Chem. Phys.* **2004**, *120*, 623.
- (69) Kim, K. H.; Kim, Y. *J. Phys. Chem. A* **2006**, *110*, 600.
- (70) Johnston, H. S.; Goldfinger, P. *J. Chem. Phys.* **1962**, *37*, 700.
- (71) Johnston, H. S.; Parr, C. A. *J. Am. Chem. Soc.* **1963**, *85*, 2544.
- (72) Raff, L. M. *J. Chem. Phys.* **1964**, *60*, 2220.
- (73) Burton, G. W.; Sims, L. B.; Wilson, J. C.; Fry, A. *J. Am. Chem. Soc.* **1977**, *99*, 3371.
- (74) Joseph, T.; Steckler, R.; Truhlar, D. G. *J. Chem. Phys.* **1987**, *87*, 7036.
- (75) Hwang, J.-K.; King, G.; Creighton, S.; Warshel, A. *J. Am. Chem. Soc.* **1988**, *110*, 5297.
- (76) Chang, Y. T.; Minichino, C.; Miller, W. H. *J. Chem. Phys.* **1992**, *96*, 4341.
- (77) Bernardi, F.; Olivucci, M.; Robb, M. A. *J. Am. Chem. Soc.* **1992**, *114*, 1606.
- (78) Warshel, A.; Åqvist, J. *J. Chem. Rev.* **1993**, *93*, 2523.
- (79) Grochowski, P.; Lesyng, B.; Bala, P.; McCammon, J. A. *Int. J. Quantum Chem.* **1996**, *60*, 1143.
- (80) Field, M. J. In *Computational Approaches to Biochemical Reactivity*; Náray-Szabó, G., Warshel, A., Eds.; Understanding Chemical Reactivity; Kluwer: Dordrecht, 1997; p 125.
- (81) Åqvist, J. In *Computational Approaches to Biochemical Reactivity*; Náray-Szabó, G., Warshel, A., Eds.; Understanding Chemical Reactivity; Kluwer: Dordrecht, 1997; p 341.
- (82) Rappe, A. K.; Pietsch, M. A.; Wisner, D. C.; Hart, J. R.; Bormann, L. M.; Skiff, W. M. *Mol. Eng.* **1997**, *7*, 385.
- (83) Bentzien, J.; Muller, R. P.; Florian, J.; Warshel, A. *J. Phys. Chem. B* **1998**, *102*, 2293.
- (84) Schmitt, U. W.; Voth, G. A. *J. Phys. Chem. B* **1998**, *102*, 5547.
- (85) Vuilleumier, R.; Borgis, D. *Chem. Phys. Lett.* **1998**, *284*, 71.
- (86) Brenner, D. W. *Phys. Status Solidi B* **2000**, *217*, 23.
- (87) Mo, Y.; Gao, J. *J. Comput. Chem.* **2000**, *21*, 1458.
- (88) Espinosa-Garcia, J. *J. Phys. Chem. A* **2001**, *105*, 8748.
- (89) van Duin, A. C. T.; Dasgupta, S.; Lorant, F.; Goddard, W. A., III *J. Phys. Chem. A* **2001**, *105*, 9396.
- (90) Warshel, A.; Parson, W. W. *Quart. Rev. Biophys.* **2001**, *34*, 563.
- (91) Brewer, M. L.; Schmitt, U. W.; Voth, G. A. *Biophys. J.* **2001**, *80*, 1691.
- (92) Hammes-Schiffer, S.; Billeter, S. R. *Int. Rev. Phys. Chem.* **2001**, *20*, 591.
- (93) Brenner, D. W.; Shenderova, O. A.; Harrison, J. A.; Stuart, S. J.; Ni, B.; Sinnott, S. B. *J. Phys.: Condens. Matter* **2002**, *14*, 783.
- (94) Ginalski, P.; Grochowski, P.; Lesyng, B.; Shugar, D. *Int. J. Quantum. Chem.* **2002**, *90*, 1129.
- (95) Olsen, P. T.; Jensen, F. *J. Chem. Phys.* **2002**, *118*, 3523.
- (96) Jensen, F.; Norrby, P.-O. *Theor. Chem. Acc.* **2003**, *109*, 1.
- (97) Bochenkova, A. K.; Suhm, M. A.; Granovsky, A. A.; Nemukhin, A. V. *J. Chem. Phys.* **2004**, *120*, 3732.
- (98) Nielson, K. D.; Van Duin, A. C. T.; Oxgaard, J.; Deng, W.-Q.; Goddard, W. A., III *J. Phys. Chem. A* **2005**, *109*, 493.
- (99) Bochenkova, A. K.; Firsov, D. A.; Nemukhin, A. V. *Chem. Phys. Lett.* **2005**, *405*, 165.
- (100) Brancato, G.; Tuckerman, M. E. *J. Chem. Phys.* **2005**, *122*, 224507.
- (101) Shurki, A.; Crown, H. A. *J. Phys. Chem. B* **2005**, *109*, 23638.
- (102) Voth, G. *Acc. Chem. Res.* **2006**, *39*, 143.

- (103) Shurki, A. *Theor. Chem. Acc.* **2006**, *116*, 253.
(104) Chakraborty, A.; Zhao, Y.; Lin, H.; Truhlar, D. G. *J. Chem. Phys.* **2006**, *124*, 44315.
(105) Schlegel, H. B.; Sonnenberg, J. L. *J. Chem. Theory Comput.* **2006**, *2*, 905.

- (106) Truhlar, D. G. *J. Comput. Chem.* **2007**, *28*, 73.
(107) Lin, H.; Truhlar, D. G. *Theor. Chem. Acc.* **2007**, *117*, 185.

CT600315H

An Integrated Path Integral and Free-Energy Perturbation–Umbrella Sampling Method for Computing Kinetic Isotope Effects of Chemical Reactions in Solution and in Enzymes

Dan Thomas Major[†] and Jiali Gao^{*,†,‡}

Department of Chemistry and Supercomputing Institute, Digital Technology Center, University of Minnesota, Minneapolis, Minnesota 55455, and Centro Nacional de Supercomputación, Programa Biología Computacional, C/ Jordi Girona 29, 08034 Barcelona, Spain

Received December 19, 2006

Abstract: An integrated centroid path integral and free-energy perturbation–umbrella sampling (PI-FEP/UM) method for computing kinetic isotope effects (KIEs) for chemical reactions in solution and in enzymes is presented. The method is based on the bisection sampling in centroid path integral simulations to include nuclear quantum effects to the classical potential of mean force. The required accuracy for computing kinetic isotope effects is achieved by coupled free-energy perturbation and umbrella sampling for reactions involving different isotopes. The use of FEP with respect to different masses results in relatively small statistical uncertainties, whereas if KIEs are computed directly by the difference in free energies obtained from the quantum mechanical potentials of mean force for different isotopes, the statistical errors are significantly greater. The PI-FEP/UM method is illustrated in two applications. The first reaction is the decarboxylation of N-methyl picolinate in water, for which the primary ¹³C and secondary ¹⁵N KIEs have been determined. The second reaction is the proton-transfer reaction between nitroethane and an acetate ion in water. In both cases, the computational results are in accord with experimental data, and the findings provide further insight into the mechanism of these reactions in water.

1. Introduction

Proton and hydride transfer reactions are ubiquitous in chemical and biological processes. Because of their relatively small mass, zero-point energy and tunneling contributions are significant in determining free-energy barriers.¹ Consequently, it is necessary to include nuclear quantum mechanical effects in computation of the rate constant.^{2,3} The incorporation of nuclear quantum effects is also important in reactions involving heavy atom transfers since one of the most direct, experimental assessments of the transition state of a chemical reaction is through measurements of kinetic

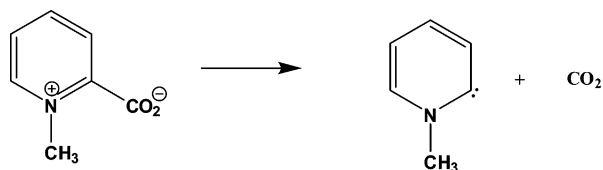
isotope effects (KIEs),⁴ which are of quantum mechanical origin. This, however, is a great challenge to computation because the measured heavy atom KIEs are typically less than a few percent, which requires an accuracy of a fraction of 0.1 kcal/mol in the computed free-energy difference between isotope substitutions. The difficult task is further exacerbated by the need to sample configurational space of the macromolecular system to achieve statistical convergence.^{5,6} Thus, it is highly desirable to develop accurate and practical methods for estimating kinetic isotope effects for chemical reactions in solution and in biological environments.⁷ In this paper, we describe an integrated path integral and free-energy perturbation/umbrella sampling (PI-FEP/UM) approach in molecular dynamics simulations using a combined quantum mechanical and molecular mechanical

* Corresponding author e-mail: gao@chem.umn.edu.

[†] University of Minnesota.

[‡] Centro Nacional de Supercomputación.

Scheme 1

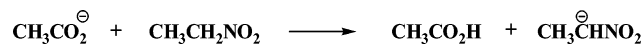


(QM/MM) potential for determining KIEs. In the integrated PI-FEP/UM method coupled with QM/MM potentials, both electronic and nuclear degrees of freedom in the reactive region are treated explicitly by quantum mechanical methods.

Of course, a variety of methods have been developed to treat nuclear quantum effects for gas-phase reactions.⁸ In principle, these techniques can be directly extended to condensed-phase systems; however, the size and complexity of these systems unfortunately make it intractable computationally. Thus, a main goal is to develop new methods, or to extend gas-phase techniques to condensed phases or biomolecular systems. One method that has been successfully introduced to computational enzymology is the ensemble-averaged variational transition-state theory with QM/MM sampling (EA-VTST-QM/MM), which has been applied to a number of enzyme systems.^{2,3,9–13} Both primary and secondary KIEs can be computed using the EA-VTST-QM/MM method, and the method includes contributions of multidimensional tunneling. In another work, a grid-based hybrid approach was used to model quantum effects in hydrogen transfer reactions by numerically solving the vibrational wavefunction of the transferring hydrogen nucleus.^{14,15} The method yielded good results for primary KIEs in several hydride transfer reactions,¹⁶ although the authors noted that a major limitation is its complexity, preventing it from extending to quantizing more than one particle.¹⁷

The third technique, which was among the first applications to incorporate nuclear quantum effects in enzyme reactions, is the quantized classical path (QCP) method developed by Hwang et al.^{18–20} The discrete Feynman path integral method²¹ has been used in a variety of applications since it offers an efficient and general approach for treating nuclear quantum effects in condensed-phase simulations.^{20,22–36} Here, we focus on applications to biomolecular systems. The centroid path integral molecular dynamics method provides a procedure that can be used to directly estimate the quantum mechanical activation free energy.^{28,37} However, these methods are computationally expensive for modeling large systems such as enzymes, especially if combined QM/MM potentials are used to represent the potential surface. The QCP method is also based on centroid path integral sampling, but it is formulated as a correction to the classical potential of mean force (PMF).^{18,19,23} Thus, the classical simulations and quantum corrections are fully separated, making it particularly attractive and efficient for modeling enzymatic reactions. Unfortunately, the QCP method has not been widely used, and it is very difficult to obtain converged results using “standard” sampling schemes. Recently, we developed a practical procedure, called BQCP,^{5,6} by extending the bisection sampling method developed by Ceperley

Scheme 2



and Pollock³⁸ for free-particle sampling to centroid path integral simulations. This has enabled us to obtain converged results through a series of validation studies.^{5,6} The remarkable free-particle sampling efficiency of the bisection scheme in centroid path integral simulations stems from the fact that every “Monte Carlo” move is accepted and is independent of the previous beads’ distribution, and it has been thoroughly discussed by Ceperley.³⁹ The BQCP method^{5,6} has been applied to a number of proton and hydride transfer reactions in solution and in enzymes.^{6,34–36} The computed KIEs are in good accord with experiments and with results from the previous EA-VTST-QM/MM method. The BQCP method has now been adopted in another QCP application.¹⁷

Although the methods discussed above are based on very different theories, a common strategy is to estimate approximately the quantum mechanical rate constant by introducing a quantum correction factor to bridge the classical transition state theory. We define

$$k \equiv k_{\text{qm}} = \gamma k_{\text{TST}} \quad (1)$$

where k_{TST} is the transition-state theory rate constant and γ is the generalized transmission coefficient,² which includes the classical dynamic recrossing factor, Γ , and the quantum correction factor κ , which is defined as follows:

$$\kappa = \frac{k_{\text{qm}}}{k_{\text{TST}}} = e^{-\beta(\Delta F_{\text{qm}}^{\ddagger} - \Delta F_{\text{TST}}^{\ddagger})} \quad (2)$$

In eq 2, $\beta = 1/k_{\text{B}}T$ with k_{B} being Boltzmann’s constant and T the temperature, and $\Delta F_{\text{qm}}^{\ddagger}$ and $\Delta F_{\text{TST}}^{\ddagger}$ are, respectively, the quantum and classical free energy of activation. Here, we have implicitly assumed that the classical and quantum Γ factors are identical. The different methods applied to enzymatic reactions to incorporate nuclear quantum effects differ in the specific approximations to estimate the free-energy difference in eq 2.

In this article, we develop an efficient sampling strategy for accurate computation of KIEs for chemical reactions in solutions and in enzymes. The method and computational details are illustrated by two systems, while the computational study also provides insights into the interpretation of the observed KIEs. The first reaction is the decarboxylation of N-methyl picolinate in water, a model for the reaction catalyzed by orotidine 5′-monophosphate decarboxylase (Scheme 1). The second is the deprotonation of nitroethane by an acetate ion, a model for the nitroalkane oxidase reaction in the first step in the oxidation of nitroalkanes to aldehydes and ketones (Scheme 2). In the former reaction, heavy-atom primary ¹³C and secondary ¹⁵N KIEs are computed, while for the latter, ²H KIE is determined.

2. Theory and Method

2.1. Centroid Path Integral Method.

In the discrete path integral method, each quantized nucleus is represented by a ring of P quasi-particles called beads, whose coordinates are

denoted as $\mathbf{r} = \{\mathbf{r}_i; i = 1, \dots, P\}$.²¹ The discrete paths are circular with $\mathbf{r}_{P+1} = \mathbf{r}_1$. For convenience, we limit the discussion to a single quantized atom embedded in a classical solvent while extension to many-quantized particles is obvious. Each bead is connected to its two neighbors via harmonic springs and is subjected to a fraction, $1/P$, of the full classical potential, $U(\mathbf{r}_i, \mathbf{S})$, where \mathbf{S} represents all classical solvent coordinates. In the centroid path integral, the centroid position, $\bar{\mathbf{r}}$, is used as the principle variable, and the canonical QM partition function of the hybrid system can be written as follows:²¹

$$Q_P^{\text{qm}} = \int d\mathbf{S} \int d\mathbf{s} \left(\frac{P}{2\pi\lambda^2} \right)^{3P/2} \int d\mathbf{R} e^{-\beta V^{\text{qm}}(\mathbf{r}, \mathbf{S})} \quad (3)$$

where $\int d\mathbf{R} = \int d\mathbf{r}_1 \dots \int d\mathbf{r}_P \delta(\bar{\mathbf{r}} = \mathbf{s})$, P is the number of quasi-particles of the discrete path, the delta function $\delta(\bar{\mathbf{r}} = \mathbf{s})$ is introduced for use in later discussion, and the centroid coordinate, $\bar{\mathbf{r}}$, of the quasi-particles, $\mathbf{r} = \{\mathbf{r}_i; i = 1, \dots, P\}$, is defined as

$$\bar{\mathbf{r}} = \frac{1}{P} \sum_{i=1}^P \mathbf{r}_i \quad (4)$$

In eq 3, the effective quantum mechanical potential $V^{\text{qm}}(\mathbf{r}, \mathbf{S})$ is given by

$$V^{\text{qm}}(\mathbf{r}, \mathbf{S}) = \frac{P}{2\beta\lambda^2} \sum_i^P (\mathbf{r}_i - \mathbf{r}_{i+1})^2 + \frac{1}{P} \sum_i^P U(\mathbf{r}_i, \mathbf{S}) \quad (5)$$

and λ^2 is the square of the de Broglie thermal wavelength of a particle of mass M :

$$\lambda^2 = \frac{\beta \hbar^2}{M} \quad (6)$$

where \hbar is Planck's constant and M is the mass of the particle.

We introduce the effective semiclassical potential $U^{\text{eff}}(\mathbf{s}; \mathbf{r}, \mathbf{S})$

$$U^{\text{eff}}(\mathbf{s} = \bar{\mathbf{r}}; \mathbf{r}, \mathbf{S}) = \frac{P}{2\beta\lambda^2} \sum_i^P (\mathbf{r}_i - \mathbf{r}_{i+1})^2 + U(\bar{\mathbf{r}}, \mathbf{S}) \quad (7)$$

where the centroid of the quantized particle is constrained at its classical position, \mathbf{s} , and they are used interchangeably below. The classical partition function Q_P^{cm} (cm is classical mechanics) is

$$Q_P^{\text{cm}} = \int d\mathbf{S} \int d\mathbf{s} e^{-\beta U(\mathbf{s}, \mathbf{S})} \left(\frac{P}{2\pi\lambda^2} \right)^{3P/2} \times \int d\mathbf{R} \exp \left[-\frac{P}{2\lambda^2} \sum_i^P (\Delta \mathbf{r}_i)^2 \right] = e^{-\beta F^{\text{cm}}} e^{-\beta F_{\text{FP}}^{\circ}} \quad (8)$$

where \mathbf{s} is the classical position vector of the quantized particle, F^{cm} and F_{FP}° are the free energies of the classical system [without the quantized free particle (FP)] and the free particle, respectively, and $\Delta \mathbf{r}_i = \mathbf{r}_i - \mathbf{r}_{i+1}$. Then, eq 3 can

be rewritten as follows

$$Q_P^{\text{qm}} = Q_P^{\text{cm}} \times \frac{\int d\mathbf{S} \int d\mathbf{s} e^{-\beta U(\mathbf{s}, \mathbf{S})} \int d\mathbf{R} \exp \left[-\frac{P}{2\lambda^2} \sum_i^P (\Delta \mathbf{r}_i)^2 \right] e^{-\beta \Delta \bar{U}(\bar{\mathbf{r}} = \mathbf{s}, \mathbf{S})}}{\int d\mathbf{S} \int d\mathbf{s} e^{-\beta U(\mathbf{s}, \mathbf{S})} \int d\mathbf{R} \exp \left[-\frac{P}{2\lambda^2} \sum_i^P (\Delta \mathbf{r}_i)^2 \right]} = e^{-\beta [F^{\text{cm}} + F_{\text{FP}}^{\circ}]} \langle e^{-\beta [F(\bar{\mathbf{r}} = \mathbf{s}, \mathbf{S}) - F_{\text{FP}}^{\circ}]} \rangle_U \quad (9)$$

In eq 9, the average $\langle \dots \rangle_U$ is obtained according the potential $U(\bar{\mathbf{r}}, \mathbf{S})$ over classical coordinates, and

$$\Delta \bar{U}(\bar{\mathbf{r}}, \mathbf{S}) = \frac{1}{P} \sum_i^P \{U(\mathbf{r}_i, \mathbf{S}) - U(\bar{\mathbf{r}}, \mathbf{S})\} \quad (10)$$

Equation 9 also defines that, for a fixed "classical" configuration $(\bar{\mathbf{r}}, \mathbf{S})$, the free-particle sampling carried out without the external potential $U(\bar{\mathbf{r}}, \mathbf{S})$ yields the partial partition function

$$Q_P^{\text{qm}}(\bar{\mathbf{r}}, \mathbf{S}) = e^{-\beta [F(\bar{\mathbf{r}}, \mathbf{S}) - F_{\text{FP}}^{\circ}]} = \langle e^{-\beta \Delta \bar{U}(\bar{\mathbf{r}}, \mathbf{S})} \rangle_{\text{FP}, \bar{\mathbf{r}}} \quad (11)$$

where $F(\bar{\mathbf{r}}, \mathbf{S})$ is the free energy of a quantized particle whose centroid position is constrained to its classical coordinate, $\bar{\mathbf{r}} = \mathbf{s}$, in the presence of the rest of the classical particles, and it is related to the free-particle averaging which is defined as

$$\langle \dots \rangle_{\text{FP}, \bar{\mathbf{r}}} = \frac{\int d\mathbf{R} \{ \dots \} \delta(\bar{\mathbf{r}}) \exp \left[-\frac{P}{2\lambda^2} \sum_i^P (\Delta \mathbf{r}_i)^2 \right]}{\int d\mathbf{R} \delta(\bar{\mathbf{r}}) \exp \left[-\frac{P}{2\lambda^2} \sum_i^P (\Delta \mathbf{r}_i)^2 \right]} \quad (12)$$

Thus, the free-particle sampling of eqs 11 and 12 yields the quantum free-energy difference relative to a reference free particle for a fixed classical configuration. The idea of using classical Monte Carlo simulations to generate particle distributions and then to use eq 12 to make quantum corrections was described by Sprik et al.²³ Later, Warshel et al. pointed out that the expression of eq 9 is particularly useful since the quantum free energy of the system can be obtained by first carrying out classical trajectories for averaging classical configurations $(\bar{\mathbf{r}}, \mathbf{S})$, then by determining the quantum contributions through free-particle sampling (eq 11).

The quantum mechanical average of the ground-state property A in the centroid path integral can be expressed as

$$\langle A \rangle = \frac{\int d\mathbf{S} \int d\mathbf{s} \int d\mathbf{R} A(\mathbf{r}, \mathbf{S}) e^{-\beta V^{\text{qm}}(\mathbf{r}, \mathbf{S})}}{\int d\mathbf{S} \int d\mathbf{s} \int d\mathbf{R} e^{-\beta V^{\text{qm}}(\mathbf{r}, \mathbf{S})}} \quad (13)$$

where the integral over $d\mathbf{R}$ is under the constraint that $\bar{\mathbf{r}} = \mathbf{s}$. In analogy with the derivation of eq 9, eq 13 can be simplified as follows:

$$\langle A \rangle = \frac{\langle \langle A(\mathbf{r}, \mathbf{S}) e^{-\beta \Delta \bar{U}(\bar{\mathbf{r}}, \mathbf{S})} \rangle_{\text{FP}, \bar{\mathbf{r}}} \rangle_U}{\langle \langle e^{-\beta \Delta \bar{U}(\bar{\mathbf{r}}, \mathbf{S})} \rangle_{\text{FP}, \bar{\mathbf{r}}} \rangle_U} \quad (14)$$

Equation 14 represents a weighted Boltzmann average of all path integrals and classical configurations. If one makes the approximation

$$\langle A(\mathbf{r}, \mathbf{S}) e^{-\beta \Delta \bar{U}(\bar{\mathbf{r}}, \mathbf{S})} \rangle_{\text{FP}, \bar{\mathbf{r}}} \approx e^{-\beta [F(\bar{\mathbf{r}}, \mathbf{S}) - F_{\text{FP}}^{\circ}]} \langle A(\mathbf{r}, \mathbf{S}) \rangle_{\text{FP}, \bar{\mathbf{r}}} \quad (15)$$

the average can be estimated as a Boltzmann weighted average by the individual quantum free energies of classical configurations:

$$\langle A \rangle \approx \sum_{\bar{\mathbf{r}}, \mathbf{S}} \frac{e^{-\beta [F(\bar{\mathbf{r}}, \mathbf{S}) - F_{\text{FP}}^{\circ}]} \langle A(\mathbf{r}, \mathbf{S}) \rangle_{\text{FP}, \bar{\mathbf{r}}}}{Q_P^{\text{qm}}} \quad (16)$$

Note that $\bar{\mathbf{r}} = \mathbf{s}$. Equation 16 has been shown to yield reasonable results for a system consisting of one electron embedded in random hard spheres.²³ If a sampling procedure can be formulated such that the classical configurations are chosen with the probability of $e^{-\beta [F(\bar{\mathbf{r}}, \mathbf{S}) - F_{\text{FP}}^{\circ}]} / Q_P^{\text{qm}}$, eq 16 may be enumerated by a simple numerical average,²³ but it is not clear how such a sampling scheme can be easily obtained.

$$\langle A \rangle \approx \sum_{\bar{\mathbf{r}}, \mathbf{S}} \langle A(\mathbf{r}, \mathbf{S}) \rangle_{\text{FP}, \bar{\mathbf{r}}} \quad (16a)$$

2.2. The Quantized Classical Path (QCP) Method.

Warshel et al. pointed out that the most significant result of the QCP method is the use of double averaging²³ in centroid path integral calculations over all configurations generated by classical trajectories.^{18,19} From eq 9, the quantum mechanical potential of mean force, defined as a function of the centroid reaction coordinate, \bar{z} , can readily be expressed as follows:

$$\begin{aligned} W^{\text{qm}}(\bar{z}) &= W^{\text{cm}}(\bar{z}) - \frac{1}{\beta} \ln \frac{Q_P^{\text{qm}}(\bar{z})}{Q^{\text{cm}}(\bar{z})} \\ &= W^{\text{cm}}(\bar{z}) - \frac{1}{\beta} \ln \langle \langle e^{-\beta \Delta \bar{U}(\bar{z})} \rangle_{\text{FP}, \bar{z}} \rangle_U \end{aligned} \quad (17)$$

where Q^{cm} is the cm partition function (without quantized free particles), and $W^{\text{qm}}(\bar{z})$ and $W^{\text{cm}}(\bar{z})$ are the centroid quantum mechanical and classical mechanical potentials of mean force, respectively. The advantage of this formulation is that one can sample the FP distribution separately at each classical configuration (i.e., centroid position) and then average over classical configurations obtained from molecular dynamics simulations.

The free-energy difference in eq 2 can then be conveniently obtained from the formula

$$\Delta F_{\text{qm}}^{\ddagger} - \Delta F_{\text{TST}}^{\ddagger} = [W^{\text{qm}}(\bar{z}_{\text{qm}}^{\ddagger}) - W^{\text{qm}}(\bar{z}_{\text{qm}}^{\text{R}})] - [W^{\text{cm}}(z_{\text{cm}}^{\ddagger}) - W^{\text{cm}}(z_{\text{cm}}^{\text{R}})] \quad (18)$$

where the symbol $\bar{z}_{\text{qm}}^{\ddagger}$ specifies the value of the centroid reaction coordinate, at which $W^{\text{qm}}(\bar{z})$ has the maximum value, and $\bar{z}_{\text{qm}}^{\text{R}}$ is the coordinate at the reactant state. Notice that the free energy of the free particle cancels out in eq 18; thus, it does not contribute to the calculation of the free-energy difference in eqs 2 and 18. Analogously, z_{cm}^{\ddagger} and z_{cm}^{R} are

the corresponding values of the classical reaction coordinate. Of course, the locations of the transition state in the quantum and classical potential of mean force are not necessarily identical.

2.3. The BQCP Method. A central issue with all path-integral formulations is the sampling method employed. A number of efficient sampling schemes have been proposed and reviewed.^{23,24,38–40} However, we had considerable difficulties achieving convergence in QCP calculations using “standard” Monte Carlo or molecular dynamics methods. Recently, we implemented the bisection method of Ceperley and Pollock to sample the free-particle distribution,^{38,39} which is based on multilevel sampling and the Lévy Brownian bridge construction,⁴¹ and we found that the convergence in eq 11 can be easily obtained.^{5,6} Since the free-particle distribution is known exactly at a given temperature, each ring-bead distribution is generated directly according to this distribution and thus 100% accepted. Furthermore, each new configuration is created independently, starting from a single initial bead position, allowing the new configuration to move into a completely different region of configurational space.

The original bisection sampling method was not developed for centroid path integral simulations, and there is no simple way of constraining the centroid position in the bisection sampling. In our implementation, we decided to first make the bisection sampling as originally proposed by Ceperley and Pollock^{38,39} and enforced the first and last beads to be identical to enclose the polymer ring.^{5,6} Then, we made a rigid-body translation of the centroid position of the new beads’ configuration to coincide with the target (classical) coordinate. Since the free-particle distribution is known exactly at a given temperature, each ring-bead distribution is generated according to this distribution and thus 100% accepted.³⁹ Furthermore, in this construction, each new configuration is created independently, starting from a single initial bead position, allowing the new configuration to move into a completely different region of configurational space. We call this sampling scheme over classical configurations, in connection with the ideas of Sprik et al.²³ and Warshel et al.’s quantized classical path,^{18,19} the BQCP method. The BQCP convergence has been thoroughly tested^{5,6} and applied to several condensed-phase and enzyme systems.^{6,34–36} Of course, the present sampling approach is not restricted to fixing the centroid position to correct the classical reaction path, and it can be used as an independent variable to obtain a “quantum” reaction path. Although this is a straightforward extension of Ceperley’s bisection sampling method,³⁹ to our knowledge, it has not been utilized previously in centroid path integral simulations, and more importantly, it allows us to achieve fast convergence.

To make convenient the discussion of the kinetic isotope effect calculations, we first describe the bisection sampling procedure and its scalability to an isotopic substitution of the quantized particle. The goal is to develop an efficient sampling scheme that facilitates an accurate prediction of KIEs. Specifically, since we’re dealing with free-particle sampling, we would like to generate entirely

uncorrelated distributions at each sampling step, to obtain maximum efficiency, while minimizing sampling noise.

Let the initial distribution of beads be $\{\mathbf{r}_1, \mathbf{r}_2, \dots, \mathbf{r}_P, \mathbf{r}_{P+1}\}$ where $P = 2^L$ is the number of beads and L is the number of bisection levels, and \mathbf{r}_1 and \mathbf{r}_{P+1} are the initial and final positions of the polymer chain. Note that the ends of the sequence in the present discussion are enclosed for a ring of beads and $\mathbf{r}_1 = \mathbf{r}_{P+1}$. To obtain a new distribution, the positions for $P - 1$ beads, $\{\mathbf{r}_2, \dots, \mathbf{r}_P\}$, will be randomly generated, starting from \mathbf{r}_1 and \mathbf{r}_{P+1} . Specifically, the bisection sampling procedure begins at the coarsest level, level 1, and the coordinate of the bead in the midpoint of the sequence is first sampled, which is placed at the geometrical center of the two ends plus a random displacement according to its (Gaussian) free-particle distribution of width $\sigma_1 = 2^{L-1}(\lambda_M^2/2P)$, where λ_M^2 is the square of de Broglie wavelength of a particle of mass M . Next, at level 2, the two new intervals $(\mathbf{r}_1, \mathbf{r}_{P/2})$ and $(\mathbf{r}_{P/2}, \mathbf{r}_{P+1})$ will be used to generate the coordinates of their two midpoints, with a distribution width of $\sigma_2 = 2^{L-2}(\lambda_M^2/2P)$. This process continues until all $P - 1$ positions are generated at level L . For convenience, which is obvious below, we set the local coordinate origin at $\mathbf{r}_1 = (0,0,0)$, and we summarize the procedure below.

Level 1:

$$\mathbf{r}_{1+P/2} = \frac{1}{2}(\mathbf{r}_1 + \mathbf{r}_{P+1}) + \lambda_M \sqrt{\frac{2^{L-2}}{P}} \eta_1 = \lambda_M \theta_{1+P/2} \quad (19)$$

where η_1 is a vector of normal distribution with zero mean and unit variance (which is obtained with the Box-Muller method⁴²), and $\theta_{1+P/2} = \sqrt{2^{L-2}/P} \eta_1$.

Level 2:

$$\begin{aligned} \mathbf{r}_{1+P/4} &= \frac{1}{2}(\mathbf{r}_1 + \mathbf{r}_{1+P/2}) + \lambda_M \sqrt{\frac{2^{L-3}}{P}} \eta_2(1) \\ &= \lambda_M \left\{ \frac{1}{2} \theta_{1+P/2} + \sqrt{\frac{2^{L-3}}{P}} \eta_2(1) \right\} = \lambda_M \theta_{1+P/4} \quad (20) \end{aligned}$$

$$\begin{aligned} \mathbf{r}_{1+3P/4} &= \frac{1}{2}(\mathbf{r}_{1+P/2} + \mathbf{r}_{P+1}) + \lambda_M \sqrt{\frac{2^{L-3}}{P}} \eta_2(2) \\ &= \lambda_M \left\{ \frac{1}{2} \theta_{1+P/2} + \sqrt{\frac{2^{L-3}}{P}} \eta_2(2) \right\} = \lambda_M \theta_{1+3P/4} \quad (21) \end{aligned}$$

where $\eta_2(1)$ and $\eta_2(2)$ are two random vectors of normal distribution.

Level k :

$$\begin{aligned} \mathbf{r}_{1+(2^{m-1})P/2^k} &= \frac{1}{2}(\mathbf{r}_{1+(2^{m-2})P/2^k} + \mathbf{r}_{1+2^m P/2^k}) + \lambda_M \sqrt{\frac{2^{L-1-k}}{P}} \eta_k(m) \\ &= \lambda_M \left\{ \frac{1}{2} [\theta_{1+(2^{m-2})P/2^k} + \theta_{1+2^m P/2^k}] + \sqrt{\frac{2^{L-1-k}}{P}} \eta_k(m) \right\} \\ &= \lambda_M \theta_{1+(2^{m-1})P/2^k} \quad (22) \end{aligned}$$

where $m = 1, \dots, 2^{k-1}$.

In general, any particle position can be expressed as

$$\mathbf{r}_i = \lambda_M \theta_i \quad i = 1, 2, \dots, P \quad (23)$$

where the vector θ_i is a random vector, properly scaled and generated according to the free-particle distribution, and associated with earlier levels of bisection sampling, as has been explicitly shown for levels 1, 2, and k in eqs 19–22. In eq 23, we have defined $\theta_1 = 0$. Finally, all beads' positions are translated such that the geometric center (centroid) of the polymer ring $\mathbf{r}_{CP} = \lambda_M (1/P \sum_i^P \theta_i)$ is made to coincide with the coordinate of the classical particle.

A key point of interest is that each of the random bead positions generated by the bisection method is proportional to the de Broglie wavelength, which is dependent on the mass of the quantized particle. We also see that the positions of the $P - 1$ sampled beads are independent of the initial position of bead number 1. Moreover, the new position of the “seed” bead, bead number 1, is also independent of the position at the previous step. This would not be the case if we perform the bisection sampling with two different endpoints. In essence, one can simply generate a library of random beads' configurations and randomly choose them in BQCP calculations, but the time needed to generate new bead positions is minimal compared to the computer time required to compute their potential energies. So, there is little advantage for creating such a library. These features make the present procedure especially efficient in centroid path integral simulations. Note that, if external potentials are applied in a Monte Carlo sampling scheme for free-particle configurations, the efficiency of the bisection sampling scheme will be significantly hampered because the beads' distribution can easily get trapped in a local minimum, making it difficult to move out.

2.4. The Integrated Path Integral–Free-Energy Perturbation/Umbrella Sampling (PI-FEP/UM) Method for Computing KIEs. In principle, one can carry out separate centroid path integral simulations to make quantum mechanical corrections to the classical potential of mean force for different isotopes. Then, one can use the activation free energies for different isotopic reactions to compute the corresponding kinetic isotope effects. However, the statistical errors associated with these separate calculations are at least 1 order of magnitude greater than the free-energy difference for different isotopic reactions, too large to be useful for computing KIEs.

We have developed a free-energy perturbation (FEP) method, in the framework of centroid path integral simulations, to obtain directly the free-energy difference from isotope substitutions along a reaction path. Two algorithms are examined below, termed the PI-UM method and the PI-FEP/UM method. Although the two methods yield similar computed KIEs, the statistical uncertainties are significantly different, with the latter PI-FEP/UM approach giving smaller uncertainties comparable to experimental results due to the use of FEP with respect to bead distribution, which is proportional to the mass of the quantized particle. Thus, the method is an FEP over mass.

Considering an atom-transfer reaction where the light atom of mass M_L is replaced by a heavier isotope of mass M_H , we use exactly the same sequence of random numbers, that is, displacement vectors $\{\theta_i\}$, to generate the bisection path integral distribution for both isotopes. Thus, the resulting coordinates of these two bead distributions differ only by the ratio of the corresponding masses:

$$\frac{\mathbf{r}_{i,L}}{\mathbf{r}_{i,H}} = \frac{\lambda_{M_L} \theta_i}{\lambda_{M_H} \theta_i} = \sqrt{\frac{M_H}{M_L}} \quad i = 1, 2, \dots, P \quad (24)$$

where $\mathbf{r}_{i,L}$ and $\mathbf{r}_{i,H}$ are the coordinates for bead i of the corresponding light and heavy isotopes. The free-energy difference, or equivalently, the ratio of the partition functions, between the heavy and light isotopes can then be determined by the formula

$$\begin{aligned} \frac{Q_L^{\text{qm}}(\bar{z})}{Q_H^{\text{qm}}(\bar{z})} &= \left\{ \frac{Q_L^{\text{qm}}(\bar{z})}{Q^{\text{cm}}(\bar{z})} \right\} \left\{ \frac{Q^{\text{cm}}(\bar{z})}{Q_H^{\text{qm}}(\bar{z})} \right\} \\ &= \frac{\langle \delta(z - \bar{z}) \langle e^{-\beta \Delta \bar{U}_L} \rangle_{\text{FP},L} \rangle_U}{\langle \delta(z - \bar{z}) \langle e^{-\beta \Delta \bar{U}_H} \rangle_{\text{FP},H} \rangle_U} \end{aligned} \quad (25)$$

where $\Delta \bar{U}_L = (1/P) \sum_i \{U(\mathbf{r}_{i,L}) - U(\bar{\mathbf{r}})\}$ and $\Delta \bar{U}_H = (1/P) \sum_i \{U(\mathbf{r}_{i,H}) - U(\bar{\mathbf{r}})\}$.

Equation 25 offers a convenient approach to determine KIEs. We first carry out classical umbrella sampling simulations to generate the classical potential of mean force (outer average). Then, for each configuration saved in the classical simulation, we carry out centroid path integral calculations by free-particle sampling to obtain the quantum mechanical correction along the classical path (inner average). The bisection samplings are performed in such a way that the same set of displacement vectors, properly scaled by the mass factor of eq 24, are used to obtain the distributions for the two different isotopes. Thus, we obtain two separate quantized potentials of mean force for the two isotopic reactions, and we call this algorithm the path integral–umbrella sampling (PI-UM) method, in which umbrella sampling is used to compute the classical mechanical PMF and the centroid path integral sampling is used to make quantum corrections. The required accuracy is achieved because the isotopic substitution represents only a slight perturbation to the original isotopic bead distribution, proportional to the square root of the ratio between the two masses. This is different than separate PI samplings for different isotopes, which is very difficult to converge to the required precision.

The second algorithm, which we refer to here as the PI-FEP/UM method, is to use the result of eq 14 to obtain the free-energy difference using free-energy perturbation between light and heavy isotopic masses. First, we note that the sampling scheme presented in eqs 23 and 24 yields the following identity for the kinetic energy term of the discrete beads:

$$\frac{P}{2\beta \lambda_{M_L}^2} \sum_i^P (\mathbf{r}_{i,L} - \mathbf{r}_{i+1,L})^2 = \frac{P}{2\beta \lambda_{M_H}^2} \sum_i^P (\mathbf{r}_{i,H} - \mathbf{r}_{i+1,H})^2 \quad (26)$$

Therefore,

$$\begin{aligned} \frac{Q_H^{\text{qm}}(\bar{z})}{Q_L^{\text{qm}}(\bar{z})} &= \left(\frac{M_H}{M_L} \right)^{3P/2} \frac{\int d\bar{\mathbf{r}} \int d\mathbf{R}_H e^{-\beta V^{\text{qm}}(\mathbf{r}_H)}}{\int d\bar{\mathbf{r}} \int d\mathbf{R}_L e^{-\beta V^{\text{qm}}(\mathbf{r}_L)}} \\ &= \frac{\int d\bar{\mathbf{r}} \int d\mathbf{R}_L e^{-\beta V^{\text{qm}}(\mathbf{r}_H)}}{\int d\bar{\mathbf{r}} \int d\mathbf{R}_L e^{-\beta V^{\text{qm}}(\mathbf{r}_L)}} \end{aligned} \quad (27)$$

where we have substituted the integration variable, $d\mathbf{R}_H = (M_L/M_H)^{3P/2} d\mathbf{R}_L$. The significance of this coordinate change is that the ratio of the partition functions for the heavy and light isotopes at reaction coordinate z can be obtained exactly by free-energy perturbation (see also eq 14) via sampling only the light (or heavy) isotopic particles:

$$\frac{Q_H^{\text{qm}}(\bar{z})}{Q_L^{\text{qm}}(\bar{z})} = \frac{\left\langle \delta(z - \bar{z}) \left\langle \exp \left[-\frac{\beta}{P} \sum_i \Delta U_i^{L \rightarrow H} \right] e^{-\beta \Delta \bar{U}_L} \right\rangle_{\text{FP},L} \right\rangle_U}{\langle \delta(z - \bar{z}) e^{-\beta [F_L(\bar{z}, \mathbf{S}) - F_{\text{FP}}^0]} \rangle_U} \quad (28)$$

where the superscripts or subscripts L and H specify computations done using light or heavy isotopes, and $\Delta U_i^{L \rightarrow H} = U(\mathbf{r}_{i,H}) - U(\mathbf{r}_{i,L})$ represents the difference in potential energy at the heavy and light bead positions $\mathbf{r}_{i,H}$ and $\mathbf{r}_{i,L}$. In eq 28, we obtain the free-energy (inner average) difference between the heavy and light isotopes by carrying out the bisection path integral sampling with the light atom and then perturbing the heavy isotope masses, i.e., positions according to eq 24. Then, the free-energy difference between the light and heavy isotope ensembles is weighted by the Boltzmann factor due to quantization of classical configurations (outer average).

An approximate approach is to employ eq 16, such that the free-energy difference between heavy and light isotopes is Boltzmann-weighted over all classical configurations:

$$\frac{Q_H^{\text{qm}}(\bar{z})}{Q_L^{\text{qm}}(\bar{z})} \approx \sum_{\mathbf{s}, \mathbf{S}} P_{P,L}^{\text{qm}}(z; \bar{\mathbf{r}} = \mathbf{s}, \mathbf{S}) \left\langle \exp \left[-\frac{\beta}{P} \sum_i \Delta U_i^{L \rightarrow H} \right] \right\rangle_{(\bar{z})\text{FP},L} \quad (29)$$

where

$$P_{P,L}^{\text{qm}}(z; \bar{\mathbf{r}} = \mathbf{s}, \mathbf{S}) = \frac{Q_{P,L}^{\text{qm}}(z; \bar{\mathbf{r}}, \mathbf{S})}{Q_{P,L}^{\text{qm}}} = \frac{e^{-\beta [F_{P,L}(z; \bar{\mathbf{r}}, \mathbf{S}) - F_{\text{FP},L}^0]}}{e^{-\beta [F_{P,L}^{\text{qm}} - F_{\text{FP},L}^0]}} \quad (30)$$

The kinetic isotope effects are computed as follows:

$$\text{KIE} = \frac{k^L}{k^H} = \left[\frac{Q_H^{\text{qm}}(\bar{z}_H^{\text{R}})}{Q_L^{\text{qm}}(\bar{z}_L^{\text{R}})} \right] \left[\frac{Q_L^{\text{qm}}(\bar{z}_L^{\text{R}})}{Q_H^{\text{qm}}(\bar{z}_H^{\text{R}})} \right] e^{-\beta [F_{\text{cm}}^{\text{R}}(\bar{z}_L^{\text{R}}) - F_{\text{cm}}^{\text{R}}(\bar{z}_H^{\text{R}})]} \quad (31)$$

where $F_{\text{cm}}^{\text{R}}(\bar{z}_L^{\text{R}})$ and $F_{\text{cm}}^{\text{R}}(\bar{z}_H^{\text{R}})$ are the free energies of the mode in the reactant (R) state that correlates with the progress coordinate z for the light and heavy isotopes. A method for estimating their values has been described.¹

3. Computational Details

3.1. Potential Energy Function. In the present study, we use a combined quantum mechanical and molecular me-

chanical potential in molecular dynamics simulations, in which the solute is represented explicitly by an electronic structure method and the solvent is approximated by the three-point charge TIP3P model for water.⁴³ The details have been described in a number of articles.^{44,45} We used the standard semiempirical Austin Model 1 (AM1) method to treat the decarboxylation reaction of N-methyl picolinate.⁴⁶ As in numerous other decarboxylation reactions, the AM1 method yielded good energetic results in comparison with high-level electronic structural results.^{47–51} In the case of the deprotonation of nitroethane by an acetate ion, the AM1 model failed to yield adequate energetic results, and a set of specific reaction parameters (SRP) was developed within the AM1 formalism to fit density functional theory results. The performance of the SRP-AM1 model has been reported previously,^{6,34} and we focus here on testing the performance of the nuclear quantum effects using the PI-FEP method.

3.2. Simulation Details. All simulations are performed using periodic boundary conditions in the isothermal–isobaric (NPT) ensemble at 25 °C and 1 atm. In the decarboxylation reaction of N-methyl picolinate, a total of 888 water molecules were included in a cubic box of about $30 \times 30 \times 30 \text{ \AA}^3$. For the deprotonation of nitroethane by an acetate ion, 898 water molecules were included in the simulations. Nonbonded electrostatics were treated by the particle-mesh Ewald summation method for QM/MM simulations.⁵² van der Waals interactions were smoothed to zero at 9.5 Å on the basis of group–group separations. The bond lengths and angles of solvent water molecules were constrained by the SHAKE algorithm,⁵³ and an integration step of 1 fs was used for all calculations.

The PMF profiles were obtained using the umbrella sampling technique.⁵⁴ In this approach, the reaction was divided into a series of “windows”, in which a biasing potential was applied to allow sufficient sampling of high-energy regions along the reaction pathway. The effect of the biasing potential was subsequently removed when the separate simulation windows are combined to produce the overall PMF by using the weighted histogram analysis method.⁵⁵ In the current simulations, 12 windows were used for the decarboxylation reaction, while 32 windows were employed in the deprotonation reaction. In both reactions, the system was slowly heated to the target temperature over the course of 25 ps and thereafter equilibrated for 100–200 ps. Subsequently, each window was further equilibrated for 25–50 ps before data collection commenced. Each window was sampled for ca. 100–150 ps, totaling at least 2 ns of sampling for the decarboxylation and ca. 4 ns for the deprotonation reaction. The reaction coordinate was defined as the distance of the cleaving C–C bond for the decarboxylation reaction and as the difference between the breaking C α –H and forming O–H bonds in the deprotonation reaction.

The BQCP simulations employed 97 800 classical configurations for each isotope (¹²C, ¹³C, ¹⁴N, and ¹⁵N) for the decarboxylation reaction, combined with 10 path-integral steps per classical step. For the deprotonation reaction, 112 807 classical configurations were used for each isotope (¹H and ²H), combined with 10 path-integral steps per

classical step. For the decarboxylation reaction, the isotope labeled atom was quantized in addition to the three neighboring atoms. For the deprotonation reaction, the nitroethane C α atom, the abstracting acetate oxygen, the transferring proton, and the secondary hydrogen were quantized. Each quantized atom was described by 32 beads. Thus, 32–36 million QM/MM energy calculations are needed in each reaction. To estimate the standard errors in the computed kinetic isotope effects, the entire path integral simulations were divided into 10 separated blocks, each treated independently. The standard uncertainties ($\pm 1\sigma$) were determined from these 10 blocks and the total averages for both the PI-UM (eq 25) and the PI-FEP/UM (eq 31) methods.

All simulations employed the CHARMM program,⁵⁶ in which the methods described here have been implemented, and all path-integral simulations used a parallel version that efficiently distributes integral calculations for the quantized beads.⁶

4. Results and Discussions

4.1. Decarboxylation Reaction of N-Methyl Picolinate in Water. The primary and secondary heavy atom kinetic isotope effects for the decarboxylation of N-methyl picolinate have been studied by Rishavy and Cleland, and this was considered as a model to probe the mechanism of orotidine 5'-monophosphate decarboxylation catalyzed by orotidine monophosphate decarboxylase (Scheme 1).^{47,57–59} Due to the small magnitude of heavy atom KIEs combined with the inherent statistical noise in condensed-phase simulations, it is very difficult to compute these quantities through computer simulations.

The reaction profile for the decarboxylation of N-methyl picolinate monotonically increases as a function of the cleaving C–C bond distance in the gas phase, reaching a plateau of 18.1 kcal/mol from MPW1PW91/6-311++(3df,2p)//MPW1PW91/6-31+G(d) calculations. The energy of reaction is 17.7 and 11.6 kcal/mol using MP2/6-311++(3df,2p) and the semiempirical AM1 model, respectively. Thus, AM1 underestimates the reaction energy by about 6 kcal/mol. At all computational levels, there is no barrier separating N-methyl picolinate and the decarboxylation product, a characteristic feature in this class of decarboxylation reactions (refs 48–51, see above). The relatively smaller energy of reaction for N-methyl picolinate decarboxylation, compared to that of orotate ($\Delta E = 36.4$ kcal/mol),⁵⁹ is due to the positive charge at the N1 position of N-methyl picolinate. Since the main goal here is to illustrate the performance of the PI-FEP/UM method, the small difference between the AM1 and high-level electronic structure results is deemed acceptable.

The potential of mean force for the decarboxylation of N-methyl picolinate was obtained as a function of the C₂–C_{O2} separation in aqueous solution at 25 °C and 1 atm (see Figure 1). Solvent effects are significant, increasing the free-energy barrier by 15.2 kcal/mol to a value of 26.8 kcal/mol, which is accompanied by a net free energy of reaction of 24.7 kcal/mol. If the error introduced by the AM1 method for the gas-phase reaction is corrected, our best estimate of the free-energy barrier is 32.9 kcal/mol for the decarboxyla-

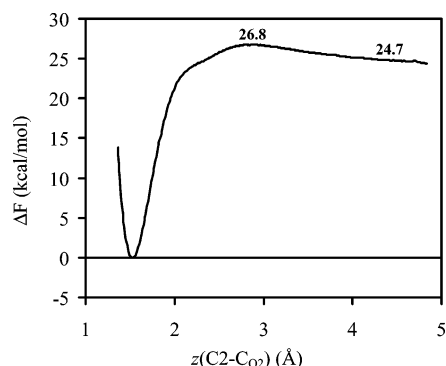


Figure 1. Classical potential of mean force as a function of the C₂-CO₂ distance of the cleaving bond for the decarboxylation reaction of N-methyl picolinate in water.

tion reaction of N-methyl picolinate in water. This is in contrast to the decarboxylation of N-methyl orotate in water, which has little solvent effect.⁴⁷ The difference is again due to the presence of the positive charge in the pyridine ring, which is annihilated in the decarboxylation reaction. However, the similarity is that there is a small solvent reorganization barrier for CO₂ recombination, which is about 2 kcal/mol.⁴⁷

The free-energy contributions to the potential of mean force by quantizing the carboxylate group and the C2 carbon in the pyridine ring are displayed in Figure 2A both for ¹²C and ¹³C at the carboxyl position, whereas the ratio of the two quantum partition functions from the PI-FEP/UM simulations is shown in Figure 2B. The nuclear quantum effects are non-negligible even for bond cleavage involving two carbon atoms, which reduce the free energy barrier by 0.45 kcal/mol. The intrinsic ¹³C primary KIE has been determined by the formula of eq 25, along with a factor correcting for the reduced mass of the reaction coordinate, which is treated as a harmonic oscillator of masses 12 (C₂) and 44 or 45 (CO₂). The PI-UM method yields a computed KIE of 1.0346 ± 0.8773 at 25 °C for the decarboxylation of N-methyl picolinate in water (Table 1). For comparison, the use of the PI-FEP/UM method resulted in a similar KIE (1.0345 ± 0.0028), but the associated statistical error is much smaller. To emphasize the sensitivity of the computational result, the computed KIE is equivalent to a free-energy difference of merely 0.0187 kcal/mol (Figure 2). Thus, even with the use of exactly the same configuration distributions, scaled by the corresponding masses of different isotopes, in path integral sampling, the fluctuation of the average quantum correction to the classical mechanical PMF is of similar magnitude as that of the computed KIE, if separated quantum mechanical PMFs are used (Figure 2A). On the other hand, the average over the exponential factor in free-energy perturbation simulations with the PI-FEP/UM method, which yields the free-energy difference between different isotopic substitutions, greatly reduces the statistical uncertainty. Experimentally, the primary ¹³C KIE for the decarboxylation of N-methyl picolinate was determined to be 1.0212 ± 0.0002 in ethylene glycol at 120 °C, which was extrapolated to a value of 1.0281 ± 0.0003 at 25 °C.⁵⁷ The agreement between the computational result and experimental value is reasonable, suggesting that the decarboxylation

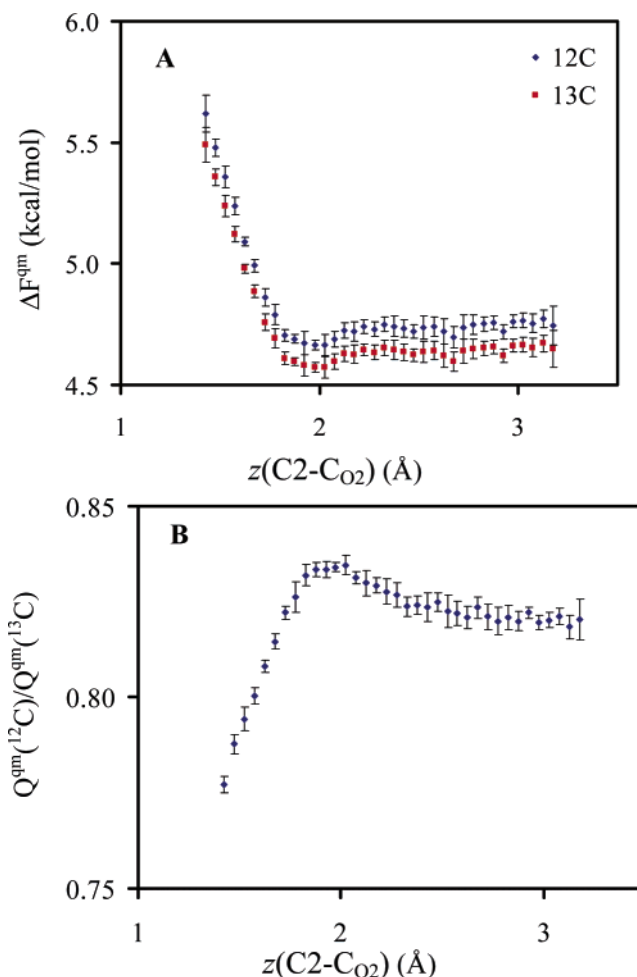


Figure 2. Nuclear quantum-mechanical free-energy corrections for the decarboxylation reaction of N-methyl picolinate in aqueous solution along the centroid reaction coordinate as defined in Figure 1. The C₂ atom of pyridinium and the carboxylate carbon and oxygen atoms are quantized. (A) Total free-energy contributions are displayed in blue for ¹²C and in red for ¹³C substitution at the carboxyl carbon position using the PI-UM algorithm. (B) The ratio of the quantum mechanical partition functions (equivalent to the free-energy difference) between ¹²C and ¹³C isotopic substitutions at the carboxyl carbon position from the PI-FEP/UM method.

Table 1. Computed and Experimental Primary ¹²C/¹³C and Secondary ¹⁴N/¹⁵N Kinetic Isotope Effects for the Decarboxylation of N-Methyl Picolinate at 25 °C in Water

	¹² k/ ¹³ k	¹⁴ k/ ¹⁵ k
exptl (120 °C) ^a	1.0212 ± 0.0002	1.0053 ± 0.0002
exptl (25 °C) ^a	1.0281 ± 0.0003	1.0070 ± 0.0003
PI-UM	1.0346 ± 0.8773	1.0067 ± 0.8862
PI-FEP/UM	1.0345 ± 0.0028	1.0083 ± 0.0016

^a In ethylene glycol with quinoline, ref 57.

reaction itself is the rate-limiting step. This is further supported by the secondary KIE discussed below.

Figure 3 depicts the nuclear quantum correction to the classical PMF by quantizing the N1 nitrogen and C2 and C6 carbons in the pyridine ring as well as the methyl carbon atom. Both ¹⁴N and ¹⁵N isotopes are used, and the ratio between their quantum mechanical distribution functions

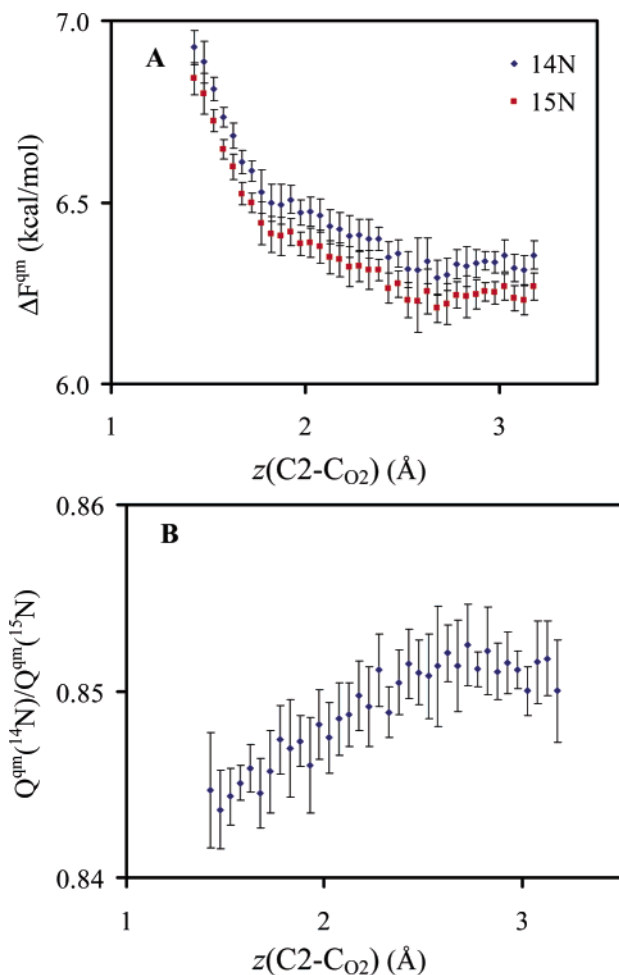


Figure 3. Nuclear quantum-mechanical free-energy corrections for the N-methyl picolinate decarboxylation reaction in aqueous solution along the centroid reaction coordinate as defined in Figure 1. Quantized atoms include the primary N_1 atom in pyridinium and the three adjacent (secondary) carbon atoms (the methyl and C_2 and C_6 carbon atoms). (A) Total free-energy contributions are shown in blue for ^{14}N and in red for ^{15}N substitution for the nitrogen atom from PI-UM calculations. (B) The ratio of the quantum partition functions (equivalent to the free-energy difference) between ^{14}N and ^{15}N isotopic substitutions for the nitrogen atom from PI-FEP/UM simulations.

along the centroid reaction coordinate is shown in Figure 3B. These calculations yield the secondary ^{15}N KIE, stemming from the loss of bending and torsional modes involving the carboxylate moiety at the transition state. Obviously, this is a very small secondary effect, and the standard fluctuations are too large when quantum corrections to the PMF for the two isotopes are used directly (Figure 3A). Fortunately, the present PI-FEP/UM method gives sufficiently stable and well-converged results as depicted in Figure 3B, and the computed secondary nitrogen KIE is computed as 1.0083 ± 0.0016 (Table 1). (The ratio of the reduced mass for the reaction coordinate for the secondary isotope effects is assumed to be one). The corresponding experimental value is 1.0070 ± 0.0003 extrapolated to 25°C .⁵⁷ The agreement between theory and experiment is also good, further sup-

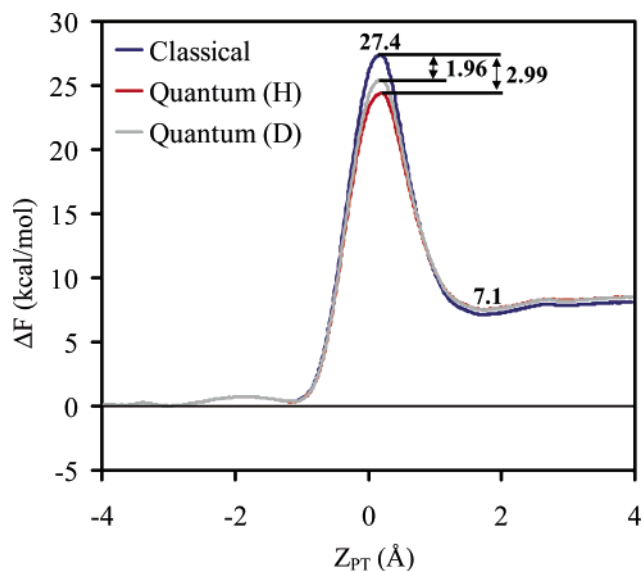


Figure 4. Classical and quantum potentials of mean force for the deprotonation of nitroethane by an acetate ion in aqueous solution. The reaction coordinate is defined as the difference of distances of the transferring proton between the donor atom (C_1) and acceptor atom (O), $Z_{\text{PT}} = r(\text{C}_1\text{-H}) - r(\text{H-O})$.

porting a unimolecular decarboxylation mechanism in this model reaction.

4.2. Deprotonation of Nitroethane by Acetate Ion in Water. The initial step in the oxidation of nitroalkanes by nitroalkane oxidase (NAO) is the abstraction of a α proton of nitroalkane.^{60,61} When the substrate is nitroethane, the deprotonation step is rate-limiting.⁶² Analyses of the crystallographic structure and mutagenesis experiments suggest that Asp402 is the base responsible for the proton abstraction.^{63,64} Recently, Valley and Fitzpatrick determined the KIEs for the dideuterated substrate $[1,1\text{-}^2\text{H}_2]$ nitroethane in NAO, and its model reaction of proton/deuteron abstraction by an acetate ion.⁶⁵ In the NAO-catalyzed reaction, the KIE was found to be 9.2 ± 0.4 , while in aqueous solution, the KIE was found to be 7.8 ± 0.1 . Here, we report the KIE results for the proton abstraction of nitroethane by an acetate ion in aqueous solution.

In the present study, we employ a reparameterized semiempirical model using the AM1 formalism, and this SRP model was fitted to the Gaussian theory 3 (G3) results, and the details of the SRP parametrization procedure and its application to the NAO enzymatic reaction have been described previously.⁶ The aim here is to examine our PI-FEP/UM method for KIE calculations, but we emphasize that the SRP model is a good one, and the computed energy of reaction for the proton abstraction of nitroethane by acetate is 8.7 kcal/mol, in adequate accord with the G3 result of 10.3 kcal/mol.^{6,34} The classical PMF for the deprotonation of nitroethane by acetate is presented in Figure 4. The computed barrier is 27.4 kcal/mol, while the computed free energy of reaction is 7.1 kcal/mol, slightly higher than the experimental value of 5.8 kcal/mol obtained from the relevant experimental $\text{p}K_{\text{a}}$.³⁴

Since light atoms are involved in the proton abstraction reaction, quantization of the “primary” and “secondary”

hydrogen atoms as well as the donor carbon atom and acceptor oxygen atom has a major impact on the computed free energy of activation, by lowering the barrier height by 3.0 kcal/mol. Thus, the estimated free energy of activation is 24.4 kcal/mol, in excellent agreement with the experimental value of 24.8 kcal/mol. This result underscores the importance of including nuclear quantum mechanical effects to accurately predict the activation free energy in reactions involving hydrogen transfers. We note that the overall barrier reduction is identical to that estimated previously using the EA-VTST-QM/MM method.³⁴ In addition, to dissect the specific contributing factors of the nuclear quantum effects, we have used the multidimensional tunneling algorithms developed by Truhlar and co-workers,⁸ extended to enzyme applications,^{1–3} to determine the average tunneling transmission factor, yielding a value of $\langle \kappa \rangle = 1.3$.³⁴ This suggests that that tunneling only makes minor contributions in the present case for the aqueous reaction. The PI-FEP/UM simulations include both zero-point and tunneling contributions that are not separable.

To directly compare the computed KIE with experimental results, which employed the dideuterated compound, 1,1-²H₂[nitroethane], we also made the same substitutions in our computation at the C_α position. The experimental KIE of 7.8 corresponds to a free-energy difference between the two isotopic reactions of 1.21 kcal/mol. Employing the PI-FEP/UM method (Figure 5A), we obtain a computed value of 6.13 ± 0.68 (Table 2), somewhat smaller than the experimental result. However, this corresponds to a free-energy error of only 0.15 kcal/mol, or 12%. Using the more efficient algorithm, the PI-FEP/UM method (Figure 5B), we obtained a computed deuterium KIE of 8.50 ± 0.01 (Table 2). It is interesting to note that there is noticeable difference in the computed deuterium primary KIE between the two computational algorithms because the effects are much greater than the heavy isotope effects. Previously, we reported a study of the same reaction in water using the EA-VTST-QM/MM method, and a total KIE of 6.0 was obtained.^{6,34}

5. Conclusions

We have described an integrated path integral and free-energy perturbation–umbrella sampling method for computing kinetic isotope effects for chemical reactions in solution and in enzymes. The approach is based on the BQCP sampling method, a combination of the bisection sampling scheme and centroid path integral simulations. The required accuracy for KIE calculations is achieved by the combined use of free-energy perturbation and umbrella sampling between different isotopic reactions. This is made possible because the bisection sampling scheme leads to a linear coordinate scaling relationship proportional to the ratio of the masses of different isotopes. Thus, the centroid path integral sampling for different quantized isotopic atoms can be similarly scaled, giving rise to small errors in free-energy perturbation/umbrella sampling simulations. The idea of making quantum mechanical corrections using the centroid path integral over configurations sampled by classical mechanical simulations has been explored previously, notably by Sprik et al. and the quantized classical path approach by

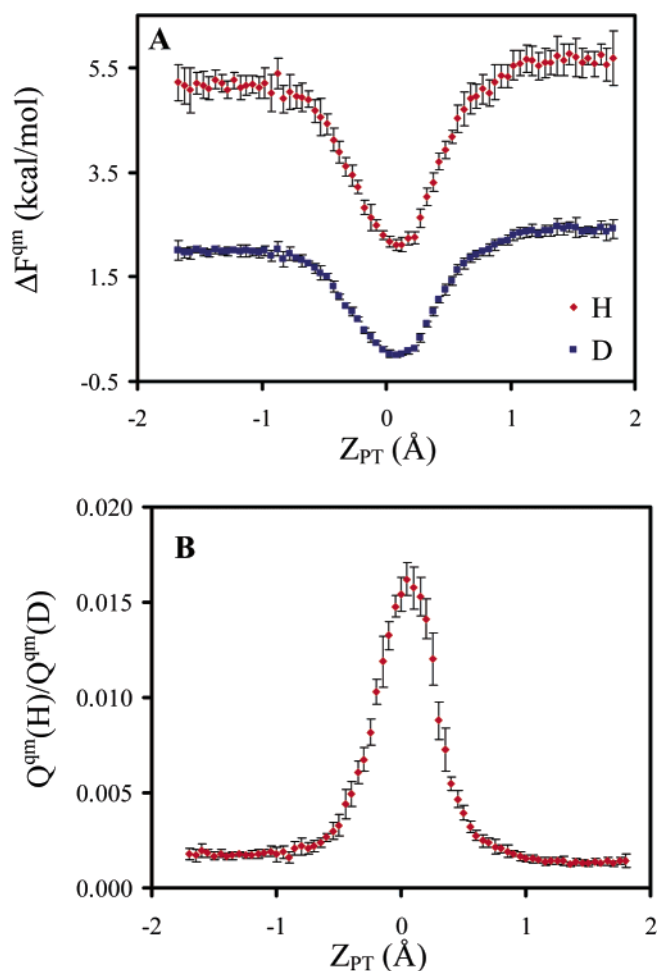


Figure 5. Nuclear quantum-mechanical free-energy correction for the deprotonation reaction of nitroethane by acetate in aqueous solution. The primary and secondary hydrogen atoms on C₁ carbon and the donor (C₁) and acceptor (O) atoms have been quantized. The reaction coordinate is defined in the legend of Figure 4. (A) The total free-energy contributions are shown in red for ¹H and in blue for ²H substitutions, and (B) the ratio of the quantum-mechanical partition functions is displayed between hydrogen and deuterium substitutions at the C₁ carbon.

Table 2. Computed and Experimental ¹H/²H Kinetic Isotope Effects for the Deprotonation of Nitroethane by Acetate at 25 °C in Water

	¹ k/ ² k
exptl ^a	7.8 ± 0.1
PI-UM	6.13 ± 0.68
PI-FEP/UM	8.50 ± 0.01

^a 25 °C in aqueous solution, ref 63.

Warshel et al., which has been applied to several enzyme systems.^{18–20,66} Here, we formulated two algorithms for computing KIEs for chemical reactions in condensed phases and in enzymes. We found that the PI-FEP/UM method yields relatively small statistical uncertainties in the computed KIEs, enabling the computed results to be compared with experimental results with reasonable confidence. However, when KIEs are obtained by taking the free-energy difference obtained from the quantum mechanical potentials of mean

force for the two isotopes, the statistical noise becomes too large to be comfortable; even the estimated KIEs are similar to those from the PI-FEP/UM calculations.

The PI-FEP/UM method is illustrated by computing the kinetic isotope effects for two chemical reactions in aqueous solution. In the first reaction, the decarboxylation of N-methyl picolinate involves heavy atom transfer reactions, and both the primary $^{12}\text{C}/^{13}\text{C}$ and the secondary $^{14}\text{N}/^{15}\text{N}$ KIEs are computed, and the results are found in good accord with experimental results. In particular, the computed primary and secondary KIEs are 1.0345 ± 0.0028 and 1.0083 ± 0.0016 , and the corresponding experimental values are 1.0281 ± 0.0003 and 1.0070 ± 0.0003 at 25 °C. In the second application, the proton-transfer reaction between nitroethane and by an acetate ion, a prototypical model for the enzymatic process by nitroalkane oxidase, was found to lower the free-energy barrier from the classical simulations by 3 kcal/mol when nuclear quantum effects are included using the PI-FEP/UM method. The computed primary deuterium isotope effect is 8.50 ± 0.01 , also in reasonable accord with experimental results (7.8 ± 0.1). The present study shows that the PI-FEP/UM method in connection with BQCP sampling allows computation of both primary and secondary kinetic isotope effects involving light as well as heavy atom transfers in solution. The method has also been applied to enzymatic reactions, providing a useful tool for the study of enzyme reaction mechanisms and for interpreting experimental KIEs.

Acknowledgment. This work has been supported in part by the National Institutes of Health and by the Army Research Laboratory through the Army High-Performance Computing Research Center (AHPARC) under the auspices of Army Research Laboratory DAAD 19-01-2-0014. J.G. thanks the Ministerio de Educación y Ciencia, España, for partial support.

References

- (1) Garcia-Viloca, M.; Alhambra, C.; Truhlar, D. G.; Gao, J. *J. Chem. Phys.* **2001**, *114*, 9953–9958.
- (2) Garcia-Viloca, M.; Gao, J.; Karplus, M.; Truhlar, D. G. *Science* **2004**, *303*, 186–195.
- (3) Pu, J.; Gao, J.; Truhlar, D. G. *Chem. Rev.* **2006**, *106*, 3140–3169.
- (4) Cleland, W. W. *Arch. Biochem. Biophys.* **2005**, *433*, 2–12.
- (5) Major, D. T.; Gao, J. *J. Mol. Graphics Modell.* **2005**, *24*, 121–127.
- (6) Major, D. T.; Garcia-Viloca, M.; Gao, J. *J. Chem. Theory Comput.* **2006**, *2*, 236–245.
- (7) Kohen, A.; Limbach, H.-H. *Isotope Effects in Chemistry and Biology*; Taylor and Francis: Boca Raton, FL, 2006.
- (8) Fernández-Ramos, A.; Millar, J. A.; Klippenstein, S. J.; Truhlar, D. G. *Chem. Rev.* **2006**, *106*, 4518–4584.
- (9) Alhambra, C.; Gao, J.; Corchado, J. C.; Villà, J.; Truhlar, D. G. *J. Am. Chem. Soc.* **1999**, *121*, 2253–2258.
- (10) Alhambra, C.; Corchado, J. C.; Sánchez, M. L.; Gao, J.; Truhlar, D. G. *J. Am. Chem. Soc.* **2000**, *122*, 8197–8203.
- (11) Alhambra, C.; Corchado, J.; Sanchez, M. L.; Garcia-Viloca, M.; Gao, J.; Truhlar, D. G. *J. Phys. Chem. B* **2001**, *105*, 11326–11340.
- (12) Gao, J.; Truhlar, D. G. *Annu. Rev. Phys. Chem.* **2002**, *53*, 467–505.
- (13) Gao, J.; Ma, S.; Major, D. T.; Pu, J.; Truhlar, D. G. *Chem. Rev.* **2006**, *106*, 3188–3209.
- (14) Billeter, S. R.; Webb, S. P.; Iordanov, T.; Agarwal, P. K.; Hammes-Schiffer, S. *J. Chem. Phys.* **2000**, *114*, 6925–6936.
- (15) Billeter, S. R.; Webb, S. P.; Agarwal, P. K.; Iordanov, T.; Hammes-Schiffer, S. *J. Am. Chem. Soc.* **2001**, *123*, 11262–11272.
- (16) Hammes-Schiffer, S. *Acc. Chem. Res.* **2006**, *39*, 93–100.
- (17) Wang, Q.; Hammes-Schiffer, S. *J. Chem. Phys.* **2006**, *125*, 184102.
- (18) Hwang, J. K.; Chu, Z. T.; Yadav, A.; Warshel, A. *J. Phys. Chem.* **1991**, *95*, 8445–8448.
- (19) Hwang, J. K.; Warshel, A. *J. Phys. Chem.* **1993**, *97*, 10053–10058.
- (20) Hwang, J.-K.; Warshel, A. *J. Am. Chem. Soc.* **1996**, *118*, 11745–11751.
- (21) Feynman, R. P.; Hibbs, A. R. In *Quantum Mechanics and Path Integrals*; McGraw-Hill: New York, 1965.
- (22) Chandler, D.; Wolynes, P. G. *J. Chem. Phys.* **1981**, *74*, 4078–4095.
- (23) Sprik, M.; Klein, M. L.; Chandler, D. *Phys. Rev. B: Condens. Matter Mater. Phys.* **1985**, *31*, 4234–4244.
- (24) Berne, B. J.; Thirumalai, D. *Annu. Rev. Phys. Chem.* **1986**, *37*, 401–424.
- (25) Voth, G. A.; Chandler, D.; Miller, W. H. *J. Chem. Phys.* **1989**, *91*, 7749–7759.
- (26) Cao, J.; Berne, B. J. *J. Chem. Phys.* **1993**, *99*, 2902–2916.
- (27) Chakrabarti, N.; Carrington, T., Jr.; Roux, B. *Chem. Phys. Lett.* **1998**, *293*, 209–220.
- (28) Jang, J.; Voth, G. A. *J. Chem. Phys.* **1999**, *111*, 2357–2370.
- (29) Marx, D.; Tuckerman, M. E.; Martyna, G. J. *Comput. Phys. Commun.* **1999**, *118*, 166–184.
- (30) Tuckerman, M. E.; Marx, D. *Phys. Rev. Lett.* **2001**, *86*, 4946–4949.
- (31) Iftimie, R.; Schofield, J. *J. Chem. Phys.* **2001**, *114*, 6763–6773.
- (32) Mielke, S. L.; Truhlar, D. G. *Chem. Phys. Lett.* **2003**, *378*, 317–322.
- (33) Olsson, M. H. M.; Siegbahn, P. E. M.; Warshel, A. *J. Am. Chem. Soc.* **2004**, *126*, 2820–2828.
- (34) Major, D. T.; York, D. M.; Gao, J. L. *J. Am. Chem. Soc.* **2005**, *127*, 16374–16375.
- (35) Major, D. T.; Nam, K.; Gao, J. L. *J. Am. Chem. Soc.* **2006**, *128*, 8114–8115.
- (36) Major, D. T.; Gao, J. L. *J. Am. Chem. Soc.* **2006**, *128*, 16345–16357.
- (37) Cao, J.; Voth, G. A. *J. Chem. Phys.* **1994**, *100*, 5093–5105.
- (38) Pollock, E. L.; Ceperley, D. M. *Phys. Rev. B: Condens. Matter Mater. Phys.* **1984**, *30*, 2555–2568.
- (39) Ceperley, D. M. *Rev. Mod. Phys.* **1995**, *67*, 279–355.

- (40) Tuckerman, M. E.; Berne, B. J.; Martyna, G. J.; Klein, M. L. *J. Chem. Phys.* **1993**, *99*, 2796–2808.
- (41) Levy, P. *Compos. Math.* **1939**, *7*, 283.
- (42) Press, W. H.; Flannery, B. P.; Teukolsky, S. A.; Vetterling, W. T. In *Numerical Recipes. The Art of Scientific Computing*, 2nd ed.; Cambridge University Press: New York, 1992; pp 279–281.
- (43) Jorgensen, W. L.; Chandrasekhar, J.; Madura, J. D.; Impey, R. W.; Klein, M. L. *J. Chem. Phys.* **1983**, *79*, 926–935.
- (44) Gao, J. *Rev. Comput. Chem.* **1995**, *7*, 119–185.
- (45) Gao, J.; Thompson, M. A. In *Combined Quantum Mechanical and Molecular Mechanical Methods*; American Chemical Society: Washington, DC, 1998; American Chemical Society Symp. Ser. #712.
- (46) Dewar, M. J. S.; Zoebisch, E. G.; Healy, E. F.; Stewart, J. J. P. *J. Am. Chem. Soc.* **1985**, *107*, 3902–3909.
- (47) Wu, N.; Mo, Y.; Gao, J.; Pai, E. F. *Proc. Natl. Acad. Sci. U.S.A.* **2000**, *97*, 2017–2022.
- (48) Gao, J. *J. Am. Chem. Soc.* **1995**, *117*, 8600–8607.
- (49) Gao, D.; Pan, Y.-K. *J. Org. Chem.* **1999**, *64*, 1151–1159.
- (50) Gao, D.; Pan, Y.-K. *J. Org. Chem.* **1999**, *64*, 4492–4501.
- (51) Acevedo, O.; Jorgensen, W. L. *J. Am. Chem. Soc.* **2005**, *127*, 8829–8834.
- (52) Nam, K.; Gao, J.; York, D. M. *J. Chem. Theory Comput.* **2005**, *1*, 2–13.
- (53) Allen, M. P.; Tildesley, D. J. In *Computer Simulation of Liquids*; Oxford University Press: Oxford, U. K., 1987.
- (54) Torrie, G. M.; Valleau, J. P. *J. Comput. Phys.* **1977**, *23*, 187–199.
- (55) Kumar, S.; Bouzida, D.; Swendsen, R. H.; Kollman, P. A.; Rosenberg, J. M. *J. Comput. Chem.* **1992**, *13*, 1011–1021.
- (56) Brooks, B. R.; Brucoleri, R. E.; Olafson, B. D.; States, D. J.; Swaminathan, S.; Karplus, M. *J. Comput. Chem.* **1983**, *4*, 187.
- (57) Rishavy, M. A.; Cleland, W. W. *Biochemistry* **2000**, *39*, 4569–4574.
- (58) Radzicka, A.; Wolfenden, R. *Science* **1995**, *267*, 90–93.
- (59) Lee, J. K.; Houk, K. N. *Science* **1997**, *276*, 942–945.
- (60) Fitzpatrick, P. F. *Acc. Chem. Res.* **2001**, *34*, 299–307.
- (61) Fitzpatrick, P. F.; Orville, A. M.; Nagpal, A.; Valley, M. P. *Arch. Biochem. Biophys.* **2005**, *433*, 157–165.
- (62) Gadda, G.; Fitzpatrick, P. F. *Biochemistry* **2000**, *39*, 1406–1410.
- (63) Valley, M. P.; Fitzpatrick, P. F. *J. Am. Chem. Soc.* **2003**, *125*, 8738–8739.
- (64) Nagpal, A.; Valley, M. P.; Fitzpatrick, P. F.; Orville, A. M. *Biochemistry* **2006**, *45*, 1138–1150.
- (65) Valley, M. P.; Fitzpatrick, P. F. *J. Am. Chem. Soc.* **2004**, *126*, 6244–6245.
- (66) Feierberg, I.; Luzhkov, V.; Aqvist, J. *J. Biol. Chem.* **2000**, *275*, 22657–22662.

CT600371K

Validation of Molecular Dynamics Simulations of Biomolecules Using NMR Spin Relaxation as Benchmarks: Application to the AMBER99SB Force Field

Scott A. Showalter and Rafael Brüschweiler*

Department of Chemistry and Biochemistry and National High Magnetic Field Laboratory, Florida State University, Tallahassee, Florida 32306

Received January 5, 2007

Abstract: Biological function of biomolecules is accompanied by a wide range of motional behavior. Accurate modeling of dynamics by molecular dynamics (MD) computer simulations is therefore a useful approach toward the understanding of biomolecular function. NMR spin relaxation measurements provide rigorous benchmarks for assessing important aspects of MD simulations, such as the amount and time scales of conformational space sampling, which are intimately related to the underlying molecular mechanics force field. Until recently, most simulations produced trajectories that exhibited too much dynamics particularly in flexible loop regions. Recent modifications made to the backbone φ and ψ torsion angle potentials of the AMBER and CHARMM force fields indicate that these changes produce more realistic molecular dynamics behavior. To assess the consequences of these changes, we performed a series of 5–20 ns molecular dynamics trajectories of human ubiquitin using the AMBER99 and AMBER99SB force fields for different conditions and water models and compare the results with NMR experimental backbone N–H S^2 order parameters. A quantitative analysis of the trajectories shows significantly improved agreement with experimental NMR data for the AMBER99SB force field as compared to AMBER99. Because NMR spin relaxation data (T_1 , T_2 , NOE) reflect the combined effects of spatial and temporal fluctuations of bond vectors, it is found that comparison of experimental and back-calculated NMR spin-relaxation data provides a more objective way of assessing the quality of the trajectory than order parameters alone. Analysis of a key mobile β -hairpin in ubiquitin demonstrates that the dynamics of mobile sites are not only reduced by the modified force field, but the extent of motional correlations between amino acids is also markedly diminished.

1. Introduction

NMR spin relaxation spectroscopy and molecular dynamics (MD) computer simulations are both widely used tools to study the dynamics of biomolecules. Although both methods probe motions on the picosecond to nanosecond range, they are highly complementary in many aspects. Spin relaxation is sensitive to reorientational dynamics of the lattice functions of spin-relaxation active interactions, such as N–H bond vectors belonging to ^{15}N – ^1H magnetic dipole–dipole inter-

actions, while MD simulations provide information on the motions of all atoms of a biomolecule.^{1–4} Due to the strong dependence of the MD simulation on the applied force field and the computational protocol,⁵ validation of simulations against experimental data is critically important. NMR spin relaxation data reflect motional amplitudes and time scales of both overall tumbling and internal motions for many sites throughout a protein and are therefore excellently suited for this task.

Comparisons of MD simulations^{6–16} with NMR relaxation data typically focus on the generalized N–H S^2 order

* Corresponding author tel.: 850-644-1768; fax: 850-644-8281; e-mail: bruschweiler@magnet.fsu.edu.

parameter by Lipari and Szabo.^{17,18} S^2 is a measure of the spatial restriction of the N–H vector in a molecule-fixed frame that takes values between 0 (large amounts of motion) and 1 (no motion) and which can be extracted from longitudinal T_1 , transverse T_2 , and heteronuclear Overhauser effect (NOE) data. Due to the underlying spin physics, the experimental S^2 order parameters only report on motions that occur on time scales comparable to or faster than the overall tumbling correlation time τ_c of the biomolecule, which is typically in the low nanosecond range. Such comparisons between MD simulations and NMR relaxation have been hampered in two important ways. First, due to the limited available computer power, MD trajectories have typically been much shorter than the overall tumbling correlation time and therefore did only reflect a subset of motions observed in NMR relaxation experiments. Therefore, the computed order parameters were on average higher than the ones of longer simulations using the same force field. Second, computed order parameters belonging to loop regions were often found to be substantially lower than their experimental counterparts, raising questions about the adequacy of the applied computational protocols or force fields. It is important to note that because these two kinds of errors have the tendency to cancel each other at least partially, agreement between calculated and experimental S^2 values could be accidental without validating the quality of the force field itself.

At the same time, the development of simplified contact models led to the remarkably accurate prediction of S^2 profiles from average 3D structures relying on very few adjustable parameters.^{19–21} This shows that the problem is generally not rooted with local features of the structural model but rather with the MD force field itself.

The situation has started to change recently due to the availability of increased computer power and adjustments made to the force fields. A correction to the CHARMM C22 force field, called CMAP, was introduced, which modifies the potential of the backbone torsion angles φ and ψ .²² The use of this corrected force field was found to improve the overall agreement between MD-derived and experimental NMR order parameters of hen lysozyme, although some discrepancies remain.²³ A similar modification was introduced into the AMBER99 force field with the result that an implicit solvent trajectory of HIV-1 protease yielded dynamics in good agreement with experimental data for that system.²⁴ Improvements provided by the AMBER99SB force field at reproducing experimental order parameters have been further demonstrated for hen lysozyme and human ubiquitin.²⁵

As MD simulations now routinely exceed in length the overall tumbling correlation times τ_c , order parameters computed over the whole trajectory include motions that are too slow to affect in significant ways T_1 , T_2 , and NOE relaxation parameters. Because these motions would not be reflected in the experimental S^2 values, their effect on calculated S^2 values introduces a bias and makes the comparison of experimental and simulation results at the order parameter level not straightforward. In fact, recent residual dipolar coupling measurements suggest that ad-

ditional motions are present on nanosecond to millisecond time scales that are not reflected in relaxation-derived S^2 values. Therefore, as MD trajectories are increasing in length, a further drop in S^2 values, at least for some protein systems, is expected.

An alternative approach for assessing the quality of a protein MD trajectory directly compares experimental and predicted T_1 , T_2 , and NOE relaxation parameters by leaving out the S^2 order parameter comparison as an intermediate step.^{16,26–28} This approach requires both a proper description of internal motions as well as an accurate modeling of overall tumbling. A related approach directly compares spectral density components $J(\omega)$,¹⁶ whereby the extraction of spectral densities from the experiment requires additional experiments or makes additional assumptions.²⁹

Here, we report the results of molecular dynamics trajectories of the well-characterized protein ubiquitin computed in the AMBER software package,³⁰ using both the AMBER99³¹ and the modified AMBER99SB^{24,25} force fields. Several sets of experimental NMR spin relaxation data have been published for ubiquitin,^{32–36} making it a valuable model system for assaying the quantitative accuracy of the MD-derived NMR relaxation parameters. Ubiquitin has also been successfully used as a model system for the MD investigation of NMR relaxation active motion in the past, yielding fundamental insight into the nature of internal protein dynamics.^{34,37,38} More recently, a 0.2 μ s ubiquitin MD trajectory calculated using the GROMOS96 43a1 force field³⁹ was reported by Nederveen and Bonvin (referred to as the “NB trajectory” from here on) from which both order parameters and spin relaxation parameters were computed.²⁸ The results of the current work indicate that the modified AMBER99SB force field performs qualitatively better than previous force fields at reproducing experimental order parameters, and it yields NMR spin relaxation parameters in near-quantitative agreement with experimental values.

2. Materials and Methods

2.1. Molecular Dynamics Simulations. Explicit solvent MD trajectories were run using the AMBER 8.0 software package³⁰ with the AMBER99³¹ and the AMBER99SB^{24,25} force field under particle mesh Ewald periodic boundary conditions.⁴⁰ Two initial configurations were generated in which ubiquitin (PDB code 1UBQ)⁴¹ was solvated with 6080 water molecules represented with either the SPC or TIP3P model⁴² such that no solute atom was within 12 Å of a box edge. The four resulting systems (AMBER99 with SPC, AMBER99 with TIP3P, AMBER99SB with SPC, and AMBER99SB with TIP3P) were energy-minimized and heated to 50 K through 10 ps of canonical (NVT) MD, with a 2 fs time step and SHAKE constraints on bonds involving hydrogen atoms⁴³ followed by heating to 150 and 300 K in successive 20 ps steps under the same conditions. Next, the systems were allowed to equilibrate in a 50 ps isothermal–isobaric (NPT) simulation in order to equilibrate the solvent density. After this initial equilibration period, an additional 5.0 ns of production MD was performed on each of the four systems under NPT conditions, and separately, 5.0 ns of production MD was performed under NVT conditions. The

result was a set of eight 5.1 ns trajectories, spanning all combinations of the two force fields, two water models, and two production run conditions. Snapshots of each trajectory were stored to disk every 1.0 ps during both the equilibration and production periods. Finally, the AMBER99 and AMBER99SB trajectories computed under NPT conditions with the SPC water model were extended for a further 15.0 ns yielding final trajectories 20.1 ns in length. Superposition of the snapshots to remove the effects of overall translation and rotation was performed within the AMBER ptraj module by superimposing the backbone heavy atoms of residues 1–72, using the snapshot at the midpoint of the production run (2.5 or 10.0 ns) as the reference structure.

2.2. Correlations Functions and Order Parameters. Bloch–Wangsness–Redfield spin relaxation theory^{44–47} expresses spin-relaxation rates induced by reorientational motion in terms of the spectral density functions:

$$J(\omega) = 2 \int_0^\infty C(t) \cos(\omega t) dt \quad (1)$$

where $C(t)$ is the time correlation function of the lattice portion of the spin interaction causing relaxation. For the relaxation of ^{15}N spins in proteins, the relevant interactions are the magnetic dipole–dipole interaction with the covalently bonded proton spin and the ^{15}N chemical shielding anisotropy. The principal axes of the tensors describing these two interactions are assumed to be collinear and parallel with the ^{15}N – ^1H bond vector. For a protein in isotropic solution, the reorientational correlation function in eq 1 takes the form

$$C(t) = \langle P_2[\mathbf{e}_{\text{LF}}(\tau) \mathbf{e}_{\text{LF}}(\tau + t)] \rangle \quad (2)$$

where P_2 is the second Legendre polynomial [$P_2 = 1/2(3x^2 - 1)$], \mathbf{e}_{LF} is a unit vector collinear with the bond vector defined relative to the laboratory frame (LF), and the angular brackets indicate averaging over time τ .

The “model-free” formalism developed by Lipari and Szabo for parametrization of the functions described in eqs 1 and 2 requires that any internal motions of the interaction vector be separable from global tumbling of the molecule.^{17,18} For isotropic overall tumbling, eq 2 may then be factored as

$$C(t) = C_0(t) C_1(t) \quad (3)$$

where $C_0(t)$ and $C_1(t)$ describe global and internal reorientation, respectively, where the correlation function $C_0(t)$ is

$$C_0(t) = e^{-t/\tau_c} \quad (4)$$

where τ_c is the rank 2 correlation time for global tumbling. The internal correlation function is approximated by^{17,18}

$$C_1(t) = \langle P_2[\mathbf{e}(\tau) \mathbf{e}(\tau + t)] \rangle \cong S^2 + (1 - S^2) e^{-t/\tau_e} \quad (5)$$

where the unit vector \mathbf{e} is defined relative to a fixed internal frame. $C_1(t)$, which is normalized [$C_1(0) = 1$], decays with an effective correlation time (τ_e) to a plateau value S^2 , the square of the generalized order parameter. The angular brackets indicate averaging over time τ . S^2 represents the spatial restriction of the motion of the interaction vector and

is determined by^{17,18,48}

$$C_1(\infty) = S^2 = 1 - \frac{4\pi}{5} \sum_{m=-2}^2 \sigma_{Y_{2m}}^2 \quad (6)$$

where $\sigma_{Y_{2m}}^2$ are the variances of the normalized spherical harmonics of rank 2, $Y_{2m}[\theta(t), \varphi(t)]$, over the trajectory and $\theta(t)$ and $\varphi(t)$ are the polar angles representing the interaction vector relative to a fixed internal frame. Equation 5 is valid for monoexponentially decaying correlation functions with a correlation time faster than the overall tumbling correlation time τ_c or for multiexponential correlation functions with all correlation times much shorter than τ_c .

Recently, a general method for calculating NMR spin relaxation parameters from MD trajectories, known as isotropic reorientational eigenmode dynamics (iRED), was introduced.³⁸ In this method, the snapshots generated from the MD trajectory are treated analytically to yield an isotropic ensemble from which a covariance matrix \mathbf{M} is computed with elements

$$M_{ij} = \frac{1}{2} \langle 3(\mathbf{e}_{\text{LF},i} \mathbf{e}_{\text{LF},j})^2 - 1 \rangle \quad (7)$$

where $\mathbf{e}_{\text{LF},i}$ and $\mathbf{e}_{\text{LF},j}$ are the normalized bond vectors, taken from the same snapshot, and the brackets indicate averaging over all snapshots. Because eq 7 contains only inner products, M_{ij} is rotationally invariant; that is, it is valid in an arbitrary frame that makes no assumptions about separability between internal and overall tumbling motions. S^2 values can be computed from \mathbf{M} by solving the eigenvalue problem $\mathbf{M}|m\rangle = \lambda_m|m\rangle$ ($m = 1, \dots, N$, where $N =$ number of interaction vectors \mathbf{e}_m) and using³⁸

$$S^2 = 1 - \sum_{m=1}^{N-5} \lambda_m ||m\rangle_j|^2 \quad (8)$$

where the sum extends over the $N-5$ eigenvectors $|m\rangle$ corresponding to internal modes with eigenvalues λ_m (i.e., all eigenvectors except those with the five largest eigenvalues). Equation 8 provides a computationally efficient way to determine order parameters without requiring the explicit removal of overall tumbling from the trajectory.

2.3. Spectral Density Functions and Spin Relaxation.

To obtain an accurate estimate for τ_c from a MD trajectory, the trajectory’s length must exceed τ_c by at least 1–2 orders of magnitude, which poses a challenge even for modern computers. Moreover, MD simulations tend to significantly underestimate τ_c . Therefore, when constructing the overall correlation function $C(t)$ from the trajectory, it is often advantageous to first compute $C_1(t)$ from the trajectory and model $C_0(t)$ with a τ_c determined experimentally. $C_1(t)$ is computed using the left part of eq 5 after first removing overall tumbling by superimposing each snapshot with respect to a reference snapshot.

Once $C_1(t)$ is computed, it can be converted by Fourier transform (eq 1) into the spectral density function needed to calculate NMR spin relaxation parameters. For this purpose, it is convenient to fit the numerical correlation function to a set of exponentials, so that the spectral density function can

be expressed analytically as a sum of Lorentzians.²⁷ The internal correlation functions are computed for the interval $t = 0, \dots, 0.3T_{\text{MD}}$, where T_{MD} is the total length of the molecular dynamics trajectory. Each correlation function is then fit to a multiexponential function:²⁷

$$C_1(t) = A_0 + \sum_{k=1}^5 A_k e^{-t/\tau_k} \quad (9)$$

subject to the normalization condition that $\sum_j A_j = 1.0$ ($j = 0, \dots, 5$), $A_k \geq 0$, and $0 \leq \tau_k$ for all k . Because it captures the long correlation time behavior of $C_1(t)$, A_0 is analogous to S^2 from the Lipari–Szabo model (eq 5).

The best-fit parameters generated from fitting the MD correlation functions to eq 9 are used in combination with the experimental value of τ_c to calculate the spectral density function:

$$J(\omega) = \frac{A_0 2\tau_c}{1 + (\omega\tau_c)^2} + \sum_{k=1}^5 \frac{A_k 2\tau'}{1 + (\omega\tau')^2} \quad (10)$$

where $\tau' = \tau_c \tau_k / (\tau_c + \tau_k)$. The spectral density functions are then used to compute the NMR observables ^{15}N T_1 , ^{15}N T_2 , and the ^1H – ^{15}N NOE using the following well-known equations:⁴⁹

$$\frac{1}{T_1} = R_1 = d_{oo}[3J(\omega_{\text{N}}) + J(\omega_{\text{H-N}}) + 6J(\omega_{\text{N+H}})] + c_{oo}\omega_{\text{N}}^2 J(\omega_{\text{N}}) \quad (11)$$

$$\frac{1}{T_2} = R_2 = \frac{1}{2}d_{oo}[4J(0) + 3J(\omega_{\text{N}}) + J(\omega_{\text{H-N}}) + 6J(\omega_{\text{H}}) + 6J(\omega_{\text{N+H}})] + \frac{1}{6}c_{oo}\omega_{\text{N}}^2 [4J(0) + 3J(\omega_{\text{N}})] \quad (12)$$

$$\text{NOE} = 1 + \frac{\gamma_{\text{H}}}{\gamma_{\text{N}}}d_{oo}T_1[6J(\omega_{\text{H+H}}) - J(\omega_{\text{H-N}})] \quad (13)$$

where $d_{oo} = (1/20)(\mu_o/4\pi)^2(h/2\pi)^2 \gamma_{\text{H}}^2 \gamma_{\text{N}}^2 \langle r_{\text{NH}}^{-3} \rangle^2$, $c_{oo} = (1/15)\Delta\sigma^2$, μ_o is the vacuum permeability, h is Planck's constant, γ_{N} and γ_{H} are the gyromagnetic ratios of ^{15}N and ^1H , respectively, $r_{\text{NH}} = 1.02 \text{ \AA}$ is the N–H bond length, and $\Delta\sigma = -160 \text{ ppm}$ is the chemical shift anisotropy of ^{15}N in an amide group. ω_{N} , ω_{H} , $\omega_{\text{N+H}}$, and $\omega_{\text{H-N}}$ are the Larmor frequencies as well as their sum and difference in radians per second of ^{15}N and ^1H spins, respectively.

The quality of the agreement between experimental and calculated values of T_1 , T_2 , and NOE was assessed in a way that is independent of their relative magnitudes. For this purpose, we define a parameter Q_{P} in analogy to the Q value used for residual dipolar couplings:⁵⁰

$$Q_{\text{P}} = \frac{\left[\frac{1}{N} \sum_{i=1}^N (P_i^{\text{obs}} - P_i^{\text{pred}})^2 \right]^{1/2}}{\left[\frac{1}{N} \sum_{i=1}^N (P_i^{\text{obs}})^2 \right]^{1/2}} \quad (14)$$

where P^{obs} and P^{pred} are the experimentally and MD-derived values, respectively, of either the parameter set $P_{\text{T}} = T_1, T_2$,

and NOE or set $P_{\text{R}} = R_1, R_2$, and NOE, and the sum runs over the residues for which both experimental and MD data are available. For P_{T} , mobile residues with large T_1 and T_2 values are emphasized, whereas for P_{R} , the influence of these residues on Q is diminished.

2.4. Torsion Angle Correlations. As the AMBER99 and AMBER99SB force fields differ in their φ and ψ torsion angle potentials,²⁵ it is important to understand what (if any) influence the reparametrization has on the extent of correlated motions among these torsion angles. A complex covariance matrix \mathbf{C} can be defined with elements⁵¹

$$C_{k,l} = \text{cov}(\cos\theta_k, \cos\theta_l) + \text{cov}(\sin\theta_k, \sin\theta_l) + \text{icov}(\cos\theta_k, \sin\theta_l) - \text{icov}(\sin\theta_k, \cos\theta_l) \quad (15)$$

where $\text{cov}(f,g) = \langle f^*g \rangle - \langle f^* \rangle \langle g \rangle$, where f and g are functions of the torsion angles $\theta_{k,l}$ (φ and ψ for each residue). In contrast to $\text{cov}(\theta_k, \theta_l)$, eq 15 does not depend on the choice of the origin of the torsion angles θ_k and θ_l .

3. Results and Discussion

3.1. Overall Effects of the AMBER99 and AMBER99SB Force Fields.

Analysis of the ubiquitin molecular dynamics trajectories computed with both the AMBER99³¹ and the AMBER99SB^{24,25} force fields indicates that all simulations are stable over the course of the production runs. The backbone C^α atom root-mean-square difference (RMSD) of each snapshot with respect to the crystal structure (excluding the mobile C-terminal tail residues 73–76) shows that, after an initial equilibration period, each of the trajectories represents an ensemble with similar RMSD values. The RMSD traces for the AMBER99 and AMBER99SB trajectories with the SPC water model under NPT conditions, which will be discussed in greater detail below, are shown in Figure 1A. The C^α RMSDs of the individual residues, which provide site-specific information regarding the extent of motion sampled throughout the protein backbone, shows clear differences between these two trajectories (Figure 1B): the extent of fluctuations in several of the loops is larger with AMBER99 than with AMBER99SB. The rigidification of the backbone torsion angles φ and ψ in AMBER99SB²⁵ is also reflected in the average angular RMSDs of φ and ψ in the hairpin loop (residues 7–10), which decreases from 20.1° to 16.3° for AMBER99SB in an NPT simulation with SPC water, while the angular RMSD values for the secondary structural elements, which are intrinsically more rigid, remain unchanged at about 7 – 12° in both trajectories.

3.2. Comparison of Calculated Order Parameters with Experiment.

Order parameters computed from MD trajectories are commonly used as a metric for comparing dynamics found in experiments and simulations. Such comparison focuses on the spatial aspects of motion but does not provide direct information on agreement of the corresponding time scales. Besides the length of the trajectory, several factors in the simulation may influence the calculated order parameters including the force field, the choice of water model, and the choice to run NVT- or NPT-type dynamics. The impact of these factors was assessed by calculating a total of eight trajectories combining the AMBER99 or

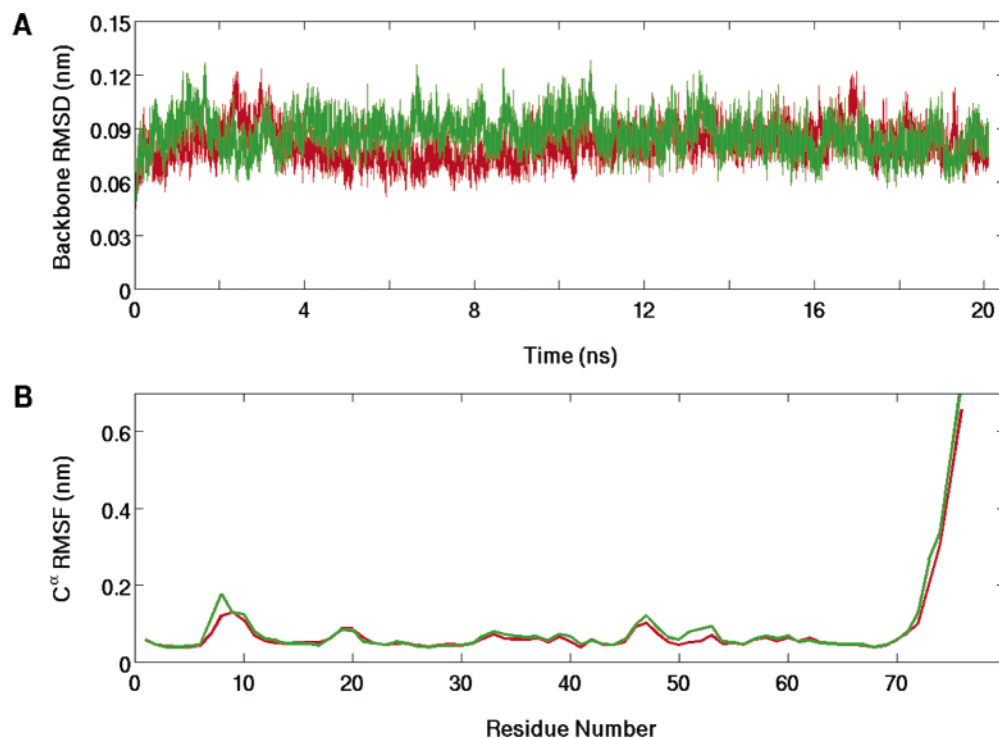


Figure 1. Backbone fluctuations over the 20 ns trajectories computed with AMBER99 (green) and AMBER99SB (red) under NPT conditions with SPC water. The backbone RMSD for all residues (A) is comparable between the two trajectories. The AMBER99 trajectory experiences larger fluctuations for many of the residues in mobile regions (B), although the backbone RMSD is similar for many residues of the most rigid regions of ubiquitin.

Table 1. Statistical Comparison of Order Parameters Calculated from Each of the 5 ns MD Trajectories with the Experimental Data Set³⁴

data set	R_p^a	R_s^b	RMSD ^c	$\langle S_{MD}^2/S_{NMR}^2 \rangle^d$
AMBER99, SPC, NPT	0.817	0.784	0.069	0.99 ± 0.11
AMBER 99, SPC, NVT	0.776	0.785	0.078	0.99 ± 0.12
AMBER 99, TIP3P, NPT	0.901	0.763	0.086	0.95 ± 0.15
AMBER 99, TIP3P, NVT	0.901	0.765	0.076	0.96 ± 0.12
AMBER 99SB, SPC, NPT	0.921	0.794	0.042	1.02 ± 0.05
AMBER 99SB, SPC, NVT	0.919	0.766	0.048	1.02 ± 0.07
AMBER 99SB, TIP3P, NPT	0.946	0.811	0.036	1.02 ± 0.04
AMBER 99SB, TIP3P NVT	0.964	0.826	0.044	1.01 ± 0.10
experimental set ³³	0.981	0.902	0.026	0.99 ± 0.05

^a Pearson's correlation coefficient between the simulation and the experimental set.³⁴ ^b Spearman's rank correlation coefficient between the simulation and the experimental set.³⁴ ^c Root-mean-square deviation between the simulation and the experimental set.³⁴ ^d Average is taken over all residues for which there are both MD and experimental data.

AMBER99SB force fields, with either the SPC or TIP3P water models, running either under NVT or NPT conditions. All eight trajectories combining these three parameter pairs were run for 5 ns of production dynamics and then analyzed to yield S^2 for each backbone N–H bond vector. The MD-derived order parameters are compared with the 61 experimentally determined values from Lienin et al.³⁴ used here as a reference. Statistics of the comparison are summarized in Table 1. In general, AMBER99SB trajectories have higher correlation coefficients, a lower RMSD, and a lower standard deviation in the S_{MD}^2/S_{NMR}^2 ratio than the corresponding AMBER99 trajectories, demonstrating that the AMBER99SB force field does a better job of reproducing experimental

order parameters. Although the statistics also indicate slightly better results for NPT conditions, the difference between NPT and NVT conditions is minimal compared to the difference caused by changing the force field. Comparing the results for the SPC and TIP3P water models suggests that the choice of water model has some, albeit small, effect on calculated order parameters.

While the agreement between the predicted S^2 values using AMBER99SB and the experimental results of Lienin et al. is overall good,³⁴ it is important to know if further improvements can realistically be expected. Tjandra et al.³³ have reported ubiquitin order parameters under conditions very similar to those of the Lienin et al.³⁴ data set. The bottom row of Table 1 shows that these two experimental data sets are well-comparable, reflecting good reproducibility and high quality, and they provide information about inherent uncertainties in experimentally derived order parameters. The correlation between the two experimental data sets is clearly higher than the correlation between the experimental data and the best MD-derived data set, which helps establish an upper limit for the agreement between simulations and experiments that can be expected under optimal circumstances.

The average S_{MD}^2/S_{NMR}^2 ratio (see the final column of Table 1) suggests that the AMBER99 trajectories slightly overestimate the dynamics of ubiquitin, while the AMBER99SB trajectories slightly underestimate them (although in both cases the difference from a 1:1 ratio is less than the standard deviation over the data set). Ratios less than one for the AMBER99 simulations are consistent with a body of literature reporting that MD trajectories based on

Table 2. Order Parameter Statistics as a Function of Trajectory Duration with Respect to the Experimental Set³⁴

data set	R_p^a	R_s^b	RMSD ^c	$\langle S_{MD}^2/S_{NMR}^2 \rangle^d$
AMBER 99, 500 ps	0.775	0.722	0.066	1.05 ± 0.16
AMBER 99, 1 ns	0.791	0.741	0.062	1.04 ± 0.14
AMBER 99, first 5 ns	0.817	0.784	0.069	0.99 ± 0.11
AMBER 99, second 5 ns	0.907	0.785	0.058	0.82 ± 0.11
AMBER 99, third 5 ns	0.730	0.760	0.071	1.01 ± 0.14
AMBER 99, fourth 5 ns	0.709	0.790	0.076	1.01 ± 0.16
AMBER 99, 10 ns	0.865	0.810	0.082	0.97 ± 0.11
AMBER 99, 20 ns	0.853	0.795	0.084	0.97 ± 0.12
AMBER 99SB, 500 ps	0.916	0.733	0.051	1.04 ± 0.06
AMBER 99SB, 1 ns	0.901	0.745	0.052	1.04 ± 0.07
AMBER 99SB, 5 ns	0.921	0.794	0.042	1.02 ± 0.05
AMBER 99SB, second 5 ns	0.942	0.801	0.042	1.03 ± 0.11
AMBER 99SB, third 5 ns	0.882	0.743	0.052	1.04 ± 0.07
AMBER 99SB, fourth 5 ns	0.808	0.760	0.060	1.04 ± 0.14
AMBER 99SB, first 10 ns	0.938	0.807	0.039	1.02 ± 0.05
AMBER 99SB, 20 ns	0.944	0.807	0.040	1.01 ± 0.07

^a Pearson's correlation coefficient between the simulation and the experimental set.³⁴ ^b Spearman's rank correlation coefficient between the simulation and the experimental set.³⁴ ^c Root-mean-square deviation between the simulation and the experimental set.³⁴ ^d Average is taken over all residues for which there are both MD and experimental data.

this and similar force fields often underestimate S^2 in loop regions.^{1,10,14–16,52}

The trajectories using the two force fields exhibit differences in their internal motional correlation times, and therefore the total length of the trajectory, T_{MD} , required to produce optimal agreement with experimental S^2 values is different for the two force fields. To demonstrate this effect, the order parameters were computed from the AMBER99 and AMBER99SB trajectories after 500 ps and 1, 5, 10, and 20 ns and compared against the experimental values (Table 2). The order parameters from the 20 ns AMBER99 and AMBER99SB trajectories are plotted as a function of the residue number, along with the experimental values of Lienin et al.³⁴ in Figure 2. For the relatively rigid sites ($S^2 \geq 0.85$), both the AMBER99 and AMBER99SB simulations tend to overestimate S^2 , regardless of the length of the trajectory, which results in $\langle S_{MD}^2/S_{NMR}^2 \rangle > 1.0$ (at least for short trajectories). A previously reported ubiquitin trajectory

calculated with the AMBER99SB force field did not display the baseline offset seen here, because the comparison was made against a different experimental data set with slightly higher order parameters, on average, for the rigid sites.^{25,33} Comparison against the Tjandra et al.³³ experimental values relieves the baseline offset but does not improve the quality of agreement otherwise (data not shown). On average, the GROMOS96 force field reproduces the order parameters of the rigid sites in ubiquitin quite well,²⁸ and the CHARMM C22/CMAP force field performs similarly well for the rigid sites of hen lysozyme.²³

By contrast, mobile regions of ubiquitin, such as the β -hairpin loop and several of the loops closer to the C-terminus of the protein, turn out to be too floppy in the AMBER99 simulation, whereas they tend to be in good agreement with experimental results in the AMBER99SB simulation (Figure 2). Plots of the AMBER99 order parameters computed after 1 and 20 ns correlated against the experimental data (Figure 3A and C) suggest that the 1 ns order parameters are the best result for the AMBER99 trajectory. This is in contrast to the AMBER99SB trajectory, which appears to improve by most of the applied statistical measures as the trajectory duration increases (Table 2 and Figure 3B,D).

Figure 2 shows that the order parameters for the mobile regions ($S^2 < 0.85$) clearly differ between the AMBER99 and AMBER99SB trajectories. While for both force fields these order parameters decrease as the total trajectory time increases (Figure 3), the rate of change is much larger for the AMBER99 force field than for AMBER99SB. Order parameters calculated over 20 ns show that the dynamics of the mobile regions are too unrestricted in the AMBER99 trajectory (Figures 2 and 3c). A similar behavior has been observed in the NB trajectory.²⁸

For AMBER99, it is clear from Table 2 and Figure 3A and C that the 1 ns trajectory does a better job of reproducing the dynamics of the mobile regions of ubiquitin than the longer trajectories. The continuous increase of the RMSD as the trajectory duration increases and the accompanying decrease in $\langle S_{MD}^2/S_{NMR}^2 \rangle$ dominated by the underestimated order parameters of the mobile regions indicates that the

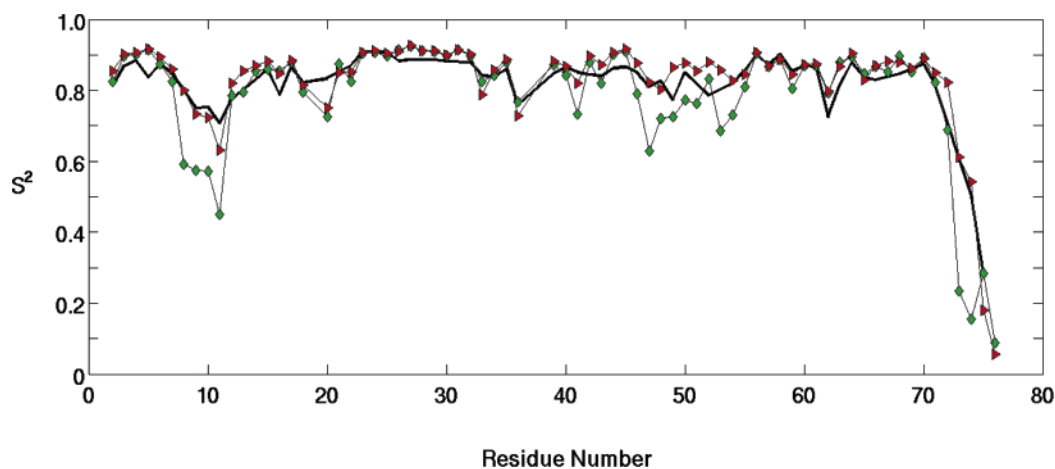


Figure 2. Ubiquitin backbone N–H bond order parameter profiles from 600 MHz NMR data (black line)³⁴ and iRED analysis of the 20 ns AMBER99 trajectory (green diamonds) and AMBER99SB (red triangles) trajectories.

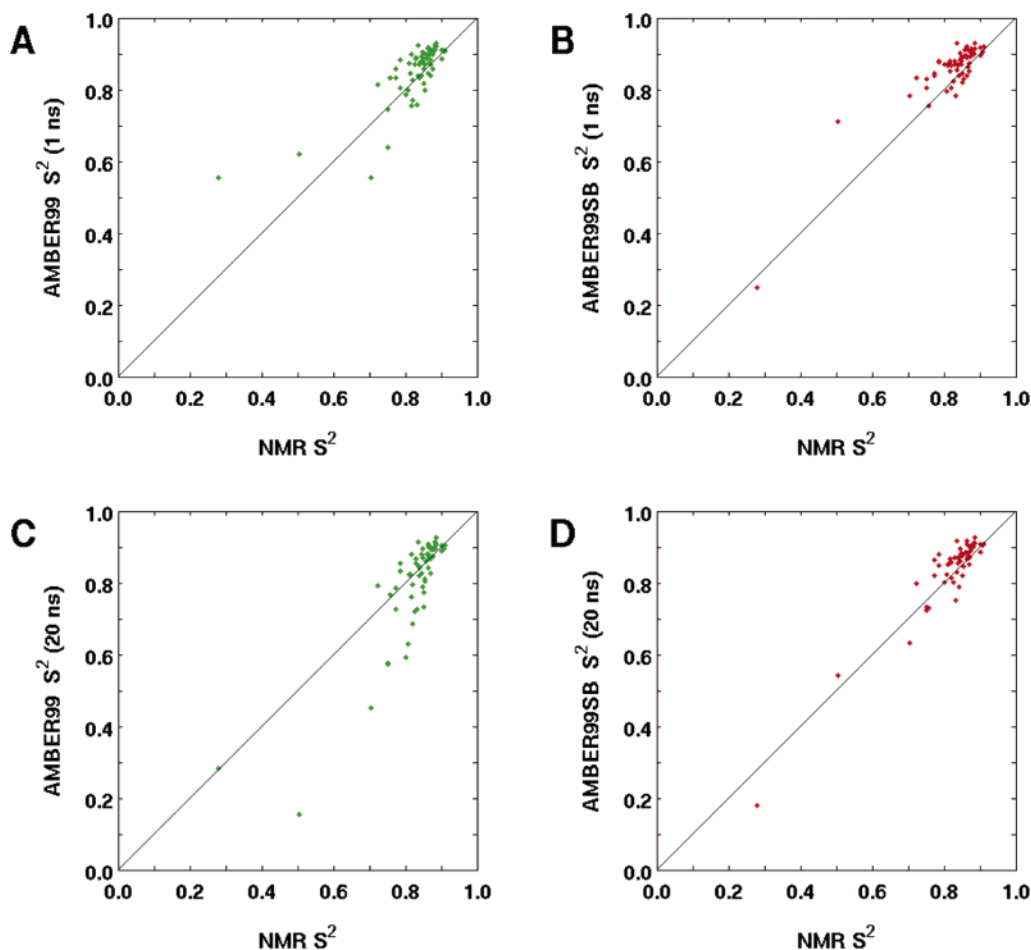


Figure 3. Ubiquitin backbone N–H bond order parameter correlation plots. Order parameters calculated from the AMBER99 trajectory at 1 ns (A), and 20 ns (C) and the AMBER99SB trajectory at 1 ns (B) and 20 ns (D) are correlated with the same experimentally derived data set in all panels.³⁴

problem lies with the force field itself rather than with poor sampling statistics, as is further demonstrated through the analysis of 10 ns subtrajectories of the AMBER99 simulation (see the Supporting Information). By contrast, it is clear from Figures 2 and 3D that the 20 ns AMBER99SB trajectory reproduces the dynamics of the mobile regions of ubiquitin well. This conclusion is supported by the decreasing RMSD and the approach of $\langle S_{\text{MD}}^2/S_{\text{NMR}}^2 \rangle$ to 1.0 (Table 2), by the similarity in the statistics from each of the four 5 ns subsets of the trajectory, and by more detailed analysis of 10 ns subtrajectories provided as Supporting Information.

This result is largely consistent with previously reported AMBER99SB ubiquitin and hen lysozyme simulations²⁵ and a hen lysozyme trajectory computed with the CHARMM C22/CMAP force field.²³ Both AMBER99SB and CHARMM C22/CMAP were produced from their parent force fields by adjusting the backbone φ and ψ torsion parameters, and the improvement at reproducing NMR order parameters indicates that these changes were made in the right direction. However, the question of whether these modified potentials properly sample the amplitudes and time scales of φ and ψ fluctuations on even longer time scales (tens of nanoseconds to milliseconds) cannot be addressed by comparison with spin-relaxation-derived S^2 values, which are insensitive to motions

with correlation times slower than global tumbling. They will have to be validated using experimental data that are sensitive to these motions, such as residual dipolar couplings.^{53–57}

3.3. Time-Correlation Functions and Relaxation Parameters. Time scales of internal dynamics can be extracted from reorientational correlation functions of each N–H bond vector calculated from a trajectory according to eq 2. For a well-sampled Markov process, the decay of the time-correlation function to a plateau is (multi)exponential. For a finite trajectory, only if a correlation function is well-converged does it approach a plateau value, which corresponds to the computed S^2 order parameter. Because the statistical error of a correlation function becomes often unacceptably large for times $t > T_{\text{MD}}/3$ (where T_{MD} is the total length of the trajectory), internal correlation functions $C_i(t)$ are computed here up to times $0.3T_{\text{MD}}$. Even then, there is a finite chance for the occurrence of rare events, for example, a local torsion angle transition, which can lead to the absence of a plateau in $C_i(t)$.

For the calculation of NMR relaxation data from a trajectory, high-quality correlation functions are required only for times $t \leq \tau_c$. Therefore, the presence of rare events is inconsequential for the NMR relaxation parameter calculation

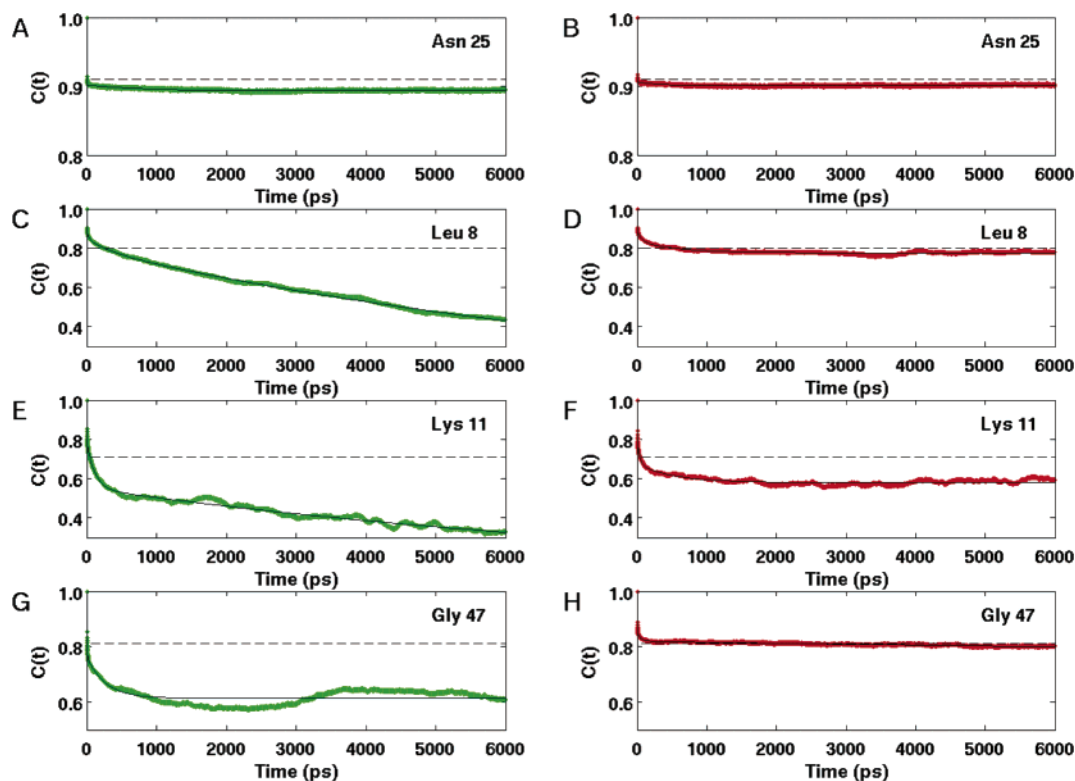


Figure 4. Ubiquitin backbone N–H bond correlation functions from the 20 ns AMBER99 trajectory (A, C, E, and G) and AMBER99SB trajectory (B, D, F, and H). The green line (AMBER99) and the red line (AMBER99SB) are the correlation functions computed from the trajectories, and the thin lines are the best fit to the correlation functions generated using eq 9. Best fit parameters for all correlation functions in this figure are presented in Table 3 (AMBER99) and Table 4 (AMBER99SB). The experimental order parameter³⁴ is represented as a dashed line in each panel for reference.

as long as the average recurrence time of such events significantly exceeds τ_c (4.1 ns for ubiquitin).

A set of 72 correlation functions $C_1(t)$ has been computed for $t \leq 6$ ns, corresponding to each of the 72 backbone ^{15}N – ^1H pairs for both 20 ns trajectories using AMBER99 and AMBER99SB. The correlation functions show different behaviors that can be subdivided into three distinct categories. The first category is exemplified by the correlation functions of Asn 25 (Figure 4A,B). They are characterized by an extremely rapid drop from $C_1(0) = 1$ to a value typically near 0.9, followed by a rapid convergence to a stable plateau value corresponding to S^2 . The very fast time-scale motions producing the initial decay reflect local librations. Their effect on spin relaxation rates is simply scaling by S^2 ; that is, the precise correlation times of these motions do not enter. Consequently, multiexponential fitting of these correlation functions to eq 9 yields only a few significantly nonzero τ_k and A_k values, with A_0 closely matching S^2 , as can be seen for Asn 25 in both the AMBER99 trajectory (Table 3) and the AMBER99SB trajectory (Table 4). Relaxation parameters of N–H bond vectors that exhibit this type of correlation function are rather well-reproduced by both the AMBER99 and the AMBER99SB trajectories.

The second category of correlation functions exhibits a rapid drop at the beginning, similar to that found for the first category, followed by decay with a correlations time $\gg 1$ ps to a plateau $S^2 \leq 0.85$. Examples of such correlation

functions are those of Leu 8 (Figure 4D), Lys 11 (Figure 4F), and Gly 47 (Figure 4H) from the AMBER99SB simulation.

The third category of correlation functions is characterized by substantial deviation from multiexponential decay behavior without a clear indication of convergence toward a plateau. Excluding the C-terminal tail, 15 correlation functions computed from the AMBER99 trajectory fall into this category (Leu 8, Thr 9, Gly 10, Lys 11, Ser 20, Ile 36, Gln 41, Ala 46, Gly 47, Lys 48, Gln 49, Leu 50, Gly 53, Arg 54, and Thr 55). All of these residues but Ile 36 display large errors in their order parameters (Figure 2). The only core domain residues in the AMBER99SB trajectory that fall into this category are Ser 20, which is also one of the residues with the worst predicted order parameter from this trajectory, and Gln 41, which also has a predicted order parameter below the experimental value.

The two categories of correlation functions reflecting significant internal mobility (categories 2 and 3) can be illustrated for residues 7–11, which form the loop region of the N-terminal β -hairpin. This is the most mobile region of ubiquitin, except for the C-terminal tail. Tables 3 and 4 include a summary of the fitting parameters for these residues from the AMBER99 and AMBER99SB trajectories, respectively. For all sites in this loop, A_0 is much lower than S^2 in the AMBER99 simulation, consistent with the absence of a plateau in the calculated correlation functions. Exponents with $\tau_k > 1.0$ ns are observed in these sites, contributing

Table 3. Exponential Fitting Parameters for the 20 ns AMBER99 Trajectory

residue number	A_0	A_1^a τ_1^b	A_2 τ_2	A_3 τ_3	A_4 τ_4	A_5 τ_5	$S^2(\text{NMR})^c$
7	0.733	0.103 11 387.104	0.025 192.394	0.006 192.392	0.027 12.236	0.107 0.013	0.850
8	0.000	0.792 9846.996	0.055 363.549	0.034 41.353	0.027 5.185	0.092 0.031	0.800
9	0.364	0.360 4201.172	0.000 1196.254	0.089 105.116	0.060 7.747	0.128 0.005	0.750
10	0.460	0.195 4109.661	0.000 3159.690	0.000 2904.702	0.125 126.644	0.219 0.015	0.750
11	0.078	0.474 9323.300	0.235 114.892	0.085 4.706	0.086 0.032	0.042 0.000	0.710
25	0.894	0.009 719.858	0.073 0.604	0.008 0.034	0.009 0.026	0.008 0.008	0.910
47	0.614	0.149 275.002	0.117 5.592	0.016 0.037	0.087 0.005	0.017 0.000	0.810

^a A_k are the amplitudes of the corresponding exponential contributions to the correlation function (eq 9). ^b Correlation times, τ_k , are given in units of picoseconds. ^c Lienin et al.³⁴

Table 4. Exponential Fitting Parameters for the 20 ns AMBER99SB Trajectory

residue number	A_0	A_1^a τ_1^b	A_2 τ_2	A_3 τ_3	A_4 τ_4	A_5 τ_5	$S^2(\text{NMR})^c$
7	0.854	0.005 340.465	0.024 340.446	0.004 340.446	0.022 21.858	0.091 0.019	0.850
8	0.775	0.008 589.888	0.006 587.012	0.048 586.469	0.056 59.368	0.108 0.014	0.800
9	0.693	0.002 879.298	0.006 879.071	0.077 39.568	0.149 0.002	0.000 0.000	0.750
10	0.693	0.005 470.807	0.004 470.333	0.037 469.508	0.084 22.166	0.176 0.007	0.750
11	0.580	0.003 540.833	0.090 539.761	0.001 539.701	0.131 36.031	0.195 0.028	0.710
25	0.901	0.006 269.870	0.068 0.603	0.008 0.034	0.009 0.014	0.008 0.002	0.910
47	0.778	0.042 9355.259	0.033 49.153	0.042 4.560	0.080 0.009	0.024 0.009	0.810

^a A_k are the amplitudes of the corresponding exponential contributions to the correlation function (eq 9). ^b Correlation times, τ_k , are given in units of picoseconds. ^c Lienin et al.³⁴

20% or more of the total amplitude of $C_1(t)$. In the examples of Leu 8 and Lys 11, a plateau is never actually reached due to the large amplitude contribution from low nanosecond time scale motion (Figure 4C, Table 3). While these motions have a notable effect on the calculated S^2 values, they are too slow to affect the relaxation parameters in a significant way. Therefore, the poor agreement between the spin relaxation parameters calculated from the AMBER99 trajectory and the experimental values (Figure 5) does not stem from these slower motions but, rather, from the large-amplitude motions on the subnanosecond time scale (note the presence of 100–400 ps τ_k associated with $A_k > 0.1$ for these residues in Table 3).

The behavior of the correlation functions for the β -hairpin vectors is quite different in the AMBER99SB trajectory, as is summarized in Table 4. Although the values of A_0 are still noticeably lower than the experimental order parameters for most sites, they are all much higher than those of the AMBER99 trajectory. Similar to the AMBER99 trajectory, the order parameter calculated for Lys 11 deviates significantly from its experimental value, despite the fact that its

correlation function is well-converged aside from being slightly noisier than some of the other correlation functions (Figure 4F). In addition to the influence of the underestimated order parameter, the discrepancy between back-calculated and experimental relaxation parameters for Lys 11 stems largely from the presence of a sizable 540 ps motional mode (Table 4), which is highly relaxation-active. Increasing the three τ_k of 540 ps to 2 ns without adjustment of any of the amplitudes A_k results in a reduction of the back-calculated T_1 from 618 to 582 ms and T_2 from 239 to 230 ms and increases NOE from 0.511 to 0.647. The agreement with the experimental values ($T_1 = 518$ ms, $T_2 = 205$ ms, and NOE = 0.608) is improved by this parameter adjustment, suggesting that the 540 ps motion dominating the back-calculated relaxation parameters in the simulation is absent in the experiment.

There are several sites outside of the β -hairpin which display significantly enhanced dynamics in the AMBER99 trajectory. The locations in primary sequence of residues with low order parameters in the AMBER99 trajectory and in the NB trajectory are similar but not identical (compare Figure

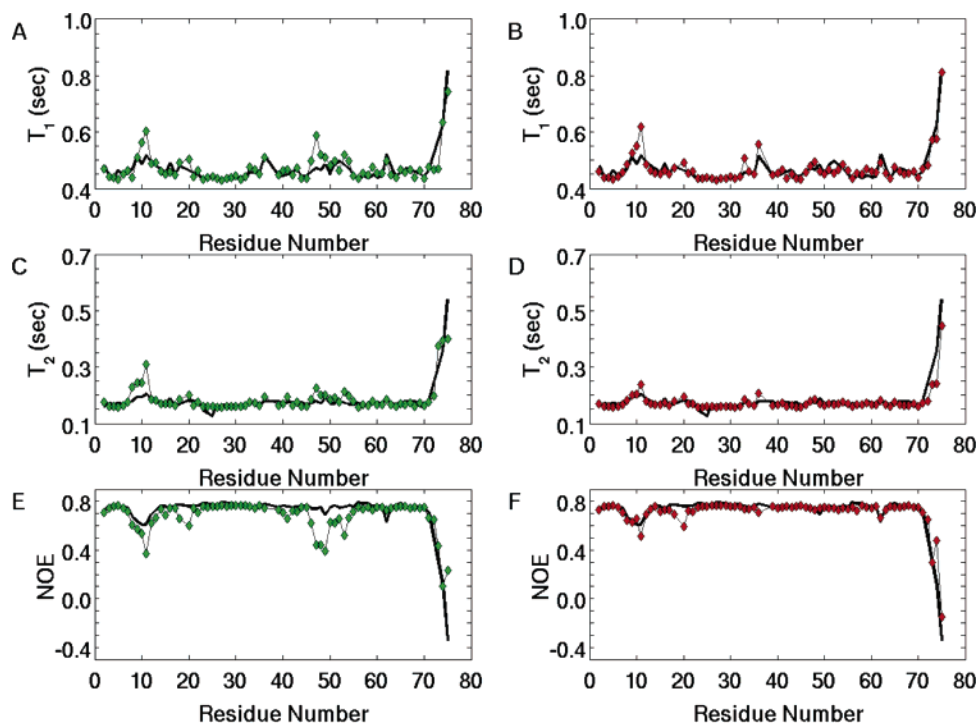


Figure 5. 600 MHz T_1 , T_2 , and NOE data predicted from the 20 ns AMBER99 (A, C, and E) and AMBER99SB (B, D, and F) trajectories. Computed values are displayed as green (AMBER99) or red (AMBER99SB) diamonds along with the experimental values³⁴ as a black line for reference.

2 with Figure 6 of ref 28), whereas the discrepancy between the MD and experimental order parameters of these sites is reduced or eliminated for all sites in the AMBER99SB trajectory. For example, the correlation function for Gly 41 (Figure 4G,H) and its fit parameters (Tables 3 and 4) indicate a significant change in dynamics caused by the change in force field. Gly 47 has a relatively high experimental order parameter ($S^2 = 0.81$),³⁴ which is very different from the value predicted from the AMBER99 simulation ($S^2 = 0.63$). In contrast, the correlation function from the AMBER99SB trajectory for Gly 47 rapidly converges to a stable asymptote (Figure 4H) and has a predicted order parameter of 0.82, in excellent quantitative agreement with experimental results ($S^2 = 0.81$).³⁴

Calculating ^{15}N T_1 and ^{15}N T_2 spin relaxation times and heteronuclear NOEs is a stringent test of an MD trajectory's quality, because it requires that both the amplitude and the time scales of spin-relaxation active motion be reproduced well. For this purpose, the fit parameters from the correlation functions are used to generate spectral densities $J(\omega)$ for each N–H bond vector along the ubiquitin backbone using eq 10. These spectral density functions are then used to calculate T_1 , T_2 , and NOE (eqs 11–13) for a magnetic field strength of 14.1 T, which corresponds to the field strength at which the reference data set was measured.³⁴ The results are shown in Figure 5. Note that residues 23–25 display chemical exchange contributions to T_2 which occur on the microsecond to millisecond time scale and are not modeled here.

On average, the AMBER99SB trajectory significantly better predicts T_1 , T_2 , and NOE than the AMBER99 trajectory (Table 5). At the level of individual residues, both the AMBER99 trajectory (Figure 5, left panels) and the AMBER99SB trajectory (Figure 5, right panels) show good

agreement with experimental results for most of the rigid residues found in secondary structural elements. However, it is again apparent that the dynamics of the β -hairpin loop (residues 7–10) and numerous other loops are severely overestimated in the AMBER99 trajectory, consistent with the order parameter analysis. The NB trajectory was also used to back-calculate the relaxation parameters of ubiquitin, and the authors found poor agreement in similar regions.²⁸ The AMBER99SB trajectory, on the other hand, reproduces the experimental relaxation times and heteronuclear NOEs well for most sites.

While the overall agreement between experimental and calculated values of T_1 , T_2 , and NOE is clearly higher for the AMBER99SB trajectory than for the AMBER99 trajectory, the different magnitudes of the individual parameters makes a quantitative comparison less straightforward. In analogy to the Q value used for residual dipolar couplings,⁵⁰ the parameters Q_T and Q_R presented in Table 5 (eq 14) allow direct quantitative comparison between the individual parameters, by renormalizing the RMSD to eliminate the influence of differences in parameter magnitudes. In general, Q_R is lower than Q_T because the influence of the C-terminal tail residues, which are less well-modeled even in the 20 ns AMBER99SB trajectory, is diminished in Q_R as compared to Q_T . This effect is seen most clearly by comparing RMSD, Q_T , and Q_R for the AMBER99SB trajectory.

The use of $Q_{T,R}$ demonstrates why comparison of simulation against experimental spin-relaxation times and heteronuclear Overhauser effects is a more objective measure of simulation quality than comparison with S^2 alone. Statistics and correlation plots (Table 2 and Figure 3) indicate that the 1 ns AMBER99 trajectory yields the highest-quality reproduction of the experimental order parameters of any

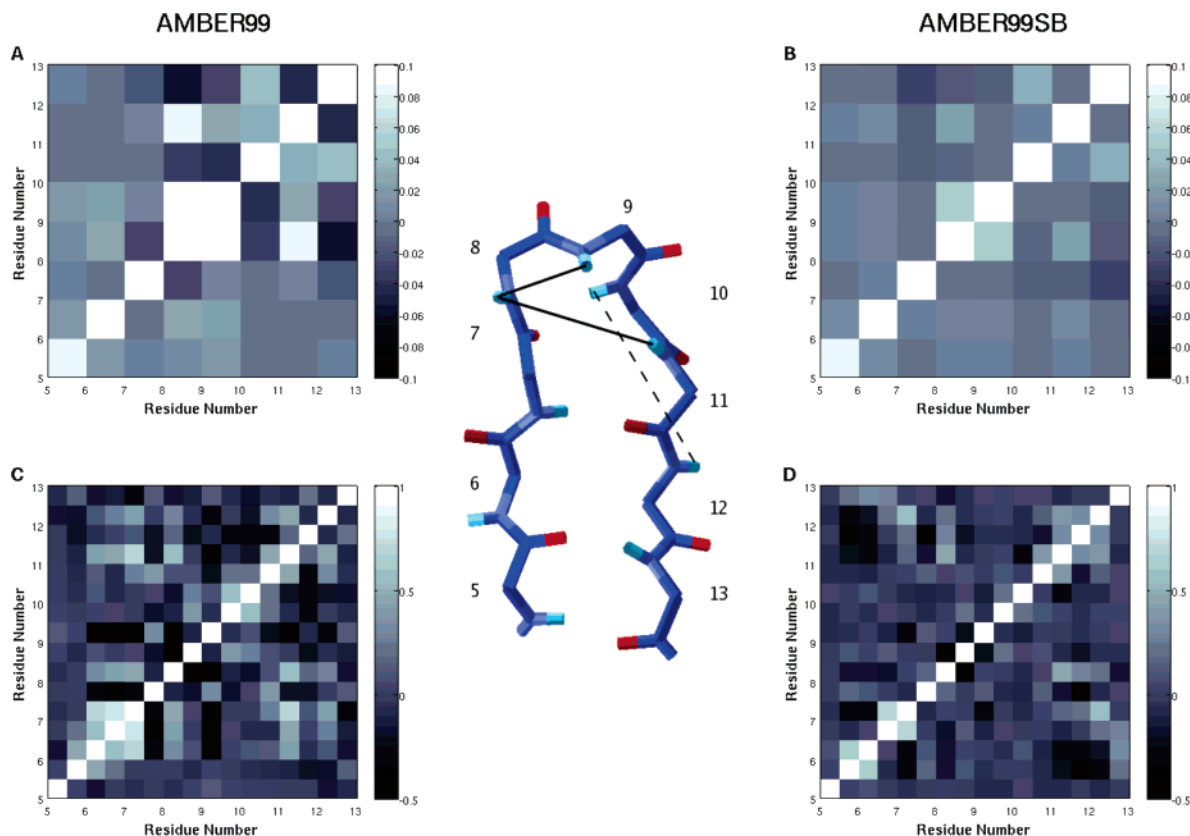


Figure 6. Internal motion correlations in the β -hairpin of ubiquitin (residues 5–12) from the 20 ns AMBER99 and AMBER99SB trajectories. Rank 2 reorientational motion of backbone N–H bond vectors is represented as the iRED covariance matrix for internal motion constructed only from the N-5 eigenvectors corresponding to internal motion for AMBER99 (A) and AMBER99SB (B). Correlations in the backbone φ and ψ torsion angles are represented by a cross-correlation matrix of the real part of eq 15 for AMBER99 (C) and AMBER99SB (D). The backbone structure diagram in the center of the figure displays the residues of the β -hairpin represented in panels A–D, with three key covariance interactions from the AMBER99SB iRED matrix mapped as solid lines (where the N–H bond vectors project out of the page) and a dashed line (where the N–H bond vectors project into the page). The imaginary part of the covariance matrix of eq 15 behaves similarly to the real part depicted in panels C and D.

Table 5. Spin Relaxation Times and Heteronuclear Overhauser Effects Calculated from the 20 ns AMBER99 and AMBER99SB Trajectories with Respect to the Experimental Data

data set ^a	R_p^b	R_s^c	RMSD ^d	Q_T^e	$(Q_R)^e$	$\langle \text{MD/NMR} \rangle^f$
AMBER99, T_1	0.866	0.744	0.029	0.061	(0.051)	1.016 ± 0.057
AMBER99, T_2	0.846	0.600	0.029	0.150	(0.091)	1.031 ± 0.118
AMBER99, NOE	0.747	0.659	0.119	0.173		0.900 ± 0.235
				$\Sigma = 0.384 (0.315)$		
AMBER99SB, T_1	0.913	0.729	0.024	0.050	(0.043)	1.006 ± 0.048
AMBER99SB, T_2	0.943	0.635	0.022	0.119	(0.062)	0.981 ± 0.072
AMBER99SB, NOE	0.938	0.517	0.066	0.091		1.030 ± 0.153
				$\Sigma = 0.260 (0.196)$		

^a Residues Ile 21 and Asn 25 are excluded from the calculation because of an exchange contribution to the experimental T_2 which would not be reproduced in the simulation. ^b Pearson's correlation coefficient between the simulation and the experimental set.³⁴ ^c Spearman's rank correlation coefficient between the simulation and the experimental set.³⁴ ^d Root-mean-square deviation between the simulation and the experimental set.³⁴ ^e Q value between the simulation and the experimental set calculated from eq 14. Values in parenthesis are calculated from R_1 , R_2 , and NOE. ^f Average is taken over all residues for which there is both MD and experimental data.

subtrajectory from that simulation, and yet the total Q_R for that trajectory ($Q_R = 0.453$) is clearly worse than that for the full 20 ns trajectory ($Q_R = 0.315$). This demonstrates that an order parameter comparison, while informative, does not provide a quantitative assessment of the quality of a trajectory because it ignores the potentially complex interplay between time scale and amplitude effects.

3.4. Dynamics of the β -Hairpin Loop. Having demonstrated that the AMBER99SB simulation reproduces well experimental order parameters, spin relaxation times, and heteronuclear Overhauser effects, the trajectory is used to study the dynamics of the turn of the β -hairpin near the N-terminus of ubiquitin in more detail. Application of the RED protocol, which is a variant of the iRED protocol used

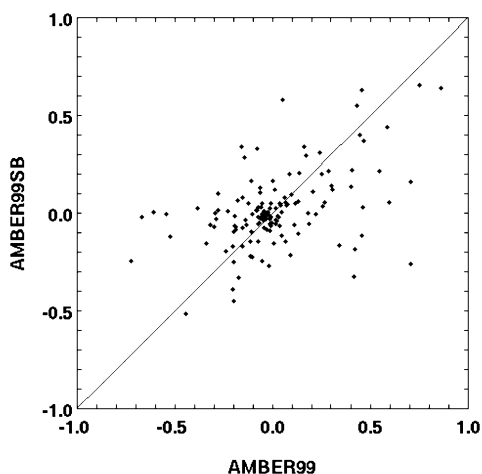


Figure 7. Comparison of torsion-angle correlation coefficients between β -hairpin matrices using AMBER99 (Figure 6C) and AMBER99SB (Figure 6D). The average correlation coefficients are 0.017 ± 0.270 for AMBER99 and 0.013 ± 0.196 for AMBER99SB. The linear correlation coefficient between the AMBER99 and the AMBER99SB correlations is $R_p = 0.48$.

in the present study, did previously show correlations in the reorientational motions of various residues in the β -hairpin loop including correlations between many of the backbone torsional degrees of freedom.³⁷ Optimization of a combined reorientational and torsional covariance matrix against experimental spin relaxation data resulted in a clear reduction of the amount of correlations among the torsional degrees of freedom.³⁷

Similarly to the previous study, both the portion of the iRED covariance matrix corresponding to internal reorientations of the β -hairpin and a matrix of correlation coefficients between the φ and ψ torsion angles for the same region constructed from the AMBER99 trajectory show significant (negative) correlations spanning the loop and its joining β strands (Figure 6A,C). In contrast, the same matrices computed from the AMBER99SB trajectory suggest lower correlations between these sites (Figure 6B,D). The matrices in Figure 6A and B are constructed by removing the eigenmodes corresponding to global reorientation from the total iRED covariance matrix, and their diagonal elements are proportional to $1 - S^2$ (eq 8). Figures 6 and 7 show that motional correlations are differentially altered and reduced on average in the AMBER99SB trajectory relative to the AMBER99 trajectory. Because it is difficult to experimentally quantify these motional correlations (off diagonal elements of the matrices in Figure 6), validation of the simulated correlations is not feasible at this time. Altered correlations are likely to have ramifications for estimating thermodynamic quantities, in particular, configurational entropies, from trajectories using AMBER99SB.

4. Conclusions

Comparison of MD simulations against NMR spin-relaxation data represents a rigorous quality test of MD simulation protocols and force fields. Presently available computational power enables routine calculation of molecular dynamics trajectories of biomolecules extending into the tens of

nanoseconds range. These simulations are reaching the point where they allow one to systematically assess and distinguish between finite conformational sampling effects and the accuracy of the force field itself.

Comparisons with NMR order parameters have long suggested that the amount of dynamics of protein loops are systematically overestimated in MD trajectories. Recent modifications of backbone potentials of both the CHARMM C22 force field and the AMBER99 force field produce significant improvements for both force fields.^{22–25} Due to the distinct sensitivity of the experimental NMR S^2 order parameters to the associated motional time scales, their usefulness as a comparison metric between simulation and relaxation data is somewhat limited. Many computed S^2 values depend on the duration of the trajectory with longer trajectories displaying on average lower computed order parameters. This is consistent with experimental evidence from residual dipolar couplings measured in multiple alignment media suggesting the presence of additional motions on nanosecond to millisecond time scales that are not captured by T_1 -type relaxation data.^{53,55–57} At present, such motions cannot be comprehensively probed by standard MD simulations; therefore, they will require other methods such as enhanced sampling techniques.

We demonstrate here that comparison directly against the “raw” relaxation parameters T_1 , T_2 , and NOE is complementary to and for fully quantitative purposes preferable over the use of S^2 parameters to assess the performance of MD simulations. Comparison based on relaxation parameters implicitly includes the complex time-scale effects of the motions on spin-relaxation parameters. While internal motional correlation times can be separately extracted from a model-free analysis^{17,18} or alternative treatments,⁵⁸ they are typically much less well-defined than the corresponding order parameters, and they also depend on the model selection procedure.⁵⁹

Because overall rotational tumbling is neither properly reproduced by current force fields nor properly sampled by trajectories in the tens of nanoseconds, a hybrid approach is used here that combines the experimentally derived overall tumbling correlation function $C_0(t)$ with the internal correlation function $C_1(t)$ calculated from the trajectory. A drawback of the method is that the relaxation parameters cannot be meaningfully predicted without accurate knowledge of the overall tumbling correlation time. However, if fit parameters using eq 9 to the internal correlation functions of MD trajectories were systematically reported in future simulations, such as the ones of Tables 3 and 4, relaxation parameters can be readily back-calculated once experimental relaxation data are available, either by using the experimentally determined overall tumbling correlation time, τ_c , or by treating τ_c as a fit parameter that optimizes agreement between the experiment and simulation. Such a procedure is a special case to the reporting of the dominant part of iRED eigenmodes together with their corresponding correlation times, from which the overall tumbling time can be modeled by fitting the correlation times of the five eigenmodes with the largest eigenvalues to the experimental data.³⁸ While in the present treatment isotropic overall tumbling is

assumed, which is adequate for ubiquitin,³³ it can be easily extended to axially symmetric or fully anisotropic overall tumbling motion.⁶⁰

We find that for ubiquitin the modified AMBER99SB force field is better at reproducing both the amplitude and time scale of spin-relaxation active internal motions than AMBER99. The overall reproduction of NMR relaxation times and the heteronuclear NOE, as well as NMR order parameters, using this force field is good, which includes the loop region of the N-terminal β -hairpin. The reduction in motional amplitudes is accompanied by both a slowdown of the intramolecular dynamics and a reduction of torsion angle correlations. Some discrepancies still remain with AMBER99SB, indicating that there is room for further improvement. Moreover, the rate of macromolecular global tumbling is systematically overestimated in MD simulations using most current water models, which will require improvements of the way explicit solvent water is modeled and how water molecules interact with the solute. Such advances would be particularly beneficial for assessing simulations of (partially) unfolded and disordered protein systems whose overall motion is not separable from internal dynamics and for which an internal order parameter is not defined any longer.^{38,61,62}

Acknowledgment. S.A.S. is the recipient of an NIH postdoctoral fellowship. This work was supported by the NSF (grant 0621482).

Supporting Information Available: The convergence of the 20 ns AMBER99 and AMBER99SB trajectories validated by detailed comparison of dynamics information generated from the first and the second half of each trajectory. This material is available free of charge via the Internet at <http://pubs.acs.org>.

References

- Case, D. A. Molecular Dynamics and NMR Spin Relaxation in Proteins. *Acc. Chem. Res.* **2002**, *35*, 325–331.
- Brüschweiler, R. New Approaches to the Dynamic Interpretation and Prediction of NMR Relaxation Data from Proteins. *Curr. Opin. Struct. Biol.* **2003**, *13*, 175–183.
- Palmer, A. G. NMR Characterization of the Dynamics of Biomacromolecules. *Chem. Rev.* **2004**, *104*, 3623–3640.
- Jarymowycz, V. A.; Stone, M. J. Fast Time Scale Dynamics of Protein Backbones: NMR Relaxation Methods, Applications, and Functional Consequences. *Chem. Rev.* **2006**, *106*, 1624–1671.
- Adcock, S. A.; McCammon, J. A. Molecular Dynamics: Survey of Methods for Simulating the Activity of Proteins. *Chem. Rev.* **2006**, *106*, 1589–1615.
- Chatfield, D. C.; Szabo, A.; Brooks, B. R. Molecular Dynamics of Staphylococcal Nuclease: Comparison of Simulation with N-15 and C-13 NMR Relaxation Data. *J. Am. Chem. Soc.* **1998**, *120*, 5301–5311.
- Chandrasekhar, I.; Clore, G. M.; Szabo, A.; Gronenborn, A. M.; Brooks, B. R., A 500-ps Molecular Dynamics Simulation Study of Interleukin-1 β in Water: Correlation with Nuclear Magnetic Resonance Spectroscopy and Crystallography. *J. Mol. Biol.* **1992**, *226*, 239–250.
- Palmer, A. G.; Case, D. A. Molecular Dynamics Analysis of NMR Relaxation in a Zinc Finger Peptide. *J. Am. Chem. Soc.* **1992**, *114*, 9059–9067.
- Wong, K. B.; Daggett, V. Barstar Has a Highly Dynamic Hydrophobic Core: Evidence from Molecular Dynamics Simulations and Nuclear Magnetic Resonance Relaxation Data. *Biochemistry* **1998**, *37*, 11182–11192.
- Stocker, U.; van Gunsteren, W. F. Molecular Dynamics Simulation of Hen Egg White Lysozyme: A Test of the GROMOS96 Force Field against Nuclear Magnetic Resonance Data. *Proteins: Struct., Funct., Genet.* **2000**, *40*, 145–153.
- Prompers, J. J.; Scheurer, C.; Brüschweiler, R. Characterization of NMR Relaxation-Active Motions of a Partially Folded A-State Analogue of Ubiquitin. *J. Mol. Biol.* **2001**, *305*, 1085–1097.
- Showalter, S. A.; Hall, K. B. A Functional Role for Correlated Motion in the N-Terminal RNA-Binding Domain of Human U1A Protein. *J. Mol. Biol.* **2002**, *322*, 533–542.
- Pang, Y.; Buck, M.; Zuiderweg, E. R. P. Backbone Dynamics of the Ribonuclease Binase Active Site Area Using Multi-nuclear (N-15 and (CO)-C-13) NMR Relaxation and Computational Molecular Dynamics. *Biochemistry* **2002**, *41*, 2655–2666.
- Philippopoulos, M.; Mandel, A. M.; Palmer, A. G.; Lim, C. Accuracy and Precision of NMR Relaxation Experiments and MD Simulations for Characterizing Protein Dynamics. *Proteins: Struct., Funct., Bioinf.* **1997**, *28*, 481–493.
- Radkiewicz, J. L.; Brooks, C. L. Protein Dynamics in Enzymatic Catalysis: Exploration of Dihydrofolate Reductase. *J. Am. Chem. Soc.* **2000**, *122*, 225–231.
- Pfeiffer, S.; Fushman, D.; Cowburn, D. Simulated and NMR-Derived Backbone Dynamics of a Protein with Significant Flexibility: A Comparison of Spectral Densities for the Beta ARK PH Domain. *J. Am. Chem. Soc.* **2001**, *123*, 3021–3036.
- Lipari, G.; Szabo, A. Model-Free Approach to the Interpretation of Nuclear Magnetic Resonance Relaxation in Macromolecules. 1. Theory and Range of Validity. *J. Am. Chem. Soc.* **1982**, *104*, 4546–4559.
- Lipari, G.; Szabo, A. Model-Free Approach to the Interpretation of Nuclear Magnetic Resonance Relaxation in Macromolecules. 2. Analysis of Experimental Results. *J. Am. Chem. Soc.* **1982**, *104*, 4559–4570.
- Zhang, F. L.; Brüschweiler, R. Contact Model for the Prediction of NMR N-H Order Parameters in Globular Proteins. *J. Am. Chem. Soc.* **2002**, *124*, 12654–12655.
- Ming, D. M.; Brüschweiler, R. Prediction of Methyl-Side Chain Dynamics in Proteins. *J. Biomol. NMR* **2004**, *29*, 363–368.
- Abergel, D.; Bodenhausen, G. Predicting Internal Protein Dynamics from Structures Using Coupled Networks of Hindered Rotators. *J. Chem. Phys.* **2005**, *123*, 204901.
- Mackerell, A. D. Empirical Force Fields for Biological Macromolecules: Overview and Issues. *J. Comput. Chem.* **2004**, *25*, 1584–1604.
- Buck, M.; Bouguet-Bonnet, S.; Pastor, R. W.; MacKerell, A. D. Importance of the CMAP Correction to the CHARMM22 Protein Force Field: Dynamics of Hen Lysozyme. *Biophys. J.* **2006**, *90*, L36–L38.

- (24) Hornak, V.; Okur, A.; Rizzo, R. C.; Simmerling, C. HIV-1 Protease Flaps Spontaneously Open and Reclose in Molecular Dynamics Simulations. *Proc. Natl. Acad. Sci. U.S.A.* **2006**, *103*, 915–920.
- (25) Hornak, V.; Abel, R.; Okur, A.; Strockbine, B.; Roitberg, A.; Simmerling, C. Comparison of Multiple AMBER Force Fields and Development of Improved Protein Backbone Parameters. *Proteins: Struct., Funct., Bioinf.* **2006**, *65*, 712–725.
- (26) Brüschweiler, R.; Roux, B.; Blackledge, M.; Griesinger, C.; Karplus, M.; Ernst, R. R. Influence of Rapid Intramolecular Motion on NMR Cross-Relaxation Rates: A Molecular Dynamics Study of Antamanide in Solution. *J. Am. Chem. Soc.* **1992**, *114*, 2289–2302.
- (27) Bremi, T.; Brüschweiler, R.; Ernst, R. R. A Protocol for the Interpretation of Side-Chain Dynamics Based on NMR Relaxation: Application to Phenylalanines in Antamanide. *J. Am. Chem. Soc.* **1997**, *119*, 4272–4284.
- (28) Nederveen, A. J.; Bonvin, A. M. J. J. NMR Relaxation and Internal Dynamics of Ubiquitin from a 0.2 μ s MD Simulation. *J. Chem. Theory Comput.* **2005**, *1*, 363–374.
- (29) Peng, J. W.; Wagner, G. Mapping of Spectral Density Functions Using Heteronuclear NMR Relaxation Measurements. *J. Magn. Reson.* **1992**, *98*, 308–332.
- (30) Case, D. A.; Cheatham, T. E.; Darden, T.; Gohlke, H.; Luo, R.; Merz, K. M.; Onufriev, A.; Simmerling, C.; Wang, B.; Woods, R. J. The AMBER Biomolecular Simulation Programs. *J. Comput. Chem.* **2005**, *26*, 1668–1688.
- (31) Wang, J. M.; Cieplak, P.; Kollman, P. A. How Well Does a Restrained Electrostatic Potential (RESP) Model Perform in Calculating Conformational Energies of Organic and Biological Molecules? *J. Comput. Chem.* **2000**, *21*, 1049–1074.
- (32) Schneider, D. M.; Dellwo, M. J.; Wand, A. J. Fast Internal Main Chain Dynamics of Human Ubiquitin. *Biochemistry* **1992**, *31*, 3645–3652.
- (33) Tjandra, N.; Szabo, A.; Bax, A. Protein Backbone Dynamics and N-15 Chemical Shift Anisotropy from Quantitative Measurement of Relaxation Interference Effects. *J. Am. Chem. Soc.* **1996**, *118*, 6986–6991.
- (34) Lienin, S. F.; Bremi, T.; Brutscher, B.; Brüschweiler, R.; Ernst, R. R. Anisotropic Intramolecular Backbone Dynamics of Ubiquitin Characterized by NMR Relaxation and MD Computer Simulation. *J. Am. Chem. Soc.* **1998**, *120*, 9870–9879.
- (35) Chang, S. L.; Tjandra, N. Temperature Dependence of Protein Backbone Motion from Carbonyl C-13 and Amide N-15 NMR Relaxation. *J. Magn. Reson.* **2005**, *174*, 43–53.
- (36) Ryabov, Y.; Fushman, D. Interdomain Mobility in Di-ubiquitin Revealed by NMR. *Proteins: Struct., Funct., Bioinf.* **2006**, *63*, 787–796.
- (37) Prompers, J. J.; Brüschweiler, R. Reorientational Eigenmode Dynamics: A Combined MD/NMR Relaxation Analysis Method for Flexible Parts in Globular Proteins. *J. Am. Chem. Soc.* **2001**, *123*, 7305–7313.
- (38) Prompers, J. J.; Brüschweiler, R. General Framework for Studying the Dynamics of Folded and Unfolded Proteins by NMR Relaxation Spectroscopy and MD Simulation. *J. Am. Chem. Soc.* **2002**, *124*, 4522–4534.
- (39) Daura, X.; Mark, A. E.; van Gunsteren, W. F. Parametrization of Aliphatic CHn United Atoms of GROMOS96 Force Field. *J. Comput. Chem.* **1998**, *19*, 535–547.
- (40) Darden, T.; York, D.; Pedersen, L. Particle Mesh Ewald - An $N \log(N)$ Method for Ewald Sums in Large Systems. *J. Chem. Phys.* **1993**, *98*, 10089–10092.
- (41) Vijaykumar, S.; Bugg, C. E.; Cook, W. J. Structure of Ubiquitin Refined at 1.8 Å Resolution. *J. Mol. Biol.* **1987**, *194*, 531–544.
- (42) Jorgensen, W. L.; Chandrasekhar, J.; Madura, J. D.; Impey, R. W.; Klein, M. L. Comparison of Simple Potential Functions for Simulating Liquid Water. *J. Chem. Phys.* **1983**, *79*, 926–935.
- (43) Ryckaert, J. P.; Ciccotti, G.; Berendsen, H. J. C. Numerical Integration of Cartesian Equations of Motion of a System with Constraints: Molecular Dynamics of n-Alkanes. *J. Comput. Phys.* **1977**, *23*, 327–341.
- (44) Wangsness, R. K.; Bloch, F. The Dynamical Theory of Nuclear Induction. *Phys. Rev.* **1953**, *89*, 728–739.
- (45) Bloch, F. Dynamical Theory of Nuclear Induction 2. *Phys. Rev.* **1956**, *102*, 104–135.
- (46) Redfield, A. G. On the Theory of Relaxation Processes. *IBM J. Res. Dev.* **1957**, *1*, 19–31.
- (47) Redfield, A. G. The Theory of Relaxation Processes. *Adv. Magn. Reson.* **1965**, *1*, 1–32.
- (48) Brüschweiler, R.; Wright, P. E. NMR Order Parameters of Biomolecules - A New Analytical Representation and Application to the Gaussian Axial Fluctuation Model. *J. Am. Chem. Soc.* **1994**, *116*, 8426–8427.
- (49) Abragam, A. *Principles of Nuclear Magnetism*; Clarendon Press: Oxford, U. K., 1961.
- (50) Ottiger, M.; Bax, A. Bicelle-Based Liquid Crystals for NMR-Measurement of Dipolar Couplings at Acidic and Basic pH Values. *J. Biomol. NMR* **1999**, *13*, 187–191.
- (51) Wang, J.; Brüschweiler, R. 2D Entropy of Discrete Molecular Ensembles. *J. Chem. Theory Comput.* **2006**, *2*, 18–24.
- (52) Smith, L. J.; Mark, A. E.; Dobson, C. M.; van Gunsteren, W. F. Comparison of MD Simulations and NMR Experiments for Hen Lysozyme: Analysis of Local Fluctuations, Cooperative Motions, and Global Changes. *Biochemistry* **1995**, *34*, 10918–10931.
- (53) Blackledge, M. Recent Progress in the Study of Biomolecular Structure and Dynamics in Solution from Residual Dipolar Couplings. *Prog. Nucl. Magn. Reson. Spectrosc.* **2005**, *46*, 23–61.
- (54) Bax, A.; Grishaev, A. Weak Alignment NMR: A Hawk-Eyed View of Biomolecular Structure. *Curr. Opin. Struct. Biol.* **2005**, *15*, 563–570.
- (55) Meiler, J.; Prompers, J. J.; Peti, W.; Griesinger, C.; Brüschweiler, R. Model-Free Approach to the Dynamic Interpretation of Residual Dipolar Couplings in Globular Proteins. *J. Am. Chem. Soc.* **2001**, *123*, 6098–6107.
- (56) Bouvignies, G.; Bernado, P.; Meier, S.; Cho, K.; Grzesiek, S.; Brüschweiler, R.; Blackledge, M. Identification of Slow Correlated Motions in Proteins Using Residual Dipolar and Hydrogen-Bond Scalar Couplings. *Proc. Natl. Acad. Sci. U.S.A.* **2005**, *102*, 13885–13890.
- (57) Tolman, J. R.; Ruan, K. NMR Residual Dipolar Couplings as Probes of Biomolecular Dynamics. *Chem. Rev.* **2006**, *106*, 1720–1736.

- (58) Meirovitch, E.; Shapiro, Y. E.; Polimeno, A.; Freed, J. H. Protein Dynamics from NMR: The Slowly Relaxing Local Structure Analysis Compared with Model-Free Analysis. *J. Phys. Chem. A* **2006**, *110*, 8366–8396.
- (59) Mandel, A. M.; Akke, M.; Palmer, A. G. Backbone Dynamics of *Escherichia coli* Ribonuclease H1: Correlations with Structure and Function in an Active Enzyme. *J. Mol. Biol.* **1995**, *246*, 144–163.
- (60) Woessner, D. Nuclear Spin Relaxation in Ellipsoids Undergoing Rotational Brownian Motion. *J. Chem. Phys.* **1962**, *37*, 647–654.
- (61) Brutscher, B.; Brüschweiler, R.; Ernst, R. R. Backbone Dynamics and Structural Characterization of the Partially Folded A State of Ubiquitin by H-1, C-13, and N-15 Nuclear Magnetic Resonance Spectroscopy. *Biochemistry* **1997**, *36*, 13043–13053.
- (62) Dyson, H. J.; Wright, P. E. Unfolded Proteins and Protein Folding Studied by NMR. *Chem. Rev.* **2004**, *104*, 3607–3622.

CT7000045

Dependence of Spurious Charge-Transfer Excited States on Orbital Exchange in TDDFT: Large Molecules and Clusters

R. J. Magyar

NIST Center for Theoretical and Computational Nanosciences (NCTCN), Gaithersburg, Maryland 20899, and Theoretical Division, Los Alamos National Laboratory, Los Alamos, New Mexico 87545

S. Tretiak*

Theoretical Division and Center for Nonlinear Studies, Los Alamos National Laboratory, Los Alamos, New Mexico 87545

Received September 9, 2006

Abstract: Time-dependent density functional theory (TDDFT) is a powerful tool allowing for accurate description of excited states in many nanoscale molecular systems; however, its application to large molecules may be plagued with difficulties that are not immediately obvious from previous experiences of applying TDDFT to small molecules. In TDDFT, the appearance of spurious charge-transfer states below the first optical excited state is shown to have significant effects on the predicted absorption and emission spectra of several donor–acceptor substituted molecules. The same problem affects the predictions of electronic spectra of molecular aggregates formed from weakly interacting chromophores. For selected benchmark cases, we show that today’s popular density functionals, such as purely local (Local Density Approximation, LDA) and semilocal (Generalized Gradient Approximation, GGA) models, are qualitatively wrong. Nonlocal hybrid approximations including both semiempirical (B3LYP) and ab initio (PBE1PBE) containing a small fraction (20–25%) of Fock-like orbital exchange are also susceptible to such problems. Functionals that contain a larger fraction (50%) of orbital exchange like the early hybrid (BHandHLYP) are shown to exhibit far fewer spurious charge-transfer (CT) states at the expense of accuracy. Based on the trends observed in this study and our previous experience we formulate several practical approaches to overcome these difficulties providing a reliable description of electronic excitations in nanosystems.

I. Introduction

Density functional theory (DFT) is one of the most promising tools to provide an accurate yet computationally feasible electronic-structure theory for large nanoscale systems, and the time-dependent extension of DFT (TDDFT) makes possible perhaps the only first principles approach to access

the optical properties of large molecular systems containing hundreds of atoms.^{1–3} Combined the two have been successful in determining ground-state geometries, vibrational spectra, and photoexcitations of many small molecules.^{4,5} These days, accurate measurements are now readily available through various absorption and emission time- and frequency-resolved spectroscopies even for large molecular systems and their assemblies. The understanding and controlled manipulation of optical properties of nanoscale molecular clusters

* Corresponding author e-mail: serg@lanl.gov.

may lead to many technological applications such as light-harvesting and photovoltaic devices^{6,7} and precision chemo- and biosensors^{8,9} to name just a few. Several comprehensive reviews of quantum-chemical methodology for UV–visible spectra of large molecules has been published recently (e.g. refs 10 and 11). So there is a clear need to apply TDDFT here.

Density functional theory formally permits the expression of the total ground-state energy and other properties of a quantum many-body system as functionals of the electron density alone and provides a formally exact scheme for solving the many-body problem.¹² TDDFT is an extension of density functional theory in which many-body excitations are associated with the poles of the exact density response.^{3,13,14} Practical density functionals are approximate and typically make use of an auxiliary orbital-based Kohn–Sham (KS) scheme in which the kinetic energy contribution of the total energy is expressed as an orbital functional. The only contribution to the total energy that must be approximated is the exchange–correlation contribution. This contribution is often approximated by functionals which depend on the electronic density locally (Local Density Approximation, LDA) or semilocally (Generalized Gradient Approximation, GGA) in a way convenient for calculations. However, more accurate functionals require further long-range information about the density which is contained in the Kohn–Sham orbitals. A step toward a general orbital exchange–correlation functional is the exact-exchange (EXX) which has recently become popular in the solid state-physics community. Results within EXX should exhibit both the proper asymptotic behavior for the effective potential, $\sim 1/r$ for finite systems, and a derivative discontinuity as the number of particles changes through integer values. Properly describing these could mean more accurate band-gaps and optical spectra. We note too that long-range effects will become important when treating the excited states of the jellium model. These problems are discussed in detail in refs 14–16.

Orbital exchange in the DFT formalism is the exact orbital contribution of exchange to the exchange–correlation functional and can be written as a Fock-like integral over the KS orbitals.^{17,18} The rewards for using orbital exchange are tempting and include more realistic potentials, better decaying KS orbitals, and more accurate excited states. However, extracting the local potential and its derivative kernel from this exact-exchange functional is difficult and in practice, is often done approximately by replacing the local exact-exchange potential by a nonlocal Hartree–Fock exchange. All current routine applications of TDDFT are based on the adiabatic approximation, where the memory effects in the time-dependent density evolution are neglected.^{19,20} The adiabatic approximation, for example, makes it impossible to describe highly correlated electronic states such as those having predominantly *double* character.²¹ It has been argued that omission of nonadiabatic effects is also solely responsible for the charge-transfer problems.²² In this paper, we show that long-range orbital-based exchange improves upon the semilocal approximations when describing charge-transfer states. This can be rationalized by noting that the hybrid

TDDFT kernel constitutes a specific case of nonadiabatic approximation.²³

One of the greatest challenges to the universal applicability of practical TDDFT is the inability of popular density functionals (and their kernels) to routinely and accurately describe certain excitations with a long-range spatial extent.^{24–27} For example, charge-transfer (CT) states correspond to excited states in which the photoexcited hole and electron do not greatly overlap due to incorrect long-range functional asymptotics and the missing discontinuity of the approximate xc-potentials with respect to particle number. Subsequently, TDDFT often predicts charge-transfer states of substantially lower energy and below optical states. A heuristic way to understand this is to consider the KS orbital excitations as zeroth-order approximations to the true excitations of the system. The TDDFT linear response formalism can be thought of as the inclusion of an effective mixing determined by the exchange–correlation kernel between the pair of occupied and unoccupied KS orbitals that constitutes the excited state. With the most commonly used approximate kernels, such as LDA and GGA models, many bound exciton states are not described at all.^{27,28} This is because the kernel is local and the orbital overlap is negligible. This problem is further complicated by the neglect of an important derivative discontinuity in most functionals. This results in a mismatch of ionization potentials between the donor and acceptor portions of molecule.²⁹ Thus, the energies of CT states are frequently so significantly lower than what they should be that these states often become the lowest energy states in calculated electronic spectra.

These TDDFT shortcomings have been well identified and explored in the case of small molecular systems and local approximations. In this work, we explore how DFT's predictive power changes when we simulate the ground and excited states of larger molecules and aggregates. In particular, we investigate the appearance of low-lying unphysical CT states which depends on the choice of density functional. We first focus on ground- and excited-state geometries in the substituted molecules. Such calculations constitute a common approach to investigate the coupling of electronic and vibrational degrees of freedom (frequently quantified as Frank–Condon overlaps) and to calculate spectroscopically observed vibrational structure in absorption and fluorescence spectral line shapes.^{30,31} We next study electronic interactions mediated by aggregation in molecular assemblies. Computation of small molecular aggregates is a typical technique to determine interchromophore interactions in molecular assemblies.^{32–34} This allows determination of aggregation type (H or J) and electronic coupling energies. The calculated information is useful for building reduced Frenkel exciton models, for example, one for Light-Harvesting Complex II (LHCII).^{35,36} Such tasks extend well beyond a standard *simple* case of ground-state geometry optimizations followed by excited-state calculations and constitute the area where the performance of TDDFT has not been consistently tested yet.

We chose representative molecules with properties that could be useful for several important technological applications: donor–donor and donor–acceptor substituted molecules and aggregates of thiophene oligomers and bacteri-

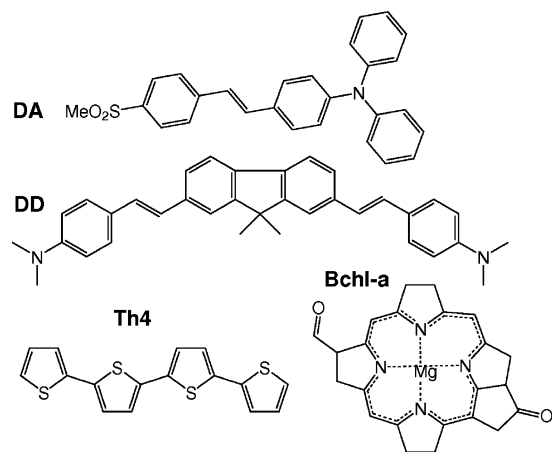


Figure 1. Chemical diagrams of the molecules studied: donor–acceptor (**DA**) and donor–donor (**DD**) substituted chromophores, thiophene oligomer (**Th4**), and bacteriochlorophyll *a* (**Bchl-a**).

ochlorophylls. Substituted organic chromophores are promising candidates in several areas, such as nonlinear optical response applications.^{37,38} The thiophenes have been exploited for applications in organic electronics related to novel display, photovoltaic, and lighting technologies.^{39,40} Finally, the chlorophylls constitute the main pigment in the biological photosynthetic light-harvesting complexes.^{35,36} Previous theoretical work within DFT on some of these systems has been carried out within the DFT formalism for donor–acceptor molecules,^{41,42} thiophenes,⁴³ and bacteriochlorophylls.^{44,45} Here our calculations examine the qualitative and quantitative aspects of TDDFT for excited-state molecular electronic structures. The results are compared for several commonly used functionals with varying fractions of Hartree–Fock (HF) exchange as implemented in standard quantum chemical packages. By tuning the fraction of HF exchange we hope to gain insight into how the orbital dependence of the exchange function affects the description of electronic excited states.

Details of our numerical modeling are presented in section II. In section III we analyze computational results obtained via different DFT approximations. Finally, we discuss the trends that emerge and summarize our findings in section IV.

II. Computational Methodology

Figure 1 shows the chemical structures of the molecules considered, including donor–acceptor **DA** ((E)-4-(4-(methylsulfonyl)styryl)-N,N-diphenylbenzenamine) and donor–donor **DD** (4,4'-[(1E,1'E)-2,2'-(biphenyl-4,4'-diyl) bis(ethene-1,1'-diyl)]bis(N,N-dimethylbenzenamine)) substituted molecules, thiophene oligomer (**Th4**), and bacteriochlorophyll-*a* (**Bchl-a**).

Ground-state geometry optimizations of the charge-neutral, singlet states of the substituted molecules have been done with the Turbomole program suite.⁴⁶ The lowest excited-state geometries were obtained next using Turbomole as well. This code is able to search for a minimum over the TDDFT excitation energy surface with respect to nuclear coordinates using analytic gradient techniques.⁴⁷ All optimizations were

performed in the gas phase using the SV basis set and one of a set of density functionals; see below. The SV and similar 6-31G basis sets are known to be an efficient blend of accuracy and manageable size for large conjugated molecules.⁴⁸ For the thiophenes and chlorophyll calculations we used geometries extracted from the experimental X-ray crystallographic data.^{49,50} In addition to the single molecule limit, we consider thiophene dimers (**2Th4**) generated from the coordinates of two nearest neighbor pairs in the unit cell.⁴⁹ For the single molecules, two **Th4** geometries exist in the crystal structure. One structure is slightly more elongated. The calculated excited-state spectra are essentially identical for both geometries. Similarly, the coordinates of $\alpha\beta$ Bchls-*a* pair (**2Bchl-a**) have been extracted from *Rs. molischianum* crystal data.⁵⁰ At the obtained geometries we calculate corresponding excited-state structures up to 20 lowest excited states using the Gaussian 03 package⁵¹ with a 6-31G basis set and density functionals corresponding to the methods used for geometry optimizations (unless specified otherwise).

We use several common density functionals with various fractions of orbital exchange, namely HF (100%), BHandHLYP (50%), PBE1PBE (25%), B3LYP (20%), TPSS–H (10%), TPSS (0%), BP86 (0%), and SVWN (0%). The set represents a gradual decreasing fraction of exchange. The treatments of correlation in each functional are not comparable and do not scale with the given fractions of exchange; however, the effects of correlation are assumed to be smaller than the relative error in the exchange amount. General trends seen as a function of the fraction of orbital exchange should persist regardless of the details of the correlation functional. We expect that functionals, including exchange, are less dramatically affected by CT problems. However, when the fraction of exchange becomes large, these functionals typically provide less accurate energetics because the cancellation of errors between exchange and correlation is reduced.⁵² For example, the BHandHLYP functional⁵³ combines semilocal exchange–correlation with orbital exchange in a 50–50 ratio. By construction, this functional handles a large fraction of long-range exchange exactly but fails to describe correlation in a compatible way.

To interpret computational trends we use a transition orbital analysis, which allows precise identification and visualization of the electronic excitations in question.⁵⁴ These transition orbitals provide a graphical real-space representation of the transition densities associated with the molecular electronic excitations computed with TDDFT. This analysis offers the most compact description of a given transition density in terms of its expansion in single KS transitions. The Gaussian 03 code was locally modified to be able to perform the transition orbital analysis.

III. Results and Discussion

Through a series of benchmark calculations, we highlight the difficulties appearing when we apply TDDFT to molecular systems of sizes important to nanoscale applications. An important issue with using TDDFT for larger molecular systems is the introduction of spurious low-energy CT states. In the following subsections, we investigate several fre-

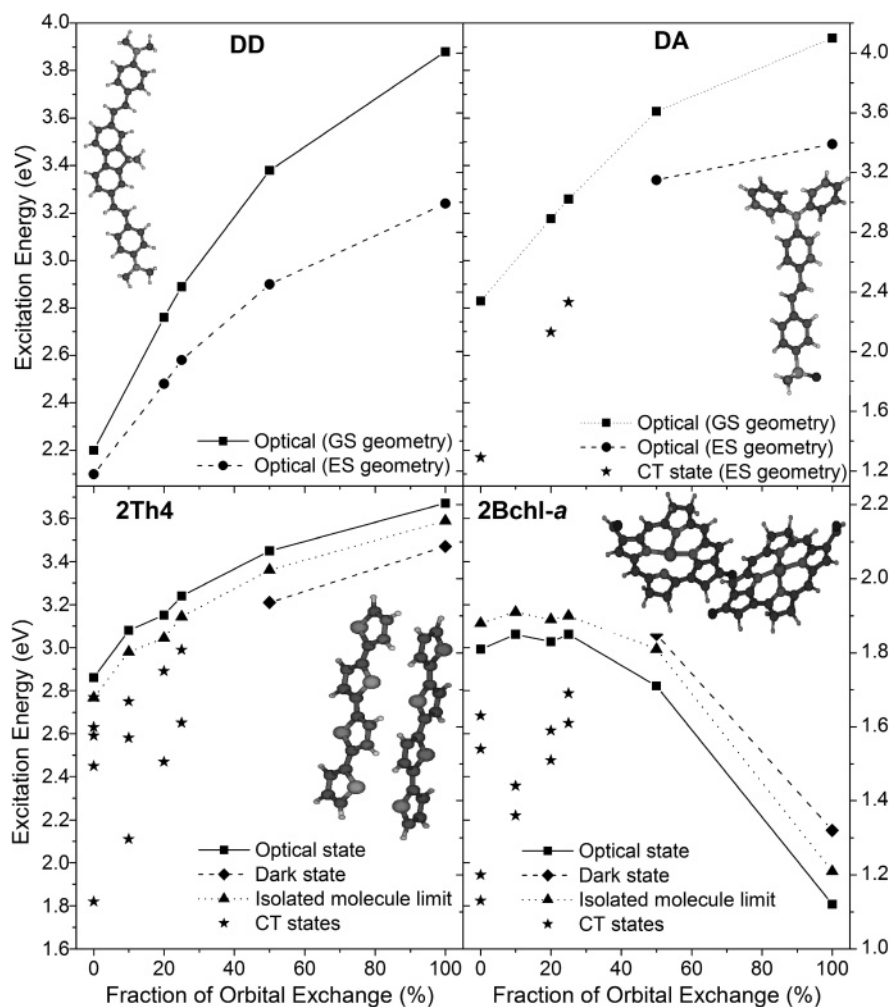


Figure 2. The calculated optical excitation energy as a function of the percentage of orbital exchange for the ground-state (GS) and the first excited-state (ES) optimized geometries of the donor–donor (DD) and donor–acceptor (DA) molecules just the GS for the 2Th4 and 2Bchl-a dimers.

quently unexpected manifestations of this problem and explore their implications.

We arbitrarily label three types of singlet excited states: ‘optical’, ‘dark’, and ‘charge transfer’. The optical excitation has a nonvanishing oscillator-strength, which means that it is possible to detect this excited state spectroscopically. The dark state refers to a low-energy electronic excitation with vanishing oscillator strength, that will not appear in the optical absorption. A CT state is a specific case of ‘dark’ state with a highly ionic nature where the photoexcited electron and hole have significant spatial separation. The oscillator strengths of CT states are expected to be weak because the overlap between the charge-transfer state and the ground state is extremely small and so are the transition dipole moments between these states. For example, in organic molecular crystals, CT states are usually higher in energy than the relevant Frenkel-exciton band of optical and dark states.⁵⁵ However, DFT methods drastically underestimate the energies of these states. For this reason, all three types of states in dimers might be mixed, and their clear distinction is not possible. The CT states become particularly troublesome in the optimization of the excited-state geometries when the target excited state is not clearly constrained by symmetry, and level crossings may occur.

A. Donor–Acceptor Substituted Chromophores. We begin this investigation by examining a relatively large (approximately 70 atoms) molecular donor–donor (DD) system. This molecule has a long π -conjugated backbone and donors (etholanimes) at both ends of the backbone. This is perhaps the easiest test case for TDDFT and offers the best opportunity for the theory to provide accurate results. The molecule has no strong electron attractors, and we do not expect large-scale charge transfer with electrons and holes migrating from/to opposite ends of the molecule. The charge transfer should be of a mild nature from the donors to the conjugated backbone. In the upper left-hand corner of Figure 2, we plot the energy of the lowest excited state versus functional for the DD molecule at both ground- and excited-state optimal geometries. The respective calculated excitation energies and their oscillator strengths are listed in Table 1. The experimental values are from refs 42 and 56. Overall, functionals with a moderate fraction of orbital exchange such as B3LYP provide the best agreement with the experimental absorption and fluorescence maxima, neglecting the proper treatment of vibronic, temperature, and nonpolar solvent effects.

The lowest-energy (band gap) transition in such conjugated molecules typically has a remarkable oscillator strength and

Table 1. Calculated Excitation Energies (eV) of the Donor–Donor (**DD**) and Donor–Acceptor (**DA**) Compounds^a

molecule	method	% exchange	GS	ES
DD	HF	100	3.88 (2.56)	3.24 (2.58)
DD	BHandHLYP	50	3.38 (2.72)	2.90 (2.80)
DD	PBE1PBE	25	2.89 (2.43)	2.58 (2.63)
DD	B3LYP	20	2.76 (2.29)	2.48 (2.53)
DD	BP86	0	2.20 (1.61)	2.1 (1.2)
DA	HF	100	4.27 (1.57)	3.39 (1.64)
DA	BHandHLYP	50	3.61 (1.40)	3.15 (1.50)
DA	PBE1PBE	25	3.02 (1.06)	2.33 (0.13)
DA	B3LYP	20	2.89 (0.99)	2.13 (0.08)
DA	BP86	0	2.34 (0.72)	1.29 (0.02)

^a The corresponding oscillator strengths f are given in parentheses. GS and ES refer to the ground-state and the first excited-state optimized molecular geometries, respectively. The SV basis set was used for all calculations. Experimental absorption and fluorescence maxima are $\omega_{\text{abs}} = 3.0$ eV and $\omega_{\text{fl}} = 2.7$ eV for **DD** and $\omega_{\text{abs}} = 3.2$ eV and $\omega_{\text{fl}} = 2.7$ eV for **DA**.

characteristically appears as a main peak in the linear absorption spectra.^{41,42} The calculated excited-state energy shifts to the blue with an increase of the fraction of orbital exchange. Likewise, the oscillator strength of the transition follows the fraction of exchange. These trends are expected since exact exchange cancels Coulomb self-interaction, and, thus, a larger fraction of orbital exchange corresponds to a contracted core. The valence states are also more tightly bound by the orbital exchange potential, but the effect is less extreme compared to the core contraction, since the HF virtual orbitals are calculated for the N+1 electron system and their energies correspond to electron affinities rather than excitation energies. Consequently, the KS orbitals become widely separated. This is consistent with results seen from noble-gas solids and atoms treated by exact-exchange DFT.⁵⁷ Since HF has even more weakly bound virtual orbitals than EXX, we expect the effect to be somewhat overemphasized. The energy of the first singlet state calculated at a relaxed excited-state geometry exhibits similar trends as a function of the fraction of orbital exchange. During excited-state geometry optimization the bonds along the conjugated backbone stretch, so that the bond-length alternation caused by uneven distribution of π -electronic density reduces.²⁸ This allows the electrons to become more delocalized, and the excited-state energy is reduced. The magnitude of the observed Stokes shift and the respective geometry changes intensify with an increase of the fraction of exchange.

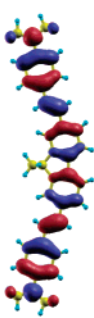
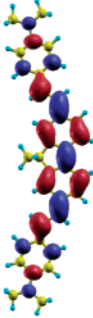
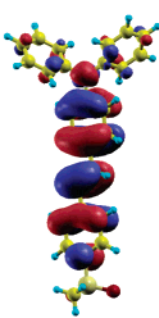
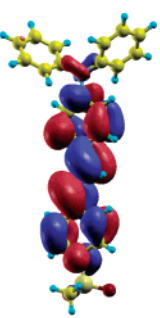
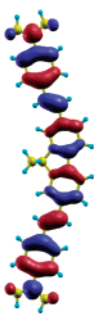
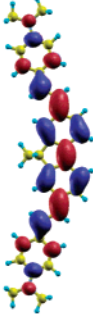
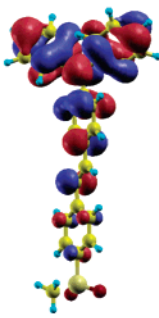
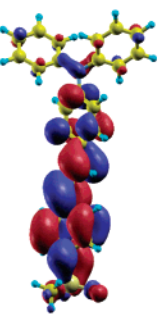
To analyze the nature of the discussed excited state, Table 2 displays the transition orbitals of the **DD** molecule obtained at the HF and BP86 limits, respectively. The two represent extremes in the locality of the functional. BP86 has only semilocal density-based exchange, while HF relies on the full orbital exchange. For the **DD** molecule, we see no qualitative difference between the HF and BP86 transition orbitals: they represent delocalized electronic state with electronic density slightly shifting toward the middle of the molecule upon photoexcitation. Transition orbitals describing emitting states are qualitatively similar to that of the absorbing state. We note that the BP86 orbitals are slightly more delocalized compared to the HF ones. This is due to

the short-range description embodied in the BP86 functional. However, there is a quantitative difference in the energetics. This is consistent with the well-known fact that local density functionals are known to perform poorly for certain properties in the limit of longer conjugated chains.²⁸ The conjugation length in this donor–donor (**DD**) molecule is perhaps too short for these semilocal functional shortcomings to become visually dramatic, but they remain energetically significant.

A more difficult test case is the donor–acceptor (**DA**) molecule in which the charge transfer between the donor and acceptor regions is energetically favorable and pronounced. It is hard to properly describe the underlying long-range interactions behind CT using a semilocal functional. The upper right-hand corner of Figure 2 shows scaling of the lowest singlet-state energy for the **DA** molecule, and the calculated data are presented in Table 1. As for the **DD** molecule, the excitation energy calculated at the ground-state geometry dramatically increases with the increasing fraction of exchange. This state is optically allowed having substantial oscillator strength. The HF transition orbitals shown in Table 2 reveal this excitation of π – π nature delocalized between donor and acceptor. Steric distortion prevents participation of terminal phenyls, and the state has only weak CT character. In contrast, BP86 transition orbitals display strong CT character in this excited state (see Table 2). Since the transition is delocalized, the overlap between electron and hole wave-functions is small, which results in a reduced oscillator strength compared to the other methods. BP86 shows to the incorrect physical behavior of semilocal functionals. The accurate numbers should lie somewhere in between HF and BP86 extremes, and this is where the hybrid TDDFT excels.⁴² The situation with semilocal functionals becomes even more problematic after excited-state optimization. While the functionals with a large percentage of orbital exchange (HF and BHandHLYP) behave normally, other methods converge to low-lying spurious CT states, where spatial overlap between an electron and a hole orbital is negligible (see Table 2), making the excitation optically forbidden (Table 1). A significant rearrangement of the molecular geometry is observed during excited-state geometry optimization, and this facilitates the crossover to the ionic CT state with a huge 1 eV Stokes shift.

To rationalize that such ionic states are artifacts of the method, we recall that the ground- and lowest-energy excited electronic states of substituted push–pull molecules are often described as a combination of neutral and zwitterionic basis states represented by the corresponding molecular resonance forms.^{58,59} The zwitterionic state assumes full separation of positive and negative charges, and, consequently, it is optically forbidden. The excited state usually possesses greater zwitterionic basis state character than the ground state. The molecular structures also become more zwitterionic in character as solvent polarity increases.⁵⁹ The semilocal functionals and functionals with a small fraction of orbital exchange do predict the ground state to be the mixture of such states; however, the excited state is described to be of solely zwitterionic character (see Table 2). In contrast, the **DA** molecule exhibits pronounced fluorescence properties,⁴²

Table 2. Hartree–Fock and BP86 Transition Orbitals of the Lowest Excited State for the Ground-State (GS) Geometries of the Donor–Donor (DD) and Donor–Acceptor (DA) Molecules^a

Molecule	Method	GS hole	GS electron	Molecule	Method	GS hole	GS electron
DD	HF			DA	HF		
DD	BP86			DA	BP86		

^a These orbitals represent the full orbital exchange and semilocal functional limits, respectively. GS refers to the ground-state optimized molecular geometry.

pointing to the strong component of the neutral basis in the excited state. The observed emission stems from the lowest vibronic state, and Kasha's rule is not violated. Thus all available experimental data point that the **DA** compound does not exhibit dual-fluorescence properties as observed on other molecular systems such as 4-(dimethyl)aminobenzonitrile (DMABN).⁶⁰ Moreover, computational excited-state geometry optimizations of the bright and the CT state for selected GGA functionals (not shown) do not change the relative state ordering. An opposite extreme is observed at the HF level when both ground and excited states have a dominant neutral component. Subsequently, the final result has a strong dependence on the fraction of orbital exchange used in the functional, which lessens the predictive power of TDDFT in applications to the polar substituted molecules.

Finally, in order to assess the basis set dependence, we performed several single point calculations on the **DA** molecule with split-valence basis sets of increasing complexity. The simplest is the 6-31G basis, then the same with polarization functions (6-31G*), then with diffuse functions (6-31+G), and with both (6-31+G*). Table 3 shows the lowest optical excitation energy for both the original Turbomole SV-optimized geometry obtained for a given functional in vacuo and then the native geometry. The latter is the optimized structure consistent with the level of theory and basis set used for excited-state calculations. Adding diffuse functions alone shifted the vertical absorption spectrum by a maximum of 0.13 eV to the red, and adding polarization functions shifted the spectrum by 0.1 eV to the red as well with the most dramatic basis set effect for pure HF. These changes are less dramatic when native geometry

is used. In practice, these molecules are often studied in solution, so we estimate solvent effects using the Polarizable Continuum Model (PCM) based on the Integral Equation Formalism^{61–64} for toluene. Adding PCM stabilized the vertical absorption maximum by 0.15 eV to the red with the most dramatic effects for the BP86 GGA kernel (see Table 3). Subsequently, using extended basis sets and solvent models leads to the overall 0.1–0.25 eV red-shifts of the excitation energies compared to plain 6-31G calculations in vacuo without changing the essential photophysics. This is a typical picture for extended molecules with delocalized π -orbitals, in contrast to small molecules of a few-atoms, where large basis sets are necessary.

B. Molecular Aggregates. In section IIIA, we have shown that TDDFT may incorrectly predict excited-state properties for large molecules with donor–acceptor character. Another interesting case, where such problems persist, is molecular aggregates. The separation distances are even larger for aggregates, and the nonlocality should play an even more important role. Modeling of molecular aggregates and assemblies can frequently be reduced to computations on characteristic dimers extracted from the underlying aggregate structure. This allows for the understanding of electronic couplings,^{33,65} excited state, and charge dynamics³⁴ seen in ultrafast optical probes. This information is important for light-harvesting and photovoltaic applications of the materials. According to molecular orbital and Hückel theory, every excited state of an isolated molecule should split into a nearly degenerate pair of states for the dimer (the Davydov's pair). The magnitude of splitting characterizes intermolecular coupling. Depending on the orientation of the molecules,

Table 3. Calculated Vertical Excitation Energies (eV) of the Donor–Acceptor (DA) Compound within Several Levels of Theory^a

method/basis set	SV geometry	native geometry
HF/6-31G	4.31 (1.59)	4.45 (1.56)
HF/6-31G*	4.21 (1.57)	4.43 (1.48)
HF/6-31+G	4.18 (1.45)	4.33 (1.41)
HF/6-31+G*	4.07 (1.43)	4.22 (1.40)
HF/6-31G PCM	4.19 (1.70)	4.35 (1.60)
HF/6-31+G* PCM	3.96 (1.57)	4.11 (1.44)
BHandHLYP/6-31G	3.71 (1.40)	3.66 (1.42)
BHandHLYP/6-31G*	3.66 (1.44)	3.66 (1.42)
BHandHLYP/6-31+G	3.61 (1.33)	3.61 (1.33)
BHandHLYP/6-31+G*	3.51 (1.33)	3.49 (1.36)
BHandHLYP/6-31G PCM	3.59 (1.54)	3.51 (1.56)
BHandHLYP/6-31+G* PCM	3.42 (1.50)	3.45 (1.44)
PBE1PBE/6-31G	3.12 (0.99)	3.04 (1.06)
PBE1PBE/6-31G*	3.05 (0.97)	3.05 (1.08)
PBE1PBE/6-31+G	3.01 (0.99)	2.96 (1.03)
PBE1PBE/6-31+G*	2.99 (1.02)	2.97 (1.05)
PBE1PBE/6-31G PCM	2.99 (1.11)	3.03 (1.08)
PBE1PBE/6-31+G* PCM	2.87 (1.13)	2.91 (1.11)
B3LYP/6-31G	2.98 (0.90)	2.91 (0.99)
B3LYP/6-31G*	2.95 (0.93)	2.93 (1.01)
B3LYP/6-31+G	2.90 (0.89)	2.90 (0.98)
B3LYP/6-31+G*	2.87 (0.91)	2.92 (0.99)
B3LYP/6-31G PCM	2.85 (1.02)	2.77 (1.14)
B3LYP/6-31+G* PCM	2.73 (1.04)	2.75 (1.18)
BP86/6-31G	2.39 (0.62)	2.34 (0.72)
BP86/6-31G*	2.37 (0.62)	2.33 (0.71)
BP86/6-31+G	2.34 (0.62)	2.27 (0.69)
BP86/6-31+G*	2.31 (0.63)	2.31 (0.72)
BP86/6-31G PCM	2.25 (0.72)	2.20 (0.86)
BP86/6-31+G* PCM	2.16 (0.74)	2.17 (0.91)

^a The corresponding oscillator strengths f are given in parentheses.

either the lower or higher energy state would acquire a larger oscillator strength. These two classes are classified as J or H aggregates, respectively.⁵⁵ In this section, we investigate both cases.

First, we examine the thiophene dimers (**2Thio4**) exemplifying the H-aggregate case. In the lower left-hand corner of Figure 2, we plot the calculated excitation energies for thiophene dimers compared to the single molecule limit. Table 4 shows the respective data. The experimental result is from ref 66. Thiophenes form H-aggregates in crystals. Experimentally, this is exemplified by a blue-shifted absorption and small fluorescence yield compared to the corresponding properties of the monomer. Parallel orientation of the molecules in a dimer results in a positive intermolecular coupling term. This shows up as a higher-lying optical state (*in phase* combination of monomer's wave functions) than the dark state (*out of phase* combination of monomer's wave functions). This picture holds relatively well for functionals with a large fraction of orbital exchange (HF and BHandHLYP): the Davydov's states split equally up and down from the isolated molecule limit (see Figure 2) and appear as a linear combination of the monomer states in the transition orbitals (see Table 5). With less than 50% exchange, several spurious charge-transfer states appear. A smaller fraction of exchange generally means a larger number

Table 4. Calculated Excitation Energies (eV) of Thiophene Oligomer (**1Th4**) and Its Dimer (**2Th4**)^a

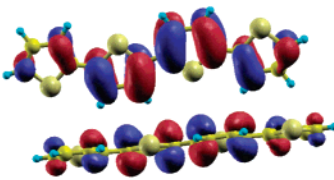
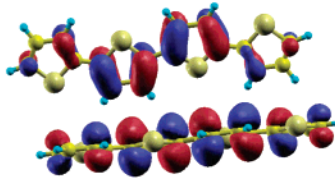
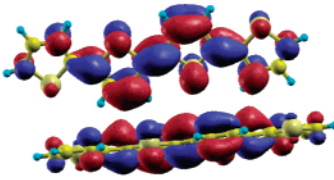
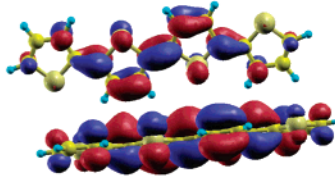
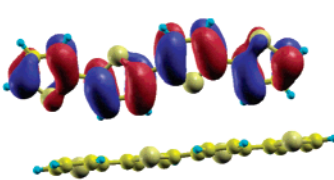
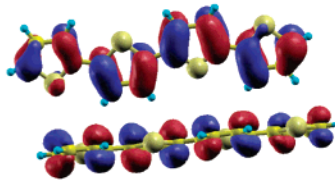
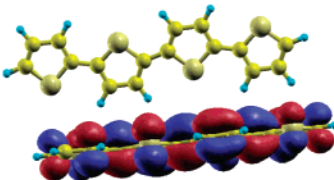
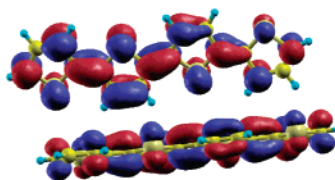
molecule	method	% exchange	optical state	dark state	no. of CT states
1Th4	HF	100	3.59 (1.47)		
1Th4	BHandHLYP	50	3.36 (1.28)		
1Th4	PBE1PBE	25	3.14 (1.26)		
1Th4	B3LYP	20	3.04 (1.22)		
1Th4	TPSS 10%	10	2.98 (1.21)		
1Th4	TPSS	0	2.82 (1.13)		
1Th4	BP86	0	2.77 (1.09)		
1Th4	SVWN	0	2.77 (1.08)		
2Th4	HF	100	3.67 (2.21)	3.47	0
2Th4	BHandHLYP	50	3.45 (2.19)	3.21	0
2Th4	PBE1PBE	25	3.24 (2.19)	2.97	1
2Th4	B3LYP	20	3.15 (1.5)	2.88	2
2Th4	TPSS 10%	10	3.08 (1.35)		3
2Th4	TPSS	0	2.92 (1.94)		4
2Th4	BP86	0	2.86 (1.86)		4
2Th4	SVWN	0	2.86 (1.83)		4

^a The corresponding oscillator strengths f are given in parentheses. Experimental absorption maximum is $\omega_{\text{abs}} = 2.7$ eV for **Th4** in solution.

of charge-transfer states below the first optical singlet. For example, LDA gives at least 4. For the BP86 GGA, the first optical state is given as state 6 instead of 2. In this case, Figure 2 shows these states as stars. They are heavily mixed with dark and optically allowed excitonic states (e.g., Table 5). We further notice that these spurious charge-transfer states disappear (shift upward in energy) with increasing separation between monomers for hybrid functionals with small amount of orbital exchange (B3LYP and PBE1PBE) but carry on for all LDA and GGA models (not shown). Subsequently, a small fraction of the HF exchange would help to predict the correct monomer limit of excitation energies in the aggregate at large intermolecular separations (> 5 Å) when the interchromophore orbital overlap vanishes but fails at smaller distances. In contrast, the CT problems persist for GGA semilocal functionals at all intermolecular separations, which agrees with the results obtained for the ethylene dimer (off-site excitations).⁶⁷ The failure of semilocal functionals to properly describe and characterize these low-lying states means that TDDFT would provide a highly unreliable description of electronic coupling and excitonic effects in such molecular aggregates.

In a second example of molecular assemblies, we consider a form of chlorophyll (**Bchl-a**) and its dimer (**2Bchl-a**) from the light-harvesting system of purple bacteria. The computational results are shown in the lower right-hand corner of Figure 2 and Table 6, and the experimental numbers are from ref 68. The $\alpha\beta$ Bchls-*a* pair forms a near J-aggregate complex as evidenced by the red-shifted first optical states in the dimer. In this case, the dark states lie above the optical ones. The full circular LHCII complex has, however, different properties suitable for efficient light-harvesting.^{35,36,68} We see an interesting trend for the chlorophyll monomers. As more orbital exchange is included, the predicted singlet energy is reduced. This is probably because of a more localized nature of the excited state and compact 2D size of the molecule. This trend may be rationalized by noting that exchange

Table 5. Transition Orbitals of Thiophene Dimer (**2Th4**)^a

Molecule	Method	State	GS hole	GS electron
2Th4	HF	1		
		2		
2Th4	BP86	1		
		6		

^a The top two and bottom two rows represent Hartree–Fock and BP86 limits. States 1 and 2 in the HF limit refer to the dark and optical transitions in the Davydov's pair, respectively. States 1 and 6 in the BP86 limit show charge-transfer character in the lowest dark and optically allowed transitions, respectively.

Table 6. Calculated Excitation Energies (eV) of Bacteriochlorophyll *a* (**1Bchl-a**) and $\alpha\beta$ Bchls-*a* Dimer (**2Bchl-a**)^a

molecule	method	% exchange	optical state	dark state	CT states
1Bchl-a	HF	100	1.21 (0.42)		
1Bchl-a	BHandHLYP	50	1.81 (0.40)		
1Bchl-a	PBE1PBE	25	1.90 (0.36)		
1Bchl-a	B3LYP	20	1.89 (0.35)		
1Bchl-a	TPSS 10%	10	1.91 (0.33)		
1Bchl-a	TPSS	0	1.88 (0.30)		
1Bchl-a	BP86	0	1.85 (0.27)		
1Bchl-a	SVWN	0	1.84 (0.27)		
2Bchl-a	HF	100	1.12 (0.90)	1.32 (0.08)	0
2Bchl-a	BHandHLYP	50	1.71 (0.89)	1.85 (0.04)	0
2Bchl-a	PBE1PBE	25	1.90 (0.54)		2
2Bchl-a	B3LYP	20	1.88 (0.61)		2
2Bchl-a	TPSS 10%	10	1.88 (0.67)		2
2Bchl-a	TPSS	0	1.84 (0.64)		4
2Bchl-a	BP86	0	1.81 (0.62)		4
2Bchl-a	SVWN	0	1.85 (0.64)		4

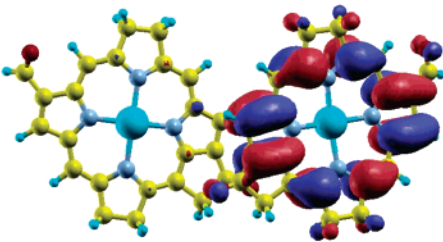
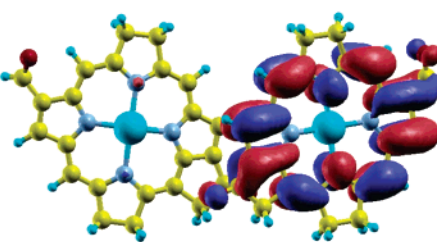
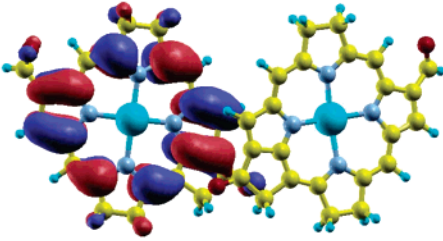
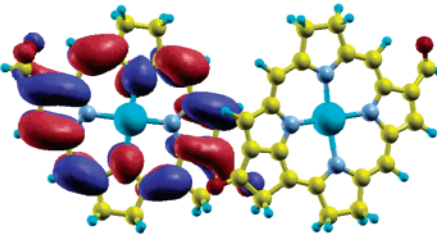
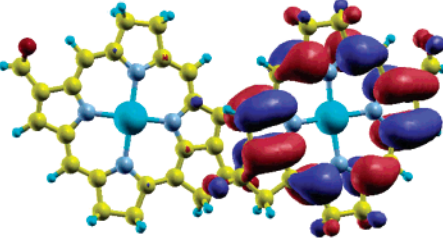
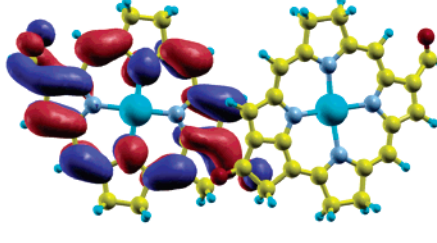
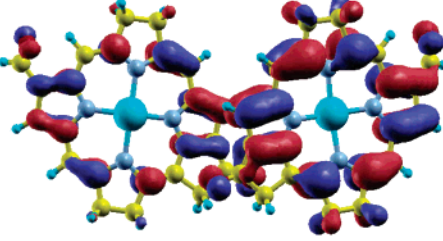
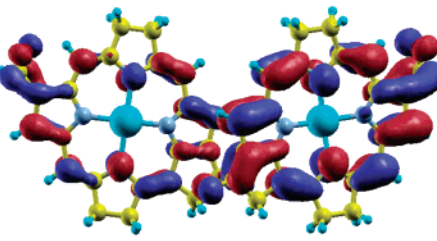
^a The corresponding oscillator strengths f are given in parentheses. The experimental absorption maximum of Q_x band of Bchls-*a* is at about 1.6 eV for a light-harvesting antenna.

creates a steeper optical potential comparable to the core contraction. The net effect would be a smaller optical gap

for orbital based functionals and a larger gap for semilocal ones. In the dimer, we observe the expected superposition of the monomer's states in the transition orbitals for HF and BHandHLYP methods. As an example, Table 7 shows the first dominant pair of transition orbitals localized on one chromophore for the first and second excited state in the HF limit. The second pair (not shown) involved the second molecule, respectively. Below 50% exchange, however, charge-transfer states begin to contaminate the optical spectra (see Table 7) making it impossible to reliably identify the states involved. Formation of such ghost states have been observed before in chlorophylls treated with TDDFT based on GGA models.^{69,70} Finally we note that recently developed functionals based on meta-GGA extensions (TPSS and TPSS-hybrid) are subject to the same charge-transfer problems as the other approaches for both thiophene and chlorophyll dimers (Tables 4 and 6). The large fraction of the orbital exchange turns out to be the only factor affecting the quality of the results.

Recent TDDFT study of a much smaller system, the ethylene dimer, shows a similar problem with CT states in the symmetric dimers.^{67,71,72} Notably, in our examples of **2Thio4** and **2Bchl-a**, the monomers are not identical. Consequently the observed CT states have nonzero net charge transferred between chromophores (see Tables 5 and 7),

Table 7. Transition Orbitals of $\alpha\beta$ Bacteriochlorophyll *a* Dimer (**2Bchl-a**)^a

Molecule	Method	State	GS hole	GS electron
Bchl-a	HF	1		
Bchl-a	HF	2		
Bchl-a	BP86	1		
Bchl-a	BP86	5		

^a The top two and bottom two rows represent Hartree–Fock and BP86 limits, respectively. States 1 and 2 in the HF limit refer to the dark and optical transitions in the Davydov’s pair, respectively. States 1 and 5 in the BP86 limit show charge-transfer character in the lowest dark and optically allowed transitions, respectively.

opposite to what has been observed in a perfectly symmetric case due to symmetry reasons.⁶⁷ In any case, it is an inaccurate xc-potential that leads to the appearance of unphysical low-lying states, generally dubbed as ‘CT states’, irrespectively if the actual charge is transferred or not upon excitation. We emphasize that physical analysis of coupling between various molecular regions is very important when deciding whether TD-DFT is applicable to ‘problematic’ cases or not: Small overlap between individual subsystems of a large system is particularly susceptible to the CT problems. Either vanishing overlap (e.g., large separations between monomers) or ‘strong’ communication (e.g., fully π -conjugated bridge) will help to offset the CT failures (i.e., here hybrid functionals with small amount of the orbital exchange may work). For example, the CT problems in donor–acceptor substituted compounds would be even more severe if the donor/acceptor subsystems are separated by

some chemical defect such as an sp^3 kink. These conclusions fully agree with the general analysis in refs 67, 71, and 72.

IV. Conclusions

In this study, we have examined the performance of the TDDFT approach for calculations of excited states. The benchmark systems include several polar donor–acceptor substituted compounds and molecular aggregates. These are typical examples of nanosized molecules currently in the focus of applied quantum chemistry. For all of the systems studied, we have employed a wide range of modern functionals including state-of-the-art meta-GGAs. Overall, today’s available density functionals often do not handle charge-transfer states properly. We see that no amount of sophistication in the currently available semilocal functionals describes the CT states successfully. These problems, however, can be overcome by including a larger fraction of orbital exchange, but this is at the expense of accuracy. We point

out that exact-exchange in density functional theory and Hartree–Fock exchange are not identical, and, in particular, they differ in their representation of virtual orbitals. EXX DFT virtual orbitals are more strongly bound than their HF analogies. This difference means that EXX-based virtual orbitals for the LUMO should be more localized than the HF analog. Consequently, our results will overemphasize the trends but not create new ones. However, the general conclusions of this work remain valid, and most of the charge-transfer problems persist.

An optimal fraction of orbital exchange is not known, and, most likely, is a system-dependent parameter. Nevertheless, it is possible to formulate several practical approaches based on the trends observed in this study and our previous experience that may overcome the outlined difficulties. We demonstrate that the excited-state geometries from TDDFT calculations using semilocal functionals can be unreliable and susceptible to CT problems. Combining of geometry optimization using functionals with 50% or more orbital exchange (e.g., HF or BHandHLYP) with excited-state calculations using functionals of lower hybrid content (e.g., B3LYP or PBE1PBE) would prevent drastic geometrical relaxation facilitating formation of ionic states.⁴² Such combinations of different methodologies have been successfully used in the past. For example, coupling of semiempirical AM1 (geometry) and INDO/S (electronic excitations) approaches has worked very well for many molecular systems.^{34,73} Alternatively, using functionals with higher fraction of the orbital exchange (e.g., BHandHLYP) for the entire calculation set would result in a qualitatively correct physical description, but the electronic excitation energies and the respective oscillator strengths would be overestimated.³⁴ Similar schemes can be applied to the excited-state description of aggregates and films: the intermolecular couplings can be derived from calculations with a high percentage of the orbital exchange (e.g., HF or BHandHLYP), whereas electronic excitations of a single chromophore can be calculated with numerically accurate DFT *workhorses* such as B3LYP or PBE1PBE. This would provide a reduced Hamiltonian description to the subsequent modeling.^{34,73} There have been several successful attempts to develop new specific functionals free of CT problems, including asymptotically corrected functionals based on HF exchange LC-TDDFT^{74,75} and CAM-B3LYP^{76–78} and ‘simple correction schemes’.^{79,80} The performance of these new functionals is yet to be thoroughly tested for extended molecular systems, and these methods need to be widely adopted in standard computational packages. We should also mention several recent *noncanonical* DFT-based approaches for electronic excitations, which address the above problems as well and are currently making their way into standard computational packages. This includes techniques based on the DFT-MRCI method,^{10,69} nonlocal density current VK functional,⁸¹ GW approximation (GWA),^{15,20} and Bethe-Salpeter equation (BSE).^{82–84}

We hope that these illustrated failures of TDDFT will motivate future work on developing exchange-correlation functionals (and kernels) which can better describe these long-range excited states.

Acknowledgment. This work was carried out under the auspices of the National Nuclear Security Administration of the U.S. Department of Energy at Los Alamos National Laboratory. The research at LANL is supported by the Center for Nonlinear Studies (CNLS) and the LANL LDRD program. This support is gratefully acknowledged.

References

- (1) Gross, E. K. U.; Dobson, J. F.; Petersilka, M. *Density Functional Theory*; Springer: Berlin, 1996; Vol. 181.
- (2) Koch, W.; Holthausen, M. C. *A Chemist's Guide to Density Functional Theory*; Wiley-VCH: Weinheim, 2000.
- (3) Casida, M. E. *Recent Advances in Density-Functional Methods*; World Scientific: Singapore, 1995; Vol. 3 of Part I.
- (4) Casida, M. E.; Jamorski, C.; Casida, K. C.; Salahub, D. R. *J. Chem. Phys.* **1998**, *108*, 4439.
- (5) Furche, F.; Burke, K. *Ann. Rep. Comp. Chem.* **2005**, *1*, 19.
- (6) Peumans, P.; Uchida, S.; Forrest, S. R. *Nature* **2003**, *425*, 158.
- (7) Markvart, T. *Prog. Quantum Electron.* **2000**, *24*, 107.
- (8) Itkis, M. E.; Borondics, F.; Yu, A. P.; Haddon, R. C. *Science* **2006**, *312*, 413.
- (9) Bartos, F. *J. Contr. Eng.* **2003**, *50*, 52.
- (10) Grimme, S. *Rev. Comp. Chem.* **2004**, *20*, 153.
- (11) Dreuw, A.; Head-Gordon, M. *Chem. Rev.* **2005**, *105*, 4009.
- (12) Hohenberg, P.; Kohn, W. *Phys. Rev.* **1964**, *136*, 864.
- (13) Runge, E.; Gross, E. K. U. *Phys. Rev. Lett.* **1984**, *52*, 997.
- (14) Onida, G.; Reining, L.; Rubio, A. *Rev. Mod. Phys.* **2002**, *74*, 601.
- (15) Rubio, A.; Balbas, L. C.; Alonso, J. A. *Phys. Rev. B* **1992**, *46*, 4891.
- (16) Serra, L.; Rubio, A. *Phys. Rev. Lett.* **1997**, *78*, 1428.
- (17) Sahni, V.; Gruenebaum, J.; Perdew, J. P. *Phys. Rev. B* **1982**, *26*, 4371.
- (18) Langreth, D. C.; Mehl, M. *J. Phys. Rev. B* **1983**, *28*, 1809.
- (19) Appel, H.; Gross, E. K. U.; Burke, K. *Phys. Rev. Lett.* **2003**, *90*, 043005.
- (20) Gonze, X.; Scheffler, M. *Phys. Rev. Lett.* **1999**, *82*, 4416.
- (21) Maitra, N. T.; Zhang, F.; Cave, R. J.; Burke, K. *J. Chem. Phys.* **2004**, *120*, 5932.
- (22) Maitra, N. T.; Burke, K.; Woodward, C. *Phys. Rev. Lett.* **2002**, *89*, 023002.
- (23) Tretiak, S.; Chernyak, V. Unpublished.
- (24) Grimme, S.; Parac, M. *ChemPhysChem* **2003**, *4*, 292.
- (25) Dreuw, A.; Head-Gordon, M. *J. Am. Chem. Soc.* **2004**, *126*, 4007.
- (26) Pogantsch, A.; Heimel, G.; Zojer, E. *J. Chem. Phys.* **2002**, *117*, 5921.
- (27) Dreuw, A.; Weisman, J. L.; Head-Gordon, M. *J. Chem. Phys.* **2003**, *119*, 2943.
- (28) Tretiak, S.; Igumenshchev, K.; Chernyak, V. *Phys. Rev. B* **2005**, *71*, 33201.
- (29) Tozer, D. J. *J. Chem. Phys.* **2003**, *119*, 12697.

- (30) Dierksen, M.; Grimme, S. *J. Phys. Chem. A* **2004**, *108*, 10225.
- (31) Tretiak, S.; Saxena, A.; Martin, R. L.; Bishop, A. R. *Phys. Rev. Lett.* **2002**, *89*, 097402.
- (32) Spano, F. C. *Ann. Rev. Phys. Chem.* **2006**, *57*, 217.
- (33) Krueger, B. P.; Scholes, G. D.; Fleming, G. R. *J. Phys. Chem. B* **1998**, *102*, 9603.
- (34) Bredas, J. L.; Beljonne, D.; Coropceanu, V.; Cornil, J. *Chem. Rev.* **2004**, *104*, 4971.
- (35) Pullerits, T.; Sundström, V. *Acc. Chem. Res.* **1996**, *29*, 381.
- (36) Fleming, G. R.; van Grondelle, R. *Phys. Today* **1994**, *47*, 48.
- (37) Goodson, T. G. *Acc. Chem. Res.* **2005**, *38*, 99.
- (38) Albota, M.; Beljonne, D.; Brédas, J. L.; Ehrlich, J. E.; Fu, J. Y.; Heikal, A. A.; Hess, S. E.; Kogej, T.; Levin, M. D.; Marder, S. R.; McCord Maughon, D.; Perry, J. W.; Rockel, H.; Rumi, M.; Subramaniam, C.; Webb, W. W.; Wu, X. L.; Xu, C. *Science* **1998**, *281*, 1653.
- (39) Dodabalapur, A.; Tousi, L.; Katz, H. E. *Science* **1995**, *268*, 270.
- (40) Sakaguchi, H.; Matsumura, H.; Gong, H.; Abouelwafa, A. M. *Science* **2005**, *310*, 1002.
- (41) Blanchard-Desce, M.; Wortmann, R.; Lebus, S.; Lehn, J.; Kramer, P. *Chem. Phys. Lett.* **1995**, *243*, 526.
- (42) Katan, C.; Terenziani, F.; Mongin, O.; Werts, M. H. V.; Porres, L.; Pons, T.; Mertz, J.; Tretiak, S.; Blanchard-Desce, M. *J. Phys. Chem. A* **2005**, *109*, 3024.
- (43) van der Horst, J. W.; Bobbert, P. A.; Michels, M. A. J.; Brocks, G.; Kelly, P. *J. Phys. Rev. Lett.* **1999**, *83*, 4413.
- (44) He, Z.; Sundstrom, V.; Pullerits, T. *J. Phys. Chem. B* **2002**, *106*, 11606.
- (45) Linnanto, J.; Korppi-Tommola, J. *Phys. Chem. Chem. Phys.* **2006**, *8*, 663.
- (46) Ahlrichs, R.; Bar, M.; Haser, M.; Horn, H.; Kolmel, C. *Chem. Phys. Lett.* **1989**, *162*, 165.
- (47) Furche, F.; Ahlrichs, R. *J. Chem. Phys.* **2002**, *117*, 7433.
- (48) Masunov, A. M.; Tretiak, S. *J. Phys. Chem. B* **2004**, *108*, 899.
- (49) Kloc, C.; Laudise, R. A.; Katz, H. E.; Haddon, R. C. *Adv. Mat.* **1998**, *10*, 379.
- (50) Koepke, J.; Hu, X. C.; Muenke, C.; Schulten, K.; Michel, H. *Structure* **1996**, *4*, 581.
- (51) Frisch, M. J.; Trucks, G. W.; Schlegel, H. B.; Scuseria, G. E.; Robb, M. A.; Cheeseman, J. R.; Montgomery, J. A., Jr.; Vreven, T.; Kudin, K. N.; Burant, J. C.; Millam, J. M.; Iyengar, S. S.; Tomasi, J.; Barone, V.; Mennucci, B.; Cossi, M.; Scalmani, G.; Rega, N.; Petersson, G. A.; Nakatsuji, H.; Hada, M.; Ehara, M.; Toyota, K.; Fukuda, R.; Hasegawa, J.; Ishida, M.; Nakajima, T.; Honda, Y.; Kitao, O.; Nakai, H.; Klene, M.; Li, X.; Knox, J. E.; Hratchian, H. P.; Cross, J. B.; Bakken, V.; Adamo, C.; Jaramillo, J.; Gomperts, R.; Stratmann, R. E.; Yazyev, O.; Austin, A. J.; Cammi, R.; Pomelli, C.; Ochterski, J. W.; Ayala, P. Y.; Morokuma, K.; Voth, G. A.; Salvador, P.; Dannenberg, J. J.; Zakrzewski, V. G.; Dapprich, S.; Daniels, A. D.; Strain, M. C.; Farkas, O.; Malick, D. K.; Rabuck, A. D.; Raghavachari, K.; Foresman, J. B.; Ortiz, J. V.; Cui, Q.; Baboul, A. G.; Clifford, S.; Cioslowski, J.; Stefanov, B. B.; Liu, G.; Liashenko, A.; Piskorz, P.; Komaromi, I.; Martin, R. L.; Fox, D. J.; T. K. Gaussian 03 (Rev. C.02); Gaussian, Inc.: Wallingford, CT, 2003.
- (52) Rassolov, V. A.; Ratner, M. A.; Pople, J. A. *J. Chem. Phys.* **2000**, *112*, 4014.
- (53) Becke, A. D. *J. Chem. Phys.* **1993**, *98*, 1372.
- (54) Martin, R. L. *J. Chem. Phys.* **2003**, *118*, 4775.
- (55) Pope, M.; Swenberg, C. E. *Electronic Processes in Organic Crystals*; Clarendon Press, Oxford University Press: Oxford, New York, 1982.
- (56) Charlot, M.; Izard, N.; Mongin, O.; Riehl, D.; Blanchard-Desce, M. *Chem. Phys. Lett.* **2006**, *417*, 297.
- (57) Magyar, R. J.; Fleszar, A.; Gross, E. K. U. *Phys. Rev. B* **2004**, *69*, 45111.
- (58) Lu, D. Q.; Chen, G. H.; Perry, J. W.; Goddard, W. A. *J. Am. Chem. Soc.* **1994**, *116*, 10679.
- (59) Moran, A. M.; Kelley, A. M.; Tretiak, S. *Chem. Phys. Lett.* **2003**, *367*, 293.
- (60) Rappoport, D.; Furche, F. *J. Am. Chem. Soc.* **2004**, *126*, 1277.
- (61) Cancès, E.; Mennucci, B.; Tomasi, J. *J. Chem. Phys.* **1997**, *107*, 3032.
- (62) Cossi, M.; Barone, V.; Mennucci, B.; Tomasi, J. *Chem. Phys. Lett.* **1998**, *286*, 253.
- (63) Mennucci, B.; Cammi, R.; Tomasi, J. *J. Chem. Phys.* **1998**, *109*, 2798.
- (64) Cossi, M.; Barone, V. *J. Chem. Phys.* **2001**, *115*, 4708.
- (65) Tretiak, S.; Middleton, C.; Chernyak, V.; Mukamel, S. *J. Phys. Chem. B* **2000**, *104*, 9540.
- (66) Birnbaum, D.; Fichou, D.; Kohler, B. E. *J. Chem. Phys.* **1992**, *96*, 165.
- (67) Hieringer, W.; Gorling, A. *Chem. Phys. Lett.* **2006**, *419*, 557.
- (68) Pullerits, T.; Hess, S.; Herek, J. L.; Sundström, V. *J. Phys. Chem. B* **1997**, *101*, 10560.
- (69) Parusel, A. B. J.; Grimme, S. *J. Phys. Chem. B* **2000**, *104*, 5395.
- (70) Sundholm, D. *Phys. Chem. Chem. Phys.* **2000**, *2*, 2275.
- (71) Hieringer, W.; Gorling, A. *Chem. Phys. Lett.* **2006**, *426*, 234.
- (72) Dreuw, A.; Head-Gordon, M. *Chem. Phys. Lett.* **2006**, *426*, 231.
- (73) Tretiak, S.; Mukamel, S. *Chem. Rev.* **2002**, *102*, 3171.
- (74) Chiba, M.; Tsuneda, T.; Hirao, K. *J. Chem. Phys.* **2006**, *124*, 144106.
- (75) Tawada, Y.; Tsuneda, T.; Yanagisawa, S.; Yanai, T.; Hirao, K. *J. Chem. Phys.* **2004**, *120*, 8425.
- (76) Peach, M. J. G.; Helgaker, T.; Salek, P.; Keal, T. W.; Lutnaes, O. B.; Tozer, D. J.; Handy, N. C. *Phys. Chem. Chem. Phys.* **2006**, *8*, 558.
- (77) Yanai, T.; Tew, D. P.; Handy, N. C. *Chem. Phys. Lett.* **2004**, *393*, 51.
- (78) Rudberg, E.; Salek, P.; Helgaker, T.; Agren, H. *J. Chem. Phys.* **2005**, *123*, 184108.
- (79) Neugebauer, J.; Gritsenko, O.; Baerends, E. J. *J. Chem. Phys.* **2006**, *124*, 214102.

- (80) Gritsenko, O.; Baerends, E. J. *J. Chem. Phys.* **2004**, *121*, 655.
- (81) Vignale, G.; Kohn, W. *Phys. Rev. Lett.* **1996**, *77*, 2037.
- (82) Ghosez, P.; Gonze, X.; Godby, R. W. *Phys. Rev. B* **1997**, *56*, 12811.

- (83) Reining, L.; Olevano, V.; Rubio, A.; Onida, G. *Phys. Rev. Lett.* **2002**, *88*, 066404.
- (84) Sottile, F.; Olevano, V.; Reining, L. *Phys. Rev. Lett.* **2003**, *91*, 056402.

CT600282K

JCTC

Journal of Chemical Theory and Computation

Quartic-Scaling Analytical Energy Gradient of Scaled Opposite-Spin Second-Order Møller–Plesset Perturbation Theory

Rohini C. Lochan,[†] Yihan Shao,[§] and Martin Head-Gordon^{*,†,‡}

Department of Chemistry, University of California, Berkeley, California 94720, Chemical Sciences Division, Lawrence Berkeley National Laboratory, Berkeley, California 94720 and Q-Chem, Inc., Pittsburgh, Pennsylvania 15213

Received September 21, 2006

Abstract: The analytical gradient of the “scaled opposite spin” (SOS-) and “modified opposite spin” (MOS-) second-order Møller–Plesset perturbation theory (MP2) methods is derived and implemented. Both energy and the first derivative can be evaluated efficiently with a fourth-order scaling algorithm by using a combination of auxiliary basis expansions and Laplace transformation techniques as opposed to the traditional fifth-order approach of MP2. A statistical analysis of 178 small molecules suggests that the new gradient scheme provides geometries of MP2 quality, indicating the reliability of the method in general chemical applications. A more specific study of the group VI transition metal carbonyl complexes indicates that the new scheme improves the MP2 description relative to available experimental data and higher-order theories. The proposed gradient scheme thus endeavors to obtain improved structural features at reduced computational cost.

I. Introduction

One of the key initial steps in any computational study or chemical application is the determination of the equilibrium molecular structure of the constituent systems. The availability of analytical gradients with respect to nuclear displacements for the specific methodology used plays a critical role in the fast and efficient identification of stable geometries or transition states.^{1,2} So far, density functional theory (DFT)³ has remained the most popular choice to obtain optimized molecular geometries in studies that especially involve large molecules, primarily due to its low computational cost and reasonable performance. However, one is constrained to choose the most appropriate functional that is suitable for a particular problem as DFT cannot be improved systematically. Also, the reliability of DFT in studies where long-range dispersive effects are important is

questionable, as present-day functionals cannot account for such interactions.^{4–8}

On the other hand, ab initio methods like second-order Møller–Plesset perturbation theory (MP2)⁹ offer the simplest systematic route to introduce dynamic correlation effects beyond the Hartree–Fock (HF) mean-field approximation¹⁰ and also account for dispersion interactions.¹¹ However, there are two important considerations that need to be addressed regarding the computational cost and the reliability of MP2 results.

(i) The cost of computing the canonical MP2 energy and analytic gradient grows formally as $\mathcal{O}(M^5)$ with system size, which limits the applicability of MP2 to large molecules. Tremendous effort has gone into developing fast and efficient lower-order scaling MP2 energy^{12–25} and gradient codes^{26–43} in the past few decades. In particular, the use of the “resolution-of-the-identity” approximation (RIMP2)^{12,14,23,40–42} has emerged as an important tool to reduce the computational prefactor of the fifth-order scaling MP2 energy and gradient algorithm, leading to significant speedups at the cost of introducing tolerable error. Then, there are the “local” MP2 (LMP2) approaches that use localized orbitals^{13,15,22} or atomic

* Corresponding author e-mail: mhg@cchem.berkeley.edu.

[†] University of California.

[‡] Lawrence Berkeley National Laboratory.

[§] Q-Chem, Inc.

truncations^{18,23} to obtain low-order scaling MP2 methods to calculate the correlation energy. Some of these methods have been made more efficient by using the RI approximation.^{22,23} Analytic gradients are available for a couple of these LMP2 approaches.^{35,43} In particular, Schütz et al. have demonstrated that their LMP2 analytic gradient scheme could scale quadratically with system size by exploiting the sparsity of the fit coefficients and employing local domains.⁴³

(ii) Although MP2 energies and geometries are known to be quite reliable for closed-shell molecules,⁴⁴ they tend to overestimate interaction energies and underestimate bond distances when compared to higher-order theories like coupled-cluster singles and doubles with a perturbative correction method [CCSD(T)]⁴⁵ or available experimental data. This is particularly true in case of stacking problems, for example, the famous benzene dimer case.⁴⁶ This trend is also observed in the prediction of metal–ligand bond dissociation energies and bond lengths in closed-shell transition metal (TM) complexes.⁴⁷ When it comes to open-shell systems like radicals and other transition metal compounds, the performance of MP2 is rather poor.⁴⁸ Also, MP2 is limited to systems where the single-reference wavefunction-based HF approximation is deemed a good starting point. Finally, approaching the basis set limit of MP2 calculations requires a large basis set description.⁴⁹ However, as mentioned earlier, MP2 displays a tendency to overestimate interaction energies, which means that this limit may or may not be more accurate than small basis set results.⁴⁶

Clearly, it is desirable to develop methodologies that are both computationally efficient and accurate. In this context, a family of “scaled” MP2 methods^{50–52} was recently proposed, which could achieve significant statistical improvements in performance across various chemical properties and also maintain the size consistency feature of MP2. The idea was first put forth by Grimme,⁵⁰ who suggested that separate scaling of the opposite-spin (OS) and same-spin (SS) components of the MP2 correlation energies (SCS-MP2)

$$E_{\text{MP2}} = c_{\text{OS}}E_{\text{OS}} + c_{\text{SS}}E_{\text{SS}} \quad (1)$$

where $c_{\text{OS}} = 6/5$ and $c_{\text{SS}} = 1/3$, could yield QCISD(T) (= quadratic configuration interaction with single and double excitations and triple excitations added perturbatively) quality results as far as relative energies are concerned.^{53–57} This method, however, does not offer any computational advantage. Following this, we recently proposed two variants of the above method, where only the OS contribution to the MP2 correlation energy is scaled while the SS contribution is neglected. In the scaled opposite-spin (SOS-MP2) approach,⁵¹ the optimal OS scaling factor that accounts for the absence of the SS contribution was found to be $c_{\text{OS}} = 1.3$. However, for nonoverlapping systems, both SCS-MP2 and SOS-MP2 provide an incorrect physical description of the long-range correlation effects. To correct this deficiency, we then proposed the modified opposite-spin (MOS-MP2)⁵² method that instead employs a distance-dependent scaling of the OS correlation energy. The two-electron operator is hence modified to

$$\hat{\Theta}_{\omega}(\mathbf{r}) = \frac{1}{\mathbf{r}} + c_{\text{MOS}} \frac{\text{erf}(\omega\mathbf{r})}{\mathbf{r}} \quad (2)$$

where the recommended value for ω is 0.6 au and $c_{\text{MOS}} = (\sqrt{2} - 1)$. Both SOS-MP2 and MOS-MP2 methods (henceforth, collectively known as OS-MP2 methods) are dependent on a single parameter unlike the two-parameter SCS-MP2 approach. In any case, the presence of empirical parameter(s) is a drawback common to all the scaled-MP2 methods as the recommended parameter value might not be suitable for every chemical application. However, in the case of the MOS-MP2 approach, it was found that the parameter ω could be tuned to improve the MP2 performance for a particular property such as barrier height determination.⁵² The OS-MP2 methods not only show statistical improvements in accuracy similar to (sometimes even better than) SCS-MP2 but are also computationally advantageous as the inherent fifth-order scaling nature with system size of the traditional MP2 can be reduced to fourth order by using a combination of auxiliary basis expansions^{12,14,58} and Laplace transformation,⁵⁹ without using any cutoffs.^{51,52} Also, by further exploiting the locality and sparsity of the expansion coefficients, the computational cost can be reduced to almost quadratic scaling.⁶⁰

In this work, we derive the analytical gradient of the fourth-order scaling OS-MP2 energy, establish that it can also be evaluated with $\mathcal{O}(M^4)$ computational effort, and validate its chemical and computational performance. This is significant as we can obtain improved results with an inherently low-order scaling MP2-type gradient without using any cutoff schemes, thereby extending the size of systems currently feasible. The analytical gradient equations presented here are exact within the use of RI and Laplace transformation approximations in the OS-MP2 energy expression. The theoretical derivation of the OS-MP2 analytical gradient is presented in section II after a brief review of the standard representations in MP2 gradient theory.

The reported gradient scheme is based on a canonical HF reference (i.e., diagonal Fock matrix), and the final gradient expression is obtained by explicitly differentiating the OS-MP2 energy equation. The fourth-order scaling result is particularly interesting because it would seem to be impossible to obtain if the quartic number of amplitudes must be manipulated explicitly to obtain effective density matrices and two-particle density matrices. However, we show this can be avoided. The proposed algorithm, discussed in section III, can be easily integrated with the existing OS-MP2 energy code and the recently proposed RIMP2 analytic gradient algorithm.⁴¹ The memory requirements for the current implementation remain quadratic, while the cubic disk space needed is doubled when compared to the OS-MP2 energy evaluation. Also, the algorithm is constructed such that it can be easily extended to accommodate the unrestricted cases and the frozen-core approximation.

In section IV, we benchmark the CPU timing performance of the proposed algorithm with a series of linear and globular polyalanine peptide (tetra-, octa-, hexadeca-) systems and compare with the timings obtained by other methods like HF, standard MP2, and RIMP2. We also show that, in

Table 1. Description of the Notation Used in the Derivation

notation	description
$\mu, \nu, \lambda, \sigma$	atomic orbital (AO)
i, j, k, l	active occupied MO
a, b, c, d	active virtual MO
p, q, r, s	any MO
K, L, M, N	auxiliary basis function
τ	Laplace quadrature point ^a
N_τ	number of quadrature points used
n	number of basis functions
o	number of active occupied MOs
v	number of active virtual MOs
N_{aux}	number of auxiliary basis functions
superscript x	derivative with respect to perturbation in the nuclear coordinate x^b
superscript (x)	derivative of the AO integrals alone (excluding MO coefficients) ^c

^a Laplace quadrature-dependent terms indicated with left superscript τ , for example, ${}^\tau X_{pq}^x$. ^b Example: $S_{pq}^x = \partial S_{pq} / \partial x$. ^c Example: $S_{pq}^{(x)} = \sum_{\mu\nu} C_{\mu p} [(\partial S_{\mu\nu}) / (\partial x)] C_{\nu q}$

general, this gradient provides reliable MP2-like geometries for small molecules through a statistical study of 178 systems, and in particular, the OS-MP2 analytical gradient helps to improve the MP2 description of difficult systems like group VI transition metal carbonyls. Finally, in section V, we present some conclusions.

II. Gradient Theory

In this section, we provide a short review of the standard representations of the MP2/RIMP2 analytic gradient and summarize the main energy expressions of the OS-MP2 theory to set the stage for the derivation of the OS-MP2 gradient. Table 1 summarizes the description of the notation/indices used hereafter.

A. Standard Representation of the Analytical MP2 Gradient. The standard representation of the analytical gradient of the conventional MP2 total energy (HF energy + correlation energy) with respect to perturbation in any nuclear coordinate, say x , can be written in the form⁶¹

$$E^x = \sum_{\mu\nu} P_{\mu\nu} H_{\mu\nu}^x + \sum_{\mu\nu} W_{\mu\nu} S_{\mu\nu}^x + \sum_{\mu\nu\lambda\sigma} \Gamma_{\mu\nu\lambda\sigma} (\mu\nu|\lambda\sigma)^x \quad (3)$$

Here, the gradient is expressed in the atomic orbital (AO) basis as the sum of three pieces, namely, the contraction of one- and two-particle density matrices, $P_{\mu\nu}$ and $\Gamma_{\mu\nu\lambda\sigma}$, with the corresponding derivatives of the one- and two-particle Hamiltonian and, third, the contraction of the energy-weighted density matrix, $W_{\mu\nu}$, with the overlap derivative. The two-particle density matrix (2-PDM) can be written as a sum of a separable and a nonseparable piece³⁰

$$\Gamma_{\mu\nu\lambda\sigma} = \Gamma_{\mu\nu\lambda\sigma}^S + \Gamma_{\mu\nu\lambda\sigma}^{\text{NS}} \quad (4)$$

The separable 2-PDM is given by

$$\Gamma_{\mu\nu\lambda\sigma}^S = \frac{1}{2} (P_{\mu\nu}^{\text{HF}} + 2P_{\mu\nu}^{(2)}) P_{\lambda\sigma}^{\text{HF}} - \frac{1}{2} (P_{\mu\sigma}^{\text{HF}} + 2P_{\mu\sigma}^{(2)}) P_{\lambda\nu}^{\text{HF}} \quad (5)$$

The definition of the MP2 correction to the density matrices, $P_{\mu\nu}^{(2)}$, $W_{\mu\nu}^{(2)}$, and $\Gamma_{\mu\nu\lambda\sigma}^{\text{NS}}$ is well-known.^{30,37,62}

In the case of RIMP2,^{12,14} the evaluation of the correlation energy is made computationally faster and efficient by using auxiliary basis expansions to express the four-index integrals in terms of three- and two-center two-electron integrals

$$I_{\text{Coulomb}} = (ia|jb) = \sum_K B_{ia}^K B_{jb}^K \quad (6)$$

where

$$B_{ia}^K = \sum_M (ia|M) V_{MK}^{-1/2} \quad (7)$$

and

$$V_{MK} = (M|K) \quad (8)$$

We note that the option of using the RI approximation in HF evaluation is not pursued here. As a consequence of the RI approximation, the three- and two-center two-electron integral derivatives also contribute toward the gradient. Therefore, the analytical gradient of the total RIMP2 energy (HF energy + RIMP2 correlation energy) takes up the form^{41,42}

$$E_{\text{RI}}^x = \sum_{\mu\nu} P_{\mu\nu} H_{\mu\nu}^x + \sum_{\mu\nu} W_{\mu\nu} S_{\mu\nu}^x + \sum_{\mu\nu\lambda\sigma} \Gamma_{\mu\nu\lambda\sigma}^S (\mu\nu|\lambda\sigma)^x + \sum_{\mu\nu} \sum_K \Gamma_{\mu\nu}^K (\mu\nu|K)^x + \sum_{KL} \gamma_{KL} (K|L)^x \quad (9)$$

where, $\Gamma_{\mu\nu}^K$ and γ_{KL} represent the RI-specific 2-PDMs, which are contracted with the three- and two-center two-electron integral derivatives, respectively. The separable 2-PDM retains the same form as eq 5. The explicit definitions of the RIMP2 correction to the density matrices are described elsewhere.^{41,42}

B. Review of OS-MP2 Energy Evaluation. Unlike conventional MP2 and RIMP2, the OS-MP2 energy (both SOS- and MOS-MP2) can be evaluated without any fifth-order step when a combination of auxiliary basis functions and a Laplace transformation is applied to the energy expression^{51,52}

$$E_{\text{OS}} = - \sum_{ia}^{\alpha} \sum_{jb}^{\beta} \frac{\bar{I}_{ia}^{jb} \bar{I}_{ia}^{jb}}{\Delta_{ia}^{jb}} \quad (10)$$

where the energy denominator is given in terms of the canonical orbital energies as $\Delta_{ia}^{jb} = (\epsilon_a - \epsilon_i) + (\epsilon_b - \epsilon_j)$. In the case of SOS-MP2, the integrals \bar{I}_{ia}^{jb} in the above equation are simply the Coulomb integrals given in eq 6, while for MOS-MP2, they are evaluated with the modified two-electron operator $\hat{\Theta}_{\omega}(\mathbf{r})$ shown in eq 2. The final working expression for computing the OS-MP2 energy can be written as

$$-E_{\text{OS}} = \sum_{\tau} w_{\tau} \sum_{KL} {}^{\tau} X_{KL}^{\alpha} {}^{\tau} X_{KL}^{\beta} \quad (11)$$

where

$$\tau X_{KL}^{\alpha} = \sum_{ia}^{\alpha} B_{ia}^K B_{ia}^L (\tau \xi_i^{\alpha})^2 \quad (12)$$

and

$$\tau \xi_i^{\alpha} = \exp[(\epsilon_i - \epsilon_a) t_{\tau}/2] \quad (13)$$

The evaluation of the \mathbf{X} matrix in eq 12 is the dominant step of order $\mathcal{O}(N_{\tau} o v N_{\text{aux}}^2)$ in the energy evaluation. Notice that the evaluation of the \mathbf{B} matrix in eq 7 also scales as $\mathcal{O}(M^4)$ with system size; however, it is independent of the Laplace quadrature and, therefore, evaluated only once in the algorithm.

C. Derivation of the Analytical OS-MP2 Gradient. We now present the formulation of the OS-MP2 analytical gradient, which retains the same standard form expressed in eq 9. However, the explicit definitions of the OS-MP2 correction to the \mathbf{P} , \mathbf{W} , Γ , and γ matrices in eq 9 are different from the case of the RIMP2 gradient.^{41,42} The formulation presented below is valid for both SOS-MP2 and MOS-MP2 analytical gradients. In the case of the MOS-MP2 gradient, the involved three-center and two-center two-electron integrals and their derivatives are evaluated using the modified two-electron operator given in eq 2. Subsequently, all terms built from these modified integrals would depend on the parameter “ ω ”.⁵²

Each piece of the OS-MP2 gradient can be evaluated with $\mathcal{O}(M^4)$ or lower computational cost, where M is the system size, unlike RIMP2 or MP2 that involve fifth-order scaling terms. This achievement is possible because the quartic number of amplitudes are *never explicitly formed*—instead, all one- and two-particle density matrices are cast in terms of more compact intermediates in the auxiliary basis, such as the \mathbf{X} matrix defined above in eq 12. For the sake of simplicity, we present the derivation for a restricted closed-shell system. However, the following derivation can be readily extended to the unrestricted case in a straightforward manner.

The OS-MP2 analytical gradient for a restricted, closed-shell system can be obtained by directly differentiating the working energy expression in eq 11, which gives

$$-\frac{1}{2} E_{\text{OS}}^x = \sum_{\tau} w_{\tau} \sum_{KL} (\tau X_{KL}^{\alpha})^x \tau X_{KL}^{\beta} \quad (14)$$

Straightforward differentiation of eqs 7, 8, 12, and 13 transforms eq 14 to

$$-\frac{1}{2} E_{\text{OS}}^x = \sum_{\tau} w_{\tau} \left[\sum_{ia}^{\alpha} \tau \Gamma_{ia}^{M,\beta} (\tau \xi_i^{\alpha})^2 \{2(ia|M)^x + t_{\tau}(ia|M)(\epsilon_i^x - \epsilon_a^x)\} + \sum_{KL} \bar{\gamma}_{KL} V_{KL}^x \right] \quad (15)$$

The details about the intermediate steps leading to the above equation are outlined in Appendix A. The three-index RI-specific 2-PDM in the above equation is given by

$$\tau \Gamma_{ia}^{M,\beta} = \sum_L \tau Y_{ML}^{\beta} B_{ia}^L \quad (16)$$

and

$$\tau Y_{ML}^{\beta} = \sum_K V_{MK}^{-1/2} \tau X_{KL}^{\beta} \quad (17)$$

The formation of the Γ matrix in the eq 16 is the dominant fourth-order step in the evaluation of the analytical gradient and scales as $\mathcal{O}(N_{\tau} o v N_{\text{aux}}^2)$. Note that this cost is isomorphic with the \mathbf{X} matrix formation in eq 12. The “Laplace quadrature independent” (indicated by bar above symbol) two-index RI-specific 2-PDM in eq 15 is given by

$$\bar{\gamma}_{KL} = \sum_{\tau} w_{\tau} \tau \gamma_{KL} \quad (18)$$

and

$$\tau \gamma_{KL} = - \sum_M \tau Y_{KM}^{\alpha} \tau Y_{ML}^{\beta} \quad (19)$$

In eq 15, the three-center, two-electron integral derivative is given by

$$(ia|M)^x = (ia|M)^{(x)} + \sum_p U_{pi}^x (pa|M) + \sum_p U_{pa}^x (ip|M) \quad (20)$$

where

$$(ia|M)^{(x)} = \sum_{\mu\nu} C_{\mu i} (\mu\nu|M)^x C_{\nu a} \quad (21)$$

The terms U_{pi}^x and U_{pa}^x in eq 20 represent the orbital responses to the displacement x . Rewriting the first term in eq 15 by inserting eq 20 gives

$$2 \sum_{\tau} w_{\tau} \sum_{ia}^{\alpha} \sum_M \tau \Gamma_{ia}^{M,\beta} (\tau \xi_i^{\alpha})^2 (ia|M)^x = 2 \sum_M \left[\sum_{\mu\nu} \bar{\Gamma}_{\mu\nu}^{M,\beta} (\mu\nu|M)^x + \sum_{\tau} w_{\tau} \sum_{ia}^{\alpha} \tau \Gamma_{ia}^{M,\beta} (\tau \xi_i^{\alpha})^2 \sum_p^{\text{all}} \{(pa|M)U_{pi}^x + (ip|M)U_{pa}^x\} \right] \quad (22)$$

In the above equation, the first term is obtained by scaling and incrementing the Γ matrix in the molecular orbital (MO) basis for every Laplace quadrature point, τ , to produce a “Laplace quadrature independent” quantity

$$\bar{\Gamma}_{ia}^{M,\beta} = \sum_{\tau} w_{\tau} \tau \Gamma_{ia}^{M,\beta} (\tau \xi_i^{\alpha})^2 \quad (23)$$

Subsequently, the $\bar{\Gamma}$ matrix is back-transformed into the AO basis by rearranging the MO coefficients in eq 21 through two fourth-order scaling steps of order $\mathcal{O}(o v n N_{\text{aux}} + o n^2 N_{\text{aux}})$

$$\bar{\Gamma}_{\mu\nu}^{M,\beta} = \sum_i^{\alpha} C_{\mu i} \left(\sum_a^{\alpha} C_{\nu a} \bar{\Gamma}_{ia}^{M,\beta} \right) \quad (24)$$

Note that the two-step back-transformation has to be performed only once as the Laplace quadrature independent $\bar{\Gamma}$ matrix is used in eq 24.

The second and third terms in eq 22 involve the occupied–occupied, occupied–virtual, virtual–occupied, and virtual–

virtual blocks of the orbital response matrix, U^x . Following the strategies used by Aikens et al.,³⁷ we make use of the closed-shell coupled-perturbed Hartree–Fock equations (see Appendix B) and the orthonormality constraint

$$U_{pq}^x + U_{qp}^x + S_{pq}^x = 0 \quad (25)$$

to manipulate the sum of the second term in eq 22 and the second term in eq 15 through some interesting algebra (see Appendix C) to arrive at

$$2 \sum_{\tau} w_{\tau} \sum_{ia}^{\alpha} \sum_M^{\text{all}} \left\{ \sum_p (pa|M) U_{pi}^x + t_{\tau} (ia|M) \epsilon_i^x \right\} \tau \Gamma_{ia}^{M,\beta} (\tau \xi_i^a)^2 = \sum_{ki}^{\alpha} \bar{P}_{ki}^{(2)} \left(\frac{Q_{ki}^x + Q_{ik}^x}{2} \right) + 2 \sum_{ci}^{\alpha} \overline{(L1)}_{ci} U_{ci}^x - \sum_{ki}^{\alpha} \overline{(L1)}_{ki} S_{ki}^x \quad (26)$$

where

$$\bar{P}_{ki}^{(2)} = \sum_{\tau} w_{\tau} \tau g_{ki}(z) \tau \Omega_{ki} \quad (27)$$

and

$$\tau \Omega_{ki} = \sum_a^{\alpha} (\tau \xi_i^a)^2 \sum_M (ka|M) \tau \Gamma_{ia}^{M,\beta} \quad (28)$$

and

$$\tau g_{ki} = \frac{\tau \xi_k^2 - \tau \xi_i^2}{\epsilon_k - \epsilon_i} = t_{\tau} \exp[(\epsilon_k + \epsilon_i)t_{\tau}/2] \frac{\sinh[(\epsilon_k - \epsilon_i)t_{\tau}/2]}{[(\epsilon_k - \epsilon_i)t_{\tau}/2]} \quad (29)$$

and

$$\overline{(L1)}_{pi} = \sum_{\tau} w_{\tau} \sum_a^{\alpha} (\tau \xi_i^a)^2 \sum_M \tau \Gamma_{ia}^{M,\beta} (pa|M) \quad (30)$$

The expressions for Q_{ki}^x are given by eqs B1 and B2. In the above equations, $\tau \xi_i = \exp(\epsilon_i t_{\tau}/2)$ and $\tau \xi_i^a = \exp(-\epsilon_a t_{\tau}/2)$. The details of the steps involved in arriving at eq 26 are indicated in Appendix C.

Similarly, the sum of the third terms in eqs 15 and 22 can be written as

$$2 \sum_{\tau} w_{\tau} \sum_{ia}^{\alpha} \sum_M^{\text{all}} \left\{ \sum_p (ip|M) U_{pa}^x - t_{\tau} (ia|M) \epsilon_a^x \right\} \tau \Gamma_{ia}^{M,\beta} (\tau \xi_i^a)^2 = \sum_{ca}^{\alpha} \bar{P}_{ca}^{(2)} \left(\frac{Q_{ca}^x + Q_{ac}^x}{2} \right) + 2 \sum_{ka}^{\alpha} \overline{(L2)}_{ka} U_{ka}^x - \sum_{ca}^{\alpha} \overline{(L2)}_{ca} S_{ca}^x \quad (31)$$

where

$$\bar{P}_{ca}^{(2)} = \sum_{\tau} w_{\tau} \tau g_{ca} \tau \Omega_{ca} \quad (32)$$

and

$$\tau \Omega_{ca} = \sum_i^{\alpha} (\tau \xi_i)^2 \sum_M (ic|M) \tau \Gamma_{ia}^{M,\beta} \quad (33)$$

and

$$\tau g_{ca} = \frac{\tau \xi_c^2 - \tau \xi_a^2}{\epsilon_c - \epsilon_a} = -t_{\tau} \exp[-(\epsilon_c + \epsilon_a)t_{\tau}/2] \frac{\sinh[-(\epsilon_c - \epsilon_a)t_{\tau}/2]}{[-(\epsilon_c - \epsilon_a)t_{\tau}/2]} \quad (34)$$

and

$$\overline{(L2)}_{pa} = \sum_{\tau} w_{\tau} \sum_i^{\alpha} (\tau \xi_i^a)^2 \sum_M \tau \Gamma_{ia}^{M,\beta} (ip|M) \quad (35)$$

The “g” function introduced in eqs 29 and 34 above is continuous at the limit of $\epsilon_i \approx \epsilon_k$ (or $\epsilon_c \approx \epsilon_a$) and tends to the finite value $t_{\tau}(\tau \xi_i)^2$ [or $-t_{\tau}(\tau \xi_i^a)^2$]. It thus ensures that the first term in eqs 26 and 31 are well-behaved when nearly degenerate orbitals are encountered.²⁵

When all of the information given above is used, the expression of the analytical gradient of the closed-shell OS-MP2 energy takes up the form

$$-\frac{1}{2} E_{\text{OS}}^x = \sum_{ik}^{\alpha} \bar{P}_{ki}^{(2)} \left(\frac{Q_{ki}^x + Q_{ik}^x}{2} \right) + \sum_{ik}^{\alpha} \overline{(L1)}_{ki} S_{ki}^x + \sum_{ca}^{\alpha} \bar{P}_{ca}^{(2)} \left(\frac{Q_{ca}^x + Q_{ac}^x}{2} \right) + \sum_{ca}^{\alpha} \overline{(L2)}_{ca} S_{ca}^x + 2 \sum_{ck}^{\alpha} \overline{(L1)}_{ck} U_{ck}^x + 2 \sum_{kc}^{\alpha} \overline{(L2)}_{kc} U_{kc}^x + 2 \sum_{\mu\nu} \sum_M \bar{\Gamma}_{\mu\nu}^{M,\beta} (\mu\nu|M)^x + \sum_{KL} \bar{\gamma}_{KL} V_{KL}^x \quad (36)$$

From this stage on, the expression for the OS-MP2 analytical gradient takes up the same form as the corresponding RIMP2 analytical gradient expression.⁴¹ Although further manipulation is required to arrive at the final standard expression given in eq 9, it involves the same strategies and techniques that were used in the derivation of the RIMP2 analytical gradient and will not be discussed in detail here. Some of the important steps following eq 36 are the assembly of the Lagrangian, followed by the iterative solution of the \mathbf{Z} -vector equation²⁷ to obtain the virtual–occupied block of the 1-PDM, \mathbf{P} , and finally, with the help of eqs B4–B6 and further rearrangements, the standard expression given in eq 9 can be obtained.^{37,41} The final expressions of the energy-weighted 1-PDM, $\bar{\mathbf{W}}$ is summarized below:

$$\text{occ-occ: } \bar{\mathbf{W}}_{ki} = -\overline{(L1)}_{ki} - \frac{1}{2}(\epsilon_i + \epsilon_k) \bar{P}_{ki} - \frac{1}{2} \sum_{pq} A_{pqki} \bar{P}_{pq} \quad (37)$$

$$\text{occ-vir: } \bar{\mathbf{W}}_{kc} = -\overline{(L2)}_{kc} \quad (38)$$

$$\text{vir-occ: } \bar{\mathbf{W}}_{ck} = -\frac{1}{2} \epsilon_k \bar{P}_{ck} \quad (39)$$

$$\text{vir-vir: } \bar{\mathbf{W}}_{ca} = -\overline{(L1)}_{ca} - \frac{1}{2} \epsilon_a \bar{P}_{ca} \quad (40)$$

The effective Lagrangian L_{ck} that goes into the \mathbf{Z} -vector equation, eq B9, is given by

$$\bar{L}_{ck} = \overline{(L1)}_{ck} + \overline{(L2)}_{ck} + \overline{(L3)}_{ck} \quad (41)$$

and

$$\overline{(L3)}_{ck} = \sum_{ij} A_{ijck} \overline{P}_{ij} + \sum_{ab} A_{abck} \overline{P}_{ab} \quad (42)$$

$\overline{(L1)}_{ai}$ and $\overline{(L2)}_{ai}$ in eq 41 are defined by eqs 30 and 35, respectively.

III. Fourth-Order Scaling Algorithm

In this section, we present the algorithmic details of the efficient fourth-order implementation of the proposed gradient method beyond the initial self-consistent field (SCF) steps. It is convenient to break up the post-SCF algorithm into the following four major sections.

A. Pre-Gradient. This section of the algorithm prepares for the evaluation of OS-MP2 energy and analytical gradient as shown in Chart 1. Similar to the OS-MP2 energy algorithm,^{51,52} the first two steps involve the formation of $V_{KL}^{-1/2}$ and $(ia|K)$, which are subsequently used to form B_{ia}^L through a simple matrix multiplication. Following this step, the three-center two-electron integrals are transposed to the order (a, i, K) going in the order of the fastest to the slowest index and stored on disk in order to efficiently form the 1-PDM contributions in the next stage of the algorithm.

B. Gradient I. This part of the algorithm involves the formation of the Laplace dependent quantities. The major steps are outlined in Chart 2. It includes the formation of the \mathbf{X} and the 2-PDM, ${}^{\tau}\Gamma$ matrix, for each Laplace quadrature point through two almost isomorphic fourth-order scaling steps, which are incidentally the dominant fourth-order steps of the OS-MP2 energy and gradient evaluation. The contributions to the occupied–occupied and virtual–virtual blocks of the 1-PDM, \mathbf{P} , are also obtained through the formation of intermediate matrices that involve two smaller fourth-order steps. The matrices, ${}^{\tau}\gamma$, ${}^{\tau}\Gamma$, and \mathbf{P} are then appropriately scaled and incremented on disk in order to form the Laplace quadrature independent quantities that will be used in the next part of the algorithm.

C. Gradient II. The RI-specific gradient entities are formed in this section. In particular, some of the small fourth-order scaling steps involved in this section are the formation of the pieces of the Lagrangian, $\mathbf{L1}$ and $\mathbf{L2}$, the two-step back-transformation of the $\overline{\Gamma}$ from a MO to AO basis, and finally contribution to the OS-MP2 gradient is obtained by contracting the three-index RI-specific 2-PDM, $\overline{\Gamma}$, with the corresponding three-center integral derivatives. Also, the analogous contribution to the gradient from the two-index RI-specific 2-PDM $\overline{\gamma}$ contracted with the two-center integral derivatives is accumulated. The outline of the major steps is shown in Chart 3.

D. Gradient III. The final section of the algorithm wraps up the evaluation of the analytical gradient. The last piece of the Lagrangian, $\mathbf{L3}$, which is a Fock-like matrix given by eq 41, is formed. It has a quartic computational cost for small systems and a quadratic cost for large systems.³⁶ With the assembly of the effective Lagrangian, the \mathbf{Z} -vector equation²⁷ can be solved self-consistently analogous to the SCF iterations, to obtain the virtual–occupied block of the 1-PDM, \mathbf{P} . Finally, the 1-PDM, \mathbf{P} ; energy-weighted 1-PDM, \mathbf{W} ; and

Chart 1. The Major Steps of the *Pregradient* Algorithmic Section along with the Details of the Ordering of Indices of the Various Entities Involved^a

	Index order	CPU	Disk
Form $V_{KL}^{-1/2}$	$\forall K, L$	N_{aux}^3	N_{aux}^2
Make $I_{ia}^K = (ia K)$	$\forall a, K, i$	$n^2 v N_{\text{aux}} + n v N_{\text{aux}}$	$ov N_{\text{aux}}$
Transpose I_{ia}^K	$\forall a, i, K$		$ov N_{\text{aux}}$
$B_{ia}^K = \sum_M (ia M) V_{MK}^{-1/2}$	$\forall a, K, i$	$ov N_{\text{aux}}^2$	$ov N_{\text{aux}}$

^a Cost of computation and order of disk storage, if necessary, are shown below.

Chart 2. The Major Steps of the *Gradient I* Algorithmic Section along with the Details of the Ordering of Indices of the Various Entities Involved^a

	Index order	CPU	Disk
Loop over quadrature points, τ			
Loop over i			
Read B_{ia}^K	$\forall a, K, \text{given } i$		
${}^{\tau}X_{kl}^{\alpha} = \sum_{\sigma} B_{ia}^K B_{i\sigma}^L$		$N_{\tau} \cdot ov N_{\text{aux}}^2$	
$E_{\text{SOS-MP2}} = \sum_{\tau} w_{\tau} \sum_{KL} {}^{\tau}X_{kl}^{\alpha} {}^{\tau}X_{kl}^{\beta}$		$N_{\tau} \cdot N_{\text{aux}}^2$	
Read $V_{MK}^{-1/2}$	$\forall M, K$		
${}^{\tau}Y_{Ml}^{\beta} = \sum_K V_{MK}^{-1/2} {}^{\tau}X_{kl}^{\beta}$		$N_{\tau} \cdot N_{\text{aux}}^3$	
$\overline{\gamma}_{KL} = \sum_{\tau} w_{\tau} \sum_M {}^{\tau}Y_{KM}^{\alpha} {}^{\tau}Y_{Ml}^{\beta}$		$N_{\tau} \cdot N_{\text{aux}}^3$	N_{aux}^2
Loop over i			
Read B_{ia}^L	$\forall a, L, \text{given } i$		
${}^{\tau}\Gamma_{ia}^{M,\beta} = \sum_L {}^{\tau}Y_{Ml}^{\beta} B_{ia}^L$		$N_{\tau} \cdot ov N_{\text{aux}}^2$	$ov N_{\text{aux}}$
Loop over M batches (batch size P)			
Read I_{ia}^M	$\forall a, k, M \in P$		
Transpose I_{ia}^M	$\forall k, a, M \in P$		
Loop over i			
Read ${}^{\tau}\Gamma_{ia}^{M,\beta}$	$\forall a, M \in P, \text{given } i$		
Accumulate ${}^{\tau}\Gamma_{ia}^{M,\beta}$	$\forall a, M \in P, \forall i$		
${}^{\tau}\Omega_{ki} = \sum_{\nu} I_{ki}^M {}^{\tau}\Gamma_{ia}^{M,\beta} \left(\frac{g_{\nu}}{\xi_{\nu}}\right)^2$		$N_{\tau} \cdot \sigma^2 v N_{\text{aux}}$	
$\overline{\Gamma}_{ia}^{M,\beta} = \sum_{\tau} w_{\tau} {}^{\tau}\Gamma_{ia}^{M,\beta} \left(\frac{\tau g_{\nu}}{\xi_{\nu}}\right)^2$	$\forall a, i, M \in P$		$ov N_{\text{aux}}$
Loop over M batches (batch size P)			
Read I_{ic}^M	$\forall c, i, M \in P$		
Loop over i			
Read ${}^{\tau}\Gamma_{ia}^{M,\beta}$	$\forall a, M \in P, \text{given } i$		
Accumulate ${}^{\tau}\Gamma_{ia}^{M,\beta}$	$\forall i, M \in P, \forall a$		
${}^{\tau}\Omega_{ca} = \sum_i I_{ic}^M {}^{\tau}\Gamma_{ia}^{M,\beta} \left(\frac{g_{\nu}}{\xi_{\nu}}\right)^2$		$N_{\tau} \cdot ov^2 N_{\text{aux}}$	
$\overline{P}_{ki} = \sum_{\tau} w_{\tau} {}^{\tau}\Omega_{ki} {}^{\tau}g_{ki}$			σ^2
$\overline{P}_{ca} = \sum_{\tau} w_{\tau} {}^{\tau}\Omega_{ca} {}^{\tau}g_{ca}$			v^2
End loop over quadrature points, τ			

^a Cost of computation and order of disk storage, if necessary, are shown below.

the separable 2-PDM, Γ^S are assembled, and the corresponding contributions to the overall gradient are obtained by the contraction with the respective nuclear derivatives.

Of the four major sections described above, in terms of algorithm and coding, only *Gradient I* is unique to the evaluation of the OS-MP2 gradient. The existing OS-MP2 energy code can be readily extended to evaluate key entities like ${}^{\tau}\Gamma$ and \mathbf{P} . The section *Gradient II* is common between RIMP2 and OS-MP2 gradient schemes,⁴¹ while the final section, *Gradient III*, is common for all MP2-based analytical gradient evaluations.^{36,41} We will therefore concentrate on only discussing the algorithmic details of *Gradient I* and refer the reader to refs 36 and 41 for further information on the other sections of the algorithm. Also, the changes that are

Chart 3. The Major Steps of the *Gradient II* Algorithmic Section along with the Details of the Ordering of Indices of the Various Entities Involved^a

	Index order	CPU	Disk
Loop over M batches (batch size P)			
Read $\bar{\Gamma}_{ia}^{M,\beta}$	$\forall a, i, M \in P$		
Back-transform: $\bar{\Gamma}_{iv}^{M,\beta} \leftarrow \bar{\Gamma}_{ia}^{M,\beta}$	$\forall v, i, M \in P$	$novN_{aux}$	noN_{aux}
Loop over M batches (batch size P)			
Read $\bar{\Gamma}_{iv}^{M,\beta}$	$\forall v, i, M \in P$		
Transpose $\bar{\Gamma}_{iv}^{M,\beta}$	$\forall i, M \in P, \forall v$		
Make $(\mu\nu M)$	$M \in P, \forall \mu, \nu$	n^2N_{aux}	
$(\bar{L}2)_{\mu\nu}^+ = \sum_{iM} \bar{\Gamma}_{iv}^{M,\beta} (\mu\nu M)$	$\forall i, \nu$	n^2oN_{aux}	no
Transform $(\mu\nu M) \rightarrow (i\nu M)$	$M \in P, \forall v, i$	n^2oN_{aux}	
Read $\bar{\Gamma}_{ia}^{M,\beta}$	$\forall a, i, M \in P$		
$(\bar{L}1)_{\alpha\nu}^+ = \sum_{iM} \bar{\Gamma}_{ia}^{M,\beta} (i\nu M)$	$\forall a, \nu$	$novN_{aux}$	nv
Loop over M batches (batch size P)			
Read $\bar{\Gamma}_{iv}^{M,\beta}$	$\forall v, i, M \in P$		
Transpose $\bar{\Gamma}_{iv}^{M,\beta}$	$M \in P, \forall v, i$		
Make $(\mu\nu M)^x$	$M \in P, \forall \nu, \mu$	n^2N_{aux}	
$E^x = \sum_{\mu\nu} \bar{\Gamma}_{\mu\nu}^{M,\beta} (\mu\nu M)^x$		n^2N_{aux}	
Read $\bar{\gamma}_{kl}$	$\forall K, L$		
Make $(K L)^x$	$\forall K, L$	N_{aux}^2	
$E^x = \sum_{kl} \bar{\gamma}_{kl} (K L)^x$			

^a Cost of computation and order of disk storage, if necessary, are shown below.

required to incorporate frozen-core approximation need to be made only in the *Gradient II* and *Gradient III* sections. As this is already implemented,^{36,41} the OS-MP2 gradient can automatically and conveniently deal with the frozen-core approximation with no further changes.

At this stage, we would also like to note that, between SOS-MP2 and MOS-MP2 analytical gradient implementations, the only major difference is the use of modified three- and two-index two-electron integrals, $\bar{I}(\omega) = I_{\text{Coulomb}} + c_{\text{MOS}} \cdot I_{\text{Erf}}(\omega)$, and integral derivatives, $\bar{I}^x(\omega) = I_{\text{Coulomb}}^x + c_{\text{MOS}} \cdot I_{\text{Erf}}^x(\omega)$, in the latter algorithm, which is obtained at almost no additional cost.⁵² Therefore, all algorithmic discussion of the SOS-MP2 gradient is applicable to the MOS-MP2 analytical gradient as well.

In this implementation of the OS-MP2 analytical gradient, we endeavor to achieve fourth-order CPU scaling, quadratic memory ($\sim 3N_{aux}^2$), cubic disk storage ($\sim 4ovN_{aux}$), and third-order I/O. In both RIMP2⁴¹ and the OS-MP2 gradient, the formation of the three-index 2-PDM is the dominating step with costs $\mathcal{O}(o^2v^2N_{aux})$ and $\mathcal{O}(N_{aux}ovN_{aux}^2)$, respectively. Similar to the discussion on the evaluation of the RIMP2 and OS-MP2 energy, there is a contest between the inherent fifth-order nature of the former and the repeated evaluation of the dominating fourth-order step for each Laplace quadrature point for the latter. However, as the system size increases, the fourth-order nature of the OS-MP2 analytical gradient would eventually kick in and considerable improvements in the CPU timing would be seen. This aspect will be discussed further in the Results and Discussion section. There are a few other competing fourth-order steps in the OS-MP2 gradient evaluation that would tend to dominate the calculation, especially for small systems. For instance, the iterative **Z**-vector solution and final assembly of **P**, **W**, and Γ^S are

isomorphic with the SCF and SCF gradient evaluations. However, these are also highly dependent on the cutoff employed for integral thresholding and convergence criterion, as we will see in the next section.

The evaluation of the analytical gradient is done mainly through a series of matrix multiplications. The upper bound on the memory requirement for these matrix multiplications is $\mathcal{O}(3N_{aux}^2)$, which is required to form, for example, eq 17. We should note here that the evaluation of the OS-MP2 energy also has the same memory requirement. In order to maintain this requirement, the three index entities are saved on disk and read, when necessary, within a loop structure that only requires quadratic memory to perform the matrix multiplication. Also, the three-index quantities are saved to disk in an order that would avoid disk-based sorting and unnecessary transpositions. For example, the three-index 2-PDM, ${}^t\Gamma$, is initially formed in the order (a, P, i) , moving from the fastest to the slowest index, which is then used in eqs 28 and 33 to form the intermediate ${}^t\Omega_{ki}$ and ${}^t\Omega_{ca}$ matrices. They are, however, subsequently transposed, incremented, and saved to the disk in the order (a, i, P) in order to reduce the number of read and seek operations on disk, when they are later used to form the **L1** and **L2** matrices in the *Gradient II* section.

In the formation of the intermediates, ${}^t\Omega_{ki}$ and ${}^t\Omega_{ca}$, through eqs 28 and 33, looping over the free indices k and i (or c and a , respectively) leads to a fourth-order I/O step. In order to avoid this, the intermediates are efficiently formed through a batching scheme over the auxiliary basis functions. For example, to form ${}^t\Omega_{ki}$ through eq 28, $(ka|M)$ and ${}^t\Gamma_{ia}^{M,\beta}$ are loaded as tiles of size ovP from disk to memory, where the batch size, P , is determined by the memory constraint discussed above, giving $P = (3N_{aux}^2 - o^2)/(2ov + v)$. The tiles of integrals $(ka|M)$ that are read in order $(a, k, M \in P)$ are subsequently transposed in memory to the order $(k, a, M \in P)$, while the tile ${}^t\Gamma_{ia}^{M,\beta}$ is accumulated in the order $(a, M \in P, i)$. A smaller batch size, $P = (3N_{aux}^2 - v^2)/(2ov + v)$, is used for the formation of ${}^t\Omega_{ca}$.

Apart from a small number of quadratic entities, the major disk storage corresponds to the three-index quantities of size ovN_{aux} . At first glance, the current gradient scheme might seem to require about $6ovN_{aux}$ disk space. This can be reduced to just $4ovN_{aux}$ by overwriting files holding intermediate quantities like ${}^t\Gamma_{ia}^{M,\beta}$ and $\bar{\Gamma}_{iv}^{M,\beta}$. In comparison to the energy calculation, the amount of disk space required to do a gradient evaluation is almost doubled. This is a modest increase. For example, to do an OS-MP2 analytical gradient calculation on a hexadeca alanine peptide with a 6-31G* basis and a double- ζ quality auxiliary basis ($o = 225$; $v = 1305$; $N_{aux} = 5390$; $n = 1610$) would imply a disk storage requirement of ~ 50 GB.

IV. Results and Discussion

In this section we evaluate the performance of the proposed method both computationally and chemically. We have implemented the quartic scaling SOS-MP2 and MOS-MP2 analytical gradient schemes in our quantum chemical software package, QCHEM 3.0.⁶³ All reported calculations were performed with QCHEM. While the discussion above

Table 2. CPU Timings Obtained on Opteron Cluster for the Force Evaluation of Polyalanine Peptides with 6-31G** Basis and the Corresponding Auxiliary Basis at Various Levels of Theory (in Seconds)

system ^b	SCF	full gradient CPU timing ^a				
		HF ^c	MP2	RIMP2	SOS-MP2	MOS-MP2
			3D			
Tetra	1153	1704	9160	4470	4106	4141
Octa	6773	9596	121 473	46 953	30 513	30 853
HexaDeca	32 751	46 305		781 151	226 751	227 251
			1D			
Tetra	847	1253	6559	3400	3010	3046
Octa	3909	5672	68 989	34 389	18 459	18 689
HexaDeca	20 379	29 098		721 879	166 379	164 979

^a Full gradient CPU timing = SCF + correlation energy + gradient. ^b Number of basis functions (n): $n_{\text{Tetra}} = 410$; $n_{\text{Octa}} = 810$; $n_{\text{HexaDeca}} = 1610$. ^c HF energy + gradient timing.

referred to the algorithm for a closed-shell case, we have also implemented the straightforward extensions necessary to perform unrestricted calculations and to use the frozen-core approximation.

A. Benchmark Timing. We have considered linear (1D) and globular (3D) polyalanine peptides (tetra-, octa-, and hexadeca-) as model systems to benchmark the computational performance of the proposed algorithm. Table 2 reports the total CPU benchmark timings obtained for the analytical force evaluation of the above systems on a 2 GHz AMD Opteron processor with a 1 GB memory limit using the 6-31G** basis with frozen-core approximation and a double- ζ valence polarized auxiliary basis set. A threshold of 10^{-12} au was employed for integral screening, while the SCF direct inversion in the iterative space (DIIS) convergence was set to 10^{-8} au for all calculations unless specified otherwise.

Table 2 clearly indicates that the use of auxiliary basis expansions brings about significant speedups in the gradient evaluation. For example, if we consider the tetrapeptides, the RIMP2 gradient evaluation is about twice as fast as the conventional MP2 gradient and costs less than 3 times that of the HF gradient. On the other hand, the SOS-MP2 and MOS-MP2 gradient timings are slightly lower than the corresponding RIMP2 timings. The similarity in timings reflects the contest between the repeated evaluation of the fourth-order scaling steps for each Laplace quadrature point in the OS-MP2 methods and the fifth-order scaling steps of RIMP2 for small systems. Also, it indicates that the crossover occurs around the 20 heavy atom regime (less than 400 basis functions) for these polypeptide systems. The SOS-MP2 and MOS-MP2 gradient timings are very similar for all systems considered, indicating that the extra cost of evaluating the modified long-range integrals and their first derivatives for the latter method is almost negligible.

As the system size increases, the fourth-order scaling behavior of the OS-MP2 analytical gradient becomes more apparent. At the octapeptide level, the OS-MP2 gradient costs about 3 times the HF gradient and is about 4 times faster than the conventional MP2 gradient. At the hexadeca level (80 heavy atom regime and about 1610 basis functions), the OS-MP2 gradient timings show significant speedups and are about 4 times faster than the corresponding RIMP2 timings. Table 2 also indicates that dimensionality of the system is

critical to the overall CPU timing. Globular systems are more expensive than the linear analogues due to the larger number of significant AO basis function pairs.

In order to take a closer look at the performance of the method, Tables 3 and 4 show the CPU timings obtained for the key steps of the SOS-MP2 energy and gradient calculation for the linear and globular polypeptides. The formation of the \mathbf{X} matrix and $\bar{\Gamma}$ matrix, solution of the \mathbf{Z} -vector equation, and assembly of the separable part of the 2-PDM (Γ^S) are among the most time-consuming steps in the evaluation of the analytical SOS-MP2 gradient. The costs of evaluating \mathbf{X} and $\bar{\Gamma}$ are isomorphic given that both terms go as $\mathcal{O}(N_{\text{tot}}N_{\text{aux}}^2)$. The latter is slightly more expensive due to the additional cost of incrementing the 2-PDM on disk for each Laplace quadrature point and becomes the dominant fourth-order step in the evaluation of the SOS-MP2 analytical gradient as the system size increases. For small systems, the solution of the \mathbf{Z} -vector equation and formation of the Γ^S matrix dominate the gradient calculation. However, these two steps [and also the formation of $(ia|P)$, other pieces of *Gradient II* and *Gradient III*] are inextricably connected to the dimensionality of the system and the cutoff for the integral screening. With a tight integral cutoff (10^{-12} au), these two steps, therefore, appear to dominate the calculation for a large system like the globular hexadecapeptide. The corresponding linear analogue clearly indicates that the \mathbf{X} and $\bar{\Gamma}$ formation becomes the most time-consuming step. In order to emphasize the effect of the integral threshold, the timings obtained for a looser cutoff (integral threshold: 10^{-10} au; DIIS convergence: 10^{-7}) are also shown in Tables 3 and 4. The looser criteria thus enable us to speed up the SCF, SCF Gradient, and Gradient III calculations by about 40%, 38%, and 27% for the globular hexadecapeptides and by about 38%, 30%, and 24% for the linear analogue, respectively. We should note here that the choice of threshold is closely related to the accuracy of the calculation. Tight tolerances are recommended if a high level of accuracy is desired. On the other hand, the various pieces of the energy [excluding $(ia|P)$ formation] and *Gradient I* evaluation are independent of the cutoff threshold as well as dimensionality of the system and, therefore, show no change in computational cost between the linear and globular analogues. We should also emphasize at this stage that the speedups obtained by the SOS-MP2 and MOS-MP2 analytical gradient lies

Table 3. Breakdown of the Dominant Fourth-Order CPU Steps in the SOS-MP2 Energy and Force/Gradient Evaluation of the Globular/Three-Dimensional Polyalanine Peptides with 6-31G** Basis and Its Corresponding Auxiliary Basis (in Seconds)

criterion ^a	tetra.3D		octa.3D		hexadeca.3D			
	8/12	7/10	8/12	7/10	8/12	7/10		
SCF	1153	717	6773	3991	32 751	19 601		
HF gradient	550	353	2823	1725	13 553	8191		
CPU	energy + gradient ^b		23 740	19 710	194 000	168 500		
energy	{	(<i>ia P</i>)	44	41	486	425	5987	5214
		B_{ia}^O	22	23	326	325	4943	4957
		X_{PQ}	150	151	2222	2221	33 870	33 990
Gradient I	{	$\bar{\Gamma}_{ia}^P$	164	167	2363	2358	35 247	35 343
		$\tau\Omega_{ki}$	24	26	303	304	2584	2538
		$\tau\Omega_{ca}$	50	49	643	649	9152	9144
Gradient II	{	$(\bar{L1})_{iv} + (\bar{L2})_{av}$	73	67	724	674	7889	6887
		$\sum_{\mu\nu M} (\mu\nu M)\bar{\Gamma}_{\mu\nu}^{M,\beta}$	80	73	620	517	5185	4546
Gradient III	{	($\bar{L3}$)	270	209	1747	1284	9279	6694
		Z vector	926	724	6099	4503	32 940	23 780
		$\Gamma_{\mu\nu\lambda\sigma}^S$	1084	867	7651	5898	41 880	30 490

^a Cutoff for integral thresholding/SCF convergence criterion. ^b CPU timing = correlation energy + SOS-MP2 gradient.

Table 4. Breakdown of the Dominant Fourth-Order CPU Steps in the SOS-MP2 Energy and Force/Gradient Evaluation of the Linear/One-Dimensional Polyalanine Peptides with 6-31G** Basis and Its Corresponding Auxiliary Basis (in Seconds)

criterion ^a	tetra.1D		octa.1D		hexadeca.1D			
	8/12	7/10	8/12	7/10	8/12	7/10		
SCF	847	554	3909	2476	20 379	12 493		
HF gradient	406	296	1763	1246	8719	5788		
CPU	energy + gradient ^b		14 550	13 230	146 000	135 000		
energy	{	(<i>ia P</i>)	36	34	337	311	4671	4466
		B_{ia}^O	23	23	322	326	4932	4942
		X_{PQ}	150	150	2218	2220	33 880	33 890
Gradient I	{	$\bar{\Gamma}_{ia}^P$	164	154	2350	2366	35 319	35 345
		$\tau\Omega_{ki}$	24	24	289	303	2582	2577
		$\tau\Omega_{ca}$	49	49	634	647	9168	9173
Gradient II	{	$(\bar{L1})_{iv} + (\bar{L2})_{av}$	59	52	501	487	5656	5245
		$\sum_{\mu\nu M} (\mu\nu M)\bar{\Gamma}_{\mu\nu}^{M,\beta}$	69	59	410	367	3532	3054
Gradient III	{	($\bar{L3}$)	183	147	828	666	4795	3577
		Z vector	627	507	2832	2304	16 760	12 720
		$\Gamma_{\mu\nu\lambda\sigma}^S$	711	573	3281	2687	19 660	15 040

^a Cutoff for integral thresholding/SCF convergence criterion. ^b CPU timing = correlation energy + SOS-MP2 gradient.

solely in the formation of the pieces of *Gradient I* as the corresponding steps in the RIMP2 gradient involve terms that are fifth-order in nature. The *Gradient II* and *Gradient III* sections are common for both OS-MP2 and RIMP2 gradient methods.

B. Chemical Tests and Application. While it is important to achieve computational speedups, we should also ensure that accuracy is not severely affected in the process. The scaled-MP2 methods, SCS-MP2, SOS-MP2, and MOS-MP2, are known to improve conventional MP2 relative energies like atomization energies, for example. Grimme et al. have also shown that the analytical SCS-MP2 gradient provides marginal statistical improvements over the MP2 geometries.⁶⁴ While this is an encouraging feature, there is no apparent computational advantage achieved by using this method. We have established in the previous sections and discussion that our OS-MP2 analytical gradient provides significant speedups relative to the RIMP2 (or SCS-MP2) analytical gradient. We will now assess the performance of the OS-MP2 analytical

gradient through a statistical study of a database of main group molecules and further specific application in transition metal chemistry.

i. Statistical Study. We have recently set up a database of molecular geometries of 178 small molecules computed at various levels of theory.⁴¹ The database consists of a variety of closed- and open-shell systems that are neutral or ionic in nature. We have used our new OS-MP2 analytical gradient techniques to obtain the structural information of these 178 molecules using two different basis sets, cc-pVDZ and cc-pVTZ.⁶⁵ Table 5 gives the statistical errors obtained relative to experimental bond lengths for various methods like conventional MP2, RIMP2, SCS-MP2, SOS-MP2, and MOS-MP2. For each basis set considered, the mean absolute deviation (MAD) and root-mean-squared (RMS) errors obtained relative to experimental data for the various flavors of MP2 are very similar. This consistency over such a diverse collection of molecules indicates that reliable geometries can be obtained from these scaled-MP2 methods. In general,

Table 5. Statistical Errors in Calculated Bond Lengths of 178 Molecules^a Relative to Experimental Bond Lengths (r_e) in Picometers

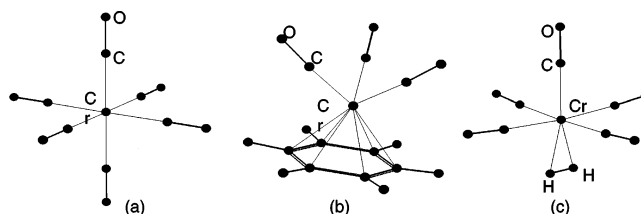
method	MAD ^b	RMS ^c	MAX ^d
cc-pVDZ			
MP2	2.776	3.698	16.862
RIMP2	2.767	3.691	16.864
SCSMP2	2.776	3.632	16.734
SOSMP2	2.791	3.639	16.668
MOSMP2	3.201	4.078	17.641
cc-pVTZ			
MP2	1.403	2.172	8.237
RIMP2	1.410	2.157	8.234
SCSMP2	1.359	2.111	8.270
SOSMP2	1.361	2.121	8.286
MOSMP2	1.828	2.443	8.184

^a See Distasio et al.⁴¹ ^b MAD: Mean absolute deviation ^c RMS: Root mean-squared deviation ^d MAX: Maximum absolute error

MOS-MP2 appears to make a slightly larger error (off by ~ 0.2 – 0.5 pm) than the other MP2 methods. MAD and RMS are found to improve for all methods by ~ 1.4 – 1.5 pm when the size of the basis set is improved from cc-pVDZ to cc-pVTZ, which indicates the value of using the larger basis set. There is an even more significant change in the maximum absolute (MAX) error (reduced by about 50%) when changing the basis set from cc-pVDZ to cc-pVTZ. These trends indicate that the OS-MP2 methods can provide reliable geometries of molecules that are in general well-described by traditional MP2.

ii. Study of Group VI Transition Metal Carbonyl Systems. Although the scaled-MP2 methods are expected to improve the conventional MP2 picture, it is not apparent in the previous statistical study. One way to establish whether improvements are obtained is to study systems that are known to be difficult for traditional MP2. Computational TM chemistry has remained a formidable challenge to the theoretical community owing to its complex electronic structure and high computational requirements.^{66,67} Over the years, DFT has proved to be the most popular methodology used to describe TM geometries and bond energies,^{66–69} while conventional ab initio methods like HF and MP2 have shown limited success with the closed-shell TM complexes.⁴⁷ Higher-correlation treatments like CCSD(T) would ideally provide reliable bond energies but are limited to small systems and cannot be routinely used due to the expensive nature of such calculations. In particular, MP2 is known to consistently underestimate the metal–ligand bond distances and, thereby, overestimate the corresponding bond energies.⁴⁷ It was established recently that the closely related scaled-MP2 method, SCS-MP2, provides an improved structural description of certain transition metal compounds. Also, when the scaling idea is extended to a higher order of the MP n series, namely, SCS-MP3, considerable improvements are obtained in description of the thermochemistry of representative TM carbonyl compounds.⁵⁷

To assess the performance of our analytical gradient implementation of SOS-MP2 and MOS-MP2, we have considered similar examples of TM–carbonyl complexes such as $M(\text{CO})_6$, $M(\text{CO})_5\text{H}_2$, and $M(\text{CO})_3(\text{C}_6\text{H}_6)$ ($M = \text{Cr}$,

**Figure 1.** Obtained SOS-MP2 optimized geometries of (a) $\text{Cr}(\text{CO})_6$, (b) $\text{C}_6\text{H}_6\text{-Cr}(\text{CO})_3$, and (c) $\text{Cr}(\text{CO})_5(\text{H}_2)$. For further structural details, refer to Table 6.

Mo). The geometries of these complexes were optimized at the SOS-MP2 and MOS-MP2 levels. The bond dissociation energies (D_0) of the $M\text{-CO}$ bond in $M(\text{CO})_6$ and $M(\text{CO})_3\text{-}(\text{C}_6\text{H}_6)$ and the $M\text{-H}_2$ bond in $M(\text{CO})_5\text{H}_2$ were also evaluated at the same level of theory. The Stuttgart–Bonn set^{70,71} of effective core potentials (ECP) was used to describe the TM core, while the 6-311G** basis set was used for the other lighter elements, and a triple- ζ valence polarized auxiliary basis was used as a fitting basis.⁷² All the methods considered predict octahedral (O_h) symmetry for the $M(\text{CO})_6$ complexes, C_{3v} symmetry for the $\text{C}_6\text{H}_6\text{-M}(\text{CO})_3$ systems, and C_{2v} symmetry for the $M(\text{CO})_5(\text{H}_2)$ complexes. The SOS-MP2 optimized geometries of the Cr systems considered are shown in Figure 1. Table 6 summarizes the main structural characteristics obtained when the aforementioned systems were optimized with RIMP2 and the three scaled-MP2 theories. We have also included, for purposes of comparison, the structural features obtained from DFT optimizations using two different, popular functionals, B3LYP⁷³ and BP86.^{74,75} Table 6 also indicates the relative error in various bond lengths (indicated within parenthesis) with respect to experimental data, if available.

The data provided in Table 6 suggest that RIMP2 consistently underestimates the metal–carbonyl ($M\text{-CO}$) and metal–carbon(benzene) [$M\text{-C}(\text{arene})$] bond distances [with the exception of $\text{Mo}\text{-CO}$ bond length for the complex $\text{C}_6\text{H}_6\text{-Mo}(\text{CO})_3$], consistent with previous studies. All three scaled-MP2 theories are able to correct this underestimation and predict bond distances that are closer to the experimental values. In particular, SOS-MP2 provides the best $M\text{-CO}$ and $M\text{-C}(\text{arene})$ bond lengths among the various flavors of MP2, closely followed by MOS-MP2 and SCS-MP2. For example, for the complex $\text{Cr}(\text{CO})_6$, the predicted absolute error (relative to experimental data) in the RIMP2 $\text{Cr}\text{-CO}$ bond length is reduced from 6 to 1.9 pm by SOS-MP2, while MOS-MP2 and SCS-MP2 are off by 2.4 and 3.4 pm, respectively. The geometries predicted by DFT (both B3LYP and BP86) are consistently closer to the experimental information than the MP2 family, with BP86 providing slightly better structures than B3LYP.⁶⁹ The only exception to the trend observed is the $\text{Mo}\text{-CO}$ bond distance in the complex $\text{C}_6\text{H}_6\text{-Mo}(\text{CO})_3$. In this case, RIMP2 seems to predict the best $\text{Mo}\text{-CO}$ bond length (error of 0.7 pm), while the remaining methods including the DFT results seem to overestimate the bond distance. This apparent success of RIMP2 seems fortuitous and raises doubts about the validity of the corresponding experimental data. The MP2-type methods and BP86 tend to overestimate the CO bond distances in most cases, while B3LYP tends to shorten the

Table 6. Optimized Geometrical Features (Bond Lengths) of the Group VI Transition Metal Carbonyl Complexes Obtained at the Various MP2 Levels and with the DFT Functionals Considered (in Picometers)^a

system	experiment	RIMP2	SOS-MP2	SCS-MP2	MOS-MP2	B3LYP	BP86
M–CO							
Cr(CO) ₆	191.8 ^b	185.8 (–6)	189.9 (–1.9)	188.4 (–3.4)	189.4 (–2.4)	192.1 (0.3)	190.4 (–1.4)
Mo(CO) ₆	206.3 ^b	203.8 (–2.5)	206.4 (0.1)	205.5 (–0.8)	205.7 (–0.6)	207.7 (1.4)	206.5 (0.2)
C ₆ H ₆ –Cr(CO) ₃	184.5 ^c	176.3 (–8.2)	181.3 (–3.2)	179.5 (–5)	180.8 (–3.7)	185.5 (1)	183.9 (–0.6)
C ₆ H ₆ –Mo(CO) ₃	196 ^d	196.7 (0.7)	199.1 (3.1)	198.3 (2.3)	198.7 (2.7)	198.5 (2.5)	197.9 (1.9)
Cr(CO) ₅ (H ₂)		185.6	190.2	188.6	189.6	191.8	186.6
Mo(CO) ₅ (H ₂)		179.2	183.7	182.2	183.1	191.8	190.1
		197.6	200.0	199.1	198.8	201.6	200.6
		203.3	206.0	205.1	205.3	207.2	205.9
M–C (Arene)							
C ₆ H ₆ –Cr(CO) ₃	223 ^c	216.6 (–6.4)	220.2 (–2.8)	218.8 (–4.2)	219.8 (–3.2)	225.2 (2.2)	223 (0)
C ₆ H ₆ –Mo(CO) ₃	237.6 ^d	230.6 (–7.0)	233.3 (–4.3)	232.4 (–5.2)	232.7 (–4.9)	240.8 (3.2)	238.7 (1.1)
CO							
CO	112.8 ^e	113.7 (0.9)	113.4 (0.6)	113.5 (0.7)	113.7 (0.9)	112.6 (–0.2)	113.9 (1.1)
Cr(CO) ₆	114.1 ^b	115.6 (1.5)	115.0 (0.9)	115.2 (1.1)	115.3 (1.2)	114.0 (–0.1)	115.5 (1.4)
Mo(CO) ₆	114.5 ^b	115.3 (0.8)	114.8 (0.3)	115.0 (0.5)	115.2 (0.7)	114.0 (–0.5)	115.4 (0.9)
C ₆ H ₆ –Cr(CO) ₃	115.8 ^c	117.4 (1.6)	116.3 (0.5)	116.6 (0.8)	116.8 (1.0)	115.2 (–0.6)	116.7 (0.9)
C ₆ H ₆ –Mo(CO) ₃	116.1 ^d	116.3 (0.2)	115.8 (–0.3)	115.9 (–0.2)	116.2 (0.1)	115.3 (–0.8)	116.7 (0.6)
Cr(CO) ₅ (H ₂)		116.3	115.6	115.8	115.9	114.1	115.7
Mo(CO) ₅ (H ₂)		115.7	115.2	115.3	115.4	114.3	115.7
Cr–H ₂							
Cr(CO) ₅ (H ₂)		166.4	171.5	169.6	171.1	170	171.6
Mo(CO) ₅ (H ₂)		186	189	188.1	189.6	192	190.3
H–H							
H ₂	74.2	73.8 (–0.4)	73.9 (–0.3)	73.9 (–0.3)	74.3 (0.1)	74.4 (0.2)	75.2 (1.0)
Cr(CO) ₅ (H ₂)		83.2	80.8	81.6	82	81.4	82.6
Mo(CO) ₅ (H ₂)		81.3	80.2	80.5	80.8	79.9	81.8

^a The deviation from available experimental data is indicated within parantheses for each indicated method. ^b References 79 and 80. ^c Reference 81. ^d Reference 82. ^e Reference 83.

C–O bond. However, the absolute magnitude of the error in the CO bond length is smaller than the M–CO and M–C(arene) cases discussed above. In particular, the deviation from the experimental CO bond distances appears to be lower for the scaled-MP2 methods, especially SOS-MP2, relative to RIMP2 and BP86. There is no experimental structural information currently available for the M(CO)₅H₂ systems. However, the scaled-MP2 theories continue to predict bond lengths [M–CO, M–C(arene), and CO] that are slightly longer than the RIMP2 case, consistent with the trend discussed above.

Table 7 summarizes the theoretical bond dissociation energies (D_0) obtained using the aforementioned methods. The D_0 values are obtained by correcting the electronic dissociation energy (D_e) for changes in the zero-point

vibrational energies. Subsequent thermodynamic corrections arising from the translational, vibrational, and rotational degrees of freedom, as well as pV work (assuming ideal behavior), were determined to be <2 kcal/mol for the systems considered here. This information was obtained from the vibrational frequency analysis performed on the optimized structure at each level of theory considered above. Due to the lack of analytical second derivatives for the RIMP2, SOS-MP2, SCS-MP2, and MOS-MP2 methods, the vibrational frequencies were obtained by performing numerical differentiation of the respective analytical gradients. We also note here that the calculated electronic dissociation energies have not been corrected for basis set superposition error on the basis of previous recommendations.⁴⁷ To further substantiate the calculated dissociation energies, we have also

Table 7. Calculated Bond Dissociation Energies, Namely M–CO and M–H₂, of the Various Group VI Transition Metal Carbonyls Considered at Different Levels of MP2 Theory, DFT and CCSD(T) (in kcal/mol)

system	exptl	RIMP2	SOS-MP2	SCS-MP2	MOS-MP2	B3LYP	BP86	CCSD(T) ^a
Cr(CO) ₆	36.80 ^b	56.62	44.04	48.35	48.45	34.87	41.07	41.71
	<i>e</i> ₁ ^c	(19.82)	(7.24)	(11.55)	(11.65)	(-1.93)	(4.27)	
	<i>e</i> ₂ ^d	<i>14.91</i>	<i>2.33</i>	<i>6.64</i>	<i>6.74</i>	<i>-6.84</i>	<i>-0.64</i>	
Mo(CO) ₆	40.50 ^b	46.45	38.87	41.46	41.82	38.15	41.13	39.58
	<i>e</i> ₁ ^c	(5.95)	(-1.63)	(0.96)	(1.32)	(-2.35)	(0.63)	
	<i>e</i> ₂ ^d	<i>6.87</i>	<i>-0.72</i>	<i>1.88</i>	<i>2.24</i>	<i>-1.43</i>	<i>1.54</i>	
C ₆ H ₆ –Cr(CO) ₃	51.89 ^e	74.90	54.39	60.98	60.29	43.20	51.93	
C ₆ H ₆ –Mo(CO) ₃		60.33	49.40	53.01	54.07	49.88	55.59	
Cr(CO) ₅ (H ₂)	15.00 ^f	24.69	17.51	19.95	20.14	11.44	16.51	17.64
	<i>e</i> ₁ ^c	(9.69)	(2.51)	(4.95)	(5.14)	(-3.56)	(1.51)	
	<i>e</i> ₂ ^d	<i>7.05</i>	<i>-0.13</i>	<i>2.31</i>	<i>2.50</i>	<i>-6.20</i>	<i>-1.13</i>	
Mo(CO) ₅ (H ₂)		17.81	13.81	15.12	15.82	11.05	12.48	15.16
	<i>e</i> ₂ ^d	<i>2.65</i>	<i>-1.35</i>	<i>-0.04</i>	<i>0.66</i>	<i>-4.12</i>	<i>-2.68</i>	

^a CCSD(T) calculation performed on the BP86 optimized geometry. ^b Reference 84. ^c *e*₁: error relative to experiment (indicated method – expt). ^d *e*₂: error relative to CCSD(T) [indicated method – CCSD(T)]. ^e DFT estimates from refs 77 and 78. ^f Reference 85.

performed the highly accurate CCSD(T) calculations on the BP86 optimized geometry using the same ECP and basis set as before. Due to the expensive nature of this method, we have been limited to the smaller systems, M(CO)₆ and M(CO)₅(H₂). Table 7 also provides information about the relative errors (*e*₁) between the calculated *D*₀ value and available experimental data (numbers indicated within parentheses).

The relative errors (*e*₁) indicate that RIMP2 tends to overestimate the M–CO and M–H₂ dissociation energies. This is consistent with the trend that RIMP2 tends to underestimate the M–CO bond length. The overestimation is significantly higher for Cr(CO)₆ and Cr(CO)₅(H₂) with the *e*₁ being as high as 19.8 kcal/mol and 9.7 kcal/mol, respectively, while Mo(CO)₆ is about 6 kcal/mol off. This trend is consistent with the previous studies on these compounds.⁶⁸ All the scaled-MP2 methods predict *D*₀ values that are closer to the experimental values than RIMP2, consistent with the corresponding prediction of longer M–CO and M–H₂ bond distances. The Mo–CO bond energy in the complex Mo(CO)₆ is the only case where SOS-MP2 seems to underestimate the bond energy by about 2 kcal/mol, while SCS-MP2 and MOS-MP2 are about 4–5 kcal/mol better than the RIMP2 result. In general, the SCS-MP2 and MOS-MP2 results are similar in magnitude, while SOS-MP2 is sometimes better than the former results or of comparable quality. Among the DFT methods, B3LYP tends to underestimate the bond energy while BP86 consistently provides better results.⁶⁹

The analysis so far assumes that the reference experimental values are the best available estimates of bond energies. This is not necessarily true; for example, inconsistencies between experimental and theoretical results for the Cr–(CO) first bond dissociation energy have raised doubts about the validity of the reported experimental value of 36.8 kcal/mol.^{47,76} Indeed, the more reliable CCSD(T) method computed in this study with a triple- ζ -quality basis predicts a dissociation energy of about 41.7 kcal/mol and is almost 5 kcal/mol higher than the experimental estimate.⁴⁷ Also, the scaled-MP2 methods are designed to produce QCISD(T)- or CCSD(T)-quality results. Therefore, in order to make a

fair comparison, we have also included the errors (*e*₂) obtained relative to CCSD(T) energies (italicized numbers in Table 7).

The *e*₂ errors are either lower than or similar to the obtained *e*₁ errors, indicating that the dissociation energies obtained with the scaled-MP2 methods are closer to the CCSD(T) values. In particular, the calculated SOS-MP2 bond dissociation energy for Mo(CO)₆ is about 0.7 kcal/mol lower than the corresponding CCSD(T) value. The corresponding *e*₁ error indicated that SOS-MP2 underestimated the experimental result. For the Mo(CO)₅(H₂) complex, there is no experimental M–H₂ bond energy data available. However, our CCSD(T) result indicates that the trend of RIMP2 overestimation of bond energies and improvements from the scaled-MP2 methods is still valid. Also, we should note here that, with the newly proposed SOS-MP2 and MOS-MP2 analytical gradients, you can obtain these CCSD(T)-quality energies for far lower computational cost. For example, the complete geometry optimization procedure at the SOS-MP2 level for Cr(CO)₆ took about 2.3 h on a Linux Opteron processor, while the single-point energy evaluation performed on the same processor at the CCSD(T) level alone took about 27.3 h.

For the C₆H₆–M(CO)₃ systems, we are not aware of any gas-phase experimental data available on the first dissociation energy of the M–CO bond, and these systems are computationally too big to get CCSD(T) energies. Previous DFT studies on the neutral C₆H₆–Cr(CO)₃ system estimate the first Cr–CO bond energy to be about 52 kcal/mol.^{77,78} SOS-MP2 estimates the Cr–CO bond energy to be about 54.3 kcal/mol, while SCS-MP2 and MOS-MP2 estimate about 60 kcal/mol. RIMP2 gives a much higher bond energy of 74.9 kcal/mol, while B3LYP predicts a low 43 kcal/mol. The BP86 functional predicts the bond energy to be ~52 kcal/mol, which is in agreement with previous studies.^{77,78} A similar trend is observed with the Mo analogue. These numbers are consistent with the previous discussion on the Cr–CO bond distance where RIMP2 geometry predicted a relatively short Cr–CO bond distance, while the scaled-MP2 methods are about 3–5 pm longer than RIMP2 bond distance.

V. Conclusions

In this paper, we have presented the derivation and efficient implementation of the fourth-order scaling analytical gradients of the SOS-MP2 and MOS-MP2 energies that are obtained through a combination of auxiliary basis expansions and a Laplace transformation. The theory is interesting because all fifth-order steps that arise in a conventional derivation of the opposite-spin MP2 gradient involve either four-center two-electron integrals or the pair correlation amplitudes. The former are obviously re-expressed in terms of two- and three-center quantities with the use of auxiliary basis expansions, and this paper shows that the amplitudes also likewise need never explicitly enter the gradient expressions. Instead, more compact two- and three-center intermediates in the auxiliary basis are used.

Significant computational speedups can be achieved by using these OS-MP2 analytical gradients to optimize the molecular geometry of large-sized systems. The inherent fourth-order nature of the algorithm helps to push the boundary of the size of systems currently feasible with conventional MP2 and RIMP2 methods, using reasonably sized basis sets. The largest calculation performed in this paper is the force calculation of the globular hexadeca alanine polypeptide with 1610 basis functions. The overall SOS-MP2 and MOS-MP2 force evaluation is about 3.4 times faster than the corresponding RIMP2 calculation.

Apart from the computational advantages, the OS-MP2 methods achieve either a MP2 level of accuracy or even help to improve the MP2 picture. Statistical results of the bond lengths obtained from 178 molecules indicate that the geometries obtained by the OS-MP2 methods are as good as MP2. The geometrical optimizations and subsequent calculation of the bond dissociation energies of the group VI transition metal carbonyl complexes indicate that SOS-MP2 and MOS-MP2 geometries help to significantly improve the underestimation seen in MP2 bond lengths and consequently predict M–CO and M–H₂ bond dissociation energies that are closer to experimental and CCSD(T) results.

However, one should keep in mind that methods like SOS-MP2 provide improvements in relative energies only when MP2 is known to overestimate the corresponding energy relative to higher-correlation treatments like CCSD(T).⁵² Also, given the empirical nature of these OS-MP2 methods, one should probably investigate the choice of optimal parameter while studying specific properties even though in our study the recommended parameters perform just fine. Apart from these caveats, the reduced scaling OS-MP2 gradient algorithm seems to be a fast, efficient, and accurate method that can be used to determine molecular geometries of medium- to large-sized systems.

Acknowledgment. This work was supported by the Office of Basic Energy Sciences of the U.S. Department of Energy through the Computational Nanoscience Initiative, with additional support from Q-Chem Inc. through a subcontract from the NIH SBIR award 5R44GM066484-02. R.C.L. would like to thank R. P. Steele for providing the database of 178 molecules for this study. M.H.G. is a part-owner of Q-Chem Inc.

Appendix A

Outline of Steps Leading to eq 15. Direct differentiation of eqs 7 and 12 leads to

$$[\tau X_{KL}^{\alpha}]^x = 2 \sum_{ia}^{\alpha} [B_{ia}^K]^x B_{ia}^L (\tau \xi_i^{\alpha})^2 + t_{\tau} \sum_{ia}^{\alpha} B_{ia}^K B_{ia}^L (\tau \xi_i^{\alpha})^2 [\epsilon_i^x - \epsilon_a^x] \quad (\text{A1})$$

$$[B_{ia}^K]^x = \sum_M (ia|M)^x V_{MK}^{-1/2} + \sum_M (ia|M) [V_{MK}^{-1/2}]^x \quad (\text{A2})$$

$$[V_{MK}^{-1/2}]^x = -\frac{1}{2} \sum_{NP} V_{MN}^{-1} V_{NP}^x V_{PK}^{-1/2} \quad (\text{A3})$$

Plugging eq A3 into eq A2 would then give

$$[B_{ia}^K]^x = \sum_M (ia|M)^x V_{MK}^{-1/2} - \frac{1}{2} \sum_{PQN} B_{ia}^Q V_{QN}^{-1/2} V_{NP}^x V_{PK}^{-1/2} \quad (\text{A4})$$

When the above equation is inserted into eq A1, we get

$$[\tau X_{KL}^{\alpha}]^x = 2 \sum_{ia}^{\alpha} \sum_M (ia|M)^x V_{MK}^{-1/2} B_{ia}^L (\tau \xi_i^{\alpha})^2 - \sum_{PQN}^{\tau} X_{LQ}^{\alpha} V_{QN}^{-1/2} V_{NP}^x V_{PK}^{-1/2} + t_{\tau} \sum_{ia}^{\alpha} B_{ia}^K B_{ia}^L (\tau \xi_i^{\alpha})^2 [\epsilon_i^x - \epsilon_a^x] \quad (\text{A5})$$

Subsequently, the above equation can be incorporated into eq 14 to arrive at eq 15 by introducing the terms described by eqs 16–19 and rearranging indices appropriately.

Appendix B

Summary of the Restricted Closed-Shell Coupled-Perturbed Hartree–Fock and Related Equations.^{2,37} The occupied–occupied and virtual–virtual orbital responses can be written in terms of the virtual–occupied response, orbital energy and derivatives of the overlap, one-particle Hamiltonian, and four-center two-electron integrals as shown below:

$$U_{pq}^x = \frac{Q_{pq}^x}{(\epsilon_q - \epsilon_p)} \quad (\text{B1})$$

$$Q_{pq}^x \equiv \mathcal{B}_{pq}^x + \sum_c^{\text{vir}} \sum_k^{\text{occ}} A_{pqck} U_{ck}^x \quad (\text{B2})$$

$$A_{pqrs} = 2(pq|rs) - (pr|qs) - (ps|qr) \quad (\text{B3})$$

$$\mathcal{B}_{pq}^x = F_{pq}^{(x)} - S_{pq}^{(x)} \epsilon_q - \frac{1}{2} \sum_{kl}^{\text{occ}} A_{pqlk} S_{kl}^x \quad (\text{B4})$$

$$F_{pq}^{(x)} = H_{pq}^{(x)} + \sum_k^{\text{occ}} [(pq|kk)^{(x)} - (pk|qk)^{(x)}] \quad (\text{B5})$$

$$\epsilon_p^x = Q_{pp}^x \quad (\text{B6})$$

The closed-shell coupled-perturbed Hartree–Fock equation in matrix notation is given by

$$\mathbf{A}'\mathbf{U}^x = \mathcal{B}^x \quad (\text{B7})$$

where

$$A'_{ajib} = \delta_{ab}\delta_{ij}(\epsilon_i - \epsilon_a) - A_{ajib} \quad (\text{B8})$$

The explicit assembly of the virtual–occupied orbital responses \mathbf{U}^x in eq B7 can be avoided by using the \mathbf{Z} -vector method²⁷

$$(\mathbf{A}')^T \mathbf{Z} = \mathbf{L} \quad (\text{B9})$$

where \mathbf{L} is the effective Lagrangian and the \mathbf{Z} -vector solution of the above equation corresponds to the virtual–occupied block of the 1-PDM \bar{P}_{ai} .

Appendix C

Details of the Algebraic Steps Leading to eq 26. The strategies used follow closely with that of refs 37 and 41. Expanding the summation, $\sum_p^{\text{all}} = \sum_k^{\text{occ}\alpha} + \sum_c^{\text{vir}\alpha} + \sum_l^{\text{occ}\beta} + \sum_d^{\text{vir}\beta}$, the sum of the second terms in eqs 15 and 22 can be written as

$$\begin{aligned} & \sum_{\tau} w_{\tau} \sum_{ia}^{\alpha} \sum_M^{\text{all}} \{2 \sum_p^{\text{all}} (pa|M)U_{pi}^x + t_{\tau}(ia|M)\epsilon_i^x\}^{\tau} \Gamma_{ia}^{M,\beta}(\tau \xi_i^a)^2 = \\ & \sum_{\tau} w_{\tau} \sum_{ia}^{\alpha} \sum_M^{\alpha} \{2 \sum_k^{\alpha} (ka|M)U_{ki}^x + \\ & 2 \sum_c^{\alpha} (ca|M)U_{ci}^x + t_{\tau}(ia|M)\epsilon_i^x\}^{\tau} \Gamma_{ia}^{M,\beta}(\tau \xi_i^a)^2 \quad (\text{C1}) \end{aligned}$$

When the spin orthonormality constraint in eq 25 is used, the first term in the above equation can be rewritten as

$$\begin{aligned} & 2 \sum_{\tau} w_{\tau} \sum_{ika}^{\alpha} \sum_M^{\alpha} (ka|M)U_{ki}^x \Gamma_{ia}^{M,\beta}(\tau \xi_i^a)^2 = \\ & \sum_{\tau} w_{\tau} \sum_{ika}^{\alpha} \sum_{KL}^{\alpha} (U_{ki}^x - U_{ik}^x) B_{ka}^K B_{ia}^L X_{KL}^{\beta}(\tau \xi_i^a)^2 - \\ & \sum_{\tau} w_{\tau} \sum_{ika}^{\alpha} \sum_M^{\alpha} S_{ki}^x (ka|M)^{\tau} \Gamma_{ia}^{M,\beta}(\tau \xi_i^a)^2 \quad (\text{C2}) \end{aligned}$$

As the indicies, k and i , both span over the same set of occupied α orbitals, the summation over these indicies can be expanded as $\sum_{ki}^{\alpha} = \sum_{k>i}^{\alpha} + \sum_{k<i}^{\alpha} + \sum_{k=i}^{\alpha}$. When this expansion is used and the indicies k and i are exchanged for the second term, eq C2 can then be written as

$$\begin{aligned} & = \sum_{\tau} w_{\tau} \sum_a^{\alpha} \sum_{KL}^{\alpha} \sum_{k>i}^{\alpha} (U_{ki}^x - U_{ik}^x) B_{ka}^K B_{ia}^L X_{KL}^{\beta} [(\xi_i^a)^2 - (\xi_k^a)^2] - \\ & \sum_{ki}^{\alpha} \overline{(L1)}_{ki} S_{ki}^x \quad (\text{C3}) \end{aligned}$$

We now introduce a function, ${}^{\tau}g_{ki}$, defined by eq 29 and further use eq B1 to express the above equation as

$$\begin{aligned} & = \sum_{\tau} w_{\tau} \sum_a^{\alpha} \sum_{KL}^{\alpha} \sum_{k>i}^{\alpha} (Q_{ki}^x + Q_{ik}^x) B_{ka}^K B_{ia}^L X_{KL}^{\beta}(\tau \xi_i^a)^2 {}^{\tau}g_{ki} - \\ & \sum_{ki}^{\alpha} \overline{(L1)}_{ki} S_{ki}^x \quad (\text{C4}) \end{aligned}$$

In the above equation, the energy denominator in eq B1 is effectively removed with the introduction of the function, ${}^{\tau}g_{ki}$, thereby neatly avoiding the potential singularity problem that would arise when nearly degenerate orbitals are encountered. Also, the function, ${}^{\tau}g_{ki}$, is continuous when $\epsilon_i \approx \epsilon_k$. The last term in eq C1 can be written in terms of the ${}^{\tau}g_{ki}$ function as

$$\begin{aligned} & \sum_{\tau} w_{\tau} t_{\tau} \sum_{ia}^{\alpha} \sum_M^{\alpha} (ia|M)^{\tau} \Gamma_{ia}^{M,\beta}(\tau \xi_i^a)^2 \epsilon_i^x = \\ & \sum_{\tau} w_{\tau} \sum_{KL}^{\alpha} \sum_{ia}^{\alpha} B_{ia}^K B_{ia}^L X_{KL}^{\beta}(\tau \xi_i^a)^2 {}^{\tau}g_{ii} Q_{ii}^x \quad (\text{C5}) \end{aligned}$$

Combining eqs C4 and C5, and using the inverse of the mathematical summation trick used to arrive at eq C3, we can easily write the sum of the terms considered in eq C1 as eq 26.

References

- (1) Pulay, P. *Mol. Phys.* **1969**, *17*, 197.
- (2) Yamaguchi, Y.; Osamura, Y.; Goddard, J. D.; Schaefer, H. F., III. *A New Dimension to Quantum Chemistry: Analytic Derivative Methods in ab Initio Molecular Electronic Structure Theory*; Oxford University Press: New York, 1994.
- (3) Parr, R. G.; Yang, W. *Density-Functional Theory of Atoms and Molecules*; Oxford: New York, 1989.
- (4) Kristyan, S.; Pulay, P. *Chem. Phys. Lett.* **1994**, *229*, 175–180.
- (5) Cerny, J.; Hobza, P. *Phys. Chem. Chem. Phys.* **2005**, *7*, 1624–1626.
- (6) Tsuzuki, S.; Luthi, H. P. *J. Chem. Phys.* **2001**, *114*, 3949–3957.
- (7) van Mourik, T.; Gdanitz, R. J. *J. Chem. Phys.* **2002**, *116*, 9620–9623.
- (8) Beachy, M. D.; Chasman, D.; Murphy, R. B.; Halgren, T. A.; Friesner, R. A. *J. Am. Chem. Soc.* **1997**, *119*, 5908–5920.
- (9) Møller, C.; Plesset, M. S. *Phys. Rev.* **1934**, *46*, 618–622.
- (10) Szabo, A.; Ostlund, N. S. *Modern Quantum Chemistry: Introduction to Advanced Electronic Structure Theory*; Dover Publications, Inc.: New York, 1996.
- (11) Mourik, T. V.; Wilson, A. K.; Dunning, T. H. *Mol. Phys.* **1999**, *96*, 529–547.
- (12) Feyereisen, M.; Fitzgerald, G.; Komornicki, A. *Chem. Phys. Lett.* **1993**, *208*, 359–363.
- (13) Saebo, S.; Pulay, P. *Ann. Rev. Phys. Chem.* **1993**, *44*, 213–236.
- (14) Weigend, F.; Haser, M.; Patzelt, H.; Ahlrichs, R. *Chem. Phys. Lett.* **1998**, *294*, 143.
- (15) Schütz, M.; Hetzer, G.; Werner, H. J. *J. Chem. Phys.* **1999**, *111*, 5691–5705.

- (16) Ayala, P. Y.; Scuseria, G. E. *J. Chem. Phys.* **1999**, *110*, 3660–3671.
- (17) Hetzer, G.; Schütz, M.; Stoll, H. *J. Chem. Phys.* **2000**, *113*, 9443–9455.
- (18) Lee, M. S.; Maslen, P. E.; Head-Gordon, M. *J. Chem. Phys.* **2000**, *112*, 3592–3601.
- (19) Pulay, P.; Saebo, S.; Wolinski, K. *Chem. Phys. Lett.* **2001**, *344*, 543–552.
- (20) Ayala, P. Y.; Kudin, K. N.; Scuseria, G. E. *J. Chem. Phys.* **2001**, *115*, 9698–9707.
- (21) Saebo, S.; Pulay, P. *J. Chem. Phys.* **2001**, *115*, 3975–3983.
- (22) Werner, H. J.; Manby, F. R.; Knowles, P. J. *J. Chem. Phys.* **2003**, *118*, 8149–8160.
- (23) DiStasio, R. A.; Jung, Y. S.; Head-Gordon, M. *J. Chem. Theory Comput.* **2005**, *1*, 862–876.
- (24) Subotnik, J. E.; Head-Gordon, M. *J. Chem. Phys.* **2005**, *122*, 034109.
- (25) Haser, M. *Theor. Chim. Acta* **1993**, *87*, 147–173.
- (26) Pople, J. A.; Krishnan, R.; Schelgel, H. B.; Binkley, J. S. *Int. J. Quantum Chem. Symp.* **1979**, *13*, 225.
- (27) Handy, N. C.; Schaefer, H. F. *J. Chem. Phys.* **1984**, *81*, 5031–5033.
- (28) Handy, N. C.; Amos, R. D.; Gaw, J. F.; Rice, J. E.; Simandiras, E. D. *Chem. Phys. Lett.* **1985**, *120*, 151–158.
- (29) Helgaker, T.; Jorgensen, P.; Handy, N. C. *Theor. Chim. Acta* **1989**, *76*, 227–245.
- (30) Frisch, M. J.; Headgordon, M.; Pople, J. A. *Chem. Phys. Lett.* **1990**, *166*, 275–280.
- (31) Frisch, M. J.; Headgordon, M.; Pople, J. A. *Chem. Phys. Lett.* **1990**, *166*, 281–289.
- (32) Haase, F.; Ahlrichs, R. *J. Comput. Chem.* **1993**, *14*, 907–912.
- (33) Nielsen, I. M. B. *Chem. Phys. Lett.* **1996**, *255*, 210–216.
- (34) Fletcher, G. D.; Rendell, A. P.; Sherwood, P. *Mol. Phys.* **1997**, *91*, 431–438.
- (35) El Azhary, A.; Rauhut, G.; Pulay, P.; Werner, H. J. *J. Chem. Phys.* **1998**, *108*, 5185–5193.
- (36) Head-Gordon, M. *Mol. Phys.* **1999**, *96*, 673–679.
- (37) Aikens, C. M.; Webb, S. P.; Bell, R. L.; Fletcher, G. D.; Schmidt, M. W.; Gordon, M. S. *Theor. Chem. Acc.* **2003**, *110*, 233–253.
- (38) Gerenkamp, M.; Grimme, S. *Chem. Phys. Lett.* **2004**, *392*, 229–235.
- (39) Saebo, S.; Baker, J.; Wolinski, K.; Pulay, P. *J. Chem. Phys.* **2004**, *120*, 11423–11431.
- (40) Rhee, Y. M.; DiStasio, R. A.; Lochan, R. C.; Head-Gordon, M. *Chem. Phys. Lett.* **2006**, *426*, 197–203.
- (41) DiStasio, R. A.; Steele, R. P.; Rhee, Y. M.; Shao, Y.; Head-Gordon, M. *J. Comput. Chem.* **2007**, *28*, 839–856.
- (42) Weigend, F.; Haser, M. *Theor. Chem. Acc.* **1997**, *97*, 331–340.
- (43) Schütz, M.; Werner, H. J.; Lindh, R.; Manby, F. R. *J. Chem. Phys.* **2004**, *121*, 737–750.
- (44) Helgaker, T.; Gauss, J.; Jorgensen, P.; Olsen, J. *J. Chem. Phys.* **1997**, *106*, 6430–6440.
- (45) Raghavachari, K.; Trucks, G. W.; Pople, J. A.; Head-Gordon, M. *Chem. Phys. Lett.* **1989**, *157*, 479–483.
- (46) Sinnokrot, M. O.; Sherrill, C. D. *J. Phys. Chem. A* **2004**, *108*, 10200–10207.
- (47) Frenking, G.; Antes, I.; Böhme, M.; Dapprich, S.; Ehlers, A. W.; Jonas, V.; Neuhaus, A.; Otto, M.; Stegmann, R.; Veldkamp, A.; Vydroshchikov, S. F. Pseudopotential Calculations of Transition Metal Compounds: Scope and Limitations. In *Reviews in Computational Chemistry*, Lipkowitz, K. B., Boyd, D. B., Eds.; VCH Publishers, Inc.: New York, 1996; Vol. 8.
- (48) Byrd, E. F. C.; Sherrill, C. D.; Head-Gordon, M. *J. Phys. Chem. A* **2001**, *105*, 9736–9747.
- (49) Helgaker, T.; Klopper, W.; Koch, H.; Noga, J. *J. Chem. Phys.* **1997**, *106*, 9639–9646.
- (50) Grimme, S. *J. Chem. Phys.* **2003**, *118*, 9095–9102.
- (51) Jung, Y.; Lochan, R. C.; Dutoi, A. D.; Head-Gordon, M. *J. Chem. Phys.* **2004**, *121*, 9793–9802.
- (52) Lochan, R. C.; Jung, Y.; Head-Gordon, M. *J. Phys. Chem. A* **2005**, *109*, 7598–7605.
- (53) Goumans, T. P. M.; Ehlers, A. W.; Lammertsma, K.; Wurthwein, E. U.; Grimme, S. *Chem.—Eur. J.* **2004**, *10*, 6468–6475.
- (54) Grimme, S. *Chem.—Eur. J.* **2004**, *10*, 3423–3429.
- (55) Grimme, S. *J. Phys. Chem. A* **2005**, *109*, 3067–3077.
- (56) Grimme, S.; Muck-Lichtenfeld, C.; Wurthwein, E. U.; Ehlers, A. W.; Goumans, T. P. M.; Lammertsma, K. *J. Phys. Chem. A* **2006**, *110*, 2583–2586.
- (57) Hyla-Kryspin, I.; Grimme, S. *Organometallics* **2004**, *23*, 5581–5592.
- (58) Dunlap, B. I. *J. Phys. Chem. Chem. Phys.* **2002**, *2*, 2113–2116.
- (59) Almlöf, J. *Chem. Phys. Lett.* **1991**, *181*, 319–320.
- (60) Jung, Y.; Head-Gordon, M. *J. Phys. Chem. Chem. Phys.* **2006**, *8*, 2831–2840.
- (61) Rice, J. E.; Amos, R. D. *Chem. Phys. Lett.* **1985**, *122*, 585–590.
- (62) Head-Gordon, M.; Maslen, P. E.; White, C. A. *J. Chem. Phys.* **1998**, *108*, 616–625.
- (63) Shao, Y.; Molnar, L. F.; Jung, Y.; Kussmann, J.; Ochsenfeld, C.; Brown, S. T.; Gilbert, A. T. B.; Slipchenko, L. V.; Levchenko, S. V.; O'Neill, D. P.; DiStasio, R. A.; Lochan, R. C.; Wang, T.; Beran, G. J. O.; Besley, N. A.; Herbert, J. M.; Lin, C. Y.; Van Voorhis, T.; Chien, S. H.; Sodt, A.; Steele, R. P.; Rassolov, V. A.; Maslen, P. E.; Korambath, P. P.; Adamson, R. D.; Austin, B.; Baker, J.; Byrd, E. F. C.; Dachsels, H.; Doerksen, R. J.; Dreuw, A.; Dunietz, B. D.; Dutoi, A. D.; Furlani, T. R.; Gwaltney, S. R.; Heyden, A.; Hirata, S.; Hsu, C. P.; Kedziora, G.; Khalliulin, R. Z.; Klunzinger, P.; Lee, A. M.; Lee, M. S.; Liang, W.; Lotan, I.; Nair, N.; Peters, B.; Proynov, E. I.; Pieniazek, P. A.; Rhee, Y. M.; Ritchie, J.; Rosta, E.; Sherrill, C. D.; Simmonett, A. C.; Subotnik, J. E.; Woodcock, H. L.; Zhang, W.; Bell, A. T.; Chakraborty, A. K.; Chipman, D. M.; Keil, F. J.; Warshel, A.; Hehre, W. J.; Schaefer, H. F.; Kong, J.; Krylov, A. I.; Gill, P. M. W.; Head-Gordon, M. *J. Phys. Chem. Chem. Phys.* **2006**, *8*, 3172–3191.
- (64) Gerenkamp, M.; Grimme, S. *Chem. Phys. Lett.* **2004**, *392*, 229–235.

- (65) Kendall, R. A.; Dunning, T. H., Jr.; Harris, R. J. *J. Chem. Phys.* **1992**, *96*, 6796–6806.
- (66) Frenking, G.; Wagener, T. *Encyclopedia of Computational Chemistry*; Wiley: New York, 1998; pp 3073–3084.
- (67) Veillard, A. *Chem. Rev.* **1991**, *91*, 743–766.
- (68) Ziegler, T. *Chem. Rev.* **1991**, *91*, 651–667.
- (69) Furche, F.; Perdew, J. P. *J. Chem. Phys.* **2006**, *124*, 044103.
- (70) Andrae, D.; Haussermann, U.; Dolg, M.; Stoll, H.; Preuss, H. *Theor. Chim. Acta* **1990**, *77*, 123–141.
- (71) Dolg, M.; Wedig, U.; Stoll, H.; Preuss, H. *J. Chem. Phys.* **1987**, *86*, 2123–2131.
- (72) Weigend, F.; Haser, M.; Patzelt, H.; Ahlrichs, R. *Chem. Phys. Lett.* **1998**, *294*, 143–152.
- (73) Becke, A. D. *J. Chem. Phys.* **1993**, *98*, 1372–1377.
- (74) Becke, A. D. *Phys. Rev. A: At., Mol., Opt. Phys.* **1988**, *38*, 3098–3100.
- (75) Perdew, J. P. *Phys. Rev. B: Condens. Matter Mater. Phys.* **1986**, *33*, 8822–8824.
- (76) Li, J.; Schreckenbach, G.; Ziegler, T. *J. Phys. Chem.* **1994**, *98*, 4838–4841.
- (77) Li, Y.; McGrady, J. E.; Baer, T. *J. Am. Chem. Soc.* **2002**, *124*, 4487–4494.
- (78) McGrady, J. E.; Dyson, P. J. *J. Organomet. Chem.* **2000**, *607*, 203–207.
- (79) Arnesen, S. P.; Seip, H. M. *Acta Chem. Scand.* **1966**, *20*, 2711.
- (80) Jost, A.; Rees, B.; Yelon, W. B. *Acta Crystallogr., Sect. B: Struct. Sci.* **1975**, *31*, 2649–2658.
- (81) Rees, B.; Coppens, P. *Acta Crystallogr., Sect. B: Struct. Sci.* **1973**, *29*, 2516–2528.
- (82) Burgi, H. B.; Raselli, A.; Braga, D.; Grepioni, F. *Acta Crystallogr., Sect. B: Struct. Sci.* **1992**, *48*, 428–437.
- (83) Huber, K. P.; Herzberg, G. *Molecular Spectra and Molecular Structure. IV. Constants of Diatomic Molecules*; Van Nostrand Reinhold Co.: New York, 1979.
- (84) Lewis, K. E.; Golden, D. M.; Smith, G. P. *J. Am. Chem. Soc.* **1984**, *106*, 3905–3912.
- (85) Wells, J. R.; House, P. G.; Weitz, E. *J. Phys. Chem.* **1994**, *98*, 8343–8351.

CT600292H

Fitting Molecular Electrostatic Potentials from Quantum Mechanical Calculations

Hao Hu, Zhenyu Lu, and Weitao Yang*

Department of Chemistry, Duke University, Durham, North Carolina 27709

Received September 26, 2006

Abstract: We develop here a new method to fit the molecular electrostatic potentials obtained in quantum mechanical calculations to a set of classical electrostatic multipoles, usually point charges located at atomic positions. We define an object function of fitting as an integration of the difference of electrostatic potentials in the entire 3-dimensional physical space. The object function is thus rotationally invariant with respect to the molecular orientation and varies smoothly with respect to molecular geometric fluctuations. Compared with commonly employed methods such as the Merz–Singh–Kollman and CHELPG schemes, this new method, while possessing comparable accuracy, shows greatly improved numerical stability with respect to the molecular positions and geometries. The method can be used in the fitting of electrostatic potentials for the molecular mechanics force fields and also can be applied to the calculation of electrostatic polarizabilities of molecular or atomic systems.

The electrostatic interaction is the key component of the diverse intra- and intermolecule interactions. Accurate treatment of the electrostatic interactions is a fundamental problem in the theoretical study of the structural and dynamic properties of molecular systems.¹ The ultimate method to accurately treat the electrostatic interaction is of course quantum mechanics (QM), in which the spatial and temporal distributions of electrons are determined through the process of solving the Schrödinger or Kohn–Sham equation. However, accurate *ab initio* quantum mechanical calculations are currently too expensive to be applied to large molecules of general interests in long time scale simulations. Because of the great computational efficiency, molecular mechanics (MM) has become a very effective and popular routine in the simulation of molecular processes. In the molecular mechanics, the complicated interatomic interactions are decomposed in a straightforward fashion into different terms such as the covalent terms (describing bond, bond angle, torsion, and improper dihedral energies), the van der Waals interaction, and the electrostatic interactions. The latter is usually computed as the simple Coulombic interaction between point charges on atoms, a much simplified and of course not so accurate description.

Most terms of the MM force field can be determined quite accurately. The covalent terms can be determined from high-level QM calculations or high-resolution spectroscopic studies. In both cases the parameters are found to be to a large extent transferable between molecules. The repulsive and attractive terms of the van der Waals interaction can be either computed from extremely accurate QM calculations or fitted to the condensed phase properties.^{2–6} The electrostatic force, however, is quite difficult to approximate. Right from the start, approximating the complicated quantum mechanical electron–electron interactions by simple Coulombic interactions between point charges naturally leads to the inaccuracy of the calculations. The problem is further complicated by the fact that the atomic charge is a term lacking a rigorous and consistent definition; as a result, assigning the atomic charges is a nontrivial problem. Even though, various schemes have been proposed to determine atomic charges, such as the Mulliken population analysis,^{7,8} the natural bond orbital analysis,^{9,10} the atoms in molecules analysis,¹¹ the distributed multipoles analysis (DMA),^{1,12,13} the wavefunction mapping Class IV model,^{14–17} the electrostatic potential expansion and analysis,^{18–20} and, most importantly, the electrostatic potential (ESP) fitting.^{21–23} The last method has proven to be very effective and has gained great popularity in the applications of MM simulations. The

* Corresponding author e-mail: weitao.yang@duke.edu.

idea of ESP fitting was first proposed by Momany²¹ and has subsequently been implemented in different ways such as the Merz–Singh–Kollman scheme,^{22–24} the CHELP scheme,²⁵ and the CHELPG scheme.²⁶ These schemes share the same basic idea, i.e., least-square fitting the electrostatic potentials at chosen grid points. Because different schemes employed different algorithms to construct and select the grid points, the results from different methods vary and show different numerical dependences to the QM level of theory and basis sets.²⁷ Nonetheless, it was shown that in general the charges from ESP fitting methods are less varied with respect to the change of molecular geometries, QM level of theory, and/or basis sets, when compared with other methods based on population analysis.²⁷ The ESP charges are also consistent with the chemical intuition and reproduce well the electrostatic multipolar properties of the molecules. Therefore, the atomic charges generated from ESP fitting are widely used in the simulations with the MM force fields,^{28,29} despite several well-acknowledged deficiencies such as the transferability of the charges in different molecules.³⁰

Recently, the applications of the ESP charges have been extended beyond the MM force fields to the QM/MM simulations and the molecular polarizability calculations.^{31–33} It was shown that the use of ESP charges can achieve similar accuracy to other methods such as DMA, with much less computational expense and complexity. However, it was also found that conventional ESP methods bear many numerical difficulties in the calculation of atomic polarizabilities. Specifically, ESP charges show a dependence on the orientation and position of the molecule and a strong sensitivity to the molecular geometry. To improve the quality and especially the numerical stability of ESP charges, an effective and robust way of approximating the QM electrostatic interactions by means of fitting the electrostatic potentials is desired.

We report here a new method to fit atomic ESP charges (and other multipoles) from QM calculations. While the fitting process is still carried out as a process of minimizing the difference between the electrostatic potentials from QM calculation and from atomic multipoles, we define the object function in the entire molecular volume space instead of discretely selected grid points surrounding the target molecule. The object function is thus rotationally invariant to the molecular orientation and varies smoothly upon the change of molecular geometry. As a result, with comparable numerical accuracy to existing ESP fitting methods, the new method shows great improvements on the numerical stability of the fitting results. The method will be very useful for future study of molecular polarization interactions, in a pure MM force field or in a combined QM/MM method.

Methods

We formulate the problem here as approximating the interaction between a QM molecule and a classical point charge. Given a molecular system with the electron densities solved as $\rho(\mathbf{r})$, without the consideration of the polarization effects, the electrostatic interaction between this molecule and a point charge q at position \mathbf{r}_q is

$$E_{ele} = \int \frac{\rho(\mathbf{r})q}{|\mathbf{r} - \mathbf{r}_q|} d\mathbf{r} = q \int \frac{\rho(\mathbf{r})}{|\mathbf{r} - \mathbf{r}_q|} d\mathbf{r} = qV_{QM}(\mathbf{r}_q) \quad (1)$$

where $V_{QM}(\mathbf{r}_q)$ is the QM molecular electrostatic potential at the position \mathbf{r}_q . One should note that in this equation, the potential $V_{QM}(\mathbf{r}_q)$ is solely determined by the electron densities and thus a property of the QM molecule. From this equation it is also obvious that the exact interaction energy has to be calculated from the quantum mechanically solved electron densities which span the space wherever an electron populates. In principle, this implies that an integration over the entire space is necessary. However, since the electron densities decay very rapidly from atoms, the integration in fact need only be done over a limited space where electron densities possess non-neglectable values. This space is defined as the molecular volume space in the current work.

In general there are two routes to approximately calculate this electrostatic energy. In the first approach, one may approximate the QM electron densities by classical electrostatic multipoles centered at the atomic positions. In other words, one directly seeks an approximate expression for the electron density, such as the distributed multipole analysis method. In the second approach, one could approximate the QM potential $V_{QM}(\mathbf{r}_q)$ by the potential of a set of classical electrostatic multipoles. That is, given a QM potential in space, one asks the question which set of classical electrostatic multipoles can best mimic this potential. Surely for one point in space there are countless solutions to reproduce the potential at this position; whether the specific solution is useful or not depends on how well this solution also approximates the potentials at other points in space.

Assuming again the electrostatic multipoles are centered at the atomic positions \mathbf{r}_a , the question now becomes how to determine a set of multipoles $Q(\mathbf{r}_a)$ so that

$$V(Q(\mathbf{r}_a), \mathbf{r}) \approx V_{QM}(\mathbf{r}) \quad (2)$$

where $V(Q(\mathbf{r}_a), \mathbf{r})$ is the potential from all the multipoles $Q(\mathbf{r}_a)$. The straightforward solution to this problem would be to solve the least-square minimization problem as

$$\min \left[\int (V(Q(\mathbf{r}_a), \mathbf{r}) - V_{QM}(\mathbf{r}))^2 d\mathbf{r} \right] \quad (3)$$

where the integration runs over the molecular volume space where electron densities span.

One can in principle determine a set of multipoles by directly solving the minimization problem defined in eq 3, in which each point in the molecular volume space contributes equally to the object function. Intuitively, however, a modified form of this equation with different weights for different points in space is more suitable owing to two practical considerations. On one hand, for those points near an atom, the magnitudes of the electrostatic potential are usually much larger than those of the points distant from atoms; consequently, the potentials at these points will make the most of the contribution to the minimization process and numerically beat out other points. However, the near-atom space is less important than other space in simulations with classical MM force fields: the short-range interactions are usually represented by covalent interactions which generally

omit electrostatic interactions between near neighbors, while the classical Coulombic term is an important component for long-range interactions. On the other hand, for points very distant from atoms, the values of the electrostatic potential are very small so that they should also be weighted less. That is to say, we would like to give more weight to points within the medium range to atoms as usually defined in classical simulation and give less weight to points too close or too distant to the molecule. In analog to the picture of the structure of liquid, one could imagine we are weighting heavily the points within the first neighboring shell which is of course most important in the simulations.

Similar to the original ESP fitting method, the problem is now defined as the minimization of an object function of

$$\gamma = \int W(\mathbf{r})(V(Q(\mathbf{r}_\alpha), \mathbf{r}) - V_{QM}(\mathbf{r}))^2 d\mathbf{r} \quad (4)$$

in which $W(\mathbf{r})$ is the weighting function. From the previous discussion, it appears that an ideal weighting function should approach zero at both small and large distances and exhibit a maximum between 3 and 5 Å which is typically 1.4–2.0 times of van der Waals radii; interatomic interaction between this distance is thought to be most important in molecular simulations. The original ESP^{23,24} method can also be formulated in the same way, where $W(\mathbf{r})$ is in fact defined as a discontinuous function as

$$W(\mathbf{r}) = \begin{cases} 0 & |\mathbf{r} - \mathbf{r}_\alpha| < R_{small} \\ \delta(\mathbf{r} - \mathbf{r}_{grid}) & R_{small} \leq |\mathbf{r} - \mathbf{r}_\alpha| \leq R_{large} \\ 0 & |\mathbf{r} - \mathbf{r}_\alpha| > R_{large} \end{cases} \quad (5)$$

in which the two cutoffs are chosen in the MSK method as^{23,24}

$$\begin{aligned} R_{small} &= 1.4R_{vdw} \\ R_{large} &= 2.0R_{vdw} \end{aligned} \quad (6)$$

The discontinuity of the weighting functions in the common ESP fitting methods leads to a well-known problem in the ESP fitting process, namely the numerical instability of the change of the ESP charges with respect to a structural perturbation of the molecule.

To solve this numerical problem, we propose here a new weighting function that not only meets the requirements discussed above but also allows smooth changes with respect to geometries. The new weighting function is defined as

$$W(\mathbf{r}) = \exp[-\sigma(\log \tilde{\rho}(\mathbf{r}) - \log \rho_{ref})^2] \quad (7)$$

in which $\tilde{\rho}(\mathbf{r})$ is the predefined electron densities, and ρ_{ref} is a reference electron density whose value is chosen in combination with σ to ensure the weighting function behaves as expected. The design of this weighting function is inspired by the fact that the atomic (and molecular) electron densities decay exponentially in space. By adjusting ρ_{ref} and σ , we are able to create a Gaussian-like function $W(\mathbf{r})$ which weights heavily on the points in the medium-range of the molecule.

In principle the exact QM electron density $\rho(\mathbf{r})$ can be used as $\tilde{\rho}(\mathbf{r})$ in the calculation of the weighting function.

However, this is not an optimal solution since $\rho(\mathbf{r})$ then depends on both the molecular geometry and the basis sets. The dependence to the basis sets thus complicates the problem if the derivatives of the weighting function with respect to the geometry are sought. To avoid this complication, we decide here to use the sum of the atomic electron densities as

$$\tilde{\rho}(\mathbf{r}) = \sum_A \rho_{atom}(\mathbf{r}_A, \mathbf{r}) \quad (8)$$

where $\rho_{atom}(\mathbf{r}_A, \mathbf{r})$ is the atomic density of atom A which will be predetermined. Hence, eq 4 can now be evaluated by 3-D numerical integration which is readily available in many quantum chemistry programs.

With the object function and weighting function available to carry out the minimization process, we consider the simplest case where there is only one point charge on each atom. The potential is

$$V(Q(\mathbf{r}_\alpha), \mathbf{r}) = \sum_{\alpha=1}^N \frac{q_\alpha}{|\mathbf{r} - \mathbf{r}_\alpha|} \quad (9)$$

in which q_α stands for the point charge on atom α . We also apply a constraint to ensure the charge of the molecule is constant

$$g = q_{tot} - \sum_{j=1}^N q_j = 0 \quad (10)$$

With a Lagrange Multiplier for the constraint, the final object function is

$$z = \gamma + \lambda g = \int W(\mathbf{r})(V(Q(\mathbf{r}_\alpha), \mathbf{r}) - V_{QM}(\mathbf{r}))^2 d\mathbf{r} + \lambda(q_{tot} - \sum_{j=1}^N q_j) = 0 \quad (11)$$

The solution is determined by solving the $n+1$ linear equations

$$0 = \frac{\partial z}{\partial q_k} = -2 \int W(\mathbf{r}) V_{QM}(\mathbf{r}) \frac{1}{|\mathbf{r} - \mathbf{r}_k|} d\mathbf{r} + 2 \int W(\mathbf{r}) \frac{1}{|\mathbf{r} - \mathbf{r}_k|} \sum_{j=1}^N \frac{q_j}{|\mathbf{r} - \mathbf{r}_j|} d\mathbf{r} - \lambda \quad (12)$$

and

$$0 = \frac{\partial z}{\partial \lambda} = q_{tot} - \sum_{j=1}^N q_j \quad (13)$$

This task can be accomplished by many well-established techniques such as the Single Value Decomposition (SVD).

Obviously the results of this ESP fitting scheme critically depend on the choices of two parameters in eq 7: σ and ρ_{ref} . Values of the two parameters cannot be determined by simply minimizing the object function defined in eq 4 since one could easily generate small values for the object function with an ill-defined weighting function. Alternately, we determined here to use an indirect criterion to evaluate the

quality of the fitting. That is, given a specific conformation of a target molecule, we randomly place a probe charge around this molecule at reasonable distances (e.g., 2–7 Å) and compare the electrostatic energies calculated with eq 1 and with ESP charges. The former is regarded as the exact result, where the latter is an approximated result. The criterion is defined as

$$E_{RRMSD} = \sqrt{\frac{\sum_{i=1}^N \left(\frac{E_{ele,i} - E_{ESP,i}}{E_{ESP,i}} \right)^2}{N}} \quad (14)$$

where $E_{ele,i}$ is the exact electrostatic energy defined in eq 1, $E_{ESP,i}$ is the approximated electrostatic energy calculated with ESP charges, and N is the number of trials to place the probe charges. The relative-root-mean-square-deviation (RRMSD) of energies defined in this equation thus allows us to practically measure the quality of the electrostatic interactions computed with the ESP fitted charges, which is the essence of ESP fitting.

Of course, the best-fits of two parameters σ and ρ_{ref} will vary with specific molecules. To ensure the two parameters are transferable between different molecules, the variation of fitting results with respect to the changes of σ and ρ_{ref} has to be evaluated; the variations of the fitting results in different molecules also have to be examined to identify the range of the two parameters so that they are suitable for different molecules. After that, σ and ρ_{ref} can be used in the future study of other molecules.

Computation Details

The program Gaussian03 was employed for this study.³⁴ We modified the link 1602 which was designed to carry out population analysis. We first constructed an integration grid with standard 3-D integration method used in Density Functional calculations³⁵ and then computed electrostatic potentials on the grid points with the converged electron densities. The fitting procedure was accomplished by solving eq 11. Unless specifically stated, we did not apply the constraints to reproduce the molecular dipole in the fitting process.

To determine the atomic electron densities for calculating eq 8, we carried out a UHF/aug-cc-pVQZ calculation for different atoms in the first three rows in the periodic table. Based on the well-known fact that the atomic electron densities are exponentially decaying in a piecewise manner,^{36,37} we fitted the atomic electron densities to

$$\rho_{atom}(\mathbf{r}) = \sum_{i=1}^N A_i \exp(-B_i r) \quad (15)$$

where N is the number of components decaying exponentially in each atom: $N = 1$ for H and He, 2 for Li to Ne, 3 for Na to Ar, and 4 for K to Kr. After the coefficients A_i and B_i were determined for each element, they were tabulated and stored in the program for the calculation of the weighting function. It should be noted here that the exact solution of

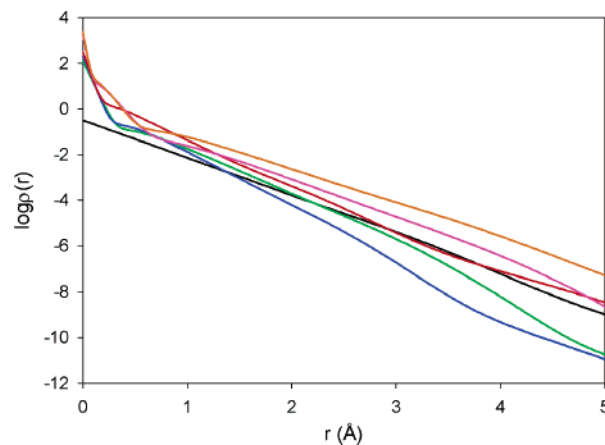


Figure 1. Atomic electron densities (in atomic units) of the elements H (black), C (green), N (blue), O (red), P (pink), and S (orange). The densities were computed by the UHF/aug-cc-pVQZ method.

atomic electron densities is not required because the uncertainties will be absorbed late in the process of determining σ and ρ_{ref} .

All QM calculations for the electrostatic potentials and electron densities were carried out at the level of B3LYP/6-31G*.^{38,39} All molecular geometries were optimized at the same level of theory prior to the ESP analysis and fitting. In current work, the standard pruned (75,302) grid implemented in Gaussian was chosen for the purpose of 3-D integration. The Merz–Singh–Kollman ESP fitting method implemented in Gaussian was used with a default setup, whenever it was used for the purpose of comparison.

To evaluate the quality of the fitting and the values of the two parameters, σ and ρ_{ref} , in the weighting function, we calculated the RRMS energy deviation defined in eq 14. In the calculation, we placed the molecule in the center and randomly placed a probe charge in the neighborhood of the molecule. For obvious reasons the probe charge would not be included in the calculation if it was too close or too far to the molecule. In general, we made selections to the position of the probe charge so that it was within 7 Å to at least one atom of the molecule and was not closer than $r_{vdW} + 0.2$ Å to any atom of the molecule. This selection ensures us to have enough samples in the space region that are most important in normal simulation studies. The standard van der Waals radii were used. Specifically, they are 1.2, 1.70, 1.55, 1.52, and 1.80 Å for the elements H, C, N, O, and S, respectively.⁴⁰ For each set of the calculations, 40,000 effective random positions were generated for the probe charge to ensure the convergence of the RRMS energy deviation (data not shown).

Results

Exponentially Decaying of Atomic Density. In the current work, the atomic densities were computed for the elements H, Li–F, and Na–Ar. Some other elements were not included in this calculation because the chosen basis sets were not available for them. The computed atomic densities for the elements H, C, N, O, P, and S are shown in Figure 1, which clearly demonstrates the exponential decaying

Table 1. Multiple Exponential Components of Atomic Electron Densities

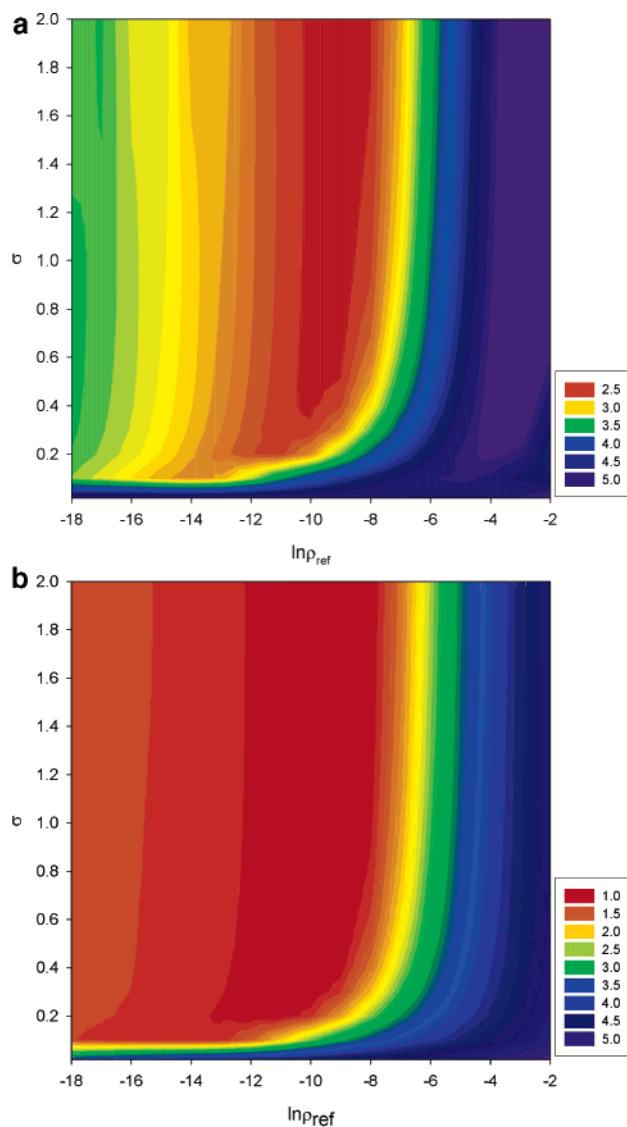
element	A	B
H ($N=1$)	0.384137961	3.90762643
C ($N=2$)	166.591448 3.23010126	29.0603279 5.01709331
N ($N=2$)	256.609200 2.58989432	31.2114908 5.45471548
O ($N=2$)	243.630909 2.53736474	26.3836036 4.29335839
P ($N=3$)	2282.83071 155.142338 1.82194667	73.7103367 15.6986998 3.38628928
S ($N=3$)	2736.19302 206.867393 2.78312612	78.9192252 17.4500522 3.51974385

behavior of the atomic electron densities. This is in agreement with the electronic shell structure where the decay also exhibits piecewise feature. As a result, the atomic electron densities can be fitted into multiple components of decaying exponentials. The fitting results for H, C, N, O, P, and S are reported in Table 1. One more important observation in Figure 1 is that the atomic electron densities of different elements tend to have similar values at the distances near van der Waals radii, even though they could be significantly different at short and long distances. This observation, plus the exponentially decaying feature of electron densities, ensures that a weighting function can be satisfactorily constructed according to eqs 7 and 8 with large weights for regions close to the vdW isosurface of a molecule.

Determination of Parameters σ and ρ_{ref} . The two parameters, σ and ρ_{ref} , in the weighting function, have to be determined in such a way that they are suitable for fitting electrostatic potentials even for different chemical molecules. For this purpose, a 2-dimensional scanning was performed for the two parameters in broad ranges, for different molecules including ethanol ($\text{CH}_3\text{CH}_2\text{OH}$), methylammonium ion (CH_3NH_3^+), methylamine (CH_3NH_2), CH_3COO^- , CH_3COOH , DMSO ($\text{CH}_3\text{S}(\text{O})\text{CH}_3$), and N-methylethanimide (NMA) ($\text{CH}_3\text{CONHCH}_3$).

Without loss of generality, we show the 2-D scanning results for ethanol and DMSO in Figure 2. It is clear when σ is too small or ρ_{ref} is too large, the quality of fitting is rather poor. The best fit was obtained when the value of ρ_{ref} is about 10^{-4} – 10^{-5} ($-10 \leq \ln\rho_{ref} \leq -8$) with reasonable values of σ . In fact, the quality of the ESP fitting is not significantly changing over a broad range of σ and ρ_{ref} . This observation becomes a quite useful result. As long as the values of σ and ρ_{ref} are within this region, they could be used in the fitting of different molecules without the loss of accuracy.

Based on these observations, we chose the values of σ and $\ln\rho_{ref}$ to be 0.8 and -9 , respectively, for the rest of the calculations. For these chosen values, we also computed E_{RRMSD} defined in eq 14 for different molecules as a test of the accuracy of the current method. The results are shown in Table 2. In general, the current method performs as well as the popular Merz–Singh–Kollman method. It must be

**Figure 2.** Variation of E_{RRMSD} with the change of $\ln\rho_{ref}$ and σ : (a) molecule ETOH and (b) molecule NMA. ρ_{ref} is in atomic units.**Table 2.** E_{RRMSD} Calculated for Various Molecules

molecule	MSK	CHELPG	current method ^a
$\text{CH}_3\text{CH}_2\text{OH}$	13.7	21.4	10.6 (4.16)
CH_3NH_2	19.3	19.4	18.7 (1.08)
CH_3NH_3^+	.00673	0.00672	0.00677 (0.00146)
CH_3COO^-	.00519	0.00482	0.00513 (0.00333)
CH_3COOH	2.20	5.93	2.19 (1.08)
DMSO	11.3	7.47	6.46 (1.59)
NMA	5.00	3.99	2.48 (1.02)

^a Data in the parentheses are E_{RRMSD} calculated including also a point dipole on each atom of the molecule. In this case, the values of the two parameters, ρ_{ref} and σ , are the same as those of the point charge only without further optimization.

reminded since E_{RRMSD} is only one criterion of many possibilities, it should never be used to draw qualitative conclusions.

The basis set dependence of the current method was also examined here. In Table 3 we show the atomic charges of the methanol molecule fitted to ESP calculated with B3LYP and different basis sets. It is shown that the charges tended

Table 3. Atomic Charges of the Methanol Molecule Determined with B3LYP and Different Basis Sets

	C	O	H ^a	H ^b	H ^c
STO-3G	0.0882	-0.4509	0.3062	0.0193	0.0179
3-21G	0.2076	-0.6367	0.4116	0.0121	-0.006605
6-31G	0.3262	-0.7258	0.4448	-0.0066	-0.0320
6-31G*	0.1809	-0.6007	0.3902	0.0193	-0.008944
6-311G*	0.1856	-0.6376	0.4154	0.0225	-0.008504
cc-pVDZ	0.2061	-0.5644	0.3642	0.00777	-0.0214
cc-pVTZ	0.1601	-0.5711	0.3695	0.0252	-0.009039
cc-pVQZ	0.1792	-0.5809	0.3702	0.0227	-0.0140
cc-pV5Z	0.1954	-0.5881	0.3707	0.0202	-0.0185
aug-cc-pVDZ	0.1985	-0.5856	0.3672	0.0194	-0.0188
aug-cc-pVTZ	0.2009	-0.5865	0.3684	0.0189	-0.0205
aug-cc-pVQZ	0.1995	-0.5862	0.3683	0.0192	-0.0200
aug-cc-pV5Z	0.2000	-0.5863	0.3683	0.0191	-0.0201

^a Hydrogen of the hydroxyl group. ^b Methyl hydrogen atom trans to the hydroxyl group. ^c Methyl hydrogen atom gauche to the hydroxyl group.

to converge to similar values when a large basis set such as cc-pVXZ or aug-cc-pVXZ is used. A similar observation has been reported before.²⁷

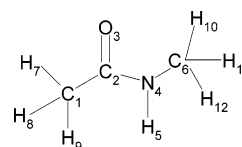
Molecular Orientation Dependence of the Fitting Results. One important advantage of the current charge fitting scheme is that the object function is defined in molecular volume space, which is not changed by the global movements of the molecule. As a result, the fitting results will not be changed by the rotation or translation of the molecule, within the limits of numerical accuracy. By contrast, conventional charge fitting schemes, such as the Merz–Singh–Kollman and the CHELPG methods, always bear such a difficulty that the fitting grid points are changing upon the rotation of the molecules. Consequently, the results of those methods are numerical unstable and fluctuate significantly. This deficiency has limited broader applications of such methods to problems which require stable fitting results.

To compare the dependences of the results on the global rotation of the molecule, we randomly translated and rotated the molecule N-methylethanamide (NMA) (CH₃CONHCH₃) 1000 times and for each orientation calculated the charges by different methods. The root-mean-square-fluctuations (RMSF) for each atomic charge were calculated and reported in Table 4. As expected, the RMSF of the charges from the CHELPG method are about the half of those in the MSK method, indicating that the CHELPG method has slightly weaker dependence on the molecular orientation and thus better numerical stability.²⁶ Importantly, the RMSF of the charges in the current method is on average about 20–30 times smaller than those in the MSK method. Therefore, the current method has the best numerical stability of the methods compared here. It should be noted that increasing the number of grid points will improve the numerical stability of both methods. However, the improvements are relatively moderate in the MSK and CHELPG methods but quite significant in the current method. In the current method, switching to a fine (99,590) grid for numerical integration will reduce the RMSF by more than an order of magnitude with the number of points only increased to 2.5 times. In

Table 4. rms Fluctuations of the Atomic Charges Determined by Different Methods

atom	MSK ^a	CHELPG	current method ^b
C1	0.02374 (0.00878)	0.0127	0.000935 (0.000114)
C2	0.01095 (0.00446)	0.00501	0.000336 (0.000049)
O3	0.00260 (0.00113)	0.00102	0.0000983 (0.000016)
N4	0.00805 (0.00389)	0.00424	0.000546 (0.000052)
H5	0.00274 (0.00125)	0.00100	0.000210 (0.000014)
C6	0.01899 (0.00851)	0.0101	0.000914 (0.000095)
H7	0.00625 (0.00236)	0.00332	0.000265 (0.000031)
H8	0.00586 (0.00217)	0.00332	0.000254 (0.000031)
H9	0.00589 (0.00220)	0.00316	0.000254 (0.000031)
H10	0.00495 (0.00219)	0.00265	0.000254 (0.000025)
H11	0.00520 (0.00233)	0.00265	0.000252 (0.000024)
H12	0.00524 (0.00230)	0.00265	0.000252 (0.000024)

^a ESP charges were fitted with default grids in Gaussian03. The data in the parentheses were fitted with a grid setup of 6 layers and 2 points per unit area, which yields a number of grid points approximately 3 times the default setup. ^b ESP charges were fitted with (75 302) a DFT grid. The data in the parentheses were fitted with (99 590) a DFT grid whose number of grids is approximately 2.5 times the former.

**Figure 3.** Structure of the molecule N-methylethanamide (NMA).

contrast, the RMSF of the MSK method is only reduced to half when the number of points is increased 3 times (Table 4).

Molecular Geometry Dependence of the Fitting Results. It is well-known that the molecular electron distribution changes with the varying of the molecular geometry. The direct consequence of this phenomenon is that the atomic charges (dipoles and quadrupoles too), calculated by fitting the electrostatic potential or by discrete multipole analysis,⁴¹ also change with a perturbation of the molecular geometries. The correlation between the atomic charges and the molecular geometries in fact provides an opportunity for designing of a polarizable force field which allows charge transfer within a molecule. For this purpose, the computed charges must be differentiable with respect to the molecular geometry, no matter whether the differentiation is carried out numerically or analytically. When analytical differentiation is difficult to achieve, the numerical method becomes the only feasible way. In such a case, the numerical uncertainty of the charges must be small enough so that its effect can be neglected in the process of numerical differentiation, otherwise, the numerical results cannot be trusted.

We carried out analysis again on the NMA molecule (Figure 3). The bond C₂–N₄ is defined as the pivot for intramolecular rotation with the relative geometries of the left and right sides of the molecule fixed. The dihedral angle O₃–C₂–N₄–H₅ was rotated for 360 degrees with 4 degrees per step. The atomic charges were computed with the MSK

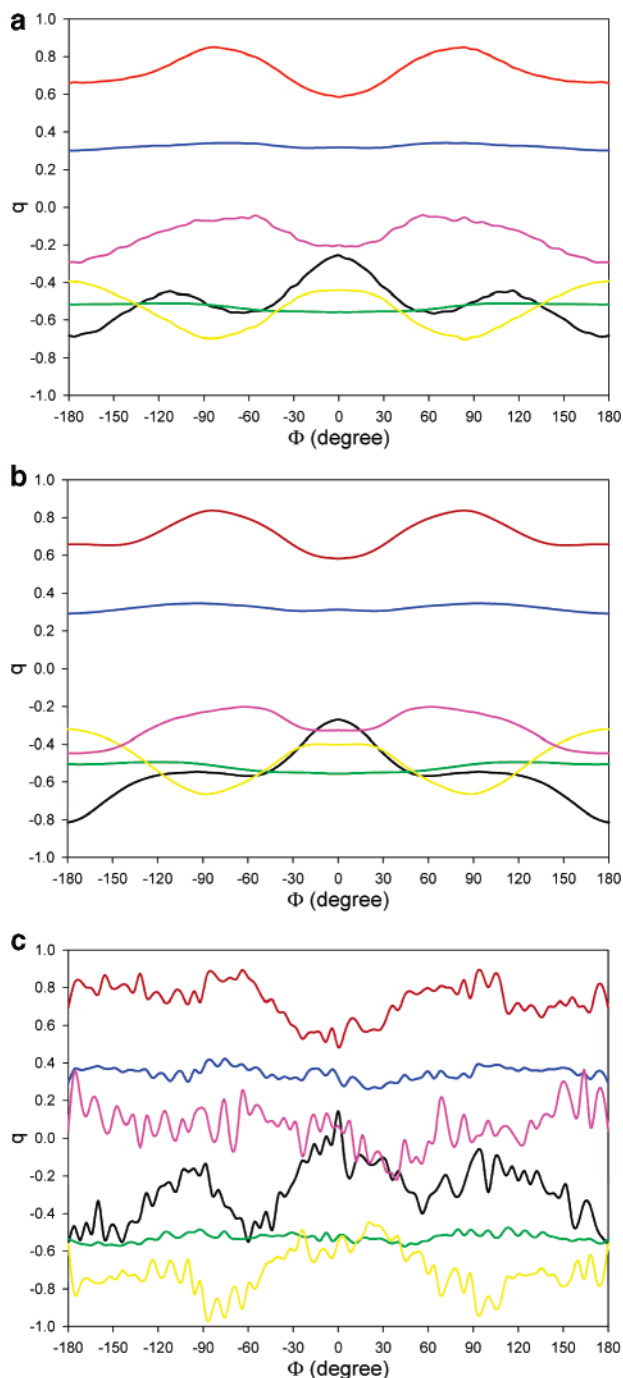


Figure 4. Variations of the ESP charges of the molecule NMA with respect to the twisting of the dihedral angle O3–C2–N4–H5. For the clarity of illustration, the charges of the hydrogen atoms of the methyl groups are not shown: (a) the Merz–Singh–Kollman method; (b) the current method; and (c) the current method with the harmonically restrained charge model (weight 0.005). The fitted charges are shown for atoms C1 (black), C2 (red), O3 (blue), N4 (yellow), H5 (green), and C6 (pink).

method and current method for each rotated conformation. The results are shown in Figure 4.

Not surprisingly, both methods consistently show the same behaviors for the changes of the atomic charges with respect to the rotation of the dihedral angle. The shape and the magnitudes of both methods share a great resemblance. This

agreement demonstrates the validity of current method. More importantly, however, the variations of the atomic charges show great discontinuity in the MSK method, while they are smoothly changing in the current method. This difference marks the most important advantage of the current method in the calculation of the atomic polarizabilities since it allows numerical differentiation with respect to geometrical perturbations to be carried out with high numerical precision.

Discussion

The motivation to utilize ESP charges in the molecular simulations is to approximate the electrostatic interaction in an atomic pairwise manner, instead of explicitly dealing with electron densities which is too complicated and too expensive. If one only cares about the quality of simulation with nonpolarizable MM force fields, the only quantity that matters here is how well the ESP charges mimic the QM electrostatic potentials. For this purpose, many methods have been developed on the basis of fitting ESP at discrete grid points in selected neighborhood regions of the target molecule. The successes of the MM simulations using fitted atomic charges strongly demonstrate the validity and usefulness of those ESP fitting methods.

When derivatives of the ESP charges are sought for the calculation of the atomic/molecular polarizability, those methods displayed numerical instability due to the nonsmooth and noncontinuous nature of the object function of fitting. Apparently, this discontinuity arises from the algorithm to construct and select the grid points for fitting. To overcome this problem, the grid points must be rotationally invariant with respect to the molecular orientation and continuously change with respect to geometrical perturbation.

From this perspective, the current method completely overcomes this problem by implementing a new algorithm to generate rotationally invariant grids, specifically the 3-D integration grids used in quantum chemistry calculations. Furthermore, there is one additional advantage for utilizing a complete set of grids in the entire molecular volume space. That is, this improves the quality of fitting when higher order multipoles are added to atomic sites. When the order of the electrostatic multipoles increases, the magnitudes of the electrostatic potential decay rapidly with a decreased order to the distance. For example, the ESP is of order r^{-1} for a monopole, r^{-2} for a point dipole, and r^{-3} for a point quadrupole. This fact suggests that for multipoles it is important to include grid points near atoms; otherwise, the results will not be as reliable as monopoles.

As suggested by the results of E_{RRMSD} (Table 2), the fitting qualities of several ESP fitting algorithms, including the current one, are comparable to each other. They all suffer the same imperfection because the implementation of the electrostatic multipoles is limited to monopole. As shown in Table 2, the deviations of electrostatic energy calculation are rather large for many molecules. Detailed inspection of the results indicates the large deviation is mostly contributed by the region closely surrounding the target molecule. In those regions, it is well-known that atomic point charges reproduce poorly the quantum mechanical ESP for two reasons. One is the complicated electrostatic potential from

Table 5. Comparison of Atomic Charges of NMA Molecule Determined with and without Restraints

atom	free	restraint ^a
C1	-0.7218	-0.0864
C2	0.6912	0.2193
O3	-0.5207	-0.4040
N4	-0.4359	-0.1971
H5	0.3120	0.2338
C6	-0.2672	-0.1590
H7	0.1602	0.0120
H8	0.2049	0.0648
H9	0.2048	0.0647
H10	0.1246	0.0769
H11	0.1239	0.0875
H12	0.1239	0.0875

^a The harmonic restraint proposed in the original paper⁴² was employed with a weight of 0.005.

the complex electron distribution in the close neighborhood of the molecule. Another reason is the charge penetration effect. To improve the fitting quality, higher order multipoles could be added to the atomic positions. As an example, the inclusion of atom-centered point dipoles will substantially improve the quality of fitting results for the current method (Table 2). Of course, the addition of a dipolar term will increase the computational cost; such a cost might be still affordable for MM force field based simulations, with the steady improvement of computers' speed.

Like many other methods, the current algorithm also bears many problems common to the ESP fitting approach. Obviously, fitting a set of electrostatic multipoles to the electrostatic potential from accurate quantum mechanical calculation is inherently a poorly posed question. Despite the subtle differences, all ESP fitting methods rely on the definition of an object function, often the rmsd of the electrostatic potentials on selected grid points. Given the complexity of the ESP surface and the drastic variation of the values on the ESP surface, it is not surprising that the fitting results are sensitive to many factors such as the choice of the grid points, the basis sets of the QM calculations, and the geometry and orientation of the molecules.

One such well-known example of the deficiencies of the ESP fitting approach is the large charges on the buried atoms of a molecule. In this case, the neighborhood spaces of those atoms are often occupied by other atoms too, and the ESP in those regions make little contribution to the object function of the fitting process. The immediate consequence is that the fitting quality is insensitive to the charges of those buried atoms, and it leads to large and numerically unstable charges on those atoms. To overcome such a difficulty, an "ad hoc" yet very effective approach has been proposed as to restrain the magnitude of the charges in the fitting process.^{42,43} This restrained minimization approach can also be applied to our method which generated a set of charges closer to common intuitions (Table 5).

One particular motivation for the development of this new method is to improve the numerical stability of the ESP fitting process, specifically in the calculation of atomic polarizabilities. The results shown in Figure 4 clearly indicated that our new method is indeed providing better

results. The dependence of the charges on the molecular geometries, in this case the dihedral angle of the peptide plane, was discovered before and was proposed as a new standpoint for designing polarizable force fields.⁴¹ Some may argue that such a geometrical dependence could be an artifact from the burying of some atoms. Especially given the magnitude of the fluctuation of the charges, one may question if such a fluctuating charge can be used in the MM force fields. Answering those questions requires a comprehensive analysis on the ESP fitting approach. Certainly as we discussed before, the burying of some atoms will influence the fitting process and ultimately will affect the fitted atomic charges. In the case of the twisting of the peptide plane here, however, the attempt to remove this effect by means of the RESP approach is ineffective. By comparing the fitting results with and without harmonic restraints (Figure 4b,c), one clearly sees that the inclusion of restraint indeed lowers the magnitude of the charge on the carbon atoms (C1 and C6) for the dihedral angle close to zero which is the normal stable conformation of this molecule. Nonetheless, the charge dependence on the dihedral angle is retained regardless of the presence of the restraints. This result suggests that the variation of the buried extent of heavy atoms is not the major source of the geometrical dependence of the fitted charges. On the other hand, even though the charges of the carbon atoms are closer to "chemical intuition" when the molecule is at the stable conformations, the overall bumpy fluctuations of the fitted RESP charges reminds us that great caution should be taken when the RESP type of "ad hoc" approximations are used. The increased roughness implies that the restraint might alter the numerical behavior of the object function in an unpredicted and unstable way so that a mathematically more elegant solution is desired (T. Heaton-Burgess, to be published). Furthermore, from our point of view, even though the fitting results without restraints may be sometimes beyond our "chemical intuitions", as long as the overall electrostatic potential of the target molecule is well approximated, the result will be accurate and will capture the essence of the electrostatic interactions.

In summary, with much improved numerical stability, the current method will make an important contribution to the calculation of the polarizability type of properties and to the development of the next generation of molecular mechanics force fields.

Instructions on how to modify the Gaussian code to implement this new algorithm can be found at <http://www.chem.duke.edu/~yang/software.htm>.

Acknowledgment. We thank Dr. Xiangqian Hu for helpful discussion and Jerry M. Parks and Steven K. Burger for proofreading the manuscript. Financial support from National Institutes of Health is acknowledged.

References

- (1) Stone, A. J. *The Theory of Intermolecular Forces*; Clarendon Press: Oxford, U.K., 1996.
- (2) Williams, D. E. Nonbonded potential parameters derived from crystalline hydrocarbons. *J. Chem. Phys.* **1967**, *47*, 4680–4684.

- (3) Scheraga, H. A. Calculations of conformations of polypeptides. *Adv. Phys. Org. Chem.* **1968**, *6*, 103–184.
- (4) Ferro, D.; Hermans, J. Semiempirical energy calculations on model compounds of polypeptides. Crystal structures of DL-acetyl-leucine N-methylamide and DL-acetyl-n-butyric acid N-methylamide. *Biopolymers* **1972**, *11*, 105–117.
- (5) MacKerell, A. D., Jr.; Bashford, D.; Bellott, M.; Dunbrack, R. L., Jr.; Evanseck, J. D.; Field, M. J.; Fischer, S.; Gao, J.; Guo, H.; Ha, S.; Joseph-McCarthy, D.; Kuchnir, L.; Kuczera, K.; Lau, F. T. K.; Mattos, C.; Michnick, S.; Ngo, T.; Nguyen, D. T.; Prodhom, B.; Reiher, W. E., III; Roux, B.; Schlenkrich, M.; Smith, J. C.; Stote, R.; Straub, J.; Watanabe, M.; Wiórkiewicz-Kuczera, J.; Yin, D.; Karplus, M. All-atom empirical potential for molecular modeling and dynamics studies of proteins. *J. Phys. Chem.* **1998**, *B 102*, 3586–3616.
- (6) Jorgensen, W. L. OPLS Force Fields. In *Encyclopedia of Computational Chemistry*; Schleyer, P. v. R., Ed.; Wiley: New York, 1998; Vol. 3, pp 1986–1989.
- (7) Mulliken, R. S. Electronic population analysis on LCAO-MO [linear combination of atomic orbital-molecular orbital] molecular wave functions. I. *J. Chem. Phys.* **1955**, *23*, 1833–1840.
- (8) Mulliken, R. S. Criteria for the construction of good self-consistent-field molecular orbital wave functions, and the significance of L.C.A.O.M.O. population analysis. *J. Chem. Phys.* **1962**, *36*, 3428–3439.
- (9) Reed, A. E.; Curtiss, L. A.; Weinhold, F. Intermolecular interactions from a natural bond orbital, donor-acceptor viewpoint. *Chem. Rev.* **1988**, *88*, 899–926.
- (10) Reed, A. E.; Weinstock, R. B.; Weinhold, F. Natural population analysis. *J. Chem. Phys.* **1985**, *83*, 735–746.
- (11) Bader, R. F. W. *Atoms in Molecules A Quantum Theory*; Oxford University Press: New York, 1990.
- (12) Stone, A. J. Distributed multipole analysis, or how to describe a molecular charge distribution. *Chem. Phys. Lett.* **1981**, *83*, 233–239.
- (13) Stone, A. J.; Alderton, M. Distributed multipole analysis methods and applications. *Mol. Phys.* **1985**, *56*, 1047–1064.
- (14) Winget, P.; Thompson, J. A.; Xidos, J. A.; Cramer, C. J.; Truhlar, D. G. Charge Model 3: A class IV charge model based on hybrid density functional theory with variable exchange. *J. Phys. Chem. A* **2002**, *106*, 10707–10717.
- (15) Li, J. B.; Williams, B.; Cramer, C. J.; Truhlar, D. G. A class IV charge model for molecular excited states. *J. Chem. Phys.* **1999**, *110*, 724–733.
- (16) Li, J. B.; Zhu, T. H.; Cramer, C. J.; Truhlar, D. G. New class IV charge model for extracting accurate partial charges from wave functions. *J. Phys. Chem. A* **1998**, *102*, 1820–1831.
- (17) Storer, J. W.; Giesen, D. J.; Cramer, C. J.; Truhlar, D. G. Class-Iv Charge Models - a New Semiempirical Approach in Quantum-Chemistry. *J. Comput.-Aided Mol. Des.* **1995**, *9*, 87–110.
- (18) Simmonett, A. C.; Gilbert, A. T. B.; Gill, P. M. W. An optimal point-charge model for molecular electrostatic potentials. *Mol. Phys.* **2005**, *103*, 2789–2793.
- (19) Sigfridsson, E.; Ryde, U. Comparison of methods for deriving atomic charges from the electrostatic potential and moments. *J. Comput. Chem.* **1998**, *19*, 377–395.
- (20) Lee, T.-S.; York, D. M.; Yang, W. A new definition of atomic charges based on a variational principle for the electrostatic potential energy. *J. Chem. Phys.* **1995**, *102*, 7549–7556.
- (21) Momany, F. A. Determination of Partial Atomic Charges from Ab Initio Molecular Electrostatic Potentials. Application to Formamide, Methanol, and Formic Acid. *J. Phys. Chem.* **1978**, *82*, 592–601.
- (22) Cox, S. R.; Williams, D. E. Representation of the molecular electrostatic potential by a net atomic charge model. *J. Comput. Chem.* **1981**, *2*, 304–323.
- (23) Singh, U. C.; Kollman, P. A. An approach to computing electrostatic charges for molecules. *J. Comput. Chem.* **1984**, *5*, 129–145.
- (24) Besler, B. H.; Merz, K. M., Jr.; Kollman, P. A. Atomic charges derived from semiempirical methods. *J. Comput. Chem.* **1990**, *11*, 431–439.
- (25) Chirlian, L. E.; Francl, M. M. Atomic charges derived from electrostatic potentials: A detailed study. *J. Comput. Chem.* **1987**, *8*, 894–905.
- (26) Breneman, C. M.; Wiberg, K. B. Determining atom-centered monopoles from molecular electrostatic potentials. The need for high sampling density in formamide conformational analysis. *J. Comput. Chem.* **1990**, *11*, 361–373.
- (27) Martin, F.; Zipse, H. Charge distribution in the water molecule - A comparison of methods. *J. Comput. Chem.* **2005**, *26*, 97–105.
- (28) Cornell, W. D.; Cieplak, P.; Bayly, C.; Gould, I. R.; Merz, K. M. J.; Ferguson, D. M.; Spellmeyer, D. C.; Fox, T.; Caldwell, J. W.; Kollman, P. A. A second generation force field for the simulation of proteins and nucleic acids. *J. Am. Chem. Soc.* **1995**, *117*, 5179–5197.
- (29) MacKerell, J. A. D.; Brooks, B.; Brooks, I. C. L.; Nilsson, L. R. B.; Won, Y.; Karplus, M. CHARMM: The energy function and its parameterization with an overview of the program. In *The Encyclopedia of Computational Chemistry*; P. v. R. S. e., Ed.; John Wiley & Sons: Chichester, 1998; Vol. 1, pp 271–277.
- (30) Chipot, C.; Angyan, J. G.; Ferenczy, G. G.; Scheraga, H. A. Transferable net atomic charges from a distributed multipole analysis for the description of electrostatic properties: a case study of saturated hydrocarbons. *J. Phys. Chem.* **1993**, *97*, 6628–6636.
- (31) Morita, A.; Kato, S. Ab Initio Molecular Orbital Theory on Intramolecular Charge Polarization: Effect of Hydrogen Abstraction on the Charge Sensitivity of Aromatic and Nonaromatic Species. *J. Am. Chem. Soc.* **1997**, *119*, 4021–4032.
- (32) Lu, Z.; Yang, W. Reaction path potential for complex systems derived from combined ab initio quantum mechanical and molecular mechanical calculations. *J. Chem. Phys.* **2004**, *121*, 89–100.
- (33) Anisimov, V. M.; Lamoureux, G.; Vorobyov, I. V.; Huang, N.; Roux, B.; Alexander, D.; MacKerell, J. Determination of Electrostatic Parameters for a Polarizable Force Field Based on the Classical Drude Oscillator. *J. Chem. Theory Comput.* **2004**, *1*, 153–168.

- (34) Frisch, M. J.; Trucks, G. W.; Schlegel, H. B.; Scuseria, G. E.; Robb, M. A.; Cheeseman, J. R.; Montgomery, J. J. A.; Vreven, T.; Kudin, K. N.; Burant, J. C.; Millam, J. M.; Iyengar, S. S.; Tomasi, J.; Barone, V.; Mennucci, B.; Cossi, M.; Scalmani, G.; Rega, N.; Petersson, G. A.; Nakatsuji, H.; Hada, M.; Ehara, M.; Toyota, K.; Fukuda, R.; Hasegawa, J.; Ishida, M.; Nakajima, T.; Honda, Y.; Kitao, O.; Nakai, H.; Klene, M.; Li, X.; Knox, J. E.; Hratchian, H. P.; Cross, J. B.; Bakken, V.; Adamo, C.; Jaramillo, J.; Gomperts, R.; Stratmann, R. E.; Yazyev, O.; Austin, A. J.; Cammi, R.; Pomelli, C.; Ochterski, J. W.; Ayala, P. Y.; Morokuma, K.; Voth, G. A.; Salvador, P.; Dannenberg, J. J.; Zakrzewski, V. G.; Dapprich, S.; Daniels, A. D.; Strain, M. C.; Farkas, O.; Malick, D. K.; Rabuck, A. D.; Raghavachari, K.; Foresman, J. B.; Ortiz, J. V.; Cui, Q.; Baboul, A. G.; Clifford, S.; Cioslowski, J.; Stefanov, B. B.; Liu, G.; Liashenko, A.; Piskorz, P.; Komaromi, I.; Martin, R. L.; Fox, D. J.; Keith, T.; Al-Laham, M. A.; Peng, C. Y.; Nanayakkara, A.; Challacombe, M.; Gill, P. M. W.; Johnson, B.; Chen, W.; Wong, M. W.; Gonzalez, C.; Pople, J. A. *Gaussian 03, C.02*; Gaussian, Inc.: Wallingford, CT, 2004.
- (35) Becke, A. D. A multicenter numerical integration scheme for polyatomic molecules. *J. Chem. Phys.* **1988**, *88*, 2547–2553.
- (36) Wang, W.-P.; Parr, R. G. Statistical atomic models with piecewise exponentially decaying electron densities. *Phys. Rev. A* **1977**, *16*, 891–902.
- (37) Weinstein, H.; Politzer, P.; Srebrenik, S. A misconception concerning the electronic density distribution of an atom. *Theor. Chim. Acta* **1975**, *38*, 159–163.
- (38) Lee, C.; Yang, W.; Parr, R. G. Development of the Colle-Salvetti correlation energy formula into a functional of the electron density. *Phys. Rev. B* **1988**, *37*, 785-.
- (39) Becke, A. D. Density-functional thermochemistry. III. The role of exact exchange. *J. Chem. Phys.* **1993**, *98*, 5648–5652.
- (40) Bondi, A. van der Waals Volumes and Radii. *J. Phys. Chem.* **1964**, *68*, 441–451.
- (41) Koch, U.; Stone, A. J. Conformational dependence of the molecular charge distribution and its influence on intermolecular interactions. *J. Chem. Soc., Faraday Trans.* **1996**, *92*, 1701–1708.
- (42) Bayly, C. I.; Cieplak, P.; Cornell, W.; Kollman, P. A. A well-behaved electrostatic potential based method using charge restraints for deriving atomic charges: the RESP model. *J. Phys. Chem.* **1993**, *97*, 10269–10280.
- (43) Cornell, W. D.; Cieplak, P.; Bayly, C. I.; Kollman, P. A. Application of RESP Charges To Calculate Conformational Energies Hydrogen Bond Energies, and Free Energies of Solvation. *J. Am. Chem. Soc.* **1993**, *115*, 9620–9631.

CT600295N

Semiempirical Molecular Orbital Scheme To Study Lanthanide(III) Complexes: PM3 Parameters for Europium, Gadolinium, and Ytterbium

Jonathan P. McNamara, Sean D. Berrigan, and Ian H. Hillier*

School of Chemistry, University of Manchester, Manchester M13 9PL, U.K.

Received October 12, 2006

Abstract: Semiempirical parameters for europium, gadolinium, and ytterbium have been developed for use in the PM3 method to allow the structure and energetics of complexes containing lanthanide(III) ions to be accurately modeled. At the semiempirical level, the lanthanide(III) ion is represented by a +3 core and has a minimal basis of $6s5d6p$ (9 atomic orbitals), the $4f$ electrons being included within the electronic core. Training sets containing up to 19 lanthanide complexes, with data computed at the density functional theory (DFT) level, have been employed for each lanthanide(III) ion. A gradient-based optimization algorithm has been used, and important modifications of the core repulsion function have been highlighted. The derived parameters lead in general to good predictions of the structure of the complexes and demonstrate improvements in the prediction of water binding energies compared to the AM1/sparkle model. For the 28 Eu(III), 28 Gd(III), and 29 Yb(III) complexes optimized at the DFT level, the PM3 average unsigned mean errors for all interatomic distances between the lanthanide(III) ion and the ligand atoms of the first coordination sphere are 0.04, 0.03, and 0.03 Å, respectively. The derived parameters are shown to be comparable to small-basis set DFT calculations in predicting the experimental structures of various lanthanide(III) complexes. The derived parameter sets provide a starting point should greater accuracy for a more restricted range of compounds be required.

Introduction

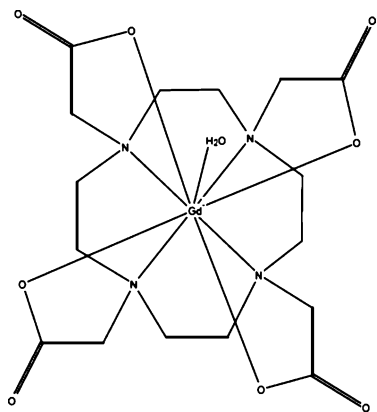
Since the late 1980s there has been an increasing interest in the physicochemical properties and reactivity of the lanthanide (Ln) elements, Ce ($Z = 58$) through to Lu ($Z = 71$) driven by their potential applications in photoluminescence^{1–4} and medical imaging.^{5–9} For example, Gd(III) complexes are currently used as “in vivo” magnetic resonance imaging (MRI) contrast agents which increase the contrast between diseased and normal tissue and/or show the status of organ function and blood flow by enhancing the water proton relaxation rate. Crucial to the design of such complexes is ensuring the complexing ligands form compounds with Gd(III) which possess high kinetic and thermodynamic stability, as the free ions are extremely toxic. As far as Gd-

(III) is concerned, the usual complexing ligands involve octadentate polyamino carboxylate (PAC) ligands such as DOTA (Chart 1).¹⁰

An understanding of the chemistry of the lanthanides is also of increasing importance in nuclear fuel reprocessing,^{11,12} where the separation of nuclear wastes containing both trivalent lanthanides and trivalent minor actinides (e.g., Am(III) and Cm(III)) is complicated by the similar chemical properties of these species. The recent upsurge in lanthanide research activity has also been driven by an interest in the use of these complexes in light conversion molecular devices, such as luminescent materials⁴ and antennae in photosensitive bioinorganic compounds.⁸

The use of quantum mechanical (QM) modeling is now well established for the understanding of structures and mechanisms involving the d -transition metal elements.^{13–15} However, there are considerable challenges for the routine

* Corresponding author phone: +44 (0) 161 275 4686; fax: +44 (0) 161 275 4734; e-mail: Ian.Hillier@manchester.ac.uk.

Chart 1. Structure of the Gadolinium(III) DOTA Complex¹⁰

application of QM approaches to the heavier elements.¹⁶ For these elements, all-electron studies are generally prohibitive due to the large number of orbitals and electrons (many of which are in the core) and the difficulties associated with the presence of open-shell $4f$ electrons. Moreover, as the periodic table is descended, relativistic effects and electron correlation become increasingly important. In addition the complexes of the heavier elements often involve high coordination numbers of the central metal atom and sterically bulky ligands (> 50 atoms) which often prohibits the use of more established ab initio methods for their study.

At present most ab initio or density functional theory (DFT) calculations make use of relativistic effective core potentials (RECP) which treat only the heavy element valence electrons and incorporate relativistic effects into the core, thus reducing the computational effort.¹⁷ Within this approach the $4f$ electrons may or may not be included within the electronic core giving the so-called “large” or “small” core approach. Calculations of $\text{Ln}(\text{NR}_2)_3$ ($\text{R} = \text{H}$ or SiH_3) at the DFT level using both large and small core RECPs indicate accurate models can be obtained by including the $4f$ electrons within the electronic core.¹⁸

To date there have been a number of high-level ab initio calculations reported on quite small lanthanide complexes. Cao and Dolg have calculated the third and fourth ionization energies of the lanthanide atoms (La to Lu) using the CASSCF method¹⁹ and have also used ab initio methods to study open-shell lanthanide dimers (Ce_2 , Pr_2 , and Gd_2)²⁰ and the lanthanum monohalides.²¹ Takeda et al. have reported stabilities of the hexafluoride anions of the lanthanides, LnF_6^{2-} and LnF_6^{3-} ($\text{Ln} = \text{Ce}$ to Lu) at the CASSCF/RECP level.²² For larger complexes, such as $[\text{Ln}(\text{DOTA})(\text{H}_2\text{O})]^{1-}$, the Hartree–Fock (HF) method with a relatively small 3-21G basis set has been shown to give quite good predictions of the structure of these complexes.^{16,23,24}

More recently, DFT has been the method of choice for including electron correlation in calculations of quite large lanthanide complexes. Cosentino et al. have reported calculations of $[\text{Gd}(\text{H}_2\text{O})_9]^{3+}$ at the HF, DFT, and MP2 levels using a 3-21G basis set for the ligand atoms and found the results to be in qualitative agreement with those obtained using larger basis sets including polarization functions.²⁴ Similarly, Smentek et al. have reported calculations of a series of lanthanide DOTA complexes which are in good agreement

with both experimental structural and energetic data.²⁵ DFT calculations showing good agreement between theory and experiment have also been reported for $\text{Ln}(\text{dpm})_3$ ($\text{Ln} = \text{La}$, Nd , Gd , Er , Yb , Ly ; $\text{dpm} = \text{dipivolumethanoate}$),²⁶ $[\text{Ln}(\text{H}_2\text{O})_9]^{3+}$ ($\text{Ln} = \text{La}$, Eu , Lu), and structures involving the 2,2':6',2''-terpyridine²⁷ and the texaphyrin ligands.²⁸ DFT methods have also been used to calculate the structures and bond strengths of the lanthanide halides, the results of which have been shown to be in good agreement with high-level CCSD(T) calculations.²⁹

Due to the difficulties in modeling lanthanide complexes a number of researchers have turned to the use of molecular mechanics (MM) methods for structure prediction.^{30,31} The use of MM techniques for studying f -block elements is sometimes problematic due to the scarcity of data for parametrization. Villa et al. fitted an empirical potential to HF calculations of $[\text{Gd}(\text{THP})\text{OH}_2]^{3+}$, $[\text{Gd}(\text{TMA})(\text{OH}_2)]^{3+}$, and $[\text{Gd}(\text{DOTMP})]^{1-}$ and were able to extend the use of the empirical parameters to study other gadolinium containing complexes.^{16,32} Consentino et al. also parametrized their MM potentials against ab initio calculations and found the quality of the parameters depended strongly on the level at which the potential energy surface was calculated.³³ Moreover, Kowall et al. have also developed potentials (including polarization) that were fitted to ab initio calculation in order to better describe Ln^{3+} –water interactions ($\text{Ln} = \text{Nd}$, Sm , Yb). These potentials were then used in classical molecular dynamics (MD) simulations to understand water exchange at tripositive lanthanide ions.³⁴ Importantly, the calculated coordination numbers of the lanthanide ions and the water exchange rate constants were found to be consistent with experimental data. More recently, van Veggel and Reinhoudt have developed Lennard-Jones parameters for La^{3+} , Nd^{3+} , Gd^{3+} , and Yb^{3+} which correctly predict the experimental free energies of hydration of these ions. In addition, these calculations, using a TIP3P water model, also yield radial distribution functions for each lanthanide ion in good agreement with the available experimental data.³⁵

However, in spite of advances in modern computation hardware and the development of DFT methods and multi-level modeling schemes (e.g., QM/MM^{36,37} and ONIOM³⁸), the computational study of lanthanide chemistry is still at the limit of computational feasibility. For this reason, in this and other areas of condensed phase modeling there has been a renaissance in the use of semiempirical molecular orbital (MO) methods. For example, we³⁹ and others⁴⁰ have successfully quantified the extreme tunneling in the enzyme methylamine dehydrogenase (MADH) using a QM/MM potential and variational transition state theory combined with semiclassical tunneling corrections. To achieve the necessary accuracy, a reparametrization of the PM3 Hamiltonian was required. The use of such specific reaction parameters (SRP), first suggested by Rossi and Truhlar,⁴¹ is central to the continuing successful exploitation of these semiempirical methods.

At present the majority of semiempirical methods (MNDO, AM1, and PM3) are based upon the NDDO approximation and have been widely applied to the study of systems containing the main group elements.^{42–44} These methods have

recently been extended⁴⁵ so that all the nonradioactive main group elements (excluding the noble gases) can now be treated using such techniques and have, in some instances, been extended to include *d*-orbitals. Thiel and Voityuk have proposed an extension of the MNDO method to include *d*-orbitals, MNDO/d, which has been successful in describing hypervalent compounds of the main group elements where *d*-orbitals are important.^{46,47} As far as transition-metal atoms are concerned we have been developing a parametrization strategy to allow the PM3 method to be used to study iron-containing proteins, focusing on iron-sulfur, iron-heme, and iron-only hydrogenases.^{48–51} The development of parameters for lanthanide elements is likely to be particularly challenging given the difficulties in accounting for the *4f* electrons and relativistic effects and due to the size of the complexing ligands (>50 atoms).

There has, however, been some progress in the development of semiempirical methods to treat the heavy elements. Culberson et al. has used the INDO method to examine the electronic structure of a series of lanthanide complexes and found the *4f* orbitals were required for the halides but were less important for the high coordination complexes.⁵² Kotzian and co-workers have also used the INDO/S-CI method (including spin-orbit coupling), to study a range of lanthanide monoxide complexes.^{53–55}

In recent years, significant progress has been made with the development of the so-called sparkle model for treating lanthanide atoms. The success of the sparkle approach is based upon the assumption that most Ln–ligand bonds are essentially electrostatic in nature and the lanthanide *4f* orbitals do not make a significant contribution to the bonding. Sparkles were originally introduced as part of the MOPAC semiempirical package and were designed to represent pure ionic charges.⁵⁶ They can be visualized as essentially a charge delocalized over the surface of a sphere, with an ionic radius of 0.7 Å, integer nuclear charges (+2, +1, –1, or –2 depending on the entity they represent), zero heat of atomization, no orbitals, and no ionization potential.⁵⁷ Crucially they are unable to donate or accept electrons. In the case of a lanthanide atom, the sparkle model involves a nuclear charge of +3, the most commonly encountered oxidation state across the series.

In 1994 the first sparkle model (within the AM1 scheme) for lanthanide complexes (SMLC) was reported for Eu(III), and the parameters were fitted to reproduce the structure of a single Eu(III) complex, [Eu(acac)₃·o-phen].⁵⁸ This model yielded Eu–ligand distances with an average Eu–ligand deviation of 0.36 Å (from experiment) which was later refined to 0.20 Å by the inclusion of two spherical Gaussian functions in the core repulsion term.⁵⁹ More recently, the SMLCII model for Eu(III) was developed which improved on the early revision by increasing the size of the training set from a single Eu(III) complex to one which included 15 complexes spanning a range of ligand environments.⁶⁰ This approach led to a significant improvement in the prediction of experimental structures for the 96 tested complexes [deviation from experiment for Ln–ligand bonds, 0.68 Å (SMLC), 0.28 Å (SMLCII), and 0.09 Å (most recent)]. The AM1 sparkle model (AM1/SMLCII) has since been extended

to nearly all lanthanide(III) elements by fitting to complexes available in the Cambridge Structural Database (CSD).⁶¹ To date AM1/sparkle parameters are available for Gd and Tb;⁶⁰ Pm and Sm;⁶² Yb,⁶³ La and Lu;⁶⁴ Dy;⁶⁵ Pr,⁶⁶ Nd;⁶⁷ and Er and Ce.⁶⁸ Very recently the Tm(III) sparkle model has been reported for use within the PM3 semiempirical scheme.⁶⁹ Both the AM1 and PM3 sparkle implementations have been extensively tested and are certainly capable of predicting structures quite close to experiment for high coordination complexes.

However, what is less clear is whether this approach is capable of describing energetic processes (e.g., the binding energy of water in [Gd(DOTA)(OH₂)]^{1–} important in developing new MRI contrast agents) or those lanthanide complexes where covalent effects may be “non-negligible” and the presence of the orbitals centered on the lanthanide atom are important.

Developing the Semiempirical Model

1. Improving the Semiempirical Sparkle Model. The success of the sparkle model is based on the assumption that lanthanide(III) ions behave like simple ions. The open-shell *4f* orbitals are shielded from external fields outside the nucleus by the closed-shell *5s* and *5p* electrons. Thus the effect of the *4f* orbitals is often assumed to be small, much in the same way as DFT or ab initio calculations using “large” core RECPs assume a negligible contribution from the *4f* orbitals to the Ln–ligand bonding.¹⁸ However, the sparkle model does assume *complete* ionization of the valence electrons, and therefore covalent effects cannot be included.⁶⁰ Freire et al. have suggested that covalent effects could be accounted for by including *s* and *p* valence orbitals on the sparkle +3 metal center.⁶⁰ In our work we have chosen to augment the AM1/sparkle model for lanthanides by adding *6s*, *5d*, and *6p* orbitals to the valence basis and account for the *4f* electrons as part of the electronic core, in line with “large” core RECP calculations.¹⁸ Thus each lanthanide atom has a core charge of +3 and *6s*, *5d*, and *6p* valence atomic orbitals. We have chosen to implement our orbital-based sparkle model within the PM3 framework.⁴⁴

2. Modification of the Core Repulsion Function. Within the NDDO approximation, the core–electron attraction ($V_{\mu\nu,B}$) and core–core repulsion (E_{AB}^{MNDO}) are usually expressed in terms of two-center two-electron integrals (eqs 1 and 2) where Z_A and Z_B correspond to the core charges, R_{AB} is the internuclear separation, and α_A and α_B are adjustable parameters.⁴²

$$V_{\mu\nu,B} = -Z_B(\mu^A \nu^A, s^B s^B) \quad (1)$$

$$E_{AB}^{\text{MNDO}} = Z_A Z_B (s^A s^A, s^B s^B) (1 + e^{-\alpha_A R_{AB}} + e^{-\alpha_B R_{AB}}) \quad (2)$$

The form of the core–electron attraction (eq 1) is common to all NDDO methods, while eq 2 gives the form of the core repulsion function used within the MNDO method.⁴² The form of the core repulsion function in AM1 and PM3 differs from that used in MNDO in that an additional term involving one to four Gaussian functions (denoted *a–c*, eq 3) is also included.^{43,44}

$$E_{AB}^{\text{AM1,PM3}} = E_{AB}^{\text{MNDO}} + \frac{Z_A Z_B}{R_{AB}} \sum_{i=1}^4 [a_{iA} e^{-b_{iA}(R_{AB}-c_{iA})^2} + a_{iB} e^{-b_{iB}(R_{AB}-c_{iB})^2}] \quad (3)$$

For methods which include *d*-orbitals (e.g., MNDO/d and AM1/d),^{46,47,70–72} it has been found that to obtain the correct balance between attractive and repulsive Coulomb interactions requires an additional adjustable parameter ρ (previously evaluated using the one-center two-electron integral, G_{ss} , eq 4), which is used in the evaluation of the two-center two-electron integrals used in these terms (eq 5):

$$\rho = \frac{1}{2G_{ss}} \quad (4)$$

$$(s^A s^A, s^B s^B) = \frac{e^2}{(R_{AB}^2 + (\rho_A + \rho_B)^2)^{1/2}} \quad (5)$$

However, in spite of these modifications, when applying these methods to the study of molybdenum complexes Voityuk and Rösch⁷⁰ found that use of the NDDO core repulsion function (eq 3) led to some systematic deviations for some Mo–X bond lengths. This led them to further modify the form of the core repulsion function for their AM1/d Hamiltonian by introducing bond specific parameters, $\alpha_{\text{Mo-X}}$ and $\delta_{\text{Mo-X}}$ (eq 6).

$$E_{\text{Mo-X}}^{\text{AM1/d}} = Z_{\text{Mo}} Z_X (s^A s^A, s^B s^B) [1 + 2\delta_{\text{Mo-X}} e^{-\alpha_{\text{Mo-X}} R_{\text{Mo-X}}}] \quad (6)$$

This modification was found to be more efficient than using Gaussian functions and has since been used in the extension of NDDO-based methods to the remaining main group elements and the AM1* parametrization of some second-row elements⁷¹ and transition metals.⁷² This is the form of the core repulsion function adopted here. Thus for each lanthanide (Eu, Gd, Yb) the PM3 Gaussian parameters *a*–*c* are set to zero, there is an additional adjustable parameter ρ , and for each Ln–X interaction there are separate $\alpha_{\text{Ln-X}}$ and $\delta_{\text{Ln-X}}$ parameters. In the AM1/d parametrization of molybdenum⁷⁰ and in our PM3 parametrization of iron,⁵¹ the core repulsion function had to be modified in the case of atom X being hydrogen. We find that in our PM3 model for the lanthanides no such modifications are required. The form of our core repulsion function differs from that used in the sparkle model which is based on the original AM1 and PM3 core repulsion function (eq 3).^{43,44}

Parametrization Strategy

1. Construction and Optimization of the Error Function. We here outline our developing strategy to obtain semiempirical parameters for the lanthanide metals, which follows closely our strategy used to obtain parameters for iron. A central feature, common to all optimization strategies, is the construction and subsequent minimization of the error function, *S*, eq 7

$$S = \sum_i w_i (q_i^{\text{semiempirical}} - q_i^{\text{reference}})^2 \quad (7)$$

where $q_i^{\text{semiempirical}}$ and $q_i^{\text{reference}}$ are the molecular quantities calculated at the semiempirical level and the corresponding reference values (usually from experiment or high-level calculation), and w_i is an appropriate weighting factor. The aim of any parameter optimization strategy is to minimize *S* efficiently and this can be achieved using either a genetic algorithm (GA)^{41,48,49,73–76} or a gradient-based algorithm.^{44,45,50,51} One of the central features of the work reported herein is the use of an efficient gradient-based optimization algorithm based upon a modified Broyden-Fletcher-Goldfarb-Shanno (BFGS) method.^{44,45,77,78} Details of this algorithm and the modifications for obtaining semiempirical parameters for transition metals have been reported previously.^{50,51} Therefore, our approach differs from the optimization of AM1/sparkle and PM3/sparkle parametrizations which used a combination of Newton–Raphson and simplex optimization methods.^{60,63}

The chosen error function (*S*, eq 7; see also Table S1 and Figure S1) for each lanthanide element contained weighted contributions from the internal coordinate gradients for each reference complex and also the relative energy (calculated at the DFT level) of the [Ln(DOTA)(OH)₂][–] structures [the square antiprismatic isomer (A) and the inverted antiprismatic isomer (IA)]. Our parametrization strategy differs from that of the AM1/sparkle approach^{60,63} in that our reference data include not only structural but also some energetic data.

2. Choice of Reference Data. Historically the reference data used in semiempirical parametrizations is obtained using a wide range of experimental techniques.^{42–45,77,78} There is, however, a growing trend to replace some of the reference data with information obtained from high-level ab initio calculations (e.g., G2 or G3 methods) or, more recently, DFT calculations.^{49–51,71,72} Such an approach is of increasing importance, particularly in the absence of experimental data or where the reliability of experimental data is questionable. Winget et al. have suggested that a semiempirical method, which behaved as well as, for example, B3LYP/6-31G*, would be a significant advance in this area.⁷¹ For this reason, in our PM3 parametrization for iron^{49–51,74} we chose to calculate all our reference data at the DFT (B3LYP)^{79–81} level using a 6-31G* basis set, and this is also the approach adopted herein.

The reference data for europium, gadolinium, and ytterbium was obtained from DFT calculations at the B3LYP level, performed using the GAUSSIAN 98⁸² and GAUSSIAN 03⁸³ suites of programs. Our choice of DFT functional is supported by the calculations of Heiberg et al. on a series of LnF complexes (Ln = Nd, Eu, Gd, Yb) where the B3LYP functional gave geometries and bond strengths in good agreement with CCSD(T) values.²⁹ The DFT calculations reported herein employed the 46 + 4*f*ⁿ electron RECP of Dolg et al., which treats the outermost 11 electrons explicitly, with valence ground configurations 5*s*²5*p*⁶6*s*²5*d*¹ for the lanthanide atom and 5*s*²5*p*⁶6*s*⁰5*d*⁰ for the lanthanide(III) cation.⁸⁴ The remaining 46 + 4*f*ⁿ electrons are placed in the core. The 3-21G basis set was chosen for the ligand atoms as it has been found to give structures and conformational energies of [Gd(H₂O)₉]³⁺ in qualitative agreement with those obtained using basis sets including polarization functions.²⁴

Table 1. Bond Lengths (Å) and Bond Angles (deg) for the LnX₃ (X = H, CH₃, F, Cl, Br, NH₂) Complexes Calculated at the DFT,^a AM1/Sparkle, and PM3 Levels of Theory

ligand ^b		average value				
		Eu	Gd	Yb		
H	distances	DFT	2.058	2.046	1.996	
		PM3	1.996	2.018	2.041	
		AM1/sparkle	1.003	0.837	0.814	
	angles	DFT	111.7 (0.0)	111.6 (0.1)	114.2 (0.0)	
		PM3	103.1 (0.0)	106.0 (0.0)	110.5 (0.0)	
		AM1/sparkle	120.0 (0.1)	120.0 (0.1)	120.0 (0.0)	
	CH ₃	distances	DFT	2.437	2.426	2.367
			PM3	2.393	2.425	2.433
			AM1/sparkle	2.040	2.093	2.096
angles		DFT	107.8 (0.1)	107.8 (0.0)	109.6 (0.0)	
		PM3	110.8 (0.0)	113.3 (0.0)	116.0 (0.0)	
		AM1/sparkle	120.0 (0.0)	120.0 (0.0)	120.0 (0.0)	
F		distances	DFT	2.073	2.063	2.006
			PM3	2.080	2.055	2.036
			AM1/sparkle	2.290	2.315	2.252
	angles	DFT	115.5 (0.0)	116.3 (0.4)	118.9 (0.4)	
		PM3	108.8 (0.0)	110.0 (0.0)	114.2 (0.0)	
		AM1/sparkle	120.0 (0.0)	120.0 (0.0)	120.0 (0.0)	
	Cl	distances	DFT	2.556	2.541	2.476
			PM3	2.524	2.524	2.480
			AM1/sparkle	2.308	2.333	2.265
angles		DFT	119.6 (0.7)	118.6 (0.9)	120.0 (0.3)	
		PM3	106.2 (0.0)	108.6 (0.0)	120.0 (0.0)	
		AM1/sparkle	120.0 (0.0)	120.0 (0.0)	120.0 (0.2)	
Br		distances	DFT	2.696	2.683	2.618
			PM3	2.601	2.671	2.610
			AM1/sparkle	2.299	2.323	2.259
	angles	DFT	120.0 (0.0)	120.0 (0.0)	120.0 (0.0)	
		PM3	120.0 (0.0)	120.0 (0.0)	120.0 (0.0)	
		AM1/sparkle	120.0 (0.0)	120.0 (0.0)	120.0 (0.0)	
	NH ₂	distances	DFT	2.253	2.241	2.179
			PM3	2.257	2.253	2.167
			AM1/sparkle	2.200	2.211	2.196
angles		DFT	120.0 (0.1)	120.0 (0.1)	120.0 (0.1)	
		PM3	114.4 (0.0)	117.3 (0.0)	120.0 (0.0)	
		AM1/sparkle	120.0 (3.9)	120.0 (0.0)	120.0 (4.9)	

^a B3LYP/6-31G* and quasi-relativistic ECP of ref 84 for the lanthanide atom. ^b Ln–X distances are essentially equivalent in each complex. (In parentheses) unsigned mean deviation of bond angles.

However, for the lanthanide tricoordinated complexes (H, Me, F, Cl, Br, NH₂, Table 1) the ligand atoms were calculated using the 6-31G* basis set. Our semiempirical model in which the 4*f* electrons are placed in the core has been parametrized against DFT calculations in which the 4*f* electrons are also placed within the electronic core.

For each lanthanide, in addition to the 6 tricoordinated complexes (Table 1) we also selected up to 10 complexes from the CSD (Tables S2–S4, Figures S2–S4).⁶¹ In line with the parametrization of the AM1/sparkle model, these

complexes involved a range of coordinating ligands such as β -diketones, nitrates, mono-, bi-, tri-, and polydentate ligands.^{60,63} We also chose at least one dilanthanide complex for each training set (Figures S2–S4). In view of the importance of the DOTA ligand (Chart 1) in MRI contrast agents we also included three structures involving the DOTA ligand within our training sets [A isomer with and without water and the IA isomer with water, Table 2]. The training sets for Eu, Gd, and Yb contained up to 19 reference structures. Each of the reference complexes was optimized at the DFT level, the structures of which are given in Tables 1, 2, and S2–S4. Our parametrization for the lanthanides thus differs from that for the AM1/sparkle model^{60,63} in that our reference data are entirely calculated at the DFT level (rather than being obtained from crystal structures alone).

All semiempirical calculations were performed using our local semiempirical package (Manchester University Semi-Empirical, MUSE) program.⁴⁸ We have implemented the semiempirical method PM3 method including *d*-orbitals^{46,47} and for comparison have also implemented the AM1/sparkle model⁶⁰ within our program and validated our algorithm against the available published data.^{60,63} We note that for the location of minima on the potential energy surface, our program uses the GAUSSIAN 03⁸³ optimization suite, whereas the published AM1/sparkle model makes use of the optimization algorithms within the MOPAC suite of programs.⁵⁷

3. Parametrization. Our initial goal was to obtain parameters for gadolinium. Stewart suggests that the two most common methods for generating initial sets of parameters are to use parameters from a previous method or to use values derived from a similar element.⁴⁵ In our case, neither of these approaches were possible due to the absence of either AM1 or PM3 published parameters for gadolinium. We also note that due to the different functional form of the AM1/sparkle model⁶⁰ and our orbital-based model we were unable to make use of the existing sparkle parameters for gadolinium for initial estimates of our core repulsion parameters.

The one-center terms, U_{ss} , U_{dd} , G_{ss} , G_{sd} , G_{dd} , and H_{sd} , were obtained by fitting these parameters (using a GA⁸⁵) to the energies of 12 electronic states of the neutral and ionized gadolinium atom.⁸⁶ The parameter U_{pp} was also estimated from experimental data. Thus the one-center lanthanide parameters, where the 4*f* electrons are part of the electronic core can be obtained in essentially the same way as for first-row transition metals.⁴⁸ The remaining parameters (G_{pp} , β_s , β_p , β_d , ξ_{ss} , ξ_p , ξ_d) were assigned different values for different parametrization runs. The core electron attraction and core repulsion parameters, ρ , δ_{Gd-X} , and α_{Gd-X} , were set equal to 1.0, 1.5, and 2.0. Importantly, in our approach *all* the semiempirical parameters were adjusted, with constraints placed upon individual parameters to prevent them from wandering toward unrealistic values, which may have limited their transferability. We note that even though we allowed the one-center terms U_{ss} , U_{dd} , G_{ss} , G_{sd} , G_{dd} , and H_{sd} to change from the GA optimized values, the relative energies of the different states of the neutral and charged gadolinium atom are in good agreement with experimental data (Table S5).

Table 2. Experimental and Calculated Average Distances (Å) and Dihedral Angles (deg) for the Lanthanide(III) DOTA Complexes

distance ^a	Eu ^c	Gd ^d	Yb
DFT ^b			
Isomer A			
N	2.699	2.690	2.645
O	2.343	2.328	2.264
φ	39.4	39.5	40.2
Isomer IA + H ₂ O			
N	2.734 (2.680)	2.729 (2.663)	2.715 ^e
O	2.381 (2.394)	2.365 (2.367)	2.298 ^e
O (H ₂ O)	2.538 (2.480)	2.530 (2.463)	2.436 ^e
φ	39.7 (38.7)	39.9 (38.5)	40.8 ^e
Isomer IA + H ₂ O			
N	2.746	2.741	2.722
O	2.393	2.378	2.315
O (H ₂ O)	2.523	2.519	2.441
φ	-28.8	-29.1	-29.0
PM3			
Isomer A			
N	2.697	2.700	2.645
O	2.384	2.359	2.284
φ	38.1	37.5	37.7
Isomer A + H ₂ O			
N	2.716	2.718	2.672
O	2.416	2.391	2.317
O (H ₂ O)	2.523	2.497	2.436
φ	38.3	37.7	37.7
Isomer IA + H ₂ O			
N	2.756	2.755	2.710
O	2.418	2.392	2.319
O (H ₂ O)	2.523	2.497	2.434
φ	-24.4	-23.0	-23.8
AM1/Sparkle			
Isomer A			
N	2.603	2.617	2.525
O	2.389	2.397	2.325
φ	35.4	38.0	36.9
Isomer A + H ₂ O			
N	2.608	2.627	2.530
O	2.398	2.409	2.330
O (H ₂ O)	2.397	2.413	2.297
φ	36.1	38.6	36.7
Isomer IA + H ₂ O			
N	2.613	2.639	2.534
O	2.403	2.415	2.333
O (H ₂ O)	2.429	2.418	2.298
φ	-20.2	-22.4	-19.9

^a φ is the twist angle between the basal plane occupied by four amine nitrogens and a capped plane occupied by the carboxylate oxygens of the acetate arms. ^b B3LYP/3-21G and quasi-relativistic ECP of ref 84 for the lanthanide atom. ^c (In parentheses) average experimental values.⁸⁹ ^d (In parentheses) average experimental values.⁹⁰ ^e For comparison experimental values for the Lu structural parameters are N = 2.614 Å, O = 2.279 Å, O(H₂O) = 2.417 Å, and φ = 39.6°.⁹⁵

Thus our parametrization scheme includes energetic data as well as structural data. We also note that our *s* and *p* Slater exponents (ξ_s , ξ_p) are quite close to those used in the INDO/S method for these lanthanides, whereas the Slater *d* exponents

Table 3. PM3 Parameters for Europium(III), Gadolinium(III), and Ytterbium(III)

parameter ^{a,b}	units	Eu	Gd	Yb
U_{ss}	eV	-18.826233	-18.911102	-18.650043
U_{pp}	eV	-7.389669	-7.242997	-7.350925
U_{dd}	eV	-20.425142	-20.259917	-19.196298
G_{ss}	eV	6.016223	6.053780	6.007332
G_{pp}	eV	6.583764	6.629378	6.637371
G_{dd}	eV	8.686045	8.771641	8.779865
G_{sd}	eV	6.539961	6.584258	6.593397
H_{sd}	eV	0.709285	0.620633	0.667674
β_s	eV	-7.731346	-7.592416	-7.727729
β_p	eV	-3.185841	-3.038541	-3.151070
β_d	eV	-5.068540	-4.952733	-4.988789
ξ_s	bohr ⁻¹	1.481590	1.459057	1.459151
ξ_p	bohr ⁻¹	1.655881	1.614106	1.649188
ξ_d	bohr ⁻¹	1.748437	1.705403	1.826745
ρ	bohr	2.003400	1.704389	1.972353
δ_{Ln-H}	dimensionless	2.003450	2.058686	2.062443
δ_{Ln-C}	dimensionless	1.995470	2.041816	1.976463
δ_{Ln-N}	dimensionless	1.982809	1.921203	1.932329
δ_{Ln-O}	dimensionless	1.964953	1.909225	1.907816
δ_{Ln-F}	dimensionless	1.939396	1.971044	1.915106
δ_{Ln-S}	dimensionless	1.974976	2.126802	1.954339
δ_{Ln-Cl}	dimensionless	2.077221	2.061006	2.051176
δ_{Ln-Br}	dimensionless	2.077995	2.229090	2.142167
δ_{Ln-Ln}	dimensionless	3.959263	4.007627	3.969686
α_{Ln-H}	Å ⁻¹	1.802290	1.823080	1.721239
α_{Ln-C}	Å ⁻¹	1.767034	1.756414	1.744168
α_{Ln-N}	Å ⁻¹	1.826384	1.864247	1.959332
α_{Ln-O}	Å ⁻¹	1.886109	1.925632	1.977981
α_{Ln-F}	Å ⁻¹	1.983411	2.090731	2.044649
α_{Ln-S}	Å ⁻¹	1.869981	1.834960	1.947567
α_{Ln-Cl}	Å ⁻¹	1.734821	1.770806	1.800099
α_{Ln-Br}	Å ⁻¹	1.728463	1.731540	1.764436
α_{Ln-Ln}	Å ⁻¹	1.556393	1.516730	1.558195

^a For complexes containing B, δ_{Ln-B} and α_{Ln-B} were set equal to the corresponding values for C; for complexes containing P, δ_{Ln-P} and α_{Ln-P} were set equal to the corresponding values for N; for complexes containing Si, δ_{Ln-Si} and α_{Ln-Si} were set equal to the corresponding values for C. ^b For comparison INDO/S Slater exponents are as follows: ξ_s 1.656 (Eu), 1.678 (Gd), 1.812 bohr⁻¹ (Yb); ξ_p 1.448 (Eu), 1.463 (Gd), 1.549 bohr⁻¹ (Yb); ξ_d 2.229 (Eu), 2.243 (Gd), and 2.279 bohr⁻¹ (Yb).⁵²

(ξ_d) are somewhat smaller than the corresponding INDO/S values (Table 3).⁵²

For gadolinium, each parametrization run involved the optimization of 33 parameters (including 18 bond specific terms) and a reference training set of 18 complexes, of which 7 contained more than 50 atoms. We carried out several parametrization runs starting from different initial parameter values, reference training sets, and weighting factors in the error function. Each explicit function and gradient calculation typically involved some 1200 SCF and force calculations, and due to the size of the reference structures the most time-consuming part of each SCF calculation was the transformation of the Cartesian forces (for each structure) into internal forces. Each parametrization run usually required less than 10 explicit gradient evaluations. In line with Stewart's algorithm^{44,45} we also found that during the initial stages of the optimization the value of the error function (*S*, eq 7) dropped rapidly, partly due to the crude initial guess of the core repulsion parameters (ρ , δ_{Gd-X} , and α_{Gd-X}). The error

function evaluated using the final optimized parameters was typically less than 20% of the function evaluated using the initial parameters. The final gadolinium parameters are given in Table 3. It is worth pointing out that since our modified BFGS algorithm avoids explicit geometry optimization,^{50,51} there is the possibility of obtaining parameters that yield very small gradients for the reference structures but that, upon geometry optimization, predict structures quite different from the reference ones. By including a relatively large number of reference structures and coordination environments we hope to minimize this effect (Tables S6–S8).

We found during our initial attempts to obtain lanthanide parameters for the $[\text{Ln}(\text{DOTA})(\text{OH}_2)]^{1-}$ complexes, that there was a tendency for the Ln–N distances to be overestimated by up to 0.2 Å, and for the dilanthanide complexes, the Ln–Ln distances were quite poorly predicted, deviating from the DFT values by up to 0.4 Å. These problems were somewhat overcome by scaling these internal coordinate gradients by quite large weighting factors relative to the other internal coordinate gradients (Table S1). Parameters for europium and ytterbium were obtained as follows. In line with Stewart's suggestion,⁴⁵ initial values for europium parameters were derived from the optimized gadolinium parameters but with the core repulsion parameters ρ , $\delta_{\text{Gd-X}}$, and $\alpha_{\text{Gd-X}}$ reset to the values 1.0, 1.5, and 2.0. However, deriving the initial ytterbium parameters from those for gadolinium led to a set of parameters which yielded *d*-orbital populations that were too large to be consistent with the expected trends across the lanthanide series. Therefore the initial ytterbium parameters were extrapolated from the parameters of europium and gadolinium.

The final ytterbium parameters (Table 3) are quite close to the corresponding gadolinium ones, the largest change occurs for the ρ parameter which has increased by 16%, and, of the 32 optimized ytterbium parameters, only eight of these differ from the gadolinium ones by more than 5% (Table 3). Similarly, only three of the optimized ytterbium parameters differ by more than 5% from the europium ones, the largest difference being for the $\alpha_{\text{Ln-N}}$ parameter, which decreases by 7% (Table 3). Generally speaking, the observed parameter changes in going from Gd to Yb (separated by Tb, Dy, Ho, Er, and Tm) and also Eu to Yb appear to be quite small. Stewart⁴⁵ suggests interpolation or extrapolation as ways of obtaining initial estimates for parameters; given the closeness of the Yb parameters to those of Eu and Gd, extrapolation may be possible, without further optimization, to obtain parameters for other lanthanides close to the ones reported herein (e.g., Sm, Tb, Tm, Lu). However, it is important to recognize that the observed parameter changes may also be influenced not only by the properties of the elements themselves but also by the different training sets used (Tables S6–S8).

This parametrization strategy differs from our previous work in developing PM3 parameters for iron^{50,51} in that we are able to obtain useful parameter sets without including data concerning the charges, spin densities, and $\langle S^2 \rangle$ value of the reference complexes. Moreover, we found that inclusion of the DFT atomic charges (scaling factor 2000 e^{-1}) did not significantly improve the final results. This was

Table 4. Average UME and $\text{UME}_{\text{Ln-X}}$ (vs Experiment) for Complexes Used by Other Workers^{60,63} in the AM1/Sparkle Parametrization of Europium, Gadolinium, and Ytterbium^a

element ^b	DFT ^c	PM3 ^d	AM1/sparkle ^d
europium (15)			
$\text{UME}_{\text{Ln-X}}$	0.0514	0.0607 (0.0588)	0.0767 (0.0673)
UME^e	0.0982	0.1174 (0.1132)	0.1547 (0.1514)
gadolinium (15)			
$\text{UME}_{\text{Ln-X}}$	0.0587	0.0574 (0.0592)	0.0676 (0.0669)
UME^e	0.1306	0.1198 (0.1141)	0.1532 (0.1584)
ytterbium (15)			
$\text{UME}_{\text{Ln-X}}$	0.0514	0.0516 (0.0630)	0.0653 (0.0835)
UME^e	0.1247	0.0967 (0.0934)	0.1667 (0.2007)

^a For individual UMEs and $\text{UME}_{\text{Ln-X}}$ values refer to Tables S9–S11. ^b (In parentheses) number of complexes used for each element. ^c B3LYP/3-21G and quasi-relativistic ECP of ref 84 for the lanthanide atom. ^d (In parentheses) complexes calculated at the DFT level only. ^e Complexes containing more than one lanthanide atom were omitted: Eu (DOPCEQ, NUHIX and QECGOU); Gd (CULNIG10 and YAVSUJ); and Yb (NIJFER and XEWZOO).

probably due to the fact that in our model our reference lanthanide complexes were all closed-shell. Importantly, the performance of our present approach with respect to any chosen molecular property can be tuned by a suitable adjustment of the weighting factors (Table S1).

The resulting parameters were then tested on a range of complexes not included in the reference training set to select those parameters giving the most balanced results. In line with our parametrization of iron⁵¹ and the recently reported AM1* parametrization,⁷¹ our goal in this work was to obtain sets of reasonable parameters which performed well for as many chemical applications as possible. As a result the final optimized parameters for Eu, Gd, and Yb (Table 3) do not necessarily correspond to those that yielded the lowest value of the error function. In this work we only report core repulsion parameters ($\delta_{\text{Ln-X}}$ and $\alpha_{\text{Ln-X}}$) for complexes in our training set. However, for the large majority of lanthanide(III) complexes in the CSD⁶¹ the lanthanide ion is directly coordinated by either oxygen or nitrogen. Thus for atoms not directly coordinated to the lanthanide ion, for which we have not derived core repulsion parameters, the parameters of a closely related element can be used (e.g., for silicon use carbon etc., Table 3).

Computational Results

In order to measure the accuracy to which our model is capable of reproducing the reference structures, we have calculated the unsigned mean error (UME) for (i) the interatomic distances (R) between all the atoms of the coordination polyhedron (UME) and (ii) the interatomic distances (R) between the lanthanide central ion and the atoms directly coordinated to this atom ($\text{UME}_{\text{Ln-X}}$).⁵⁹ The UME (or $\text{UME}_{\text{Ln-X}}$) for any given structure (in Å) is calculated using eq 8

$$\text{UME} = \frac{1}{n} \sum_{i=1}^n |R_{\text{reference}} - R_{\text{calculated}}| \quad (8)$$

The average UME and $\text{UME}_{\text{Ln-X}}$ are also reported for different sets of complexes (Tables 4, 5, and S6–S14).

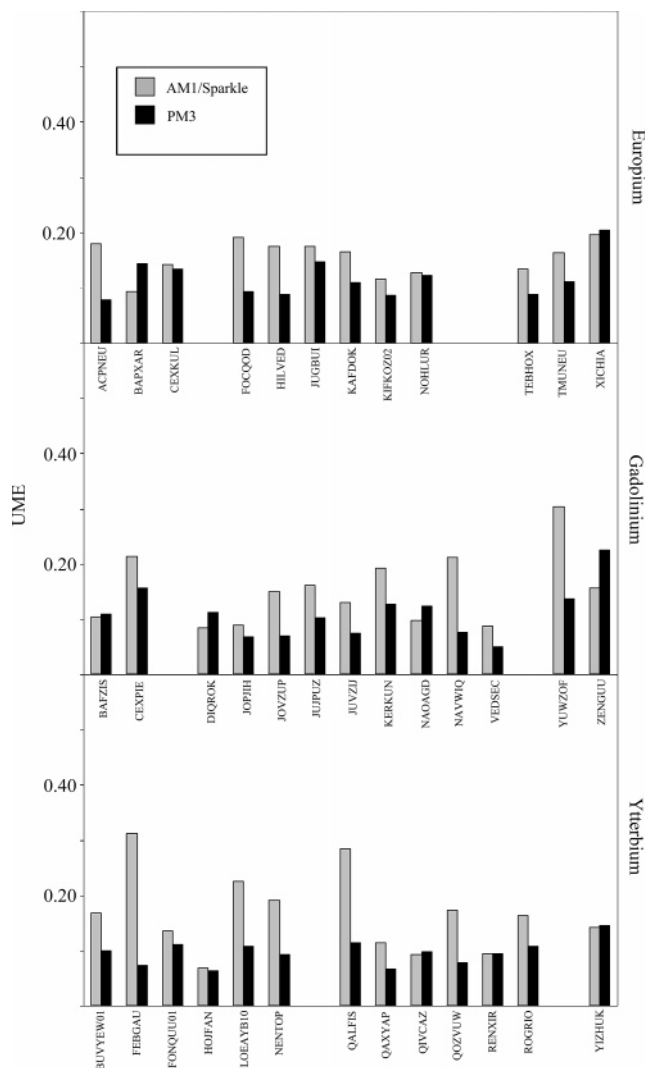


Figure 1. UME (Å) (vs experiment) for the complexes used by other workers^{60,63} in the AM1/sparkle parametrization of europium, gadolinium, and ytterbium. Refer to Tables S9–S11 for individual UMEs. Complexes containing more than one lanthanide atom were omitted: Eu (DOPCEQ, NUXHIX, and QECGOU); Gd (CULNIG10 and YAVSUJ); and Yb (NIJFER and XEWZOO).

1. Calculation of Crystal Structures Using DFT. We have evaluated the performance of our chosen DFT method and the PM3 model in predicting the experimental structures (obtained from the CSD⁶¹) of complexes from the training sets used by other workers^{60,63} in the parametrization of the AM1/sparkle model. For comparison we have also calculated these structures using our implementation of the AM1/sparkle method. The average UME and UME_{Ln-X} values for the europium, gadolinium, and ytterbium complexes are summarized in Table 4 and also Figure 1 (see also Tables S9–S11).^{60,63}

Evidently, our chosen DFT method yields Ln–ligand distances close to the experimental values with UME_{Ln-X} of 0.0514, 0.0587, and 0.0514 Å for the europium, gadolinium, and ytterbium complexes, respectively (Table 4). Importantly for the prediction of crystal geometries, the average UME indicate that the PM3 model generally predicts structures a little closer to experiment for gadolinium and

Table 5. Average UME and UME_{Ln-X} (vs DFT^a) for Complexes in the Europium, Gadolinium, and Ytterbium PM3 Training Sets^b

element ^c	AM1/sparkle ^d	PM3 ^d
europium		
UME_{Ln-X}	0.1984 (0.1005)	0.0355 (0.0329)
UME^e	0.2812 (0.1570)	0.0963 (0.0896)
gadolinium		
UME_{Ln-X}	0.1875 (0.0821)	0.0254 (0.0316)
UME^e	0.2725 (0.1296)	0.0720 (0.0735)
ytterbium		
UME_{Ln-X}	0.1801 (0.0873)	0.0283 (0.0292)
UME^e	0.2835 (0.1752)	0.0677 (0.0807)

^a B3LYP/3-21G and quasi-relativistic ECP of ref 84 for the lanthanide atom. ^b For individual UME and UME_{Ln-X} values refer to Tables S6–S8. ^c (In parentheses) number of complexes used for each element. ^d (In parentheses) values *not* including LnX_3 ($X = H, CH_3, Cl, F, Br, NH_2$). ^e Complexes containing more than one lanthanide atom were omitted: Eu (DOPCEQ); Gd (ACAQGD01 and YAVSUJ); and Yb (XEWZOO).

ytterbium than does the DFT method [Eu, 0.1132 (PM3), 0.0982 (DFT); Gd, 0.1141 (PM3), 0.1306 (DFT); Yb 0.0934 (PM3), 0.1247 Å (DFT)]. This finding is somewhat surprising given that the PM3 parameters were developed using DFT structures alone. Intuitively the quality of the PM3 structures should at best be as good as the DFT ones. The fact that PM3 predicts structures a little closer to experiment is likely to be due to a fortuitous cancellation of errors, probably as a result of the approximations inherent in the parameter optimization algorithm. One such approximation is that for each reference structure, the parameters are adjusted until the forces on the atoms of each structure are minimized, rather than performing explicit geometry optimization.

The average UME values at the PM3 level for these structures [0.1174 (Eu), 0.1198 (Gd), 0.0967 Å (Yb)] are smaller than the corresponding AM1/sparkle values [0.1547 (Eu), 0.1532 (Gd), 0.1667 Å (Yb)] even though the PM3 model was parametrized to reproduce DFT gas-phase geometries and not crystal structures (Table 4). It would appear the PM3 model is a notable improvement over the existing AM1/sparkle model and can even rival DFT for accuracy in predicting the structures of various lanthanide crystal complexes. Figure 1 shows a plot of the UMEs (vs experiment) calculated for each of the europium, gadolinium, and ytterbium crystal structures. Overall the PM3 model generally gives smaller UMEs for the crystal structures than does the AM1/sparkle model. It is not surprising that the PM3 model is superior to the AM1/sparkle model given its increased flexibility due to the greater number of adjustable parameters. Importantly, despite the increase in the number of parameters for our PM3 model compared to the AM1/sparkle model⁶⁰ the actual increase in calculation time is negligible.

2. Calculation of Complexes in the PM3 Training Sets. We first discuss the average UME and UME_{Ln-X} for the PM3 and AM1/sparkle calculations for each PM3 training set (summarized in Table 5 and Figure 2; see also Tables S6–S8) to measure the accuracy to which they can reproduce the results of the DFT calculations. Figure 2 shows a plot of

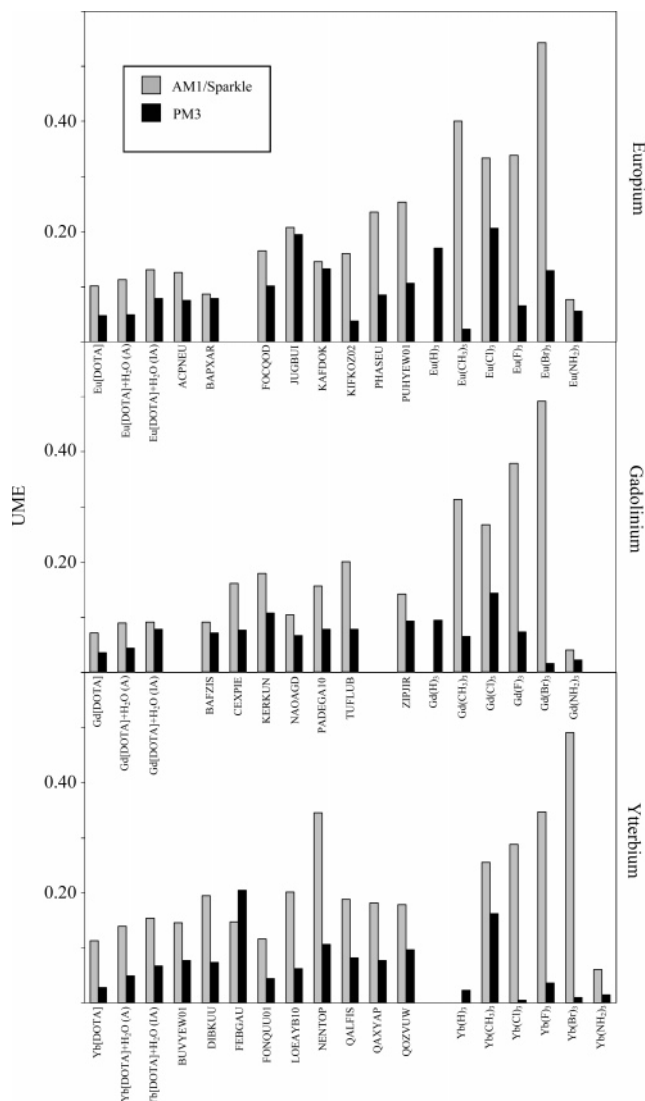


Figure 2. UME (Å) (vs DFT) for complexes in the europium, gadolinium, and ytterbium PM3 training sets. Refer to Tables S6–S8 for individual UMEs. Complexes containing more than one lanthanide atom were omitted: Eu (DOPCEQ); Gd (ACAQGD01 and YAVSUJ); and Yb (XEWZOO). AM1/sparkle UMEs for LnH₃ complexes were also omitted: Eu (1.3616 Å); Gd (1.5713 Å); and Yb (1.5625 Å).

the UMEs for each of the complexes in the europium, gadolinium, and ytterbium training sets. As expected the UMEs (vs DFT) for each structure are considerably smaller at the PM3 level than at the AM1/sparkle level. For each lanthanide, the average UME_{Ln-X} for each training set indicates the PM3 structures are very close to those at the DFT level [0.0355 (Eu), 0.0254 (Gd), and 0.0283 Å (Yb)]. Not surprisingly, the PM3 average UME_{Ln-X} are considerably better than those calculated using the AM1/sparkle parameters given that the AM1/sparkle model was parametrized to reproduce crystal structures [0.1984 (Eu), 0.1875 (Gd), 0.1801 Å (Yb)].^{60,63} These findings are also reflected in the average UME_{Ln-X} when considering only the poly coordinated complexes (Table 5). The average UME (which reflects the ability of the semiempirical model to reproduce the geometry of the coordination polyhedron) are significantly smaller at the PM3 level [0.0963 (Eu), 0.0720 (Gd), 0.0677

Table 6. Relative Energies (kcal mol⁻¹) of the Complexes Involving the DOTA Ligand, Calculated at the DFT, AM1/Sparkle, and PM3 Levels of Theory

complex ^b	Eu	Gd	Yb
DFT ^a			
[Ln(DOTA)] ¹⁻ (A) + H ₂ O	0.0	0.0	0.0
[Ln(DOTA)(OH ₂)] ¹⁻ (A)	-42.7	-42.7	-40.7
[Ln(DOTA)(OH ₂)] ¹⁻ (IA)	-36.8	-36.7	-33.7
$\Delta E(A-IA)$	-5.9	-6.0	-7.0
PM3			
[Ln(DOTA)] ¹⁻ (A) + H ₂ O	0.0	0.0	0.0
[Ln(DOTA)(OH ₂)] ¹⁻ (A)	-23.7	-31.2	-22.6
[Ln(DOTA)(OH ₂)] ¹⁻ (IA)	-21.4	-28.9	-17.6
$\Delta E(A-IA)$	-2.3	-2.3	-5.0
AM1/Sparkle			
[Ln(DOTA)] ¹⁻ (A) + H ₂ O	0.0	0.0	0.0
[Ln(DOTA)(OH ₂)] ¹⁻ (A)	4.7	-17.8	-5.6
[Ln(DOTA)(OH ₂)] ¹⁻ (IA)	16.5	-6.6	6.1
$\Delta E(A-IA)$	-11.8	-11.2	-11.7

^a B3LYP/3-21G and quasi-relativistic ECP of ref 84 for the lanthanide atom. ^b ΔE is the relative energy of the A and IA isomers of [Ln(DOTA)(OH₂)]¹⁻.

Å (Yb)] than at the AM1/sparkle level [0.2812 (Eu), 0.2725 (Gd), 0.2835 Å (Yb)]. We turn now to discuss the complexes involving the DOTA ligand calculated using our new PM3 model.

[Ln(DOTA)(OH₂)]¹⁻ (Ln = Eu, Gd, or Yb). The mean Ln–ligand distances of the complexes involving the DOTA ligand calculated at the DFT (B3LYP), AM1/sparkle, and PM3 level along with the available experimental data are given in Table 2. The relative energies of the [Ln(DOTA)(OH₂)]¹⁻ isomers (A and IA) calculated at the DFT, AM1/sparkle, and PM3 levels are reported in Table 6.

It is now well understood that in solution [Ln(DOTA)]⁻ complexes exist in two interconverting diastereomeric forms which differ in their arrangement of the acetate arms. For each form, the arrangement of the nitrogen and acetate oxygen atoms (which define two parallel squares) are twisted by an angle φ , yielding square antiprismatic (A) ($\varphi \sim 40^\circ$) and inverted antiprismatic (IA) ($\varphi \sim -20^\circ$) geometries. In solution the ninth coordination site is occupied by a single water molecule which undergoes rapid exchange with the surrounding bulk solvent and enhances the water proton relaxation rate.^{87,88}

We first compare our DFT calculations with the available experimental data (Table 2).^{89,90} Evidently, at the DFT level the Ln–N and the Ln–OH₂ distances are overestimated, whereas the Ln–O(DOTA) interactions are well-described at this level (Table 2). Previous calculations at the HF/3-21G level (46 + 4th ECP for lanthanides) have shown that for the [Ln(DOTA)(OH₂)]¹⁻ complex (Ln = La, Gd, Ho, Lu) there is a decrease in the calculated metal–ligand distances across the series coupled with a decrease in the stability of the nonacoordinated A isomer.²³ Thus our DFT structures of these complexes are in good agreement with the HF values in that there is a significant decrease in the metal–ligand distances from Eu through to Yb. For example, for the hydrated A isomer of the DOTA complex, the Ln–OH₂ distance decreases from 2.538 to 2.436 Å in going from

Eu to Yb (Table 2). In agreement with the calculations of Consentino et al. the Ln–O(DOTA) distances of the A isomer are predicted to be shorter than those of the IA isomer (Table 2).²³ Also, the general trend in increasing φ angles (Yb > Gd > Eu) for the nonacoordinated species reflects the decreasing ionic radius across the series leading to more compact structures (Table 2).

We turn now to the semiempirical calculations of the DOTA complexes. For each of the complexes (at both PM3 and AM1/sparkle level) the Ln–ligand distances decrease across the series as Eu > Gd > Yb. The PM3 Ln–OH₂ distances (isomer A) decrease going from Eu to Yb [2.523 (Eu), 2.497 (Gd), and 2.436 Å (Yb)] and are close to the corresponding values calculated at the DFT level (2.538, 2.530, 2.436 Å, Table 2). However, the AM1/sparkle Ln–OH₂ distances (A isomer) are less well predicted being ca. 0.1 Å shorter than the DFT values (Table 2). Similarly, the AM1/sparkle Ln–N distances for each structure are generally too short by some 0.1 Å or greater (Table 2).

As the ionic radius of the lanthanide cation decreases, the ninth coordination site at the metal center becomes less accessible; the structure around the ion becoming more compact. As a result the stability of the nonacoordinated species (isomers A and IA) should decrease, relative to the nonhydrated complex (isomer A).²³ This is indeed the trend predicted from the DFT calculations as the relative stability of the A and IA isomers decreases from –42.7 and –36.8 (Eu) to –40.7 and –33.7 (Yb) kcal mol^{–1}, respectively (Table 6). However, at both the PM3 and AM1/sparkle levels the trend is less clear. Evidently at the PM3 level the binding energies of the water molecules for the Eu, Gd, and Yb (isomer A) complexes (–23.7, –31.2, and –22.6 kcal mol^{–1}, Table 6) are much closer to the corresponding DFT values (–42.7, –42.7, and –40.7 kcal mol^{–1}) than for the AM1/sparkle model (4.7, –17.8, and –5.6 kcal mol^{–1}, Table 6). Overall, the PM3 estimates for the water-binding energies are quite poor and to achieve better estimates of energetic properties will probably require a greater number of energetic data in the fitting function, in line with our fitting function used to obtain parameters for iron.⁵¹ Here, we note that the observed trend in our DFT calculations mirrors that of previous DFT studies (B3LYP/6-311G**) on a series of [Ln(DOTA)(OH₂)]^{1–} complexes in which the water binding *free* energy decreases across a series as La > Gd > Ho > Lu (–3.84, –2.64, –0.81, and 0.20 kcal mol^{–1}).²³ Surprisingly, for this same series of complexes the Ln–OH₂ distances are found to also decrease as 2.635, 2.515, 2.462, and 2.424 Å, respectively (HF/3-21G in vacuo) in line with experiment.²³

We finally note that the relative energies of the A and IA isomers at both the PM3 and AM1/sparkle levels are quite close to the corresponding DFT values (Table 6), although we find that the PM3 method underestimates and the AM1/sparkle model overestimates the relative stabilities (Table 6).

CSD Complexes. The UME and the UME_{Ln–X} values for each complex in the PM3 training sets are given in Tables S6–S8. The mean Ln–ligand bond distances for each

complex are given in Tables S2–S4. Within each training set for Eu, Gd, and Yb there are a range of lanthanide coordination environments including β -diketone, nitrate, mono-, bi-, tri-, and polydentate ligands as well as dilanthanide complexes (Figures S2–S4). Each structure was obtained from the CSD⁶¹ and optimized at the B3LYP/3-21G level using the quasi-relativistic 46 + 4fⁿ ECP of Dolg et al.⁸⁴ for the lanthanide atoms. We now compare structures both from the AM1/sparkle model and from our new PM3 model with those calculated at the DFT level.

Europium(III) Complexes. The training set for europium (Tables S2 and S6) involved 9 structures with up to decaoordination of the central Eu(III) ion (PHASEU and PUHYEW01); the largest complex containing 66 atoms (KAFDOK). At the PM3 level, the closest agreement between PM3 and DFT was found for the KIFKOZ02 complex (UME = 0.0381 Å, Table S6), whereas the largest discrepancy was calculated for the JUGBUI complex (UME = 0.1943 Å, Table S6). We find the europium–water oxygen distances are quite well predicted in the dieuropium complex [DOPCEQ, 2.534 (PM3), 2.501 Å (DFT), Table S2] and also in the complexes involving the terpyridine [PUHYEW01, 2.530 (PM3), 2.492 Å (DFT), Table S2] and trihydroxyhexane ligands [FOCQOD, 2.469 (PM3), 2.520 Å (DFT), Table S2]. Similarly, the europium–nitrate oxygen distances at the PM3 level are in satisfactory agreement with the DFT calculations [FOCQOD, JUGBUI, PHASEU, PUHYEW01, 2.492, 2.540, 2.550, 2.563 Å (PM3); 2.465, 2.493, 2.509, 2.574 Å (DFT), Table S2]. Finally we note that for the dieuropium complex involving bidentate acetate ligands (DOPCEQ), the Eu–Eu distance is somewhat underestimated at the PM3 level [3.852 Å (PM3), 3.983 Å (DFT), Table S2].

Gadolinium(III) Complexes. The training set for gadolinium (Tables S3 and S7) involved 9 structures with up to decaoordination of the central Gd(III) ion (PADEGA10); the largest complex containing 61 atoms (ZIPJIR). The smallest difference between the PM3 and DFT calculations is found for the complex involving oxydiacetate (NAOAGD, UME = 0.0665 Å, Table S7), while the largest discrepancy is calculated for the coordination polyhedron of the thiocyanate complex (KERKUN, UME = 0.1081 Å, Table S7). At the PM3 level the Gd–Gd distances in the two digadolinium complexes are predicted with varying degrees of success. In the complex involving primarily bidentate acetate ligands (ACAQGD01) the PM3 Gd–Gd distance differs from that of the DFT structure by 0.06 Å (Table S3), whereas in the complex involving the bridging nitrate ligands (YAVSUJ), the PM3 Gd–Gd is too short by some 0.16 Å (Table S3). The PM3 calculations of the complexes involving water mirror those of europium in that the gadolinium–water oxygen distances are well predicted at this level in a range of coordination environments (ACAQGD01, KERKUN, YAVSUJ, ZIPJIR, Table S3). Furthermore, the gadolinium–nitrogen distances are also well described in the BAFZIS, KERKUN, PADEGA10, and ZIPJIR complexes differing from the DFT values by 0.01–0.06 Å (Table S3).

Ytterbium(III) Complexes. The training set for ytterbium (Tables S4 and S8) involved 10 structures with up to

nonacoordination of the central Yb(III) ion; the largest complex contained some 98 atoms (XEWZOO). The largest discrepancy between the DFT and the PM3 structures occurs for the FEBGAU complex, the UME being 0.2041 Å (Table S8) which suggests a notable distortion of the coordination polyhedron at the PM3 level. The closest agreement with DFT is calculated for the complex involving the terpyridine ligand (FONQUU01, UME = 0.0446 Å, Table S8). Again, the Ln–water oxygen distances are quite well predicted at the semiempirical level in a range of different coordination environments [NENTOP, QALFIS, QOZVUW; 2.414, 2.410, 2.393 Å (PM3); 2.387, 2.366, 2.439 Å (DFT), Table S4]. Good agreement is also found in the ytterbium–nitrogen distances where the largest difference between DFT and PM3 is calculated for the LOEAYB10 complex, the PM3 values being on average some 0.06 Å longer than the DFT ones (Table S4). We note in the diytterbium complex (XEWZOO) the Yb–Yb distance is quite poorly predicted [4.234 (PM3), 4.623 Å (DFT), Table S4]. Such complexes are quite difficult to calculate accurately, given their large degree of conformational flexibility.

LnX₃ (Ln = Eu, Gd or Yb; X = H, Me, F, Cl, Br, or NH₂). There have been a number of theoretical studies of the lanthanide(III) trihalides which have sought to clarify the nature of the bonding, particularly the degree of covalent character in these species.^{17,91,92,93} DFT calculations suggest the interaction is predominantly ionic especially for the lighter halogens and lanthanides, while for the more polarizable bromide or iodide there is some non-negligible ligand-to-metal charge transfer.⁹¹

The AM1/sparkle model has been parametrized primarily to reproduce structures of high coordination complexes, and therefore its ability to predict the geometries of low coordination complexes is not clear.^{60,63} Since our goal in this work is to develop a completely general set of lanthanide parameters, we have also included a range of tricoordinated lanthanide(III) complexes in our training sets. Here, the use of the modified core repulsion function (eq 6)^{45,50,51,70–72} allows for the fine-tuning of the structures where different atoms (other than nitrogen or oxygen) are directly coordinated to the lanthanide(III) ion. The structures of the tricoordinated lanthanide(III) complexes calculated at the DFT, AM1/sparkle, and PM3 level are given in Table 1. In Table S15, the *d*-orbital populations and charges (calculated at the DFT and PM3 level) for each of the tricoordinated complexes are also reported.

We first note that our DFT calculations are in good agreement with the calculations of Perrin et al. using the B3PW91 functional.⁹¹ The hydride and alkyl complexes are strongly pyramidal and for fluoride a pyramidal structure is preferred, but for the heavier halides the complexes become increasingly planar. The calculations of Perrin et al.⁹¹ suggest the Ln–X bond is predominantly ionic, and the pyramidalization of the complexes is related to the involvement of the valence *d* orbitals in the Ln–X bond. Therefore those complexes with the least population of the lanthanide *d* orbitals are found to be more pyramidal, while the increasing covalency with the heavier halides stabilizes the planar interactions through *d*_π–*p*_π interactions.

The calculated Ln(III)–ligand distances are quite well reproduced at the PM3 level (Table 1), although we note that the trend of decreasing Ln(III)–X distances across the series (Eu to Yb) shown by DFT is not well defined; only for fluoride, chloride, and amide does the PM3 trend reflect that of the DFT calculations (Table 1). However, at the PM3 level the calculations correctly predict the hydride, alkyl, and fluoride complexes to be pyramidal, although the degree of pyramidalization is overestimated for hydride and fluoride complexes and underestimated for the alkyl complexes (Table 1). Evidently, despite these discrepancies, the PM3 model is a significant improvement over the AM1/sparkle model^{60,63} which predicts all the structures to be trigonal planar. Clearly, the inclusion of atomic orbitals and the use of a modified core repulsion function has led to a significant improvement of the semiempirical description of these complexes. However, the trends in the *d* orbital occupations and atomic charges are less well reproduced (Table S15). For each ligand (H, Me, F, Cl, Br, NH₂) DFT predicts a decrease in the *d* orbital populations and an increase in the atomic charge moving from left to right across the lanthanide series (Eu, Gd, Yb). The trend in decreasing *d* orbital populations across the series (for each ligand) is essentially mirrored by the PM3 calculations even though the magnitude and trends in the atomic charges are quite different from the DFT calculations (Table S15). For the halides, the *d* orbital populations for any given lanthanide are calculated to be F < Cl < Br at the DFT level, whereas at the PM3 level this order is reversed. The inclusion and suitable weighting of the atomic charges and orbital occupations in the error function or the appropriate modification of the ligand atom parameters may help to alleviate this problem.

3. Calculation of Complexes not in the PM3 Training Sets. In the development of the AM1/sparkle model, each parameter set has been extensively tested in the calculation of a range of complexes from the CSD.⁶¹ For this reason we decided to test our parameters for Eu, Gd, and Yb on up to 10 additional complexes (each optimized at the DFT level) from the CSD. We have therefore compared our PM3 calculations on a total of 28 (Eu), 28 (Gd), and 29 (Yb) complexes calculated at the DFT level, which we believe is sufficient to reflect a range of coordination environments. The UME for the additional complexes are given in Tables S12–S14. We can see that in general the agreement is extremely satisfactory.

For *all* Eu(III), Gd(III), and Yb(III) complexes considered herein, the average UME_{Ln–X} PM3 values for all interatomic distances between the lanthanide(III) ion and the ligand atoms of the first coordination sphere are 0.04, 0.03, and 0.03 Å, respectively (summarized in Table 7). These are smaller than the AM1/sparkle values of 0.09 Eu(III), 0.07 Gd(III), and 0.07 Yb(III), for their respective test sets. As far as the average UME are concerned (Table 7), the PM3 values are notably smaller (approximately half) than the corresponding AM1/sparkle values, which suggests the inclusion of lanthanide centered orbitals is important in describing the angular arrangement of ligands. We note that due to the computational expense of optimizing each of our test

Table 7. Comparison of the Average UME and UME_{Ln-x} (Å) for the PM3 and AM1/Sparkle Models

	Eu	Gd	Yb
PM3 (vs DFT ^a)			
UME_{Ln-x}	0.04	0.03	0.03
UME ^b	0.10	0.09	0.07
structural comparisons	28	28	29
AM1/sparkle (vs CSD ^c)			
UME_{Ln-x}	0.09 ^d	0.07 ^d	0.07 ^e
UME	0.19 ^d	0.18 ^d	0.15 ^e
structural comparisons	96 ^d	70 ^d	47 ^e

^a B3LYP/3-31G and quasi-relativistic ECP of ref 84 for the lanthanide atoms (6-31G* for the tricoordinated complexes). ^b Complexes containing more than one lanthanide atom were omitted: Eu (DOPCEQ); Gd (ACAQGD01 and YAVSUJ); and Yb (XEWZOO). ^c Cambridge Structural Database. ^d Reference 60. ^e Reference 63.

structures at the DFT level our test sets are smaller than those for the AM1/sparkle model.^{60,63}

Conclusions

There are considerable difficulties in carrying out accurate “high level” DFT or ab initio calculations on lanthanide containing complexes. In particular, all-electron studies are generally prohibitive due to the large number of electrons and orbitals associated with the lanthanide atoms themselves; there are also difficulties in treating the 4f electrons and accounting for both relativistic effects and electron correlation. These problems have in part been addressed by the use of relativistic effective core potentials which incorporate relativistic effects into the core therefore reducing the computational effort for SCF calculations.¹⁸ Further approximations can be made, such as the inclusion of the 4f electrons into the core, without significantly compromising the accuracy of the final results.

Semiempirical methods take these approximations much further. The AM1/sparkle model for lanthanides has been quite successful in describing a range of highly coordinated lanthanide complexes.^{60,63} The sparkle model relies on the fact that for many lanthanide complexes the Ln–ligand bonds are largely electrostatic in nature. While the approximations in such a model appear to be quite severe, the AM1/sparkle model does quite well in predicting the coordination polyhedron of various lanthanide(III) complexes. Since the sparkle model assumes complete ionization of the valence electrons, covalent effects which may in some complexes be non-negligible cannot be included. Therefore in this work we have sought to build upon the suggestion by Freire et al. that covalent effects could be accounted for in semiempirical sparkle calculations by the inclusion of a set of orbitals on the sparkle atom.⁶⁰ Thus our PM3 model takes the approximations inherent in a DFT/RECP calculation further, but the approximations used are less severe compared to the AM1/sparkle approach.

Although semiempirical MO methods are formally minimal basis methods, we find that our parametrized PM3 model is generally comparable to DFT calculations using a 3-21G basis and the quasi-relativistic core potential of Dolg et al.⁸⁴ for the complexes calculated herein. The closeness of the PM3 results to the DFT calculations indicates we have been

quite successful in developing a model and an appropriate parametrization strategy for obtaining semiempirical parameters for trivalent lanthanide complexes. Furthermore, our model is also shown to be essentially superior to the AM1/sparkle model for predicting crystal structures even though our model has been parametrized to reproduce DFT calculations. This is not surprising in view of the flexibility resulting from the number of adjustable parameters included in the PM3 model. We have sought to obtain a parameter set that will allow a large range of lanthanide(III)–ligand interactions to be considered. The results presented here show that in general we have been quite successful in being able to predict the structural and to a lesser extent the more demanding energetic quantities of these species. We could, most probably, achieve greater accuracy by including a larger number of energetic reference data in our training sets, a larger training set, and possibly obtaining initial one-center parameters for europium and ytterbium directly from experimental data rather than using the gadolinium parameters for initial estimates. As with DFT calculations using RECPs, a given semiempirical core is only likely to be valid for a given formal oxidation state of the lanthanide atom.⁹⁴ Therefore the current model may not be successful in describing processes which involve a change in the formal oxidation state of the lanthanide. However, we believe the parameter set presented here would represent a good starting point for further refinement of the PM3 model for the elements (Eu, Gd, Yb) reported herein and the remaining lanthanide metals.

Acknowledgment. We thank EPSRC for support of this work and Dr. James J. P. Stewart for helpful discussions.

Supporting Information Available: Tables S1–S15, Figures S1–S4, and the Cartesian coordinates of all CSD⁶¹ structures and DOTA complexes optimized at the DFT level. This material is available free of charge via the Internet at <http://pubs.acs.org>.

References

- Bouno-Core, G. E.; Li, H.; Marciniak, B. *Coord. Chem. Rev.* **1990**, *99*, 55.
- de Sá, G. F.; Malta, O. L.; de Mello Donegá, C.; Simas, A. M.; Longo, R. L.; Santa-Cruz, P. A.; da Silva, E. F., Jr. *Coord. Chem. Rev.* **2000**, *196*, 165.
- Parker, D.; Dickins, R. S.; Puschmann, H.; Crossland, C.; Howard, J. A. K. *Chem. Rev.* **2002**, *102*, 1977.
- Kido, J.; Okamoto, Y. *Chem. Rev.* **2002**, *102*, 2357.
- Lauffer, R. B. *Chem. Rev.* **1987**, *87*, 901.
- Choppin, G. R.; Schaab, K. M. *Inorg. Chim. Acta* **1996**, *252*, 299.
- Aime, S.; Botta, M.; Fasano, M.; Terreno, E. *Chem. Soc. Rev.* **1998**, *27*, 19.
- Thunus, L.; Lejeune, R. *Coord. Chem. Rev.* **1999**, *184*, 125.
- Caravan, P.; Ellison, J. J.; McMurphy, T. J.; Lauffer, R. B. *Chem. Rev.* **1999**, *99*, 2293.
- DOTA = 1,4,7,10-tetraaza-1,4,7,10-tetrakis(carboxymethyl)cyclododecane.

- (11) OECD/NEA. *Actinide and Lanthanide Product Partitioning and Transmutation*; Proceedings of the Fifth Information Exchange Meeting, Mol, Belgium, November 25–27, 1998.
- (12) OECD/NEA. *Actinide and Fission Product Partitioning and Transmutation*; Proceedings of the Seventh Information Exchange Meeting, Jeju, Republic of Korea, October 14–16, 2002.
- (13) Morgado, C. A.; McNamara, J. P.; Hillier, I. H.; Sundararajan, M. *Mol. Phys.* **2005**, *103*, 905.
- (14) Sundararajan, M.; Hillier, I. H.; Burton, N. A. *J. Phys. Chem. A* **2006**, *110*, 785.
- (15) Sundararajan, M.; Surendren, R. A.; Hillier, I. H. *Chem. Phys. Lett.* **2005**, *418*, 92.
- (16) Villa, A.; Cosentino, U.; Pitea, D.; Moro, G.; Maiocchi, A. *J. Phys. Chem. A* **2000**, *104*, 3421.
- (17) Cundari, T. R.; Sommerer, S. O.; Strohecker, L. A.; Tippett, L. *J. Chem. Phys.* **1995**, *103*, 7058.
- (18) Maron, L.; Eisenstein, O. *J. Phys. Chem. A* **2000**, *104*, 7140.
- (19) Cao, X.; Dolg, M. *Chem. Phys. Lett.* **2001**, *349*, 489.
- (20) Cao, X.; Dolg, M. *Mol. Phys.* **2003**, *101*, 1967.
- (21) Cao, X.; Dolg, M. *J. Theor. Comput. Chem.* **2005**, *4*, 583.
- (22) Takeda, K.; Tsuchiya, T.; Nakano, H.; Taketsugu, T.; Hirao, K. *J. Mol. Struct. (Theochem)* **2001**, *537*, 107.
- (23) Cosentino, U.; Villa, A.; Pitea, D.; Moro, G.; Barone, V.; Maiocchi, A. *J. Am. Chem. Soc.* **2002**, *124*, 4901.
- (24) Cosentino, U.; Moro, G.; Pitea, D.; Calabi, L.; Maiocchi, A. *J. Mol. Struct. (Theochem)* **1997**, *392*, 75.
- (25) Smentek, L.; Hess, B. A.; Cross, J. P.; Manning, H. C.; Bornhop, D. J. *J. Chem. Phys.* **2005**, *123*, 244302.
- (26) Girichev, G. V.; Giricheva, N. I.; Haaland, A.; Kuzmina, N. P.; Samdal, S.; Strenalyuk, T. N.; Tverdova, N. V.; Zaitseva, I. G. *Inorg. Chem.* **2006**, *45*, 5179.
- (27) Guillaumont, D. *J. Phys. Chem. A* **2004**, *108*, 6893.
- (28) Cao, X.; Dolg, M. *Mol. Phys.* **2003**, *101*, 2427.
- (29) Heiberg, H.; Gropen, O.; Laerdahl, J. K.; Swang, O.; Wahlgren, U. *Theor. Chem. Acc.* **2003**, *110*, 118.
- (30) Cundari, T. R. *J. Chem. Soc., Dalton Trans.* **1998**, 2771.
- (31) Fossheim, R.; Dugstad, H.; Dahl, S. G. *Eur. J. Med. Chem.* **1995**, *30*, 539.
- (32) THP = 1,4,7,10-tetrakis (2-hydroxypropyl)-1,4,7,10-tetraazacyclododecane; TMA = 1,4,7,10-tetrakis[(*N*-methylcarbamoyl)methyl]-1,4,7,10-tetraazacyclododecane; DOTMP = 1,4,7,10-tetraazacyclododecane-1,4,7,10-tetrakis(methyl-nemethylphosphinate).
- (33) Cosentino, U.; Moro, G.; Pitea, D.; Villa, A.; Fantucci, P. C.; Maiocchi, A.; Uggeri, F. *J. Phys. Chem. A* **1998**, *102*, 4606.
- (34) Kowall, T.; Foglia, F.; Helm, L.; Merbach, A. E. *J. Am. Chem. Soc.* **1995**, *117*, 3790.
- (35) van Veggel, C. J. M.; Reinhoudt, D. N. *Chem. Eur. J.* **1999**, *5*, 90.
- (36) Field, M. J.; Basch, M.; Karplus, M. *J. Comput. Chem.* **1990**, *11*, 700.
- (37) Gao, J.; Xia, X. *Science* **1992**, *258*, 631.
- (38) Maseras, F.; Morokuma, K. *J. Comput. Chem.* **1995**, *16*, 1170.
- (39) Tresadern, G.; Wang, H.; Faulder, P. F.; Burton, N. A.; Hillier, I. H. *Mol. Phys.* **2003**, *101*, 2775.
- (40) Alhambra, C.; Luz Sanchez, M.; Corchado, J.; Gao, J.; Truhlar, D. G. *Chem. Phys. Lett.* **2001**, *347*, 512.
- (41) Rossi, I.; Truhlar, D. G. *Chem. Phys. Lett.* **1995**, *233*, 231.
- (42) Dewar, M. J. S.; Thiel, W. *J. Am. Chem. Soc.* **1977**, *99*, 4899.
- (43) Dewar, M. J. S.; Zoebisch, E. G.; Healy, E. F.; Stewart, J. J. P. *J. Am. Chem. Soc.* **1993**, *115*, 5348.
- (44) Stewart, J. J. P. *J. Comput. Chem.* **1989**, *10*, 209.
- (45) Stewart, J. J. P. *J. Mol. Model.* **2004**, *10*, 155.
- (46) Thiel, W.; Voityuk, A. A. *Theor. Chim. Acta* **1992**, *81*, 391.
- (47) Thiel, W.; Voityuk, A. A. *Theor. Chim. Acta* **1996**, *93*, 315.
- (48) Mohr, M.; McNamara, J. P.; Wang, H.; Rajeev, S. A.; Ge, J.; Morgado, C.; Hillier, I. H. *Faraday Discuss.* **2003**, *124*, 413.
- (49) Sundararajan, M.; McNamara, J. P.; Hillier, I. H.; Wang, H.; Burton, N. A. *Chem. Phys. Lett.* **2005**, *404*, 9.
- (50) McNamara, J. P.; Sundararajan, M.; Hillier, I. H. *J. Mol. Graphics Modell.* **2005**, *24*, 128.
- (51) McNamara, J. P.; Sundararajan, M.; Hillier, I. H.; Ge, J.; Campbell, A.; Morgado, C. *J. Comput. Chem.* **2006**, *27*, 1307.
- (52) Culberson, J. C.; Knappe, P.; Rösch, N.; Zerner, M. C. *Theor. Chim. Acta* **1987**, *71*, 21.
- (53) Kotzian, M.; Rösch, N. *J. Phys. Chem.* **1992**, *96*, 7288.
- (54) Kotzian, M.; Rösch, N.; Zerner, M. C. *Theor. Chim. Acta* **1992**, *81*, 201.
- (55) Kotzian, M.; Rösch, N. *J. Mol. Spectrosc.* **1991**, *147*, 346.
- (56) Stewart, J. J. P. *J. Comput.-Aided Mol. Des.* **1990**, *4*, 1.
- (57) Stewart, J. J. P. *MOPAC 2000 Manual*; Fujitsu Ltd.: 1999. <http://home.att.net/~mopacmanual> (accessed September 2006).
- (58) de Andrade, A. V. M.; da Costa, N. B., Jr.; Simas, A. M.; de Sá, G. F. *Chem. Phys. Lett.* **1994**, *227*, 349.
- (59) Rocha, G. B.; Freire, R. O.; da Costa, N. B., Jr.; de Sá, G. F.; Simas, A. M. *Inorg. Chem.* **2004**, *13*, 2346.
- (60) Freire, R. O.; Rocha, G. B.; Simas, A. M. *Inorg. Chem.* **2005**, *44*, 3299.
- (61) Allen, F. H. *Acta Crystallogr., Sect. B: Struct. Sci.* **2002**, *58*, 380.
- (62) Freire, R. O.; da Costa, N. B., Jr.; Rocha, G. B.; Simas, A. M. *J. Chem. Theor. Comput.* **2006**, *2*, 64.
- (63) Freire, R. O.; Rocha, G. B.; Simas, A. M. *J. Comput. Chem.* **2005**, *26*, 1524.
- (64) Freire, R. O.; da Costa, N. B., Jr.; Rocha, G. B.; Simas, A. M. *J. Phys. Chem. A* **2006**, *110*, 5897.
- (65) da Costa, N. B., Jr.; Freire, R. O.; Rocha, G. B.; Simas, A. M. *Inorg. Chem. Commun.* **2005**, *8*, 831.
- (66) Freire, R. O.; da Costa, N. B., Jr.; Rocha, G. B.; Simas, A. M. *J. Organomet. Chem.* **2005**, *690*, 4099.
- (67) Bastos, C. C.; Freire, R. O.; Rocha, G. B.; Simas, A. M. *J. Photochem. Photobiol., A* **2006**, *177*, 225.
- (68) Freire, R. O.; do Monte, E. V.; Rocha, G. B.; Simas, A. M. *J. Organomet. Chem.* **2006**, *691*, 2584.
- (69) Freire, R. O.; Rocha, G. B.; Simas, A. M. *Chem. Phys. Lett.* **2006**, *425*, 138.

- (70) Voityuk, A. A.; Rösch, N. *J. Phys. Chem. A* **2000**, *104*, 4089.
- (71) Winget, P.; Horn, A. H. C.; Selçuki, C.; Martin, B.; Clark, T. *J. Mol. Model.* **2003**, *9*, 408.
- (72) Winget, P.; Clark, T. *J. Mol. Model.* **2005**, *11*, 439.
- (73) Cundari, T. R.; Deng, J.; Fu, W. *Int. J. Quantum Chem.* **2000**, *77*, 421.
- (74) Sundararajan, M.; McNamara, J. P.; Mohr, M.; Wang, H.; Hillier, I. H. *Biochem. Soc. Trans.* **2005**, *33*, 20.
- (75) Brothers, E. N.; Merz, K. M., Jr. *J. Phys. Chem. B* **2002**, *106*, 2779.
- (76) Hutter, M. C.; Reimers, J. R.; Hush, N. S. *J. Phys. Chem. B* **1998**, *102*, 8080.
- (77) Stewart, J. J. P. *J. Comput. Chem.* **1989**, *10*, 221.
- (78) Stewart, J. J. P. *J. Comput. Chem.* **1991**, *12*, 320.
- (79) Becke, A. D. *J. Chem. Phys.* **1993**, *98*, 5648.
- (80) Miehlich, B.; Savin, A.; Stoll, H.; Preuss, H. *Chem. Phys. Lett.* **1989**, *157*, 200.
- (81) Lee, C.; Yang, W.; Parr, R. G. *Phys. Rev. B* **1988**, *37*, 785.
- (82) Frisch, K.-M.; Trucks, G. W.; Schlegel, H. B.; Scuseria, G. E.; Robb, M. A.; Cheeseman, J. R.; Zakrzewski, V. G.; Montgomery, J. A., Jr.; Stratmann, R. E.; Burant, J. C.; Dapprich, S.; Millam, J. M.; Daniels, A. D.; Kudin, K. N.; Strain, M. C.; Farkas, O.; Tomasi, J.; Barone, V.; Cossi, M.; Cammi, R.; Mennucci, B.; Pomelli, C.; Adamo, C.; Clifford, S.; Ochterski, J.; Petersson, G. A.; Ayala, P. Y.; Cui, Q.; Morokuma, K.; Malick, D. K.; Rabuck, A. D.; Raghavachari, K.; Foresman, J. B.; Cioslowski, J.; Ortiz, J. V.; Stefanov, B. B.; Liu, G.; Liashenko, A.; Piskorz, P.; Komaromi, I.; Gomperts, R.; Martin, R. L.; Fox, D. J.; Keith, T.; Al-Laham, M. A.; Peng, C.-Y.; Nanayakkara, A.; Gonzalez, C.; Challacombe, M.; Gill, P. M. W.; Johnson, B. G.; Chen, W.; Wong, M. W.; Andres, J. L.; Head-Gordon, M.; Replogle, E. S.; Pople, J. A. *Gaussian 98, Revision A.7*; Gaussian Inc.: Pittsburgh, PA, 1998.
- (83) Frisch, M. J.; Trucks, G. W.; Schlegel, H. B.; Scuseria, G. E.; Robb, M. A.; Cheeseman, J. R.; Montgomery, J. A., Jr.; Vreven, T.; Kudin, K. N.; Burant, J. C.; Millam, J. M.; Iyengar, S. S.; Tomasi, J.; Barone, V.; Mennucci, B.; Cossi, M.; Scalmani, G.; Rega, N.; Petersson, G. A.; Nakatsuji, H.; Hada, M.; Ehara, M.; Toyota, K.; Fukuda, R.; Hasegawa, J.; Ishida, M.; Nakajima, T.; Honda, Y.; Kitao, O.; Nakai, H.; Klene, M.; Li, X.; Knox, J. E.; Hratchian, H. P.; Cross, J. B.; Bakken, V.; Adamo, C.; Jaramillo, J.; Gomperts, R.; Stratmann, R. E.; Yazyev, O.; Austin, A. J.; Cammi, R.; Pomelli, C.; Ochterski, J. W.; Ayala, P. Y.; Voth, G. A.; Salvador, P.; Dannenberg, J. J.; Zakrzewski, V. G.; Dapprich, S.; Daniels, A. D.; Strain, M. C.; Farkas, O.; Malick, D. K.; Rabuck, A. D.; Raghavachari, K.; Foresman, J. B.; Ortiz, J. V.; Cui, Q.; Baboul, A. G.; Clifford, S.; Cioslowski, J.; Stefanov, B. B.; Liu, G.; Liashenko, A.; Piskorz, P.; Komaromi, I.; Martin, R. L.; Fox, D. J.; Keith, T.; Al-Laham, A.; Peng, C. Y.; Nanayakkara, A.; Challacombe, M.; Gill, P. M. W.; Johnson, B.; Chen, W.; Wong, M. W.; Gonzalez, C.; Pople, J. A. *Gaussian 03, Revision C.02*; Gaussian, Inc.: Wallingford, CT, 2004.
- (84) Dolg, M.; Stoll, H.; Savin, A.; Preuss, H. *Theor. Chim. Acta* **1989**, *75*, 173.
- (85) Levine, D. *PGAPack, Version 1.0*; Mathematics and Computer Science Division Argonne National Laboratory: Argonne, IL, 1995.
- (86) Ralchenko, Y.; Jou, F.-C.; Kelleher, D. E.; Kramida, A. E.; Musgrove, A.; Reader, J.; Wiese, W. L.; Olsen, K. *NIST Atomic Spectra Database, Version 3.1.0*; National Institute of Standards and Technology: Gaithersburg, MD, September 4, 2006.
- (87) Aime, S.; Botta, M.; Fasano, M.; Terreno, E. *Acc. Chem. Res.* **1999**, *32*, 941.
- (88) Botta, M. *Eur. J. Inorg. Chem.* **2000**, 399.
- (89) Spirelet, M. R.; Rebizant, J.; Desreux, J. F.; Loncin, M. F. *Inorg. Chem.* **1984**, *23*, 359.
- (90) Kumar, K.; Allen, Chang, C.; Francesconi, L. C.; Dischino, D. D.; Malley, M. F.; Gougoutas, J. Z.; Tweedle, M. F. *Inorg. Chem.* **1994**, *33*, 3567.
- (91) Perrin, L.; Maron, L.; Eisenstein, O. *Faraday Discuss.* **2003**, *124*, 25.
- (92) Adamo, C.; Maldivi, P. *J. Phys. Chem. A* **1998**, *102*, 6812.
- (93) Lanza, G.; Fragalà, I. L. *Chem. Phys. Lett.* **1996**, *255*, 341.
- (94) Eisenstein, O.; Maron, L. *J. Organomet. Chem.* **2002**, *647*, 190.
- (95) Aime, S.; Barge, A.; Botta, M.; Fasano, M.; Ayala, J. D.; Bombieri, G. *Inorg. Chem. Acta* **1996**, *246*, 423.

CT600304G

Computation of Accurate Activation Barriers for Methyl-Transfer Reactions of Sulfonium and Ammonium Salts in Aqueous Solution

Hakan Gunaydin,[†] Orlando Acevedo,[‡] William L. Jorgensen,^{*,‡} and K. N. Houk^{*,†}

Department of Chemistry and Biochemistry, University of California, Los Angeles, California 90095-1569, and Department of Chemistry, Yale University, 225 Prospect Street, New Haven, Connecticut 06520-8107

Received December 11, 2005

Abstract: The energetics of methyl-transfer reactions from dimethylammonium, tetramethylammonium, and trimethylsulfonium to dimethylamine were computed with density functional theory, MP2, CBS-QB3, and quantum mechanics/molecular mechanics (QM/MM) Monte Carlo methods. At the CBS-QB3 level, the gas-phase activation enthalpies are computed to be 9.9, 15.3, and 7.9 kcal/mol, respectively. MP2/6-31+G(d,p) activation enthalpies are in best agreement with the CBS-QB3 results. The effects of aqueous solvation on these reactions were studied with polarizable continuum model, generalized Born/surface area (GB/SA), and QM/MM Monte Carlo simulations utilizing free-energy perturbation theory in which the PDDG/PM3 semiempirical Hamiltonian for the QM and explicit TIP4P water molecules in the MM region were used. In the aqueous phase, all of these reactions proceed more slowly when compared to the gas phase, since the charged reactants are stabilized more than the transition structure geometries with delocalized positive charges. In order to obtain the aqueous-phase activation free energies, the gas-phase activation free energies were corrected with the solvation free energies obtained from single-point conductor-like polarizable continuum model and GB/SA calculations for the stationary points along the reaction coordinate.

Introduction

The transfer of methyl groups is a widely observed process in biological pathways; methyl groups are routinely transferred to reaction intermediates during the synthesis of a variety of compounds such as lignin, phenylpropene, some alkaloids, and phospholipids.^{1–4} Enzymes that catalyze methyl-transfer reactions generally utilize compounds with active methyl substituents such as S-adenosyl-L-methionine (SAM).^{1–7} The cofactor SAM is involved in several transmethylation reactions, such as the synthesis of neurotransmitters in the brain.^{5,6} Catechol *O*-methyl-transferase utilizes SAM as the methyl source for the methylation of cytosine,

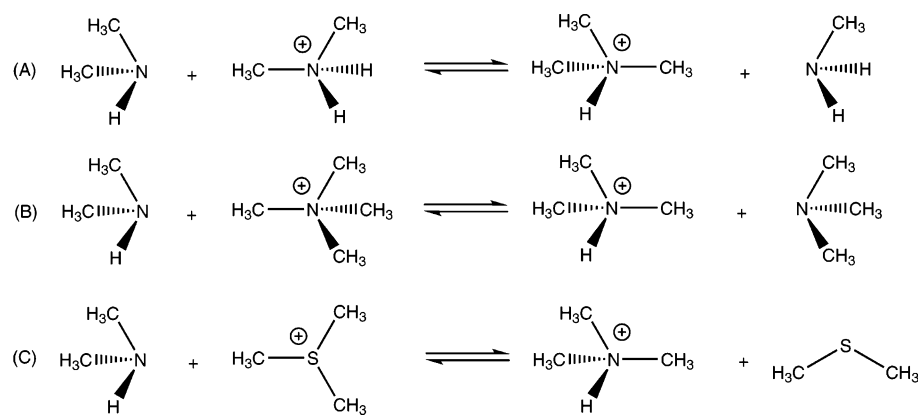
adenine, and catechol.^{7,8} Modification of adenine within DNA through the transfer of a methyl group is a common defense mechanism in biological organisms that enables them to distinguish host DNA from viral DNA.⁸ In addition, three different types of methyl-transfer enzymes are known to utilize SAM to transfer methyl groups to DNA.⁹

In order to understand the magnitude of the enzymatic acceleration of methyl-transfer reactions, it is important to know the rate of methyl-transfer reactions in water in the absence of protein (background reaction). These uncatalyzed rate constants (k_{noncat}) are used to calculate the rate enhancements ($k_{\text{cat}}/k_{\text{noncat}}$) and proficiencies [$(k_{\text{cat}}/K_M)/k_{\text{noncat}}$] of the enzymes.¹⁰ For slow reactions, Wolfenden and Callahan have estimated uncatalyzed rates by measuring the rate constants at elevated temperatures and extrapolating them to room temperature.¹⁰ An alternative approach is to compute the activation energies of these uncatalyzed reactions. In order

* Corresponding authors. E-mail: houk@chem.ucla.edu (K.N.H.), william.jorgensen@yale.edu (W.L.J.).

[†] University of California, Los Angeles.

[‡] Yale University.

Scheme 1. Methyl-Transfer Reactions in Aqueous Phase Studied by Wolfenden

to estimate the aqueous-phase rate constants with good accuracy, reliable solvation energies need to be generated. This is a very challenging problem that has attracted much attention. Warshel and Weiss have approached this problem by developing the empirical valence bond (EVB) method to generate an approximate potential energy surface for reactions in solution.^{11a} EVB was used to compute the activation energies for a variety of background reactions with reasonable accuracy; these were subsequently compared to enzymatic reactions.¹¹ Warshel demonstrated that enzymes provide a more efficient charge stabilization environment for the transition structures (TSs) by anchoring side-chain and backbone dipoles in appropriate orientations.^{11b} The free-energy profile for the hydrolysis of the phosphate ester in solution was also studied using Langevin dipoles and polarized continuum methods.^{11c} Detailed investigation for the general base-catalyzed methanolysis of formamide was also carried out, and it was found that the gas-phase reaction

paths did not provide an adequate model for the reactions in solution, emphasizing the need for accurate solvation methods.^{11d}

Wolfenden and Callahan measured the activation parameters of the three methyl-transfer reactions that are shown in Scheme 1.¹⁰ The rate of the uncatalyzed methyl-transfer reaction from trimethylsulfonium to dimethylamine in the aqueous phase was used to obtain the catalytic rate enhancement of the enzyme histamine N-methyl-transferase that catalyzes the metabolism of histamine and is responsible for the termination of the neurotransmitter action of histamine in the brain.^{6,10} It was found that this enzyme enhances the rate of the methyl-transfer reaction by 5×10^{13} .¹⁰ The rate enhancement of catechol *O*-methyltransferase, which catalyzes the transfer of the methyl group from SAM to an oxygen nucleophile, is reported to be on the order of 10^{17} by using the same uncatalyzed rate constant for this enzyme.¹⁰

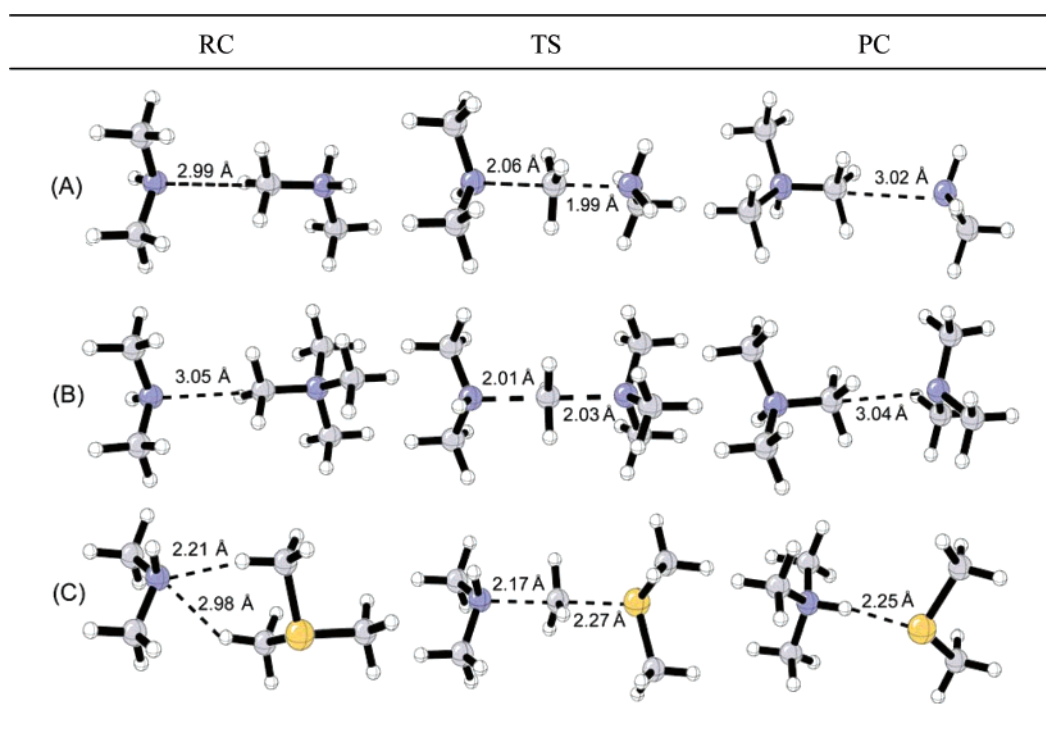


Figure 1. Geometries of stationary points for reactions A, B, and C located at the B3LYP/6-31+G(d,p) level. RC: reactive complex, TS: transition state, PC: product complex. Full geometrical parameters are given in the Supporting Information.

The factors controlling the catalytic efficiency of catechol *O*-methyltransferase have been investigated theoretically.¹² Roca et al. calculated the activation free energy of methyl-transfer reactions from trimethylsulfonium to the catecholate ion in water and from SAM to the catecholate ion in water and in an enzyme environment by making use of the quantum mechanics/molecular mechanics (QM/MM) methodology.^{12a} The QM/MM computed activation free energy for the aqueous methyl-transfer reaction (26.9 kcal/mol) was found to be in reasonable agreement with the experimental estimate (30.8 kcal/mol) of this methyl-transfer reaction. The reasons behind the efficiency of the enzymatic reaction over the aqueous-phase reaction have been discussed in detail.^{12a} In addition, the same catalytic and aqueous-phase reactions have been studied by using quantum mechanics/free-energy simulations (QM-FE) by Kuhn and Kollman.^{12b} The QM-FE barriers for the enzymatic and aqueous-phase methyl-transfer reactions are reported to be 24.5 and 29.5 kcal/mol, respectively. Bruice and Zheng have calculated the gas-phase and condensed-phase activation energies for trimethylsulfonium to the catecholate ion by using quantum mechanics.^{12c} On the basis of molecular dynamics simulations, it has been shown that the enzyme active site does not change significantly upon binding to either reactants or the transition structure for this methyl-transfer reaction.^{12d} Bruice and co-workers have also shown that SAM and catecholate ions spend significant amounts of time in the “near attack conformer” (NAC) and came to the conclusion that the basis of the catalytic power of the catechol *O*-methyltransferase arises from populating the NACs.^{12d,e}

Transfer of a methyl group from trimethylsulfonium to pyridine has been computed previously with the B3LYP/6-31+G(d) level in the gas phase.¹³ Effects of solvation on the activation barrier of this reaction with different solvents were investigated. Theoretical calculations revealed that, when the gas-phase density functional theory (DFT) activation free energies were corrected with QM/MM/Monte Carlo (MC) solvation corrections, the computed (25.9 kcal/mol) and experimental (29.6 kcal/mol) activation free energies were in good agreement.¹³ In addition, the steric effects of various S_N2 reactions involving chloride and five different chlorocarbons have been computed in the gas phase with CBS-QB3 and PDDG/PM3 methods.¹⁴ The transition-state carbon–chlorine distances computed with CBS-QB3 and PDDG/PM3 were found to be essentially the same in both methods.¹⁴ Solvation corrections for these reactions were calculated using QM/MM/MC simulations as well as the conductor-like polarizable continuum model (CPCM) method, and both methods gave similar condensed-phase activation enthalpies.¹⁴

The aim of the research described in this paper was to test various quantum mechanical and solvation methods for simple methyl-transfer reactions to determine the appropriate level of theory necessary to reproduce the kinetics of aqueous-phase reactions with high accuracy. The gas-phase reaction mechanisms were computed with DFT, Møller–Plesset perturbation theory, and CBS-QB3 methods. Solvation corrections were obtained with the CPCM, generalized Born/surface area (GB/SA), and free-energy QM/MM/MC

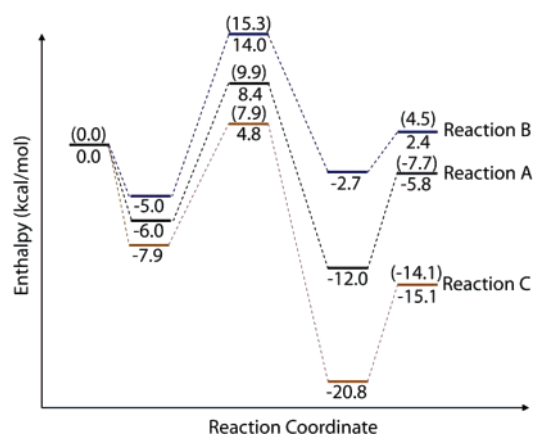


Figure 2. Enthalpies (kcal/mol) calculated with B3LYP/6-31+G(d,p) for the gas phase. CBS-QB3 values for the reactants, transition states, and products are given in parentheses.

Table 1. Activation Enthalpies of Reactions A, B, and C (kcal/mol)

method	reaction A	reaction B	reaction C
B3LYP/6-31G(d)	6.0	11.5	2.2
B3LYP/6-31G(d,p)	6.0	11.7	2.4
B3LYP/6-31+G(d,p)	8.4	14.0	4.8
MPW1K/6-31+G(d,p)	12.4	17.9	9.0
MP2/6-31G(d)	8.7	13.9	5.9
MP2/6-31+G(d,p)	9.8	14.7	7.0
CBS-QB3	9.9	15.3	7.9

Table 2. Activation Free Energies of Reactions A, B, and C (kcal/mol)

method	reaction A	reaction B	reaction C
B3LYP/6-31+G(d,p)	17.9	24.2	13.6
MP2/6-31+G(d,p)	19.9	25.3	16.4
CBS-QB3	19.4	24.8	18.0

simulations using the PDDG/PM3 semiempirical Hamiltonian for the solute and TIP4P water molecules for the solvent.

Methodology

The gas-phase energetics were computed with DFT,^{15,16} MP2,¹⁷ and CBS-QB3¹⁸ levels of theory by using Gaussian 98¹⁹ and Gaussian 03.²⁰ For DFT calculations, the B3LYP^{21,22} functional with 6-31G(d), 6-31G(d,p), and 6-31+G(d,p) basis sets and the MPW1K²³ functional with the 6-31+G(d,p) basis set were used. For MP2 calculations, 6-31G(d) and 6-31+G(d,p) basis sets were used. The accuracies of these methods and basis sets were tested against the more accurate CBS-QB3 activation energies.

Solvation effects for these reactions were studied by using the CPCM²⁴ method and GB/SA^{25–27} as implemented in the BOSS program.²⁸ Single-point CPCM and GB/SA calculations were utilized for all of the stationary points located in the gas phase in order to obtain the solvation free energies for the reactants, products, and transition structures. The gas-phase activation free energies were corrected with these solvation corrections to estimate the activation free energies

Table 3. Enthalpies of the Reactant Complexes (RC), Transition Structures (TS), Product Complexes (PC), and Products (P) Relative to the Reactants (R) at Infinite Separation (kcal/mol) [BS1:6-31G(d), BS2:6-31+G(d,p)]

	reaction A				reaction B				reaction C			
	B3LYP		MP2	CBS-QB3	B3LYP		MP2	CBS-QB3	B3LYP		MP2	CBS-QB3
	BS1	BS2	BS2		BS1	BS2	BS2		BS1	BS2	BS2	
R	0	0	0	0	0	0	0	0	0	0	0	0
RC	-7.4	-6.0	-8.1		-6.3	-5.0	-2.1 ^a		-9.8	-7.9	-13.3	
TS	6.0	8.4	9.8	9.9	11.5	14.0	14.7	15.3	2.2	4.8	7.0	7.9
PC	-12.5	-12.0	-15.5		-4.7	-2.7	2.2 ^a		-31.5	-20.8	-33.0	
P	-4.8	-5.8	-7.8	-7.7	1.7	2.4	4.4	4.5	-17.7	-15.1	-17.3	-14.1

^a Thermal corrections are obtained from HF calculations with the same basis set.

in the aqueous phase. Benchmarking studies showed that, when CM1A^{29,30} charges are used in conjunction with GB/SA solvation corrections, experimental hydration free energies can be reproduced with a high accuracy.^{25–27} The GB/SA solvation free energies for the methyl-transfer reactions studied here were computed by using the methodology described by refs 25–27.

QM/MM/MC simulations from BOSS were used to obtain the hydration free energies with explicit solute–solvent interactions by making use of statistical averaging of the possible configurations. The QM/MM method has been established as a good technique for studying the chemical reactions in both solution and enzyme environments.³¹ Several QM/MM methods have been utilized, and these methods differ in their treatment of the quantum mechanical and/or molecular mechanics regions.³¹ An overview of the applications of the QM/MM method for studying enzyme reactivity has been published by Gogonea.^{31a} In order to determine the effect of solvation on the reaction coordinate, free-energy perturbation (FEP) calculations were carried out in the NPT ensemble. In these FEP calculations, the solutes were treated in the QM region and water molecules were described in the MM region. The configurational space was explored using the Metropolis Monte Carlo algorithm. This method has been shown to give excellent results for S_N2 reactions,¹⁴ nucleophilic aromatic substitution reactions,^{32a} Kemp decarboxylations,^{32b,c} and Cope elimination^{32d} reactions. In these FEP simulations, the reaction coordinates were explored with increments of 0.01 Å by the sampling of all other degrees of freedom from separated reactants to the products through transition states. Since this procedure requires ca. 15 million single-point QM calculations per system, the use of the fast semiempirical PDDG/PM3³³ QM method was necessary. The solvent water molecules were represented with the TIP4P water model.³⁴ For electrostatic contributions to the solute–solvent energy, unscaled CM1 charges were calculated for the solute with the PDDG/PM3 Hamiltonian. For each heavy atom of the solutes, one water molecule was extracted from the pre-equilibrated solvent box of 750 water molecules to make space for the solutes. Simulations were run at 25 °C and 1 atm. In each simulation, equilibration of 2.5 M configurations was followed by averaging of 5 M configurations. In this method, the interaction between the QM region and MM region is treated through nonbonded electrostatic interactions and Lennard-Jones parameters. Solute–solvent and solvent–solvent intermolecular cutoff distances of 10 Å were applied on the

Table 4. Solvation Free Energies ($\Delta G_{\text{Solvation}}$; kcal/mol) Computed with Single-Point CPCM Calculations at the B3LYP/6-31G(d) Level^a

	$\Delta G_{\text{Solvation}}$		
	reaction A	reaction B	reaction C
R1	-4.0	-4.0	-4.0
R2	-65.4	-51.7	-42.1
RC	-59.5	-46.9	-37.6
TS	-52.5	-47.5	-40.3
PC	-54.2	-52.5	-42.8
P	-64.4	-62.4	-61.1

^a R1 represents dimethyl amine, and R2 represents the second reactant in each reaction.

basis of center of mass separations. A feathering of the intermolecular interactions within 0.5 Å of the cutoff was applied. This methodology gives accurate results for charged and neutral species.^{14,32}

Results and Discussion

Gas-Phase Calculations. Methyl transfers from charged ammonium or sulfonium compounds to neutral amines proceed via an S_N2 reaction mechanism. The methyl group inverts during the reaction in a backside displacement process. The geometries for the stationary points obtained at this level of theory are given in Figure 1, and the corresponding potential energy surfaces for these S_N2 reactions in the gas phase, computed at the B3LYP/6-31+G(d,p) level of theory, are shown in Figure 2. In the gas phase, all three reactions proceed through the formation of reactant and product ion–dipole complexes (RC and PC, respectively, in Figure 1) whose energies are lower than the sum of the reactant energies. The geometries for the ion–dipole complexes were located by following the imaginary frequencies of the transition structures along the reaction path toward reactants and products by intrinsic reaction coordinate (IRC) calculations and then optimizing the last IRC geometries. In order to test the accuracy of various types of calculations, enthalpies are computed with different basis sets and functionals at the DFT and MP2 levels, and these enthalpies are compared to the more accurate CBS-QB3 results (Table 1). Diffuse functions are found to be crucial for the accurate description of these methyl-transfer reactions. MP2/6-31+G(d,p) activation enthalpies for all three reactions agree best with the activation enthalpies obtained at the CBS-QB3 level. B3LYP/6-31+G(d,p) activation barriers are in good agreement with CBS-QB3 activation barriers for the methyl-

Table 5. Aqueous Phase Reaction and Activation Free Energies and Experimental Activation Free Energies (kcal/mol)^a

	reaction A				reaction B				reaction C			
	B3LYP 6-31+G(d,p)	MP2 6-31+G(d,p)	CBS- QB3	exp ¹⁰	B3LYP 6-31+G(d,p)	MP2 6-31+G(d,p)	CBS- QB3	exp ¹⁰	B3LYP 6-31+G(d,p)	MP2 6-31+G(d,p)	CBS- QB3	exp ¹⁰
R	0	0	0	0	0	0	0	0	0	0	0	0
RC	10.7	8.1			10.7	18.4 ^b			7.9	4.3		
TS	34.8	36.8	36.3	34.4	32.4	33.5	33.0	33.5	19.4	22.2	23.8	28.1
PC	10.1	5.8			9.5	16.8 ^b			-8.0	-22.5		
P	-1.1	-3.1	-3.0		-4.6	-2.6	-2.6		-31.1	-32.5	-28.6	

^a The solvation effects are computed with single-point CPCM calculations at the B3LYP/6-31G(d) level. ^b Thermal corrections are obtained from HF calculations with the same basis set.

Table 6. Activation Free Energies Computed at the B3LYP/6-31+G(d,p) Level with Different Cavity Methods

	$\Delta G_{\text{Sol}}^{\ddagger}$		
	reaction A	reaction B	reaction C
UAHF	34.8	31.5	19.2
UA0	33.7	31.2	21.5
UAKS	34.7	31.5	19.2
UFF	35.3	30.1	25.2
BONDI	40.5	37.8	28.5
PAULING	41.0	38.4	28.7
exp ¹⁰	34.4	33.5	28.1

transfer reactions from ammonium salts but not for the methyl-transfer reaction from trimethyl sulfonium salt. All of the B3LYP/6-31+G(d,p) activation barriers for the methyl-transfer reactions studied here are found to be lower than the CBS-QB3 activation barriers as expected, since the DFT method is known to underestimate the activation barriers for S_N2 reactions.³⁵ The CBS-QB3 method generates thermodynamic properties with high accuracy for a variety of molecules, and it has been shown that, for S_N2 reactions, the estimated activation enthalpies differ by 0.5 kcal/mol from even higher accuracy methods like W1³⁶ and W2³⁷ or other coupled cluster methods.³⁸ Therefore, CBS-QB3 activation enthalpies are assumed to produce the best gas-phase results for these reactions among the methods applied. MPW1K/6-31+G(d,p) gave the highest estimates of the activation enthalpies for all three reactions among the methods applied (Table 1). The activation free energies for these reactions in the gas phase with B3LYP/6-31+G(d,p), MP2/6-31+G(d,p), and CBS-QB3 methods are given in Table 2. The energies of the all stationary points located with DFT and MP2 levels of theory with 6-31G(d) and 6-31+G(d,p) basis sets are given in Table 3.

In the gas phase, reaction A is estimated to be exothermic, and reaction B is estimated to be endothermic (Table 3). The only difference between these two reactions is the different

substituents on the methyl-donor compounds (Scheme 1). In reaction A, the methyl donor dimethylammonium has two hydrogens and two methyl groups, whereas in reaction B, the methyl donor tetramethylammonium has four methyl groups. This increases the reaction enthalpy by 12.2 kcal/mol and the activation enthalpy by 5.4 kcal/mol at the CBS-QB3 level. Possible reasons for the changes in the reaction and activation enthalpies for these two reactions are (i) the electron-donating alkyl substituents on the ammonium cation stabilize the reactants more than the neutral products, and therefore, the transition structure for reaction B is higher in energy than the transition structure for reaction A and (ii) the steric effects generated by the methyl groups might raise the activation enthalpy of reaction B more than that of reaction A. Reaction C involves breaking a carbon-sulfur bond and forming a carbon-nitrogen bond. Therefore, the energetics of this reaction are controlled by the relative strengths of the weaker carbon-sulfur bond on the reactants side and stronger carbon-nitrogen bond on the products side, which causes an early transition structure (Figure 1) and low activation barrier for this reaction.

Aqueous-Phase Calculations. Solvation corrections for the reactions were first computed by single-point CPCM calculations at the B3LYP/6-31G(d) level (Table 4). The polar solvent, water, stabilizes reactants and products with localized charges more than the TSs with delocalized positive charges. Therefore, the activation free energies of the reactions are increased substantially by the aqueous solvent. The RCs are found to be higher in energy than the reactants in the aqueous phase for all three reactions (Table 5).

CBS-QB3 computed activation free energies with single-point CPCM solvation corrections are in good agreement with the available experimental data for reactions A and B but deviate by 3.6 kcal/mol for reaction C (Table 5). The average absolute error for the estimation of the activation free energies with the single-point CPCM corrections for the CBS-QB3 optimized geometries with respect to the experi-

Table 7. Aqueous Phase Reaction and Activation Free Energies Computed at the CBS-QB3 and B3LYP/6-31+G(d) Levels and Experimental Activation Free Energies (kcal/mol)^a

	reaction A			reaction B			reaction C		
	B3LYP	CBS-QB3	exp	B3LYP	CBS-QB3	exp	B3LYP	CBS-QB3	exp
R	0.0	0.0	0.0	0.0	0.0	0.0	0.0	0.0	0.0
TS	28.4	29.9	34.4	27.7	28.3	33.5	30.1	34.6	28.1
P	-0.2	-2.1		-2.9	-0.9		-3.5	-2.0	

^a The solvation free energies are computed with single-point GB/SA calculations for CBS-QB3 geometries.

Table 8. GB/SA Solvation Free Energies (kcal/mol) for CBS-QB3 Gas-Phase Geometries

	ΔG_{Solv}		
	reaction A	reaction B	reaction C
R1	-3.4	-3.4	-3.4
R2	-63.8	-50.3	-65.3
TS	-56.7	-50.2	-52.1
P	-61.5	-58.7	-57.3

mental activation free energies is found to be 1.9 kcal/mol with the UA0 cavity model.

The sum of the gas-phase activation free energies obtained at the B3LYP/6-31+G(d,p) level of theory and solvation free energies computed with different cavity methods at the same level are given in Table 6. These values constitute estimates of the condensed-phase activation free energies and, therefore, are compared to the experimental values to assess the accuracy of the $\Delta\Delta G_{\text{Sol}}^{\ddagger}$'s obtained with different cavity models. The condensed-phase activation free energy for reaction C seems to be correlated better with the experimental value when the solvation corrections are computed with the UFF, BONDI, and PAULING cavity models, but the agreement between the experimental and computed values gets worse in the case of reactions A and B with these cavity models. The activation free energies with the BONDI and PAULING cavity models are systematically higher than the corresponding reactions with the UA0 cavity model (~ 7 kcal/mol). The average absolute errors for the computed activation free energies are 2.3 and 3.2 kcal/mol with the UFF and UA0 cavity models, respectively. The UFF cavity model appears to generate more reliable solvation free energies for the methyl-transfer reactions even though this cavity method was shown to produce larger deviations from experimental hydration energies in a more general benchmark.³⁹

Aqueous-phase activation free energies for the methyl-transfer reactions computed by correcting the gas-phase CBS-QB3 activation free energies with GB/SA solvation corrections are given in Table 7. In order to obtain the solvation free energies for the DFT gas-phase geometries, the charges

for the DFT structures have been computed with the CM1 charge method by making use of the AM1³⁰ semiempirical Hamiltonian. After this step, CM1A charges were used to calculate the solvation free energies for the reactants, products, and transition structures with the GB/SA solvation method (Table 8). The average absolute error is found to be 5.4 kcal/mol with the GB/SA solvation corrections for the estimation of the activation free energies.

QM/MM/MC is another well-established method for the calculation of $\Delta G_{\text{Sol}}^{\ddagger}$ for chemical reactions. The QM/MM/MC explicit solvation method is a robust way of calculating accurate solvation free energies with explicit solute-solvent interactions.³²

To permit a detailed elucidation of the changes in aqueous solvation along the reaction path, the QM/MM/MC treatment was used with the computation of free-energy profiles using FEP theory. The QM calculations were performed during the MC/FEP calculations using PDDG/PM3, and the solute geometries were fully sampled (see Methodology). The B3LYP/6-31+G(d,p) and PDDG/PM3 computed gas-phase transition structures of the three methyl-transfer reactions were very similar to the ones found by MC/FEP calculations (Figure 3). Radial distribution functions obtained between the carbon of the methyl group being transferred during the reaction (carbon 2 in Figure 3) and the oxygen of the surrounding water molecules at the TSs are shown in Figure 4. The PDDG/PM3 gas-phase activation enthalpies 31.3, 36.6, and 26.8 kcal/mol for reactions A, B, and C, respectively, differed notably from CBS-QB3 values despite the similarities between the predicted TSs (Table 1). Smooth free-energy profiles of the aqueous-phase reactions using a 0.01 Å increment predicted free energies of activation of 49.2, 50.1, and 39.3 kcal/mol from the PDDG/PM3/MM/MC simulations with cratic entropy corrections.⁴⁰ Even though PDDG/PM3/MM/MC simulations did not reproduce experimental activation free energies, the experimental trend was reproduced with these simulations.

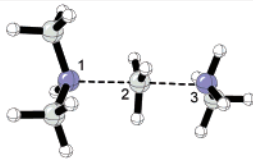
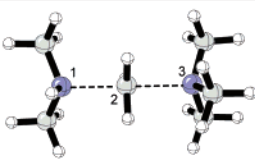
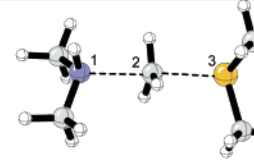
Method	Transition state geometries and distances (Å) for reactions		
	A	B	C
			
	d(1-2)/d(2-3)	d(1-2)/d(2-3)	d(1-2)/d(2-3)
DFT	2.07 / 2.00	2.01 / 2.05	2.16 / 2.30
PDDG/PM3(gas)	1.98 / 1.96	2.00 / 2.01	2.00 / 2.24
PDDG/PM3(MC)	1.95 / 1.99	2.01 / 2.03	2.03 / 2.23

Figure 3. Geometrical comparison between gas-phase B3LYP/6-31+G(d,p) and PDDG/PM3 optimized transition state geometries in the gas phase and with the QM/MM/MC simulations. The structures from left to right are transition structure geometries for reactions A, B, and C.

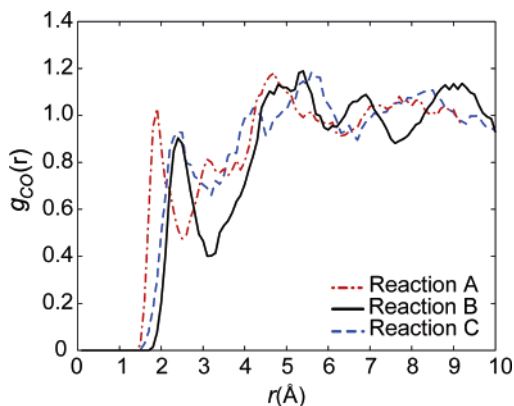


Figure 4. Radial distribution functions obtained from QM/MM/MC simulations for CBS-QB3 transition structures for reactions A, B, and C. r corresponds to the distance from carbon of the transferring methyl group to the water oxygens at the transition structures.

Conclusions

Activation enthalpies of the methyl-transfer reactions in the gas phase can be computed with reasonable accuracy with the B3LYP/6-31G(d,p) and MP2/6-31+G(d,p) levels of theory. Diffuse functions are found to be important in order to estimate the activation enthalpies accurately in the gas phase. Correcting the gas-phase CBS-QB3 free energies with the aqueous phase solvation free-energy corrections from CPCM calculations gave the free energy of activation with an average error of 1.9 kcal/mol. The PDDG/PM3 method overestimated the aqueous-phase activation free energies, but the qualitative trend was estimated correctly by this method.

Acknowledgment. We are grateful to the National Science Foundation and the NIH (Grant GM-32136) for financial support of this research. The computations were performed on the UCLA Academic Technology Services Hoffman Beowulf cluster.

Note Added after ASAP Publication. This article was released ASAP on March 10, 2007 with minor errors throughout the paper. The correct version was posted on March 19, 2007.

Supporting Information Available: Coordinates for all of the B3LYP/6-31+G**, MP2/6-31+G**, CBS-QB3, and PDDG/PM3 optimized structures. This material is available free of charge via the Internet at <http://pubs.acs.org>.

References

- (1) Shields, D. J.; Altarejos, J. Y.; Wang, X.; Agellon, L. B.; Vance, D. E. *J. Biol. Chem.* **2003**, *278*, 35826–35836.
- (2) Zubieta, C.; Kota, P.; Ferrer, J.-L.; Dixon, R. A.; Noel, J. P. *Plant Cell* **2002**, *14*, 1265–1277.
- (3) Akashi, T.; Sawada, Y.; Shimada, N.; Sakurai, N.; Aoki, T.; Ayabe, S. *Plant Cell Physiol.* **2003**, *44*, 103–112.
- (4) Lavid, N.; Schwab, W.; Kafkas, E.; Kock-Dean, M.; Bar, E.; Larkov, O.; Ravid, U.; Lewinsohn, E. *J. Agric. Food Chem.* **2002**, *50*, 4025–4030.
- (5) Pancheri, P.; Scapicchio, P.; Chiaie, R. D. *Am. J. Clin. Nutr.* **2002**, *76*, 1158S–61S.
- (6) Wang, L.; Thomae, B.; Eckloff, B.; Wieben, E.; Weinshilboum, R. *Biochem. Pharmacol.* **2002**, *64*, 699–710.
- (7) Osipiuk, J.; Walsh, M. A.; Joachimiak, A. *Nucleic Acids Res.* **2003**, *31*, 5440–5448.
- (8) Chen, L.; MacMillan, A. M.; Chang, W.; Ezaz-Nikpay, K.; Lane, W. S.; Verdine, G. L. *Biochemistry* **1991**, *30*, 11018–11025.
- (9) Schluckebier, G.; O’Gara, M.; Saenger, W.; Cheng, X. *J. Mol. Biol.* **1995**, *247*, 16–20.
- (10) Callahan, B. P.; Wolfenden, R. *J. Am. Chem. Soc.* **2003**, *125*, 310–311.
- (11) (a) Warshel, A.; Weiss, R. M. *J. Am. Chem. Soc.* **1980**, *102*, 6218–6226. (b) Warshel A. *Proc. Natl. Acad. Sci. U.S.A.* **1978**, *75*, 5250–5254. (c) Florian, J.; Warshel, A. *J. Phys. Chem. B* **1998**, *102*, 719–734. (d) Strajbl, M.; Florian, L.; Warshel, A. *J. Am. Chem. Soc.* **2000**, *122*, 5354–5366.
- (12) (a) Roca, M.; Marti, S.; Andres, J.; Moliner, V.; Tunon, I.; Bertran, J.; Williams, I. H. *J. Am. Chem. Soc.* **2003**, *125*, 7726–7737. (b) Kuhn, B.; Kollman, P. A. *J. Am. Chem. Soc.* **2000**, *122*, 2586–2596. (c) Zheng, Y.-J.; Bruice, T. C. *J. Am. Chem. Soc.* **1997**, *119*, 8137. (d) Lau, E. Y.; Bruice, T. C. *J. Am. Chem. Soc.* **2000**, *122*, 7165–7171. (e) Kahn, K.; Bruice, T. C. *J. Am. Chem. Soc.* **2000**, *122*, 46–51.
- (13) Castejon, H.; Wiberg, K. B.; Sklenak, S.; Hinz, W. *J. Am. Chem. Soc.* **2001**, *123*, 6092–6097.
- (14) Vayner, G.; Houk, K. N.; Jorgensen, W. L.; Brauman, J. I. *J. Am. Chem. Soc.* **2004**, *126*, 9054–9058.
- (15) Parr, R. G.; Yang, W. *Density Functional Theory of Atoms and Molecules*; Oxford University Press: New York, 1989.
- (16) Handy, N. C. *Density Functional Theory*, In *Lecture Notes in Quantum Chemistry*; Roos, B. O., Ed.; Springer-Verlag: Berlin, 1994; Vol. 2, pp 91–123.
- (17) Møller, C.; Plesset, M. S. *Phys. Rev.* **1934**, *46*, 618–622.
- (18) Montgomery, J. A., Jr.; Frisch, M. J.; Ochterski, J. W.; Petersson, G. A. *J. Chem. Phys.* **1999**, *110*, 2822–2827.
- (19) Frisch, M. J.; Trucks, G. W.; Schlegel, H. B.; Scuseria, G. E.; Robb, M. A.; Cheeseman, J. R.; Zakrzewski, V. G.; Montgomery, J. A., Jr.; Stratmann, R. E.; Burant, J. C.; Dapprich, S.; Millam, J. M.; Daniels, A. D.; Kudin, K. N.; Strain, M. C.; Farkas, O.; Tomasi, J.; Barone, V.; Cossi, M.; Cammi, R.; Mennucci, B.; Pomelli, C.; Adamo, C.; Clifford, S.; Ochterski, J.; Petersson, G. A.; Ayala, P. Y.; Cui, Q.; Morokuma, K.; Malick, D. K.; Rabuck, A. D.; Raghavachari, K.; Foresman, J. B.; Cioslowski, J.; Ortiz, J. V.; Stefanov, B. B.; Liu, G.; Liashenko, A.; Piskorz, P.; Komaromi, I.; Gomperts, R.; Martin, R. L.; Fox, D. J.; Keith, T.; Al-Laham, M. A.; Peng, C. Y.; Nanayakkara, A.; Gonzalez, C.; Challacombe, M.; Gill, P. M. W.; Johnson, B. G.; Chen, W.; Wong, M. W.; Andres, J. L.; Head-Gordon, M.; Replogle, E. S.; Pople, J. A. *Gaussian 98*, revision A.5; Gaussian, Inc.: Pittsburgh, PA, 1998.
- (20) Frisch, M. J.; Trucks, G. W.; Schlegel, H. B.; Scuseria, G. E.; Robb, M. A.; Cheeseman, J. R.; Montgomery, J. A., Jr.; Vreven, T.; Kudin, K. N.; Burant, J. C.; Millam, J. M.; Iyengar, S. S.; Tomasi, J.; Barone, V.; Mennucci, B.; Cossi, M.; Scalmani, G.; Rega, N.; Petersson, G. A.; Nakatsuji, H.; Hada, M.; Ehara, M.; Toyota, K.; Fukuda, R.; Hasegawa, J.; Ishida, M.; Nakajima, T.; Honda, Y.; Kitao, O.; Nakai, H.; Klene, M.; Li, X.; Knox, J. E.; Hratchian, H. P.; Cross, J. B.; Bakken, V.; Adamo, C.; Jaramillo, J.; Gomperts, R.; Stratmann, R. E.; Yazyev, O.; Austin, A. J.; Cammi, R.;

- Pomelli, C.; Ochterski, J. W.; Ayala, P. Y.; Morokuma, K.; Voth, G. A.; Salvador, P.; Dannenberg, J. J.; Zakrzewski, V. G.; Dapprich, S.; Daniels, A. D.; Strain, M. C.; Farkas, O.; Malick, D. K.; Rabuck, A. D.; Raghavachari, K.; Foresman, J. B.; Ortiz, J. V.; Cui, Q.; Baboul, A. G.; Clifford, S.; Cioslowski, J.; Stefanov, B. B.; Liu, G.; Liashenko, A.; Piskorz, P.; Komaromi, I.; Martin, R. L.; Fox, D. J.; Keith, T.; Al-Laham, M. A.; Peng, C. Y.; Nanayakkara, A.; Challacombe, M.; Gill, P. M. W.; Johnson, B.; Chen, W.; Wong, M. W.; Gonzalez, C.; Pople, J. A. *Gaussian 03*, revision C.02; Gaussian, Inc.: Wallingford, CT, 2004.
- (21) Becke, A. D. *J. Chem. Phys.* **1993**, *98*, 5648–5652.
- (22) Lee, C.; Yang, W.; Parr, R. G. *Phys. Rev. B: Condens. Matter Mater. Phys.* **1988**, *37*, 785–789.
- (23) Lynch, B. J.; Fast, P. L.; Harris, M.; Truhlar, D. G. *J. Phys. Chem. A* **2000**, *104*, 4811–4815.
- (24) Barone, V.; Cossi, M. *J. Phys. Chem. A* **1998**, *102*, 1995–2001.
- (25) Hasel, W.; Hendrickson, T. L.; Still, W. C. *Tetrahedron Comput. Methodol.* **1988**, *1*, 103–116.
- (26) Jorgensen, W. L.; Ulmschneider, J. P.; Tirado-Rives, J. *J. Phys. Chem. B* **2004**, *108*, 16264–16270.
- (27) Udier-Blagovic, M.; De Tirano, P. M.; Pearlman, S. A.; Jorgensen, W. L. *J. Comput. Chem.* **2004**, *25*, 1322–1332.
- (28) Jorgensen, W. L.; Tirado-Rives, J. *J. Comput. Chem.* **2005**, *26*, 1689–1700.
- (29) Storer, J. W.; Giesen, D. J.; Cramer, C. J.; Truhlar, D. G. *J. Comput.-Aided Mol. Des.* **1995**, *9*, 87–110.
- (30) Dewar, M. J. S.; Zoebisch, E. G.; Healy, E. F.; Stewart, J. J. P. *J. Am. Chem. Soc.* **1985**, *107*, 3902–3909.
- (31) (a) Gogonea, V. *Internet Electron. J. Mol. Des.* **2002**, *1*, 173–184. (b) Warshel A.; Levitt M. *J. Mol. Biol.* **1976**, *103*, 227–249. (c) Singh, U. C.; Kollman, P. A. *J. Comput. Chem.* **1986**, *7*, 718–730. (d) Field, M. J.; Bash, P. A.; Karplus, M. *J. Comput. Chem.* **1990**, *11*, 700–733. (e) Maseras, F.; Morokuma, K. *J. Comput. Chem.* **1995**, *16*, 1170–1179. (f) Guimaraes, C. R. W.; Udier-Blagovic, M.; Jorgensen, W. L. *J. Am. Chem. Soc.* **2005**, *127*, 3577–3588. (g) Guimaraes, C. R. W.; Repasky, M. P.; Chandrasekhar, J.; Tirado-Rives, J.; Jorgensen, W. L. *J. Am. Chem. Soc.* **2003**, *125*, 6892–6899.
- (32) (a) Acevedo, O.; Jorgensen, W. L. *Org. Lett.* **2004**, *6*, 2881–2884. (b) Acevedo, O.; Jorgensen, W. L. *J. Am. Chem. Soc.* **2005**, *127*, 8829–8834. (c) Acevedo, O.; Jorgensen, W. L. *J. Org. Chem.* **2006**, *71*, 4896–4902. (d) Acevedo, O.; Jorgensen, W. L. *J. Am. Chem. Soc.* **2006**, *128*, 6141–6144.
- (33) (a) Repasky, M. P.; Chandrasekhar, J.; Jorgensen, W. L. *J. Comput. Chem.* **2002**, *23*, 1601–1622. (b) Tubert-Brohman, I.; Guimaraes, C. R. W.; Repasky, M. P.; Jorgensen, W. L. *J. Comput. Chem.* **2003**, *25*, 138–150. (c) Tubert-Brohman, I.; Guimaraes, C. R. W.; Jorgensen, W. L. *J. Chem. Theory Comput.* **2005**, *1*, 817–823.
- (34) Jorgensen, W. L.; Chandrasekhar, J.; Madura, J. D.; Impey, W.; Klein, M. L. *J. Chem. Phys.* **1983**, *79*, 926–935.
- (35) Glukhovtsev, M. N.; Bach, R. D.; Pross, A.; Radom, L. *Chem. Phys. Lett.* **1996**, *260*, 558–564.
- (36) Martin, J. M. L.; De Oliveria, G. *J. Chem. Phys.* **1991**, *111*, 1843–1856.
- (37) Parthiban, S.; De Oliveria, G.; Martin, J. M. L. *J. Phys. Chem. A* **2001**, *105*, 895–904.
- (38) Botchwina, P. *Theor. Chem. Acc.* **1998**, *99*, 426–428.
- (39) Takano, Y.; Houk, K. N. *J. Chem. Theory Comput.* **2005**, *1*, 70–77.
- (40) Yu, B. Y. *J. Pharm. Sci.* **2001**, *90*, 2099–2102.

CT050318N

JCTC

Journal of Chemical Theory and Computation

Active-Space Equation-of-Motion Coupled-Cluster Methods through Quadruples for Excited, Ionized, and Electron-Attached States

Peng-Dong Fan, Muneaki Kamiya, and So Hirata*

*Quantum Theory Project, Department of Chemistry, University of Florida,
Gainesville, Florida 32611-8435*

Received August 17, 2006

Abstract: Several variants of the equation-of-motion coupled-cluster (EOM-CC) method with singles (one-hole or one-particle), doubles (two-hole-one-particle or two-particle-one-hole), and a selected set of triples (three-hole-two-particle or three-particle-two-hole) and/or quadruples (four-hole-three-particle or four-particle-three-hole) have been implemented by computerized symbolic algebra. They are applicable to excitation energies (EE), ionization potentials (IP), and electron affinities (EA), excited-state dipole moments, and transition dipole moments of both closed- and open-shell species and are abbreviated as EE/IP/EA-EOM-CCSD t , EE/IP/EA-EOM-CCSD tq , and EE/IP/EA-EOM-CCSD tq , where the small letters indicate the use of active-space cluster and EE/IP/EA operators. They are also parallel executable and accelerated by the use of spin, spatial, and permutation symmetries. The remarkable effectiveness of the methods in capturing nondynamical correlation effects has been demonstrated by their applications to the vertical excitation energies of C₂, the adiabatic excitation energies and dipole moments of the CH radical, the adiabatic excitation energies of the CH₂ diradical, the adiabatic excitation energies and dipole moments of formaldehyde, the vertical ionization energies of N₂, and the vertical electron affinities of C₂. The effectiveness is found to decline when the basis set is extended, causing the active space to become relatively small and also less well-defined. As a remedy, we propose a composite method that combines higher-rank active-space methods with smaller basis sets for nondynamical correlation and lower-rank nonactive-space methods with larger basis sets for dynamical correlation, which is shown to work well for an excited-state potential energy curve of hydrogen fluoride.

I. Introduction

The most accurate and compact single-reference coupled-cluster (CC) descriptions^{1–4} of electronic transitions can be furnished by the equation-of-motion (EOM) CC method^{5–10} and the related CC linear response (LR)^{11–17} and symmetry-adapted-cluster configuration-interaction (SAC-CI) methods.^{18,19} They can handle not only excitation energies (EE)^{7–10,20–25} but also ionization potentials (IP)^{26–31} and electron affinities (EA).^{32–35} The lowest-order member of the EOM-CC hierarchy for excitation energies (EE-EOM-

CC), i.e., the EE-EOM-CC with singles and doubles (EE-EOM-CCSD),^{7–10,25} has been established as a reliable method for dominantly single excitations. Its performance deteriorates when the excited states have significant double excitation components from the ground state, when the ground state itself is quasidegenerate, or when the entire excited-state potential energy surfaces are considered. Similarly, EOM-CCSD for ionization energies and electron affinities, i.e., IP-^{26–29} and EA-EOM-CCSD,^{32,33} prove inadequate for shake-up or shake-on transitions and when the effect of orbital relaxation is substantial. In these cases, higher-order EE/IP/EA-EOM-CC methods, such as those through triples

* Corresponding author e-mail: hirata@qtp.ufl.edu.

(EE-,^{20,23} IP-,^{30,31,36} and EA-EOM-CCSDT^{34,35}) and through quadruples (EE-,^{37,38} IP-,³¹ and EA-EOM-CCSDTQ,³⁵) become necessary. However, the high-rank polynomial size dependence of the computational cost of these methods, e.g., $O(n^8)$ of EE-EOM-CCSDT and $O(n^{10})$ of EE-EOM-CCSDTQ (n is the number of orbitals), prohibits their applications to large molecules, despite their correct theoretical size dependence (size extensivity and intensivity). The high-order EE/IP/EA-EOM-CC calculations are by no means routine, although the electronic states that demand these treatments are not uncommon.

The essential effects of higher-order excitation operators can nevertheless be incorporated in the coupled-cluster (CC) method at a low cost by the ansatz of Adamowicz and co-workers,^{39–41} defining the active-space CC methods. It restricts higher-order cluster T operators to those that involve user-defined active orbitals, in ways that do not impair size extensivity. When nondynamical correlation effects calling for the high-order CC methods are plainly associated with a small set of orbitals, the active-space methods designating these orbitals as active can provide the most compact descriptions of these effects. The active-space CC methods through triples (CCSD t) and quadruples (CCSD tq and CCSDT q) (the small letters in acronyms indicate restricted triples and/or quadruples) have been implemented into parallel execution programs by us⁴² with the aid of computerized symbolic algebra. Kállay and co-workers implemented a general-order CC method⁴³ with their string-based algorithm and subsequently incorporated the active-space ansatz into this.⁴⁴

It is not unreasonable to expect that this class of methods is even more effective for excited, ionized, and electron-attached states because the proportion of double excitation, shake-up ionization, shake-on electron-attachment, and higher-ranked contributions in the wave functions can be much greater (and can reach unity) than the double excitation contributions in ground-state wave functions. The active-space ansatz was hence extended to excited states by Kowalski and Piecuch,^{22,23} who reported the formalisms of EE-EOM-CCSD with active-space triples (EE-EOM-CCSD t) and quadruples (EE-EOM-CCSD tq) and an implementation of EE-EOM-CCSD t , where, in addition to T , higher-order excitation R (or deexcitation L) operators were restricted. Kowalski et al.⁴⁵ also reported a semiautomated parallel implementation of EE-EOM-CCSD t . Slipchenko and Krylov⁴⁶ implemented the spin-flip EOM-CCSD(2,3) method in addition to the usual spin-conserving counterpart, where only R and L included active-space triples, while T reached up to doubles. Gour et al.^{47–49} applied the scheme to ionization energies and electron affinities, in which ionization $R^{(N-1)}$ and electron-attachment $R^{(N+1)}$ operators were restricted, implementing IP-EOM-CCSD t and EA-EOM-CCSD t . Kállay and Gauss³⁸ reported a general-order EE-EOM-CC for energies and properties employing the string-based algorithm that was fitted with the ability to apply active-space restrictions on any of the high-order cluster and linear excitation operators. Köhn and Olsen⁵⁰ generalized the active space by further dividing it into many subspaces and combined them

with a general-order CC method in an algorithm similar to the string-based algorithm of Kállay and Surján.⁴³

For a fixed active space size, the size dependence of computational cost remains $O(n^6)$ for EE-EOM-CCSD t and EE-EOM-CCSD tq and $O(n^5)$ for IP/EA-EOM-CCSD t and IP/EA-EOM-CCSD tq . In addition to this remarkable speedup, the active-space EOM-CC approach has several unmatched advantages: it substantiates the state-selective multireference CC method in a transparent and unambiguous single-reference framework; it reduces to the full EOM-CC methods when all orbitals are active; it can rival the full EE/IP/EA-EOM-CC methods in the ability to include essential high-order correlation and EE/IP/EA effects with a small active space; and it is size extensive for total energies and size intensive for transition energies.

In this article, we report implementations of a number of extensions to this method which have been made with the essential aid of the symbolic algebra system (Tensor Contraction Engine or TCE)^{37,51–54} completely automating the time-consuming and error-prone processes of formula derivations and computer implementations involved. The original contributions of the present study are the following. We present the algebraic, order-by-order (as opposed to the so-called determinant-^{55–58} or string-based^{38,43}) implementations of the EE/IP/EA-EOM-CCSD t , EE/IP/EA-EOM-CCSD tq , and EE/IP/EA-EOM-CCSDT q methods and their numerous variants differing from each other in detailed definitions of active-space cluster and EE/IP/EA operators. Being based on spin-orbital formalisms, these TCE-synthesized programs can compute the excitation, ionization, and electron-attachment energies of closed- and open-shell molecules. Their execution is accelerated by distributed- or replicated-data load-balancing parallelism and the use of various symmetries (spin symmetry, real Abelian point-group symmetry, and index permutations). We also furnish the active-space EE-EOM-CC programs with the capability to compute transition dipole moments (and oscillator strengths) and excited-state dipole moments. This capability requires the left-hand-side eigenvectors of the non-Hermitian CC effective Hamiltonian in addition to the right-hand-side eigenvectors that are sufficient for excitation energies alone. The left-hand-side eigenvector corresponding to the ground state is related to the so-called Λ vector of the CC analytical gradient theory.⁵⁹ The Λ vectors and the ground-state dipole moments with the active-space CC (CCSD t , CCSD tq , and CCSDT q) methods have also become available by the present developments.

We also document the results of benchmark calculations of these active-space EOM-CC methods for the vertical excitation energies of C₂, the adiabatic excitation energies and dipole moments of the low-lying excited states of the CH radical, the adiabatic excitation energies and dipole moments of the low-lying excited states of formaldehyde, the adiabatic excitation energies of the CH₂ diradical, the vertical ionization energies of N₂, and the electron affinities of C₂. They attest to the remarkable accuracy of the active-space methods with the minimum active spaces: e.g., the errors from the full configuration-interaction (FCI) results in the vertical excitation energy to the ¹ Δ_g state of C₂

diminish rapidly from 2.1 eV (EOM-CCSD) to 0.24 eV (EOM-CCSD t) and to -0.06 eV (EOM-CCSD tq) as we introduce the active-space triples and quadruples. These applications also expose the methods' weaknesses. The effectiveness of the active-space triples and quadruples is increasingly less when the higher-than-double excitation effects are characterized as dynamical correlation and as the basis set is extended and the active space becomes relatively smaller and less well-defined. In lieu of the usual remedy of (variationally) optimizing the active orbitals,^{60–62} we propose a composite method that combines higher-rank active-space methods with smaller basis sets for nondynamical correlation and lower-rank nonactive-space methods with larger basis sets for dynamical correlation, which is shown to work well for an excited-state potential energy curve of hydrogen fluoride.

II. Theory

In the EE-EOM-CC theory, the k th excited state of an atom or a molecule is defined as

$$|\Psi_k\rangle = R(k)|\Psi_0\rangle \quad (1)$$

where

$$|\Psi_0\rangle = \exp(T)|\Phi\rangle \quad (2)$$

is the ground-state CC wave function and $R(k)$ is a linear excitation operator. The k dependence of $R(k)$ will be dropped hereafter whenever it is not essential. $|\Phi\rangle$ is a single-reference wave function—usually, a Hartree–Fock (HF) determinant—and T is the cluster operator. The R and T operators are defined as

$$R = \sum_{n=0}^m R_n \quad (3a)$$

$$R_n = \left(\frac{1}{n!}\right)^2 r_{a_1 \dots a_n}^{i_1 \dots i_n} C^{a_1} \dots C^{a_n} C_{i_n} \dots C_{i_1} \quad (3b)$$

and

$$T = \sum_{n=1}^m T_n \quad (4a)$$

$$T_n = \left(\frac{1}{n!}\right)^2 t_{a_1 \dots a_n}^{i_1 \dots i_n} C^{a_1} \dots C^{a_n} C_{i_n} \dots C_{i_1} \quad (4b)$$

respectively, where $r_{a_1 \dots a_n}^{i_1 \dots i_n}$ and $t_{a_1 \dots a_n}^{i_1 \dots i_n}$ are amplitudes, and C^{a_n} (C_{i_n}) are the creation (annihilation) operators and m determines the rank of the EE-EOM-CC method. Indices i_1, \dots, i_n and a_1, \dots, a_n designate the occupied spin-orbitals in the reference $|\Phi\rangle$ and unoccupied spin-orbitals, respectively. We use, whenever possible, the Einstein summation convention over the repeated upper and lower indices.

The amplitudes $t_{a_1 \dots a_n}^{i_1 \dots i_n}$ of the T operator can be obtained by solving the CC equations

$$\langle \Omega | \bar{H}_N | \Phi \rangle = 0 \quad (5)$$

where $|\Omega\rangle$ is a manifold of single through m -tuple excitation determinants and \bar{H}_N is a similarity-transformed Hamiltonian defined as

$$\bar{H}_N = \exp(-T)H_N \exp(T) = [H_N \exp(T)]_C \quad (6a)$$

$$H_N = H - \langle \Phi | H | \Phi \rangle \quad (6b)$$

where H is the usual electronic Hamiltonian. $[H_N \exp(T)]_C$ means that H_N and T must be diagrammatically connected. Substituting eq 1 into the Schrödinger equation and projecting it onto the determinant manifolds created by acting R on the reference $|\Phi\rangle$, we obtain

$$\langle \Omega | \bar{H}_N R | \Phi \rangle = (E_{\text{corr}} + \omega) \langle \Omega | R | \Phi \rangle \quad (7)$$

or

$$\langle \Omega | (\bar{H}_N R)_C | \Phi \rangle = \omega \langle \Omega | R | \Phi \rangle \quad (8)$$

to determine R and excitation energy ω , where E_{corr} is the correlation energy which can be calculated by

$$\langle \Phi | \bar{H}_N | \Phi \rangle = E_{\text{corr}} \quad (9)$$

Since \bar{H}_N is non-Hermitian, it has distinct left- and right-hand-side eigenvectors. Both of them are needed for molecular properties, such as dipole moments and transition dipole moments. The L operator, which generates the left-hand-side eigenvectors of \bar{H}_N , is defined as

$$L = \sum_{n=0}^m L_n \quad (10a)$$

$$L_n = \left(\frac{1}{n!}\right)^2 l_{i_1 \dots i_n}^{a_1 \dots a_n} C^{i_1} \dots C^{i_n} C_{a_n} \dots C_{a_1} \quad (10b)$$

and satisfies the condition

$$\langle \Phi | L \bar{H}_N | \Omega \rangle = (E_{\text{corr}} + \omega) \langle \Phi | L | \Omega \rangle \quad (11)$$

or

$$\langle \Phi | (L \bar{H}_N)_L | \Omega \rangle = \omega \langle \Phi | L | \Omega \rangle \quad (12)$$

where $(L \bar{H}_N)_L$ means that L and \bar{H}_N must be diagrammatically linked.

Once we have the biorthogonal left- and right-hand-side eigenvectors of \bar{H}_N , the dipole moments can be calculated by¹⁰

$$\langle d \rangle_{(k)} = \langle \Phi | L(k) [d \exp(T)]_C R(k) | \Phi \rangle \quad (13)$$

where d is a dipole operator, and transition dipole moments can be calculated by¹⁰

$$\langle dd \rangle_{(kl)} = \langle \Phi | L(k) [d \exp(T)]_C R(l) | \Phi \rangle \times \langle \Phi | L(l) [d \exp(T)]_C R(k) | \Phi \rangle \quad (14)$$

The dipole and transition dipole moments calculated by the EOM-CC approach, eqs 13 and 14, are identical to those by the CC LR theory in the FCI limit, while there can be subtle differences in the approximate calculations.⁶³

The EE-EOM-CCSDT^{20,23} and EE-EOM-CCSDTQ^{37,38} methods are obtained by truncating eqs 3a, 4a, 5, and 10a after $n = 3$ and 4, i.e., by setting $m = 3$ and 4, respectively. In the active-space EE-EOM-CC methods, we restrict the $T_3, T_4, R_3, R_4, L_3,$ and L_4 operators to their subsets defined

in terms of the active spin-orbitals. To do so, we partition all spin-orbitals into core, active occupied, active unoccupied, and virtual spin-orbitals. We designate core spin-orbitals by i, j, k , active occupied spin-orbitals by I, J, K , active unoccupied spin-orbitals by A, B, C , and virtual spin-orbitals by a, b, c . The core and active occupied orbitals are those that are occupied in reference wave function $|\Phi\rangle$, and the active space is chosen by the user at runtime.

The restricted R_3 operators can be defined by using the excitations in which at least one, two, or three occupied and unoccupied spin-orbitals are active, and they are designated by $r_3^{(1)}$, $r_3^{(2)}$, and $r_3^{(3)}$, respectively, and written as

$$r_3^{(1)} = \left(\frac{1}{6}\right)^2 r_{ABC}^{iJK} C^A C^B C^C C_K C_J C_i \quad (15)$$

$$r_3^{(2)} = \left(\frac{1}{6}\right)^2 r_{ABC}^{iJK} C^A C^B C^C C_K C_J C_i \quad (16)$$

and

$$r_3^{(3)} = \left(\frac{1}{6}\right)^2 r_{ABC}^{IJK} C^A C^B C^C C_K C_J C_I \quad (17)$$

The restricted T_3 ($\{t_3^{(i)} | 1 \leq i \leq 3\}$), T_4 ($\{t_4^{(i)} | 1 \leq i \leq 4\}$), R_4 ($\{r_4^{(i)} | 1 \leq i \leq 4\}$), L_3 ($\{l_3^{(i)} | 1 \leq i \leq 3\}$), and L_4 ($\{l_4^{(i)} | 1 \leq i \leq 4\}$) operators are defined analogously.

Replacing T_3 , R_3 , and L_3 in the EE-EOM-CCSDT ansatz by $t_3^{(i)}$, $r_3^{(i)}$, and $l_3^{(i)}$, we obtain EE-EOM-CCSDT(I) ($i = 1$),^{22,23,45} EE-EOM-CCSDT(II) ($i = 2$),⁴⁵ and EE-EOM-CCSDT(III) ($i = 3$).⁴⁵ EE-EOM-CCSDT q , EE-EOM-CCSDT q (II), EE-EOM-CCSDT q (III), and EE-EOM-CCSDT q (IV) can likewise be defined by replacing T_4 , R_4 , and L_4 in the EOM-CCSDT q equations by $t_4^{(i)}$, $r_4^{(i)}$, and $l_4^{(i)}$ ($1 \leq i \leq 4$), respectively. The use of $t_3^{(1)}$, $r_3^{(1)}$, $l_3^{(1)}$, $t_4^{(2)}$, $r_4^{(2)}$, and $l_4^{(2)}$ in EE-EOM-CCSDT q leads to EE-EOM-CCSDT q .²² Obviously, we can concoct many other variants by combining these active-space triples and quadruples in EE-EOM-CCSDT q . For instance, with the use of $t_3^{(3)}$, $r_3^{(3)}$, $l_3^{(3)}$, $t_4^{(4)}$, $r_4^{(4)}$, and $l_4^{(4)}$, we arrive at a method that can be called EE-EOM-CCSDT(III) q (IV). If one active-space restriction is imposed on all of T_n , R_n , and L_n for a given rank n , the resulting method is size extensive and intensive. Equations 5, 8, and 12 with restricted T_n , R_n , and L_n ($n = 3, 4$) and a manifold Ω with restricted triple and quadruple excitation determinants need to be solved to determine the unknown coefficients in these methods.

The IP- and EA-EOM-CC methods can be formulated by replacing the R operator and manifold $|\Omega\rangle$ in eqs 1, 7, and 8 by $R^{(N\mp 1)}$, which are defined as

$$R^{(N-1)} = \sum_{n=1}^m R_n^{(N-1)} \quad (18)$$

$$R_n^{(N-1)} = \frac{1}{n!(n-1)!} r_{a_1 \dots a_{n-1}}^{i_1 \dots i_n} C^{a_1 \dots a_{n-1}} C_{i_n} \dots C_{i_1} \quad (19)$$

and

$$R^{(N+1)} = \sum_{n=1}^m R_n^{(N+1)} \quad (20)$$

$$R_n^{(N+1)} = \frac{1}{n!(n-1)!} r_{a_1 \dots a_n}^{i_1 \dots i_{n-1}} C^{a_1 \dots a_n} C_{i_{n-1}} \dots C_{i_1} \quad (21)$$

Accordingly, the manifolds $|\Omega^{(N-1)}\rangle$ and $|\Omega^{(N+1)}\rangle$ are spanned by $|\Phi_i\rangle$, $|\Phi_{ij}^a\rangle$, $|\Phi_{ijk}^{ab}\rangle$, etc., and $|\Phi^a\rangle$, $|\Phi_i^{ab}\rangle$, $|\Phi_{ij}^{abc}\rangle$, etc., respectively.

The IP/EA-EOM-CCSDT and IP/EA-EOM-CCSDT q methods are defined by eqs 4, 5, 18, and 19 with $m = 3$, and 4, respectively. Their active-space variants restrict the T_3 , T_4 , $R_3^{(N\mp 1)}$, and $R_4^{(N\mp 1)}$ operators to their subsets. Since the $R_3^{(N\mp 1)}$ operators have an unequal number of creation and annihilation operators, the restriction can be imposed in one of the following two ways

$$r_3^{(N-1),A,(1)} = \left(\frac{1}{12}\right) r_{BC}^{iJK} C^B C^C C_K C_J C_i \quad (22)$$

or⁴⁷

$$r_3^{(N-1),B,(1)} = \left(\frac{1}{12}\right) r_{bc}^{iJK} C^b C^c C_K C_J C_i \quad (23)$$

Likewise, the active-space $R_4^{(N-1)}$ operator can be either

$$r_4^{(N-1),A,(1)} = \left(\frac{1}{144}\right) r_{BCd}^{ijkl} C^B C^C C^d C_L C_K C_J C_i \quad (24)$$

$$r_4^{(N-1),A,(2)} = \left(\frac{1}{144}\right) r_{BCd}^{ijkl} C^B C^C C^d C_L C_K C_J C_i \quad (25)$$

or

$$r_4^{(N-1),B,(1)} = \left(\frac{1}{144}\right) r_{bcd}^{ijkl} C^b C^c C^d C_L C_K C_J C_i \quad (26)$$

$$r_4^{(N-1),B,(2)} = \left(\frac{1}{144}\right) r_{BCd}^{ijkl} C^B C^C C^d C_L C_K C_J C_i \quad (27)$$

The restricted $R_3^{(N+1)}$ and $R_4^{(N+1)}$ can be defined analogously.

Replacing T_3 by $t_3^{(1)}$ and $R_3^{(N\mp 1)}$ by $r_3^{(N\mp 1),A,(1)}$ ($r_3^{(N\mp 1),B,(1)}$) in IP/EA-EOM-CCSDT leads to the IP/EA-EOM-CCSDT-A and -B methods, which have been proposed by Gour et al.⁴⁷ The IP/EA-EOM-CCSDT q -A and -B and IP/EA-EOM-CCSDT q -A and -B methods can also be defined completely analogously. The size dependence of the computational costs of the A variants is one-rank lower than that of the B counterparts in the step of solving $R^{(N\mp 1)}$ (the common CCSD step incurs the same cost for both). Both methods are size extensive for total energies and intensive for transition energies.

III. Computer Implementation

In our previous report on the active-space CC methods for the ground state,⁴² we described the salient modifications to the symbolic algebra system TCE needed for it to perform the automated formula derivation and computer implementation of these methods. One important feature of the TCE-synthesized programs is the tiling algorithm, which has also been proposed and implemented by Windus and Pople⁶⁴ as the “block-tensor” algorithm. In this algorithm, orbitals are grouped into tiles, and every tile is a set of orbitals which have the common attributes of hole/particle distinction, spatial symmetry, and spin symmetry. Once the tiles are defined, tensor contractions and additions can be carried out by the tilewise matrix multiplications and additions, taking account of the spin, spatial, and permutation symmetries.⁵¹

The TCE has been extended to handle various active-space ansatz by simply adding the active/inactive attribute to each tile.⁴² In the TCE-synthesized EE-EOM-CCSD t program, for instance, the tiles of the amplitudes $t_3^{(1)} ({}_{ijK}^{abc})$, $r_3^{(1)} ({}_{ijK}^{abc})$, and $l_3^{(1)} ({}_{ijK}^{abc})$ that are stored and used in contractions are limited to those that have at least one active particle tile index and at least one active hole tile index. The numbers of eqs 5, 7, and 11 are likewise reduced since only the tiles of triples excitations in Ω that have at least one active particle tile index and one active hole tile index are retained. Many tiles of intermediate quantities of active-space EE-EOM-CC calculations can also be excluded. Only those tiles that satisfy the universal formula, $n_B \geq n_C - n_D + n_A$, need to be considered, where n_B is the number of superscript (or subscript) active external indices in the intermediate (the external indices are the indices in Ω), n_C is equal to i in $t_n^{(i)}$, $r_n^{(i)}$, or $l_n^{(i)}$, n_D is the number of superscript (or subscript) external indices of Ω , and n_A is the number of superscript (or subscript) external indices in the intermediate.

The TCE has also been extended to handle the IP/EA-EOM-CC approaches through quadruples.^{31,35} To allow the $R^{(N\mp 1)}$ operators in the ansatz, we have added a new attribute to each of the creation and annihilation operators and each of the indices of physical tensors (molecular integrals, excitation amplitudes, and so forth), which distinguishes the usual operators and indices from those that are associated with a continuum operator. One additional rule is introduced: a continuum operator can only be contracted with another continuum operator,³¹ when evaluating an expectation value of normal-ordered second-quantized operators using Wick's theorem. Once the active-space logic and the IP/EA extension are combined, the TCE can be used to generate the active-space IP/EA-EOM-CC codes as well as active-space EE-EOM-CC codes.

The EE-EOM-CCSD t , EE-EOM-CCSD t (II), and EE-EOM-CCSD t (III) methods have been implemented in a single algorithmic framework that switches among these three and also EE-EOM-CCSD t according to a runtime parameter set by the user of the program. The EE-EOM-CCSD tq , EE-EOM-CCSD t (I) q (III), EE-EOM-CCSD t (I) q (IV), EE-EOM-CCSD t (II) q (III), EE-EOM-CCSD t (II) q (IV), EE-EOM-CCSD t (III) q (IV), EE-EOM-CCSD tq , EE-EOM-CCSD tq (II), EE-EOM-CCSD tq (III), and EE-EOM-CCSD tq (IV) can also be executed by a single algorithm that also encompasses EE-EOM-CCSD tq . The IP and EA variants, IP/EA-EOM-CCSD t -A and -B, IP/EA-EOM-CCSD tq -A and -B, and IP/EA-EOM-CCSD tq -A and -B, are implemented in the same fashion. When using the formula $n_B \geq n_C - n_D + n_A$, a continuum index can be either ignored altogether or counted as an active, external index toward n_B , n_D , and n_A . The former choice defines the A variant and the latter the B variant.

These programs are parallel executable on the basis of a distributed- or replicated-data, load-balancing algorithm, adjust tile sizes automatically according to the user specified memory limit, and make use of the spin (within spin-orbital formalisms), spatial (real Abelian), and permutation symmetries. They can be applied to atoms and molecules of any number of electrons and any spin multiplicity (with certain

Table 1. Vertical Excitation Energies (in eV) of C₂

theory	active space	${}^1\Pi_u$	${}^1\Delta_g$	${}^1\Pi_g$	${}^1\Sigma_u^+$
FCI ^a	...	1.385	2.293	4.494	5.602
EE-EOM-CCSD ^b	...	+0.090	+2.054	+1.708	+0.197
EE-EOM-CCSD t^b	...	+0.034	+0.407	+0.088	+0.113
EE-EOM-CCSD t	(2,2)	-0.077	+0.244	+0.070	+0.123
EE-EOM-CCSD t	(2,7)	-0.038	+0.282	+0.063	+0.097
EE-EOM-CCSD tq^b	...	+0.001	+0.024	-0.007	+0.013
EE-EOM-CCSD tq	(2,2)	-0.083	-0.057	+0.065	+0.061
EE-EOM-CCSD tq	(2,7)	-0.056	-0.034	+0.027	+0.027
EE-EOM-CCSD tq	(2,2)	-0.004	+0.036	+0.007	+0.012
EE-EOM-CCSD tq	(2,7)	-0.002	+0.034	+0.001	+0.013
EE-EOM-CCSD t (EII)	(2,2)	-0.131	+1.527	+1.312	+0.204
EE-EOM-CCSD t (EIII)	(2,2)	+0.089	+2.054	+1.707	+0.197
EE-EOM-CCSD t (E)q(III)	(2,2)	-0.077	+0.243	+0.070	+0.123
EE-EOM-CCSD t (E)q(IV)	(2,2)	-0.077	+0.244	+0.070	+0.123
EE-EOM-CCSD t (EII)q(III)	(2,2)	-0.131	+1.526	+1.312	+0.204
EE-EOM-CCSD t (EII)q(IV)	(2,2)	-0.131	+1.527	+1.312	+0.204
EE-EOM-CCSD t (EIII)q(IV)	(2,2)	+0.089	+2.054	+1.707	+0.197
EE-EOM-CCSD tq (II)	(2,2)	+0.020	+0.118	+0.102	+0.047
EE-EOM-CCSD tq (III)	(2,2)	+0.034	+0.406	+0.088	+0.113
EE-EOM-CCSD tq (IV)	(2,2)	+0.034	+0.407	+0.088	+0.113

^a Reference 66. ^b Reference 37.

molecular size limits). They are a part of the NWChem computational chemistry program suite.⁶⁵

The code verification has been done by the comparison with an independent implementation of the same methods using the determinant-based algorithm⁵⁶ for the right-hand-side eigenvalue problem. The TCE-synthesized codes for the left-hand-side eigenvalue problem have been verified to give the identical eigenvalues as the right-hand-side codes. We have observed the speedup by a factor of 10 and 3 for EE-EOM-CCSD tq and EE-EOM-CCSD tq , respectively, relative to EE-EOM-CCSD tq , for the excitation energies of C₂ with a modified cc-pVDZ basis set.⁶⁶ The parallel algorithms employed here are unchanged from our prior studies,^{37,42,45,51–54} and their performance can be inferred from the data given therein.^{42,51,52}

IV. Applications

A. Vertical Excitation Energies of C₂. The active-space EE-EOM-CC results for C₂, a molecule notorious for the multideterminant ground-state wave function at the equilibrium geometry, are shown in Table 1. The FCI results⁶⁶ in this table are listed as the vertical excitation energies, while the other entries are the differences from the FCI. We have used 2.348 bohr⁶⁶ as the internuclear distance and the cc-pVDZ basis set⁶⁷ with an additional diffuse function for each valence orbital⁶⁶ in the frozen core approximation. Two types of active space have been used: the first selects the two highest occupied and two lowest unoccupied α - and β -spin orbitals as active orbitals. The second uses two active occupied and seven unoccupied α - and β -spin orbitals. We use “(2,2)” to designate the first and “(2,7)” the second active space.

Four low-lying excited states ${}^1\Pi_u$, ${}^1\Delta_g$, ${}^1\Pi_g$, and ${}^1\Sigma_u^+$ have been examined. The ${}^1\Delta_g$ and ${}^1\Pi_g$ states are dominated by doubly excited determinant contributions, noticeable by the significant improvement in excitation energies brought to by

Table 2. Adiabatic Excitation Energies (T_e /eV) and Dipole Moments (μ /D) of the Ground and Low-Lying Excited States of CH

theory ^a	$\tilde{X}^2\Pi$		$\tilde{a}^4\Sigma^-$		$\tilde{A}^2\Delta$		$\tilde{B}^2\Sigma^-$		$\tilde{C}^2\Sigma^+$	
	T_e	μ	T_e	μ	T_e	μ	T_e	μ	T_e	μ
CCSD/aug-cc-pVDZ ^b	0.00	1.39	0.95	0.65	3.33	0.81	4.41	0.91	5.29	0.72
CCSD/aug-cc-pVTZ ^b	0.00	1.42	1.03	0.65	3.28	0.81	4.62	0.90	5.48	0.71
CCSDT/aug-cc-pVDZ ^b	0.00	1.37	0.66	0.65	3.02	0.81	3.27	1.27	4.07	0.87
CCSDT/aug-cc-pVDZ	0.00	1.38	0.76	0.67	3.12	0.82	3.42	1.20	4.18	0.88
CCSDT/aug-cc-pVTZ ^b	0.00	1.39	0.74	0.65	2.94	0.81	3.27	1.27	4.03	0.87
CCSDT/aug-cc-pVTZ	0.00	1.41	0.86	0.66	3.07	0.82	3.50	1.17	4.19	0.88
CCSDTQ/aug-cc-pVDZ ^b	0.00	1.37	0.65	0.65	3.00	0.81	3.26	1.27	4.04	0.86
CCSDTq/aug-cc-pVDZ	0.00	1.38	0.76	0.67	3.12	0.82	3.42	1.20	4.17	0.88
CCSDTq/aug-cc-pVDZ	0.00	1.37	0.65	0.65	3.01	0.81	3.26	1.27	4.04	0.86
experiment	0.00	1.46 ± 0.06 ^c	0.74 ^d	...	2.88 ^e	0.77 ± 0.07 ^f	3.23 ^g	...	3.94 ^e	...

^a CCSD represents CCSD for the ground state $\tilde{X}^2\Pi$ or EE-EOM-CCSD for the rest. Likewise, CCSDT, CCSDTQ, CCSDt, CCSDtq, and CCSDTq represent either the CC or EE-EOM-CC methods. ^b Reference 37. ^c Reference 73. ^d Reference 74. ^e Reference 72. ^f Reference 75. ^g Reference 71.

the inclusion of triples (EE-EOM-CCSDT). For $^1\Delta_g$, EE-EOM-CCSDt with (2,2) active space gives +0.244 eV difference from the FCI results. Hence, it is as accurate as EE-EOM-CCSDT, which suffers from the slightly greater error of +0.407 eV. EE-EOM-CCSDtq and EE-EOM-CCSDTq further reduce the deviations to -0.057 eV and +0.036 eV and rival EE-EOM-CCSDTQ in accuracy. We can make similar observations in the results of the $^1\Pi_g$ state. The $^1\Sigma_u^+$ and $^1\Pi_u$ states are approximated by single determinants, and only marginal (< 0.1 eV) improvements relative to EE-EOM-CCSD are obtainable by EE-EOM-CCSDT. For the $^1\Sigma_u^+$ state, in particular, EE-EOM-CCSDt, EE-EOM-CCSDtq, and EE-EOM-CCSDTq all exhibit rapid convergence to the FCI results.

When the active space is extended to (2,7), all of the results of the active-space methods improve. However, the improvement is very small and in the order of 0.01 eV for the EE-EOM-CCSDt and EE-EOM-CCSDtq methods, and in the order of 0.001 eV for the EE-EOM-CCSDTq method, attesting to the effectiveness of the active-space methods with a minimum active space.

We have also examined the relative performance of various definitions of active-space triples and quadruples with active space (2,2). The EE-EOM-CCSDt(III) energies constitute no improvement over the EE-EOM-CCSD ones, while the EE-EOM-CCSDt(II) energies are in marginally closer agreement to the FCI values by 0.4–0.5 eV for excited states with two-electron character. This indicates that the use of “t(I)=t” ansatz for active-space triples is essential as “t(II)” can capture too small a portion of significant triples contributions and “t(III)” is even less meaningful. EE-EOM-CCSDt(I)-q(III), EE-EOM-CCSDt(II)-q(III), EE-EOM-CCSDt(III)-q(III), and EE-EOM-CCSDTq(III) simply reproduce the results of EE-EOM-CCSDt(I)=EE-EOM-CCSDt, EE-EOM-CCSDt(II), EE-EOM-CCSDt(III), and EE-EOM-CCSDT, respectively. The “q(III)” and hence also “q(IV)” variants of active-space quadruples are inadequate. The “q(II)” is the crudest meaningful approximation and is employed in EE-EOM-CCSDtq. The effectiveness of “q(I)=q” in EE-EOM-CCSDTq is already emphasized (see above).

B. Adiabatic Excitation Energies and Dipole Moments of the CH Radical. Table 2 compiles the adiabatic excitation

energies and dipole moments of low-lying excited states ($\tilde{a}^4\Sigma^-$, $\tilde{A}^2\Delta$, $\tilde{B}^2\Sigma^-$, and $\tilde{C}^2\Sigma^+$) of the CH radical. We have used the aug-cc-pVDZ and aug-cc-pVTZ^{67,68} basis sets with the frozen core approximation. The equilibrium bond lengths have been taken from experiment, and they are 1.1197868 Å,⁶⁹ 1.0977 Å,⁷⁰ 1.1031 Å,⁶⁹ 1.1640 Å,⁷¹ and 1.1143 Å⁷² for states $\tilde{X}^2\Pi$, $\tilde{a}^4\Sigma^-$, $\tilde{A}^2\Delta$, $\tilde{B}^2\Sigma^-$, and $\tilde{C}^2\Sigma^+$, respectively. The active space adopted is minimum, consisting of (2,2) for the α -spin orbitals and (1,3) for the β -spin orbitals. The symmetries of the active-space orbitals are a_1 , b_2 , b_1 , and a_1 for α -spin orbitals and a_1 , b_1 , a_1 , and b_2 for β -spin orbitals. The experimental values of excitation energies and dipole moments have been taken from refs 71–75.

For the $\tilde{a}^4\Sigma^-$ and $\tilde{A}^2\Delta$ states, the differences in excitation energies between EE-EOM-CCSD and EE-EOM-CCSDT are about 0.3 eV. EE-EOM-CCSDt yields the excitation energy within 0.1 eV of EE-EOM-CCSDT, recovering only $2/3$ of the contribution due to triples. The effect of quadruples is minimal, which is in the order of 0.01 eV. The marked decrease in the effectiveness of EE-EOM-CCSDt for these states is ascribed to the fact that the triples effects are better described as dynamical correlation, unsuitable to be treated by active-space triples. The dipole moments of these states obtained from EE-EOM-CCSD, EE-EOM-CCSDT, and EE-EOM-CCSDTQ are essentially identical. There is no indication that the active-space methods introduce significant errors. The accurate agreement between EE-EOM-CCSDt/aug-cc-pVDZ or EE-EOM-CCSDtq/aug-cc-pVDZ and experiment⁷⁴ is fortuitous.

In the excitation energies to the $\tilde{B}^2\Sigma^-$ and $\tilde{C}^2\Sigma^+$ states, the triples effects reach more than 1 eV, reflecting greater two-electron character of these states. The deviation between EE-EOM-CCSDt and EE-EOM-CCSDT is about 0.15 eV, and the former captures 88% of correlation due to triples. For $\tilde{C}^2\Sigma^+$, the deviation is 0.11 eV, and EE-EOM-CCSDt recovers 91% of correlation due to triples. Generally, the EE-EOM-CCSDt with an adequate minimum active space seems capable of exhausting nondynamical correlation due to triples (e.g., associated with two-electron character in excited states), leaving only dynamical correlation due to triples on the order of 0.1–0.2 eV with aug-cc-pVDZ for this molecule. The inclusion of active-space triples clearly

Table 3. Adiabatic Excitation Energies (T_e /eV) and Dipole Moments (μ /D) of the Ground State and the Lowest-Lying Singlet Excited State of Formaldehyde

state	theory	T_e	μ
1A_1	CCSD/aug-cc-pVDZ ^a	0.00	2.34
	CCSD/aug-cc-pVTZ ^a	0.00	2.38
	CCSDT/aug-cc-pVDZ ^a	0.00	2.33
	CCSDt/aug-cc-pVDZ	0.00	2.34
	Experiment	0.00	2.33 ^b
1A_2	EE-EOM-CCSD/aug-cc-pVDZ ^a	3.64	1.28
	EE-EOM-CCSD/aug-cc-pVTZ ^a	3.73	1.27
	EE-EOM-CCSDT/aug-cc-pVDZ ^a	3.49	1.48
	EE-EOM-CCSDt/aug-cc-pVDZ	3.49	1.43
	experiment	3.49 ^c	1.56 \pm 0.07 ^d

^a Reference 37. ^b Reference 77. ^c Reference 78. ^d Reference 79.

leads to improved agreement between calculated and observed^{71,72} excitation energies of these states.

When the basis set size is increased to aug-cc-pVTZ, EE-EOM-CCSDt becomes slightly less effective. For $\tilde{B}^2\Sigma^-$ and $\tilde{C}^2\Sigma^+$, the differences between EE-EOM-CCSDt and EE-EOM-CCSDT are 0.23 and 0.16 eV, respectively, with the active-space triples recovering 83 and 89% of correlation due to all triples. A similar observation can be made for active-space quadruples. This may be explained as follows. The greater fidelity in describing the dynamical correlation effects (but not necessarily the nondynamical ones) is afforded by larger basis sets. Hence the increase in basis set size widens the gap between the conventional method and its active-space counterparts, as the latter are limited in capturing dynamical correlation due to triples (and/or quadruples).

There are significant differences between EE-EOM-CCSD and EE-EOM-CCSDT in the dipole moments of the $\tilde{B}^2\Sigma^-$ and $\tilde{C}^2\Sigma^+$ states. They amount to 0.36 and 0.15 D, respectively. On the other hand, no difference can be seen between the EE-EOM-CCSDT and EE-EOM-CCSDTQ values. EE-EOM-CCSDt reduces these differences to 0.07 and 0.01 D for the $\tilde{B}^2\Sigma^-$ and $\tilde{C}^2\Sigma^+$ states with the aug-cc-pVDZ basis set and 0.1 and 0.01 D with the aug-cc-pVTZ basis set. The higher-order active-space EE-EOM-CC methods display equal (or even greater) effectiveness in recovering correlation effects on the excited-state dipole moments.

C. Adiabatic Excitation Energies and Dipole Moments of Formaldehyde. Next we examine the dipole moment of the ground (1A_1) state and the adiabatic excitation energy and dipole moment of the lowest-lying excited (1A_2) state of formaldehyde (Table 3). The planar equilibrium geometry of the ground state 1A_1 is $r_{CH} = 1.116$ Å, $r_{CO} = 1.208$ Å, and $a_{HCH} = 116.5^\circ$,⁷⁶ and the nonplanar equilibrium geometry of the 1A_2 state is $r_{CH} = 1.103$ Å, $r_{CO} = 1.323$ Å, $a_{HCH} = 118.1^\circ$, and CH_2 out-of-plane angle = 34.0° .⁷⁶ We have chosen (3,2) active space, and the frozen core approximation has been used. The symmetries of the active-space orbitals are $a_1, b_1, b_2, a_1,$ and b_2 for the planar geometry and $a', a', a'', a',$ and a' for the nonplanar geometry.

For the ground state, the CCSD and CCSDT dipole moments agree within 0.01 D, and the triples effect is essentially null. The CCSDt result is within 0.01 D of these

Table 4. Adiabatic Excitation Energies (in eV) to Low-Lying Excited States of the CH_2^a

	theory ^b	\tilde{a}^1A_1	\tilde{b}^1B_1	\tilde{c}^1A_1
EE-EOM-CCSD/aug-cc-pVDZ		0.48	1.57	3.72
EE-EOM-CCSDT/aug-cc-pVDZ		0.43	1.54	2.65
EE-EOM-CCSDt/aug-cc-pVDZ		0.45	1.56	2.81
EE-EOM-CCSDTQ/aug-cc-pVDZ		0.43	1.54	2.67
EE-EOM-CCSDtq/aug-cc-pVDZ		0.45	1.56	2.83
EE-EOM-CCSDTq/aug-cc-pVDZ		0.43	1.54	2.68
EE-EOM-CCSD/aug-cc-pVTZ		0.46	1.46	3.89
EE-EOM-CCSDT/aug-cc-pVTZ		0.41	1.43	2.53
EE-EOM-CCSDt/aug-cc-pVTZ		0.43	1.44	2.79

^a The ground state is \tilde{X}^3B_1 . ^b The EE-EOM-CC methods represent the corresponding CC methods for the \tilde{a}^1A_1 state.

two values and also of the experimental finding (2.33 D).⁷⁷ The adiabatic excitation energy to the 1A_2 undergoes a decrease of 0.15 eV upon inclusion of the triples by EE-EOM-CCSDT. EE-EOM-CCSDt recovers this downward shift accurately, which may indicate that this is caused by nondynamical correlation or the rearrangement of electrons in the active space. Although the basis set effect is still significant, the closer agreement between EE-EOM-CCSDT or EE-EOM-CCSDt and experiment (3.49 eV)⁷⁸ than EE-EOM-CCSD is meaningful. The excited-state dipole moment also increases from 1.28 to 1.48 D on going from EE-EOM-CCSD to EE-EOM-CCSDT. The EE-EOM-CCSDt predicts 1.43 D, recovering 3/4 of the triples effect, and in much closer agreement with experiment (1.56 \pm 0.07D).⁷⁹

D. Adiabatic Excitation Energies of CH_2 . Some of the low-lying singlet states of CH_2 are said to have diradical character,^{80–83} which warrants a high-order CC description. We have calculated the adiabatic excitation energies to the $\tilde{a}^1A_1, \tilde{b}^1B_1,$ and \tilde{c}^1A_1 states from the ground \tilde{X}^3B_1 state, which requires the methods that can handle transitions from open to closed shells such as the spin-orbital EE-EOM-CC methods developed in this work (Table 4). The geometries used are $r_e = 1.0775$ Å, $\theta_e = 133.29^\circ$ (\tilde{X}^3B_1); $r_e = 1.1089$ Å, $\theta_e = 101.89^\circ$ (\tilde{a}^1A_1); $r_e = 1.0748$ Å, $\theta_e = 141.56^\circ$ (\tilde{b}^1B_1); $r_e = 1.0678$ Å, $\theta_e = 170.08^\circ$ (\tilde{c}^1A_1).⁸³ The aug-cc-pVDZ and aug-cc-pVTZ basis sets^{67,68} have been used with the frozen core approximation. The active spaces are (2,3) for the singlet states and (3,2) for the α -spin orbitals and (1,4) for the β -spin orbitals of the triplet state. The symmetries of the active-space orbitals are $b_2, a_1, b_1, a_1,$ and b_2 for the singlet states and $b_2, a_1, b_1, a_1,$ and b_2 for α -spin orbitals and $b_2, a_1, b_2, a_1,$ and b_1 for β -spin orbitals of the triplet state.

The singlet–triplet separation of CH_2 , i.e., the energy difference between the \tilde{a}^1A_1 and \tilde{X}^3B_1 states, has been used to assess the accuracy of theoretical methods.^{81,84–86} These studies showed that CCSDT or its perturbative approximation CCSD(T) is the minimum level of theory for its quantitative description. Previously, we demonstrated that the CCSDt method with (3,3) or (2,2) active space is another inexpensive alternative to CCSDT with only a small penalty in accuracy (within 0.2 kcal/mol).⁴² The results in Table 4 reiterate the importance of the triples effect in the splitting in which the difference between CCSD and CCSDT is approximately -0.05 eV. However, unlike our previous CCSDt work,

CCSDt/aug-cc-pVnZ with (2,3) active space captures only 60% of the triples effect as opposed to 80–90% by CCSDt/cc-pVnZ with (3,3) or (2,2) active space.⁴² We have confirmed that this varied performance is simply the consequence of the diffuse functions of aug-cc-pVnZ basis sets that tend to make the low-lying unoccupied orbitals less suitable for active orbitals.

The \tilde{b}^1B_1 state is dominated by a single determinant, and hence the difference between EE-EOM-CCSD and EE-EOM-CCSDT in the excitation energy is less than 0.03 eV. The active-space methods nevertheless reduce the error but only slightly to 0.01–0.02 eV. The \tilde{c}^1A_1 state, on the other hand, can be viewed as a diradical, and the EE-EOM-CCSD excitation energy has an error in excess of 1 eV, which is characteristic of severe multideterminant character in the wave function. EE-EOM-CCSDt reduces this large error to mere 0.16 eV with the aug-cc-pVDZ basis set and to 0.26 eV with the aug-cc-pVTZ basis set. This also suggests that again the effectiveness of the active-space diminishes with increasing basis set sizes, and the remaining dynamical correlation on the order of 0.1–0.3 eV needs to be accounted for by other means. The quadruple effect is small and is about 0.02 eV. EE-EOM-CCSDTq can capture half of it.

E. Dissociation of Hydrogen Fluoride in the Excited 1A_1 State. One of the weaknesses of the active-space methods identified above is that its effectiveness declines with increasing basis set sizes. A larger basis set allows the nonactive-space methods to capture a greater proportion of dynamical correlation, but it does not benefit the active-space methods with fixed active-space sizes. Furthermore, the larger the basis set, the low-lying unoccupied orbitals become more diffuse, planewave-like, and less suitable as active orbitals. A remedy to this problem is to (variationally) optimize the orbitals in the active space, and such approaches in the context of CC theory have been reported, e.g., by Sherrill et al.⁶⁰ and by Krylov et al.^{61,62}

We propose a much simpler alternative of using a multiresolution composite method⁸⁶ which combines higher-rank active-space methods with smaller basis sets for nondynamical correlation and lower-rank nonactive-space methods with larger basis sets for dynamical correlation. This not only circumvents the undesirable basis-set dependence of the active-space methods but also reduces the overall computational cost. We apply the scheme to bond breaking of hydrogen fluoride in the first excited (1A_1) state, where the multideterminant effect is again prominent. The following formula has been used to approximate the total energy

$$E = E_{\text{CIS}(5Z)} + [E_{\text{CCSD}(QZ)} - E_{\text{CIS}(QZ)}] + [E_{\text{CCSD}_t(\text{TZ})} - E_{\text{CCSD}(\text{TZ})}] + [E_{\text{CCSD}_{tq}(\text{DZ})} - E_{\text{CCSD}_t(\text{DZ})}] \quad (28)$$

where subscripts and parentheses indicate the method (CCSD, CCSDt, etc. are understood to stand for EE-EOM-CCSD, EE-EOM-CCSDt, etc.) and basis sets (the cc-pVnZ series) with which individual energy components are computed. The active space consists of (3,1). The symmetries of the active-space orbitals are a_1 , b_1 , b_2 , and a_1 at bond length of 2.0 bohr and b_2 , b_1 , a_1 , and a_1 at bond lengths in the range of 3.0–9.0 bohr. The active space is essentially unchanged with bond lengths.

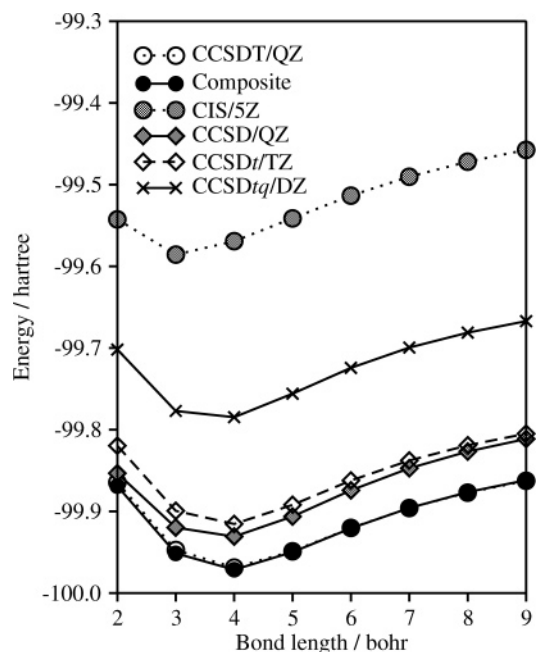


Figure 1. The energies of hydrogen fluoride in the first excited (1A_1) state as a function of bond length. The CCSD, CCSDt, etc. label the corresponding EE-EOM-CC calculations and the composite calculations are based on eq 28.

The potential energy curves obtained by this composite method as well as by some of its components are depicted in Figure 1. The accuracy of the composite method rivals that of the EE-EOM-CCSDT/cc-pVQZ method, which is considerably more expensive than the composite method, as attested by the close agreement between the two curves. It is also noticed that none of the energy components is remotely as close to the EE-EOM-CCSDT/cc-pVQZ curve as their composite. For instance, the deviation between EE-EOM-CCSD/cc-pVQZ, which is the best performing component in eq 28, and EE-EOM-CCSDT/cc-pVQZ ranges between 11 and 51 mE_h , while that between the composite method and EE-EOM-CCSDT/cc-pVQZ is no more than 5 mE_h anywhere. In addition, the EE-EOM-CCSD/cc-pVQZ curve is clearly nonparallel to the EE-EOM-CCSDT/cc-pVQZ curve at shorter bond lengths, which is not the case with the curve obtained by the composite method. These results support the tacit assumption underlying this method that the basis-set dependence of nondynamical correlation is small and the dynamical and nondynamical correlation energies are separable.

F. Vertical Ionization Energies of N_2 . The performance of the active-space IP-EOM-CC methods has been assessed by the calculation of the vertical ionization energies of N_2 (refs 30 and 31) (Table 5). The equilibrium bond distance 1.097685 Å has been taken from ref 72. The active space is (3,3), and the frozen core approximation has been used. The symmetries of the active-space orbitals are a_1 , b_2 , b_1 , b_2 , and a_1 .

The $\tilde{X}^2\Sigma_g^+$, $\tilde{A}^2\Pi_u$, and $\tilde{B}^2\Sigma_u^+$ states of N_2^+ are the so-called Koopmans states, and the IP-EOM-CCSD descriptions are already accurate. The contributions of triples (quadruples) with the cc-pVDZ basis set are -0.08 eV (-0.04 eV), -0.29 eV (-0.01 eV), and -0.11 eV (-0.08 eV), respectively, in

Table 5. Vertical Ionization Energies (in eV) of N₂

theory	$\tilde{X}^2\Sigma_g^+$	$\tilde{A}^2\Pi_u$	$\tilde{B}^2\Sigma_u^+$	$\tilde{C}^2\Sigma_u^+$
IP-EOM-CCSD/cc-pVDZ	15.18	16.93	18.47	28.78
IP-EOM-CCSDT/cc-pVDZ	15.10	16.64	18.36	25.28
IP-EOM-CCSDt-A/cc-pVDZ	15.13	16.66	18.42	25.74
IP-EOM-CCSDt-B/cc-pVDZ	15.07	16.61	18.33	25.24
IP-EOM-CCSDTQ/cc-pVDZ	15.06	16.63	18.28	24.99
IP-EOM-CCSDtq-A/cc-pVDZ	15.10	16.66	18.35	25.60
IP-EOM-CCSDtq-B/cc-pVDZ	15.03	16.60	18.26	24.99
IP-EOM-CCSDTq-A/cc-pVDZ	15.06	16.63	18.28	25.04
IP-EOM-CCSDTq-B/cc-pVDZ	15.06	16.63	18.28	24.99
IP-EOM-CCSD/cc-pVTZ	15.56	17.18	18.83	29.50
IP-EOM-CCSDT/cc-pVTZ	15.44	16.90	18.67	25.63
IP-EOM-CCSDt-A/cc-pVTZ	15.54	16.98	18.81	26.42
IP-EOM-CCSDt-B/cc-pVTZ	15.38	16.83	18.61	25.53
IP-EOM-CCSD/cc-pVQZ	15.68	17.28	18.94	29.71
IP-EOM-CCSDT/cc-pVQZ	15.55	16.99	18.77	25.76
IP-EOM-CCSDt-A/cc-pVQZ	15.66	17.10	18.93	26.73
IP-EOM-CCSDt-B/cc-pVQZ	15.47	16.90	18.70	25.63

the three states. The IP-EOM-CCSDt-A method captures a respectable portion of the triples, which are -0.05 eV, -0.27 eV, and -0.05 eV. The IP-EOM-CCSDt-B variant seems to work slightly better, although it tends to overshoot the triples contributions by 0.03 eV, at a significantly higher computational cost. Both IP-EOM-CCSDTq-A and -B reproduce the IP-EOM-CCSDTQ results. IP-EOM-CCSDtq-A and -B are equally effective in capturing the quadruples effects, but they retain the errors caused by the active-space treatment of triples. When the basis set is extended to cc-pVTZ and cc-pVQZ, IP-EOM-CCSDt-A approaches IP-EOM-CCSD in its performance, and IP-EOM-CCSDt-B becomes increasingly superior to IP-EOM-CCSDt-A as the latter adopts the more compact $R^{(N-1)}$ operator.

The $\tilde{C}^2\Sigma_u^+$ state is the destination of a satellite ionization transition with substantial triples effects, which amount to +3.50 eV, +3.87 eV, and +3.95 eV according to the calculations with the cc-pVDZ, cc-pVTZ, and cc-pVQZ basis sets, respectively. Both IP-EOM-CCSDt-A and -B methods capture a majority of the triples contributions, while the B variant is again distinctly superior to the A counterpart. With cc-pVDZ, IP-EOM-CCSDt-A is in error (from IP-EOM-CCSDT) by +0.46 eV, whereas IP-EOM-CCSDt-B is by only -0.04 eV. With larger basis sets, the gap in performance between the A and B variants widens. Essentially the same observation can be made for the active-space quadruples contributions. IP-EOM-CCSDtq-A incurs the error of +0.61 eV from IP-EOM-CCSDTQ, which can be minimized by IP-EOM-CCSDtq-B to 0.01 eV.

G. Vertical Electron Affinities of C₂. The electron affinities of C₂ pose perhaps the severest multideterminant problem for the EA-EOM-CC methods. The EA-EOM-CCSD method is known to predict incorrectly that the two lowest-lying excited states ($\tilde{A}^2\Pi_u$ and $\tilde{B}^2\Sigma_u^+$) of C₂⁻ are unstable toward autoionization and C₂⁻ can exist only in the ground state ($\tilde{X}^2\Sigma_g^+$).³⁵ In Table 6, we have compiled the active-space EA-EOM-CC results of the vertical electron affinities of C₂ computed at the equilibrium bond distance 1.243 Å (ref 72) with the aug-cc-pVDZ, aug-cc-pVTZ, and

Table 6. Vertical Electron Affinities (in eV) of C₂

theory	$\tilde{X}^2\Sigma_g^+$	$\tilde{B}^2\Sigma_u^+$	$\tilde{A}^2\Pi_u$
EA-EOM-CCSD/aug-cc-pVDZ	3.13	-1.64	-0.43
EA-EOM-CCSDT/aug-cc-pVDZ	3.00	0.62	1.84
EA-EOM-CCSDt-A/aug-cc-pVDZ	2.87	0.54	1.90
EA-EOM-CCSDt-B/aug-cc-pVDZ	2.87	0.57	1.93
EA-EOM-CCSDTQ/aug-cc-pVDZ	3.00	0.74	2.28
EA-EOM-CCSDtq-A/aug-cc-pVDZ	2.88	0.46	2.17
EA-EOM-CCSDtq-B/aug-cc-pVDZ	2.88	0.50	2.21
EA-EOM-CCSDTq-A/aug-cc-pVDZ	3.00	0.71	2.26
EA-EOM-CCSDTq-B/aug-cc-pVDZ	3.00	0.71	2.26
EA-EOM-CCSD/aug-cc-pVTZ	3.30	-1.39	-0.63
EA-EOM-CCSDT/aug-cc-pVTZ	3.17	0.69	1.95
EA-EOM-CCSDt-A/aug-cc-pVTZ	2.99	0.61	2.05
EA-EOM-CCSDt-B/aug-cc-pVTZ	3.00	0.64	2.08
EA-EOM-CCSD/aug-cc-pVQZ	3.35	-1.22	-0.69
EA-EOM-CCSDT/aug-cc-pVQZ	3.21	0.72	1.97
EA-EOM-CCSDt-A/aug-cc-pVQZ	3.02	0.63	2.07
EA-EOM-CCSDt-B/aug-cc-pVQZ	3.01	0.66	2.11

aug-cc-pVQZ basis sets and the frozen core approximation. The active space is (3,3). The symmetries of the active-space orbitals are a_u , b_u , b_u , a_g , a_u , and b_g for the aug-cc-pVDZ basis set and a_u , b_u , b_u , a_g , a_u , and a_g for aug-cc-pVTZ and QZ basis sets.

The electron affinity associated with the $\tilde{X}^2\Sigma_g^+$ state can be predicted reasonably accurately by either EA-EOM-CCSD or EA-EOM-CCSDT. Both EA-EOM-CCSDt-A and -B overshoot the triples effects. Consequently they do not necessarily reduce the differences in the electron affinity between EA-EOM-CCSD from EA-EOM-CCSDT, which are in the range of 0.13–0.14 eV. Again, this is because the active-space methods are not effective for dynamical correlation, which seems to constitute the majority of the triples effects of this state. The quadruples contribution in the electron affinity of this state is virtually null.

In the $\tilde{B}^2\Sigma_u^+$ state, the differences between EA-EOM-CCSD and EA-EOM-CCSDT are substantial, reaching 2.26 eV. The active-space methods reduce these differences to mere -0.09 eV (EA-EOM-CCSDt-A) and -0.06 eV (EA-EOM-CCSDt-B). The quadruples effect is relatively small, which is 0.12 eV, and the EA-EOM-CCSDtq-A and -B variants are not particularly useful. EA-EOM-CCSDTq-A and -B, however, reproduce EA-EOM-CCSDTQ within just 0.03 eV. A similar observation can be made to the $\tilde{A}^2\Pi_u$ state, except that the quadruples effect is more significant and amounts to 0.44 eV. EA-EOM-CCSDtq-A and -B capture 0.33 and 0.37 eV of this effect, respectively, which are about 80% of the quadruples effect. EA-EOM-CCSDTq-A and -B recover 0.42 eV or 95%.

V. Concluding Remarks

We have implemented and tested a wide range of approximations in the category of high-order active-space EOM-CC. They contain cluster and linear operators through quadruples for excited states, through four-hole-three-particle for ionized states, and through four-particle-three-hole for electron-attached states. The methods that include active-space triples of the type $t(I)=t$ and/or active-space quadruples

of the type $q(\text{I})=q$ or $q(\text{II})$ can reproduce the corresponding nonactive-space EE/IP/EA-EOM-CC methods for dominantly two-electron or higher-order transitions. The use of minimum active spaces in EE/IP/EA-EOM-CCSD t , EE/IP/EA-EOM-CCSD tq , or EE/IP/EA-EOM-CCSD Tq leads to accurate predictions for energies and related one-electron properties at a fraction of computational cost required in EE/IP/EA-EOM-CCSD T or EE/IP/EA-EOM-CCSD TQ . This article presents the most comprehensive exposition of this class of methods and their performance assessment, made possible by computerized symbolic algebra automating the formula derivation and implementations of the methods.

The active-space methods are found to be not as effective for the states that are already describable by EE/IP/EA-EOM-CCSD (e.g., within 0.1 eV of EE/IP/EA-EOM-CCSD T), where the triples effects are dynamical correlation. In a related note, the performance of the active-space methods gradually deteriorates with increasing basis set sizes. With a larger basis set, low-lying unoccupied orbitals become diffuse, planewave-like, and inadequate for active space. This undesirable basis-set dependence constitutes the most serious weakness of the active-space methods in the absence of any provision to optimize them such as those reported in refs 60–62. In this article, we have proposed and examined a much simpler alternative of using different basis sets for different methods or energy components. Our calculations on excited-state potential energy curves of hydrogen fluoride have demonstrated that nondynamical correlation effects can be isolated and are less sensitive to basis set sizes and can be described separately by the active-space methods with relatively small basis sets, while the dynamical correlation effects are treated by nonactive-space methods with more extensive basis sets.

Acknowledgment. This work has been supported by the National Science Foundation (CHE 0450462) and by the U.S. Department of Energy, Office of Basic Energy Sciences (DE-FG02-04ER15621). Some calculations were performed by using the Molecular Science Computing Facility in the William R. Wiley Environmental Molecular Sciences Laboratory, a national scientific user facility sponsored by the U.S. Department of Energy's Office of Biological and Environmental Research and located at the Pacific Northwest National Laboratory, operated for the Department of Energy by Battelle.

References

- (1) Coester, F. *Nucl. Phys.* **1958**, *7*, 421.
- (2) Coester, F.; Kümmel, H. *Nucl. Phys.* **1960**, *17*, 477.
- (3) Čížek, J. *J. Chem. Phys.* **1966**, *45*, 4256.
- (4) Čížek, J. *Adv. Chem. Phys.* **1969**, *14*, 35.
- (5) Emrich, K. *Nucl. Phys. A* **1981**, *351*, 379.
- (6) Emrich, K. *Nucl. Phys. A* **1981**, *351*, 397.
- (7) Sekino, H.; Bartlett, R. J. *Int. J. Quantum Chem. Symp.* **1984**, *18*, 255.
- (8) Geertsen, J.; Rittby, M.; Bartlett, R. J. *Chem. Phys. Lett.* **1989**, *164*, 57.

- (9) Comeau, D. C.; Bartlett, R. J. *Chem. Phys. Lett.* **1993**, *207*, 414.
- (10) Stanton, J. F.; Bartlett, R. J. *J. Chem. Phys.* **1993**, *98*, 7029.
- (11) Monkhorst, H. J. *Int. J. Quantum Chem. Symp.* **1977**, *11*, 421.
- (12) Ghosh, S.; Mukherjee, D.; Bhattacharyya, S. *Mol. Phys.* **1981**, *43*, 173.
- (13) Dalgaard, E.; Monkhorst, H. J. *Phys. Rev. A* **1983**, *28*, 1217.
- (14) Takahashi, M.; Paldus, J. *J. Chem. Phys.* **1986**, *85*, 1486.
- (15) Koch, H.; Jørgensen, P. *J. Chem. Phys.* **1990**, *93*, 3333.
- (16) Koch, H.; Jensen, H. J. A.; Jørgensen, P.; Helgaker, T. *J. Chem. Phys.* **1990**, *93*, 3345.
- (17) Rico, R. J.; Head-Gordon, M. *Chem. Phys. Lett.* **1993**, *213*, 224.
- (18) Nakatsuji, H.; Hirao, K. *Int. J. Quantum Chem.* **1981**, *20*, 1301.
- (19) Nakatsuji, H.; Ohta, K.; Hirao, K. *J. Chem. Phys.* **1981**, *75*, 2952.
- (20) Kucharski, S. A.; Włoch, M.; Musiał, M.; Bartlett, R. J. *J. Chem. Phys.* **2001**, *115*, 8263.
- (21) Watts, J. D.; Bartlett, R. J. *J. Chem. Phys.* **1994**, *101*, 3073.
- (22) Kowalski, K.; Piecuch, P. *J. Chem. Phys.* **2000**, *113*, 8490.
- (23) Kowalski, K.; Piecuch, P. *J. Chem. Phys.* **2001**, *115*, 643.
- (24) Piecuch, P.; Bartlett, R. J. *Adv. Quantum Chem.* **1999**, *34*, 295.
- (25) Del Bene, J. E.; Watts, J. D.; Bartlett, R. J. *J. Chem. Phys.* **1997**, *106*, 6051.
- (26) Nooijen, M.; Snijders, J. G. *Int. J. Quantum Chem. Symp.* **1992**, *26*, 55.
- (27) Nooijen, M.; Snijders, J. G. *Int. J. Quantum Chem.* **1993**, *48*, 15.
- (28) Stanton, J. F.; Gauss, J. *J. Chem. Phys.* **1994**, *101*, 8938.
- (29) Stanton, J. F.; Gauss, J. *J. Chem. Phys.* **1994**, *111*, 8785.
- (30) Musiał, M.; Kucharski, S. A.; Bartlett, R. J. *J. Chem. Phys.* **2003**, *118*, 1128.
- (31) Kamiya, M.; Hirata, S. *J. Chem. Phys.* **2006**, *125*, 074111.
- (32) Nooijen, M.; Bartlett, R. J. *J. Chem. Phys.* **1995**, *102*, 3629.
- (33) Nooijen, M.; Bartlett, R. J. *J. Chem. Phys.* **1995**, *102*, 6735.
- (34) Musiał, M.; Bartlett, R. J. *J. Chem. Phys.* **2003**, *119*, 1901.
- (35) Kamiya, M.; Hirata, S. *J. Chem. Phys.* **2007**, in press.
- (36) Musiał, M.; Bartlett, R. J. *Chem. Phys. Lett.* **2004**, *384*, 210.
- (37) Hirata, S. *J. Chem. Phys.* **2004**, *121*, 51.
- (38) Kállay, M.; Gauss, J. *J. Chem. Phys.* **2004**, *121*, 9257.
- (39) Oliphant, N.; Adamowicz, L. *Int. Rev. Phys. Chem.* **1993**, *12*, 339.
- (40) Piecuch, P.; Oliphant, N.; Adamowicz, L. *J. Chem. Phys.* **1993**, *99*, 1875.
- (41) Piecuch, P.; Adamowicz, L. *J. Chem. Phys.* **1994**, *100*, 5792.
- (42) Fan, P.-D.; Hirata, S. *J. Chem. Phys.* **2006**, *124*, 104108.
- (43) Kállay, M.; Surján, P. R. *J. Chem. Phys.* **2001**, *115*, 2945.

- (44) Kállay, M.; Szalay, P. G.; Gauss, J. *J. Chem. Phys.* **2002**, *117*, 980.
- (45) Kowalski, K.; Hirata, S.; Włoch, M.; Piecuch, P.; Windus, T. L. *J. Chem. Phys.* **2005**, *123*, 074319.
- (46) Slipchenko, V. L.; Krylov, I. A. *J. Chem. Phys.* **2005**, *123*, 084107.
- (47) Gour, J. R.; Piecuch, P.; Włoch, M. *J. Chem. Phys.* **2006**, *123*, 134113.
- (48) Gour, J. R.; Piecuch, P. *J. Chem. Phys.* **2006**, *125*, 234107.
- (49) Gour, J. R.; Piecuch, P.; Włoch, M. *Int. J. Quantum Chem.* **2006**, *106*, 2854.
- (50) Köhn, A.; Olsen, J. *J. Chem. Phys.* **2006**, *125*, 174110.
- (51) Hirata, S. *J. Phys. Chem. A* **2003**, *107*, 9887.
- (52) Hirata, S.; Fan, P.-D.; Auer, A. A.; Nooijen, M.; Piecuch, P. *J. Chem. Phys.* **2004**, *121*, 12197.
- (53) Hirata, S. *J. Chem. Phys.* **2005**, *122*, 094105.
- (54) Hirata, S. *Theor. Chem. Acc.* **2006**, *116*, 2.
- (55) Hirata, S.; Bartlett, R. J. *Chem. Phys. Lett.* **2000**, *321*, 216.
- (56) Hirata, S.; Nooijen, M.; Bartlett, R. J. *Chem. Phys. Lett.* **2000**, *326*, 255.
- (57) Kállay, M.; Surján, P. R. *J. Chem. Phys.* **2000**, *113*, 1359.
- (58) Olsen, J. *J. Chem. Phys.* **2000**, *113*, 7140.
- (59) Salter, E. A.; Trucks, G. W.; Bartlett, R. J. *J. Chem. Phys.* **1989**, *90*, 1752.
- (60) Sherrill, C. D.; Krylov, A. I.; Byrd, E. F. C.; Head-Gordon, M. *J. Chem. Phys.* **1998**, *109*, 4171.
- (61) Krylov, A. I.; Sherrill, C. D.; Byrd, E. F. C.; Head-Gordon, M. *J. Chem. Phys.* **1998**, *109*, 10669.
- (62) Krylov, A. I.; Sherrill, C. D.; Head-Gordon, M. *J. Chem. Phys.* **2000**, *113*, 6509.
- (63) Koch, H.; Kobayashi, R. J. A.; de Merás, A. S.; Jørgensen, P. *J. Chem. Phys.* **1993**, *100*, 4393.
- (64) Windus, T. L.; Pople, J. A. *Int. J. Quantum Chem. Suppl.* **1995**, *29*, 485.
- (65) NWChem, *A Computational Chemistry Package for Parallel Computers, version 4.7*; Straatsma, T. P.; Aprà, E.; Windus, T. L.; Bylaska, E. J.; de Jong, W.; Hirata, S.; Valiev, M.; Hackler, M. T.; Pollack, L.; Harrison, R. J.; Dupuis, M.; Smith, D. M. A.; Nieplocha, J.; Tipparaju, V.; Krishnan, M.; Auer, A. A.; Brown, E.; Cisneros, G.; Fann, G. I.; Fruchtl, H.; Garza, J.; Hirao, K.; Kendall, R.; Nichols, J. A.; Tsemekhman, K.; Wolinski, K.; Anchell, J.; Bernholdt, D.; Borowski, P.; Clark, T.; Clerc, D.; Dachsel, H.; Deegan, M.; Dyall, K.; Elwood, D.; Glendening, E.; Gutowski, M.; Hess, A.; Jaffe, J.; Johnson, B.; Ju, J.; Kobayashi, R.; Kutteh, R.; Lin, Z.; Littlefield, R.; Long, X.; Meng, B.; Nakajima, T.; Niu, S.; Rosing, M.; Sandrone, G.; Stave, M.; Taylor, H.; Thomas, G.; van Lenthe, J.; Wong, A.; Zhang, Z. Pacific Northwest National Laboratory, Richland, WA, 2005.
- (66) Christiansen, O.; Koch, H.; Jørgensen, P.; Olsen, J. *Chem. Phys. Lett.* **1996**, *256*, 185.
- (67) Dunning, T. H., Jr. *J. Chem. Phys.* **1989**, *90*, 1007.
- (68) Kendall, R. A.; Dunning, T. H., Jr.; Harrison, R. J. *J. Chem. Phys.* **1992**, *96*, 6796.
- (69) Zachwieja, M. *J. Mol. Spectrosc.* **1995**, *170*, 285.
- (70) Nelis, T.; Brown, J. M.; Evenson, K. M. *J. Chem. Phys.* **1990**, *92*, 4067.
- (71) Kepa, R.; Para, A.; Rytel, M.; Zachwieja, M. *J. Mol. Spectrosc.* **1996**, *178*, 189.
- (72) Huber, K. P.; Herzberg, G. *Molecular Spectra and Molecular Structure: Constants for Diatomic Molecules*; Van Nostrand Reinhold: New York, 1979.
- (73) Phelps, D. H.; Dalby, F. W. *Phys. Rev. Lett.* **1966**, *16*, 3.
- (74) Kasdan, A.; Herbst, E.; Lineberger, W. C. *Chem. Phys. Lett.* **1975**, *31*, 78.
- (75) Steimle, T. C.; Nachman, D. F.; Fletcher, D. A.; Brown, J. M. *J. Mol. Spectrosc.* **1989**, *138*, 222.
- (76) Takagi, K.; Oka, T. *J. Phys. Soc. Jpn.* **1963**, *18*, 1174.
- (77) Fabricant, B.; Krieger, D.; Muenter, J. S. *J. Chem. Phys.* **1977**, *67*, 1576.
- (78) Clouthier, D. J.; Ramsay, D. A. *Ann. Rev. Phys. Chem.* **1983**, *34*, 31.
- (79) Freeman, D. E.; Klemperer, W. *J. Chem. Phys.* **1966**, *45*, 52.
- (80) Yamaguchi, Y.; Sherrill, C. D.; Schaefer, H. F., III. *J. Phys. Chem.* **1996**, *100*, 7911.
- (81) Cramer, C. J.; Dulles, F. J.; Storer, J. W.; Worthington, S. E. *Chem. Phys. Lett.* **1994**, *218*, 387.
- (82) Bauschlicher, C. W.; Langhoff, S. R.; Taylor, P. R. *J. Chem. Phys.* **1987**, *87*, 387.
- (83) Sherrill, C. D.; Leininger, M. L.; Van Huis, T. J.; Schaefer, H. F., III. *J. Chem. Phys.* **1998**, *108*, 1040.
- (84) Van Huis, T. J.; Yamaguchi, Y.; Sherrill, C. D.; Schaefer, H. F., III. *J. Phys. Chem. A* **1997**, *101*, 6955.
- (85) Hoffman, B. C.; Yamaguchi, Y.; Schaefer, H. F., III. *J. Phys. Chem. A* **1999**, *103*, 1886.
- (86) Hirata, S.; Yanai, T.; Harrison, R. J.; Kamiya, M.; Fan, P.-D. *J. Chem. Phys.* **2007**, *126*, 024104.

CT600270C

Self-Consistent Strictly Localized Orbitals

Pierre-François Loos and Xavier Assfeld*

*Equipe de Chimie et Biochimie Théoriques, UMR 7565 CNRS-UHP,
Institut Jean Barriol (FR CNRS 2843), Faculté des Sciences et Techniques,
Nancy-Université, B.P. 239, 54506 Vandœuvre-lès-Nancy Cedex, France*

Received October 30, 2006

Abstract: Among all the Quantum Mechanics/Molecular Mechanics (QM/MM) methods available to describe large molecular systems, the Local Self-Consistent Field/MM (LSCF/MM) one uses frozen doubly occupied Strictly Localized Bonding Orbital (SLBO) to connect the QM fragment to the one treated at the MM level. This approach is correct as long as the QM part is large enough to minimize the artifacts that could arise because of the fixed SLBO. If one wants to decrease the size of the QM subsystem, one clearly needs to help the SLBO to relax according to the variations of the global wave function. Also, the SLBO have to adjust itself according to the modification of the surrounding if we want to improve the method. Here, we present a modification of the original LSCF method called Optimized LSCF (OLSCF) where each SLBO is allowed to mix with its corresponding Strictly Localized Anti Bonding Orbital (SLABO) resulting in an adjustment of the two-electron bond described by a self-consistent SLBO (SCSLBO). We test the new methodology against the modification of the QM part (internal perturbation) and against the variation of the surroundings (external perturbation) represented either by a dielectric continuum or by a classical point charge. In each case the initial SLBO is the symmetric C–C SLBO of the ethane molecule. It is shown that the optimized SCSLBO presents a final polarity in perfect agreement with what could be expected as the result of a reaction to the internal or external perturbation.

1. Introduction

During the past decade, the interest of theoreticians for macromolecular systems, or more globally large systems, has grown enormously. This is a direct consequence of the tremendous improvement of computers, both from the storage (memory and/or hard drive) and the CPU points of view. However, one has to bear in mind that studying chemical reactions in such systems (i.e. locating transition states) is still out of reach for the casual methods of quantum chemistry, despite the computer enhancement. To be able to treat such large molecular systems, the community of quantum chemists has developed new methods that combine different levels of theory. The total system is divided in several parts, each one described at a given level of theory. The levels of theory are chosen such that, for each part, the

most important physical phenomenon is correctly handled. Various schemes (combinations) are possible. For example, the part of the macromolecule undergoing the chemical reaction (generally few atoms) needs to be treated with high level (for example, correlated *ab initio*) techniques. This is called Quantum Mechanics (QM) level. The neighboring region, larger than the QM one, where consecutive reactions can take place—for example proton transfer rearrangement like in the bacteriorhodopsin molecule—can be described with a less time demanding method, typically a semiempirical one. Let us call this level QM' to avoid confusion with the former QM level. The remaining atoms of the macromolecule, which play a nontrivial and nonisotropic role by means of electrostatic and mechanic interactions, are often handled with Molecular Mechanics (MM) force fields. Finally the surrounding solvent can be included explicitly via a classical force field (MM') or implicitly using a

* Corresponding author e-mail: Xavier.Assfeld@cbt.uhp-nancy.fr.

polarizable continuum (Self-Consistent Reaction Field, SCRF). The combination of these four levels of theory gives rise to a QM/QM'/MM:MM' or QM/QM'/MM:SCRF method, if one uses the “/” symbol to represent the separation between two parts connected by a chemical bond and the “:” character when no chemical bond connects the two parts. One could of course think of more complicated combinations, but the most widely known and used schemes of hybrid method are certainly the QM/MM and the QM:MM ones.¹

Let us focus our attention on the methods that need the “/”, i.e. when covalent chemical bonds are formally cut to divide the system. Many solutions have been proposed and applied to circumvent the so-called dangling bond problem.^{2–13} If used carefully each scheme will correctly handle the connection between the two parts. We refer the interested reader to a recent review for further details.¹⁴ In this article we will restrain our discussion on the Local Self-Consistent Field combined with MM (LSCF/MM)^{15–18} way to treat such connection.

The connecting bond is described by a frozen doubly occupied Strictly Localized Bonding Orbital (SLBO). By frozen we mean that the expansion coefficients of the basis functions in the SLBO are kept constant during the wave function optimization (during the Self-Consistent Field (SCF) procedure). Trivially the SLBO is readjusted by rotation and renormalization if the geometry is changed during either a geometry optimization or a molecular dynamics step. Thanks to the transferability principle, the SLBO is generally obtained from a preliminary calculation on a small model molecule that possesses the chemical bond of interest. Freezing the SLBO implies that it is the same whatever the state of the QM part is. This can only be correct if the size of the QM part is large enough to reduce the interaction between the frozen SLBO and the global wave function to something negligible. It is a severe limitation if one is willing to perform reactive dynamic calculations, since the required CPU time will be enormous and unreachable with normal computer equipment. The corollary is that to have the size of the QM part reduced, it is necessary that the SLBO can relax somehow. In order to keep the QM size as small as possible we propose a modification of the LSCF method—based on quantum mechanics only (not of the hybrid LSCF/MM method yet)—called Optimized LSCF (OLSCF), in which the SLBOs can readjust themselves according to the variation of the global wave function (called internal perturbation) and to the variation of the surroundings (called external perturbation). The LSCF method needs SLBO, the OLSCF one produces Self-Consistent SLBO (SCSLBO).

This paper is organized as follows. Section 2 deals with the general principle of the method. The basic equations of the OLSCF method are established in section 3. Finally, some illustrative calculations are gathered in section 4 and discussed in the fifth section. Our aim is to prove that the OLSCF method is able to correctly represent the polarity variation of the SCSLBO when the surroundings change and that these changes are consistent with the general chemical sense, before adapting the new methodology to the QM/MM framework.

2. Principle

The LSCF method allows the optimization of a wave function at the Hartree–Fock level, or equivalently at the Kohn–Sham level in the Density Functional Theory (DFT) framework, knowing that some predefined (spin-)orbitals must remain unchanged. The predefined orbitals can be of any shape and occupied or not. Any post-HF method can follow the LSCF optimization. All orbitals are orthogonal.

Our aim is to allow SLBOs, expanded on the basis functions of the two atoms defining the bond, to remain strictly localized but to have some degrees of freedom to adjust themselves according to the surroundings. We decide to mix the doubly occupied SLBO to its corresponding empty Strictly Localized Anti-Bonding Orbital (SLABO). Hence, each connecting bond will be described with a doubly occupied SCSLBO that is a linear combination of the initial SLBO and SLABO, i.e. we give one electronic degree of freedom to the bond. To avoid the delocalization of the SCSLBO, we do not mutually orthogonalize the SLBOs nor the SLABOs. The variational Molecular Orbitals (MO) are mutually orthogonal and orthogonal to each {SLBO, SLABO} pair.

The mixing of the SLBO and the SLABO is not new. Many studies have been performed in the 1980s mainly by P. Surján,^{19–24} and even before in the 1960s and 1970s with the PCILO method of J.-P. Malrieu,^{25–27} and related methods.^{28–31} Here, we are less ambitious since only a few bonds, those connecting two parts described at different levels of theory, will be treated like that.

3. Theory

SLBO. Let us consider a closed shell system of $2n$ electrons treated with the spin restricted formalism, for simplicity. The generalization to the unrestricted case is trivial. We use a set of atom centered basis functions $\{|\phi_\mu\rangle\}_{\mu=1}^K$. Let say that L SLBOs $\{|l_i\rangle\}_{i=1}^L$ are considered, with $L < K$. They are developed onto the basis functions of the two atoms X_i and Y_i defining the bonds number i .

$$|l_i\rangle = \sum_{\mu \in X_i} a_{\mu i} |\phi_\mu\rangle + \sum_{\nu \in Y_i} a_{\nu i} |\phi_\nu\rangle \quad (1)$$

These SLBOs are obtained from usual localization procedures^{32–37} on small model molecules. The strict localization is attained by zeroing the coefficients of basis functions belonging to atom different from X_i or Y_i , if necessary.³⁸

They can be written in a shorter form introducing normalized hybrid orbitals (HO)

$$|l_i\rangle = a_{X_i} |h_i^{X_i}\rangle + a_{Y_i} |h_i^{Y_i}\rangle \quad (2)$$

where $h_i^{X_i}$ is a HO belonging to atom X_i and used in the i th SLBO l_i .

SLABO. The corresponding SLABOs, noted $\{|l_i^*\rangle\}_{i=1}^L$, can be obtained with different manners, and we list four of them below.

(1) They can be obtained the same way SLBOs are created with the usual localization techniques^{32–37} applied on the virtual orbitals of a small model molecule.

(2) However, as the size of the basis set increases, the number of virtual orbitals increases also, and the convergence of the localization is more difficult to achieve. In that case one can just project the SLBO found with a smaller basis (SB) set on the large basis (LB) set

$$|l_i^*\rangle_{\text{LB}} = \sum_{\mu, \nu}^{LB} |\phi_\mu\rangle (S^{-1})_{\mu\nu} \langle \phi_\nu | l_i^*\rangle_{\text{SB}} \quad (3)$$

where $S_{\mu\nu}$ is the overlap integral between the functions ϕ_μ and ϕ_ν of the large basis set.

(3) SLABOs can also be defined with the elaborate method proposed by M. Head-Gordon and co-workers.³⁹

(4) Finally, it is also possible to derive the antibonding orbital directly from the bonding one.^{20,40} The sign of the coefficients of the basis functions of one atom is reversed, and the resulting function is renormalized.

$$\begin{aligned} |l_i^*\rangle &= N_i^* (a_{X_i} |h_i^{X_i}\rangle - a_{Y_i} |h_i^{Y_i}\rangle) \\ &= a_{X_i}^* |h_i^{X_i}\rangle + a_{Y_i}^* |h_i^{Y_i}\rangle \end{aligned} \quad (4)$$

One has to note that for the first three possibilities, the SLBO and the corresponding SLABO are not developed over the same hybrid orbitals, whereas the fourth method expands the SLBO and the SLABO over the same two HOs.

In this article the two first procedures are used since they are easy to get and because they give more reliable results, based on preliminary calculations.

MO. To determine the variational MOs we use the same procedure as the one we developed for the LSCF method 10 years ago.¹⁵ The only exception is that the predefined orbitals (all pairs of SLBO and SLABO) are not orthogonal. First, we recall the steps followed in the LSCF method:

- Requirement: the MOs are orthogonal to the frozen orbitals (FOs). Hence, we expand the MO over basis functions that are already orthogonal to the FOs.

- Basis functions orthogonal to the FOs: each basis function ϕ_μ from the original basis set $\{|\phi_\mu\rangle\}_{\mu=1}^K$ is projected out of the subspace defined by the FOs. To have a simple expression of the projection operator, the FOs are mutually orthogonalized, generally by means of the Löwdin procedure

$$|\tilde{\phi}_\mu\rangle = [1 - \sum_i^L R_{\mu i}^2]^{-1/2} [|\phi_\mu\rangle - \sum_i^L |ol_i\rangle \langle ol_i | \phi_\mu\rangle] \quad (5)$$

where $R_{\mu i}$ is the overlap integral between the basis function ϕ_μ and the orthonormalized FO ol_i , $\langle \phi_\mu | ol_i\rangle$.

- Removing the linear dependencies: since L FOs were predefined, the new set of K basis functions has at least L linear dependencies. They are removed by means of the canonical orthogonalization procedure.⁴¹ The set of $(K - L)$ resulting basis functions is exactly what is needed to expand the MOs.

The only difference with the new OLSCF method is that to avoid the delocalization of the SLBOs and SLABOs we keep them strictly localized and thus possibly nonorthogonal. The projection operator is then modified

$$\begin{aligned} |\tilde{\phi}_\mu\rangle &= [1 - \sum_i^{2L} \sum_j^{2L} T_{\mu i} (D^{-1})_{ij} T_{\mu j}]^{-1/2} [|\phi_\mu\rangle - \\ &\quad \sum_i^{2L} \sum_j^{2L} |l_i\rangle (D^{-1})_{ij} \langle l_j | \phi_\mu\rangle] \end{aligned} \quad (6)$$

with D_{ij} being the overlap integral between the FOs l_i and l_j , $\langle l_i | l_j\rangle$, and $T_{\mu i}$ is the overlap integral between the basis function ϕ_μ and the FO l_i , $\langle \phi_\mu | l_i\rangle$. One has to note that here i and j run over the SLBOs and the SLABOs and that l_i can be a SLBO or a SLABO. This transformation can be done with the matrix M whose elements are given by

$$\begin{aligned} M_{\mu\nu} &= [1 - \sum_i^{2L} \sum_j^{2L} T_{\mu i} (D^{-1})_{ij} T_{\nu j}]^{-1/2} \\ &\quad [\delta_{\mu\nu} - \sum_i^{2L} \sum_j^{2L} \sum_\eta a_{\nu i} (D^{-1})_{ij} a_{\eta j} S_{\eta\mu}] \end{aligned} \quad (7)$$

where $\delta_{\mu\nu}$ is the Kronecker symbol, and $S_{\eta\mu}$ is the overlap integral between functions ϕ_η and ϕ_μ .

This projection is followed by the canonical orthogonalization to remove the $2L$ linear dependencies. The orthogonalization is performed with a matrix named X . The conjunction of these two steps lead to the definition of a matrix, named $B = MX$, that transforms the original basis set of K nonorthogonal functions into a set of $(K - 2L)$ functions mutually orthogonal and orthogonal to the SLBOs and SLABOs. This B matrix plays, for the OLSCF method, exactly the same role the Löwdin matrix ($X = S^{-1/2}$) plays in the SCF procedure.

The other point one has to take care of in the OLSCF (or LSCF) method is the definition of the density matrix. In the LSCF method, the density matrix (P^L) due to the occupied frozen orbitals must be added to the one resulting from the variational MOs (P^O) to give the total density matrix $P^T = P^L + P^O$. Here, thanks to the orthogonality of the MOs (mutually orthogonal and orthogonal to the strictly localized orbitals (SLOs)) the total density matrix can also be split into the two usual components P^O and P^L . However, due to the nonorthogonality of the SLOs the density matrix due to the occupied predefined orbital requires special attention. One matrix element of the P^L matrix is written as

$$P_{\mu\nu}^L = 2 \sum_j^L a_{\mu j} \tilde{a}_{\nu j} \quad (8)$$

where $\tilde{a}_{\nu j}$ are the expansion coefficients of the dual orbitals (DOs).²⁴

$$\tilde{a}_{\nu j} = \sum_i^{2L} a_{\nu i} (D^{-1})_{ij} \quad (9)$$

The DOs $\{|\tilde{l}_i\rangle\}_{i=1}^{2L}$ are orthogonal to the set of SLO $\{|l_i\rangle\}_{i=1}^{2L}$ ($\langle l_i | \tilde{l}_j\rangle = \delta_{ij}$), but the two sets are not mutually orthogonal $\langle l_i | l_j\rangle = D_{ij}$ and $\langle \tilde{l}_i | \tilde{l}_j\rangle = \tilde{D}_{ij}$. The SLOs and the DOs form a biorthogonal basis set.⁴² Although it is possible to express the energy and the Roothaan equation as functions of the initial nonorthogonal orbitals,⁴³ it requires a lot of modifications of the existing code. However, the DOs

propose a very simple form very close to the usual one. With the definition of the density matrix given above (eq 8) the Fock matrix elements and the electronic energy can be obtained with the traditional formula (the nonorthogonality is hidden in the density matrix)

$$F_{\mu\nu} = H_{\mu\nu}^c + \sum_{\lambda,\sigma} P_{\lambda\sigma}^T \left[(\mu\nu|\lambda\sigma) - \frac{1}{2}(\mu\sigma|\lambda\nu) \right] \quad (10)$$

$$E = \sum_{\mu,\nu} P_{\mu\nu}^T H_{\mu\nu}^c + \frac{1}{2} \sum_{\mu,\nu} \sum_{\lambda,\sigma} P_{\mu\nu}^T P_{\lambda\sigma}^T \left[(\mu\nu|\lambda\sigma) - \frac{1}{2}(\mu\sigma|\lambda\nu) \right] \quad (11)$$

where we have used the usual notation for the various integrals. Equation 11 is equivalent to half the trace of the matrix product ($\mathbf{P}^T(\mathbf{H}+\mathbf{F})$). At this point we have all the tools to obtain the MOs.

SCSLBO. For each pair (l_i, l_i^*) composed of a SLBO and its corresponding SLABO expanded over the basis functions of the two atoms defining the connecting bond, we build a 2×2 Fock matrix

$$\begin{pmatrix} \langle l_i | \hat{F} | l_i \rangle & \langle l_i^* | \hat{F} | l_i \rangle \\ \langle l_i | \hat{F} | l_i^* \rangle & \langle l_i^* | \hat{F} | l_i^* \rangle \end{pmatrix} \quad (12)$$

with

$$\langle l_i | \hat{F} | l_i \rangle = \sum_{\mu,\nu} a_{\mu i} a_{\nu i} F_{\mu\nu} \quad (13)$$

where $F_{\mu\nu}$ comes from eq 10.

This matrix is transformed in a basis where the SLBO is orthogonal to the SLABO, with either a Löwdin or a Gram-Schmidt orthogonalization and further diagonalized. The two eigenvectors correspond to the new SLBO and SLABO that we call SCSLOs. From these new functions a new density matrix \mathbf{P}^L can be formed and new MOs can be sought. The whole process is conducted until convergence is reached. It is summarized in the algorithm given below.

Algorithm. We have implemented this method in our modified version of the package Gaussian 03.⁴⁴

(1) Determine the SLBOs and SLABOs on model molecules. Orthogonalize the SLABO to its SLBO, with the Löwdin or the Gram-Schmidt method.

(2) Orthogonalize the basis functions with respect to all SLOs, i.e. build the matrix \mathbf{M} .

(3) Perform the canonical orthogonalization of the new basis set with the matrix \mathbf{X} .

(4) Get an initial guess of the density matrix.

(5) Build in the Fock matrix \mathbf{F} .

(6) Transform \mathbf{F} in the orthogonal basis: $\mathbf{F}' = \mathbf{B}' \mathbf{F} \mathbf{B}$.

(7) Diagonalize \mathbf{F}' : $\epsilon = \mathbf{C}' \mathbf{F}' \mathbf{C}'$ where ϵ is the diagonal $(K-2L) \times (K-2L)$ matrix of the eigenvalues.

(8) Backtransform in the original basis: $\mathbf{C} = \mathbf{B} \mathbf{C}'$.

(9) Compute the density matrix due to the MOs, \mathbf{P}^Q .

(10) Diagonalize the 2×2 Fock matrix, for each (l_i, l_i^*) pair to get the SCSLOs.

(11) Compute the density matrix due to the SCSLBOs, \mathbf{P}^L .

Table 1. Half Mulliken Electronic Population of the C–C Bond Orbitals (in Electron) of the Carbon Atom Bonded to the X Ligand in the CH_3CX_3 Molecules (i.e. Bond Polarity)^c

X	Pipek-Mezey			Boys-Foster	
	HF/6-31G*	HF/6-311G** ^a	HF/6-311G** ^b	HF/6-31G*	HF/6-311G** ^b
SCSLBO					
H	0.500	0.500	0.500	0.500	0.500
Li	0.479	0.481	0.472	0.490	0.484
BH ₂	0.521	0.519	0.529	0.504	0.507
CH ₃	0.529	0.524	0.539	0.509	0.516
NH ₂	0.559	0.553	0.576	0.524	0.539
OH	0.586	0.581	0.612	0.538	0.560
F	0.592	0.594	0.621	0.545	0.571
SLBO					
H	0.500	0.500	0.500	0.500	0.500
Li	0.415	0.460	0.460	0.430	0.475
BH ₂	0.518	0.544	0.544	0.519	0.548
CH ₃	0.498	0.529	0.529	0.498	0.529
NH ₂	0.527	0.580	0.580	0.524	0.575
OH	0.546	0.579	0.579	0.544	0.574
F	0.523	0.559	0.559	0.515	0.553

^a SLABO obtained at the HF/6-311G**. ^b SLABO obtained at the HF/6-31G* and projected on the 6-311G** basis set. ^c The SCSLBOs result from an OLSCF calculation. Their polarities are given in the upper part of the table. The SLBOs are obtained as usual (see the Theory section) after a traditional SCF calculation. Their polarities are given in the lower part of the table.

(12) Compute $\mathbf{P}^T = \mathbf{P}^Q + \mathbf{P}^L$.

(13) Exit test. If not satisfied go back to step 5.

4. Test Results

In order to show that with our new formalism a given SLBO can adjust itself with respect to either an internal modification or to the surroundings variation we perform three series of calculations.

For the first one, we consider the $\text{H}_3\text{C}-\text{CX}_3$ molecules ($\text{X}=\text{H}, \text{Li}, \text{BH}_2, \text{NH}_3, \text{OH}, \text{F}$) for which the initial SLBO and SLABO are determined on the ethane molecule. Two levels of theory (HF/6-31G* and HF/6-311G**) and two localization schemes (Boys-Foster,³² BF, and Pipek-Mezey,³³ PM) are considered. The polarity (P) of the optimized SCSLBO is represented as half the electronic population (q) due to this SCSLBO on the carbon atom connected to the X substituents (C_X) computed with the Mulliken partitioning.⁴⁵

$$P = \frac{q_{C_X}}{2} = \sum_{\mu} \sum_{\nu}^{\in C_X \text{ AO}} c_{\mu i} c_{\nu i} S_{\mu\nu} \quad (14)$$

For comparison, the polarity of the SLBO obtained with the BF or PM a posteriori criterion on a SCF optimized wave function is also provided. The geometries were optimized at the SCF level. The polarities are gathered in Table 1.

The second series is concerned with the influence of the solvent. The solvent is represented by a polarizable continuum with the help of the SCRf method developed previously in our group.^{46,47} The initial SLBO is determined on the ethane molecule at the B3LYP/6-311++G** level of theory with the help of the PM localization scheme and

Table 2. Half Mulliken Electronic Population (in Electron) of the Carbon Atom Bearing the NH₂ Group in the β -Alanine Molecule (i.e. Bond Polarity), Due to the SCSLBO and to the SLBO(PM)^a

form	phase	SCSLBO	SLBO(PM)
neutral	gas	0.495	0.501
	solvent	0.495	0.493
zwitterionic	gas	+0.0004	-0.0079
	solvent	0.553	0.637
	Δ	-0.0246	-0.0854

^a Δ is the difference of polarity between the solvent and the gas phases.

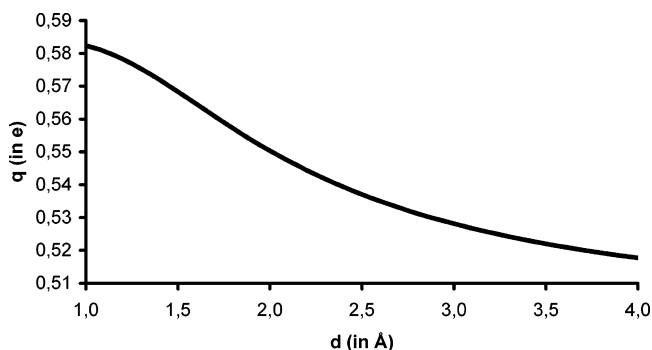


Figure 1. Half Mulliken electronic population (q , in electron) of the carbon atom nearest to the classical point charge due to the SCSLBO (i.e. bond polarity), as a function of the distance (d , in Å) between the positive point charge and the nearest carbon atom of the ethane molecule. The point charge is placed on the line defined by the two carbon atoms.

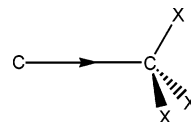
transferred on the central C–C bond of the β -alanine molecule in its neutral and zwitterionic forms, H₂N–CH₂–CH₂–COOH and H₃N⁺–CH₂–CH₂–COO⁻, respectively. Calculations are performed in the gas phase and in solution at the B3LYP/6-311++G** level of theory. The geometries are optimized at this same level in solvent phase only and without frozen orbital. The polarities of the SCSLBO are given in Table 2. For comparison purposes, pure B3LYP/6-311++G** calculations are carried out and followed by a PM localization procedure to obtained SLBOs. The polarity of the SLBO of the central C–C bond is given in Table 2. Polarities correspond to half the electronic population, arising from the SLO, of the carbon atom bearing the NH₂ group.

Finally, the effect of a surrounding classical point charge ($q = +|e|$) is studied in the third series, to anticipate QM/MM calculations. The chosen molecule is ethane. The starting SLBO comes from a preceding calculation on the C₂H₆ molecule at the HF/6-311G** level of theory with the PM criterion. The point charge is placed on the line defined by the two carbon atoms. The distance between the point charge and the nearest carbon atom is varied from 1 to 4 Å. The polarity of the SCSLBO, represented as half the electronic population due to this SCSLBO of the C atom nearest to the point charge, is sketched in Figure 1.

5. Discussion

From the results presented in Table 1, one can readily extract that the polarity (i.e. half the electronic population, due to

Scheme 1. Polarization of the C–C SLBO by the Electronegative Substituents X



the SCSLBO only, of the carbon atom connected to the X substituents) increases when the electronegativity of the substituent increases. This result is in perfect agreement with the usual “chemical sense” (see Scheme 1). Although not exactly identical, this trend is the same whatever the level of theory is (double- or triple- ζ), whatever the localization criterion is (BF or PM), and whatever the SLBO is (projected from double- ζ or not). However, it seems that the PM SLOs give a larger polarization than the BF ones.

To have a point of comparison, we run traditional SCF calculations on all molecules, and we determine the C–C Localized Molecular Orbital (LMO) for each molecule with either the PM or the BF criterion at all levels of theory. These LMOs were further transformed in SLBOs, and their polarities are given in the second part of Table 1. If one compares the polarity of the SCSLBO with the one obtained for the SLBO, one can remark that the values are quite similar although not identical. The increase of the electronic population with the increasing electronegativity of the ligands, for the SLBO, is not as straight as it is for SCSLBO. For SLBO, the polarity seems to drop down for the CH₃ and the F ligand. This is due to the fact that these SLBOs are obtained by rotation of all the occupied molecular orbitals of the molecule and thus reflect the global effect of the ligands on the total wave function. Of course this effect cannot be fully reproduced by the polarity of just one function even if it is a SCSLBO. Anyway, we can conclude that the SCSLBOs correctly show the expected trend and that they adequately adjust themselves according to the chemical modification of the molecule.

The values given in Table 2 show that the SCSLBO and the SLBO are not much modified by the solvent effects for the neutral form of the β -alanine molecule. The difference of electronic population between the gas and the solvent phase is small in both cases. For the zwitterionic molecule, the electronic polarization induced by the solvent is at least ten times stronger than for the neutral isomer. We can put that in parallel with the electrostatic solvation free energy that is also small for the neutral form, 14.5 kcal·mol⁻¹, compared to the one of the zwitterionic form, 59.7 kcal·mol⁻¹. The polarization of the SCSLBO is less than the one of the SLBO, albeit both present the same tendency. Again, this discrepancy can be attributed to the global character of the SLBO and to the local nature of the SCSLBO. Anyway, it is shown that the SCSLBO reacts correctly with respect to the perturbation of an external electric field (here produced by the dielectric continuum).

Finally, before the adaptation of the OLSCF scheme to the QM/MM formalism, we decide to focus our attention to the action of a classical charge on the polarity of the SCSLBO. One can see (Figure 1) that the stronger the interaction, i.e. the shorter the distance between the classical

charge and the molecule, the stronger the polarization of the SCSLBO. That is exactly what could be expected and is encouraging for the future implementation in a QM/MM framework.

6. Conclusion

In this first step, we propose a modification of the LSCF method—based on quantum mechanics only (not the LSCF/MM hybrid method)—which allows the relaxation of strictly localized bonding orbitals according to the variation of the surroundings and/or of the quantum state. The new method is named Optimized LSCF (OLSCF). For each SLBO, a SLABO is defined, and the mixing of these two functions gives the electronic degree of freedom responsible for the relaxation of the orbital. The new methodology is tested against the modification of the molecule itself, against the influence of the surrounding solvent (modeled by means of a polarizable continuum), and against the presence of a classical point charge. In all three cases investigated here, it is shown that the SCSLBOs properly adjust themselves to the situation. According to these encouraging results, we will further apply our new technique to the QM/MM formalism and to the QM/QM' method in forthcoming papers.

Acknowledgment. P.-F.L. and X.A. are deeply indebted to Professor Jean-Louis Rivail for the initial idea leading to this new development and for many fruitful discussions.

References

- Moreau, Y.; Assfeld, X. In *Lecture Series on Computer and Computational Sciences*; Maroulis, G., Simos, T., Eds.; Koninklijke Brill NV: Leiden, The Netherlands, 2005; Vol. 3, pp 1–9.
- Ranganathan, S.; Gready, J. E. *J. Phys. Chem. B* **1997**, *101*, 5614–5618.
- Cummins, P. L.; Gready, J. E. *J. Phys. Chem. B* **2000**, *104*, 4503–4510.
- Das, D.; Eurenium, K. P.; Billings, E. M.; Sherwood, P.; Chatfield, D. C.; Hodoscek, M.; Brooks, B. R. *J. Chem. Phys.* **2002**, *117*, 10534–10547.
- Maseras, F.; Morokuma, K. *J. Comput. Chem.* **1995**, *16*, 1170–1179.
- Zhang, Y.; Lee, T.-S.; Yang, W. *J. Chem. Phys.* **1999**, *110*, 46–54.
- Antes, I.; Thiel, W. *J. Phys. Chem. A* **1999**, *103*, 9290–9295.
- DiLabio, G. A.; Hurley, M.; Christiansen, P. A. *J. Chem. Phys.* **2002**, *116*, 9578–9584.
- Gao, J.; Amara, P.; Alhambra, C.; Field, M. J. *J. Phys. Chem. A* **1998**, *102*, 4714–4721.
- Pu, J.; Gao, J.; Truhlar, D. G. *J. Phys. Chem. A* **2004**, *108*, 632–650.
- Lin, H.; Truhlar, D. G. *J. Phys. Chem. A* **2005**, *109*, 3991–4004.
- Kairys, V.; Jensen, J. H. *J. Phys. Chem. A* **2000**, *104*, 6656–6665.
- Murphy, R. B.; Philipp, D. M.; Friesner, R. A. *J. Comput. Chem.* **2000**, *21*, 1442–1457.
- Lin, H.; Truhlar, D. G. *Theor. Chem. Acc.* **2007**, *117*, 185–199.
- Assfeld, X.; Rivail, J.-L. *Chem. Phys. Lett.* **1996**, *263*, 100–106.
- Ferré, N.; Assfeld, X.; Rivail, J.-L. *J. Comput. Chem.* **2002**, *23*, 610–624.
- Moreau, Y.; Loos, P.-F.; Assfeld, X. *Theoret. Chem. Acc.* **2004**, *112*, 228–239.
- Fornili, A.; Loos, P.-F.; Sironi, M.; Assfeld, X. *Chem. Phys. Lett.* **2006**, *427*, 236–240.
- Surján, P.; Mayer, I. *Theor. Chim. Acta* **1981**, *59*, 603–607.
- Mayer, I.; Surján, P. *J. Chem. Phys.* **1984**, *80*, 5649–5658.
- Surján, P.; Révész, M.; Mayer, I. *J. Chem. Soc., Faraday Trans. 2* **1981**, *77*, 1129–1131.
- Surján, P. *J. Mol. Struct. (THEOCHEM)* **1988**, *169*, 95–104.
- Surján, P. *Chem. Phys. Lett.* **1985**, *117*, 386–388.
- Surján, P. *Chem. Phys. Lett.* **1982**, *92*, 483–485.
- Diner, S.; Malrieu, J.-P.; Clavery, P. *Theor. Chim. Acta* **1969**, *13*, 1–17.
- Malrieu, J.-P.; Clavery, P.; Diner, S. *Theor. Chim. Acta* **1969**, *13*, 18–45.
- Malrieu, J.-P. In *Semiempirical methods in electronic structure calculation*; Segal, G. A., Ed.; Plenum: New York, 1977.
- Kvasnika, V. *Theor. Chim. Acta* **1974**, *34*, 61–65.
- Cullen, J. M.; Zerner, M. C. *Int. J. Quantum Chem.* **1982**, *22*, 497–535.
- Boča, A. *Theor. Chim. Acta* **1982**, *61*, 179–192.
- Barone, V.; Douady, J.; Ellinger, Y.; Subra, R. *J. Chem. Soc., Faraday Trans. 2* **1979**, *75*, 1597–1611.
- Foster, J. M.; Boys, S. F. *Rev. Mod. Phys.* **1960**, *32*, 300–302.
- Pipek, J.; Mezey, P. *J. Chem. Phys.* **1989**, *90*, 4916–4926.
- Weinstein, H.; Pauncz, R.; Cohen, M. In *Advances in Atomic and Molecular Physics*; Academic Press: New York, 1971; Vol. 7, p 97.
- Magnasco, V.; Perico, A. *J. Chem. Phys.* **1972**, *47*, 971–981.
- Fornili, A.; Moreau, Y.; Sironi, M.; Assfeld, X. *J. Comput. Chem.* **2006**, *27*, 515–523.
- Fornili, A.; Sironi, M.; Raimondo, M. *J. Mol. Struct. (THEOCHEM)* **2003**, *632*, 157–172.
- Functions obtained with the ELMO method³⁷ are already strictly localized.
- Subotnik, J. E.; Head-Gordon, M. *J. Chem. Phys.* **2005**, *122*, 034109.
- Reed, A. E.; Curtiss, L. A.; Weinhold, F. *Chem. Rev.* **1988**, *88*, 899–926.
- Szabo, A.; Ostlund, N. S. *Modern Quantum Chemistry: Introduction to Advanced Structure Theory*; Dover Publications Inc.: Mineola, NY, 1989; p 144.
- McDouall, J. J. W. *Theor. Chim. Acta* **1992**, *83*, 339–350.
- Stoll, H.; Wagenblast, G.; Preuss, H. *J. Am. Chem. Soc.* **1978**, *100*, 7742–7743.

- (44) *Gaussian 03, Revision C.03*; Frisch, M. J.; Trucks, G. W.; Schlegel, H. B.; Scuseria, G. E.; Robb, M. A.; Cheeseman, J. R.; Montgomery, J. A., Jr.; Vreven, T.; Kudin, K. N.; Burant, J. C.; Millam, J. M.; Iyengar, S. S.; Tomasi, J.; Barone, V.; Mennucci, B.; Cossi, M.; Scalmani, G.; Rega, N.; Petersson, G. A.; Nakatsuji, H.; Hada, M.; Ehara, M.; Toyota, K.; Fukuda, R.; Hasegawa, J.; Ishida, M.; Nakajima, T.; Honda, Y.; Kitao, O.; Nakai, H.; Klene, M.; Li, X.; Knox, J. E.; Hratchian, H. P.; Cross, J. B.; Bakken, V.; Adamo, C.; Jaramillo, J.; Gomperts, R.; Stratmann, R. E.; Yazyev, O.; Austin, A. J.; Cammi, R.; Pomelli, C.; Ochterski, J. W.; Ayala, P. Y.; Morokuma, K.; Voth, G. A.; Salvador, P.; Dannenberg, J. J.; Zakrzewski, V. G.; Dapprich, S.; Daniels, A. D.; Strain, M. C.; Farkas, O.; Malick, D. K.; Rabuck, A. D.; Raghavachari, K.; Foresman, J. B.; Ortiz, J. V.; Cui, Q.; Baboul, A. G.; Clifford, S.; Cioslowski, J.; Stefanov, B. B.; Liu, G.; Liashenko, A.; Piskorz, P.; Komaromi, I.; Martin, R. L.; Fox, D. J.; Keith, T.; Al-Laham, M. A.; Peng, C. Y.; Nanayakkara, A.; Challacombe, M.; Gill, P. M. W.; Johnson, B.; Chen, W.; Wong, M. W.; Gonzalez, C.; Pople, J. A. Gaussian, Inc.: Wallingford, CT, 2004.
- (45) Mulliken, R. S. *J. Chem. Phys.* **1955**, *23*, 1833–1840.
- (46) Rinaldi, D.; Bouchy, A.; Rivail, J.-L.; Dillet, V. *J. Chem. Phys.* **2004**, *120*, 2343–2350.
- (47) Rinaldi, D.; Bouchy, A.; Rivail, J.-L. *Theor. Chem. Acc.* **2006**, *116*, 664–669.

CT6003214

The Hydrated Electron as a Pseudo-Atom in Cavity-Bound Water Clusters

Alexis Taylor,[†] Chérif F. Matta,^{†,‡} and Russell J. Boyd^{*,†}

*Department of Chemistry, Dalhousie University, Halifax, NS, Canada B3H 4J3, and
Department of Chemistry and Physics, Mount Saint Vincent University,
Halifax, NS, Canada B3M 2J6*

Received November 9, 2006

Abstract: Anionic water clusters, $(\text{H}_2\text{O})_n^-$, of various sizes, $n = 1-8$, have been investigated using high-level ab initio calculations and the quantum theory of atoms in molecules, which provides a topological analysis of the electron density. The results of the current study indicate that the distribution of the excess electron is dependent on the geometry of the cluster. Non-nuclear attractors (NNAs), with associated pseudo-atomic basins and populations, are observed only in the highly symmetric clusters in which several non-hydrogen-bonded (NHB) hydrogen atoms are oriented toward a central cavity. For the latter cases, the non-nuclear attractor can be considered a pseudo-atom, possessing a significant portion of the excess electron within the cavity, consistent with the cavity-bound model of the solvated electron. In some cases, the population of the NNA is more than 0.2 electrons, and it contributes in excess of 20 kJ/mol to the energy of the system. Furthermore, the less symmetric systems, which tend to orient the NHB hydrogen atoms away from the center of the cluster, tend to delocalize the excess electron to a greater extent over several atoms at the surface of the cluster, consistent with the surface-bound model of the excess electron.

I. Introduction

While the solvated electron in water has been the focus of many experimental and theoretical studies, the microscopic structure of this species remains the subject of intense theoretical and experimental interest.¹⁻³¹ Water is the universal solvent; it is ubiquitous throughout our natural environment, from biological systems to interstellar space. For instance, hydrated electrons (anionic water clusters) are known to react with O_2 to produce the superoxide anion, O_2^- .^{32,33} This reaction can occur in various conditions, in clouds, where O_2^- can destroy ozone,³⁴ to biological systems, where O_2^- is involved in cell death, aging, and various disease processes.³⁵ Given that anionic water has such a profound influence on a large variety of systems, a thorough understanding of its properties and behavior is essential.

As early as 1810, Humphry Davy observed that, when alkali metals are exposed to ammonia, the resulting solution has an intense blue color. The following century saw a great deal of research that focused on this phenomenon and sought to determine the cause. Although it was well-established that these solutions behave as electrolytes, possessing high conductivity and magnetic susceptibility,³⁶ it was not until nearly 100 years after Davy's observations that Kraus suggested that the solutions contain sodium cations and free electrons,³⁷ and that the latter are responsible for the intense color.

The discovery of solvated electrons in ammonia solutions led naturally to the assumption that solvated electrons might be observed in water. Indeed, water's larger dipole moment and stronger hydrogen-bonding capability facilitate the ionization of metals. However, it was another 50 years before hydrated electrons were generated by pulse radiolysis and observed in water.³⁸⁻⁴⁰ In addition, it was found that this species was highly reactive and could be destroyed through

* Corresponding author e-mail: Russell.Boyd@dal.ca.

[†] Dalhousie University.

[‡] Mount Saint Vincent University.

various processes. For example, free electrons are easily removed from solution by recombination with the protons produced from the autoionization of water. Thus, the hydrated electron exhibits a short, pH-dependent lifetime.⁴¹

Subsequent studies by Haberland and co-workers^{27–30} established that the hydrated electron was not only produced in bulk solvent but also in clusters of a finite size, forming anionic water clusters, $(\text{H}_2\text{O})_n^-$. Furthermore, water molecules in small clusters do not experience autoionization as tends to occur in bulk solvent, and thus the lifetime of the hydrated electron should be greater in these small clusters. This distinction proved advantageous for investigations into the nature of the hydrated electron, which has since been studied extensively both experimentally and theoretically (see Beyer et al.¹² and references therein).

Many methods are employed to generate solvated electrons: injection of energetic electrons into the solvent,^{38–40} photoionization of water or a suitable precursor by ultraviolet radiation,^{22,41–43} interaction of alkali metal surfaces with water,⁴⁴ supersonic expansion to generate neutral clusters followed by irradiation with a low-energy electron beam to generate the anions,^{45,46} and laser vaporization.^{12,47} Furthermore, several spectroscopic methods may be employed to detect the solvated electrons once they are generated, such as photoelectron and infrared spectroscopy and mass spectrometry. However, while there are many experimental methods available to produce hydrated electrons, and several techniques to detect them, the problem that remains is how to determine the exact structure, and consequently the nature, of the hydrated electron. Is the excess electron density largely localized to a region of space within the water clusters or is it smeared out and distributed over the electronegative oxygen atoms?

Two general models concerning the structure of the solvated electron have been proposed:^{1,2,8,23,31,48–57} the surface-bound model (frequently referred to as the dipole-bound model) and the cavity-bound model. The cavity-bound model predicts the electron to be localized to a particular region in space within the center of the cluster, while the surface-bound model predicts the electron to be delocalized over several atoms on the surface of the cluster. Theoretical methods have been extensively employed to probe the electronic structure of anionic water clusters. Various *ab initio* and density functional theory (DFT) methods have been applied to smaller clusters^{7,11,13–16,20,21,58–64} as well as molecular dynamic simulations of the bulk solvent.^{24,26,48,65–67} It was suggested by Turi et al.⁵⁶ that the hydrated electron exists solely in the surface-bound state for clusters smaller than 45 water molecules, $(\text{H}_2\text{O})_{45}^-$. However, this was recently contradicted in a study by Khan,¹ in which $(\text{H}_2\text{O})_{14}^-$ exhibits both surface- and cavity-bound states depending on the geometry of the cluster. Furthermore, Khan also noted that the two states were nearly identical in energy. While the cavity model is experimentally supported by the appreciable volume increase upon the injection of electrons into the solvent,⁶⁸ it is still unclear as to which model provides a better description.

The quantum theory of atoms in molecules (QTAIM)^{69–73} is based on the topological analysis of the electron density,

$\rho(\mathbf{r})$, and is used to predict bonding interactions and atomic properties.⁷⁴ The electron density exhibits maxima at the locations of the nuclei (or, more generally, the attractors) and lines of maximum electron density linking bonded nuclei, that is, bond paths. The resulting network of nuclei and bond paths represents the molecular graph for a given system. A *single* bond path always links the nuclei of chemically bonded atoms regardless of the bond order.⁷⁴ The bond path is always accompanied by a virial path, a line of maximally stabilizing potential energy density linking the same bonded nuclei.⁷⁵ The presence of a bond path and its associated virial path provides a definitive criterion for bonding, especially in ambiguous or borderline cases.⁷⁶ A bond path between nuclei is always accompanied by an interatomic surface (IAS) between the bonded atoms, and this IAS must satisfy the zero-flux condition⁶⁹

$$\nabla\rho(\mathbf{r})\cdot\mathbf{n}(\mathbf{r}) = 0 \quad (1)$$

for all \mathbf{r} 's on the surface $S(\mathbf{r})$, where $\nabla\rho(\mathbf{r})$ is the gradient of the electron density and $\mathbf{n}(\mathbf{r})$ is a unit vector normal to the surface. This IAS partitions the system into atomic regions or basins. The atoms defined in this manner, based on the topology of the electron density, were brought into coincidence with the quantum mechanically derived atoms in a molecule⁷⁷ starting from Schwinger's principle of stationary action.⁷⁸ The atoms in a molecule were shown to behave as "proper open quantum systems"⁷⁷ which are described by equations of motion in correspondence to closed total systems.⁷⁹ The atoms in molecules, when defined as proper open systems, recover and predict a wide range of experimental observations.⁸⁰

The zero-flux surface consists of a set of $\nabla\rho(\mathbf{r})$ trajectories that originate at infinity and terminate at a single point in the electron density where $\nabla\rho(\mathbf{r}) = 0$, known as the bond critical point (BCP). Two other trajectories originate at the BCP, and each of these terminates at one of the nuclei involved in the bonding, thereby defining the bond path. In addition to satisfying the zero-flux condition, all nonperiodic systems must satisfy the Poincaré–Hopf relationship

$$n - b + r - c = 1 \quad (2)$$

where n stands for the number of attractors (e.g., nuclei), b for the number of bond paths, r for the number of rings, and c for the number of cages.⁸¹

An important feature of QTAIM is its ability to predict non-nuclear attractors (NNAs), which by definition are maxima in the electron density at a location other than that of the nuclei. The occurrence of NNAs is rare and was first theoretically predicted in alkali metal clusters^{82–84} and later observed experimentally in metallic beryllium and magnesium.^{85,86} NNAs behave as attractors in the basins of proper open systems bounded by a zero-flux surface and satisfy the above equation (eq 1), just as atomic nuclei behave topologically. For this reason, a NNA and its associated basin bounded by zero-flux surfaces are termed "pseudo-atoms" in a molecule, cluster, or crystal. Furthermore, for any system containing a NNA, the Poincaré–Hopf relationship (eq 2) must be modified to include both nuclei (or nuclear critical points, NCPs) and non-nuclear attractors (i.e., $n = \text{NCP} + \text{NNA}$).

QTAIM is used in this work to study the properties of the pseudo-atomic basin associated with the hydrated electron and to shed light on questions such as: is the excess electron localized to a specific region in space, or is it delocalized over the entire system? If the hydrated electron exists as a localized entity within the cluster, it will appear as a non-nuclear attractor. If, however, the excess electron is delocalized over the entire system, no NNA will be observed, and the excess charge will be distributed over several atoms in the system.

Besides its physical foundations, the advantage of real space partitioning of the electron population entailed by QTAIM over population analyses such as Mulliken population analysis (MPA) becomes particularly apparent when we consider the case of the solvated electron. QTAIM is able to predict NNAs and consequently determine the population of the associated pseudo-atomic basins. Therefore, should the excess electron exist as a localized entity in an interstitial space not associated with any atom in the cluster, QTAIM can determine exactly to what extent this occurs. Conversely, a MPA of the same system (or any other scheme which assigns atomic populations on the basis of contributions from atom-centered basis functions) would, by necessity, delocalize the excess electron and assign a zero population to any region in space lacking basis functions at its center. Hence, population analyses based on the contributions of basis functions to an atomic population cannot be used to study the solvated electron. The use of QTAIM in the analysis of the hydrated electron is a novel approach and, to our knowledge, has not been reported elsewhere.

II. Computational Details

All structures were optimized at the UMP2(full)/6-31++G-(2d,2p) level of theory and frequencies calculated at that level to ensure local minima have been located. Unpublished DFT results were also obtained at the B3LYP/6-31++G(2d,2p) level of theory and were found to give qualitatively similar results with minor differences in geometric parameters. The spin contamination was never in excess of 0.083% for any of the studied clusters. To validate our discussion of atomic energies, we obtained the energies and wavefunctions always at the same level of theory used for the geometry optimization. [To report atomic (and pseudo-atomic) energies, one cannot optimize the geometry with one basis set and obtain the wavefunction using a larger one as is commonly (and often justifiably) done to refine the electron density and several other atomic and molecular properties. This approach would invalidate the discussion of atomic and pseudo-atomic energies due to nonvanishing forces on the nuclei, each contributing an origin-dependent virial term. Thus, all wavefunctions in this work were obtained at the same level of theory used in the geometry optimization.]

All electronic structure calculations were performed using Gaussian 03.⁸⁷ Molecular graphs were obtained using AIM2000,⁸⁸ while the AIMPAC suite of programs,⁸⁹ implemented in the AIMALL97 software,⁹⁰ was used to analyze the electron densities and obtain atomic properties. The distribution of the excess electron was determined from the charge difference between the anionic cluster and the

Table 1. Relative Energies (kJ/mol) of the Anionic and Neutral Water Clusters

system		anion ^a	neutral
(H ₂ O)		0	-89.7
(H ₂ O) ₂	2A	0	-58.2
	2B	+1.4	-58.2
(H ₂ O) ₄	4A	0	-46.5
	4B	+13.2	-57.2
(H ₂ O) ₆	6A	0	+7.4
	6B	-34.9	-57.5
(H ₂ O) ₈	8A	0	-80.7
	8B	-12.5	-80.7

^a The cavity-forming anionic clusters (A) were assigned a relative energy of zero for any given cluster size.

corresponding neutral cluster in the anionic geometry. The spin density isosurfaces, the spin density being the difference between the α - and β -spin densities, that is, $\rho^{\text{spin}}(\mathbf{r}) \equiv \rho^{\alpha}(\mathbf{r}) - \rho^{\beta}(\mathbf{r})$, were obtained using GaussView.⁹¹ All reported spin density isosurfaces are the 0.001 au isosurface unless otherwise stated. Higher and lower densities were shown to give the same qualitative results.

A note should be made about the color scheme employed in the figures. Various critical points appear in the molecular graphs and are colored as follows: BCPs are red dots, ring critical points (RCPs) are yellow dots, cage critical points (CCPs) are green dots, and NNAs are pink dots. The larger spheres represent the nuclei, employing the usual color scheme of oxygen as red spheres and hydrogen as white.

III. Results and Discussion

A. Water Anion, (H₂O)⁻. The obvious starting point for any investigation into anionic water clusters is the monomer. Both anionic, (H₂O)⁻, and neutral water were optimized at the UMP2(full)/6-31++G(2d,2p) level of theory, and the O-H bond lengths and the H-O-H bond angles were compared for the two cases. As may be expected, the addition of a single electron has little effect on the overall geometry, with an increase in the O-H bond of 0.013 Å and a decrease in the bond angle of 2.8°. However, while the structural changes are minor, the energetic changes are more significant; the anionic water molecule is 89.7 kJ/mol higher in energy than the neutral structure (see Table 1 for relative energies).

QTAIM was employed to determine the distribution of the excess electron, which was calculated from the difference between the atomic charges in the anionic structure and those in the corresponding neutral structure of the same geometry. The data indicate that a large portion of the excess electron is accommodated on the hydrogen atoms, 0.27 electrons (e⁻) on each H atom with the remainder on the O atom, 0.44 e⁻ (Table 2). As one might expect, a greater proportion of the excess electron is accommodated on the oxygen atom when compared to a single hydrogen atom, due to its greater electronegativity. However, collectively, the hydrogen atoms accommodate a greater proportion of the excess electron. Analysis of the spin populations reveals a similar trend to that observed in the charge distribution, with a spin population of 0.42 on the oxygen atom and 0.29 on each hydrogen. The spin density plot graphically illustrates the distribution

Table 2. Selected Atomic Properties of the Anionic Water Clusters

cluster	atom	atomic charge (anion)	charge difference ^a (anion – neutral)	spin population	energy ^b (kJ/mol)
(H ₂ O) ⁻	O1	-1.6047	-0.4449	0.4197	
	H2	0.3072	-0.2727	0.2850	
	H3	0.3070	-0.2729	0.2852	
2A⁻	O1	-1.3992	-0.2409	0.2036	
	H2	0.4537	-0.1255	0.1442	
	H3	0.4529	-0.1263	0.1448	
2B⁻	O1	-1.2806	-0.0613	0.0369	
	H2	0.6491	+0.0237	0.0032	
	H3	0.5461	-0.0292	0.0216	
	O4	-1.5476	-0.3749	0.3526	
	H5	0.3223	-0.2736	0.2872	
	H6	0.3239	-0.2720	0.2859	
4A⁻	O1	-1.3451	-0.1234	0.1020	
	H2	0.6443	-0.0018	0.0022	
	H3	0.4356	-0.1399	0.1609	
NNA		-0.0281	-0.0281	0.0277	-3.2
	O1	-1.3423	-0.1094	0.1028	
	H2	0.6442	-0.0014	0.0037	
4B⁻	H3	0.4596	-0.1380	0.1420	
	O1	-1.2853	-0.0733	0.0502	
	H2	0.6331	-0.0018	0.0025	
6A⁻	H3	0.5281	-0.0486	0.0732	
	NNA	-0.2318	-0.2318	0.2257	-21.5
	H1	0.6345	-0.0025	0.0001	
6B⁻	H2	0.6465	+0.0070	0.0002	
	H3	0.6347	-0.0038	0.0005	
	H4	0.6506	-0.0027	0.0002	
	O5	-1.2763	-0.0204	0.0053	
	O6	-1.2759	-0.0272	0.0048	
	O7	-1.2868	-0.0378	0.0145	
	O8	-1.2649	-0.0325	0.0148	
	H9	0.6274	+0.0134	0.0013	
	H10	0.6087	+0.0107	0.0014	
	H11	0.6274	+0.0249	0.0037	
	H12	0.5682	-0.0011	0.0229	
	H13	0.5471	-0.0443	0.0460	
	O14	-1.3159	-0.0821	0.0597	
	H15	0.6506	+0.0161	0.0046	
O16	-1.4779	-0.3026	0.2830		
8A⁻	H17	0.3294	-0.2756	0.2935	
	H18	0.3839	-0.2257	0.2362	
	O1	-1.2818	-0.0550	0.0372	
	H2	0.6496	-0.0005	0.0009	
	H3	0.5362	-0.0400	0.0589	
	NNA	-0.2164	-0.2164	0.2101	-17.9
8B⁻	O1	-1.3647	-0.0980	0.1018	
	H2	0.6600	-0.0038	0.0021	
	H3	0.5105	-0.0900	0.0878	
	O4	-1.3253	-0.0553	0.0528	
	H5	0.6353	-0.0008	0.0031	
	H6	0.6348	-0.0021	0.0032	

^a Charge difference was determined from the difference between the atomic charge in the anion and the atomic charge in the corresponding neutral cluster in the anionic geometry. ^b Only the total energies of the NNA basins (in kJ/mol) are reported here, since the energies of the other atoms are of too large to be reported in kJ/mol.

of the excess spin, which is predominantly located near the hydrogen atoms (Figure 1).

B. Anionic Water Dimers, (H₂O)₂⁻. The optimization of the anionic monomer was followed naturally by an investigation of dimeric clusters. Two structures were investigated and optimized as seen in Figure 2, a cagelike structure in which the hydrogen atoms of the two water molecules are oriented toward one another, effectively forming a cavity between the two molecules (**2A⁻**), and an approximately linear structure that exhibits the typical hydrogen-bonding arrangement (**2B⁻**).

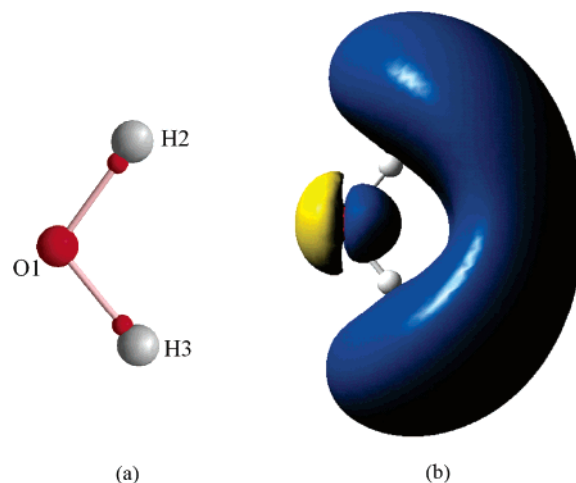


Figure 1. Molecular graph (a) of the water anion, (H₂O)⁻, illustrating the bond critical points (BCP) between the nuclei and (b) the +0.001 and -0.001 au spin density isosurfaces (blue and yellow, respectively).

The molecular graph of **2A⁻** reveals that there is a long-range oxygen–oxygen interaction (~5.2 Å) between the two water molecules as indicated by the BCP between the atoms. Once again, the H atoms accommodate a large portion of the excess electron, 0.13 e⁻ each, while the O atoms possess a slightly larger fraction at 0.24 e⁻, a trend that is mirrored in the spin populations of 0.14 and 0.20 for the hydrogen and oxygen atoms, respectively. The spin density plot of **2A⁻** (Figure 2) indicates that a large portion of the unpaired electron is found within the cavity formed by the two water molecules. Conversely, **2B⁻** tends to accommodate the excess electron preferably on the hydrogen-bond acceptor water molecule (0.27 e⁻ on each H atom and 0.37 e⁻ on the O atom from the integration data and spin populations of 0.29 and 0.35 for those same atoms; Table 2).

When the results of the two dimers are compared, it is obvious that there is a marked difference between the two systems. The highly symmetric **2A⁻** structure distributes the excess electron to a specific region within the center of the cluster, satisfying the notion of a cavity-bound hydrated electron. On the other hand, **2B⁻** delocalizes the electron over one of the water molecules, largely accommodating it on the surface of the cluster such that it may be considered surface-bound. However, it should also be noted, in either case (surface- or cavity-bound), the excess electron is largely accommodated by the NHB hydrogen atoms.

Additionally, structure **2A⁻** is marginally more stable than **2B⁻** by 1.4 kJ/mol. Although the energy difference is not very significant, it is interesting to note that the unusual cagelike arrangement has a stability similar to that of the typical water dimer upon the addition of an electron.

The geometries of each anionic dimer were subsequently used as initial structural coordinates for the optimization of a neutral cluster. Upon optimization, both structures prefer to adopt the typical hydrogen-bonding scheme, forming structure **2B** (Figure 2) which is very similar to **2B⁻** with some minor differences in geometric parameters [most notably a slightly longer hydrogen bond between the molecules and a smaller α angle (Figure 3)]. As may be

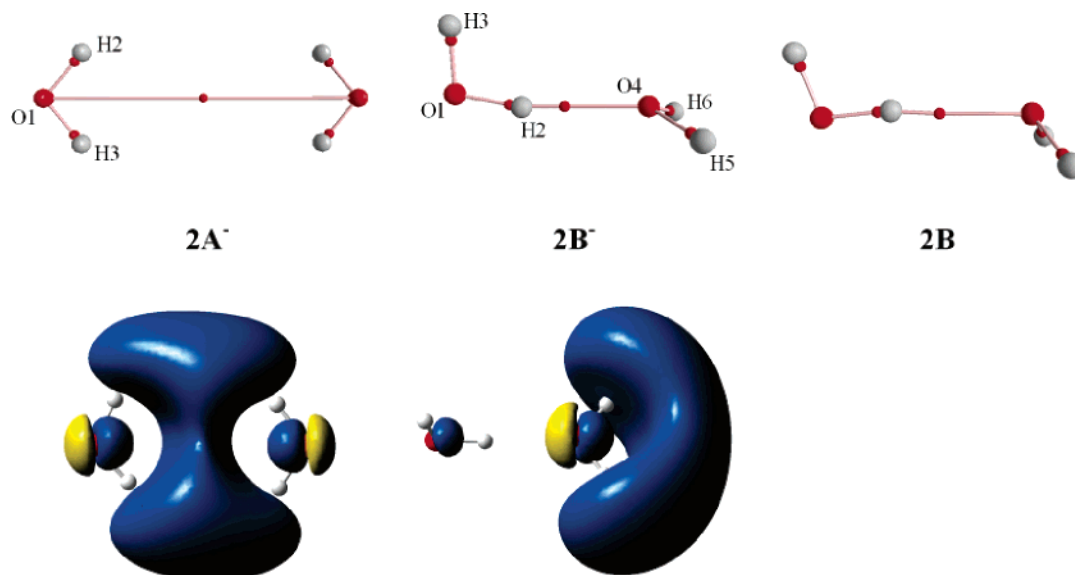


Figure 2. Molecular graphs of the optimized anionic dimer structures, $2A^-$ and $2B^-$, with their 0.001 au spin density plots shown below each structure as well as the optimized structure of the neutral water dimer, $2B$.

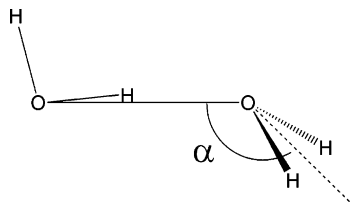


Figure 3. Neutral water dimer illustrating the α angle, the angle between the line connecting the oxygen atoms and the line bisecting the hydrogen atoms of the hydrogen-bond acceptor.

Table 3. Vertical Electron Dissociation Energies (VDE; eV) for the Anionic Water Clusters

system	VDE ^a	system	VDE ^a
monomer	0.918	6A	-0.476
2A	0.310	6B	-0.291
2B	0.573	8A	-0.613
4A	0.252	8B	0.696
4B	0.546		

^a VDEs were calculated from the difference between the anion and the energy of the neutral cluster in the anion geometry.

expected, the neutral structure was the most stable of the three dimers investigated, almost 60 kJ/mol more stable than either of the anionic structures (Table 1).

Vertical electron dissociation energies (VDEs) were calculated from the energy difference between the anion and that of the corresponding neutral cluster in the anionic geometry. It was found that structure $2A^-$, the cavity-bound state, had a smaller VDE value, 0.310 eV, compared to that of $2B^-$, 0.573 eV, the surface-bound state (Table 3). This trend of smaller VDE values for the cavity-bound model compared to the surface-bound model is observed in all of the clusters studied and is in agreement with previous work in the field.⁵⁶

It should be emphasized that other geometries are possible for the dimeric case previously discussed as well as the larger systems to be described below. First and foremost, the goal

of the current study was to determine whether non-nuclear attractors exist topologically in anionic water clusters. Furthermore, for the systems in which NNAs are found, various characteristics of those systems were probed and compared to systems in which NNAs are absent. Therefore, the main focus was the comparison of two types of clusters for each cluster size investigated: those in which several NHB hydrogen atoms are contained within the cavity and those in which they protrude from the surface of the cluster. The current study is by no means an exhaustive search for all possible cluster geometries.

C. Anionic Water Tetramers, $(H_2O)_4^-$. Two tetrameric structures were investigated, both with four water molecules hydrogen-bonded in a single ring. $4A^-$ possesses a 4-fold axis of symmetry, with the NHB hydrogen atoms (or the out-of-plane H atoms) all pointed in the same direction, while in $4B^-$ the NHB hydrogen atoms alternate directions forming a cluster with a 2-fold axis of symmetry (Figure 4). Electronic structure optimizations reveal that $4A^-$ is more stable than $4B^-$ by 13.2 kJ/mol (Table 1), indicating that $4A^-$ is the energetically favored structure formed upon the addition of a single electron to the two systems investigated.

Although the two tetrameric structures share some similar features, a major difference becomes apparent from the QTAIM analysis: $4A^-$ possesses a NNA situated above the non-hydrogen-bonded H atoms, while $4B^-$ exhibits no such NNA. Because of this NNA in $4A^-$, five RCPs and one CCP are also observed (and are indeed necessary to satisfy the Poincaré–Hopf relationship), whereas $4B^-$ exhibits only one RCP (Figure 4). According to QTAIM, all maxima in the electron density are bounded by zero-flux surfaces, which separate each attractor from its neighbors. NNAs are no exception to this rule; they are bounded by zero-flux surfaces, which define a pseudo-atomic basin in which electron density resides. Indeed, the NNA can be considered to be a pseudo-atom, and QTAIM can be used to determine its electron population, which in the case of $4A^-$ is 0.03 e⁻ (and a spin population of 0.03), as well as its contribution to the overall

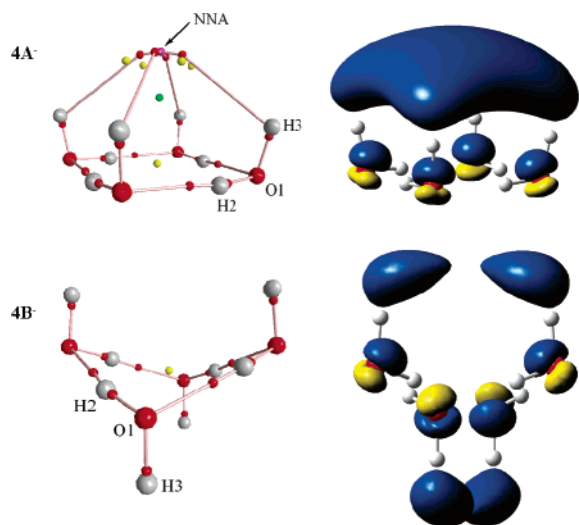


Figure 4. Molecular graphs of $4A^-$ and $4B^-$ as well as their 0.001 au spin density plots shown beside each structure. Note the appearance of the non-nuclear attractor (NNA) in the $4A^-$ system (pink sphere).

energy, 3.2 kJ/mol (Table 2), and a pseudo-atomic volume of 11.8 au. As a frame of reference for atomic volumes observed in these anionic clusters, we note that the hydrogen-bonded H atoms typically have volumes of 10 to 15 au; the NHB hydrogen atoms range from 30 to 90 au, and the oxygen atoms range from 140 to 200 au. Although the actual population and energy of the pseudo-atomic basin are small in this case, the fact that the NNA is predicted for this geometry is significant, indicating that it exists topologically within the electron density.

Furthermore, the spin density plots (Figure 4) can be used to illustrate the difference between the two systems, namely, that $4A^-$ localizes the excess electron to a specific region above the plane of the four water molecules (accommodating $0.14 e^-$ and $0.12 e^-$ on each NHB H atom and O atom, respectively, and $0.03 e^-$ on the NNA with a similar trend in the spin populations; Table 2) while $4B^-$ distributes the electron over the NHB hydrogen atoms ($0.14 e^-$ each) and the O atoms ($0.11 e^-$ each), essentially binding the electron to the surface of the cluster.

The subsequent optimizations of the two systems as neutral clusters resulted in two new structures that retain the general features of the anions. The most notable change is the position of the NHB hydrogen atoms, which move away from the center of the rings, ultimately flattening the entire systems (Figure 5). Additionally, $4B$ is no longer “V-shaped” like its anionic counterpart. The energy differences between the anion and neutral for $4A$ and $4B$ are -46.5 kJ/mol and -57.2 kJ/mol, respectively (see Table 1 for relative energies). While both of the neutral structures are more stable than their corresponding anion as expected, it is interesting to note that $4A$ is less destabilized by the addition of a single electron than $4B$.

D. Anionic Water Hexamers, $(H_2O)_6^-$. As with the tetrameric structures, two types of systems were investigated: a highly symmetric hexamer ($6A^-$) possessing a 3-fold axis of symmetry and a cavity between two planes of hydrogen-bonded trimers and a less symmetric system ($6B^-$)

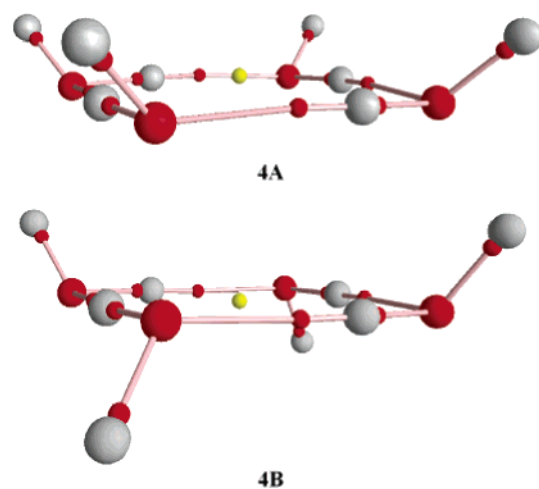


Figure 5. Optimized structures of the neutral water tetramers $4A$ and $4B$ (N.B., the neutral structures maintain a similar arrangement to the anionic clusters but flatten out considerably).

which has a structure similar to a prism but is distorted at one end (Figure 6). Once again, the highly symmetric structure, $6A^-$, which possesses several NHB hydrogen atoms all directed toward the center of the cavity, exhibits a NNA. However, the hexameric cluster exhibits two key differences compared to the tetrameric case: (i) the NNA is now located in the center of the cavity formed by the water molecules, and (ii) the population of the NNA basin is much more significant, accommodating $0.23 e^-$ (spin population of 0.23), contributing 21.5 kJ/mol to the overall energy of the system (Table 2) and a larger pseudo-atomic volume of 93.3 au. The spin populations for both $6A^-$ and $6B^-$ correlate well with the integration data and are graphically illustrated in the spin density plots (Figure 6). The excess electron in $6A^-$ is largely contained within the cavity, corresponding to the historical notion of the hydrated electron. On the other hand, $6B^-$ exhibits no such NNA, and upon investigation of the spin density plot (Figure 6), it is clear that this system largely accommodates the excess electron on a single water molecule on the surface of the cluster (with 0.23 and $0.28 e^-$ on the H atoms involved and $0.30 e^-$ on the oxygen; Table 2), similar to the distribution observed in the $2B^-$ system.

Subsequently, both structures were optimized as neutral species, resulting in geometrically similar structures compared to the anionic species. In particular, $6A$ maintained the same arrangement of the water molecules as $6A^-$; however, the two planes are now closer together, and the NHB hydrogen atoms are bent away from the center of the cluster (Figure 6). Furthermore, the relative energies of these two species reveal that $6A^-$, the anion, is marginally more stable than $6A$, the neutral, by 7.4 kJ/mol. Even though the energy difference itself is negligible, the fact remains that this is the only system in which the anion and the corresponding neutral cluster are nearly equal in energy. Indeed, in most of the systems, the neutral cluster is more stable by approximately 50 kJ/mol or more. Although $6B^-$ is more stable than $6A^-$ by 34.9 kJ/mol, it is interesting to note that the addition of an electron to $6A$ actually has a slight

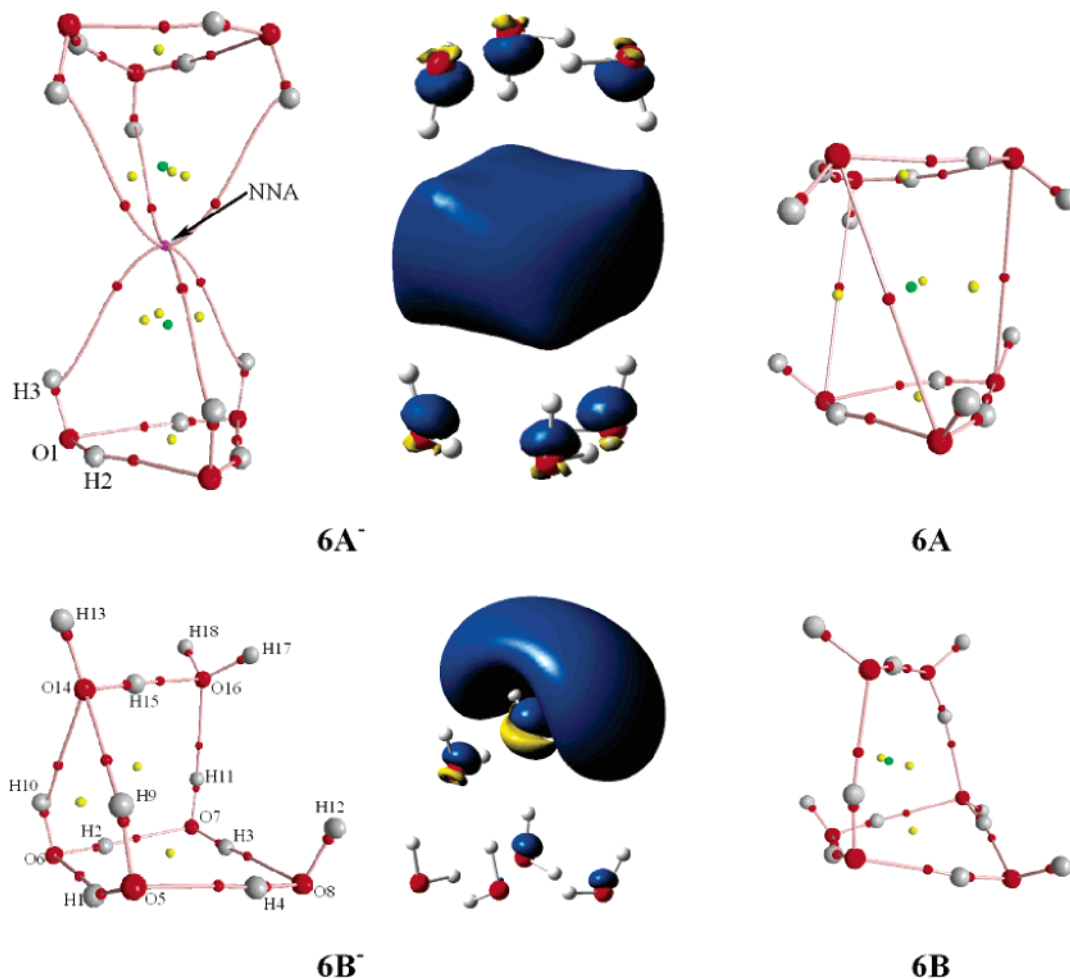


Figure 6. Molecular graphs of $6A^-$ and $6B^-$ with the 0.001 au spin density plots shown adjacent to each structure as well as the optimized structures of the neutral clusters $6A$ and $6B$. Note the appearance of the NNA in the $6A^-$ system found in the center of the cavity formed between the two trimers.

stabilizing effect (or at least a negligible effect) while $6B$ experiences a marked destabilization of 22.6 kJ/mol.

E. Anionic Water Octamers, $(H_2O)_8^-$. The final systems investigated were two anionic water octamers, constructed by placing two tetrameric planes on top of one another. The more symmetric of the two systems, $8A^-$, consists of two hydrogen-bonded planes of tetramers like $4A^-$ stacked so that the NHB hydrogen atoms are directed toward one another and the center of the cavity. However, the two stacked planes are not mirror images; one plane is rotated 45° relative to the other (Figure 7), maintaining the 4-fold axis of symmetry. The second system, $8B^-$, consists of two stacked tetramers like $4B$ (neutral arrangement), forming a cube such that four of the water molecules have NHB hydrogen atoms directed away from the center of the cube while the other four water molecules form two hydrogen bonds each, giving the entire system a 2-fold axis of symmetry (Figure 7).

The more symmetric of the two systems, $8A^-$, exhibits a NNA at the center of the cavity, as may be expected on the basis of the hexameric results and the similarity between the two systems. The integration data reveal that this NNA possesses a significant portion of the excess electron, 0.22 e^- (spin population of 0.21), contributes 17.9 kJ/mol to the overall energy of the system, and occupies a pseudo-atomic

volume of 89.0 au. The remainder of the excess electron is largely accommodated on the NHB hydrogen atoms and the O atoms. Conversely, the $8B^-$ system exhibits no such NNA and tends to accommodate the excess electron on the O atoms and the NHB hydrogen atoms as per the other systems (see Table 2 for the exact charge distribution and spin populations). The different distributions are graphically illustrated in the spin density plots (Figure 7).

Upon optimization of the systems as neutral species, it was noted that the final neutral structure was the same for both cases, $8B$ (Figure 7), which is very similar to $8B^-$ with some minor changes in bond lengths and angles. Comparing the relative energies of all eight-membered species, $8B$ is more stable than either anion by more than 60 kJ/mol (Table 1). Moreover, $8B^-$ is merely 12.5 kJ/mol more stable than $8A^-$; one would expect $8B^-$ to be significantly more stable since it closely resembles the preferred neutral geometry. This last observation illustrates that although the two different distributions of the hydrated electron are qualitatively very different, they are in fact very similar energetically.

IV. Conclusions

QTAIM has been used to probe the nature of the solvated electron in small water clusters, $(H_2O)_n^-$, for $n = 1-8$. The

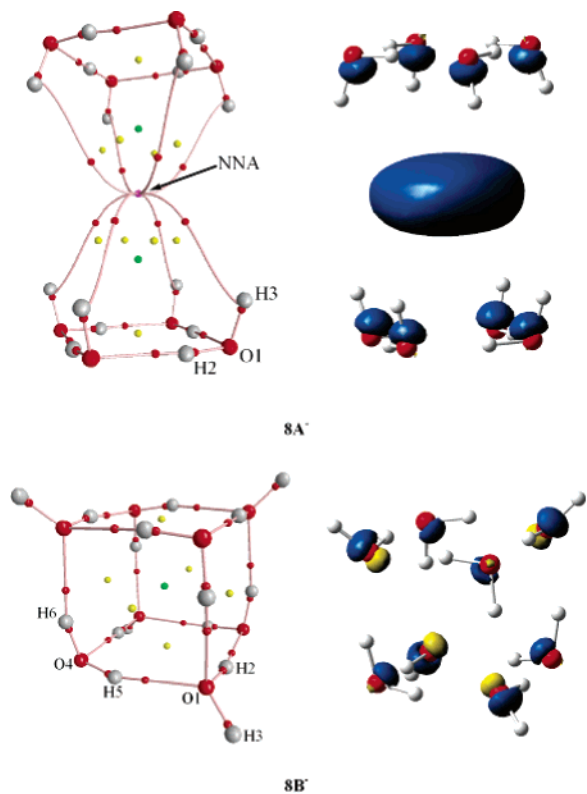


Figure 7. Molecular graphs of $8A^-$ and $8B^-$ with the 0.001 au spin density plots shown adjacent to each structure. Similar to the $6A^-$ system, a NNA appears in the center of the cavity formed between the two tetramers.

results indicate that the hydrated electron can take on one of several arrangements depending on the geometry of the cluster. Highly symmetric clusters, that can form a cavity between the water molecules and have several non-hydrogen-bonded H atoms directed toward this center ($2A^-$, $4A^-$, $6A^-$, and $8A^-$), favor the archetypical notion of the cavity-bound hydrated electron. Although clusters as small as four water molecules ($4A^-$) exhibit NNAs, only the larger clusters ($6A^-$ and $8A^-$) possess NNAs or pseudo-atoms with significant populations and energies (upward of 0.2 electrons and energy contributions in excess of 20 kJ/mol). On the other hand, the less symmetric clusters tend to distribute the excess electron on the surface of the cluster, either delocalized over the entire surface ($4B^-$ and $8B^-$) or localized on one specific water molecule ($2B^-$ and $6B^-$). A surface-bound solvated electron is observed in those cases where the NHB hydrogen atoms are directed away from the surface of the cluster while the cavity-bound model prevails when the NHB hydrogen atoms are oriented toward the center of the cavity. In general, the hydrated electron is accommodated on the non-hydrogen-bonded H atoms and the oxygen atoms, and it is the orientation of these non-hydrogen-bonded H atoms that dictates the distribution of the hydrated electron.

Acknowledgment. The authors gratefully acknowledge the Natural Sciences and Engineering Research Council of Canada, Dalhousie University, and the Killam Trusts for financial support. We thank Dr. Todd Keith for providing AIMALL97.

References

- (1) Khan, A. *J. Chem. Phys.* **2006**, *125*, 024307.
- (2) Sommerfeld, T.; Jordan, K. D. *J. Am. Chem. Soc.* **2006**, *128*, 5828.
- (3) Coe, J. V.; Arnold, S. T.; Eaton, J. G.; Lee, G. H.; Bowen, K. H. *J. Chem. Phys.* **2006**, *125*, 014315.
- (4) Baldacchino, G.; De Waele, V.; Monard, H.; Sorgues, S.; Gobert, F.; Larbre, J. P.; Vigneron, G.; Marignier, J. L.; Pommeret, S.; Mostafavi, M. *Chem. Phys. Lett.* **2006**, *424*, 77.
- (5) De Waele, V.; Sorgues, S.; Pernot, P.; Marignier, J. L.; Monard, H.; Larbre, J. P.; Mostafavi, M. *Chem. Phys. Lett.* **2006**, *423*, 30.
- (6) Neumann, S.; Eisfeld, W.; Sobolewski, A. L.; Domcke, W. *J. Phys. Chem. A* **2006**, *110*, 5613.
- (7) Lee, H. M.; Suh, S. B.; Tarakeshwar, P.; Kim, K. S. *J. Chem. Phys.* **2005**, *122*, 044309.
- (8) Khan, A. *Chem. Phys. Lett.* **2005**, *401*, 85.
- (9) Hammer, N. I.; Shin, J. W.; Headrick, J. M.; Diken, E. G.; Roscioli, J. R.; Weddle, G. H.; Johnson, M. A. *Science* **2004**, *306*, 675.
- (10) Balaj, O. P.; Siu, C. K.; Balteanu, L.; Beyer, M. K.; Bondybey, V. E. *Int. J. Mass Spectrom.* **2004**, *238*, 65.
- (11) Zhan, C. G.; Dixon, D. A. *J. Phys. Chem. B* **2003**, *107*, 4403.
- (12) Beyer, M. K.; Fox, B. S.; Reinhard, B. M.; Bondybey, V. E. *J. Chem. Phys.* **2001**, *115*, 9288.
- (13) Kulkarni, S. A.; Bartolotti, L. J.; Pathak, R. K. *J. Chem. Phys.* **2000**, *113*, 2697.
- (14) Weigend, F.; Ahlrichs, R. *Phys. Chem. Chem. Phys.* **1999**, *1*, 4537.
- (15) Smith, D. M. A.; Smets, J.; Adamowicz, L. *J. Chem. Phys.* **1999**, *110*, 3804.
- (16) Chen, H. Y.; Sheu, W. S. *J. Chem. Phys.* **1999**, *110*, 9032.
- (17) Tsurusawa, T.; Iwata, S. *Chem. Phys. Lett.* **1999**, *315*, 433.
- (18) Ayotte, P.; Weddle, G. H.; Bailey, C. G.; Johnson, M. A.; Vila, F.; Jordan, K. D. *J. Chem. Phys.* **1999**, *110*, 6268.
- (19) Kim, J.; Becker, I.; Cheshnovsky, O.; Johnson, M. A. *Chem. Phys. Lett.* **1998**, *297*, 90.
- (20) Lee, S.; Kim, J.; Lee, S. J.; Kim, K. S. *Phys. Rev. Lett.* **1997**, *79*, 2038.
- (21) Kim, K. S.; Park, I. J.; Lee, S.; Cho, K.; Lee, J. Y.; Kim, J.; Joannopoulos, J. D. *Phys. Rev. Lett.* **1996**, *76*, 956.
- (22) Kimura, Y.; Alfano, J. C.; Walhout, P. K.; Barbara, P. F. *J. Phys. Chem.* **1994**, *98*, 3450.
- (23) Coe, J. V.; Lee, G. H.; Eaton, J. G.; Arnold, S. T.; Sarkas, H. W.; Bowen, K. H.; Ludewigt, C.; Haberland, H.; Worsnop, D. R. *J. Chem. Phys.* **1990**, *92*, 3980.
- (24) Barnett, R. N.; Landman, U.; Makov, G.; Nitzan, A. *J. Chem. Phys.* **1990**, *93*, 6226.
- (25) Hamaka, H. F.; Robinson, G. W.; Marsden, C. J. *J. Phys. Chem.* **1987**, *91*, 3150.
- (26) Wallqvist, A.; Thirumalai, D.; Berne, B. J. *J. Chem. Phys.* **1986**, *85*, 1583.
- (27) Haberland, H.; Schindler, H. G.; Worsnop, D. R. *Ber. Bunsen-Ges.* **1984**, *88*, 270.

- (28) Haberland, H.; Ludewigt, C.; Schindler, H. G.; Worsnop, D. R. *J. Chem. Phys.* **1984**, *81*, 3742.
- (29) Haberland, H.; Langosch, H.; Schindler, H. G.; Worsnop, D. R. *J. Phys. Chem.* **1984**, *88*, 3903.
- (30) Armbruster, M.; Haberland, H.; Schindler, H. G. *Phys. Rev. Lett.* **1981**, *47*, 323.
- (31) Copeland, D. A. *J. Chem. Phys.* **1970**, *53*, 1189.
- (32) Stemmler, K.; von Gunten, U. *Atmos. Environ.* **2000**, *34*, 4241.
- (33) Buxton, G. V.; Greenstock, C. L.; Helman, W. P.; Ross, A. B. *J. Phys. Chem. Ref. Data* **1988**, *17*, 513.
- (34) Chameides, W. L. *Science* **1998**, *281*, 1152.
- (35) Beal, M. F. *Trends Neurosci.* **2000**, *23*, 298.
- (36) Weyl, W. *Ann. Phys. (Weinheim, Ger.)* **1864**, *121*, 601.
- (37) Kraus, C. A. *J. Am. Chem. Soc.* **1908**, *30*, 1323.
- (38) Hart, E. J.; Boag, J. W. *J. Am. Chem. Soc.* **1962**, *84*, 4090.
- (39) Boag, J. W.; Hart, E. J. *Nature* **1963**, *197*, 45.
- (40) Keene, J. P. *Nature* **1963**, *197*, 47.
- (41) Schindewolf, U. *Angew. Chem., Int. Ed. Engl.* **1968**, *7*, 190.
- (42) Migus, A.; Gauduel, Y.; Martin, J. L.; Antonetti, A. *Phys. Rev. Lett.* **1987**, *58*, 1559.
- (43) Jortner, J.; Ottolenghi, M.; Stein, G. *J. Phys. Chem.* **1964**, *68*, 247.
- (44) Walker, D. C. *Can. J. Chem.* **1966**, *44*, 2226.
- (45) Knapp, M.; Echt, O.; Kreisle, D.; Recknagel, E. *J. Chem. Phys.* **1986**, *85*, 636.
- (46) Knapp, M.; Echt, O.; Kreisle, D.; Recknagel, E. *J. Phys. Chem.* **1987**, *91*, 2601.
- (47) Balaj, O. P.; Balteanu, I.; Fox-Beyer, B. S.; Beyer, M. K.; Bondybey, V. E. *Angew. Chem., Int. Ed.* **2003**, *42*, 5516.
- (48) Barnett, R. N.; Landman, U.; Cleveland, C. L.; Jortner, J. *J. Chem. Phys.* **1988**, *88*, 4429.
- (49) Feng, D. F.; Kevan, L. *Chem. Rev.* **1980**, *80*, 1.
- (50) Kevan, L. *Acc. Chem. Res.* **1981**, *14*, 138.
- (51) Fueki, K. *J. Am. Chem. Soc.* **1973**, *95*, 1398.
- (52) Gaathon, A.; Jortner, J. In *Electrons in Fluids*; Jortner, J., Kestner, N. R., Eds.; Springer: Berlin, 1973; p 429.
- (53) Schnitker, J.; Rossky, P. J. *J. Chem. Phys.* **1987**, *86*, 3471.
- (54) Rossky, P. J.; Schnitker, J. *J. Phys. Chem.* **1988**, *92*, 4277.
- (55) Khan, A. *J. Chem. Phys.* **2003**, *118*, 1684.
- (56) Turi, L.; Sheu, W. S.; Rossky, P. J. *Science* **2005**, *309*, 914.
- (57) Tauber, M. J.; Mathies, R. A. *J. Am. Chem. Soc.* **2003**, *125*, 1394.
- (58) Kim, J.; Lee, J. Y.; Oh, K. S.; Park, J. M.; Lee, S.; Kim, K. S. *Phys. Rev. A* **1999**, *59*, R930.
- (59) Kim, J.; Suh, S. B.; Kim, K. S. *J. Chem. Phys.* **1999**, *111*, 10077.
- (60) Suh, S. B.; Lee, H. M.; Kim, J.; Lee, J. Y.; Kim, K. S. *J. Chem. Phys.* **2000**, *113*, 5273.
- (61) Novakovskaya, Y. V.; Stepanov, N. F. *J. Phys. Chem. A* **1999**, *103*, 10975.
- (62) Clary, D. C.; Benoit, D. M. *J. Chem. Phys.* **1999**, *111*, 10559.
- (63) Rao, B. K.; Kestner, N. R. *J. Chem. Phys.* **1984**, *80*, 1587.
- (64) Kestner, N. R.; Jortner, J. *J. Phys. Chem.* **1984**, *88*, 3818.
- (65) Landman, U.; Barnett, R. N.; Cleveland, C. L.; Scharf, D.; Jortner, J. *J. Phys. Chem.* **1987**, *91*, 4890.
- (66) Barnett, R. N.; Landman, U.; Cleveland, C. L.; Jortner, J. *J. Chem. Phys.* **1988**, *88*, 4421.
- (67) Barnett, R. N.; Landman, U. *Phys. Rev. Lett.* **1993**, *70*, 1775.
- (68) Jortner, J. *J. Chem. Phys.* **1959**, *30*, 839.
- (69) Bader, R. F. W. *Atoms in Molecules: A Quantum Theory*; Oxford University Press: Oxford, U. K., 1990.
- (70) Bader, R. F. W.; Nguyen Dang, T. T. *Adv. Quantum Chem.* **1981**, *14*, 63.
- (71) Bader, R. F. W. *Chem. Rev.* **1991**, *91*, 893.
- (72) Popelier, P. L. A. *Atoms in Molecules: An Introduction*; Prentice Hall: London, 2000.
- (73) Matta, C. F.; Boyd, R. J. *The Quantum Theory of Atoms in Molecules: From Solid State to DNA and Drug Design*; Wiley-VCH: Weinheim, Germany, 2007.
- (74) Bader, R. F. W. *J. Phys. Chem. A* **1998**, *102*, 7314.
- (75) Keith, T. A.; Bader, R. F. W.; Aray, Y. *Int. J. Quantum Chem.* **1996**, *57*, 183.
- (76) Bader, R. F. W.; Matta, C. F. *Organometallics* **2004**, *23*, 6253.
- (77) Bader, R. F. W. *Phys. Rev. B* **1994**, *49*, 13348.
- (78) Schwinger, J. *Phys. Rev.* **1951**, *82*, 914.
- (79) Bader, R. F. W.; Popelier, P. L. A. *Int. J. Quantum Chem.* **1993**, *45*, 189.
- (80) Matta, C. F.; Bader, R. F. W. *J. Phys. Chem. A* **2006**, *110*, 6365.
- (81) Collard, K.; Hall, G. G. *Int. J. Quantum Chem.* **1977**, *12*, 623.
- (82) Gatti, C.; Fantucci, P.; Pacchioni, G. *Theor. Chim. Acta* **1987**, *72*, 433.
- (83) Cao, W. L.; Gatti, C.; Macdougall, P. J.; Bader, R. F. W. *Chem. Phys. Lett.* **1987**, *141*, 380.
- (84) Mei, C. J.; Edgecombe, K. E.; Smith, V. H.; Heilingbrunner, A. *Int. J. Quantum Chem.* **1993**, *48*, 287.
- (85) Iversen, B. B.; Larsen, F. K.; Souhassou, M.; Takata, M. *Acta Crystallogr., Sect. B* **1995**, *51*, 580.
- (86) Iversen, B. B.; Larsen, F. K. In *Collected Abstracts, XVII Congress, International Union of Crystallography, Seattle, Washington, August 8–17, 1996*; International Union of Crystallography: Seattle, Washington, 1996.
- (87) Frisch, M. J.; Trucks, G. W.; Schlegel, H. B.; Scuseria, G. E.; Robb, M. A.; Cheeseman, J. R.; Montgomery, J. J. A.; Vreven, T.; Kudin, K. N.; Burant, J. C.; Millam, J. M.; Iyengar, S. S.; Tomasi, J.; Barone, V.; Mennucci, B.; Cossi, M.; Scalmani, G.; Rega, N.; Petersson, G. A.; Nakatsuji, H.; Hada, M.; Ehara, M.; Toyota, K.; Fukuda, R.; Hasegawa, J.; Ishida, M.; Nakajima, T.; Honda, Y.; Kitao, O.; Nakai, H.; Klene, M.; Li, X.; Knox, J. E.; Hratchian, H. P.; Cross, J. B.; Bakken, V.; Adamo, C.; Jaramillo, J.; Gomperts, R.; Stratmann, R. E.; Yazyev, O.; Austin, A. J.; Cammi, R.; Pomelli, C.; Ochterski, J. W.; Ayala, P. Y.; Morokuma, K.; Voth, G. A.; Salvador, P.; Dannenberg, J. J.; Zakrzewski, V. G.; Dapprich, S.; Daniels, A. D.; Strain, M. C.; Farkas, O.; Malick, D. K.; Rabuck, A. D.; Raghavachari, K.;

Foresman, J. B.; Ortiz, J. V.; Cui, Q.; Baboul, A. G.; Clifford, S.; Cioslowski, J.; Stefanov, B. B.; Liu, G.; Liashenko, A.; Piskorz, P.; Komaromi, I.; Martin, R. L.; Fox, D. J.; Keith, T.; Al-Laham, M. A.; Peng, C. Y.; Nanayakkara, A.; Challacombe, M.; Gill, P. M. W.; Johnson, B.; Chen, W.; Wong, M. W.; Gonzalez, C.; Pople, J. A. *Gaussian 03*, Revision B.05; Gaussian, Inc.: Wallingford, CT, 2004.

- (88) Biegler-Konig, F.; Schonbohm, J.; Bayles, D. *J. Comput. Chem.* **2001**, 22, 545.

- (89) Biegler-Konig, F. W.; Bader, R. F. W.; Tang, T. *J. Comput. Chem.* **1982**, 3, 317.

- (90) Keith, T. A. *AIMALL97 for DOS/Windows*, private communication, 1997.

- (91) Dennington, R., II; Keith, T.; Millam, J.; Eppinnett, K.; Hovell, W. L.; Gilliland, R. *GaussView*, Version 3.09; Semichem, Inc.: Shawnee Mission, KS, 2003.

CT600334W

Exploiting QM/MM Capabilities in Geometry Optimization: A Microiterative Approach Using Electrostatic Embedding

Johannes Kästner,^{*,†,‡} Stephan Thiel,[†] Hans Martin Senn,[†] Paul Sherwood,[‡] and Walter Thiel[†]

Max-Planck-Institut für Kohlenforschung, Kaiser-Wilhelm-Platz 1, D-45470 Mülheim an der Ruhr, Germany, and Computational Science and Engineering Department, CCLRC Daresbury Laboratory, Daresbury, Warrington WA4 4AD, United Kingdom

Received November 28, 2006

Abstract: We present a microiterative adiabatic scheme for quantum mechanical/molecular mechanical (QM/MM) energy minimization that fully optimizes the MM part in each QM macroiteration. This scheme is applicable not only to mechanical embedding but also to electrostatic and polarized embedding. The electrostatic QM/MM interactions in the microiterations are calculated from electrostatic potential charges fitted on the fly to the QM density. Corrections to the energy and gradient expressions ensure that macro- and microiterations are performed on the same energy surface. This results in excellent convergence properties and no loss of accuracy compared to standard optimization. We test our implementation on water clusters and on two enzymes using electrostatic embedding, as well as on a surface example using polarized embedding with a shell model. Our scheme is especially well-suited for systems containing large MM regions, since the computational effort for the optimization is almost independent of the MM system size. The microiterations reduce the number of required QM calculations typically by a factor of 2–10, depending on the system.

I. Introduction

Combined quantum mechanical/molecular mechanical (QM/MM) methods are increasingly applied to model large systems, from solid state^{1,2} over surface catalysis³ to biological systems.^{4–6} In this approach, the chemically reactive part is described with an accurate, but computationally demanding, quantum mechanical method, while the environment is treated by force fields. These are computationally highly efficient but unable to describe chemical reactions, such as the breaking or forming of bonds. The systems frequently considered nowadays contain several tens to a few hundred QM atoms and many thousands of MM atoms.

When higher-level QM methods [ab initio or density functional theory (DFT)] are used in QM/MM treatments, the QM calculation generally takes much longer than the

MM calculation. For a given size of the QM region, an extension of the MM region does not noticeably increase the computation time for a given configuration. Geometry optimizations, however, need more and more energy and gradient evaluations the larger the system becomes. As one QM calculation is in principle required for each such evaluation, the computational effort of QM/MM structure optimizations increases steeply with system size.

Microiterative QM/MM optimization schemes have been proposed^{7–15} that exploit the computational advantage of treating a major part of the system with MM methods: the system is divided into an inner region including, but not limited to, the QM part and an outer region covering the rest of the system, as illustrated in Figure 1. In microiterative schemes, the regions are optimized separately. One can either use an adiabatic scheme,^{7–9,11,15} that is, fully optimize the outer region after each optimization step of the inner region, or use an alternating scheme,^{10,12} in which each region is completely optimized with the other one frozen. Both

* Corresponding author e-mail: J.Kaestner@dl.ac.uk.

[†] Max-Planck-Institut für Kohlenforschung.

[‡] CCLRC Daresbury Laboratory.

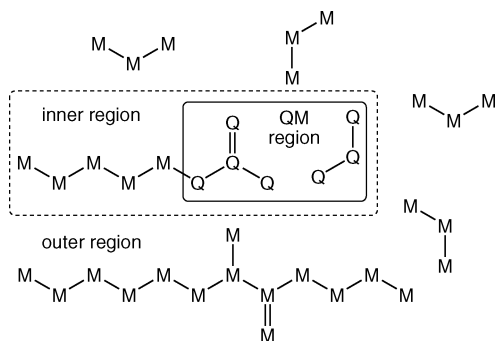


Figure 1. Partitioning of the system: Atoms in the QM region are described quantum mechanically, the remainder by molecular mechanics. Macroiterations are performed in the inner region, which has to include all QM atoms. Microiterations are performed in the outer region.

schemes are iterated until both regions are converged. This work uses the adiabatic scheme to minimize the number of required QM calculations.

Computation time is saved because the number of costly optimization steps in the inner region (macroiterations) is reduced, at the expense of the number of optimization steps in the outer region (microiterations). In mechanical QM/MM embedding, the interaction between the QM and the MM parts is calculated at the force-field level. Thus a microiterative scheme can be applied straightforwardly.^{7,13,15}

Using electrostatic QM/MM embedding, the electrostatic interaction between the QM and the MM parts is evaluated by the QM code. This in principle requires a QM calculation even if only MM atoms are moved during the microiterations. Thus, some approximations are necessary in order to reduce the CPU demand. The density of the QM part may be frozen during the microiterations, which almost retains the convergence of the optimizer compared with full QM calculations¹⁴ and saves some computation time as only one-electron integrals have to be evaluated. Alternatively, charges that represent the electrostatic potential of the QM part (ESP charges) may be used to calculate the electrostatic QM/MM interaction in the microiterations. Without corrections, this leads to different potential-energy surfaces for the micro- and macroiterations, which hampers convergence.¹⁴ If ESP charges are used for the electrostatic QM/MM interaction in both the macro- and microiterations, convergence is good,^{10,12} but the QM/MM Hamiltonian is altered. To correct the gradient obtained from ESP charges, one can use the exact QM/MM forces at the initial geometry of the microiterations plus the change in the gradient provided by ESP charges during the microiterations.¹¹ This latter approach is adopted in our work.

Besides the computational cost of the QM calculations, the time required for the optimizer itself becomes an issue for systems with several thousand atoms if the optimizer scales worse than linearly with system size.

Two types of optimizers are frequently employed in atomistic simulations. First-order methods like steepest descent or conjugate gradient methods take only the gradient of the total energy with respect to the nuclear coordinates into account. The computation time for evaluating the search direction is small and generally scales as $\mathcal{O}(N)$, with N being

the number of degrees of freedom to be optimized. However, in general, many energy and gradient evaluations are required to achieve convergence. First-order methods are suited for large systems if the energy and gradient evaluations are very fast (as, e.g., in MM). By contrast, second-order methods, including Newton–Raphson, partitioned rational function optimization,¹⁶ or the Broyden–Fletcher–Goldfarb–Shanno^{17–20} (BFGS) algorithm, make use of the Hessian. Therefore, they require fewer steps until convergence, but the time to evaluate each search step scales as $\mathcal{O}(N^3)$. The limited-memory BFGS^{21,22} (L-BFGS) variant utilizes Hessian information accumulated from the gradients over the history of the optimization and thus scales as $\mathcal{O}(N)$ in both CPU time and memory requirements. It is particularly suited for large-scale optimizations and is therefore employed in this work.

The choice of coordinates also has major effects on the scaling and convergence behavior of the optimizer. Cartesians are easy and efficient to handle, but highly coupled, which impedes convergence. Internal coordinates, such as Z-matrix coordinates, are less coupled, but they are biased. Redundant internal coordinates can be constructed in an unbiased manner, but their redundancy may spoil convergence, as changes in the coordinates do not necessarily lead to changes in the energy. For all variants of internal coordinates covering the whole system, the conversion between internals and Cartesians (which are needed to calculate the energy) scales as $\mathcal{O}(N^3)$, and internals are thus impractical for large systems. We use hybrid delocalized internal coordinates⁹ (HDLC), where both the time and memory requirements scale as $\mathcal{O}(N)$. This scaling behavior is achieved by dividing the system into fragments and using internals only within each fragment.

In section II, we present a microiterative scheme for geometry optimization in QM/MM calculations which has been implemented in the general-purpose QM/MM software package ChemShell^{23,24} as an extension to the HDLC optimizer.⁹ In section III, we describe its performance in a variety of QM/MM calculations using semiempirical and DFT methods as QM components and standard as well as polarizable force fields (shell models) as MM components. These calculations were carried out using the ChemShell software interfaced to MNDO,²⁵ TURBOMOLE,^{26–30} and GAMESS-UK^{31,32} as QM codes and GROMOS³³ and GULP³⁴ as MM codes; the DL_POLY code included in ChemShell was used for CHARMM.³⁵ We show that the microiterative scheme reduces the computation times for QM/MM geometry optimizations with electrostatic embedding typically by a factor of 2–10.

II. Theory

II.A. Definitions and Notation. We apply an additive QM/MM scheme with link atoms where the total QM/MM energy is defined as

$$E = E_{\text{qm}}(x_{\text{qm}}) + E_{\text{qm/mm}}(x_{\text{qm}}, x_{\text{mm}}) + E_{\text{mm}}(x_{\text{mm}}) \quad (1)$$

with E_{qm} depending on the coordinates of the QM atoms x_{qm} and E_{mm} depending on the coordinates of the MM atoms x_{mm} . The term $E_{\text{qm/mm}}$ includes all energy contributions coupling the QM and the MM parts:

$$E_{\text{qm/mm}} = E_{\text{Q}} + E_{\text{vdW}} + E_{\text{FF}} \quad (2)$$

that is, the electrostatic QM/MM interaction E_{Q} , the van der Waals interaction E_{vdW} , and the force field terms E_{FF} at the boundary. The latter stem from covalent bonds between QM and MM atoms. Within the electrostatic embedding scheme, the QM code calculates $E_{\text{qm}} + E_{\text{Q}}$, while the MM code computes the remaining terms $E_{\text{mm}} + E_{\text{vdW}} + E_{\text{FF}}$. To avoid overpolarization of the QM density at the boundary, we use a charge-shift scheme.²³ The charge of the MM atom of the link is redistributed onto the MM atoms bonded to it. Thus, the overall charge is conserved. To conserve also the dipole moment, pairs of point charges of opposite sign are added to these neighboring MM atoms.

During the microiterations, the electrostatic interaction E_{Q} is approximated by the point-charge interaction energy $E_{\text{Q-ESP}}$ between the ESP charges on the QM atoms and the force-field charges on the MM atoms. We thus need to calculate the approximate energy

$$E_{\text{ESP}} = E_{\text{qm}} + E_{\text{Q-ESP}} + E_{\text{vdW}} + E_{\text{FF}} + E_{\text{mm}} \quad (3)$$

The QM energy E_{qm} is calculated at each macroiteration and remains constant during the microiterations. The second term $E_{\text{Q-ESP}}$ takes into account any modifications of MM charges arising from the applied link-atom treatment (i.e., from the charge-shift scheme, see above). In the modular structure of ChemShell, it is computed by a separate dedicated routine, while the remaining three terms in eq 3 are again provided by the MM code.

We adopt the convention to use superscripts 0 and 1 to label quantities that refer to macroiterations and microiterations, respectively. The total QM/MM energy E^0 and its gradient $G^0 = \partial E^0 / \partial x^0$ are evaluated only during the macroiterations (coordinates x^0), while the approximate energy E_{ESP}^1 and the associate gradient are computed also during the microiterations (coordinates x^1). The energy E^1 and the gradient G^1 that are actually used in the microiterations need to coincide with E^0 and G^0 , respectively, when the geometries are identical ($x^0 = x^1$). Their proper choice will be discussed below.

II.B. Microiterative Optimization Algorithm. As already mentioned in the Introduction, we adopt the L-BFGS optimization algorithm in HDLCs, both in the inner and outer regions, as it scales linearly with system size and shows comparable convergence to other second-order optimizers. A trust-radius approach (for details, see ref 9) is used to determine the step size. This allows the optimizer to reject steps.

The general flow of the microiterative geometry optimizer is outlined in Chart 1. All energies E correspond to total energies, including QM and MM contributions. A standard L-BFGS optimization, without microiterations, would consist of cycles between steps 1, 3–5, and 7 only.

Overall convergence requires converged macro- and microiterations. As full QM/MM calculations define the convergence of the macroiterations, the accuracy of standard optimization is retained even when ESP charges are used in the microiterations.

In Chart 1, the ESP charges are calculated in step 2, prior to the macroiterative step 5 that moves the QM atoms. They are then used in the subsequent microiterations at a QM geometry that is different from the one for which they have been determined. This approach, denoted as Q1, introduces some error, but requires only one QM calculation in each macroiteration. Alternatively, one could include a second QM calculation and ESP charge evaluation in analogy to steps 1 and 2 at step 6, in what we call scheme Q2. We tested both approaches and found Q1 to be superior. This comparison is presented in sections 3.2 and 3.3.

II.C. Energy and Gradient Corrections in the Microiterations. The crucial point for fast convergence is the matching of the energy surfaces of the macroiterations and the microiterations. In the former, the energy is calculated with a full QM treatment. In the microiterations, however, no QM calculation is done, and the energy is calculated by replacing the QM density with ESP charges. These provide sufficiently accurate electrostatic forces on MM atoms far from the QM part but do not account for the shielding experienced by MM atoms within the QM density. Following a previous proposal,¹¹ we use a corrected gradient during the microiterations, that is, in step 6a of Chart 1:

$$G^1 = \frac{\partial E^1}{\partial x_{\text{outer}}} = \frac{\partial E_{\text{ESP}}^1}{\partial x_{\text{outer}}} + G_{\text{corr}}^0 \quad (4)$$

with

$$G_{\text{corr}}^0 = \left. \frac{\partial E^0}{\partial x_{\text{outer}}} \right|_{x_{\text{outer}}^0} - \left. \frac{\partial E_{\text{ESP}}^0}{\partial x_{\text{outer}}} \right|_{x_{\text{outer}}^0} \quad (5)$$

where the correction G_{corr}^0 is calculated using the geometry from the last full macroiterative QM calculation, that is, step 1. Hence, we only assume that the ESP charges can faithfully reproduce the *change* in the gradient contribution from the electrostatic QM/MM interaction during the microiterations. The derivatives in eqs 4 and 5 are restricted to the coordinates x_{outer} of the outer region since the coordinates of the inner region remain fixed.

To achieve optimal convergence behavior, the energy expression has to match the gradient expression; that is, the gradient has to be the derivative of the energy. The approximate energy E_{ESP}^1 does not correspond to the gradient in eq 4 due to the appearance of G_{corr}^0 and can thus not be used as a criterion for accepting or rejecting steps in step 6d of Chart 1 where the current energy is compared to that from the preceding microiteration (or from the preceding macroiteration in the case of the first microiteration). The energy expression for step 6d is

$$E^1 = E_{\text{ESP}}^1 + E^0 - E_{\text{ESP}}^0 + G_{\text{corr}}^0 (x_{\text{outer}}^1 - x_{\text{outer}}^0) \quad (6)$$

where x_{outer}^1 are the current coordinates of the outer region and x_{outer}^0 are the respective coordinates from the last macroiterative QM calculation. As can be verified easily, the gradient in eq 4 is the derivative of eq 6 with respect to x_{outer}^1 . The expressions for the energy E^1 and the gradient G^1 ensure a smooth connection between microiterations and macroiterations: in the case of identical geometries ($x^0 =$

Chart 1. Program Flow of the Microiterative Optimization Algorithm Q1

- Step 1: Perform a QM/MM calculation with a full QM calculation to obtain the QM/MM energy E^0 and the gradient G^0 at geometry x^0 .
- Step 2: Calculate ESP charges fitted on the fly to the actual electron density. Recalculate the approximate energy E_{ESP}^0 using ESP charges instead of the QM density for the electrostatic QM/MM interaction. Calculate the gradient correction G_{corr}^0 from Eq. (5).
- Step 3: If this is not the first macroiteration, test the acceptance of the step. Reject it if E^0 has increased compared with E^0 of the previous macroiteration. In this case reset the coordinates of the whole system to those used in the previous macroiteration, and halve the step size.
- Step 4: If the step is accepted, terminate if the convergence criteria are met.
- Step 5: Make one L-BFGS step in the inner region using the gradient obtained in step 1.
- Step 6: Enter the microiterations
- Step 6.a: Make an L-BFGS step in the outer region using the gradient from Eq. (4).
- Step 6.b: If the convergence criteria are met, exit the microiterative loop and continue at step 7.
- Step 6.c: Calculate the energy (E_{ESP}^1) and the associated gradient using ESP charges.
- Step 6.d: If the energy E^1 (see Eq. (6)) has increased, reject the step and reduce the step size.
- Step 6.e: Continue at step 6.a.
- Step 7: Continue with macroiterations at step 1.

x^1), eqs 6 and 4 recover E^0 and G^0 , respectively. Close to convergence, the geometry will change only very slightly in the microiterations and the approximations through ESP charges become exact.

We generally find good convergence of the overall optimization scheme when using the above energy and gradient expressions during the microiterations. While the gradient correction has been proposed before,¹¹ we are not aware of any previous discussion of a matching energy expression, eq 6, which is crucial for proper convergence. The use of ESP charges in the microiterations will be justified further in section 3.2 through comparisons with optimizations employing frozen QM densities and full self-consistent field (SCF) calculations for the QM region.

The L-BFGS memory, that is, the number of steps used to accumulate Hessian information, is retained during the macroiterations. Whenever a new cycle of microiterations is started, however, the L-BFGS optimizer for the microiterations is reset. The trust radius from the last microiteration cycle is retained as a starting value. This turned out to lead to faster convergence than resetting the trust radius to a fixed value.

II.D. Convergence Criteria. The adiabatic microiterative scheme requires in principle a fully converged outer region in each macroiteration. As this is difficult to achieve in practice, we include the coordinate space of both the inner and outer region into the active space for the L-BFGS algorithm of the macroiterations. In this case, partial convergence of the microiterations is sufficient to reach overall convergence.¹⁵ This can be achieved by using a tighter (smaller) convergence criterion for the microiterations than for the macroiterations. The larger the ratio of the convergence criteria of the macroiterations and the microiterations is, the more MM steps, and accordingly less QM steps, are required to achieve convergence. While this ratio is user-definable in our implementation, we adopt a value of 10 throughout this work.

The convergence criteria for standard optimizations and macroiterations are taken from Gaussian 94.³⁶ An optimization is considered converged when all of the following four criteria are fulfilled (all values in atomic units, au). (i) The maximum gradient component has to be lower than $c = 0.00045$; this value can be specified by the user; (ii) $^{2/3}c$ is used as a criterion for the root-mean-square (RMS) of the

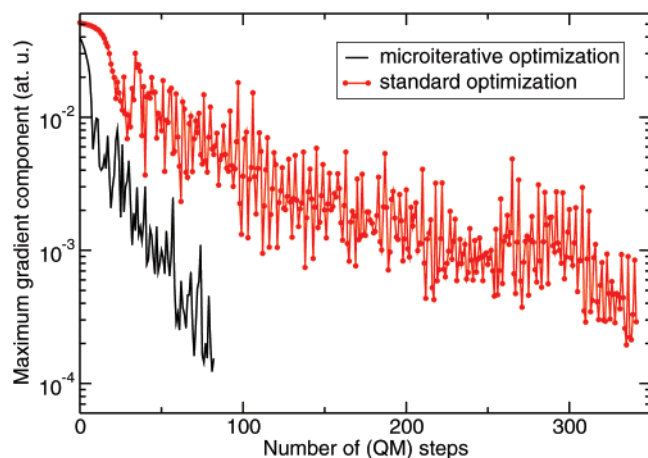


Figure 2. Maximum gradient component (one of the four convergence criteria) during microiterative optimization (only macroiterations shown) and standard optimization. This example refers to PHBH; the microiterative run was done with the parameters of the first line in Table 3.

gradient, (iii) $4c$ for the maximum step size, and (iv) $8/3c$ for the RMS of the step vector.

The convergence of the proposed scheme is illustrated in Figure 2. One of the four convergence criteria is plotted against the number of QM calculations. The microiterative optimization converges significantly faster, that is, requires fewer QM steps, than the standard optimization.

III. Results and Discussion

III.A. Scaling Behavior of the Optimizer. To show that the CPU time of an optimization is roughly independent of the MM system size, we optimized the geometry of water clusters in spheres of increasing size. Three water molecules in the center of the sphere served as the QM part and inner region. They were described by the semiempirical AM1 Hamiltonian.³⁷

The MM water molecules were represented by the TIP3P³⁸ model, which constrains all internal coordinates. Only the relative orientations were optimized, leaving six degrees of freedom per water molecule. All 4404 water molecules with at least one atom within 25 Å of the center were cut out of equilibrated bulk water. Different active regions were defined, with radii of 5, 10, 15, and 20 Å. All atoms within the active region were optimized, while those outside were kept frozen and thus provided some kind of boundary potential. The microiterative optimizations were done according to Chart 1 using the standard Q1 approach.

Table 1 shows that the overall effort, measured by the number of QM steps in a microiterative optimization, changes with system size, but in a non-monotonic way, for a given size of the QM region. This is a well-known behavior of optimization algorithms in complex systems, which has often been encountered in the present work: unproductive search directions are tried and rejected in one case, while they may be directly avoided in the other case. In Table 1, the system with 9588 degrees of freedom apparently was especially easy to optimize. It needed less steps than the next smaller system (4644 degrees of freedom) in the microiterative scheme as well as in standard optimization.

Table 1. Optimization of Spherical TIP3P Water Clusters with a Radius of 25 Å (See Text)^a

active region	DOF	microit.		std. QM	ΔE
		QM	MM		
5 Å	1662	62	2292	259	+23
10 Å	4644	62	2621	517	-57
15 Å	9588	56	3328	471	-19
20 Å	17 424	90	3640	801	-72

^a The radius of the active region is given in the first column. DOF is the number of degrees of freedom being optimized. The following columns give the number of QM and MM calculations in microiterative optimization and the number of QM calculations in a standard QM/MM optimization. ΔE denotes the energy difference between the result of the microiterative and the standard optimizations in kilojoules per mole (positive if the former leads to a higher energy, and negative otherwise).

Generally speaking, optimizations of the kind considered currently only reach local minima. Since many close-lying minima are present in complex systems, different optimizers take different paths and may converge to different local minima. This happened in all four cases in Table 1. When standard and microiterative optimizations converge to the same minimum, the energy from the latter is generally slightly lower, because of the tighter convergence criteria used for the outer region of the system.

A noticeable difference between the systems with active regions of different size is the number of microiterations preceding the first macroiteration: 146, 654, 627, and 1031 initial microiterations are needed for the four systems in Table 1, respectively. These steps cover the major part of the optimization of the outer region. The following macro- and microiterations take more or less the same number of steps for all active regions considered.

We have also tested the systems with just one water molecule in the QM part and inner region. A total of 85, 48, 28, and 61 QM calculations are required to converge the different active regions, respectively. Thus, in this case, the smallest system needed the most steps to converge, again a result of the non-monotonic behavior discussed above.

The number of QM calculations required in a standard QM/MM optimization is shown in Table 1 as a reference. It is obvious that this number is greatly reduced in the microiterative optimizations, by a factor of 4–9. This indicates the speedup for QM/MM optimizations with high-level QM methods (*ab initio* or DFT) where the computational effort is dominated by the QM calculation. The speedup is somewhat smaller for semiempirical QM/MM optimizations since the computation time for the MM part is not completely negligible in this case.

III.B. ESP Charges versus Frozen Density and Full SCF Calculations. To check the approximate treatment of electrostatics in the microiterations, we performed test calculations on the example introduced in the previous section (a spherical TIP3P water cluster with a 5 Å active region; see first line of Table 1). The exact evaluation of the electrostatic QM/MM interaction energy would employ full SCF calculations. Successive approximations involve the use of frozen QM densities and ESP charges; the latter are consistent with the frozen QM densities in scheme Q2,

Table 2. Comparison of Different Methods for Evaluating the Electrostatic QM/MM Interaction Energy in the Microiterations (See Text) during Optimization of a Spherical TIP3P Water Cluster (See First Line of Table 1)^a

electrostatics	macroit.	microit.	ΔE
SCF calculations Q2	44 (88)	1443	+23
frozen density Q2	47 (94)	1359	+16
ESP charges Q2	80 (160)	2528	+47
ESP charges Q1	62 (62)	2292	+23

^a The second column lists the number of macroiterations until convergence (in parentheses: total number of QM calculations during macroiterations). The third column gives the number of microiterations (QM calculations in the SCF case). ΔE denotes the energy difference between the result of the microiterative and the standard optimization in kilojoules per mole.

whereas those from scheme Q1 are determined at a slightly different geometry and are therefore even more approximate (see section 2.2).

Table 2 shows that full SCF calculations during the microiterations lead to the fastest convergence (44 macroiterations), closely followed by the calculations with the frozen QM density (47 macroiterations). Representing the QM density by ESP charges in scheme Q2 slows down convergence (80 macroiterations), which—surprisingly and probably fortuitously—becomes faster again with scheme Q1 (62 macroiterations). The final energies are comparable in all four cases and virtually identical for the best and the most approximate treatment applied (see Table 2, first and last lines). The present results confirm that the overall convergence behavior of our microiterative optimizer is not very sensitive to the treatment of electrostatics in the microiterations. Under these circumstances, the use of ESP charges is clearly justified considering the huge savings in computation time compared with the use of frozen QM densities (or even full SCF calculations).

III.C. Charge-Fitting Procedures. The approximation of the density by point charges can be done in various ways. We only consider charges derived from the electrostatic potential. One can fit the potential at different positions in space, for example, on a shell around the QM part or at the positions of the nearest MM atoms. The fitting itself can be done without constraints, resulting in ESP charges, or with restrictions keeping the fitted charges at low values, yielding so-called restrained electrostatic potential (RESP) charges.³⁹

We tested the effect of different charge-fitting schemes on the optimization process using the enzyme *p*-hydroxybenzoate hydroxylase (PHBH). The QM part contained 49 atoms: *p*-hydroxybenzoate and the isoalloxazine part of the hydroperoxyflavin cofactor of PHBH. Polar groups, such as carboxylates, and atoms buried within the QM part, for which ESP charges are not well-defined, pose significant challenges to the charge fitting. Thus, this example should provide a stringent test for charge-fitting schemes. Again, AM1 was used as the QM method, while the GROMOS force field was chosen to describe the MM environment. Details of the system setup are available elsewhere.^{40,41} We optimized an active region with 8847 degrees of freedom, composed of the QM part and all residues with at least one atom within 15 Å of the substrate. The optimizations were started from

Table 3. Comparison of Different Charge-Fitting Procedures in the Microiterative Optimization of PHBH (See Text)^a

	# pt.	QM	MM	ΔE (kJ mol ⁻¹)	
MM atoms	98	ESP	88	4851	-22.9
shell	98	ESP	100	4373	-23.1
MM atoms	98	RESP	91	3854	-24.2
shell	98	RESP	94	4354	-23.9
shell	400	ESP	104	4404	-23.0
standard optimization			363	0	0

^a The first three columns specify the location of the fitting points (MM atoms vs points on a shell), their number ($2N_{\text{qm}} = 98$), and the type of fitting (ESP vs RESP). The next two columns give the number of required QM and MM calculations. The last column lists the final energy relative to that obtained from a standard optimization. All microiterative optimizations are significantly better converged than the standard optimization due to the tight convergence criterion in the outer region.

a MD snapshot taken from umbrella sampling simulations equilibrated at $T = 300$ K.⁴²

This system exhibits one covalent link between the QM part and the MM part. The MM atom of the link and the MM atoms bonded to it were included in the inner region. With this choice, all atoms affected by the charge-shift scheme²³ are treated by the macroiterations.

Table 3 summarizes the results of optimizations with different charge-fitting schemes applied. Overall, the efficiency of the optimizer depends only slightly on the charge-fitting scheme. For N_{qm} (number of QM atoms) charges to be fitted, $2N_{\text{qm}}$ fitting points are sufficient (i.e., 98 in this case). Using the positions of the MM atoms with the smallest distance to their nearest QM atom seems slightly more efficient (88 QM steps) than using points on a shell of 1.5 times the van der Waals distance of the QM atoms (100 steps). ESP and RESP charges lead to a similar convergence behavior (100 vs 94 and 88 vs 91 steps, respectively), but a slightly lower energy is obtained in both cases when using RESP charges, and fewer MM steps are required. Finally, using 400 points to fit the potential rather than 98 has little effect on the convergence (104 vs 100 steps).

In our implementation, the choice of the fitting method is left to the user. However, for an arbitrary system, a shell of fitting points may be better than the MM positions, as the latter may be distributed unevenly, preventing an accurate fit.

We have also tested on this system the alternative scheme Q2 introduced in section 2.2. With all other parameters set as in the first line of Table 3, 178 QM calculations (i.e., 89 macroiterations) were needed to reach convergence for Q2, compared to 88 when using Q1, and the same optimized energy of -22.9 kJ mol⁻¹ was obtained (see Table 3). These results again show the validity of the approximate scheme Q1.

Finally, we note that a standard optimization requires typically almost 4 times more QM calculations than the microiterative approach (see Table 3) and yields a minimum that is 23–24 kJ mol⁻¹ higher in energy. This is caused by the relatively loose convergence criteria applied to the whole system: 10 times tighter criteria are used for the outer region in the microiterative optimizations. If 3 times tighter criteria

(i.e., $c = 0.00\ 015$ au) are used in the standard optimization, 557 iterations are needed (i.e., 5–6 times more than with the microiterative scheme), but the resulting energy of -23.8 kJ mol $^{-1}$ is close to the microiterative results. This indicates that the standard optimization does reach the same local minimum as the microiterative scheme, when the convergence criteria are sufficiently tightened.

III.D. Energy Minimization in Enzymes. We chose the enzyme fluorinase to compare actual CPU times rather than the number of QM steps. The DFT calculations used for the QM system take substantially more computation time than the force-field calculations. The system was set up in analogy to our previous work.⁴³ The fluorinase catalyzes the S_N2 attack of fluoride on *S*-adenosyl-L-methionine (SAM). The QM part consisted of the 39 atoms of fluoride and the 5'-(*S,S*-dimethylsulfonio)-5'-deoxyadenosine part of SAM. The CHARMM22³⁵ force field was used for the MM calculations with the DL_POLY force-field engine included in ChemShell. A group-based cutoff of 20 au was applied for the MM interactions, while no cutoff was used for the QM/MM interactions. The QM calculations were done with TURBO-MOLE interfaced to ChemShell at the DFT (BP86) level with the TZVP basis⁴⁴ augmented by diffuse functions (1005 basis functions in total). They were message-passing-interface-parallelized over four AMD Opteron 848 processors with a clock rate of 2.2 GHz. A trimer unit of the enzyme with 17 596 atoms, including 4272 water molecules, was used, of which only one active site was solvated. All residues or water molecules within 8 Å of SAM or F $^{-}$ were included in the optimization. Water was again described by the TIP3P model, with all three internal degrees of freedom constrained. This resulted in 3960 degrees of freedom to be optimized. Fluoride and the whole SAM group (153 degrees of freedom) served as the inner region in the microiterative optimizations.

In contrast to all cases discussed up to now, we started from a structure already optimized under a constraint that keeps the system close to the transition state, rather than from an MD snapshot. This is a severe test for the microiterative scheme, as the structural changes occur predominantly within the QM region rather than uniformly throughout the system.

Nevertheless, the microiterative scheme required only 51% of the time for a standard optimization which took 139 CPU hours. A total of 53 QM steps were required until convergence was reached, rather than 119 steps in the standard calculation. The fact that relatively less CPU time (49%) is saved compared to the change in the number of QM calculations (55%) is due to two factors: (1) The number of MM energy evaluations increased from 119 to 4610. Thus, the MM calculations accounted for less than 0.1% of the overall time in the standard optimization but for 2% in the microiterative optimization. (2) Each QM step in the microiterative scheme takes some 2% longer than in the standard optimization, as the ESP charges have to be evaluated in addition. The tighter convergence criterion for the MM part resulted in a tiny energy lowering by 0.04 kJ mol $^{-1}$. We did not attempt to converge an MD snapshot due to the potentially high computational cost of a standard optimization.

III.E. Polarizable Force Fields for Surface Catalysis.

The applicability of the microiterative optimizer to solid-state embedding was tested by optimizing the structure of a defect at the MgO (001) surface. We modeled the MgO surface as a hemispherical cluster in analogy to previous work.^{3,45} GAMESS-UK^{31,32} was used as the QM code and GULP³⁴ with a shell model⁴⁶ (i.e., a polarizable force field) as the MM code. The polarization of the MM part adds another layer of iterations to the calculations. Whenever a full QM/MM energy is evaluated, the QM and MM calculations are iterated until the mutual polarization of the QM and MM parts has converged.

This example is intended as a proof of principle, showing that the microiterative optimization works and converges well for a shell model. The system needed 30 QM steps and 459 MM steps in the microiterative optimization, compared to 34 optimization steps in the standard optimization, and it reached the same minimum, the final energy being slightly lower (by 3.5 kJ mol $^{-1}$) in the microiterative case. With only four QM calculations saved, the benefits of the microiterative scheme are less pronounced in this example, presumably because the optimization started from a well-ordered rather than a disordered structure (such as an MD snapshot).

IV. Conclusion

We have described an optimization scheme for the QM/MM approach with electrostatic embedding. In each QM optimization step (macroiteration), the MM atoms in the outer region are fully relaxed in microiterations, during which the QM density is approximated by ESP charges to allow for an efficient computation of the electrostatic QM/MM interactions. Suitable energy and gradient expressions for the microiterations ensure an excellent convergence behavior of the overall algorithm. The inner region treated by macroiterations must contain all QM atoms but may be extended to include additional MM atoms. The algorithm retains the accuracy of a standard QM/MM optimization scheme, while saving typically a factor of 2–10 in CPU time for the examples discussed. It has been implemented in the modular QM/MM program package ChemShell.

We have considered two variants, Q1 and Q2, which evaluate the ESP charges at different stages of the algorithm. In Q1, they are calculated prior to each macroiterative step and then used at a geometry of the inner region that is slightly different, whereas they are redetermined at this geometry in Q2. Variant Q1 is preferred over Q2 because it requires only half the computational effort and performs well in the test cases studied. We have also compared several charge-fitting procedures (such as ESP vs RESP) and found that the convergence behavior is largely independent of these choices.

The force-field calculations in the microiterations are fast compared to full QM/MM calculations, and they relax the MM part efficiently. The overall computational cost of such an optimization is thus essentially independent of the MM system size, for a given size of the QM part. The microiterative optimization algorithm is particularly beneficial for systems in which the MM part as well as the QM part are far from the minimum, as is often the case for MD snapshots as starting points. In systems where the MM part is almost

relaxed but the QM part is not, the microiterative scheme will show only a minor, if any, advantage over the conventional optimization.

Using the ChemShell implementation, we have demonstrated the applicability of the microiterative optimization scheme for a number of different systems: a water cluster, fully or partially solvated proteins, and a surface defect. We believe that the proposed microiterative optimizer will increase the range of applicability of QM/MM methods because it enables large-scale QM/MM optimizations with electrostatic embedding.

Acknowledgment. S.T. thanks Salomon Billeter for helpful discussions. This work was supported by the Deutsche Forschungsgemeinschaft, Grant SFB 663/C4.

References

- (1) Brändle, M.; Sauer, J. *J. Am. Chem. Soc.* **1998**, *120*, 1556.
- (2) Sierka, M.; Sauer, J. *Faraday Discuss.* **1997**, *106*, 41.
- (3) Sushko, P. V.; Shluger, A. L.; Catlow, C. R. A. *Surf. Sci.* **2000**, *450*, 153.
- (4) Åqvist, J.; Warshel, A. *Chem. Rev.* **1993**, *93*, 2523.
- (5) Gao, J.; Ma, S.; Major, D. T.; Nam, K.; Pu, J.; Truhlar, D. G. *Chem. Rev.* **2006**, *106*, 3188.
- (6) Senn, H. M.; Thiel, W. In *Atomistic Approaches in Modern Biology – From Quantum Chemistry to Molecular Simulations*; Reiher, M., Ed.; Springer: Berlin, Germany, 2007; Topics in Current Chemistry, Vol. 268, pp 173–290.
- (7) Maseras, F.; Morokuma, K. *J. Comput. Chem.* **1995**, *16*, 1170.
- (8) Turner, A. J.; Moliner, V.; Williams, I. H. *Phys. Chem. Chem. Phys.* **1999**, *1*, 1323.
- (9) Billeter, S. R.; Turner, A. J.; Thiel, W. *Phys. Chem. Chem. Phys.* **2000**, *2*, 2177.
- (10) Zhang, Y.; Liu, H.; Yang, W. *J. Chem. Phys.* **2000**, *112*, 3483.
- (11) Murphy, R. B.; Philipp, D. M.; Friesner, R. A. *J. Comput. Chem.* **2000**, *21*, 1442.
- (12) Hall, R. J.; Hindle, S. A.; Burton, N. A.; Hillier, I. H. *J. Comput. Chem.* **2000**, *21*, 1433.
- (13) Vreven, T.; Morokuma, K.; Farkas, Ö.; Schlegel, H. B.; Frisch, M. J. *J. Comput. Chem.* **2003**, *24*, 760.
- (14) Prat-Resina, X.; Bofill, J. M.; González-Lafont, A.; Lluch, J. M. *Int. J. Quantum Chem.* **2004**, *98*, 367.
- (15) Vreven, T.; Frisch, M. J.; Kudin, K. N.; Schlegel, H. B.; Morokuma, K. *Mol. Phys.* **2006**, *104*, 701.
- (16) Banerjee, A.; Adams, N.; Simons, J.; Shepard, R. *J. Phys. Chem.* **1985**, *89*, 52.
- (17) Broyden, C. G. *J. Inst. Math. Appl.* **1970**, *6*, 76.
- (18) Fletcher, R. *Comput. J.* **1970**, *13*, 317.
- (19) Goldfarb, D. *Math. Comp.* **1970**, *24*, 23.
- (20) Shanno, D. F. *Math. Comp.* **1970**, *24*, 647.
- (21) Liu, D. C.; Nocedal, J. *Math. Prog. B* **1989**, *45*, 503.
- (22) Nocedal, J. *Math. Comp.* **1980**, *35*, 773.
- (23) Sherwood, P.; de Vries, A. H.; Guest, M. F.; Schreckenbach, G.; Catlow, C. R. A.; French, S. A.; Sokol, A. A.; Bromley, S. T.; Thiel, W.; Turner, A. J.; Billeter, S.; Terstegen, F.; Thiel, S.; Kendrick, J.; Rogers, S. C.; Casci, J.; Watson, M.; King, F.; Karlsen, E.; Sjøvoll, M.; Fahmi, A.; Schäfer, A.; Lennartz, C. *THEOCHEM* **2003**, *632*, 1.
- (24) ChemShell, a Computational Chemistry Shell. <http://www.chemshell.org> (accessed Nov 28, 2006).
- (25) Thiel, W. *MNDO99*, version 6.1; Max-Planck-Institut für Kohlenforschung: Mülheim an der Ruhr, Germany, 2004.
- (26) Ahlrichs, R.; Bär, M.; Häser, M.; Horn, H.; Kölmel, C. *Chem. Phys. Lett.* **1989**, *162*, 165.
- (27) Treutler, O.; Ahlrichs, R. *J. Chem. Phys.* **1995**, *102*, 346.
- (28) Eichkorn, K.; Treutler, O.; Öhm, H.; Häser, M.; Ahlrichs, R. *Chem. Phys. Lett.* **1995**, *242*, 652.
- (29) Eichkorn, K.; Weigend, F.; Treutler, O.; Ahlrichs, R. *Theor. Chem. Acc.* **1997**, *97*, 119.
- (30) Sierka, M.; Hogekamp, A.; Ahlrichs, R. *J. Chem. Phys.* **2003**, *118*, 9136.
- (31) GAMESS-UK is a package of ab initio programs. <http://www.cfs.dl.ac.uk/games-uk/index.shtml> (accessed Nov 28, 2006).
- (32) Guest, M. F.; Bush, I. J.; van Dam, H. J. J.; Sherwood, P.; Thomas, J. M. H.; van Lenthe, J. H.; Havenith, R. W. A.; Kendrick, J. *Mol. Phys.* **2005**, *103*, 719.
- (33) van Gunsteren, W. F.; Billeter, S. R.; Eising, A. A.; Hünenberger, P. H.; Krüger, P.; Mark, A. E.; Scott, W. R. P.; Tironi, I. G. *Biomolecular Simulation: The GROMOS96 Manual and User Guide*; vdf and BIOMOS b.v.: Zürich, Switzerland, 1996.
- (34) Gale, J. D. *J. Chem. Soc., Faraday Trans.* **1997**, *93*, 629.
- (35) MacKerell, A. D., Jr.; Bashford, D.; Bellott, R. L.; Dunbrack, R. L., Jr.; Evanseck, J. D.; Field, M. J.; Fischer, S.; Gao, J.; Guo, H.; Ha, S.; Joseph-McCarthy, D.; Kuchnir, L.; Kuczera, K.; Lau, F. T. K.; Mattos, C.; Michnick, S.; Ngo, T.; Nguyen, D. T.; Prodhom, B.; Reiher, W. E., III; Roux, B.; Schlenkrich, M.; Smith, J. C.; Stote, R.; Straub, J.; Watanabe, M.; Wiorkiewicz-Kuczera, J.; Yin, D.; Karplus, M. *J. Phys. Chem. B* **1998**, *102*, 3586.
- (36) Frisch, M. J.; Trucks, G. W.; Schlegel, H. B.; Gill, P. M. W.; Johnson, B. G.; Robb, M. A.; Cheeseman, J. R.; Keith, T.; Petersson, G. A.; Montgomery, J. A.; Raghavachari, K.; Al-Laham, M. A.; Zakrzewski, V. G.; Ortiz, J. V.; Foresman, J. B.; Cioslowski, J.; Stefanov, B. B.; Nanayakkara, A.; Challacombe, M.; Peng, C. Y.; Ayala, P. Y.; Chen, W.; Wong, M. W.; Andres, J. L.; Replogle, E. S.; Gomperts, R.; Martin, R. L.; Fox, D. J.; Binkley, J. S.; Defrees, D. J.; Baker, J.; Stewart, J. P.; Head-Gordon, M.; Gonzalez, C.; Pople, J. A. *Gaussian 94*, rev. c.3; Gaussian, Inc.: Pittsburg, PA, 1995.
- (37) Dewar, M. J. S.; Zoebisch, E. G.; Healy, E. F.; Stewart, J. J. P. *J. Am. Chem. Soc.* **1985**, *107*, 3902.
- (38) Jorgensen, W. L.; Chandrasekhar, J.; Madura, J. D.; Impey, R. W.; Klein, M. L. *J. Chem. Phys.* **1983**, *79*, 926.
- (39) Bayly, C. I.; Cieplak, P.; Cornell, W.; Kollman, P. A. *J. Phys. Chem.* **1993**, *97*, 10269.
- (40) Senn, H. M.; Thiel, S.; Thiel, W. *J. Chem. Theory Comput.* **2005**, *1*, 494.
- (41) Kästner, J.; Senn, H. M.; Thiel, S.; Otte, N.; Thiel, W. *J. Chem. Theory Comput.* **2006**, *2*, 452.

- (42) Kästner, J.; Thiel, W. *J. Chem. Phys.* **2005**, *123*, 144104.
- (43) Senn, H. M.; O'Hagan, D.; Thiel, W. *J. Am. Chem. Soc.* **2005**, *127*, 13643.
- (44) Schäfer, A.; Huber, C.; Ahlrichs, R. *J. Chem. Phys.* **1994**, *100*, 5829.
- (45) Sokol, A. A.; Bromley, S. T.; French, S. A.; Catlow, C. R. A.; Sherwood, P. *Int. J. Quantum Chem.* **2004**, *99*, 695.
- (46) Dick, B. G.; Overhauser, A. W. *Phys. Rev.* **1958**, *112*, 90.

CT600346P

Structural, Energetic, and Infrared Spectra Insights into Methanol Clusters $(\text{CH}_3\text{OH})_n$, for $n = 2-12, 16, 20$. ONIOM as an Efficient Method of Modeling Large Methanol Clusters

Marcos M. Pires and Vincent F. DeTuri*

Department of Chemistry, Ithaca College, Ithaca, New York 14850

Received November 29, 2006

Abstract: An investigation of gas-phase methanol clusters $(\text{CH}_3\text{OH})_n$, where $n = 2-12, 16$, and 20, was completed with a range of computational methods: PM3, Hartree–Fock, B3LYP, MP2, and their combination using an ONIOM (our own n -layered integrated molecular orbital and molecular mechanics) method. Geometries, binding energies, and vibrational frequencies are reported. For all ab initio optimized structures, the cyclic isomer was found to be the most stable structure of all isomers investigated. The scaled OH frequency shift for $n = 1-4$ is found to be in good agreement with experimentally measured shifts. An ONIOM method, with the methyl group calculated at the low level and the hydroxyl group at the high level, proved to be an excellent way of reducing computational expense. The calculated enthalpies, geometries, and infrared spectra using an ONIOM method were comparable to that of a high-level calculation. Clusters were solvated using the integral equation formalism for the polarized continuum model method to compare with the microsolvation studies.

Introduction

The study of hydrogen-bonded clusters has been the subject of intense interest in the past decade, with water and methanol molecules receiving the greatest amount of attention.¹ Water is the most thoroughly investigated hydrogen-bonded cluster but is quite different from methanol. Water can form up to four hydrogen bonds, two as proton acceptors (via the lone-pair electrons on oxygen) and two as proton donors. Methanol generally only forms three strong hydrogen bonds, two as proton acceptors (via the lone-pair electrons on oxygen) and one as a proton donor. The methyl CH bonds may form weak hydrogen-bonding interactions. The bulky methyl group and the dipole it produces give methanol a more complex and asymmetrical cluster compared with water. This study aims to understand microscopic properties of methanol and relate those to the macroscopic properties. Specifically, we set out to determine the number of methanol molecules necessary to mimic the enthalpy of vaporization and geometric properties of bulk methanol. However, model-

ing a limited cluster size without molecular dynamics (MD) does not represent bulk methanol.

Much of the stabilization of methanol clusters comes from the very sensitive electronic interaction of the hydrogen bond. Thus, hydrogen-bonding fluids are described by the strength and number of hydrogen bonds formed. In water clusters of $n = 5-19$, the bonding energy calculated per hydrogen bond reproduces the binding energy of ice at 0 K better than the bonding energy calculated per water.² The dangling hydrogen bonds in the cluster contribute little to the energy stabilization of water. In methanol clusters, each molecule can donate only one hydrogen bond, a difference from water that has many structural and electronic consequences. An intriguing feature of hydrogen-bonded networks is that the acceptance of one hydrogen bond actually promotes the donation of an additional hydrogen bond in a process known as cooperativity or nonadditivity. The cooperativity effects have been previously calculated by ab initio methods for methanol clusters $(\text{CH}_3\text{OH})_n$ for $n = 2-6$ isolated in a vacuum at the HF/aug-cc-pVDZ//HF/6-31G(d,p) level.³ While, hydrophobic forces are also known to be part of the interaction within a methanol

* Corresponding author e-mail: vdeturi@ithaca.edu.

network, it is generally believed that the number of hydrogen bonds is what dominates the intermolecular interactions in hydrogen-bonded clusters.³

Density functional calculations, B3LYP/6-31+G(d), have been previously carried out on methanol clusters (CH₃OH)_n for $n = 2-6$ isolated in a vacuum⁴ and also at the B3LYP/6-31G(d) level for $n = 2-12$ in a vacuum.⁵ Computational results indicate that the cyclic methanol clusters are the global minima when compared with chain, branched-cyclic, and branched-chain arrangements.^{4,5} Cyclic structures maximize the number of hydrogen bonds and display an increase in cooperativity, thus yielding more favorable interactions among the members of the cluster.

Until recently, previous research on methanol clusters had been limited to single-digit numbers of molecules, and the few studies that examine higher levels, (CH₃OH)_n for $n = 6-9$, were limited to minimal ab initio methods or less accurate methods.^{1,6} A recent study investigated methanol clusters for $n = 2-12$ at the B3LYP/6-311+G(d,p)//B3LYP/6-31G(d) level.⁵ It does not appear that methanol clusters have been studied computationally for cluster sizes greater than 12 molecules using an ab initio method. MD and Monte Carlo (MC) methods have been employed on much larger clusters (up to 256 methanol molecules);⁷ however, they are limited by parametrization designed for small methanol clusters. It is not practical to account for 256 methanol molecules by an ab initio method, but an understanding of $n = 2-12$, 16, and 20 methanol clusters at a high-level ab initio method will improve the parameter set.

Herein, we also report the application of the ONIOM (our own n -layered integrated molecular orbital and molecular mechanics)⁸ method to hydrogen-bonded methanol clusters. The ONIOM method has emerged as an efficient method to study hydrogen-bonding systems and microsolvation approximations.⁹⁻¹¹ A major advantage of the ONIOM method is its versatility. It comes in many flavors, thus making it possible to specify the appropriate method and level of theory of choice for individual atoms. In our study of methanol clusters, we use the integrated molecular orbital and molecular orbital method. The technique of applying a molecular orbital treatment to both layers has been successfully tested for non-methanol systems.¹⁰ This means that both the high-level layer and the low-level layer will receive molecular orbital treatments.

There are many implications in the research of gas-phase methanol clusters that go beyond just the elucidation of how these macromolecular structures behave. Methanol molecules in large clusters are expected to have properties that are more similar to methanol in the condensed phase than to single methanol molecules. In particular, studies relating to methanol clusters may facilitate the modeling of complexation of solutes in methanol since it is well-known that the first solvation shell is particularly crucial in this respect. Solvation of organic acids by methanol has already been studied and so has proton transfer in methanol.¹²⁻¹⁴ The principal goal of this work is to characterize the geometric, energetic, and vibrational features of methanol clusters by successively increasing the cluster size up to 20 molecules. Initially, we set out to identify the lowest-energy isomers for (CH₃OH)_n

where $n = 1-10$. The number of local minima of larger systems makes it difficult to thoroughly sample all of the different conformers for each size of methanol clusters at a high level of ab initio theory. However, we believe it is not necessary to find every minimum for a specific methanol cluster size. As we study them from the smaller cluster sizes to the larger ones, we should observe a pattern that will be mimicked with each additional methanol. Such patterns are not uncommon for hydrogen-bonded cluster networks. As Maheshwary et al. discovered with water clusters,¹⁵ (H₂O)_n where $n = 4, 8, 12, 16$, and 20 are cuboids while (H₂O)₁₀ and (H₂O)₁₅ are fused pentameric structures. Moreover, structures that contained one water molecule more than the cuboid series such as $n = 9, 13$, and 17 were very similar in structure to their cuboid correspondents.

Not all previously reported structures of extensively sized methanol clusters are in agreement.¹ It has been suggested that, for methanol clusters up to $n = 17$, the clusters do not have a dominant structure.⁷ In molecular beam electric deflection experiments, the dimer was the predominant structure observed for methanol.⁷ While it is possible for clusters to be in flux, that is, constant restructuring of the cluster size, many experimental results indicate that methanol can have a predictable pattern.¹⁶

Computational Methods

All calculations were carried out using the Gaussian 98 suite of programs¹⁷ or the Gaussian 03 suite of programs.¹⁸

A common impediment to ab initio computational research of methanol clusters is the computational time required to model large clusters greater than six methanol molecules. Our first approach was to model many different conformers of each sized cluster, where $n = 1-10$, using the semiempirical method PM3. Geometry-optimized structures from the PM3 calculations were used as a starting point for HF/6-31+G(d,p) calculations. The addition of a diffuse basis set seems appropriate for a system in which hydrogen bonds contribute to the overall geometry and stabilization energy. Several of the lowest-energy PM3 structures were geometry-optimized at the HF/6-31+G(d,p) level. Basis set superposition error was calculated using the counterpoise keyword in Gaussian 03W on the optimized structures.^{19,20} Additional calculations were employed using the hybrid density functional methods B3LYP and MP2. A number of basis sets were also investigated, 6-31G(d), 6-31+G(d,p), and 6-311+G(d,p).

An ONIOM method²¹ serves as an appropriate method to reduce the computational time it takes to describe methanol clusters. ONIOM methods were initially compared to one-layered calculations to verify their efficiency. Our two-level layer scheme replaces the methyl group with a hydrogen link atom in the high-level layer. This translates into a major reduction of computational time since each methanol molecule contributes 18 electrons in the real system and 10 in the high-level system. Frequency calculations were used to verify the minima in geometry optimizations and provide thermochemical corrections to calculate the enthalpy and Gibbs energy at 298 K.

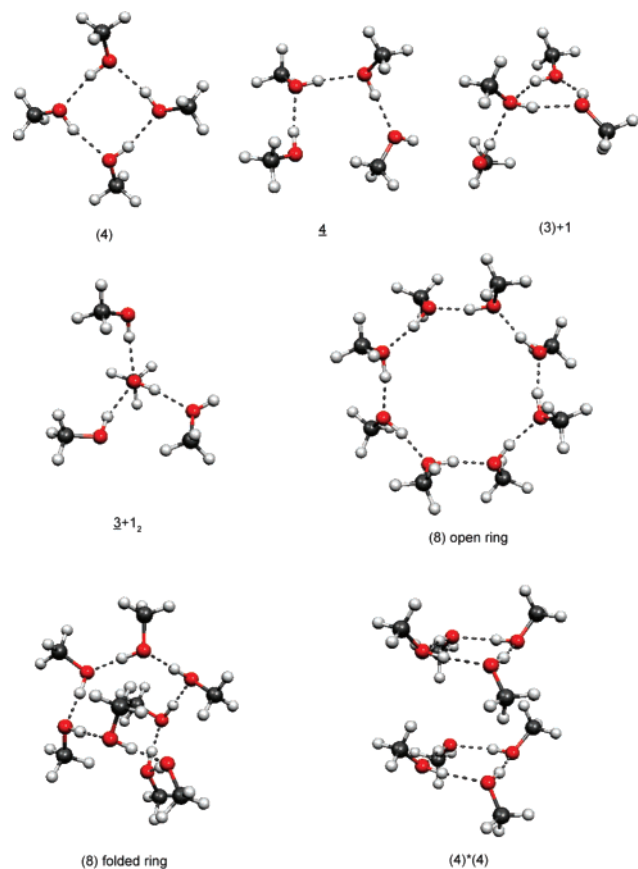


Figure 1. Representative geometries for several clusters using notation discussed in the text: ring tetramer (4), chain tetramer 4, cyclic trimer with attached methanol (3)+1, branched tetramer $3+1_2$, (8) flat or open ring, (8) folded ring, and (4)*(4) stacked cluster.

To facilitate the representation of different combinations of same size structures, the following notations will be used: (X) represents a ring of size X; \underline{X} represents a chain structure of size X; (X)+Y represents a ring of size X with an attached chain of size Y; (X)*(Y) represents a ring of size X stacked with a ring of size Y; and $\underline{X}+Y$ represents a chain of size X with a chain attached of size Y (sometimes the location of the attachment is also specified to make the representation clearer). Figure 1 diagrams several different methanol structures.

The average energy of a single methanol molecule in a (MeOH) $_n$ cluster can be calculated as $\bar{E}_n = E_n/n$. Comparing this energy to that of a single methanol in the gas phase, E_1 , gave the per methanol stabilization energy calculated using eq 1.

$$\Delta\bar{E}_n = \frac{E_n}{n} - E_1 \quad (1)$$

For a large cluster size, where n approaches Avogadro's number, the per methanol stabilization energy is equivalent to the enthalpy of solvation $\Delta\bar{E}_n = \Delta_{\text{sol}}H$ or $\text{MeOH}(\text{g}) \rightarrow \text{MeOH}(\text{l})$. Equation 1 was used to compare the per methanol energy of n -sized clusters with the enthalpy of solvation. Inclusion of thermochemical values from a frequency analysis corrects the electronic energy to an enthalpy value and a Gibbs energy at 298 K.

The strength of a single hydrogen bond between methanol molecules is calculated by taking the difference in energy between the monomer and the dimer, $E_2 - E_1$. This difference in energy is compared to the increased energy found from one structure to the next structure after the addition of one methanol molecule. Hydrogen bond strength was estimated using eq 2.

$$E_{\text{Hbond}} = (E_n - E_{n-1}) - (E_2 - E_1) \quad (2)$$

The energy stabilization from a single hydrogen bond is a measure of the energy difference between adding a hydrogen-bonding methanol molecule and an isolated methanol molecule. Some effects are not fully accounted for by using this method—mainly geometric rearrangements and dielectric forces.

Solvent effects using a dielectric medium were approximated using the integral equation formalism for the polarized continuum model (IEFPCM) method^{22–24} on fully optimized clusters. The solvation energy was calculated by taking the difference between the gas-phase electronic energy and the solvent-wrapped electronic energy.

Results and Discussion

Cluster Geometry at the HF/6-31+G(d,p) Level. Semiempirical calculations were used to quickly scan a large range of isomers for each cluster size.

Conformers calculated using semiempirical methods that might be candidates as the most stable structure are tabulated in Table S1 in the Supporting Information. Initial geometries prior to optimization were constructed by guessing reasonable structures. Attempts at using a simulated annealing process or dynamics search were less effective and more costly at identifying unique cluster geometries.

Additional calculations were done at the HF/6-31+G(d,p) level for the $n = 2-7$ clusters on the three lowest-energy PM3 structures. The results from the HF/6-31+G(d,p) calculations are summarized in Table S2 of the Supporting Information. Basis set superposition errors are reported for each calculation and tabulated in Table S2 (Supporting Information). As the number of methanol molecules increases, the basis set superposition error also increases. In general, the ring structures show a greater correction than the branched or chain clusters due to the greater number of hydrogen-bonding interactions. The counterpoise correction for the cyclic structures as a function of cluster size gives a straight line with a slope of 3.2 ± 0.1 kJ/mol. Thus, the per methanol cluster energy should include a correction of 3 kJ/mol. This offset does not change the relative energy difference between the clusters; it only changes the absolute value compared with experimental results for the 6-31+G(d,p) basis. The calculated dipole moments of the clusters are reported in Table S2 (Supporting Information) along with the geometric data of the OH bond, OO distance, and OHO angle. The addition of methanol molecules to clusters larger than six seems to have little or no effect on the bond lengths and bond angles of the hydrogen-bonding hydroxyl groups participating in hydrogen bonds. For the chain systems, the free OH bond length does not change significantly as the chain length increases. The per methanol energy for each

cluster geometry at the HF/6-31+G(d,p) level is summarized in Table S2 of the Supporting Information.

Three trimer conformers were studied at the HF/6-31+G(d) level: a flat ring structure (3), a chain $\underline{3}$, and a single methanol molecule with two molecules attached to the two possible acceptor sites $\underline{2}+1$. The flat ring structure (3) had the lowest optimized energy at the HF/6-31+G(d,p) level of theory, consistent with previous studies.^{25,26} The equilibrium geometry for the cyclic trimer is flat, resulting in poor overlap of the sp^3 orbitals compared to the noncyclic structures. However, the stabilization afforded by the additional hydrogen bonds compensates for the less favorable orbital overlap in the cyclic structure.

The cyclic tetramer arrangement with the methyl groups alternating between above and below the plane of the ring is the most stable of all arrangements. This configuration is in the S_4 point group. Other isomers were also considered, such as a cyclic tetramer with C_i symmetry and a (3)+1 isomer. As expected, both the C_i symmetry, and (3)+1 optimized structures were higher in energy than the S_4 tetramer.

The double acceptor–donor configuration serves as a branching point for an extended methanol cluster. The $\underline{3}+1_2$ isomer has been previously observed and characterized by Zwier and co-workers⁴ and Boyd and Boyd.⁵ The hydrogen bond donated by the branching methanol molecule is strengthened by accepting two hydrogen bonds from methanol molecules. However, the two hydrogen bonds to the branching molecule are weaker than a single hydrogen bond. Thus, the $\underline{3}+1_2$ structure is less stable than the cyclic (4) structure.

The pentamer isomers studied at the HF/6-31+G(d,p) level of theory were the (5), (4)+1, and (3)+1+1 structures. The ring structure has the lowest equilibrium energy of the three, being lower by 15.82 kJ/mol than the (4)+1 structure and 18.81 kJ/mol lower than the (3)+1+1 structure. The arrangement of alternating above–below methyl groups to the plane of the ring is mostly observed here, except for the necessary pairing of two methyl groups because of the odd number of molecules.

The four (CH₃OH)₆ structures studied at this level of theory were (6), (5)+1, (4)+1₁+1₂, and (4)+1₁+1₃. The ring structure is lower in energy by 12.40 kJ/mol, 25.66 kJ/mol, and 29.75 kJ/mol, respectively. It is evident from this set of data that there is a tendency for small methanol clusters to be in small rings. All four isomers had the same number of hydrogen bonds; thus, there must be a variable besides the absolute number of hydrogen bonds that leads to the stability of methanol structures. As discussed with the tetramer molecule, a branch point in the methanol cluster geometry could lead to an overall weakening of the total strength of the hydrogen bonds.

The ring octamer molecule (8) is lower in energy than the (4)*(4). In both structures, the methanol molecules are all single acceptors and single donors. The (8) and (4)*(4) structures are postulated to be very similar in energy if the two tetramers are able to find an arrangement in which they facilitate each other's stabilization. After several attempts to stack the two tetramers in different orientations with

several different computational methods, the gas-phase octamer ring still is more stable than two stacked tetramer rings. It is possible that gas-phase structures simply do not have the proper dielectric assistance to force a geometric change in order for the two rings to conform around each other; however, this might be observed for liquid methanol.

At the HF/6-31+G(d,p) level, the lowest-energy structures for $n = 1-8$ are flat rings with the methyl groups being above, below, or approximately coplanar with the ring plane. The different cyclic structures vary by patterns of orientation of the methyl groups. Of the isomers investigated, the most stable structures are rings with an equal number of monomers above and below the plane. Other patterns such as above–above–below ($n = 4$) and above–below–in plane–above–below–in plane ($n = 6$) are slightly less stable. Rings with an odd number of monomers have no symmetry. As examples of such rings, the patterns of methyl group orientations are above–above–below ($n = 3$) and above–below–above–below–in plane ($n = 5$). Similar structures with different orientations of the methyl groups differ only by very small barriers of rotation.

All structures beyond the octamer at the HF/6-31+G(d,p) level of theory show a distinctive inclination toward a ring structure. However, beyond eight methanol molecules, there is no longer an “open” ring system; the ring system for $n = 9-12$ is “pinched”. As the cluster of the methanol increases in size, it may begin to approximate liquid methanol. Bulk solvent effects have not been included in the optimization of the structures, and the expectation is that the clusters will attempt to minimize its volume. The “open” ring structure for $n > 8$ leads to an excluded volume; it is more favorable for clusters of $n > 8$ to form a “pinched” ring structure and fill the excluded volume with a dielectric.

At the HF/6-31+G(d,p) level of theory, the ring structures are found to be most stable for $n = 1-12$. The ring structure provides the maximum number of hydrogen bonds, when compared to chain and branched structures of the same size. Attempts to stack tetramers, both in an eclipsed nature and not, failed to produce meaningful results.

Table S2 (Supporting Information) tabulates the energy of clusters of size $n = 1-12$ calculated at the HF/6-31+G(d,p) level. Comparison of the average energy per methanol calculated using eq 1 indicates that for the ring systems of $n \geq 6$ the average energy of a single methanol is about -30 kJ/mol. The average energy to convert from a cyclic structure to a chain cluster is about 27 kJ/mol with a greater energy needed to convert the larger conformers. The average energy of a methanol molecule in a chain is about 5 kJ/mol higher than the energy of a methanol molecule in a cyclic structure. This small energy difference indicates that there is only a slight preference for a single methanol to remain in a ring system over a chain system.

Single-point energy calculations at the B3LYP/6-311+G(d,p) and MP2/6-311+G(d,p) levels were performed using the HF/6-31+G(d,p) optimized geometries. The B3LYP and MP2 results are tabulated in the Supporting Information, and the per methanol energy was calculated using eq 1. The higher-level energy calculations are consistent with the HF level of theory. Although the absolute energies are different,

Table 1. Geometry-Optimized Structures at the B3LYP Level Compared with Those at the HF Level

cluster	HF/6-31+G(d,p)				B3LYP/6-31G(d)				B3LYP/6-311+G(d,p)			
	dipole debye	$\bar{\tau}_{\text{OH}}^a$ Å	$\bar{\tau}_{\text{OO}}^b$ Å	$\bar{\alpha}_{\text{OHO}}^c$ deg	dipole debye	$\bar{\tau}_{\text{OH}}^a$ Å	$\bar{\tau}_{\text{OO}}^b$ Å	$\bar{\alpha}_{\text{OHO}}^c$ deg	dipole debye	$\bar{\tau}_{\text{OH}}^a$ Å	$\bar{\tau}_{\text{OO}}^b$ Å	$\bar{\alpha}_{\text{OHO}}^c$ deg
(MeOH) ₁	1.9729	0.942			1.6943	0.969			1.8894	0.961		
(MeOH) ₂	3.2917	0.947	2.967	178.9	2.8777	0.977	2.810	159.7	3.1518	0.970	2.873	176.2
(MeOH) ₃	2.7089	0.949	2.887	148.9	1.0560	0.986	2.745	152.3	0.8355	0.976	2.772	149.8
(MeOH) ₄	0.0166	0.952	2.863	166.8	0.0005	0.994	2.703	168.7	0.0036	0.983	2.725	167.0
(MeOH) ₅	0.5184	0.953	2.846	174.3	0.8582	0.995	2.692	176.4	0.6905	0.985	2.712	175.5
(MeOH) ₆	0.0007	0.953	2.832	176.2	0.0021	0.995	2.683	174.4	0.0007	0.986	2.705	178.9
(MeOH) ₇	0.0915	0.953	2.828	175.5	2.4285	0.995	2.690	174.9				
(MeOH) ₈ ^d	0.0043	0.953	2.828	174.5	0.0450	0.993	2.677	169.9	0.0670	0.985	2.697	176.3
(MeOH) ₈ ^e					0.1030	0.995	2.699	176.7	0.1112	0.986	2.715	176.5
(MeOH) ₉	0.3864	0.953	2.830	174.5	2.1366	0.994	2.686	173.1				
(MeOH) ₁₀	1.3795	0.953	2.832	175.1	1.2243	0.994	2.695	173.3				
(MeOH) ₁₁	1.7175	0.953	2.829	175.1	2.7031	0.994	2.687	173.2				
(MeOH) ₁₂	1.3207	0.953	2.831	175.2	2.0521	0.994	2.695	174.1				

^a Average O–H bond length for hydrogen-bonding hydroxyl groups. ^b Average O–O distance between hydrogen-bonding methanol molecules. ^c Average O–H–O angle between hydrogen-bonding methanol molecules. ^d Structure is a flat ring. ^e Structure is a folded ring.

the trends are identical. At around five methanol molecules, the energy per methanol levels out to a consistent value.

Cluster Geometry at the B3LYP Level. Calculations at the HF/6-31+G(d,p) level of theory indicate that cyclic methanol clusters are lower in energy than chain clusters for $n = 3$ –12. When the HF/6-31+G(d,p) geometry-optimized structures were used as an initial geometry, cluster geometries were further optimized using the B3LYP/6-31G(d) level of theory for $n = 1$ –12 and using the B3LYP/6-311+G(d,p) level of theory for $n = 1$ –6 and 8. The geometry optimizations using the B3LYP method are tabulated and compared with HF calculations in Table 1. At the levels of theory reported in Table 1, it was not practical to extend the system beyond $n = 12$. For the B3LYP/6-31G(d) geometry optimizations for $n = 7$, the structure started as a flat ring structure and proceeded to fold. For the $n = 8$ system, the flat ring structure local minimum is 21 kJ/mol higher in energy than that for a folded ring system. And for $n = 9$, the geometry optimization started as a flat ring structure and optimized to a folded ring structure as well. Optimized geometries for $n > 6$ all converged to a folded or puckered OH ring structure instead of a flat OH ring structure. Interestingly, at the B3LYP/6-311+G(d,p) level, the flat $n = 8$ structure is 7 kJ/mol lower in energy than the folded structure, which contradicts the findings from the B3LYP/6-31G(d) level of theory. The flat structure for $n = 8$ is also the lowest-energy structure at the HF/6-31+G(d,p) level of theory. The folded and flat $n = 8$ structures are local true minima with no negative frequencies.

In general, the geometries optimized at the B3LYP level are consistent with that of the HF calculations. For $n \geq 4$, the average OH and OO distances converge to a constant value as the number of methanol molecules increases. For the $n = 4$ geometry, there is some ring strain for the OHO angle, but for the $n > 4$ geometries, the average OHO angle is consistent as the number of methanol molecules increases. The trends in the geometry optimization are generally insensitive to the level of theory except for the $n = 8$ cluster.

Our primary interest in this study is to identify an ab initio method to quickly and accurately model large methanol

systems, specifically those governed by hydrogen bonding. The electronic energy is compared between the MP2/6-311+G(d,p)//B3LYP/6-31G(d) level of theory for $n = 1$ –4 and 8 and the B3LYP/6-311+G(d,p) level of theory for $n = 1$ –6 and 8 to the B3LYP/6-31G(d) level of theory. The B3LYP/6-31G(d) level is an inexpensive level of theory, and yet it appears to do a reasonable job in modeling large clusters. We have found that the B3LYP/6-31G(d) level produces nearly identical geometries (within 1%) to the geometries yielded by the 6-311+G(d,p) extended basis set. Our selection of the B3LYP/6-31G(d) level as an adequate method for obtaining reasonable methanol cluster geometries is consistent with findings by Boyd and Boyd.⁵ For the geometry optimization of the structures, B3LYP/6-31G(d) is the level of theory of choice, and a larger basis set can be used to improve the accuracy of the energy calculation.⁵

Small clusters of $n = 3$ –12 prefer to form a ring system over a branched ring system or chain structure.⁵ A cyclic geometry maximizes the number hydrogen bonds where each methanol donates one hydrogen bond and accepts one hydrogen bond and methyl groups can rotate to minimize steric effects. Branched structures with a methanol accepting two hydrogen bonds leads to a methanol that accepts no hydrogen bonds and is a less favorable overall geometry. As the systems increase in size, the rings begin to pucker and fold, thus minimizing an excluded volume in the middle of the cluster.

Cluster Frequencies. Analytical second derivatives are calculated at the B3LYP/6-31G(d), HF/6-31+G(d,p), and B3LYP/6-311+G(d,p) levels for $n = 1$ –6 and 8. The relative difference between the gas-phase OH stretching frequency $\nu_{\text{OH}}(1)$ and the cluster of size n average OH stretching frequency $\bar{\nu}_{\text{OH}}(n)$ is calculated using eq 3.

$$\frac{\bar{\nu}_{\text{OH}}(n) - \nu_{\text{OH}}(1)}{\nu_{\text{OH}}(1)} \times 100 \quad (3)$$

Mirroring the average bond length for clusters of size $n \geq 4$, the average difference between the OH stretching frequency of the cluster and a single methanol converge. The

Table 2. Summary of per Methanol Enthalpy at 298 K and Gibbs Energy at 298 K Reported in kJ/mol^a

cluster	B3LYP/6-31G(d)				HF/6-31+G(d,p)						B3LYP/6-311+G(d,p)	
	B3LYP/6-31G(d)		MP2/6-311+G(d,p)		HF/6-31+G(d,p)		B3LYP/6-311+G(d,p)		MP2/6-311+G(d,p)		B3LYP/6-311+G(d,p)	
	ΔH_{298}	ΔG_{298}	ΔH_{298}	ΔG_{298}	ΔH_{298}	ΔG_{298}	ΔH_{298}	ΔG_{298}	ΔH_{298}	ΔG_{298}	ΔH_{298}	ΔG_{298}
(MeOH) ₂	-12	4	-10	5	-7	7	-8	5	-10	4	-9	6
(MeOH) ₃	-28	-2	-20	6	-16	10	-18	8	-22	5	-19	6
(MeOH) ₄	-36	-6	-29	1	-19	8	-24	4	-28	0	-26	3
(MeOH) ₅	-37	-6			-22	9	-26	4	-30	0	-28	4
(MeOH) ₆	-38	-6			-22	8	-27	3	-31	-1	-29	3
(MeOH) ₈					-22	8	-27	4	-31	-1		
(MeOH) ₈ ^b	-39	-3	-34	2							-28	7
MAD	1		7		17		13		8		10	

^a The MAD (mean average deviation) compares the $n = 4, 5, 6,$ and 8 clusters with the experimental value of $\Delta H_{298} = -38.4$ kJ/mol. ^b Folded ring geometry for (MeOH)₈.

relative difference using the B3LYP method for the 6-311+G(d,p) basis and the 6-31G(d) basis is about 12%, and the average HF/631+G(d,p) difference is about 5%. When the B3LYP method is used, there is very little difference between the 6-311+G(d,p) basis and the 6-31G(d) basis. The absolute difference in the gas-phase OH stretching frequency using the B3LYP method is 94 cm⁻¹ or 2%. Vibrational frequencies at each level of theory for clusters $n = 1-6$ and 8 can be found in the Supporting Information. To evaluate the quality of the frequency calculations, the calculated IR-active OH stretching modes are compared with known experimental values.^{25,27,28} The calculated stretching frequencies are scaled by the appropriate scaling factors of 0.9173 for the HF/6-31+G(d,p) level of theory, 0.9806 for the B3LYP/6-31G(d) level of theory, and 0.98 for the B3LYP/6-311+G(d,p) level of theory. After scaling, the B3LYP/6-31G(d) level of theory has a mean average deviation (MAD) = 30 cm⁻¹ and comes closest to reproducing the experimental OH stretching frequencies. The B3LYP/6-311+G(d,p) level of theory has a MAD = 65 cm⁻¹ and is comparable to the B3LYP/6-31G(d) level of theory. The HF/6-31+G(d,p) level of theory has the largest mean absolute deviation of 308 cm⁻¹ but is still within 10% of the experimental values.

The frequency comparison for each structure and the relative cluster energy indicate that the B3LYP/6-31G(d) level of theory is sufficiently accurate in modeling the neutral methanol cluster geometry.

Cluster Energetics. Thermochemical analysis from the analytical second derivatives provides a correction to calculate the enthalpy and Gibbs energy at 298 K. The per methanol enthalpy at 298 K is calculated using scaled vibrational energies.²⁹ These values are reported in Table 2 and compared with the experimental value³⁰ of -38.4 ± 0.3 kJ/mol. It is evident from the tabulation that, of all the methods used in this study, the B3LYP/6-31G(d) level of theory yields values that are most similar to the experimental values. Also, only the B3LYP/6-31G(d) level of theory gave a negative Gibbs energy at 298 K (Table 2) for the $n = 3-8$ clusters. A negative Gibbs energy implies a favorable structure. The most stable clusters are the $n = 4-6$ at the B3LYP/6-31G(d) level of theory when the entropy of complexation is considered. The $n = 4-6$ and 8 clusters at the MP2/6-311+G(d,p)/HF/6-31+G(d,p) level have a Gibbs energy of 0 or -1 kJ/mol. Other levels of theory investigated

generated positive Gibbs energies, implying that the clusters are not stable. It is possible that there are deficiencies in the entropy calculation from vibrational frequencies.

ONIOM Calculations. For clusters of five to six methanols, the average hydrogen-bond lengths and average solvation energies approach an asymptotic value. To accurately represent a large methanol system including a hydrogen-bonding network and dielectric effects, the cluster should consist of more than six methanol molecules. Accurate geometries and energies for bulky systems must include hydrogen bonding; however, as the cluster size increases the computational resources become costly. The methyl group of methanol does not directly participate in hydrogen-bonding interactions but is significant in aligning the dipole of methanol and contributes to the dielectric strength of the system. To accurately and efficiently model a large methanol system beyond $n = 12$, we use a two-level ONIOM method. The real (CH₃OH)_{*n*} system is modeled at a computationally inexpensive level of theory, and the hydrogen-bonding network (OH)_{*n*} system is modeled at a high level of theory, with hydrogen as a link atom in the high layer.

Geometry optimizations were performed on the cyclic methanol tetramer (4) and compared to one-layer calculations. In order to find the optimum set of low and high level of theory for the two-layered method, multiple combinations of two-level ONIOM calculations were tried on the methanol tetramer. The values for OH length, OO length, and OHO angle are tabulated in Table 3. The values are sorted by their deviations from the B3LYP/6-31G(d) level of theory. The cheapest method within a 2% accuracy to the B3LYP/6-31G(d) level of theory is the B3LYP/6-31G(d):PM3 level of theory. Treating the methyl groups with the AM1 level gives comparable results. We found that using HF/STO-3G on the low layer yields the most accurate values, but a HF/STO-3G calculation is not significantly cheaper than a full B3LYP/6-31G(d) calculation.

With the optimized ONIOM conditions in hand, we proceeded to apply the B3LYP/6-31G(d):PM3 level of theory to methanol clusters $n = 1-12, 16,$ and 20 . The geometric results and the per methanol single-point electronic energies are shown in Table 4. The ONIOM calculations reduced the computational time by a factor of 6 compared with calculations at the B3LYP/6-31G(d) level. For example, a single optimization step for the $n = 5$ cluster on a 32-bit Intel

Table 3. Geometry Comparisons of Cyclic Methanol Tetramer^a

method	\bar{r}_{OH}	\bar{r}_{OO}	$\bar{\alpha}_{\text{OHO}}$	$\delta(\bar{r}_{\text{OH}})$	$\delta(\bar{r}_{\text{OO}})$	$\delta(\bar{\alpha}_{\text{OHO}})$
B3LYP/6-31G(d)	0.994	2.703	168.7	0.0%	0.0%	0.0%
B3LYP/6-31G(d):HF/STO-3G	0.994	2.703	168.7	0.0%	0.0%	0.0%
B3LYP/6-31+G(d)	0.989	2.714	167.8	-0.5%	0.4%	-0.5%
B3LYP/6-31+G(d,p):HF/STO-3G	0.989	2.716	167.8	-0.5%	0.5%	-0.6%
B3LYP/6-31G(d):AM1	0.999	2.733	168.6	0.5%	1.1%	0.0%
B3LYP/6-31G(d):PM3	0.991	2.754	168.7	-0.3%	1.9%	0.0%
B3LYP/6-31+G(d):HF/6-31G(d)	0.986	2.722	167.1	-0.8%	0.7%	-0.9%
B3LYP/6-311+G(d,p)	0.983	2.725	167.0	-1.1%	0.8%	-1.0%
MP2/6-31G(d):AM1	0.993	2.780	168.2	-0.1%	2.8%	-0.3%
MP2/6-31G(d):PM3	0.986	2.798	168.2	-0.8%	3.5%	-0.3%
B3LYP/6-311+G(d):AM1	0.986	2.762	164.2	-0.8%	2.2%	-2.7%
B3LYP/6-31+G(d,p):PM3	0.984	2.774	165.0	-1.0%	2.6%	-2.2%
MP2/6-31+G(d,p):HF/STO-3G	0.984	2.787	164.6	-1.0%	3.1%	-2.5%
B3LYP/6-311+G(d,p):PM3	0.978	2.795	164.4	-1.6%	3.4%	-2.6%
PM3	0.964	2.731	162.6	-3.1%	1.0%	-3.6%
MP2/6-311+G(d,p):PM3	0.971	2.809	163.6	-2.3%	3.9%	-3.0%
HF/6-31G(d,p)	0.953	2.830	166.9	-4.1%	4.7%	-1.1%
HF/6-31+G(d,p)	0.952	2.863	166.8	-4.2%	5.9%	-1.2%
HF/6-31+G(d):HF/STO-3G	0.958	2.891	163.9	-3.7%	7.0%	-2.8%
HF/6-31+G(d,p):PM3	0.951	2.919	163.7	-4.4%	8.0%	-3.0%

^a Average O–O bond distance, average O–H bond distance, and average O–H–O angle. Distances are reported in angstroms, and angles are reported in degrees. The deviation from the B3LYP/6-31G(d) optimization is reported.

Table 4. Geometry-Optimized Structures at the ONIOM B3LYP/6-31G(d):PM3 Level

cluster	dipole debye	OH ^a Å	OO ^b Å	OHO ^c deg	$\Delta\bar{E}_n^d$	ΔH_{298}^e	ΔG_{298}^f
(MeOH) ₁	1.5477	0.965					
(MeOH) ₂	1.4228	0.974	2.911	163.1	-14	-11	4
(MeOH) ₃	1.0858	0.984	2.799	153.0	-32	-27	0
(MeOH) ₄	0.0006	0.991	2.754	168.7	-40	-35	-3
(MeOH) ₅	1.4581	0.991	2.752	174.5	-41	-36	-2
(MeOH) ₆	0.0286	0.990	2.752	176.7	-41	-36	0
(MeOH) ₇	0.6323	0.991	2.754	177.2	-42	-37	-1
(MeOH) ₈	0.1997	0.991	2.755	176.1	-43	-37	1
(MeOH) ₉	4.1048	0.991	2.750	176.2	-44	-39	1
(MeOH) ₁₀	1.4764	0.990	2.754	174.3	-43	-37	1
(MeOH) ₁₁	2.2169	0.991	2.753	175.7	-42	-37	2
(MeOH) ₁₂	2.0048	0.991	2.750	176.7	-44	-38	1
(MeOH) ₁₆	5.2732	0.991	2.753	173.6	-44	-38	3
(MeOH) ₂₀ ^g	3.7549	0.991	2.757	173.9	-45	-38	4

^a Average O–H bond length for hydrogen-bonding hydroxyl groups. ^b Average O–O distance between hydrogen-bonding methanol molecules. ^c Average O–H–O angle between hydrogen-bonding methanol molecules. ^d Per methanol electronic energy. ^e Per methanol enthalpy at 298 K. ^f Per methanol Gibbs energy at 298 K. ^g The geometry is (19)+1; see text for details.

processor running Windows using the ONIOM method required approximately 6 min, whereas the B3LYP/6-31G(d) level required approximately 35 min to process the same optimization. On average, the ONIOM method did not require more optimization steps to find a minimum. Figure 2 diagrams the geometry-optimized structures from the ONIOM calculations. Results from the B3LYP/6-31G(d) calculations are also tabulated in Table 4. At most, the ONIOM calculated enthalpy at 298 K is 3 kJ/mol different than the B3LYP/6-31G(d) calculations for $n = 1-6$ and 8. Thus, B3LYP/6-31G(d):PM3 is a suitable model for calculating small- and intermediate-sized methanol clusters. The

two-level ONIOM was applied to even larger clusters, expanding this study up to $n = 20$ by investigating $n = 1-12$, 16, and 20. The relative energetic and geometric parameters converge after about $n = 6$ and extend out to $n = 20$; therefore, the clusters $n = 13-15$ and $17-19$ were not examined. The $(\text{CH}_3\text{OH})_{20}$ cluster was optimized several times, and the lowest-energy cluster was a (19)+1 branched ring. Several attempts were made to retain a (20) ring system but were unsuccessful. This indicates that there may be an upper limit to the size of a ring system. The open-ring systems are no longer favorable for $n > 6$, and around $n = 20$, branched folded ring systems appear to be more favorable than cyclic systems.

The strength of a single hydrogen bond is estimated for each cluster using eq 2. Table 5 tabulates the results from additional hydrogen bonds at the B3LYP/6-31G(d) level of theory and using the B3LYP/6-31G(d):PM3 ONIOM method. Stabilization by a single hydrogen bond in methanol clusters reaches a maximum at $n = 3$.

Table 6 summarizes the single-point energies using the IEFPCM model on the B3LYP/6-31G(d) optimized structures. The average solvation energy is -21 kJ/mol, which does not correlate well with the experimental value of -38.4 kJ/mol. The solvation energy also varies depending on the size of the methanol cluster. For example, clusters of $n = 2$ have the greatest solvation energy of -34 kJ/mol, while the $n = 3$ cluster has a solvation energy of -13 kJ/mol.

Conclusion

We tested several different levels of theory in finding single-point energies for large methanol clusters. The general trend of the energy per methanol molecule for all methods is very similar; after approximately four or five methanol molecules, the energy per methanol leveled off and started to approach an asymptotical value. Several ab initio and ONIOM methods

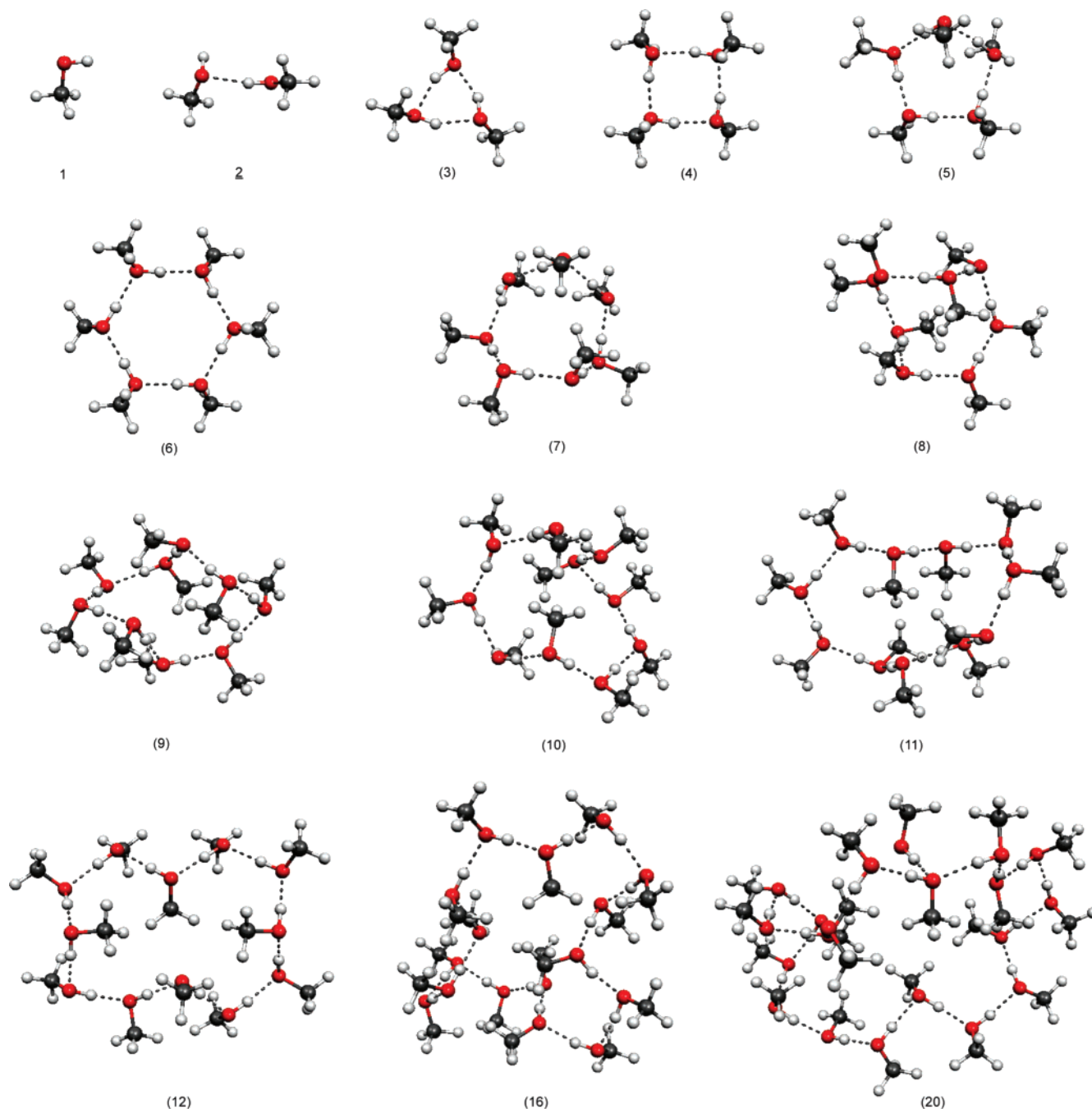


Figure 2. Geometry-optimized structures at the ONIOM (B3LYP/6-31G(d):PM3) level.

are applied to the system. When the results for the ONIOM method are compared to that of nonlayered calculations, it becomes evident that the considerably faster ONIOM method models the cluster to complete satisfaction. Geometric, energetic, and vibrational data support this conclusion. The advantage of the ONIOM method is that it provides the accuracy of a high-level calculation for the hydrogen-bonding network of methanol but requires the computation resources of a much smaller system. The geometry of methanol clusters is established for one-layer systems using density functional theory methods and a basis set, including diffuse and polarization functions. The ONIOM calculations are able to efficiently and accurately reproduce the geometry of the methanol clusters. The frequency analysis provided thermochemical corrections to calculate enthalpy and Gibbs energy

at 298 K to compare with the experimental enthalpy of solvation and Gibbs energy of solvation. Our implementation of the ONIOM method reduces the size of the high-level calculation from an 18-electron system to a 10-electron system. A major advantage to this reduction is that one is able to double the size of the system using the same computational resources. A modification to the ONIOM method that treats all two-body interactions with a high-level QM method and the many-body interactions with a low-level QM should allow greater reduction in the cost of accurate calculations of methanol clusters.³¹

For methanol clusters with $n \leq 6$, the geometries optimize to an open-ring structure. Large methanol clusters $n > 6$ optimized to a folded ring or pinched ring structure. Comparisons between single-ring structures, branched struc-

Table 5. Hydrogen-Bond Stabilization Effects Calculated Using eq 2 Comparing Electronic Energy at the B3LYP/6-31G(d) and B3LYP/6-31G(d):PM3 Levels Using the ONIOM Method

cluster	B3LYP/6-31G(d)	B3LYP/6-31G(d):PM3
(MeOH) ₃	-40	-39
(MeOH) ₄	-35	-33
(MeOH) ₅	-17	-16
(MeOH) ₆	-16	-11
(MeOH) ₇	-17	-24
(MeOH) ₈	-25	-19
(MeOH) ₉	-1	-20
(MeOH) ₁₀	-19	-5
(MeOH) ₁₁	-11	-11
(MeOH) ₁₂	-23	-27

^a Energies are reported in kJ/mol.**Table 6.** Single-Point Solvation Energy and Optimized Geometry Energy at the B3LYP/6-31G(d) Level Using the IEFPCM Method^a

cluster	E_{solv}	per MeOH	cluster	E_{solv}	per MeOH
(MeOH) ₁	-22		(MeOH) ₅	-16	-24
(MeOH) ₂	-34	-10	(MeOH) ₆	-15	-24
(MeOH) ₃	-13	-16	(MeOH) ₇	-18	-25
(MeOH) ₄	-13	-23	(MeOH) ₈	-19	-26

^a Energies are reported in kJ/mol.

tures, and multiple-ring structures indicate that single-ring systems are lower in energy. As the clusters become larger, the fluidity of the structure increases, and the global minimum at 0 K may be a pinched ring system. However, at thermal energies, a large cluster may readily sample branched structures and multiple-ring structures. Methanol clusters receive the most stabilization from hydrogen bonds, and the ring structures maximize the number of hydrogen bonds, resulting in optimized OHO angles, OO distances, and OH distances. In a ring system, one methanol molecule will act as both a donor and acceptor of a hydrogen bond. Ring structures provide the most spacing between the bulky methyl groups, further elevating the preference for rings over a branched or chain system for a static geometry.

Small clusters consisting of up to six methanol molecules do not necessarily represent bulk properties. However, our results indicate that cluster properties begin to reach an asymptotic limit after six methanol molecules are calculated in a cluster.

Acknowledgment. We thank the Camille & Henry Dreyfus Foundation and Ithaca College for funding. Ryan Adler, Jonathan Hershenson, Brian Hoyt, and Erica Schlesinger aided in the preliminary and final calculations on dielectric wrapping.

Supporting Information Available: Table S1 tabulates several of the PM3 calculations of the clusters. Tables S2 and S3 tabulate the HF/6-31+G(d,p) geometries and electronic energies in hartrees. Table S4 compares the single-point electronic energies in hartrees at the HF/6-31+G(d,p) geometry for a B3LYP/6-311+G(d,p) and MP2/6-311+G(d,p) energy calculation. Table S5 compares the electronic

energies in hartrees at several levels of theory. Table S6 tabulates calculated unscaled vibrational frequencies. Cartesian coordinates for all clusters at the HF/6-31+G(d,p), B3LYP/6-31G(d), B3LYP/6-311+G(d,p), ONIOM(B3LYP/6-31G(d):PM3), and IEFPCM B3LYP/6-31G(d) levels are reported. Frequencies for all ONIOM cluster geometries are also reported. This material is available free of charge via the Internet at <http://pubs.acs.org>.

References

- (1) Buck, U.; Huisken, F. *Chem. Rev.* **2000**, *100*, 3863–3890.
- (2) Su, J. T.; Xu, X.; Goddard, W. A., III *J. Phys. Chem. A* **2004**, *108*, 10518–10526.
- (3) Sum, A. K.; Sandler, S. I. *J. Phys. Chem. A* **2000**, *104*, 1121–1129.
- (4) Hagemester, F. C.; Gruenloh, C. J.; Zwier, T. S. *J. Phys. Chem. A* **1998**, *102*, 82–94.
- (5) Boyd, S. L.; Boyd, R. J. *J. Chem. Theory Comput.* **2007**, *3*, 54–61.
- (6) Buck, U.; Siebers, J.; Wheatley, R. J. *J. Chem. Phys.* **1998**, *108*, 20–32.
- (7) Wright, D.; El-Shall, M. S. *J. Chem. Phys.* **1996**, *105*, 11199–11208.
- (8) Svensson, M.; Humbel, S. F. R. D. J.; Matsubara, T.; Sieber, S.; Morokuma, K. *J. Phys. Chem.* **1996**, *100*, 19357–19363.
- (9) Re, S.; Morokuma, K. *J. Phys. Chem. A* **2001**, *105*, 7185–7197.
- (10) Tschumper, G. S.; Morokuma, K. *THEOCHEM* **2002**, *592*, 137–147.
- (11) Hopkins, B. W.; Tschumper, G. S. *Int. J. Quantum Chem.* **2004**, *96*, 294–302.
- (12) Lin, X.; Zhao, C.; Phillips, D. L. *J. Org. Chem.* **2005**, *70*, 9279–9287.
- (13) Koch, H. F.; Mishima, M.; Zuilhof, H. *Ber. Bunsen. Ges.* **1998**, *102*, 567–572.
- (14) DeTuri, V. F.; Koch, H. F.; Koch, J. G.; Lodder, G.; Mishima, M.; Zuilhof, H.; Abrams, N. M.; Anders, C. E.; Biffinger, J.; Han, P.; Kurland, A. R.; Nichols, J. M.; Ruminski, A. M.; Smith, P. R.; Vasey, K. *J. Phys. Org. Chem.* **2006**, *19*, 308–317.
- (15) Maheshwary, S.; Patel, N.; Sathyamurthy, N.; Kulkarni, A. D.; Gadre, S. R. *J. Phys. Chem. A* **2001**, *105*, 10525–10537.
- (16) Tschumper, G. S.; Gonzales, J. M.; Schaefer, H. F., III *J. Chem. Phys.* **1999**, *111*, 3027–3034.
- (17) Frisch, M. J.; Trucks, G. W.; Schlegel, H. B.; Gill, P. M. W.; Johnson, B. G.; Robb, M. A.; Cheeseman, J. R.; Keith, T.; Petersson, G. A.; Montgomery, J. A.; Raghavachari, K.; Al-Laham, M. A.; Zakrzewski, V. G.; Ortiz, J. V.; Foresman, J. B.; Cioslowski, J.; Stefanov, B. B.; Nanayakkara, A.; Challacombe, M.; Peng, C. Y.; Ayala, P. Y.; Chen, W.; Wong, M. W.; Andres, J. L.; Replogle, E. S.; Gomperts, R.; Martin, R. L.; Fox, D. J.; Binkley, J. S.; Defrees, D. J.; Baker, J.; Stewart, J. P.; Head-Gordon, M.; Gonzalez, C.; Pople, J. A. *Gaussian 98*; Gaussian, Inc.: Pittsburgh, PA, 1998.
- (18) Frisch, M. J.; Trucks, G. W.; Schlegel, H. B.; Scuseria, G. E.; Robb, M. A.; Cheeseman, J. R.; Montgomery, J. J. A.; Vreven, T.; Kudin, K. N.; Burant, J. C.; Millam, J. M.; Iyengar, S. S.; Tomasi, J.; Barone, V.; Mennucci, B.; Cossi, M.; Scalmani, G.; Rega, N.; Petersson, G. A.; Nakatsuji, H.;

- Hada, M.; Ehara, M.; Toyota, K.; Fukuda, R.; Hasegawa, J.; Ishida, M.; Nakajima, T.; Honda, Y.; Kitao, O.; Nakai, H.; Klene, M.; Li, X.; Knox, J. E.; Hratchian, H. P.; Cross, J. B.; Bakken, V.; Adamo, C.; Jaramillo, J.; Gomperts, R.; Stratmann, R. E.; Yazyev, O.; Austin, A. J.; Cammi, R.; Pomelli, C.; Ochterski, J. W.; Ayala, P. Y.; Morokuma, K.; Voth, G. A.; Salvador, P.; Dannenberg, J. J.; Zakrzewski, V. G.; Dapprich, S.; Daniels, A. D.; Strain, M. C.; Farkas, O.; Malick, D. K.; Rabuck, A. D.; Raghavachari, K.; Foresman, J. B.; Ortiz, J. V.; Cui, Q.; Baboul, A. G.; Clifford, S.; Cioslowski, J.; Stefanov, B. B.; Liu, G.; Liashenko, A.; Piskorz, P.; Komaromi, I.; Martin, R. L.; Fox, D. J.; Keith, T.; Al-Laham, M. A.; Peng, C. Y.; Nanayakkara, A.; Challacombe, M.; Gill, P. M. W.; Johnson, B.; Chen, W.; Wong, M. W.; Gonzalez, C.; Pople, J. A. *Gaussian 03*, revision C.02; Gaussian, Inc.: Wallingford, CT, 2004.
- (19) Simon, S.; Duran, M.; Dannenberg, J. J. *J. Chem. Phys.* **1996**, *105*, 11024–11031.
- (20) Boys, S. F.; Bernardi, F. *Mol. Phys.* **1970**, *196*, 553–566.
- (21) Maseras, F.; Morokuma, K. *J. Comput. Chem.* **1995**, *16*, 1170–1179.
- (22) Cancès, M. T.; Mennucci, B.; Tomasi, J. *J. Chem. Phys.* **1997**, *107*, 3032–3041.
- (23) Cossi, M.; Barone, V. M. B.; Tomassi, J. *Chem. Phys. Lett.* **1998**, *286*, 253–260.
- (24) Mennucci, B.; Tomasi, J. *J. Chem. Phys.* **1997**, *106*, 5151–5158.
- (25) Provencal, R.; Paul, J. B.; Roth, K.; Chapo, C.; Casaes, R. N.; Saykally, R. J.; Tschumper, G. S.; Schaefer, H. F., III *J. Chem. Phys.* **1999**, *110*, 4258–4267.
- (26) Mó, O.; Yáñez, M.; Elguero, J. *J. Chem. Phys.* **1997**, *107*, 3592–3601.
- (27) Fu, H. B.; Hu, Y. J.; Bernstein, E. R. *J. Chem. Phys.* **2006**, *124*, 024302.
- (28) Shimanouchi, T. In *NIST Chemistry WebBook, NIST Standard Reference Database Number 69*; Linstrom, P. J., Mallard, W. G., Eds.; National Institute of Standards and Technology: Gaithersburg, MD, 2005.
- (29) Scott, A. P.; Radom, L. *J. Phys. Chem.* **1996**, *100*, 16502–16513.
- (30) Afeefy, H. Y.; Liebman, J. F.; Stein, S. E. In *NIST Chemistry WebBook, NIST Standard Reference Database Number 69*; Linstrom, P. J., Mallard, W. G., Eds.; National Institute of Standards and Technology: Gaithersburg, MD, 2005.
- (31) Tschumper, G. S. *Chem. Phys. Lett.* **2006**, *427*, 185–191.

CT600348X

JCTC

Journal of Chemical Theory and Computation

Alchemical Variations of Intermolecular Energies According to Molecular Grand-Canonical Ensemble Density Functional Theory

O. Anatole von Lilienfeld^{*,†} and M. E. Tuckerman^{†,‡}

*Department of Chemistry, New York University, New York, New York 10003, and
Courant Institute of Mathematical Sciences, New York University, New York 10003*

Received January 3, 2007

Abstract: Molecular grand-canonical density functional theory [*J. Chem. Phys.* **2006**, *125*, 154104] is employed for the alchemical variation of intermolecular energies due to changes in the chemical composition of small molecules. We investigate the interaction of a fixed binding target, formic acid, with a restricted chemical space, corresponding to an isoelectronic 10-proton system which includes molecules such as CH₄, NH₃, H₂O, and HF. Differential expressions involving the nuclear chemical potential are derived, numerically evaluated, tested with respect to finite difference results, and discussed regarding their suitability as gradients of the intermolecular energy with respect to compositional variations.

I. Introduction

A. Chemical Space. The fundamental challenge of compound design, that is, the reverse engineering of chemical compounds with predefined specific properties, originates in the high-dimensional and combinatorial nature of chemical space.¹ Chemical space is the hyperspace of a given set of molecular observables that is spanned by the grand-canonical variables (particle densities of electrons and nuclei) which define the chemical composition of stable molecules or material. Exploration of this space via screening techniques, such as combinatorial high-throughput techniques or in silico evaluation exploiting quantitative structure–property relationships, consistently faces the problem of having to deal with the factorial scaling of the cardinal number which is due to the combinatorial character of chemical composition, atomic connectivities, and conformational configurations. Consequently, more “rational” endeavors have been undertaken to tackle this problem more deterministically.^{2–7}

Unless one possesses knowledge about the relevant chemical space a priori, a first-principles scheme is required for its unbiased exploration since chemical bonding patterns, the number of atoms, and atomic numbers must become vari-

ables. Such a scheme can be formulated using the principles of physical chemistry and seeks to address the question of how a compound’s property changes upon variation of its chemical composition. Recently, we presented a rigorous physical framework for this purpose by introducing a molecular multicomponent grand-canonical extension⁸ of Kohn–Sham density functional theory (KS–DFT).^{9,10} How chemical space is distinguished from the well-defined notion of phase space is somewhat arbitrary, as has been extensively discussed and investigated in the context of variations in the electronic chemical potential and the number of electrons in ref 8. In the present work, we focus on the complementary aspect of chemical space, namely, the study of the nuclear chemical potential and the proton density defining the nuclear charge distribution. Specifically, we will investigate how intermolecular energies, important molecular observables which are ubiquitous in all self-assembly processes, depend on the chemical composition of neutral and isoelectronic molecules. The procedure presented herein is prototypical in showing how to rationally “dial-in” certain intermolecular potential energies via compositional and structural changes and without any screening.

Reliable estimates of noncovalent interactions between molecular entities are notoriously difficult to obtain from first principles since they require an accurate description of the relatively weak and long-ranged mutual polarization of

* Corresponding author e-mail: ovt203@nyu.edu.

† Department of Chemistry.

‡ Courant Institute of Mathematical Sciences.

molecular entities. Within KS–DFT, the accuracy of current approximations to the exact exchange–correlation potential in describing intermolecular potentials can vary significantly^{11–13,31,32} To achieve an accuracy that is state-of-the-art, the generalized gradient approximation to the exchange–correlation potential employed herein has been augmented by an atom-centered London dispersion correction as introduced, assessed, and employed in refs 14–17.

B. Motivation. Before presenting the numerical results, a brief summary of the idea of compound design is given in order to provide the necessary background. It was proposed by one of us⁵ that the problem of tuning intermolecular energies through alchemical variations can be mapped onto a minimization problem in a variable space spanned by the electron and proton densities. Within density functional theory, any observable, \mathcal{O} , can be expressed in terms of a statistical mechanical average of a functional of the electron density which, due to the Hohenberg–Kohn theorem, is uniquely defined by the total number of electrons, N_e , and the external potential due to the nuclear charge distribution, $Z(\mathbf{r})$. If a target observable, \mathcal{O}_0 , is known a priori, a variational principle, $\mathcal{P} \geq 0$, can be applied to the general penalty functional

$$\mathcal{P} = (\mathcal{O}_0 - \mathcal{O}[N_e, Z])^2 \quad (1)$$

\mathcal{P} can be minimized by varying the proton distribution, $Z(\mathbf{r})$, and the number of electrons, N_e , defining the observable, \mathcal{O} , of the system. Variation with respect to the particle number, however, suggests the use of a grand-canonical ensemble theory. First- and second-order derivatives of \mathcal{P} with respect to Z and N_e are thus “grand-canonical derivatives”,⁸ reminiscent of chemical potentials and are likely, as is standard in all gradient-based optimization algorithms,¹⁸ to significantly enhance the efficiency of any algorithm which minimizes \mathcal{P} in the elementary particle space of protons and electrons. If the system contains N_n nuclei at positions $\mathbf{R}_1, \dots, \mathbf{R}_{N_n}$, then the atomic number of the l th nucleus will be $Z(\mathbf{R}_l)$. Thus, taking into account the inhomogeneity of possible proton distributions, the number of degrees of freedom available in chemical space is $1 + N_n$, the additional degree of freedom arising from the fact that the electron number N_e is one additional minimization parameter.

The functional \mathcal{P} is stationary if

$$0 = \frac{\delta \mathcal{P}}{\delta Z(\mathbf{r})} = 2(\mathcal{O}[N_e, Z] - \mathcal{O}_0) \frac{\delta \mathcal{O}[N_e, Z]}{\delta Z(\mathbf{r})} \quad (2)$$

and

$$0 = \frac{\partial \mathcal{P}}{\partial N_e} = 2(\mathcal{O}[N_e, Z] - \mathcal{O}_0) \frac{\partial \mathcal{O}[N_e, Z]}{\partial N_e} \quad (3)$$

Clearly, the local nature of the proton density is reflected in the \mathbf{r} dependence of the derivative $\delta \mathcal{P} / \delta Z(\mathbf{r})$.

When considering the change of molecular observables due to noninteger variations of elementary particles, it must be recognized that, in actuality, isolated charge densities integrate to integers. This can be accounted for by either assuming integer steps in N_e and $Z(\mathbf{r})$ or by requiring \mathcal{O} to

be a state function that can be changed along arbitrary paths, specifically via continuous variables, permitting the *virtual* existence of fractional numbers of electrons and protons.

Two further subtleties arise: (1) unless the band gap is zero, potential energy derivative discontinuities emerge for variation in the number of electrons at integer occupation numbers;^{19,20} (2) if unphysical, negatively charged “protons” are to be avoided, then for all $Z(\mathbf{r}) = 0$, the derivative of \mathcal{O} with respect to $Z(\mathbf{r})$ is only defined for $dZ(\mathbf{r}) \rightarrow 0^+$. The latter constraint, however, must be relaxed when considering the transmutational, or alchemical, case, $\delta \mathcal{O} / \delta Z(\mathbf{R}_l)$, when a given atomic number, that is, $Z(\mathbf{R}) > 0$, is allowed both to increase and to decrease.

II. Theory—Nuclear Gradients of Intermolecular Energies

A. The Intermolecular Nuclear Chemical Potential. For this study, the observable \mathcal{O} has been chosen to be an intermolecular potential energy. Since this quantity is a state function, its value can be tuned using fractional particle variables. We limit ourselves to the variation in the proton density. Nuclear grand-canonical gradients are derived, computed, and assessed in order to determine their utility for the control of intermolecular energies through compositional and structural tuning. The electronic analog to the nuclear chemical potential, the electronic chemical potential, μ_e , as well as changes in N_e , have already been investigated within applications of the molecular grand-canonical ensemble DFT introduced in ref 8.

The total potential energy of interaction, E^{int} , of an arbitrary substrate (s) with a binding template (t) is defined as

$$E^{\text{int}} = E^{t+s} - E^t - E^s \quad (4)$$

In order to maximize the energy of interaction, we set $\mathcal{O} = E^{\text{int}}[N_e, Z]$ and $\mathcal{O}_0 = -\infty$ and find a simplified variational principle, namely, $\mathcal{A}[N_e, Z] \geq 0$. \mathcal{P} is minimal when the gradients of \mathcal{O} are zero and the second-order derivatives are positive. In the following, we will denote the nuclear chemical potential of our intermolecular energy as $\mu_n^{\text{int}}(\mathbf{r}) = \delta E^{\text{int}} / \delta Z(\mathbf{r})$. According to eq 4, these gradients are

$$\begin{aligned} \mu_n^{\text{int}}(\mathbf{r}) &= \frac{\delta E^{t+s}}{\delta Z(\mathbf{r})} - \frac{\delta E^s}{\delta Z(\mathbf{r})} - \frac{\delta E^t}{\delta Z(\mathbf{r})} \\ &= \mu_n^{t+s}(\mathbf{r}) - \mu_n^s(\mathbf{r}) - \mu_n^t(\mathbf{r}) \end{aligned} \quad (5)$$

Note that $\mu_n^{\text{int}}(\mathbf{r})$ is constructed from functional derivatives of the total potential energy with respect to the proton distribution as they are generally formulated in terms of a continuous nuclear charge distribution as discussed in ref 8. It becomes evident that the intermolecular nuclear chemical potential, $\mu_n^{\text{int}}(\mathbf{r})$, corresponds to the difference between the nuclear chemical potentials,⁸ $\mu_n(\mathbf{r})$, of the complex, $t + s$, and the isolated systems, t and s . Note that, due to the indistinguishability and the spatial distribution of the proton distribution, $\mu_n^t(\mathbf{r})$ is not zero since a variation of the proton density in the vicinity of an isolated template affects its total potential energy value.

As shown in ref 8, one can use a modified electrostatic potential

$$\bar{V}^{\text{ESP}}(\mathbf{r}) = \int d\mathbf{r}' \frac{Z(\mathbf{r}') \text{erf}[\sigma|\mathbf{r} - \mathbf{r}'|] - \rho(\mathbf{r}')}{|\mathbf{r} - \mathbf{r}'|} \quad (6)$$

for $\mu_n(\mathbf{r})$, where the parameter σ is chosen to be sufficiently small to exclude the Coulomb repulsion between protons only within the same nucleus. Here, $\rho(\mathbf{r})$ represents the electron, and $Z(\mathbf{r}) = \sum_I N_I \delta(\mathbf{R}_I - \mathbf{r})$ is the proton density, N_I being the atomic number of atom I . These two particle densities must fulfill the constraint that they integrate to their total number, N_e and N_p for the electrons and protons, respectively.

From eq 5, the intermolecular nuclear chemical potential can be expressed as

$$\mu_n^{\text{int}}(\mathbf{r}) = \bar{V}_{t+s}^{\text{ESP}}(\mathbf{r}) - \bar{V}_s^{\text{ESP}}(\mathbf{r}) - \bar{V}_t^{\text{ESP}}(\mathbf{r}) \quad (7)$$

Apparently, the change of the total potential energy of interaction with respect to the variation of the number of protons at \mathbf{r} in the system corresponds to the difference in the modified electrostatic potential between the complex and the isolated moieties. If one considers the “vertical” derivative (vert), for which all geometries in the evaluation of eq 7 are kept rigid, that is, $\{\mathbf{R}_I\}$ is constant, the nuclear contribution to the difference in the modified electrostatic potentials cancels, and one finally finds

$$\begin{aligned} \left. \frac{\delta E^{\text{int}}}{\delta Z(\mathbf{r})} \right|_{\{\mathbf{R}_I\}} &= \mu_n^{\text{int}}(\mathbf{r}) \\ &= \int d\mathbf{r}' \frac{\rho^s(\mathbf{r}') + \rho^t(\mathbf{r}') - \rho^{t+s}(\mathbf{r}')}{|\mathbf{r} - \mathbf{r}'|} \end{aligned} \quad (8)$$

This expression is exact and does not involve any fractional atomic numbers per se. Consequently, it is not limited to the use of a plane-wave basis set but could also be evaluated within localized basis function calculations. The numerical applications of this study aim at assessing eq 8 for its meaning and utility when navigating through chemical space in order to control the interaction between a fixed target binding template t and the variable substrate s . For comparison, finite difference estimates, μ_n^{fd} , of the derivative in eq 5 have also been evaluated for rigid geometries according to

$$\mu_n^{\text{fd}}(\mathbf{r}) = \frac{E^{\text{int}}[Z + dZ] - E^{\text{int}}[Z]}{dZ(\mathbf{r})} \quad (9)$$

where $E^{\text{int}}[Z + dZ] = E^{t+s}[Z + dZ] - E^t[Z + dZ] - E^s[Z + dZ]$ and $dZ(\mathbf{r}) \rightarrow 0^+$ at all \mathbf{r} where $Z(\mathbf{r}) = 0$.

B. Definitions Employed. Formic acid has been selected to represent a rigid binding target t . This is an arbitrary choice, solely motivated by the fact that formic acid can act as hydrogen-bond donor and acceptor and consequently corresponds to a realistic, meaningful, yet simple (though nontrivial) target model. For the substrate s , we have chosen to limit the chemical space of interest to $N_e = N_p = 10$ and all the molecules containing a central atom “interpolated” between the carbon ($Z_c = 6$) and fluorine ($Z_c = 9$) and a number of hydrogen protons, N_H , defined by $N_H = 10 - Z_c$.

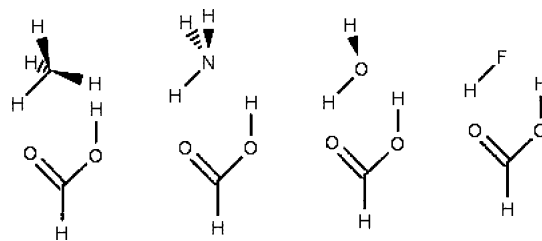


Figure 1. Sketch of the four supramolecular complexes which represent realistic members of all the possible 10-proton systems interacting with formic acid.

This defines an inhomogeneous spatial distribution of 10 protons in the electronic Kohn–Sham Hamiltonian within the Born–Oppenheimer approximation and includes compounds such as CH_4 , NH_3 , H_2O , and HF . While this restriction of chemical space keeps the number of systems requiring evaluation tractable, there is no loss of generality since the entire scheme is general enough that any other compounds could be used as templates (targets) or substrates.

In order to facilitate the analysis and to ensure smooth alchemical variations, several geometrical constraints have been imposed throughout all calculations. These constraints for determining the interaction energy *vertically* as

$$E^{\text{int}} = E^{\text{fa}+s} - E^{\text{fa}} - E^s \quad (10)$$

that is, without any further geometry optimization of the isolated moieties for the systems displayed in Figure 1, are described in the subsections of section IV. In eq 10, E^{fa} is the energy of the isolated formic acid and $E^{\text{fa}+s}$ is the energy of the complex.

For the alchemical variations of the intermolecular energies, six arbitrary quantum chemical “ λ paths” have been considered, as discussed for chemical space in ref 8. The usual parameter λ ($0 \leq \lambda \leq 1$) is used to measure the progress of the state function of interest, E^{int} , for going reversibly from state A to state B,

$$E^{\text{int}}(\lambda = 0) = E_A^{\text{int}}, \text{ and } E^{\text{int}}(\lambda = 1) = E_B^{\text{int}} \quad (11)$$

where the states are of different chemical composition, see refs 21–23 for discussion. The transmutation of CH_4 into NH_3 is controlled by λ_1 ; λ_2 controls the $\text{NH}_3 \rightarrow \text{H}_2\text{O}$ transmutation, and λ_3 transforms H_2O into HF . These transformations have been carried out first for geometrically rigid complexes starting with an optimized methane structure and then for a transformation where the structure of the 10-proton system has been relaxed at every point of λ . As the number of protons in the central atom is continuously increased, the atomic number of one of the protons in the surrounding hydrogen atoms is simultaneously decreased from 1 to 0. Which of the hydrogens has been chosen for annihilation can be recognized from inspection of Figure 1.

Alternatively, many other, more efficient or convenient λ paths could have been imagined. For example, three of the

four hydrogen protons in CH₄ could have been simultaneously annihilated while increasing the atomic number of the central atom correspondingly until HF is reached. However, such a path would not enable the system to “pass through” the realistic points in chemical space which correspond to NH₃ and H₂O. Realistic points in chemical space have only integer proton distributions. A systematic way to ensure that a maximal number of realistic points is visited would be to restrict the path to a single certain site in the system until a full proton has been added or removed.

III. Computational Details

All KS–DFT calculations have been carried out using the generalized gradient approximation BLYP^{24–26} to the exact exchange–correlation potential as implemented in the plane-wave code CPMD²⁷ together with the analytical pseudopotentials from refs 28 and 29, a large plane-wave energy cutoff of 100 Ry, periodic boundary conditions, and converged box sizes. London dispersion-corrected atom-centered potentials (DCACPs) as introduced and employed in refs 14–17 and 30 have been used for all atoms. The corresponding reference is the MP2/aug-cc-pVTZ (counterpoise-corrected) level of theory. Noninteger atomic numbers have been obtained through linear scaling of all the parameters $\{\sigma_i\}$ occurring in the analytical pseudopotential of hydrogen, $\{\sigma_i(\lambda)\} = \{\lambda\sigma_i\}$, through linear interpolation between the parameters for carbon, nitrogen, oxygen, and fluorine.

IV. Results and Discussion

A. Intermolecular Energies and Electronic Structure for Integer Atomic Numbers. Total interaction energies, E^{int} , for the four integer atomic number complexes with formic acid and as sketched out in Figure 1 amount to attractive interaction energies of 6.2, 34.1, 33.3, and 48.6 kJ/mol for CH₄, NH₃, H₂O, and HF, respectively. These values have been obtained as follows: first, the geometry of the isolated formic acid was optimized; second, the various substrate (s) geometries were relaxed in the presence of the rigid formic acid and under the constraint that the heavy atoms of the substrate as well as that hydrogen that interacts with the carbonyl oxygen of the formic acid are in the same plane as the formic acid.

At one extreme, CH₄ with its weak octupole moment exhibits only a relatively small attraction to formic acid, while at the other, HF acts with its strong dipole moment as a good hydrogen-bond donor. NH₃ and H₂O both yield comparable interaction energies of ~ 34 kJ/mol. This can be rationalized by referring to the relative atomic electronegativities of nitrogen and oxygen. While the NH bond in ammonia is less polar than the OH bond in water, the lone-pair electrons of the nitrogen are more polarizable than the lone pair on the oxygen in H₂O. Consequently, while NH₃ is a weaker hydrogen-bond donor than H₂O, it is also a stronger hydrogen-bond acceptor, resulting in an overall comparable interaction energy.

This explanation is consistent with the effect on the electronic structure due to the binding, $\Delta\rho = \rho^{\text{fa+s}} - \rho^{\text{s}} - \rho^{\text{fa}}$, and along the change from CH₄ to HF as displayed in Figure 2. Specifically, when considering that isosurface

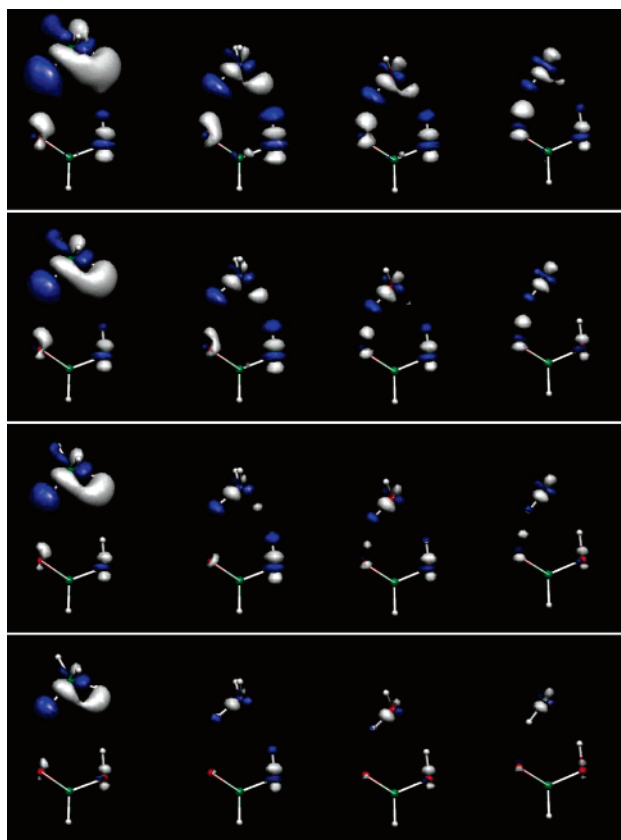


Figure 2. Isosurfaces of the difference in electron density, $\Delta\rho(\mathbf{r})$, due to the interaction of formic acid, $\Delta\rho(\mathbf{r}) = \rho^{\text{fa+s}}(\mathbf{r}) - \rho^{\text{fa}}(\mathbf{r}) - \rho^{\text{s}}(\mathbf{r})$, with the four 10-proton systems CH₄, NH₃, H₂O, and HF (left to right). Negative values are blue and represent depletion of the electron density upon binding; positive values are white and correspond to an increase of electron density due to binding. The isosurfaces are plotted for cutoff values of 5, 7.5, 10, and 15% of the respective absolute maximal value (top to bottom).

which corresponds to a 10% cutoff value (second from the bottom), it becomes evident that, for ammonia, the intermolecular electron density is first increased between the nitrogen lone pair and the acidic hydrogen of formic acid, while for water, the intermolecular electron density is first increased between the water proton and the carbonyl oxygen. Furthermore, an index of the relative strength of the interaction due to the mutual polarization can be estimated from the electronic structure plots with $\text{CH}_4 < \text{NH}_3 \approx \text{H}_2\text{O} < \text{HF}$: at a 10% cutoff, the lobe of intermolecular density is largest for HF, roughly equal for NH₃ and H₂O, and nonexistent for CH₄.

B. Intermolecular Energies and Electronic Structure for Noninteger particle Distributions. Results for the six continuous distinct alchemical changes (λ paths) of the intermolecular energy are plotted as a function of the atomic number of the heavy atom in Figure 3. In the case of the structurally relaxed λ paths, the first and third λ paths, that is, between CH₄ and NH₃ (λ_1) and between H₂O and HF (λ_3), the interaction energy falls off according to a power law, which is reminiscent of the scaling of atomic energies with atomic numbers. NH₃ and H₂O, however, are connected through a single, very shallow minimum (λ_2), implying that

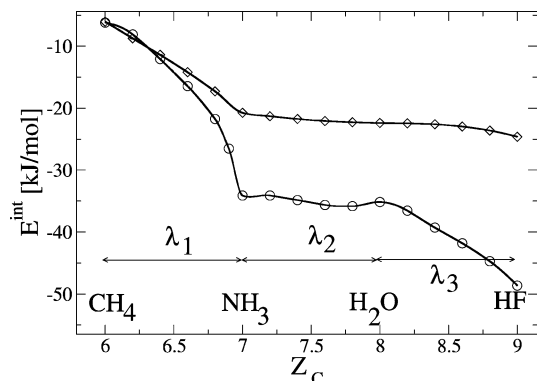


Figure 3. Potential energy of interaction with formic acid for the six λ paths when going from CH₄ ($Z_c = 6$) to HF ($Z_c = 9$) in steps of 0.2 recorded as a function of the atomic number of the central atom, Z_c . The circles correspond to intermolecular energies for substrates which are relaxed in the presence of the rigid formic acid. The diamonds correspond to intermolecular energies obtained for a generally rigid geometry which was optimized for the methane–formic acid complex without any constraint and then kept fixed for all other λ values. The straight lines represent corresponding interpolations.

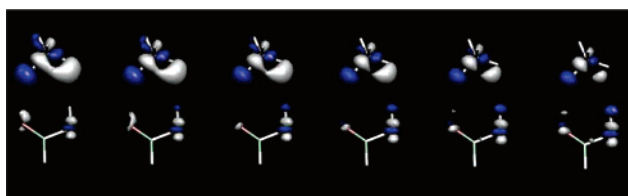


Figure 4. Isosurfaces of the difference in electron density, $\Delta\rho(\mathbf{r})$, due to the interaction with formic acid, $\Delta\rho(\mathbf{r}) = \rho^{\text{fa+s}}(\mathbf{r}) - \rho^{\text{fa}}(\mathbf{r}) - \rho^{\text{s}}(\mathbf{r})$, for the geometrically rigid λ_1 path. Surfaces are displayed for $\lambda_1 = 0.0$ (CH₄), 0.2, 0.4, 0.6, 0.8, and 1.0 (NH₃) (left to right, see also Figure 3). Negative values are blue and represent depletion of the electron density upon binding; positive values are white and correspond to an increase of electron density due to binding. The isosurfaces are plotted for a cutoff value of 10% of the respective absolute maximal value.

the corresponding gradient of the interaction energy, corresponding to the gradient of the plot in Figure 3, must be small between NH₃ and H₂O. In the case of the geometrically rigid λ paths, however, the rapid decrease with λ_1 is much weaker, leading to only $\sim 60\%$ of the interaction energy of ammonia in the relaxed case. λ_2 is a plateau as in the relaxed case. Most interestingly, the effect of the imposed rigidity becomes clearly significant for λ_3 , which leads only to very small changes in the interaction energy, implying an underestimation by more than 50% compared to the relaxed formic acid–HF complex.

In Figure 4, isosurfaces of the change in electron density due to the binding, $\Delta\rho = \rho^{\text{fa+s}} - \rho^{\text{s}} - \rho^{\text{fa}}$, are displayed for the geometrically rigid λ_1 path (CH₄ \rightarrow NH₃). One can clearly see how the electronic structure continuously adapts to the variation in the proton distribution and how the vanishing hydrogen nucleus of CH₄ loses its influence on the electronic structure.

Overall, the results above indicate the presence of a relatively simple and continuous grand-canonical potential-energy hypersurface. Thus, one can imagine including entropic effects through extended ab initio molecular dynamics schemes. However, derivative discontinuities are expected when switching the λ , that is, when considering the derivatives of the interaction energy in Figure 3 for $E^{\text{int}}(\lambda_1 = 1, \lambda_2 = \lambda_3 = 0; \text{NH}_3)$ and $E^{\text{int}}(\lambda_1 = \lambda_2 = 1, \lambda_3 = 0; \text{H}_2\text{O})$. In other words

$$\lim_{d\lambda \rightarrow 0} \frac{E^{\text{int}}(\lambda_1 = 1 - d\lambda, \lambda_2 = \lambda_3 = 0)}{d\lambda} \neq \lim_{d\lambda \rightarrow 0} \frac{E^{\text{int}}(\lambda_1 = 1, \lambda_2 = d\lambda, \lambda_3 = 0)}{d\lambda} \quad (12)$$

and

$$\lim_{d\lambda \rightarrow 0} \frac{E^{\text{int}}(\lambda_1 = 1, \lambda_2 = 1 - d\lambda, \lambda_3 = 0)}{d\lambda} \neq \lim_{d\lambda \rightarrow 0} \frac{E^{\text{int}}(\lambda_1 = \lambda_2 = 1, \lambda_3 = d\lambda)}{d\lambda} \quad (13)$$

In the case of NH₃, the left side of eq 12 describes the trend in the interaction energy when creating a fourth proton and decreasing the atomic number of the central nitrogen atom toward carbon. This tendency appears to be uncoupled from the tendency of the interaction energy to annihilate the third proton in NH₃ and to increase the atomic number of the central nitrogen atom toward oxygen (right side of that equation). The same is true for eq 13. Consequently, if the force of a given λ transformation is to be measured, care should be taken regarding the correct choice of the corresponding linear combinations of alchemical potentials.

The interaction energy for the geometrically rigid and relaxed alchemical paths in Figure 3 diverges rapidly already between CH₄ and NH₃. This suggests that, for a quantitative integration over the forces of the state function along the transformation, it is crucial to “decouple” frequently the canonical geometrical degrees of freedom from the grand-canonical variations in particle distribution space. Hence, if adiabaticity is desired between the degrees of freedom corresponding to momenta and positions and the degrees of freedom corresponding to the particle number,²³ the step in λ space must be chosen to be sufficiently small. This raises the problem of dealing with noninteger proton densities. That is, while a molecular grand-canonical scheme that is restricted to integer atomic numbers might yield the right trends, it is likely to be quantitatively inaccurate when employed within a molecular dynamics²³ or thermodynamic integration scheme.^{21,22} This is an issue that will be dealt with in subsequent studies.

C. The Nuclear Chemical Potential for Integer Proton Distributions. Isosurfaces of the intermolecular nuclear chemical potentials, $\mu_n^{\text{int}}(\mathbf{r})$, according to eq 8 are shown in Figure 5. One can recognize how the change in interaction energy due to a positive charge perturbation varies from CH₄ to HF. When the isosurface cutoff is gradually increased, one can also identify the regions and the number of extrema of $\mu_n^{\text{int}}(\mathbf{r})$. In order to assess the correctness of eq 8 for

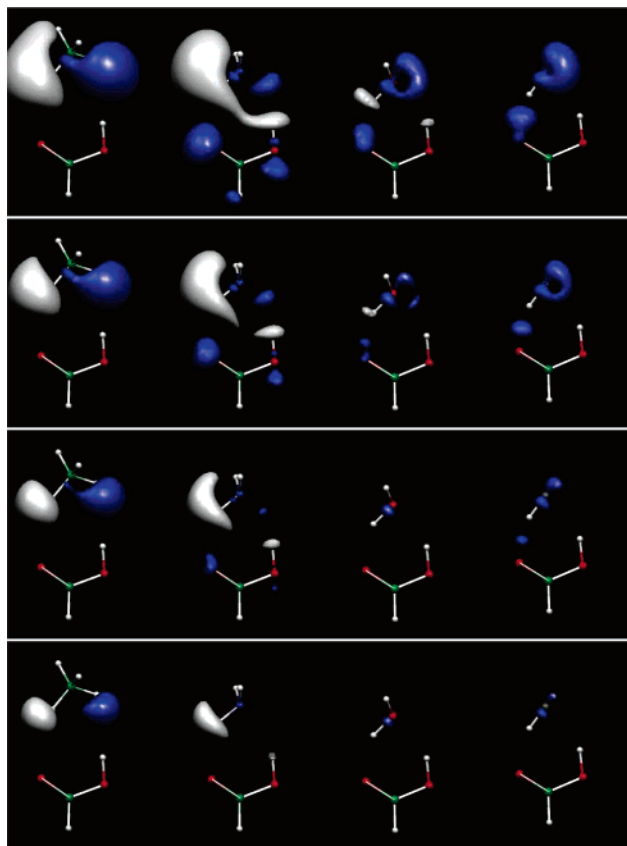


Figure 5. Isosurfaces of the nuclear chemical potential of the interaction energy of formic acid (according to eq 8) with the four 10-proton systems CH₄, NH₃, H₂O, and HF (left to right). The surfaces are plotted for cutoff values of 30, 40, 50, and 60% of the respective absolute maximal value (top to bottom). Negative values are blue and predict an increase; positive values are white and predict a decrease of interaction energy due to proton density variation.

computing this quantity, numerical values of the intermolecular nuclear chemical potential (displayed in Figure 5) at spatial positions where the function is maximal or minimal are presented in Table 1 along with finite difference estimates resulting from the change in interaction energy due to the presence of 0.1% of a proton at the same spatial locations according to eq 9. The finite difference results deviate negligibly by at most 0.2 kJ/mol from the results computed according to eq 8.

Estimates for alchemical potentials, $\{\mu_n^{\text{int}}(\mathbf{R}_i)\}$, have likewise been obtained from volumetric data (at grid points closest to corresponding atomic positions) for the geometrically rigid alchemical path. The “left-hand-side derivative” results for the integer atomic number cases CH₄, NH₃, and H₂O are reported in Table 1, together with finite difference results due to a 1% proton perturbation of the atomic number. Clearly, while the overall agreement with the finite difference prediction is still acceptable, it is less accurate than it is for the intermolecular nuclear chemical potential at spatial positions where there is no nucleus. Furthermore, the agreement with finite difference results is significantly better when applied to vanishing hydrogens than when applied to an increase in atomic number by the addition of protons to heavier nuclei.

Table 1. Intermolecular Nuclear Chemical Potentials, $\mu_n^{\text{int}}(\mathbf{r})$

	CH ₄	NH ₃	H ₂ O	HF
$\mu_n^{\text{int}}(\mathbf{r}_{\text{min}})$	-32.4	-42.2	-122.8	-156.6
$\mu_n^{\text{fd}}(\mathbf{r}_{\text{min}})$	-32.3	-42.1	-123.0	-156.5
$\mu_n^{\text{int}}(\mathbf{r}_{\text{max}})$	34.6	61.8	57.9	32.4
$\mu_n^{\text{fd}}(\mathbf{r}_{\text{max}})$	34.7	61.9	58.0	32.4
$\mu_n^{\text{int}}(\mathbf{R}_{\text{H}})$	-21.5	8.7	-6.7	
$\mu_n^{\text{fd}}(\mathbf{R}_{\text{H}})$	-18.5	7.2	-7.7	
$\mu_n^{\text{int}}(\mathbf{R}_{\text{C}})$	-2.5	-4.7	-13.6	
$\mu_n^{\text{fd}}(\mathbf{R}_{\text{C}})$	-7.3	-9.5	-8.9	

^a Values are obtained according to eq 8 and as extracted from the volumetric data displayed in Figure 5 at positions at which μ_n^{int} is maximal, \mathbf{r}_{max} , or Minimal, \mathbf{r}_{min} . For comparison, μ_n^{fd} is given as a finite difference perturbation of the energy of interaction due to the presence of 0.1% of a proton. For the geometrically fixed alchemical path, intermolecular alchemical potentials, $\mu_n^{\text{int}}(\mathbf{R})$, with respect to an increase in proton number are given at the positions of the vanishing hydrogens, $\mu_n^{\text{int}}(\mathbf{R}_{\text{H}})$, and at the position of the central atom, $\mu_n^{\text{int}}(\mathbf{R}_{\text{C}})$, along with corresponding finite difference estimates. Since no λ path involves a Z_{c} larger than that for fluorine, no values are presented for HF. A linear combination of the alchemical potentials would correspond to the right-hand-side derivatives of the geometrically rigid intermolecular energy curve in Figure 3. All μ_n^{int} values are given in kJ/mol.

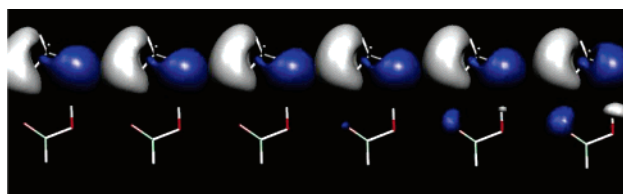


Figure 6. Isosurfaces of the nuclear chemical potential of the interaction energy, $\mu_n^{\text{int}}(\mathbf{r})$ (according to eq 8), for the geometrically rigid λ_1 path from CH₄ to NH₃. $\lambda_1 = 0.0$ (CH₄), 0.2, 0.4, 0.6, 0.8, and 0.1 (NH₃) (left to right, see Figure 3). The surfaces are plotted for a cutoff value of 30% of the respective absolute maximal value. Negative values are blue and predict an increase; positive values are white and predict a decrease of interaction energy due to proton density variation.

D. The Nuclear Chemical Potential for Noninteger Proton Distributions. In order to investigate this effect in more detail, alchemical potentials of the intermolecular energy have been computed according to eq 8, $\mu_n^{\text{int}}(\mathbf{R}_i)$, and according to the finite difference in eq 9 with 1% proton perturbation, $\mu_n^{\text{fd}}(\mathbf{R}_i)$, along the geometrically rigid alchemical transformations CH₄ ($\lambda_1 = 0$) \rightarrow NH₃ ($\lambda_1 = 1$), NH₃ ($\lambda_2 = 0$) \rightarrow H₂O ($\lambda_2 = 1$), and H₂O ($\lambda_3 = 0$) \rightarrow HF ($\lambda_3 = 1$) in λ steps of 0.0, 0.2, 0.4, 0.6, and 0.8 (see Figure 3). For the purpose of further illustration, isosurfaces of $\mu_n^{\text{int}}(\mathbf{r})$ along the λ_1 path are also displayed in Figure 6.

The overall correlation of these results is remarkably good (see Figure 7), and the derivative discontinuities in Figure 3 are reproduced. However, the correlation is not as good as it is for the nonalchemical nuclear chemical potentials, and we find that the aforementioned trend, namely, that the alchemical potential at the vanishing hydrogen correlates better with the finite difference results than the alchemical potential of the central atom, is also confirmed. Specifically, Figure 7 appears to indicate a systematic error in the computation of the alchemical potential of the central atom

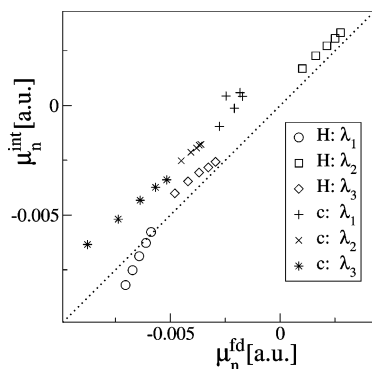


Figure 7. Alchemical potentials according to eq 8, $\{\mu_n^{\text{int}}(\mathbf{R}_i)\}$, versus finite difference results, μ_n^{fd} , at the position of the vanishing hydrogens (H) and the central atom (c). Results have been collected for the three, geometrically rigid transformations CH_4 ($\lambda_1 = 0$) \rightarrow NH_3 ($\lambda_1 = 1$), NH_3 ($\lambda_2 = 0$) \rightarrow H_2O ($\lambda_2 = 1$), and H_2O ($\lambda_3 = 0$) \rightarrow HF ($\lambda_3 = 1$) in λ steps of 0.0, 0.2, 0.4, 0.6, and 0.8.

according to eq 8; that is, there is a constant shift of ~ 0.002 au by which the finite difference results are underestimated. The strongest deviation is found for the λ_1 path.

A possible reason for this behavior might be the use of the electrostatic potential at positions where pseudopotentials are localized, that is, regions in space where the electron density is artificially reduced to zero, which in turn leads to an approximate result for the otherwise exact result from eq 8. Alternatively, the geometrical constraints might be a reason. Methods to remedy this deficiency will be considered in future studies using either eq 8 directly for electron densities obtained within all electron calculations, exploiting an appropriate linear combination of total potential energy derivatives with respect to pseudopotential parameters as proposed in refs 5 and 30, or accounting for geometrical relaxation.

V. Conclusion

Using the molecular grand-canonical ensemble density functional theory framework introduced in refs 5 and 8, we have studied potential energies of interaction and how they are connected for continuously varying a 10-proton system from CH_4 to HF via NH_3 and H_2O in the presence of a formic acid binding target. The effects on interaction energies, electronic structures, and electrostatic potentials due to the alchemical variations for gradually transforming CH_4 into HF (via NH_3 and H_2O) have been illustrated.

Predictions of the nuclear chemical potential of the interaction energy compare well to finite difference results, showing unambiguously the suitability of the molecular grand-canonical DFT ensemble approach for indexing where in space protons should be annihilated or created if an enhancement in the interaction energy is sought. While the alchemical potential of second-row elements leads to expected trends, it is estimated only approximately within the presented computational setup. Further investigations will be required in order to achieve satisfactory accuracy in predicting this quantity, which is crucial for the guided exploration of chemical space.

The advantage of such a molecular grand-canonical scheme compared to individual geometry optimizations is that, in order to perform the latter, one must know which compounds to consider a priori. A molecular grand-canonical theory, on the other hand, not only provides the means to perform geometry optimizations but can also help to identify those compounds which are more relevant than others.

We conclude that, in combination with the theoretical framework and the results of the calculations presented in ref 8, numerical evidence has been collected that, within molecular grand-canonical ensemble DFT, the elementary particle number variation of electrons and protons and of their corresponding intensive conjugates, the electronic and the nuclear chemical potential, is perfectly feasible. The procedure presented here should prove useful for devising more efficient and de novo compound design algorithms involving the unbiased control of intermolecular energies via compositional tuning.

Acknowledgment. O.A.v.L. acknowledges the SNF postdoctoral research grant no. PBEL2-110243. M.E.T. acknowledges funding from NSF CHE-0121375 and NSF CHE-0310107.

References

- (1) Kirkpatrick, P.; Ellis, C. *Nature* **2004**, *432*, 823.
- (2) Wolverton, C.; Zunger, A. *Phys. Rev. Lett.* **1998**, *81*, 606.
- (3) Franceschetti, A.; Zunger, A. *Nature* **1999**, *402*, 60.
- (4) Jóhannesson, G. H.; Bligaard, T.; Ruban, A. V.; Skriver, H. L.; Jacobsen, K. W.; Nørskov, J. K. *Phys. Rev. Lett.* **2002**, *88*, 255506.
- (5) von Lilienfeld, O. A.; Lins, R.; Rothlisberger, U. *Phys. Rev. Lett.* **2005**, *95*, 153002.
- (6) Wang, M.; Hu, X.; Beratan, D. N.; Yang, W. *J. Am. Chem. Soc.* **2006**, *128*, 3228.
- (7) Keinan, S.; Hu, X.; Beratan, D. N.; Yang, W. *J. Phys. Chem. A* **2007**, *111*, 176.
- (8) von Lilienfeld, O. A.; Tuckerman, M. E. *J. Chem. Phys.* **2006**, *125*, 154104.
- (9) Hohenberg, P.; Kohn, W. *Phys. Rev.* **1964**, *136*, B864.
- (10) Kohn, W.; Sham, L. J. *Phys. Rev.* **1965**, *140*, A1133.
- (11) Koch, W.; Holthausen, M. C. *Hydrogen Bonds and Weakly Bound Systems*. In *A Chemist's Guide to Density Functional Theory*, 2nd ed.; Wiley-VCH Verlag GmbH: Weinheim, Germany, 2001; Vol. B, pp 217–238.
- (12) Zhao, Y.; Truhlar, D. G. *J. Chem. Theory Comput.* **2005**, *1*, 415.
- (13) Ortman, F.; Bechstedt, F.; Schmidt, W. G. *Phys. Rev. B: Condens. Matter Mater. Phys.* **2006**, *73*, 205101.
- (14) von Lilienfeld, O. A.; Tavernelli, I.; Rothlisberger, U.; Sebastiani, D. *Phys. Rev. Lett.* **2004**, *93*, 153004.
- (15) von Lilienfeld, O. A.; Tavernelli, I.; Rothlisberger, U.; Sebastiani, D. *Phys. Rev. B: Condens. Matter Mater. Phys.* **2005**, *71*, 195119.
- (16) von Lilienfeld, O. A.; Andrienko, D. *J. Chem. Phys.* **2006**, *124*, 054307.
- (17) Tkatchenko, A.; von Lilienfeld, O. A. *Phys. Rev. B: Condens. Matter Mater. Phys.* **2006**, *73*, 153406.

- (18) Press, W. H.; Teukoldky, S. A.; Vetterling, W. T.; Flannery, B. P. *Minimization or Maximization of Functions. In Numerical Recipes in Fortran 77*, 2nd ed.; Cambridge University Press: Cambridge, U. K., 1992; Vol. 1, pp 387–436.
- (19) Perdew, J. P.; Parr, R. G.; Levy, M.; Balduz, J. L. *Phys. Rev. Lett.* **1982**, *49*, 1691.
- (20) Perdew, J. P.; Levy, M. *Phys. Rev. Lett.* **1983**, *51*, 1884.
- (21) Kirkwood, J. G. *J. Chem. Phys.* **1935**, *3*, 300.
- (22) Pearlman, D. A.; Govinda Rao, B. *Free Energy Calculations: Methods and Applications*; Jorgensen, W. L. *Free Energy Changes in Solution. In Encyclopedia of Computational Chemistry*, 2nd ed.; Ragué von Schleyer, P., Allinger, N., Clark, T., Gasteiger, J., Kollman, P., Schaefer, H. F., III, Eds.; John Wiley & Sons Ltd: West Sussex, U. K., 1998; Vol. 2, pp 1036–1070.
- (23) Abrams, J. B.; Rosso, L.; Tuckerman, M. E. *J. Chem. Phys.* **2006**, *125*, 074115.
- (24) Becke, A. D. *Phys. Rev. A: At., Mol., Opt. Phys.* **1988**, *38*, 3098.
- (25) Lee, C.; Yang, W.; Parr, R. G. *Phys. Rev. B: Condens. Matter Mater. Phys.* **1988**, *37*, 785.
- (26) Colle, R.; Salvetti, D. *Theor. Chim. Acta* **1975**, *37*, 329.
- (27) Hutter, J. *Computer code CPMD*, version 3.11; IBM Corp./Max-Planck Institute-FKF: Stuttgart, Germany, 1990–2006/1997–2001.<http://www.cpmc.org> (accessed Jan. 1, 2007).
- (28) Goedecker, S.; Teter, M.; Hutter, J. *Phys. Rev.: Condens. Matter Mater. Phys.* **1996**, *54*, 1703.
- (29) Krack, M. *Theor. Chim. Acta* **2005**, *114*, 145.
- (30) von Lilienfeld, O. A.; Tavernelli, I.; Rothlisberger, U.; Sebastiani, D. *J. Chem. Phys.* **2005**, *122*, 014113.
- (31) Langreth, D. C.; Dion, M.; Rydberg, H.; Schroder, E.; Hyldgaard, P.; Lundqvist, B. I. *Int. J. Quantum Chem.* **2005**, *101*, 599.
- (32) Tao, J.; Perdew, J. P. *J. Chem. Phys.* **2005**, *122*, 114102.

CT700002C

JCTC Journal of Chemical Theory and Computation

Stabilities and Spin Distributions of Benzannulated Benzyl Radicals

Yongqiang Sui,[†] Rainer Glaser,^{*,†} Ujjal Sarkar,[†] and Kent Gates^{†,‡}

Departments of Chemistry and Biochemistry, University of Missouri—Columbia, Columbia, Missouri 65211

Received March 5, 2007

Abstract: The effects have been studied of mono- and dibenzannulation of a benzyl radical with hybrid density functional theory (B3LYP) and quadratic configuration interaction theory (QCISD). Bond dissociation energies and enthalpies are reported that were determined at the common level QCISD/6-311G**//B3LYP/6-31G* for the benzylic C–H bonds of toluene **1H**, the monobenzannulated polycyclic aromatic hydrocarbons (PAH) 1- and 2-methylnaphthalene **2H** and **3H**, the dibenzannulated PAHs 9-methylanthracene **4H** and 9-methylphenanthrene **5H**, and the model hydrocarbons 1-phenylpropene **6H** and propene **7H**. The conformational preferences and the symmetries of **1H–7H** and of their corresponding radicals **1–7** have been determined. The analysis of the electron and spin density distributions of radicals **1–7** at the QCI level are reported, and these high-level data are discussed in comparison to results obtained with density functional theory and with an awareness of a general perception shaped by Hückel molecular orbital theory. The results show in a compelling fashion that electron and spin delocalization onto an annulated arene is not the decisive principle for stabilization of the benzyl radicals formed by homolysis of the methylated PAHs C₁₀H₇–CH₃ and C₁₄H₉–CH₃, and instead, the analysis of QCI spin density distributions suggests that spin delocalization onto annulated arenes is avoided as much as possible while spin polarization does occur to a significant extent.

Introduction

The homolysis of toluene to yield a benzyl radical is discussed in many textbooks on organic chemistry as the *prima facie* example of the benefits of electron and spin delocalization (Chart 1). The hyperfine coupling in electron spin resonance (ESR) spectra shows that spin delocalization occurs, and quantum chemistry shows the spin delocalization to occur with some spin polarization (Figure 1). Dust and Arnold argued that increased spin delocalization should increase radical stability and proposed a relation between ESR hyperfine coupling constants and radical stabilization.¹ The textbook view on spin delocalization permeates the modern research literature,^{2–5} and for example, Wu et al.⁵ concluded from their studies of neutral para-substituted

toluenes that “both electron-donating and electron-withdrawing groups reduce the bond dissociation energy (BDE) of the benzylic C–H bond [by 0–3 kcal/mol] because both groups cause spin delocalization from the benzylic radical center.”

While restricted Hartree–Fock (HF) theory presents a good starting point for the computation of closed-shell molecules, studies of radicals are more challenging for a number of reasons.⁶ Restricted and unrestricted open-shell HF (ROHF and UHF, respectively) theories^{7,8} have been developed. While ROHF theory completely neglects spin polarization, UHF theory suffers from spin contamination (i.e., an overestimation of spin polarization). Spin contamination of the UHF solution can be remedied,^{9,10} but spin polarization intrinsically is a correlation effect, and correlated methods are required to compute meaningful spin density distributions.^{11–13} In practice, this is often accomplished by post-Hartree–Fock treatments¹⁴ either with perturbation

* Corresponding author e-mail: glaserr@missouri.edu.

[†] Department of Chemistry.

[‡] Department of Biochemistry.

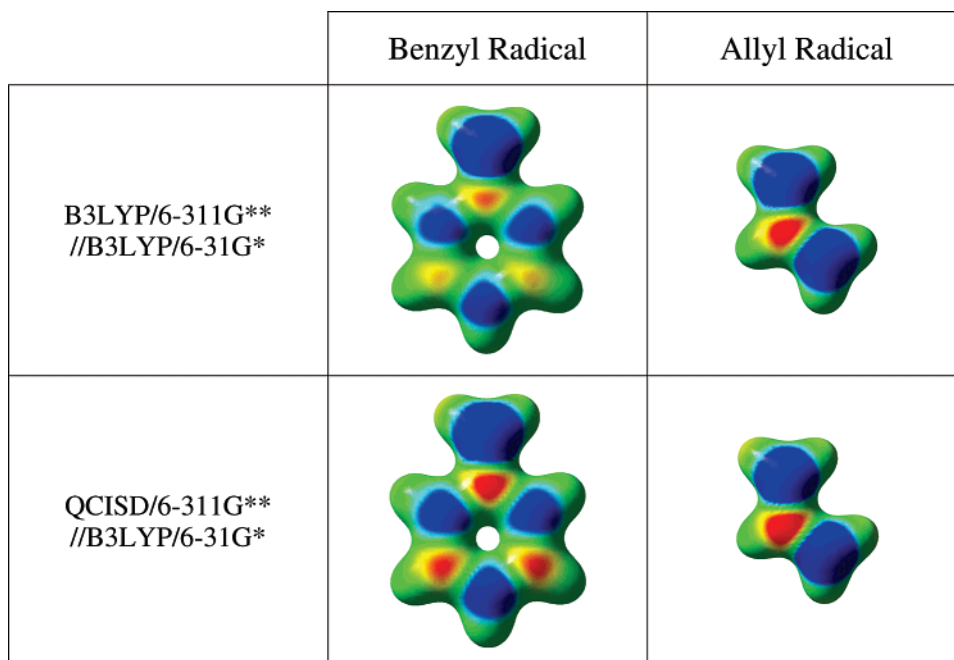
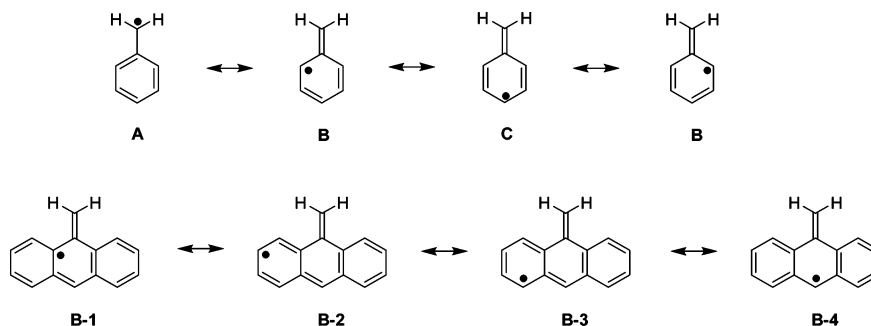


Figure 1. Spin density distributions of benzyl and allyl radicals color-coded (-4.432×10^{-3} to 4.432×10^{-3}) and displayed on isosurfaces of the electron densities (value 0.04).

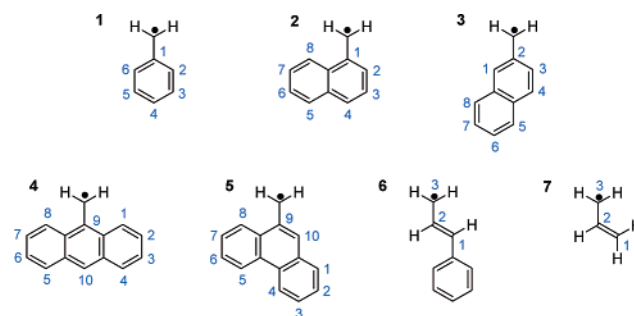
Chart 1. Spin Delocalization in Benzyl Radical **1** and Its Dibenzannulated Derivative **4**



methods (i.e., Møller–Plesset perturbation theory¹⁵) or configuration interaction treatments (i.e., quadratic configuration interaction, QCI, theory¹⁶). Studies of radicals have become more frequent with the availability of density functional methods, and the usual spin contaminations are moderate.^{17,18} This knowledge has been the implicit justification for the use of density functional theory (DFT) methods even though problems with spin-projected density functional theory are known.^{19,20} Aside from the theoretical challenges, computations of radicals push the limits of computational feasibility because unrestricted theory doubles the number of orbitals and thereby greatly increases the post-HF task. Hence, accurate studies of benzene-sized radicals are scarce, higher-level studies of benzannulation effects of radicals have not been reported, and the conceptual knowledge about spin density distributions in benzannulated systems has not been well-developed.

In this article, we report the results of a theoretical study of benzannulation on the stabilities and the spin distributions of benzyl radical **1** and its benzannulated derivatives **2–5** (Chart 2). Allyl radicals **6** and **7** serve as models for **5**. Bond dissociation energies and enthalpies are reported that were determined at the common level QCISD/6-311G**//B3LYP/

Chart 2. Benzyl Radical **1**, Benzannulated Benzyl Radicals **2–5**, Model System **6**, and Allyl Radical **7**



6-31G* for the benzylic C–H bonds of toluene **1H**, the monobenzannulated polycyclic aromatic hydrocarbons (PAHs) 1- and 2-methylnaphthalene **2H** and **3H**, the dibenzannulated PAHs 9-methylanthracene **4H** and 9-methylphenanthrene **5H**, and the model hydrocarbons 1-phenylpropene **6H** and propene **7H**. Conformational preferences and symmetries of **1H–7H** and **1–7** have been explored. Analyses of the electron and spin density distributions of radicals **1–7** have been performed at the DFT and QCI levels, and the results

Table 1. Bond Dissociation Energies, Enthalpies, and Free Energies^a

parameter and theor. level		1H	2H	3H	4H	5H	6H	7H
BDE	B3LYP/6-31G* :=A	94.90	93.82	94.21	88.50	94.28	87.23	92.19
	B3LYP/6-311G**//A	94.12	94.16	94.76	88.94	94.63	87.47	92.60
	QCISD/6-311G**//A	95.34	96.60	96.66	91.73	99.38	89.13	91.62
BDH ₀	B3LYP/6-31G*	86.48	85.23	85.77	80.16	85.57	79.01	83.57
	B3LYP/6-311G**//A	85.70	84.38	85.13	79.41	84.74	78.07	82.80
	QCISD/6-311G**//A	86.92	88.00	88.21	83.38	90.67	80.91	83.00
BDH ₂₉₈	B3LYP/6-31G*	87.07	85.96	86.38	80.77	86.37	79.62	84.30
	B3LYP/6-311G**//A	86.28	85.12	85.75	80.02	85.54	78.67	83.53
	QCISD/6-311G**//A	87.50	88.73	88.83	84.00	91.47	81.52	83.73
BDG	B3LYP/6-31G*	79.57	77.69	78.61	72.81	77.84	72.17	76.20
	B3LYP/6-311G**//A	78.79	76.85	77.97	72.06	77.01	71.23	75.43
	QCISD/6-311G**//A	80.01	80.47	81.05	76.03	82.94	74.07	75.63

^a All energies in kilocalories per mole.

are discussed in the context of “common knowledge” shaped by Hückel molecular orbital (HMO) theory.

Theoretical and Computational Methods

Structures were optimized at the B3LYP/6-31G* level and characterized by vibrational analysis using restricted and unrestricted wavefunctions for **1H–7H** and **1–7**, respectively.²¹ The closed-shell hydrocarbons are *C_s*-symmetric and, except for toluene, the *C_s* plane coincides with the molecular plane. Except for **4**, the radicals also are *C_s*-symmetric and planar, and radicals **1** and **7** are *C_{2v}*-symmetric. Unexpectedly, we find that radical **4** shows a slight preference for a nonplanar *C_s*-symmetric structure; that is, its CH₂ group is moved out of the best plane of the anthracene. The structures of all radicals were optimized without symmetry constraints and starting with slightly asymmetric initial guess structures so that the resulting de facto symmetries were established for the minima and confirmed by the analytical computations of the Hessian matrices. Details of the potential energy surface analysis are provided in the Supporting Information, and the data include Cartesian coordinates and molecular models of the optimized structures, total energies *E*_{tot}, vibrational zero-point energies VZPE, thermal energies TE, and molecular entropies *S*.

Bond dissociation energies BDE = Δ*E*(R–H → R• + H•), enthalpies BDH₀ = Δ(*E* + VZPE) and BDH₂₉₈ = Δ(*E* + TE), and free energies BDG = Δ(*E* + TE – 298.15*S*) are summarized in Table 1. These values were first determined with the data obtained at the level of optimization, B3LYP/6-31G* (:= level “A”). More accurate energies were computed with the 6-311G** basis set in two ways: again with the B3LYP method and then also with the quadratic configuration interaction method QCISD. These single-point energy calculations were based on the structures determined at the level B3LYP/6-31G* (:= A), for example, B3LYP/6-311G**//A and QCISD/6-311G**//A, and the BDH and BDG data in Table 1 include the thermal corrections determined at the level of optimization.

Electron and spin densities were computed for all systems at the levels B3LYP/6-311G**//A (:= level “B”) and QCISD/6-311G**//A (:= level “C”) and for comparison also with extended HMO theory.²² Electronic structures were examined by natural population analysis²³ and by inspection

of surface maps of spin density distributions. Pertinent results are summarized in Table 2, and details are provided in the Supporting Information.

Spin density distributions are illustrated as surface maps in Figure 1 for the prototypical benzyl and allyl radicals and in Figure 2 for radicals **2–6**. The generation of such a surface begins with the determination of an isodensity surface of the molecular electron density for a given value of the electron density. We employed the same isodensity surface in all cases, and specifically the one computed at level “B”. The value of the spin density is then determined for the entire isosurface, and its distribution is presented via color-coding. Regions shown in blue indicate high α-spin density; those shown in green are relatively spin-free, and regions shown in red show the accumulation of β-spin density.

Calculations were performed with Gaussian 03²⁴ on the 64-processor SGI Altix system of MU Research Support Computing. Even though the performance of this system is quite astounding, the magnitude of the computational task presented by the present study still posed challenges. The QCISD calculations of the large radicals **4** and **5** required the option “tran=IJAB” so that the integral transformation was possible with the available disk space usage (ca. 1 TB) and, in fact, proceeded with a rather small disk usage (ca. 25 GB). Even then, these radicals were too large to compute the QCI density by the default process. Instead, the value of CONVER had to be reduced such that the convergence on the wavefunction was set to 10^{–6}. Control calculations of the spin density distribution and the natural bond order data of the allyl radical with default and less-restrictive CONVER settings showed that the spin density distribution had converged.

Results and Discussion

Experimental Bond Dissociation Energies. The accurate measurement of the bond dissociation energy of toluene has been difficult. Early on, the bond dissociation energy of toluene in the gas phase was thought to be as low as Δ*H*₂₉₈ = 77.5 kcal/mol,²⁵ whereas the modern values are close to 90 kcal/mol. In 1990, Hippler and Troe²⁶ reported Δ*H*₂₉₈ = 90.4 ± 1 and Δ*H*₀ = 88.9 ± 1 kcal/mol, and these values were based on the direct measurements of the rate constants of the forward and backward reactions of the equilibrium

Table 2. Spin Density Distributions in Radicals 1–7

parameter	1	2	3	4	5	6	7
B3LYP/6–311G**							
CH ₂	0.68	0.59	0.64	0.40	0.59	0.46	0.62
C _{ipso} (CH ₂)	–0.14	–0.15	–0.14	–0.14	–0.15	–0.17	–0.20
C _i –CH ₂	0.54	0.44	0.50	0.26	0.44	0.29	0.40
C _o –H	0.21	0.30	0.11		0.38	0.50	0.62
C _m –H	–0.10	–0.12	–0.09				
C _p –H	0.23	0.30		0.42			
C _o in CH	0.21	0.31	0.11		0.39	0.52	0.62
C _m in CH	–0.10	–0.12	–0.09				
C _p in CH	0.24	0.31		0.43			
C _o in CR		0.12		0.17	0.06		
C _m in om–CR		–0.07		–0.10	–0.04		
C _m in mp–CR			–0.08		–0.09	–0.10	
C _p in CR			0.13		0.13	0.15	
C ₂ H ₂	0.11	0.18	0.03				
om–C ₂ C ₄ H ₄		0.09		0.16	0.01		
mp–C ₂ C ₄ H ₄			0.15		0.17	0.21	
QCISD/6–311G**							
CH ₂	0.69	0.60	0.65	0.42	0.60	0.46	0.61
C _{ipso} (CH ₂)	–0.20	–0.22	–0.21	–0.21	–0.22	–0.22	–0.23
C _i –CH ₂	0.49	0.38	0.43	0.22	0.38	0.24	0.38
C _o –H	0.26	0.36	0.18		0.45	0.57	0.63
C _m –H	–0.15	–0.19	–0.15				
C _p –H	0.29	0.36		0.48			
C _o in CH	0.26	0.38	0.19		0.47	0.59	0.66
C _m in CH	–0.15	–0.20	–0.16				
C _p in CH	0.30	0.37		0.50			
C _o in CR		0.18		0.24	0.13		
C _m in om–CR		–0.13		–0.17	–0.12		
C _m in mp–CR			–0.15		–0.16	–0.17	
C _p in CR			0.20		0.21	0.19	
C ₂ H ₂	0.11	0.17	0.03				
om–C ₂ C ₄ H ₄		0.09		0.15	0.02		
mp–C ₂ C ₄ H ₄			0.14		0.15	0.19	
Extended Hückel Theory							
CH ₂	0.53	0.41	0.47	0.23	0.41	0.33	0.50
C _{ipso} (CH ₂)	0.00	0.00	0.00	0.00	0.00	0.00	0.00
C _i –CH ₂	0.53	0.41	0.47	0.23	0.41	0.33	0.50
C _o –H	0.15	0.21	0.05		0.29	0.38	0.50
C _m –H	0.00	0.00	0.00				
C _p –H	0.17	0.22		0.29			
C _o in CH	0.15	0.21	0.05		0.29	0.38	0.50
C _m in CH	0.00	0.00	0.00				
C _p in CH	0.17	0.22		0.29			
C _o in CR		0.06		0.09	0.02		
C _m in om–CR		0.00		0.00	0.00		
C _m in mp–CR			0.00		0.00	0.00	
C _p in CR			0.08		0.09	0.09	
C ₂ H ₂	0.15	0.21	0.05				
om–C ₂ C ₄ H ₄		0.16		0.24	0.05		
mp–C ₂ C ₄ H ₄			0.23		0.25	0.29	

C₆H₅–CH₃ ⇌ C₆H₅–CH₂• + •H. The value Δ*H*₂₉₈ = 88.5 ± 1.5 kcal/mol was given in the 1994 review by Berkowitz et al.,²⁷ and in 1996, Ellison et al.²⁸ reported the values Δ*H*₃₀₀ = 89.8 ± 0.6 and Δ*H*₀ = 88.1 ± 0.6 kcal/mol. These values were derived from the measurement of Δ*G*₃₀₀ for the gas-phase equilibrium C₆H₅–CH₃ + CH₃O[–] ⇌ C₆H₅–CH₂[–] + CH₃OH in conjunction with the knowledge of Δ*S*₃₀₀ for this

equilibrium, the gas phase acidity of methanol, the electron affinity of the benzyl radical, and an estimation of the thermal correction (Δ*H*₀ = Δ*H*₃₀₀ – 1.6 ± 0.2 kcal/mol). With the more recent value for the gas-phase acidity of methanol reported by Ervin and DeTuri in 2002²⁹ as Δ*G*₂₉₈ = 375.5 ± 0.6 kcal/mol and 0.4 kcal/mol higher than the earlier value, the derivation by Ellison et al. results in 0.4 kcal/mol

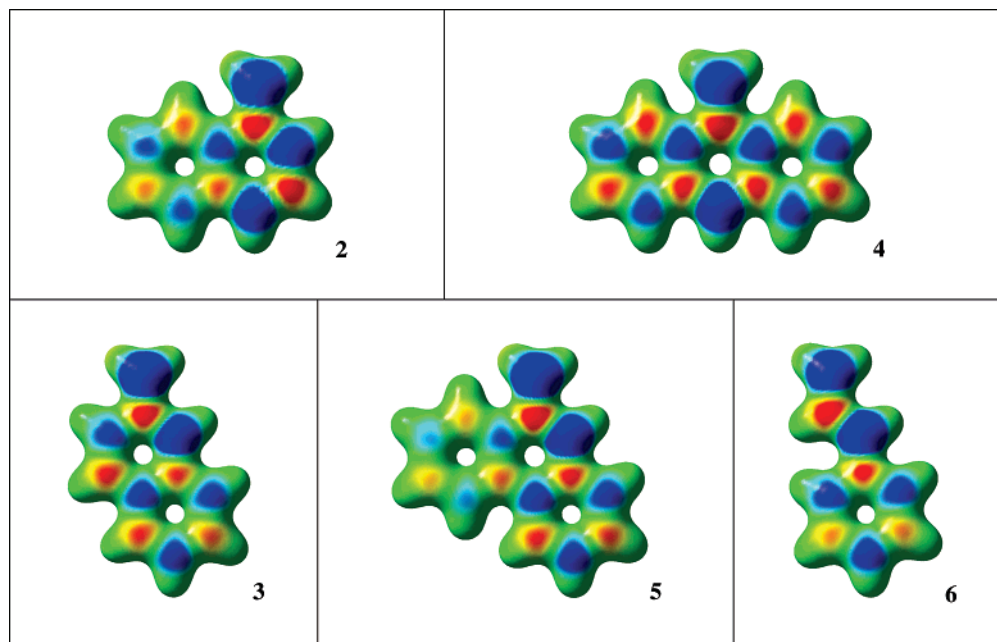


Figure 2. Spin density distributions of benzannulated benzyl radicals **2–5** and model **6**. Spin densities are color-coded as in Figure 1 from -4.432×10^{-3} to 4.432×10^{-3} and displayed on isosurfaces of the electron densities (value 0.04).

increases to the values $\Delta H_{300} = 90.2 \pm 0.6$ and $\Delta H_0 = 88.6 \pm 0.6$ kcal/mol. Thus, there exists complete agreement between the measurements of the bond dissociation energy of toluene by the two different approaches.

Benzannulation is thought to provide additional radical stabilization because benzannulation is thought to result in additional electron and spin delocalization as indicated for radical **4** in Chart 1 (**B-1–B-4** etc.). Yet, the experimental and theoretical records on benzannulated benzyl radicals are scarce, and this assumption has never been really tested. Finkelshtein's compilation indicates reductions of the bond dissociation energies of 1-methylnaphthalene and 9-methylanthracene by 3.4 and 4.4 kcal/mol for single and double benzannulation, respectively.³⁰ The bond dissociation energies computed by Bauschlicher and Langhoff at the B3LYP/4-31G level for 1-methylnaphthalene, 1-methylanthracene, and 9-methylanthracene are respectively 0.7, 0.6, and 3.7 kcal/mol lower than for toluene.³¹ The suggestion that monoannulation would have but a negligible effect on the benzylic C–H bond dissociation energy was stated without comment in spite of its apparent inconsistency with the available experimental data.³⁰

Computed Bond Dissociation Energies. The hydrocarbons all are neutral, nonpolar, and strain-free; basis set effects are expected to be small, and they are; and BDE(A) and BDE(B) data are in excellent agreement. Unless noted otherwise, the bond dissociation enthalpies $\text{BDH}_{298}(\text{B})$ are discussed, and the results are as follows: (1) Monoannulation hardly alters the benzylic C–H bond dissociation energy. The $\text{BDH}_{298}(\text{B})$ data for **1–3** are almost the same, 85.6 ± 0.5 kcal/mol. (2) Dibenzannulation in the anthracene derivative reduces the BDH value by ca. 6 kcal/mol. (3) Dibenzannulation in the phenanthrene derivative results in a BDH value that falls in the range of 85.6 ± 0.5 kcal/mol for **1H–3H**.

We first sought corroboration of the finding that $\text{BDH}_{298}(\text{2H})$ and $\text{BDH}_{298}(\text{3H})$ are only *slightly* reduced compared to $\text{BDH}_{298}(\text{1H})$ only to find that the QCISD calculations show that the $\text{BDH}_{298}(\text{C})$ values for **2H** and **3H** actually are slightly *higher* than for **1H**. The difference between the BDH_{298} values of **2H** and **3H** relative to **1H** change from -1.2 and -0.5 at level B to $+1.2$ and $+1.3$ at level C, respectively, and these changes are about 2 kcal/mol. The respective differences for the larger systems **4H** and **5H** are significantly larger, and they can be as high as about 5 kcal/mol; the difference between the BDH_{298} values of **4H** and **5H** relative to **1H** change from -6.3 and -0.7 at level B to -3.5 and $+4.0$ at level C, respectively. It is common practice to seek corroboration at higher levels. It also is common practice to seek this corroboration only for small systems and to then argue that the insights gained for the small systems would carry over to larger systems. The latter approach, as common and as accepted as it is, fails quite significantly in the present case!

The theoretical methods employed in the present study give BDH_{298} values for toluene that are about 2–4 kcal/mol lower than the experimental value (vide infra), and the BDH_{298} value derived at the QCISD/6-311G**//B3LYP/6-31G* level is within 2.5 kcal/mol. The bond dissociation energy of propene allows for a second direct comparison with experimental data of high quality. With the modern gas-phase acidity of methanol,²⁹ the equilibrium measurements by Ellison et al.²⁸ yield $\Delta H_{300} = 89.2 \pm 0.4$ and $\Delta H_0 = 87.8 \pm 0.4$ kcal/mol, and these values need to be compared to the computed values of $\text{BDH}_{298} = 83.7$ and $\text{BDH}_0 = 83.0$ kcal/mol (Table 1). The allyl data suggest that the agreement of the computed and experimental benzyl data is perhaps better than one can generally expect at this theoretical level. Nevertheless, to achieve these high levels of agreement between experiment and theory for homolyses is quite

remarkable. For homolyses, the underestimation of the bond dissociation energy is systematic because the UHF treatments of the hydrocarbon radicals are more complete than the RHF treatments of the hydrocarbons. The post-HF methods must correct, and the QCISD method accomplishes this very effectively. Furthermore, the computed thermal correction for the bond dissociation enthalpy of toluene is $\text{BDH}_{298}(\mathbf{1H}) - \text{BDH}_0(\mathbf{1H}) = 0.6$ kcal/mol (Table 1) and about 1 kcal/mol lower than the thermal correction employed in the experimental studies.^{26,28} Part of the underestimation of the bond dissociation enthalpy is thus due to errors in the computed thermal energy correction. Overall, we can be quite confident that the wavefunctions of the radicals are of high quality, and considering that trends in general are less sensitive to the completeness of the theoretical method, it is justified and safe to conclude the following: “Benzannulation per se” does not necessarily lower the benzylic C–H bond dissociation energy. Compared to $\text{BDH}_{298}(\mathbf{1H})$, the BDH_{298} values of $\mathbf{2H}$ and $\mathbf{3H}$ are about 1 kcal/mol higher, the BDH_{298} value of $\mathbf{(5H)}$ is about 4 kcal/mol higher, and only $\text{BDH}_{298}(\mathbf{4H})$ is about 3.5 kcal/mol lower.

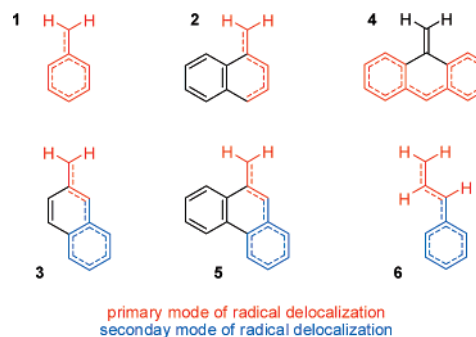
Spin Density Distributions. Complete sets of q^S data computed for radicals $\mathbf{1-7}$ with DFT and QCI densities are given in Table 2. The spin density distributions computed for benzyl and allyl radicals are illustrated in Figure 1, and the DFT and QCISD results are in qualitative agreement in these cases. However, even the qualitative agreement does not carry over to the benzannulated systems, and the spin density distributions shown for radicals $\mathbf{2-6}$ in Figure 2 were determined at the QCISD level.

The spin delocalization in the allyl radical must result in equal α -spin densities of the CH_2 groups, and the methodological differences only can effect the spin polarization. Spin delocalization in the benzyl radical is much more interesting because there are no such symmetry constraints, and consequently, whether spin delocalization occurs, to what extent spin delocalization occurs, and how spin delocalization effects spin polarization, all of these questions now become dependent on the correlation method. The $q^S(\text{CH}_2)$ data computed with the DFT and QCI densities are very similar, but the consequences of the spin delocalization are qualitatively different in significant ways, and we discuss the QCI-derived q^S data.

Spin delocalization in the benzyl radical leaves about two-thirds of one full α spin on the CH_2 group, and the delocalization of one-third of an α spin leads to strong spin polarization: the spin densities on the ortho ($\approx 0.26\alpha$) and para ($\approx 0.29\alpha$) CH groups add up to 2–3 times the amount of delocalized total spin, and C_{ipso} ($\approx 0.2\beta$) and the meta CH groups ($\approx 0.15\beta$) carry β -spin populations.

The illustrations in Figure 2 show in a compelling fashion that spin delocalization onto a benzannulated fragment is *not* the decisive principle and that the spin distribution remaining in the benzyl fragment depends on the type of benzannulation. In $\mathbf{2}$, the spin population on the annulated ortho C atom declines and those on the ortho and para CH groups increase, and the resulting spin density closely resembles that of the homoallyl radical (Chart 3). In $\mathbf{3}$, all the spin delocalization occurs to that ortho CH group that is part of a second benzyl

Chart 3. Avoidance of Benzyl Delocalization as Primary Delocalization Mode: Allyl and Homoallyl Systems and Alternative Benzyl Systems as Secondary Modes of Radical Delocalizations



system, and the electronic structure of the 1-phenylallyl radical $\mathbf{6}$ results. This same electronic structure also characterizes radical $\mathbf{5}$, and its second benzannulated ring is essentially spin-free. Spin delocalization occurs via nonannulated bonds in $\mathbf{2}$, $\mathbf{3}$, and $\mathbf{5}$, and this is not possible in $\mathbf{4}$. Nonetheless, upon homolysis, massive spin delocalization onto the para CH group does occur [$q^S(\text{C}_p\text{H}) \approx 0.5\beta$], and the spin populations of the $\text{C}_2\text{C}_4\text{H}_4$ fragments are lower than in $\mathbf{1}$. Hence, $\mathbf{4}$ features the electronic structure of a 2,2'-ethylenylene-bridged diphenylmethyl radical. The overall spin on the $\text{C}_{\text{ipso}}-\text{CH}_2$ fragment amounts to a mere 0.2α , and the essence of $\mathbf{4}$ is its diphenylmethyl radical nature.

Radicals $\mathbf{3}$, $\mathbf{5}$, and $\mathbf{6}$ are of special interest because they contain 1-phenylallyl moieties and allow for a direct comparison of the propensity for benzyl-type spin delocalization. The ortho CH group and the C_o atoms of $\mathbf{3}$, $\mathbf{5}$, and $\mathbf{6}$ show α -spin populations that are greatly increased as compared to the respective moieties in $\mathbf{1}$ and $\mathbf{2}$, respectively, and well-recognizable “allyl radical spin systems” result. The important point here is the finding that this delocalization of spin density onto the phenyl substituted C atom would allow for benzyl-type delocalization into the “annulated arene” (shown in blue in Chart 3) and that such benzyl-type delocalization actually occurs *much less* than in radicals $\mathbf{1}$ and $\mathbf{4}$ where benzyl-type delocalization is the only option. The same argument applies to $\mathbf{2}$ where the para CH group and C_p carry large α -spin populations but benzyl-type delocalization into the “annulated ring” is only modest.

The spin density analysis thus explains the low value for the benzylic C–H bond dissociation energy of $\mathbf{4H}$: Homolysis creates the diphenylmethyl radical $\mathbf{4}$, whereas radicals $\mathbf{2}$, $\mathbf{3}$, $\mathbf{5}$, and $\mathbf{6}$, on the other hand, are homoallyl or phenylallyl systems. There is one-half of an α -spin density on the C_pH group of $\mathbf{4}$, that is, the “methyl moiety” of the diphenylmethyl radical (cf. **B-4** in Chart 1). Compared to the benzyl radical itself, the second benzene leads to the additional delocalization of merely 0.1 of an unpaired α spin! This very fact shows that delocalization per se is not the general principle for stabilization it is thought to be—not even when benzyl radical stabilization is the only option. The key insight here is that radical $\mathbf{4}$ is not stabilized because twice as much spin delocalization occurs as in the benzyl radical itself. Rather, radical $\mathbf{4}$ can achieve spin delocalization while minimizing

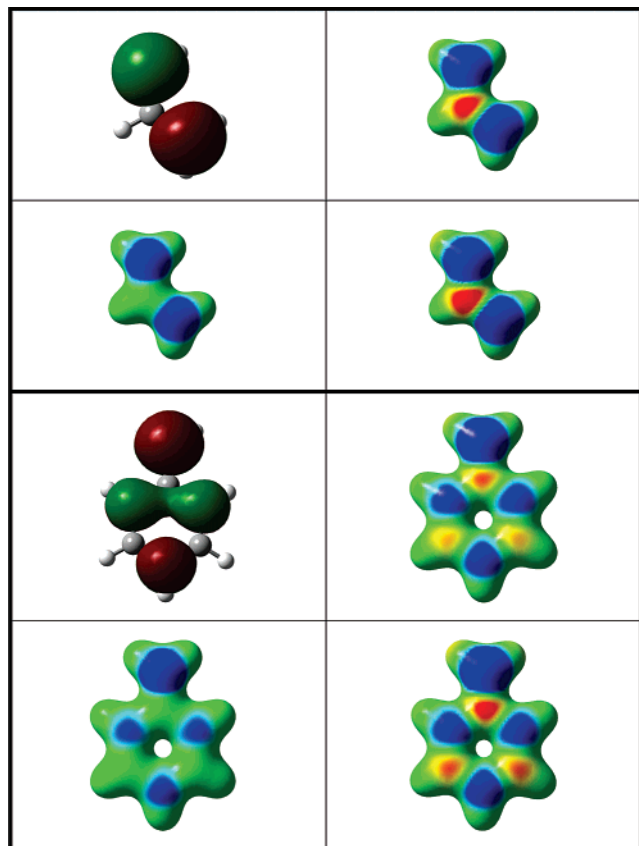


Figure 3. Conceptualization of the spin density distributions in the allyl radical (top) and benzyl radical (bottom). For each radical are shown the HOMO (top, left) and mapped surface plots of the spin densities computed with Hückel theory (bottom, left), density functional theory (top, right), and quadratic CI theory (bottom, right).

the destabilization associated with “spin delocalization onto an aromatic ring.”

Spin Delocalization and/or Spin Polarization. The qualitative patterns of the spin delocalizations can be predicted by any linear combination of atomic orbitals molecular orbital (LCAO-MO) theory: from Hückel theory^{32–34} and extended Hückel theory³⁵ to Hartree–Fock theory^{36,37} by inspection of the shape of the highest occupied molecular orbital (HOMO) or by spin density analysis.^{38,39} Quantitative methods for spin density analysis must account for spin polarization and require electron correlation, that is, the application of post-HF methods in the context of MO theory. On the other hand, spin polarization enters naturally in valence bond (VB) thought culture.⁴⁰ The DFT and the QCI methods recover the α -spin distribution pattern suggested by VB resonance theory, but these methods differ greatly in their effectiveness.

In HMO theory, spin density distribution usually is discussed by inspection of the HOMO. To provide for a direct comparison by way of the DFT and QCISD spin-density mapped electron density surfaces of Figures 1 and 2, we computed such surfaces also at the HMO level using extended HMO theory. Figures 3–5 show the results for the prototypical radicals **1** and **7**, the annulated systems, and the diannulated systems, respectively. The HMO spin-density mapped electron density surface for the benzyl radical shown

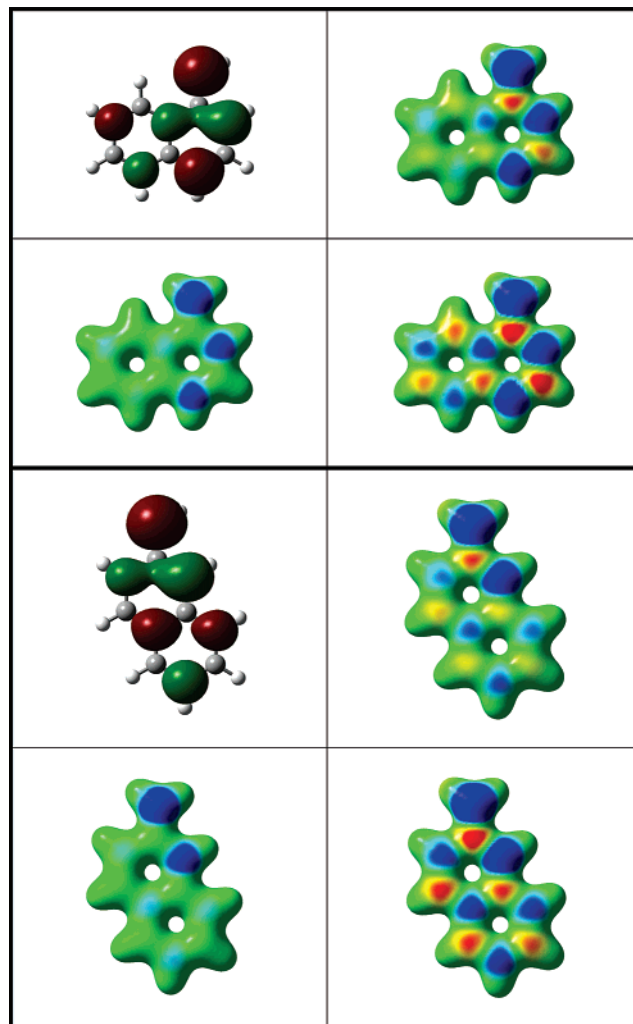


Figure 4. Conceptualization of the spin density distributions of the benzannulated benzyl radicals **2** (top) and **3**. See caption to Figure 3.

in Figure 3 features much less α -spin accumulations on the ortho and para positions as compared to the DFT and QCISD methods; this is the graphical manifestation of the fact that spin delocalization has significant consequences on spin polarization! Many organic chemists might react with disbelief when confronted with the HMO spin-density mapped electron density surfaces for **2–6** because there is hardly any spin delocalization into the arenes.

Figures 3–5 show in a compelling fashion that the spin density distributions cannot be understood, not even qualitatively, without consideration of spin polarization. QCISD theory shows significantly more spin polarization and extends over a longer range as compared to the B3LYP method. While molecule-wide spin polarization occurs, there is a tendency to keep the extent of spin delocalization into the annulated arenes *as low as possible*. Spin delocalization into an arene comes at a cost because spin delocalization *requires* spin polarization and thereby causes electronic structures that are less ideal from the perspective of aromaticity.⁴¹

Conclusion

Chemists use valence bond theory whenever they engage in “electron-pushing”, and doing so for radicals creates the

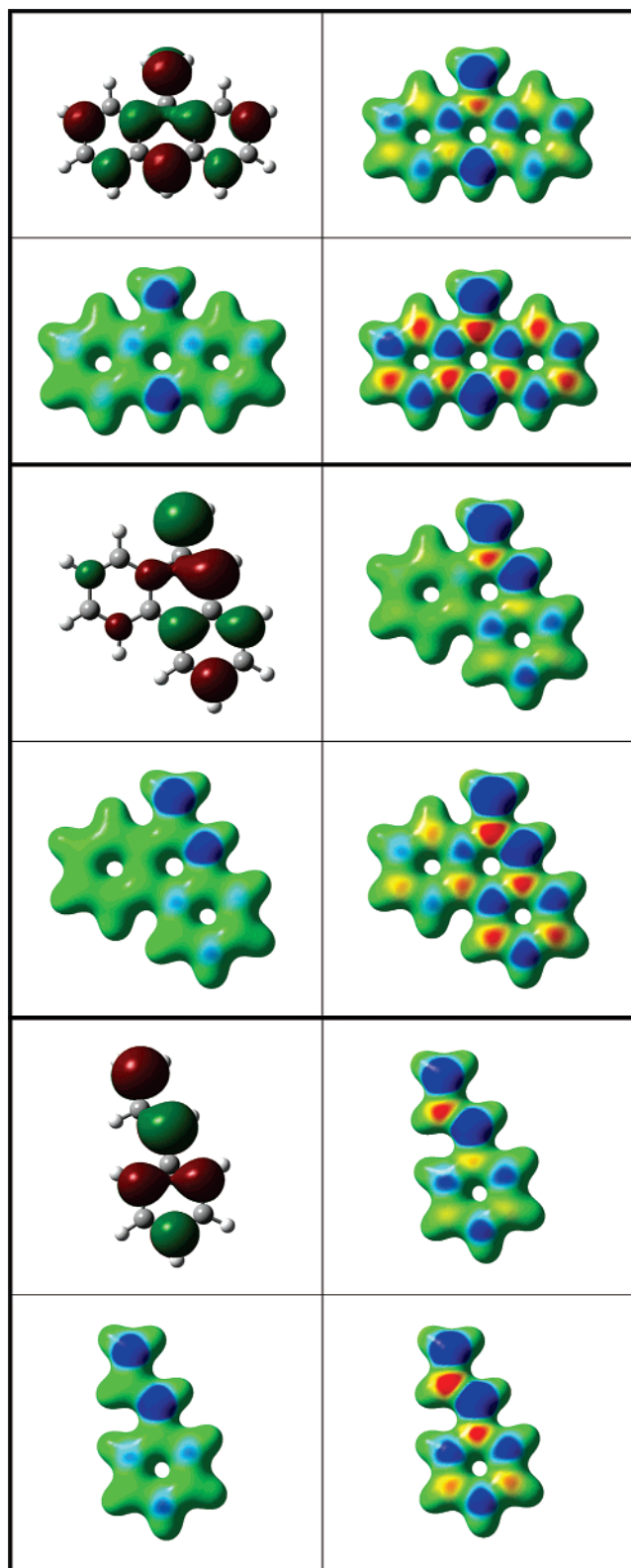


Figure 5. Conceptualization of the spin density distributions of the dibenzannulated benzyl radicals **4** (top) and **5** (center) and of model **6**. See caption to Figure 3.

perception of the possibility of molecule-wide spin delocalization in conjugated systems. On the other hand, whenever chemists employ computational methods, they are likely to use an uncorrelated LCAO-MO method, and doing so creates the perception of limiting spin delocalization over the HOMO region of the molecule. Neither of these viewpoints is

satisfactory. At the core of this problem is a general lack of understanding of “spin polarization” outside of the small circle of theorists. Graduate education in chemistry must begin to include at least qualitative discussions of the effects of spin polarization as a fundamental concept for long-distance communication in molecules. It is hoped that the present article contributes to furthering this long-term goal.

As a more immediate result, the present contribution demonstrates the need for experimental measurements of bond dissociation energies of the benzannulated systems. These data are most pertinent in and of themselves and as the key reference for theoretical studies that will advance fundamental conceptions about bonding.

From the theoretical perspective, the present paper highlights significant differences between the wavefunctions computed with the most widely used implementation of density functional theory and the QCISD method. Considering the computational demand of large-molecule calculations with QCI theory, one wonders whether DFT-based methods can be developed that account more fully for spin-polarization with regard to both magnitude and reach.

Acknowledgment. We acknowledge helpful communications with Dr. Paul Wenthold about the bond dissociation energy of toluene. We thank Drs. Gordon Springer, Larry Sanders, and Slava Zagrzewki for their continued advice about hardware and software issues. This work was supported in part by the MU Research Board (RB #2358). We gratefully acknowledge support of MU Research Computing by Federal Earmark NASA Funds for Bioinformatics Consortium Equipment and additional financial support from Dell, SGI, Sun Microsystems, TimeLogic, and Intel.

Supporting Information Available: Details of the potential energy surface analyses (Cartesian coordinates, total energies E_{tot} , thermal energies TE , thermal entropies S) and details of the electronic structure analyses (atom charges q , atom spin populations q^S). This material is available free of charge via the Internet at <http://pubs.acs.org>.

References

- (1) Dust, J. M.; Arnold, D. R. *J. Am. Chem. Soc.* **1983**, *105*, 1221–1227.
- (2) Creary, X. *Acc. Chem. Res.* **2006**, *39*, 761–771.
- (3) Wen, Z.; Li, Z.; Shang, Z.; Cheng, J.-P. *J. Org. Chem.* **2001**, *66*, 1466–1472.
- (4) Adam, W.; Kita, F.; Harrer, H. M.; Nau, W. M.; Zipf, R. *J. Org. Chem.* **1996**, *61*, 7056–7065.
- (5) Wu, Y. D.; Wong, C. L.; Chan, K. W.; Ji, G. Z.; Jiang, X. K. *J. Org. Chem.* **1996**, *61*, 746–750.
- (6) Bally, T.; Borden, W. T. *Rev. Comput. Chem.* **1999**, *13*, 1–97.
- (7) Hehre, W. J.; Radom, L.; Schleyer, P. v.; Pople, J. *Ab Initio Molecular Orbital Theory*; Wiley-Interscience: New York, 1986.
- (8) Cramer, C. J. *Essentials of Computational Chemistry: Theories and Models*, 2nd ed.; John Wiley & Sons: New York, 2004.

- (9) Lunell, S. *Chem. Phys. Lett.* **1972**, *13*, 93–96.
- (10) Pauncz, R. *Fundam. World Quantum Chem.* **2003**, *1*, 155–181.
- (11) Schlegel, H. B. *J. Phys. Chem.* **1988**, *92*, 3075–3078.
- (12) Chen, W.; Schlegel, H. B. *J. Chem. Phys.* **1994**, *101*, 5957–5968.
- (13) Glaser, R.; Chen, G. S.; Grützmacher, H. *J. Comput. Chem.* **1997**, *18*, 1023–1035.
- (14) Pople, J. A. *Rev. Mod. Phys.* **1999**, *71*, 1267–1274.
- (15) Wilson, S. *Handb. Mol. Phys. Quantum Chem. 2003* **2003**, *2*, 314–373.
- (16) He, Z.; Kraka, E.; Cremer, D. *Int. J. Quantum Chem.* **1996**, *57*, 157–172.
- (17) Koch, W.; Holthausen, M. C. *A Chemist's Guide to Density Functional Theory*, 2nd ed.; Wiley-VCH: Weinheim, Germany, 2001.
- (18) Parr, R. G.; Weitao, Y. *Density-Functional Theory of Atoms and Molecules*; Oxford University Press: Oxford, U. K., 1994; International Series of Monographs on Chemistry.
- (19) Wittbrodt, J. M.; Schlegel, H. B. *J. Chem. Phys.* **1996**, *105*, 6574–6577.
- (20) Noodleman, L.; Lovell, T.; Han, W.-G.; Li, J.; Himo, F. *Chem. Rev.* **2004**, *104*, 459–508.
- (21) ReePeng, C.; Ayala, P.; Schlegel, H. B.; Frisch, M. J. *J. Comput. Chem.* **1996**, *17*, 49–56.
- (22) Hoffmann, R. *J. Chem. Phys.* **1964**, *40*, 2474–2478.
- (23) Reed, A. E.; Weinstock, R. B.; Weinhold, F. *J. Chem. Phys.* **1985**, *83*, 735–746.
- (24) Frisch, M. J.; Trucks, G. W.; Schlegel, H. B.; Scuseria, G. E.; Robb, M. A.; Cheeseman, J. R.; Montgomery, J. A., Jr.; Vreven, T.; Kudin, K. N.; Burant, J. C.; Millam, J. M.; Iyengar, S. S.; Tomasi, J.; Barone, V.; Mennucci, B.; Cossi, M.; Scalmani, G.; Rega, N.; Petersson, G. A.; Nakatsuji, H.; Hada, M.; Ehara, M.; Toyota, K.; Fukuda, R.; Hasegawa, J.; Ishida, M.; Nakajima, T.; Honda, Y.; Kitao, O.; Nakai, H.; Klene, M.; Li, X.; Knox, J. E.; Hratchian, H. P.; Cross, J. B.; Bakken, V.; Adamo, C.; Jaramillo, J.; Gomperts, R.; Stratmann, R. E.; Yazyev, O.; Austin, A. J.; Cammi, R.; Pomelli, C.; Ochterski, J. W.; Ayala, P. Y.; Morokuma, K.; Voth, G. A.; Salvador, P.; Dannenberg, J. J.; Zakrzewski, V. G.; Dapprich, S.; Daniels, A. D.; Strain, M. C.; Farkas, O.; Malick, D. K.; Rabuck, A. D.; Raghavachari, K.; Foresman, J. B.; Ortiz, J. V.; Cui, Q.; Baboul, A. G.; Clifford, S.; Cioslowski, J.; Stefanov, B. B.; Liu, G.; Liashenko, A.; Piskorz, P.; Komaromi, I.; Martin, R. L.; Fox, D. J.; Keith, T.; Al-Laham, M. A.; Peng, C. Y.; Nanayakkara, A.; Challacombe, M.; Gill, P. M. W.; Johnson, B.; Chen, W.; Wong, M. W.; Gonzalez, C.; Pople, J. A. *Gaussian 03*, revision D.01; Gaussian, Inc.: Wallingford, CT, 2004.
- (25) Szwarc, M. *J. Chem. Phys.* **1948**, *16*, 128–136.
- (26) Hippler, H.; Troe, J. *J. Phys. Chem.* **1990**, *94*, 3803–3806.
- (27) Berkowitz, J.; Ellison, G. B.; Gutman, D. *J. Phys. Chem.* **1994**, *98*, 2744–2765.
- (28) Ellison, G. B.; Davico, G. E.; Bierbaum, V. M.; DePuy, C. H. *Int. J. Mass Spectrom. Ion Processes* **1996**, *156*, 109–131.
- (29) Ervin, K. M.; DeTuri, V. F. *J. Phys. Chem. A* **2002**, *106*, 9947–9956.
- (30) Finkelshtein, E. I. *J. Phys. Org. Chem.* **2001**, *14*, 543–550.
- (31) Bauschlicher, C. W.; Langhoff, S. R. *Mol. Phys.* **1999**, *96*, 471–476.
- (32) Streitwieser, A. *Molecular Orbital Theory for Organic Chemists*; John Wiley & Sons: New York, 1961; p 392ff.
- (33) Carsky, P.; Zahradnik, R. *J. Phys. Chem.* **1970**, *74*, 1249–1254.
- (34) Nowakowski, J. *Theor. Chim. Acta* **1970**, *18*, 133–142.
- (35) Hoffmann, R.; Bissell, R.; Farnum, D. G. *J. Phys. Chem.* **1969**, *73*, 1789–1800.
- (36) Gey, E.; Hennig, H.; Stoesser, R. *Z. Phys. Chem. (Liepzig)* **1974**, *255*, 395–400.
- (37) Klimo, V.; Tino, J. *Int. J. Quantum Chem.* **1976**, *10*, 761–769.
- (38) Glaser, R.; Choy, G. S.-C. *J. Phys. Chem.* **1993**, *97*, 3188–3198.
- (39) Glaser, R.; Choy, G. S.-C. *J. Phys. Chem.* **1994**, *98*, 11379–11393.
- (40) Wu, W.; Zhong, S.; Shaik, S. *Chem. Phys. Lett.* **1998**, *292*, 7–14.
- (41) Shurki, A.; Hiberty, P. C.; Dijkstra, F.; Shaik, S. *J. Phys. Org. Chem.* **2003**, *16*, 731–745.

CT700051J

JCTC

Journal of Chemical Theory and Computation

Energy Conservation in Adaptive Hybrid Atomistic/ Coarse-Grain Molecular Dynamics

Bernd Ensing,^{*,†} Steven O. Nielsen,[‡] Preston B. Moore,[§] Michael L. Klein,^{||} and Michele Parrinello[†]

Department of Chemistry and Applied Biosciences, ETH Zurich USI-Campus, Via Giuseppe Buffi 13, Lugano, CH-6900 Switzerland, Department of Chemistry, University of Texas at Dallas, 2601 North Floyd Road, Richardson, Texas 75083-0688, Department of Chemistry and Biochemistry, University of the Sciences in Philadelphia, Philadelphia, Pennsylvania 19104, and Center for Molecular Modeling, Department of Chemistry, University of Pennsylvania, Philadelphia Pennsylvania 19104-6323

Received November 3, 2006

Abstract: Multiscale computer simulation algorithms are required to describe complex molecular systems with events occurring over a range of time and length scales. True multiscale simulations must solve the interface, or hand-shaking, problem of coupling together different levels of description in different spatial regions of the system. If the spatial regions of different resolution move over time, or if material is allowed to flow over the inter-region boundaries, a mechanism must be introduced into the multiscale algorithm to allow material to dynamically change its representation. While such a mechanism is highly desirable in many instances, it is fraught with technical difficulties. Here, we present a molecular dynamics simulation algorithm which is multiscale in both time and space. We supplement the potential and kinetic energy expressions with auxiliary terms in order to recover the total energy as a conserved quantity, even when the total number of degrees of freedom changes during the simulation. This is crucial for a proper assessment of the quality of adaptive hybrid algorithms, and in particular, it allows us to tune the hierarchy of RESPA levels to optimize the integration scheme.

I. Introduction

In computer simulation, multiscale methods break the calculation up into parts to be treated at different levels of resolution or accuracy. Multiscale methods are therefore more economical, allowing for larger systems, longer time scales, or simply less resources than calculations performed entirely at the most demanding level. An example of a successful multiscale approach in molecular simulation is the quantum mechanical/molecular mechanical (QM/MM) treatment of enzymatic proteins, in which the chemically active region of the enzyme is modeled with an accurate QM method,

while the remaining protein scaffold and the aqueous environment are described with a classical MM force field.^{1,2}

In this paper, we present a hybrid atomistic/coarse-grain molecular dynamics method which allows parts of a molecular system to be simulated in full atomistic detail while treating the rest of the system at a coarse-grain (CG) resolution. Here, CG refers to a dimensional reduction by lumping atoms together into single interaction sites, that way drastically reducing the number of particles and pair interactions in the calculation. CG simulations can therefore access much longer time scales and larger system sizes than canonical molecular dynamics (MD) and has found successful application in the modeling of polymer melts,^{3,4} biomembranes,⁵ and proteins.^{6,7}

The idea of combining an atomistic with a lower-resolution description is not new. Carloni et al. joined atomistic MD with a Go-type of model for the simulation of proteins,^{8,11}

* Corresponding author e-mail: bernd.ensing@phys.chem.ethz.ch.

[†] ETH Zurich USI-Campus.

[‡] University of Texas at Dallas.

[§] University of the Sciences in Philadelphia.

^{||} University of Pennsylvania.

while Koumoutsakos et al. linked atomistic MD to a continuum description to model nanoscale fluid mechanics.¹² Kurkuoglu et al. studied protein motions at mixed levels of coarse-graining within an elastic network approach,⁹ and Voth et al. used a force-field-fitting approach to parametrize atom–CG bead interactions in a mixed atomistic and coarse-grained MD simulation.¹⁰ A particularly advantageous approach was recently introduced by Kremer et al. which allows particles to change their representation from atomistic to CG and vice versa during a MD simulation,^{13,14} while Abrams presented a similar adaptive dual-resolution method within a Monte Carlo approach.¹⁵

It is important that molecules can adapt their representation when they diffuse over the region boundaries in order to maintain the spatial separation in regions of different resolution. On very short time scales and in rigid molecular systems, such diffusion is minimal, so that a nonadaptive approach can be sufficient. This is often the case in the aforementioned QM/MM simulation of enzymes. On the other hand, when the chemical (QM-treated) region is solvent-exposed and protons or water molecules take part in the chemistry, MM-treated water molecules can replace the QM ones, so that the chemistry is not correctly described unless the representation adapts. Also, when the phenomenon of high-resolution interest displaces through the system, an adaptive scheme is required. The QM/MM treatment of the propagation of a crack in a brittle solid, in which only the atoms in the advancing crack tip region are modeled at the QM tight-binding level of theory, is an example of such an adaptive approach.¹⁶

In the case of an atomistic/CG molecular dynamics treatment, the method is especially aimed to study molecular motions on long time scales, making it natural to seek an adaptive algorithm. Coarse-graining is typically applied to model soft matter, and the range of phenomena in this field that could be studied with an adaptive hybrid atomistic/coarse-grained description is only limited by our imagination but could include diffusion of molecules and ions in swollen polymers, conformational dynamics in proteins, ligand docking, physisorption at a solid/liquid interface, permeation and diffusion in biomembranes, and so forth.

To set up a (particle-based) dual-resolution simulation, the system is, arbitrarily, spatially divided into a high-resolution atomistic region (AR) and a low-resolution CG region (CGR). For example, the AR can be defined within a sphere of fixed-radius centered on a specific particle. This way, the AR follows the tagged particle and evolves when particles move through the spherical boundary. A standard force field can be employed for the evolution of the individual atoms in the AR, whereas the particles in the CGR are evolved using a CG force field—for example, one fitted against the atomistic force field using force-matching methods^{17,18} or inverse Monte Carlo techniques.¹⁹ The coupling between the two regions is done at the CG level by first mapping the AR into its CG representation (which involves grouping the atoms into larger particles) and then evaluating the cross interactions with the CG force field, after which the effective forces on the CG particles in the AR are distributed mass-weighted over their constituent atoms.¹³

Difficulties arise when particles are allowed to diffuse over the regional boundaries and change their atomistic/coarse-grain (A/CG) representation on the fly. In particular, instantaneous switching of the atomistic potentials into the CG ones or vice versa would cause spurious jumps in the forces and velocities of the particles. Instead, the discontinuity between the AR and CGR is bridged by an intermediate *healing region* (HR), in which crossing particles gradually acquire their new representation. In the scheme of Kremer et al., this is done using force scaling.¹³ Instead, here, we will scale the potentials, the advantages of which are the main focus of this paper. Second, we exploit the reversible RESPA multi-time-step approach,²⁰ evaluating rapidly oscillating forces, such as those arising from bond interactions between atoms, more frequently than the slowly fluctuating nonbonded forces. The natural hierarchy of RESPA levels commonly employed in atomistic simulations generalizes in a straightforward manner to the A/CG situation, allowing us to tune the molecular dynamics integrator optimally across the entire system.

II. Method

The present hybrid scheme assigns both atomistic and coarse-grain positions and velocities throughout the entire system. Given an atomistic configuration and a CG mapping (i.e., a grouping of the atoms into CG particles), the coarse-grained representation is readily computed, taking for each CG position the center of mass of its constituent atoms and likewise for the velocities. Recently, some of us developed an efficient algorithm to obtain an atomistic configuration from a CG one, the so-called inverse mapping, which is not straightforward because of missing information.²¹ Molecules in the AR and HR are evolved at the atomistic level, and their CG positions (and velocities) are updated in the RESPA substep for the evaluation of the inter-region interactions. In the CGR, the CG particles are evolved, and their corresponding atomistic positions and velocities are frozen relative to these centers.

The accuracy of the integration of the equations of motion (i.e., the quality of the simulation) is evaluated by monitoring the total energy, which is a conserved quantity of the system. The total energy in a hybrid system is composed of the sum of kinetic and potential energies of the distinct spatial regions, plus the energy that is exchanged with extended variables (e.g., those of a thermostat), plus the change in kinetic and potential energies due to particles that adapt their resolution.

The total kinetic energy, K , is

$$K = \sum_{\alpha \in (\text{AR}, \text{HR})} \sum_{i \in \alpha} \frac{p_i^2}{2m_i} + \sum_{\alpha \in \text{CGR}} \frac{p_\alpha^2}{2M_\alpha} + \Delta K_\alpha^{\text{A/CG}} \quad (1)$$

where, for each CG particle α in the AR and HR, we sum the kinetic energy of its constituent atoms, i (with p the momentum and m the mass), and for each CG particle in the CGR, its kinetic energy, plus an extra term $\Delta K_\alpha^{\text{A/CG}}$:

$$\Delta K_\alpha^{\text{A/CG}} = \sum_{i \in \alpha} \frac{\tilde{p}_i^2}{2m_i} - \frac{\tilde{p}_\alpha^2}{2M_\alpha} \quad (2)$$

This term is the surplus kinetic energy that is associated with the atomistic representation of a CG particle but which is “integrated out” upon coarse-graining. Its value is computed at the start of the simulation and is then updated whenever a particle α crosses the CGR/HR boundary, adding or subtracting the kinetic energy difference between the two representations of the particle. To distinguish the momenta in eq 2 from the normal instantaneous momenta in eq 1, we add here and hereafter a tilde to indicate a book-keeping property that is only updated upon adaptation of a particle’s resolution and frozen in between.

The potential-energy function is separated into interactions that are confined between sites within a single CG particle and interactions between sites spanning more than one CG particle. The first type of interactions, termed *intra-CG particle* interactions and shown in eq 3, consists of atomistic potentials, Φ_{ij} , where i and j are atoms belonging to the same CG particle α . They are evaluated in the AR and HR but not in the CGR where the atoms are frozen with respect to the CG particle they are associated with. Similar to the kinetic energy, an extra term, $\Delta W_{\alpha}^{\text{intraCG}}$, arises to account for this frozen inherent atomistic potential energy, $\tilde{\Phi}$, within each CG particle in the CGR; its value is recorded at the start of the simulation, after which it is updated whenever a particle crosses the CGR/HR boundary.

$$V^{\text{intraCG}} = \sum_{\alpha \in (\text{AR}, \text{HR})} \sum_{\substack{i \in \alpha \\ j \in \alpha}} \Phi_{ij} + \sum_{\alpha \in (\text{CGR})} \Delta W_{\alpha}^{\text{intraCG}} \quad (3)$$

$$\Delta W_{\alpha}^{\text{intraCG}} = \sum_{\substack{i \in \alpha \\ j \in \alpha}} \tilde{\Phi}_{ij} \quad (4)$$

All other interactions, termed *inter-CG particle* interactions, are governed by eq 5. That is, the interaction between CG particles α and β is composed of the scaled CG potential $\Phi_{\alpha\beta}$ and the scaled atomistic interactions Φ_{ij} between atoms i and j belonging to α and β , respectively, with the scaling factor λ a number between 0 and 1.

$$V^{\text{interCG}} = \sum_{\alpha} \left\{ \sum_{\beta > \alpha} \lambda_{\alpha\beta} \Phi_{\alpha\beta} + \sum_{\beta > \alpha} (1 - \lambda_{\alpha\beta}) \sum_{\substack{i \in \alpha \\ j \in \alpha}} \Phi_{ij} + \Delta W_{\alpha}^{\text{interCG}} \right\} \quad (5)$$

Equation 5 also contains an extra term, $\Delta W_{\alpha}^{\text{interCG}}$, that accounts for the changes in V^{interCG} when particles change their A/CG character.

For an infinitely thin HR, the scaling factor, λ , becomes simply a Heaviside step function, Θ , that is equal to unity if one or both particles are in the CGR and is equal to 0 otherwise. In such a case of instantaneous resolution switching, $\Delta W_{\alpha}^{\text{interCG}}$ can be explicitly expressed and computed as the energy difference in V^{interCG} when particle α crosses the region boundary, analogous to the auxiliary terms in eqs 2 and 4:

$$\Delta W_{\alpha}^{\text{interCG}} = \Theta \sum_{\alpha} \left(\tilde{\Phi}_{\alpha\beta} - \sum_{\substack{i \in \alpha \\ j \in \alpha}} \tilde{\Phi}_{ij} \right) \quad (6)$$

Note however that, contrary to the other two auxiliary terms

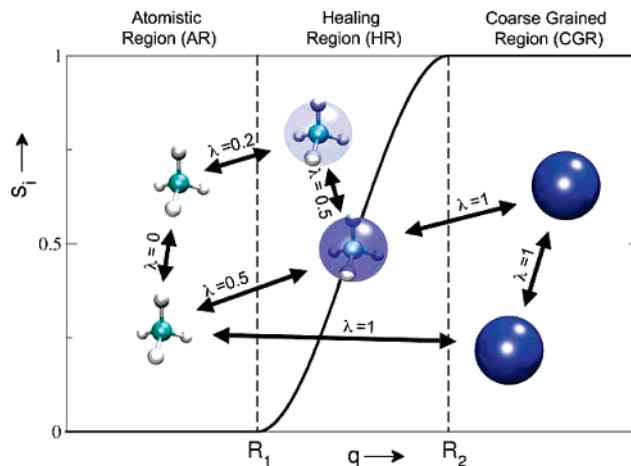


Figure 1. Switch function s shown as a function of an arbitrary distance q . Here, $s = 0$ for each CG particle (and its atoms) within a sphere $q < R_1$ (atomistic region) and $s = 1$ for particles outside $q > R_2$ (coarse-grained region). Pair interactions are scaled by $\lambda = \max[s_1, s_2]$.

$\Delta K_{\alpha}^{\text{A/CG}}$ and $\Delta W_{\alpha}^{\text{intraCG}}$, which are local and consist of constant (frozen) intra-CG atomistic contributions of particles in the CGR, evaluation of $\Delta W_{\alpha}^{\text{interCG}}$ requires nonlocal information including inter-CG atomistic interactions that are not constant, which would nullify the efficiency of the CG representation. That is, we can indeed store that part of the kinetic and potential energies that become inherent to the CG bead when a particle α moves from the AR to the CGR by taking the energy difference (using eqs 2, 4, and 6), but when this particle returns to the AR and the inherent energies become explicit again, $\Delta W_{\alpha}^{\text{interCG}}$ is of course not the same as when it left the AR, thus rendering the absolute value of $\Delta W_{\alpha}^{\text{interCG}}$ meaningless. Instead, we will only book-keep the changes to this term when molecules change representation, where we make use of a smoothly changing scaling function, λ , in the HR in the following manner.

The scaling factor is equal to

$$\lambda_{\alpha\beta} = \max[s(\mathbf{r}_{\alpha}), s(\mathbf{r}_{\beta})] \quad (7)$$

where s_{α} is the fraction of CG character of particle α , which depends on its position \mathbf{r} relative to the regional boundaries as illustrated in Figure 1. For particles in the AR, s is 0; in the CGR, s is 1, and in the HR, s has an intermediate value, signifying a hybrid character. Here, we take s to be a simple polynomial function of the distance q between the particle and a fixed position that smoothly switches from 0 to 1 between the AR/HR boundary at R_1 and the HR/CGR boundary at R_2 :

$$s_{\alpha}(q) = \begin{cases} 0 & \text{if } q < R_1 \\ (q - R_1)^2(3R_2 - R_1 - 2q)/(R_2 - R_1)^3 & \text{if } R_1 \leq q \leq R_2 \\ 1 & \text{if } q > R_2 \end{cases} \quad (8)$$

Let us consider for a moment the forces on the particles by taking the derivatives of the potential $V = V^{\text{intraCG}} + V^{\text{interCG}}$, namely eq 3 plus eq 5. The derivatives of the first part give

the usual contributions to the forces; however, applying the chain rule to the scaled potentials in V^{interCG} results in forces of the following shape:

$$f_{\alpha} = -\lambda(\mathbf{r}_{\alpha}, \mathbf{r}_{\beta}) \frac{\partial \Phi(\mathbf{r}_{\alpha}, \mathbf{r}_{\beta})}{\partial \mathbf{r}_{\alpha}} - \frac{\partial \lambda(\mathbf{r}_{\alpha}, \mathbf{r}_{\beta})}{\partial \mathbf{r}_{\alpha}} \Phi(\mathbf{r}_{\alpha}, \mathbf{r}_{\beta}) - \dots \quad (9)$$

Here, the usual forces $\partial \Phi / \partial \mathbf{r}_{\alpha}$ are recognized in the first term, scaled by λ , but the second term introduces a new force, consisting of the derivative of the scaling function multiplied by the potential. This term is only nonzero for particles in the HR and gives rise to a force on these particles that changes their A/CG character, $s(\mathbf{r})$, which is seen to be spurious.

To understand the origin of this new force, consider an atomistic torsion potential, $V_{ijkl}^{\text{dihedral}}$, spanning two CG particles ($i, j \in \alpha$, and $k, l \in \beta$) located in the HR. The molecule can now lose this torsional potential energy in two ways: (1) by gaining kinetic energy in the usual physical manner via a motion in the direction of the first term in eq 9 or 2 by moving in the direction of the second term (i.e., toward the CGR) so that the potential is scaled down to 0. The second term thus causes a spurious flux of particles through the HR. Note, however, that the loss of the atomistic torsional potential energy that causes this force should be canceled by CG potential terms (on average) and that any instantaneous differences should be taken as inherent CG energy, stored in $\Delta W^{\text{interCG}}$. In other words, even though we do not have an explicit expression for $\Delta W^{\text{interCG}}$ in the case of smoothly scaled potentials, we can keep track of the energy flow from and to $\Delta W^{\text{interCG}}$ because we know its derivative as minus the second term in eq 9.²²

With the second term in the force expression canceled, only the first term, namely, the scaled force, is left in the equations of motion. To obtain the total energy, however, we need to accurately book-keep the amount of nonlocal ‘‘inter-GC particle’’ potential energy that transfers from explicit (atomistic) into the inherent CG term, $\Delta W^{\text{interCG}}$. This is done in a manner analogous to the thermodynamic integration applied in free-energy perturbation methods. That is, the energy flow is evaluated by integration of the derivative of W^{interCG} (i.e., minus the second term in eq 9) on the fly for particles moving in the HR:

$$\Delta \Delta W^{\text{interCG}} = \int_{\Delta \mathbf{r}} \sum_{\substack{\alpha \in \text{HR} \\ \beta \in \text{AA, HR}}} \Phi(\mathbf{r}) \frac{d\lambda}{d\mathbf{r}} d\mathbf{r}' \approx \sum_t \sum_{\substack{\alpha \in \text{HR} \\ \beta \in \text{AA, HR}}} \Phi(\mathbf{r}) \frac{ds(q_{\alpha})}{dq_{\alpha}} \Delta q_{\alpha} \quad s_{\alpha} > s_{\beta} \quad (10)$$

where the sum runs over all scaled inter-CG interactions (including the atomistic ones) between CG particles α and β and the integral is approximated by a Riemann’s sum over time steps t , making use of the fact that the change in λ equals the change in s of the particle (α) with maximum s (see eq 7). Here, Δq is the displacement of the particle in the direction of changing s (i.e., toward or from the CGR).

The main function of the HR is to facilitate the introduction of atomistic detail when a CG particle leaves the CGR. Without a HR, instantaneous switching to the atomistic

interactions would lead to large repulsive forces due to overlaps of the nonequilibrated atoms. Rather, the atomistic interactions are turned on gradually across the width of the healing region. In addition, many-body interactions, such as bend and torsion potentials spanning more than one CG particle, are evaluated as in eq 5, where λ is determined by the particle with the maximum CG character.

All particles are coupled to individual Nose–Hoover thermostat chains, which are frozen when the particles are not explicitly evolved upon crossing regional boundaries (namely, for CG particles in the AR and HR and for atoms in the CGR). Coupling of the atoms to thermostats in the healing region is particularly important for two reasons. First, the particles that leave the CGR have atomistic velocities that were stored from the last time they left the AR (or were drawn from a random distribution at time zero) and, thus, need to be updated before entering the AR. Second, the atomistic positions of such particles also need to be equilibrated because these particles tend to be too high on the atomistic potential energy surface. This excess potential energy is transformed into kinetic energy while the atoms cross the HR heading toward the AR, which is conveniently removed with a thermostat. Consequently, we expect to see a decreasing $\Delta W^{\text{interCG}}$, as molecules moving from the CGR toward the AR on average have a higher atomistic potential than molecules moving in the opposite direction (e.g., consider also the case of eq 6), with a slope with opposite sign and equal magnitude as the potential energy of the thermostat (see the Supporting Information for an illustration). The requirement of thermostats excludes the calculation of transport properties, although in principle, it is possible to only couple particles in the HR to a thermostat and reduce the influence on the dynamics in the other regions.

In the rest of this paper, we will illustrate the method by applying it to two model systems: first, a single two-particle molecule moving across the regional boundaries and, second, a periodic box of dense methane.

III. Applications

A. Simple Bead and Spring Molecule Changing Representation. Figure 2 illustrates the first application, namely, a single molecule that is represented at both the atomistic and CG levels by two atoms connected with a bond. The only difference is the force constant of the harmonic bond potential, which is 10 times smaller in the CGR than in the AR. The AR is a two-dimensional slab of thickness $2r_{\text{AR}} = 10 \text{ \AA}$, flanked on both sides by a 5- \AA -thick HR and an outer CGR. The cubic box with edge length $L = 30 \text{ \AA}$ is subject to periodic boundary conditions, and the molecule has a velocity parallel to the AR slab normal vector that takes it 6 ps to move through the entire box. The $\Delta K^{\text{A/CG}}$ and $\Delta W^{\text{intraCG}}$ terms are 0 in this special case of a one-to-one mapping, and the remaining nonzero $\Delta W^{\text{interCG}}$ term allows us to test the integration scheme. The solid black lines show the total energy (with and without the correction) when the molecule is oriented with the bond stretch vibration perpendicular to the velocity, while the red lines show the energies in the case of parallel orientation (see also the yellow inset). The dashed lines show the correction, W^{interCG} . The inset in the

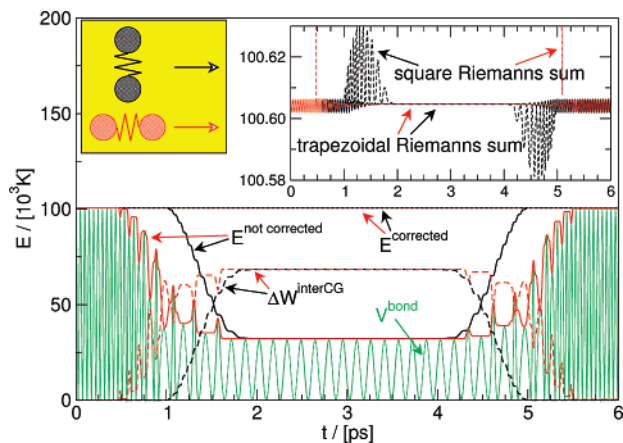


Figure 2. Total energy of a two-atom molecule that moves from the AR via a HR into the CGR (where the bond is $10\times$ weaker) and back. Black lines: molecule orientation perpendicular to its velocity. Red lines: parallel orientation (see the yellow inset). Green line: potential energy during the parallel orientation trajectory. The inset shows the superiority of the trapezoidal Riemann's sum (eq 11).

upper right-hand corner of Figure 2 zooms in on the fluctuations of the total energy, showing strong oscillations when the integral is estimated by the straightforward rectangular Riemann's sum of eq 10, which uses only the end-point evaluation of the function on the interval Δq (not taking into account the "midpoint rule" of integration). Much better total energy conservation is obtained by including the function value at the start point of the time-step interval and taking the average (making use of the "trapezoid rule"):

$$\Delta\Delta W^{\text{interCG}} = \sum_t \sum_{\substack{\alpha \in \text{HR} \\ \beta \in \text{AA, HR}}} \frac{1}{2} \left[\Phi_t(\mathbf{r}) \frac{ds_t(q_\alpha)}{dq_\alpha} + \Phi_{t-1}(\mathbf{r}) \frac{ds_{t-1}(q_\alpha)}{dq_\alpha} \right] \Delta q_\alpha \quad s_\alpha > s_\beta \quad (11)$$

Clearly, the integration scheme works to recover the total energy as a conserved quantity in this example of adaptive hybrid MD.

B. Hybrid Molecular Dynamics of Liquid Methane. The second, more realistic, illustration is a cubic box containing 8000 methane molecules. The box has an edge length of 79.9 Å and is subject to periodic boundary conditions. In a spherical AR with a radius of 8 Å, the CH_4 molecules are represented in atomistic detail with flexible bonds and bends.²³ The AR is surrounded by a 4-Å-thick spherical healing region. Both regions are centered on a noninteracting dummy particle that is fixed in space, but in other test simulations, we have also used a methane molecule to center these regions, in which case the AR and HR follow the motion of that methane molecule. In the outlying CGR, the molecules are represented by a single van der Waals sphere using Jorgensen's united atom model.²⁴ The density of methane in this setup is 0.418 g/mL, which is close to the actual density of liquid methane (at 1 atm and 111.5 K) of 0.423 g/mL.

The multi-time-step approach is employed with an outer time step of 2 fs and substeps in which the CG long-range

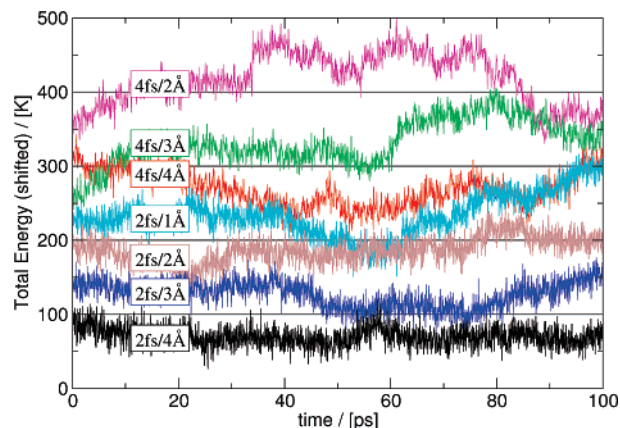


Figure 3. Total energies (shifted for comparison) of hybrid MD simulations of 8000 methane molecules, using different time steps and healing region widths. The energy is well-conserved using a time step of 2 fs and a HR width of 4 Å.

van der Waals interactions are updated once, the CG short-range Van der Waals interactions twice, the atomistic long-range and short-range van der Waals and electrostatics twice and four times, respectively, and the bond and bend interactions 32 times (for further details, see the Supporting Information). A further speedup is gained by treating the periodic boundary conditions for the AR and HR in the CG representation, which is allowed when the longest distance in those regions is smaller than half of the shortest box edge. For systems with charged CG particles, the long-range electrostatics are taken into account using Ewald summation at the CG level.

As seen in the first example above, the best total energy conservation is reached by averaging $\Phi d\lambda/dq$ in the integration scheme (eq 11). Implemented in that form, however, requires storing $\Phi d\lambda/dq$ of the previous time step ($t - 1$) for all scaled interactions. Instead, we can rewrite eq 11 in sums of $\Phi d\lambda/dq$ that have the same displacement Δq . The displacement is determined by the interacting particle with the maximum CG character, so that the number of terms to be stored is only as large as the number of CG particles in the HR.

In Figure 3, the total energy from the first 100 ps of this hybrid MD simulation is compared with those from hybrid simulations using different outer time steps and different HR widths. A clear trend can be observed of total energy conservation improvement with decreasing time-step and increasing HR-width.

Further details on the analysis of a 600 ps trajectory of the best combination are found in the Supporting Information. The numbers of methane molecules in the AR, HR, and CGR were 34.0 ± 2.3 , 77.5 ± 3.8 , and 7889.4 ± 3.8 , respectively. The radial distribution functions, mean square displacements, and velocity autocorrelation functions of the hybrid MD simulation averaged over the methane atoms in the AR show excellent agreement with those from a purely atomistic MD simulation of a box of 1000 methane molecules.

IV. Conclusions

We have presented a hybrid atomistic/CG MD method that allows particles to change resolution on the fly. By introduc-

ing auxiliary terms to the kinetic and potential energy expressions, we recover the total energy as a conserved quantity, even when the total number of degrees of freedom changes during the simulation. These auxiliary energy terms should be seen as the inherent energy of the CG particles that is “integrated out” upon the dimensional reduction and becomes explicit again when switching back to the atomistic representation. Using a reversible RESPA multistep integration scheme, our method has the benefits of being truly multiscale in both time and space. Conserving energy is particularly important in hybrid MD, as it is the fundamental property used to evaluate the choice of the subtime steps and the size of the intermediate healing region with respect to the quality of the simulation. In particular for hybrid MD simulations of more complex systems than methane, in which case it is expected that a wider healing region is required, we now have the machinery in place to assess the quality of hybrid MD.

Supporting Information Available: Technical details and analysis of the hybrid MD simulation of methane, including a short illustrative mpeg movie. This material is available free of charge via the Internet at <http://pubs.acs.org>.

References

- (1) Carloni, P.; Rothlisberger, U.; Parrinello, M. *Acc. Chem. Res.* **2002**, *35*, 455.
- (2) Warshel, A. *Annu. Rev. Biophys. Biomol. Struct.* **2003**, *32*, 425.
- (3) Baschnagel, J.; Binder, K.; Doruker, P.; Gusev, A. A.; Hahn, O.; Kremer, K.; Mattice, W. L.; Muller-Plathe, F.; Murat, M.; Paul, W.; Santos, S.; Suter, U. W.; Tries, V. *Adv. Polym. Sci.* **2000**, *152*, 41.
- (4) Muller-Plathe, F. *Chem. Phys. Chem.* **2002**, *3*, 754.
- (5) Nielsen, S. O.; Lopez, C. F.; Srinivas, S.; Klein, M. L. *J. Phys.: Condens. Matter* **2004**, *16*, R481.
- (6) Go, N. *Annu. Rev. Biophys. Bioeng.* **1983**, *12*, 183.
- (7) Brown, S.; Fawzi, N. J.; Head-Gordon, T. *Proc. Natl. Acad. Sci. U.S.A.* **2003**, *100*, 10712.
- (8) Neri, M.; Anselmi, C.; Cascella, M.; Maritan, A.; Carloni, P. *Phys. Rev. Lett.* **2005**, *95*, 218102.
- (9) Kurkcuoglu, O.; Jernigan, R. L.; Doruker, P. *Polymer* **2004**, *45*, 649.
- (10) Shi, Q.; Izvekov, S.; Voth, G. A. *J. Phys. Chem. B* **2006**, *110*, 15045.
- (11) Neri, M.; Anselmi, C.; Carnevale, V.; Vargiu, A. V.; Carloni, P. *J. Phys.: Condens. Matter* **2006**, *18*, S347.
- (12) Werder, T.; Walther, J. H.; Koumoutsakos, P. *J. Comput. Phys.* **2005**, *205*, 373.
- (13) Praprotnik, M.; Delle Site, L.; Kremer, K. *J. Chem. Phys.* **2005**, *123*, 224106.
- (14) Praprotnik, M.; Delle Site, L.; Kremer, K. *Phys. Rev. E: Stat., Nonlinear, Soft Matter Phys.* **2006**, *73*, 066701.
- (15) Abrams, C. *J. Chem. Phys.* **2005**, *123*, 234101.
- (16) Csányi, G.; Albaret, T.; Payne, M. C.; DeVita, A. *Phys. Rev. Lett.* **2004**, *93*, 175503.
- (17) Ercolessi, F.; Adams, J. B. *Europhys. Lett.* **1994**, *26*, 583.
- (18) Izvekov, S.; Parrinello, M.; Burnham, C. J.; Voth, G. J. *Chem. Phys.* **2004**, *120*, 10896.
- (19) Lyubartsev, A. P.; Laaksonen, A. *Phys. Rev. E: Stat., Nonlinear, Soft Matter Phys.* **1995**, *52*, 3730.
- (20) Tuckerman, M.; Berne, B. J.; Martyna, G. J. *J. Chem. Phys.* **1992**, *97*, 1990.
- (21) Nielsen, S. O.; Ensing, B.; Moore, P. B.; Klein, M. L. Coarse Grain to Atomistic Mapping Algorithm: A Tool for Multi-scale Simulations. In *Advances in Hierarchical and Multi-Scale Simulations of Materials*; Mohanty, S., Ross, R. B., Eds.; Publisher: Taylor and Francis: Oxford, U. K., 2006; in press.
- (22) This is easily shown to be true in the infinitely thin HR case for which we have an explicit expression for $\Delta W^{\text{interCG}}$ (eq 6), and the forces are thus given by $f_a = -\Theta(q - R_2)(\partial\Phi/\partial\mathbf{r}) - \Phi[\partial\Theta(q - R_2)/\partial\mathbf{r}] - \Theta(-q + R_2)(\partial\tilde{\Phi}/\partial\mathbf{r}) - \tilde{\Phi}[\partial\Theta(-q + R_2)/\partial\mathbf{r}]$. Indeed, the second term is canceled by the derivative of $\Delta W^{\text{interCG}}$ (third and fourth terms), because the third term is zero in all regions and the fourth term equals minus the second term, as the derivative of the Heaviside step function is the δ function, $\delta(q - R_2)$, which equals unity at the HR/CG boundary R_2 where $\Phi = \tilde{\Phi}$ and zero otherwise.
- (23) Sun, Y.; Spellmeyer, D.; Pearlman, D. A.; Kollman, P. J. *Am. Chem. Soc.* **1992**, *114*, 6798.
- (24) Jorgensen, W.; Madura, J.; Swenson, C. *J. Am. Chem. Soc.* **1984**, *106*, 6638.

CT600323N

JCTC

Journal of Chemical Theory and Computation

Improving Docking Accuracy through Molecular Mechanics Generalized Born Optimization and Scoring

Matthew R. Lee* and Yaxiong Sun

*Department of Molecular Structure, Amgen Inc., One Amgen Center Drive,
Thousand Oaks, California 91320-1799*

Received November 20, 2006

Abstract: Docking methods are typically used within the biopharmaceutical industry for the challenging purposes of suggesting putative binding modes of new chemotypes and for virtual screening. When attempting to satisfy the far more simplistic yet fundamentally important goal of reproducing and identifying the correct binding mode from a cocrystal, all docking methods fail at a rather significant rate, demonstrating room for further improvement in docking methodology. We report a hierarchical method that yields results comparable to the industry-leading docking packages GOLD, Glide, and Surflex. By first using a fast, simple, well-established method, UCSF DOCK 4.0, to rigidly dock conformational ensembles, we successfully generate the correct binding mode in all but 4 of a standard, publicly available set of 79 cocrystals from the PDB. Among these 4 failures (1glq, 1tmn, 1rds, and 8gch), all are highly flexible, highly charged, and not druglike. Subsequently, all resultant docking poses were optimized and scored in the protein with molecular mechanics, using a standard MMGB energy function. In total, this hierarchical method identified the correct binding in 71 of 79 cases (90%), an unprecedented level of accuracy on this highly benchmarked test set. Furthermore, the publicly available energy functions employ only physically based force fields without parameter fitting from this or any other docking test sets.

Introduction

A fundamentally important challenge facing any docking algorithm is the ability to generate and identify the native binding mode of a ligand in its protein target, since failure to reliably accomplish this objective necessarily implies greater difficulty in identifying the correct binding mode for other small molecules, as these programs have been designed to do. However, three known issues have precluded levels of redocking accuracy much greater than 70–80%: (i) insufficient sampling of a complex energy landscape, (ii) inaccuracies in the scoring functions, and (iii) uncertainties in the experimental structures themselves. While the third issue cannot be addressed, other than to identify and discard such problematic cases from consideration, the docking community has long understood the first two issues as distinct

from one another and hence worked on ways to address them independently.

In the vast majority of cases, particularly for reasonably sized small molecules, the orientational space for a ligand in a protein is not an intractable problem; only a limited number of low-energy ligand conformers exist at room temperature, and a limited number of poses for each conformer will fit in the protein. In most instances, the total number of sterically permissible poses should be well within the accessible computational time frame of any docking package. Failure to generate the native pose, in most instances, likely stems from an arbitrary limitation on the docking engine resulting from overly restrictive default parameters. In this work, we assess this issue of docking completeness with the earliest, most longstanding of docking methods, UCSF DOCK 4.0,¹ which also is one of the simpler approaches.

In order to address the second issue of scoring accuracy, the docking community has recently drifted away from

* Corresponding author e-mail: mrlee@amgen.com.

energy functions that are entirely physically based, toward empirical scoring functions that involve parameter fitting to reproduce experimental binding energies and/or statistical distributions of atomic interactions in protein–ligand complexes. Like all methods that involve parameter fitting, however, the quality of the results depends on the robustness of the training set. Validations on test sets that do not exhibit significant overlap with the training sets fare worse than validations on test sets possessing greater resemblance to the training sets. One of the potential problems often overlooked is the druglikeness characterization of the training and test sets. In this regard, accurate physically based molecular mechanics energy functions can be applied with a greater level of confidence onto new systems not represented by protein–ligand databases, which have been used for training empirical functions. Historically, one of the major obstacles in using molecular mechanics force fields has been how to account for the solvation energy. Over the past decade, however, advances in the field of continuum solvent models have been made and combined successfully with molecular mechanics energies for accurately reproducing relative binding energies. Perhaps the most popular continuum solvent model has been the Generalized Born approximation which, together with a molecular mechanics energy, gives rise to Molecular Mechanics Generalized Born (MMGB) binding energies. This was first summarized in a review article by Kollman and co-workers² and has been applied successfully over the past couple of years on an increasingly diverse set of molecular recognition cases for accurate binding energy predictions,^{3–11} for virtual screening,¹² and compared alongside other scoring functions for discriminating native from binding site decoy conformations.¹³ However, to date these methods have not been applied explicitly to docking validation studies, in large part due to a perception that reliable implementation of such methods would be computationally prohibitive. In this work, we present a fast, accurate, general hierarchical approach that incorporates an MMGB energy into optimization and scoring procedures as the final stages of a docking process, the culmination of many different attempts on how best to fold these latter methods into the overall docking protocol.

Methods

Test Sets. Over the past decade, a number of papers have assessed the accuracy of different docking methods in correctly predicting the experimental binding mode, with many of these papers using all or part of the publicly available “GOLD benchmark” data set, a total of 134 complexes from the PDB, most of which were curated and reported in 1997 in order to validate GOLD’s effectiveness.¹¹ In 2003, a reduced “81 complex set” was published¹² that removed complexes with more than 15 rotatable bonds, covalent attachments, and obvious errors in structure and that has published data for many other docking methods. With an interest in comparatively assessing the binding mode accuracy of our docking approach with that of others, we also selected this highly benchmarked test set for validation purposes. However, we removed two additional entries: (i) 1lpm, because the ligand menthyl hexyl phosphonate is covalently bound to the gamma oxygen of Ser269 and (ii)

6rsa, because the ligand uridine vanadate contains an unusual vanadium atom, for which the methods in this work lack parameters. We refer to the remaining complexes as the “GOLD 79 set”; note this includes the newer PDB entries of 2ack instead of 1ack and 4aah instead of 3aah.

While the GOLD 79 set spans a diverse range of protein classes and its ligands have a reasonable average of 5 rotatable bonds, the vast majority of these ligands show little resemblance to compounds that would result from a medicinal chemistry effort. Many of them look to be closely related to the endogenous ligands for the protein targets, which are generally of high concentration in vivo and hence low affinity. Among oral drugs, the normal distributions for a number of descriptors that are widely recognized to be important for oral bioavailability have been characterized.¹³ The normal range, defined as the limits spanning two standard deviations from the average, the 5th to 95th percentile, for molecular weight is 164 to 589, and for cLogP –1.9 to 6.3. In contrast, this test set consists of compounds for which 67% are in the normal range of molecular weight range of oral drugs and 70% are in the normal range of cLogP, as summarized in Table 1. In addition, and perhaps more problematic, is that these ligands have an average of 1.5 charged groups, with 36 (46%) having two or more charges and 16 (20%) having three or more charges.

In the interest of assessing accuracy of our docking method on a more pharmaceutically relevant test set, we culled through the PDB database and identified 14 targets with the greatest number of cocrystal entries, all of which are well validated targets of historical interest in the biopharmaceutical industry (Table 5). For these targets, we selected one representative complex from each and created what we refer to as the “PDB recurrent 14 set”. Not surprisingly, 13 of 14 fall within two standard deviations from the average cLogP of oral drugs, and all 14 are within the statistically normal distribution of oral drugs for molecular weight, number of rotatable bonds, and numbers of hydrogen bond donors and acceptors. In addition, these compounds have an average of 0.8 total charges groups, with two (14%) having two or more charges and one (7%) having three or more charges.

Ligand Conformational Ensembles and Ligand Preparation. While the redocking of a ligand’s bound conformation from the native complex has been used to compare accuracies in satisfying a fundamental docking objective of correctly predicting the native binding mode,¹⁴ a more challenging and practical comparison is that of redocking a ligand’s conformational ensemble. Without any a priori knowledge of which small molecule conformer a protein prefers, a truly objective method must consider all low-energy conformers. Using the bound conformer from the native complex does not provide a useful indication for the power of a docking run, because it greatly simplifies the problem by not having to deal with the following known difficulties: (i) comparing the native conformer’s binding energy with that from other ligand conformations that can fit in the active site pocket in dissimilar ways and (ii) characterizing the energy landscape of a ligand and incorporating each conformer’s energy of stability penalty into the scoring function.

Table 1. Properties of the GOLD 79 Set^a

PDB code	MW	cLogP	# rotatable bonds	# H-bond donors	# H-bond acceptors	# + charges	# - charges
1abe	150	-2.2	0	4	5	0	0
1acj	199	3.5	0	2	1	0	1
1ack	166	-2.4	2	1	1	0	1
1acm	255	-3.2	6	1	8	4	0
1aco	174	-1.6	4	0	6	3	0
1aha	135	-0.1	0	2	4	0	0
1atl	339	2.7	9	2	5	1	0
1baf	397	1.9	7	4	8	0	1
1bbp	583	2.7	11	3	8	2	0
1bma	522	7.0	12	3	3	0	1
1cbs	300	6.4	5	0	2	1	0
1cbx	208	1.0	5	0	4	2	0
1com	226	-1.8	4	1	6	2	0
1coy	288	3.1	0	1	2	0	0
1dbb	314	3.8	1	0	2	0	0
1dbj	290	3.6	0	1	2	0	0
1dr1	237	-3.2	2	4	7	0	0
1dwd	523	1.5	9	4	6	0	1
1eap	343	1.5	10	1	6	3	0
1epb	300	6.4	5	0	2	1	0
1etr	509	1.3	10	5	6	1	1
1fen	270	8.2	4	0	0	0	0
1fkg	450	6.3	10	0	4	0	0
1fki	438	5.1	0	0	6	0	0
1frp	336	-3.5	6	3	12	4	0
1glq	443	-1.3	13	3	9	2	1
1hdc	571	6.6	6	0	7	2	0
1hdy	194	1.6	0	1	1	0	0
1hri	309	4.1	9	0	3	0	0
1hsl	156	-2.1	3	2	3	1	1
1hyt	208	1.0	5	0	4	2	0
1lah	134	-1.9	4	2	2	1	2
1lcp	168	-0.5	3	1	3	2	1
1ldm	89	-1.7	1	1	3	1	0
1lic	307	6.2	15	0	3	0	0
1lna	247	-0.7	8	3	3	1	2
1lst	148	-1.3	5	2	2	1	2
1mdr	166	0.8	2	1	3	1	0
1mrg	135	-0.1	0	2	4	0	0
1mrk	267	-1.7	2	5	8	0	0

PDB code	MW	cLogP	# rotatable bonds	# H-bond donors	# H-bond acceptors	# + charges	# - charges
1mrk	267	-1.7	2	5	8	0	0
1nco	661	1.9	8	4	12	0	1
1phg	226	1.5	3	0	3	0	0
1rds	589	-10.5	8	6	16	2	0
1rob	323	-2.5	4	3	10	2	0
1snc	402	-2.9	6	1	11	4	0
1srj	292	4.0	3	1	5	1	0
1stp	244	-0.3	5	2	4	1	0
1tka	424	-0.8	8	5	10	4	1
1tmn	481	3.8	13	3	5	2	1
1tng	114	2.0	1	1	0	0	1
1tni	150	2.4	4	1	0	0	1
1tnl	134	1.5	1	1	0	0	1
1trk	425	-1.4	8	2	11	4	1
1ukz	427	-3.9	6	3	14	4	0
1ulb	151	-1.2	0	3	4	0	0
1wap	205	0.3	3	2	2	0	1
2ada	270	-1.7	2	4	9	0	0
2ak3	347	-3.2	4	3	11	2	0
2cgr	384	4.0	8	2	6	1	0
2cht	228	-1.8	2	1	6	2	0
2cmd	192	-2.4	5	1	7	3	0
2ctc	166	0.5	3	1	3	1	0
2dbl	419	5.0	6	0	5	1	0
2gbp	180	-2.2	1	5	6	0	0
2lgs	148	-2.2	4	1	4	2	1
2phh	138	0.3	1	1	3	1	0
2r07	347	4.1	8	0	3	0	0
2sim	291	-3.1	5	5	8	1	0
3aah	238	-0.9	3	1	9	3	0
3cpa	266	2.7	5	3	5	1	1
3hvt	120	0.8	1	1	4	0	0
3ptb	231	1.1	1	2	0	0	1
3tpi	330	-2.1	6	2	3	1	1
4cts	132	-1.6	3	0	5	2	0
4dfr	454	-1.2	9	3	12	2	0
6abp	150	-2.2	0	4	5	0	0
6rnt	345	-2.4	4	3	11	2	0
7tim	171	-2.6	3	2	6	2	0
8gch	333	-0.5	7	4	4	1	1
AVG	286	0.5	4.7	1.9	5.3	1.1	0.4
Median	267	-0.1	4	2	5	1	0

^a The four DOCK 4.0 failures are highlighted in red (see Table 2).

For the sake of completeness, we sought to create exhaustive conformational ensembles. To this end, we used Amgen's internally developed program FLAME,¹⁵ which uses the OpenEye toolkits¹⁶ OEChem and CASE and incorporates a genetic algorithm to search the torsional space resulting from using discrete 10° dihedral angles for each rotatable bond (36 total angles per torsion). With the exception of hydroxyl groups, dihedral angles that included hydrogen atoms were not considered rotatable during the conformational search. Conformers were discarded if they were either less than 0.2 Å away of an existing member of the ensemble, in terms of root-mean-square deviation of all heavy atom Cartesian coordinates, or 10 kcal/mol above the global energy minimum conformer, according to the MMFF94¹⁷ force field, including the partial atomic charges, with a Sheffield solvation term.¹⁶ In addition, the maximum number of conformers per ligand was set to 200; in cases where less than 200 conformers were generated, the conformational ensemble is considered exhaustive.

Ligands were extracted from the PDB and converted to mol2 format with explicit hydrogens, using the OEChem toolkit,¹⁶ which has the advantages of assigning bond orders and of ionizing basic amines and acids. In each case, the resulting mol2 file was visually inspected to ensure that the bond order was in agreement with its 2D representation on the Brookhaven PDB Web page, with a few rare instances leading to incorrect bond orders; in every instance, the ionization states were in agreement. In a few cases, the ionization state reported in the complex's original reference did not match with this canonical ionization state. Tacrine, the ligand in 1acj, contains a 4-aminoisoquinoline that is considered neutral on both the Brookhaven Web page and by the OEChem toolkit but has experimentally been determined to contain a highly basic nitrogen in the ring,¹⁸ which in turn forms a hydrogen bond with a backbone carbonyl oxygen in the complex. Unexpectedly, L-leucine phosphonic acid, the ligand in 1lcp, reportedly binds with a neutralized phosphate group.¹⁹ Last, the ligand from 4aah, pyrroloquino-

line quinoline, reportedly employs a neutralized carboxylate oxygen (O2A) in order to hydrogen bond with the carboxylate group of Glu55.²⁰

Protein Preparation. To prepare the proteins for redocking, all water molecules, cofactors, counterions, and ligands were stripped from each complex. (As a lone exception, two crystallographic water molecules were kept in 1lna, which are tightly bound to the counterion.) Hydrogen atoms were added and charges were added according to the Cornell et al.²¹ all-atom force field. All histidine residues in direct or indirect contact with the ligands, cofactors, or counterions were visually inspected and assigned the appropriate tautomeric or charged state, based on what appeared to be most energetically favorable in the absence of ligands and cofactors. By default, histidine residues were assigned the tautomeric state in which the delta nitrogen is protonated (HID), modified to the alternative tautomer if the epsilon nitrogen was better served as the lone protonated nitrogen (HIE) or in rare instances assigned the charged state when both nitrogen atoms needed to serve as hydrogen bond donors (HIP) in the absence of ligand and cofactors. Similarly, tyrosine, serine, and threonine residues in close proximity to the active site small molecules were visually inspected to make sure that the dihedral of the hydroxyl group placed the proton in the more appropriate environment. Finally, fully charged residues, such as aspartic acids under physiological conditions, were also carefully inspected to see if two residues with like charges directed the termini of their side chains toward each other. In such cases, we neutralize one of the two residues, as in the case of 1trk, where we used the neutralized form of Glu162. Prior to the docking and optimization, cofactors and counterions in the active site were added back in.

DOCK 4.0. Regardless of which software is used, generating the native pose upon docking an exhaustive conformational ensemble of the native ligand into its cognate protein structure should be a solvable task. If the docking run fails to produce the native pose, this likely reflects a sampling issue, either resulting from an insufficient ligand conformational ensemble or from sampling issues within the docking engine itself, as is the case with the default parameters in DOCK 4.0, where we made changes to a number of the input parameters and added an additional parameter. Perhaps most importantly, we affect the sampling by turning on the bump filter and minimization and have DOCK 4.0 search along a largely shape-based energy function; the intermolecular energy score is turned on, while leaving electrostatics off by setting the electrostatic scale to 0. Ligand orientation is also turned on, and, in order to reduce the probability of insufficiently exploring the entire orientational space, we increase the default of 100 maximum orientations to 50 000 while saving the top 15 minimized orientations in terms of intermolecular energy. The chief sampling parameter for matching, the distance tolerance is also modified from 0.25 to 0.6 to allow for greater variance from the site points. Because there are several very small ligands with less than 10 heavy atoms, the distance minimum parameter is set to 0 in order to allow all pairs of atoms to match. Finally, in order to effect a soft-shell steric overlap

potential to allow for resultant poses that might be more amenable to subsequent optimization into the native state, we leave the vdW scaling factor at the default value of 1 but have modified the source code to allow for a user-specified maximum energy for any atom, which we set at 3 kcal/mol in this work.

With DOCK 4.0, one must generate site points that create an inverse image of the binding site on which each conformer is docked. In this study, the site points were obtained by randomly perturbing the Cartesian coordinates for each heavy atom of the bound conformer, by up to 1 Å in each dimension for up to a total of 1.73 Å, and saving one-third of these resulting coordinates as site points, albeit with a minimum of five points. In our experience, the exact site point positions do not affect docking results significantly for the protocols used in this study. For comparison, we verified this on the PDB Recurrent 14 Set, by using the sphgen accessory that comes with DOCK 4.0 to generate site points, and this had no impact on the quality of docked results in terms of the ability to generate the native binding mode.

Optimization. An approach with growing popularity is to rely on a docking program to generate final poses that are subsequently used for scoring by an energy function which is independent from that which was used to dock the compounds. One of the known limitations of DOCK 4.0 and many other algorithms used for rigid-body docking is the inability to effect the requisite gently relaxation of torsions, angles, and bond lengths in response to the local environment of the protein binding site that distinguishes the bound conformation from any member of its conformational ensemble. (These discrepancies can arise because, while any method for generating conformational ensembles can sample exhaustively over the conformational space resulting from a given number of discrete torsions over each rotatable bond, it cannot sample exhaustively over a continuum of torsions.) Another widespread problem is not accounting for the plasticity of a protein in response to the ligand, although this type of simplification does not present a considerable obstacle on redocking exercises, except in cases where steric clashes and other local inaccuracies in the experimental structures exist. Subsequent to rigid-body docking of a conformational ensemble in the rigid protein and prior to scoring, in order to help address the limited sampling issues discussed above, we subjected each pose that emerged from DOCK 4.0 to a molecular mechanics optimization routine, comparing the effectiveness of several different protocols, varying ligand and protein flexibility.

In the Glide validation paper,²² the authors discuss the importance of relaxing a protein in the presence of its cognate ligand, prior to the redocking exercise, in order to anneal away “untenable steric clashes often found in crystallographically determined protein sites”, to which hard 12–6 Lennard-Jones vdW potentials are extremely sensitive. Like Glide, the methods described in this work also use the hard repulsive potentials in both the optimization and in the scoring. We evaluate our method, by performing the ligand optimization both in the presence of a rigid relaxed protein, analogous to the Glide validation study, and in the presence of the less biased original PDB heavy atom positions that

are flexible during the optimization. All optimizations in this work were carried out with Amber 7,²³ using the Cornell et al.²¹ force field for proteins, the GAFF²⁴ force field for small molecules, and the default continuum solvent implementation, which is described in greater detail below in the following section. In our early implementation of the MMGB optimization method, we observed a number of resultant small molecules with conformations that we deemed unacceptable, particularly for the following functional groups: sulfonamides, phosphates, anilinic nitrogens, amides, nitriles, and alkynes. To correct for these problems, we commented out some of the GAFF parameters and modified a number of others by increasing the force constant to exaggerate preferences for desired small molecule free-state conformations (available in the Supporting Information).

In order to generate a relaxed representation on the protein active site that is subsequently used for ligand optimization in a rigid protein, we first defined a flexible residue list to include amino acids in the original PDB complex that show steric overlap with the native ligand pose and those fully charged amino acids that are in direct contact with the inhibitor. Because both proteins and ligands include explicit hydrogen atoms, we define amino acids in overlap with the ligand as those containing any atom less than 2 Å from any atom of the ligand. Starting with the original PDB complex, these flexible residues were crudely minimized in the presence of the entire complex until a loose convergence criterion of 5.0 kcal/mol·Å for the root-mean-square of the Cartesian elements of the energy gradient (DRMS) was reached. The flexible residues in the complex were then subjected to a 2 ps molecular dynamics simulated annealing schedule from 100 to 400 K over the first picosecond and from 400 K down to 5 K over the second picosecond, followed by a final minimization with a tighter convergence criterion, a DRMS of 0.6 kcal/mol·Å. Ligands were removed, and the resulting protein structure was used for rigid protein optimization of every resulting pose produced by Dock. In the presence of this relaxed protein, each docked pose is crudely minimized restraint-free, while the protein is held frozen, until the DRMS reaches 5.0 kcal/mol·Å. At this point, final optimized poses were created by either (i) restraint-free minimization alone until the DRMS reaches 0.6 kcal/mol·Å or (ii) 2 ps of restraint-free simulated annealing molecular dynamics followed by restraint-free minimization. In total, we ran each docked conformer through two separate rigid protein optimizations.

As an alternative approach to optimizing the docked poses in a rigid relaxed protein, we also optimized them in the original PDB protein conformation, while allowing for plasticity of the protein in response to the ligand, a protocol which we refer to as flexible protein optimization. After placing each pose in the protein, a flexible residue list was determined based solely on the 2 Å distance cutoff designation for steric clashes. These flexible residues then conform to each individual docked pose through crude minimization (DRMS of 5.0 kcal/mol·Å) and 2 ps of simulated annealing molecular dynamics, while keeping the ligand and all other residues frozen. We then add ligand flexibility back into the

system by allowing both ligand and flexible protein residues to respond to each other and move simultaneously through a crude minimization (DRMS of 5.0 kcal/mol·Å), followed by either minimization alone or by simulated annealing molecular dynamics and minimization. During the latter part of the flexible protein optimization, ligand flexibility was run either restraint-free or with a positional restraint of 0.5 kcal/mol·Å on all heavy atoms. In total, we ran each docked conformer through four separate flexible protein optimizations: (1) minimization alone with ligand restraint, (2) minimization alone without ligand restraint, (3) dynamics and minimization with ligand restraint, and (4) dynamics and minimization without ligand restraint. All molecular dynamics simulations were carried out in the presence of an implicit continuum solvent model, which we describe in the next section.

During the validation phase of this approach, we experimented with many alternative optimization protocols, varying the equilibration and relaxation, the simulated annealing schedule, the length of the molecular dynamics production run, and the extent of minimization. We arrived at the protocol described in this work as that which involved the minimum threshold number of CPU cycles necessary to lead to robust optimization of bound poses. Given that the production dynamics run entails only 2 ps of simulation time, the optional molecular dynamics addition adds minimal overhead to this approach (discussed in greater detail below).

MMGB Energy for Scoring. Over the past several years, molecular mechanics, together with continuum solvent representations, have been used to predict binding energies,² according to the following series of equations:

$$\Delta G_{\text{bind}} = (\Delta H_{\text{bind}} + \Delta \Delta G_{\text{solv}}) - T\Delta S \quad (1)$$

$$\Delta H_{\text{bind}} = H_{\text{complex}} - (H_{\text{protein}} + H_{\text{ligand}}) \quad (2)$$

$$\Delta G_{\text{solv}} = \Delta G_{\text{solv,np}} + \Delta G_{\text{solv,polar}} \quad (3)$$

The enthalpy terms of eq 2 are taken from the molecular mechanics energy. For estimating the polar contribution to the free energy of solvation ($\Delta G_{\text{solv,polar}}$), bulk medium can be treated as a continuum solvent, and the generalized Born equation used²⁵ is

$$\Delta G_{\text{elec}} = \sum_{i=1}^N \sum_{j=i+1}^N \frac{q_i q_j}{\epsilon r_{ij}} - \frac{1}{2} \left(1 - \frac{1}{\epsilon}\right) \sum_{i=1}^N \frac{q_i^2}{a_i} \quad (4)$$

where r_{ij} represents the interatomic distance between atoms i and j , and a_i is the effective Born radius for atom i . In its true form, the effective Born radius for a given atom in a system is that which would lead the generalized Born equation to return the correct electrostatic energy of the system when all other atoms are discharged and serve only as an effective dielectric medium between the atom and the solvent.

Still and co-workers subsequently incorporated an approximation to the generalized Born equation into a molecular mechanics equation,²⁶ in which the two terms are

combined into a single expression that is a function of both r_{ij} and a_i :

$$\Delta G_{\text{solv,polar}} = -\frac{1}{2} \left(1 - \frac{1}{\epsilon} \right) \sum_{i=1}^N \sum_{j=i+1}^N \frac{q_i q_j}{f(r_{ij}, a_{ij})} \quad (5a)$$

$$f(r_{ij}, a_{ij}) = \sqrt{(r_{ij}^2 + a_{ij}^2 e^{-D})} \quad (5b)$$

$$a_{ij} = \sqrt{a_i a_j} \quad (5c)$$

$$D = \frac{r_{ij}^2}{(2a_{ij})^2} \quad (5d)$$

For all of our calculations, we used the default generalized Born approximation model²⁷ that comes with AMBER 7.

The nonpolar contribution to solvation includes the cost of creating a solute-sized cavity in solvent and the free energy of inserting the discharged solute into that cavity, which has been found experimentally in hydrocarbons to be linearly related to the solvent accessible surface area (SASA):

$$\Delta G_{\text{solv,nonpol}} = \gamma \cdot \text{SASA} + b \quad (6)$$

The γ coefficient is set to 5.42 cal/mol·Å², and b is set to 920 cal/mol. While we included this nonpolar solvation term in our binding energy calculations, the differences in surface areas between various bound poses of a single ligand are minor and do not have a significant effect on the relative binding energies of different poses. Even when comparing different ligands, this effect is generally insignificant.

In this work, we ignore the ΔS term of eq 1, which is a valid approximation when comparing predicted binding energies among different conformers of the same ligand. This omission, however, can bias toward larger, more flexible ligands when comparing different compounds with largely varying degrees of freedom.

Because our final binding energy score is predominantly a measure of the molecular mechanics enthalpic energy and the generalized Born polar solvation terms, we refer to it as the MMGB energy, which is of the following form

$$\begin{aligned} \Delta G_{\text{bind}} \cong \Delta \text{MMGB}_{\text{bind}} &= \Delta H_{\text{bind}} + \Delta \Delta G_{\text{solv}} = \\ &(E_{\text{MM}} + \Delta G_{\text{solv,GBA}} + \gamma \cdot \text{SASA} + b)_{\text{complex}} - (E_{\text{MM}} + \\ &\Delta G_{\text{solv,GBA}} + \gamma \cdot \text{SASA} + b)_{\text{ligand}} - (E_{\text{MM}} + \Delta G_{\text{solv,GBA}} + \\ &\gamma \cdot \text{SASA} + b)_{\text{protein}} \quad (7) \end{aligned}$$

where E_{MM} is the AMBER molecular mechanics energy resulting from the Cornell et al. force field²¹ for proteins and the GAFF force field²⁴ for small molecules, and $\Delta G_{\text{solv,GBA}}$ is the AMBER implementation of the generalized Born approximation equation.²⁷

Four Different MMGB Optimization and Scoring Protocols. For each system in the test sets, we performed one docking run and passed each of the resultant docked poses into rigid protein optimizations and flexible protein optimizations. Rigid protein optimizations were run restraint free with minimization alone or with molecular dynamics followed by minimization. Because molecular dynamics involves thermal energy, thereby sampling along a free

energy landscape rather than along the enthalpic energy landscape, it populates local minima differently than a minimization alone optimization. As a result, we separate the scoring protocols in accordance to the extent of optimization carried out, with each rigid protein optimization resulting in its own independent score, “MMGB Rigid Min” or “MMGB Rigid MD/Min” in Tables 2–5.

Flexible protein optimizations were also run with minimization alone or with molecular dynamics followed by minimization. However, distinct from the rigid protein optimizations, flexible protein optimizations were run both with and without a positional restraint on the ligand and flexible protein residues, for a total of 4 flexible protein optimizations. One of the potential problems during the dynamics optimization stage is that slightly unfavorable contacts with the protein can drive the ligand out of the binding site, despite its geometric proximity to the native state. For the rigid protein scheme, the relaxation of untenable interactions precluded such problematic contacts from arising during the optimization, but for the flexible protein scheme, ligands were run both with and without the aforementioned 0.5 kcal/mol·Å positional restraints on ligand heavy atoms. This assures that each docked pose can respond to the protein environment resulting from soft-shell docking both restraint free and also with a gentle tether in place. But while the flexible protein optimization with and without positional restraints on the ligand leads to different final optimized poses, they are combined into a single set with MMGB energies compared alongside one another. Thus, the two minimization alone flexible protein optimizations for each docked pose (with and without restraint) are considered together as the “MMGB Flex Min” protocol, and the two molecular dynamics and minimization flexible protein optimizations are considered together as the “MMGB Flex MD/Min” protocol. For all 4 protocols, the final MMGB binding energy is calculated on the final minimized structure in the absence of restraints. The entire process flow of our 4 protocols is summarized in Figure 1.

In addition to the four protocols compared in this work, our implementation of the MMGB optimization and scoring stages allows for even greater user control over how to run the optimization, all from the command line. The user can select specific residues in addition to or in place of those within a specified distance of the ligand’s input pose. Water molecules can be explicitly added and treated as part of the “protein”; when treated as rigid, the hydrogen atoms remain flexible to optimize their positions that are generally not included in the PDB entry. Instead of running molecular dynamics for 2 ps, when greater conformational motion is desired, the user can increase the time frame to the desired level. Side-chain-only motion for flexible residues can be specified. The magnitude of the positional restraint on the inhibitor is also modifiable. Depending on the nature of the problem, we routinely generate models using various permutations of these variables.

Results
Completeness of Conformational Ensembles and Rigid Docking. By imposing an arbitrary limit of 200 maximum conformers per ensemble, we knowingly precluded en-

Table 3. rmsds of Best Scoring Poses^a

PDB code	FlexX	GOLD	Surflex	Glide	UCSF Dock 4.0	MMGB Rigid		MMGB Flex	
						Min	MD/Min	Min	MD/Min
1abe	1.16	0.86	0.27	0.17	3.34	0.46	0.30	0.54	2.69
1acj	0.49	4.00	3.89	0.28	5.31	0.35	0.25	4.75	4.75
1ack	2.21	4.99	1.18	0.97	4.74	1.82	1.42	1.85	0.89
1acm	1.39	0.81	1.43	0.29	5.50	1.03	1.08	1.51	1.04
1aco	0.96	0.86	3.39	1.02	2.43	0.35	0.36	0.68	0.43
1aha	0.56	0.51	0.37	0.11	2.98	0.36	0.41	0.37	0.48
1atl	2.06	1.37	7.01	0.94	3.51	2.55	0.47	0.60	3.51
1baf	8.27	6.12	6.52	0.76	2.10	6.14	6.47	5.72	5.72
1bbp	3.75	8.22	1.07	4.96	8.36	1.55	1.62	4.45	1.58
1bma	13.41	1.03	1.00	9.31	5.05	0.85	0.63	1.73	0.97
1cbs	1.68	2.05	1.77	1.96	1.93	0.42	0.67	2.16	2.82
1cbx	1.35	0.54	0.70	0.36	5.83	1.05	1.04	0.75	7.89
1com	1.62	1.28	0.86	3.64	1.03	1.46	1.78	0.73	3.97
1coy	1.06	0.86	0.54	0.28	7.91	1.27	0.49	0.65	1.14
1dbb	0.81	1.17	0.54	0.41	0.99	0.59	0.85	0.71	1.30
1dbj	1.22	0.72	0.88	0.20	5.99	0.85	0.46	0.78	0.57
1dr1	5.64	1.41	1.25	1.47	5.66	1.53	0.47	1.58	0.71
1dwd	1.66	1.71	1.68	1.32	4.64	0.62	1.34	0.63	0.60
1eap	3.72	3.00	4.89	2.32	5.03	0.88	0.82	1.14	2.17
1epb	2.77	2.08	2.87	1.78	3.17	2.60	1.39	2.68	2.23
1etr	7.24	4.23	4.05	1.48	3.54	0.41	0.69	2.16	2.09
1fen	1.39	1.19	1.18	0.66	0.51	1.32	1.18	0.62	0.49
1fkg	7.59	1.81	1.81	1.25	6.23	1.42	1.99	1.61	1.61
1fki	0.59	0.71	0.70	1.92	0.73	0.51	1.06	0.47	0.41
1frp	1.89	0.66	0.75	0.27	3.85	0.55	0.68	2.49	1.85
1glq	6.43	1.35	5.68	0.29	7.37	1.91	0.52	4.92	2.65
1hdc	11.74	10.49	1.80	0.58	11.05	2.40	1.03	11.14	10.75
1hdy		0.94	0.66	1.74	0.38	1.61	0.52	1.74	1.75
1hri	10.23	14.01	1.98	1.59	2.43	1.65	2.41	1.70	2.33
1hsl	0.59	0.97	0.51	1.31	1.25	1.87	1.13	2.01	1.87
1hyt	1.62	1.10	0.55	0.28	5.45	1.18	1.61	1.17	0.62
1lah	0.28	0.27	0.30	0.13	1.03	0.24	0.23	0.33	0.45
1lcp	1.65	0.98	2.01	1.98	2.48	0.93	1.46	1.32	1.30
1ldm	0.74	1.00	0.44	0.30	5.52	1.35	1.35	1.53	4.70
1lic	5.07	10.78	3.46	4.87	5.03	1.23	1.25	1.33	2.35
1ina	5.40	3.44	0.88	0.95	5.51	1.04	2.56	1.18	5.82
1lst	0.71	0.87	0.33	0.14	1.24	0.67	0.58	0.42	0.68
1mdr	0.88	0.36	0.68	0.52	1.99	1.57	1.58	1.50	1.55
1mrg	0.81	0.57	0.70	0.30	2.96	0.50	0.31	3.03	0.36
1mrk	3.55	1.01	0.85	1.20	3.55	0.84	1.37	2.21	2.75

PDB code	FlexX	GOLD	Surflex	Glide	UCSF Dock 4.0	MMGB Rigid		MMGB Flex	
						Min	MD/Min	Min	MD/Min
1nco	8.26	1.18	8.26	6.99	2.00	10.47	0.64	2.32	1.40
1phg	4.44	1.35	4.44	4.32	1.42	0.40	0.37	0.52	4.93
1rds	9.83	4.78	9.83	3.75	10.46	9.29	2.03	6.11	2.03
1rob	0.82	3.75	0.82	1.85	5.51	0.75	0.51	1.13	2.99
1snc	4.92	2.36	4.92	1.91	4.88	1.25	1.20	1.69	1.75
1srj	0.39	0.42	0.39	0.58	7.01	2.35	0.83	0.67	1.07
1stp	0.51	0.69	0.51	0.59	0.76	0.55	0.53	0.56	0.69
1tka	1.96	1.88	1.96	2.28	1.64	1.69	1.77	1.63	1.51
1tmn	1.30	1.68	1.30	2.80	9.65	3.94	3.48	4.06	2.35
1tng	0.22	0.95	0.22	0.19	3.18	0.65	0.32	0.66	0.26
1tni	2.97	1.98	2.97	2.18	3.68	1.65	2.00	2.54	2.98
1tnl	2.26	0.56	2.26	0.23	4.35	0.65	0.71	1.61	4.42
1trk	1.22	0.76	1.22	1.64	1.08	0.86	1.55	1.63	1.87
1ukz	0.77	2.87	0.77	0.37	1.04	0.46	0.59	1.90	1.12
1ulb	0.77	0.32	0.77	0.28	1.07	0.56	0.63	0.62	0.54
1wap	0.30	0.42	0.30	0.12	0.83	0.30	0.25	0.29	0.31
2ada	0.32	0.40	0.32	0.53	6.13	0.44	0.40	0.59	0.33
2ak3	0.60	5.08	0.60	0.71	3.75	0.91	0.72	0.90	0.68
2cgr	1.63	0.99	1.63	0.38	1.71	0.93	1.38	0.93	4.87
2cht	0.42	0.59	0.42	0.42	1.00	0.70	0.48	0.53	0.56
2cmd	1.60	1.68	1.60	0.65	3.78	0.65	0.48	1.43	3.17
2ctc	0.38	0.32	0.38	1.61	2.78	0.41	0.51	1.81	0.31
2dbl	0.81	1.31	0.81	0.69	1.40	0.97	0.92	1.21	1.48
2gbp	0.63	0.39	0.63	0.15	0.45	0.50	0.31	0.55	0.68
2lgs	1.22	4.41	1.22	7.55	2.62	1.48	1.67	4.53	1.71
2phh	0.44	0.72	0.44	0.38	0.89	0.60	0.59	0.59	0.61
2r07	1.35	8.23	1.35	0.48	1.14	0.99	0.99	1.08	2.91
2sim	1.10	0.92	1.10	0.92	4.34	1.01	1.28	1.01	1.35
3aah	5.93	0.42	0.68	0.30	0.32	0.32	0.33	0.29	0.35
3cpa	2.53	1.58	1.90	2.40	1.46	4.14	8.44	3.66	1.98
3hvt	10.26	1.12	1.64	0.77	0.80	0.82	0.62	0.94	0.98
3ptb	0.55	0.96	0.54	0.27	3.12	0.23	0.35	0.27	0.18
3tpi	1.07	0.80	0.52	0.49	2.09	0.27	0.23	0.46	0.49
4cts	1.53	1.57	2.20	0.19	2.11	0.30	0.30	3.67	3.69
4dfr	1.40	1.44	1.60	1.12	8.56	1.16	0.64	4.31	3.36
6abp	1.12	1.08	0.28	0.40	3.13	2.76	0.28	2.06	3.23
6rnt	4.79	1.20	7.03	2.22	7.15	2.79	1.01	1.78	1.77
7tim	1.49	0.78	1.20	0.14	4.60	0.60	0.47	1.04	0.73
8gch	8.91	0.86	4.51	0.30	4.18	3.57	4.77	3.59	2.96
AVG	2.76	2.06	1.84	1.36	3.59	1.42	1.14	1.80	2.03
Median	1.40	1.11	1.14	0.70	3.15	0.93	0.72	1.38	1.55
n	78	79	79	79	79	79	79	79	79
n (< 2.0)	51	60	60	65	26	67	71	57	49
% (< 2.0)	65%	76%	76%	82%	33%	85%	90%	72%	62%
n (< 2.5)	54	63	63	70	33	70	74	64	55
% (< 2.5)	69%	80%	80%	89%	42%	89%	94%	81%	70%

^a Coloring is the same as in Table 2. In addition, for cases that MMGB scoring failed with the MMGB Rigid MD/Min protocol, their PDB codes are in magenta cells.

sembles of highly flexible molecules from being exhaustive, with the expectation that 200 would still be sufficient in the majority of cases for DOCK 4.0 to find the native binding mode. In the GOLD 79 set, ligands from 64 of the complexes (81%) were exhaustive, as is the case when the FLAME run completes prior to reaching the limit of 200 conformers. Among the 15 ligands where the ensemble was not complete, the 200 representative conformers still provided sufficient coverage of conformational space for DOCK 4.0 to generate the native binding pose in all but two exceptions, thermolysin (1tmn) and ribonuclease Ms (1rds), which contain exceptionally flexible ligands having 13 and 8 rotatable bonds, respectively. In addition, among the 64 exhaustive conformational ensembles, DOCK 4.0 failed to produce the binding pose on two other cases, gamma-chymotrypsin (8gch) and glutathione S-transferase (1glq), which also contain highly flexible ligands with 7 and 13 rotatable bonds, respectively. The structures of these four docking failures are shown in

Figure 2. In total, the rigid docking by DOCK 4.0 of FLAME conformational ensembles described in this work succeeded at the 2 Å rmsd level in 75 of GOLD 79 set cases (95%). One of the key results reported in the validation paper of Surflex¹² is that its failure rate for returning a pose within 2.5 Å was 5/81 cases (6%) and half that of GOLD. By that measure of evaluation, our conventional use of DOCK 4.0, as described in the methods section, demonstrates a 0% failure rate, the two MMGB Min scoring protocols maintained the 0% failure rate, while the two MMGB MD/Min protocols introduced one failure (8gch) for a 1% failure rate (Table 2).

Among the ligands in the PDB recurrent 14 set, all conformational ensembles were exhaustive, and rigid docking succeeded at the 2 Å rmsd level in all cases in finding the native state.

Accuracy of MMGB Optimization and Scoring. While docking methods should be expected to generate the native

Table 2. Lowest rmsds Found in Surflex and Four MMGB Protocols^a

PDB code	Surflex	UCSF Dock 4.0	MMGB Rigid		MMGB Flex	
			Min	MD/Min	Min	MD/Min
1abe	0.18	1.81	0.46	0.30	0.53	0.18
1acj	0.81	0.43	0.28	0.25	0.27	0.29
1ack	0.50	0.82	0.72	1.06	0.76	0.75
1acm	1.35	1.27	0.75	0.64	1.15	0.76
1aco	0.63	0.77	0.34	0.34	0.51	0.32
1aha	0.26	0.69	0.28	0.35	0.30	0.29
1atl	1.05	1.16	0.55	0.47	0.54	0.71
1baf	1.10	1.04	0.69	0.69	0.52	0.80
1bbp	1.06	1.96	0.59	1.09	1.59	1.30
1bma	0.86	1.02	0.83	0.63	0.95	0.77
1cbs	0.52	0.75	0.42	0.40	0.52	0.45
1cbx	0.70	0.75	1.03	1.04	0.75	0.81
1com	0.64	0.94	0.49	0.91	0.64	0.45
1coy	0.32	1.48	1.13	0.36	0.47	0.49
1dbb	0.28	0.89	0.57	0.58	0.71	0.38
1dbj	0.57	1.00	0.81	0.46	0.78	0.57
1dr1	0.29	0.96	0.53	0.36	0.76	0.32
1dwd	0.93	0.74	0.62	0.92	0.63	0.48
1eap	0.92	1.09	0.86	0.59	0.99	0.57
1epb	1.52	1.08	0.82	0.51	0.93	0.72
1etr	3.01	1.57	0.41	0.65	0.49	0.44
1fen	0.79	1.42	0.36	0.38	1.00	0.36
1fkg	1.52	1.35	1.26	0.61	1.26	0.68
1fki	0.64	0.76	0.51	1.06	0.43	0.41
1frp	0.50	0.69	0.52	0.51	0.58	0.58
1glq	3.49	2.07	1.91	0.52	2.04	0.95
1hdc	1.47	1.84	1.60	0.97	1.72	1.26
1hdy	0.41	0.64	0.41	0.44	0.83	0.70
1hri	1.96	1.22	0.92	0.64	1.04	0.91
1hsl	0.35	1.25	0.81	0.27	1.09	0.87
1hyt	0.53	0.79	0.58	0.51	0.54	0.49
1lah	0.25	0.68	0.20	0.21	0.33	0.21
1lcp	0.54	0.61	0.56	0.35	0.45	0.44
1ldm	0.38	1.21	0.86	0.36	1.21	0.92
1lic	2.19	1.00	0.53	0.96	0.62	0.57
1lna	0.60	0.98	0.70	1.60	0.56	1.00
1lst	0.23	0.55	0.29	0.18	0.19	0.18
1mdr	0.45	0.74	0.92	0.87	0.72	0.77
1mrg	0.60	0.76	0.49	0.31	0.65	0.36
1mrk	0.75	0.77	0.84	1.12	0.95	0.90
1nco	6.69	1.89	1.84	0.64	1.87	0.78
1phg	0.41	0.53	0.35	0.36	0.38	0.37
1rds	4.79	2.25	2.34	1.23	2.29	1.24
1rob	0.56	0.67	0.50	0.44	0.56	0.31
1snc	2.44	1.36	1.25	1.10	1.43	1.10
1srj	0.35	0.61	0.44	0.57	0.55	0.52
1stp	0.46	0.70	0.30	0.33	0.43	0.28
1tka	1.49	1.12	0.90	1.36	0.87	0.51
1tmn	0.65	2.24	2.14	1.21	2.17	0.98
1tng	0.20	0.78	0.44	0.23	0.66	0.26
1tni	1.33	0.83	0.70	0.96	0.70	0.76
1tnl	0.23	0.66	0.58	0.42	0.59	0.50
1trk	0.78	1.00	0.51	0.43	0.76	0.50
1ukz	0.25	1.01	0.42	0.54	0.78	0.52
1ulb	0.58	0.75	0.56	0.33	0.50	0.54
1wap	0.24	0.46	0.29	0.24	0.29	0.23
2ada	0.29	0.82	0.44	0.34	0.39	0.32
2ak3	0.58	0.65	0.37	0.58	0.50	0.47
2cgr	0.89	0.71	0.77	0.77	0.86	0.72
2cht	0.42	0.55	0.49	0.45	0.45	0.49
2cmd	1.49	0.74	0.65	0.47	0.70	1.02
2ctc	0.32	1.19	0.41	0.31	0.95	0.31
2dbl	0.66	0.93	0.89	0.67	0.90	0.61
2gbp	0.27	0.45	0.50	0.27	0.45	0.31
2lgs	0.79	1.69	1.30	1.36	1.24	1.19
2phh	0.41	0.48	0.45	0.47	0.47	0.43
2r07	1.09	0.65	0.57	0.57	0.61	0.64
2sim	0.35	0.46	0.36	0.42	0.38	0.24
3aah	0.33	0.32	0.27	0.31	0.26	0.26
3cpa	0.66	1.02	0.57	0.58	0.62	0.55
3hvt	1.61	0.38	0.31	0.28	0.36	0.33
3ptb	0.37	0.67	0.21	0.21	0.27	0.18
3tpi	0.37	0.36	0.27	0.21	0.37	0.49
4cts	0.53	1.37	0.30	0.29	1.16	0.38
4dfr	1.24	1.53	1.00	0.58	1.41	1.25
6abp	0.14	1.56	1.52	0.28	1.54	0.24
6rnt	4.68	1.72	1.61	0.80	1.66	1.13
7tim	0.34	0.90	0.50	0.38	0.48	0.60
8gch	0.96	2.35	2.45	2.53	2.38	2.85
AVG	0.95	1.01	0.72	0.61	0.81	0.62
Median	0.60	0.86	0.57	0.51	0.66	0.52
n	79	79	79	79	79	79
n (< 2.0)	72	75	76	78	75	78
% (< 2.0)	91%	95%	96%	99%	95%	99%
n (< 2.5)	74	79	79	78	79	78
% (< 2.5)	94%	100%	100%	99%	100%	99%

^a The four cases that DOCK 4.0 failed to have their PDB codes highlighted in red. In the table body, rmsd values exceeding 3.0 Å are in red cells; those that are less than 2.0 Å are considered correct and are in cyan cells.

pose in the vast majority if not all cases, the more challenging problem of identifying the native pose as the most energetically favorable is considerably more formidable and can depend heavily on how one handles characterization of the protein. FlexX, GOLD, Surflex, and the MMGB Flex protocols make no modifications to the original PDB coordinates, while Glide and the MMGB Rigid protocols relax steric overlaps and other unfavorable geometries of the protein in the presence of the native ligand pose found in the PDB entry. Not surprisingly, protocols which reorganize the protein around the native ligand pose perform significantly better. Table 3 summarizes and compares the results of our 4 different MMGB scoring protocols with DOCK 4.0 itself, and the literature results that have been reported for FlexX, Gold, Surflex, and Glide.

Two key findings reported in the Glide validation paper are that (1) the top scoring poses by Glide exceeded the 2 Å rmsd at a significantly lower rate than that of FlexX, Gold,

and Surflex and that (2) Glide results in a lower average rmsd than the other methods. While Glide prepares the protein sites by performing a series of restrained minimizations on the entire protein–ligand complex, with a 10 kcal/mol·Å² positional restraint on all heavy atoms, we relax only those residues within 2 Å of the inhibitor and other charged residues which are in direct contact with the inhibitor. On the GOLD 79 set, Glide reports failure at the 2 Å level on 14 cases²² (18%), while the closely related MMGB Rigid Min protocol fails on 12 cases (15%) and the MMGB Rigid MD/Min protocol fails on only 8 cases (10%). In terms of rmsd for the top scoring poses, an average of 1.36 Å is accomplished by Glide, 1.42 Å for the MMGB Rigid Min protocol, and 1.15 Å for the MMGB Rigid MD/Min protocol (Table 3). As Glide only minimizes the ligand in the presence of the rigid relaxed protein, it is not surprising that its results are essentially equivalent to that of the MMGB Rigid Min protocol. In contrast, the greater sampling afforded by

Table 4. Effect of Including Poses within 3 kcal/mol of the MMGB Global Minimum^a

PDB code	MMGB Rigid						MMGB Flex					
	Min			MD/Min			Min			MD/Min		
	lowest MMGB	lowest RMSD within 3 kcal/mol	# binding modes within 3 kcal/mol	lowest MMGB	lowest RMSD within 3 kcal/mol	# binding modes within 3 kcal/mol	lowest MMGB	lowest RMSD within 3 kcal/mol	# binding modes within 3 kcal/mol	lowest MMGB	lowest RMSD within 3 kcal/mol	# binding modes within 3 kcal/mol
AVG	1.42	1.16	1.2	1.15	0.91	1.3	1.80	1.53	1.4	2.03	1.49	1.7
Median	0.93	0.80	1	0.72	0.63	1	1.38	1.14	1	1.55	1.02	1
n	79	79	79	79	79	79	79	79	79	79	79	79
n (< 2.0)	67	71	68	71	75	60	57	63	58	49	63	51
% (< 2.0)	85%	90%	86%	90%	95%	76%	72%	80%	73%	62%	80%	65%
n (< 2.5)	70	73		73	76		64	67		55	68	
% (< 2.5)	89%	92%		92%	96%		81%	85%		70%	86%	

^a Binding modes are considered new and distinct when they are more than 2 Å rmsd away from any other pose in an existing binding mode. As greater flexibility is incorporated during the optimization, more binding modes emerge within 3 kcal/mol of the global MMGB energy minimum.

molecular dynamics leads to a marked improvement in both the failure rate at the 2 Å rmsd level and in the average rmsd of the lowest energy poses.

While comparing the single pose of the lowest MMGB energy with the native pose is unequivocally objective, when using this method in support of lead optimization, we share not only the model of the absolute global MMGB minimum but also other binding modes residing within a reasonably small yet somewhat arbitrary range above the global minimum. Among a set of bound poses, one can define unique binding modes by first calculating the pairwise heavy atom rmsds and then requiring that no two members within a single binding mode (conformational family) be within a certain arbitrary rmsd distance apart. Using a 2 Å rmsd cutoff, we find that the majority of the test cases (ranging from 65–86% as shown in Table 4) result in a single binding mode for all poses within 3 kcal/mol of the global MMGB minimum, regardless of which MMGB optimization and scoring protocol we employ. Not surprisingly, as more flexibility is added into the system, the average number of discrete binding modes within 3 kcal/mol of the global minimum increases, and the number of cases with a single binding mode decreases accordingly, as seen in Table 4, reading from left to right. Accounting for protein flexibility as well as the use of molecular dynamics during optimization both lead to greater binding mode diversity within 3 kcal/mol of the global minimum. When taking into account additional binding modes within a 3 kcal/mol cutoff on the GOLD 79 set, we find that the MMGB Rigid Min failure rate improves from 15% to 10%, while that of the MMGB Rigid MD/Min failure rate improves from 10% to 5%.

When assessing closely related analogs of a single series, for which one member has been cocrystallized, the use of the MMGB Rigid protocols may be appropriate. However, optimization of the protein around the ligand introduces bias toward the correct answer in accordance with preferences of the force field that is used for the protein relaxation. Moreover, this treatment can lead to greater difficulty when attempting to dock more distantly related analogues. Our main goal at the onset of implementing this MMGB optimization/scoring stage was to allow for protein residues

to respond on-the-fly to the presence of each ligand's docked poses. While the option to rigidify the protein leads to unparalleled results in docking accuracy, the freedom to allow for dynamic protein flexibility has proven more useful in our work, albeit less accurate, when attempting to dock ligands disparate from the cognate one (data not presented). Encouragingly, when comparing the MMGB flexible protein optimization protocols to that of the other popular docking methods which use the original PDB coordinates, we find comparable accuracy. While FlexX, GOLD, and Surflex report failure rates at the 2 Å level of 35%, 24%, and 24% for the best scoring poses, respectively, the MMGB Flex Min protocol fails at a rate of 28%, and the MMGB Flex MD/Min fails at a rate of 37% (Table 3). When also considering conformers within 3 kcal/mol of the global minimum, these rates drop to 20% for both MMGB protocols (Table 4). When comparing the average rmsd for the poses with the best scores, those from the MMGB flexible protein protocols are highly similar to those from GOLD and Surflex.

While the MMGB Flex approach performs favorably on the nondruglike GOLD 79 set, Table 5 illustrates that it performs just as well on the pharmaceutically relevant PDB recurrent 14 set. Interestingly, while the Min outperformed the MD/Min optimization on the GOLD 79 set, we find little difference between the two optimization schedules on this more well-behaved test set; both fail at the 2 Å level on 4 of the 14 cases (29%), with lowj as the single failure in common, and the average rmsds for the lowest energy MMGB poses are 1.5 Å and 1.4 Å. One aspect, that the two optimization routines show some disparity in, is the quality of conformers within 3 kcal/mol of the global MMGB minimum, where the added molecular dynamics lead to a marked improvement. While taking these additional bound poses into consideration leads to better docking accuracy in both cases, decreasing the number of failures from 4 down to two (Min) and to one (MD/Min), the average rmsd of the best conformers drops considerably more in the MD/Min protocol from 1.52 Å to 0.86 Å (the mean improves from 1.43 Å to 0.49 Å).

While we ran the two MMGB Rigid protocols on the GOLD 79 set in order to run our approach in a manner comparable to that reported by Glide, we ran only the more unbiased MMGB Flex protocols on PDB recurrent 14 set. In the same way, we routinely generate models for medicinal chemistry compounds by using the MMGB protocols on original PDB coordinates, without relaxing them around the cognate ligand.

Limitations and Sources of Failure. In order to better understand the limitations of this approach, we attempt to identify the sources of failures. As alluded to above, DOCK 4.0 failed to generate a pose within 2 Å rmsd of the native pose in 4 cases. In one (1glq) of those four DOCK 4.0 failures, MMGB Rigid optimization successfully drew a non-native starting pose to the native state and scored it with the most favorable MMGB energy. In the other three cases, all of the docked poses were beyond the radius of convergence of our optimization routines. Among the remaining 75 in the GOLD 79 set, the most successful protocol, MMGB Rigid MD/Min, failed on 5 additional cases (7%) due to unambiguous scoring problems with MMGB: 1baf, 1lhr,

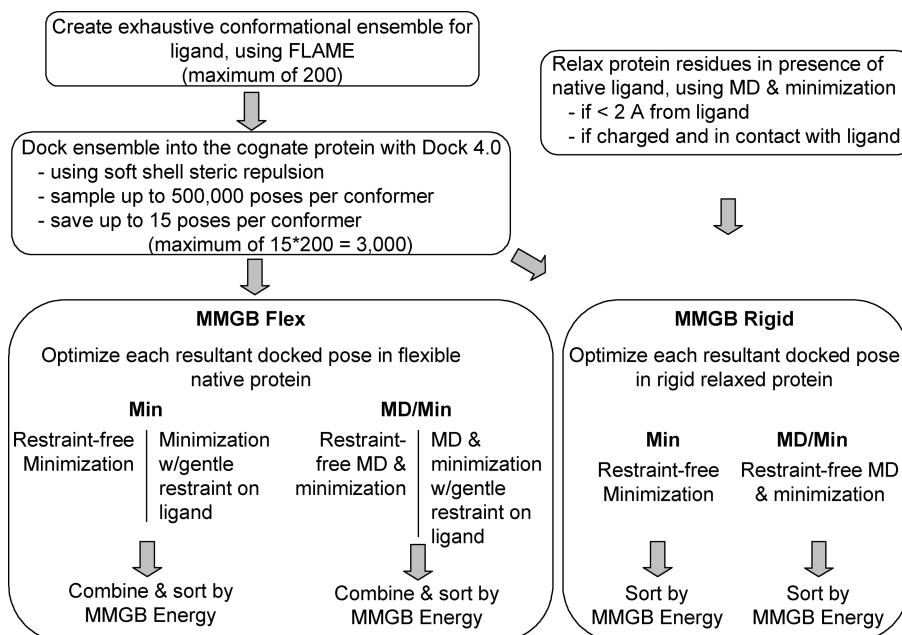


Figure 1. Process flow of the hierarchical dock/optimization/MMGB protocol. A total of 4 different MMGB optimization and scoring protocols were compared. When using a flexible protein, incoming poses for each of the two protocols were optimized both with and without restraints, and resultant poses were combined into a single protocol-specific pool and sorted according to their MMGB energies which are calculated in each of the 4 protocols on the final minimized snapshot in the absence of restraints.

Table 5. MMGB Flex Results on the PDB Recurrent 14 Set^a

PDB code	MW	cLogP	# rot. bonds	# H-bond don.	# H-bond acc.	# - charges	# + charges	Protein	UCSF Dock 4.0		MMGB Flex					
									best RMSD	best score	best RMSD	lowest MMGB	lowest RMSD within 3 kcal/mol	best RMSD	lowest MMGB	best RMSD within 3 kcal/mol of top
1c88	271	-0.8	3	2	5	2	1	Tyrosine Phosphatase 1B	0.36	0.43	0.20	0.38	0.38	0.21	0.32	0.32
1df8	244	-0.3	5	2	4	1	0	Streptavidin	0.46	2.46	0.35	0.37	0.35	0.21	0.38	0.38
1iqm	462	4.7	6	1	4	0	1	Coagulation Factor XA	0.88	9.11	0.82	1.84	1.22	0.58	2.00	1.21
1ke7	393	0.6	3	2	5	0	0	CDK2	1.71	4.91	1.70	5.24	5.24	1.54	1.98	1.54
1o2r	382	4.2	4	4	3	0	0	Beta-Trypsin	0.57	9.43	0.37	1.84	1.25	0.24	1.54	0.34
1oq5	381	4.4	4	1	3	0	0	Carbonic Anhydrase II	0.61	5.43	0.46	0.50	0.46	0.41	2.83	2.72
1owj	384	3.5	4	3	2	0	0	Urokinase-type Plasminogen Activator	1.39	1.55	1.29	2.96	1.56	0.69	3.63	1.96
1rt4	336	4.9	6	1	2	0	0	HIV-1 Rev Transcriptase	0.74	0.92	0.63	0.74	0.74	0.23	0.62	0.23
1sj0	465	6.3	6	3	5	0	1	Estrogen Receptor	1.01	2.57	0.87	2.54	0.91	0.42	1.32	0.85
1vcj	350	1.5	8	3	5	1	1	Neuraminidase	0.65	1.00	0.46	0.88	0.88	0.47	1.73	0.47
1x70	408	0.7	5	1	3	0	1	Dipeptidyl Peptidase IV	0.77	2.05	0.60	1.56	1.56	0.35	1.18	0.50
1xoq	403	3.0	7	1	4	0	0	cAMP-specific 3',5' cyclic PDE4d	0.48	1.27	0.40	0.45	0.40	0.35	0.61	0.38
1yc1	368	1.9	4	3	7	1	0	HSP90-alpha	1.38	2.56	1.16	2.45	2.45	0.67	0.71	0.71
7upj	480	6.4	6	2	5	0	0	HIV-1 Protease	1.34	3.61	1.21	1.49	1.49	0.48	2.42	0.48
	381	2.9	5.1	2.1	4.1	0.4	0.4	AVG	0.88	3.38	0.75	1.66	1.35	0.49	1.52	0.86
	383	3.2	5	2	4	0	0	Median	0.76	2.51	0.62	1.53	1.07	0.42	1.43	0.49
	14	14	14	14	14	14	14	n	14	14	14	14	14	14	14	14
								n (< 2.0)	14	5	14	10	12	14	10	13
								% (< 2.0)	100%	36%	100%	71%	86%	100%	71%	93%

^a Among this smaller, pharmaceutically relevant test set, MMGB Flex protocols share only one failure in common when considering the lowest MMGB energy, 1owj. The correct binding mode is present within 3 kcal/mol of the global minimum for both protocols.

1lna, 1tni, and 3cpa, which are illustrated in Figure 3. Encouragingly, among four of these five MMGB scoring failures, at least one of the other MMGB protocols succeeded in correctly identifying the binding mode.

In 1baf, the native pose of the hapten ligand for the murine monoclonal antibody AN02 fails to rank as best with any of

the MMGB optimization/scoring protocols. While the crystallographic structure stacks the hydrophobic center of the ligand's piperidin-1-ol functional group against the protein's negatively charged carboxylate oxygen atom from Asp49, the MMGB energy prefers a bound orientation in which the ligand maintains the same general shape by flipping the

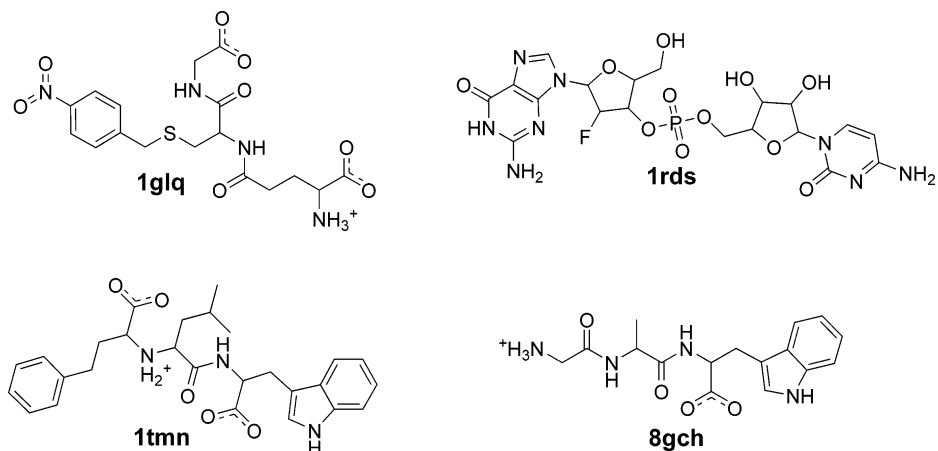


Figure 2. Structures of 4 docking failures from the GOLD 79 set. The four cases from the GOLD 79 set that DOCK 4.0 failed to generate the native pose for are all highly flexible. Conformational ensembles for 1rds and 1tmn did not run exhaustively within the arbitrary limit of 200 maximum conformers per small molecule.

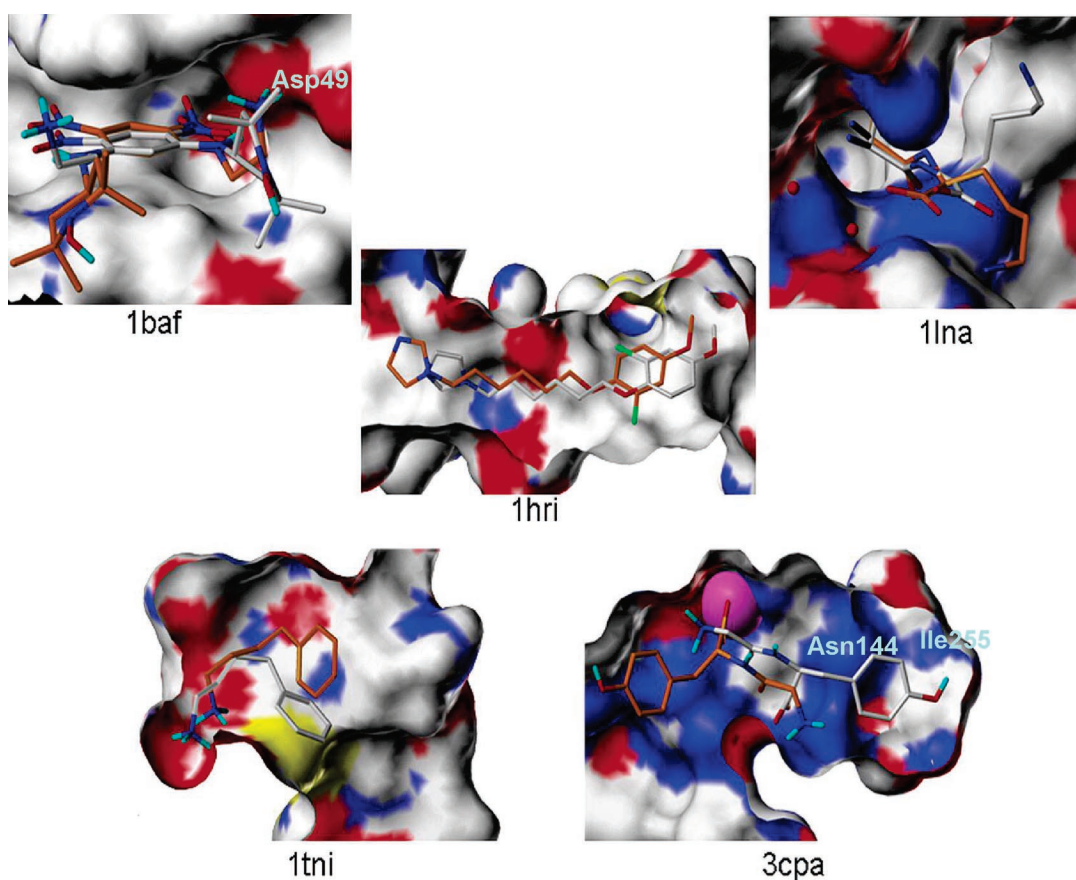


Figure 3. Five MMGB scoring failures. Solvent accessible surfaces are shown for the five MMGB scoring failures from the MMGB Rigid MD/Min protocol with both the native crystallographic binding mode of the ligand, colored in white, and for the pose at the global MMGB binding energy minimum, colored in orange. 1baf and 1lna have shallow binding pockets and open to bulk solvent, whereas with 1lri, 1tni, and 3cpa, surface cutouts are rendered in order to better illustrate the binding modes. The magenta sphere in 3cpa is the tightly bound zinc counterion.

dinitrobenzene 180° and satisfying Asp49 with an ionic interaction involving its positively charged basic ethyl amine. By analyzing the various components of the MMGB energy, we find that the crystallographic binding mode exhibits a largely positive (repulsive) electrostatic interaction energy, which agrees with the intuitive response one would have upon visual inspection of this binding mode. Important to note, however, is that the docking approach does find the

crystallographic binding mode for the hapten and assigns a net negative (favorable) binding energy, despite the positive electrostatics term. When given a choice between satisfying a protein side-chain carboxylate with a charged group of opposite sign or an aromatic ring, MMGB and all physically based energy functions as well as most knowledge-based scoring functions will prefer the former, although knowledge-based methods may be able to dampen this effect

out more. Thus, it is not surprising that most docking methods had problems with this target. As we occasionally find in cases such as 1baf, some crystallographic structures seem to go against the grain of a conventional understanding. In these rare instances, physically based energy functions will invariably fail to properly rank order the native state as best unless artificial tricks are implemented.

In two of the MMGB scoring failures, 1lna and 1tni, MMGB favors poses that differ from the crystallographic structures only in the positioning of highly flexible groups directed out toward the solvent front. It is not surprising that MMGB scoring fails on cases like these, where the native ligand pose only partially occupies a wide pocket and there are few stabilizing interactions from the protein on the highly flexible ligand side chain. In a somewhat related scoring failure, MMGB prefers a pose for 1hri that is a rigid body translation of the native pose in a loose cylindrically shaped binding pocket, with a long aliphatic chain spanning the bulk of the long axis. In terms of lead optimization, the MMGB-preferred poses for these three cases are roughly correct, showing accurate geometries for the anchoring regions of the ligands in the binding sites, with binding modes that would be sufficient to generate new ideas for improving potency.

The fifth MMGB scoring failure comes from 3cpa, a highly charged system in which the native pose places a neutralized basic amine in contact with a zinc counterion, while also desolvating the amide NH₂ of the Asn144 side chain and the backbone NH of Ile255 with a hydrophobic edge of the ligand's ethylphenol. MMGB prefers a pose in which the ligand's carboxylate group satisfies the positively charged zinc counterion and the polar pocket, lined by Asn144 and Ile255, is left unfilled by the ligand and thereby blocked from bulk solvent.

Computational Cost of Optimization and Scoring. With our arbitrary limits of 200 maximum conformers per ensemble and 15 poses saved per conformer, any given complex will pass on a maximum of 3000 poses to the optimization and scoring phase (Figure 1), which for a typical system consumes roughly 3–10 min of CPU-time per pose on an Intel Pentium III 1 GHz processor. Thus, on a standard MMGB Flex run, where we employ 200 CPU's from our Pentium III Linux cluster, each optimization protocol takes at most 3 h of wall-clock time per system (for both Flex Min and Flex MD/Min); simpler runs such as the MMGB Rigid ones take at most 1 h of wall-clock timer per system. While a detailed description is not within the scope of this work, we also use the flexible protein MMGB optimization and scoring protocol as a follow-up for database virtual screens, typically evaluating 50 000 to 100 000 docked poses in an overnight run on our cluster.

Discussion

Performance on GOLD 79 Set Does Not Necessarily Carry Over to a More Druglike Test Set. While the compounds in the PDB recurrent 14 set have properties consistent with those that we model on a regular basis in support of drug discovery projects, the GOLD 79 set shows little similarity. Because the energy functions in our general approach were never trained on protein–ligand complexes,

they are insensitive to the disparity between the druglike PDB recurrent 14 set and the nondruglike GOLD 79 set. This can be seen in the comparable docking accuracy performance of the unbiased flexible protein among the two sets. In contrast, virtually all the scoring functions that are currently implemented in docking suites have been largely trained to perform well on test sets that show high similarity to and overlap with the GOLD 79 set. Unfortunately, there is not a pharmaceutically relevant test set that has been well benchmarked, and the transferability of high accuracy for empirical and knowledge-based scoring functions to test sets consisting of only druglike compounds remains to be seen.

Increasing Protein Flexibility during Optimization Extends Radius of Convergence, While Decreasing Accuracy of Scoring. With our implementation of the MMGB optimization, the degree of protein flexibility can be fine-tuned to appropriately take into account the nature of problem. In some instances, where medicinal chemists seek to probe the space of a deep, well-defined pocket, Rigid MMGB Min has functioned best and provided excellent agreement with experimental structure–activity relationships (data not presented). While Tables 3–5 indicate that added protein flexibility tends, in general, to decrease overall docking accuracy for redocking exercises, in general by introducing more false positives, certain instances clearly benefit from the added sampling afforded by the use of molecular dynamics during the optimization. On the druglike targets in Table 5, three of the four minimization alone failures were successful with the Flex MD/Min protocol. In many internal drug discovery projects, we have applied the MMGB Flex MD/Min protocol to a chemical series very different from one for which the cocrystal has been solved. In some instances, we predicted new binding modes, which were verified as correct by subsequent crystallographic structures and were made possible only after substantial movement of the protein, which the MMGB optimization captured. For lead optimization, we often use FLAME¹⁵ to align new compounds against the native pose from a lead compound's cocrystal and then rely on the MMGB Flex MD/Min to tell us which compounds align well and fit without any protein movement of the existing protein crystal structure, which compounds align with poses having steric clashes with the protein that can be annealed away on-the-fly, and which compounds lead only to poses with insurmountable overlap with the protein or otherwise unfavorable MMGB binding energies. Increasing protein flexibility during the optimization phase increases the power at the expense of some accuracy.

Sources of Greater Uncertainty in the MMGB Scoring: Highly Charged Systems and Trapped Solvent Pockets. MMGB has difficulty with highly charged systems, particularly those in which the noncharged regions show loose fitting. The correct balance between desolvation of protein and ligand with that of the interaction energy is hard to achieve. Also, we find that MMGB scoring does not sufficiently penalize buried channels or pockets that are sufficiently large enough for water molecules, as is the case in 3cpa. While our discussion above of MMGB scoring failures focused only on those from the MMGB Rigid MD/

Min protocol, Tables 2 and 3 indicate that additional MMGB scoring failures arose during the MMGB Flex protocols where some alternate low-energy binding modes emerge as more favorable, as was often the case on highly charged systems and other instances, in which the lowest energy binding mode buried a water pocket. A recent advance in the Generalized Born solvation model that corrects the molecular volume³¹ by using the molecular surface as opposed to the van der Waals surface may help to alleviate some of this error.

An important consequence of protein relaxation is the repositioning of amino acids in accordance with the preferences of the force field, a change that can have a profound effect on the local position of fully charged residues in a highly charged complex, which can be significant despite a small rmsd between all of the protein's relaxed and original non-hydrogen atoms of 0.3 Å or less. While the elimination of troublesome steric clashes can be required for favorable dispersion contact energies of properly docked conformers, any relaxation of the protein active site can introduce bias toward the shape of the native ligand state in accordance with the energy function used to optimize the protein, particularly for highly charged complexes.

Important Points To Consider When Incorporating MMGB into the Docking Process. While the methods described are general and should work, in principle, with any robust physically based energy function and implicit solvent model, the way that these physically based energy functions are implemented is important. The protocols we report in this paper are the result of significant trial and error. In particular, the most important consideration is keeping the vast majority of the protein fixed during the optimization. This serves to reduce the noise, particularly those regions not comprising the binding site. Otherwise, the thermal fluctuation of an entire protein introduces error bars with magnitudes that dwarf the magnitude of the binding energies, thereby making it too difficult to detect the signal among the noise. This approximation of keeping the protein largely rigid naturally does not account for differing degrees of protein distortion when comparing MMGB energies from different binding modes, thereby leading to larger error bars when comparing ligands that bind very differently to the same protein and when comparing MMGB binding energies of different proteins. Alternatively stated, the MMGB energies in this work are not useful for comparing relative binding energies between different proteins or between very different conformations of a single protein. Another important consideration is a final minimization following any molecular dynamics run to a given gradient, so that local minima are compared, instead of relying on the approximation that all systems will reach the bottom of their energy wells in a fixed number of minimization steps or relying on the more egregious approximation that minimization need not be run at all. Given that the depth of an energy well on a molecular dynamics free energy landscape is exceedingly greater than relative differences in binding energies between different poses, one would have to adequately sample a given energy well and capture a sufficient number of snapshots to make a Boltzmann-weighted average well represented. This would

presumably entail molecular dynamics simulations significantly longer than the 2 ps used in this work. We instead make the approximation that most energy wells are deep and hence have Boltzmann-weighted averages that are dominated by energies at the bottom of the well, which we capture through simple minimizations. The advantage of our approximation is higher throughput and applicability to virtual screening in a reasonable time frame.

The approach in this work is not tied to DOCK for the generation of poses. Most of the popular docking packages should be capable of exhaustive runs that consistently generate the native pose in a maximum of a few CPU hours, as DOCK 4 was able to in this work, despite its reported inability to do effectively while using the default parameters³² for nonexhaustive runs. The optimization aspect of this approach with user control over protein flexibility at a contact distance and/or residue level does add more computer time but provides features not available with other methods. While the optimization and scoring may require orders of magnitude more total CPU time, given the ubiquity and cost-effectiveness of Linux-based clusters, the added value of MMGB optimization and scoring requires less than a few hours of wall-clock time. When the goal is to predict the binding mode as accurately as possible, sacrificing a few hours on a Linux cluster as opposed to a few hours on a single machine is a small sacrifice, particularly when this allows for protein flexibility and use of a reliable physically-based scoring function.

Summary

With recent advances in the field of continuum solvent models, we explored the idea of incorporating a purely physically based MMGB energy into the docking process not only that can lead to unparalleled levels of success in redocking accuracy but also that can be run with varying degrees of protein and/or ligand flexibility during an optimization stage. This, in turn, makes for a robust hierarchical docking approach which satisfies a gamut of docking problems faced during the lead identification to lead optimization stages of drug discovery.

Supporting Information Available: Changes made to the GAFF parameters to exaggerate preferences for more suitable small molecule conformations. This material is available free of charge via the Internet at <http://pubs.acs.org>.

References

- (1) Ewing, T. J. A.; Makino, S.; Skillman, A. G.; Kuntz, I. D. DOCK 4.0: Search strategies for automated molecular docking of flexible molecule databases. *J. Comput.-Aided Mol. Des.* **2001**, *15* (5), 411–428.
- (2) Kollman, P. A.; Massova, I.; Reyes, C.; Kuhn, B.; Huo, S. H.; Chong, L.; Lee, M.; Lee, T.; Duan, Y.; Wang, W.; Donini, O.; Cieplak, P.; Srinivasan, J.; Case, D. A.; Cheatham, T. E. Calculating structures and free energies of complex molecules: Combining molecular mechanics and continuum models. *Acc. Chem. Res.* **2000**, *33* (12), 889–897.
- (3) Adekoya, O. A.; Willassen, N. P.; Sylte, I. Molecular insight into pseudolysin inhibition using the MM-PBSA and LIE methods. *J. Struct. Biol.* **2006**, *153* (2), 129–144.

- (4) Coi, A.; Tonelli, M.; Ganadu, M. L.; Bianucci, A. M. Binding free energy calculations of adenosine deaminase inhibitors. *Bioorg. Med. Chem.* **2006**, *14* (8), 2636–2641.
- (5) Luo, C.; Xu, L. F.; Zheng, S. X.; Luo, Z.; Jiang, X. M.; Shen, J. H.; Jiang, H. L.; Liu, X. F.; Zhou, M. D. Computational analysis of molecular basis of 1 : 1 interactions of NRG-1 beta wild-type and variants with ErbB3 and ErbB4. *Proteins, Struct., Funct., Bioinformatics* **2005**, *59* (4), 742–756.
- (6) Mamolo, M. G.; Zampieri, D.; Vio, L.; Ferraglia, M.; Ferrone, M.; Pricl, S.; Scialino, G.; Banfi, E. Antimycobacterial activity of new 3-substituted 5-(pyridin-4-yl)-3H-1,3,4-oxadiazol-2-one and 2-thione derivatives. Preliminary molecular modeling investigations. *Bioorg. Med. Chem.* **2005**, *13* (11), 3797–3809.
- (7) Murray, J. B.; Meroueh, S. O.; Russell, R. J. M.; Lentzen, G.; Haddad, J.; Mobashery, S. Interactions of designer antibiotics and the bacterial ribosomal aminoacyl-tRNA site. *Chem. Biol.* **2006**, *13* (2), 129–138.
- (8) Nunez-Aguero, C. J.; Escobar-Llanos, C. M.; Diaz, D.; Jaime, C.; Garduno-Juarez, R. Chiral discrimination of ibuprofen isomers in beta-cyclodextrin inclusion complexes: experimental (NMR) and theoretical (MD, MM/GBSA) studies. *Tetrahedron* **2006**, *62* (17), 4162–4172.
- (9) Villacanas, O.; Rubio-Martinez, J. Reducing CDK4/6–p16-(INK4a) interface: Computational alanine scanning of a peptide bound to CDK6 protein. *Proteins, Struct., Funct., Bioinformatics* **2006**, *63* (4), 797–810.
- (10) Xu, Y.; Wang, R. X. A computational analysis of the binding affinities of FKBP12 inhibitors using the MM-PB/SA method. *Proteins, Struct., Funct., Bioinformatics* **2006**, *64* (4), 1058–1068.
- (11) Lyne, P. D.; Lamb, M. L.; Saeh, J. C. Accurate prediction of the relative potencies of members of a series of kinase inhibitors using molecular docking and MM-GBSA scoring. *J. Med. Chem.* **2006**, *49* (16), 4805–4808.
- (12) Huang, N.; Kalyanaraman, C.; Bernacki, K.; Jacobson, M. P. Molecular mechanics methods for predicting protein-ligand binding. *Phys. Chem. Chem. Phys.* **2006**, *8* (44), 5166–5177.
- (13) Ferrara, P.; Gohlke, H.; Price, D. J.; Klebe, G.; Brooks, C. L. Assessing Scoring Functions for Protein-Ligand Interactions. *J. Med. Chem.* **2004**, *47* (12), 3032–3047.
- (14) Jones, G.; Willett, P.; Glen, R. C.; Leach, A. R.; Taylor, R. Development and validation of a genetic algorithm for flexible docking. *J. Mol. Biol.* **1997**, *267* (3), 727–748.
- (15) Jain, A. N. Surflex: fully automatic flexible molecular docking using a molecular similarity-based search engine. *J. Med. Chem.* **2003**, *46* (4), 499–511.
- (16) Vieth, M.; Siegel, M. G.; Higgs, R. E.; Watson, I. A.; Robertson, D. H.; Savin, K. A.; Durst, G. L.; Hipkind, P. A. Characteristic physical properties and structural fragments of marketed oral drugs. *J. Med. Chem.* **2004**, *47* (1), 224–232.
- (17) Kellenberger, E.; Rodrigo, J.; Muller, P.; Rognan, D. Comparative evaluation of eight docking tools for docking and virtual screening accuracy. *Proteins* **2004**, *57* (2), 225–242.
- (18) Cho, S. J.; Sun, Y. X. FLAME: A program to flexibly align molecules. *J. Chem. Inf. Model* **2006**, *46* (1), 298–306.
- (19) *OEChem Toolkits*; OpenEye Scientific Software: Santa Fe, NM.
- (20) Halgren, T. A. Merck Molecular Force Field .1. Basis, Form, Scope, Parameterization, and Performance of Mmff94. *J. Comput. Chem.* **1996**, *17* (5–6), 490–519.
- (21) Albert, A.; Goldace, R. J. The strength of heterocyclic bases. *J. Chem. Soc.* **1948**, 2240–2249.
- (22) Strater, N.; Lipscomb, W. N. Transition State Analogue L-Leucinephosphonic Acid Bound to Bovine Lens Leucine Aminopeptidase - X-Ray Structure at 1.65 Angstrom Resolution in a New Crystal Form. *Biochemistry* **1995**, *34* (28), 9200–9210.
- (23) Xia, Z. X.; Dai, W. W.; Zhang, Y. F.; White, S. A.; Boyd, G. D.; Mathews, F. S. Determination of the Gene Sequence and the Three-Dimensional Structure at 2.4 Angstrom Resolution of Methanol Dehydrogenase from *Methylophilus W3a1*. *J. Mol. Biol.* **1996**, *259* (3), 480–501.
- (24) Cornell, W. D.; Cieplak, P.; Bayly, C. I.; Gould, I. R.; Merz, K. M.; Ferguson, D. M.; Spellmeyer, D. C.; Fox, T.; Caldwell, J. W.; Kollman, P. A. A second generation force field for the simulation of proteins, nucleic acids, and organic molecules. *J. Am. Chem. Soc.* **1995**, *117* (19), 5179–5197.
- (25) Friesner, R. A.; Banks, J. L.; Murphy, R. B.; Halgren, T. A.; Klicic, J. J.; Mainz, D. T.; Repasky, M. P.; Knoll, E. H.; Shelley, M.; Perry, J. K.; Shaw, D. E.; Francis, P.; Shenkin, P. S. Glide: a new approach for rapid, accurate docking and scoring. 1. Method and assessment of docking accuracy. *J. Med. Chem.* **2004**, *47* (7), 1739–49.
- (26) Case, D. A.; Pearlman, D. A.; Caldwell, J. W.; Cheatham III, T. E.; Wang, J. M.; Ross, W. S.; Simmerling, C. L.; Darden, T. A.; Merz, K. M.; Stanton, R. V.; Cheng, A. L.; Vincent, J. J.; Crowley, M.; Tsui, V.; Gohlke, H.; Radmer, R. J.; Duan, Y.; Pitera, J.; Massova, I.; Seibel, G. L.; Singh, U. C.; Weiner, P. K.; Kollman, P. A. *AMBER 7*; University of California: San Francisco, 2002.
- (27) Wang, J. M.; Wolf, R. M.; Caldwell, J. W.; Kollman, P. A.; Case, D. A. Development and testing of a general amber force field. *J. Comput. Chem.* **2004**, *25* (9), 1157–1174.
- (28) Constanciel, R.; Contreras, R. Self-Consistent Field-Theory of Solvent Effects Representation by Continuum Models - Introduction of Desolvation Contribution. *Theor. Chim. Acta* **1984**, *65*, 1–11.
- (29) Still, W. C.; Tempczyk, A.; Hawley, R. C.; Hendrickson, T. Semianalytical, treatment of solvation for molecular mechanics and dynamics. *J. Am. Chem. Soc.* **1990**, *112*, 6127–6129.
- (30) Tsui, V.; Case, D. A. Calculations of the absolute free energies of binding between RNA and metal ions using molecular dynamics simulations and continuum electrostatics. *J. Phys. Chem. B* **2001**, *105* (45), 11314–11325.
- (31) Mongan, J.; Simmerling, C.; McCammon, J. A.; Case, D. A.; Onufriev, A. Generalized Born Model with a Simple, Robust Molecular Volume Correction. *J. Chem. Theory Comput.* **2007**, *3* (1), 156–169.
- (32) Warren, G. L.; Andrews, C. W.; Capelli, A. M.; Clarke, B.; LaLonde, J.; Lambert, M. H.; Lindvall, M.; Nevins, N.; Semus, S. F.; Senger, S.; Tedesco, G.; Wall, I. D.; Wolven, J. M.; Peishoff, C. E.; Head, M. S. A critical assessment of docking programs and scoring functions. *J. Med. Chem.* **2006**, *49* (20), 5912–5931.

Additive and Classical Drude Polarizable Force Fields for Linear and Cyclic Ethers

Igor Vorobyov,[†] Victor M. Anisimov,[†] Shannon Greene,[†] Richard M. Venable,[‡]
Adam Moser,^{‡,§} Richard W. Pastor,[‡] and Alexander D. MacKerell, Jr.*[†]

Department of Pharmaceutical Sciences, School of Pharmacy, University of Maryland, Baltimore, Maryland 21201, and Laboratory of Computational Biology, National Heart, Lung, and Blood Institute, National Institutes of Health, Bethesda, Maryland 20892

Received November 30, 2006

Abstract: Empirical force field parameters consistent with the CHARMM additive and classical Drude based polarizable force fields are presented for linear and cyclic ethers. Initiation of the optimization process involved validation of the aliphatic parameters based on linear alkanes and cyclic alkanes. Results showed the transfer to cyclohexane to yield satisfactory agreement with target data; however, in the case of cyclopentane direct transfer of the Lennard-Jones parameters was not sufficient due to ring strain, requiring additional optimization of these parameters for this molecule. Parameters for the ethers were then developed starting with the available aliphatic parameters, with the nonbond parameters for the oxygens optimized to reproduce both gas- and condensed-phase properties. Nonbond parameters for the polarizable model include the use of an anisotropic electrostatic model on the oxygens. Parameter optimization emphasized the development of transferable parameters between the ethers of a given class. The ether models are shown to be in satisfactory agreement with both pure solvent and aqueous solvation properties, and the resulting parameters are transferable to test molecules. The presented force field will allow for simulation studies of ethers in condensed phase and provides a basis for ongoing developments in both additive and polarizable force fields for biological molecules.

1. Introduction

The ether moiety is an important functional group in molecules of biological and industrial importance. For instance, tetrahydrofuran (THF) is a model for ribose, deoxyribose, fructose, and other furanoses, and tetrahydropyran (THP) is a model for glucose and other pyranoses. Therefore, accurate parametrization of THF and THP is necessary for the development of both nucleic acid and carbohydrate force fields. Concerning linear ethers, dimethyl

ether (DME), diethyl ether (DEE), and dimethoxyethane (DMOE) are commonly used organic solvents that are often utilized in a biological context, an example being the use of polyethylene glycol for the stabilization of protein based drugs for which DMOE is an ideal model compound.

From the physical chemical point of view ethers include a combination of the nonpolar aliphatic groups and polar oxygen atoms capable of participating in hydrogen bonds, including strong electrostatic interactions with cations. However, beyond that local hydrogen-bonding capacity, ethers are still relatively nonpolar, as evidenced by their small dipole moments and dielectric constants (e.g., the dipole moment of DEE is 1.15 and the dielectric constant is 4.24),¹ which has led to their use as solvents for organic synthesis. Therefore, the development of an empirical force field for this class of compounds requires attaining the right balance

* Corresponding author phone: (410)706-7442; fax: (410)706-5017; e-mail: amackere@rx.umaryland.edu. Corresponding author address: 20 Penn Street, Baltimore, MD 21201.

[†] University of Maryland.

[‡] National Institutes of Health.

[§] Current address: Department of Chemistry, University of Minnesota, 207 Pleasant St SE, Minneapolis, MN 55455.

of dispersion, electrostatic and repulsive forces governing the structure and dynamics of ethers in condensed phases and, thus, correctly describing a wide range of their properties. Facilitating such parameter development is the wide range of experimental data on the ethers. This includes a variety of data on the pure solvents¹ as well as free energies of solvation.² The availability of such data allows for an adequate training set of compounds to rigorously optimize the model as well as test compounds to validate the force field.

To date several empirical force fields for ethers have been presented. Linear ether (dimethyl ether (DME), methyl ethyl ether (MEE), DEE) parameters were developed as part of the MMFF94 force field.³ Recently, parameters for both linear and cyclic ethers were developed in the framework of the MM4 force field of Allinger and co-workers.^{4–8} Both MMFF94 and MM4 force fields provide accurate descriptions of the gas-phase properties of ethers including equilibrium geometries, vibrational frequencies, and torsional barriers. However, neither MM4 nor MMFF94 force fields were tested in condensed-phase simulations.

Emphasis on the reproduction of condensed-phase properties was placed in the development of the alkyl ether parameters determined in the framework of OPLS united atom (OPLS-UA)⁹ and all-atom models (OPLS-AA).¹⁰ In addition, OPLS parameters for THF were developed for the simulation of short polypeptides in this solvent.¹¹ In other work all-atom additive THF parameters were developed for use in MD simulations using an automatic optimization approach based on the simplex algorithm.^{12,13} Ether parameters have also been developed for AMBER united-atom and all-atom force fields^{14–16} and were tested using the compounds THF, dimethyl ether, and methyl ethyl ether model compounds.

Smith and co-workers have developed both additive and polarizable models of polyethylene oxide (PEO), its oligomers, and related compounds including DMOE. These efforts emphasized understanding the structure–property relationship in polymer electrolytes comprised of a PEO-based matrix, which was doped with lithium salts.^{17–23} The developed force field parameters for linear ethers were tested against a wide range of experimental structural, dynamic, and thermodynamic condensed-phase properties.

In this work we present a force field for both linear and cyclic ethers in the context of the CHARMM empirical force fields. Both an additive model and a polarizable model, based on a classical Drude oscillator, are considered. Motivation for the proposed work includes efforts in our laboratory to develop an additive force field for carbohydrates compatible with the CHARMM all-atom additive biomolecular force fields.^{24–27} In addition, efforts are ongoing toward the development of a polarizable force fields for biomolecules based on a classical Drude oscillator. Those efforts have included the development parameters for water,^{28,29} ethanol, alkanes,³⁰ and aromatics³¹ along with the development of a general protocol for determination of the partial atomic charges and polarizabilities which was used to generate a preliminary polarizable force field for DNA.³² More recently, an atom based anisotropic polarizable model has been developed,³³ which is applied in the proposed work.

2. Computational Methods

QM calculations were performed using the Gaussian 03 program suite.³⁴ Geometry optimizations were performed at the MP2(fc)/6-31G(d) level. The MP2/6-31G(d) level of theory has been found to provide molecular geometries consistent with gas-phase experimental data.³⁵ MP2/cc-pVTZ single-point energy calculations were performed on MP2/6-31G(d) optimized structures to obtain accurate estimates of molecular dipole moments, relative conformational energies, and torsional energy profiles. It was recently determined^{36,37} that MP2/cc-pVTZ/MP2/6-31G(d) and MP2/cc-pVTZ/MP2-cc-pVTZ relative energies are quite similar for a number of small model compounds including alcohols and THP, motivating the use of the more economical hybrid method.

QM calculations on the complexes of model compounds with rare gas atoms (He and Ne) were performed at the MP3/6-311++G(3d,3p) level³⁸ with the intramolecular geometries fixed at the MP2/6-31G(d) optimized structures. The location of the minima were obtained using two distance scans based on MP3/6-311++G(3d,3p) single point energy calculations. The scans involved a preliminary 0.1 Å scan to identify the region of the energy minimum followed by a 0.01 Å scan from which the minimum was identified.

QM calculations on the complexes of model compounds with water molecule were performed using the gas-phase MP2/6-31G(d) optimized conformers of the model compound and the gas-phase experimental geometry of water molecule ($R(\text{OH}) = 0.9572 \text{ \AA}$, $\angle\text{HOH} = 104.52^\circ$). For the additive CHARMM force field, constrained HF/6-31G(d) optimization of the complexes was performed where both monomer geometry and orientation were fixed, and only the interaction distance was optimized, as previously performed.^{27,39} The optimized interaction distance and energy scaled by a factor of 1.16 were used as reference values for consistency with the CHARMM22 parameter development protocol.²⁷ The same protocol was applied for the polarizable model with MP2/6-31G(d) used to identify the water-model compound interaction minima with the interaction energies obtained via LMP2/cc-pVQZ(-g) single point calculations using the program Jaguar.⁴⁰ This level of theory provides an accurate estimate of the gas-phase interaction energies and geometries for a number of hydrogen-bonded dimers⁴¹ at a reasonably low computational cost due to the use of the local MP2 (LMP2) method,^{42,43} where only a subset of the virtual orbitals is used for the calculation of the perturbed wavefunction.

To obtain experimental target data for bond, valence angle, and dihedral angle distributions for the model compounds, surveys of the Cambridge Structural Database⁴⁴ were performed. Each model compound was used as a search template with acyclic R (i.e., R = C or H) substituent(s) allowed. Distorted structures, structures containing errors, ones with R-factor > 0.1, and powder structures were excluded from the surveys. Organometallic compounds and structures containing ions were also excluded, since the close proximity of ions and/or metals can substantially influence values of internal parameters. The histograms for the geometric parameter distribution were plotted using the program Vista.⁴⁵

Their most probable values were obtained as the average of the values contributing to the largest peak on the histogram.

Empirical force field calculations were performed with the program CHARMM.^{46,47} Polarizability was introduced using the classical Drude oscillator model by attaching massless charged particles to the core of polarizable atoms (e.g., only non-hydrogen atoms in the present model) via a harmonic spring with a force constant, k_D . The partial atomic charge of a polarizable atom q is redistributed between the Drude particle and atomic core. The sign of the charges on Drude particles q_D is chosen to be negative by analogy with the electron charge.³² The magnitudes of q_D can be unambiguously determined from the atomic polarizabilities using the relationship $\alpha = q_D^2/k_D$. The charge on the atomic core q_c is determined by subtracting the Drude charge from the charge on the atom-Drude pair q , such that each atom-Drude pair forms a dipole $q_D \cdot d$ where d is the displacement vector going from the atomic core to its Drude particle. Thus, the electrostatic energy term U_{elec} in the additive potential energy function was modified to include Coulombic interactions between atomic cores and Drude particles. As in the additive CHARMM force field, interactions between core atomic charges q_c are excluded for 1–2 and 1–3 atom pairs. However, the U_{elec} term is modified to take into account screened 1–2 and 1–3 dipole interactions between Drude oscillators.⁴⁸ The screening is implemented through the smearing of the charge on the Drude particle and real atom using a Slater distribution with a dimensionless parameter 2.6.

In addition to the modified electrostatic term, the term U_{self} describing the self-energy of a polarizable atom via the harmonic term $0.5d\mathbf{K}^{(D)}d$ is included in the potential energy function.³² The Drude force constant is generally treated as isotropic; however, for hydrogen bond acceptor atoms it is treated as a tensor $\mathbf{K}^{(D)}$, where the diagonal elements $K_{xx}^{(D)}$, $K_{yy}^{(D)}$, and $K_{zz}^{(D)}$ determine the stiffness of the atom-Drude bond in three orthogonal directions (defined using a local intramolecular reference frame) allowing for anisotropic polarizability; note that the higher values of K correspond to lower polarizability along a given direction. The case of $K_{xx}^{(D)} = K_{yy}^{(D)} = K_{zz}^{(D)} = k_D$ corresponds to the isotropic polarizability and is applied to all the carbon atoms in the present study. For oxygen the atomic polarizability anisotropy was defined as $K_{xx}^{(D)} = 1100$, $K_{yy}^{(D)} = 800$, and $K_{zz}^{(D)} = 1100$ kcal/(mol·Å²) as determined for methanol.³³ The same anisotropic model was used for the ethers since O in both alcohols and ethers has the same sp³ hybridization state and thus is expected to have similar shape of the polarization response. The intramolecular frame defining the polarization anisotropy was with the x -axis in the plane along the COC bisector, the y -axis is perpendicular to the COC plane, and the z -axis is orthogonal to both x and y axes. The isotropic atomic polarizability with $k_D = 1000$ kcal/(mol·Å²) was applied to all carbon atoms.

In addition to the anisotropic polarizability, two virtual charge sites away from the atomic core were added to the ether oxygen atom to account for the asymmetry in the electron charge density around that atom. The sites are

traditionally attributed to the presence of lone pairs (LPs), i.e. an electron pair in the valence shell of the atom not involved in the formation of a covalent bond. Such a model adjustment has been shown to better predict the anisotropy of the interactions of a water molecule in different orientations about hydrogen bond acceptors as compared to atom centered charges.^{33,49} The determination of the LP partial charges are included in the fitting procedure. However, their positions were not optimized during the fitting but rather adjusted manually based on achieving as small as possible root-mean-square error (RMSE) of empirical vs QM electrostatic potentials (ESP) and the qualitative reproduction of the variation of the local QM ESP around the oxygen atom.³³ The CHARMM LONEPAIR facility was used for the placement of the virtual particles.

Partial atomic charges and atomic polarizabilities for the Drude polarizable model were determined from restrained fitting to the B3LYP/aug-cc-pVDZ perturbed electrostatic potential (ESP) maps using MP2/6-31G(d) optimized geometries, as previously described.³² The ESP grid points were located on concentric nonintersecting Connolly surfaces around the ether molecule. In order to determine both atomic polarizabilities and partial atomic charges from the single fitting procedure, a series of perturbed ESP maps was generated by placing point charges of magnitude +0.5e on Connolly surfaces along chemical bonds, around the ether oxygen atoms (to probe lone pairs) and in the gaps between the initially placed ions to achieve nearly equidistant coverage of the molecular shape. Connolly surfaces of perturbation charges and grid points were generated with size factors 2.2 (charges and grid), 3.0 (grid), 4.0 (charges), 5.0 (grid), and 6.0 (grid). The size factor multiplied by the vdW radius of the corresponding atom determines its distance from the corresponding Connolly surface. In addition, for the oxygens, additional perturbation ions and grid points with a size factor of 1.3 were included. This proximal surface, along with the grid at 2.2, takes into account the details of the electrostatic environment of the molecule around the region where hydrogen-bond and other direct interactions take place, whereas the more distal surfaces provide a more accurate description of the dipolar and polarizability response of the entire molecule since the point charge approximation works well at larger distances. During fitting parabolic restraints were applied to the initial values of both the charges and polarizabilities with the weighting factor of 10⁻⁵ Å⁻² for all atoms except for ether oxygens, for which 10⁻¹ Å⁻² was used in order to maintain its electroneutrality. Additionally, a flat well potential with the half-width of 0.1e was used for atomic polarizabilities. Fitting to the same charge and polarizability values was imposed for chemically equivalent atoms. For the oxygen atoms the charge was moved to LP particles during the fitting procedure, while the polarizability was maintained on the atomic core of the parent oxygen. Thus, each LP effectively receives one-half of the O charge, with the oxygen having a charge of zero. Initial values for the partial atomic charges were from the additive CHARMM model, and for atomic polarizabilities Miller's ahp polarizability values α_{ahp} were modified to account for the non-hydrogen only polarizable model being used.^{32,50}

Molecular dynamics (MD) simulations were performed at 298.15 K and 1 atm pressure using the new velocity Verlet integrator⁵¹ implemented in CHARMM. A Nosé-Hoover thermostat with a relaxation time of 0.1 ps was applied to all real atoms to control the global temperature of the system. A modified Andersen-Hoover barostat with a relaxation time of 0.1 ps was used to maintain the system at constant pressure. Condensed-phase MD simulations were performed using periodic boundary conditions and SHAKE to constrain covalent bonds involving hydrogens.⁵² Electrostatic interactions were treated using particle-mesh Ewald (PME) summation⁵³ with a coupling parameter 0.34 and sixth-order spline for mesh interpolation. Nonbond pair lists were maintained out to 14 Å, and a real space cutoff of 12 Å was used for the electrostatic and Lennard-Jones terms with the latter truncated via an atom-based force switch algorithm,⁵⁴ unless noted. Long-range contributions to the van der Waals terms were corrected for as previously described.^{55,56} The extended Lagrangian double-thermostat formalism⁵¹ was used in all polarizable MD simulations where a mass of 0.4 amu was transferred from real atoms to the corresponding Drude particles. The amplitude of their oscillation was controlled with a separate low-temperature thermostat (at $T = 1.0$ K) to ensure that their time course approximates the SCF regimen.⁵¹

A box of 128 molecules was used for the pure solvent simulations of all model compounds. It was shown previously that this number of molecules is adequate to achieve convergence for Drude polarizable MD simulations of neat liquid propane to within 0.5% for both molecular volumes and heats of vaporization.³⁰ To obtain adequate sampling, ten independent MD simulations were run for 150 ps for the box of each model compound with different initial velocities, and the final 100 ps were used for the analysis. The results of 10 simulations were averaged to get liquid-phase properties and the standard deviations were calculated. The molecular volumes were calculated as the average volume of the monomer in the box, whereas the heats of vaporization were obtained using a difference between the average potential energy of the molecule in the gas phase and the average potential energy of the monomer in the liquid-phase plus thermal correction RT .⁵⁷ Gas-phase simulations required to calculate heats of vaporization were performed using Langevin dynamics in the SCF regimen in the case of the polarizable models. The same Drude force constants as in the condensed-phase simulations were used along with infinite nonbonded cutoffs. The friction coefficient of 5.0 ps^{-1} was applied to all real atoms. Gas-phase simulations were run individually for all 128 molecules in the respective boxes for a duration of 1000 ps with the monomer result being averaged over all 128 individual simulations. The static dielectric constants ϵ of neat liquid ethers and cycloalkanes were calculated from the dipole moment fluctuations of the box as described before.²⁹ The high-frequency optical dielectric constant ϵ_∞ was estimated from the Clausius-Mossotti equation, which relates ϵ_∞ to the molecular polarizability.^{29,58} For additive CHARMM force field simulations ϵ_∞ was set to 1.

Free energies of aqueous solvation were obtained via free energy perturbations (FEP)^{59,60} using the staged protocol

developed by Deng and Roux.⁶¹ The protocol from our previous study for calculating solvation free energy of alkanes³⁰ with minor modifications was utilized in this work. The solvation free energies were computed as a sum of the electrostatic, dispersive, and repulsive contributions. Each term was obtained as a difference in the free energy of the solute in water and in vacuum. The weighted histogram analysis method (WHAM)⁶² was used to obtain the repulsive term of the FE, whereas thermodynamic integration (TI) was used to obtain the electrostatic and dispersive components of the free energies from the simulations. The nonbonded parameter truncation scheme applied in FEP simulations was different from that used for regular MD simulations: energy instead of force switch cutoff and no long-range LJ corrections were used since these options are currently not supported by the existing FEP code. Gas-phase simulations were performed using Langevin dynamics as described above. Separate FEP simulations consisting of 10 ps of equilibration and 50 ps of production run were performed for a given value of the coupling and/or staging parameter. Three sets of simulations with different initial structures and/or initial velocities were performed for both gas- and aqueous-phase FEP calculations from which averages and standard deviations were determined.

3. Results and Discussion

3.A. Initial Parameters and Optimization Strategy. Force field parameters were optimized to maximize the quality of the agreement with various target data while still maintaining a reasonable level of transferability. Internal parameters were initially transferred directly from CHARMM27 with additional optimization, typically to the dihedral parameters, performed as required. Electrostatic parameters were obtained, in the case of the additive model, based on reproduction of the interactions with water as well as the target condensed-phase properties. In the additive model atomic charges for all H atoms of CH_x groups were assigned to be 0.09 for consistency with the CHARMM22 and 27 force fields. The partial atomic charge of carbon atoms in CH_x groups of cycloalkanes or ethers, excluding those covalently bound to an oxygen, were adjusted to make the moiety electroneutral (i.e., -0.27 for CH_3 and -0.18 for CH_2). Atomic charges of oxygens and the adjacent carbons were determined iteratively based on the reproduction of the reference dipole moment and interactions with water. With the polarizable model, the charges and polarizabilities were obtained from the ESP fitting procedure described in the methods. The atomic polarizabilities were scaled by a factor of 0.7, consistent with that used in the SWM4-NDP water model.²⁸ Validation of the use of scaling was based on the reproduction of free energies of solvation as described below.

Adjustment of the Lennard-Jones parameters represents the most difficult aspect of the optimization process. Initial LJ parameters were from CHARMM27. Additional optimization was motivated by the necessity of the model to adequately reproduce the target condensed-phase properties. In addition, rare gas-model compound interactions were used as target data as developed by Yin and MacKerell.³⁸ In the remainder of this section the motivation for the optimization

Table 1. Pure Solvent Properties of the Alkanes Using the Modified Aliphatic LJ Parameters^a

compound	experimental data ^b			C27r ^c		C27m ^d	
	<i>T</i> (K)	<i>V</i> _m	ΔH_{vap}	<i>V</i> _m	ΔH_{vap}	<i>V</i> _m	ΔH_{vap}
ethane	184.6	91.8	3.53	91.8 ± 0.9	3.42 ± 0.03	91.8 ± 0.8	3.42 ± 0.03
propane	231.1	125.7	4.51	126.0 ± 0.6	4.28 ± 0.03	124.7 ± 1.1	4.51 ± 0.04
butane	272.7	160.5	5.37	164.1 ± 1.3	5.05 ± 0.13	160.4 ± 0.9	5.33 ± 0.07
isobutane	261.4	162.5	5.12	162.3 ± 1.6	4.82 ± 0.06	160.5 ± 1.0	4.99 ± 0.05
heptane	298.2	244.9	8.76	248.2 ± 0.9	7.24 ± 0.16	243.4 ± 1.1	8.69 ± 0.12
	312.2	249.1	8.53	254.3 ± 1.6	6.97 ± 0.16	249.2 ± 1.5	8.45 ± 0.14
decane	298.2	325.2	12.28	327.7 ± 1.9	10.29 ± 0.22	322.4 ± 1.2	12.48 ± 0.17
	312.2	330.0	12.01	336.0 ± 1.6	9.86 ± 0.22	327.4 ± 1.7	12.27 ± 0.20

^a Molecular volumes *V*_m are in Å³; heats of vaporization ΔH_{vap} are in kcal/mol. ^b Experimental data are from ref 1. ^c CHARMM27 parameters are from ref 38 with modified alkane dihedral parameters from ref. 25. ^d C27r parameters with modified Lennard-Jones parameters from ref 30.

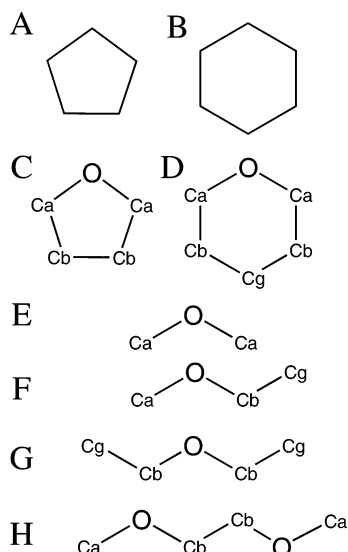


Figure 1. Model compounds: (A) cyclopentane, CPEN; (B) cyclohexane, CHEX; (C) tetrahydrofuran, THF; (D) tetrahydropyran, THP; (E) dimethyl ether, DME; (F) methyl ethyl ether MEE; (G) diethyl ether, DEE (H) 1,2-dimethoxyethane, DMOE. Atom names correspond to the atom types used in the definition of the parameters (Table S1, Supporting Information).

performed on the individual model compounds (Figure 1) is presented for the additive model followed by the polarizable one. This is followed by an overview of the results for the final selected models. Final parameters for all species are included in Table S1 of the Supporting Information.

3.B. Motivation for Selection of Final Models: Additive Force Field. As the aliphatic moieties represent a significant portion of the ethers the initial step of the parameter development was re-evaluation of the alkane parameters. This involved testing the additive linear alkanes parameters, with the LJ parameters previously developed for the Drude polarizable model, C27m,³⁰ along with the revised alkane dihedral parameters, C27r.²⁵ As may be seen in Table 1, these parameters yielded good agreement with the pure solvent properties for a range of alkanes up to decane. These parameters, which involved changes in the LJ parameters of the CH carbon and the LJ well depths of the aliphatic CH₂ hydrogens, represent a significant improvement over the original CHARMM aliphatic parameters,³⁸ especially in the case of the longer alkanes.

As a major goal of the present work was the development of models for cyclic ethers for use in biomolecules, tests

Table 2. Molecular Volumes and Heats of Vaporization for Cycloalkanes and Ethers^e

	<i>T</i> , K	exper	additive	%err	Drude	%err
Cyclopentane (CPEN)						
<i>V</i> _m	298.15	157.3^a	155.5 ± 0.8	-1.2	156.9 ± 0.9	-0.3
ΔH_{vap}	298.15	6.82^b	6.86 ± 0.03	0.6	6.76 ± 0.06	-0.9
Cyclohexane (CHEX)						
<i>V</i> _m	298.15	180.6^b	182.7 ± 1.0	1.2	182.4 ± 0.8	1.0
ΔH_{vap}	298.15	7.89^b	7.66 ± 0.05	-3.0	7.67 ± 0.04	-2.8
Tetrahydrofuran (THF)						
<i>V</i> _m	298.15	135.6^b	134.7 ± 0.5	-0.7	134.0 ± 0.8	-1.2
ΔH_{vap}	298.15	7.65^b	7.70 ± 0.04	0.7	7.80 ± 0.06	2.0
Tetrahydropyran (THP)						
<i>V</i> _m	298.15	162.3^b	164.3 ± 0.9	1.2	165.3 ± 0.3	1.8
ΔH_{vap}	298.15	8.26^b	8.25 ± 0.07	-0.2	8.27 ± 0.02	0.1
Diethyl Ether (DEE)						
<i>V</i> _m	298.15	173.9^a	172.4 ± 1.1	-0.9	171.8 ± 1.0	-1.2
ΔH_{vap}	298.15	6.48^b	6.87 ± 0.11	6.1	6.80 ± 0.10	4.9
Dimethoxyethane (DMOE)						
<i>V</i> _m	298.15	173.6^a	176.5 ± 1.1	1.7	176.6 ± 0.8	1.7
ΔH_{vap}	298.15	8.79^b	8.80 ± 0.24	0.1	8.79 ± 0.1	0.0
Dimethyl Ether (DME)						
<i>V</i> _m	248.34	104.9^c	106.4 ± 1.1	1.4	106.6 ± 0.9	1.6
ΔH_{vap}	248.34	5.14^b	5.19 ± 0.10	0.9	4.94 ± 0.05	-3.9
Methyl Ethyl Ether (MEE)						
<i>V</i> _m	273.20	137.5^d	138.9 ± 0.9	1.1	137.5 ± 0.6	-0.4
ΔH_{vap}	280.60	5.90^b	5.90 ± 0.08	0.1	5.72 ± 0.06	-3.1

^a Experimental data are from ref 87. ^b Experimental data are from ref 1. ^c Experimental data are from ref 88. ^d Experimental data are from ref 89. ^e Molecular volumes *V*_m are in Å³; heats of vaporization ΔH_{vap} are in kcal/mol.

Table 3. Solvation Free Energies in Aqueous Solution for Cycloalkanes and Ethers^a

	exper	additive	diff	Drude	diff
CPEN	1.20	0.73 ± 0.21	-0.47	0.81 ± 0.39	-0.39
CHEX	1.23	0.89 ± 0.45	-0.34	1.42 ± 0.21	0.19
THF	-3.47	-3.34 ± 0.19	0.13	-3.78 ± 0.15	-0.31
THP	-3.12	-3.35 ± 0.05	-0.23	-3.20 ± 0.83	-0.08
DEE	-1.76	-2.00 ± 0.35	-0.24	-1.60 ± 0.11	0.16
DMOE	-4.84	-4.52 ± 0.59	0.32	-3.78 ± 0.59	1.06
DME	-1.92	-1.44 ± 0.32	0.48	-1.25 ± 0.22	0.67
MEE		-1.74 ± 0.22		-1.38 ± 0.16	

^a Solvation free energies are in kcal/mol. See Table 2 and Figure 1 for compound names. Experimental data are from ref 2.

were next undertaken to verify if the linear alkane parameters were appropriate for cyclopentane and cyclohexane. In the case of cyclohexane, good agreement was obtained for the pure solvent properties (Table 2) and for the free energies of solvation (Table 3) indicating that those parameters were acceptable. In contrast, with cyclopentane direct transfer of the alkane parameters to the five-membered ring leads to the molecular volume of 162.0 ± 1.2 Å³ and heat of vaporization 6.39 ± 0.08 kcal/mol, which are 4.5 and -6.2% differences from experiment (Table 2), respec-

Table 4. Ether Gas-Phase Interaction Energies with a Water Molecule^a

molec	conf	orient	QM (HF)		additive			QM (LM2/MP2)		Drude		
			Rmin	IE	Rmin	IE	dIE	Rmin	IE	Rmin	IE	dIE
THF	C2	O1_180	2.01	-6.39	1.72	-5.87	0.52	1.95	-5.45	1.77	-5.24	0.20
THF	C2	O1_120	1.98	-6.95	1.73	-6.51	0.44	1.90	-5.95	1.75	-5.93	0.02
THF	Cs	O1_180	2.02	-5.99	1.72	-6.06	-0.07	1.96	-5.09	1.77	-5.32	-0.23
THF	Cs	O1_120	2.01	-6.47	1.73	-6.47	0.00	1.93	-5.47	1.75	-5.80	-0.33
THF	RMSE						0.48					0.32
THP	chair	O1_180	2.01	-6.05	1.71	-6.23	-0.18	1.94	-5.23	1.78	-5.02	0.21
THP	chair	O1_120	2.01	-6.34	1.72	-6.49	-0.16	1.92	-5.54	1.77	-5.47	0.08
THP	RMSE						0.17					0.16
DEE	tt	O3_180	2.03	-5.99	1.75	-6.14	-0.15	1.94	-5.41	1.82	-5.03	0.38
DEE	tt	O3_120	2.02	-6.76	1.76	-6.50	0.26	1.91	-6.00	1.81	-5.32	0.68
DEE	gt	O3_180	2.02	-6.16	1.75	-5.69	0.47	1.93	-5.60	1.83	-4.46	1.15
DEE	gt	O3_120	2.04	-6.47	1.83	-6.04	0.44	1.92	-5.99	1.88	-4.94	1.05
DEE	gg	O3_180	2.01	-6.21	1.74	-5.42	0.78	1.94	-5.49	1.84	-4.01	1.48
DEE	gg	O3_120	2.08	-5.88	1.89	-5.22	0.66	1.96	-5.44	1.95	-4.08	1.36
DEE	RMSE						0.51					1.09
MEE	t	O3_180	2.02	-5.94	1.75	-5.69	0.25	1.94	-5.24	1.82	-4.62	0.62
MEE	t	O3_120	2.02	-6.46	1.76	-6.12	0.34	1.92	-5.78	1.81	-5.01	0.78
MEE	g	O3_180	2.01	-6.09	1.75	-5.22	0.87	1.94	-5.56	1.83	-4.04	1.51
MEE	g	O3_120	2.04	-6.24	1.83	-5.69	0.55	1.94	-5.81	1.88	-4.67	1.13
MEE	RMSE						0.56					1.07
DME	s	O2_180	2.02	-5.87	1.75	-5.24	0.63	1.95	-5.01	1.82	-4.23	0.78
DME	s	O2_180	2.02	-6.10	1.76	-5.73	0.37	1.94	-5.47	1.81	-4.71	0.76
DME	RMSE						0.51					0.77
DMOE	ttt	O2_180	2.01	-5.78	1.75	-5.32	0.46	1.93	-5.22	1.81	-4.48	0.73
DMOE	ttt	O2_120	2.02	-5.95	1.77	-5.27	0.67	1.92	-5.42	1.81	-4.65	0.77
DMOE	ttt	O2_240	2.05	-5.16	1.79	-4.71	0.45	1.94	-5.27	1.82	-4.36	0.91
DMOE	ttt	O5_180	2.01	-5.78	1.75	-5.32	0.46	1.93	-5.22	1.81	-4.48	0.73
DMOE	ttt	O5_120	2.02	-5.95	1.77	-5.27	0.67	1.92	-5.42	1.81	-4.65	0.77
DMOE	ttt	O5_240	2.05	-5.16	1.79	-4.71	0.45	1.94	-5.27	1.82	-4.36	0.91
DMOE	ggt	O2_180	2.02	-5.59	1.76	-4.80	0.79	1.95	-5.04	1.83	-3.92	1.12
DMOE	ggt	O2_120	2.02	-5.83	1.77	-5.23	0.60	1.93	-5.19	1.82	-4.25	0.93
DMOE	ggt	O2_240	2.18	-3.79	1.92	-2.98	0.81	2.01	-4.01	1.95	-3.22	0.79
DMOE	ggt	O5_180	2.02	-5.38	1.75	-4.91	0.47	1.94	-5.04	1.81	-4.26	0.78
DMOE	ggt	O5_120	2.03	-5.75	1.78	-5.10	0.65	1.93	-5.14	1.82	-4.44	0.70
DMOE	ggt	O5_240	2.05	-4.86	1.79	-4.32	0.54	1.94	-4.93	1.82	-4.24	0.70
DMOE	tgg	O2_180	2.16	-4.64	1.83	-4.66	-0.02	2.03	-4.28	1.86	-4.02	0.27
DMOE	tgg	O2_120	2.74	-3.68	2.40	-2.60	1.08	2.21	-3.19	1.94	-4.65	-1.46
DMOE	tgg	O2_240	2.07	-4.57	1.80	-4.10	0.47	1.95	-4.81	1.82	-4.24	0.57
DMOE	tgg	O5_180	2.00	-6.64	1.74	-6.31	0.34	1.94	-5.69	1.83	-4.51	1.18
DMOE	tgg	O5_120	2.01	-6.39	1.75	-6.07	0.33	1.92	-5.57	1.80	-4.84	0.73
DMOE	tgg	O5_240	2.56	-5.12	2.02	-6.10	-0.98	2.29	-3.95	2.40	-2.55	1.40
DMOE	RMSE						0.62					0.90

^a Interaction energies (IE) are in kcal/mol; minimum interaction distances (Rmin) are in Å. QM data are either from scaled HF/6-31G(d)//HF/6-31G(d) (reference for additive model) or LMP2/cc-pVQZ//MP2/6-31G(d) calculations (reference for Drude model).

tively. This level of disagreement appears to be associated with strain in the smaller ring, as evidenced by increased bond lengths and the smaller angles in the 5-membered ring versus both the 6-membered ring and linear alkanes as evident from both experimental gas phase and crystal as well as QM geometric data (see Tables S2–S5 of the Supporting Information). Based on the experimental heats of vaporization a strain energy of 5.3 kcal/mol has been estimated for cyclopentane versus a negligible strain energy of -0.4 kcal/mol for cyclohexane.⁶³ It is therefore suggested that the strain impacts the dispersion/repulsion interactions of the molecule, requiring additional optimization of the LJ and internal parameters.

Additional support for the optimization of LJ parameters specific for cyclopentane comes from Bader's atoms in molecules theory. It was shown that the atomic properties of methyl and methylene groups in linear hydrocarbons such as charges, energies, and volumes are transferable across a series,^{64,65} which is consistent with the use of the same nonbonded force field parameters. However, in cycloalkanes, due to geometric strain, differences from "standard" alkane CH₂ group atomic properties were observed for cyclopropane and to a lower degree for cyclobutane and cyclopentane. The differences in the atomic energies correlated with the experimental strain energies.⁶⁵ A noticeable increase in the atomic volume for C and decrease for H atom in cyclopropane and cyclobutane compared to average alkane

values were also observed.⁶⁴ No such changes were detected for cyclohexane.^{64,65} Since atomic volumes and energy might be at least qualitatively correlated to LJ radii and well depths, the requirement for unique parameters for CPEN can be thus justified.

Additional optimization of the cyclopentane LJ parameters followed the standard CHARMM procedure.³⁸ Following this additional optimization the resulting parameters yield excellent agreement for the pure solvent properties (Table 2) with errors well within the target values of 2%, and provided smaller fluctuations about average differences and ratios of interaction energies and distances with respect to QM data for complexes with rare gases (Table 5 and Figure 3). Moreover, the free energy of solvation is in acceptable agreement with experiment, being too favorable by ~0.5 kcal/mol (Table 3). These LJ parameters were then used in THF during the subsequent optimization of that molecule.

Additive force field parameters were developed for the cyclic ethers, THF and THP, starting with the CH₂ group parameters for cyclopentane and cyclohexane, respectively. In the final models identical partial atomic charges and the LJ parameters of the oxygen for the two compounds were shown to reproduce interactions with water (Table 4) as well as pure solvent properties (Table 2) and the free energies of aqueous solvation (Table 3). Concerning the interactions with water, the empirical

Table 5. Root-Mean-Square Fluctuations about the Average Differences and Ratios with Respect to QM Data for the Minimum Interaction Distances and Energies for Complexes of Cycloalkanes with Helium and Neon^a

	helium				neon			
	R_{\min}		IE		R_{\min}		IE	
	differ	ratio	differ	ratio	differ	ratio	differ	ratio
Cyclopentane (CPEN)								
C27r	0.0579	0.0089	17.08	0.116	0.0358	0.0101	33.64	0.0358
additive	0.0486	0.0055	16.72	0.111	0.0259	0.0065	31.76	0.0350
Drude	0.0486	0.0055	16.68	0.112	0.0259	0.0065	32.73	0.0347
Cyclohexane (CHEX)								
C27r	0.0492	0.0082	20.23	0.128	0.0249	0.0061	37.03	0.0390
additive	0.0535	0.0092	22.26	0.141	0.034	0.0089	40.28	0.0428
Drude	0.0535	0.0092	21.88	0.139	0.034	0.0089	41.84	0.0422

^a Interaction energies (IE) are in microHartrees (mkH); minimum interaction distances (R_{\min}) are in Å.

values are in good agreement with the target scaled HF/6-31G* values for the interaction energies, while the distances are underestimated by ~ 0.3 Å. Such an offset is consistent with previous studies showing the need for decreased minimum interaction distances in the empirical model to reproduce the density of the pure solvent.^{26,27} Use of the same nonbond parameters for the oxygens indicates the transferability of the model. However, the optimized internal parameters were different reflecting the strain associated with the formation of the five-membered ring for THF, similar to that for cyclopentane.

Following completion of the cyclic ethers, the linear ethers, dimethyl ether (DME), methyl ethyl ether (MEE), diethyl ether (DEE), and dimethoxyethane (DMOE) were studied. For these compounds the oxygen LJ parameters from cyclic ethers were used directly with additional optimization of the oxygen partial atomic charges and the internal parameters undertaken. The oxygen partial charges were adjusted to better reproduce the neat liquid properties as well as interactions with water and solvation free energies across the series of compounds. In the final model the same charges were used for the oxygen and adjacent carbons in all the linear ethers. Such transferability is desirable to allow for the parameters to be applied to other ethers; however, due to simplicity of the model, it makes it impossible to reproduce all target properties with the same degree of accuracy. Thus, the final model, with a partial charge of -0.34 on the oxygens, yields good agreement for the pure solvent properties (Table 2) for all model compounds except for DEE, for which the heat of vaporization was overestimated by 6.1%. In addition, the free energy of solvation is too unfavorable by 0.5 and 0.3 kcal/mol (Table 3) for DME and DMOE, respectively, while it is slightly too favorable for DEE by 0.2 kcal/mol. These results correlate well with the interaction energies with water, which are underestimated with respect to the target data for DME, MEE, and DMOE but are in good agreement for the *tt* conformer of DEE (Table 4). Efforts to correct for the overestimation of the heat of vaporization for DEE by decreasing the partial charge on O to -0.30 lead to the reduction of this error to 2.7%. However, this DEE model underestimates the interaction energies with

water (by 0.5–0.8 kcal/mol for the *tt* conformer) and solvation free energy by approximately 0.5 kcal/mol compared to target values. Moreover, the transfer of these parameters to other linear ethers leads to a substantial underestimation of the heat of vaporization (by 4.9% for DME, 3.9% for MEE and 3.0% for DMOE). Thus, the partial charge on oxygen was set to the value of -0.34 for all linear ethers in the additive model.

3.C. Motivation for Selection of Final Models: Drude Polarizable Force Field. A similar strategy as applied to the additive model was used for the development of the polarizable ether parameters. For cyclohexane direct transfer of the linear alkane charges, polarizabilities, LJ, and internal parameters lead to an underestimation of the heat of vaporization by 3.2% (not shown), while the free energy of solvation was too favorable by 0.8 kcal/mol (not shown). This motivated the refitting of the electrostatic parameters via the QM ESP approach and the scaling of the final polarizabilities by 0.7, as performed for the SWM4-NDP water model,²⁸ aromatic,³¹ and polar-neutral species (A. D. MacKerell, Jr. et al., work in progress). This model yielded pure solvent properties in satisfactory agreement with experiment (Table 2) and, importantly, an improved free energy of solvation (Table 3). With cyclopentane, direct transfer of the linear alkane parameters again gave poor pure solvent properties (the molecular volume was too large by 5.3%, whereas the heat of vaporization was underestimated by 8.0%), and the free energy of solvation was too favorable by ca. 0.5 kcal/mol, as occurred in the additive model. Accordingly, optimized LJ and internal parameters were taken from the additive cyclopentane model, and these were initially combined with the electrostatic alkane parameters. This model did show significant improvements in the pure solvent properties (the errors in both molecular volume and heat of vaporization were less than 1%) although the free energy of solvation, as with cyclohexane, was too favorable by ~ 0.7 kcal/mol. Accordingly, charge and polarizability QM ESP fitting was performed with the polarizabilities scaled by 0.7, as with cyclohexane, yielding the final Drude model. This model again gave good agreement for the pure solvent properties (Table 2) and improved agreement for the free energy of solvation (Table 3), with the calculated value being ~ 0.4 kcal/mol more favorable than the experimental value. Thus, satisfactory polarizable models of cyclohexane and cyclopentane required explicit fitting of the charges and polarizabilities with the scaling of fitted polarizabilities by 0.7. Such scaling has been used for the aromatic and polar neutral species in the Drude model but not for the linear alkanes. The need to perform such scaling suggests that the cyclic structure of the compounds may alter their electrostatic properties, perhaps via more correlation effects due to their cyclic nature, making them behave more like polar compounds.

Initial parameters for the internal and LJ terms in the Drude polarizable model of the cyclic ethers were taken from the additive models. Partial atomic charges and atomic polarizabilities were obtained from the ESP fitting procedure, with atomic charges scaled to reproduce the reference dipole moments and the polarizabilities scaled by a factor of 0.7.

By analogy with the additive models, for THF and THP the optimized LJ parameters of the cyclopentane and cyclohexane models, respectively, were used for the C and H atoms. The LJ parameters of the oxygens were then adjusted to reproduce the pure solvent and aqueous solvation properties. The resulting models are in good agreement with experiment for both the pure solvent (Table 2) and the free energies of solvation (Table 3). The interactions energies with water are also in good agreement with the target QM data with the maximum difference being 0.3 kcal/mol (Table 4).

As with the cyclic ethers, internal parameters for the polarizable linear ethers were obtained from the additive model with the LJ parameters from the polarizable alkane force field. Charges and polarizabilities were from the ESP fitting procedure for DEE with fitted charges scaled to reproduce the experimental dipole moment and with fitted polarizabilities scaled by 0.7. These electrostatic parameters were then adjusted to produce neutral terminal CH₃ groups and then transferred to the other linear ethers, DME, MEE, and DMOE. Except for some dihedral parameters, most internal parameters were directly transferred from the corresponding additive models. To obtain a fully transferable polarizable Drude ether model and to be consistent with the additive model, oxygen LJ parameters from THF and THP models were also used for linear ethers. The resultant parameters provide reasonable agreement for both the pure solvent (Table 2) and aqueous solvation properties (Table 3). As for the additive model, the heat of vaporization of DEE is substantially overestimated (4.9%), whereas those for DME and MEE are underestimated by 3.9 and 3.1%, respectively (Table 2). However, the molecular volumes for all models were within 2% of the experimental values (Table 2). This level of agreement is similar to that of another polarizable model reported for dimethyl ether.¹⁸ The solvation free energies are in satisfactory agreement with experiment, with the value for DEE being just 0.2 kcal/mol less favorable than the reference value, whereas those for DME and DMOE are too unfavorable by 0.7 and 1.1 kcal/mol, respectively. Such poor performance for DMOE might be related to sampling problems; additional studies are required to address this issue. It should be also noted that this linear ether model systematically underestimates the interaction energies with water, especially for DME and DMOE (Table 4), which is consistent with the trends in the solvation free energies (Table 3). Thus, the transferability of LJ parameters across ether series can be achieved, but for some compounds the agreement with experimental data needs to be sacrificed. Since the main focus of this study is the development of the ether parameters to be used in a biomolecular force field, we concentrated on the derivation of THF and THP parameters as templates for furanoses and pyranoses, respectively. The development of more accurate linear ether parameters, which are also important in biological molecules (e.g., for linkages in oligo- and polysaccharides), may require more extensive studies beyond the scope of the present work.

It should be noted that it is possible to achieve a very good agreement for a wide range of molecular properties for a particular compound. For instance, by optimizing LJ parameters of the oxygen atom we were able to obtain a

Drude polarizable DEE model, which is in very good agreement for pure solvent properties (0.1% error for both molecular volume and heat of vaporization), aqueous solvation free energy (less than 0.1 kcal/mol error), and interaction energy with water (0 and 0.3 kcal/mol error for two different interaction orientations for the *tt* conformer). However, the transfer of LJ and electrostatic parameters to other linear ethers does not provide satisfactory results for condensed-phase properties: heats of vaporization are underestimated by 10.2, 8.1, and 6.8% for DME, MEE, and DMOE, respectively.

3.D. Detailed Analysis of Final Models. A variety of target data was used in the optimization of the present force field for ethers, as discussed above. In this section, the overall level of agreement with respect the various target data is presented with emphasis on the results not discussed in the preceding sections.

Gas-Phase Properties. Intramolecular parameters associated with the bond, valence angle, and dihedral angle terms in the energy function were optimized to reproduce a variety of gas-phase QM and experimental data. Presented in Tables S3–S9 of the Supporting Information is the target data along with the empirical optimized geometries for the model compounds studied. Overall the level of agreement is excellent. In virtually all cases the differences are within the target ranges of 0.02 Å, 2° and 2° for the bonds, valence angles, and dihedrals, respectively. Intramolecular parameter optimization also analyzed the vibrational spectra. As shown in Tables S10–S14 of the Supporting Information the overall level of agreement is good. Note that emphasis was placed on the treatment of the lowest frequency modes as these correspond to those that have the largest impact in MD simulations. However, for some of the lowest frequency modes, sacrifices were made in the vibrational data to allow for better reproduction of the relative energies of different conformations of the target molecules.

Table 6 lists the relative conformational energies and dipole moments of selected conformations for all model compounds. In general, the conformational energies reproduce the target MP2/cc-pVTZ//MP2/6-31G(d) data well. The energy of the planar D_{5h} structure of cyclopentane is underestimated in the empirical models, although the energy is high enough to avoid significant sampling of this structure in MD simulations; this trend extends to THF. With cyclohexane the energies of the twist conformation are higher in the empirical models than in the QM calculations, while in THP the higher energy conformations are underestimated in the empirical models. For the cyclic ethers, the present QM data are consistent with previously reported data for THF,^{67,68} including pseudorotation profiles^{69–73} and THP.^{74–76} Similar trends are observed in the linear alkanes with the higher energy conformations slightly overestimated in the empirical models of DEE and MEE, while they are slightly underestimated in DMOE. For DEE the experimental conformational energy difference between *gt* and *tt* is 1.14 kcal/mol in solution,⁷⁷ versus the gas-phase value of 1.36 kcal/mol, indicating potential solution effects on the conformational properties. Overall, these results along with the conformational energy surfaces shown in Figures S1–S13 of the

Table 6. Gas-Phase Relative Conformational Energies and Dipole Moments for Cycloalkanes and Ethers^a

	relative energies			dipole moments			
	QM	additive	Drude	exper	QM	additive	Drude
Cyclopentane (CPEN)							
C2	0.00	0.00	0.00	0.02	0.05	0.02	
Cs	0.00	0.00	0.00	0.02	0.05	0.02	
D5h	6.07	4.57	3.76	0.00	0.00	0.00	
Cyclohexane (CHEX)							
chair	0.00	0.00	0.00	0.00	0.00	0.00	
twist	6.17	6.52	6.58	0.00	0.00	0.00	
Tetrahydrofuran (THF)							
C2	0.00	0.00	0.00	1.75	1.78	1.97	1.69
Cs	0.15	0.30	0.15	1.75	1.56	2.12	1.78
C2v	4.47	3.34	2.84	1.77	1.99	1.70	
Tetrahydropyran (THP)							
chair	0.00	0.00	0.00	1.58	1.44	2.03	1.58
twist25	5.67	5.62	5.22	1.43	2.03	1.61	
twist14	6.74	6.32	6.48	1.63	1.98	1.67	
boat25	6.76	6.53	6.42	1.33	1.98	1.62	
boat14	7.48	7.01	6.41	1.62	2.05	1.64	
Diethyl Ether (DEE)							
tt	0.00	0.00	0.00	1.15	1.11	1.81	1.20
gt	1.36	1.37	1.52	1.21	1.79	1.23	
gg	2.66	2.94	3.24	1.29	1.78	1.21	
Methyl Ethyl Ether (MEE)							
t	0.00	0.00	0.00	1.17	1.19	1.84	1.25
g	1.38	1.40	1.53	1.30	1.81	1.27	
Dimethyl Ether (DME)							
s	0.00	0.00	0.00	1.30	1.29	1.86	1.30
Dimethoxyethane (DMOE)							
ttt	0.00	0.00	0.00	0.00	0.00	0.00	
gg't	0.21	0.25	0.37	1.64	2.04	1.45	
tgt	0.26	0.90	0.03	1.35	2.30	1.67	
gtt	1.41	1.35	1.19	1.64	2.37	1.66	
tgg	1.50	2.47	1.29	2.40	3.64	2.46	
ggg	1.51	3.47	2.35	1.20	2.66	1.86	
ggg'	1.68	1.66	1.62	1.91	2.55	1.84	
gtg'	2.84	2.48	2.41	0.00	0.00	0.00	
gtg	2.91	2.63	2.30	2.19	3.10	2.12	

^a Relative energies are in kcal/mol; dipole moments are in Debye. Experimental data are from ref 1. QM data are from MP2/cc-pVTZ//MP2/6-31G(d) calculations.

Supporting Information support the ability of the empirical models to reproduce the target QM data.

Dipole moments of the selected conformations of the model compounds are also included in Table 6. In all cases the values for the additive model overestimate the experimental and QM target values. This is expected due to the need to implicitly overpolarize the additive model as required for treating the condensed phase due to the omission of explicit polarizability in the model.³⁹ With the polarizable model, the empirical values are in good agreement with the target values, a clear advantage of the polarizable model over the additive model that is anticipated to play an important role when the model is applied to environments of different polarities. There is a tendency of the polarizable model to underestimate the change in the dipole as function of

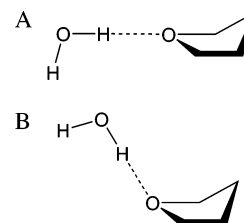


Figure 2. Interaction orientations of the C2 conformer of THF with water for the (A) orientation O1_180, where the water molecule is in the C–O1–C plane and (B) orientation O1_120 where the H atom of water molecule is oriented toward the lone pair position.

conformation (e.g., THP and DMOE) although this trend is within acceptable limits.

Interactions of the ethers with individual water molecules (Table 4) are worth additional discussion. Overall, the empirical values are less favorable than the target scaled HF/6-31G(d) or LMP2/cc-pVQZ(-f)//MP2/6-31G(d) QM target data for the additive and polarizable models, respectively. This is despite the additive model overestimating the dipole moments, while the polarizable models are in good agreement with the target QM and experimental data. Moreover, the condensed-phase properties are also generally in good agreement for the two empirical models. This discrepancy may be associated with the assumption in the present work that aliphatic LJ parameters are applied to the carbons adjacent to the oxygens, whereas it may be more appropriate to use “smaller” radii due to a more polar nature of these atoms. Consistent with this is the magnitude of the less favorable empirical versus QM values being smaller for the cyclic ethers relative to the linear ethers, suggesting that the constrained nature of the ring may minimize secondary interactions of the water with the surrounding aliphatic groups.

Other interesting trends in the ether–water interactions are the minimum interaction distances and the relative energies of the linear (i.e., O_180, Figure 2) and the lone pair (i.e., O_120) interactions. Overall, the empirical interaction distances are shorter than the QM values, as required to obtain the correct condensed-phase properties as previously discussed.³⁹ The differences are generally less in the polarizable model. This is due in part to the use of MP2 for the treatment of electron correlation in the respective target data, where the improved treatment of dispersion interactions leads to the QM minimum interaction distances being systematically shorter than the HF results. However, the minimum distances in the polarizable model are systematically longer by approximately 0.05 Å than in the additive model. Thus, the inclusion of the polarization in the force field leads to a decrease in the extent by which the empirical model must underestimate the gas phase to obtain the correct condensed-phase properties, another indication of the capability of the polarizable model to more accurately treat a wider range of environments. Concerning the relative interaction energies of the O_180 versus O_120 orientations, the empirical models typically reproduce the QM relative energies quite well. This is especially true with the polarizable model and is associated, in part, with the inclusion of virtual sites

Table 7. Dielectric Constants of Neat Liquid Cycloalkanes and Ethers^a

molecule	<i>T</i>	exper	additive	error	Drude	error
CPEN	298.15	1.96	1.02 ± 0.00	-0.94	1.63 ± 0.00	-0.33
CHEX	298.15	2.02	1.02 ± 0.00	-1.00	1.66 ± 0.00	-0.36
THF	298.15	7.43	5.42 ± 0.33	-2.01	6.80 ± 0.78	-0.63
THP	298.15	5.54	4.97 ± 0.60	-0.58	5.03 ± 0.20	-0.51
DEE	298.15	4.24	4.96 ± 0.53	0.72	3.53 ± 0.34	-0.71
DMOE	298.15	7.22	6.76 ± 0.74	-0.46	5.61 ± 0.82	-1.60
DME	248.34	6.53	9.71 ± 1.01	3.18	6.36 ± 0.18	-0.17

^a Experimental data are from ref 1.

representative of lone pairs and anisotropic polarizability on the acceptor oxygen atom.

Condensed-Phase Properties. The majority of the discussion in the preceding sections involved the condensed-phase properties, such that only issues not addressed above and additional results will be presented in this section. While the condensed-phase properties are treated in a satisfactory way in both the additive and polarizable models (Tables 2 and 3), there are discrepancies associated with the enforced use of identical parameters for the individual classes studied. Comparison of the differences with respect to experiment indicates the errors to be somewhat smaller for the additive model versus the polarizable model. For example, the average absolute percent differences for the heats of vaporization and molecular volumes are 1.1% and 1.5% for the additive model, respectively, and 1.3% and 2.2% for the polarizable model, respectively. Similarly, the average absolute differences for the free energies of solvation are 0.32 and 0.41 kcal/mol for the additive and polarizable models, respectively. While the increased discrepancies in the polarizable model are somewhat disappointing, it may possibly be attributable to the enforced transfer of the nonbond parameters. By explicitly treating polarization, the electrostatic model is suggested to be more sensitive to subtle changes in chemical structure as compared to the additive model. This additional sensitivity leads to the enforced transferability having a more negative impact in the polarizable model, leading to the poorer agreement with experiment as compared to the additive force field. Consistent with this are studies on polarizable models of the alcohols where, based on a fluctuating charge formalism, different oxygen LJ parameters were required to accurately treat methanol and ethanol,^{78,79} and in a model based on a induced dipole model it was not possible to accurately reproduce the molecular volumes for the alcohol series when the same parameters were applied to the hydroxyl.⁸⁰ However, it should be reiterated that the polarizable model has the clear benefit of more accurately treating gas-phase properties as compared to the additive model while still satisfactorily treating the condensed phase, indicating the capability of the polarizable model to more accurately treat a range of condensed-phase environments from hydrophobic to highly polar.

Beyond the densities and thermodynamic properties several other properties of the ethers in the condensed phase were analyzed. Presented in Table 7 are the dielectric constants for the pure liquids. Overall the polarizable model is in better agreement with experiment, though exceptions are present. With the cyclic alkanes, the polarizable model is significantly

better than the additive model, as expected as the dielectric at infinite frequency of the electric field, which is associated with the electronic polarizability of the model, dominates the total value. For the ethers, the additive model shows some significant variations from experiment, both under- and overestimating those values in the cases of THF and DME, respectively. In the polarizable model there is a systematic trend to underestimate the experimental values, with the largest discrepancy being dimethoxyethane. This trend is associated with the scaling of the polarizabilities. The use of the unscaled polarizabilities tends to increase calculated dielectric constant of both linear and cyclic ethers: e.g. DEE increases from 3.53 to 4.14, just 0.1 less than the experimental value, and THF increases from 6.80 to 8.04, which is ~0.6 greater than the experimental estimate. However, since the remainder of the condensed-phase properties are in satisfactory agreement with experiment, the use of the scaled polarizabilities was maintained. An additional advantage of this choice is the need for such scaling in order to perform condensed-phase simulations of macromolecules. Different approaches have been used to deal with this phenomenon. For example, in the DNA simulation performed in our laboratory it was necessary to scale the polarizabilities by 0.7 to achieve a stable simulation.³² Moreover, in an induced dipole model of proteins it was necessary to damp the polarization response between the side chains of acidic residues, Met and Tyr with TIP4Q water using a screening function,³³ while in a protein fluctuating charge model the hardness values were scaled by 1.15⁸¹ leading to a damping of the polarization response.

One of the significant advantages of the polarizable models is the ability to more accurately treat condensed phases of different polar character as was shown previously for ion distribution near the water–air interface,^{82,83} ion permeation through ion channel proteins,^{84,85} and peptide folding.⁸⁶ To investigate the capability of the model to adapt to different environments, the dipole distributions were obtained for THF and diethyl ether from vacuum, aqueous solution, and pure solvent simulations. Presented in Figure 4A,B are the dipole distributions for THF and DEE for both the additive and polarizable models. For the additive model the dipole distributions are nearly identical for the gas phase, pure solvent, and aqueous solution results, with maxima in the vicinity of 2 and 1.8 Debye for THF and DEE, respectively. Such a result is expected associated with the overestimation of the dipole in the additive model and the lack of polarizability, such that the changes in the dipole moments are only due to changes in the geometry. In contrast, the differences in dipole distributions in the different environments in the polarizable model are significant. The increase in the distributions upon going from the gas to condensed phase is obvious. In the pure solvents the increase in the dipole moment versus gas phase is larger in THF than in DEE, a result consistent with the electrostatic energy contributing 13 versus 7% of the heat of vaporization in these liquids, respectively, such that the larger electrostatic contribution in THF leads to the larger increase in the dipole distribution. Upon going to aqueous solution a similar trend is observed, where the increase in the dipole distribution is

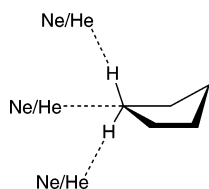


Figure 3. Interaction orientations of the C2 conformer of cyclopentane with the rare gases helium and neon. Only the hydrogens on the carbon interacting with the rare gases are shown for clarity.

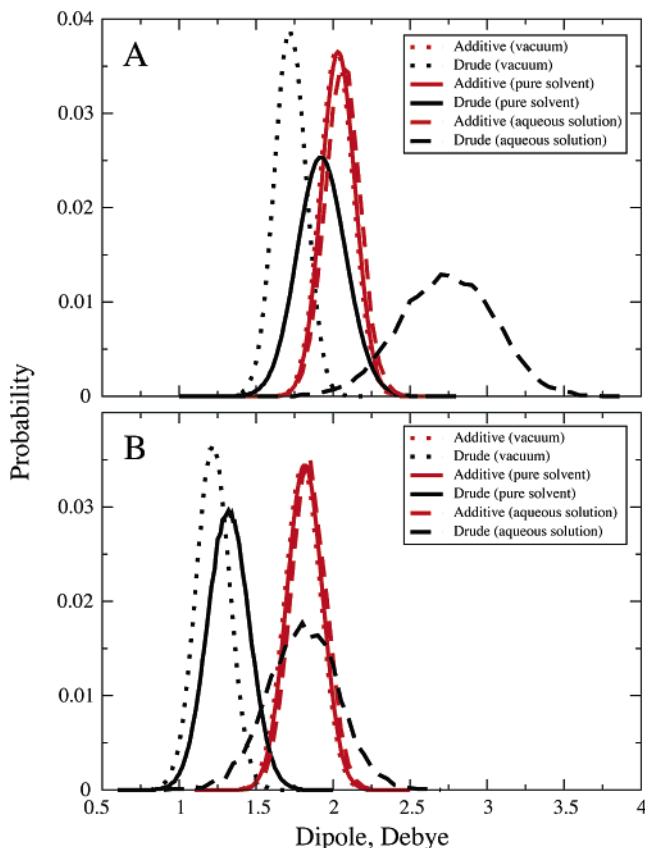


Figure 4. Dipole moment distributions for the gas, pure solvent and aqueous phases of THF (panel A) and DEE (panel B) at 298 K for both additive and Drude polarizable force fields.

larger in THF than in DEE. This is consistent with the electrostatic contribution to the free energies of solvation being -4.3 in THF and -3.2 kcal/mol in DEE, with the larger electrostatic contribution leading to the larger increase in the dipole distribution. Overall, the dipole moment in THF increases by approximately 1.1 Debye upon going from the gas phase to aqueous solution, while the corresponding value is 0.6 Debye in DEE, consistent with a greater role of electrostatics in THF.

Comparison of the additive versus polarizable dipole distributions is also interesting. As mentioned above, the additive dipole distributions are similar regardless of environment and are larger than the gas-phase values. With THF the additive distributions are slightly greater than that of the polarizable model for the pure solvent but are significantly lower than that of the polarizable dipole distribution in aqueous solution. In contrast with DEE, the additive dipole distributions are significantly higher than that of the polariz-

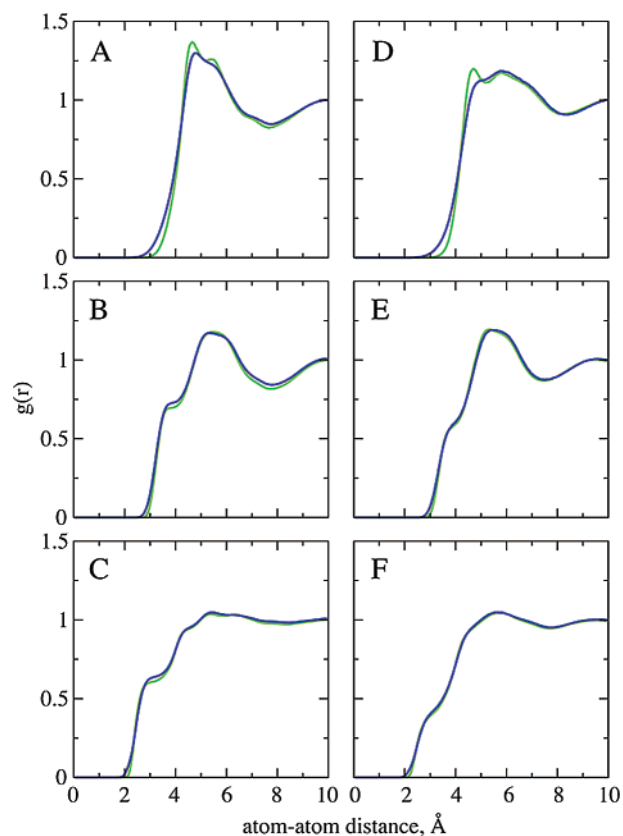


Figure 5. Radial distribution functions (RDF) for neat liquid THF (panels A–C) and DEE (panels D–F) at 298 K. O···O (A and D), C···O (B and E), and O···H (C and F) RDFs are shown for both the Drude (blue line) and additive (green line) models.

able pure solvent results, while the maxima corresponds with that of the polarizable model in aqueous solution. While the exact meaning of the differences in relative dipole distributions in the additive versus polarizable models for THF vs DEE is difficult to interpret, the observations further emphasize the utility of the polarizable models in being more responsive to the polarity of the environment as well as the inherent limitation of the additive model in treating condensed-phase properties. Last, the results indicate a more important role of electrostatics in the condensed-phase properties of THF versus DEE, consistent with the differences observed in linear versus cyclic alkanes discussed above.

An important feature of empirical force field based calculations is that ability to obtain an atomic detail picture of condensed phases, a picture that is often difficult to obtain via experimental methods. To investigate whether the polarizable model was giving a significantly different atomic detail picture as compared to the additive models, radial distribution functions (RDF) for the THF and DEE pure solvents were analyzed. For the RDFs involving the atoms in the aliphatic moieties (i.e., C–C, C–H, and H–H RDFs) the results were very similar, though not identical, for the two models (not shown). However, RDFs involving the oxygen atom did show some differences. Presented in Figure 5 are the O–O, O–C, and O–H RDFs for both DEE and THF. In all three plots the RDF shows sampling at shorter distances in the polarizable model. This is interesting when one considers that the minimum interaction energy distances

Table 8. Pure Solvent Properties for Test Compounds^e

	experiment	additive	%err	Drude	%err
Molecular Volumes, Å ³					
MPE	171.3^a	173.5 ± 0.7	1.3	172.8 ± 1.1	0.9
MBE	198.0^a	200.1 ± 1.2	1.1	199.0 ± 0.7	0.5
EPE	200.3^a	200.4 ± 0.7	0.0	199.6 ± 0.9	-0.3
MTHF	166.7^c	163.0 ± 0.6	-2.2	162.5 ± 0.4	-2.5
Heats of Vaporization, kcal/mol					
MPE	6.60^b	6.70 ± 0.07	1.6	6.60 ± 0.12	0.0
MBE	7.74^b	7.87 ± 0.11	1.7	7.75 ± 0.12	0.1
EPE	7.51^b	7.86 ± 0.09	4.7	7.80 ± 0.12	3.8
MTHF	8.13^d	8.66 ± 0.05	6.5	8.82 ± 0.05	8.5

^a Experimental data are from ref 90. ^b Experimental data are from ref 1. ^c Experimental data are from ref 87. ^d Experimental data are from ref 91. ^e Abbreviations: MPE – methyl propyl ether, MBE – methyl butyl ether, EPE – ethyl propyl ether, MTHF – 2-methyl tetrahydrofuran.

for the interactions of water with the ether oxygens are systematically longer in the polarizable model (Table 4), suggesting that the explicit inclusion of polarizability in the model leads to “softer” interactions of the oxygen with its environment despite the use of the LJ 6-12 model to treat dispersion and exchange-repulsion in both models. Additional differences are evident in the two models at longer distances in the RDFs with the most obvious occurring in the O...O RDF. In the additive model there is a well-defined peak at 4.6 Å followed by a second peak at 5.5 Å. In contrast, the polarizable model has a broader, single peak with the maximum at 4.8 Å followed the broad peak with evidence of a small depression in the peak at 5.2 Å. Thus, the polarizable model is giving a different atomic detail picture as compared to the additive model in addition to differences in the dipole distributions and other properties discussed above.

3.E. Validation of the Developed Force Field. To validate the developed ether force field pure solvent calculations were performed on additional model compounds, including longer chain linear ethers (methyl propyl ether, methyl butyl ether, and ethyl propyl ether) and 2-methyl THF. The results are presented in Table 8. For the new compounds, the molecular volumes and most heats of vaporization are in satisfactory agreement with experimental values. For the linear ethers the largest differences are in the heats of vaporization of ethyl propyl ether which are overestimated by 4.7 and 3.8% in the additive and the Drude models, respectively, similar to the overestimation observed for DEE (Table 2). With the only cyclic test molecule, the molecular volumes are somewhat underestimated, and the heats of vaporization are overestimated with both force fields. The significant overestimation of the heat of vaporization may be associated with the addition of a methyl group on the carbon adjacent to the ether oxygen. While the origins and possible solution of these differences are beyond the scope of the present work, the overall quality of the agreement with experiment for the test molecules demonstrates the transferability of the developed LJ and electrostatic parameters.

4. Conclusion

Presented are both additive and polarizable force fields for linear and cyclic ethers. The initial stage of the optimization was the evaluation of the linear alkane parameters in cycloalkanes. While the linear alkane parameters transferred well to cyclohexane, they were not appropriate for cyclopentane. This is indicated to be due to strain in the smaller ring leading to the need for alternative LJ parameters for that model. In addition, for the polarizable model it was observed that the charges and polarizabilities from the linear alkanes were not appropriate for both cycloalkanes, requiring explicit determination of the electrostatic parameters via the QM fitting procedure followed by scaling of the polarizabilities by 0.7. These steps are suggested to be due to the cyclic alkanes having a more polar character due to more correlated electronic effects associated with their cyclic structures.

The alkane parameters were then used directly in the ethers, with the new cyclopentane based parameters used in THF, with the only LJ parameters optimized being those of oxygen. In the additive models, the charges on the oxygen, with appropriate adjustments of the adjacent carbons, were optimized based on interactions with water, while the charges were determined via the QM ESP approach for the polarizable model. Selected internal parameters, primarily associated with dihedrals, were optimized as required. To facilitate the transferability of the parameters, the LJ parameters and electrostatic parameters for all the linear ethers were constrained to be identical for the respective electrostatic models. However, due to the ring strain discussed above, the electrostatic parameters of THF were allowed to differ from THP, although in the additive model the same charge was found to be appropriate for both compounds. Further, the LJ parameters of the oxygens were identical for all ethers of a given electrostatic model.

Optimization of the parameters based on the above restraints yielded models that are in satisfactory agreement with both pure solvent properties and free energies of aqueous solvation. As is typical for additive models, this was achieved via implicit overpolarization of the charge distribution such that the gas-phase dipole moments and interactions with water were overestimated. In contrast, the polarizable model allowed both gas phase and condensed-phase properties to be reproduced reasonably well. This represents a major advantage of the polarizable model that should allow it to more accurately treat ethers in a wider variety of environments ranging from hydrophobic to aqueous solution. This is emphasized by the changes in the dipole distribution of THF and DEE in MD simulations of the gas phase, in aqueous solution, and in the pure solvents. In addition, RDFs show that differences in the atomic interactions, especially those involving the oxygens, occur in the polarizable versus additive models.

Somewhat disappointing is the inability of the polarizable model to yield overall improvements in condensed-phase properties as compared to the additive model. Given the extra degrees of freedom in the polarizable model it would be assumed that improved agreement should be achieved. The reason this was not achieved is suggested to be due to the restraints in the parametrization enforced to facilitate trans-

ferability. Due to the polarizable electrostatic model being more sensitive to the environment, including intramolecular contributions, the use of the restraints in the parameters appears to have a larger negative impact than in the additive model, where the electrostatic properties are not affected by the environment. Future studies will address this issue.

Acknowledgment. Financial support from the NIH (GM51501 and GM72558) is acknowledged, and the DOD ACS Major Shared Resource Computing and PSC Pittsburgh Supercomputing Center are thanked for their generous CPU allocations.

Supporting Information Available: Optimized force field parameters; experimental, QM and CHARMM calculated molecular geometries, and vibrational frequencies; QM and force field based torsional energy profiles. This material is available free of charge via the Internet at <http://pubs.acs.org>.

References

- (1) *CRC Handbook Chemistry and Physics*, 84th ed.; Lide, D. R., Ed.; CRC Press: Boca Raton, 2003; p 2616.
- (2) Kelly, C. P.; Cramer, C. J.; Truhlar, D. G. *J. Chem. Theory Comput.* **2005**, *1*, 1133.
- (3) Halgren, T. A. *J. Comput. Chem.* **1996**, *17*, 490.
- (4) Allinger, N. L.; Chen, K. H.; Lii, J. H.; Durkin, K. A. *J. Comput. Chem.* **2003**, *24*, 1447.
- (5) Lii, J. H.; Chen, K. H.; Allinger, N. L. *J. Phys. Chem. A* **2004**, *108*, 3006.
- (6) Lii, J. H.; Chen, K. H.; Allinger, N. L. *J. Comput. Chem.* **2003**, *24*, 1504.
- (7) Lii, J. H.; Chen, K. H.; Durkin, K. A.; Allinger, N. L. *J. Comput. Chem.* **2003**, *24*, 1473.
- (8) Lii, J. H.; Chen, K. H.; Grindley, T. B.; Allinger, N. L. *J. Comput. Chem.* **2003**, *24*, 1490.
- (9) Briggs, J. M.; Matsui, T.; Jorgensen, W. L. *J. Comput. Chem.* **1990**, *11*, 958.
- (10) Jorgensen, W. L.; Maxwell, D. S.; Tirado-Rives, J. *J. Am. Chem. Soc.* **1996**, *118*, 11225.
- (11) Helfrich, J.; Hentschke, R. *Macromolecules* **1995**, *28*, 3831.
- (12) Girard, S.; Muller-Plathe, F. *Mol. Phys.* **2003**, *101*, 779.
- (13) Faller, R.; Schmitz, H.; Biermann, O.; Muller-Plathe, F. *J. Comput. Chem.* **1999**, *20*, 1009.
- (14) Cornell, W. D.; Cieplak, P.; Bayly, C. I.; Gould, I. R.; Merz, K. M.; Ferguson, D. M.; Spellmeyer, D. C.; Fox, T.; Caldwell, J. W.; Kollman, P. A. *J. Am. Chem. Soc.* **1995**, *117*, 5179.
- (15) Weiner, S. J.; Kollman, P. A.; Case, D. A.; Singh, U. C.; Ghio, C.; Alagona, G.; Profeta, S.; Weiner, P. *J. Am. Chem. Soc.* **1984**, *106*, 765.
- (16) Weiner, S. J.; Kollman, P. A.; Nguyen, D. T.; Case, D. A. *J. Comput. Chem.* **1986**, *7*, 230.
- (17) Borodin, O.; Smith, G. D. *J. Phys. Chem. B* **2003**, *107*, 6801.
- (18) Borodin, O.; Smith, G. D. *J. Phys. Chem. B* **2006**, *110*, 6279.
- (19) Bedrov, D.; Smith, G. D. *J. Phys. Chem. B* **1999**, *103*, 10001.
- (20) Bedrov, D.; Smith, G. D. *J. Phys. Chem. B* **1999**, *103*, 3791.
- (21) Bedrov, D.; Pekny, M.; Smith, G. D. *J. Phys. Chem. B* **1998**, *102*, 996.
- (22) Bedrov, D.; Borodin, O.; Smith, G. D. *J. Phys. Chem. B* **1998**, *102*, 5683.
- (23) Bedrov, D.; Borodin, O.; Smith, G. D. *J. Phys. Chem. B* **1998**, *102*, 9565.
- (24) Foloppe, N.; MacKerell, A. D., Jr. *J. Comput. Chem.* **2000**, *21*, 86.
- (25) Klauda, J. B.; Brooks, B. R.; MacKerell, A. D., Jr.; Venable, R. M.; Pastor, R. W. *J. Phys. Chem. B* **2005**, *109*, 5300.
- (26) MacKerell, A. D., Jr.; Wiykiewicz-Kuczera, J.; Karplus, M. *J. Am. Chem. Soc.* **1995**, *117*, 11946.
- (27) MacKerell, A. D., Jr.; Bashford, D.; Bellott, M.; Dunbrack Jr., R. L.; Evanseck, J.; Field, M. J.; Fischer, S.; Gao, J.; Guo, H.; Ha, S.; Joseph, D.; Kuchnir, L.; Kuczera, K.; Lau, F. T. K.; Mattos, C.; Michnick, S.; Ngo, T.; Nguyen, D. T.; Prodhom, B.; Reiher, I.; W. E.; Roux, B.; Schlenkrich, M.; Smith, J.; Stote, R.; Straub, J.; Watanabe, M.; Wiorkiewicz-Kuczera, J.; Yin, D.; Karplus, M. *J. Phys. Chem. B* **1998**, *102*, 3586.
- (28) Lamoureux, G.; Harder, E.; Vorobyov, I. V.; Roux, B.; MacKerell, A. D., Jr. *Chem. Phys. Lett.* **2006**, *418*, 245.
- (29) Lamoureux, G.; MacKerell, A. D., Jr.; Roux, B. *J. Chem. Phys.* **2003**, *119*, 5185.
- (30) Vorobyov, I. V.; Anisimov, V. M.; MacKerell, A. D., Jr. *J. Phys. Chem. B* **2005**, *109*, 18988.
- (31) Lopes, P. E. M.; Lamoureux, G.; Roux, B.; MacKerell, A. D., Jr. *J. Chem. Theory Comput.* **2007**, *3*, in press.
- (32) Anisimov, V. M.; Lamoureux, G.; Vorobyov, I. V.; Huang, N.; Roux, B.; MacKerell, A. D., Jr. *J. Chem. Theory Comput.* **2005**, *1*, 153.
- (33) Harder, E.; Anisimov, V. M.; Vorobyov, I. V.; Lopes, P. E. M.; Noskov, S. Y.; MacKerell, A. D., Jr.; Roux, B. *J. Chem. Theory Comput.* **2006**, *2*, 1587.
- (34) Frisch, M. J.; Trucks, G. W.; Robb, M. A.; Scuseria, G. E.; Schlegel, H. B.; Cheeseman, J. R.; Montgomery, J. J. A.; Vreven, T.; Kudin, K. N.; Burant, J. C.; Millam, J. M.; Iyengar, S. S.; Tomasi, J.; Barone, V.; Mennucci, B.; Cossi, M.; Scalmani, G.; Rega, N.; Petersson, G. A.; Nakatsuji, H.; Hada, M.; Ehara, M.; Toyota, K.; Fukuda, R.; Hasegawa, J.; Ishida, M.; Nakajima, T.; Honda, Y.; Kitao, O.; Nakai, H.; Klene, M.; Li, X.; Knox, J. E.; Hratchian, H. P.; Cross, J. B.; Bakken, V.; Adamo, C.; Jaramillo, J.; Gomperts, R.; Stratmann, R. E.; Yazyev, O.; Austin, A. J.; Cammi, R.; Pomelli, C.; Ochterski, J. W.; Ayala, P. Y.; Morokuma, K.; Voth, G. A.; Salvador, P.; Dannenberg, J. J.; Zakrzewski, V. G.; Dapprich, S.; Daniels, A. D.; Strain, M. C.; Farkas, O.; Malick, D. K.; Rabuck, A. D.; Raghavachari, K.; Foresman, J. B.; Ortiz, J. V.; Cui, Q.; Baboul, A. G.; Clifford, S.; Cioslowski, J.; Stefanov, B. B.; Liu, G.; Liashenko, A.; Piskorz, P.; Komaromi, I.; Martin, R. L.; Fox, D. J.; Keith, T.; Al-Laham, M. A.; Peng, C. Y.; Nanayakkara, A.; Challacombe, M.; Gill, P. M. W.; Johnson, B.; Chen, W.; Wong, M. W.; Gonzalez, C.; Pople, J. A. *Gaussian 03, Revision C.02*; Gaussian, Inc.: Wallingford, CT, 2004.
- (35) Foloppe, N.; Nilsson, L.; MacKerell, A. D., Jr. *Biopolymers (Nucleic Acid Sciences)* **2002**, *61*, 61.
- (36) Greene, S.; Guvench, O.; MacKerell, A. D., Jr. unpublished data, 2006.
- (37) Woodcock, H. L.; Moran, D.; Pastor, R. W.; MacKerell, A. D., Jr.; Brooks, B. R. *Biophys. J.*, in press.

- (38) Yin, D.; MacKerell, A. D., Jr. *J. Comput. Chem.* **1998**, *19*, 334.
- (39) MacKerell, A. D., Jr. *J. Comput. Chem.* **2004**, *25*, 1584.
- (40) *Jaguar*, 4.2 ed.; Schrodinger, Inc.: Portland, OR, 2000.
- (41) Huang, N.; MacKerell, A. D., Jr. *J. Phys. Chem. B* **2002**, *106*, 7820.
- (42) Saebo, S.; Pulay, P. *Annu. Rev. Phys. Chem.* **1993**, *44*, 213.
- (43) Saebo, S.; Tong, W.; Pulay, P. *J. Chem. Phys.* **1993**, *98*, 2170.
- (44) Allen, F. H. *Acta Crystallogr. B* **2002**, *58*, 380.
- (45) CCDC. *Vista - A Program for the Analysis and Display of Data Retrieved from the CSD*; Cambridge Crystallographic Data Centre: Cambridge, England, 1994.
- (46) MacKerell, A. D.; Jr.; Brooks, B.; Brooks, C. L., III; Nilsson, L.; Roux, B.; Won, Y.; Karplus, M. CHARMM: The Energy Function and Its Parameterization with an Overview of the Program. In *Encyclopedia of Computational Chemistry*; Schleyer, P. v. R., Allinger, N. L., Clark, T., Gasteiger, J., Kollman, P. A., Schaefer, H. F., III, Schreiner, P. R., Eds.; John Wiley & Sons: Chichester, 1998; Vol. 1, p 271.
- (47) Brooks, B. R.; Brucoleri, R. E.; Olafson, B. D.; States, D. J.; Swaminathan, S.; Karplus, M. *J. Comput. Chem.* **1983**, *4*, 187.
- (48) Thole, B. T. *Chem. Phys.* **1981**, *59*, 341.
- (49) Dixon, R. W.; Kollman, P. S. *J. Comput. Chem.* **1997**, *18*, 1632.
- (50) Miller, K. J. *J. Am. Chem. Soc.* **1990**, *112*, 8533.
- (51) Lamoureux, G.; Roux, B. *J. Chem. Phys.* **2003**, *119*, 3025.
- (52) Ryckaert, J. P.; Ciccotti, G.; Berendsen, H. J. C. *J. Comput. Phys.* **1977**, *23*, 327.
- (53) Darden, T.; York, D.; Pedersen, L. *J. Chem. Phys.* **1993**, *98*, 10089.
- (54) Steinbach, P. J.; Brooks, B. R. *J. Comput. Chem.* **1994**, *15*, 667.
- (55) Allen, M. P.; Tildesley, D. J. *Computer Simulation of Liquids*; Clarendon Press: Oxford, 1987; p 408.
- (56) Lague, P.; Pastor, R. W.; Brooks, B. R. *J. Phys. Chem. B* **2004**, *108*, 363.
- (57) Ben-Naim, A. *Statistical Thermodynamics for Chemists and Biochemists*; Plenum Press: New York, 1992; p 720.
- (58) Bonin, K. D.; Kresin, V. V. *Electric-dipole polarizabilities of atoms, molecules, and clusters*; World Scientific: Singapore River Edge, NJ, 1997; p 247.
- (59) Kollman, P. A. *Chem. Rev.* **1993**, *93*, 2395.
- (60) Simonson, T. Free Energy Calculations. In *Computational Biochemistry and Biophysics*; Becker, O. M., MacKerell, A. D., Jr., Roux, B., Watanabe, M., Eds.; Marcel Dekker, Inc.: New York, 2001; p 169.
- (61) Deng, Y.; Roux, B. *J. Phys. Chem. B* **2004**, *108*, 16567.
- (62) Kumar, S.; Bouzida, D.; Swendsen, R. H.; Kollman, P. A.; Rosenberg, J. M. *J. Comput. Chem.* **1992**, *13*, 1011.
- (63) Boatz, J. A.; Gordon, M. S.; Hilderbrandt, R. L. *J. Am. Chem. Soc.* **1988**, *110*, 352.
- (64) Bader, R. F. W.; Carroll, M. T.; Cheeseman, J. R.; Chang, C. *J. Am. Chem. Soc.* **1987**, *109*, 7968.
- (65) Wiberg, K. B.; Bader, R. F. W.; Lau, C. D. H. *J. Am. Chem. Soc.* **1987**, *109*, 1001.
- (66) Borodin, O.; Smith, G. D. *J. Phys. Chem. B* **2006**, *110*, 6293.
- (67) Strajbl, M.; Florian, J. *Theor. Chem. Acc.* **1998**, *99*, 166.
- (68) Strajbl, M.; Baumruk, V.; Florian, J. *J. Phys. Chem. B* **1998**, *102*, 1314.
- (69) Rayon, V. M.; Sordo, J. A. *J. Chem. Phys.* **2005**, *122*, 204303.
- (70) Gallinella, E.; Cadioli, B.; Flament, J. P.; Berthier, G. *J. Mol. Struct. (Theochem)* **1994**, *121*, 137.
- (71) Cadioli, B.; Gallinella, E.; Coulombeau, C.; Jobic, H.; Berthier, G. *J. Phys. Chem.* **1993**, *97*, 7844.
- (72) Berthier, G.; Cadioli, B.; Gallinella, E.; Aamouche, A.; Ghomi, M. *J. Mol. Struct. (Theochem)* **1997**, *390*, 11.
- (73) Berthier, G.; Cadioli, B.; Gallinella, E. *Theor. Chem. Acc.* **2000**, *104*, 223.
- (74) Freeman, F.; Kasner, M. L.; Hehre, W. J. *J. Phys. Chem. A* **2001**, *105*, 10123.
- (75) Freeman, F.; Kasner, J. A.; Kasner, M. L.; Hehre, W. J. *J. Mol. Struct. (Theochem)* **2000**, *496*, 19.
- (76) Ionescu, A. R.; Berces, A.; Zgierski, M. Z.; Whitfield, D. M.; Nukada, T. *J. Phys. Chem. A* **2005**, *109*, 8096.
- (77) Halgren, T. A. *J. Comput. Chem.* **1999**, *20*, 730.
- (78) Patel, S.; Brooks, C. L. *J. Chem. Phys.* **2005**, *122*, 024508.
- (79) Patel, S.; Brooks, C. L. *J. Chem. Phys.* **2005**, *123*, 164502.
- (80) Gao, J. L.; Habibollazadeh, D.; Shao, L. *J. Phys. Chem.* **1995**, *99*, 16460.
- (81) Patel, S.; Brooks, C. L., III. *J. Comput. Chem.* **2004**, *25*, 1.
- (82) Archontis, G.; Leontidis, E.; Andreou, G. *J. Phys. Chem. B* **2005**, *109*, 17957.
- (83) Jungwirth, P.; Tobias, D. J. *Chem. Rev.* **2006**, *106*, 1259.
- (84) Allen, T. W.; Andersen, O. S.; Roux, B. *Proc. Natl. Acad. Sci. U.S.A.* **2004**, *101*, 117.
- (85) Allen, T. W.; Andersen, O. S.; Roux, B. *Biophys. Chem.* **2006**, *124*, 251.
- (86) Soto, P.; Mark, A. E. *J. Phys. Chem. B* **2002**, *106*, 12830.
- (87) Poling, B. E.; Prausnitz, J. M.; O'Connell, J. P. *The properties of gases and liquids*, 5th ed.; McGraw-Hill: New York, 2001; p 752.
- (88) Wu, J. T.; Liu, Z. G.; Bi, S. S.; Meng, X. Y. *J. Chem. Eng. Data* **2003**, *48*, 426.
- (89) Liu, Z. Y.; Chen, Z. C. *Chem. Eng. J. Bioch. Eng.* **1995**, *59*, 127.
- (90) Obama, M.; Oodera, Y. *J. Chem. Eng. Data* **1985**, *30*, 1.
- (91) Chicos, J. S.; Acree, W. E., Jr. *J. Phys. Chem. Ref. Data* **2003**, *32*, 519.

Improved Boundary Element Methods for Poisson–Boltzmann Electrostatic Potential and Force Calculations

Benzhuo Lu^{*,†,‡,§} and J. Andrew McCammon^{†,‡,§,||}

*Howard Hughes Medical Institute, Center for Theoretical Biological Physics,
Department of Chemistry and Biochemistry, and Department of Pharmacology,
University of California at San Diego, La Jolla, California 92093-0365*

Received January 3, 2007

Abstract: A patch representation differing from the traditional treatments in the boundary element method (BEM) is presented, which we call the constant “node patch” method. Its application to solving the Poisson–Boltzmann equation (PBE) demonstrates considerable improvement in speed compared with the constant element and linear element methods. In addition, for the node-based BEMs, we propose an efficient interpolation method for the calculation of the electrostatic stress tensor and PB force on the solvated molecular surface. This force calculation is simply an $O(N)$ algorithm (N is the number of elements). Moreover, our calculations also show that the geometric factor correction in the boundary integral equations significantly increases the accuracy of the potential solution on the boundary, and thereby the PB force calculation.

1. Introduction

In the 20 years since the first boundary element method (BEM) paper on continuum electrostatics of biological systems,¹ computational scientists have made extensive contributions to the methodological generalization, optimization, and performance improvements in this area. These works include the extension from solving the Poisson equation (PE) and the linear Poisson–Boltzmann equation (PBE),^{2,3} to solving the nonlinear PBE,^{4–6} from the single molecule case to that of two or more molecules,^{7–9} the implementation of accelerating techniques,^{9–16} studies on the conditioning of the produced linear system,^{9,14,17} the method for rigorous force calculations,^{8,9,18} and applications to molecular mechanics or dynamics simulation.^{19–22} However, the practical utility of BEM is still very limited in biological electrostatic studies, though it has been widely recognized in engineering applications. Despite its high accuracy of solution and the reduction of system degrees of freedom

relative to other numerical approaches such as the finite difference and finite element methods, BEM has its own difficulties: challenges of mesh generation for biomolecules, singular and hypersingular surface integrals, and numerous integral operations. The main hurdle to its practical usage is the speed. We recently made progress on this by using a new version of the fast multipole method (FMM)⁹ to achieve a CPU performance comparable or even superior to that of some other numerical methods. This work also focuses on the speed improvement. Two typical low-order BEMs are the constant element method (unknowns are constant in each element) and the linear element method (unknowns are located at the nodes of an element). In this work, we construct a boundary “patch” (or element) differing from the normal facet patch (e.g., triangular element) based on the same mesh and also make a constant unknown approximation in this patch. We call this the constant “node patch” method and demonstrate that this method allows considerable acceleration of the BEM calculation and maintains a similar calculation accuracy. In addition, the details of a fast interpolation method are given for the PB force calculation for the node-based BEMs including the linear element methods and our node patch method. This interpolation method is simply of order N and much faster than our previous $O(N^2)$ algo-

* Corresponding author phone: 858-822-0168; fax: 858-534-4974; e-mail: blu@mccammon.ucsd.edu.

† Howard Hughes Medical Institute.

‡ Center for Theoretical Biological Physics.

§ Department of Chemistry and Biochemistry.

|| Department of Pharmacology.

arithms.^{8,18} Finally, we also show that the geometric correction to the normal boundary integral equation (nBIE) leads to a much more accurate potential solution, and thereby a much more accurate force calculation.

2. Boundary Integral Equation

2.1. Normal Boundary Integral Equation. In the widely used BEMs to solve the PBE (see refs 2 and 7), the electrostatic potential is expressed as a boundary integral form

$$\phi_p^{\text{int}} = \oint_S \left[G_{pt} \frac{\partial \phi_t^{\text{int}}}{\partial n} - \frac{\partial G_{pt}}{\partial n} \phi_t^{\text{int}} \right] dS_t + \frac{1}{D_{\text{int}}} \sum_k q_k G_{pk}, \quad p, k \in \Omega \quad (1)$$

$$\phi_p^{\text{ext}} = \oint_S \left[-u_{pt} \frac{\partial \phi_t^{\text{ext}}}{\partial n} + \frac{\partial u_{pt}}{\partial n} \phi_t^{\text{ext}} \right] dS_t, \quad p \in \bar{\Omega} \quad (2)$$

where ϕ_p^{int} is the potential at position p inside the molecular domain Ω , q_k is the k th source point charge of the molecule, $S = \partial\Omega$ is its boundary, e.g., solvent-accessible surface, ϕ_p^{ext} is the potential at position p outside domain Ω , D_{int} (D_{ext}) is the interior (exterior) dielectric constant, and n is the outward normal vector at the integral point t . G and u are the fundamental solutions of the PE and the PBE, respectively, where r_{pq} denotes the distance between two points p and q

$$G_{pq} = \frac{1}{4\pi\epsilon r_{pq}} \quad (3)$$

$$u_{pq} = \exp(-\kappa r_{pq}) / 4\pi\epsilon r_{pq} \quad (4)$$

and κ is the reciprocal of the Debye–Hückel screening length determined by the ionic strength of the solution.

When point p approaches surface S , and the boundary conditions $\phi^{\text{int}} = \phi^{\text{ext}}$ and $D_{\text{int}}(\nabla\phi^{\text{int}} \cdot n) = D_{\text{ext}}(\nabla\phi^{\text{ext}} \cdot n)$ are considered, eqs 1 and 2 become a set of self-consistent boundary integral equations (denoted as nBIEs)

$$\frac{1}{2} f_p = \oint_S^{\text{PV}} \left[\epsilon G_{pt} h_t - \frac{\partial G_{pt}}{\partial n} f_t \right] dS_t + \frac{1}{D_{\text{int}}} \sum_k q_k G_{pk}, \quad p \in S \quad (5)$$

$$\frac{1}{2} f_p = \oint_S^{\text{PV}} \left[-u_{pt} h_t + \frac{\partial u_{pt}}{\partial n} f_t \right] dS_t, \quad p \in S \quad (6)$$

where PV denotes the principal value integral to avoid the singular point when $t \rightarrow p$ in the integral equations, $f = \phi^{\text{ext}}$, $h = \nabla\phi^{\text{ext}} \cdot n$, and $\epsilon = D_{\text{ext}}/D_{\text{int}}$.

In our former work,⁸ we extended this form to an interacting system with an arbitrary number of molecules and gave a set of corresponding iterative equations for force calculation.

2.2. Geometric Modification. For a nonsmooth boundary as represented by a practically discretized mesh, the following rigorous BIEs can be obtained when p approaches the boundary using a limiting process from the original eqs 1 and 2:

$$\alpha_p f_p = \oint_S^{\text{PV}} \left[\epsilon G_{pt} h_t - \frac{\partial G_{pt}}{\partial n} f_t \right] dS_t + \frac{1}{D_{\text{int}}} \sum_k q_k G_{pk}, \quad p \in S \quad (7)$$

$$(1 - \alpha_p) f_p = \oint_S^{\text{PV}} \left[-u_{pt} h_t + \frac{\partial u_{pt}}{\partial n} f_t \right] dS_t, \quad p \in S \quad (8)$$

where the coefficient constant α_p is dependent on the local surface geometry of the node p . For a smooth surface, α_p is $1/2$. For a vertex of a polyhedron, which is not a smooth point of the surface, the coefficient α_p is equal to $A_p/4\pi$, where A_p is the interior solid angle at the node. The constant $1/2$ is as usually used in the previous BEM PB works, but this work will show that the use of the geometry-dependent coefficient does make a significant improvement in the PB solution, especially the potentials on the surface and the PB force on the molecule. For a mesh with flat elements, the interior solid angle at node p can be calculated by the following formula: where n_p is the total number of neighboring elements of p ,

$$A_p = \sum_i^{n_p} \beta_i - (n_p - 2) * \pi \quad (9)$$

and the interior dihedral angle β_i at an attached i th edge formed by two neighboring faces with normal vectors, for example, n_1 and n_2 , respectively, satisfies $\beta_i = \arccos(-n_1 \cdot n_2)$.

There are only weak and strong singular integrals appearing in the above equations, which can be analytically treated by using coordinate transformation and series expansion.^{18,23,24}

2.3. Derivative Boundary Integral Formulation. By linearly combining the derivative forms of eqs 5 and 6, the derivative BIEs (dBIEs) can be obtained:³

$$\left(\frac{1}{2\epsilon} + \frac{1}{2} \right) f_p = \oint_S^{\text{PV}} \left[(G_{pt} - u_{pt}) h_t - \left(\frac{1}{\epsilon} \frac{\partial G_{pt}}{\partial n} - \frac{\partial u_{pt}}{\partial n} \right) f_t \right] dS_t + \frac{1}{D_{\text{ext}}} \sum_k q_k G_{pk}, \quad p \in S \quad (10)$$

$$\left(\frac{1}{2} + \frac{1}{2\epsilon} \right) h_p = \oint_S^{\text{PV}} \left[\left(\frac{\partial G_{pt}}{\partial n_0} - \frac{1}{\epsilon} \frac{\partial u_{pt}}{\partial n_0} \right) h_t - \frac{1}{\epsilon} \left(\frac{\partial^2 G_{pt}}{\partial n_0 \partial n} - \frac{\partial^2 u_{pt}}{\partial n_0 \partial n} \right) f_t \right] dS_t + \frac{1}{D_{\text{ext}}} \sum_k q_k \frac{\partial G_{pk}}{\partial n_0}, \quad p \in S \quad (11)$$

where n is the unit normal vector at point t and n_0 is the unit normal vector at point p .

The dBIEs lead to a well-conditioned system of algebraic equations. These dBIEs have been extended to systems with arbitrary numbers of biomolecules, and the solution has been accelerated with an efficient FMM in our former work.⁹

For a discretized mesh that is not smooth in numerical realization, the geometric correction for dBIEs has not been well-implemented in the BEM PB solver, though we have demonstrated the success of applying hypersingular integration techniques to calculate the gradient of potential on the surface as a postprocessing procedure.¹⁸ The direct evaluation

of all the singular integrals and the other terms such as the additional free terms that appear in the geometrically modified BIEs have been theoretically studied.^{24,25} The implementation including both the free-term modification and the hypersingular integration techniques for the derivative BEM (dBEM) PB solver has not been demonstrated and is beyond the scope of this work.

3. A Constant “Node Patch” Method

One of the methods often used in BEM is that the unknowns f or h on an element (face) are treated as constants. Therefore, the number of unknowns is equal to the number of elements. This is the lowest-order BEM method, the so-called “constant element” approach. This treatment is convenient for numerical implementation. Another widely used treatment is the linear element method, in which f and h at a position in an element are obtained by linear interpolation from the values (unknowns) on the three nodes (for a triangular element). Therefore, the number of unknowns is equal to the number of nodes and is almost half of the number of elements for a triangulated surface (according to Euler’s formula for a polyhedron). The disadvantage of a node-based method is the introduction of additional complexities in numerical implementation. The advantage is that it can achieve better accuracy of the solution and seems to gain higher computational speed because the number of unknowns is reduced by about half.

In either kind of the BEMs, most operations are the far-field integrations. When an element patch ΔS_i (also denoted as its area) is far from the evaluation point p , in the constant element treatment, the boundary integrals on this patch are approximated as

$$\int_{\Delta S_i} G_{pi} h_i dS \approx h_i G_{pi} \Delta S_i \quad (12)$$

$$\int_{\Delta S_i} \frac{\partial G_{pi}}{\partial n} f_i dS \approx f_i \nabla G_{pi} \cdot n_i \Delta S_i \quad (13)$$

where n_i is the unit normal vector of the i th element and the i th position is taken as the element center. In the above formulas, constant approximations of f and h are used, which is the meaning of “constant element” treatment, and the values of function G and its derivative are also approximated as constants on the integral patch because of the far-field approximation. For near-patch integration, a normal quadrature method is used. Similar treatments apply to the integrations for the kernel u and its derivative, as well as for the other second-derivative terms if the dBIEs are used.

Here, we construct a patch around each node, instead of directly using the facet patch (element), and suppose that f and h are constants on this new “node patch”. We call this the constant “node patch” treatment. A simple way to construct these new patches is illustrated in Figure 1 in which an example “node patch” at the i th node that has five neighboring elements is constructed. All the centroids $\{O_l, l = 1, \dots, 5\}$ of the five adjacent triangles and the midpoints $\{C_l, l = 1, \dots, 5\}$ of the attached five edges are listed, and then the area formed by $\{O_1, C_1, O_2, C_2, \dots, O_5, C_5, O_1\}$ is the new patch that we want. Therefore, there is one-third of the area

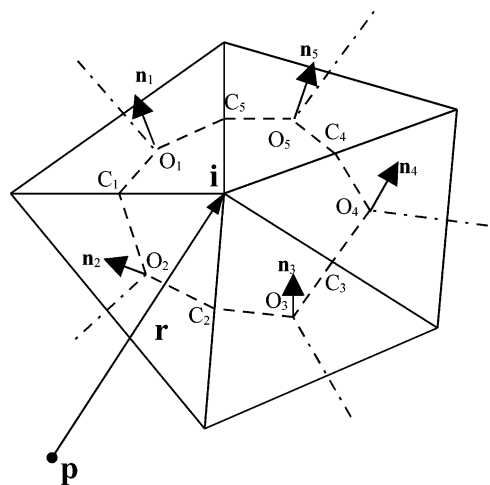


Figure 1. “Node” patch constructed on a triangular mesh. O and n are the centroid and normal vector of an element, respectively, and C is the middle point of an edge.

of each neighboring triangle occupied by the “node patch” ΔS_i . The other patches are similarly constructed. All the node patches connect and cover the whole surface. Now, the far-field integrals on the new patch ΔS_i become

$$\int_{\Delta S_i} G_{pi} h_i dS \approx h_i G_{pi} \Delta S_i^a \quad (14)$$

$$\int_{\Delta S_i} \frac{\partial G_{pi}}{\partial n} f_i dS \approx f_i \nabla G_{pi} \cdot \Delta S_i^b \quad (15)$$

where, supposing all neighboring elements of i th node form a set $\{L\}$,

$$\Delta S_i^a = \frac{1}{3} \sum_{l \in \{L\}} \Delta S_l \quad (16)$$

$$\Delta S_i^b = \frac{1}{3} \sum_{l \in \{L\}} \Delta S_l n_l \quad (17)$$

where n_l is the unit normal vector of the l th neighboring element, ΔS_l is the area of the l th adjacent triangular element, and ΔS_i^b here should also be considered as a vector. As in the constant element treatment, for near-patch integration, a normal quadrature method is used. Similar treatments apply to the integrations for the kernel u and its derivative, as well as for the other second-derivative terms if the dBIEs are used.

There are three main advantages of this “node patch” treatment in the BEM. First, as aforementioned, the unknowns are reduced by almost half relative to the constant element method, and the computational time on solving the resulting linear system in each iteration step or in direct matrix inversion is also reduced by the same factor. The only additional computation is a preprocessing of some geometric coefficients ΔS_i^a and ΔS_i^b as in eqs 16 and 17, which can be saved for repeated usage in the iterative solving procedure. The CPU cost of this preprocessing represents a negligible portion of the whole PBE solution time. However, this time reduction (by about half) due to reduced unknowns in our constant node patch method does not hold in the normal linear element approach, though the number of unknowns

is the same as the number of nodes. The reason is that there are more additional numerical operations (interpolations and quadratures) for the integration on every element. Therefore, in the iterative solving procedure, though the unknowns in the linear element approach are reduced by about half, the total computational time is not reduced much. If direct matrix inversion is used, time saving is expected due to the fact that the linear system size is reduced and all the matrix coefficients are just calculated once; however, the iterative method has to be used for any sizable biological system.

Thus, compared with the constant element method, the constant “node patch” method can save considerable computational time. This will also be demonstrated in numerical tests. And because both methods use similar assumptions (constant f and h in a patch), and are based on the same mesh resolution, there is no loss in the accuracy of the solution. It is worth noting that the linear element treatment that uses linear interpolation to get f and h in a patch instead of using a constant approximation should achieve relatively higher computational accuracy.

The second advantage, which is not so explicit, lies in the case when it is necessary to store the matrix coefficients from the “near points” (local list) integration. The local list is typically given by cutoff criteria or the FMM local neighborhood list output if FMM is implemented. It is found that, relative to the linear element method, our constant “node patch” method tremendously saves time searching and locating the local list in order to store the calculated coefficients in a practical matrix storage format, for example, the Harwell–Boeing sparse matrix format (HB),²⁶ or modified sparse column (row) format. In the linear element treatment, the CPU cost for this part is large enough to be comparable with the whole PBE solution time. The BEM mesh is a kind of unstructured mesh. In the linear element method, each matrix coefficient relates to a node pair (the unknowns are located at nodes), while the local list is normally given as an element list because the integrations are performed on each element and need the nodal value interpolations. Therefore, the node pair information needs to be searched from the element list. Another fact to be considered is that each node is normally shared by several elements; therefore, each matrix coefficient corresponding to a node pair has contributions from the integrations on all the connected elements. Due to these reasons, storing the calculated coefficients (from geometric integrals) requires complex embedded loops to search in both element and node indices to locate the position in the storage frame. For example, four embedded loops in our original implementation are required for the whole matrix storage, which makes the coefficient saving not obviously more efficient than the direct matrix–vector multiplication calculation in every iteration step. However, for our node patch method, or similarly the constant element approach, the local list is also a node list; therefore, the location in the sparse matrix of the coefficient corresponding to each local point is straightforward by counting the local nodes and looking at their indices. This can finally save CPU time in the whole iterative solution procedure.

The third advantage, as with other node-based methods such as the linear element method, is that it is convenient to compute the potential and its gradient (not only the normal derivative) at any position near or on the molecular surface for stress and force calculation through an interpolation method. As shown in the following section, a simple linear interpolation can be performed in a constructed prism, where only the potential f and its normal derivative h on the nodes are required. It might be more complicated to calculate the gradient of potential at an arbitrary surface point in the constant element method.

4. Interpolation Method for Calculation of the Gradient of the Potential

Our previous work^{8,18} introduced two rigorous methods, a variational approach and a hypersingular integral method, for the PB force calculation. Both are order N^2 algorithms. Here, we'll introduce an interpolation method that is simply of order N . In an ionic solution, the full stress tensor on the boundary should include an additional term accounting for the ionic pressure besides the conventional Maxwell stress tensor.²⁷ It is

$$T_{ij} = D_{\text{ext}} E_i E_j - \frac{1}{2} D_{\text{ext}} E^2 \delta_{ij} - \frac{1}{2} D_{\text{ext}} \kappa^2 \phi^2 \delta_{ij} \quad (18)$$

where E is the electrostatic field and δ_{ij} is the Kronecker δ function. Therefore, to obtain the boundary stress tensor, the derivative of the potential, that is, the negative of E on the boundary, should be known.

To get the gradient of the potential on the surface, a potential function in the vicinity of the molecular surface can be constructed using an interpolation method. From the potential data on the nodes of a triangulated surface, we can construct a C^1 or C^2 modeled potential field on the surface, for example, by using piecewise trivariate polynomials that are defined on a three-dimensional triangulation called the simplicial hull and defined over the domain surface.²⁸ Because, in our case, we not only know the potential values but also know their normal derivatives on the nodes, a more efficient and simple way can be taken to construct the approximated potential functions on the surface by using both the potential and its normal derivative values. The idea is to construct a small three-sided prism attached on each triangular element on the surface in which a piecewise interpolated function is defined. The prism is defined by the triangular element and the three normal vectors on the nodes as shown in Figure 2.

A concern that has to be tackled is that the normal vector \mathbf{V} at a node (vertex) on a surface mesh is not defined due to the discontinuity. Hence, the calculation or assignment of this normal vector is not trivial. The normal vector at the node is also required in the node-based dBEMs including the node patch dBEM presented in this work, because the vector n_0 at the point p appears in the dBIEs 10 and 11. Several averaging methods may be used, such as direct averaging from the neighbor facet normals, neighbor angle weighting, neighbor facet area weighting, or using weights from facet normals and supposing adjacent vertices are inscribed in a sphere.²⁹ If the mesh is generated from software

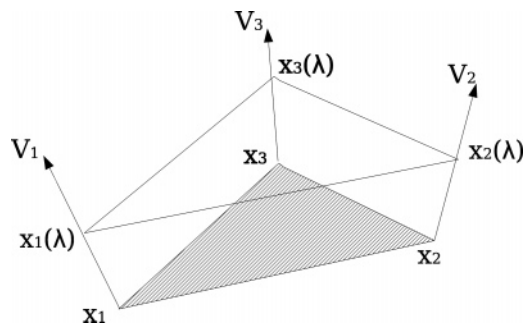


Figure 2. Prism constructed on a triangular element. The shadowed triangle is one of the boundary elements; V_1 , V_2 , and V_3 are three unit normal vectors at the three nodes; and λ is a parameter to describe the third dimension of the prism.

such as MSMS³⁰ that can output the normal vectors, the data can be directly used and need not be calculated again. We have tested these methods for vertex normal calculations for both spherical cavity and protein cases. Preliminary results seem to show that no one method is superiorly accurate and preferred. The overall PB solutions obtained with different normal vector definitions do not differ much except for some points where the local geometry is very uneven, and the final energy calculations are close to each other. Here, the simplest way is adopted to calculate the normal vector:

$$cV_p = \sum_{\text{adjacent faces}} n_i \quad (19)$$

where n_i is the normal vector of the adjacent i th element of node p and c is a factor used to normalize the unit vector V_p .

Any point in a triangle can be described using two parameters (parametric coordinates), for example, (ξ, η) . On the normal direction, we use another parameter λ to locate the position. For example, a point on the normal direction of node i has coordinates $X_i(\lambda) = X_i + \lambda V_i$, $i = 1-3$, where X_i is the position of i th node and V_i is its unit normal vector. It is easy to see that $X_i(0) = X_i$. And the potential value at $X_i(\lambda)$ can be approximated as $f_i(\lambda) = f_i + \lambda h_i$ when λ is small enough. Here, it is supposed that the potential derivative in the normal direction V_i at the i th node is equal to the PB solution h_i . We'll discuss this later. Then, for the same λ at three nodes, the three points $\{X_1(\lambda), X_2(\lambda), X_3(\lambda)\}$ form a new parametric triangle layer. Therefore, the position and function values at any point in this layer can be interpolated using the parametric coordinates (ξ, η, λ) as

$$X(\xi, \eta, \lambda) = (1 - \xi - \eta)(X_1 + \lambda V_1) + \xi(X_2 + \lambda V_2) + \eta(X_3 + \lambda V_3) \quad (20)$$

$$f(\xi, \eta, \lambda) = (1 - \xi - \eta)(f_1 + \lambda h_1) + \xi(f_2 + \lambda h_2) + \eta(f_3 + \lambda h_3) \quad (21)$$

where f_i denotes the potential at the i th node, and h_i denotes its derivative in the normal direction V_i . The trivariate function $f(\xi, \eta, \lambda)$ is then constructed to model the potential in the vicinity of the surface element. When $\lambda = 0$, the triangle layer is reduced to the surface element. All the prisms connect and cover the whole molecular surface without

overlap. The interpolated function is piecewise C^1 continuous on the whole molecular surface; therefore, the gradient can be calculated everywhere. Because we only want to calculate the potential gradient on the molecular surface, $\lambda = 0$, this makes the approximation of the interpolation (small λ) on the normal direction acceptable. The gradient of the potential at any point $(\xi, \eta, \lambda = 0)$ on the surface can be obtained from the following relationship:

$$\begin{pmatrix} f_x \\ f_y \\ f_z \end{pmatrix} = J^{-1} \begin{pmatrix} f_\xi \\ f_\eta \\ f_{\lambda=0} \end{pmatrix} \quad (22)$$

where J is the coordinate transformation matrix from (ξ, η, λ) to (x, y, z) at $\lambda = 0$. These function derivatives are the required fields in eq 18.

Now, the Maxwell tensor \mathbf{T} can be calculated using eq 18, and the PB force F and torque M acting on a molecule are calculated by integrations

$$F = \int_S \mathbf{T}(x) dS(x) \quad (23)$$

$$M = \int_S r_c(x) \times [\mathbf{T}(x) dS(x)] \quad (24)$$

where $r_c(x)$ is a vector from the center of mass of the target molecule to the surface point x and the dot and cross vector multiplication are applied to the vector and tensor quantities.

It is worth it to note that this force calculation procedure can be further improved. As stated above, the PB solution h_i is also taken as the potential derivative in the node normal direction V_i , which is a rough approximation. In the BEM formula, h should be considered as the projection of the potential gradient in the surface normal direction at each quadrature (integration) point. Therefore, a better approximation is that the value h_i at node i is the projection of the potential gradient (not known) at the node in the adjacent element normal direction (all the projections on the adjacent elements equal the same h_i due to the linear element treatment). Normally, the projection of the potential gradient on the node normal vector V_i may deviate from the value h_i to some extent, which is dependent on the mesh geometry. Therefore, the potential gradient at each node, denoted as \bar{H}_i , can be fitted from the above consideration. We calculate the value and direction of each \bar{H}_i through minimizing the quantity

$$\sum_{l \in \{L\}} (\bar{H}_i \cdot n_l - h_i)^2 \quad (25)$$

where $\{L\}$ is the collection of the adjacent elements of the i th node. And it is found from the above interpolation procedure that the prism construction actually only needs an (arbitrary) vector, not necessarily the normal vector, and the directional derivative on this vector at each node. Therefore, the interpolation procedure for force calculation based on the set $\{\bar{H}_i\}$ is similar to that on the set $\{V_i, h_i\}$ and should lead to better results, especially for very irregular mesh geometry.

5. Results and Discussion

5.1. Performance Comparison of Different Patch Treatments. In the iterative PBE solver, the surface integration

Table 1. Performance Comparison of the Constant Node Patch (First Line) and Linear Element (Second Line) Approaches^a

mesh size (vertices and faces)	CPU time dissection			$E_{\text{solvation}}$ (kcal/mol)	error in f_i (%)	error in h_i (%)
	coeff saving	GMRES	total			
162, 340	0.01	0.07	0.10	-82.3	9.1	2.8
	0.11	0.08	0.20	-84.7	8.0~9.3	3.6~6.5
642, 1280	0.08	0.37	0.51	-81.3	4.5	1.3
	0.42	0.40	0.83	-82.7	3.6~5.0	1.4~3.3
4841, 9678	0.88	9.39	11.49	-544.3		
	13.17	10.07	26.23	-554.8		
7525, 15046	6.38	11.90	20.05	-531.5		
	33.53	12.33	50.49	-537.8		

^a Both calculations use the derivative BIE forms, and seven quadrature points are taken for each local element integration in the linear element method. The first two meshes are for spherical cavity calculations, the last two meshes for a protein (fasciculinII). Protein surface mesh is generated using the program MSMS.³⁰ As a reference, the exact Born solvation energy $E_{\text{solvation}}$ of a unit spherical cavity is -80.9 kcal/mol, and the protein solvation energy is decreased to -522.0 kcal/mol when higher resolution mesh is used.

is performed during each iterative step (implicit matrix–vector multiplication). To accelerate the speed and also consider the memory requirement, some matrix coefficients related to the local integration (corresponding to a sparse matrix) are saved, while the far-field integrations are directly calculated. The task for the coefficient saving includes two main parts: coefficient computation and its position placement in a practical matrix-saving format. A compressed sparse column format is used in the current code (similar to HB format). When the local matrix coefficients are saved, the main work in each GMRES iteration step is the far-field integration. This part can be accelerated by the already implemented FMM.⁹

Table 1 provides a comparison of the calculation speed and accuracy between the constant node patch and the linear element BEMs. Calculations are made for both a spherical cavity case and a protein case. As an example, Figure 3 shows the surface mesh and potential of the protein molecule (fasciculinII) calculated using the current node patch method. It is found that in all the cases the CPU time costs in the GMRES iterations of both BEMs are very close. Because we just use one quadrature point in the linear element method, that is, equivalent to the constant element treatment, for far-element integration, this only makes a small difference in the calculation speed (when FMM is used) compared with the constant node patch treatment. However, there is much difference in the sparse matrix-saving step between the two approaches, and it is also found that this is basically the origin of the difference of the total CPU times for the PBE solution by the two BEMs. It is worth it to point out that in the linear element method the most time-consuming step lies in the position placement of the matrix coefficients to be stored, which is much more expensive than the coefficient calculation operations. The CPU time cost of this step is comparable with the total time cost of the PBE solution. As mentioned in the method section, the reason is that in the linear element method both the (unstructured) node and element indices are required to search for the coefficient storage positions, and

we have to use several embedded search loops in the code to reach these. In the constant node patch method, on the other hand, each calculated coefficient to be saved only corresponds to one node in the local node list; therefore, the position location is straightforwardly indicated by the node index itself. This significantly saves CPU time and becomes practical if some matrix coefficients need to be stored.

The accuracies of both potential solution and energy calculation are also well-maintained in the node patch method. In the sphere case, the solution error with the constant node patch approximation is stable (nearly stays at a same value), which is reasonable, while the error varies over a range with the linear element method due to different shapes of the triangular elements on the sphere. In addition, the constant element method is also tested and shows lower accuracy than the linear element method as discussed above. For example, for the above sphere case with a 642 node mesh, the constant element method results in an energy of -84.9 kcal/mol. And the speed is also much slower than our constant node patch method (data not shown here).

5.2. Effects of the Geometric Factor Modification. We check the effects on the PBE solution of using the geometric correction coefficient α_p instead of $1/2$ in the left-hand side of the BIEs 7 and 8. The test is performed on a single sphere model, in which a unit positive charge is positioned at the center of a unit sphere (radius of 1 Å). The relative interior and exterior dielectric constants are set as 2 and 80, respectively. The ionic concentration is 0. Table 2 shows the BEM solution values obtained with the normal BIEs with coefficient $1/2$, and with the geometry-dependent coefficients on the first five nodes of the mesh. The analytical values are also shown as references.

It is found that the normal BEM (nBEM, based on the nBIEs) gives a solution on the nodes with around $\sim 8\%$ relative errors, while the geometrically corrected BEM makes surprising improvements in the potential solution f , with less than 0.05% relative error. However, the normal derivative of the potential, h , is not improved. This may be due to the fact that in the left-hand sides of both eqs 7 and 8 the geometric correction only explicitly couples with f . This indicates that the geometric correction on the dBIE may improve the accuracy of both f and h , which will be studied in the future work related to the aforementioned free terms and hypersingular integrals that appear in the dBIE.

5.3. Force Calculations. For a test model, we calculate the electrostatic interaction forces between two spherical molecules and compare with those computed by our previous methods.^{8,18} We choose two point charges in a vacuum, in which each charge is surrounded by a unit sphere discretized by 320 flat triangular elements (162 nodes). Both charges are put on the x axis, so that the nonzero force component is along the x direction; that is, F_x , and the other two components F_y and F_z are zero in theory. Figure 4 shows the forces along the x direction F_x as a function of the distance between the two point charges calculated using the present interpolation method, a hypersingular integral method, the variational approach, and the analytical formula. It is found that the interpolation method based on the PB solution with geometric correction in the nBIEs is the most accurate

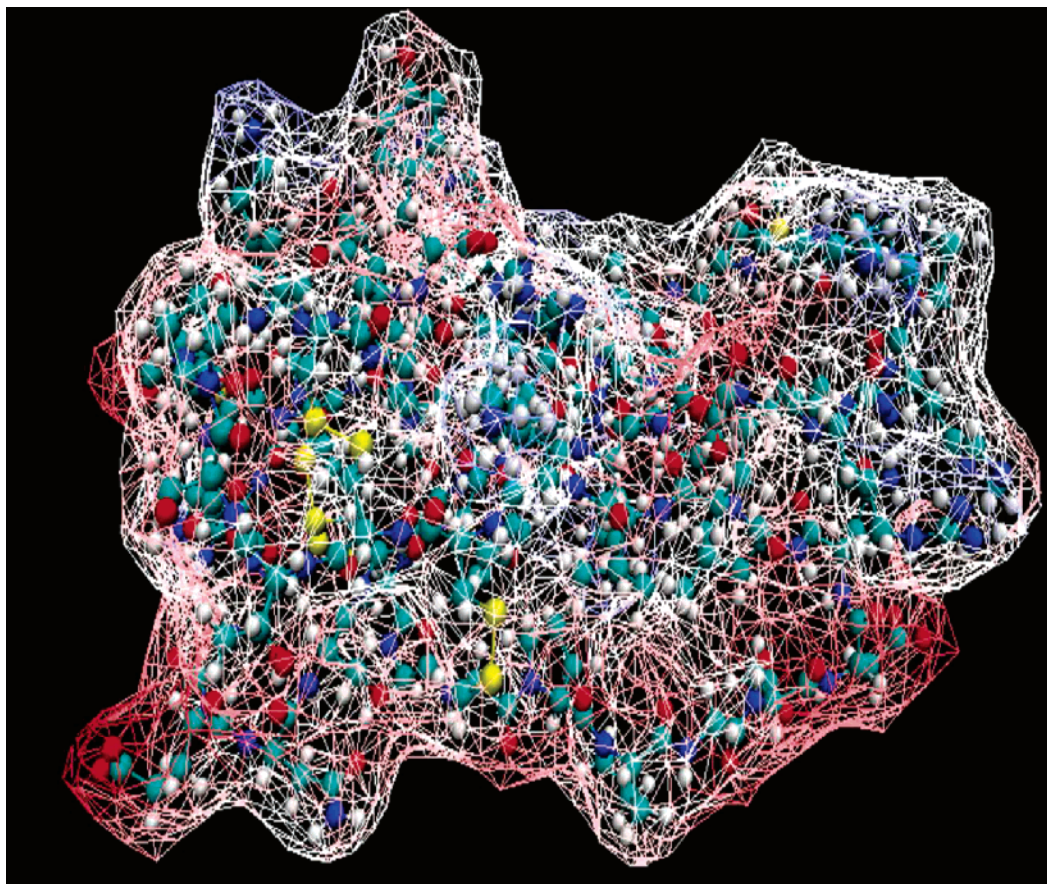


Figure 3. Surface mesh and potential map of fasciculinII. The mesh wireframe is colored from red to blue to represent the potential increasing from negative to positive values. The figure is generated using VMD³¹ by running a tcl script

Table 2. The BEM Solution at the First Five Nodes on a Unit Spherical Surface^{a,b}

node index	<i>x</i>	<i>y</i>	<i>z</i>	f_{analy}	h_{analy}	f_{N} (err%)	h_{N} (err%)	f_{M} (err%)	h_{M} (err%)
1	0.000	0.000	1.000	4.150	-4.150	4.485 (8.077)	-4.202 (1.272)	4.150 (0.002)	-4.202 (1.258)
2	0.273	0.000	0.962	4.150	-4.150	4.499 (8.406)	-4.200 (1.208)	4.150 (0.004)	-4.203 (1.272)
3	0.084	0.260	0.962	4.150	-4.150	4.500 (8.444)	-4.192 (1.022)	4.150 (-0.001)	-4.196 (1.131)
4	0.526	0.000	0.851	4.148	-4.146	4.518 (8.924)	-4.174 (0.668)	4.147 (-0.027)	-4.186 (0.950)
5	0.362	0.263	0.894	4.151	-4.152	4.527 (9.054)	-4.219 (1.616)	4.152 (0.023)	-4.233 (1.945)

^a f_{N} and h_{N} are the potential and its normal derivative, respectively, obtained with the normal BIE, and f_{M} and h_{M} are from the geometrically modified BIE. f_{analy} and h_{analy} are the corresponding analytical values. The errors (shown in the parentheses) are relative to the analytical results and in percentages. The corresponding units are in angstroms, moles, and kilocalories. ^b Calculations use the normal BIE form on a surface mesh with 162 nodes and 320 elements.

one among three approaches, and the calculated forces F_x nearly overlap with the analytical results over the whole distance range. However, if the force interpolation is based on the normal BIE solution without geometric correction, then the results are not so accurate as those of the other two methods (see the blue dot line in Figure 4). This means that the accuracy of the interpolation method heavily depends on the solution accuracy of the PBE.

The superior advantage of the interpolation method for force calculation is its calculation efficiency. In the above test case, in which 30 calculation points (distances) were selected, the CPU time on an Intel Pentium IV (2 GHz) for the whole nBEM calculation is 28.3 s for the variational

approach, 23.0 s for the hypersingular integral method, and 12.0 s for the present interpolation method. Moreover, as shown in the method description, the CPU time spent on the force calculation is simply proportional to the number of boundary elements of the target molecule.

6. Conclusions

New boundary patches around each node in the BEM are simply constructed on the basis of the usual triangulated mesh. This kind of BEM can be considered as a compromise of the traditional constant element method (constant node patch now) and the linear element method (unknowns located at nodes) and draws upon the advantages of both methods:

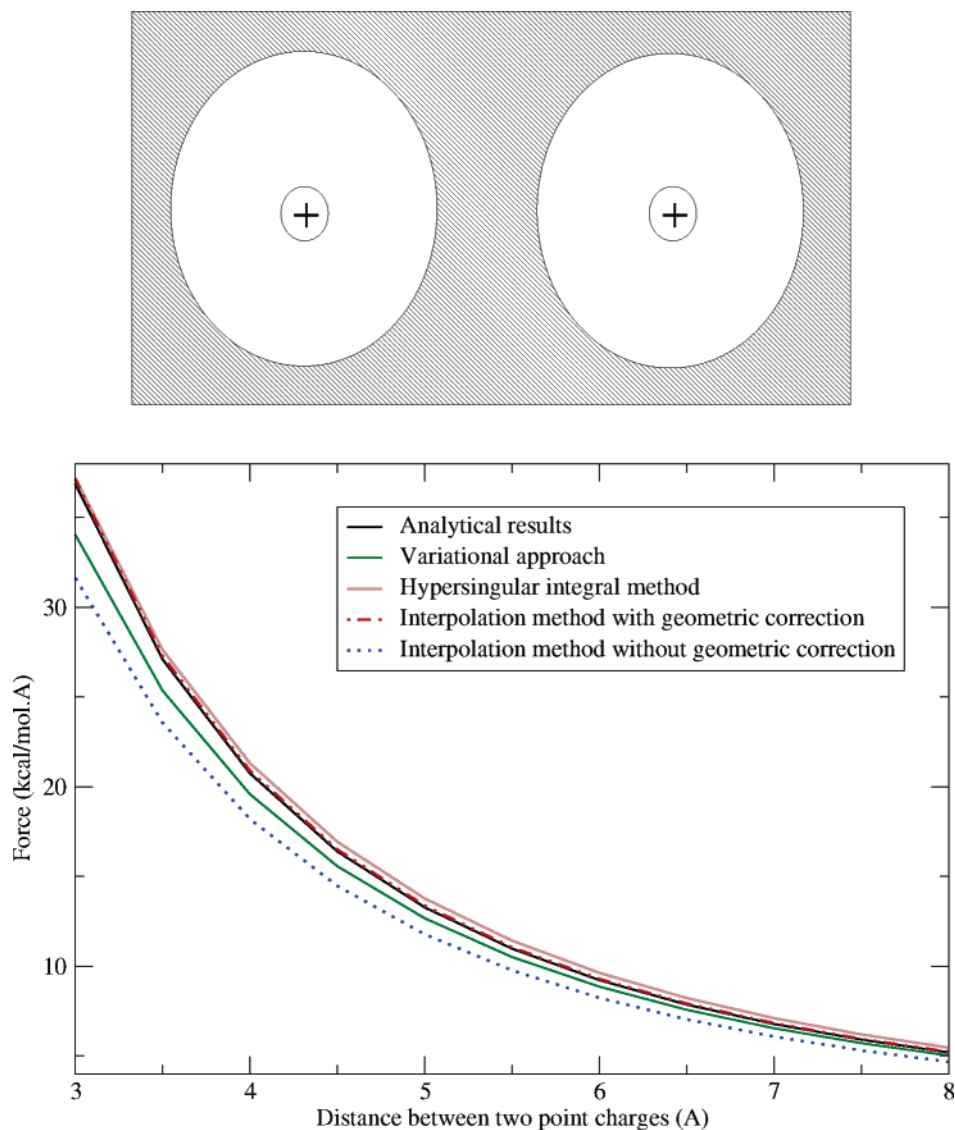


Figure 4. Calculations of electrostatic forces between two spheres using different approaches with normal BIE form. The data from the hypersingular integral method and variational approach are taken from refs 8 and 18.

reduction of the unknowns, simplified numerical complexity, and convenience for coefficient storage. Because the same mesh resolution is still kept, the calculation accuracy is not lost, and our numerical results on both sphere and protein cases also demonstrate this.

In addition, we describe an efficient interpolation approach for force calculation that is proper for any kind of node-based BEM. This is simply of order N with a small prefactor. The accuracy of force calculation by this approach is determined by the accuracy of the PBE solution, f and h . Our calculations also show that the geometry factor correction in BIE can significantly improve the accuracy of potential solution on the surface, thereby improving the accuracy of force calculation using the interpolation approach.

The code will be made available by the authors.

Acknowledgment. We would like to thank Prof. Chandrajit Bajaj for discussion of the interpolation method, Dr. Xiaolin Cheng for his help, and Dr. Justin Gullingsrud for visualization aid. This work was supported in part by

the NIH, NSF, the Howard Hughes Medical Institute, National Biomedical Computing Resource, the NSF Center for Theoretical Biological Physics, SDSC, the W. M. Keck Foundation, and Accelrys, Inc.

References

- (1) Zauhar, R. J.; Morgan, R. S. *J. Mol. Biol.* **1985**, *186*, 815–820.
- (2) Yoon, B. J.; Lenhoff, A. M. *J. Comput. Chem.* **1990**, *11*, 1080–1086.
- (3) Juffer, A. H.; Botta, E. F. F.; Vankeulen, B. A. M.; Vanderploeg, A.; Berendsen, H. J. C. *J. Comput. Phys.* **1991**, *97*, 144–171.
- (4) Vorobjev, Y. N.; Grant, J. A.; Scheraga, H. A. *J. Am. Chem. Soc.* **1992**, *114*, 3189–3196.
- (5) Zhou, H. X. *J. Chem. Phys.* **1994**, *100*, 3152–3162.
- (6) Boschitsch, A. H.; Fenley, M. O. *J. Comput. Chem.* **2004**, *25*, 935–955.
- (7) Zhou, H. X. *Biophys. J.* **1993**, *65*, 955–963.

- (8) Lu, B. Z.; Zhang, D. Q.; McCammon, J. A. *J. Chem. Phys.* **2005**, *122*, 214102.
- (9) Lu, B. Z.; Cheng, X. L.; Huang, J. F.; McCammon, J. A. *Proc. Natl. Acad. Sci. U.S.A.* **2006**, *103*, 19314–19319.
- (10) Bharadwaj, R.; Windemuth, A.; Sridharan, S.; Honig, B.; Nicholls, A. *J. Comput. Chem.* **1995**, *16*, 898–913.
- (11) Zauhar, R. J.; Varnek, A. *J. Comput. Chem.* **1996**, *17*, 864–877.
- (12) Vorobjev, Y. N.; Scheraga, H. A. *J. Comput. Chem.* **1997**, *18*, 569–583.
- (13) Totrov, M.; Abagyan, R. *Biopolymers* **2001**, *60*, 124–133.
- (14) Boschitsch, A. H.; Fenley, M. O.; Zhou, H. X. *J. Phys. Chem. B* **2002**, *106*, 2741–2754.
- (15) Bordner, A. J.; Huber, G. A. *J. Comput. Chem.* **2003**, *24*, 353–367.
- (16) Kuo, S. S.; Altman, M. D.; Bardhan, J. P.; Tidor, B.; White, J. K. Fast Methods for Simulation of Biomolecule Electrostatics. In *ICCAD '02: Proceedings of the 2002 IEEE/ACM International Conference on Computer-Aided Design*; ACM Press: New York, 2002.
- (17) Liang, J.; Subramaniam, S. *Biophys. J.* **1997**, *73*, 1830–1841.
- (18) Lu, B. Z.; Cheng, X. L.; Hou, T. J.; McCammon, J. A. *J. Chem. Phys.* **2005**, *123*, 084904.
- (19) Zauhar, R. J. *J. Comput. Chem.* **1991**, *12*, 575–583.
- (20) Wan, S. Z.; Wang, C. X.; Xiang, Z. X.; Shi, Y. Y. *J. Comput. Chem.* **1997**, *18*, 1440–1449.
- (21) Wang, C. X.; Wan, S. Z.; Xiang, Z. X.; Shi, Y. Y. *J. Phys. Chem. B* **1997**, *101*, 230–235.
- (22) Lu, B. Z.; Wang, C. X.; Chen, W. Z.; Wan, S. Z.; Shi, Y. Y. *J. Phys. Chem. B* **2000**, *104*, 6877–6883.
- (23) Pozrikidis, C. *A Practical Guide to Boundary-Element Methods with the Software Library BEMLIB*; Chapman and Hall: London, 2002.
- (24) Guiggiani, M. Formulation and Numerical Treatment of Boundary Integral Equations with Hypersingular Kernels. In *Singular Integrals in Boundary Element Methods*; Sladek, V., Sladek, J., Eds.; Computational Mechanics Publications: Southampton, U. K., 1998.
- (25) Frangi, A.; Guiggiani, M. *Z. Angew. Math. Mech.* **2001**, *81*, 651–664.
- (26) Duff, I. S.; Grimes, R. G.; Lewis, J. G. *ACM Trans. Math. Software* **1989**, *15*, 1–14.
- (27) Gilson, M. K.; Davis, M. E.; Luty, B. A.; McCammon, J. A. *J. Phys. Chem.* **1993**, *97*, 3591–3600.
- (28) Bajaj, C. L.; Xu, G. Modeling Scattered Function Data on Curved Surfaces. In *Pacific Graphics '94: Proceeding of the Second Pacific Conference on Fundamentals of Computer Graphics*; World Scientific Publishing Co., Inc.: River Edge, NJ, 1994.
- (29) Max, N. *J. Graph. Tools* **1999**, *4*, 1–6.
- (30) Sanner, M. F.; Olson, A. J.; Spehner, J. C. *Biopolymers* **1996**, *38*, 305–320.
- (31) Humphrey, W.; Dalke, A.; Schulten, K. *J. Mol. Graphics* **1996**, *14*, 33–38.

CT700001X

Theoretical Investigation of Excited States of Oligothiophenes and of Their Monocations

Ulrike Salzner*

Bilkent University, Department of Chemistry, 06800 Bilkent, Ankara, Turkey

Received November 27, 2006

Abstract: Excitation energies of neutral thiophene oligomers with chain lengths of up to 25 rings and charged thiophene oligomers with chain lengths of up to 20 rings were calculated with time-dependent Hartree–Fock and time-dependent density functional theory (TDDFT). As recently for polyene cations, very good agreement is found between TDDFT and high-level ab initio calculations and with experimental results wherever data are available. For short thiophene oligomer cations, two sub-band transitions are predicted; for long chains, a third transition develops. Defects are found to be delocalized in bare cations; the inclusion of counterions induces localization. Despite the strong influence of counterions on the geometry, the influence of counterions on the spectra is small for the first two sub-band peaks. Since counterions are directly involved in the electron transitions contributing to the third sub-band peak of longer oligomers, the inclusion of counterions lowers the energy of this absorption peak. The agreement between theoretical spectra based on delocalized geometries and experimental spectra shows that defect localization (electron phonon coupling) is not the underlying cause of the two sub-band transitions. Investigation of the electronic configurations that contribute to the excited states does not confirm the nature of the transitions predicted with the polaron model.

Introduction

Polythiophene (PT) is an organic semiconductor that increases its conductivity by several orders of magnitude upon oxidation (p-doping).¹ During the doping process, the strong π – π^* absorption of the neutral polymer in the UV spectrum decreases in intensity and shifts to higher energy. At the same time, two new features start developing at lower energy.² Doping is therefore associated with a shift in the absorption energy and causes a color change. The evolution of the absorption peaks is crucial for understanding electrochromic properties and for characterizing the charge carriers produced during doping.

The doping process of organic polymers differs from that of inorganic semiconductors since oxidation of organic molecules causes geometry and band structure changes. A widely accepted model for rationalizing the doping process is that at low doping levels polarons form, which combine into bipolarons as the doping proceeds.^{3–7} Polarons are

radical cations that consist of the combined distortion of electronic and geometric structures (electron–phonon coupling). The associated distortion from aromatic to quinoid structure is generally believed to be “self-localized” over a short chain segment because for neutral PT the quinoid form is higher in energy than the aromatic form. Therefore, the cation is believed to keep the quinoid chain segment as short as possible. Bipolarons are dicationic species that consist of two positive charges that are separated by a quinoid chain segment. For bipolarons, self-localization results from a competition between electronic repulsion between the two like charges and the tendency to minimize the lengths of the quinoid segment. Polarons are associated with three sub-band transitions in the UV/vis spectrum, bipolarons with two. Since doped PT exhibits two features in the UV spectrum and since bipolarons are spinless, the low electron spin resonance (ESR) signal for doped PT was originally considered evidence for bipolaron formation.^{6,7}

As solid organic polymers are highly disordered, UV bands are relatively broad and peak assignments are difficult. To

* E-mail: salzner@fen.bilkent.edu.tr.

get around the problems with polydispersity and disorder, many researchers prefer working with well-characterized thiophene oligomers instead of with polymers.⁸ Comparing oligomer with polymer properties revealed that properties of neutral PT are well-reproduced with systems as short as semi- and octithiophene,^{9,10} although excitation energies of neutral oligothiophenes (OTs) in solution decrease up to a chain length of about 20 rings. Between chain lengths of 20 and 27 rings, excitation energies hardly change, but the intensity of the maximum absorption peak continues to rise.^{11–14} These findings indicate that effective conjugation lengths in PT might be rather short. Therefore, OTs are probably more realistic models for PT than infinitely long polymers.

Similarly, doping experiments of short OTs in solution^{15–25} showed that OT radical cations reproduce spectral properties of PT upon doping. In solution, radical cations could be obtained for bithiophene and longer oligomers, while dications require chain lengths of at least six thiophene rings. In contrast to predictions of the polaron–bipolaron model, radical cations (polarons) exhibit two peaks in the UV spectrum and dications (bipolarons) show only one.^{16,19–22,24,26–32} Thus, doped PT might contain polarons rather than bipolarons. Low ESR signals in doped PT are not inconsistent with polaron formation since interacting polarons also may have singlet ground states.³³ Especially at low temperatures, cations have a tendency to dimerize. Since dimerization is more likely in a solid than in dilute solution, spinless π dimers of radical cations offer an explanation for conductivity in the absence of spins.^{19–21,24} An alternative rationalization for the small ESR signals in doped PT was suggested when experiments revealed that duodecithiophene and longer OTs give rise to UV spectra that are consistent with spinless interacting polaron pairs located on the same chain.^{32,34,35}

Theoretical investigations of excited states for bi- and terthiophene cations have been carried out at the complete active space self-consistent field CASSCF³⁶ and CASPT2³⁷ levels of theory. The calculations agree with the experimental solution data and predict two excitations for radical cations. The excitations are multiconfigurational, indicating that the polaron–bipolaron model, which is based on single electron transitions, is oversimplified. Unfortunately, CASPT2 calculations cannot be extended to larger systems. In fact, the active space for the terthiophene cation had to be reduced, since a complete active space containing 17 π electrons is computationally too demanding. Excited states of longer OTs have been studied with intermediate neglect of differential overlap combined with singles excitations configuration interaction (INDO/SCI),³⁸ with the equation of motion coupled cluster (INDO/EOM-CCSD) method,³⁹ and with time-dependent density functional theory (TDDFT).⁴⁰ Two transitions were confirmed for polarons in OT monocations.

Evidence is therefore mounting that the polaron–bipolaron model does not fully explain optical properties of conducting polymers upon doping. Therefore, high-level calculations on longer oligomers are needed. In a recent paper,⁴¹ excited states of polyene cations were investigated with TDDFT. Comparison of TDDFT excitation energies for oligomers up to $C_{10}H_{12}^+$ with multireference perturbation theory (MRMP)

values and with experimental results indicated that TDDFT produces reliable excitation energies for short- and medium-sized polyene cations.⁴¹ Geometry optimizations of longer odd-numbered closed-shell polyene cations with Møller–Plesset perturbation theory truncated at second order (MP2) and with a DFT hybrid functional (B3P86 with 30% Hartree–Fock exchange) gave very similar results with respect to defect sizes. Comparison of excitation energies of odd-numbered closed-shell polyene cations with time-dependent Hartree–Fock (TDHF) theory indicated that TDDFT does not deteriorate for cations in the long chain lengths limit.⁴¹ Since these results are very encouraging, TDHF and TDDFT are employed here to investigate spectral properties of neutral oligothiophenes and oligothiophene cations.

Methods

Thiophene oligomers with 2–25 thiophene units were optimized in neutral states and with 2–20 rings in charged states with density functional theory employing the B3P86 hybrid functional^{42,43} with 30% HF exchange⁴⁴ (B3P86-30%) and Stevens–Basch–Krauss pseudopotentials with polarized split-valence basis sets (CEP-31G*).^{45,46} The amount of HF exchange in the B3P86 functional was originally increased from 20% to 30% to reproduce absorption maxima of polyenes with orbital energy differences.^{44,47} It was shown later that the B3P86-30%/CEP-31G* level of theory also gives reasonable estimates of band gaps of PT and polypyrrole^{44,48} and provides accurate structures of polyenes.⁴¹ Moreover, TDDFT calculations with the B3P86-30% functional give excellent agreement with experimental results for excited states of polyene cations.⁴¹ These findings are in agreement with results of other groups that showed that about 20–40% HF exchange is necessary to produce good geometries,⁴⁹ band gaps,⁵⁰ energy level spacings as compared to peak positions in photoelectron spectra,⁵¹ and vibronic structures of electronic absorption spectra,^{52,53} while the type of exchange functional itself makes little difference.^{47,53}

Neutral and charged species were kept planar and obey C_{2h} (even number of rings) or C_{2v} (odd number of rings) symmetries. For 6T, the effect of planarization was evaluated by comparing excitation energies of planar and twisted forms. Radicals were shown to have planar ground states by Zade and Bendikov.⁴⁰ The effect of counterions was probed on 3T-Cl₃, 9T-Cl₃, 13T-Cl₃, and 19T-Cl₃ complexes. Cl₃[−] is used as a model for iodine doping. The counterions were placed at the center of the chain and in the plane of the backbone rather than above the chain. In agreement with electrostatics, placement of the anion next to the slightly positively charged hydrogen atoms corresponds to the minimum energy structure. No covalent bond formation as with Cl^{−54} was observed during structure optimization with Cl₃[−] as the counterion. In contrast to polyene radical cations,⁴¹ there is very little spin contamination for OT radical cations when the B3P86-30% functional is used. The expectation value for the spin operator for 20T⁺ is 0.76. The highest value, 0.84, was obtained for the complexes with Cl₃[−]. There was therefore no need to employ the restricted open-shell formalism. In contrast, HF wave functions are strongly spin-contaminated

with an expectation value of the spin operator of 1.16 already for the bithiophene cation. Thus, HF and MP2 were not considered for radical cations.

Excited states for neutral species were calculated with TDHF and TDB3P86-30% employing the CEP-31G* basis set. Studies on polyenes have shown that this basis set is sufficient for calculations of extended systems since no change was observed beyond hexatriene when diffuse functions were added.⁵⁵ Although TDDFT has been shown in numerous studies to provide good excitation spectra,^{52,56–63} there is one major exception. The 1 ¹Bu excited state of large conjugated systems, the very transition that gives rise to the band gap in conducting polymers, is predicted to lie too low in energy.^{41,53,55,57,59,61,63–70} The underestimation of the excitation energy is associated with the fact that the 1 ¹Bu excited state has ionic character in a valence-bond interpretation (compare ref 71 treating polyenes). In general, the underestimation of TDDFT excitation energies for conjugated π systems increases with increasing ionic character of the excited state and with increasing size of the system.⁶⁶ For this reason, TDDFT is not employed here for neutral thiophene oligomers. Careful comparison of TDHF excitation energies with high-level ab initio predictions and with experimental spectra of polyenes and of OTs has shown that TDHF reproduces the 1 ¹Bu excitation energies of large conjugated systems very well.^{41,72–74} Thus, TDHF/CEP-31G* is employed here to determine the excitation energies and to define the sub-band region of the neutral species.

In general, TDDFT was shown to be able to treat radicals successfully.⁵⁸ In a recent investigation, it turned out that, despite the failure of TDDFT for the neutral conjugated systems, excited states of polyene cations and radical cations⁴¹ are reproduced accurately compared to experimental results and compared to MRMP calculations. Grozema et al. observed the same good performance of TDDFT for thienylene vinylene oligomer dications.⁷⁵ Moreover, the quality of the polyene radical cation excited states was found to be independent of the amount of HF exchange since results with the B3P86-30% and BP86 functionals were almost identical for the first two excited states of polyene cations. Differences start showing, however, for higher-lying excited states.⁴¹ Since the failure of TDDFT for neutral systems depends on the ionic character of the excited states,⁶⁶ it is not surprising that TDDFT performs better for the excited states of radical cations which are quite different in nature⁷¹ compared to those of the neutral species. OT radical cations were therefore treated with time-dependent pure DFT (TDBP86) and with TDB3P86-30%. Excitation energies for cations were computed up to the TDHF transition energy of the neutral species. For 20T⁺, excitation energies up to the third strong peak were obtained, since for 16T⁺ and 19T⁺ no further sub-band peaks were found. For long oligomer cations, up to 40 excited states had to be considered.

Finally, solvent effects in the presence of dichloromethane were determined for neutral 6T, 2T⁺, 3T⁺, 8T⁺, 9T-Cl₃, and 13T-Cl₃ with the polarized continuum model (PCM) as implemented in G03.^{76–94} All calculations are done with Gaussian 03, revision D02.⁹⁵

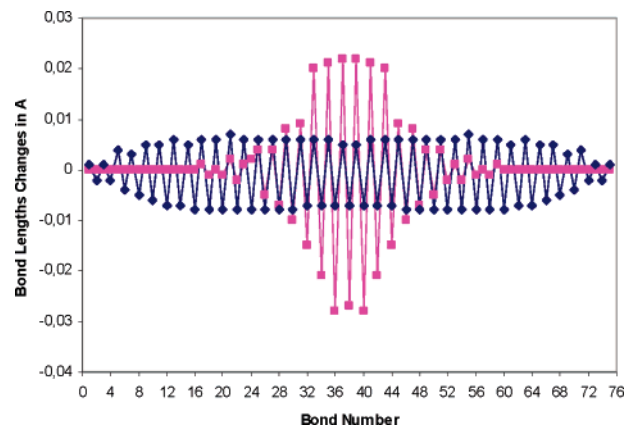


Figure 1. Bond length changes in 19T⁺ (blue diamonds) and 19T-Cl₃ (pink squares) compared to neutral 19T. Bond lengths shown are those of C–C and C=C bonds numbered from the beginning to the end of the chain.

Results

Geometry of Cations. In agreement with recent studies,^{75,96–102} the B3P86-30%/CEP-31G* level of theory produces delocalized defects for radical cations in the absence of counterions. In Figure 1, bond length changes in the radical cation in the absence and in the presence of a counterion with respect to the neutral species are plotted for the longest OT investigated here, 19T⁺ and the 19T-Cl₃ complex. The geometry distortion in the bare cation is distributed evenly in the middle of the chain. Toward the end, the geometry distortion decreases, with the terminal rings being hardly affected, but no convergence of the defect size with increasing chain length seems to occur. The defect delocalization is not a consequence of spin contamination, since the expectation value for the spin operator for 19T⁺ is only 0.77, corresponding closely to a pure doublet with an $\langle S^2 \rangle$ value of 0.75. In the presence of a counterion, the defect is localized over 11 thiophene rings. The main distortion affects the inner three rings, which are quinoid, and falls off quickly over the next four rings. The last four terminal rings are undistorted compared to the neutral system.

The geometries of the bare cation and of the complex with one counterion differ considerably. The energetic effect of these structural differences was evaluated by removing the counterion and performing a single-point calculation on the cation at the geometry of the complex (19T⁺//19T-Cl₃). The energy difference between the optimized cation and the cation at the geometry of the complex is 1.76 kcal/mol (0.09 kcal/mol per ring). Thus, potential energy surfaces of OT radical cations are very flat. This agrees with findings for polyene cations.⁴¹

The distribution of the positive charge in 19T⁺, 19T-Cl₃, and 19T⁺//19T-Cl₃ is plotted versus the ring number in Figure 2. In the bare cation, there is a relatively even distribution of the charge over the entire molecule with two slight maxima at rings 5 and 15 and slightly less charge in the middle. For 19T⁺//19T-Cl₃, a slight shift of the charge toward the middle is observed. This charge shift can be attributed to electron–phonon coupling. In the presence of the counterion, a sharp peak of the positive charge is obtained at the central ring that falls off exponentially toward the chain

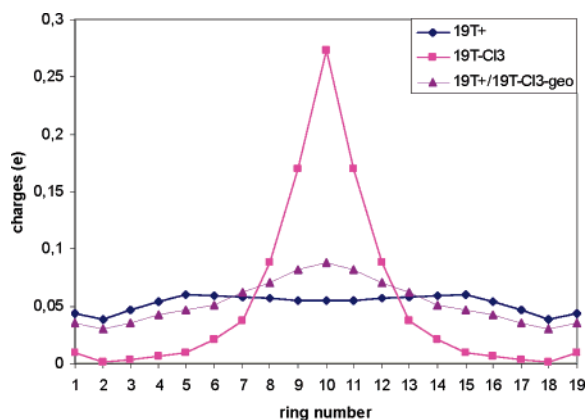


Figure 2. Distribution of the positive charge in $19T^+$, in $19T^+$ with the backbone structure of $19T-Cl_3$, and in $19T-Cl_3$. Rings are numbered from the beginning to the end of the chain.

ends. The three species therefore represent polymers with a localized defect ($19T-Cl_3$), with a delocalized defect ($19T^+$), and with a localized structural defect but delocalized charge distribution ($19T^+//19T-Cl_3$).

Excited States. Neutral Thiophene Oligomers. No gas-phase data exist for thiophene oligomers. Solvent effects on excitation energies are therefore unknown. Thiophene oligomers absorb and emit at different energies in room-temperature (RT) solutions; in a matrix, absorption and emissions occur at the same value and coincide with the room-temperature emission.^{103–106} Differences between RT solution and matrix data were attributed to planarization of the twisted thiophene chains upon cooling. To assess influences of the solvent and nonplanarity theoretically, sexithiophene (6T) was optimized at the MP2/CEP-31G* level with planar and nonplanar structures. MP2 was employed since the B3P86-30%/CEP-31G* level of theory does not produce a nonplanar geometry. The nonplanar form of 6T with an optimized twist angle of 25° is 1.44 kcal/mol more stable than the planar form. The TDHF excitation energy to the 1^1B_u state of the nonplanar form is 3.04 eV, 0.32 eV higher than that of the planar conformation. For the nonplanar form, the excitation energy was also computed in the presence of CH_2Cl_2 with the PCM.^{76–91} Inclusion of the solvent lowers the excitation energy by 0.09 eV.

By comparison with polyene data, for which experimental solvent effects are 0.3–0.4 eV¹⁰⁷ and calculated solvent effects are ~ 0.28 eV,⁷⁴ it becomes clear that solvent effects are smaller for thiophene oligomers than for polyenes and that calculated solvent effects are underestimated compared to experimental results. A reasonable estimate is therefore that solvent effects decrease excitation energies by about 0.2 eV. Additional differences with experimental results arise since vertical excitation energies are used, which means that zero-point energy (ZPE) differences between ground and excited states are neglected and that Franck–Condon (FC) factors were not calculated explicitly. Inclusion of the latter two corrections can lead to a lowering of the excitation energy of about 0.3 eV.¹⁰⁸

Taking the corrections together, 0.2 eV (solvent) + 0.3 eV (ZPE and FC) – 0.32 eV (planarization) = 0.18 eV,

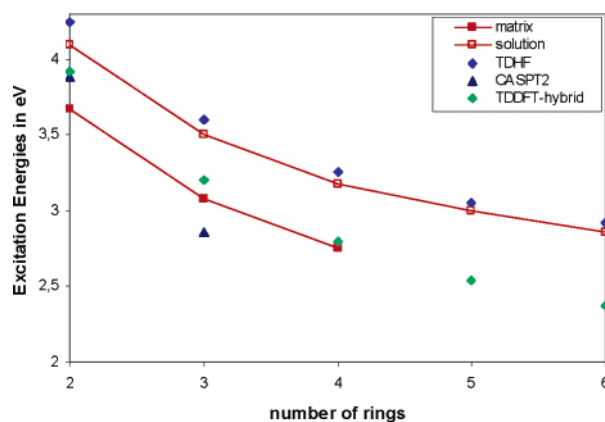


Figure 3. $1B_u$ excitation energies (λ_{max} values) for neutral thiophene oligomers in RT solution,¹⁰³ in matrix,^{104–106} at the CASPT2 level,³⁷ at the TDHF/CEP-31G*//B3P86-30%/CEP-31G* level, and at the TDB3P86-31G*//B3P86-30%/CEP-31G* level.

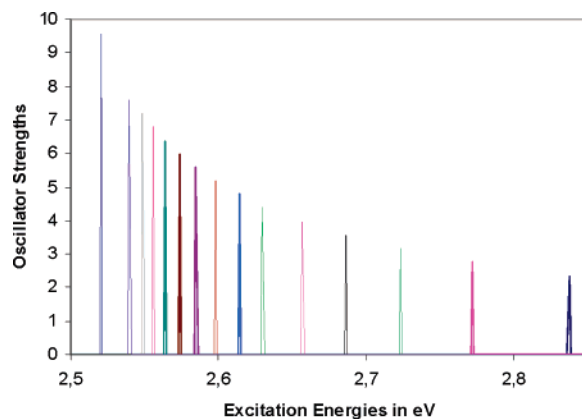


Figure 4. First allowed absorption peaks for neutral thiophene oligomers with 7–20 and 25 thiophene rings at the TDHF/CEP-31G* level.

vertical excitation energies calculated for planar thiophene oligomers in the gas phase should lie in the vicinity of experimental RT solution and definitely above matrix data. Experimental (λ_{max} values) and theoretical excitation energies are compared in Figure 3.

The CASPT2³⁷ value for bithiophene seems to be a bit low, lying between experimental RT solution and matrix values. Terthiophene was treated with a reduced active space since 18 π electrons are still too many to be treated fully.³⁷ This might explain the severe underestimation of the excitation energy since the value is below the matrix data despite the absence of a solvent in the calculations. Note that the CASPT2 value lies also below the TDDFT result for 3T. The TDDFT value agrees with CASPT2 for bithiophene, but for longer oligomers, TDDFT excitation energies fall off faster than the experimental values and approach the matrix data already for 4T. The results would be useless in the long chain limit. In contrast, TDHF values appear to be very accurate. This confirms that TDHF is the best method, especially for long oligomers, to estimate the maximum absorption in long thiophene oligomers.

Figure 4 shows the progression of TDHF excitation energies and oscillator strengths for 7T–25T. Spectra of all

Table 1. Excitation Energies in eV, Oscillator Strength, and Main Electron Configurations in the Excited States (Weight % for CASPT2, CI Coefficients for TDDFT) for the Bithiophene Cation at CASPT2³⁷ and TDDFT Levels of Theory

	1 ² A _u	2 ² B _g	2 ² A _u	3 ² A _u
CASPT2 ³⁷	1.54 (0.010) H-1 → H 63% H → L 9%	1.78 (–) H-2 → H 75%	1.95 (0.062) H-3H → 54% H → L 18% H-1 → H 7%	2.78 (0.607) H → L 44% H-3 → H 18% H-1 → H 5%
TDBP86	1.55 (0.002) H-1 → H 1.00	1.74 (–) H-2 → L 1.00	2.15 (0.029) H-3 → H 0.78 H → L 0.65	3.23 (0.463) H → L 0.71 H-3 → H 0.46
TDB3P86-30%	1.94 (0.002) H-1 → H 0.97 H-2 → H 0.25 H → L 0.23	2.14 (–) H-3 → L 1.00 ^a	2.25 (0.061) H-2 → H 0.84 H → L 0.60 H-1 → H 0.29	3.23 (0.477) H → L 0.77 H-2 → H –0.47 H-2 → H 0.25
in CH ₂ Cl ₂	1.95 (0.003)	2.16 (–)	2.21 (0.11)	3.06 (0.54)
expt. ^b			2.10 (weak)	2.92 (strong)
expt. ^c			2.14 (weak)	2.95 (strong)

^a That H-2 and H-3 are reversed with TDBP86 as compared to TDB3P86-30% is due to the near degeneracy of these energy levels. The near degeneracy is caused by the crossing of the states arising from HOMO and HOMO-1 levels of the thiophene repeat unit (compare ref 48).
^b Electron absorption in freon glass at 77 K, ref 36. ^c Electron absorption in acetonitrile in the presence of TCNE, ref 25.

species are dominated by one strong absorption peak that shifts to lower energy and increases in oscillator strengths as chain lengths increase. The peak is dominated by the highest occupied molecular orbital–lowest unoccupied molecular orbital (HOMO–LUMO) transition with a coefficient of about 0.6 for short oligomers. At long chain lengths, the coefficient of the leading excitation decreases (to 0.39 for 25T), as lower- and higher-lying orbitals start contributing. For long oligomers, there are also some additional weaker features with oscillator strengths of $\sim 1/10$ that of the strong peak and at 0.2–0.4 eV higher energies. The weak features are not included in Figure 4 for clarity. The difference between the excitation energies of 19T and 20T is 0.009 eV. Adding five more rings decreases the excitation energy by 0.02 eV to a value of 2.52 eV for 25T. Experimentally, there is no more change in the excitation energies beyond 20T, while absorption intensities and conductivities keep increasing in going from 20T to 27T.¹¹

Cations. Assessment of the TDDFT Results. Since the performance of unrestricted (U)TDDFT excited-state calculations for radical cations of conjugated systems is not well-established, the accuracy of the results is investigated by comparing the 2T⁺ and 3T⁺ data with CASPT2 results.³⁷ Rubio et al. reported the four lowest excited states for 2T⁺ and the five lowest excited states for 3T⁺. Like the present TDDFT results, CASPT2 excitation energies were obtained on ground-state structures of the radical cations and correspond to vertical excitation energies in the gas phase. Structure optimizations were done at the UB3PW91/cc-pVDZ level of theory. The main difference between the structures obtained at B3P86-30%/CEP-31G* and the ones reported by Rubio et al. is that all bonds are about 0.01 Å longer with B3P86-30%/CEP-31G*. Comparison with B3P86-30%/6-31G* structures shows that the bond length increase is caused by the pseudopotentials. B3P86-30%/CEP-31G* structures of polyenes are, however, in close agreement with experimental results.⁴¹

Following the same nomenclature as Rubio et al.,³⁷ energy levels are labeled HOMO, HOMO-1, LUMO, LUMO+1,

and so on. In a CASSCF wave function, there are no orbital energies, but states and orbitals can be matched by comparing their symmetries. The wave function of the ion was shown to be dominated by a single electron configuration obtained by removing one electron from the HOMO of the neutral species. This electron configuration has a weight of 84% for 2T⁺ and 79% for 3T⁺ in the CASSCF wave function. The term “HOMO” is also used for radical cations in which the HOMO is then only half-occupied. The HOMO (semio-occupied molecular orbital, SOMO) corresponds to polaron level 1 (pol1) in solid-state nomenclature. All excited states are dominated by single excitations, doubles having total contributions between 4 and 7%.³⁷ This justifies the use of a single-electron method like TDDFT.

In open-shell DFT calculations, separate spin-orbitals are obtained for electrons with α and β spin. Upon ionization, one electron with β spin is removed. For radical cations, α and β orbitals have different energies. The half-occupied HOMO (SOMO) of the cation in the CASPT2 wave function corresponds to the pair of the HOMO of the α electrons and the LUMO of the β electrons in the unrestricted TDDFT formalism. HOMO-1 is the pair of α and β orbitals lying below the HOMO/LUMO pair and so on. In this way, the CASPT2 states and UTDDFT orbitals can be matched although the energies of α - and β -spin orbitals are not identical. Excited states arise as combinations of single-electron transitions within the α - and β -orbital spaces. Since there are no transitions between α - and β -orbital spaces, the energetic shift of α versus β orbitals is irrelevant for analyzing the nature of the electronic states. A thorough comparison of the composition of the CASPT2 wave functions³⁷ for the excited states with the configurations contributing to the excited states in UTDDFT calculations revealed a close correspondence. UTDDFT and CASPT2 excited states of 2T⁺ are compared in Table 1. Note that the electron configurations are given as weight percents for CASPT2, while the TDDFT values are CI coefficients.

The first feature in the spectrum at the CASPT2 level arises from a linear combination of the HOMO-1 → HOMO

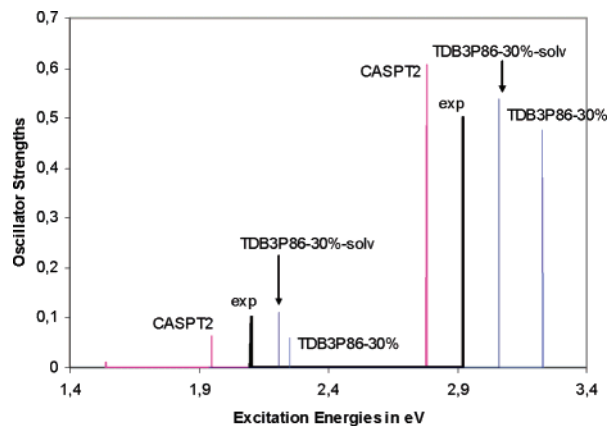


Figure 5. Excitation spectra for $2T^+$ compared to experimental results at the CASPT2 and TDB3P86-30% levels of theory. The experimental oscillator strengths were arbitrarily set to 0.1 and 0.5.

(H-1 \rightarrow H) and HOMO \rightarrow LUMO (H \rightarrow L) transitions with the same sign. This leads to partial cancellation of the electric dipole transition moment vectors.⁷¹ Since the two transition energies differ for OT radical cations, in contrast to those in polyene radical cations,⁷¹ the first excited state is dominated by the H-1 \rightarrow H transition. As a result, the cancellation of the electric dipole transition moment vectors is incomplete and there is oscillator strength in this first peak. The strong (fourth) peak arises from the linear combination of the same two transitions with opposite signs and is dominated by the H \rightarrow L transition. The opposite sign combination leads to addition of the electric dipole transition moment vectors and a higher oscillator strength. The third peak arises from the H-3 \rightarrow H transition with some contributions from H-1 \rightarrow H and H \rightarrow L transitions. Rubio et al.³⁷ assigned peaks 3 and 4 to the experimentally observed absorptions.

The same four lowest excited states as predicted by CASPT2 are also found with UTDDFT calculations. The TDDFT excitation energies obtained with the hybrid functional are between 0.3 and 0.4 eV higher than that at CASPT2; the nature of the excited states and the oscillator strengths match qualitatively. There is a very close agreement for the two higher-energy peaks between TDBP86 and TDB3P86-30% results. The general trend is that pure TDDFT finds some of the peaks at lower energy than the TDDFT hybrid. It is therefore clear that TDDFT produces qualitatively correct results with hybrid and pure DFT functionals.

To probe the solvent effect, TDDFT-hybrid calculations were carried out in the presence of dichloromethane, a common solvent for OT radical cations.^{16,26} Changing the solvent is not expected to lead to different results.⁷⁴ The solvent hardly influences the low-energy transitions but lowers the strong absorption peak in energy. This brings the TDDFT-hybrid results in close agreement with experimental results. Figure 5 shows that CASPT2 gas-phase values are slightly lower than experimental excitation energies. Inclusion of a solvent would therefore deteriorate the agreement with experimental results. Thus, TDDFT-hybrid results seem to match experimental results at least as well and maybe better than CASPT2 values.

A similar comparison as for $2T^+$ is summarized for $3T^+$ in Table 2. In addition, the effect of a counterion in the absence and in the presence of a solvent has been examined for $3T^+$. In contrast to $2T^+$, the H-3 \rightarrow L transition leads to a peak with very low oscillator strength for $3T^+$. At the same time, the first peak, the linear combination of the H-1 \rightarrow H and H \rightarrow L transition with same sign, gains oscillator strength. Thus, the first visible peaks in the spectra of $2T^+$ and $3T^+$ are of different electronic origin. The trends regarding the excitation energies are the same as for $2T^+$. CASPT2 values are lower than gas-phase data; TDB3P86-30% are higher. TDBP86 values lie in between but closer to TDB3P86-30%. The difference between the strong peaks with and without HF exchange is about 0.1 eV. Inclusion of a solvent tends to lower excitation energies. The influence of the counterion, especially in the presence of the solvent, is very small.

Interesting is the splitting of the strong absorption peak predicted by CASPT2.³⁷ This splitting is reproduced with TDBP86-30% but not with TDBP86. It also depends on the medium as the splitting disappears with a counterion and reappears when the solvent is added. We will see below that peak splitting appears only for $3T^+$ and vanishes for longer OT radical cations. TDBP86 produces splitting for $4T^+$, which also vanishes for all other chain lengths. Thus, it seems that the splitting of the strong peak into two closely spaced features is caused by subtle configuration mixing and depends on the energy levels, which in turn depend on chain length. This theoretical "fine structure" might not be observable in the experiment. Figure 6 summarizes the results and shows that TDDFT is very reliable and probably more accurate than CASPT2.

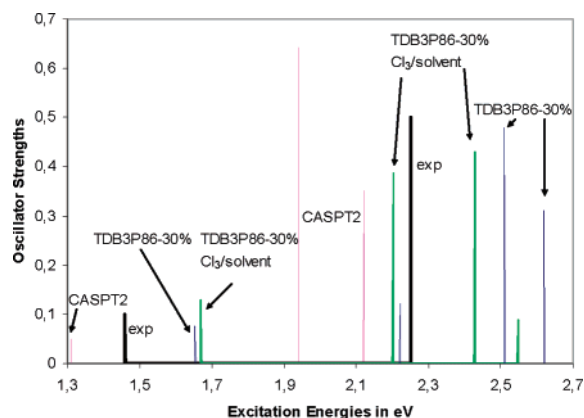
Chain-Length Dependence of Excitation Spectra. Having established the reliability of the TDDFT results, the chain-length dependence of the excitation energies can be investigated. Excited states in the energy range below the TDHF excitation energies of the neutral species were obtained at the TDB3P86-30%/CEP-31G* and TDBP86/CEP-31G* levels of theory. The results are summarized in Table 3 and compared to experimental values where available. Weak features with oscillator strengths below 0.3 are omitted unless they correspond to peaks that grow in intensity with increasing chain lengths.

For oligomers with two to six six-rings, TDDFT predicts two sub-band transitions arising from the combination of H-1 \rightarrow H and H \rightarrow L transitions with the same and with opposite signs. The low-energy feature has low oscillator strength but increases in intensity upon chain-length extension as the H-1 \rightarrow H transition becomes more dominant in the excited-state wave function. The increase in intensity with increasing chain length is in agreement with experimental results.¹⁶ TDB3P86-30% and TDBP86 results are in close agreement with each other, overestimating experimental values by up to 0.28 eV (neglecting solvent effects). Solvent effects on excitation energies evaluated at the TDBP86 level for $8T^+$ are smaller than for $2T^+$ and $3T^+$, 0.11 eV, and bring the excitation energies to within 0.1–0.2 eV of the experimental values. Although solvents effects have a small

Table 2. Excitation Energies in eV, Oscillator Strength, and Main Electron Configurations in the Excited States (Weight % for CASPT2, CI Coefficients for TDDFT) for the Terthiophene Cation at CASPT2³⁷ and TDDFT Levels of Theory

	1 ² B ₁	2 ² B ₁	3 ² B ₁	2 ² A ₂	3 ² A ₂
CASPT2 ³⁷	1.31 (0.051) H-1 → H 47% H → L 24%	1.94 (0.643) H → L 28% H-1 → H 23% H-2 → H 14%	2.12 (0.351) H-2 → H 51% H → L 16%	2.21 (0.002) H-3 → L 63%	2.50 (<0.001) H-4 → L 38% H → L+1 19% H-1 → L 16%
TDBP86	1.52 (0.038) H-1 → H 0.75 H → L 0.59	2.56 (0.84) H → L 0.71 H-1 → H -0.40	1.73 (0.023) H-2 → H 0.93 ^a	1.76 (<0.001) H-3 → L 1.00	2.14 (-) H-4 → L 0.99
TDB3P86-30%	1.65 (0.076) H-1 → H 0.85 H → L 0.63	2.51 (0.480) H → L 0.59 H-1 → H 0.28 H-4 → H 0.61	2.62 (0.313) H-4 → H 0.76 ^a H → L 0.51 H-1 → H 0.28	2.22 (0.120) H-2 → H 0.93	2.27 (0.001) H-3 → H 0.97
TDB3P86-30% in CH ₂ Cl ₂	1.65 (0.146)	2.21 (0.442)	2.42 (0.387)	2.33 (0.002)	2.56 (0.076)
with Cl ₃ ⁻	1.75 (0.057)	2.49 (0.033)	2.61 (0.658)	2.19 (0.094)	2.37 (0.003)
with Cl ₃ ⁻ in CH ₂ Cl ₂	1.67 (0.129)	2.20 (0.386)	2.43 (0.430)	2.36 (0.003)	2.55 (0.087)
Expt. ^b	1.46 (weak)	2.25 (strong)			

^a That H-2, H-3, and H-4 are reversed with TDBP86 as compared to TDB3P86-30% is due to the near degeneracy of these energy levels. The near degeneracy is caused by the crossing of the states arising from HOMO and HOMO-1 levels of the thiophene repeat unit (compare ref 48). ^b Electron absorption in acetonitrile ref 22.

**Figure 6.** Excitation spectra for 3T⁺ compared to experimental results at the CASPT2 and TDDFT levels of theory. The experimental oscillator strengths were arbitrarily set to 0.1 and 0.5.

influence on the excitation energies, there are significant shifts in oscillator strengths.

For 8T⁺, the first peak in the spectrum consists almost entirely of the H-1 → H electron configuration. The second peak originates from the H → L transition, but additional electronic configurations contribute. Due to this configuration mixing, the H → L transition splits into two separate peaks at 1.45 and at 2.56 eV. The new peak at 2.56 eV has a low oscillator strength for 8T⁺ but increases rapidly in intensity with increasing chain lengths while a fourth sub-band absorption that appears at 2.74 eV vanishes in the long chain limit. Stick spectra for 2T⁺ through 8T⁺ at TDB3P86-30% are compared in Figure 7. Some differences start to arise between TDB3P86-30% and TDBP86 predictions as the second absorption in the 8T⁺ spectrum is split into two closely spaced (~0.14–0.15 eV) peaks and the third transition lies lower in energy and has a higher oscillator strength.

For 12T⁺, the two additional sub-band transitions lie at 2.14 and 2.47 eV, slightly below the TDHF interband transition of neutral 12T at 2.63 eV. Due to configuration mixing, the lower component of the H → L transition (second

peak) that dominates spectra of short oligomers decreases in intensity with increasing chain length. Starting with 12T⁺, the H-1 → H transition and the higher component of the H → L transition have higher oscillator strengths than the original H → L transition. The contributions of various electronic transitions to the three main peaks at TDB3P86-30% are represented graphically in Figure 8 for 12T⁺. Transitions with coefficients above 0.3 were considered. It might be confusing that the HOMO-1 of the β electrons lies above the HOMO of the α electrons in Figure 8. As described above, the energetic shift between α and β energy levels can be ignored, since no transitions occur between α and β energy levels. The semioccupied HOMO according to Rubio et al.'s³⁷ nomenclature corresponds therefore still to the α-HOMO/β-LUMO pair of spin-orbitals. In Figure 8, Rubio's nomenclature is applied and the α-HOMO/β-LUMO pair is designated as HOMO for α and β electrons. Therefore, the first transition at 0.46 eV, which is dominated by a single electron transition, is the H-1 → H transition. Peaks 2 and 3 have strong H → L contributions but mix with H-1 → L+1 and H-2 → L transitions.

For 14T⁺ and longer OT cations, the higher-lying component of the H → L transition (peak 3) becomes the dominant peak in the spectrum. The second peak, which was the strongest for short oligomers, is the weakest in the long chain length limit. Figure 9 shows that a huge absorption is predicted for peak 3 at about 0.5 eV below the interband transition of the neutral species. Using geometries with localized defects produces the sub-band transition with almost the same energy but with about half of the oscillator strength. Nonetheless, even with a localized defect, the third peak remains the strongest absorption in the spectrum for long oligomers. The fourth peak in the 2.4–2.7 eV region that is rather intense for 10T⁺ through 14T⁺ is absent for 16T⁺ and 19T⁺.

Since TDB3P86-30% and TDBP86 spectra differ in the high-energy sub-band region of longer OT cations, stick spectra for 8T⁺ through 20T⁺ are plotted at the TDBP86

Table 3. Excitation Energies in eV and Oscillator Strengths (in Parenthesis) for Thiophene Oligomer Cations

	method	E1	E2	E3	E4
4T ⁺	TDB3P86-30%	1.34 (0.18)	2.11 (1.22)		
	TDBP86	1.22 (0.10)	2.09 (0.26)	2.17 (0.94)	
	expt. ¹⁶	1.16	1.92		
5T ⁺	TDB3P86-30%	1.12 (0.33)	1.86 (1.53)		
	TDBP86	1.01 (0.18)	1.86 (1.38)		
	expt. ¹⁶	0.98	1.72		
6T ⁺	TDB3P86-30%	0.96 (0.53)	1.68 (1.70)		
	TDBP86	0.88 (0.29)	1.66 (1.64)		
	expt. ¹⁶	0.84	1.59		
	expt. ³⁴	0.83	1.58		
8T ⁺	TDB3P86-30%	0.74 (1.00)	1.45 (1.75)	2.56 (0.16)	2.74 (0.11)
	TDBP86	0.70 (0.57)	1.39 (0.81)	1.53 (0.21)	2.16 (0.63)
	in CH ₂ Cl ₂	0.64 (0.29)	1.28 (1.70)	1.43 (0.56)	2.18 (0.53)
9T ⁺	TDB3P86-30%	0.65 (1.23)	1.37 (1.67)	2.42 (0.38)	2.68 (0.09)
	TDBP86	0.65 (0.73)	1.29 (0.88)/	1.36 (0.83)	2.00 (0.78)
	expt. ³²	0.67	1.46		
9T-Cl ₃	TDB3P86-30%	0.86 (0.84)	1.47 (1.67)	1.71 (0.31)	not calculated
	in CH ₂ Cl ₂	0.76 (1.36)	1.37 (1.64)	1.67 (0.12)	
10T ⁺	TDB3P86-30%	0.58 (1.44)	1.30 (1.55)	2.30 (0.65)	2.63 (0.32)
	TDBP86	0.57 (0.86)	1.28 (1.41)	1.86 (0.46)	1.88 (0.75)
12T ⁺	TDB3P86-30%	0.46 (1.76)	1.21 (1.21)	2.14 (1.38)	2.47 (0.55)
	TDBP86	0.48 (1.14)	1.18 (1.35)	1.69 (1.04)	1.70 (0.38)
	expt. ³²	0.59/0.62	1.42/1.45	2.68	
13T ⁺	TDB3P86-30%	0.41 (1.86)	1.17 (1.07)	2.08 (1.90)	2.41 (0.54)
13T ⁺ //13T-Cl ₃	TDB3P86-30%	0.45 (1.87)	1.19 (1.44)	2.03 (0.90)/2.28 (0.28)	2.45 (0.72)
13T-Cl ₃	TDB3P86-30%	0.77 (1.31)	1.24 (0.88)	1.58 (1.52)	2.60 (0.58)
	in CH ₂ Cl ₂	0.64 (1.83)	1.21 (1.03)	1.50 (0.92)	2.34 (0.33)/
					2.49 (0.99)/
					2.58 (0.40)
14T ⁺	TDB3P86-30%	0.37 (1.93)	1.14 (0.93)	2.05 (2.47)	2.38 (0.60)
	TDBP86	0.40 (1.32)	1.15 (1.15)	1.57 (1.39)/1.59 (0.65)	2.06 (0.76)
16T ⁺	TDB3P86-30%	0.31 (1.99)	1.09 (0.71)	2.00 (3.54)	
	TDBP86	0.34 (1.44)	1.12 (0.94)	1.48 (1.62)	
				1.50 (0.66)	
19T ⁺	TDB3P86-30%	0.24 (1.99)	1.05 (0.50)	1.95 (5.12)	
19T ⁺ //19T-Cl ₃	TDB3P86-30%	0.27 (2.21)	0.99 (0.64)	1.86 (2.75)	2.17 (1.36)
19T-Cl ₃	TDB3P86-30%	0.71 (1.50)	1.07 (0.35)	1.34 (1.30)	1.46 (0.56)
			1.63 (0.95)	2.29 (1.67)	2.37 (1.20)
20T ⁺	TDB3P86-30%	0.23 (1.97)	1.03 (0.44)	1.95 (5.61)	
	TDBP86	0.26 (1.56)	1.11 (0.71)	1.37 (1.92)/1.40 (0.55)	

level in Figure 10. The prediction of additional sub-band transitions is confirmed with TDBP86. However, with pure TDDFT, several of the peaks are split into multiple components. The third peak for 20T⁺ lies lower in energy than with the hybrid functional. In addition, the electronic configurations of the transitions are different, having less contribution from the H → L excitation and more contributions involving higher and lower energy levels. These findings seem to be consistent with the more compressed band structure produced with pure DFT. Considering the general performances of pure DFT and DFT-hybrid, showing that DFT-hybrid produces better band gaps,^{44,48–50} and more accurate relative energies of occupied orbitals,⁵¹ it seems that the peak positions obtained with the hybrid functional are more reliable.

Effect of Counterions. Since experimental work showed that the doping process is similar no matter which dopant is used,¹⁰⁹ only Cl₃[−] counterions were employed here. The structure of 13T-Cl₃ is shown in Figure 11. The charge transfer from the thiophene chain to the counterion is 0.96e in 9T-Cl₃, in 13T-Cl₃, and in 19T-Cl₃ according to natural bond order analysis.¹¹⁰ The complete charge transfer indicates that OT cations and counterions form ion pairs that interact electrostatically.

As shown in Figure 2 for 19T-Cl₃, the positive charge is highest in the three central rings. The charges decrease gradually toward the second to last ring from the chain end and increase somewhat in the terminal ring. Cl₃ complexes have therefore localized defects in terms of structure and electron distribution with defect sizes of about 11 rings. 9T⁺

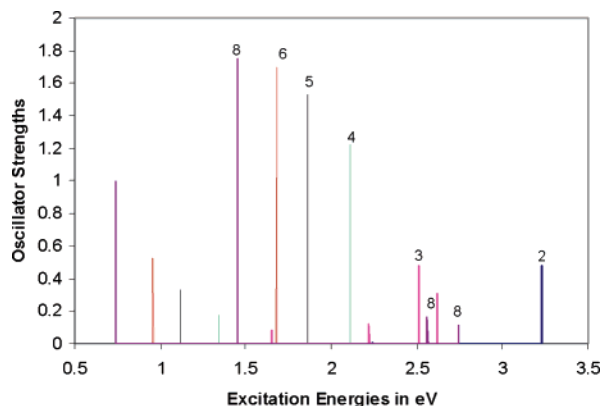


Figure 7. Stick spectra for $2T^+$ through $8T^+$ at the TDB3P86-30% level.

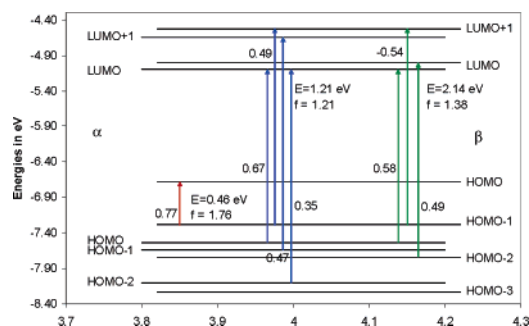


Figure 8. Electronic configurations contributing to the three strong sub-band transitions in $12T^+$ at the TDB3P86-30% level. The numbers close to the arrows give the coefficients of the transitions. β -electron energy levels are shifted right with respect to the α levels. The orbitals are labeled according to Rubio et al.'s³⁷ nomenclature, which is described in the text.

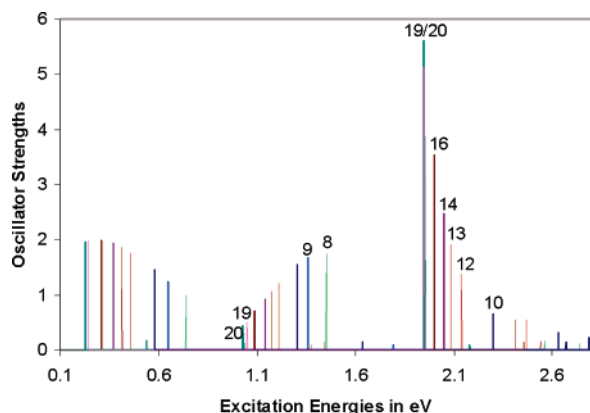


Figure 9. Stick spectra for $8T^+$ through $20T^+$ at the TDB3P86-30% level.

is therefore too short for having a converged defect, and $13T^+$ has only about the size of the localized defect. For $19T^+$, true localization effects can be expected.

TDB3P86-30% excitation energies for $9T-Cl_3$, $13T-Cl_3$, and $19T-Cl_3$ are included in Table 3. Compared to $9T^+$, the excitation energies of $9T-Cl_3$ shift as follows. The first excited state lies 0.21 eV higher in energy, and its oscillator strength is reduced from 1.23 to 0.84. The second excitation energy is increased by 0.10 eV without a change in oscillator strength. The third excited state lies 0.72 eV lower in energy with a similar oscillator strength as in the absence of the

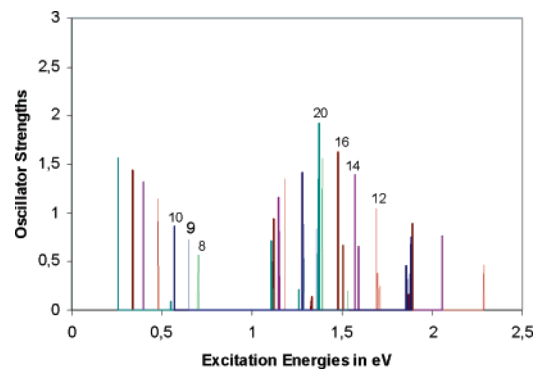


Figure 10. Stick spectra for $8T^+$ through $20T^+$ at the TDBP86 level.

counterion. Thus, the main effect of the counterion is lowering of the third peak. There are only small changes in excitation energies and the oscillator strength when a solvent is considered.

Compared to $13T^+$, the first excitation energy of $13T-Cl_3$ increases by 0.36 eV. The energy of the second transition increases by 0.06 eV. Both peaks decrease in oscillator strength. The third transition lies 0.5 eV lower in the presence of a counterion. The electronic configurations contributing to these states are depicted in Figure 12. One of the electron configurations contributing to the third peak directly involves the counterion. This explains the strong effect of the counterion on this transition. Otherwise, there is little change in the nature of the absorption peaks compared to $12T^+$ (Figure 8). Removing the counterion without letting the structure relax results in absorption energies that differ by less than 0.05 eV from those of $13T^+$. The changes between $13T^+$ and $13T-Cl_3$ are therefore not due to structural localization but caused by changes in the electron distribution. Adding a solvent splits the peak that arises in the 2.4–2.6 eV region of the cation and complex into three components. Otherwise, the influence of the solvent on the spectrum is small.

The inclusion of a counterion increases the energies of the first two peaks of $19T-Cl_3$ by 0.47 and 0.02 eV compared to $19T^+$. Instead of the strong peak at 1.95 eV, there are five absorptions between 1.3 and 2.3 eV in the presence of the counterion. The two peaks at 1.07 and 1.34 eV have H \rightarrow L contributions but are multiconfigurational. The two features at 1.46 and 1.63 eV have major contributions (coefficients of 0.55 and 0.69) from transitions that originate from a Cl_3^- orbital (HOMO-6). The peaks at 2.29 and 2.37 eV originate from H-1 \rightarrow L+1 and H \rightarrow L+2 transitions. Removing the counterion reverses the changes to a large extent as three peaks are predicted for structurally localized $19T^+//19T-Cl_3$ that differ by only up to 0.09 eV from those of $19T^+$. The biggest difference between $19T^+$ with a delocalized defect and $19T^+$ with a structurally localized defect is that the third peak loses oscillator strength, 5.12 versus 2.75. Thus, the effect of structural localization is moderate; the effect of the counterion is substantial, since it is directly involved in some of the electronic transitions. This latter effect might differ with other counterions. In general, the spectral region of the third peak is very sensitive to

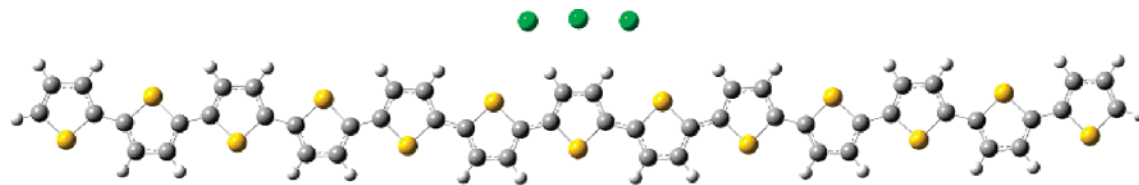


Figure 11. Optimized structure of 13T-Cl₃.

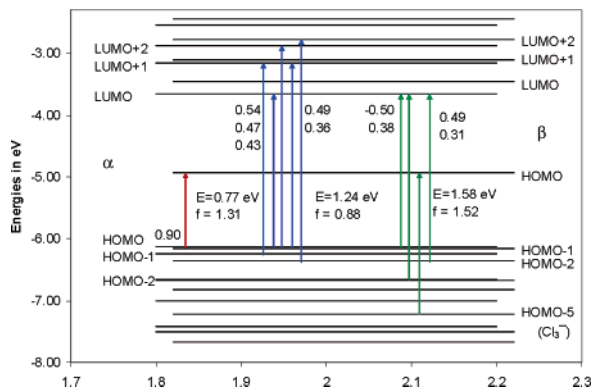


Figure 12. Electronic configurations contributing to the three strong sub-band transitions in 13T-Cl₃ at the TDB3P86-30% level. The numbers close to the arrows give the coefficients of the transitions. β -electron energy levels are shifted right with respect to the α levels.

changes in the method and in the geometry and to the presence of a counterion and a solvent. This region of the spectrum requires further study.

Comparison between Theory and Experiment. For short OT cations, a comparison between theory and experiment is straightforward as the two bands predicted by theory match experimental values well. The influence of counterions is small, and solvent effects lower the theoretical excitation energies, improving the agreement between theory and experiment. As the chains get longer, theory predicts a third band that increases rapidly in oscillator strength. This sub-band transition appears at a chain length of eight rings; for 12T⁺, three peaks of comparable oscillator strength are predicted. Doping of 12T with perchlorate in dichloromethane³² and of 13T with FeCl₃ in dichloromethane³⁴ was reported. The bands of the 13T cation at 0.85 and 1.67 eV are close to those at 0.88 and 1.75 eV for the second doping stage of 12T. Since these values are close to those for 6T⁺, the features were attributed to two polarons located on the same chain. Haare et al.,³² however, reported an earlier doping stage with bands at 0.59–0.62 and 1.42–1.45 eV. These bands belong most likely to the monocations and are used for comparison here. The theoretical predictions of 0.46 and 1.21 eV for 12T⁺ and 0.45 and 1.19 eV for 13T⁺ are a little lower than the experimental values.

In addition, to the two well-known features comparably intense peaks are predicted at 2.14 and 2.08 eV for 12T⁺ and 13T⁺. The appearance of these additional peaks close to the interband transition of the neutral oligomer is important as doping experiments on 12T³² showed that, in contrast to shorter OTs, the interband transition did not disappear but was reduced to half its size. This was rationalized in terms

of a disproportionation of 12T⁺ into neutral 12T and the dication. The present results indicate that the unexpected peak may be the third peak of the radical cation. Similar findings were reported in a theoretical and experimental study by Grozema et al.⁹⁷ As chain lengths increase further, the third peak is predicted to dominate the spectrum of the radical cations. Such a peak has never been discussed explicitly in experimental studies, but the spectra presented by Nakanishi et al.³⁴ for 41T⁺ show a strong absorption slightly below that of the neutral oligomer at low doping levels. These findings will need further analysis.

Discussion

Comparison with experimental and CASPT2 results shows that TDDFT-hybrid excitation energies and oscillator strengths are reliable and almost quantitatively correct. For short oligothiophene cations, TDDFT employing hybrid and pure DFT functionals leads to very similar excitation spectra. The same agreement was obtained for closed-shell polyene cations.⁴¹ In contrast, hybrid functionals do not work for polyene radical cations because of large spin contaminations. For long chain systems, pure TDDFT and TDDFT-hybrid predictions completely agree for the low-energy peaks, and both predict an additional strong sub-band transition. Pure TDDFT tends, however, to place certain peaks lower in energy than TDDFT-hybrid. Since pure DFT produces too small band widths and too small energy gaps, TDDFT-hybrid is probably more reliable.

The appearance of two low-energy peaks in PT instead of one in polyacetylene (PA)⁴¹ can be traced back to the different H-1 \rightarrow H and H \rightarrow L energy gaps. For both systems, there exist, in principle, two excited states which arise from combinations of H-1 \rightarrow H and H \rightarrow L with the same and with opposite signs.^{36,37,71} The combination with the same signs leads to cancellation of the electric dipole transition moment vectors and has a low oscillator strength. For polyene radical cations, the cancellation is almost complete since the energy of the two transitions is practically the same. Thus, the first transition is not observed. For OTs, the cancellation is incomplete because the energy-level difference is not the same. As a result, the low-energy excited state is dominated by H-1 \rightarrow H and has oscillator strength. The high-energy excited state is dominated by H \rightarrow L. For medium-sized OTs with around 10 rings, both excited states have similar oscillator strengths. Thus, the different numbers of peaks in PA and PT do not correspond to different localized species (solitons vs bipolarons) as predicted by the polaron model.

The polaron model^{5,111} was developed on the basis of calculations applying the Su–Schrieffer–Heeger (SSH) Hamiltonian.¹¹² According to this model, localized intragap

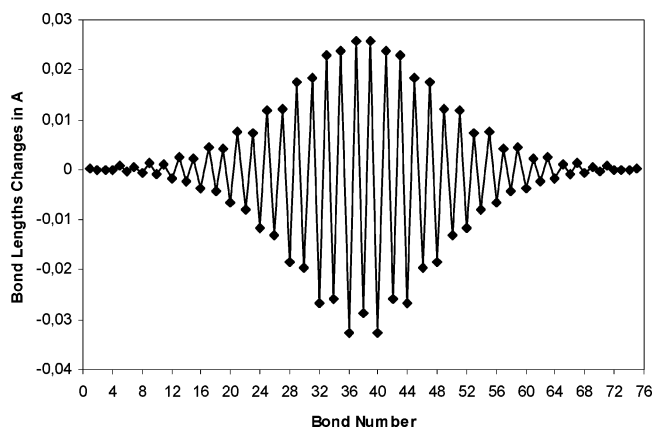


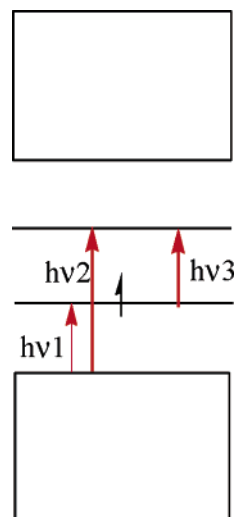
Figure 13. Bond length changes in $12T^+$ compared to neutral $12T$ at the BHandHLYP/CEP-31G* level of theory.

states arise from kinks (solitons) or bound kink–antikink pairs (polarons), both of which extend over 15–20 lattice spacings. Big emphasis is therefore placed on the “self-localization” of defects.⁴ Applied to polypyrrole, localization over four rings was obtained for polarons at the SSH level.¹¹³ Localized defects were reproduced for polyene cations in the absence of counterions at the restricted modified neglect of diatomic overlap (MNDO) level “modified to deal with open shell systems (by placing “1/2 electron” of each spin in the open shell ...)”.¹¹⁴ A polaron size of four rings was also determined for PT with the SSH¹¹⁵ method and with MNDO calculations on $6T^+$.⁶ Thiophene cations with up to nine rings were optimized at the semiempirical AM1 level, employing restricted open-shell Hartree–Fock (ROHF) wave functions³⁸ because ROHF “better reproduces the localization of the charge carriers along the chain as compared to the unrestricted unrestricted Hartree–Fock (UHF) approach.”¹¹⁶ An upper limit for the defect size of five rings was estimated in this way. It was shown more recently, however, that, while it is true that UHF overestimates the width of solitons of neutral polyenes, ROHF underestimates it.¹¹⁷ Localized defects were also obtained with two-configuration SCF.⁵⁴ Defect localization was confirmed for thiophene cations with UMP2 and DFT-hybrid (BHandHLYP),⁹⁸ in contrast to pure DFT results.¹¹⁸

The problem with *ab initio* and HF-based semiempirical calculations on polarons is that wave functions of open-shell species are spin-contaminated, and the problem grows as the chains get longer. Therefore, one must choose between spin-contaminated and restricted wave functions, the former leading to delocalized defects, the latter to localized ones. The above summary shows that the calculations concerning defect sizes have been adjusted in one way or another to reproduce the localized defects predicted with the SSH method. Localization of polarons has therefore never been *proven* at higher levels of theory. Here, it is found that open-shell DFT-hybrid calculations produce delocalized defects *in the absence of spin-contamination*.

Since the localized defects at the BHandHLYP/3-21G* level⁹⁸ are at odds with the findings of this work, geometries of $12T$, $12T^+$, and $19T^+$ were optimized at the BHandHLYP/CEP-31G* level. The bond length changes upon ionization are shown in Figure 13 for $19T^+$. While it is true that the

Scheme 1



defect is more localized with BHandHLYP than with B3P86-30%, the defect still spreads over all but the last two rings in $19T^+$. This corresponds to a defect size of 15 rings. The energy lowering during the optimization starting with the B3P86-30% geometry is 1.96 kcal/mol. Thus, the potential energy surface is confirmed to be very flat, and highly accurate calculations would be required to determine the geometry with certainty. The half and half (HandH) functional includes 50% HF exchange. Therefore, it does not come as a surprise that the expectation values of the spin-operator are 1.15 for $12T^+$ and 1.30 for $19T^+$. Increasing the amount of HF exchange to 50% simply reintroduces the spin-contamination problem of *ab initio* methods. The BHandHLYP geometry is therefore not reliable and is no proof for polaron localization.

Apart from the problem with spin-contamination, HF calculations lack dynamic correlation. Since the driving force for defect localization is supposed to be the energy difference between quinoid and aromatic structures, Moro et al.⁹⁶ tested the performance of HF, MP2, and DFT with respect to this energy difference for $2T$. It turned out that HF overestimates the preference for the aromatic form by 30 kcal/mol compared to MP2 and BLYP, which predict preferences of 15.5 and 13 kcal/mol, respectively. In agreement with these results, DFT-hybrid defect sizes were shown to agree with MP2 ones for solitons in odd-numbered polyene cations.⁴¹ Thus, DFT-B3P86-30% geometries do not suffer from overdelocalization of defects compared to MP2. This discussion suggests that DFT-hybrid geometries are reliable for conjugated systems and that the delocalized defects predicted for radical cations are not a DFT artifact. Additional evidence against defect localization comes from a comparison of INDO/SCI excitation energies obtained at ROHF/AM1 and DFT structures, which shows that the originally very poor agreement with experimental results^{38,116} improves when delocalized DFT structures are employed.⁹⁷

The delocalized nature of the defect agrees with earlier pure DFT results,^{118–120} which showed, moreover, that any defect localization decreases further in a three-dimensional lattice compared to isolated chains. Thus, the most accurate calculations performed on polarons to this date suggest that

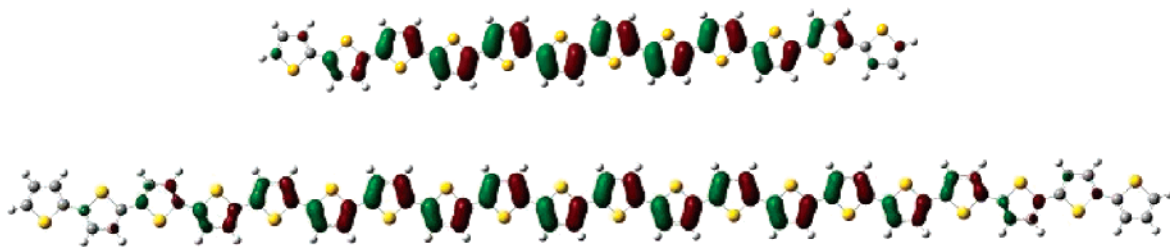


Figure 14. HOMO orbitals of 12T and 20T at the B3P86-30% level of theory.

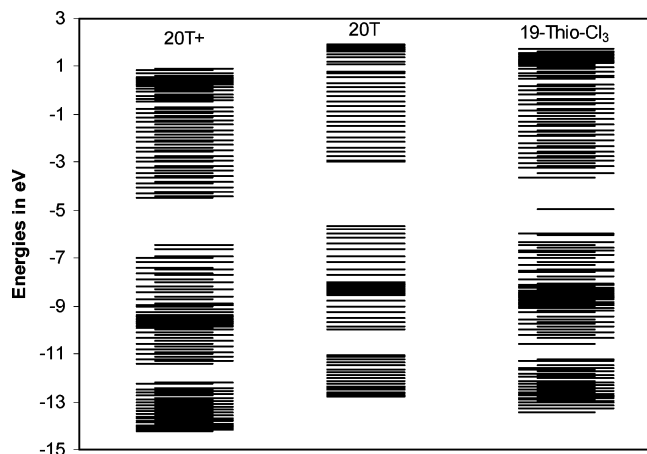


Figure 15. π -orbital energies of 20T, 20T⁺, and 19T-Cl₃ at the UTDB3P86-30% level of theory. β -orbital energies are shifted right with respect to α levels.

these defects are delocalized. This is exactly what qualitative molecular orbital theory predicts. As the electron is removed from a molecular orbital that is delocalized almost over the entire molecule, except for the terminal rings (compare Figure 14), the finding of a delocalized defect that involves all but the terminal rings makes perfect sense. Why should ionization involve only five thiophene rings? Experimental evidence for localization is necessarily obtained in the presence of counterions. In the presence of counterions, DFT predicts defect localization over 11 rings.

According to the polaron model, oligothiophene cations should have two new energy levels placed symmetrically in the band gap. These gap states are believed to be a consequence of the formation of a geometrically localized defect upon ionization. The two intragap states give rise to three sub-band transitions (Scheme 1): $h\nu_1$ forms a valence band to HOMO, $h\nu_2$ forms a valence band to the second intragap state, and $h\nu_3$ forms a band between the two intragap states.

In Figure 15, the π -orbital energies are plotted for 20T, 20T⁺, and 19T-Cl₃. Due to their chain length, these cations may serve as models for polymers. Although the meaning of DFT orbital energies is a matter of debate,^{121–123} a comparison of energy levels obtained with B3LYP and peaks in ultraviolet photoelectron spectra revealed agreement regarding relative energies of the occupied orbitals although the ionization potentials applying Koopmans's theorem are too low.⁵¹ Combined with the accurate band gaps predicted at the B3P86-30% level,⁴⁴ orbital energy plots should give rather accurate relative positions of the occupied and unoccupied energy levels. Figure 15 does not confirm the

energy-level diagram as shown in Scheme 1. There are no two symmetrically placed levels in the gap for the cation with and without counterions. For 20T⁺, the highest β level at -6.42 eV is empty and belongs to the lower polaron level together with the highest occupied α orbital at -6.96 eV. The other β level at -6.62 eV is occupied. Thus, pol1 is very close to the valence band. pol2 is merged with the conduction band. This might be attributed to the lack of defect localization. In the presence of the counterion, and therefore with defect localization, only the empty β level moves up. There is still no pol2 in the gap.

Despite the absence of the two intragap states, TDDFT correctly predicts sub-band transitions. These transition are obtained at virtually the same energies with delocalized and with localized defects. Thus, defect localization cannot be the reason for the sub-band transitions. Analysis of the nature of these excited states at the CASPT2 and TDDFT level shows that the $h\nu_1$ and $h\nu_3$ transitions, which correspond to H-1 \rightarrow H and H \rightarrow L transitions, couple with the same and opposite signs to give rise to a weak low-energy and a strong higher-energy absorption peak. Scheme 1 is therefore inconsistent with the electronic nature of these first two excited states. Moreover, the H \rightarrow L transition couples with additional transitions especially in the long chain limit. The last transition $h\nu_2$, corresponding to H-1 \rightarrow L, is not predicted at the CASPT2 and TDDFT levels of theory.

Conclusions

Although TDDFT has problems with excited states of neutral conjugated π systems, TDDFT gives very good results for conjugated cations and radical cations. This conclusion is based on a comparison of TDDFT excitation energies with CASPT2 data on 2T⁺ and 3T⁺ and with experimental results for long OT radical cations. While hybrid functionals produce large spin contamination for polyene radical cations, spin contamination is virtually absent in open-shell calculations on oligothiophene radical cations. Therefore, the more reliable hybrid functionals can be used for OT radical cations.

For short- to medium-sized oligomers, two sub-band transitions are obtained. In the long chain limit, TDDFT predicts one additional intense sub-band transition. Experimental data on 12T⁺ and 41T⁺ seem to confirm the existence of such a transition close to the interband transition of the neutral system.

The two lower-energy sub-band features of OT radical cations have the same electronic origin as the single sub-band peak in polyene radicals and radical cations. In both systems of H-1 \rightarrow H and H \rightarrow L, transitions mix with the same and opposite signs. With equal transition energies as

in polyene radical cations, the low-energy peak has no oscillator strength and the high-energy peak is very strong. With different excitation energies as in OT radical cations, the low-energy peak becomes visible. Thus, polarons may give rise to one, two, or three sub-band peaks depending on the system and on the conjugation length.

DFT methods predict delocalized defects in the absence of spin contamination. Usually, the reliability of DFT methods regarding this issue is questioned since DFT tends to overestimate conjugation. One should not forget, however, that the polaron model is based on Hückel-type calculations that lack a self-consistent treatment of Coulomb repulsions. Localized defects are only reproduced with semiempirical and ab initio methods that lack dynamic electron correlation and are based on restricted open-shell wave functions. Since the potential energy surfaces are very flat, most of the discrepancies between the results with different methods are caused by the small energy changes that are associated with distortions of the structures.

Spectra obtained for radical cations with optimized structures and with nonoptimized structures containing a localized structural defect are very similar. This proves beyond any doubt that defect localization is not the reason for the occurrence of sub-band transitions.

Spectra calculated in the presence of counterions differ especially for longer systems from those of bare cations due to a change in the electron density and due to direct involvement of the counterion in some of the electronic transitions.

With all due caution that should be applied when approximate methods are used and only isolated molecules are investigated, it must be stated that the present results are in contradiction with almost every aspect of the polaron model. Instead of the strong self-localization, there are very flat potential energy surfaces. The same sub-band transitions are obtained in the absence as in the presence of defect localization. The nature of the electronic transitions is more complicated than predicted with the polaron model as all of the peaks involve a combination of several electronic configurations. In the long chain limit, due to the closely spaced orbital energies, extensive configuration mixing contributes to the excited states. Care is therefore recommended when using the polaron model.

Acknowledgment. This work is supported by TÜBİTAK (TBAG-2461) and by Bilkent University. I would like to thank Dennis Salzner for writing a program that extracts orbital energies from Gaussian 03 output files for plotting.

References

- (1) Skotheim, T. A. *Handbook of Conducting Polymers*; Marcel Dekker: New York, 1986.
- (2) Chung, T.-C.; Kaufman, J. H.; Heeger, A. J.; Wudl, F. *Phys. Rev. B: Condens. Matter Mater. Phys.* **1984**, *30*, 702.
- (3) Brédas, J. L.; Thémans, B.; Fripiat, J. G.; André, J.-M.; Chance, R. R. *Phys. Rev. B: Condens. Matter Mater. Phys.* **1984**, *29*, 6761.
- (4) Brédas, J. L.; Street, G. B. *Acc. Chem. Res.* **1985**, *18*, 309.
- (5) Heeger, A. J.; Kivelson, S.; Schrieffer, J. R.; Su, W.-P. *Rev. Mod. Phys.* **1988**, *60*, 781.
- (6) Stafström, S.; Brédas, J. L. *Phys. Rev. B: Condens. Matter Mater. Phys.* **1988**, *38*, 4180.
- (7) Patil, A. O.; Heeger, A. J.; Wudl, F. *Chem. Rev.* **1988**, *88*, 183.
- (8) *Electronic Materials: The Oligomer Approach*; Müllen, K., Wegener, G., Eds.; Wiley-VCH: Weinheim, Germany, 1997.
- (9) Taliani, C.; Blinov, L. M. *Adv. Mater.* **1996**, *8*, 353.
- (10) Fichou, D.; Teulade-Fichou, M.-P.; Horowitz, G.; Demanze, F. *Adv. Mater.* **1997**, *9*, 75.
- (11) Nakanishi, H.; Sumi, N.; Aso, Y.; Otsubo, T. *J. Org. Chem.* **1998**, *63*, 8632.
- (12) Otsubo, T.; Nakanishi, H.; Aso, Y. *Synth. Met.* **1999**, *101*, 604.
- (13) Sumi, N.; Nakanishi, H.; Ueno, S.; Takimiya, K.; Aso, Y.; Otsubo, T. *Bull. Chem. Soc. Jpn.* **2001**, *74*, 979.
- (14) Otsubo, T.; Aso, Y.; Takimiya, K. *Bull. Chem. Soc. Jpn.* **2001**, *74*, 1789.
- (15) Fichou, D.; Horowitz, G.; Garnier, F. *Synth. Met.* **1990**, *39*, 125.
- (16) Fichou, D.; Horowitz, G.; Xu, B.; Garnier, F. *Synth. Met.* **1990**, *39*, 243.
- (17) Guay, J.; Diaz, A.; Wu, R.; Tour, J. M. *J. Am. Chem. Soc.* **1993**, *115*, 1869.
- (18) Guay, J.; Kasai, P.; Diaz, A.; Wu, R.; Tour, J. M.; Dao, L. H. *Chem. Mater.* **1992**, *4*, 1097.
- (19) Hill, M. G.; Mann, K. R.; Miller, L. L.; Penneau, J.-F. *J. Am. Chem. Soc.* **1992**, *114*, 2728.
- (20) Hill, M. G.; Penneau, J.-F.; Zinger, B.; Mann, K. R.; Miller, L. L. *Chem. Mater.* **1992**, *4*, 1106.
- (21) Bäuerle, P.; Segelbacher, U.; Maier, A.; Mehring, M. *J. Am. Chem. Soc.* **1993**, *115*, 10217.
- (22) Wintgens, V.; Valat, P.; Garnier, F. *J. Phys. Chem.* **1994**, *98*, 228.
- (23) Yu, Y.; Gunic, E.; Zinger, B.; Miller, L. L. *J. Am. Chem. Soc.* **1996**, *118*, 1013.
- (24) Zinger, B.; Mann, K. R.; Hill, M. G.; Miller, L. L. *Chem. Mater.* **1992**, *4*, 1113.
- (25) Evans, C. H.; Scaiano, J. C. *J. Am. Chem. Soc.* **1990**, *112*, 2694.
- (26) Fichou, D.; Xu, B.; Horowitz, G.; Garnier, F. *Synth. Met.* **1991**, *41*, 463.
- (27) Guay, J.; Diaz, A.; Wu, R.; Tour, J. M.; Dao, L. H. *Chem. Mater.* **1992**, *4*, 254.
- (28) Hotta, S.; Waragai, K. *J. Phys. Chem.* **1993**, *97*, 7427.
- (29) Horowitz, G.; Yassar, A.; von Bardeleben, H. J. *Synth. Met.* **1994**, *62*, 245.
- (30) Furukawa, Y. *J. Phys. Chem.* **1996**, *100*, 15644.
- (31) Graf, D. D.; Duan, R. G.; Campbell, J. P.; Miller, L. L.; Mann, K. R. *J. Am. Chem. Soc.* **1997**, *119*, 5888.
- (32) Haare, J. A. E. H.; Havinga, E. E.; van Dongen, J. L. J.; Janssen, R. A. J.; Cornil, J.; Brédas, J. L. *Chem.—Eur. J.* **1998**, *4*, 1509.
- (33) Tol, A. J. W. *Synth. Met.* **1995**, *74*, 95.

- (34) Nakanishi, H.; Sumi, N.; Ueno, S.; Takimiya, K.; Aso, Y.; Otsubo, T.; Komaguchi, K.; Shiotani, M.; Ohta, N. *Synth. Met.* **2001**, *119*, 413.
- (35) Nessakh, B.; Horowitz, G.; Garnier, F.; Deloffre, F.; Srivastava, P.; Yassar, A. *J. Electroanal. Chem.* **1995**, *399*, 97.
- (36) Keszthelyi, T.; Grage, M. M.-L.; Offersgard, J. F.; Wilbrandt, R.; Svendsen, C.; Sonnich Mortensen, O.; Pedersen, J. K.; Jensen, H. J. A. *J. Phys. Chem. A* **2000**, *104*, 2808.
- (37) Rubio, M.; Ortí, E.; Pou-Amerigo, R.; Merchán, M. *J. Phys. Chem. A* **2001**, *105*, 9788.
- (38) Cornil, J.; Beljonne, D.; Brédas, J. L. *J. Chem. Phys.* **1995**, *103*, 842.
- (39) Ye, A.; Shuai, Z.; Kwon, O.; Brédas, J. L.; Beljonne, D. *J. Chem. Phys.* **2004**, *121*, 5567.
- (40) Zade, S. S.; Bendikov, M. *Chem.—Eur. J.* **2006**, in press.
- (41) Salzner, U. *J. Chem. Theory Comput.* **2007**, *3*, 219.
- (42) Becke, A. D. *J. Chem. Phys.* **1993**, *98*, 5648.
- (43) Perdew, J. P. *Phys. Rev. B: Condens. Matter Mater. Phys.* **1986**, *33*, 8822.
- (44) Salzner, U.; Lagowski, J. B.; Pickup, P. G.; Poirier, R. A. *J. Phys. Chem.* **1998**, *102*, 2572.
- (45) Stevens, W.; Basch, H.; Krauss, J. *J. Chem. Phys.* **1984**, *81*, 6026.
- (46) Stevens, W. J.; Krauss, M.; Basch, H.; Jasien, P. G. *Can. J. Chem.* **1992**, *70*, 612.
- (47) Salzner, U.; Lagowski, J. B.; Pickup, P. G.; Poirier, R. A. *J. Comput. Chem.* **1997**, *18*, 1943.
- (48) Salzner, U.; Lagowski, J. B.; Poirier, R. A.; Pickup, P. G. *Synth. Met.* **1998**, *96*, 177.
- (49) Kertesz, M.; Choi, C. H.; Yang, S. *Chem. Rev.* **2005**, *105*, 3448.
- (50) Choi, C. H.; Kertesz, M.; Karpfen, A. *J. Chem. Phys.* **1997**, *107*, 6712.
- (51) Sanchez-Carrera, R. S.; Coropceanu, V.; da Silva, D. A.; Friedlein, R.; Osikowicz, W.; Murdey, R.; Suess, C.; Salaneck, W. R.; Bredas, J. L. *J. Phys. Chem. B* **2006**, *110*, 18904.
- (52) Bauernschmitt, R.; Ahlrichs, R. *Chem. Phys. Lett.* **1996**, *256*, 454.
- (53) Dierksen, M.; Grimme, S. *J. Phys. Chem. A* **2004**, *108*, 10225.
- (54) Irle, S.; Lischka, H. *J. Chem. Phys.* **1997**, *107*, 3021.
- (55) Salzner, U. *Curr. Org. Chem.* **2004**, *8*, 569.
- (56) Bauernschmitt, R.; Ahlrichs, R.; Henrich, F. H.; Kappes, M. M. *J. Am. Chem. Soc.* **1998**, *120*, 5052.
- (57) Hirata, S.; Head-Gordon, M.; Bartlett, R. J. *J. Chem. Phys.* **1999**, *111*, 10774.
- (58) Hirata, S.; Head-Gordon, M. *Chem. Phys. Lett.* **1999**, *302*, 375.
- (59) Hsu, C.-P.; Hirata, S.; Head-Gordon, M. *J. Phys. Chem. A* **2001**, *105*, 451.
- (60) Della Sala, F.; Heinze, H. H.; Görling, A. *Chem. Phys. Lett.* **2001**, *339*, 343.
- (61) Ma, J.; Li, S.; Liang, Y. *Macromolecules* **2002**, *35*, 1109.
- (62) Hieringer, W.; van Gisbergen, S. J. A.; Baerends, E. J. *J. Phys. Chem. A* **2002**, *106*, 10380.
- (63) Dreuw, A.; Head-Gordon, M. *Chem. Rev.* **2005**, *105*, 4009.
- (64) Cai, Z.-L.; Sendt, K.; Reimers, J. R. *J. Chem. Phys.* **2002**, *117*, 5543.
- (65) Sala, F. D.; Görling, A. *Int. J. Quantum Chem.* **2003**, *91*, 131.
- (66) Parac, M.; Grimme, S. *Chem. Phys.* **2003**, *292*, 11.
- (67) Dreuw, A.; Weisman, J. L.; Head-Gordon, M. *J. Chem. Phys.* **2003**, *119*, 2943.
- (68) Dreuw, A.; Head-Gordon, M. *J. Am. Chem. Soc.* **2004**, *126*, 4007.
- (69) Dierksen, M.; Grimme, S. *J. Chem. Phys.* **2004**, *120*, 3544.
- (70) Salzner, U. Conjugated Organic Polymers: From Bulk to Molecular Wire. In *Handbook of Theoretical and Computational Nanotechnology*; Rieth, M., Schommers, W., Eds.; ASP: Valencia, CA, 2006; Vol. 8, pp 203.
- (71) Kawashima, Y.; Nakayama, K.; Nakano, H.; Hirao, H. *Chem. Phys. Lett.* **1997**, *267*, 82.
- (72) Luo, Y.; Ågren, H.; Stafström, S. *J. Chem. Phys.* **1994**, *98*, 7782.
- (73) Luo, Y.; Ruud, K.; Norman, P.; Jonsson, D.; Ågren, H. *J. Phys. Chem. B* **1998**, *102*, 1710.
- (74) Li, Y. Modeling Solvent Effects on Excitation Energies for Polyenes. Master's Thesis, Bilkent University, Ankara, Turkey, 2006.
- (75) Grozema, F. C.; van Duijnen, P. T.; Siebbeles, L. D.; Goossens, A.; Leeuw, S. W. *J. Phys. Chem. B* **2004**, *108*, 16139.
- (76) Miertus, S.; Scrocco, E.; Tomasi, J. *J. Chem. Phys.* **1981**, *55*, 117.
- (77) Miertus, S.; Tomasi, J. *J. Chem. Phys.* **1982**, *65*, 239.
- (78) Cossi, M.; Cammi, R.; Tomasi, J. *Chem. Phys. Lett.* **1996**, *255*, 327.
- (79) Cancès, M. T.; Mennucci, B.; Tomasi, J. *J. Chem. Phys.* **1997**, *107*, 3032.
- (80) Barone, V.; Cossi, M.; Tomasi, J. *J. Chem. Phys.* **1997**, *107*, 3210.
- (81) Cossi, M.; Barone, V.; Mennucci, B.; Tomasi, J. *Chem. Phys. Lett.* **1998**, *286*, 253.
- (82) Barone, V.; Cossi, M.; Tomasi, J. *J. Comput. Chem.* **1998**, *19*, 404.
- (83) Barone, V.; Cossi, M. *J. Phys. Chem. A* **1998**, *102*, 1995.
- (84) Mennucci, B.; Tomasi, J. *J. Chem. Phys.* **1997**, *106*, 5151.
- (85) Mennucci, B.; Cancès, M. T.; Tomasi, J. *J. Phys. Chem. B* **1997**, *101*, 10506.
- (86) Tomasi, J.; Mennucci, B.; Cancès, M. T. *THEOCHEM* **1999**, *464*, 211.
- (87) Cammi, R.; Mennucci, B.; Tomasi, J. *J. Phys. Chem. A* **1999**, *103*, 9100.
- (88) Cossi, M.; Barone, V.; Robb, M. A. *J. Chem. Phys.* **1999**, *111*, 5295.
- (89) Cammi, R.; Mennucci, B.; Tomasi, J. *J. Phys. Chem. A* **2000**, *104*, 5631.
- (90) Cossi, M.; Barone, V. *J. Chem. Phys.* **2000**, *112*, 2427.

- (91) Cossi, M.; Barone, V. *J. Chem. Phys.* **2001**, *115*, 4708.
- (92) Cossi, M.; Rega, N.; Scalmani, G.; Barone, V. *J. Chem. Phys.* **2001**, *114*, 5691.
- (93) Cossi, M.; Scalmani, G.; Rega, N.; Barone, V. *J. Chem. Phys.* **2002**, *117*, 43.
- (94) Cossi, M.; Rega, N.; Scalmani, G.; Barone, V. *J. Comput. Chem.* **2003**, *24*, 669.
- (95) Frisch, M. J.; Trucks, G. W.; Schlegel, H. B.; Scuseria, G. E.; Robb, M. A.; Cheeseman, J. R.; Montgomery, J. A., Jr.; Vreven, T.; Kudin, K. N.; Burant, J. C.; Millam, J. M.; Iyengar, S. S.; Tomasi, J.; Barone, V.; Mennucci, B.; Cossi, M.; Scalmani, G.; Rega, N.; Petersson, G. A.; Nakatsuji, H.; Hada, M.; Ehara, M.; Toyota, K.; Fukuda, R.; Hasegawa, J.; Ishida, M.; Nakajima, T.; Honda, Y.; Kitao, O.; Nakai, H.; Klene, M.; Li, X.; Knox, J. E.; Hratchian, H. P.; Cross, J. B.; Bakken, V.; Adamo, C.; Jaramillo, J.; Gomperts, R.; Stratmann, R. E.; Yazyev, O.; Austin, A. J.; Cammi, R.; Pomelli, C.; Ochterski, J. W.; Ayala, P. Y.; Morokuma, K.; Voth, G. A.; Salvador, P.; Dannenberg, J. J.; Zakrzewski, V. G.; Dapprich, S.; Daniels, A. D.; Strain, M. C.; Farkas, O.; Malick, D. K.; Rabuck, A. D.; Raghavachari, K.; Foresman, J. B.; Ortiz, J. V.; Cui, Q.; Baboul, A. G.; Clifford, S.; Cioslowski, J.; Stefanov, B. B.; Liu, G.; Liashenko, A.; Piskorz, P.; Komaromi, I.; Martin, R. L.; Fox, D. J.; Keith, T.; Al-Laham, M. A.; Peng, C. Y.; Nanayakkara, A.; Challacombe, M.; Gill, P. M. W.; Johnson, B.; Chen, W.; Wong, M. W.; Gonzales, C.; Pople, J. A. *Gaussian 03*, Revision D.01; Gaussian, Inc.: Wallingford, CT, 2004.
- (96) Moro, G.; Scalmani, G.; Cosentino, U.; Pitea, D. *Synth. Met.* **2000**, *108*, 165.
- (97) Grozema, F. C.; Candeias, L. P.; Swart, M.; van Duijnen, P. T.; Wildeman, J.; Hadziioanou, G.; Siebbeles, L. D. A.; Warman, J. M. *J. Chem. Phys.* **2002**, *117*, 11366.
- (98) Geskin, V. M.; Dkhissi, A.; Brédas, J. L. *Int. J. Quantum Chem.* **2003**, *91*, 350.
- (99) Dkhissi, A.; Beljonne, D.; Lazzaroni, R.; Louwet, F.; Groenendaal, L.; Brédas, J. L. *Int. J. Quantum Chem.* **2003**, *91*, 517.
- (100) Geskin, V. M.; Grozema, F. C.; Siebbeles, L. D. A.; Beljonne, D.; Brédas, J. L.; Cornil, J. *J. Phys. Chem. B* **2005**, *109*, 20237.
- (101) Champagne, B.; Spassova, M. *Phys. Chem. Chem. Phys.* **2004**, *6*, 3167.
- (102) Monev, V.; Spassova, M.; Champagne, B. *Int. J. Quantum Chem.* **2005**, *104*, 354.
- (103) Martinez, F.; Voelkel, R.; Naegele, D.; Naarmann, H. *Mol. Cryst. Liq. Cryst.* **1989**, *167*, 227.
- (104) Birnbaum, D.; Kohler, B. E. *J. Chem. Phys.* **1989**, *90*, 3506.
- (105) Birnbaum, D.; Kohler, B. E. *J. Chem. Phys.* **1991**, *95*, 4783.
- (106) Birnbaum, D.; Fichou, D.; Kohler, B. E. *J. Chem. Phys.* **1992**, *96*, 165.
- (107) D'Amico, K. L.; Manos, C.; Christensen, R. L. *J. Am. Chem. Soc.* **1980**, *102*, 1777.
- (108) Guillaume, M.; Champagne, B.; Zutterman, F. *J. Phys. Chem. A* **2006**, *110*, 13007.
- (109) Fincher, C. R., Jr.; Ozaki, M.; Heeger, A. J.; MacDiarmid, A. G. *Phys. Rev. B: Condens. Matter Mater. Phys.* **1979**, *19*, 4140.
- (110) Reed, A. E.; Curtiss, L. A.; Weinhold, F. *Chem. Rev.* **1988**, *88*, 899.
- (111) Fesser, K.; Bishop, A. R.; Campbell, D. K. *Phys. Rev. B: Condens. Matter Mater. Phys.* **1983**, *27*, 4804.
- (112) Su, W. P.; Schrieffer, J. R.; Heeger, A. J. *Phys. Rev. B: Condens. Matter Mater. Phys.* **1980**, *22*, 2099.
- (113) Brédas, J. L.; Scott, J. C.; Yakushi, K.; Street, G. B. *Phys. Rev. B: Condens. Matter Mater. Phys.* **1984**, *30*, 1023.
- (114) Boudreaux, D. S.; Chance, R. R.; Brédas, J. L.; Silbey, R. *Phys. Rev. B: Condens. Matter Mater. Phys.* **1983**, *28*, 6927.
- (115) Brédas, J. L.; Wudl, F.; Heeger, A. J. *Solid State Commun.* **1987**, *63*, 577.
- (116) Cornil, J.; Beljonne, D.; Brédas, J. L. *J. Chem. Phys.* **1995**, *103*, 834.
- (117) Bally, T.; Hrovat, D. A.; Thatcher Borden, W. *Phys. Chem. Chem. Phys.* **2000**, *2*, 3363.
- (118) Brocks, G. *Synth. Met.* **1999**, *102*, 914.
- (119) Vogl, P.; Campbell, C. K. *Phys. Rev. Lett.* **1989**, *62*, 2012.
- (120) Vogl, P.; Campbell, C. K. *Phys. Rev. B: Condens. Matter Mater. Phys.* **1990**, *41*, 12797.
- (121) Perdew, J. P.; Levy, M. *Phys. Rev. Lett.* **1983**, *51*, 1884.
- (122) Baerends, E. J.; Gritsenko, O. V. *J. Phys. Chem. A* **1997**, *101*, 5383.
- (123) Stowasser, R.; Hoffmann, R. *J. Am. Chem. Soc.* **1999**, *121*, 3414.

JCTC Journal of Chemical Theory and Computation

Theory for Quantum Interference Signal from an Inhomogeneously Broadened Two-Level System Excited by an Optically Phase-Controlled Laser-Pulse Pair

Shin-ichiro Sato*

Division of Biotechnology and Macromolecular Chemistry, Graduate School of Engineering, Hokkaido University, Sapporo 060-8628, Japan

Received January 9, 2007

Abstract: A useful expression for the quantum interference (QI) signal was derived for an inhomogeneously broadened two-level system when it was excited by an optically phase-controlled laser-pulse pair. It was shown that the QI signal oscillates as a function of a relative optical phase, with the reduced angular frequency given by the relation $\omega_a = (\Gamma^2\omega_0 + \gamma_g^2\Omega)/(\gamma_g^2 + \Gamma^2)$, where γ_g and Γ are standard deviations of the system's absorption and the laser spectra both having a Gaussian line shape, respectively, and ω_0 and Ω are the center angular frequency of the system absorption and the carrier angular frequency of the laser, respectively.

1. Introduction

Control of quantum interference (QI) of molecular wavefunctions excited by a pair of femtosecond laser pulses that have a definite optical phase is one of the basic schemes for the control of versatile quantum systems including chemical reactions. The QI technique with the pulse pair, or the double pulse, has been applied to several atomic, molecular systems in the gas phase^{1–3} and condensed phases.^{4–8} A basic theory of the double-pulse QI experiment for a two-level molecular system in the gas phase has been given in the original paper by Scherer et al.^{1,2} In their beautiful work, they derived the expression for the QI signal from a two-level system including a molecular vibration. However, the effect of inhomogeneous broadening, which is not very significant in the gas phase, has not been taken into account.

In this study, we derive a compact and useful expression for the QI signal for an inhomogeneously broadened two-level system in condensed phases, when the system was excited by an optically phase-controlled laser-pulse pair. In general, the homogeneous broadening gives a Lorentz profile:

$$S_L(\omega) = \frac{1}{2\pi} \frac{\gamma_1}{(\omega_0 - \omega)^2 + (\gamma_1/2)^2} \quad (1)$$

On the other hand, the inhomogeneous broadening gives a Gauss profile:

$$S_G(\omega) = \frac{1}{\sqrt{\pi} \gamma_g} e^{-(\omega - \omega_0)^2/\gamma_g^2} \quad (2)$$

When both the homogeneous and inhomogeneous broadening exist, the spectral profiles are given by a convolution of $S_L(\omega)$ with $S_G(\omega)$, namely, a Voigt profile:

$$S_V(\omega) = \int_{-\infty}^{\infty} d\omega' S_L(\omega') S_G(\omega + \omega_0 - \omega') \quad (3)$$

As pointed out by Scherer et al., the QI signal is the free-induction decay and the Fourier transform of the optical spectral profile. According to the convolution theorem in the Fourier transform, the expression for the QI signal should, in principle, have the form:

$$\text{QI}(t_d) = \text{FT}[S_V(\omega)] = \text{FT}[S_L(\omega)] \text{FT}[S_G(\omega)] \propto \cos[\omega_0 t_d] \exp\left[-\frac{\gamma_1 t_d}{2}\right] \exp\left[-\frac{\gamma_g^2 t_d^2}{4}\right] \quad (4)$$

where t_d is a time delay between the laser-pulse pair. However, in the above discussion, the laser pulse is assumed to be impulsive; that is, the effects of a finite time width or a spectral width of the actual laser pulse are not taken into account. The purpose of this paper is to derive the expression for the QI signal that includes the effects of nonimpulsive

* E-mail: s-sato@eng.hokudai.ac.jp.

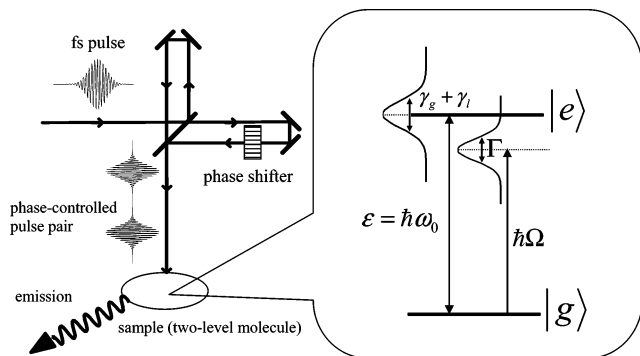


Figure 1. Schematic drawing of the QI experiment with a phase-controlled laser-pulse pair.

laser pulses which possess a Gaussian pulse shape. The procedure for derivation has two steps: first, we derive the expression for the homogeneously broadened two-level system, and then we obtain the expression for the inhomogeneously broadened system by integrating the result of the homogeneously broadened system weighted by the inhomogeneous spectral distribution function.

2. Theory

2.1. Homogeneously Broadened Two-Level System. Let us consider a two-level electronic system interacting with a phase-controlled femtosecond-laser pulse pair (Figure 1). When the ground-state energy is assumed to be zero, that is, the system is referenced to the molecular frame, the electronic Hamiltonian for the two-level system with the homogeneous broadening is given by

$$\hat{H} = (\epsilon - i\gamma_1/2)|e\rangle\langle e| \quad (5)$$

where γ_1 is a homogeneous relaxation constant that stands for a radiative or a nonradiative decay constant. An electronic transition dipole operator is expressed as

$$\hat{\mu} = \mu_{eg}(|e\rangle\langle g| + |g\rangle\langle e|) \quad (6)$$

The interaction Hamiltonian between the system and a photon field is given by

$$\hat{V} = -\hat{\mu} E(t) \quad (7)$$

where photoelectric field $E(t)$ in the double-pulse QI experiments is given by the sum of E_1 and E_2 , each of which has a Gaussian profile:

$$E(t) = E_1(t) + E_2(t) \quad (8)$$

where τ is a standard deviation of each laser pulse in the

$$E_1(t) = E_0 \exp[-t^2/(2\tau^2)] \cos(\Omega t) \quad (9)$$

$$E_2(t) = E_0 \exp[-(t - t_d)^2/(2\tau^2)] \cos[\Omega(t - t_d)] \quad (10)$$

time domain and related to a standard deviation Γ of each laser pulse in the frequency domain by $\tau = 1/\Gamma$, and Ω is a common carrier frequency of the laser pulses. The phase shift of the photon field is defined as delay time:⁹ the delay time t_d between double pulses is finely controlled with attoseconds order in the optical phase-controlled experiments. This

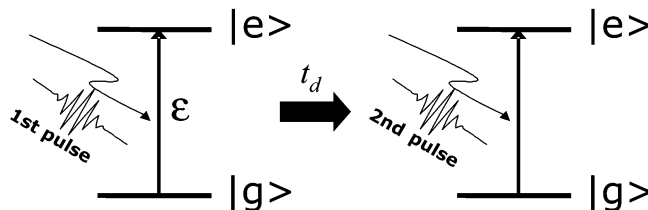
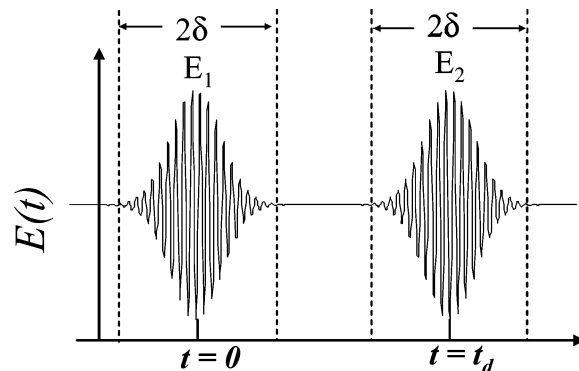


Figure 2. Time domains: free evolution and interaction with laser pulses.

definition is natural in the optical phase-shift experiments as pointed out by Albrecht et al.¹⁰

To derive the expression for the QI signal, we divide the time region into the free-evolution regions and the interaction regions (Figure 2). Then, the time evolution of the system from the initial electronic state $|\psi(t = -\infty)\rangle = |g\rangle$ is given by the equation

$$|\psi(t)\rangle = \hat{U}(t - t_d - \delta)\hat{W}_2\hat{U}(t_d - 2\delta)\hat{W}_1|g\rangle \quad (11)$$

where the time evolution operator in the absence of the photon field is defined by

$$\hat{U}(t, t') = \exp[-i\hat{H}(t - t')/\hbar] \quad (12a)$$

or by replacing as $\Delta t = t - t'$

$$\hat{U}(\Delta t) = \exp[-i\hat{H}\Delta t/\hbar] \quad (12b)$$

Within the framework of the first-order perturbation theory,¹¹ the time evolution operator \hat{W}_j ($j = 1, 2$) in the presence of the photon field is given by

$$\begin{aligned} \hat{W}_j &= \hat{U}(t_j + \delta, t_j - \delta) \\ &= \left\{ 1 - \frac{1}{i\hbar} \int_{t_j - \delta}^{t_j + \delta} dt' \hat{U}(t_j - t') \hat{\mu} E_j(t') \hat{U}(t' - t_j) \right\} \\ &= \hat{U}(2\delta) \left\{ 1 - \frac{1}{i\hbar} \int_{t_j - \delta}^{t_j + \delta} dt' \hat{U}(t_j - t') \hat{\mu} E_j(t') \hat{U}(t' - t_j) \right\} \\ &\equiv \hat{U}(2\delta) \left(1 - \frac{1}{i\hbar} \hat{F}_j \right) \end{aligned} \quad (13)$$

The substitution of eq 13 into eq 11 yields

$$|\psi(t)\rangle = \hat{U}(\delta) \left[\hat{U}(t) + \frac{i}{\hbar} \hat{U}(t) \hat{F}_1 + \frac{i}{\hbar} \hat{U}(t - t_d) \hat{F}_2 \hat{U}(t_d) \right] |g\rangle \quad (14)$$

where \hat{F} is defined as an electronic transition operator, and $\hat{U}(\delta)$ a global phase factor, which will be neglected hereafter, because it does not affect final results in the state-density

matrix. The projection of eq 14 onto the excited state $|e\rangle$ gives

$$\begin{aligned}\langle e|\psi(t)\rangle &= \left\langle e \left| \left[\hat{U}(t) + \frac{i}{\hbar} \hat{U}(t) \hat{F}_1 + \frac{i}{\hbar} \hat{U}(t-t_d) \hat{F}_2 \hat{U}(t_d) \right] |g\rangle \right. \right\rangle \\ &= \frac{i}{\hbar} \langle e | [\hat{U}(t) \hat{F}_1 + \hat{U}(t-t_d) \hat{F}_2 \hat{U}(t_d)] |g\rangle \\ &= \frac{i}{\hbar} \{ \exp[-i\omega_0 - \gamma/2)t] \langle e | \hat{F}_1 |g\rangle + \\ &\quad \exp[-i\omega_0 - \gamma/2)(t-t_d)] \langle e | \hat{F}_2 |g\rangle \} \quad (15)\end{aligned}$$

where $\omega_0 = \epsilon/\hbar$. The matrix element of an electronic transition operator \hat{F}_j is calculated as

$$\begin{aligned}\langle e | \hat{F}_j |g\rangle &= \langle e | \int_{t_j-\delta}^{t_j+\delta} dt' \hat{U}(t_j-t') \hat{\mu} \hat{U}(t'-t_j) |g\rangle E_j(t') \\ &= \mu_{eg} \langle e | \int_{t_j-\delta}^{t_j+\delta} dt' \hat{U}(t_j-t') (|g\rangle \langle e| + \\ &\quad |e\rangle \langle g|) \hat{U}(t'-t_j) |g\rangle E_j(t') \\ &= \mu_{eg} \int_{t_j-\delta}^{t_j+\delta} dt' \langle e | U(t_j-t') |e\rangle \langle g | U(t'-t_j) |g\rangle E_j(t') \\ &= \mu_{eg} \int_{t_j-\delta}^{t_j+\delta} dt' e^{-i(\omega_0 - i\gamma/2)(t_j-t')} E_j(t') \quad (16)\end{aligned}$$

When a rotating-wave approximation is used, the matrix element is further calculated as

$$\begin{aligned}\langle e | \hat{F}_j |g\rangle &= \frac{1}{2} E_0 \mu_{eg} \int_{-\infty}^{+\infty} dx e^{-i(\omega_0 - \Omega)x} e^{-\gamma|x/2 - x^2/(2\tau^2)} \\ &= \sqrt{\frac{\pi}{2}} E_0 \mu_{eg} \tau \exp\left[\frac{\{\gamma_1 + i2(\omega_0 - \Omega)\}^2 \tau^2}{8} \right] \equiv F \times \\ &\quad \exp\left\{ \frac{\tau^2}{8} [\gamma_1^2 - 4(\omega_0 - \Omega)^2 + i4\gamma_1(\omega_0 - \Omega)] \right\} \quad (17)\end{aligned}$$

The substitution of eq 17 into eq 15 yields

$$\langle e | \psi(t, t_d) \rangle = \frac{iF}{\hbar} \exp[-i\omega_0 - \gamma/2)t] \{ 1 + \exp[(i\omega_0 + \gamma/2)t_d] \} \exp\left[\frac{\{\gamma_1 + i2(\omega_0 - \Omega)\}^2 \tau^2}{8} \right] \quad (18)$$

The absolute square of eq 18 gives the density matrix element $\rho_{ee}(t, t_d, \omega_0, \Omega)$ for the excited state

$$\begin{aligned}\rho_{ee}(t, t_d, \omega_0, \Omega) &= \langle e | \psi(t, t_d) \rangle \langle \psi(t, t_d) | e \rangle \\ &= \frac{2F^2}{\hbar^2} e^{\gamma_1^2/(4\Gamma^2)} e^{-(\omega_0 - \Omega)^2/\Gamma^2} \{ e^{-\gamma t} + e^{-\gamma(t-t_d)} + \\ &\quad e^{-\gamma t/2} e^{-\gamma(t-t_d)/2} \cos[\omega_0 t_d] \} \quad (19)\end{aligned}$$

The first and second term give population decays of the excited state created by the first and second pulses, respectively. The third term is the interference term that is the product of coherence decays and an oscillating term.

2.2. Inhomogeneously Broadened System. In the previous section, the inhomogeneous broadening was not taken into consideration. The effects of inhomogeneous decay can be taken into account by summing up ρ_{ee} that originates from inhomogeneously broadened spectral components.¹² When the inhomogeneous spectrum function is given by a Gaussian

in eq 2, the expectation value of the excited-state density function can be written as

$$\begin{aligned}\langle \rho_{ee}(t_d, \omega_0, \Omega) \rangle &= \int_{-\infty}^{+\infty} d\omega S_G(\omega, \omega_0) \rho_{ee}(t_d, \omega, \Omega) \\ &= \frac{F^2}{\hbar^2} e^{\gamma_1^2/(4\Gamma^2)} \int_{-\infty}^{+\infty} d\omega S_G(\omega, \omega_0) e^{-(\omega - \Omega)^2/\Gamma^2} \\ &\quad \{ e^{-\gamma t} + e^{-\gamma(t-t_d)} + \\ &\quad e^{-\gamma t/2} e^{-\gamma(t-t_d)/2} \cos(\omega t_d) \} \quad (20)\end{aligned}$$

In the above equation, the two-center Gaussian functions can be rewritten as a one-center Gaussian function:

$$\begin{aligned}S_G(\omega, \omega_0) e^{-(\omega - \Omega)^2/\Gamma^2} &= \frac{1}{\sqrt{\pi} \gamma_g} e^{-(\omega - \omega_0)^2/\gamma_g^2} e^{-(\omega - \Omega)^2/\Gamma^2} \\ &= \frac{1}{\sqrt{\pi} \gamma_g} \exp\left[-\frac{(\omega_0 - \Omega)^2}{\gamma_g^2 + \Gamma^2} \right] \times \\ &\quad \exp\left[-\frac{\gamma_g^2 + \Gamma^2}{\gamma_g^2 \Gamma^2} \left(\omega - \frac{\Gamma^2 \omega_0 + \gamma_g^2 \Omega}{\gamma_g^2 + \Gamma^2} \right)^2 \right] \quad (21)\end{aligned}$$

By defining a reduced decay constant γ_a and a reduced frequency ω_a equation 21 becomes a simple form:

$$\frac{1}{\gamma_a^2} \equiv \frac{\gamma_g^2 + \Gamma^2}{\gamma_g^2 \Gamma^2} \quad (22a)$$

$$\omega_a \equiv \frac{\Gamma^2 \omega_0 + \gamma_g^2 \Omega}{\gamma_g^2 + \Gamma^2} \quad (22b)$$

$$\begin{aligned}S_G(\omega, \omega_0) e^{-(\omega - \Omega)^2/\Gamma^2} &= \frac{1}{\sqrt{\pi} \gamma_g} \exp\left[-\frac{(\omega_0 - \Omega)^2}{\gamma_g^2 + \Gamma^2} \right] \times \\ &\quad \exp\left[-\frac{(\omega - \omega_a)^2}{\gamma_a^2} \right] \quad (23)\end{aligned}$$

By carrying out the Gauss integral and the Fourier-type integral of the Gaussian function, the final form of eq 20 becomes

$$\begin{aligned}\langle \rho_{ee}(t, t_d, \omega_0, \Omega) \rangle &= \frac{\gamma_a F^2}{\gamma_g \hbar^2} \exp\left[\frac{\gamma_1^2}{4\Gamma^2} - \frac{(\omega_0 - \Omega)^2}{\gamma_g^2 + \Gamma^2} \right] \{ e^{-\gamma t} + \\ &\quad e^{-\gamma(t-t_d)} + 2 \cos[\omega_a t_d] e^{-\gamma t/2} e^{-\gamma(t-t_d)/2} e^{-(\gamma_a^2 t_d^2/4)} \} \quad (24)\end{aligned}$$

In the typical QI experiments, the QI signal is obtained as the total fluorescence integrated over time. Thus, the QI signal is calculated from eq 24 as the following:

$$\begin{aligned}\text{QI}(t_d) &= - \int_{t_d}^{\infty} dt \frac{d\langle \rho_{ee}(t, t_d, \omega_0, \Omega) \rangle}{dt} = \langle \rho_{ee}(t = t_d, t_d, \omega_0, \Omega) \rangle \\ &= \frac{\gamma_a F^2}{\gamma_g \hbar^2} \exp\left[\frac{\gamma_1^2}{4\Gamma^2} - \frac{(\omega_0 - \Omega)^2}{\gamma_g^2 + \Gamma^2} \right] \{ 1 + e^{-\gamma t_d} + \\ &\quad 2 \cos[\omega_a t_d] e^{-(\gamma t_d/2)} e^{-(\gamma_a^2 t_d^2/4)} \} \quad (25)\end{aligned}$$

In the above derivation, the pure dephasing was not taken into account, and a transverse relaxation time constant T_2 and a longitudinal relaxation constant T_1 are related by

$$\frac{1}{T_2} = \frac{\gamma_1}{2} = \frac{1}{2T_1} \quad (26)$$

However, in general, there also exists a pure dephasing γ^* that is brought about from elastic solute–solvent collisions.¹³ Thus, the transverse relaxation time constant should be rewritten as

$$\frac{1}{T_2} = \frac{\gamma_1}{2} + \gamma^* = \frac{1}{2T_1} + \frac{1}{T_2^*} \quad (27)$$

The final expression for the QI signal is given by

$$\text{QI}(t_d) = \frac{\gamma_a F^2}{\gamma_g \hbar^2} \exp\left[\frac{1}{(2T_1\Gamma)^2} - \frac{(\omega_0 - \Omega)^2}{\gamma_g^2 + \Gamma^2}\right] \{1 + e^{-(t_d/T_1)} + 2 \cos[\omega_a t_d] e^{-(t_d/T_2)} e^{-(\gamma_a^2 t_d^2/4)}\} \quad (28)$$

3. Discussion

By comparing the third term in eq 28 with eq 4, we notice that ω_0 and γ_g in the impulsive excitation are replaced by ω_a and γ_a , respectively, in the nonimpulsive excitation. These reduced constants, of course, approach ω_0 and γ_g in the limiting case of impulsive laser pulses; that is, when $\Gamma \gg \gamma_g$, the following relations can be deduced:

$$\omega_a \cong \omega_0, \gamma_a \cong \gamma_g \quad (29)$$

In the reverse limiting case of $\gamma_g \gg \Gamma$, that is, in the case of a quasi continuum wave (CW) laser, we notice that

$$\omega_a \cong \Omega, \gamma_a \cong \Gamma \quad (30)$$

Under this condition, if we further assume that $1/T_2 \gg \Gamma$, the QI signal can be approximately written as

$$\text{QI}(t_d) = \frac{\Gamma F^2}{\gamma_g \hbar^2} \exp\left[\frac{1}{(2T_1\Gamma)^2} - \frac{(\omega_0 - \Omega)^2}{\gamma_g^2 + \Gamma^2}\right] \{1 + e^{-t_d/T_1} + 2 \cos[\Omega t_d] e^{-(t_d/T_2)}\} \quad (31)$$

This result may be the time-domain expression for the hole-burning experiments. These two extreme situations are schematically drawn in Figure 3. Figure 3 infers that the overlap of the laser-pulse spectrum with the absorption spectrum plays a role in the effective spectral width for the system excited by the nonimpulsive laser pulse.

Figure 4 shows the interference term of QI signals calculated for intermediate cases. The red sinusoidal curve of the QI signal was calculated for $\gamma_g = 100 \text{ cm}^{-1}$ and $\Gamma = 200 \text{ cm}^{-1}$, while the blue one was calculated for $\gamma_g = 200 \text{ cm}^{-1}$ and $\Gamma = 100 \text{ cm}^{-1}$. All the other parameters were common for the two calculations. The frequency of the QI signal is altered by the ratio of γ_g to Γ for the cases of nonzero detuning (e.g., $\omega_0 - \Omega \neq 0$). This dependence of

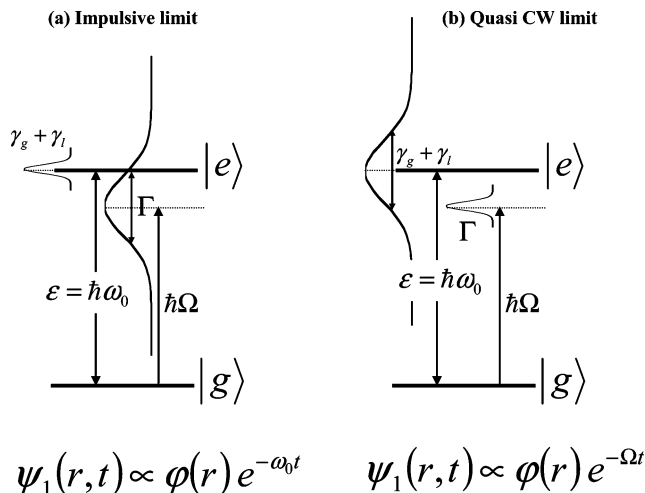


Figure 3. Limiting cases: impulsive laser (left) and quasi CW laser (right).

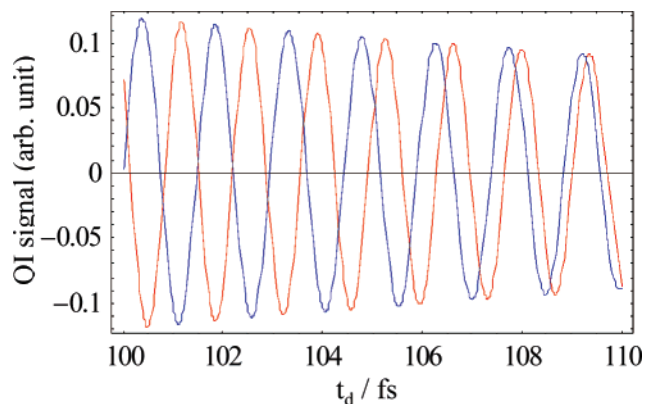


Figure 4. QI signals simulated for the intermediate cases. The parameters specific for each curve were $\gamma_g = 100 \text{ cm}^{-1}$ and $\Gamma = 200 \text{ cm}^{-1}$ (for the red curve), $\gamma_g = 200 \text{ cm}^{-1}$ and $\Gamma = 100 \text{ cm}^{-1}$ (for the blue curve). The common parameters for the two curves were $\omega_0 = 25\,000 \text{ cm}^{-1}$, $\Omega = 22\,000 \text{ cm}^{-1}$, $\gamma_1 = 100 \text{ cm}^{-1}$, and $\gamma^* = 25 \text{ cm}^{-1}$.

the QI frequency ω_a on γ_g can be usefully applied to the determination of an inhomogeneous decay component; that is, in the QI experiments, the precise determination of each frequency parameter, ω_a , ω_0 , and Ω , will aid to deduce the inhomogeneous decay constant by the relation

$$\gamma_g = \left| \frac{\omega_0 - \omega_a}{\omega_a - \Omega} \right|^{1/2} \Gamma \quad (32)$$

which can be derived from eq 22b.

4. Summary

We have shown that the decays of the QI signal obtained by the nonimpulsive excitation can be written as the product of exponential decay and Gaussian decay, and the Gaussian decay constant is given by

$$\frac{1}{\gamma_a^2} \equiv \frac{\gamma_g^2 + \Gamma^2}{\gamma_g^2 \Gamma^2}$$

We have also shown that the frequency of the QI signal is given by

$$\omega_a \equiv \frac{\Gamma^2 \omega_0 + \gamma_g^2 \Omega}{\gamma_g^2 + \Gamma^2}$$

In general, it is often difficult to fit the optical absorption spectrum with Voigt functions in the frequency domain, because the Voigt function includes the convolution integral, and one often finds several parameter sets of the least-squared fits. This situation makes it difficult to separate homogeneous components from inhomogeneous components in the frequency-domain spectrum. In contrast, the fitting procedure is rather easier in the QI experiment, once the expression that includes the effect of laser-pulse width is given. This is because the homogeneous and inhomogeneous components are the simple product in the QI experiment. By analyzing the frequency-domain spectrum and the time-domain QI profile simultaneously (e.g., global fit), the reliable determination of homogeneous and inhomogeneous components of relaxations becomes possible.

Acknowledgment. This work was supported by Grants-in-Aid for Scientific Research (B) (No. 17350001) from the Ministry of Education, Science, Sports and Culture of Japan.

References

- (1) Scherer, N. F.; Carlson, R. J.; Matro, A.; Du, M.; Ruggiero, A. J.; Romero-Rochin, V.; Cina, J. A.; Fleming, G. R.; Rice, S. A. Fluorescence-Detected Wave Packet Interferometry: Time Resolved Molecular Spectroscopy with Sequences of Femtosecond Phase-Locked Pulses. *J. Chem. Phys.* **1991**, *95*, 1487.
- (2) Scherer, N. F.; Matro, A.; Ziegler, L. D.; Du, M.; Carlson, R. J.; Cina, J. A.; Fleming, G. R. Fluorescence-Detected Wave Packet Interferometry. II. Role of Rotations and Determination of the Susceptibility. *J. Chem. Phys.* **1991**, *96*, 4180.
- (3) Ohmori, K.; Katsuki, H.; Chiba, H.; Honda, M.; Hagihara, Y.; Fujiwara, K.; Sato, Y.; Ueda, K. Real-Time Observation of Phase-Controlled Molecular Wave-Packet Interference. *Phys. Rev. Lett.* **2006**, *96*, 093002.
- (4) Bonadeo, N. H.; Erland, J.; Gammon, D.; Park, D.; Katzer, D. S.; Steel, D. G. Coherent Optical Control of the Quantum State of a Single Quantum Dot. *Science* **1998**, *282*, 1473.
- (5) Mitsumori, Y.; Mizuno, M.; Tanji, S.; Kuroda, T.; Minami, F. Coherent Transients Involving 2p Excitons in ZnSe. *J. Lumin.* **1998**, *76–77*, 113.
- (6) Htoon, H.; Takagahara, T.; Kulik, D.; Baklenov, O. A. L.; Holmes, J.; Shih, C. K. Interplay of Rabi Oscillations and Quantum Interference in Semiconductor Quantum Dots. *Phys. Rev. Lett.* **2002**, *88*, 087401.
- (7) Sato, S.-i.; Nishimura, Y.; Sakata, Y.; Yamazaki, I. Coherent Control of Oscillatory Excitation Transfer in Dithia-1,5[3,3]-anthracenophane by a Phase-Locked Femtosecond Pulse Pair. *J. Phys. Chem. A* **2003**, *107*, 10019.
- (8) Fushitani, M.; Bargheer, M.; Hr, M. G.; Schwentner, N. Pump-Probe Spectroscopy with Phase-Locked Pulses in the Condensed Phase: Decoherence and Control of Vibrational Wavepackets. *Phys. Chem. Chem. Phys.* **2005**, *7*, 3143.
- (9) Xu, L.; Spielmann, C.; Poppe, A.; Brabec, T.; Krausz, F.; Hänsch, T. W. Route to Phase Control of Ultrashort Light Pulses. *Opt. Lett.* **1996**, *21*, 2008.
- (10) Albrecht, A. W.; Hybl, J. D.; Faeder, S. M. G.; Jonas, D. M. Experimental Distinction between Phase Shifts and Time Delays: Implications for Femtosecond Spectroscopy and Coherent Control of Chemical Reactions. *J. Chem. Phys.* **1999**, *111*, 10934.
- (11) Louisell, W. H. The Interaction Picture; Time-Dependent Perturbation Theory, Dyson Time Ordering Operator. In *Quantum Statistical Properties of Radiation*; John Wiley & Sons, Inc: New York, 1973; pp 57–68.
- (12) Allen, L.; Eberly, J. H. Free Induction Decay. In *Optical Resonance and Two-Level Atoms*; Dover: New York, 1975; pp 10–12.
- (13) Louisell, W. H. The Markoff Approximation in the Schrödinger Picture. In *Quantum Statistical Properties of Radiation*; John Wiley & Sons, Inc: New York, 1973; pp 336–360.

CT7000073

Revised Implicit Solvent Model for the Simulation of Surfactants in Aqueous Solutions. 2. Modeling of Charged Headgroups at Oil–Water Interface

Shintaro Morisada,[†] Hiroyuki Shinto,* and Ko Higashitani

Department of Chemical Engineering, Kyoto University,
Nishikyo-ku, Kyoto 615-8510, Japan

Received October 23, 2006

Abstract: The revised implicit solvent model (ISM-2) for the simulation of cationic surfactants in water was proposed in the previous study (*J. Phys. Chem. B* 2005, 109, 11762): no water molecules of the solvent are explicitly treated, and their effects are incorporated using the solvent-averaged interactions between the surfactant segments in water, where the interactions between the hydrocarbon sites of the surfactants are allowed to vary depending on their surroundings. In the present study, the representation of a charged headgroup at the liquid–liquid interface between the hydrocarbon oil and the implicit water has been improved, where the free energy change due to the transfer of the charged headgroup across the interface is taken into account. The present model (ISM-3) has been applied to the molecular dynamics simulations of (i) the single preformed micelle of 30 *n*-decyltrimethylammonium chloride (C₁₀TAC) cationic surfactants in water and (ii) 343 C₁₀TAC surfactants uniformly dispersed in water, where the corresponding systems are also simulated using the ISM-2 for comparison. The first simulations showed that the ISM-3 as well as the ISM-2 is applicable to the simulation of the preformed micelle of the average aggregate size for C₁₀TAC. The second simulations demonstrated that the ISM-3 can represent the surfactant self-assembling plausibly, while the ISM-2 fails to do so because of the rude treatment of the charged headgroups at the interface. The results will be compared with those from experiments and atomistic model simulations.

1. Introduction

Shape, stability, and average size of surfactant aggregates in solutions have been of great interest for researchers and engineers in many fields. The surfactant aggregates have been investigated at the molecular level using the molecular dynamics (MD) and the Monte Carlo (MC) simulations,^{1–13} which are popular tools for atomistic description of matter and materials.^{14–16} However, the quantitative simulation of the surfactants in a solution computationally costs too much, because a huge number of the solvent molecules must be

treated besides the solute molecules of interest. If the solvent molecules can be treated implicitly, the computational cost is drastically reduced, which makes the quantitative simulations of surfactant solutions more accessible to the researchers and the engineers. Such implicit treatment of the solvent is referred to as an implicit solvent model (ISM),¹⁷ where the effects of the solvent are incorporated into the interactions between the solutes. When the concentration of the solutes is not very high, the effective interactions between them are plausibly represented by the potential of mean force (PMF), which is the solvent-averaged free energy as a function of the configuration of the solutes.

In our previous study,¹⁸ the ISM was proposed for the simulation of cationic surfactants in water, where the effective interactions between the surfactant segments are given by assuming the site–site pair additivity of the PMFs

* Corresponding author phone: +81-75-383-2672; fax: +81-75-383-2652; e-mail: shinto@cheme.kyoto-u.ac.jp.

[†] Present address: Department of Environmental Chemistry and Engineering, Tokyo Institute of Technology, Nagatsuta, Midori-ku, Yokohama 226-8502, Japan.

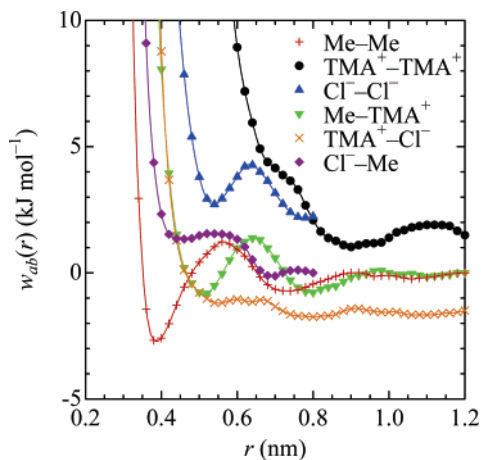


Figure 1. Potentials of mean force for solute pairs in ambient water at infinite dilution. The solid lines are the guides for the eyes.

in water at infinite dilution. The ISM was then revised to represent the hydrocarbon interior of the surfactant aggregates more appropriately: in this revised model (ISM-2), the interactions between the hydrophobic sites of the surfactants are varied depending on their surroundings, namely, the local hydrocarbon density.¹⁹ It is noted that Lazaridis et al.²⁰ also reported similar implicit solvent simulations of the zwitterionic surfactants.

Using the ISM-2, we have simulated the self-assembly of the cationic surfactants in water to encounter the strange result, as will be seen in section 3.2: only a few aggregates became large, and the other surfactants remained as monomers or small aggregates, where the large aggregates often included the charged headgroups of the surfactants in the hydrocarbon interior. This result is considered to be implausible because the charged headgroups should exist in water more favorably than in the hydrocarbon interior. The aim of the present study is to improve the ISM-2 by correcting the representation of the charged headgroups.

In this paper, we improve the representation of a charged headgroup at the liquid–liquid interface between the hydrocarbon oil and the implicit water, where the free energy change due to the transfer of the charged headgroup across the interface is taken into account. This model (ISM-3) is applied to the MD simulations of the aqueous surfactant solutions starting from two types of initial configurations: (i) a single preformed micelle of the surfactants in water and (ii) the surfactant monomers uniformly dispersed in water. To clarify the effect of the revision in the ISM-3, the simulation results are compared with those from the ISM-2.

2. Simulation Methods

2.1. Implicit Solvent Models. We consider *n*-decyltrimethylammonium chloride [$\text{CH}_3(\text{CH}_2)_9\text{-N}(\text{CH}_3)_3^+\text{Cl}^-$ or C_{10}TAC] and water as a cationic surfactant and a solvent, respectively. To construct the force field for the surfactant molecule in water using the PMFs, the following technique was employed. The hydrophilic and the hydrophobic groups of the surfactant were approximated by a tetramethylammonium ion [$(\text{CH}_3)_4\text{N}^+$ or TMA^+] and a chain of methane molecules (CH_4 or Me), respectively.^{18,19} Figure 1 shows the

Table 1. Molecular Geometry of t_{10}h^+ Surfactant

	bond length (nm)	bond angle (deg.)
t-t	0.153	
t-h ⁺	0.280	
t-t-t		109.5
t-t-h ⁺		126.4

PMFs $w_{ab}(r)$ for 6 different binary combinations with Me , TMA^+ , and Cl^- in ambient water at infinite dilution, which were computed using the atomistic model MD simulations in our previous studies.²¹ The surfactant of $\text{CH}_3(\text{CH}_2)_9\text{-N}(\text{CH}_3)_3^+\text{Cl}^-$ was mimicked as $(\text{Me})_{10}\text{-TMA}^+\text{Cl}^-$, that is, $\text{t}_{10}\text{h}^+\text{Cl}^-$, where t and h⁺ denote the hydrophobic and the hydrophilic sites, respectively.

2.1.1. Previous Model (ISM-2).¹⁹ All the intermolecular interactions were given by assuming the site–site pair additivity of the PMFs, except for the interaction between the hydrophobic sites (see eq 3). The PMFs for separations beyond the range of the computed PMFs (i.e., $r > 0.8$ or 1.2 nm) were given by

$$w_{ab}(r) = \frac{1}{4\pi\epsilon_r^w\epsilon_0} \frac{Q_a Q_b}{r} \quad (1)$$

where Q_a is the point charge of site a , ϵ_0 is the permittivity of the vacuum, and ϵ_r^w is the relative permittivity of water; the experimental value of $\epsilon_r^w = 77.6$ at $T = 300$ K was used.²²

As for the intramolecular interactions of the t_{10}h^+ surfactant, the PMF between the t and the h⁺ sites (see Figure 1) and the corrected PMF between the t sites (see eq 3) were included, only when these sites were separated at least four bonds. The bond lengths and the bond angles were fixed at constant values, as listed in Table 1. The torsional potential of Ryckaert and Bellemans²³ was used for t-t-t-t and t-t-t-h⁺

$$u_{\text{torsion}}(\phi) = \sum_{n=0}^5 k_n \cos^n \phi \quad (2a)$$

$$\left. \begin{aligned} k_0 &= +1.541 \times 10^{-20} \text{J} \\ k_1 &= +2.019 \times 10^{-20} \text{J} \\ k_2 &= -2.179 \times 10^{-20} \text{J} \\ k_3 &= -0.508 \times 10^{-20} \text{J} \\ k_4 &= +4.357 \times 10^{-20} \text{J} \\ k_5 &= -5.230 \times 10^{-20} \text{J} \end{aligned} \right\} \quad (2b)$$

where ϕ is the dihedral angle, and $\phi = 0$ corresponds to the trans conformation.

The ISM family^{18,19} is based on the PMFs composed of the direct and the solvent-induced interactions. However, the solvent-induced interactions between the hydrophobic sites are negligible in the interior of the surfactant aggregates such as micelles, because water molecules hardly exist there. The interaction force between the hydrophobic sites, f_{tt} , was then represented by the PMF and the Lennard-Jones (LJ) terms

$$f_{tt} = -(1 - \alpha_{ia,jb}) \cdot \frac{dw_{\text{MeMe}}(r)}{dr} - \alpha_{ia,jb} \cdot \frac{du_{\text{LJ}}(r)}{dr} \quad (3a)$$

$$u_{\text{LJ}}(r) = 4\epsilon_t \left[\left(\frac{\sigma_t}{r} \right)^{12} - \left(\frac{\sigma_t}{r} \right)^6 \right] \quad (3b)$$

where $w_{\text{MeMe}}(r)$ is the PMF for the Me–Me pair in Figure 1, $\epsilon_t = 0.994 \times 10^{-21}$ J, and $\sigma_t = 0.3923$ nm; the latter two are the energy and the size parameters of the LJ potential for *n*-alkane, respectively.²³ The distribution parameter $\alpha_{ia,jb}$ is allowed to vary from 0 to 1, depending on the local packing ratio of the hydrocarbon sites around sites *a* and *b* of interest.

To define the local packing ratio of the hydrocarbon around the hydrophobic site *a* on molecule *i*, Γ_{ia}^t , we regarded every hydrophobic site as a sphere of radius $\sigma_t/2$ and then computed the portion that the spherical shell of inner radius $\sigma_t/2$ and outer radius σ_t around site *a* cuts out from the spheres of all the other sites, as illustrated in Figure 2. The spherical shell around site *a* on molecule *i* cuts out from the sphere of site *b* on molecule *j*, the shaded portion, whose volume $V_{ia,jb}^t$ is

$$V_{ia,jb}^t(r_{ia,jb}) = \begin{cases} (13\pi/192)\sigma_t^3, & r_{ia,jb} < \sigma_t \\ \frac{\pi\sigma_t^4}{12r_{ia,jb}} \left(\frac{r_{ia,jb}}{\sigma_t} - \frac{3}{2} \right)^2 \left[\left(\frac{r_{ia,jb}}{\sigma_t} + \frac{3}{2} \right)^2 - 3 \right], & \sigma_t \leq r_{ia,jb} \leq 3\sigma_t/2 \\ 0, & r_{ia,jb} > 3\sigma_t/2 \end{cases} \quad (4)$$

It also cuts the other shaded portion from the spheres of the neighboring sites ($=a \pm 1, a \pm 2, a \pm 3, a \pm 4$); this volume is denoted by V_{ia}^t . Consequently, the local packing ratio Γ_{ia}^t is defined as

$$\Gamma_{ia}^t = \frac{1}{V_{\text{cp}}^t} \left[V_{ia}^t + \sum_{b \in i, |b-a| \geq 5} \beta_b V_{ia,ib}^t(r_{ia,ib}) + \sum_{j \neq i} \sum_{b \in j} \beta_b V_{ia,jb}^t(r_{ia,jb}) \right] \quad (5)$$

where the first, second, and third terms in the brackets correspond to the contributions from the intramolecular neighboring sites, the other intramolecular sites, and all the hydrophobic sites of the other molecules, respectively. In eq 5, $V_{\text{cp}}^t \equiv V_{ia,jb}^t(\sigma_t) \times 12 = (13\pi/16)\sigma_t^3$ is the closest packing volume for the nonbonded identical spheres of radius $\sigma_t/2$, and β_b is a factor to avoid overestimating the net volume occupied by molecule *j* (e.g., the simple summation of $V_{ia,jb}^t$ over site *b* on molecule *j* causes overestimation of the volume of the overlapping space between the spherical shell of site *a* on molecule *i* and a chain of the spheres on molecule *j*). The distribution parameter $\alpha_{ia,jb}$ is given as a function of the local packing ratio around sites *a* and *b* of interest, $\Gamma_{ia,jb}^t$:

$$\alpha_{ia,jb} = 0.5 + 0.5 \tanh \left[\frac{\Gamma_{ia,jb}^t - 0.5}{0.135} \right] \quad (6a)$$

$$\Gamma_{ia,jb}^t = \max(\Gamma_{ia}^t, \Gamma_{jb}^t) - V_{ia,jb}^t(r_{ia,jb})/V_{\text{cp}}^t \quad (6b)$$

In the present study, V_{ia}^t and β_b were chosen as the constant values depending on the hydrophobic sites of the

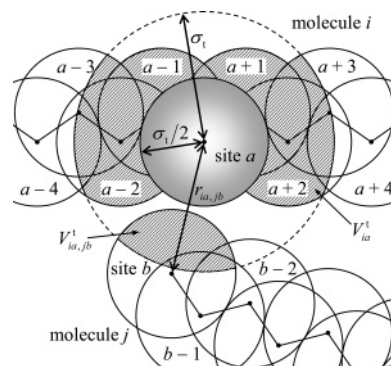


Figure 2. Illustration of hydrophobic chains of two molecules. The spherical shell of inner radius $\sigma_t/2$ and outer radius σ_t around site *a* on molecule *i* cuts out from the sphere of site *b* on molecule *j*, the shaded portion, whose volume is indicated by $V_{ia,jb}^t$. The other shaded portion is cut out from the spheres of the neighboring sites ($=a \pm 1, a \pm 2, a \pm 3, a \pm 4$); this volume is denoted by V_{ia}^t .

Table 2. Parameters of Eqs 5 and 9 for $t_{10}h^+$ Surfactant

	V_{ia}^t/V_{cp}^t	V_i^h/V_{cp}^h	β_b
h^+		0.093	
t1	0.54		0.58
t2	0.48		0.56
t3, ..., t7	0.44		0.53
t8	0.42		0.53
t9	0.33		0.59
t10	0.22		0.75

surfactant, the all-trans conformation of which was assumed for the sake of convenience. The values of parameters V_{ia}^t and β_b are listed in Table 2, where the hydrophobic sites are numbered 1, ..., 10 from the *t* next to h^+ to the end *t*. It should be noted that the values of V_{ia}^t and β_b in Table 2 are slightly different from those in Table 3 of ref 19, because of the difference in definition of V_{ia}^t .

2.1.2. Present Model (ISM-3). Solute transfer across the interface between two immiscible liquids is accompanied by the free energy change resulting from the difference of the solvation states; therefore, the force perpendicular to the liquid–liquid interface acts on the solute at the interface.^{24,25} Likewise, when the surfactants assemble to form an aggregate in water, their charged headgroups situated at the interface between the hydrocarbon core and water feel such forces, which are neglected in the ISM-2. In the present model (ISM-3), these forces, \mathbf{f}_h , were modeled as a pseudo-single-body force depending on the local density of hydrocarbon sites around a charged headgroup and were incorporated into the ISM-2 mentioned above.

The force \mathbf{f}_h was represented as a function of the local packing ratio of the hydrophobic sites around the hydrophilic site h^+ on molecule *i*, Γ_i^h

$$\mathbf{f}_h = 0.5 f_0 [\cos \{2\pi(\Gamma_i^h - 0.5)\} + 1] \frac{\mathbf{r}_i^h - \mathbf{r}_i^{t2}}{|\mathbf{r}_i^h - \mathbf{r}_i^{t2}|} \quad (7)$$

where \mathbf{r}_i^h and \mathbf{r}_i^{t2} are the positions of h^+ and *t2* sites, respectively, and $f_0 = 4.5 \times 10^{-10}$ N is the maximum force

derived from the theory of Ulstrup and Kharkats²⁴ with the relative permittivity of liquid alkane $\epsilon_r^o = 1.9$. The definition of Γ_i^h is similar to that of Γ_{ia}^t described in section 2.1.1. We regarded the hydrophilic site h^+ as a sphere of radius $\sigma_h/2 = 0.285$ nm and then calculated the portion that the spherical shell of inner radius $\sigma_h/2$ and outer radius $r_o \equiv (\sigma_h + \sigma_t)/2$ around the site h^+ cuts out from the spheres of the hydrophobic sites. The volume of the portion that the spherical shell around the site h^+ on molecule i cuts out from the sphere of hydrophobic site b on molecule j , V_{ijb}^h , is

$$V_{ijb}^h(r_{ijb}^h) = \begin{cases} (\pi/192)(16 - 3\sigma_t/r_o)\sigma_t^3, & r_{ijb}^h < r_o \\ \frac{\pi\sigma_t^4}{12r_{ijb}^h} \left[\frac{r_{ijb}^h}{\sigma_t} - \left(\frac{r_o}{\sigma_t} + \frac{1}{2} \right) \right]^2 \left[\frac{r_{ijb}^h}{\sigma_t} + \left(\frac{r_o}{\sigma_t} + \frac{1}{2} \right) \right]^2 - 4 \left(\frac{r_o}{\sigma_t} + \frac{1}{2} \right)^2 + 6 \frac{r_o}{\sigma_t}, & r_o \leq r_{ijb}^h \leq r_o + \sigma_t/2 \\ 0, & r_{ijb}^h > r_o + \sigma_t/2 \end{cases} \quad (8)$$

Note that eq 8 is identical to eq 4 when $r_o = \sigma_t$ (i.e., $\sigma_h = \sigma_t$). The volume of the portion cut out from the spheres of four neighboring hydrophobic sites ($=t1, t2, t3, t4$) is denoted by V_i^h . The local packing ratio Γ_i^h is then defined as

$$\Gamma_i^h = \frac{1}{V_{cp}^h - V_i^h} \left[\sum_{b \in i, b \geq 15} \beta_b V_{i,ib}^h(r_{i,ib}^h) + \sum_{j \neq i} \sum_{b \in j} \beta_b V_{i,jb}^h(r_{i,jb}^h) \right] \quad (9)$$

where β_b is the same parameter as in eq 5 and Table 2; $V_{cp}^h \equiv V_{i,ib}^h(r_o) \times 24 = (\pi/8)(16 - 3\sigma_t/r_o)\sigma_t^3$ is an approximation of the closest packing volume for the spheres of radius $\sigma_t/2$ around the sphere of radius $\sigma_h/2$. In the right-hand side of eq 9, V_i^h does not appear in the brackets [...], but does in the denominator to normalize Γ_i^h , because it should never contribute to the force of eq 7 acting on the site h^+ of the surfactant molecule. One should compare eq 9 of Γ_i^h with eq 5 of Γ_{ia}^t , where V_{ia}^t differently appears in the right-hand side to contribute to the interaction force of eq 3a between the hydrophobic sites. Like V_{ia}^t , V_i^h was chosen as the constant value given in Table 2, with the all-trans conformation of the surfactant being assumed.

Table 3. Simulation Systems

system	no. of solutes		side length L (nm)	concn C_{surf} (M)	initial configuration of surfactants	model
	$t_{10}h^+$	Cl^-				
A.1	30	30	7.927	0.1	micelle	ISM-2
A.2	30	30	7.927	0.1	micelle	ISM-3
B.1	343	343	17.86	0.1	monomers	ISM-2
B.2	343	343	17.86	0.1	monomers	ISM-3

2.2. Simulation Details. The systems simulated are summarized in Table 3: (A) a single micelle composed of 30 $t_{10}h^+Cl^-$ surfactants in water at $C_{surf} = 0.1$ M and (B) 343 $t_{10}h^+Cl^-$ surfactants uniformly dispersed in water at $C_{surf} = 0.1$ M. Both the ISM-2 and the ISM-3 were employed in systems A and B to clarify how much the ISM-3 improves the representation of the surfactant solutions. The surfactant

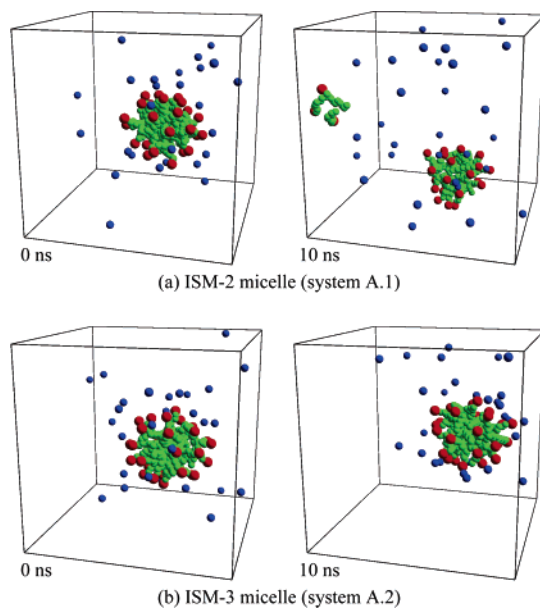


Figure 3. Snapshots of a micelle of 30 $t_{10}h^+Cl^-$ surfactants in water at $C_{surf} = 0.1$ M (system A) at time $t = 0$ and 10 ns: (a) the ISM-2 and (b) the ISM-3. Green, red, and blue spheres denote t, h^+ , and Cl^- , respectively. The simulation cell is depicted by the lines.

concentration of $C_{surf} = 0.1$ M employed in the present study is higher than the critical micelle concentration (cmc) of $C_{10}TAC$ in ambient water, 0.05–0.065 M.^{26,27} A cubic box with 3D periodicity was employed, which included the finite number of the solutes and had the side length L as listed in Table 3. The equations of motion for all the interaction sites were integrated by the leapfrog algorithm with the time step of $\Delta t = 0.005$ ps. The bond lengths and the bond angles of the $t_{10}h^+$ surfactant were fixed by the SHAKE method.¹⁵ The temperature of the systems was kept at $T = 300$ K, using the Nosé–Hoover thermostat¹⁵ with a time constant of $\tau_T = 1$ ps. The Coulomb contributions of eq 1 to the PMF were handled by the Ewald summation,¹⁵ while the rest of the contributions were considered only within the range of the computed PMFs (i.e., $r \leq 0.8$ or 1.2 nm). In eqs 4–6, 8, and 9, the local packing ratios, Γ_{ia}^t and Γ_i^h , were calculated at every time step. During the simulations, the configuration was stored every 0.1 ps for the subsequent analysis.

2.2.1. Single Micelle in Water (System A). A single micelle initially composed of 30 $t_{10}h^+Cl^-$ surfactants in water was simulated using the ISM-2 (system A.1) or the ISM-3 (system A.2). It is noted that the average size of the aggregates, N_{av} , for $C_{10}TAC$ is estimated as $N_{av} = 30$, according to an extrapolation of the experimental results for C_nTAC : $N_{av} = 44, 62,$ and 84 for $n = 12,$ ²⁸ $14,$ ²⁹ and $16,$ ³⁰ respectively. The initial configuration of a micelle was prepared following section 2.4.2 of ref 18, where the time was set at $t = 0$ (see Figure 3), and the system was allowed to evolve over 10 ns.

2.2.2. Surfactant Self-Assembly in Water (System B). An aqueous solution of 343 $t_{10}h^+Cl^-$ surfactants at $C_{surf} = 0.1$ M was simulated using the ISM-2 (system B.1) or the ISM-3 (system B.2). The number and the concentration of the

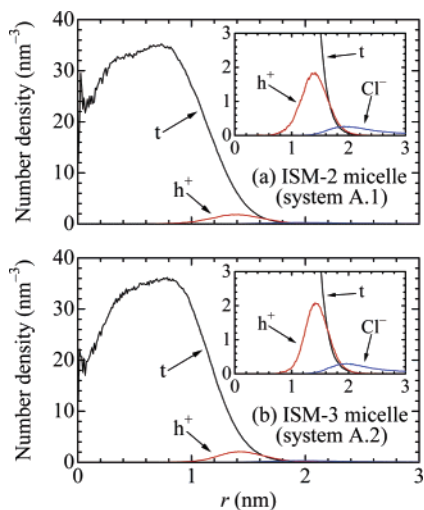


Figure 4. Number densities of t , h^+ , and Cl^- for a micelle of 30 $t_{10}h^+Cl^-$ surfactants in water (system A), as a function of the distance from the center of mass of the micelle, r . (a) the ISM-2 and (b) the ISM-3. Each density is the result averaged over 20 000 configurations during the last 2 ns of the 10-ns simulation. The inset focuses on the densities of the charged sites.

surfactants employed seem to be sufficient for the simulation of the surfactant self-assembly, compared with the average size of the aggregates ($N_{av} = 30$) and the cmc (0.05–0.065 M), respectively. The initial configuration of the surfactants was prepared as follows: (i) the center of mass of a $t_{10}h^+$ surfactant in all-trans conformation was placed at one of the $7 \times 7 \times 7$ lattice points, and the surfactant was then randomly rotated around the lattice point; (ii) likewise, the rest of the surfactants were positioned at the lattice points; and (iii) the Cl^- counterions were placed at random positions such that they never overlapped with each other and the surfactants. Starting from this configuration where the time was set at $t = 0$ (Figure 6a), the system was allowed to evolve over 25 ns.

3. Results and Discussion

In the following two subsections, we investigate the single preformed micelles of 30 surfactants in water (system A) and the self-assembling of surfactants in water (system B) using MD simulations with the ISM-2 and the ISM-3.

3.1. Single Micelle in Water. Figure 3 displays the snapshots of the micelles of 30 $t_{10}h^+Cl^-$ surfactants simulated with the ISM-2 (system A.1) and the ISM-3 (system A.2). For both the models, several surfactants repeatedly dissociated from and associated with the micelle during the 10-ns simulations. At $t = 10$ ns, the ISM-2 and the ISM-3 micelles were composed of 27 and 30 surfactants, respectively; hereafter, a surfactant is considered to belong to the aggregate when the minimum site-to-site separation between the tail of the surfactant and those of the surfactants in the aggregate is less than 0.48 nm, at which the Me–Me PMF equals zero as in Figure 1. Judging from similar snapshots of the ISM-2 and the ISM-3 micelles, the force on the h^+ sites represented by eq 7 seems to have no significant influence on the behavior of single preformed micelles.

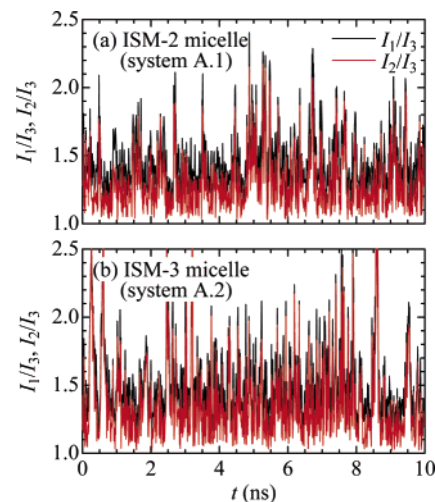


Figure 5. Values of I_1/I_3 (black lines) and I_2/I_3 (red lines) for a micelle of 30 $t_{10}h^+Cl^-$ surfactants in water (system A), as a function of time t : (a) the ISM-2 and (b) the ISM-3. The principal moments of inertia of the micelle are represented by I_1 , I_2 , and I_3 , where $I_1 \geq I_2 \geq I_3$. Each plot is the result averaged over 2 ps.

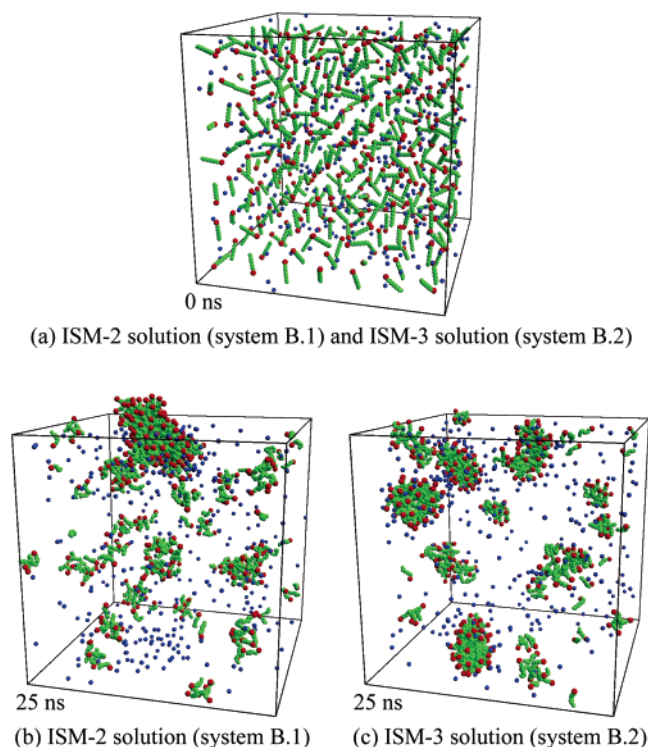


Figure 6. Snapshots of 343 $t_{10}h^+Cl^-$ surfactants in water at $C_{surf} = 0.1$ M (system B): (a) the initial configuration of the ISM-2 and the ISM-3 solutions; (b) the final configuration of the ISM-2 solution; and (c) the final configuration of the ISM-3 solution. Green, red, and blue spheres denote t , h^+ , and Cl^- , respectively. The simulation cell is depicted by the lines.

3.1.1. Internal Structure. To investigate the internal structure of the micelle, the number densities of t sites, h^+ sites, and Cl^- counterions were calculated as a function of the distance from the center of mass of the micelle, r , using the configurations for $t = 8$ –10 ns. Figure 4 exhibits the obtained density profiles. For the ISM-2 micelle, the t sites form a hydrocarbon interior of the micelle at $r \leq 2.0$ nm,

while the h^+ sites exist at the surface of the hydrocarbon core, as in Figure 4a. The Cl^- counterions are located outside of the micelle and favorably reside near the h^+ sites. These profiles coincide with those of the atomistic model MD study, where a micelle of 30 $C_{10}TAC$ surfactants was simulated in 2166 water molecules at $C_{surf} = 0.67$ M for 0.215 ns.³¹ Although the density profiles for the ISM-3 micelle are almost the same as those for the ISM-2 micelle, the profile of the h^+ sites for the ISM-3 micelle has a somewhat higher peak at $r \approx 1.4$ nm and a smaller foothill at $t < 1.4$ nm (see the insets of Figure 4). This is because the h^+ sites of the surfactants in the ISM-3 micelle are pushed out of the hydrocarbon interior by the forces of eq 7 depending on the hydrocarbon densities around them.

3.1.2. Shape and Stability. The principal moments of inertia of the micelle, I_1 , I_2 , and I_3 ($I_1 \geq I_2 \geq I_3$), were calculated to obtain detailed information on the shape and the stability of the micelle. Figure 5 shows the values of I_1/I_3 and I_2/I_3 as a function of time t , where each plot is the result averaged over 2 ps. The values of I_1/I_3 and I_2/I_3 for the ISM-2 and the ISM-3 micelles are larger than unity, indicating that both the micelles have an ellipsoidal shape. The sharp and high peaks of I_1/I_3 and I_2/I_3 result from the dissociation/association of some surfactants from/with the micelle. The values of I_1/I_3 and I_2/I_3 for the ISM-3 micelle fluctuate a bit more significantly than those for the ISM-2 micelle, suggesting that the ISM-3 micelle is slightly less stable than the ISM-2 micelle.

3.1.3. Comparison between ISM-2 and ISM-3. In the previous study,¹⁹ we demonstrated that the ISM-2 successfully represents the preformed micelle of surfactants in water, by comparison with the results of the atomistic model MD study³¹ and the NMR study.³² As seen in Figures 3–5, the behaviors of the ISM-2 and the ISM-3 micelles closely resemble each other, except that there are slight differences in the density profile of the h^+ sites and the values of I_1/I_3 and I_2/I_3 . This indicates that the corrected treatment of the h^+ sites in the ISM-3 hardly influences the representation of the single preformed micelle of $N = 30$, which is the average size of the aggregates for $C_{10}TAC$. Nonetheless, this correction in the ISM-3 significantly improves the representation of surfactant self-assembling, as will be demonstrated in section 3.2.

3.2. Surfactant Self-Assembly in Water. We have ascertained that the ISM-3 can plausibly represent the surfactant micelle of the proper size, as mentioned in section 3.1. Next, we consider the aqueous solution of 343 $t_{10}h^+Cl^-$ surfactants simulated using the ISM-2 (system B.1) and the ISM-3 (system B.2).

Figure 6 displays the snapshots of the aqueous surfactant solutions for the ISM-2 and the ISM-3, where the $t_{10}h^+$ surfactants and the Cl^- counterions at $t = 0$ are completely disaggregated, as expected from the procedure explained in section 2.2.2. At $t = 25$ ns, the surfactants in the ISM-2 solution spontaneously assembled to form a large aggregate of $N = 117$, and the other surfactants existed as monomers or aggregates of $N < 10$, as in Figure 6b. In Figure 6c for the ISM-3 solution, on the other hand, the surfactants formed several aggregates of different sizes,

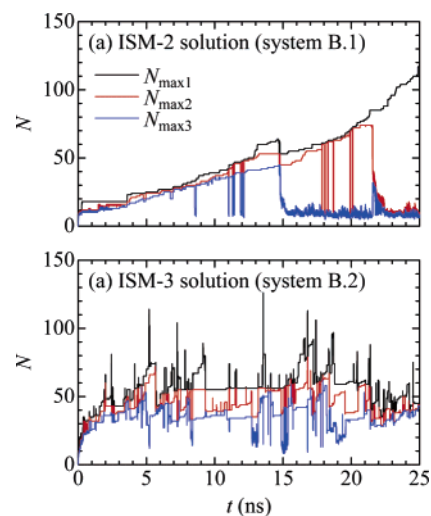


Figure 7. Three maximum sizes N_{max1} (black lines), N_{max2} (red lines), and N_{max3} (blue lines) of surfactant aggregates in $C_{surf} = 0.1$ M solution of 343 $t_{10}h^+Cl^-$ surfactants (system B), as a function of time t . (a) the ISM-2 and (b) the ISM-3.

where the sizes of the three largest aggregates were 46, 44, and 43 at $t = 25$ ns.

3.2.1. Growth Process of Aggregates. To investigate the growth process of the surfactant aggregates, we calculated three maximum sizes of the aggregates, N_{max1} , N_{max2} , and N_{max3} , at every configuration stored during the 25-ns simulation. Figure 7 shows the resultant values of N_{max1} , N_{max2} , and N_{max3} as a function of time t . As seen in Figure 7a, these maximum sizes of the aggregates in the ISM-2 solution gradually increase until $t \leq 14.7$ ns, and then the largest aggregate of $N_{max1} = 63$ breaks apart into monomers and small aggregates. At $t = 21.5$ ns, the second largest aggregate of $N_{max2} = 74$ falls apart. Thereafter, only one large aggregate continues to grow until $t = 25$ ns, as also seen in Figure 6b. For the ISM-3 solution, the values of N_{max1} , N_{max2} , and N_{max3} greatly fluctuate at $t = 2$ –25 ns as seen in Figure 7b. The sharp and high peaks of N_{max1} , N_{max2} , and N_{max3} correspond to the temporary association between surfactant aggregates. The continuous fluctuations of N_{max1} , N_{max2} , and N_{max3} in Figure 7b indicate that the growth and the breakup of the surfactant aggregates repeatedly occur in the ISM-3 solution. Thus, the growth process of the surfactant aggregates in the ISM-3 solution is quite different from that in the ISM-2 solution shown in Figure 7a; the latter is considered to be an artifact resulting from the rude treatment of the h^+ sites at the interface between the hydrocarbon core and the implicit water.

3.2.2. Surroundings of Charged Headgroups. We carefully observed the snapshots of the ISM-2 solution to find that the h^+ sites of the ISM-2 surfactants intruded into the hydrocarbon interiors of the large aggregates, whereas the Cl^- counterions never existed there. The former result is implausible because the charged headgroups should exist in water more favorably than in the hydrocarbon interior. To clarify the difference in the surroundings of the h^+ sites between the ISM-2 and the ISM-3 solutions, we counted the number of the t sites in the coordination shell around each h^+ site, $n_{h \rightarrow t}$, and then calculated the probability distribution

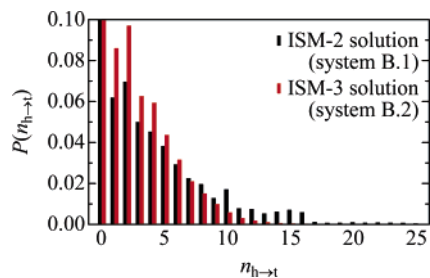


Figure 8. Probability distributions of the h^+ sites with the coordination number n_{h-t} of the t sites in the shell around each h^+ site, $P(n_{h-t})$, in the ISM-2 solution (black bars) and the ISM-3 solution (red bars). The value of $P(n_{h-t})$ at $n_{h-t} = 0$ and the average coordination number respectively equal to $P(0) = 0.59$ and $\bar{n}_{h-t} = 2.18$ for the ISM-2 and $P(0) = 0.56$ and $\bar{n}_{h-t} = 1.61$ for the ISM-3. Each n_{h-t} includes only the intermolecular contributions. Each distribution is the result averaged over 50 000 configurations during the last 5 ns of the 25-ns simulation.

of the h^+ sites with n_{h-t} , $P(n_{h-t})$. Here, each n_{h-t} includes only the intermolecular sites, and the coordination shell was defined as the region of $r_{h-t} \leq 6.4$ nm, at which the PMF for the Me-TMA⁺ pair exhibits the first maximum between two minima as in Figure 1.

The resultant probability distributions are shown in Figure 8, where the probabilities of $n_{h-t} > 0$ are highlighted and those of $n_{h-t} = 0$ are 0.59 and 0.56 for the ISM-2 and the ISM-3 solutions, respectively. The probabilities of $n_{h-t} = 1-6$ for the ISM-2 solution are lower than those for the ISM-3 solution, while the probabilities of $n_{h-t} \geq 7$ are higher. The average coordination numbers were also calculated and found to be $\bar{n}_{h-t} = 2.18$ and 1.61 for the ISM-2 and the ISM-3 solutions, respectively. These results suggest that the h^+ sites of the ISM-2 surfactants easily exist in the hydrophobic environment compared with those of the ISM-3 surfactants. In general, the size of an aggregate of ionic surfactants in water is determined by a balance between two interactions: (i) the solvent-induced hydrophobic attraction among the hydrocarbon chains and (ii) the electrostatic repulsion among the charged headgroups, which are located at the interface between the resultant hydrocarbon core and water. The former causes the surfactant aggregation, while the latter limits it. In the ISM-2 solution, the h^+ sites often intruded into the hydrocarbon interiors, which leads to weakening of the electrostatic repulsion among the h^+ sites. This is a reason why the aggregates of the ISM-2 surfactants become much larger than those of the ISM-3 surfactants, as shown in Figures 6b, 7a, and 9a.

By contrast, the behaviors of the ISM-2 and the ISM-3 preformed micelles in system A are fairly similar to each other, as mentioned in section 3.1. According to eqs 7–9, the revision in the ISM-3 has a noticeable influence on the behavior of the surfactant only when its h^+ site is contiguous to the t sites other than its neighboring t sites. Such a situation infrequently arose in system A, because most of the surfactants in the preformed micelle stably existed as an aggregate with the h^+ sites pointing outward and the hydrophobic tails of the t sites pointing inward during the simulation. Thus, the simulation of the preformed micelle

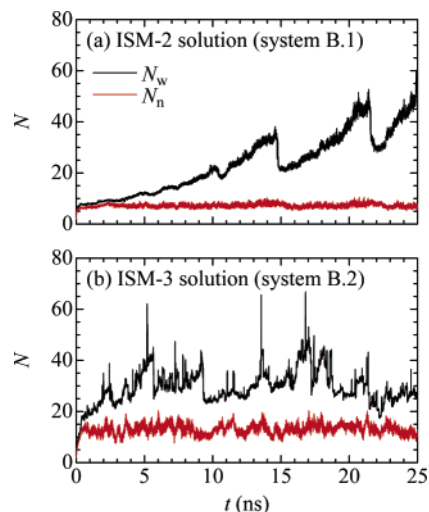


Figure 9. Weight average size N_w (black lines) and number average size N_n (red lines) of the surfactant aggregates in $C_{\text{surf}} = 0.1$ M solution of 343 $t_{10}h^+Cl^-$ surfactants (system B), as a function of time t . (a) the ISM-2 and (b) the ISM-3.

of the proper size is inappropriate for examination into how the revision in the ISM-3 impacts on the surfactant behavior.

It is worth noting that the PMFs for interactions of h^+ with the sites (h^+ , t , and Cl^-) used in our ISMs are based on a tetramethylammonium cation $[(CH_3)_4N^+]$ instead of a trimethylammonium cation $[(CH_3)_3N^+]$. In this strict sense, one should think that our h^+ site represents a headgroup plus its bonding methylene group, $[(CH_3)_3N^+-CH_2-]$, and our $t_{10}h^+Cl^-$ surfactant corresponds to $C_{11}TAC$ rather than $C_{10}TAC$, which leads to the slightly different values of N_{av} and cmc. However, the conclusions drawn from the present simulations are unaffected.

3.2.3. Size of Aggregates. Figure 9 shows the number average size and the weight average size of the aggregates, N_n and N_w , as a function of time t , which are respectively defined as

$$N_n = \frac{\sum_{N>1} k_N N}{\sum_{N>1} k_N} \quad (10a)$$

$$N_w = \frac{\sum_{N>1} k_N N^2}{\sum_{N>1} k_N N} \quad (10b)$$

where k_N is the number of the aggregates of size N .^{33,34} It is worth noting that the light, neutron, and X-ray scattering measurements, which are the popular methods to estimate the average size of surfactant aggregates, give the weight average size of the aggregates, N_w . The average size of the aggregates for $C_{10}TAC$, $N_{\text{av}} = 30$, corresponds to N_w because it is an estimate using an extrapolation of the experimental results obtained by the light scattering^{28,29} and the X-ray scattering.³⁰ As seen in Figure 9a, N_n in the ISM-2 solution is almost constant around 7, while N_w continuously increases during the 25-ns simulation, except for the sharp drops at t

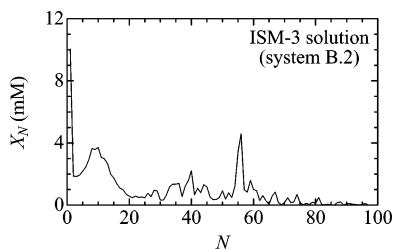


Figure 10. Size distribution of surfactant aggregates in $C_{\text{surf}} = 0.1$ M ISM-3 solution of 343 $t_{10}h^+Cl^-$ surfactants (system B.2). The average concentration of the surfactants in aggregates of size N is denoted by X_N . Each plot is the result averaged over 20 000 configurations taken every 1 ps during the last 20 ns of the 25-ns simulation.

= 14.7 and 21.5 ns corresponding to the breakups of the large aggregates shown in Figure 7a. Finally, N_w exceeds the average size of the aggregates $N_{\text{av}} = 30$ for $C_{10}TAC$ and reaches 53.4 at $t = 25$ ns. For the ISM-3 solution, both N_n and N_w seem to converge and fluctuate around constant values at least at $t > 5$ ns as in Figure 9b. The averages of N_n and N_w over $t = 5-25$ ns are 13.3 and 30.6, respectively; the latter value for N_w agrees very well with the experimental estimate of $N_{\text{av}} = 30$.

For the ISM-3 solution, the aggregate size distribution was calculated using the configurations for $t = 5-25$ ns, which are considered to be equilibrated judging from the variations of the maximum sizes of the aggregates (Figure 7b) and of the average sizes (Figure 9b). Figure 10 shows the resultant size distribution of the aggregates, where X_N denotes the average concentration of the surfactants in the aggregates of size N . The aggregates in the ISM-3 solution exhibit several favorable sizes of $N < 100$, and the maximum peak is observed at $N = 56$. However, the size distribution in Figure 10 is not smooth enough because of the lack of the sufficient samplings. Although we performed the ISM-3 simulations using the single CPU computers in the present study, the use of the massive parallel computers may enable us to carry out the long-time simulations of the large-scale systems for the sufficient samplings. This will be our future study.

4. Conclusions

We have recently proposed a series of the ISMs for the simulation of cationic surfactants in water, where no water molecules of solvent are explicitly treated and their effects are incorporated using the solvent-averaged interactions, namely PMFs.^{18,19} In our previous study, the ISM was revised to improve the representation of the hydrocarbon interior of the surfactant aggregates: in this revised ISM (ISM-2),¹⁹ the interactions between the hydrophobic sites of the surfactants are varied depending on the hydrocarbon densities around them, while in the original ISM,¹⁸ all the interactions between the surfactant segments are given by the PMFs regardless of their surroundings. In the present study, we have additionally improved the representation of a charged headgroup of the liquid-liquid interface between the hydrocarbon oil and the implicit water, where the free energy change due to the transfer of the charged headgroup across the interface is taken

into account. The present model (ISM-3) has been applied to the MD simulations of (i) a single preformed micelle composed of 30 $C_{10}TAC$ cationic surfactants in water and (ii) 343 $C_{10}TAC$ surfactants uniformly dispersed in water, where the corresponding systems were also simulated using the ISM-2 for comparison. The first simulations showed that the ISM-3 as well as the ISM-2 is applicable to the simulation of the preformed micelle of the average aggregate size for $C_{10}TAC$, judging from the internal structure, the shape, and the stability of the micelle. In the second simulations, the ISM-2 solution gave the strange result that only a few surfactant aggregates became large and the other surfactants remained as monomers or small aggregates; for the ISM-3 solution, on the other hand, the surfactant self-assembling was plausibly represented in the sense that the weight average size of the aggregates agreed very well with the experimental estimate.

The ISM-3 simulation of aqueous surfactant solutions computationally costs far less than the atomistic model simulations do, where the water molecules of the solvent are explicitly treated in addition to the solutes of interest. The other feature of the ISM-3 is that it allows us to change the concentration of the surfactants and the counterions involved without changing the computational cost because of the implicit treatment of the water molecules. In the near future, we will investigate the effects of the surfactant concentration and the salt addition on the surfactant behavior, with the help of these advantages of the ISM-3 simulation.

Acknowledgment. This work was partly supported by the Grants-in-Aid (No. 15206085/16760606) for Scientific Research from the Ministry of Education, Culture, Sports, Science and Technology in Japan.

References

- (1) Klein, M. L. *J. Chem. Soc., Faraday Trans.* **1992**, *88*, 1701.
- (2) Smit, B. In *Computer Simulation in Chemical Physics*; Allen, M. P., Tildesley, D. J., Eds.; NATO Advanced Study Institute Series C; Kluwer: Dordrecht, The Netherlands, 1993; Vol. 397, Chapter 12.
- (3) Pastor, R. W. *Curr. Opin. Struct. Biol.* **1994**, *4*, 486.
- (4) Esselink, K.; Hilbers, P. A. J.; Karaborni, S.; Siepmann, J. I.; Smit, B. *Mol. Simul.* **1995**, *14*, 259.
- (5) Karaborni, S.; Smit, B. *Curr. Opin. Colloid Interface Sci.* **1996**, *1*, 411.
- (6) Larson, R. G. *Curr. Opin. Colloid Interface Sci.* **1997**, *2*, 361.
- (7) Jakobsson, E. *Trends Biochem. Sci.* **1997**, *22*, 339.
- (8) Bandyopadhyay, S.; Tarek, M.; Klein, M. L. *Curr. Opin. Colloid Interface Sci.* **1998**, *3*, 242.
- (9) Shelley, J. C.; Shelley, M. Y. *Curr. Opin. Colloid Interface Sci.* **2000**, *5*, 101.
- (10) Feller, S. E. *Curr. Opin. Colloid Interface Sci.* **2000**, *5*, 217.
- (11) Forrest, L. R.; Sansom, M. S. P. *Curr. Opin. Struct. Biol.* **2000**, *10*, 174.
- (12) Schmid, F. In *Computational Methods in Surface and Colloid Science*; Borówko, M., Ed.; Surfactant Science Series 89; Marcel Dekker: New York, 2000; Chapter 13.

- (13) Saiz, L.; Bandyopadhyay, S.; Klein, M. L. *Biosci. Rep.* **2002**, 22, 151.
- (14) Allen, M. P.; Tildesley, D. J. *Computer Simulation of Liquids*; Clarendon Press: Oxford, U.K., 1987.
- (15) Frenkel, D.; Smit, B. *Understanding Molecular Simulation: From Algorithms to Applications*, 2nd ed.; Academic Press: San Diego, CA, 2002.
- (16) Rapaport, D. C. *The Art of Molecular Dynamics Simulation*, 2nd ed.; Cambridge University Press: Cambridge, U.K., 2004.
- (17) Roux, B.; Simonson, T. *Biophys. Chem.* **1999**, 78, 1.
- (18) Shinto, H.; Morisada, S.; Miyahara, M.; Higashitani, K. *Langmuir* **2004**, 20, 2017.
- (19) Morisada, S.; Shinto, H.; Higashitani, K. *J. Phys. Chem. B* **2005**, 109, 11762.
- (20) Lazaridis, T.; Mallik, B.; Chen, Y. *J. Phys. Chem. B* **2005**, 109, 15098.
- (21) (a) Shinto, H.; Morisada, S.; Miyahara, M.; Higashitani, K. *J. Chem. Eng. Jpn.* **2003**, 36, 57. (b) Shinto, H.; Morisada, S.; Higashitani, K. *J. Chem. Eng. Jpn.* **2004**, 37, 1345. (c) Shinto, H.; Morisada, S.; Higashitani, K. *J. Chem. Eng. Jpn.* **2005**, 38, 465.
- (22) The Chemical Society of Japan. *Kagaku-binran Kiso-hen II*, 4th ed.; Maruzen: Tokyo, Japan, 1993.
- (23) Ryckaert, J.-P.; Bellemans, A. *Faraday Discuss. Chem. Soc.* **1978**, 66, 95.
- (24) Ulstrup, J.; Kharkats, Y. I. *Russ. Electrochem.* **1993**, 29, 386.
- (25) Schweighofer, K.; Benjamin, I. *J. Phys. Chem. A* **1999**, 103, 10274.
- (26) Bacaloglu, R.; Blaskó, A.; Bunton, C. A.; Cerichelli, G.; Ortega, F. *J. Phys. Chem.* **1990**, 94, 5062.
- (27) Klevens, H. B. *J. Am. Oil Chem. Soc.* **1953**, 30, 74.
- (28) Ozeki, S.; Ikeda, S. *Bull. Chem. Soc. Jpn.* **1981**, 54, 552.
- (29) Imae, T.; Ikeda, S. *J. Phys. Chem.* **1986**, 90, 5216.
- (30) Reiss-Husson, F.; Luzzati, V. *J. Phys. Chem.* **1964**, 68, 3504.
- (31) Böcker, J.; Brickmann, J.; Bopp, P. *J. Phys. Chem.* **1994**, 98, 712.
- (32) Stilbs, P.; Walderhaug, H.; Lindman, B. *J. Phys. Chem.* **1983**, 87, 4762.
- (33) Mukerjee, P. *J. Phys. Chem.* **1972**, 76, 565.
- (34) Nagarajan, R. *Langmuir* **1994**, 10, 2028.

CT600311T

A Base-Sugar–Phosphate Three-Layer ONIOM Model for Cation Binding: Relative Binding Affinities of Alkali Metal Ions for Phosphate Anion in DNA

Neethu Sundaresan[†] and Cherumuttathu H. Suresh^{*‡}

Chemical Sciences and Technology Division and Computational Modeling and Simulation Section, Regional Research Laboratory (Council of Scientific and Industrial Research), Trivandrum 695019, India

Received July 28, 2006

Abstract: A three-layer ONIOM approach was used to study the interactions of hydrated alkali metal ions such as Li⁺, Na⁺, and K⁺ with a DNA fragment containing two phosphate groups, three sugar units, and a G••C base pair modeled in the anion and dianion states. Among the three metal-binding combinations studied herein (outer-sphere, inner-sphere monodentate, and inner-sphere bidentate), the outer-sphere binding mode showed the highest binding energy (BE) for hydrated Li⁺ ions (103.1 kcal/mol) while the hydrated Na⁺ and K⁺ ions preferred the inner-sphere monodentate binding modes to the phosphate group of the anionic DNA fragment (BE = 87.9 and 98.2 kcal/mol for Na⁺ and K⁺, respectively). These data on the binding mechanisms of Li⁺, Na⁺, and K⁺ ions and the higher binding affinity of Li⁺ ions compared to Na⁺ and K⁺ ions in the anion model system of DNA are in good agreement with the previous experimental findings. On the other hand, in the dianion state, Li⁺ preferred inner-sphere monodentate, whereas Na⁺ and K⁺ ions preferred the outer-sphere structures. The neutral anion model ion revealed a more realistic picture of DNA–alkali metal ion interactions compared to the non-neutral dianion model systems.

I. Introduction

DNA, the highly anionic polyelectrolyte in a living cell, is stabilized by an array of cationic species, including metal ions. Metal cations are known to play a crucial role in both stabilizing and destabilizing the DNA double helix.^{1–4} They can coordinate DNA at several sites, of which the major sites are the phosphate groups, the sugar moiety, the base keto oxygens (O2 of thymine and O6 of guanine on the interior of the double helix), and the ring nitrogens (N7 of adenine and guanine on the exterior and N3 of adenine and guanine) (see Figure 1), the different coordinations depending on the concentration and type of metal ions. The affinity of a cation for a specific site on a polynucleotide is a general function of its charge, hydration-free energy, coordination geometry,

and coordinate bond-forming capacity.^{5,6} Both alkali and alkaline earth metal ions are known to stabilize the DNA predominantly by neutralizing the negatively charged sugar–phosphate backbone.^{7–9} Coordination of phosphate moieties by cations is essential for catalytic enzymatic reactions, the processes involving the transfer of genetic information and the synthesis of oligonucleotides and so forth.^{10,11}

The DNA–metal ion interactions are governed by several parameters such as the nature of the metal, its size, and its charge, which influence the conformation of DNA by direct or indirect interaction through the water molecules with the basic sites of the nucleotides.¹² As monovalent cations are generally less strongly solvated than divalent cations, they tend to interact with DNA purely electrostatically without making hydrogen bonds from metal-coordinated water molecules.¹³

Molecular dynamic (MD) simulations, solution NMR, and crystallographic results agree that the monovalent cations

* Corresponding author e-mail: sureshch@gmail.com

[†] Chemical Sciences and Technology Division.

[‡] Computational Modeling and Simulation Section.

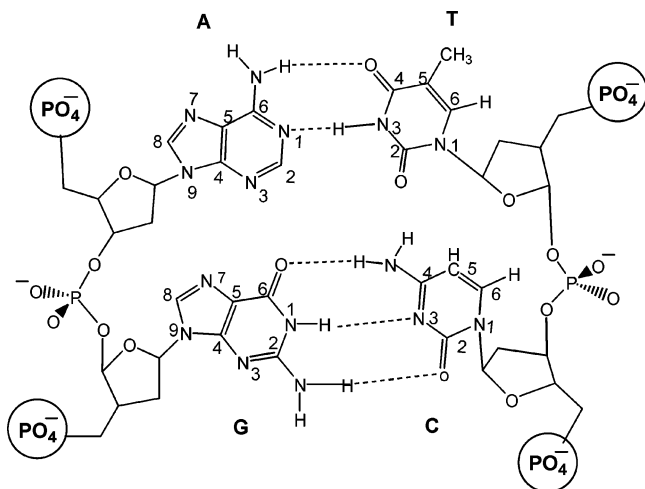


Figure 1. Schematic diagram of A••T and G••C base pairs linked by phosphate groups.

Na^+ , K^+ , Rb^+ , and Cs^+ prefer direct binding (inner-sphere) at the ApT step in the A-track in the minor groove of DNA.^{14,15} Li^+ is reported to interact with the minor groove via a water bridge.¹⁶

A recent study carried out by Wilson and co-workers on MD simulations of 10 ns and longer on DDD (Dickerson–Drew dodecamer with sequence CGCGAATTCGCG),¹⁷ and by Feig and Pettitt on the DNA duplex (A5G5)•(C5T5), with Na^+ as the counterion observed a correlation between the entrance of Na^+ into the minor groove and groove narrowing.¹⁸ Among the alkali metal ions, Na^+ and K^+ are widely distributed in most of the biological systems and are involved in a variety of cellular functions.¹⁹

Most of the previous theoretical studies devoted to metal–DNA binding by Sponer et al.,^{20–25} Petrov et al.,^{26–28} and other groups^{29–36} were carried out on small model systems such as base pairs, nucleotides, dimethyl phosphate anions, solvated metal ions, and so forth, could shed new insights into the mechanisms of metal binding to nucleic acids. In native DNA, the electronegative oxygen atoms of the phosphate group are projected toward the exterior of the double helix, and the small models are largely ineffective in replicating such geometrical constraints.

So, it was thought worthwhile that a study with a model system where negative oxygen atoms of the phosphate group project toward the exterior would be more comparable to the native DNA structure. In the present study, the selected model is a guanine–cytosine base-pair region (G••C region), which also contains the related two sugar units (one connected to the guanine fragment and the other connected to cytosine fragment) and the associated two phosphate groups (one free anionic phosphate group at the cytosine end, which is the anion model). Because of the structural restrictions imposed by the sugar units, we hope that in the present model the phosphate geometry will be maintained as in native DNA. DNA being an anionic polyelectrolyte, one would expect excess negative charge on the DNA segments. Therefore, to compare the effect of excess charge on DNA fragments on the interactions of alkali metal ions with DNA, besides the anion model, we have considered a dianionic model possessing two negative phosphate ends.

In the present work, we have adopted a three-layer ONIOM method [a hybrid of quantum mechanical and molecular mechanics methods (QM–MM)] to study the interaction of hydrated alkali metal ions with the anionic and dianionic DNA fragments. As negatively charged phosphate groups are the major contributors to the polyanionic nature of the DNA macromolecule, the present study will mainly be focused on the interaction of biologically important metal ions such as Li^+ , Na^+ , and K^+ ions with the phosphate groups of DNA.

II. Computational Details and Models

A. Three-Layer ONIOM Model. In this work, we will be utilizing a three-layer ONIOM method, developed by Morokuma and co-workers,^{37–39} to study the metal ion interactions with the DNA segment. ONIOM is a general hybrid method, which can combine molecular orbital as well as molecular mechanics methods, and it is reported to be an efficient tool for accurately calculating chemical interactions in large systems.^{40,41}

In the present study, a typical system used for ONIOM calculation is given in Figure 2. We name this model HPSG••CSP[−]••M_{hyd}⁺, where HP stands for the protonated phosphate group at the guanine end, SG stands for the sugar and the connected guanine, the dotted line indicates the hydrogen-bond interaction between the guanine and cytosine, CSP[−] stands for the cytosine and the connected sugar units and the phosphate anion, M_{hyd}⁺ is the hydrated metal ion, and the dotted line between CSP[−] and M_{hyd}⁺ represents the interaction between the two units. In the case of alkali metal ions, typically, four water molecules are found in their first solvation shell, and accordingly we use the M⁺(H₂O)₄ model for the hydrated metal ion (for selected cases, higher coordination possibilities of the metal ions are also modeled). It may be noted that, in the HPSG••CSP[−]••M_{hyd}⁺ model, the net charge is zero. Therefore, in order to study the effect of excess charge on the M_{hyd}⁺–DNA interactions, we have also studied a dianion model which is designated as (H₂O)₂••PSG••CSP[−]. Here also, an ONIOM model similar to the one in Figure 2 is used, wherein the P[−] at the cytosine end is in the high level and the P[−] at the guanine end is in the medium level. In order to have a realistic picture, the guanine end is microsolvated with a water dimer, which is also in the medium layer. According to the ONIOM terminology, the model HPSG••CSP[−]••M_{hyd}⁺ is divided into three layers, namely, (i) a high layer, (ii) a medium layer, and (iii) a low layer, which are illustrated in Figure 2. The high layer contains the critical part of the reacting system, namely, the phosphate group and interacting hydrated metal ion, which is treated at the B3LYP/6-31G(d) level of density functional theory (DFT).^{42–44} The G••C base pair, the sugar units, and the phosphate group at the guanine end were treated at the medium level of theory by using the semiempirical PM3 method.⁴⁵ The use of the PM3 method in the medium layer will incorporate some electronic effects into the system, and it will also help the delocalization of the charge centered on the phosphate moieties. The sugar units in the low layer are treated with a universal force field.⁴⁶ Since there are no electrons in the MM layer, the phosphate

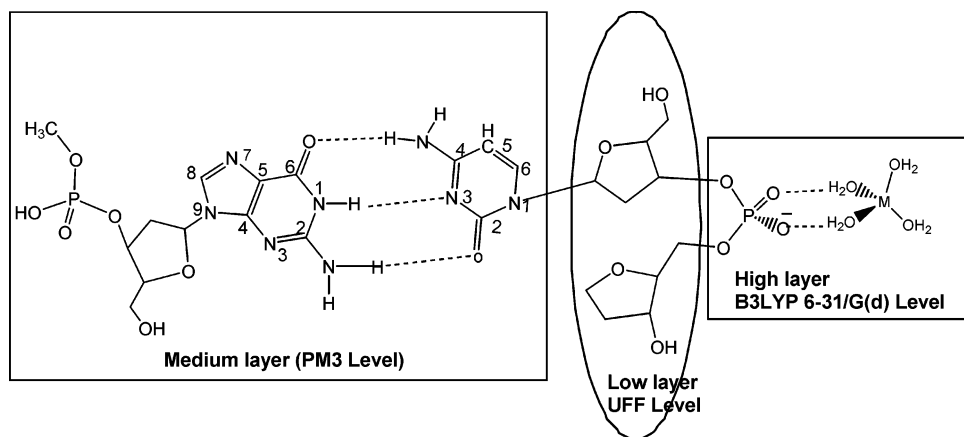


Figure 2. Scheme of the real and model systems used in the ONIOM calculations for DNA–hydrated-metal interaction.

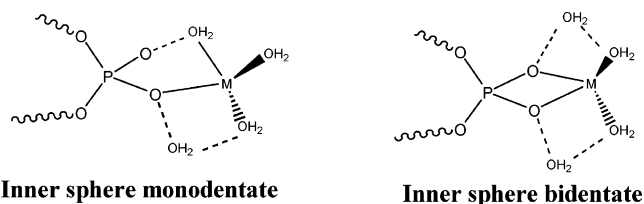


Figure 3. Scheme of the different binding modes selected to study hydrated alkali metal ions and phosphate anion interactions.

group will not interact electronically with this layer, and therefore great twisting of the phosphate groups leading to phosphate and G••C interaction may be prevented. Great twisting of the phosphate groups is less likely to occur in DNA molecules because of the rigid double-stranded structure. Therefore, we expect that the steric effect imposed by the sugar unit can be retained in the MM layer, and at the same time, the direct electronic interaction between the QM layer and the medium layer can be prevented, which in turn will help the phosphate moiety to project toward the exterior of the DNA fragment. Therefore, it is felt that the three-layer ONIOM model will serve as a good model for the study of phosphate and hydrated-metal ion interactions in DNA systems. For interaction energy calculations, structures of hydrated metal ions are fully optimized at the B3LYP/6-31G(d) level of theory (see the Supporting Information, SI, for the structures).

The binding mode given in Figure 2 is the outer-sphere combination of the hydrated metal and the phosphate group. Inner-sphere monodentate and inner-sphere bidentate combinations (Figure 3) are also commonly observed in metal-binding interactions with electron-rich centers. It may be noted that, in the models given in Figure 3, one or two water molecules will have to move out from the tetra-hydration shell of the metal (one for mono- and two for bidentate) to make room for the direct metal–phosphate oxygen bonds. This assumption is reasonable because alkali metal ions prefer three to four metal–oxygen direct bond connections. For instance, in a theoretical study of alkali metal ion–water interaction conducted with models of $M^+(H_2O)_n$, Glendeing and Feller⁴⁷ have found that, for larger clusters ($n = 4–6$), one or two water molecules often occupy the secondary solvation shell.^{9,14,48} The possibilities of higher coordination

geometries for the metal ions will also be considered to a limited extent.

B. Interaction Energy Calculations. In the present calculations, the following geometry types are optimized with the three-layer ONIOM method, namely, (i) the bare anion $HPSG\bullet\bullet CSP^-$, (ii) the bare dianion $(H_2O)_2\bullet\bullet^- PSG\bullet\bullet CSP^-$, (iii) the metal–anion $HPSG\bullet\bullet CSP^- \bullet\bullet M^+(H_2O)_4$, and (iv) the metal–dianion $(H_2O)_2\bullet\bullet^- PSG\bullet\bullet CSP^- \bullet\bullet M^+(H_2O)_4$ systems. In type i and type ii geometries, the main interaction is between the bases G and C, while in types iii and iv structures, both the base pair interaction and the hydrated metal ion and phosphate anion interaction occur. Therefore, we can estimate the following interaction energies.

For G••C base pair interaction energy in the free anion

$$E1 = E(HPSG) + E(CSP^-) - E(HPSG\bullet\bullet CSP^-) + E1_{BSSE} \quad (1)$$

For G••C base pair interaction energy in the bare dianion

$$E2 = E[(H_2O)_2\bullet\bullet^- PSG] + E(CSP^-) - E[(H_2O)_2\bullet\bullet^- PSG\bullet\bullet CSP^-] + E2_{BSSE} \quad (2)$$

For G••C base pair interaction energy in the metal bound anion systems

$$E3 = E(HPSG) + E(CSP^- \bullet\bullet M_{hyd}^+) - E(HPSG\bullet\bullet CSP^- \bullet\bullet M_{hyd}^+) + E3_{BSSE} \quad (3)$$

For G••C base pair interaction energy in the metal bound dianion systems

$$E4 = E[(H_2O)_2\bullet\bullet^- PSG] + E(CSP^- \bullet\bullet M_{hyd}^+) - E[(H_2O)_2\bullet\bullet^- PSG\bullet\bullet CSP^- \bullet\bullet M_{hyd}^+] + E4_{BSSE} \quad (4)$$

For metal ion–phosphate interaction energy in the anion systems

$$E5 = E(HPSG\bullet\bullet CSP^-) + E(M_{hyd}^+) - E(HPSG\bullet\bullet CSP^- \bullet\bullet M_{hyd}^+) + E5_{BSSE} \quad (5)$$

For hydrated metal ion–phosphate interaction energy in the dianion systems

$$E_6 = E[(\text{H}_2\text{O})_2 \bullet\bullet\text{PSG}\bullet\bullet\text{CSP}^-] + E(\text{M}_{\text{hyd}}^+) - E[(\text{H}_2\text{O})_2 \bullet\bullet\text{PSG}\bullet\bullet\text{CSP}^- \bullet\bullet\text{M}_{\text{hyd}}^+] + E_6_{\text{BSSE}} \quad (6)$$

E is the total energy of the systems given in parenthesis. In order to get a reasonable estimate of the E values, the single-point energies of the ONIOM-optimized structures of all the anionic ($\text{HPSG}\bullet\bullet\text{CSP}^- \bullet\bullet\text{M}_{\text{hyd}}^+$) and dianionic [$(\text{H}_2\text{O})_2 \bullet\bullet\text{PSG}\bullet\bullet\text{CSP}^- \bullet\bullet\text{M}_{\text{hyd}}^+$] systems are calculated at the B3LYP/6-31G(d) level. Further, E values at the B3LYP/6-31G(d) level are calculated for the fragment structures HPSG, $(\text{H}_2\text{O})_2 \bullet\bullet\text{PSG}$, and CSP^- taken from their respective full systems. Names in regular font are of the fully optimized ONIOM level structures, and those in italics are of the fragment structures taken from the fully optimized systems. The $E_{1\text{BSSE}}$ to $E_{6\text{BSSE}}$ values are the BSSE corrections to be obtained by employing the counterpoise correction method of Boys and Bernardi.⁴⁹ The BSSE-corrected interaction energy is used for comparing the stability of different structures.

III. Results and Discussion

A. Bare Anion and Dianion Models of a DNA Fragment.

The ONIOM-level-optimized geometries of the bare anion and dianion models of the DNA fragment are given in Figure 4a and b, respectively. As expected, in the optimized geometries, the P–O bonds that are not connected to the sugar units are projected outward with respect to the $\text{G}\bullet\bullet\text{C}$ base pair. The low level of MM theory proved useful, particularly to treat the steric effect of these sugar units, which are mainly responsible for this structural feature. The extra electrons in the systems are delocalized over the exposed P–O bonds, and as a result, they show more double-bond character than the P–O bonds connected to the sugar units. For instance, in the QM layer, the exposed P–O distance is in the range of 1.498–1.501 Å, while the P–O bond connected to the sugar unit is in the range of 1.700–1.712 Å. In DNA systems, the P–O bonds showing double-bond character are typically seen at a distance of 1.48–1.51 Å, and the present results are in good agreement with this. However, the distance obtained for the P–O bond connected to the sugar unit is larger than the typically observed value in the range of 1.59–1.64 Å in DNA systems^{50,51} (later, we will see better values for the longer P–O bond distances in systems containing hydrated metal ions). Shortening of the P–O bond length is mainly due to strong solvation or a counterion effect in DNA systems.

Although understanding the nature of interactions between the DNA phosphate group and the alkali metal ion was the primary objective of the present work, the ONIOM models used in the current study could also provide information on the stability of the $\text{G}\bullet\bullet\text{C}$ base pair in the anion, dianion, and their metal-containing systems. This is possible because the PM3 method, being well-parametrized for organic molecules, applied at the $\text{G}\bullet\bullet\text{C}$ base pair region can yield reliable structural features. For instance, in both the anion and dianion models, the aromatic rings of the $\text{G}\bullet\bullet\text{C}$ base pair are nearly in the same plane, which agrees well with the planar $\text{G}\bullet\bullet\text{C}$ structures often found in DNA systems. Further, the hydrogen-bond length parameters obtained for the $\text{G}\bullet\bullet\text{C}$ base pair region show good agreement with the results obtained by

Sponer et al. at the RI-MP2/TZVPP level (a planar structure with $\text{O}_{6(\text{G})}-\text{N}_{4(\text{C})} = 2.750$ Å, $\text{N}_{1(\text{G})}-\text{N}_{3(\text{C})} = 2.900$ Å, and $\text{N}_{2(\text{G})}-\text{O}_{2(\text{C})} = 2.891$ Å).⁵² Moreover, for a free $\text{G}\bullet\bullet\text{C}$ base pair optimized at the PM3 level, the distances obtained for the $\text{O}_{6(\text{G})}-\text{N}_{4(\text{C})}$, $\text{N}_{1(\text{G})}-\text{N}_{3(\text{C})}$, and $\text{N}_{2(\text{G})}-\text{O}_{2(\text{C})}$, are 2.813, 2.800, and 2.850 Å, respectively, and the corresponding values obtained for the anion and dianion models are nearly the same. The distances observed for the ordered triplet ($\text{O}_{6(\text{G})}-\text{N}_{4(\text{C})}$, $\text{N}_{1(\text{G})}-\text{N}_{3(\text{C})}$, $\text{N}_{2(\text{G})}-\text{O}_{2(\text{C})}$) in the $\text{G}\bullet\bullet\text{C}$ base pair for free anion and dianion models are (2.820, 2.804, 2.828 Å) and (2.810, 2.814, 2.847 Å), respectively, suggesting that the hydrogen-bond interactions at the $\text{N}_{1(\text{G})}-\text{N}_{3(\text{C})}$ and $\text{N}_{2(\text{G})}-\text{O}_{2(\text{C})}$ regions in the dianion model are weaker than that found in the anion model, which can be attributed to the enhanced electrostatic repulsive interaction arising from anionic guanine and anionic cytosine ends. Further, a well-defined water dimer interaction is also present in the guanine end of the dianion model, which would provide a microsolvation environment to the phosphate moiety. It may be noted that, in the case of both anion and dianion models, the bond lengths $\text{N}_{(\text{G})}-\text{C}_{(\text{sugar})}$, $\text{N}_{(\text{C})}-\text{C}_{(\text{sugar})}$, and $\text{C}_{(\text{sugar})}-\text{O}_{(\text{phosphate})}$ observed at the boundary that separates the QM layer from the MM layer (DFT/MM and PM3/MM boundaries) are in good agreement with the corresponding distances in the DNA systems (Figure 4).

In the free anion and dianion models, the BSSE-corrected $\text{G}\bullet\bullet\text{C}$ base pair interaction energy values are calculated according to eqs 1 and 2, respectively, and a value of $E_1 = 29.6$ kcal/mol for the anion and $E_2 = 7.3$ kcal/mol for the dianion is obtained.⁵³ These values are already reported in a recent article, and the smaller base pair interaction energy in the dianion model is attributed to the repulsive electrostatic interaction between the negatively charged guanine and the negatively charged cytosine fragments.

B. Anion and Dianion Models for Hydrated Alkali Metal Ion Interactions. Geometries of $\text{HPSG}\bullet\bullet\text{CSP}^- \bullet\bullet\text{M}^+(\text{H}_2\text{O})_4$ Anion Models.

The binding of alkali metal ions such as Li^+ , Na^+ , and K^+ to the anionic phosphate group in the anion model with different binding mechanisms is optimized at the ONIOM level according to the scheme given in Figures 2 and 3. In these models, the primary solvation shell of the metal ion is modeled with four water molecules because, normally, tetrahydration is observed in alkali metal ions (see the SI for a discussion on the hydrated structures of metal ions).⁴⁷ In Figure 5a, the full optimized geometry for the outer-sphere coordination of $\text{Li}^+(\text{H}_2\text{O})_4$ with the $\text{HPSG}\bullet\bullet\text{CSP}^-$ model is depicted. In order to have a closer look at the hydrated metal region interacting with the phosphate anion, the QM region of the ONIOM optimized geometry of the outer-sphere coordination of $\text{Li}^+(\text{H}_2\text{O})_4$ is also presented in Figure 5b. Only the QM regions in the cases of inner-sphere monodentate and bidentate structures of Li^+ are presented in Figure 5c and d, respectively (see SI for the full geometry). In all three of the binding modes, Li–O bonds are more or less in a tetrahedral arrangement. In mono- and bidentate structures, Li–O bonds to the water molecule (1.950, 1.961, 1.985, 1.912, and 1.933 Å) are shorter than the Li–O bonds to the phosphate oxygen (2.010, 2.141, and 2.160 Å).

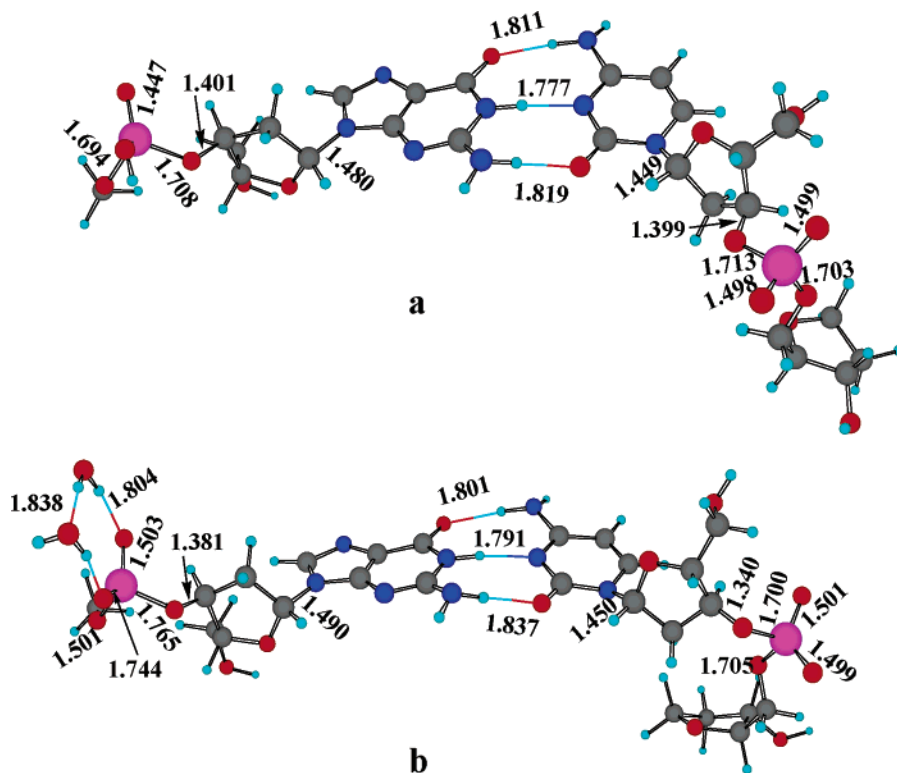


Figure 4. Optimized structures of bare (a) anion ($\text{HPSG}\bullet\bullet\text{CSP}^-$) and (b) dianion $[(\text{H}_2\text{O})_2\text{-PSG}\bullet\bullet\text{CSP}^-]$ model systems. All bond lengths are in angstroms.

In the case of the outer-sphere structure of Na^+ , the $\text{Na}-\text{O}$ bonds around the metal ion show a substantial distortion from the tetrahedral arrangement. For instance, in this geometry, the $\text{O}7-\text{Na}-\text{O}8$ angle is found to be 134.6° , which is quite large compared to a tetrahedral angle. In fact, Na , $\text{O}6$, $\text{O}7$, and $\text{O}8$ atoms are nearly in the same plane as the sum of the angles $\angle\text{O}6\text{NaO}7$, $\angle\text{O}6\text{NaO}8$, $\angle\text{O}7\text{NaO}8$, which is found to be 359.1° . Compared to the Li^+ -induced outer-sphere structure, the distortion from tetrahedral arrangement is quite large in the Na^+ -induced structure because, in the latter system, the $\text{Na}-\text{O}$ bond is expected to be weaker than the $\text{Li}-\text{O}$ bond in the former system. Further, the $\text{O}5\bullet\bullet\text{H}-\text{O}8$ hydrogen-bond interaction between the two metal-bound water molecules (Figure 6a) would also facilitate the tetrahedral distortion in the Na^+ -induced structure. Compared to the outer-sphere structure, $\text{Na}-\text{O}$ bond connections found in the inner-sphere mono- and bidentate structures are largely in a tetrahedral arrangement around the metal (Figure 6b and c), and this feature is also very similar to the corresponding Li^+ geometries.

In the case of K^+ , the outer-sphere structure was not found. All attempts to find the outer-sphere coordination always led to the inner-sphere monodentate structure. In the monodentate system, the $\angle\text{O}7\text{KO}5$ angle is found to be 164.7° and the sum of the angles $\angle\text{O}5\text{KO}6$, $\angle\text{O}5\text{KO}7$, and $\angle\text{O}6\text{KO}7$ is 359.9° . It means that the arrangement of the $\text{K}-\text{O}$ bonds in the system is very similar to the arrangement of the $\text{Na}-\text{O}$ bond in the outer-sphere structure of Na^+ . On the other hand, the bidentate structure retained the tetrahedral arrangement of the $\text{K}-\text{O}$ bonds (Figure 6 e).

The average values of the metal-oxygen distances are 1.971 and 2.288 Å for outer-sphere structures of Li^+ and

Na^+ , respectively, and those for the inner-sphere monodentate structures are 1.977, 2.302, and 2.694 Å for Li^+ , Na^+ , and K^+ , respectively. Slightly higher values of 2.037, 2.324, 2.691 Å are observed for the average metal-oxygen distances in the bidentate structures of Li^+ , Na^+ , and K^+ , respectively. It can be understood that the average metal-oxygen distances increase with an increase in size of the metal ion. However, it does not change much with respect to the different binding modes preferred by the metal ions. In general, the $\text{P}-\text{O}$ bond interacting with the hydrated metal ($\text{P}-\text{O}1$ and $\text{P}-\text{O}2$) showed a small amount of elongation, whereas the other two $\text{P}-\text{O}$ bonds ($\text{P}-\text{O}3$ and $\text{P}-\text{O}4$ connected to the sugar unit) showed a small amount of shortening as compared to the corresponding bonds in the free anion (see the SI for detailed bond length information). For instance, the average of $\text{P}-\text{O}1$ and $\text{P}-\text{O}2$ distances was 1.525 Å, and the average of $\text{P}-\text{O}3$ and $\text{P}-\text{O}4$ distances was 1.669 Å.

C. Geometries of $(\text{H}_2\text{O})_2 \bullet\bullet\text{-PSG}\bullet\bullet\text{CSP}^- \bullet\bullet\text{M}^+(\text{H}_2\text{O})_4$ Dianion Models. The dianion model is selected in order to understand the effect of excess negative charge on the DNA fragment on the metal ion-DNA interaction. The QM regions of the ONIOM-optimized geometries of different binding modes of $\text{Li}^+(\text{H}_2\text{O})_4$, $\text{Na}^+(\text{H}_2\text{O})_4$, and $\text{K}^+(\text{H}_2\text{O})_4$ are presented in Figure 7 (see the SI for the full systems). In the dianion model, the outer-sphere model for Li^+ and the inner-sphere bidentate model for K^+ could not be located. In the case of inner-sphere mono- and bidentate structures of the metals, $\text{Li}-\text{O}$ bonds are arranged in a tetrahedral fashion around the metal. The outer-sphere Na^+ -induced structure is very unique as it shows the arrangement of all four of the oxygen atoms of the water molecules and the

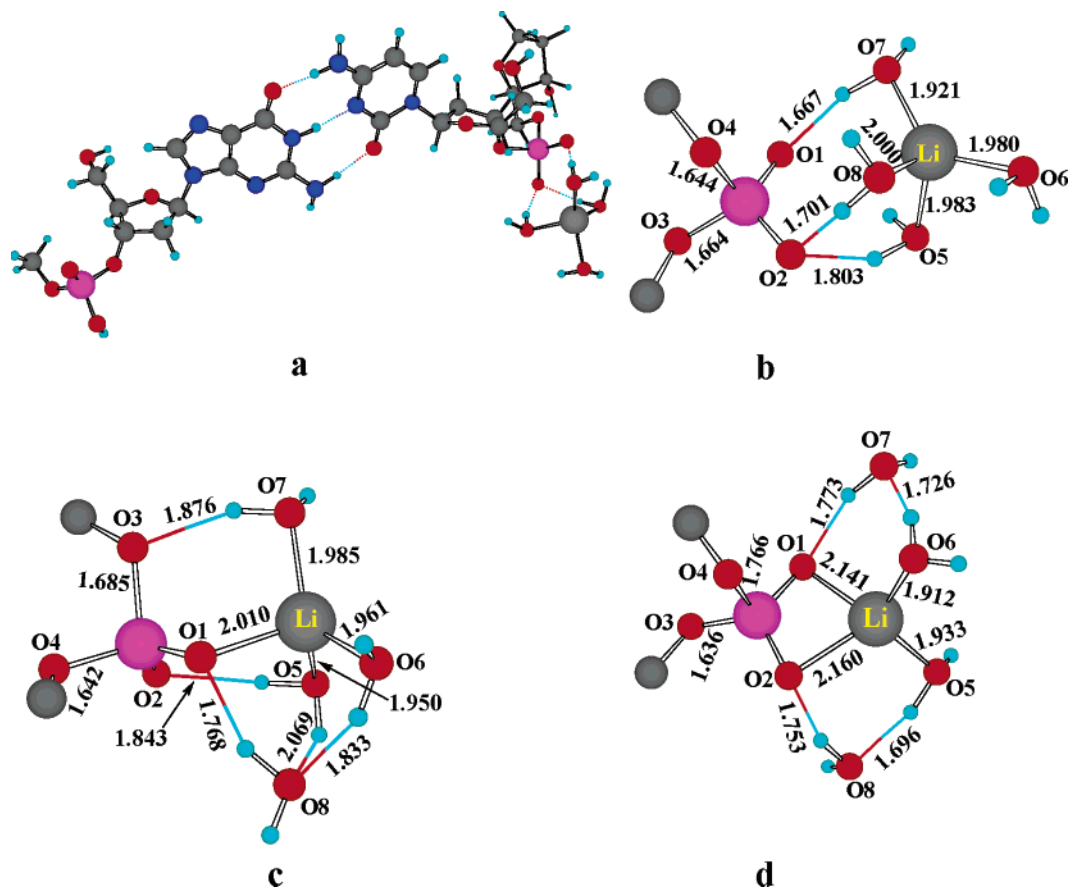


Figure 5. HPS••CSP••Li⁺(H₂O)₄ anion model (a) ONIOM-level optimized full geometry for outer-sphere binding. Parts b, c, and d are the QM region of the ONIOM optimized geometries for outer-sphere binding, inner-sphere monodentate binding, and the inner-sphere bidentate binding, respectively. All bond lengths are in angstroms.

metal in nearly the same plane, meaning that a large distortion from a tetrahedral to a square planar arrangement takes place during the formation of the complex. On the other hand, the tetrahedral arrangement of the Na–O bonds is not much distorted during the formation of the inner-sphere monodentate structure. In both the K⁺-induced outer-sphere and inner-sphere monodentate structures, the K–O bonds around the metal are largely distorted from the tetrahedral arrangement, and in the former case, the part of the structure defined by four water molecules and the metal can be best described as a square pyramid in which the apical position is occupied by a K atom.

In the dianion structures, the average metal–oxygen distances are 1.964, 2.024, 2.365, 2.291, 2.751, and 2.652 Å for inner-sphere monodentate Li⁺, inner-sphere bidentate Li⁺, outer-sphere Na⁺, inner-sphere monodentate Na⁺, outer-sphere K⁺, and inner-sphere monodentate K⁺, respectively. All of these values are shorter than the corresponding values found in the respective anion models. This means that a tighter metal–phosphate binding is occurring in the dianion model than in the anion models. However, these binding interactions have only a small influence on the exposed P–O bond lengths, as they showed an average distance of 1.515 Å, which is in fact smaller than the corresponding value found in the anion models. On the other hand, compared to anion models, the metal–phosphate binding interaction in the dianion models led to a further shortening of the P–O

bonds connected to the sugar units, as they showed an average P–O distance of 1.654 Å.

D. Interaction Energies. The G••C base pair interaction energy data of the three different binding modes (outer-sphere and inner-sphere monodentate and bidentate) of the hydrated alkali metal ions in the dianion model are given in Table 1. For anion and dianion models, eqs 3 and 4 are used to calculate these energies (E3 for anion and E4 for dianion models). It may be seen that, irrespective of the metal ions and their different binding modes, base pair interaction energy in the anion model is nearly close to 25.0 kcal/mol, which is 4.6 kcal/mol smaller than the E1 value of the G••C pair in the free anion model. In the anion models, the average value of the three hydrogen-bond lengths for the G••C base pair is in the range of 1.802–1.805 Å (see the Supporting Information for a distance table), meaning that the hydrogen-bond interactions in all the hydrated metal–anion model systems are nearly unchanged, which is in agreement with the nearly identical interaction energy values. Similarly, in all of the dianion cases, the base pair interaction energy (E4) is nearly identical to 21.0 kcal/mol. However, this E4 value is 4.0 kcal/mol smaller than the E3 value obtained for the anion models, indicating that the excess negative charge on the DNA fragment is weakening the G••C hydrogen-bond strength. On the other hand, compared to the G••C base pair interaction in the free dianion model (E2), the E4 value is 13.7 kcal/mol higher in magnitude. This can be attributed

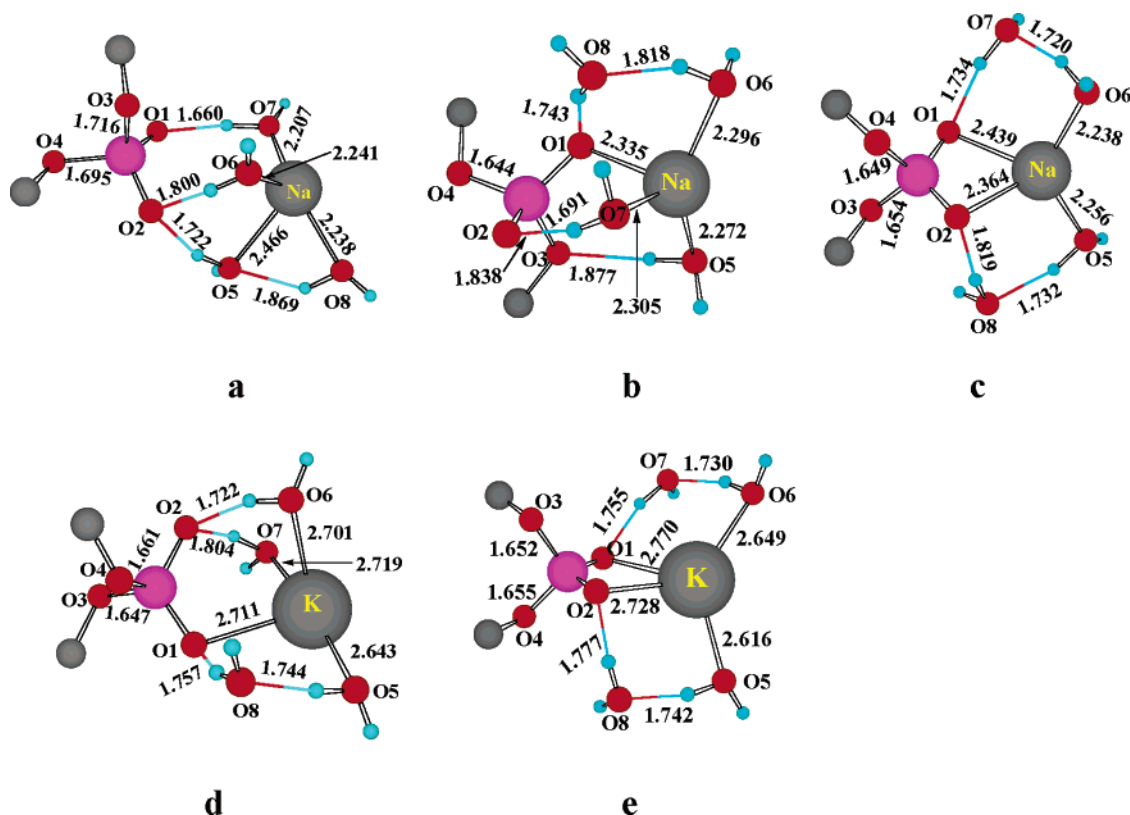


Figure 6. Anion models for $\text{HPS}\bullet\bullet\text{CSP}^{\bullet\bullet}\text{Na}^+(\text{H}_2\text{O})_4$ and $\text{HPS}\bullet\bullet\text{CSP}^{\bullet\bullet}\text{K}^+(\text{H}_2\text{O})_4$. The QM layer of the ONIOM optimized geometry for (a) outer-sphere binding of Na^+ (b and d) inner sphere monodentate binding, and (c and e) the inner sphere bidentate binding. All bond lengths are in angstroms.

mainly to the decrease in the repulsive electrostatic interaction in the dianion–metal system as a result of the neutralization of the charge on the cytosine end. Compared to the anion–metal systems, the average values of the three hydrogen-bond lengths (1.810–1.813 Å) in the G–C pair of dianion–metal systems are increased as a result of the weakening of the G••C base pair interaction.

Table 2 depicts the metal ion–phosphate interaction energy data for tetrahydrated Li^+ , Na^+ , and K^+ ions with anion and dianion models in the outer-sphere, inner-sphere monodentate, and inner-sphere bidentate binding modes. For anion and dianion models, eqs 5 and 6 are used to calculate these energies (E_5 for anion and E_6 for dianion models), respectively. In the case of the anion model of lithium, the E_5 values show the following order of stability: outer-sphere > inner-sphere monodentate > inner-sphere bidentate. The outer-sphere coordination with a binding energy (BE) of 103.1 kcal/mol is superior to the values of 88.9 and 76.9 kcal/mol obtained for the inner-sphere mono- and bidentate structures, respectively. On the other hand, in the case of the anion model of Na^+ , all three of the modes of binding have nearly identical strengths, with the inner-sphere bidentate having the highest value of 87.9 kcal/mol for the BE. The anion model of K^+ showed the highest stability for the inner-sphere monodentate structure ($E_5 = 98.2$ kcal/mol). As a whole, the E_5 values suggest that, in the anion models, the binding strength is in the order $\text{Li}^+ > \text{K}^+ > \text{Na}^+$.

The energy data of tetrahydrated alkali metal–phosphate anion interactions of the dianion models in Table 2 suggest a substantial increase in the metal phosphate BE in all types

of binding modes when compared with the corresponding values obtained in the case of the anion models. For instance, compared to the inner-sphere monodentate anion model, the inner-sphere monodentate dianion model of Li^+ showed an increase in the BE by 41%.

In the case of Li^+ binding to the dianion model, the E_6 values obtained for inner-sphere monodentate and inner-sphere bidentate are 125.7 and 118.9 kcal/mol, respectively, which suggests that Li^+ prefers the inner-sphere monodentate binding mode. In contrast, in the anion model, the stable binding mode observed with the Li^+ ion was the outer-sphere one, which implies that the charge of the model system is crucial in deciding the type of binding.

The difference in the binding mechanism could be due to the fact that, as the dianion model has higher negative potential, it holds the lithium ion closer to the DNA fragment than the anion fragment accompanied by the removal of water from the hydrated Li^+ (dehydration), resulting in an inner-sphere monodentate binding mode. Moreover, in the case of inner-sphere binding, the metal–oxygen distances are shorter than that in the anion model. Unlike lithium, in the case of Na^+ and K^+ , it can be understood from the E_6 values that they prefer the outer-sphere binding mode in the dianion model. Whereas in the anion model, the most stable binding mechanisms observed with Na^+ and K^+ were inner-sphere bidentate and monodentate, respectively. However, it should be noted that the inner-sphere bidentate structure could not be located for Na^+ in the dianion model. It can therefore be concluded that the binding modes of alkali metal ions largely depend on the charge of the DNA fragment.

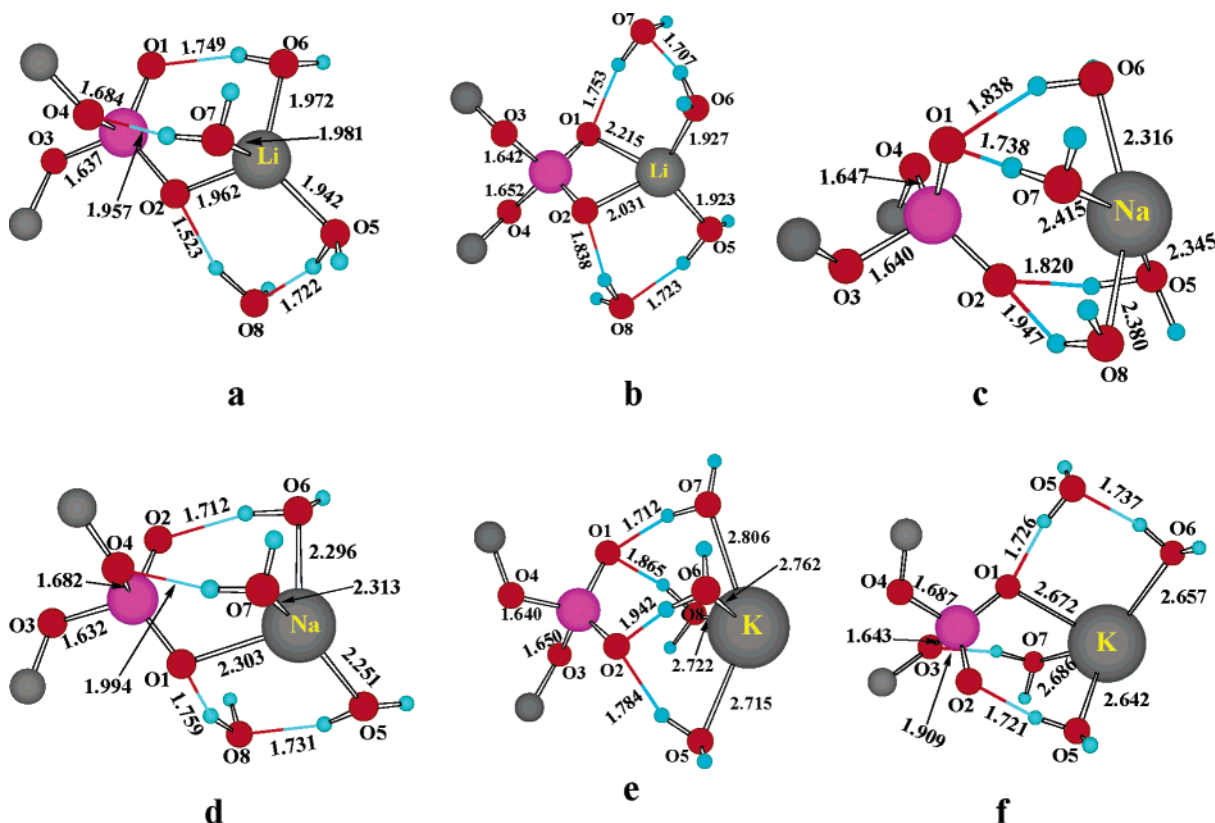


Figure 7. The $[(\text{H}_2\text{O})_2\text{PSG}\cdots\text{CSP}^-\cdots\text{M}^+(\text{H}_2\text{O})_4]$ dianion models for alkali metal ions. Parts a and b are the inner-sphere mono- and bidentate structures for the Li^+ ion, respectively. Parts c and d are the outer-sphere and inner-sphere monodentate structures of the Na^+ ion, respectively; parts e and f are outer- and inner-sphere monodentate structures for the K^+ ion, respectively. All bond lengths are in angstroms.

Table 1. BSSE-Corrected G••C Base Pair Interaction Energy in Anion (E3) and Dianion (E4) Models^a

model systems	outer-sphere		inner-sphere monodentate		inner-sphere bidentate	
	E3 (anion)	E4 (dianion)	E3 (anion)	E4 (dianion)	E3 (anion)	E4 (dianion)
Li^+	25.2 (4.7)	not found	25.4 (4.6)	21.0 (4.7)	25.9 (4.7)	20.8 (4.8)
Na^+	24.7 (4.7)	20.5 (4.8)	25.3 (4.6)	20.6 (4.8)	25.1 (4.7)	not found
K^+	not found	20.6 (4.9)	24.9 (4.6)	20.7 (4.9)	25.2 (4.7)	not found

^a Values in parentheses are the BSSE corrections. All values are in kilocalories per mole.

Table 2. Phosphate–Hydrated Metal Ion Interaction Energy in Anion (E5) and Dianion (E6) Models^a

model systems	outer-sphere		inner-sphere monodentate		inner-sphere bidentate	
	E5 (anion)	E6 (dianion)	E5 (anion)	E6 (dianion)	E5 (anion)	E6 (dianion)
Li^+	103.1 (9.4)	not found	88.9 (9.9)	125.7 (9.2)	76.9 (11.4)	118.9 (12.8)
Na^+	86.1 (9.1)	118.5 (11.0)	86.4 (9.9)	116.0 (10.5)	87.9 (11.5)	not found
K^+	not found	114.2 (12.6)	98.2 (10.5)	114.6 (9.9)	86.4 (10.5)	not found

^a Values in parentheses are the BSSE corrections. All values are in kilocalories per mole.

E. Possibilities of Higher Coordination Geometries. In the previous sections, all of the models were made with four water molecules in the first solvation shell of the metal ion. Although this may be a valid assumption, the higher coordination possibilities exist particularly in the case of Na^+ and K^+ ions because of the larger size of their coordination sphere.^{54–57} In the case of Li^+ , the commonly observed coordination number is four.^{58–61} However, there are examples where this cation shows a penta coordination, which

mainly arises when it interacts with a multidentate ligand such as a crown ether. In the case of Na^+ , octahedral coordination with six nearest-neighbor oxygen interactions is reported in protein structures.⁶² In such structures, many of the Na–O interactions are furnished by carboxylate groups of an amino acid residue as well as the carbonyl group of the peptide bond. From a combined quantum chemical statistical simulation study on the hydration of Na^+ , Öhrn and Karlström⁵⁸ have recently proposed a value close to five

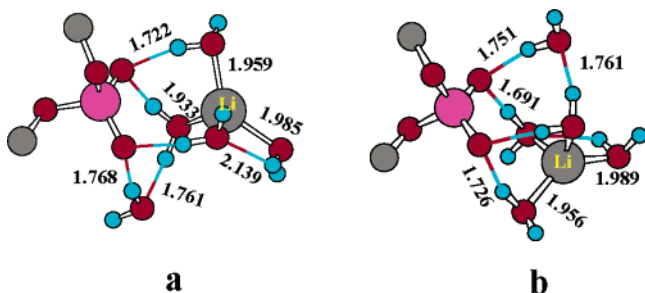


Figure 8. Optimized structures taken from the full model of (a) $\text{HPS}\bullet\bullet\text{CSP}^-\bullet\bullet\text{Li}^+(\text{H}_2\text{O})_5$ and (b) $(\text{H}_2\text{O})_2\bullet\bullet\text{-PSG}\bullet\bullet\text{CSP}^-\bullet\bullet\text{Li}^+(\text{H}_2\text{O})_5$. All bond lengths are in angstroms.

for the average coordination number for Na^+ , while other workers have reported this value to be around six.^{63,64} In the case of K^+ , coordination numbers even higher than six are located. For instance, in a recent study, Di Cera and co-workers⁶⁵ have reported the high-resolution structure of thrombin containing seven $\text{K}^+\text{-O}$ bonding interactions. In the present work, the reported structures in Figures 6a,d and 7c,e,f show a large bare region around the metal center, suggesting further coordination possibilities with water molecules. This aspect is explored to a limited extent by further ONIOM-level calculations on model structures containing five and six water molecules around the metal center.

The initial geometry of the $\text{HPS}\bullet\bullet\text{CSP}^-\bullet\bullet\text{Li}^+(\text{H}_2\text{O})_5$ anion model is made by adding one water molecule to the most stable outer-sphere $\text{HPS}\bullet\bullet\text{CSP}^-\bullet\bullet\text{Li}^+(\text{H}_2\text{O})_4$ complex so that the newly added water is within the Li-O bonding region (~ 2.0 Å). Similarly, to the most stable inner-sphere dianion model $(\text{H}_2\text{O})_2\bullet\bullet\text{-PSG}\bullet\bullet\text{CSP}^-\bullet\bullet\text{Li}^+(\text{H}_2\text{O})_4$, one more water molecule is added in the Li-O bonding region to obtain the $(\text{H}_2\text{O})_2\bullet\bullet\text{-PSG}\bullet\bullet\text{CSP}^-\bullet\bullet\text{Li}^+(\text{H}_2\text{O})_5$ dianion system. In both of the cases, the final optimized geometry (Figure 8) showed a tetrahedral coordination of four water molecules around the Li^+ and the fifth water molecule was moved out to the second solvation shell. Further addition of water molecules is expected to keep the tetra coordination around the Li^+ , and therefore their geometries are not optimized.

The initial geometries of $\text{HPS}\bullet\bullet\text{CSP}^-\bullet\bullet\text{Na}^+(\text{H}_2\text{O})_5$ and $\text{HPS}\bullet\bullet\text{CSP}^-\bullet\bullet\text{Na}^+(\text{H}_2\text{O})_6$ models for ONIOM optimization are made by adding the appropriate number of water molecules at the Na-O bonding distances (2.3 Å). The same strategy is used in the case of dianion models as well (cf. Figure 9 for optimized structures). The anion model $\text{HPS}\bullet\bullet\text{CSP}^-\bullet\bullet\text{Na}^+(\text{H}_2\text{O})_5$ turns out to be an inner-sphere monodentate structure wherein only three of the water molecules showed strong coordination to the metal ion. On the other hand, the dianion model showed the outer-sphere coordination with four strong Na-O bonding interactions. In this case, the fifth water molecule is moved out from the coordination sphere to keep hydrogen-bonding interactions with one of the phosphate oxygen atoms and another water in the first solvation shell. Although $\text{HPS}\bullet\bullet\text{CSP}^-\bullet\bullet\text{Na}^+(\text{H}_2\text{O})_5$ is described as an outer-sphere structure, the $\text{Na-O}_{(\text{phosphate})}$ distance of 2.579 Å suggests significant interaction between the corresponding atoms. The anion and the dianion models with six water molecules possess outer-sphere coordination,

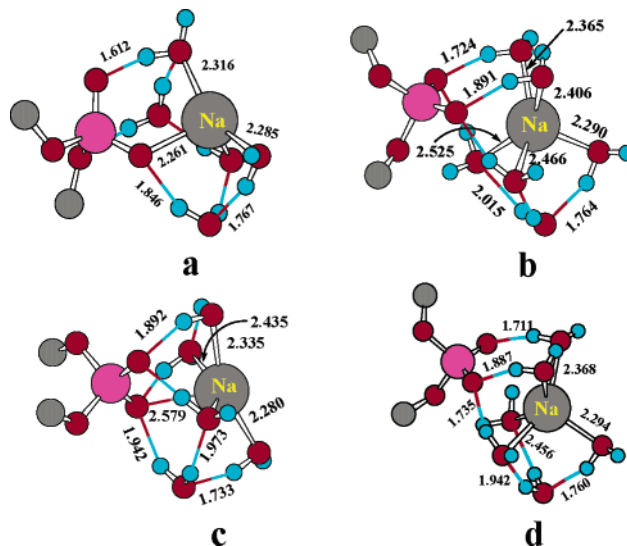


Figure 9. Optimized structures taken from the full model of (a) $\text{HPS}\bullet\bullet\text{CSP}^-\bullet\bullet\text{Na}^+(\text{H}_2\text{O})_5$, (b) $\text{HPS}\bullet\bullet\text{CSP}^-\bullet\bullet\text{Na}^+(\text{H}_2\text{O})_6$, (c) $(\text{H}_2\text{O})_2\bullet\bullet\text{-PSG}\bullet\bullet\text{CSP}^-\bullet\bullet\text{Na}^+(\text{H}_2\text{O})_5$, and (d) $(\text{H}_2\text{O})_2\bullet\bullet\text{-PSG}\bullet\bullet\text{CSP}^-\bullet\bullet\text{Na}^+(\text{H}_2\text{O})_6$. All bond lengths are in angstroms.

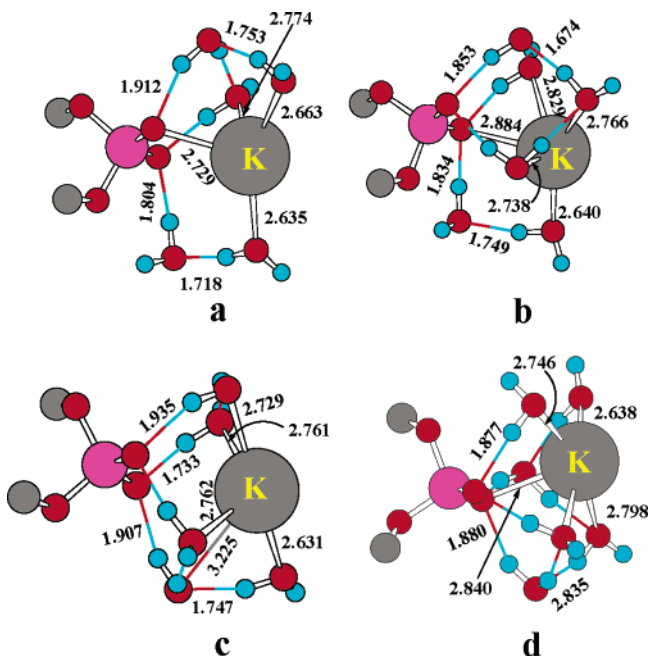


Figure 10. Optimized structures taken from the full model of (a) $\text{HPS}\bullet\bullet\text{CSP}^-\bullet\bullet\text{K}^+(\text{H}_2\text{O})_5$, (b) $\text{HPS}\bullet\bullet\text{CSP}^-\bullet\bullet\text{K}^+(\text{H}_2\text{O})_6$, (c) $(\text{H}_2\text{O})_2\bullet\bullet\text{-PSG}\bullet\bullet\text{CSP}^-\bullet\bullet\text{K}^+(\text{H}_2\text{O})_5$, and (d) $(\text{H}_2\text{O})_2\bullet\bullet\text{-PSG}\bullet\bullet\text{CSP}^-\bullet\bullet\text{K}^+(\text{H}_2\text{O})_6$. All bond lengths are in angstroms.

and both of the structures are nearly identical, showing direct coordination of five water molecules to the metal center. In this case, the nearest $\text{Na-O}_{(\text{phosphate})}$ distance is found to be 2.840 Å.

For the systems containing K^+ , further additions of water molecules are carried out with the inner-sphere $\text{HPS}\bullet\bullet\text{CSP}^-\bullet\bullet\text{K}^+(\text{H}_2\text{O})_4$ (cf. Figure 6d) and the outer-sphere $(\text{H}_2\text{O})_2\bullet\bullet\text{-PSG}\bullet\bullet\text{CSP}^-\bullet\bullet\text{K}^+(\text{H}_2\text{O})_4$ models (cf. Figure 7e). The ONIOM-level optimized geometries are presented in Figure 10. Both of the anion models (with five and six water molecules) show inner-sphere monodentate coordination of the metal ion to the phosphate. In $\text{HPS}\bullet\bullet\text{CSP}^-\bullet\bullet\text{K}^+(\text{H}_2\text{O})_5$,

Table 3. Phosphate–Hydrated Metal Ion Interaction Energy in Anion and Dianion Models^a

model systems	anion		dianion	
	E7 for M ⁺ (H ₂ O) ₅	E8 for M ⁺ (H ₂ O) ₆	E9 for M ⁺ (H ₂ O) ₅	E10 for M ⁺ (H ₂ O) ₆
Li ⁺	98.1 (10.5)		121.1 (10.4)	
Na ⁺	87.9 (11.1)	85.5 (12.0)	117.3 (11.8)	117.0 (12.1)
K ⁺	96.2 (11.7)	97.6 (12.2)	115.6 (12.5)	114.1 (14.1)

^a Values in parentheses are the BSSE corrections. All values are in kilocalories per mole.

three water molecules are directly bonded to the K⁺, while in HPS••CSP⁻••K⁺(H₂O)₆, four water molecules show strong interaction with the K⁺. Interestingly, the (H₂O)₂••PSG••CSP⁻••K⁺(H₂O)₅ dianion model possesses outer-sphere coordination while the (H₂O)₂••PSG••CSP⁻••K⁺(H₂O)₆ is inner-sphere monodentate. In both of the dianion systems, four water molecules are directly bonded to the metal center. It may be noted that, even with five or six water molecules, full coverage of the coordination sphere of both Na⁺ and K⁺ is not achieved. Interestingly, these metal centers are unable to keep six M⁺–O-type bonding interactions, and it is felt that through the mediation of water molecules in the secondary solvation shell such coordination may arise. For instance, in HPS••CSP⁻••Na⁺(H₂O)₆, the water molecule in the secondary solvation shell (cf. Figure 9b) is helpful to maintain the rigidity of the penta-coordinated metal ion in it.

The BSSE-corrected BE values E7, E8, E9, and E10 are calculated to quantify the interaction of the hydrated metal ion to the phosphate moiety (Table 3). E7 and E8 represent the interaction of M⁺(H₂O)₅ and M⁺(H₂O)₆ with the anion, while E9 and E10 represent the interaction of M⁺(H₂O)₅ and M⁺(H₂O)₆ with the dianion, respectively. A comparison of the energy values in Tables 2 and 3 suggests that, in the case of Li⁺, the maximum BE to both the anion and the dianion is obtained when it is hydrated with four water molecules. Similarly, dianion models containing Na⁺(H₂O)₄ and the anion model containing K⁺(H₂O)₄ show more BE than their corresponding penta- and hexa-hydrated metal centers. In contrast to this, in the anion models, the penta-hydrated Na⁺ system shows binding strength equal to that of the tetra-hydrated inner-sphere bidentate structure (BE = 87.9 kcal/mol). Among all the dianion models of K⁺, the (H₂O)₂••PSG••CSP⁻••K⁺(H₂O)₅ system has the highest BE (115.6 kcal/mol).

IV. Conclusions

The interactions of hydrated Li⁺, Na⁺, and K⁺ ions to the phosphate group of DNA are studied by modeling a DNA fragment both in an anion (one negative charge) and a dianion (two negative charges) state with the phosphate geometry maintained as in native DNA (projected toward the exterior) using a three-layer ONIOM-based QM–MM method. Three combinations of metal ion–DNA binding were studied, which included the outer-sphere, inner-sphere monodentate, and inner-sphere bidentate patterns. Among the alkali metal ions, Li⁺ is known to have the highest affinity for DNA in aqueous solutions in terms of counterion

interactions.⁶⁶ The present results are in good agreement with this as, among all the structures, Li⁺ showed the highest BE in both anion and dianion models, where the former is of 103.1 kcal/mol [outer-sphere HPS••CSP⁻••Li⁺(H₂O)₄] and the latter is 125.7 kcal/mol [inner-sphere monodentate (H₂O)₂••PSG••CSP⁻••Li⁺(H₂O)₄]. Comparison of all the structures with the highest BE shows that the binding strength of the metal ions follows the order Li⁺ > K⁺ > Na⁺ in the anion models, while it is Li⁺ > Na⁺ > K⁺ in the dianion models. Experimental reports have shown that Li⁺ ions prefer outer-sphere binding to DNA¹⁶ and stabilizes the water structure around DNA,⁵⁰ and Na⁺ and K⁺ ions bind to DNA in an inner-sphere manner,^{14,15} which is in good agreement with the binding behavior of these ions with the anion model, as the structures with the highest binding energies are outer-sphere HPS••CSP⁻••Li⁺(H₂O)₄, inner-sphere monodentate HPS••CSP⁻••Na⁺(H₂O)₅, and inner-sphere monodentate HPS••CSP⁻••K⁺(H₂O)₄. This suggests that the neutral anion model is quite suitable for studying the interactive behavior of alkali metal ions compared to the dianion model where the net charge on the system is not neutral. In the dianion models, the Coulombic electrostatic interaction between the dianion system and the positively charged hydrated metal ion is higher than that of the anion system and the hydrated metal ions. Therefore, all dianion models showed a higher binding energy than the anion models. It appears that, when the net charge on the DNA–metal system is not zero, the results are not in agreement with the experiment. Our previous work⁵³ on the binding behavior of alkaline earth metals (dipositively charged) on a DNA fragment revealed similar results where only the dianion model having net zero charge showed the right binding behavior, as found in the experiments.

Acknowledgment. We thank the Council of Scientific and Industrial Research, Government of India, for the support of this work. We also thank Dr. C. K. S. Pillai for fruitful discussions.

Supporting Information Available: Optimized geometries of all the structures and a discussion on the hydrated metal ions. This material is available free of charge via the Internet at <http://pubs.acs.org>.

References

- (1) Eichhorn, G. L. *Adv. Inorg. Biochem.* **1981**, 3, 1.
- (2) Martin, R. B. *Acc. Chem. Res.* **1985**, 18, 32.
- (3) Saenger, W. *Principles of Nucleic Acid Structure*; Springer-Verlag: New York, 1994.
- (4) Sigel, H. *Chem. Soc. Rev.* **1993**, 22, 255.
- (5) Glusker, J. P. *Adv. Protein Chem.* **1991**, 42, 1.
- (6) Misra, V. K.; Draper, D. E. *Biopolymers* **1998**, 48, 113.
- (7) Alexander, R. S.; Kanyo, Z. F.; Chirlian, L. E.; Christianson, D. W. *J. Am. Chem. Soc.* **1990**, 112, 933.
- (8) Laughton, C. A.; Luque, F. J.; Orozco, M. *J. Phys. Chem.* **1995**, 99, 11591.
- (9) Schneider, B. K.; Kabelac, M.; Hobza, P. *J. Am. Chem. Soc.* **1996**, 118, 12207.

- (10) Bamann, E.; Trapmann, H.; Fischler, F. *Biochem. Z.* **1954**, 328, 89.
- (11) Marzilli, L. G.; Kistenmacher, T. J.; Eichhorn, G. L. *Nucleic Acid-Metal Ion Interactions*; John Wiley and Sons: New York, 1980; Vol. 1.
- (12) Missailides, S.; Anastassopoulou, J.; Fotopoulos, N.; Theophanides, T. *Asian J. Phys.* **1997**, 6, 481.
- (13) Chiu, T. K.; Dickerson, R. E. *J. Mol. Biol.* **2000**, 301, 915.
- (14) Tereshko, V.; Wilds, C. J.; Minasov, G.; Prakash, T. P.; Maier, M. A.; Howard, A.; Wawrzak, Z.; Manoharan, M.; Egli, M. *Nucleic Acids Res.* **2001**, 29, 1208.
- (15) Stelwagen, N. C.; Magnusdottir, S.; Gelfi, C.; Righeti, P. *G. J. Mol. Biol.* **2001**, 305, 1025.
- (16) Zheng, J.; Li, Z.; Wu, A.; Zhou, H. *Biophys. Chem.* **2003**, 104, 37.
- (17) Hamelberg, D.; McFail-Isom, L.; Williams, L. D.; Wilson, W. D. *J. Am. Chem. Soc.* **2000**, 122, 10513.
- (18) Feig, M.; Pettitt, B. M. *Biophys. J.* **1999**, 77, 1769.
- (19) Sigel, H. *Metal-DNA Chemistry*; American Chemical Society: Washington, D. C., 1989; Vol. 159.
- (20) Sponer, J.; Burda, J. V.; Leszczynski, J.; Hobza, P. *J. Biomol. Struct. Dyn.* **1999**, 17, 61.
- (21) Sponer, J.; Hobza, P. *Collect. Czech. Chem. Commun.* **2003**, 68, 2231.
- (22) Sponer, J.; Leszczynski, J.; Hobza, P. *THEOCHEM* **2001**, 573, 43.
- (23) Sponer, J.; Sabat, M.; Burda, J. V.; Leszczynski, J.; Hobza, P.; Lippert, B. *J. Biol. Inorg. Chem.* **1999**, 4, 537.
- (24) Sponer, J. E.; Sychrovsky, V.; Hobza, P.; Sponer, J. *Phys. Chem. Chem. Phys.* **2004**, 6, 2772.
- (25) Munoz, J.; Sponer, J.; Hobza, P.; Orozco, M.; Luque, F. J. *J. Phys. Chem. B* **2001**, 105, 6051.
- (26) Petrov, A. S.; Funseth-Smotzer, J.; Pack, G. R. *Int. J. Quantum Chem.* **2005**, 102, 645.
- (27) Petrov, A. S.; Lamm, G.; Pack, G. R. *J. Phys. Chem. B* **2002**, 106, 3294.
- (28) Petrov, A. S.; Lamm, G.; Pack, G. R. *J. Phys. Chem. B* **2004**, 108, 6072.
- (29) Bandyopadhyay, D.; Bhattacharya, D. *J. Biomol. Struct. Dyn.* **2003**, 21, 447.
- (30) Bertran, J.; Rodriguez-Santiago, L.; Sodupe, M. *J. Phys. Chem. B* **1999**, 103, 2310.
- (31) Zeizinger, N.; Burda, J. V.; Sponer, J.; Kapsa, V.; Leszczynski, J. *J. Phys. Chem. A* **2001**, 105, 8086.
- (32) Murashov, V. V.; Leszczynski, J. *J. Phys. Chem. B* **1999**, 103, 8391.
- (33) Rodger, A.; Sanders, K. J.; Hannon, M. J.; Meistermann, I.; Parkinson, A.; Vidler, D. S.; Haworth, I. S. *Chirality* **2000**, 12, 221.
- (34) Marincola, F. C.; Denisov, V. P.; Halle, B. *J. Am. Chem. Soc.* **2004**, 126, 6739.
- (35) Kankia, B. I. *Biopolymers* **2004**, 74, 232.
- (36) Jerkovic, B.; Bolton, P. H. *Biochemistry* **2001**, 40, 9406.
- (37) Svensson, M.; Humbel, S.; Froese, R. D. J.; Matsubara, T.; Sieber, S.; Morokuma, K. *J. Phys. Chem.* **1996**, 100, 19357.
- (38) Humbel, S.; Sieber, S.; Morokuma, K. *J. Chem. Phys.* **1996**, 105, 1959.
- (39) Dapprich, S.; Komaromi, I.; Byun, K. S.; Morokuma, K.; Frisch, M. J. *THEOCHEM* **1999**, 461–462, 1.
- (40) Tschumper, G. S.; Morokuma, K. *THEOCHEM* **2002**, 592, 137.
- (41) Re, S.; Morokuma, K. *J. Phys. Chem. A* **2001**, 105, 7185.
- (42) Becke, A. D. *J. Chem. Phys.* **1993**, 98, 5648.
- (43) Becke, A. D. *Phys. Rev. A: At., Mol., Opt. Phys.* **1988**, 38, 3098.
- (44) Hariharan, P. C.; Pople, J. A. *Mol. Phys.* **1974**, 27, 209.
- (45) Stewart, J. J. P. *J. Comput. Chem.* **1989**, 10, 209.
- (46) Rappé, A. K.; Casewit, C. J.; Colwell, K. S.; Goddard, W. A., III; Skiff, W. M. *J. Am. Chem. Soc.* **1992**, 114, 10024.
- (47) Glendening, E. D.; Feller, D. *J. Phys. Chem.* **1995**, 99, 3060.
- (48) Egli, M. *Chem. Biol.* **2002**, 9, 277.
- (49) Boys, S. F.; Bernardi, F. *Mol. Phys.* **1970**, 19, 553.
- (50) Campbell, N. H.; Evans, D. A.; Lee, M. P.; Parkinson, G. N.; Neidle, S. *Bioorg. Med. Chem. Lett.* **2006**, 16, 15.
- (51) Hays, F. A.; Teegarden, A. T.; Jones, Z. J. R.; Harms, M.; Raup, D.; Watson, J.; Cavaliere, E.; Ho, P. S. *Proc. Natl. Acad. Sci. U.S.A.* **2005**, 102, 7157.
- (52) Sponer, J.; Jurecka, P.; Hobza, P. *J. Am. Chem. Soc.* **2004**, 126, 10142.
- (53) Sundaresan, N.; Pillai, C. K. S.; Suresh, C. H. *J. Phys. Chem. A* **2006**, 110, 8826.
- (54) Jungwirth, P.; Tobias, D. J. *J. Phys. Chem. B* **2002**, 106, 6361.
- (55) Várnai, P.; Zakrzewska, K. *Nucleic Acids Res.* **2004**, 32, 4269.
- (56) Draper, D. E.; Grilley, D.; Soto, A. M. *Annu. Rev. Biophys. Biomol. Struct.* **2005**, 34, 221.
- (57) Hud, N. V.; Smith, F. W.; Anet, F. A. L.; Feigon, J. *Biochemistry* **1996**, 35, 15383.
- (58) Öhrn, A.; Karlström, G. *J. Phys. Chem. B* **2004**, 108, 8452.
- (59) Obst, S.; Bradaczek, H. *J. Phys. Chem.* **1996**, 100, 15677.
- (60) Loeffler, H. H. R. B. M. *J. Chem. Phys.* **2002**, 117, 110.
- (61) Duan, Z. H.; Zhang, Z. G. *Mol. Phys.* **2003**, 101, 1501.
- (62) Nayal, M.; Di Cera, E. *J. Mol. Biol.* **1996**, 256, 228.
- (63) Tòth, G. *J. Chem. Phys.* **1996**, 105, 5518.
- (64) Degrève, L.; de Pauli, V. M.; Duarte, M. A. *J. Chem. Phys.* **1997**, 106, 655.
- (65) Carrell, C. J.; Bush, L. A.; Mathews, F. S.; Di Cera, E. *Biophys. Chem.* **121**, 177.
- (66) Lyubartsev, A. P.; Laaksonen, A. *J. Biomol. Struct. Dyn.* **1998**, 16, 579.

De novo Folding of Two-Helix Potassium Channel Blockers with Free-Energy Models and Molecular Dynamics

Aina Quintilla, Evgeni Starikov, and Wolfgang Wenzel*

Forschungszentrum Karlsruhe, Institute für Nanotechnologie, P.O. Box 3640,
76021 Karlsruhe, Germany

Received August 24, 2006

Abstract: We report the predictive de novo folding of three two-helix proteins using the free-energy protein forcefield PFF01. Starting from random initial conformations 40–90% of the members of the simulated ensembles converge to near-native conformations. The energetically lowest conformations approach the conserved part of the native conformations to within 1.64, 1.86, and 1.84 Å for 1WQC, 1WQD, and 1WQE, respectively. An analysis of the low-lying conformations predicts the correct topology of the disulfide bridges, which are formed in additional simulations with a constraining potential. The free energy landscapes of these proteins are very simple, suggesting them as candidates for all-atom molecular dynamics simulations. In five independent simulations we find the formation of the correct secondary structure and several folding events into the tertiary structure.

1. Introduction

The development of methods that simulate the protein folding process at the all-atom level and the elucidation of its mechanism are among the important outstanding problems of biophysical chemistry.^{1–4} Significant new insights arise from de novo folding studies of small proteins and peptides.^{5–8} We have recently demonstrated a feasible strategy for all-atom protein structure prediction^{9–11} in a minimal thermodynamic approach. We developed an all-atom free-energy forcefield for proteins (PFF01), which is primarily based on physical interactions.¹¹ We already demonstrated the reproducible and predictive folding of several proteins with 20–60 amino acids.^{9,12–14}

While many β -hairpin systems have been investigated both experimentally and theoretically,^{15–17} there is a relative scarcity of small two-helix peptides that are known to fold experimentally into well-defined tertiary structure. Since two-helix proteins constitute a minimal model, in which to investigate the interplay of hydrophobic collapse, secondary structure formation and the formation of native contacts, the identification of such systems may be helpful to elucidate

the protein folding mechanism. We have previously folded the widely studied 23 amino acid trp-cage protein,^{6,12,18,19,20–22} which has spurred many theoretical investigations because of its fast folding time.

In this investigation we fold three homologous potassium channel blockers,²³ which exhibit a parallel two-helix bundle. We find that all three peptides fold reproducibly into stable tertiary structures, with very simple free-energy funnels. We demonstrate through molecular dynamics simulation that the lack of competing metastable conformations makes these proteins ideal candidates for folding studies to elucidate the interplay of secondary and tertiary structure formation.^{15,24,25}

2. Methods

2.1. Forcefield. We have recently developed an all-atom (with the exception of apolar CH_n groups) free-energy protein forcefield (PFF01) that models the low-energy conformations of proteins with minimal computational demand.^{26,10,11} The forcefield parametrizes the internal free energy of the protein (excluding backbone entropy) and contains the following nonbonded interactions:

* Corresponding author phone: +49-7247-82-6383. E-mail: wenzel@int.fzk.de; Web: <http://www.fzk.de/biostruct>.

$$V(\{\vec{r}_i\}) = \sum_{ij} V_{ij} \left[\left(\frac{R_{ij}}{r_{ij}} \right)^{12} - 2 \left(\frac{R_{ij}}{r_{ij}} \right)^6 \right] + \sum_{ij} \frac{q_i q_j}{\epsilon_{g(i)g(j)} r_{ij}} + \sum_i \sigma_i A_i + \sum_{\text{hbonds}} V_{\text{hb}} \quad (1)$$

Here r_{ij} denotes the distance between atoms i and j and $g(i)$ the type of the amino acid i .

The Lennard-Jones parameters (V_{ij} , R_{ij} for potential depths and equilibrium distance) depend on the type of the atom pair and were adjusted to satisfy constraints derived from a set of 138 proteins of the PDB database.^{26–28} The nontrivial electrostatic interactions in proteins are represented via group-specific dielectric constants ($\epsilon_{g(i)g(j)}$ depending on the amino acids to which the atoms i and j belong). The partial charges q_i and the dielectric constants were derived in a potential-of-mean-force approach.²⁹ Interactions with the solvent were first fit in a minimal solvent accessible surface model³⁰ parametrized by free energies per unit area σ_i to reproduce the enthalpies of solvation of the Gly-X-Gly family of peptides.³¹ A_i corresponds to the area of atom i that is in contact with a fictitious solvent. Hydrogen bonds are described via dipole–dipole interactions included in the electrostatic terms and an additional short-range term for backbone–backbone hydrogen bonding (CO to NH) which depends on the OH distance, the angle between N, H, and O along the bond, and the angle between the CO and NH axis.¹¹

In the folding process under physiological conditions the degrees of freedom of a peptide are confined to rotations about single bonds. In our simulation we therefore consider only moves around the side-chain and backbone dihedral angles, which are attempted with 30% and 70% probability, respectively. The moves for the side-chain angles are drawn from an equidistributed interval with a maximal change of 5 degrees. Half of the backbone moves are generated in the same fashion; the remainder is generated from a move library that was designed to reflect the natural amino acid dependent bias toward the formation of α -helices or β -sheets. The probability distribution of the move library was fitted to experimental probabilities observed in the PDB database.³² While driving the simulation toward the formation of secondary structure, the move library introduces no bias toward helical or sheet structures beyond that encountered in nature.

2.2. Optimization Methods. The low-energy part of the free energy landscape of proteins is extremely rugged due to the comparatively close packing of the atoms in the collapsed ensemble. Rugged potential energy surfaces are characterized by the existence of many low-lying minima, which are separated by high-energy barriers. For this reason, the global optimum of such a surface is difficult to obtain computationally. Simple methods, such as steepest descent or simulated annealing, are almost always trapped in metastable conformations.

Efficient optimization methods must therefore speed up the simulation by avoiding high-energy transition states, by adapting large scale moves wherever possible, or by accepting unphysical intermediates. One of the simplest ideas to effectively eliminate high-energy transition states of the free-

energy surface is the basis of the basin hopping technique,^{33,34} also known as Monte Carlo with minimization. This method simplifies the original potential energy surface by replacing the energy of each conformation with the energy of a nearby local minimum. This replacement eliminates the high-energy barriers that are responsible for the freezing problem in simulated annealing. In many cases the additional minimization effort to find a local minimum for each starting configuration is more than compensated by the increase of efficiency of the stochastic search on the simplified potential energy surface. The basin hopping technique and derivatives²⁷ have been used previously to study the potential energy surface of model proteins³⁵ and all atom protein models.^{22,36–38}

In contrast to previous work, we use a simulated annealing process³⁹ for the minimization step. The temperature is decreased geometrically from its starting to the final value of $T_f = 2\text{K}$. Following an optimized protocol³⁸ the starting temperature T_s is drawn randomly from a distribution $p(T_s) \sim \exp(T_s/T_0)$. The performance of the method is only weakly dependent on the choice of T_0 , which was chosen as 750 K for all simulations reported here.

While each simulated annealing run is typically much more expensive than a local minimization using gradient based techniques, it can nevertheless be competitive for very rugged potential energy surfaces, or when the computation of the gradient of the potential is prohibitive. The number of moves in each individual basin hopping cycle, is increased with the square root of the cycle number m as $N = 10\,000 \times \sqrt{m}$.

At the end of one annealing step the new conformation was accepted if its energy difference to the current configuration was no higher than a given threshold energy ϵ_T , an approach proven optimal for certain optimization problems.⁴⁰ Throughout this study we use a threshold acceptance criterion of 1 kcal/mol.

2.3. Molecular Dynamics. Starting from the same unfolded conformation as above, we performed all-atom implicit water molecular dynamics simulation using the AMBER8 simulation package⁴¹ with the AMBER99 force-field⁴² using the Born/SASA solvation model.^{43–45,8} The simulation was performed at the linux cluster of the KIST supercomputational materials lab with up to 16 processors in parallel. The system was first minimized by steepest descent. We generated five trajectories with 50 ns total simulation time each, three at 300 K and two at 325 K. After minimization the simulations are heated independently to their final temperature. Simulations were performed using Langevin temperature coupling and electrostatic interactions without cutoff.

3. Results

3.1. Free-Energy Folding Simulations. Structures for the peptides 1WQC, 1WQD, and 1WQE with 26, 27, and 23 amino acids, respectively, were retrieved from the PDB database⁴⁶ and unfolded by setting all backbone dihedral angles to random values until nonclashing conformations were obtained. The starting conformations had backbone root-mean-square deviations (RMSB) of 11.8 Å, 7.8 Å, and 9.7 Å to the native conformations of 1WQC, 1WQD, and



Figure 1. Overlay of the experimental (in red, first model) and the folded conformations (in blue) of 1WQC, 1WQD, and 1WQE, respectively.

Table 1. Length, Sequence, and Disulfide-Bridge Topology (Numbers of the Amino Acids) for the Peptides 1WQC, 1WQD, and 1WQE

name	#AA	sequence	DS1	DS2
1WQC	26	DPCYEVLQQHGNVKECEEACKHPVE	3/21	7/17
1WQD	27	DPCYEVLQQHGNVKECEEACKHPVEY	3/21	7/17
1WQE	23	NDPCEEVCIQHTGDVKACEEACQ	4/22	8/18

1WQE, respectively—they had no secondary structure. Table 1 shows the sequences of the peptides, which have a very high degree of homology. We note that all three peptides are stabilized by two disulfide bridges, as indicated in the table.

For each of the peptide we performed 20 independent basin hopping simulations with 200 cycles each using the protocol described above. In order to avoid any bias toward the native conformation, there was no potential representing the disulfide bridges in these simulations. Figure 2 shows the convergence of the energy and the RMSB deviation for 1WQC vs the number of function evaluations as a representative example.

Tables 2–4 summarize the energies, RMSB deviations, and secondary structure for the final population of these simulations. There are 30 NMR models for each of the peptides, which differ in the unstructured tail-fragments after amino acid 20 of the sequence. The table therefore reports the RMSB deviation to the closest model and the RMSB deviation to the structurally conserved part of each peptide.

All three proteins were folded predictively to very good resolution. Predictive folding is achieved, when near-native

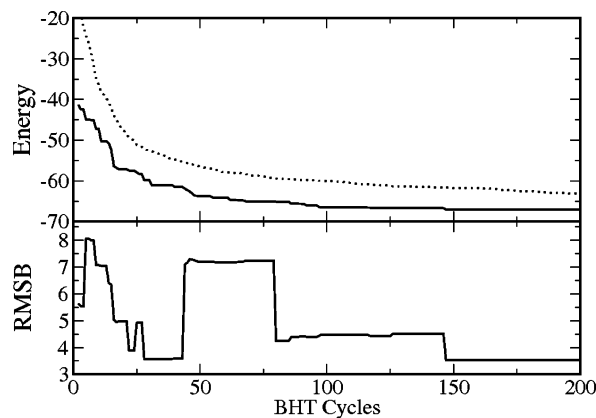


Figure 2. Convergence of best and mean energy (top panel, in kcal/mol) and RMSB (bottom panel, in Å) as a function of the number of basin hopping cycles for the simulations of 1WQC. Note that early in the simulation, one of the non-native conformations was lowest in energy, before it was overtaken by a near-native conformation. For simplicity the RMSB deviation was measured against the first, not the best NMR model.

Table 2. Final Population of Decoys of the Basin Hopping Simulations for 1WQC^a

RMSB	RMSB _{1–20}	energy	secondary structure
2.90	1.64	−67.10	CHHHHHHHHHHTCHHHHHHHHHHHHC
3.21	1.67	−66.80	CHHHHHHHHHHTCHHHHHHHHTTTTC
2.60	1.95	−65.40	CHHHHHHHHHHTCHHHHHHHHSCCC
6.31	4.07	−65.40	CHHHHHHHHHHTSCSHHHHHHHHSCCC
3.85	2.01	−65.00	CHHHHHHHHHHTSCHHHHHHHHTSSCC
2.55	1.92	−64.70	CHHHHHHHHHHTSHHHHHHHHSCCC
3.08	1.52	−64.40	CHHHHHHHHHHTCCHHHHHHHHHHHHC
3.98	2.32	−64.20	CHHHHHHHHHHTSCHHHHHHHHTTTTC
3.34	1.74	−63.90	CHHHHHHHHHHTSCHHHHHHHHHHHHC
4.83	2.15	−63.40	CHHHHHHHHHHTSCHHHHHHHHTSCCC
6.45	4.57	−62.80	CHHHHHHHHHHTCCHHHHHHHHHHHHC
6.38	4.45	−62.40	CHHHHHHHHHHTCCHHHHHHHHHHHHC
6.34	4.41	−62.40	CHHHHHHHHHHTCCHHHHHHHHHHHHC
6.30	4.42	−62.30	CHHHHHHHHHHTCCHHHHHHHHHHHHC
2.45	1.67	−62.10	CHHHHHHHHHHTCCHHHHHHHHSCCC
3.74	2.81	−61.70	CHHHHHHHHHHTCCCCHHHHHSCCC
3.26	1.75	−60.80	CHHHHHHHHHHSSHHHHHHHHCSSCC
5.01	2.85	−59.70	CHHHHHHHHHCHHHHHHHHHHTSSCC
3.14	1.92	−59.60	CHHHHHHHHSSHCHHHHHHHHHHHHC
6.19	4.82	−58.30	CHHHHHHSCCTTCHHHHHHHHSCCC

^a We computed the minimal RMSB deviation (in Å) to the 30 experimental models of the full protein and of amino acids 1–20, respectively. The secondary structure was computed with DSSP:⁶⁷ H, T, S, and C designate helix, turn, strand, and coil conformations, respectively.

structures dominate the low-energy spectrum of the simulated ensemble. In a free-energy forcefield the native conformation is selected on the basis of its estimate of internal free-energy in comparison to other conformations with well-defined secondary and tertiary structure. This is in contrast to MD or REM investigations, where occupation probability determines the thermodynamically stable conformation. Thus finding a particular conformation repeatedly with the lowest energy, as was observed for ALL proteins studied here, predicts the native conformation. Not in all simulations that reach the native conformation all stabilizing tertiary interac-

Table 3. Final Population of Decoys of the Basin Hopping Simulations for 1WQD^a

RMSB	RMSB ₁₋₂₀	energy	secondary structure
3.23	1.86	-69.30	CHHHHHHHHHHHSCHHHHHHTCHHHHC
2.82	1.91	-68.70	CHHHHHHHHHHSSHHHHHTCHHHHC
3.87	1.93	-68.70	CHHHHHHHHHHTCHHHHHHHHHHHHC
2.92	2.08	-68.50	CHHHHHHHHHHSSHHHHHTCHHHHC
4.89	1.72	-68.40	CHHHHHHHHHHTSHHHHHHHHCTTTC
3.43	3.32	-68.40	CCSHHHHHHHHTSCHHHHHHTTCCC
3.93	1.93	-68.00	CHHHHHHHHHHTCHHHHHHHHHHHHC
3.27	1.99	-67.70	CHHHHHHHHTSCHHHHHHTHHHHHC
3.30	2.51	-66.10	CHHHHHHHHHHCHHHHHHTHHHHHC
4.26	4.05	-66.10	CHHHHHHHHTTTTCHHHHHHHHHHHHC
3.63	3.67	-65.50	CHHHHHHHHHHCHHHHHHTTCCC
3.67	3.68	-65.50	CHHHHHHHHHHCHHHHHHTTCCC
2.96	2.79	-65.50	CCCHHHHHHHHTSCHHHHHHTTSCC
3.67	3.72	-64.70	CHHHHHHHHHHCHHHHHHTTCCC
4.05	1.77	-63.90	CHHHHHHHHTCSSHHHHHHHHHHHC
4.61	4.60	-63.50	CHHHHHHHHHHTCCHHHHHHHHHHHHC
3.27	2.09	-63.40	CHHHHHHHHTSCHHHHHHSSHHHHHC
3.67	3.70	-63.30	CHHHHHHHHTTCHHHHHHTTCCC
5.16	2.97	-62.60	CHHHHHHHHHSCHHHHHHCTTTC
3.56	2.29	-60.20	CHHHHHHHHTTCHHHHHHHHHHHHC
4.01	3.91	-60.20	CHHHHHHSCSSCHHHHHHTTCCC

^aWe computed the minimal RMSB deviation (in Å) to the 30 experimental models of the full protein and of amino acids 1–20, respectively. The secondary structure was computed with DSSP:⁶⁷ H, T, S, and C designate helix, turn, strand, and coil conformations, respectively.

Table 4. Final Population of Decoys of the Basin Hopping Simulations for 1WQE^a

RMSB	RMSB ₁₋₂₀	energy	secondary structure
1.90	1.84	-57.00	CHHHHHHHHHHTCHHHHHHHHC
1.64	1.63	-56.90	CHHHHHHHHHHTCHHHHHHHHC
1.66	1.66	-56.90	CHHHHHHHHHHTCHHHHHHHHC
1.70	1.67	-56.80	CHHHHHHHHHHTSHHHHHHHHC
1.70	1.69	-56.50	CHHHHHHHHHHTCCHHHHHHHHC
1.68	1.67	-56.50	CHHHHHHHHHHTCCHHHHHHHHC
2.13	2.10	-56.50	CHHHHHHHHHHTCCHHHHHHHHC
1.74	1.72	-56.50	CHHHHHHHHHHTCCHHHHHHHHC
1.73	1.70	-56.40	CHHHHHHHHHHTCCHHHHHHHHC
1.72	1.70	-56.40	CHHHHHHHHHHTCCHHHHHHHHC
1.68	1.67	-56.30	CHHHHHHHHHHTCCHHHHHHHHC
1.74	1.71	-56.30	CHHHHHHHHHHTCCHHHHHHHHC
1.69	1.66	-56.30	CHHHHHHHHHHTCCHHHHHHHHC
2.12	2.14	-56.20	CHHHHHHHHHHTCCHHHHHHHHC
1.69	1.66	-56.20	CHHHHHHHHHHTCCHHHHHHHHC
1.69	1.67	-56.10	CHHHHHHHHHHTCCHHHHHHHHC
1.71	1.68	-56.10	CHHHHHHHHHHTCCHHHHHHHHC
2.18	2.14	-55.00	CHHHHHHHHHHCSCHHHHHHHHC
2.04	2.02	-54.70	CHHHHHHHHHHCSCHHHHHHHHC
5.73	4.54	-54.40	CHHHHHHHHTCCSCHHHHHHHHC
4.71	3.84	-53.50	CHHHHHHHHTTSCCHHHHHHHHC

^aWe computed the minimal RMSB deviation (in Å) to the 30 experimental models of the full protein and of amino acids 1–20, respectively. The secondary structure was computed with DSSP:⁶⁷ H, T, S, and C designate helix, turn, strand, and coil conformations, respectively.

tions are fully formed. As a result there may be many more near-native conformations that are slightly higher in energy. We found the lowest 3, 9, and 18 of 20 simulations to converge to near-native conformations of 1WQC, 1WQD,

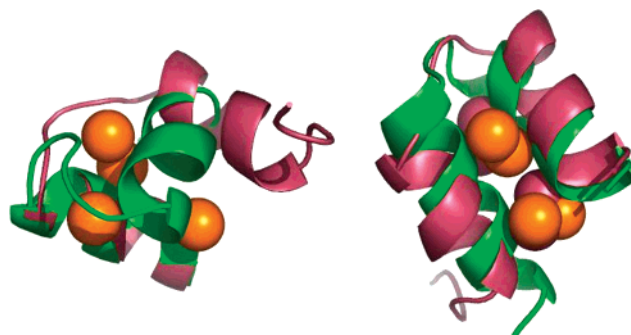


Figure 3. Left panel: Misfolded conformation (green) of 1WQC, corresponding to the fourth decoy in Table 2. Right: Folded conformation (green) of 1WQC in the presence of disulfide bridges in the simulation. The sulfur atoms are shown in orange, the experimental model in red.

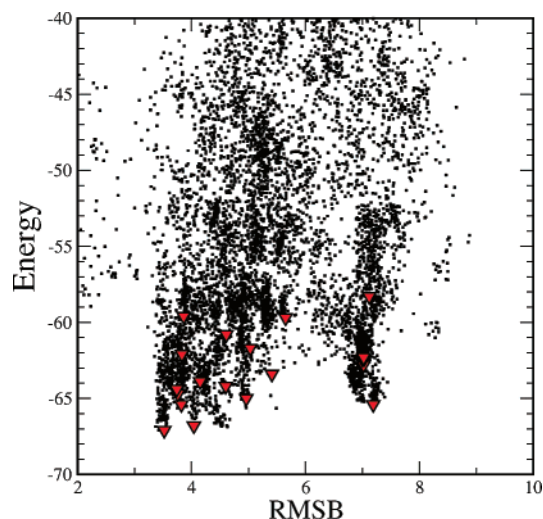


Figure 4. Plot of the energy vs the RMSB in all accepted conformations in the simulations for 1WQC, the triangles show the best conformations of the 20 simulations. There are only two structural clusters in the free-energy landscape with characteristic RMSB deviations of around 3 and 6 Å to the experimental model.

and 1WQE, respectively. The data demonstrate that the simulation method is very robust: 50% (1WQC), 40% (1WQD), and 90% (1WQE) of the simulations converge to conformations with RMSB deviations of less than 2 Å to the native conformation.

In Figure 1 we show the overlay of the lowest energy conformations with the respective experimental model. The figure demonstrates the high degree of similarity of the folded and experimental conformations. It is interesting to note that the addition of just one amino acid from 1WQC to 1WQD leads to a noticeable change in structure that is reproduced in the theoretical model.

3.2. Analysis of the Free-Energy Landscape. Next we turn to the surface of the internal free-energy (excluding backbone entropy) of 1WQC as a representative example of the three peptides. Figure 4 shows energy versus RMSB for all accepted configurations at the end of basin hopping cycles (from all simulations). The triangles indicate the terminal configurations of the individual simulations. We clearly see two broad funnels of conformations, which terminate into

low-energy structures with 3.4 Å and about 7.0 Å RMSB deviation to the native conformation, respectively. The configuration corresponding to the non-native funnel is shown in the left panel of Figure 3. This conformation is inconsistent with the formation of the correct number of native disulfide bridges of this peptide. There is only one, very broad folding funnel consistent with the native disulfide bridge topology. For this reason, the proteins studied here may be ideal examples to follow the kinetics of protein folding with molecular dynamics or replica exchange methods.^{47–49}

3.3. Simulations with Disulfide Bridges. Inspection of the final conformation of the simulations reported above suggests correct pairing for the native disulfide bridges, even if the distances between the sulfur atoms are too large in the absence of any constraining potential. We have therefore added a constraining potential, which varied with the square root of the distance between the sulfur atoms in the correct disulfide bridge topology

$$V_{ss} = V_0 \sum \sqrt{(d_i - d_0)}$$

where d_i is the distance between the sulfur atoms in the i th disulfide bridge, and $V_0 = 5$ kcal/mol, $d_0 = 2$ Å was the target distance for all disulfide bridges (typical experimental values are 2.05 Å). The functional form of the potential was chosen to obtain an appreciable force even for small bond mismatches. In the main simulation the disulfide bridge potential was only applied to the correct disulfide bridge pairing. In exploratory simulations we had applied the potential also to other pairings, but for the protein under investigation here these pairings were incommensurate with the helical starting structures formed in the unbiased simulations discussed in the previous section. Application of the incorrect pairings thus either led to conformations in which the sulfur atoms did not approach one another closely or where the helices were destroyed. In both cases the free energy increased significantly compared to the converged structures described below.

Starting from the final population of 1WQC of the preceding section, we performed 50 additional basin hopping cycles using the annealing cycle described in the methods section. The results of the simulations are summarized in Table 5. Find more near-native conformations and the energetic gap between the native and non-native conformations more than doubles from 1.7 kcal/mol to 3.9 kcal/mol. Because most of the structural differences between the native and the non-native structures arise in the unstructured tail, which is not directly affected by the formation of disulfide bridges, the overall RMSB deviation did not improve much.

This example demonstrates that unconstrained simulations can be used to predict the native topology of disulfide bridge formation, which can be later refined in constrained simulations to form ideal disulfide contacts.

3.4. Molecular Dynamics Folding Simulations. The free energy surface of 1WQE, as illustrated in Figure 4, is much more simple than that encountered for other proteins we have investigated so far.^{10,14} However the internal free-energy estimate does not contain backbone entropy; stabilization of

Table 5. Final Population of Decoys of the Basin Hopping Simulations for 1WQC with the Constraining Potential^a

RMSB	RMSB _{1–20}	energy	secondary structure
2.94	1.59	–56.50	CHHHHHHHHHHTCHHHHHHHHHHHHC
2.61	1.79	–56.20	CHHHHHHHHHHTSHHHHHHHHTSSCC
3.17	1.67	–54.80	CHHHHHHHHHHTSHHHHHHHHTTTTC
3.33	1.77	–53.50	CHHHHHHHHHHTSCHHHHHHHHTTTTC
3.12	1.47	–53.40	CHHHHHHHHHHTCCHHHHHHHHHHHHC
3.42	1.69	–53.10	CHHHHHHHHHHTSCHHHHHHHHHHHHC
2.83	1.35	–52.80	CHHHHHHHHHHTCCHHHHHHHHHHHHC
4.61	1.86	–52.60	CHHHHHHHHHHTSCHHHHHHHHTSSCC
2.76	1.88	–51.20	CHHHHHHHHHHTCCHHHHHHHHHHSCCC
2.33	1.48	–50.60	CHHHHHHHHHHTCCHHHHHHHHHHSCCC
3.33	1.79	–46.70	CCCHHHHHHHHTSCHHHHHHHHTTTTC
3.45	2.27	–46.50	CHHHHHHHHHHTSTTCHHHHHHSCCC
3.31	1.99	–46.50	CHHHHHHHHSSSCHHHHHHHHHHHHC
6.11	3.98	–45.30	CHHHHHHHHHHTSCSHHHHHHHHSCCC
5.80	4.16	–44.20	CCCHHHHHHHHTSCHHHHHHHHHHHHC
5.74	4.19	–44.00	CCCHHHHHHHHTSCHHHHHHHHHHHHC
5.96	4.27	–43.80	CCCHHHHHHHHTCCHHHHHHHHHHHHC
5.73	4.26	–43.20	CCCHHHHHHHHTSCHHHHHHHHHHHHC
4.99	2.67	–42.90	CHHHHHHHHHCHHHHHHHHHHTSSCC
4.24	3.71	–36.30	CHHHHHHHHTCCTTCTHHHHHHHSCCC

^aWe computed the minimal RMSB deviation (in Å) to the 30 experimental models of the full protein and of amino acids 1–20, respectively. The secondary structure was computed with DSSP.⁶⁷ H, T, S, and C designate helix, turn, strand, and coil conformations, respectively.

one particular conformation with respect to all others does not mean that this conformation is stable with respect to the unfolded ensemble. To settle this question kinetic or thermodynamic simulations must be performed. We have therefore performed all-atom implicit water molecular dynamics simulations for this protein as described in the methods section. The results for the deviation of the actual conformation from the native structure and the two helices are shown in Figure 5. The simulations equilibrate quickly into a rapidly fluctuating ensemble with an average overall rmsd deviation between 5 and 8 Å. When we analyze the rmsd deviation of the helical segments however (Helix 1: 1–11, Helix 2: 15–21), we find that the entire simulation is dominated with conformations that are within 1–2 Å of the respective fragment of the protein. We have also analyzed the helix propensity as a function of time for each amino acid as a function of time, as measured by DSSP. Figure 6 demonstrates a very strong helical content for both segments, but the propensity of helix formation may be forcefield dependent (see below). The figure illustrates very nicely that numerous folding and unfolding events occur for each helix. Both helices disappear completely for short time windows during the simulation, only to form again on a 10 ps time scale.

Next we analyze the sulfur–sulfur distance between CYS8–CYS18 and CYS4–22 as a function of time (lower panels in Figure 5). These distances also fluctuate strongly, averaging more than 10 Å during the simulations. On occasion, however, some of the sulfur atoms approach each other to within 3–4 Å, i.e., close enough for a disulfide bridge to form. On isolated instances, which occur in three of the five simulations (in one simulation two times independently), folding events occur in which both pairs of

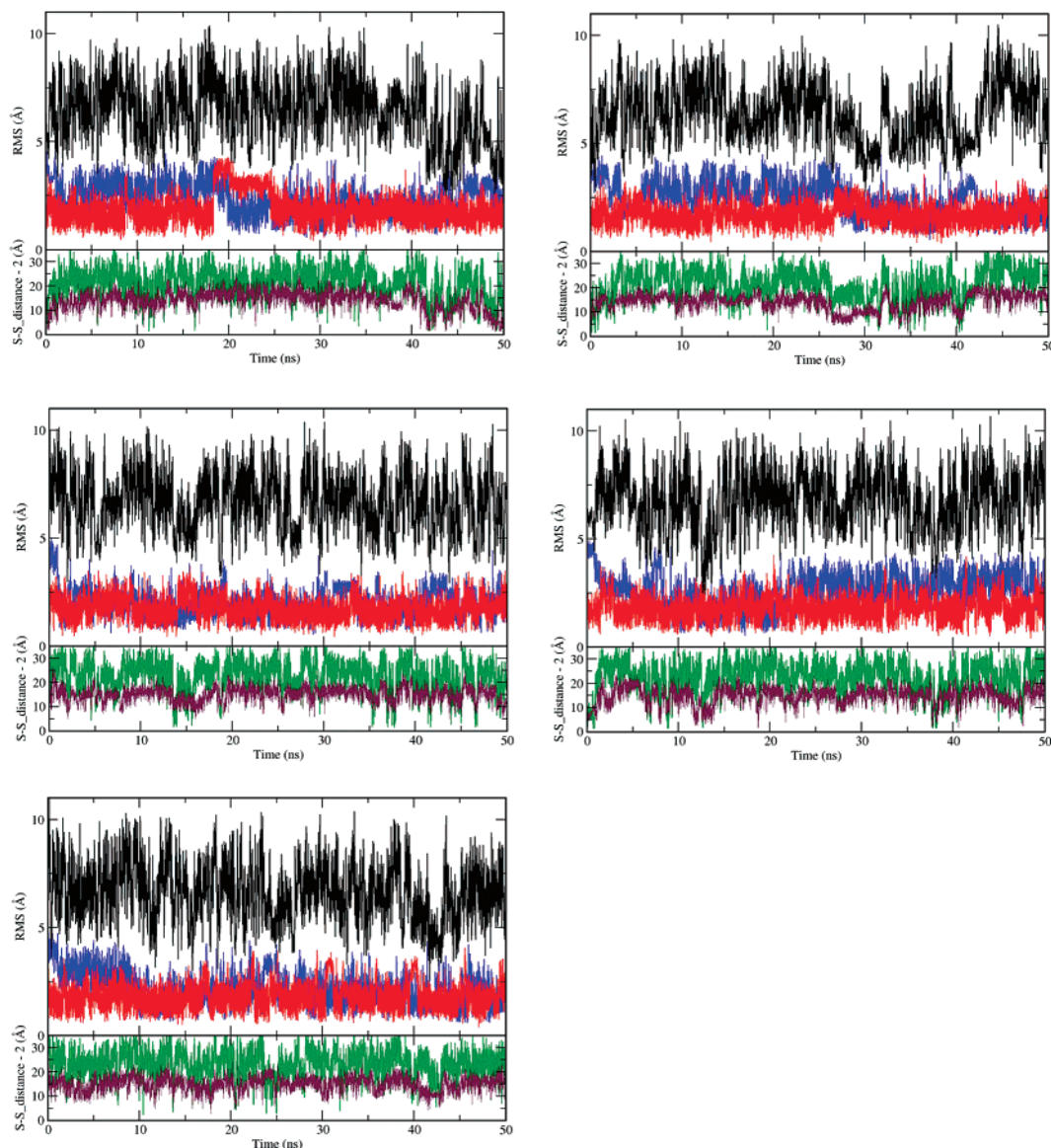


Figure 5. Analysis of the molecular dynamics trajectories as a function of simulation time. The top panel of each graph shows the rmsd of the actual conformation to the native conformation (black) and for the helical fragments only (red: helix 1–11, blue: helix 15–21). The lower panel always shows the deviation of the sulfur–sulfur distance for a potential disulfide bridge (at 2 Å distance) for the amino acids forming the first (green, CYS8–CYS18) and the second disulfide bridge (brown, CYS4–CYS22).

sulfur atoms approach one another (see Figure 7), while both helices are preformed. In those occurrences (which last several ps), the simulations attain all-atom RMSDs to native of 3.43 Å, 3.80 Å, and 3.47 Å, respectively. The intrahelix rmsd vary between 2.1 and 2.5 Å for helix 1 and between 0.8 and 1.0 Å for helix 2 in this time frame.

4. Discussion

From this analysis emerges a picture of the folding process for 1WQE: the low-energy part of the folding funnel is characterized by fluctuating conformation in which both helices are preformed. Both helices fold and unfold repeatedly during the simulation. As the protein explores this landscape it occasionally visits conformations that can lead to the formation of the correct disulfide bridges that would stabilize the native conformation. We note that neither the MD simulations nor the free-folding simulations in PFF01 produced conformations that are consistent with a non-native

disulfide bridge pairing. These events can occur in sequence on a time scale below 1 ns but happen even concurrently on a time scale of the order of 100 ns.

These observations agree with the predictions of the free-energy folding investigation reported above. The free-energy model also predicts the existence of an exclusively helical low-energy ensemble, which collapses into the native conformation at the bottom of the free-energy funnel. Because the free-energy model contains no backbone entropy, the native conformation is found with high probability in the free-energy approach, even though it is not stable (without disulfide bridges) under physiological conditions.

These results are best put into perspective in the context of the framework^{50–52} or diffusion-collision^{53,54} approach of protein folding, where secondary structure fragments of the protein assemble first, which then assume their final tertiary structure by docking into one another. The folding process may thus conceptually be divided into two steps: the

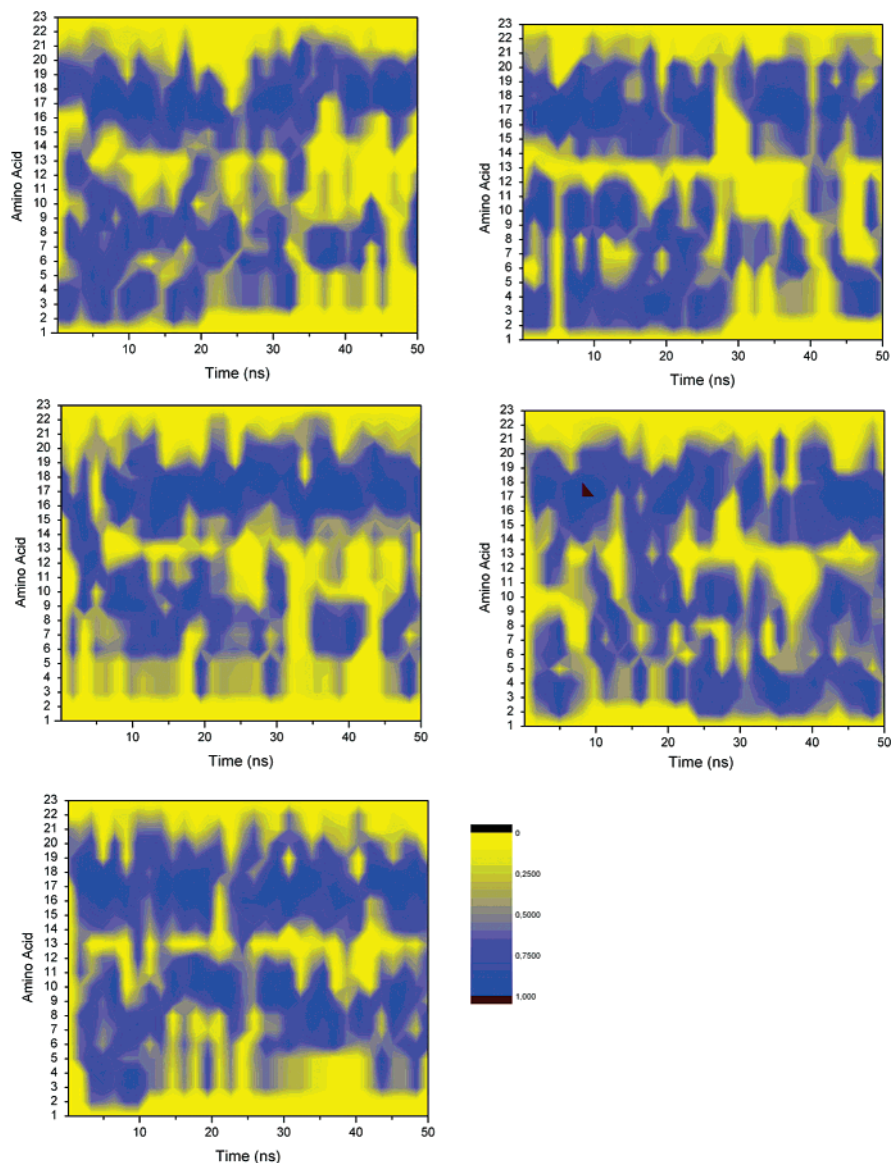


Figure 6. Time average over a 100-ps moving window of the helix propensity of each amino acid in the molecular dynamics simulations. In the native conformation the first helix spans amino acids 1–11, and the second helix spans amino acids 14–21, respectively. The scale for helix probability is the same in all panels.

assembly of the secondary structure precursors and the final collapse into the tertiary structure. For the proteins described here the latter requires the formation of disulfide bridges for enthalpic stabilization. We note that both simulations suggest the existence of preformed helical sections; for the specific systems in question the failure to connect the disulfide bridges in any other than the native topology from the low-energy conformations further supports the idea that the helices must be largely formed for the assembly of tertiary structure. However, in accordance with the funnel paradigm of protein folding,^{3,4} there is no single unique intermediate conformation that must be passed in the folding process to the native state. Instead our simulations suggest the existence of a wide ensemble of two-helix structures that precede the final collapse to the native conformation. In this final collapse there is a huge loss of configurational entropy that is apparently not compensated by the weak hydrophobic free-energy gain (increase in solvent entropy) afforded by this

small system. Therefore an enthalpic contribution from the disulfide bridges is required to stabilize the native conformations.

In this picture the folding time is determined by the rate of helix formation and the rate of disulfide bridge formation. Many present molecular dynamics forcefields, in particular those with implicit solvent models,⁸ may contain a bias toward on particular secondary structure. The combination of Amber99/GBSA that was used in the present study was reported to overemphasize helical secondary structure elements.^{55–58} This would influence the frequency with which the helical precursors for disulfide bridge formation are visited, and further studies are required for quantitative results.

5. Conclusions

In this study we have demonstrated the reproducible folding of three small two-helix proteins, which were recently

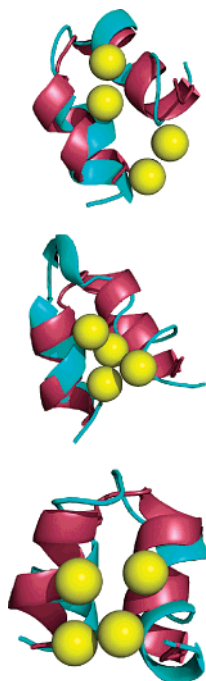


Figure 7. Figure: Overlay of conformations of three folding events from different trajectories of the molecular dynamics simulations (in blue) with the experimental conformation (red). Both helices perfectly formed in all simulations and agree well with the native conformation in their tertiary alignment. Both pairs of sulfur atoms approach each other concurrently for the formation of the disulfide bridges in the correct topology. The sulfur atoms of the MD simulations (not of the native conformation) are shown.

discovered to function as potassium channel blockers. Our simulations yielded final populations which reproducibly and predictively approach the native conformations to within 2 Å. Near native conformations are selected alone on the basis of their free-energy. The three peptides have a high degree of homology but nevertheless differ slightly in the tertiary and secondary structures.

We found that many independent simulations converge to the native conformations, which were predictively selected on the basis of the energy criterion of our force field PFF01. Our characterization of the low-energy part of their free energy surface suggests the existence of very broad and simple folding funnels.^{3,4} Folding of the protein thus proceeds by a diffusion-collision mechanism⁵³ where preformed helices approach one another occasionally to form the disulfide bridges which ultimately stabilize the native conformation.

This prediction was validated in five independent implicit solvent all-atom molecular dynamics simulations, which demonstrated that the individual helix segments preform in equilibrium under physiological conditions. On a time scale of 50 ns we observed several folding events to near native conformation, which validated the folding scenario discussed above.

Our results indicate that for these peptides secondary structure formation precedes hydrophobic collapse,^{59,60} in contrast to most standard folding scenarios. This raises the intriguing question whether it is possible to substitute the

cysteine residues to hydrophobic residues leading to hydrophobic collapse of the preformed helical ensemble into a well-defined tertiary structure that requires no stabilization by disulfide bridges. Such design exercises may help to guide the design of stable hydrophobic cores for such small proteins, which would have implications for important challenges in protein design, e.g., for zinc-finger design.^{61–65} In a recent folding study we could demonstrate that the ATF zinc finger (PDB code 1BHI) folds in the absence of the ion into a preformed ensemble with 3 Å of the native conformation, in a scenario similar to that encountered here.⁶⁶

Acknowledgment. We thank the Deutsche Forschungsgemeinschaft (grants WE 1863/10-2, WE 1863/14-1) and the Kurt Eberhard Bode Stiftung for financial support. Part of the simulations were performed at the KIST teraflop cluster.

References

- (1) Baker, D.; Sali, A. Protein structure prediction and structural genomics. *Science* **2001**, *294*, 93–96.
- (2) Schonbrunn, J.; Wedemeyer, W. J.; Baker, D. Protein structure prediction in 2002. *Curr. Opin. Struct. Biol.* **2002**, *12*, 348–352.
- (3) Dill, K. A.; Chan, H. S. From Levinthal to pathways to funnels: The “new view” of protein folding kinetics. *Nat. Struct. Biol.* **1997**, *4*, 10–19.
- (4) Onuchic, J. N.; Luthey-Schulten, Z.; Wolynes, P. G. Theory of protein folding: The energy landscape perspective. *Annu. Rev. Phys. Chem.* **1997**, *48*, 545–600.
- (5) Snow, C. D.; Nguyen, H.; Pande, V. S.; Gruebele, M. Absolute comparison of simulated and experimental protein folding dynamics. *Nature* **2002**, *420*, 102–106.
- (6) Simmerling, C.; Strockbine, B.; Roitberg, A. All-atom structure prediction and folding simulations of a stable protein. *J. Am. Chem. Soc.* **2002**, *124*, 11258–11259.
- (7) Snow, C. D.; Qiu, L.; Du, D.; Gai, F.; Hagen, S. J.; Pande, V. S. Trp zipper folding kinetics by molecular dynamics and temperature-jump spectroscopy. *Proc. Natl. Acad. Sci. U.S.A.* **2004**, *101*, 4077–4082.
- (8) Chen, J.; Im, W.; Brooks, C. L., III. Balancing solvation and intramolecular interactions: Toward a consistent generalized born force field. *J. Am. Chem. Soc.* **2006**, *128*, 3728–3736.
- (9) Schug, A.; Herges, T.; Wenzel, W. Reproducible protein folding with the stochastic tunnelling method. *Phys. Rev. Lett.* **2003**, *91*, 158102.
- (10) Herges, T.; Wenzel, W. Reproducible in-silico folding of a three-helix protein and characterization of its free energy landscape in a transferable all-atom forcefield. *Phys. Rev. Lett.* **2005**, *94*, 018101.
- (11) Herges, T.; Wenzel, W. An All-Atom Force Field for Tertiary Structure Prediction of Helical Proteins. *Biophys. J.* **2004**, *87*, 3100–3109.
- (12) Schug, A.; Wenzel, W. All-atom folding of the trp-cage protein in an all-atom forcefield. *Europhys. Lett.* **2004**, *67*, 307–313.
- (13) Schug, A.; Wenzel, W. Predictive in-silico all-atom folding of a four helix protein with a free-energy model. *J. Am. Chem. Soc.* **2004**, *126*, 16736–16737.

- (14) Herges, T.; Wenzel, W. Free energy landscape of the villin headpiece in an all-atom forcefield. *Structure (London)* **2005**, *13*, 661.
- (15) Dinner, A. R.; Sali, A.; Smith, L. J.; Dobson, C. M.; Karplus, M. Understanding protein folding via free energy surfaces from theory and experiment. *Trends Struct. Biol.* **2001**, *25*, 331.
- (16) Pande, V. S.; Rokhsar, D. S. Molecular dynamics simulations of unfolding and refolding of a beta-hairpin fragment of protein G. *Proc. Natl. Acad. Sci. U.S.A.* **1999**, *96*, 9062–9067.
- (17) Bonvin, A. M. J. J.; van Gunsteren, W. F. beta-hairpin stability and folding: Molecular dynamics studies of the first beta-hairpin of tendamistat. *J. Mol. Biol.* **2000**, *296*, 255–268.
- (18) Neidigh, J. W.; Fesinmeyer, R. M.; Anderson, N. H. Designing a 20-residue protein. *Nat. Struct. Biol.* **2002**, *9*, 425–430.
- (19) Qiu, L.; Pabit, S. A.; Roitberg, A. E.; Hagen, S. J. Smaller and faster: The 20-residue trp-cage protein folds in 4 microseconds. *J. Am. Chem. Soc.* **2002**, *124*, 12952.
- (20) Pitera, J.; Swope, W. Understanding folding and design: Replica-exchange simulations of “trp-cage” miniproteins. *Proc. Natl. Acad. Sci. U.S.A.* **2003**, *100*, 13280–13285.
- (21) Zhou, R. Trp-cage: Folding free energy landscape in explicit water. *Proc. Natl. Acad. Sci. U.S.A.* **2003**, *100*, 13280–13285.
- (22) Schug, A.; Verma, A.; Herges, T.; Lee, K. H.; Wenzel, W. Comparison of stochastic optimization methods for all-atom folding of the trp-cage protein. *ChemPhysChem* **2005**, *6*, 2640–2646.
- (23) Chagot, B.; Pimentel, C.; Da, L.; Pil, J.; Tytgat, J.; Nakajima, T.; Corzo, G.; Darbon, H.; Ferrat, G. An unusual fold for potassium channel blockers: Nmr structure of three toxins from the scorpion *opisthacanthus madagascariensis*. *Biochem. J.* **2005**, *388*, 263–271.
- (24) Dinner, A. R.; Lazaridis, T.; Karplus, M. Understanding beta-hairpin formation. *Proc. Natl. Acad. Sci. U.S.A.* **1999**, *96*, 9068–9073.
- (25) Themis, Lazaridis, Martin, Karplus. “new view” of protein folding reconciled with the old through multiple unfolding simulations. *Science* **1997**, *278*, 1928–1931.
- (26) Herges, T.; Merlitz, H.; Wenzel, W. Stochastic optimization methods for biomolecular structure prediction. *J. Assoc. Lab. Autom.* **2002**, *7*, 98–104.
- (27) Abagyan, R. A.; Totrov, M. Biased probability Monte Carlo conformation searches and electrostatic calculations for peptides and proteins. *J. Mol. Biol.* **1994**, *235*, 983–1002.
- (28) Herges, T.; Schug, A.; Wenzel, W. Exploration of the free energy surface of a three helix peptide with stochastic optimization methods. *Int. J. Quantum Chem.* **2004**, *99*, 854–893.
- (29) Avbelj, F.; Moult, J. Role of electrostatic screening in determining protein main chain conformational preferences. *Biochemistry* **1995**, *34*, 755–764.
- (30) Eisenberg, D.; McLachlan, A. D. Solvation energy in protein folding and binding. *Nature* **1986**, *319*, 199–203.
- (31) Sharp, K. A.; Nicholls, A.; Friedman, R.; Honig, B. Extracting hydrophobic free energies from experimental data: relationship to protein folding and theoretical models. *Biochemistry* **1991**, *30*, 9686–9697.
- (32) Pedersen, J. T.; Moult, J. Protein folding simulations with genetic algorithms and a detailed molecular description. *J. Mol. Biol.* **1997**, *269*, 240–259.
- (33) Nayeem, A.; Vila, J.; Scheraga, H. A. A comparative study of the simulated-annealing and monte carlo-with-minimization approaches to the minimum-energy structures of polypeptides: [met]-enkephalin. *J. Comput. Chem.* **1991**, *12*, 594–605.
- (34) Leitner, D. M.; Chakravarty, C.; Hinde, R. J.; Wales, D. J. Global optimization by basin-hopping and the lowest energy structures of Lennard-Jones clusters containing up to 110 atoms. *Phys. Rev. E* **1997**, *56*, 363.
- (35) Wales, D. J.; Dewbury, P. E. J. Effect of salt bridges on the energy landscape of a model protein. *J. Chem. Phys.* **2004**, *121*, 10284–10290.
- (36) Mortenson, P. N.; Wales, D. J. Energy landscapes, global optimization and dynamics of poly-alanine Ac(ala) 8 nhme. *J. Chem. Phys.* **2004**, *114*, 6443–6454.
- (37) Mortenson, P. N.; Evans, D. A.; Wales, D. J. Energy landscapes of model polyalanines. *J. Chem. Phys.* **2002**, *117*, 1363–1376.
- (38) Verma, A.; Schug, A.; Lee, K. H.; Wenzel, W. Basin hopping simulations for all-atom protein folding. *J. Chem. Phys.* **2006**, *124*, 044515.
- (39) Kirkpatrick, S.; Gelatt, C. D.; Vecchi, M. P. Optimization by simulated annealing. *Science* **1983**, *220*, 671–680.
- (40) Schneider, J.; Morgenstern, I.; Singer, J. M. Bouncing towards the optimum: Improving the results of monte carlo optimisation algorithms. *Phys. Rev. E* **1998**, *58*, 5085–5095.
- (41) Case, D. A.; Darden, T. A.; Cheatham, T. E., III; Simmerling, C. L.; Wang, J.; Duke, R. E.; Luo, R.; Merz, K. M.; Wang, B.; Pearlman, D. A.; Crowley, M.; Brozell, S.; Tsui, V.; Gohlke, H.; Mongan, J.; Hornak, V.; Cui, G.; Beroza, P.; Schafmeister, C.; Caldwell, J. W.; Ross, W. S.; Kollman, P. A. *Amber 8*; University of California, San Francisco, 2004.
- (42) Wang, J. M.; Cieplak, P.; Kollman, P. A. How well does a restrained electrostatic potential (resp) model perform in calculating conformational energies of organic and biological molecules? *J. Comput. Chem.* **2000**, *21*, 1049.
- (43) Born, M. Volumes and hydration warmth of ions. *Z. Phys.* **1920**, *1*, 45–48.
- (44) Hawkins, G. D.; Kramer, C. J.; Truhlar, D. B. Pairwise solute descreening of solute charges from a dielectric medium. *Chem. Phys. Lett.* **1995**, *246*, 122–129.
- (45) Hawkins, G. D.; Kramer, C. J.; Truhlar, D. B. Parametrized models of aqueous free energies of solvation based on pairwise solute descreening of solute charges from a dielectric medium. *J. Phys. Chem.* **1996**, *100*, 19824–19839.
- (46) Berman, H. M.; Westbrook, J.; Feng, Z.; Gillil, G.; Bhat, T. N.; Weissig, H.; Shindyalov, I. N.; Bourne, P. E. The protein data bank. *Nucl. Acids Res.* **2000**, *28*, 235–242.
- (47) Hukushima, K.; Nemoto, K. Exchange monte carlo method and application to spin glass simulations. *J. Phys. Soc. Jpn.* **1996**, *65*, 1604–1608.

- (48) Marinari, E.; Parisi, G. Simulated tempering: a new Monte Carlo scheme. *Eur. Phys. Lett.* **1992**, *19*, 451–458.
- (49) Garcia, A. E.; Onuchic, N. Folding a protein in a computer: An atomic description of the folding/unfolding of protein A. *Proc. Natl. Acad. Sci. U.S.A.* **2003**, *100*, 13898–13903.
- (50) Ptitsyn, O. B. Sequential mechanism of protein folding. *Dokl. Akad. Nauk SSSR* **1973**, *210*, 1213–1215.
- (51) Kim, P. S.; Baldwin, R. L. Intermediates in the folding reactions of small proteins. *Annu. Rev. Biochem.* **1990**, *59*, 631–660.
- (52) Dyson, H. J.; Wright, P. E. Peptide conformation and protein folding. *Curr. Opin. Struct. Biol.* **1993**, *3*, 60–65.
- (53) Karplus, M.; Weaver, D. L. Protein folding dynamics: The diffusion-collision model and experimental data. *Protein Sci.* **1994**, *3*, 650–668.
- (54) Islam, S. A.; Karplus, M.; Weaver, D. L. Application of the diffusion-collision model to the folding of three-helix bundle proteins. *J. Mol. Biol.* **2002**, *318*, 199–215.
- (55) Yoda, T.; Sugita, Y.; Okamoto, Y. Comparisons of force fields for proteins by generalized-ensemble simulations. *Chem. Phys. Lett.* **2004**, *386*, 460–467.
- (56) Wang, T.; Wade, R. Force field effects on a β -sheet protein domain structure in thermal unfolding simulations. *J. Chem. Theor. Comput.* **2005**, *2*, 140–148.
- (57) Lwin, T. Z.; Luo, R. Force field influences in beta-hairpin folding simulations. *Protein Sci.* **2006**, *15*, 2642–2655.
- (58) Hornak, V.; Abel, R.; Stockbrine, B.; Roitberg, A.; Simmerling, C. Comparison of multiple amber force fields and development of improved protein backbone parameters. *Proteins: Struct., Funct., Bioinformatics* **2006**, *65*, 712–725.
- (59) Šali, A.; Shakhnovich, E.; Karplus, M. How does a protein fold? *Nature* **1994**, *369*, 248–251.
- (60) Lazaridis, T.; Karplus, M. ‘‘new view’’ of protein folding reconciled with the old through multiple unfolding simulations. *Science* **1997**, *278*, 1928–1931.
- (61) Lee, M. S.; Gippert, G. P.; Soman, K. V.; Case, D. A.; Wright, P. E. Threedimensional solution structure of a single zinc finger dna-binding domain. *Science* **1989**, *245*, 635–637.
- (62) Kochoyan, M.; Keutmann, H. T.; Weiss, M. A. Architectural rules of the zinc-finger motif: Comparative two-dimensional nmr studies of native and ‘‘aromatic-swap’’ domains define a ‘‘weakly polar switch’’. *Proc. Natl. Acad. Sci. U.S.A.* **1991**, *88*, 8455–8459.
- (63) Choo, Y.; Isalan, M. Advances in zinc finger engineering. *Curr. Opin. Struct. Biol.* **2000**, *10*, 411–416.
- (64) Laity, J. H.; Lee, B. M.; Wright, P. E. Zinc finger proteins: new insights into structural and functional diversity. *Curr. Opin. Struct. Biol.* **2001**, *11*, 39–49.
- (65) (65) Urnov, F. D.; Miller, J. C.; Lee, Y. L.; Beausejour, C. M.; Rock, J. M.; Augustus, S.; Jamieson, A. C.; Porteus, M. H.; Gregory, P. D.; Holmes, Michael C. Highly efficient endogenous human gene correction using designed zinc-finger nucleases. *Nature* **2005**, *435*, 646–651.
- (66) Gopal, S. M.; Wenzel, W. De-novo folding of the DNA-binding ATF-2 zinc finger motif in an all-atom free energy forcefield. *Angew. Chem., Int. Ed.* **2006**, *118*, 7890–7892.
- (67) Kabsch, W.; Sander, C. Dictionary of protein secondary structure: pattern recognition of hydrogen-bonded and geometrical features. *Biopolymers* **1983**, *22*, 2577–2637.

CT600274A

JCTC Journal of Chemical Theory and Computation

Rapid, Accurate, and Precise Calculation of Relative Binding Affinities for the SH2 Domain Using a Computational Grid

Philip W. Fowler,[‡] Sebastien Geroult,[§] Shantenu Jha,[‡] Gabriel Waksman,^{§,||} and Peter V. Coveney^{*,‡}

Centre for Computational Science, Department of Chemistry, University College London, 20 Gordon Street, London WC1H 0AJ, U.K., School of Crystallography, Birkbeck College, University of London, Malet Street, London WC1E 7HX, U.K., and Department of Biochemistry & Molecular Biology, University College London, Gower Street, London WC1E 6BT, U.K.

Received October 24, 2006

Abstract: We describe and apply a method that reduces the time taken to calculate binding free energies using thermodynamic integration. This method uses a stack of grid software, which we call STIMD, that allows the scientist to easily distribute the necessary simulations around a computational grid thereby accelerating the process. We use this method to study how a series of phosphopeptides binds to the Src SH2 domain. The binding of phosphopeptides to the Src SH2 domain is described by the “two-pronged plug two-holed socket” model, and we investigate this model by reducing the length of the aliphatic side chain that engages the second of the two sockets through two successive alchemical mutations. Seven different values of $\Delta\Delta G$ have been calculated, and we report good agreement with experiment. We then propose an extension to this model using the insights gained from a free energy component analysis.

1. Introduction

Measuring the free energy of binding, ΔG , is a vital step in studying the interaction between any two molecules. Although theoretically exact techniques exist for calculating values of ΔG (e.g., free energy perturbation and thermodynamic integration), they require large amounts of computer time, and the values they yield are not always accurate or precise. Many research groups are developing theoretical approaches which hopefully both use less computer time and are accurate, for example LIE,¹ Jarzynski's equality,^{2,3} MM-PBSA,^{4–6} λ -dynamics,⁷ ABF,⁸ and 4D-PMF.⁹ Existing techniques continue to be improved, for example through the use of replica exchange algorithms^{10–12} and Bennett's

acceptance ratio^{13,14} and through the development of new approaches for assessing when simulations have equilibrated.¹⁵ We shall not discuss the different theories here but direct the reader to one of the recent excellent reviews.^{16–18} Despite several comparative studies^{11,19,20} it is not clear which techniques are the most accurate or even if such a general conclusion can be made. Whichever technique is chosen, for each value of ΔG one must typically run and analyze a number of similar molecular dynamics or Monte Carlo simulations. This not only requires access to a commodity cluster and preferably a supercomputer but also takes a long time and is a difficult and tedious task. For theoretically based calculations to complement experiment and be useful, one must be able to run a calculation in a reasonable time.²¹ We use grid computing to accelerate a free energy calculation so that it takes less than a week, a period of time that we suggest is the upper limit for free energy calculations to be useful. The method (i.e., the underlying software and design) is general and may be adapted, if appropriate, to other free energy techniques.

* Corresponding author phone: +44 20 7679 4850; fax: +44 20 7679 1501; e-mail: p.v.coveney@ucl.ac.uk.

[‡] Department of Chemistry, University College London.

[§] Birkbeck College, University of London.

^{||} Department of Biochemistry & Molecular Biology, University College London.

In this paper we shall describe how we have reduced the time taken to run calculations using thermodynamic integration to less than a week by using high performance parallel and grid computing. This has allowed us to study in detail how phosphopeptides bind to the SH2 domain of the Src kinase, and we shall validate our results against published experimental data. Our method relies heavily on a collection of grid technologies, which we call STIMD (steered thermodynamic integration using molecular dynamics), that we have described in more detail elsewhere.²²

We have chosen to use thermodynamic integration since it is an established and accepted free energy technique, the enthalpy ($\Delta\Delta H$) and entropy ($T\Delta\Delta S$) change can be calculated, a free energy component analysis can be performed, and last it requires many (10–50) simulations to be run for each value of $\Delta\Delta G$ and is therefore well-suited to deployment on a computational grid. The speedup achieved is simply due to the simultaneous running of all the λ -simulations; this can be described as a second tier of parallelization since each of the simulations is itself running on multiple computer processors. This is not novel since it must be done, for example, when using a replica exchange algorithm,^{10–12} but we believe this is the first use of a computational grid to accurately and precisely calculate values of $\Delta\Delta G$.

There are two main benefits to the STIMD method: first it is easier for the scientist to run a calculation and second each calculation takes less time. Being able to quickly calculate a value of $\Delta\Delta G$ allows us either to repeat calculations to improve our confidence in the results or to study more than one mutation. Mistakes are less likely to be made during the calculation, and one can also investigate how changing the method affects the accuracy and precision of the calculations. These advantages will become apparent when we examine our results, but we shall first discuss why an understanding of the binding of phosphopeptides to the Src SH2 domain is both interesting and important.

2. Background

SH2 domains are small protein subunits. They bind to phosphorylated tyrosine residues and are key components of tyrosine kinase mediated signal cascades.²³ SH2 domains are considered by some to be the prototypical protein–protein interaction domain.²⁴ There are many different SH2 domains; for example more than 80 SH2 domains have been identified in the human genome.²⁵ Over the last 15 years there has been an intense academic and industrial effort aimed at developing small molecules that inhibit specific SH2 domains, including that of the Src kinase. The hope is that these drugs could be used to treat a diverse range of conditions, from cancer to osteoporosis to autoimmune diseases.^{23,26,27} We shall refer to phosphorylated tyrosine residues using both the single (pY) and multiple (pTyr) amino acid residue notations, and the pTyr residue and the three C-terminal residues of the phosphopeptide are conventionally labeled +0, +1, +2, and +3. We shall also adopt the standard SH2 structural nomenclature established by Waksman et al.²⁸ to identify specific residues (e.g., Tyr β D5) or elements of secondary structure (e.g., the β D β -sheet).

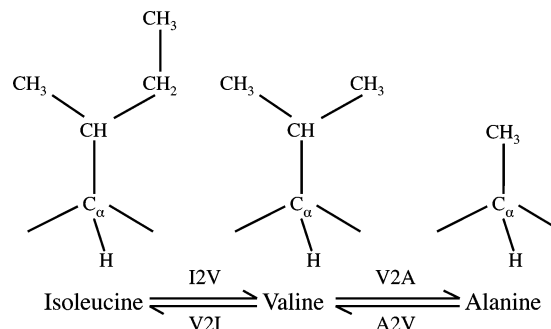


Figure 1. The simple hierarchy of aliphatic amino acid residues studied. The alchemical mutations are labeled using single-letter amino acid notation. For example the valine to alanine mutation is labeled V2A.

The X-ray crystallographic structure of the Src SH2 domain revealed that it is a compact protein domain composed of a central β -sheet surrounded by two α -helices.²⁹ The regions between the α -helices and the central β -sheet form two sockets; the first engages the pTyr residue, while the second binds the amino acid residue at the +3 position. A “two-pronged plug two-holed socket” model has been proposed to explain the binding of phosphopeptides to the Src SH2 domain.²⁸ The second of these sockets preferentially binds hydrophobic amino acid residues and is dubbed the “+3 binding pocket”. Other structural and biophysical studies have indicated that only the pTyr residue and the +1, +2, and +3 residues contribute significantly to the binding event.^{28,30,31} Subsequent isothermal titration calorimetry (ITC) experiments demonstrated that the pTyr residue accounts for about half of the binding free energy,³² and therefore SH2 domains bind a wide range of phosphopeptides.

In this paper we shall investigate how progressively shortening the length of the aliphatic side chain of the amino acid at the +3 position affects the binding of phosphopeptides to the Src SH2 domain. This will help us understand how phosphopeptides engage with the +3 binding pocket and therefore what form an artificial inhibitor might take. We shorten the side chain by mutating the phosphopeptide from PQpYEEIPI to PQpYEEVPI to PQpYEEAPI (see Figure 1). For each of the two mutations, isoleucine to valine (I2V) and valine to alanine (V2A), the differences in binding free energies, $\Delta\Delta G$, entropies, $T\Delta\Delta S$, and enthalpies, $\Delta\Delta H$, are calculated. Values are also calculated for the reverse mutations (A2V, V2I) to provide a further estimate of the error. These values are then compared to two sets of experimental values which have been measured previously using isothermal titration calorimetry.^{33,34}

The magnitude of the estimated error must be small if we are to both distinguish between the two mutations and detect any effect on the precision of our calculations when the method is altered. The magnitudes of the errors for the binding free enthalpies and entropies are at least an order of magnitude larger than the error for the binding free energy^{35,36} and hence requiring that the magnitude of the errors in the values of $\Delta\Delta H$ and $T\Delta\Delta S$ be reasonably small will ensure that the magnitude of the error in the value of $\Delta\Delta G$ is smaller still. These criteria ensure that, although the mutations are

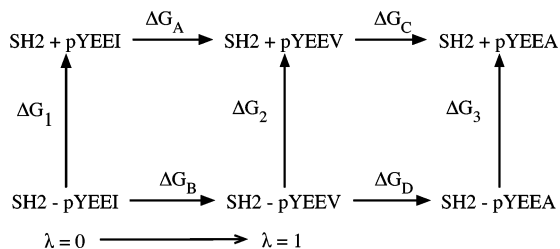


Figure 2. The combined thermodynamic cycle for the V2A and I2V mutations studied here. A ‘+’ indicates that the two species are bound, and a ‘-’ indicates that they are unbound. The progress parameter, λ , is shown for the cycle on the left.

themselves comparatively small, this is a challenging problem, and one that is a good test of our method.

SH2 domains have been studied using a range of different computational free energy approaches.^{22,37–42} Woo and Roux⁴² recently described an interesting approach to calculating ΔG using a combined potential of mean force and free energy perturbation approach. They applied it to the binding of a pYEEI phosphopeptide to the Lck SH2 domain and obtained reasonable agreement with experimental data, although the magnitude of the error is relatively large (2–3 kcal/mol). To minimize our error we shall limit ourselves to calculating how the binding free energy changes when a single amino acid is mutated (i.e., $\Delta\Delta G$); if this is successful, then we can consider calculating a value of ΔG for a phosphopeptide, either by using a conventional “double-decoupling” approach or by accelerating a newer free energy technique using our grid-based method.

3. Method

We shall first outline in section 3.1 the theory of thermodynamic integration and discuss the use of thermodynamic cycles. We shall describe in section 3.2 how we accelerate thermodynamic integration calculations. Finally, we shall explain in section 3.3 how the individual simulation models were constructed and what simulation protocols were used.

3.1. Thermodynamic Integration. We shall calculate the difference in the binding free energy, $\Delta\Delta G$, using the thermodynamic cycle drawn in Figure 2. The vertical paths denote the binding of the different phosphopeptides to the Src SH2 domain, while the horizontal paths denote the change in free energy when the amino acid residue at the +3 position is mutated from, for example, isoleucine to valine. We shall refer to these last free energies as *alchemical* since one molecule is transmuted, or mutated, into another. A parameter, λ , describes the progress between the physical states ($0 \leq \lambda \leq 1$): when $\lambda = 0$ the phosphopeptide is pYEEI and when $\lambda = 1$ it is pYEEV, but when $\lambda = 0.5$ it is in an intermediate state.

Since the free energy is a state function, we can write the difference in binding free energy, $\Delta\Delta G$, in terms of the alchemical free energies, $\Delta G'$, which converge more quickly. This leads to the following relationships

where ΔG_A and ΔG_C are the alchemical free energies when

$$\Delta\Delta G_{I2V} = \Delta G_A - \Delta G_B$$

$$\Delta\Delta G_{I2V} = \Delta G_C - \Delta G_D$$

the phosphopeptide is bound to the SH2 domain, and ΔG_B and ΔG_D are the alchemical free energies when the phosphopeptide is solvated (see Figure 2).

Thermodynamic integration⁴³ is “theoretically exact” in the classical approximation, although in practice approximations are introduced via the method, for example the use of a classical forcefield to describe the potential. The method also assumes that one can adequately sample phase space. The alchemical free energy, $\Delta G'$, is given by

$$\Delta G' = \int_0^1 \left\langle \frac{\partial U(\mathbf{p}, \mathbf{r}, \lambda)}{\partial \lambda} \right\rangle_\lambda d\lambda \quad (1)$$

where \mathbf{p} and \mathbf{r} are the canonical momenta and positions of all the atoms, λ is the progress parameter as defined above, $U(\mathbf{p}, \mathbf{r}, \lambda)$ is the potential energy of the microstate, and the angled brackets indicate that an ensemble average is to be taken at the specified value of λ . We chose to generate the Boltzmann-factor weighted ensemble of structures using molecular dynamics (MD) since a Monte Carlo approach would be less efficient in this case due to the flexibility of the unbound phosphopeptide. The alchemical entropy, $T\Delta S'$, is calculated via

$$T\Delta S' = \frac{1}{k_B T} \int \left(\left\langle \frac{\partial U}{\partial \lambda} \right\rangle_\lambda \langle U \rangle_\lambda - \left\langle \frac{\partial U}{\partial \lambda} U \right\rangle_\lambda \right) d\lambda \quad (2)$$

where T is the absolute temperature, and k_B is Boltzmann’s constant.^{35,44} The presence of the potential energy terms, U , in eq 2 leads to the estimated error for $T\Delta S'$ being 1–2 orders of magnitude larger^{35,36} than that for $\Delta G'$. The alchemical enthalpy, $\Delta H'$, is then inferred via $\Delta G = \Delta H - T\Delta S$.

If the potential energy function, U , in eq 1 is pairwise additive, then we can rewrite U as a sum, $U_1 + U_2, \dots$, where we have divided the atoms into groups. This allows us to rewrite eq 1 as a sum of integrals

$$\Delta G' = \int_0^1 \left\langle \frac{\partial U_1(\mathbf{p}, \mathbf{r}, \lambda)}{\partial \lambda} \right\rangle_\lambda d\lambda + \int_0^1 \left\langle \frac{\partial U_2(\mathbf{p}, \mathbf{r}, \lambda)}{\partial \lambda} \right\rangle_\lambda d\lambda + \dots$$

and therefore we can also write the free energy as a sum, $\Delta G = \Delta G_1 + \Delta G_2, \dots$. These components are not state functions, and hence their values are dependent upon the path taken.⁴⁵ This approach is known as free energy component analysis and is a useful method for estimating which groups of atoms contribute significantly to a binding event.^{46,47} The results, however, must be carefully interpreted due to their path dependence.⁴⁸

3.2. The STIMD Method. To calculate an alchemical free energy using eq 1 one must measure the ensemble average of $(\partial U/\partial \lambda)$ at several different values of λ and then numerically integrate the function to yield $\Delta G'$. We shall refer to this set of simulations used to compute the ensemble averages as “ λ -simulations”. It is customary to run these λ -simulations sequentially, i.e., the last conformation of the n th λ simulation is used as the initial conformation of the $(n+1)$ th λ simulation. We speed up the calculation by simply running all of the λ simulations simultaneously. It is usually difficult to apply this approach to the study of protein mutations using MD for two reasons. First, the number of computer proces-

sors required to efficiently and quickly run an entire calculation is very large even for a small protein like the SH2 domain. Second, it is usually assumed that the accuracy of the calculation is improved by allowing the simulation unit cell to equilibrate at each value of λ before starting the next λ simulation. The first problem is addressed by our use of high performance and grid computing; we shall test the second assumption later. We also discuss and define grid computing⁴⁹ in detail elsewhere.^{50,51}

The key step in our method was the interfacing of our chosen classical molecular dynamics package, NAMD2.5,^{52,53} with the RealityGrid steering library.⁵⁴ This piece of grid middleware was developed as part of the U.K. e-Science pilot project RealityGrid and is freely available for download via that project's Web site.⁵⁵ Once interfaced with the steering library, an application can be remotely monitored and restarted, checkpoints can be taken, and variables can be steered.⁵⁴ The remote launching functionality is implemented using the Globus Toolkit 2⁵⁶ (GT2). This grid infrastructure is described in more detail by Fowler et al.²²

The scientist uses the launcher, a local application, to launch each λ simulation onto the computational grid. This grid may consist of several high performance computers or it may consist of only one depending on circumstance or demand. Another local application, the steerer, which also exists in personal digital assistant⁵⁷ and Web-based forms, is then used to remotely monitor and control one or more λ simulations. If the simulations are not being run simultaneously, then a checkpoint is taken at the appropriate time and used to seed the next λ simulation. If this new simulation is on a different computer, then the relevant simulation files are automatically copied to the new machine. In summary, the scientist only interacts with two local applications, and they do not need to log in to the remote machines that form the computational grid. Of course, the same simulations may still be launched in the conventional way, but it is our experience that it is easy to make mistakes while keeping track of tens of simulations running on several different computers. Several STIMD calculations have been performed which combined the U.S. TeraGrid⁵⁸ and the U.K. National Grid Service⁵⁹ to create a single large federated intercontinental computational grid. We used six of the supercomputers in this computational grid, and we note and welcome the recent trend toward providing interactive access to high performance computers as this is necessary for methods like ours.⁶⁰

One major disadvantage of this method is that one must install and maintain several different pieces of software, including GT2, on the local computer from where all the simulations are launched and controlled. At the time of writing we have adopted the Application Hosting Environment⁶¹ (AHE), a set of tools that has been developed in our group, which only requires a local installation of Java 1.4.2. This makes it much easier for new users to start launching jobs onto a computational grid. The AHE is freely available for download from the U.K. Open Middleware Institute.⁶² It does not, at present, allow a user to steer the variables of a remote simulation, but this is not necessary for running a thermodynamic integration on a computational grid. Unlike

Table 1. Sizes of the Bound and Unbound Src SH2 Protein Complexes Studied^a

mutation	system	waters	ions	atoms
Ile to Val	bound	6621	4 Cl ⁻	21 676
	unbound	2333	3 Na ⁺	7153
Val to Ala	bound	6621	4 Cl ⁻	21 673
	unbound	2286	3 Na ⁺	7009

^a The reverse mutations are identical in size to the forward mutations.

our original method the AHE automatically retrieves the simulation files from the remote computational resource and stores them in a local folder. One can launch and monitor simulations either through a graphical user interface or using command line tools. The former method is easier, but the latter is more appropriate when one is launching several jobs at once. Neither the RealityGrid steering library-based method or the AHE helps the scientist create the initial files required for a free energy simulation. This unfortunately remains a tedious and often error-prone task.

3.3. Details of the Molecular Dynamics Simulations. We shall now describe how the simulation cells were constructed and how individual molecular dynamics simulations were run. The free energy calculations were performed with NAMD2.5^{52,53} using the dual topology method to construct the alchemical atoms.⁶³ Only those atoms with different forcefield parameters were duplicated in the dual topology alchemical residues. This means that for the V2A alchemical residue the side chain is split at the C_α atom, whereas for the I2V alchemical residue it is split at the C_β atom. The Alchemify program was used to turn off the nonbonded interactions between vanishing and appearing atoms.⁶⁴

All the initial structures were derived from the X-ray crystallographic structure of the octapeptide PQpYEEIPI bound to the Src SH2 domain.²⁸ No crystallographic waters were included. We chose to use explicit water since both the alchemical residue in the unbound system and the phosphopeptide-protein interface are exposed to solvent. Each structure was neutralized with NaCl counterions and was placed in a box of TIP3P water⁶⁵ such that the minimum distance from the protein or peptide to the surface of the box was 12 Å. The CHARMM27 forcefield,⁶⁶ which includes parameters for the pTyr residue,⁶⁷ was used. The sizes of the unbound and bound systems are listed in Table 1.

The potential energy of the system was first minimized for 500 steps. The positions of the protein heavy atoms were then fixed, and the hydrogen atoms and water molecules were allowed to evolve for 200 ps at a temperature of 298 K. This is the same temperature as the isothermal titration calorimetry experiments.^{33,34} The positions of the backbone atoms of the protein and the phosphopeptide were then restrained by a small harmonic potential with a spring constant of 2 kcal mol⁻¹ Å⁻². Next the entire system was warmed from 108 to 298 K in steps of 10 K over 200 ps. The magnitude of the restraining spring constant was then reduced to 0.5 kcal mol⁻¹ Å⁻², and the system was evolved for 10 ps with the temperature held at 298 K by a Langevin thermostat. The restraints were then removed, and the system was evolved for a further 10 ps. Finally, a Berendsen barostat was applied to maintain the pressure at 1.01 kPa, and the simulation was

Table 2. The Seven Calculations Performed^a

mutation	name	Δt (fs)	α	direction
Val to Ala	V2Aa	1	0.17	forward
	V2Ab	2	0.17	forward
	V2Ac	2	0	forward
	V2Ad	2	1	forward
	A2V	2	0.17	reverse
Ile to Val	I2V	2	0.17	forward
	V2I	2	0.17	reverse

^a We shall refer to each calculation by the name given here (e.g., V2Aa). To allow an integration time step, Δt , of 2 fs the length of all bonds that include a hydrogen atom are constrained using the SHAKE⁶⁸ and SETTLE⁶⁹ algorithms. No constraints are required for $\Delta t = 1$ fs. α is defined to be the proportion of the n th λ simulation that has elapsed before the $(n+1)$ th λ simulation is started. For example $\alpha = 1$ corresponds to running the λ simulations sequentially and $\alpha = 0$ to launching all the λ simulations simultaneously.

equilibrated for at least 2 ns in the isothermal–isobaric (NPT) ensemble at the smallest value of λ .

SHAKE⁶⁸ and SETTLE⁶⁹ algorithms were applied to allow a 2 fs integration time step. The particle mesh Ewald approach⁷⁰ was used to compute the electrostatic forces, and the van der Waals forces were cut off at 12 Å with a switching distance of 10 Å. NAMD does not have a softcore or separation-shifted van der Waals potential,⁷¹ and therefore we used the conventional Lennard-Jones 6–12 van der Waals potential. This leads to the so-called “end-point catastrophe” as atoms vanish. To minimize this effect the 17 values of λ were nonuniformly spaced: $\lambda = 0.02, 0.1, 0.3, 0.5, 0.6, 0.7, 0.8, 0.84, 0.88, 0.91, 0.93, 0.94, \dots, 0.99$. We shall discuss the problems introduced by the use of a hardcore van der Waals potential later.

Each λ simulation was run for a duration of 2.5 ns making a total of 85 ns per calculation requiring 11.5k CPU hours to run. Due to the lack of continuity in the Lennard-Jones 6–12 form of the van der Waals potential it is not possible to run simulations at the endpoints, $\lambda = 0$ and $\lambda = 1$. These values of $(\partial U/\partial \lambda)$ were extrapolated by fitting functions to the electrostatic and van der Waals components as described elsewhere.^{46,47}

The next step was to estimate the correlation and equilibration times. Computing the statistical inefficiency¹⁵ provides a method of determining the correlation time, τ . The statistical inefficiency of both the $\Delta G'$ and λ data sets indicated that $\tau \sim 4\text{--}10$ ps (data not shown) and therefore the data sets were split into 250 bins of width $\tau = 10$ ps. A single value of $\Delta \Delta G$ or $T\Delta \Delta S$ was calculated from each bin, and errors were estimated using the batch averaging method.⁷² In an attempt to determine the equilibration time, we applied a recently suggested method of testing for normality temporally reversed $\Delta G'$ or λ data sets.¹⁵ This was not conclusive (data not shown), most likely because of the complexity of the mutations²² compared to the simpler models the technique was validated on.

4. Results

We performed seven different calculations; these are listed in Table 2. We shall first determine if the calculations are equilibrated and converged before comparing the results to experimental data. Then we shall evaluate the effect of

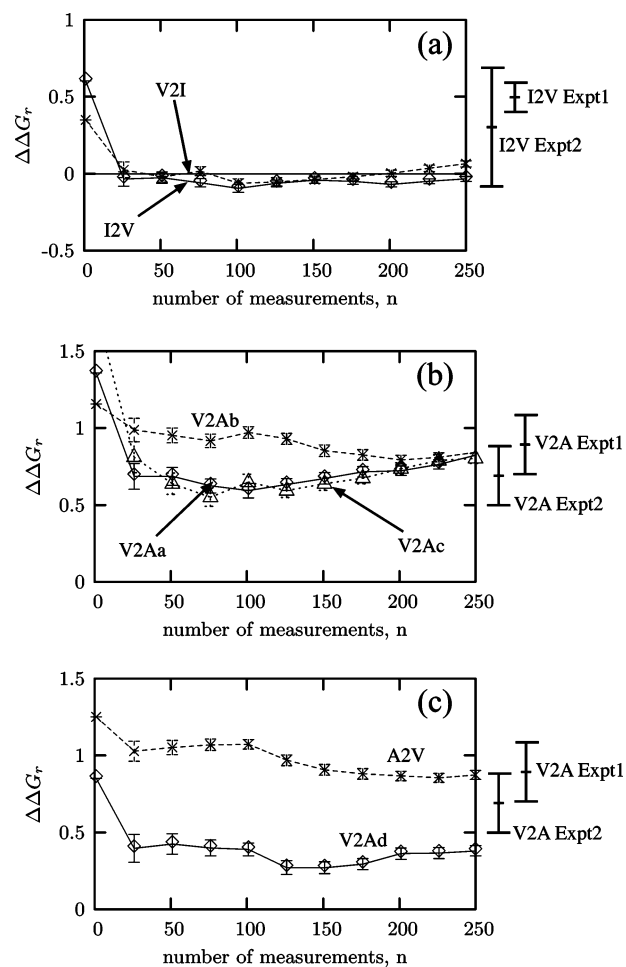


Figure 3. The differences in the binding free energies are not sensitive to the amount of data included in their calculation. This is shown by the reverse cumulative averages, $\Delta \Delta G_r$, of the isoleucine to valine (I2V) and valine to alanine (V2A) mutations. The results from the reversed mutations, e.g., valine to alanine (A2V), have been multiplied by (-1) to allow direct comparison with the forward mutations. The experimental values, including their error ranges, are also plotted. All energies are in kcal/mol.

altering the length of the integration time step and the value of α (see Table 2 for a definition). Last we shall investigate which parts of the system are important in the binding of the pYEEI phosphopeptide to the Src SH2 domain using a free energy component analysis.

The λ simulations will probably contain some unequilibrated data, which, if included in our calculations, will reduce the accuracy and precision of the calculated value of $\Delta \Delta G$. It is therefore important that we assess whether all the λ simulations are both equilibrated and converged. Here we adopt a suggestion made by Yang et al.¹⁵ and compute the reverse cumulative average of $\Delta \Delta G$. This is plotted in Figure 3. The values of $\Delta \Delta G$ are not very sensitive to the amount of data included in their calculation, and furthermore all values (with the exception of V2Ad) converge during the first 0.5 ns to within the error of the experimental values. This indicates that, for these mutations, either the unequilibrated regions have little effect on the calculated values of $\Delta \Delta G$ or the equilibration time is much longer than 2.5 ns,

Table 3. Calculated and Experimentally Measured Thermodynamic Variables for the V2A and I2V Mutations^a

calculation	$\Delta\Delta G$	$\Delta\Delta H$	$T\Delta\Delta S$
I2V Expt 1	0.5 ± 0.1	2.3 ± 0.4	1.8 ± 0.4
I2V Expt 2	0.3 ± 0.4	-1.1 ± 0.6	-1.4 ± 0.7
I2V	0.0 ± 0.1	1.5 ± 0.9	1.5 ± 0.9
V2I	0.1 ± 0.1	-0.7 ± 1.0	-0.7 ± 1.0
V2A Expt 1	0.9 ± 0.2	0.3 ± 0.4	-0.6 ± 0.4
V2A Expt 2	0.7 ± 0.2	0.9 ± 0.4	-0.2 ± 0.4
V2Aa	0.8 ± 0.1	-1.0 ± 1.3	-1.8 ± 1.3
V2Ab	0.8 ± 0.1	-1.2 ± 1.7	-2.0 ± 1.7
V2Ac	0.8 ± 0.1	0.3 ± 1.4	-0.5 ± 1.4
V2Ad	0.4 ± 0.1	0.2 ± 1.3	-0.2 ± 1.3
A2V	-0.9 ± 0.1	-2.0 ± 1.3	-1.1 ± 1.3

^a The experimental results are taken from two separate studies, which we shall label Expt1³³ and Expt2.³⁴ See Table 2 for an explanation of the different mutations. All values are quoted with a precision of 0.1 kcal/mol, and all energies are in kcal/mol.

and hence we are unable to resolve any time-dependent behavior. We shall assume the former is true and will include all the data in our calculations. Interestingly, the I2V calculations converge more rapidly which we would expect given they have fewer alchemical degrees of freedom. Likewise, examining the reverse cumulative averages of the alchemical free energies shows that $\Delta G'$ for the bound systems converges more slowly than $\Delta G'$ for the unbound system (data not shown). This reflects the relatively slow rearrangements of the phosphopeptide and the protein around the alchemical residue compared to the faster rearrangements of the water and the phosphopeptide.

Values of $\Delta\Delta G$, $\Delta\Delta H$, and $T\Delta\Delta S$ were calculated using the entire trajectories for each of the seven calculations; these are given in Table 3 and are plotted in Figure 4. For comparison two sets of results from isothermal titration calorimetry experiments^{33,34} are also given. The errors estimated for the calculated $\Delta\Delta G$ values (see the Method section) are smaller than the estimated experimental errors, and there is also good agreement between the forward and reverse mutations. All the calculated $\Delta\Delta G$ values agree with the experimental results, to within experimental error. As expected, the estimated errors for our calculated values of $T\Delta\Delta S$ and $\Delta\Delta H$ are more than an order of magnitude larger than those of $\Delta\Delta G$, and therefore while our calculated values of $T\Delta\Delta S$ and $\Delta\Delta H$ are accurate, they are not precise enough to be useful. We estimate that reducing the estimated error to under 0.5 kcal/mol would require all the λ simulations to be extended in duration by an order of magnitude. This demonstrates the importance of developing new techniques that improve sampling.

We shall now compare the different calculated values of $\Delta\Delta G$ for the V2A mutation to determine the effect of altering our method as described in Table 2. Since there is no measurable difference between the values of $\Delta\Delta G$ for the V2Aa and V2Ab mutations, we conclude that using SHAKE and SETTLE to restrain the lengths of the hydrogen to heavy atom bonds has no effect on the accuracy or precision of our calculations. This is useful as it allows us to speed up our calculations by using an integration time step of 2 fs. Our method fundamentally relies on there being no effect

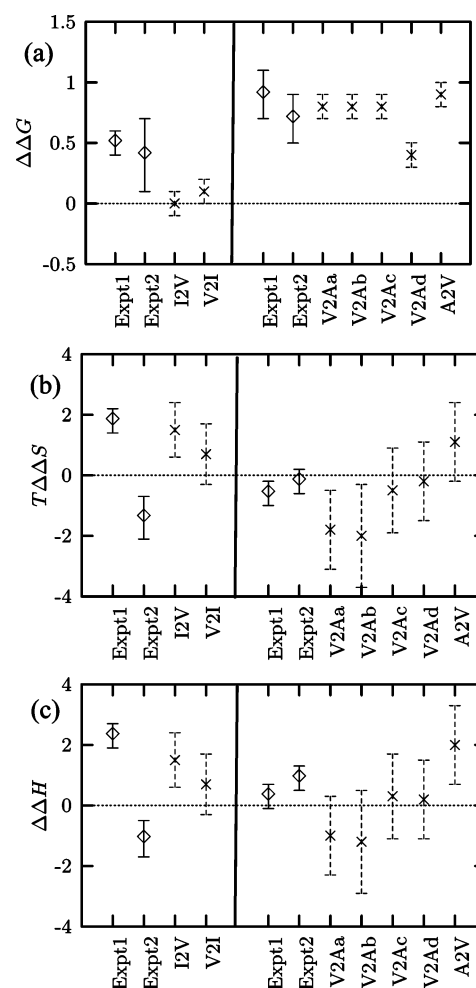


Figure 4. There is good agreement between our calculated values of $\Delta\Delta G$ and the experimental values (a). There is reasonable agreement between our calculated values of $T\Delta\Delta S$ (b) and $\Delta\Delta H$ (c) and the experimental values. The results from the reversed mutations, e.g., valine to alanine (A2V), have been multiplied by (-1) to allow direct comparison with the forward mutations. All energies are in kcal/mol.

on the accuracy of our calculations if we launch all the λ simulations simultaneously ($\alpha = 0$) or nearly simultaneously (e.g., $\alpha = 0.17$) compared to launching the λ simulations consecutively. To test this assumption we ran three free energy calculations (V2Ac,b,d) with values of $\alpha = 0, 0.17$, and 1.

The values of $\Delta\Delta G$ when $\alpha = 0$ and 0.17 (V2Ab,c) agree with experiment. This suggests that, for this mutation at least, there is no effect on the accuracy of the calculation if we launch all the λ simulations simultaneously. Our computed value of $\Delta\Delta G$ when $\alpha = 1$ (V2Ad) does not agree with the experimental values, although this is not conclusive given the magnitude of the error bars. Launching all the λ simulations consecutively may therefore affect the accuracy of the calculation. This could be due to error accumulating in the λ simulations and dominating any reduction in the equilibration time achieved by launching the λ simulations consecutively.

We examined the relative free energy profiles of all the mutations (see the Supporting Information) to investigate these effects in more detail. There are no large changes with

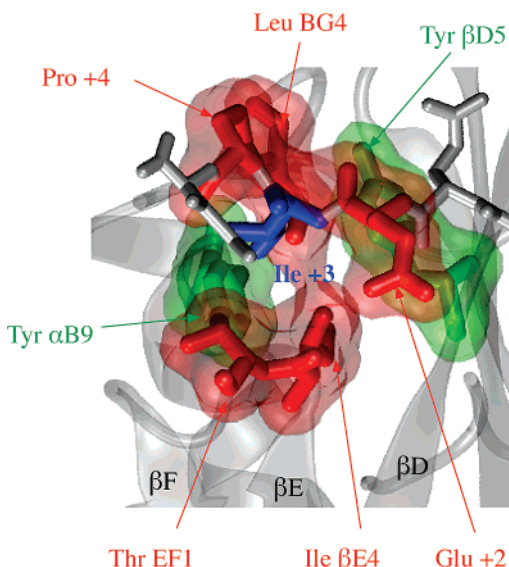


Figure 5. A schematic representation showing which amino acid residues of the Src SH2 domain favor (in green) or hinder (in red) the binding of isoleucine over alanine in the +3 binding pocket. Not indicated are the effects of the remainder of the protein, the solvent, and the alchemical residue itself which all favor the binding of isoleucine. The alchemical residue at the +3 position is drawn in dark blue, and the remainder of the phosphopeptide and the protein domain are drawn in gray.

λ in the relative free energy profiles for all of the V2A mutations. This indicates that, to a first approximation, all of the λ windows contribute a similar amount to the final value of $\Delta\Delta G$. In addition the shapes of all the profiles for the V2A mutations are similar with any differences being gradually accumulated, and therefore we cannot attribute the loss of accuracy for the V2Ad mutation to a single λ window.

Finally, we shall present the results of a free energy component analysis for all the calculations with $\alpha = 0.17$ and a time step of 2 fs (I2V, V2I, V2Ab, and A2V). All the atoms were assigned to one of 23 groups. The majority of these were amino acid residues, but larger groups, for example the entire solvent, were also defined (see the Supporting Information). The values of the free energy components are path-dependent and therefore should not be regarded as quantitative. They may, however, indicate whether or not a group of atoms, for example a residue, favors one of the mutated side chains over the other. The free energy components for the forward and reverse calculations were first averaged, and the results for the I2V and V2A mutations were added to create a single data set for the isoleucine to alanine (I2A) mutation. We assume that any group with a nonzero free energy component plays a role in the binding of the phosphopeptide. The results are shown qualitatively in Figure 5.

According to our analysis the solvent, the alchemical residue itself, the remainder of the Src SH2 domain, and Tyr β D5 and Tyr α B9 all favor the binding of the longer side chain of isoleucine. Three of the residues that surround the +3 binding pocket, Ile β E4, Thr EF1, and Leu β G4, in addition to the amino acid residues in the +2 and +4 positions, all favor the binding of the shorter side chain of alanine. The strength with which the aliphatic side chain

engages the +3 binding pocket is therefore found to be a balance between favorable interactions with the two tyrosines deep within the pocket and repulsive steric clashes with the adjacent amino acid residues on the phosphopeptide and those surrounding the pocket.

5. Discussion

We have rapidly, accurately, and precisely calculated how the binding free energy changes as we mutate the +3 residue of the pYEEI phosphopeptide from isoleucine to valine to alanine. This was done using a grid-based method that we call STIMD. The development of such methods is necessary if we are both to subject the growing number of competing free energy theories to broader comparative studies and to use these techniques in a more routine way. We have also calculated values of $\Delta\Delta H$ and $T\Delta\Delta S$ for both mutations; however, while the values agreed with known experimental values, the calculated errors were too large to be useful. Being able to run thermodynamic integration calculations quickly and with relative ease allowed us to run forward and reverse calculations, test and optimize our method, and examine two different mutations. We found that either accelerating the calculation by using an integration time step of 2 fs or launching all the λ simulations simultaneously did not affect the accuracy or precision of $\Delta\Delta G$. This result is crucial as our method relies on being able to launch all the λ simulations simultaneously, and hence in future we will be able to more quickly calculate changes in binding free energy for this system. Finally we presented the results of a free energy component analysis.

The exact information determined by a free energy component analysis cannot be determined experimentally. The strength of an interaction between two amino acid residues may be assessed by calculating the coupling free energy, ΔG_c , using double mutant cycles.^{45,47} Comparing these results to existing experimental data provides a further route for validating our method, and where there is no experimental data or it is inconclusive, we can then make predictions about the influence individual amino acid residues have on the binding of the phosphopeptide. Coupling free energy studies confirm that the individual contributions of the studied amino acid residues are weak.^{33,73} The magnitude of the experimental errors, however, are similar to the magnitude to the coupling free energies which makes comparison difficult. The experimental results suggest that Tyr β D5, Leu β G4, and Glu +2 favor the binding of isoleucine, whereas our findings indicate that Tyr β D5 favors, and both Leu β G4 and Glu +2 hinder, the binding of isoleucine. These conclusions are tentative given the magnitudes of the experimental errors, the lack of an exact correspondence between free energy components and ΔG_c , and theoretical concerns over the interpretation of free energy components. The effect of mutating Tyr α B9 has not, however, been studied experimentally, and we therefore predict that mutating it to alanine will reduce the specificity of the Src SH2 domain for the canonical phosphopeptide pYEEI. This would confirm the importance of the pocket defined by the aromatic rings of Tyr α B9 and Tyr β D5 in binding pYEEI.

Our free energy component analysis also predicted that the solvent favors the binding of the longer side chain of isoleucine. It is difficult for experiment to investigate the role of water in protein–protein interactions, and this, therefore, is an example of where the computational approach is potentially useful. We hypothesize that the complex network of water-mediated hydrogen bonds that forms between the backbone of the alchemical atom and Lys β D6 and Arg β D'1 (see the Supporting Information) is disrupted by the mutation. Interestingly, despite including no crystallographic waters in our simulations, a water molecule is observed hydrogen bonding to the backbone of the +3 amino acid residue for the entire duration of several λ simulations. This water molecule is also resolved in several X-ray crystal structures,^{28,74} while similar water-mediated hydrogen-bonded networks have been observed by experiment⁷⁵ and computational study.³⁹ We hypothesize that, through these bridging waters, Lys β D6 and Arg β D'1 contribute to the binding of aliphatic side chains in the +3 binding pocket. This is supported by a bioinformatics study⁷⁶ which indicates that both these residues contribute to the selectivity of Src SH2 domains despite being ~ 6 Å away from the phosphopeptide. We predict that mutating these residues will also reduce the specificity of the Src SH2 domain for pYEEL.

Using a free energy component analysis we have identified which residues hinder and which encourage the binding of the longer side chain of isoleucine in the +3 binding pocket. The “two-pronged plug two-holed socket” model simply characterizes the +3 binding pocket as hydrophobic and therefore implies that all the residues lining the pocket encourage the binding of hydrophobic side chains. Our results therefore constitute an improvement on this model and may be tested by combined mutagenesis and isothermal titration calorimetry experiments. Improving our understanding of how SH2 domains bind phosphopeptides will help resolve whether specific SH2 domains can be inhibited by druglike molecules²⁷ and whether these will be useful, given the potential for crosstalk between different SH2 domains within tyrosine kinase mediated signal cascades.²⁴

It should be recognized that there are limitations in a study of this nature. First, we used a standard Lennard Jones 6–12, or “hardcore”, van der Waals potential, and therefore, due to the lack of continuity in $(\partial U/\partial \lambda)$, we could not run simulations with $\lambda = 0$ or 1 but instead had to extrapolate the values of $(\partial U/\partial \lambda)$ at these points. This is a source of error. Furthermore, if we had been able to use a softcore or “separation-shifted” van der Waals potential,⁷¹ then not only would we have avoided this problem but also the λ simulations would have converged significantly faster. Although there are molecular dynamics codes that have softcore van der Waals potentials implemented (e.g., CHARMM), these do not currently scale very well on parallel computers. Instead we chose to use NAMD which scales very well on parallel computers but does not have a softcore potential. Using NAMD allowed us to run simulations of comparatively long durations in a short space of time, and we hope that studies of this nature will encourage the implementation of a softcore potential in codes such as NAMD. Finally, the accuracy of free energy calculations also

relies on the phase space being adequately sampled. Applying a replica exchange algorithm^{10–12} to all the λ simulations running on the computational grid would improve the sampling.

Acknowledgment. We thank Dr. Shunzhou Wan and our other RealityGrid collaborators, in particular the Supercomputing, Visualisation and e-Science group at Manchester University. We are also grateful for the computational time provided by the U.K. National Grid Service. This work was supported by EPSRC via RealityGrid grant GR/R67699. Access to the U.S. TeraGrid was provided by the National Science Foundation under NRAC grant MCA04N014. Use of UKLight was supported by the Exploitation of Switched Lightpaths for E-Science Applications PPARC/EPSC/MRC project, grant number GR/T04465/01. EPSRC also provided a Ph.D. studentship for P.W.F.

Supporting Information Available: Relative free energy profiles for the V2A and I2V mutations (Figure 1), which groups were used for the free energy component analysis (Figure 2), an example of the water-mediated hydrogen-bonded network (Figure 3), and raw numerical results. This material is available free of charge via the Internet at <http://pubs.acs.org>

References

- Åqvist, J.; Medina, C.; Samuelsson, J.-E. *Protein. Eng.* **1994**, *7*, 385–391.
- Jarzynski, C. *Phys. Rev. E* **1997**, *56*, 5018–5035.
- Ytreberg, F. M.; Zuckerman, D. M. *J. Chem. Phys.* **2004**, *120*, 10876–10879.
- Srinivasan, J.; Cheatham, T. E., III; Cieplak, P.; Kollman, P. A.; Case, D. A. *J. Am. Chem. Soc.* **1998**, *120*, 9401–9409.
- Vorobjev, Y. N.; Almagro, J. C.; Hermans, J. *Proteins* **1998**, *32*, 399–413.
- Lee, M. S.; Olson, M. A. *Biophys. J.* **2006**, *90*, 864–877.
- Damodaran, K. V.; Banba, S.; Brooks, C. L., III *J. Phys. Chem. B* **2001**, *105*, 9316–9322.
- Hénin, J.; Chipot, C. *J. Chem. Phys.* **2004**, *121*, 2904–3004.
- Rodinger, T.; Howell, P. L.; Pomès, R. *J. Chem. Phys.* **2005**, *123*, 034104.
- Woods, C. J.; Essex, J. W.; King, M. A. *J. Phys. Chem. B* **2003**, *107*, 13703–13710.
- Rodinger, T.; Howell, P. L.; Pomès, R. *J. Chem. Theor. Comput.* **2006**, *2*, 725–731.
- Rick, S. W. *J. Chem. Theor. Comput.* **2006**, *2*, 939–946.
- Lu, N.; Singh, J. K.; Kofke, D. A. *J. Chem. Phys.* **2003**, *118*, 2977–2984.
- Shirts, M. R.; Pande, V. S. *J. Chem. Phys.* **2005**, *122*, 144107.
- Yang, W.; Bitetti-Putzer, R.; Karplus, M. *J. Chem. Phys.* **2004**, *120*, 2618–2628.
- Rodinger, T.; Pomès, R. *Curr. Opin. Struct. Biol.* **2005**, *15*, 164–170.
- Kofke, D. A. *Fluid Phase Equilib.* **2005**, *228–229*, 41–48.
- Adcock, S. A.; McCammon, J. A. *Chem. Rev.* **2006**, *106*, 1589–1615.

- (19) Rodriguez-Gomez, D.; Garve, E.; Pohorille, A. *J. Chem. Phys.* **2004**, *120*, 2563–2578.
- (20) Ytreberg, F. M.; Swendsen, R. H.; Zuckerman, D. M. *J. Chem. Phys.* **2006**, *125*, 184114.
- (21) Chipot, C.; Pearlman, D. A. *Mol. Simul.* **2002**, *28*, 1–12.
- (22) Fowler, P. W.; Jha, S.; Coveney, P. V. *Philos. Trans. R. Soc. London, Ser. A* **2005**, *363*, 1999–2015.
- (23) Machida, K.; Mayer, B. J. *Biochim. Biophys. Acta* **2005**, *1747*, 1–25.
- (24) Pawson, T.; Nash, P. *Science* **2003**, *300*, 445–452.
- (25) Venter, J. C. et al. *Science* **2001**, *291*, 1304–1352.
- (26) Waksman, G.; Kumaran, S.; Lubman, O. *Expert Rev. Mol. Med.* **2004**, *6*, 1–18.
- (27) Shakespeare, W. C. *Curr. Opin. Chem. Biol.* **2001**, *5*, 409–415.
- (28) Waksman, G.; Shoelson, S. E.; Pant, N.; Cowburn, D.; Kuriyan, J. *Cell* **1993**, *72*, 779–790.
- (29) Waksman, G.; Kominos, D.; Robertson, S. C.; Pant, N.; Baltimore, D.; Birge, R. B.; Cowburn, D.; Hanafusa, H.; Mayer, B. J.; Overduin, M.; Resh, M. D.; Rios, C. B.; Silverman, L.; Kuriyan, J. *Nature* **1992**, *358*, 646–653.
- (30) Songyang, Z. et al. *Cell* **1993**, *72*, 767–778.
- (31) Eck, M. J.; Shoelson, S. E.; Harrison, S. C. *Nature* **1993**, *362*, 87–91.
- (32) Bradshaw, J. M.; Mitaxov, V.; Waksman, G. *J. Mol. Biol.* **1999**, *293*, 971–985.
- (33) Bradshaw, J. M.; Waksman, G. *Biochemistry* **1999**, *38*, 5147–5154.
- (34) Bradshaw, J. M.; Gruzca, R. A.; Ladbury, J. E.; Waksman, G. *Biochemistry* **1998**, *37*, 9083–9090.
- (35) Wan, S.; Stote, R.; Karplus, M. *J. Chem. Phys.* **2004**, *121*, 9539.
- (36) Pearlman, D. A.; Rao, B. G. Free energy calculations: Methods and Applications. In *Encyclopedia of Computational Chemistry*; Schleyer, P. v. R., Ed.; Wiley: Chichester, 1999; Vol. 2, pp 1036–1061.
- (37) Henriques, D. A.; Ladbury, J. E.; Jackson, R. M. *Protein Sci.* **2000**, *9*, 1975–1985.
- (38) Geroult, S.; Virdee, S.; Waksman, G. *Chem. Biol. Drug Des.* **2006**, *67*, 38–45.
- (39) Price, D. L.; Jorgensen, W. L. *J. Comput.-Aided Mol. Des.* **2001**, *15*, 681–695.
- (40) Suenaga, A.; Hatakeyama, M.; Ichikawa, M.; Yu, X.; Futatsugi, N.; Narumi, T.; Fukui, K.; Terada, T.; Taiji, M.; Shirouzu, M.; Yokoyama, S.; Konagaya, A. *Biochemistry* **2003**, *42*, 5195–5200.
- (41) Donnini, S.; Juffer, A. *J. Comput. Chem.* **2003**, *25*, 393–411.
- (42) Woo, H.-J.; Roux, B. *Proc. Natl. Acad. Sci. U.S.A.* **2005**, *102*, 6825–6830.
- (43) Kirkwood, J. G. *J. Chem. Phys.* **1935**, *3*, 300–313.
- (44) Peter, C.; Oostenbrink, C.; van Dorp, A.; van Gunsteren, W. F. *J. Chem. Phys.* **2004**, *120*, 2652–2661.
- (45) Mark, A. E.; van Gunsteren, W. F. *J. Mol. Biol.* **1994**, *240*, 167–176.
- (46) Wan, S.; Coveney, P. V.; Flower, D. R. *J. Immunology* **2005**, *175*, 1715–1723.
- (47) Michielin, O.; Karplus, M. *J. Mol. Biol.* **2002**, *324*, 547–569.
- (48) Boresch, S.; Archontis, G.; Karplus, M. *Proteins: Struct., Funct., Genet.* **1994**, *20*, 25–33.
- (49) Foster, I.; Kesselman, C.; Tuecke, S. *Int. J. Supercomput. Appl.* **2001**, *15*, 200–224.
- (50) Coveney, P. V.; Fowler, P. W. *J. R. Soc. Interface* **2005**, *2*, 267–280.
- (51) Coveney, P. V., Ed.; Scientific Grid Computing. *Philos. Trans. R. Soc. London, Ser. A* **2005**, *363*(1833), 1705–2053.
- (52) Kalé, L.; Skeel, R.; Bhandarkar, M.; Brunner, R.; Gursoy, A.; Krawetz, N.; Phillips, J.; Shinozaki, A.; Varadara, jan, K.; Schulten, K. *J. Comput. Phys.* **1999**, *151*, 283–312.
- (53) Phillips, J.; Braun, R.; Wang, W.; Gumbart, J.; Tajkhorshid, E.; Villa, E.; Chipot, C.; Skeel, R. D.; Kalé, L.; Schulten, K. *J. Comput. Chem.* **2005**, *26*, 1781–1802.
- (54) Pickles, S. M.; Haines, R.; Pinning, R. L.; Porter, A. R. *Philos. Trans. R. Soc. London, Ser. A* **2005**, *363*, 1843–1853.
- (55) RealityGrid. <http://www.realitygrid.org> (accessed Feb 23, 2007).
- (56) The Globus Alliance. <http://www.globus.org> (accessed Feb 23, 2007).
- (57) Kalawsky, R. S.; Nee, S. P.; Holmes, I.; Coveney, P. V. *Philos. Trans. R. Soc. London, Ser. A* **2005**, *363*, 1885–1894.
- (58) The TeraGrid. <http://www.teragrid.org> (accessed Feb 23, 2007).
- (59) The National Grid Service. <http://www.ngs.ac.uk> (accessed Feb 23, 2007).
- (60) Coveney, P. V.; Jha, S.; Pickles, S. *CSAR Focus* **2005**, *14*, 16–18.
- (61) Coveney, P. V.; Saksena, R. S.; Zasada, S. J.; McKeown, M.; Pickles, S. *Comput. Phys. Commun.* **2007**, *176*, 406–418.
- (62) The Open Middleware Institute. <http://www.omii.ac.uk> (accessed Feb 23, 2007).
- (63) Dixit, S. B.; Chipot, C. *J. Phys. Chem. A* **2001**, *105*, 9795–9799.
- (64) Hémin, J. Alchemify, an X-PLOR PSF post-processor for alchemical free energy calculations in NAMD. <http://www.edam.uhp-nancy.fr/Alchemify/> (accessed Feb 23, 2007).
- (65) Jorgensen, W. L.; Chandrasekhar, J.; Madura, J. D.; Impey, R. W.; Klein, M. L. *J. Chem. Phys.* **1983**, *79*, 926–935.
- (66) MacKerell, A. D. et al. *J. Phys. Chem. B* **1998**, *102*, 3586–3616.
- (67) Feng, M.-H.; Philippopoulos, M.; MacKerell, A. D. J.; Lim, C. *J. Am. Chem. Soc.* **1996**, *118*, 11265–11277.
- (68) Ryckaert, J.-P.; Ciccotti, G.; Berendsen, H. J. C. *J. Comput. Phys.* **1977**, *23*, 327–341.
- (69) Miyamoto, S.; Kollman, P. A. *J. Comput. Chem.* **1992**, *13*, 952–962.

- (70) Darden, T.; York, D.; Pedersen, L. *J. Chem. Phys.* **1993**, *98*, 10089–10092.
- (71) Zacharias, M.; Straatsma, T. P.; McCammon, J. A. *J. Chem. Phys.* **1994**, *100*, 9025–9031.
- (72) Frenkel, D.; Smit, B. *Understanding Molecular Simulation*, 2nd ed.; Academic Press: London, 2002; p 529.
- (73) Bradshaw, J. M.; Mitaxov, V.; Waksman, G. *J. Mol. Biol.* **2000**, *299*, 521–535.
- (74) Lubman, O. Y.; Waksman, G. *J. Mol. Biol.* **2003**, *328*, 655–668.
- (75) Chung, E.; Henriques, D. A.; Renozi, D.; Zvelebil, M.; Waksman, G.; Robinson, C. V.; Ladbury, J. E. *Structure* **1998**, *6*, 1141–1151.
- (76) Sheinerman, Felix, B.; Al-Lazikani, B.; Honig, B. *J. Mol. Biol.* **2003**, *334*, 823–841.

CT6003017

Calculation of a Complete Enzymic Reaction Surface: Reaction and Activation Free Energies for Hydride-Ion Transfer in Dihydrofolate Reductase

Peter L. Cummins, Ivan V. Rostov, and Jill E. Gready*

Computational Proteomics Group, John Curtin School of Medical Research,
Australian National University, P.O. Box 334, Canberra ACT 2601, Australia

Received October 25, 2006

Abstract: We present a two-dimensional grid method for the calculation of complete free-energy surfaces for enzyme reactions using a hybrid quantum mechanical/molecular mechanical (QM/MM) potential within the semiempirical (PM3) QM approximation. This implementation is novel in that parallel processing with multiple trajectories (replica-exchange molecular dynamics simulations) is used to sample configuration space. The free energies at each grid point are computed using the thermodynamic integration formalism. From the free-energy surface, the minimum free-energy pathway for the reaction can be defined, and the computed activation and reaction energies can be compared with experimental values. We illustrate its use in a study of the hydride-transfer step in the reduction of dihydrofolate to tetrahydrofolate catalyzed by *Escherichia coli* dihydrofolate reductase with bound nicotinamide adenine dinucleotide phosphate cofactor. We investigated the effects of changing the QM region, ionization state of the conserved active-site Asp27 residue, and polarization contributions to the activation and reaction free energy. The results clearly show the necessity for including the complete substrate and cofactor molecules in the QM region, and the importance of the overall protein (MM) electrostatic environment in determining the free energy of the transition state (TS) and products relative to reactants. For the model with ionized Asp27, its inclusion in the QM region is essential. We found that the reported [Garcia-Viloca, M.; Truhlar, D. G.; Gao, J. J. *Mol. Biol.* **2003**, *327*, 549] stabilization of the TS due to polarization is an artifact that can be attributed to truncation of the electrostatic interactions between the QM and MM atoms. For neutral (protonated) Asp27, our calculated reaction free energy of -4 ± 2 kcal/mol agrees well with the experimental value of -4.4 kcal/mol, although the corresponding activation free-energy estimate is still high at 21 ± 2 kcal/mol compared with the experimental value of 13.4 kcal/mol. The results are less supportive of the ionized Asp27 model, which gives rise to a much higher activation barrier and favors the reverse reaction.

Introduction

Dihydrofolate reductase (DHFR) is a key enzyme¹ that catalyzes the reduction of folate to dihydrofolate (DHF) and DHF to tetrahydrofolate (THF), cycling the THF cofactors required for the synthesis of DNA and other precursors. It

has been the subject of much theoretical investigation. Aspects of the mechanism that have been studied using computational methods include kinetic isotope effects,^{2,3} transition-state (TS) geometry,⁴ the ionization state of active-site residues,^{5,6} the role of dynamical structural fluctuations in promoting hydride transfer,^{7–9} and the effects of electronic polarization of the active site.^{10–12} Methods employed vary

* Corresponding author e-mail: Jill.Gready@anu.edu.au.

from simple geometry optimization to the use of molecular dynamics (MD), or combinations of both. The ultimate goal of these studies is to understand how DHFR facilitates its reaction. While many general theories have been proposed^{13–15} to rationalize the catalytic activity of enzymes, to test these theories using computational methods, and to provide a detailed picture of how a particular enzyme catalyzes a particular reaction, we must first have a sufficiently accurate description of the basic physical and chemical processes involved. Combined quantum mechanical/molecular mechanical (QM/MM) methods have become very popular as a basis for such a description. In the 30 years since the pioneering work of Warshel and Levitt,¹⁶ QM/MM methods have undergone considerable development,^{17–31} providing a computationally efficient way of including the effects of solvent and enzyme environments on a reaction center. The total energy of the system, as an explicit function of the reaction coordinate (r), is given by the sum of the QM and MM energies plus a QM/MM interaction term:

$$E(r) = E_{\text{QM}}(r) + E_{\text{QM/MM}}(r) + E_{\text{MM}} \quad (1)$$

As it must allow for the breaking and formation of chemical bonds, the reaction coordinate is contained within the QM region and, as indicated in eq 1, is an explicit function of E_{QM} and $E_{\text{QM/MM}}$ only.

However, in order to compute reaction free energies that are directly comparable with experimental quantities, it is necessary to perform appropriate statistical mechanical averaging^{32,33} along the predefined reaction coordinate. While *ab initio* or density functional (DFT) QM methods can yield a more reliable description of reaction energies than the more efficient semiempirical PM3 or AM1 methods, their relatively high computational cost generally prohibits statistical mechanical calculations for enzymic systems.^{29,31} Thus, despite the known limitations of semiempirical methods in terms of their overall chemical accuracy, the primary need to compute free-energy changes associated with chemical processes has led to their continued application in studies of enzymic reaction mechanisms, including that of DHFR.^{6,7} They are particularly useful for problems where systematic trends or alternative mechanisms are of interest, rather than cases where absolute accuracy in computed reaction free energies is required.

Regardless of the level of QM used—*ab initio*, DFT, or semiempirical—a primary consideration when applying QM/MM methods is the choice of QM region. The positioning of the QM/MM boundary is arbitrary, except that it should not divide the reaction coordinate. Although chemical intuition and critical analysis of the active-site structure can be used to guide choices, ultimately, they require validation by performing a number of calculations with QM regions of varying size and composition.

The reductions in DHFR take place via the transfer of a hydride ion from the nicotinamide adenine dinucleotide phosphate (NADPH) cofactor bound to the enzyme. The hydride-ion transfer also requires that a proton be transferred to the substrate (S), so that the overall reaction proceeds according to



The active site of *Escherichia coli* DHFR is shown in Figure 1. For this particular redox reaction, it is commonly believed that the substrate is protonated first, prior to hydride-ion transfer.³⁴ Protonation produces an increase in positive charge on the substrate, thereby activating it toward acceptance of the negatively charged hydride ion. Our recent computational studies^{5,6} have provided some evidence that protonation of the conserved Asp/Glu that hydrogen bonds the substrate may also form part of the activation mechanism. The neutral (protonated) and ionized forms of Asp27 are depicted in Figure 1, H bonded to W206 and O4 of the substrate pterin ring. Despite its apparent importance in binding the substrate to DHFR, this residue has been omitted from the QM region in a large number of other QM/MM studies^{2–4,7,9–12} of the hydride-ion transfer mechanism. Another QM/MM study has also suggested that electronic polarization of the QM region by the MM region is an essential feature of TS stabilization for the hydride-ion transfer in DHFR.¹² The choice of QM region is critical to an understanding of the origin of these proposed polarization effects as polarization is clearly a function of the QM/MM boundary; that is, the QM region is polarized by the partial charges in the MM region.

In the present study, we have used MD simulation methods to perform an *a priori* calculation of the free-energy change for the hydride-ion transfer in DHFR. In order to perform the necessarily large number of simulations efficiently, we use the semiempirical PM3-QM/MM approximation^{6,27,35,36} for the force field in the MD and parallel processing capabilities of state-of-the-art computer clusters. From our simulations, we have determined the reaction coordinate corresponding to the minimum pathway on the free-energy surface for the hydride-ion transfer. Thus, we have a precise definition of the activation and reaction free energies for direct comparison with experimental results. This minimum free-energy path (MFEP) provides a convenient integration path for carrying out further investigative simulations to study the effects of changing the size and composition of the QM region, the ionization state of Asp27, and the polarization contribution to the free energy. Due to the approximations of the semiempirical QM method used in generating the MFEP, we also performed some higher-level *ab initio* and DFT QM/MM calculations along the MFEP to assist in validation.

Methods

Solvated Enzyme and QM/MM Model. Initial coordinates for *E. coli* DHFR were obtained from the DHFR·FOL·NADP⁺ complex in the Protein Data Bank (1rx2).³⁷ In this structure, the mobile M20 loop is in the closed conformation, which is thought to be necessary for the hydride-ion transfer to take place. Hydrogens were added to this structure using Insight II³⁸ to form the DHFR·DHFH⁺·NADPH complex. This complex, together with the 153 crystallographic water molecules, was solvated in a 36-Å-radius sphere containing 4962 additional water molecules. To maintain the system at constant density, the water molecules between 32 and 36 Å

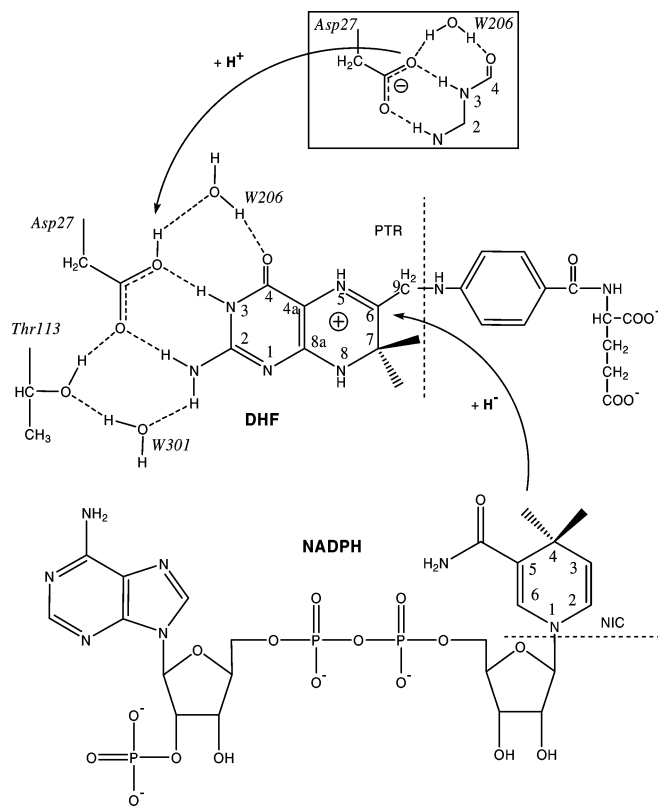


Figure 1. Active site in *E. coli* DHFR with N5-protonated 7,8-dihydrofolate (DHFH⁺) substrate and NADPH cofactor. DHFH⁺ is shown H-bonded to both the protonated carboxylate (carboxylic acid) and ionized (carboxylate) side chain of the conserved Asp27 residue. Other possible H-bond interaction sites, with Thr113 and water molecules W206 and W301, are shown as indicated from X-ray structures of *E. coli* DHFR complexes available in the Protein Data Bank.

were held fixed at their initial positions during the MD simulation to form a rigid outer shell of solvent, leaving a total of 3229 waters free to move. Where necessary, hydrogen (link) atoms were added to the QM region at the QM/MM boundaries. The force field of Cornell et al.³⁹ for the protein atoms and the TIP3P model⁴⁰ for water were used for the MM terms. The hybrid force field and parametrization procedure used for the nonbonded electrostatic and van der Waals (vdW) interactions between the QM and MM regions has been described in detail previously.^{27,39,40} Briefly, the QM/MM term is given by

$$E_{\text{QM/MM}} = \text{tr}(\mathbf{P}\mathbf{V}) + E_{\text{vdW}} \quad (3)$$

where \mathbf{P} is the density matrix and \mathbf{V} is the one-electron matrix for the interaction between the QM atoms and the partial charges (q) of the MM atoms. The matrix elements of \mathbf{V} have the form

$$V_{\mu\nu} = \sum_k q_k(\mu\nu, ss) \quad (4)$$

where the summation is over MM atoms and $(\nu\mu, ss)$ are the semiempirical approximations for the one-electron integrals. The electrostatic interactions between atoms in the QM and MM regions were not subject to any cutoff in the calculations of the MFEP. All residues in the MM region were subject

to a 12 Å cutoff for the electrostatic terms. An 8 Å cutoff was applied to all vdW interactions between residues. In order to reduce the computational time, we also adopted a multiple time-step approach in which the electrostatic forces due to interactions beyond 8 Å were computed once every 10 time steps.

Minimum Free-Energy Path. We used a two-dimensional (2D) grid-based method in order to determine the MFEP. This type of approach has been used extensively to calculate adiabatic and free-energy surfaces for chemical reactions in both aqueous^{41–43} and enzymic^{17,44,45} environments. More recently, potential of mean force calculations in 2D have been carried out in order to generate free-energy surfaces for investigating concerted reactions.^{46,47} Thus, grid methods would seem a natural choice when two parameters are required for a complete description of a reaction pathway in complex molecular environments such as enzymes.

The MFEP was determined using a QM region (Asp27·DHFH⁺·NADPH) consisting of the N5-protonated substrate and cofactor molecules and the carboxylic acid (–CH₂–COOH) side chain of Asp27 (see Figure 1). In eq 1, we wrote the general reaction coordinate as $r = (r_1, r_2)$, where the C6–H4 and C4–H4 bond distances involving the hydride ion (H4) to be transferred are given by r_1 and r_2 , respectively. In order to locate reactant, product, and transition states on the reaction free-energy surface, we first define a set of curvilinear reaction paths $\{x\}$ with $x \geq 1$ for the path parameter and $0 \leq \lambda \leq 1$ for the coupling parameter which drives the system between reactant and product states.⁴⁸ The $\lambda = 0$ and $\lambda = 1$ states correspond to reactant-side and product-side states, respectively. The equations for these paths are given (in Å) by

$$r_1(x, \lambda) = 3.4 - 2.4[1 - (1 - \lambda)^x] \quad (5a)$$

and

$$r_2(x, \lambda) = 1 + 2.4\lambda^x \quad (5b)$$

with values of $\{x\} = \{1.3, 1.5, 2.0, 2.5, 3.0, 4.0\}$; that is, a total of six paths were used to construct the free-energy surface. The λ -coupling parameter was divided into 21 discrete values using $\Delta\lambda = 0.05$. Thus, we obtain a grid of $6 \times 21 = 126$ points (x, λ) ; independent MD simulations were performed at these points for the free-energy calculation.

Reaction Path Simulations. The configurational sampling in these simulations was performed using the replica exchange molecular dynamics (REMD) method.^{49,50} The REMD simulations consisted of independent trajectories (replicas) that were generated simultaneously (i.e., in parallel) on a Compaq AlphaServer and SGI Altix 3700Bx2 cluster. The trajectories were assigned temperatures in the range 290–320 K with unique initial velocity distributions. The trajectories were run using a time step of 0.001 ps, with hydrogen masses set to 2 amu. Temperature exchanges were attempted every 0.02 ps. As the temperature range used is quite narrow (290–320 K), we perform an average over the temperature to obtain a single value for the free energy. We note that the efficiency of REMD over conventional MD

has been questioned recently,⁵¹ but this is not of concern here. In this study, we needed to exploit the advantages of parallel methods to reduce the wall time (i.e., the real time it takes to complete a calculation), as opposed to CPU time, to a reasonable time frame; this can be achieved by using either the REMD formalism or parallel computation of conventional MD trajectories.

To evaluate the required free energies, we used the thermodynamic integration (TI) formalism.^{32,33} The free-energy change between 0 and a given value of λ along path x is exactly

$$\Delta G(x,\lambda) = \int_{a=0}^{a=\lambda} \left\langle \frac{\partial E[r(x,\alpha)]}{\partial \alpha} \right\rangle_a d\alpha \quad (6)$$

where, in the present calculations, we have approximated the integrand in eq 6 by the sum over a finite number of time intervals

$$\left\langle \frac{\partial E[r(x,\alpha)]}{\partial \alpha} \right\rangle_\alpha \cong \frac{1}{N_{\text{time}}} \sum_{i=1}^{N_{\text{time}}} \langle E_i(x,\alpha) \rangle \quad (7)$$

with the subaverages over the number of processors in the REMD given by

$$\langle E_i(x,\alpha) \rangle = \frac{1}{N_{\text{proc}}} \sum_{j=1}^{N_{\text{proc}}} \frac{\partial E_{ij}[r(x,\alpha)]}{\partial \alpha} \quad (8)$$

Following Ho et al.,⁴³ the SHAKE algorithm⁵² was used to fix distances r given by eq 5 at the 126 (x,λ) grid points. However, as we use TI to compute the Hamiltonian derivatives with respect to the λ coupling parameter, our approach to constraint distance contributions is formally the same as that described by Pearlman.⁵³ The average value in eq 6 was computed as the average of the set of five moving averages with a time interval of $\Delta t = 1$ ps, for a total of 12 time intervals (12 ps), that is, $N_{\text{time}} = 12$ in eq 7. The total number of derivatives that are computed is given by the product of the fixed number of time intervals, which numbered 12, and the number of processors (N_{proc}). In the present simulations, we used sampling parameters of $N_{\text{proc}} = 12$ (total of 144 derivatives per λ) and $N_{\text{proc}} = 48$ (total of 576 derivatives per λ) for the calculation of the MFEP. For each value of λ , the REMD was run prior to the start of sampling for at least 100 ps to ensure adequate equilibration. All REMD simulations were performed using Molecular Orbital Programs for Simulations (MOPS).⁵⁴

To compute the necessary energy derivatives at the PM3-QM/MM level in eq 8, we first write the total system energy given by eq 1 in the form

$$E = \text{tr}[\mathbf{P}\mathbf{H}] + \epsilon \quad (9)$$

where \mathbf{H} is the QM Hamiltonian matrix, \mathbf{P} is the density matrix, and ϵ are the remaining terms in the expression for the energy which do not depend explicitly on \mathbf{P} . We then make use of the Hellmann–Feynman theorem to obtain

$$\frac{\partial E}{\partial \alpha} = \text{tr} \left[\mathbf{P} \frac{\partial \mathbf{H}}{\partial \alpha} \right] + \frac{\partial \epsilon}{\partial \alpha} \quad (10)$$

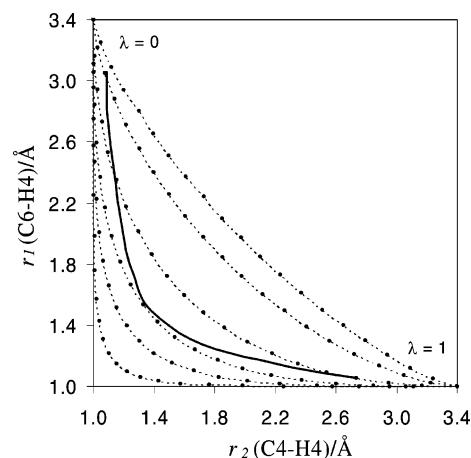


Figure 2. Reaction paths (dashed lines) used in the calculation of the minimum free-energy path (MFEP) (solid line) as a function of the C6–H4 and C4–H4 distances (Å). The MFEP was determined for λ ranging from 0.10 to 0.85 using a sampling parameter of $N_{\text{proc}} = 48$. The dots (filled circles) indicate the points at which the MD simulations were performed for paths corresponding to $\{x\} = 1.3, 1.5, 2.0, 2.5, 3.0,$ and 4.0 (1.3 gives the path with smallest curvature, 4.0 the path with highest curvature).

The derivatives of \mathbf{H} and ϵ were conveniently obtained by finite difference ($\Delta\alpha = \pm 0.001$), using the density matrix \mathbf{P} computed at α ; at the semiempirical level, performing analytic evaluation of these derivatives does not provide any advantage in terms of precision or efficiency. Calculation of the energy derivatives (on the basis of configurational sampling at the PM3-QM/MM level along the MFEP) were also carried out using the ONIOM (QM/MM) method with electronic embedding^{28,30} as implemented in the Gaussian 03 (G03) program.⁵⁵ Derivatives were obtained at the Hartree–Fock (HF) and DFT (B3LYP) levels using the 6-31G* basis and the formula

$$\frac{\partial E}{\partial \alpha} = \frac{\partial r_1}{\partial \alpha} \frac{\partial E}{\partial r_1} + \frac{\partial r_2}{\partial \alpha} \frac{\partial E}{\partial r_2} \quad (11)$$

where the derivatives of the energy E with respect to r_1 and r_2 were computed analytically (using G03) at the configurations generated in the PM3-QM/MM level simulations.

Results and Discussion

Minimum Free-Energy Path. The reaction paths (eq 5) are plotted in Figure 2. The (x,λ) -grid points at which the individual MD simulations were carried out are indicated by dots. The free-energy surface computed using $N_{\text{proc}} = 12$ based on these grid points is illustrated in Figure 3. The isoenergy contours (2D projections in the x,λ plane) clearly show the reactant ($\lambda \sim 0.1$) and product ($\lambda \sim 0.85$) potential wells. The solid line in Figure 2 represents the MFEP obtained using a sampling parameter of $N_{\text{proc}} = 48$. N_{proc} corresponds to the number of computer processors and is equivalent to the number of independent trajectories at each point (x,λ) in the free-energy calculation. This MFEP was found by a least-squares fitting of the path $\{x\}$ free-energy curves (dots in Figure 2) to a low-order (quadratic or cubic)

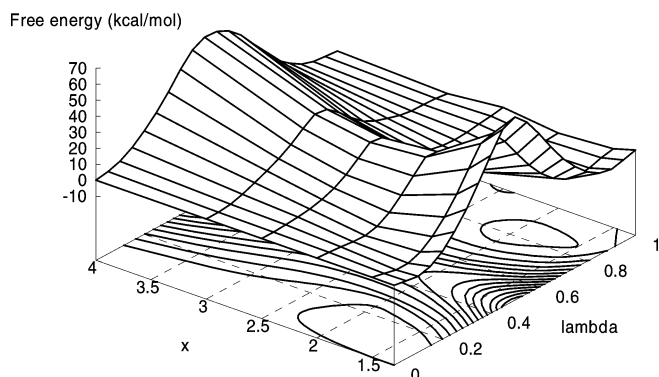


Figure 3. 3D and isoenergy contour representation of the PM3 free-energy surface. Free energy (kcal/mol) plotted as function of reaction path $\{x\}$ and λ coupling parameter (λ) for the hydride transfer to DHFH⁺ in DHFR.

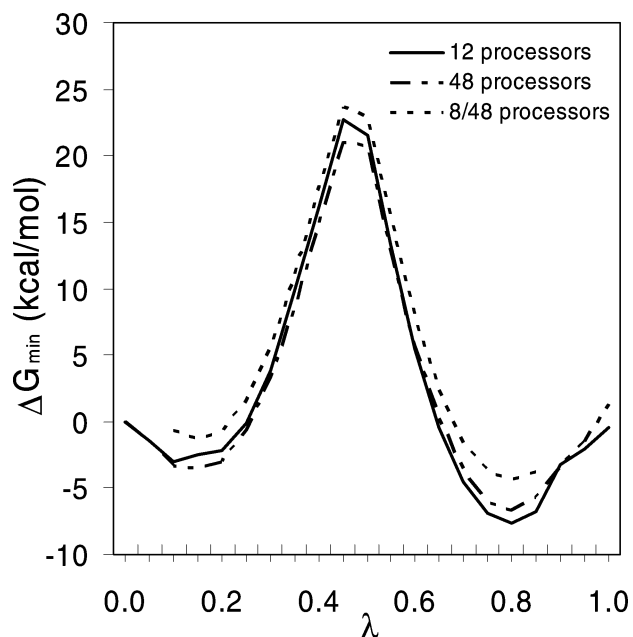


Figure 4. Change in free energy ΔG_{\min} relative to $\lambda = 0$ for $N_{\text{proc}} = 12$ and $N_{\text{proc}} = 48$. The curve labeled 8/48 is not a ΔG_{\min} (see text) but was calculated from independent simulations using $N_{\text{proc}} = 8$ at the points (x_{\min}, λ) along the minimum free-energy path generated using $N_{\text{proc}} = 48$ (see Figure 3).

polynomial for each value of λ . We were unable to fit the free-energy curves for $\lambda < 0.1$ and $\lambda > 0.85$ values due to the fact that paths close to the end points ($\lambda = 0$ and $\lambda = 1$) rapidly converge (see Figure 2), forcing the actual small free-energy differences to be comparable with statistical sampling errors in the simulations.

The MFEP using the QM region for Asp27·DHFH⁺·NADPH was obtained for two values of the sampling parameter, $N_{\text{proc}} = 12$ and $N_{\text{proc}} = 48$, which we will refer to as MFEP/12 and MFEP/48, respectively. We denote as x_{\min} the value of x at which the free energy (as computed by the fitted polynomial) is a minimum value, given by ΔG_{\min} , for a given value of the coupling parameter, λ . The free energy, ΔG_{\min} , is shown in Figure 4, together with the free energy obtained from a subsequent simulation with $N_{\text{proc}} = 8$, calculated by following the MFEP/48 path. Note that the simulations with $N_{\text{proc}} = 8$ were carried out only for values

Table 1. Reaction Path Parameters for Reactant, Transition State, and Product Complexes

parameter ^a	reactant	TS	product
λ	0.1	0.475	0.8
x_{\min} ($N_{\text{proc}} = 12$)	1.48	2.415	2.05
x_{\min} ($N_{\text{proc}} = 48$)	1.45	2.45	2.07
$R(\text{C6-H4})/\text{\AA}$	3.06	1.50	1.09
$R(\text{C4-H4})/\text{\AA}$	1.09	1.40	2.52

^a For PM3-QM/MM model simulations with Asp27(neutral)·DHFH⁺·NADPH in QM region.

of λ ranging from 0.10 to 0.85. For the $N_{\text{proc}} = 12$ and 48 simulations used to determine the MFEP/12 and MFEP/48 paths, we averaged the free energy over x for all points, including $\lambda < 0.10$ and $\lambda > 0.85$. Note that the displacement between the ΔG_{\min} curves for $N_{\text{proc}} = 8$ and 48 is due to the fact that the calculations start from different λ values, that is, $\lambda = 0.10$ and $\lambda = 0$, respectively.

Figure 4 reveals that there are no major differences in the results between different levels of sampling in the MD simulations. The free-energy change obtained by integration between $\lambda = 0$ and $\lambda = 1$, $\langle \Delta G(1) \rangle$, where the average $\langle \rangle$ is over paths $\{x\}$, was calculated to be -0.47 ± 2.35 kcal/mol for $N_{\text{proc}} = 12$ and 1.21 ± 2.16 kcal/mol for $N_{\text{proc}} = 48$. Note that, theoretically, the standard deviation in $\langle \Delta G(1) \rangle$ should be zero (see Figure 2) as the reaction paths start and finish at common points. Thus, the nonzero standard deviation of $\sim \pm 2$ kcal/mol serves as a reliable estimate of the final error bars associated with incomplete sampling.

From the MFEP defined by coordinates (x_{\min}, λ) , we can determine values for x and λ that are appropriate for reactants, TS, and products; these values are given in Table 1. The C6-H4 and C4-H4 distances in angstrom units, also given in Table 1, were obtained by substituting these values of x_{\min} and λ into eq 5 for the curvilinear reaction paths shown in Figure 2. These distances were found to vary insignificantly (within ± 0.01 Å) between the two levels ($N_{\text{proc}} = 12$ and 48) of sampling.

QM Regions (with Protonated Asp27). The free-energy curves for different choices of the QM region are shown in Figures 5 and 6. These results are for protonated Asp27 only, with no cutoffs applied to electrostatic interactions between the QM and MM regions. They were obtained from simulations using $N_{\text{proc}} = 8$ and MFEP/48. In Figure 5, the complete DHFH⁺ substrate and NADPH cofactor molecules are included in the QM region. The other enzyme fragments (W206, W301, and Thr113) that could be included (see Figure 1) interact with these reactant molecules exclusively via nonbonded interactions. It can be seen that the free-energy changes along the MFEP vary insignificantly (i.e., within the estimated statistical sampling error of ± 2 kcal/mol) among these choices of QM region. This suggests that the PM3-QM/MM force-field description we have used can adequately account for these types of nonbonded interactions. In contrast, Figure 6 shows that using smaller pterin (PTR) and nicotinamide (NIC) fragments (see Figure 1) of the substrate and cofactor in the QM region leads to much larger deviations from the reference MFEP. These results demonstrate that, at least for the neutral (protonated) state of Asp27, the minimum QM region need contain only the complete

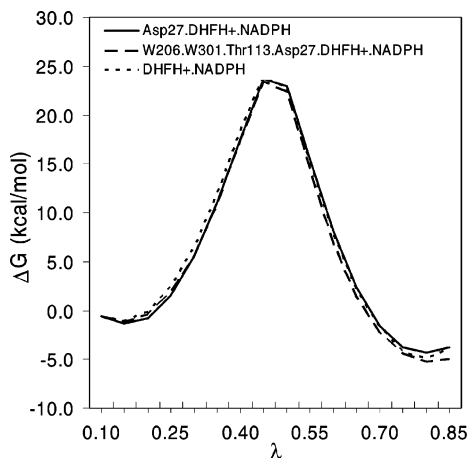


Figure 5. Free-energy change ($N_{\text{proc}} = 8$ and MFEP/48) relative to reactant state at $\lambda = 0.1$ for QM regions consisting of the substrate and cofactor molecules (DHFH⁺·NADPH), and with additional active-site species forming H bonds with DHFH⁺·NADPH (see Figure 1). Asp27 is neutral (protonated).

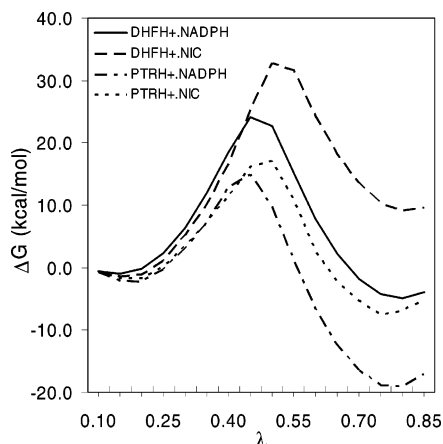


Figure 6. Free-energy change ($N_{\text{proc}} = 8$ and MFEP/48) relative to reactant state at $\lambda = 0.1$ for QM regions consisting of substrate and cofactor molecules (DHFH⁺·NADPH), or combinations of nicotinamide-ring (NIC), and pterin-ring (PTRH⁺) fragments (see Figure 1). Asp27 is neutral (protonated).

substrate and cofactor molecules. Note that many previous studies on DHFR include smaller fragments of these two species.^{2–13} However, as demonstrated by the results in Figure 6, these choices represent very different reactions in terms of the free-energy change relative to the reactant state, and, although we do not compute them in the present study, represent somewhat different MFEPs. Hence, on this basis alone, we may also expect to find differences in the geometry of the TS, depending on the choice of QM region.^{4–6}

Ionization State of Asp27. The results in Figures 7 and 8 were obtained from simulations using $N_{\text{proc}} = 8$ and MFEP/48, without cutoffs applied to electrostatic interactions between the QM and MM regions. As shown in Figure 7, if Asp27 is included in the MM region, the ionized state of Asp27 presents only a small perturbation on the neutral reference state. However, if ionized Asp27 is included in the QM region, a very different free-energy curve is obtained. The model with the ionized state gives rise to an endothermic reaction with a higher activation barrier, consistent with our

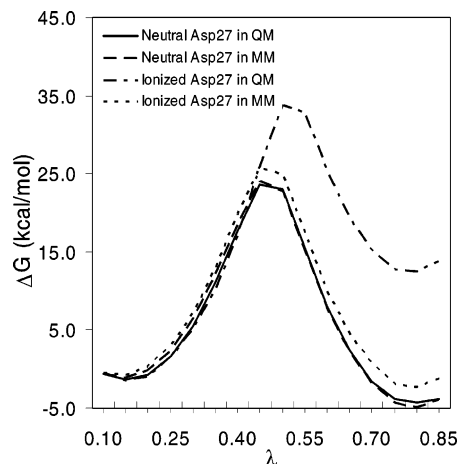


Figure 7. Free-energy change ($N_{\text{proc}} = 8$ and MFEP/48) relative to reactant state at $\lambda = 0.1$ for neutral and ionized states of Asp27 with QM regions Asp27·DHFH⁺·NADPH (Asp27 in QM region) and DHFH⁺·NADPH (Asp27 in MM region).

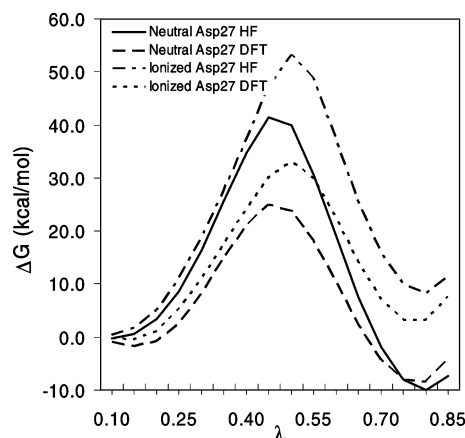


Figure 8. Free-energy change ($N_{\text{proc}} = 8$ and MFEP/48) relative to reactant state at $\lambda = 0.1$ calculated at the HF and DFT QM/MM levels for neutral and ionized states of Asp27 with QM region Asp27·DHFH⁺·NADPH.

earlier QM/MM free energy simulations for the 8-methylpterin substrate.⁵⁶ As shown in Figure 8, the results are qualitatively similar if ab initio HF and DFT QM/MM methods are used to compute the free energies (based on the configurational sampling at the PM3-QM/MM level); that is, the reaction tends to be endothermic with a higher activation free energy. We have noted similar behavior between protonated and ionized Asp27 in previous geometry optimization studies using simplified model systems for the hydride transfer reaction.⁶ The PM3, HF, and DFT methods predict very similar reaction free energies. As expected, HF overestimates the activation free energy relative to DFT, due to a lack of electron correlation in the former. The free-energy curve for PM3 is quite similar to that obtained for DFT.

From the PM3 data for neutral Asp (Figure 7), we estimate the free energy of reaction to be -4 ± 2 kcal/mol, compared with the experimental value of -4.4 kcal/mol.⁵⁷ The corresponding activation free energy of 24 ± 2 kcal/mol is considerably higher than the experimental value of 13.4 kcal/

Table 2. Polarization Contribution to the Free Energy (kcal/mol) at the Transition State, TS, at $\lambda = 0.475$, and Products at $\lambda = 0.80$, Relative to the Reactant State at $\lambda = 0.1$

system	method	TS ($\lambda = 0.475$)	products ($\lambda = 0.80$)
neutral Asp27 in QM	PM3	5.5 (−9.9) ^a	1.9 (−14.1)
	HF	4.5	6.1
	DFT	2.9	4.8
in MM	PM3	7.1 (−9.3)	5.5 (−10.7)
ionized Asp27 in QM	PM3	2.5 (−9.0)	4.5 (−14.1)
	HF	7.9	7.3
	DFT	9.1	9.7
in MM	PM3	8.7 (−11.1)	7.2 (−8.6)

^a Free energies in parentheses were calculated using a 12 Å radius for the neglect of nonbonded interactions between atoms in the QM and MM regions.

mol.⁵⁷ Note that in the present simulations all atomic motions have been treated classically. If we include the 3 kcal/mol correction term for the effects of quantized vibrations,² we estimate a value of 21 ± 2 kcal/mol for the activation free energy. The DFT calculations yield a similar result for the activation free energy of ca. 25 kcal/mol (Figure 8). This result is unexpected given that in vacuo calculations on fragment complexes^{6,7} show that PM3 consistently produces higher energy barriers compared with single-point DFT calculations carried out at the corresponding PM3 optimized geometries. The results in Table 2 show that this discrepancy cannot be rationalized in terms of polarization of the reaction center by the enzyme, as the difference in TS polarization free energy between PM3 and DFT amounts to only 2.6 kcal/mol (neutral Asp27). However, we also found from our fragment study⁶ that optimization of the geometries at the DFT level can give barrier energies quite different from those for single-point calculations at PM3 or some other lower level of geometry optimization. This analysis suggests there may be some important differences between the semiempirical and DFT energy surfaces.

Polarization Free Energy. The polarization free energy arises from distortion of the continuous electron charge distribution of the QM region in the electrostatic field of the discrete point charges in the MM region. The polarization contribution to the free-energy change along the reaction coordinate may thus be defined as

$$\Delta\Delta G_{\text{pol}} = \Delta G(\mathbf{P}) - \Delta G(\mathbf{P}_0) \quad (12)$$

where \mathbf{P} is the density matrix of the QM region obtained from a calculation in which the charge field of the MM region polarizes the QM region and \mathbf{P}_0 is obtained when this charge field is switched off in the calculation of the density matrix. Note that $\Delta G(\mathbf{P})$ and $\Delta G(\mathbf{P}_0)$ are computed from separate simulations. The polarization free energies at the TS ($\lambda = 0.475$) and product state ($\lambda = 0.8$), relative to the reactant state ($\lambda = 0.1$), are shown in Table 2 and were obtained from simulations using $N_{\text{proc}} = 8$ and MFEP/48. The results obtained in the present study using a 12 Å radius as the cutoff for the neglect of interactions between the QM and MM regions (Table 2) are very similar to the 9 kcal/mol stabilization of the TS relative to reactants that was

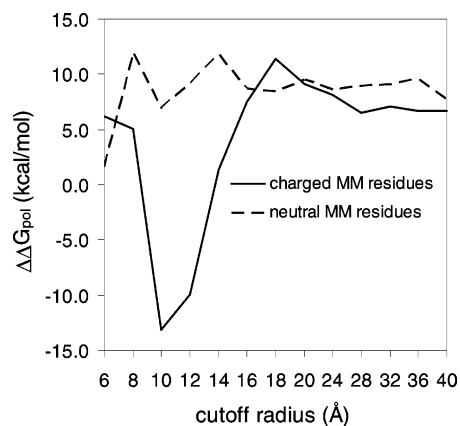


Figure 9. Polarization contribution (PM3 level) to the activation free energy as a function of cutoff for neglect of QM/MM interactions for both charged and neutral residues (see text) in the MM region, with Asp27·DHFH⁺·NADPH (neutral Asp27) as the QM region.

obtained by Garcia-Viloca et al.¹² using the same cutoff. However, on removing the cutoff for the QM/MM interaction, we found that polarization by the whole enzyme actually *destabilizes* the TS relative to reactants. The PM3-QM/MM polarization free energies are in broad agreement with the corresponding results obtained using the higher-level HF and DFT QM/MM methods. Thus, we may conclude, at least for this system, that the computationally less demanding semiempirical PM3 method can account for the bulk of the polarization effect and produce reliable estimates of the relative polarization free energies. Note also that the polarization free-energy differences between neutral and ionized Asp27, and the effect on the polarization free energy of moving Asp27 between QM and MM regions, are also not very large. But note again that the effect on the *total* free-energy differences due to these changes can be substantially greater.

The large increase in the magnitude of the polarization contribution obtained using a 12 Å cutoff can be explained largely in terms of the dipoles formed by ion pairs in the enzyme being split as a result of the application of the (residue-based) cutoff to the QM/MM interactions. The anomalous charge effect produced by the split dipole can be eliminated simply by neutralizing all acidic and basic residues in the MM region of the enzyme. However, rather than physically adding or deleting protons on the enzyme in order to gauge the magnitude of the split dipole effect, we have simply added a constant partial charge to each of the atoms in the ionized residues to enforce electrical neutrality. This was done only for the calculation of the free energy and not for the calculation of forces in the MD, so it does not otherwise affect the MD trajectory. The polarization component as a function of cutoff distance is shown Figure 9. In the calculation of the free energy using the normal residue charge state, the dip in the polarization contribution at around 12 Å is evident. However, the fluctuations with respect to cutoff distances are greatly reduced when all MM residues are made neutral.

Conclusions

In summary, using the semiempirical PM3-QM/MM method together with the TI formalism,^{32,33,53} we mapped a sufficiently large part of the free-energy surface to allow us to obtain a precise MFEP for the hydride-ion transfer catalyzed by DHFR. For an accurate representation of the free-energy change along the reaction path, we found that it was necessary to include the whole substrate and cofactor molecules in the QM region of the active-site complex. For a model where the conserved active-site Asp27 residue is considered to be ionized, it also must be included in the QM region. Our calculations also show that electronic polarization by the enzyme actually *increases* the free energy of activation for the hydride-ion transfer and does not stabilize products either. Furthermore, we found that this polarization contribution was very sensitive to the neglect of electrostatic interactions between QM and MM atoms beyond a cutoff radius.

The MEFP obtained for the neutral state of Asp27 was found to be more consistent with the experimentally determined activation and reaction free energies⁵⁷ than that for the ionized state. This result adds further support to our findings in previous studies^{5,6} that protonation of Asp27 is an essential factor in the activation mechanism. However, as complementary DFT calculations along the MEFP showed some discrepancies which may be due to the accuracy of the semiempirical representation of the free-energy surface, we are working on further methodological refinements which will allow a more definitive assessment of the Asp27 protonation mechanism.

Acknowledgment. We acknowledge support from Australian Research Council (ARC) Grants DP0346292 and DP0665816, the ANU (Australian National University) IAS (Institute of Advanced Studies) block grant, and APAC (Australian Partnership for Advanced Computing) National Facility and ANU Supercomputer Facility computer-time grants.

References

- Blakely, R. L. In *Advances in Enzymology and Related Areas in Molecular Biology*; Meister, A., Eds.; John Wiley: New York, 1995; Vol. 70, pp 23–102.
- Garcia-Viloca, M.; Truhlar, D. G.; Gao, J. *Biochem.* **2003**, *42*, 13558–13575.
- Hammes-Schiffer, S. *Curr. Opin. Struct. Biol.* **2004**, *14*, 192–201.
- Castillo, R.; Andres, J.; Moliner, V. *J. Am. Chem. Soc.* **1999**, *121*, 12140–12147.
- Cummins, P. L.; Gready, J. E. *J. Am. Chem. Soc.* **2001**, *123*, 3418–3428.
- Cummins, P. L.; Greatbanks, S. P.; Rendell, A. P.; Gready, J. E. *J. Phys. Chem. B* **2002**, *106*, 9934–9944.
- Thorpe, I. F.; Brooks, C. L., III. *J. Phys. Chem. B* **2003**, *107*, 14042–14051.
- Thorpe, I. F.; Brooks, C. L., III. *Proteins: Struct., Funct., Bioinf.* **2004**, *57*, 444–457.
- Thorpe, I. F.; Brooks, C. L., III. *J. Am. Chem. Soc.* **2005**, *127*, 12997–13006.
- Greatbanks, S. P.; Gready, J. E.; Limaye, A. C.; Rendell, A. P. *Proteins: Struct., Funct., Genet.* **1999**, *37*, 157–165.
- Greatbanks, S. P.; Gready, J. E.; Limaye, A. C.; Rendell, A. P. *J. Comput. Chem.* **2000**, *21*, 788–811.
- Garcia-Viloca, M.; Truhlar, D. G.; Gao, J. *J. Mol. Biol.* **2003**, *327*, 549–560.
- Garcia-Viloca, M.; Gao, J.; Karplus, M.; Truhlar, D. G. *Science* **2004**, *303*, 186–195.
- Warshel, A. *Annu. Rev. Biophys. Biomol. Struct.* **2003**, *32*, 425–443.
- Kollman, P. A.; Kuhn, B.; Donini, O.; Perakyla, M.; Stanton, R.; Bakowies, D. *Acc. Chem. Res.* **2001**, *34*, 72–79.
- Warshel, A.; Levitt, M. *J. Mol. Biol.* **1976**, *103*, 227–249.
- Singh, U. C.; Kollman, P. A. *J. Comput. Chem.* **1986**, *7*, 718–730.
- Field, M. J.; Bash, P. A.; Karplus, M. *J. Comput. Chem.* **1990**, *11*, 700–733.
- Gao, J.; Xia, X. *Science* **1992**, *258*, 631.
- Gao, J. In *Reviews in Computational Chemistry*; Lipkowitz, K. B.; Boyd, D. B., Eds.; VHC Publishers: New York, 1996; Vol. 7, pp 119–185.
- Bakowies, D.; Thiel, W. *J. Phys. Chem.* **1996**, *100*, 10580–10594.
- Friesner, R. A.; Beachy, M. D. *Curr. Opin. Struct. Biol.* **1998**, *8*, 257–262.
- Merz, K. M., Jr.; Stanton, R. V. In *Encyclopedia of Computational Chemistry*; Wiley: New York, 1998; pp 2330–2343.
- Tomasi, J. In *Encyclopedia of Computational Chemistry*; Wiley: New York, 1998; pp 2343–2350.
- Dapprich, S.; Komaromi, I.; Byun, K. S.; Morokuma, K.; Frisch, M. J. *THEOCHEM* **1999**, *462*, 1–21.
- Murphy, R. B.; Phillipp, D. M.; Friesner, R. A. *J. Comput. Chem.* **2000**, *21*, 1442–1457.
- Luque, F. J.; Reuter, N.; Cartier, A.; Ruiz-Lopez, M. F. *J. Phys. Chem. A* **2000**, *104*, 10923–10931.
- Vreven, T.; Morokuma, K. *Theor. Chem. Acc.* **2003**, *109*, 125–132.
- Lu, Z.; Yang, W. *J. Chem. Phys.* **2004**, *121*, 89–100.
- Vreven, T.; Byun, K. S.; Komaromi, I.; Dapprich, S.; Montgomery, J. A., Jr.; Morokuma, K.; Frisch, M. J. *J. Chem. Theory Comput.* **2006**, *2*, 815–826.
- Rosta, E.; Klahn, M.; Warshel, A. *J. Phys. Chem. B* **2006**, *110*, 2934–2941.
- Mezei, M.; Beveridge, D. L. *Ann. N.Y. Acad. Sci.* **1986**, *482*, 1–23.
- Straatsma, T. P. In *Reviews in Computational Chemistry*; Lipkowitz, K. B.; Boyd, D. B., Eds.; VHC Publishers: New York, 1996; Vol. 9, pp 81–127.
- Huennekens, F. M.; Scrimgeour, K. G. In *Pteridine Chemistry*; Pfeleiderer, W., Taylor, E. C., Eds.; Pergamon Press: New York, 1964; pp 355–376.
- Cummins, P. L.; Gready, J. E. *J. Comput. Chem.* **1997**, *18*, 1496–1512.

- (36) Cummins, P. L.; Gready, J. E. *J. Comput. Chem.* **1999**, *20*, 1028–1038.
- (37) Sawaya, M. R.; Kraut, J. *Biochemistry* **1997**, *36*, 586–603.
- (38) *Insight II*, release 2000.1; Accelrys Inc.: San Diego, CA, 2002.
- (39) Cornell, W. D.; Cieplak, P.; Bayly, C. I.; Gould, I. R.; Merz, K. M., Jr.; Ferguson, D. M.; Spellmeyer, D. C.; Fox, T.; Caldwell, J. W.; Kollman, P. A. *J. Am. Chem. Soc.* **1995**, *117*, 5179–5197.
- (40) Jorgensen, W. L.; Chandrasekhar, J.; Madura, J. D.; Impey, R. W.; Klein, M. L. *J. Chem. Phys.* **1983**, *79*, 926–935.
- (41) Gao, J.; Xia, X. *J. Am. Chem. Soc.* **1993**, *115*, 9667–9675.
- (42) Bash, P. A.; Ho, L. L.; MacKerell, A. D., Jr.; Levine, D.; Hallstrom, P. *Proc. Natl. Acad. Sci. U.S.A.* **1996**, *93*, 3698–3703.
- (43) Ho, L. L.; MacKerell, A. D., Jr.; Bash, P. A. *J. Phys. Chem.* **1996**, *100*, 4466–4475.
- (44) Strajbl, M.; Florian, J.; Warshel, A. *J. Phys. Chem. B* **2001**, *105*, 4471–4484.
- (45) Cui, Q.; Karplus, M. *J. Phys. Chem. B* **2002**, *106*, 1768–1798.
- (46) Poulsen, T. D.; Garcia-Viloca, M.; Gao, J.; Truhlar, D. G. *J. Phys. Chem. B* **2003**, *107*, 9567–9578.
- (47) Rajamani, R.; Naidoo, K. J.; Gao, J. *J. Comput. Chem.* **2003**, *24*, 1775–1781.
- (48) Gready, J. E.; Rostov, I.; Cummins, P. L. In *Modelling Molecular Structure and Reactivity in Biological Systems*; Naidoo, K. J., Hann, M., Gao, J., Field, M., Brady, J., Eds.; Royal Society of Chemistry: London, 2006; pp 101–118.
- (49) Sugita, Y.; Okamoto, Y. *Chem. Phys. Lett.* **1999**, *314*, 141–151.
- (50) Mitsutake, A.; Sugita, Y.; Okamoto, Y. *Biopolymers* **2001**, *60*, 96–123.
- (51) Zuckerman, D. M.; Lyman, E. *J. Chem. Theory Comput.* **2006**, *2*, 1200–1202.
- (52) van Gunsteren, W. F.; Berendsen, H. J. C. *Mol. Phys.* **1977**, *34*, 1311–1327.
- (53) Pearlman, D. A. *J. Chem. Phys.* **1993**, *98*, 8946–8957.
- (54) Cummins, P. L. *Molecular Orbital Programs for Simulations (MOPS)*; Australian National University: Canberra, Australia, 1996.
- (55) Frisch, M. J.; Trucks, G. W.; Schlegel, H. B.; Scuseria, G. E.; Robb, M. A.; Cheeseman, J. R.; Montgomery, J. A., Jr.; Vreven, T.; Kudin, K. N.; Burant, J. C.; Millam, J. M.; Iyengar, S. S.; Tomasi, J.; Barone, V.; Mennucci, B.; Cossi, M.; Scalmani, G.; Rega, N.; Petersson, G. A.; Nakatsuji, H.; Hada, M.; Ehara, M.; Toyota, K.; Fukuda, R.; Hasegawa, J.; Ishida, M.; Nakajima, T.; Honda, Y.; Kitao, O.; Nakai, H.; Klene, M.; Li, X.; Knox, J. E.; Hratchian, H. P.; Cross, J. B.; Bakken, V.; Adamo, C.; Jaramillo, J.; Gomperts, R.; Stratmann, R. E.; Yazyev, O.; Austin, A. J.; Cammi, R.; Pomelli, C.; Ochterski, J. W.; Ayala, P. Y.; Morokuma, K.; Voth, G. A.; Salvador, P.; Dannenberg, J. J.; Zakrzewski, V. G.; Dapprich, S.; Daniels, A. D.; Strain, M. C.; Farkas, O.; Malick, D. K.; Rabuck, A. D.; Raghavachari, K.; Foresman, J. B.; Ortiz, J. V.; Cui, Q.; Baboul, A. G.; Clifford, S.; Cioslowski, J.; Stefanov, B. B.; Liu, G.; Liashenko, A.; Piskorz, P.; Komaromi, I.; Martin, R. L.; Fox, D. J.; Keith, T.; Al-Laham, M. A.; Peng, C. Y.; Nanayakkara, A.; Challacombe, M.; Gill, P. M. W.; Johnson, B.; Chen, W.; Wong, M. W.; Gonzalez, C.; Pople, J. A. *Gaussian 03*, revision C.02; Gaussian Inc.: Wallingford, CT, 2004.
- (56) Cummins, P. L.; Gready, J. E. *J. Comput. Chem.* **1998**, *19*, 977–988.
- (57) Fierke, C. A.; Johnson, K. A.; Benkovic, S. J. *Biochemistry* **1987**, *26*, 4085–4092.

CT600313B

Structural and Energetic Properties of Organometallic Ruthenium(II) Diamine Anticancer Compounds and Their Interaction with Nucleobases

Christian Gossens, Ivano Tavernelli, and Ursula Rothlisberger*

Institut des Sciences et Ingénierie Chimiques, Ecole Polytechnique Fédérale de Lausanne (EPFL), CH-1015 Lausanne, Switzerland

Received January 17, 2007

Abstract: We rationalize the chemoselectivity of the monofunctional ruthenium anticancer compound $[(\eta^6\text{-arene})\text{Ru}(\text{II})(\text{en})(\text{OH}_2)]^{2+}$ (en=ethylenediamine; arene=benzene **1**, *p*-cymene **2**) toward guanine, using static DFT (BP86) and MP2 calculations together with Car–Parrinello molecular dynamics. The calculated binding energies for the three investigated nucleobases (G, A, C) decreases in the order $\text{G}(\text{N}7) \gg \text{C}(\text{O}2) \sim \text{C}(\text{N}3) > \text{A}(\text{N}7) > \text{G}(\text{O}6) > \text{OH}_2$. The G(N7) complex is the most stable product due to a hydrogen bond of its O6 with one of the H₂N-amine groups of en, while the corresponding NH₂–H₂N(en) interaction in the adenine complex is repulsive. A very low rotational barrier of 0.17 kcal/mol (BP86) and 0.64 kcal/mol (MP2) was calculated for the arene rotation in $[(\eta^6\text{-C}_6\text{H}_6)\text{Ru}(\text{en})(\text{Cl})]^+$ (**3**) allowing complexes containing arenes with bulky side chains like *p*-cymene to minimize steric interactions with, e.g., DNA by simple arene rotation. All $[(\eta^6\text{-arene})\text{Ru}(\text{en})(\text{L})]^{2+}$ compounds exist in two stable conformers obtained for different diamine dihedral angle (NCCN) orientation, which, in the case of asymmetric ligands L, differ by up to ~2.8 kcal/mol. Car–Parrinello dynamics reveal a chelating transition state for the interconversion between N7 and O6 binding of guanine to $[(\eta^6\text{-arene})\text{Ru}(\text{en})]^{2+}$.

Introduction

The discovery of cisplatin $[\text{Pt}(\text{NH}_3)_2(\text{Cl})_2]$ ¹ as an anticancer drug^{2,3} has stimulated the search for other transition-metal complexes with even higher activity.⁴ In the last decades, this search resulted mainly in related platinum based complexes which made their way to the clinics.⁵ However, problems related to toxicity, selectivity, and resistance have limited their therapeutic application.⁶ More recently, ruthenium complexes have attracted particular attention because of their potentially high in vivo antitumor activity and selectivity, together with their low general toxicity. Some of these compounds have already entered clinical trials.^{7,8} Whereas inorganic ruthenium coordination complexes have been investigated for some years, organoruthenium compounds have moved into the focus of anticancer research only recently. So far, all of these complexes are based on a ruthenium(II) containing organometallic moieties of the type

$[(\eta^6\text{-arene})\text{Ru}]^{2+}$,^{9–12} $[(\eta^5\text{-cyclopentadienyl})\text{Ru}]^+$,^{13,14} or $[(1,4,7\text{-trithiacyclononane})\text{Ru}]^{2+}$.¹⁵ The remaining three coordination sites in these pseudo-octahedral complexes, which exhibit a so-called “piano stool” geometry, can be occupied by various monodentate or chelating ligands.

A common feature to all these compounds is the presence of at least one leaving group, as for instance the chloro ligand in $[(\eta^6\text{-arene})\text{Ru}(\text{en})(\text{Cl})]^+$ (where en=ethylenediamine). It was shown experimentally that these chloro species hydrolyze like cisplatin only at very low chloride concentration (e.g., inside a human cell), while no hydrolysis occurs at higher chloride concentrations (e.g., in the human blood stream).¹⁶ As for cisplatin, the cellular (nuclear) DNA is considered the most relevant biological target, and it was shown experimentally that a hydrolyzed ruthenium arene diamine can indeed bind to oligonucleotides.¹⁷ Crystal structures have been published showing such binding of $[(\eta^6\text{-arene})\text{Ru}(\text{en})]^{2+}$ (arene=biphenyl; 5,8,9,10-tetrahydroanthracene; 9,10-dihydroanthracene) to the N7 atom of guanine

* Corresponding author e-mail: ursula.rothlisberger@epfl.ch.

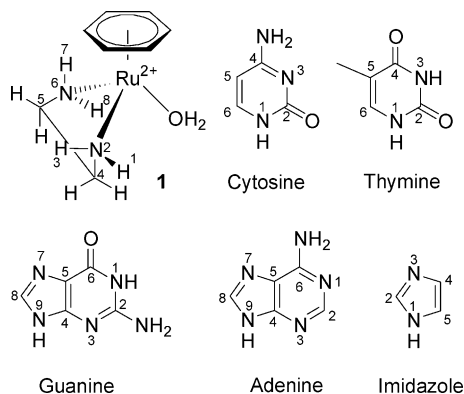


Figure 1. The hydrolyzed $[(\eta^6\text{-benzene})\text{Ru}(\text{en})(\text{OH}_2)]^{2+}$ (**1**) and nucleobases that can replace the aqua ligand. Imidazole is also shown.

derivatives, and stereospecific hydrogen bonding of the en amino hydrogen to the guanine O6 has been proposed.¹⁸

In a previous study we showed how computational tools can be applied to these organometallic systems in order to obtain energetic and structural information suitable to interpret mass spectrometric experiments.^{19,20} This work is the first of a series of studies aiming at the understanding of the atomistic steps involved in the process that starting from the hydrolysis of the aqua species leads to the binding of organoruthenium compounds to double stranded DNA (ds-DNA). Here we focus on a rigorous analysis of all elementary degrees of freedom that may be involved in the interaction of different $[(\eta^6\text{-arene})\text{Ru}(\text{II})(\text{en})(\text{L}))^{n+}$ (arene=benzene, *p*-cymene; L = Cl, H₂O, adenine, guanine, cytosine, imidazole) compounds with DNA bases. Based on this information, we calculate the corresponding thermodynamic binding energies (BE) to nucleobases with the intent to rationalize the experimentally observed preference of guanine N7 among the potential metalation sites in nucleobases (Figures 1 and S1).²¹

Computational Details

Except stated otherwise, all calculations were carried out using density functional theory at the generalized gradient approximation (GGA) level of theory as implemented in the ADF 2004.01 package.²² We used the BP86^{23,24} exchange-correlation energy functional and the “TZP” basis set of the ADF package. This basis set is of triple- ζ quality with one polarization function in the valence region and a double- ζ representation in the core region. The frozen core approximation (for electrons up to main quantum number $n = 1$ for C,N,O; up to $n = 2$ for Cl; $n = 3$ for Ru) and a spin-restricted formalism were applied. As shown in previous calculations, the investigated compounds can be treated as closed shell systems.¹⁹ The ZORA approach was used to incorporate scalar relativistic effects.²⁵ The general numerical integration (gni) precision parameter was generally increased to 5.0 except for the en dihedral calculations for which it was even increased to 10.0. For all calculations presented here, we applied very tight convergence criteria (energy: $E=1\text{E-}4$ hartree; gradients: Grad= $1\text{E-}3$ hartree/Å; Cartesian coordinates: Coord= $1\text{E-}3$ Å) as the default values are not sufficient for proper convergence. This is true in particular

for the transition state search (eigenvector following approach) in which we were forced to use even tighter convergence criteria (gni=7.0, $E=1\text{E-}5$ hartree; Grad= $1\text{E-}4$ hartree/Å; Coord= $1\text{E-}3$ Å). Forces in the frequency analysis were calculated via a 2-point numerical differentiation with gni=6.0. All transition states (TS) discussed in this text are characterized by a single imaginary frequency. The ligand binding energy (BE) was calculated as $E\{[(\text{arene})\text{Ru}(\text{en})]^{2+} + [\text{L}]\} - E\{[(\text{arene})\text{Ru}(\text{L})(\text{en})]^{2+}\}$ with all fragments fully geometry optimized. COSMO calculations were conducted on gas-phase geometries (gni=7.0, parameters as in ref 9).

For the calculations on the arene rotation we used the Gaussian03 package.²⁶ We applied the BP86 exchange-correlation energy functional with a mixed basis set using the quasirelativistic Stuttgart/Dresden semicore SDD-ECP²⁷ with a (8s7p6d)/[6s5p3d]-GTO triple- ζ valence basis set on the ruthenium atoms and 6-31+G(d) on the remaining atoms. The same basis was used for geometry optimizations at the MP2 level of theory. Investigations on the absolute orientation of the *p*-cymene ligand were performed using the BP86 functional and the LanL2DZ basis which consists of the D95V²⁸ basis for hydrogen, carbon, nitrogen, and oxygen and the Los Alamos National Laboratories effective semicore potentials (ECP) (relativistic for Ru) in combination with a double- ζ basis for chlorine and ruthenium.²⁹

The CPMD³⁰ program was used for all Car–Parrinello molecular dynamics (CPMD) calculations. In this case, an analytical local pseudopotential (PP) for hydrogen atoms and nonlocal, norm-conserving soft PPs of the Martins–Trouiller³¹ type for all other elements were used. The explicitly treated valence electrons were kept equal to the ones used in the ADF calculations. The PP for ruthenium includes scalar relativistic effects. The PPs for C, N, and O were transformed to a fully nonlocal form using the scheme of Kleinman and Bylander,³² whereas for Ru the semicore PP was integrated numerically using a Gauss-Hermite quadrature. The BP86 exchange-correlation energy functional was used with an energy cut off of 75 Rydberg, a time step of 4 au (0.097 fs), a fictitious electron mass of 400 au, an orbital convergence of $1\text{E-}6$, and a temperature of 310 K except where stated different. Figures were done with Molekel.³³

Results and Discussion

Arene Rotation. Experimental and theoretical investigations have shown the rotational energetic barrier of arene ligands in organometallic complexes to be very low (~ 0.5 kcal/mol $[(\eta^6\text{-benzene})\text{Cr}(\text{CO})_3]$, ~ 2.5 kcal/mol in $[(\eta^6\text{-C}_6\text{H}_6)\text{Ru}\{\kappa^3\text{-HB}(\text{pz})_3\}]^+$).^{34–36} In our CPMD simulations we observed even at temperatures lower than 310 K a full rotation of the benzene ligand in $[(\eta^6\text{-C}_6\text{H}_6)\text{Ru}(\text{en})(\text{N7}\{\text{G}\})]^{2+}$ (**4**) on the ps time scale. There seemed to be no effective rotational barrier for rotation at temperatures higher than 150 K. Using DFT and the BP86 functional, we calculated a rotational energy barrier in $[(\eta^6\text{-C}_6\text{H}_6)\text{Ru}(\text{en})(\text{Cl})]^+$ (**3**) of 0.17 kcal/mol in correspondence with the rotated geometry in Figure 2. A frequency analysis showed a very small vibrational energy (15 cm^{-1}) for the slowest frequency mode associated to the arene, which corresponds to a pure rotation of the arene with respect to the $[\text{Ru}(\text{en})(\text{Cl})]^+$ moiety. MP2

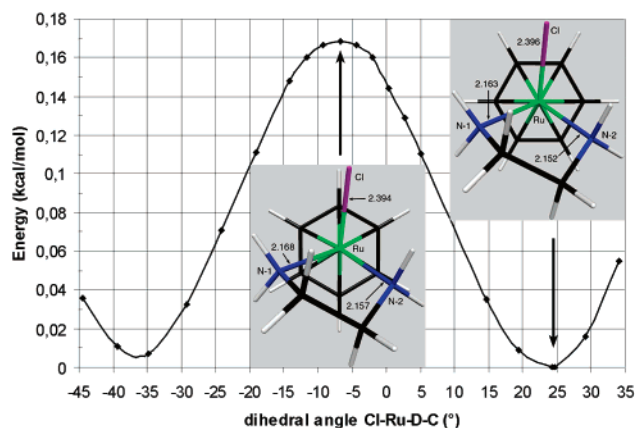


Figure 2. Rotational energy barrier (kcal/mol) of benzene in $[(\eta^6\text{-C}_6\text{H}_6)\text{Ru}(\text{en})(\text{Cl})]^+$ (**3**).

geometry optimization on the DFT energy minimum and maximum (constraint to -7.5°) gave an energy difference of 0.64 kcal/mol. The maximum does correspond to a conformation in which Cl, N-1, N-2 and the corresponding aromatic arene carbons are not eclipsed. Here, the L–Ru–D–C dihedral angles (L = Cl, N-1, N-2; D = arene centroid) are all staggered by -7° to -8° . The same holds for the energy minimum in which the dihedral angles are shifted by -33° to -36° . Interestingly, the ruthenium ligand bond lengths are not affected by the arene rotation. Therefore the nonequivalence of the Ru–N1 and Ru–N2 bonds (difference of 0.01 Å) must have a different origin (see section: dihedral angle of ethylenediamine).

Conformation of *p*-Cymene. The determination of a minimum energy geometry for the ruthenium complexes with a benzene ligand is straightforward. In contrast, the additional degrees of freedom due to the conformation of the methyl and in particular of the *i*-Pr group in the *p*-cymene (1-methyl-4-isopropylbenzene) ligand are of importance for the global stability of $[(\eta^6\text{-cymene})\text{Ru}(\text{en})(\text{L})]^{n+}$ complexes and have to be taken into account. Since the electronic contribution to the rotational barrier is very small, the main contribution comes from steric interactions of the arene with the [Ru(en)(L)] $^{n+}$ moiety. We calculated the conformational minimum of isolated *p*-cymene in vacuo. It shows one hydrogen of its 1-methyl group in the plane of the ring and the two others each one above and one below the aromatic plane. Similar, the *i*-Pr hydrogen lies in the plane of the arene, and one methyl group points above and the other below this plane. To our knowledge, no crystal structure of [cymeneRu(en)(nucleobase)] $^{2+}$ has been published so far. Recent NMR (NOESY) studies³⁷ have addressed the question of the relative conformation of the *p*-cymene ligand with respect to the [Ru(R₁R₂NCH₂CH₂NR₁R₂)(Cl)] $^+$ moiety, however, without addressing the issue related to the conformations of the *i*-Pr group relative to the benzene moiety. They propose as the most abundant conformation the one in which the cymene methyl group is eclipsed to one en nitrogen (in their study, both en nitrogens are assumed to be equivalent), and the *i*-Pr group is located in the less hindered region between the other en-nitrogen and a chloro ligand (Figure 6 in ref 37). This is in agreement with the published crystal structure of $[(\eta^6\text{-cymene})\text{Ru}(\text{en})(\text{Cl})]^+$.¹⁷ Our calculations confirm this

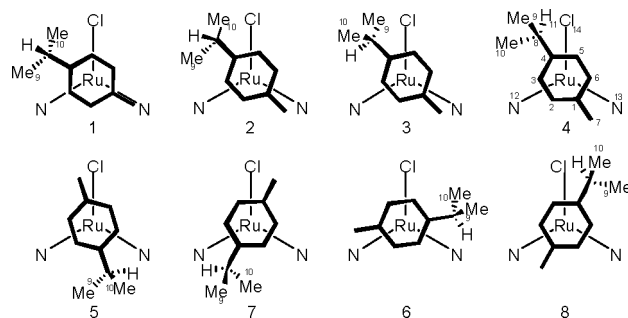


Figure 3. Schematic drawings of geometry optimized structures of $[(\eta^6\text{-cymene})\text{Ru}(\text{en})(\text{Cl})]^+$ showing a top view along the arene-centroid ruthenium axes.

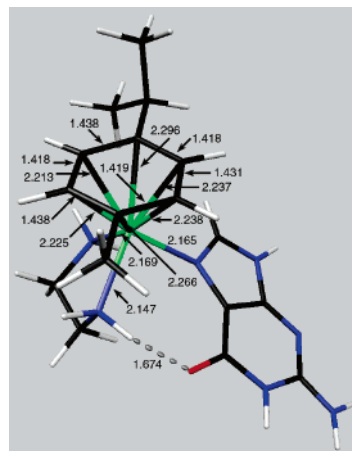


Figure 4. Energy minimized structure of $[(\eta^6\text{-cymene})\text{Ru}(\text{en})(\text{N7}\{\text{G}\})]^{2+}$.

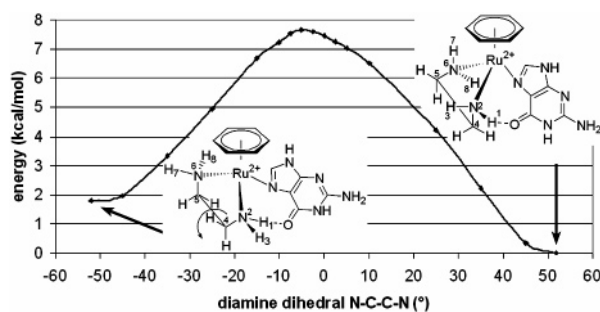


Figure 5. Potential energy (kcal/mol) upon variation of the en dihedral ($\text{N}^6\text{-C}^5\text{-C}^4\text{-N}^2$) in $[(\eta^6\text{-benzene})\text{Ru}(\text{en})(\text{N7}\{\text{G}\})]^{2+}$.

finding (Table 1). However, the above-mentioned crystal structure shows the two methyl groups of the *i*-Pr pointing downward to the ruthenium site. In contrast, at the DFT (BP86, B3LYP, BLYP) and MP2 level of theory we do not find a corresponding energy minimum for this geometry in vacuo, and therefore we conclude that its stabilization may be due to crystal packing effects. Moreover, we do not observe a perfectly eclipsed structure of 7-Me and en 13-N as in the crystal (**1** in Figure 3). Instead, we identified a global minimum in which 7-Me is located in between 12-N and 13-N, and the *i*-Pr group occupies the space between the 12-N and Cl (**4** in Figure 3). The 9-Me is nearly perpendicular to the arene plane pointing away from the ruthenium, while 10-Me points away from the chloro ligand. Starting the optimization from the crystal structure (**1** in Figure 3)

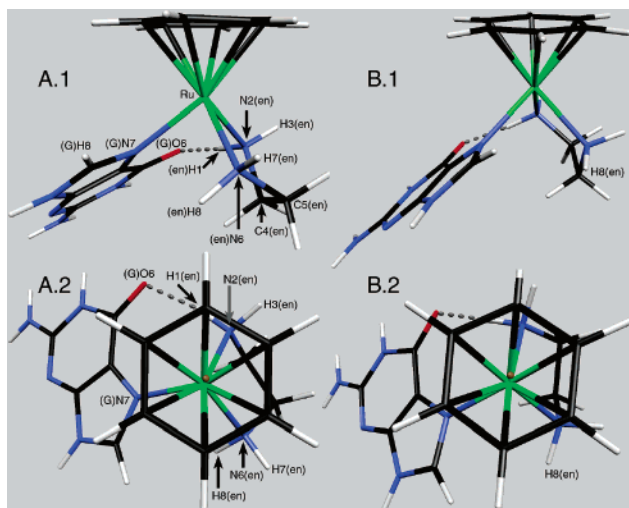


Figure 6. The two stable en conformers of $[(\eta^6\text{-benzene})\text{Ru}(\text{en})(\text{N7}\{\text{G}\})]^{2+}$ show different orientations of the H8(en). In the more stable conformer (left: A.1 (side view), A.2 (top view)), the N6–H8 bond is parallel to the Ru–N7(G) bond, whereas it points away from guanine in the less stable conformer (right: B.1 (side), B.2 (top)).

yields a local minimum (2 in Figure 3) in which 10-Me lies in the arene plane and the 11-hydrogen points away from the complex. However, this structure is 1.85 kcal/mol higher in energy than the global minimum. All geometry optimizations starting directly from the crystal were trapped in this local minimum. Another local minima was identified by further rotating the *i*-Pr group relative to the aromatic moiety (3 in Figure 3). In this structure the 9-Me points toward the Cl which turns out to be less unfavorable than minimum 2 but with an energy which is still 1.09 kcal/mol higher than the global minimum.

Multiple conformations of the arene relative to the $[\text{Ru}(\text{en})(\text{Cl})]^+$ moiety have been sampled. They reveal the importance of the en (N–C–C–N) dihedral angle in $[(\eta^6\text{-arene})\text{Ru}(\text{en})(\text{L})]^{n+}$ complexes. The existing literature has treated the $[\text{Ru}(\text{en})(\text{Cl})]^+$ moiety as an object of C_s symmetry, with a mirror plane (σ) passing through the ruthenium atom, the chloro ligand, and the midpoint between the two en nitrogen atoms (N12/N13). Our results show that this symmetry does not exist, even approximately. The conformer pairs 3/6, 4/8, and 5/7 in Figure 3 therefore cannot be considered enantiomer pairs. Geometry optimizations, starting from the modified structures 3', 4', and 5' in which the cymene has been σ -mirrored compared to the original compounds (3, 4, and 5) while keeping the $[\text{Ru}(\text{en})(\text{Cl})]^+$ moiety unchanged, converge toward the structures 6, 8, and 7, respectively. This explains the difference in energy between the conformers forming the different pairs (Table 1), which amounts to 0.8 kcal/mol, 0.2 kcal/mol, and 0.9 kcal/mol, respectively, and which can only be associated with different en dihedral angle conformations (see section: dihedral angle of ethylenediamine).

The second most stable conformation (5 in Figure 3) shows the *i*-Pr group occupying the space between the two en nitrogens. Again, the cymene is most stable in a conformation that resembles that of its isolated form. As can be seen from

Table 1, the en dihedral does not change in all these conformers, nor does any ligand bond length. In fact, it is the steric interaction of both the 8-C and the 7-Me to the other ligands (Cl, N12, and N13) that has to be optimized in order to minimize the total energy of the complex. In total, our results are in full agreement with the NMR experiment of ref 37. However, our findings show that the assumption of an energy minimum in which the 7-Me is fully eclipsed is most probably not correct but can be traced back to a crystallographic artifact in the solid state.

The energy landscape becomes even more complex once the symmetric chloro ligand is replaced by a less symmetric ligand, e.g., guanine. As binding to dsDNA is thought to be the biologically relevant step, we started from a *p*-cymene conformer taken from a QM/MM study in which the $[(\eta^6\text{-cymene})\text{Ru}(\text{en})]^{2+}$ moiety is bound to a 12-mer dsDNA and the *i*-Pr group points in the direction of the DNA major groove.^{38,39} We performed 1.4 ps of unconstrained Car–Parrinello molecular dynamics (CPMD) starting from $[(\eta^6\text{-cymene})\text{Ru}(\text{en})(\text{N7}\{\text{G}\})]^{2+}$. The system was first equilibrated for 0.4 ps at 150 K and then heated successively up to 450 K. During the entire simulation time, the strong H-bond between the O6(G) and the en-NH₂ group proved to be stable. In fact, this H-bond acts like a second weak coordination bond between the guanine ligand and the ruthenium moiety, providing additional thermal stability to the complex. The cymene did only slightly fluctuate between the initial conformer and a second one, in which the vector connecting the 7-Me and 8-C is parallel to the en N12–N13 axis. As no conformational change of the *i*-Pr group was observed and because of the agreement with the results reported above for the chloro species, we took this structure as a starting point for further geometry optimizations. The resulting conformer shows, like the most stable chloro species (4 in Figure 3), one methyl group of the *i*-Pr nearly perpendicular (82.4°) to the arene plane, while the other points away from the guanine H8 (Figure 4).⁴⁰ In this structure, the *i*-Pr group occupies the free region of space in between the N7(G) and the en-NH₂, which is larger than the space between the O6(G) and the corresponding en-NH₂, as the latter are kept close together by a strong H-bond. The average aromatic bond of the arene is slightly elongated compared to the isolated cymene (1.427 vs 1.401 Å). Moreover, the aromaticity is perturbed as shown by the alternating C–C bond lengths (1.438 vs 1.418 Å). The two Ru–N(en) bonds are not identical but differ by 0.022 Å. We observed a similar picture in the analogous benzene compound **4** in which they differ by 0.028 Å (2.166 on N7 side vs 2.138 on O6 side). Surprisingly, the difference in bond length is also evident in $[\text{benzeneRu}(\text{en})(\text{Cl})]^+$, even though in this case it amounts only to 0.013 Å. This indicates that the two en amino groups are not equivalent even in the case in which the other ligands around the ruthenium center are highly symmetric. Interestingly, in the case of all investigated guanine(N7) complexes, the difference in the two Ru–N(en) bond lengths does not invert when the diamine dihedral angle (NCCN) inverts. This indicates that it is more the global environment due to the guanine ligand (N7, O6) than the direct interactions of the en-NH₂ or the arene that causes this asymmetry.

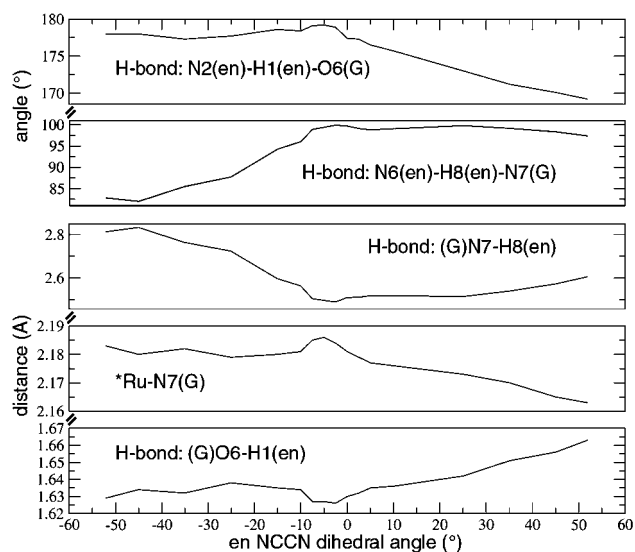
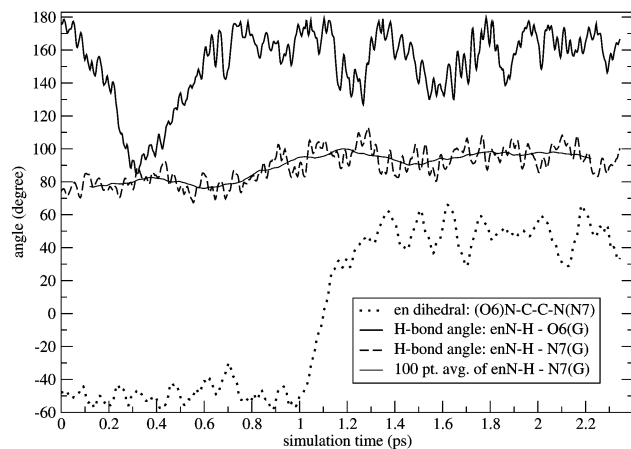
Table 1. Relative Energies, Selected Dihedral Angles (deg), and Distances (Å) of Representative *p*-Cymene Conformations in [cymeneRu(en)(Cl)]⁺ as Depicted in Figure 3

	1	2	3	4	5	6	7	8
energy	crystal ^c	1.85	1.09	0.00	0.07	0.27	0.93	0.19
N ¹² –C–C–N ¹³	52.6	50.4	50.4	50.5	50.3	50.4	50.5	50.4
Cl–Ru–D ^a –C ⁷	–118.3	–137.1	–137.0	–150.9	28.9	–26.9	105.9	152.4
C ⁵ –C ⁴ –C ⁸ –H ¹¹	–89.2	–113.7	144.5	38.5	146.8	36.217	33.4	139.8
C ⁸ –Cl/N ^{12/13 b}	4.069	4.002	4.070	3.686	3.648	3.886	3.958	3.688
C ⁷ –Cl/N ^{12/13 b}	3.271	3.639	3.626	3.806	3.839	3.638	3.605	3.830

^a D: centroid of arene. ^b Distance between carbon and Cl or N¹² or N¹³ (whatever atom is closest). ^c Geometry optimization (keeping only the cymene carbon atoms frozen) yielded 7.30 kcal/mol.

Dihedral Angle of Ethylenediamine (en). Another important conformational degree of freedom consists in an inversion of the dihedral angle (N²C⁴C⁵N⁶) of the chelating diamine ligand (Figures 5, 6, and S2). In contrast to compounds with small, highly symmetric ligands like halogens, the two conformers are no longer energetically equivalent in the case of a less symmetric ligand L, such as guanine. For the purines, guanine and adenine, we found that one of the diamine conformers is always more stable, namely the one, in which the N6(en)–H8(en) bond is nearly parallel to the Ru–L (L = N7{A/G}, O6{G}) bond (Figures 6, 12, and S2). Whereas a diamine dihedral angle change does not cause a significant energy difference in the case of symmetric ligands (H₂O, imidazole), it amounts up to 1.8 kcal/mol for guanine (see Figure 5). This explains why in all reported crystal structures of the type [(η⁶-arene)Ru(en*)(N7{G*})]²⁺ (*=various modifications) only this conformer is observed.^{18,41} The TS between the two stable conformers was calculated to be at a dihedral angle of ~ –5°. For the transition from a negative to a positive dihedral angle, the activation energy amounts to 5.9 kcal/mol and 7.7 kcal/mol for the transition from the negative to the positive. This barrier height can be overcome easily in a biological system. This result shows that the en dihedral could easily adapt to a changing environment, a flexibility which may become essential during the approach of the ruthenium complex to a guanine in dsDNA.

Both the arene and the guanine ligand can easily adapt to changes in the geometry of the [Ru(en)]²⁺ moiety. The H-bond between the O6(G) and the en-NH₂ is maintained in all geometry optimizations along the dihedral angle profile. Along the path connecting the less stable to the more stable conformer (Figure 5), we observed the following trends. As can be seen from Figure 7, the (G)O6–H1(en) hydrogen bond is getting weaker and elongates from 1.629 to 1.663 Å, while the (en)N2–H1(en)–O6(G) angle decreases from 178° to 169°. Simultaneously, the Ru–N7(G) bond is getting stronger with a consequent shortening of 0.02 Å (2.183 vs 2.163 Å). However, the largest change concerns the (en)H8 orientation. It points to the N7(G) in the more stable conformer and away from the guanine in the less stable conformer (Figures 6, 7, and S2). As a consequence the (G)-N7–H8(en) distance shortens by 0.217 Å in the more stable conformer (from 2.813 to 2.606 Å) and at the same time the angle (en)N6–H8(en)–N7(G) increases from 82.8° to 97.4°. This results in a sort of H-bond between the (en)H8 and the N7(G) in addition to the Ru–N7 bond which overcompensates the weakening of the (en)N2–H1(en)–O6(G) H-bond.

**Figure 7.** Selected distances (Å) and H-bond angles (deg) upon variation of the diamine (NCCN) dihedral in [(η⁶-benzene)Ru(en)(N7{G})]²⁺. Numbering as in Figure 5.**Figure 8.** Selected dihedral and H-bond angles during a CPMD simulation of [(η⁶-benzene)Ru(en)(N7{G})]²⁺ at 310 K.

In a CPMD simulation at 310 K, we observed a rapid conformational change of the diamine dihedral angle. The transition from the negative to the positive dihedral angle (Figure 5) occurs within the first 1 ps (Figure 8). After an initial distortion of the H-bond angle (G)O6–H1(en)–N2(en), we observe a strengthening of this H-bond, characterized by an average angle of 160° and an average (G)O6–H1(en) distance of 1.7 Å (Figures 8 and 9). The shortening of the Ru–N7(G) bond length observed in the static approach

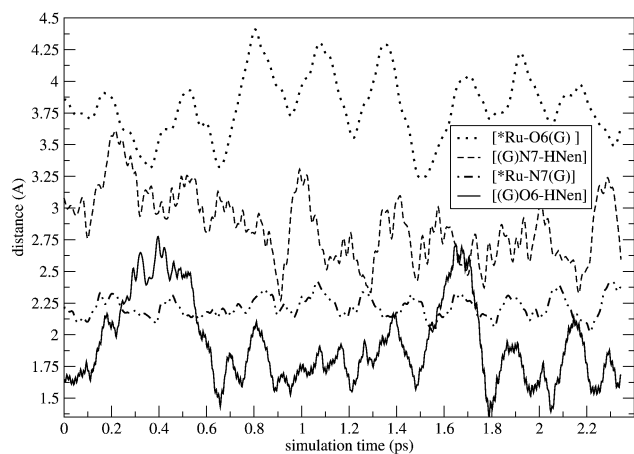


Figure 9. Selected distances during a CPMD simulation of $[(\eta^6\text{-benzene})\text{Ru}(\text{en})(\text{N7}\{\text{G}\})]^{2+}$ at 310 K.

is not easily detectable in the MD simulation due to the thermal fluctuation and the short sampling. In contrast, one can clearly see the shortening of the (G)N7–H8(en) that precedes the NCCN dihedral flip (Figure 9). Starting from an initial value of ~ 3 Å, the hydrogen atom approaches the N7 as close as 2.25 Å just before the dihedral angle flip and relaxes to distances around 2.6 Å after the transition. A similar strengthening was observed for the “H-bond” angle between (en)N6–H8(en)–N7(G), which fluctuates around 80° before the dihedral transition and around 95° afterward. It is worth mentioning that during the simulation, the benzene rotated by $\sim 180^\circ$.

Thermodynamic Stability of Aqua vs Nucleobase Complexes. At typical chloride concentrations found inside human cells, compounds of the type $[(\eta^6\text{-arene})\text{Ru}(\text{en})(\text{Cl})]^+$ undergo substantial aquation.¹⁶ The chloro ligand acts as leaving group to form the corresponding aqua species $[(\eta^6\text{-arene})\text{Ru}(\text{en})(\text{OH}_2)]^{2+}$, which itself is very prompt to undergo a ligand exchange reaction and to form a Ru–N or Ru–O bond with a nucleobase.¹⁶ In the presence of all four different DNA nucleobases, experiments show a very high selectivity for the N7 atom of guanine. For the most relevant nucleobase binding sites, a decrease in reactivity and relative stabilities is observed in the order $\text{G}(\text{N7}) \gg \text{C}(\text{N3}) \gg \text{A}(\text{N7}, \text{N1})$ (Figure S1).⁴² Our computed ligand binding energies (BE) in vacuo (Table 2) and in “aqueous solution” (Table 2) show exactly the same trend as measured experimentally, and, moreover, they allow to quantify the thermodynamic stability of the biological relevant Ru–nucleobase complexes over the aqua species.⁴³ All nucleobases form stronger bonds with the ruthenium moiety than with a water ligand. Therefore, from a thermodynamic point of view, the aqua species should undergo a spontaneous ligand exchange reaction with a nucleobase when the activation energy is not too high. However, the presence of possible side reactions may prevent such a ligand exchange to occur. In addition, the eventual low concentration of the nucleobase in aqueous solution may favor a permanent hydrolysis of the Ru–nucleobase product once it is formed. The in vacuo BEs (Table 2) for the nucleobase and aqua ligands for the benzene complexes are 3.1 (H_2O) to 7.3 (guanine) kcal/mol higher than for *p*-cymene compounds, which is most probably due to repulsive steric

interactions of the more bulky cymene with the monodentate ligands. We already observed the same trend in the case of the monodentate pta ligand in cymene vs benzene $[(\eta^6\text{-arene})\text{Ru}(\text{Cl})_2(\text{pta})]$ compounds.¹⁹ However, configurational and conformational changes in the aliphatic side chains of the arene have hardly any effect on the orbitals of the complex.²⁰ Figures 10–13 show the optimized structures for the most stable conformers of $[(\eta^6\text{-arene})\text{Ru}(\text{en})(\text{L})]^{2+}$ (L = guanine, cytosine, imidazole, adenine, and aqua) for benzene and cymene, respectively. All complexes have the characteristic geometry of a three legged “piano stool” (Tables 3 and S1). The planar arene is η^6 -bound to the ruthenium center, and the chelating ethylenediamine shows the typical dihedral angle of $\sim 52^\circ$. The remaining coordination site is occupied by a nucleobase ligand which prefers to bind via the aromatic sp^2 nitrogen atom in the case of guanine and adenine. For cytosine we calculated a more stable complex when it is bound via its carbonyl $\text{C2}=\text{O}$. In all these complexes, the ruthenium atom lies nearly in the aromatic plane of the nucleobase. The gas-phase BEs are substantially reduced when we simulated an aqueous environment using the conductor-like screening model (COSMO). Moreover, we observe significant shifts of the relative stabilities in particular for complexes containing solvent accessible exocyclic oxygen (Table 2).

The highest BE was computed for the guanine(N7)–ruthenium complex. Here, a very strong H-bond between the $\text{C6}=\text{O}$ of guanine and a proton of the en amino group contributes to the stability of the system. The obtained minimal structure shows the formation of a 7-membered ring between $\text{Ru}-\text{G}\{\text{N7}, \text{C5}, \text{C6}, \text{O6}\}-\text{en}\{\text{H1}, \text{N2}\}$ (Figure 6). The same happens in an analogous complex in which the guanine binds via its O6 to the ruthenium center (Figures 12 and 13). This $\text{Ru}-\text{O6}(\text{G})$ complex shows a hydrogen bond between the N7(G) and an en hydrogen. The relative stability of the $\text{Ru}-\text{N7}(\text{G})$ vs the $\text{Ru}-\text{O6}(\text{G})$ complex changes substantially when we simulate the systems in an aqueous environment. Whereas the $\text{Ru}-\text{O6}$ complex is in vacuo only slightly (3 kcal/mol) less stable than the $\text{Ru}-\text{N7}$ complex, this difference amounts to 11.3 kcal/mol in the solvation model (Table 2). Apparently, the O6 has a stronger solvent interaction in the $\text{Ru}-\text{N7}$ complex in which it is less buried and therefore more solvent accessible than in the $\text{Ru}-\text{O6}$ complex. The sp^2 hybridized cyclic N7(G), however, does not show further stabilization in solution once it has formed a hydrogen bond to an en- NH_2 group.

Similarly, cytosine can either bind to ruthenium via its N3 or $\text{C2}=\text{O}$ atoms. In the N3 case, a 6-membered ring $\text{Ru}-\text{G}\{\text{N3}, \text{C2}, \text{O2}\}-\text{en}\{\text{H1}, \text{N2}\}$ is formed by a strong H-bond via the adjacent cytosine $\text{C2}=\text{O}$ to one en- NH_2 . However, the other en amino group is repulsive toward the cytosine $\text{C4}-\text{NH}_2$ group. In order to reduce this strain, the cytosine $\text{C4}-\text{NH}_2$ group changes slightly hybridization from sp^2 to sp^3 . This not only allows for H-bonding but also contributes to the destabilization of the complex, as the $\text{C4}-\text{NH}_2$ group can no longer take part in the aromatic system. On the other hand, when the cytosine is binding to the ruthenium via its $\text{C2}=\text{O}$ atom, the steric interaction between these two amino groups is reduced due to the fact that they are more distant (Figure

Table 2. Gas Phase and Solution (COSMO) Ligand Binding Energies of $[(\eta^6\text{-arene})\text{Ru}(\text{en})(\text{L})]^{2+}$ ^a

arene			OH ₂	A(N7)	Im(N3)	C(N3)	C(O2)	G(N7)	G(O6)
<i>p</i> -cymene		abs.	23.5 (n.a.)	44.5 (43.2)	54.0 (n.a.)	58.6 (57.5)	66.5 (66.1)	70.2 (68.7)	66.8 (64.7)
benzene	gas	abs.	26.6 (n.a.)	51.3 (49.7)	60.3 (n.a.)	65.4 (64.7)	73.7 (73.0)	77.5 (76.3)	74.5 (71.7)
		rel.	0.0	24.7	33.7	38.8	47.1	50.9	47.9
	COSMO	abs.	16.5	23.3	31.1	24.7	25.0	32.7	21.4
		rel.	0.0	6.8	14.6	8.2	8.5	16.2	4.9

^a BEs for the less stable diamine conformer are given in brackets. Energies in kcal/mol; benzene structures as depicted in Figure 10, cymene structures as in Figure 11; identical orientation of the cymene ligand in both en conformers.

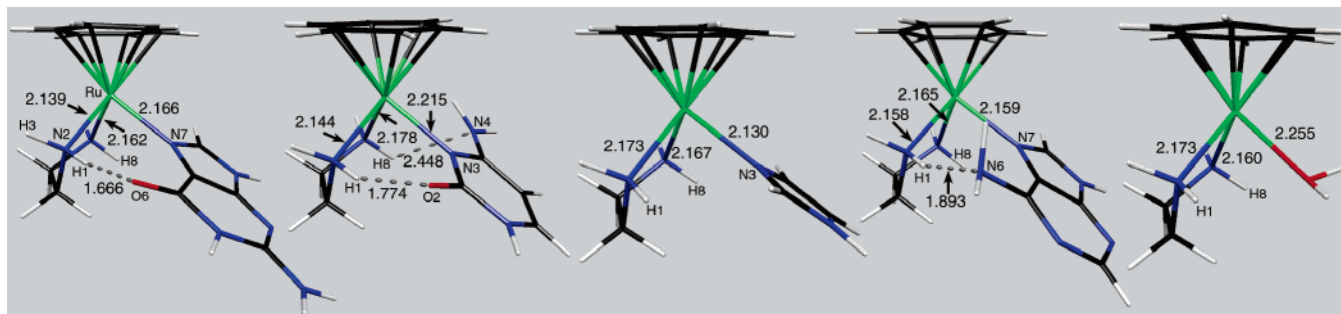


Figure 10. Energy minimized $(\eta^6\text{-benzene})\text{Ru}(\text{en})(\text{L})]^{2+}$ with L = guanine, cytosine, imidazole, adenine, and aqua (from left to right) binding via nitrogen. Only the most stable en conformers are shown.

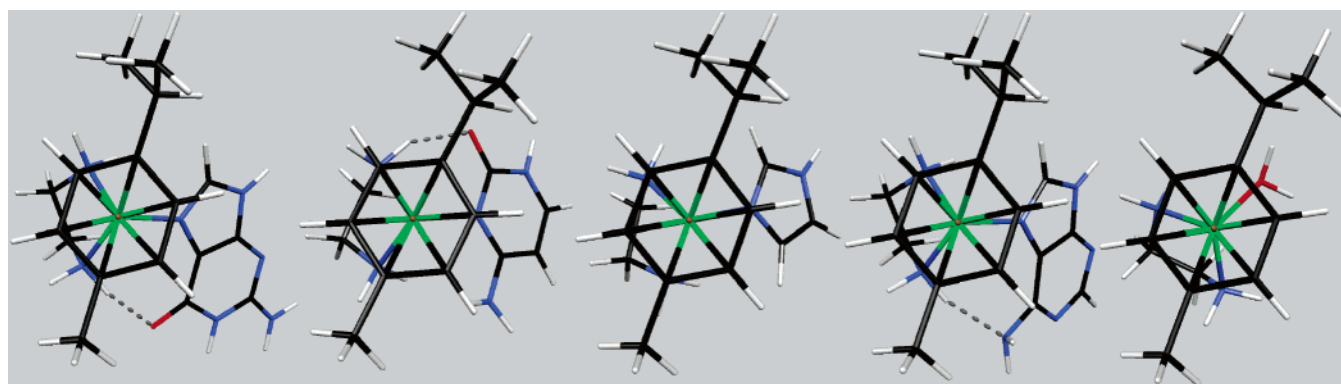


Figure 11. Energy minimized $(\eta^6\text{-cymene})\text{Ru}(\text{en})(\text{L})]^{2+}$ with L = guanine, cytosine, imidazole, adenine, and aqua (from left to right) binding via nitrogen. Only the most stable en conformers are shown.

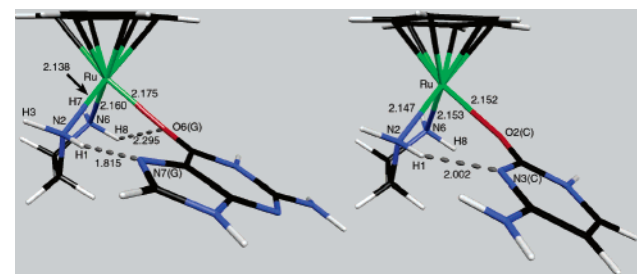


Figure 12. Energy minimized $(\eta^6\text{-benzene})\text{Ru}(\text{en})(\text{L})]^{2+}$ (L = guanine(left), cytosine(right)) binding via oxygen. Only the most stable en conformers are shown.

12, 13). In this configuration, it is the cytosine N2 atom that now forms an H-bond with the en amino hydrogen H1 (Figure 12). As a consequence, the Ru–O2(cytosine) complex is in vacuo 8.3 kcal/mol more stable than the Ru–N3-(cytosine) complex. However, using the COSMO hydration method this difference reduces to only 0.3 kcal/mol (Table 2). As in the case of guanine–O6, hydration of the exo-cyclic C=O is crucial for the stabilization of the Ru–N3(cytosine) complex.⁴⁴

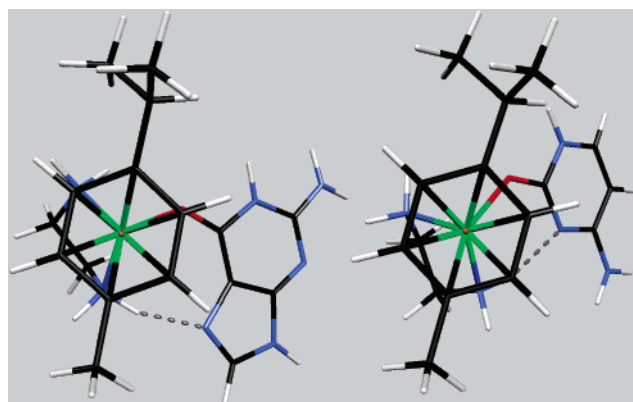


Figure 13. Energy minimized $(\eta^6\text{-cymene})\text{Ru}(\text{en})(\text{L})]^{2+}$ (L = guanine(left), cytosine(right)) binding via oxygen. Only the most stable en conformers are shown.

Interestingly, the complex in which adenine is bound via its N7 atom is significantly less stable (in vacuo 26.2; with COSMO 9.4 kcal/mol) than the analogous guanine compound. This rationalizes the experimental observation that guanine is exclusively preferred over adenine. In the

Table 3. Selected Geometries of the More Stable En Conformer of $[(\eta^6\text{-benzene})\text{Ru}(\text{en})(\text{L})]^{2+}$ ^a

	OH ₂	A(N7)	Im(N3)	C(N3)	G(N7)
Ru–D ^b	1.721 (1.715)	1.740 (1.742)	1.736 (1.732)	1.738 (1.741)	1.734 (1.735)
Ru–N6 _{en}	2.160 (2.163)	2.165 (2.168)	2.167 (2.177)	2.178 (2.185)	2.166 (2.169)
Ru–N2 _{en}	2.173 (2.179)	2.158 (2.169)	2.173 (2.176)	2.144 (2.147)	2.138 (2.147)
Ru–L	2.255 (2.264)	2.159 (2.162)	2.130 (2.133)	2.215 (2.227)	2.163 (2.165)
N6 _{en} –Ru–N2 _{en}	78.0 (78.0)	77.9 (77.7)	77.9 (77.8)	77.8 (77.8)	78.4 (78.1)
L–Ru–N6 _{en}	79.9 (79.4)	85.0 (84.8)	85.3 (85.0)	87.1 (86.8)	84.9 (85.2)
L–Ru–N2 _{en}	83.3 (85.4)	87.5 (87.7)	85.6 (86.5)	85.1 (85.5)	86.8 (87.3)
D–Ru–L	130.9 (128.7)	127.9 (128.2)	127.7 (127.7)	128.1 (128.7)	127.8 (127.5)
D–Ru–N6 _{en}	132.6 (133.4)	130.7 (130.6)	131.4 (131.1)	132.9 (131.8)	132.0 (132.0)
D–Ru–N2 _{en}	132.0 (132.3)	130.5 (130.6)	131.4 (131.2)	128.4 (128.7)	129.7 (129.6)
N2 _{en} –C–C–6 _{en}	52.1 (51.9)	52.3 (52.3)	53.1 (53.0)	51.8 (51.9)	52.0 (51.8)

^a In parentheses $[(\eta^6\text{-cymene})\text{Ru}(\text{en})(\text{L})]^{2+}$. Distances in Å, angles in degrees; benzene structures as depicted in Figure 10, cymene as in Figure 11, numbering in analogy to Figure 5. ^b Centroid of ring.

adenine–ruthenium complex, the amino group in the adenine C6 position is sp^3 hybridized. In this way it forms a weak H-bond with its lone pair to an en-hydrogen and thereby reduces the repulsion between both of the amino-hydrogens on the en and the adenine.

In order to better understand the role played by the different substitutions in the 6-position of guanine (C6=O) and adenine (C6–NH₂), we have also investigated the binding affinity of imidazole (Im) to the ruthenium complex. Its BE turns out to be in between the BE of guanine and adenine indicating that the adjacent donor groups on the 6-membered purine ring play an important role in the enhancement of the overall thermodynamic stability of the complexes. Moreover, this result suggests that the amino group in adenine is not directly involved in a stabilizing H-bond with the en moiety of the ruthenium complex. One possible explanation for this observation is related to the change of hybridization ($sp^2 \rightarrow sp^3$) that the adenine amino group undergoes to adapt to the diamine ligand. It reduces the H–H repulsion with the en-H1 and moreover allows for H-bonding via its lone pair. However, the loss of the π -contribution of the NH₂ to the aromatic system of the ring is responsible for the lower BE of adenine compared to guanine.

Comparing the COSMO BEs of the A(N7), Im(N3), and G(N7) complexes, one can see the strong influence of hydration on the C6=O of guanine. Whereas hydration reduces the relative stability of the A(N7) versus the Im(N3) complex only slightly (vacuum 9.0 vs with COSMO 7.8 kcal/mol), we calculated a significant stabilization of the G(N7) complex compared to the Im(N3) complex (in vacuo 17.2 vs with COSMO 1.6 kcal/mol). These results suggest that in solution the adenine C6–NH₂ group is responsible for a destabilization of ~ 7.8 kcal/mol, whereas the guanine C6=O adds via its H-bond an additional ~ 1.6 kcal/mol to the overall BE. Overall, we observed large solvent effects, but the main trends are conserved for all ruthenium complexes, namely the preference of binding to nucleobases over water and the strong preference of N7 binding to guanine.

Finally, it is worth mentioning that the aqua complex shows very similar geometries compared to the chloro species and analogous crystal structures.¹⁶ Moreover, the structural parameters of the benzene and cymene complexes are almost identical (Table 3).

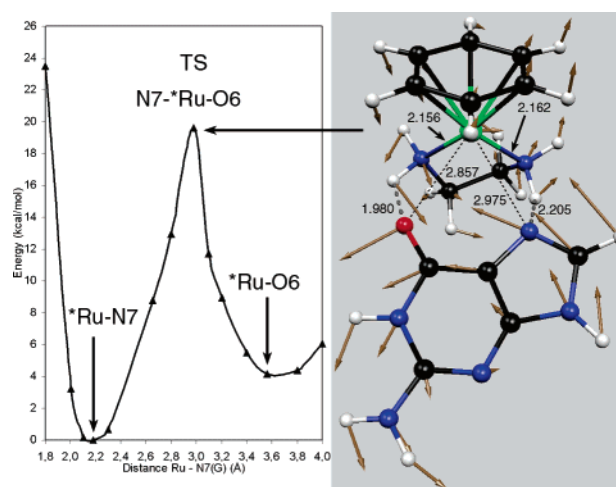


Figure 14. Potential energy of $[(\eta^6\text{-benzene})\text{Ru}(\text{en})(\text{guanine})]^{2+}$ as a function of the ruthenium–N7(G) distance for the interconversion between the Ru–N7(G) and Ru–O6(G) complex.

Interconversion of N7 to O6 Binding of Guanine. The coordination of guanine to the $[(\eta^6\text{-benzene})\text{Ru}(\text{en})]^{2+}$ results in the formation of stable complexes via both the guanine O6 or N7 atoms, as can be seen from Table 2. We therefore investigated the intramolecular exchange reaction from N7- to O6-coordination since such a process might be of relevance during the reaction of guanine with $[(\eta^6\text{-benzene})\text{Ru}(\text{en})(\text{OH}_2)]^{2+}$. To this end we performed constrained CPMD simulations along the Ru–N7(G) distance which allows for relaxation of the system along all other thermally accessible degrees of freedom. Constraint geometry optimization of snapshots taken from these CPMD simulations yielded structures and potential energies for increasing Ru–N7 distances which are shown in Figures 14 and 15. The O6(G) keeps H-bonding to an en–NH₂ group and does not respond very slowly to changes in the Ru–N7 bond length. However, once the Ru–N7 distance is longer than ~ 2.8 Å, the system can overcome an activation barrier to form a Ru–O6(G) complex. The increase of the Ru–N7(G) distance is closely followed by the formation of a hydrogen bond between N7(G) and en–NH₂. Simultaneously, the O6(G) binds to the ruthenium center and the hydrogen bond to the en–NH₂ breaks. A frequency analysis of the identified transition state (TS) connecting the two states Ru–N7(G)

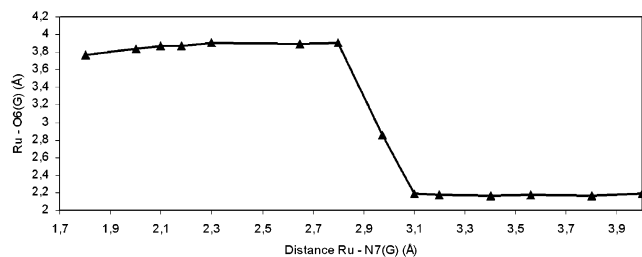


Figure 15. Distances of Ru–O6(G) in $[(\eta^6\text{-benzene})\text{Ru}(\text{en})\text{-}(\text{guanine})]^{2+}$ as a function of the ruthenium–N7(G) distance for the interconversion between the Ru–N7(G) and Ru–O6(G) complex.

and Ru–O6(G) gives one imaginary frequency (visualized as arrows in Figure 14). At this geometry, the ruthenium distance to the O6 (2.857 Å) is slightly shorter than the Ru–N7 distance (2.975 Å). Both, the N7 and the O6 atoms each form a hydrogen bond to one of the en-NH₂ groups with distances 2.205 Å/1.980 Å and angles 130.8°/124.4°, respectively. The activation energy for this interconversion process amounts to 19.6 kcal/mol starting from the Ru–N7(G) complex and 15.4 kcal/mol starting from the Ru–O6(G) complex.

Conclusions

We have demonstrated that the rotational energy barrier of the arene in $[(\eta^6\text{-arene})\text{Ru}(\text{en})(\text{L})]^{n+}$ is very small. The main stability factor is related to the minimization of the steric repulsion with all other ligands. In the case of *p*-cymene we find our results in excellent agreement with experimental data. Consequently, even bulkier arenes in complexes of the type $[(\eta^6\text{-arene})\text{Ru}(\text{en})(\text{OH}_2)]^{2+}$ should be able to adapt, by simple rotation, to the biological relevant target dsDNA. This result suggests that force field parametrizations, which rely on nonbonded interactions only, can be applied for the simulation of ruthenium–arene interactions in these complexes. The ethylenediamine dihedral angle plays an important role in the calculation of accurate BEs. However, the barrier to internal rotation, separating the different potential minima, can be overcome at room temperature, and therefore the complex can easily adapt to any potentially relevant biological binding site. The H-bonding pattern of these complexes is extremely nontrivial, and therefore *ab initio* MD becomes an essential tool for the unbiased search of possible reaction free energy profiles. It was also shown that a reasonable reaction coordinate for the description of the Ru–N7(G) bond formation has to take into account additional degrees of freedom, in particular the Ru–O6(G) distance. All tested nucleobases showed higher BEs to $[(\eta^6\text{-arene})\text{Ru}(\text{en})]^{2+}$ than an aqua ligand both in vacuo and with the COSMO solvation model. In agreement with experiments, the guanine(N7) binding to ruthenium was shown to be thermodynamically the most stable. In solution, the guanine C6=O stabilizes the guanine–ruthenium complex by ~1.6 kcal/mol, whereas the adenine C6-NH₂ destabilizes the analogous adenine complex by ~7.8 kcal/mol. In conclusion, our gas-phase calculations are confirmed by our calculations with the COSMO solvation model.

Acknowledgment. Support from the Swiss National Science Foundation (Grant No 200021-100242/1) is gratefully acknowledged.

Supporting Information Available: Additional figures and tables. This material is available free of charge via the Internet at <http://pubs.acs.org>.

References

- (1) Rosenberg, B.; Camp, L. v.; Krigas, T. Inhibition of Cell Division in *Escherichia coli* by Electrolysis Products from a Platinum Electrode. *Nature* **1965**, *205*, 698–699.
- (2) Furtés, M. A.; Alonso, C.; Pérez, J. M. Biochemical modulation of cisplatin mechanisms of action: Enhancement of antitumor activity and circumvention of drug resistance. *Chem. Rev.* **2003**, *103*, 645–662.
- (3) Wang, D.; Lippard, S. J. Cellular processing of platinum anticancer drugs. *Nature Rev. Drug Discovery* **2005**, *4*, 307–320.
- (4) Clarke, M. J.; Zhu, F.; Frasca, D. R. Non-platinum chemotherapeutic metallopharmaceuticals. *Chem. Rev.* **1999**, *99*, 2511–2533.
- (5) Wong, E.; Giandomenico, C. M. Current status of platinum-based antitumor drugs. *Chem. Rev.* **1999**, *99*, 2451–2466.
- (6) Chu, G. Cellular Response to Cisplatin. *J. Biol. Chem.* **1994**, *269*, 787–790.
- (7) Depenbrock, H.; Schmelcher, S.; Peter, R.; Keppler, B. K.; Weirich, G.; Block, T.; Rastetter, J.; Hanauske, A. R. Preclinical activity of trans-indazolium [tetrachlorobisindazolone] (III) (NSC 666158; IndCR; KP 1019) against tumor colony-forming units and hematopoietic progenitor cells. *Eur. J. Cancer* **1997**, *33*, 2404–2410.
- (8) Sava, G.; Alessio, E.; Bergamo, A.; Mestroni, G. Sulfoxide ruthenium complexes: non-toxic tools for the selective treatment of solid tumor metastases. In *Topics in Biological Inorganic Chemistry*; Clarke, M. J., Sadler, P. J., Eds.; Springer: Berlin, Germany, 1999; Vol. 1, pp 143–169.
- (9) Wang, F.; Habtemariam, A.; van der Geer, E. P. L.; Fernandez, R.; Melchart, M.; Deeth, R. J.; Aird, R.; Guichard, S.; Fabbiani, F. P. A.; Lozano-Casal, P.; Oswald, I. D. H.; Jodrell, D. I.; Parsons, S.; Sadler, P. J. Controlling ligand substitution reactions of organometallic complexes: Tuning cancer cell cytotoxicity. *Proc. Natl. Acad. Sci. U.S.A.* **2005**, *102*, 18269–18274.
- (10) Sclaro, C.; Bergamo, A.; Brescacin, L.; Delfino, R.; Cocchietto, M.; Laurenczy, G.; Geldbach, T. J.; Sava, G.; Dyson, P. J. In Vitro and in Vivo Evaluation of Ruthenium(II)-Arene PTA Complexes. *J. Med. Chem.* **2005**, *48*, 4161–4171.
- (11) Gopal, Y. N. V.; Jayaraju, D.; Kondapi, A. K. Inhibition of Topoisomerase II Catalytic Activity by Two Ruthenium Compounds: A Ligand-Dependent Mode of Action. *Biochemistry* **1999**, *38*, 4382–4388.
- (12) Gaiddon, C.; Jeannequin, P.; Bischoff, P.; Pfeffer, M.; Sirlin, C.; Loeffler, J. P. Ruthenium (II)-derived organometallic compounds induce cytostatic and cytotoxic effects on mammalian cancer cell lines through p53-dependent and p53-independent mechanisms. *J. Pharmacol. Exp. Ther.* **2005**, *315*, 1403–1411.

- (13) Akbayeva, D. N.; Gonsalvi, L.; Oberhauser, W.; Peruzzini, M.; Vizza, F.; Brueggeller, P.; Romerosa, A.; Sava, G.; Bergamo, A. Synthesis catalytic properties and biological activity of new water soluble ruthenium cyclopentadienyl PTA complexes [(C5R5)RuCl(PTA)2] (R = H, Me; PTA = 1,3,5-triaza-7-phosphaadamantane). *Chem. Commun.* **2003**, 264–265.
- (14) Romerosa, A.; Campos-Malpartida, T.; Lidrissi, C.; Saoud, M.; Serrano-Ruiz, M.; Peruzzini, M.; Garrido-Cardenas, J. A.; Garcia-Maroto, F. Synthesis, Characterization, and DNA Binding of New Water-Soluble Cyclopentadienyl Ruthenium(II) Complexes Incorporating Phosphines. *Inorg. Chem.* **2006**, *45*, 1289–1298.
- (15) Serli, B.; Zangrando, E.; Gianferrara, T.; Scolaro, C.; Dyson, P. J.; Bergamo, A.; Alessio, E. Is the aromatic fragment of piano-stool ruthenium compounds an essential feature for anticancer activity? The development of New RuII-[9]aneS3 analogues. *Eur. J. Inorg. Chem.* **2005**, 3423–3434.
- (16) Wang, F.; Chen, H.; Parsons, S.; Oswald, I. D. H.; Davidson, J. E.; Sadler, P. J. Kinetics of aquation and anation of ruthenium(II) arene anticancer complexes, acidity and X-ray structures of aqua adducts. *Chem. Eur. J.* **2003**, *9*, 5810–5820.
- (17) Morris, R. E.; Aird, R. E.; Murdoch, P. d. S.; H. Chen, J. C.; Hughes, N. D.; Parsons, S.; Perkin, A.; Boyd, G.; Jodrell, D. I.; Sadler, P. J., Inhibition of cancer cell growth by ruthenium(II) arene complexes. *J. Med. Chem.* **2001**, *44*, 3616–3621.
- (18) Chen, H.; Parkinson, J. A.; Parsons, S.; Coxall, R. A.; Gould, R. O.; Sadler, P. J. Organometallic ruthenium(II) diamine anticancer complexes: Arene-nucleobase stacking and stereospecific hydrogen-bonding in guanine adducts. *J. Am. Chem. Soc.* **2002**, *124*, 3064–3082.
- (19) Dorcier, A.; Dyson, P. J.; Gossens, C.; Rothlisberger, U.; Scopelliti, R.; Tavernelli, I. Binding of Organometallic Ruthenium(II) and Osmium(II) Complexes to an Oligonucleotide: A Combined Mass Spectrometric and Theoretical Study. *Organometallics* **2005**, *24*, 2114–2123.
- (20) Scolaro, C.; Geldbach, T. J.; Rochat, S.; Dorcier, A.; Gossens, C.; Bergamo, A.; Cocchietto, M.; Tavernelli, I.; Sava, G.; Rothlisberger, U.; Dyson, P. J. Influence of Hydrogen-Bonding Substituents on the Cytotoxicity of RAPTA Compounds. *Organometallics* **2006**, *25*, 756–765.
- (21) Reedijk, J. Improved understanding in platinum antitumor chemistry. *Chem. Commun.* **1996**, 801–806.
- (22) Baerends, E. J.; Autschbach, J.; Bérces, A.; Bickelhaupt, F. M.; Bo, C.; Boerrigter, P. M.; Cavallo, L.; Chong, D. P.; Deng, L.; Dickson, R. M.; Ellis, D. E.; van Faassen, M.; Fan, L.; Fischer, T. H.; Fonseca Guerra, C.; van Gisbergen, S. J. A.; Groeneveld, J. A.; Gritsenko, O. V.; Grüning, M.; Harris, F. E.; van den Hoek, P.; Jacob, C. R.; Jacobsen, H.; Jensen, L.; van Kessel, G.; Kootstra, F.; van Lenthe, E.; McCormack, D. A.; Michalak, A.; Neugebauer, J.; Osinga, V. P.; Patchkovskii, S.; Philipsen, P. H. T.; Post, D.; Pye, C. C.; Ravenek, W.; Ros, P.; Schipper, P. R. T.; Schreckenbach, G.; Snijders, J. G.; Solà, M.; Swart, M.; Swerhone, D.; te Velde, G.; Vernooijs, P.; Versluis, L.; Visscher, L.; Visser, O.; Wang, F.; Wesolowski, T. A.; van Wezenbeek, E.; Wiesenekker, G.; Wolff, S. K.; Woo, T. K.; Yakovlev, A. L.; Ziegler, T. *ADF, 2004.01*; SCM, Theoretical Chemistry, Vrije Universiteit: Amsterdam, The Netherlands, 2004.
- (23) Becke, A. D. Density-functional thermochemistry. III. The role of exact exchange. *J. Chem. Phys.* **1993**, *98*, 5648–52.
- (24) Perdew, J. P. Density-functional approximation for the correlation energy of the inhomogeneous electron gas. *Phys. Rev. B* **1986**, *33*, 8822–8824.
- (25) Lenthe, E. v.; Ehlers, A. E.; Baerends, E. J. Geometry optimization in the Zero Order Regular Approximation for relativistic effects. *J. Chem. Phys.* **1999**, *110*, 8943–8953.
- (26) Frisch, M. J.; Trucks, G. W.; Schlegel, H. B.; Scuseria, G. E.; Robb, M. A.; Cheeseman, J. R.; Montgomery, J. A., Jr.; Vreven, T.; Kudin, K. N.; Burant, J. C.; Millam, J. M.; Iyengar, S. S.; Tomasi, J.; Barone, V.; Mennucci, B.; Cossi, M.; Scalmani, G.; Rega, N.; Petersson, G. A.; Nakatsuji, H.; Hada, M.; Ehara, M.; Toyota, K.; Fukuda, R.; Hasegawa, J.; Ishida, M.; Nakajima, T.; Honda, Y.; Kitao, O.; Nakai, H.; Klene, M.; Li, X.; Knox, J. E.; Hratchian, H. P.; Cross, J. B.; Bakken, V.; Adamo, C.; Jaramillo, J.; Gomperts, R.; Stratmann, R. E.; Yazyev, O.; Austin, A. J.; Cammi, R.; Pomelli, C.; Ochterski, J. W.; Ayala, P. Y.; Morokuma, K.; Voth, G. A.; Salvador, P.; Dannenberg, J. J.; Zakrzewski, V. G.; Dapprich, S.; Daniels, A. D.; Strain, M. C.; Farkas, O.; Malick, D. K.; Rabuck, A. D.; Raghavachari, K.; Foresman, J. B.; Ortiz, J. V.; Cui, Q.; Baboul, A. G.; Clifford, S.; Cioslowski, J.; Stefanov, B. B.; Liu, G.; Liashenko, A.; Piskorz, P.; Komaromi, I.; Martin, R. L.; Fox, D. J.; Keith, T.; Al-Laham, M. A.; Peng, C. Y.; Nanayakkara, A.; Challacombe, M.; Gill, P. M. W.; Johnson, B.; Chen, W.; Wong, M. W.; Gonzalez, C.; Pople, J. A. *Gaussian 03, Revision B.03*; Gaussian, Inc.: Wallingford, CT, 2004.
- (27) Andrae, D.; Haeussermann, U.; Dolg, M.; Stoll, H.; Preuss, H. Energy-adjusted ab initio pseudopotentials for the second and third row transition elements. *Theor. Chem. Acc.* **1990**, *77*, 123–41.
- (28) Dunning, T. H.; Hay, P. J. *Gaussian Basis Sets for Molecular Calculations*; Plenum: New York, 1976; Vol. 3, pp 1–28.
- (29) Hay, P. J.; Wadt, W. R. Ab initio effective core potentials for molecular calculations. Potentials for potassium to gold including the outermost core orbitals. *J. Chem. Phys.* **1985**, *82*, 299–310.
- (30) *CPMD*; Copyright IBM Corp 1990–2006; Copyright MPI für Festkörperforschung Stuttgart 1997–2001.
- (31) Troullier, N.; Martins, J. L. Efficient pseudopotentials for plane-wave calculations. *Phys. Rev. B* **1991**, *43*, 1993–2006.
- (32) Kleinman, L.; Bylander, D. M. Efficacious form for model pseudopotentials. *Phys. Rev. Lett.* **1982**, *48*, 1425–8.
- (33) Flükiger, P.; Lüthi, H. P.; Portmann, S.; Weber, J. *MOLEKEL, Version 4.0*; Swiss Center for Scientific Computing: Manno, Switzerland, 2000.
- (34) Bhambri, S.; Bishop, A.; Kaltsoyannis, N.; Tocher, D. A. Synthesis NMR studies molecular orbital calculations on cyclohexadienyl derivatives of (h6-arene)tris(pyrazolyl)-ruthenium(II) compounds. *Dalton Trans.* **1998**, 3379–3390.
- (35) Albright, T. A. Rotational barriers and conformations in transition metal complexes. *Acc. Chem. Res.* **1982**, *15*, 149–55.
- (36) Braga, D. Dynamical processes in crystalline organometallic complexes. *Chem. Rev.* **1992**, *92*, 633–65.
- (37) Zuccaccia, D.; Macchioni, A. An Accurate Methodology to Identify the Level of Aggregation in Solution by PGSE NMR

- Measurements: The Case of Half-Sandwich Diamino Ruthenium(II) Salts. *Organometallics* **2005**, *24*, 3476–3486.
- (38) Gossens, C.; Tavernelli, I.; Rothlisberger, U. Rational design of organoruthenium anticancer compounds. *Chimia* **2005**, *59*, 81–84.
- (39) Colombo, M. C.; Gossens, C.; Tavernelli, I.; Rothlisberger, U. From Enzymatic Catalysis to Anticancer Drugs: QM/MM Car-Parrinello Simulations of Biological Systems. In *Modelling Molecular Structure and Reactivity in Biological Systems*; Naidoo, K. J., Brady, J., Field, M., Gao, J., Hann, M., Eds.; Royal Society of Chemistry: Cambridge, U.K., 2006; Special Vol. WATOC 2005, pp 85–100.
- (40) This corresponds nearly to the most stable conformer found for the isolated *p*-cymene species in which the dihedral is 62.7° and the *i*-Pr hydrogen lies in the arene plane.
- (41) Chen, H.; Parkinson, J. A.; Novakova, O.; Bella, J.; Wang, F.; Dawson, A.; Gould, R.; Parsons, S.; Brabec, V.; Sadler, P. J. Induced-fit recognition of DNA by organometallic complexes with dynamic stereogenic centers. *Proc. Natl. Acad. Sci. U.S.A.* **2003**, *100*, 14623–14628.
- (42) Chen, H.; Parkinson, J. A.; Morris, R. E.; Sadler, P. J. Highly selective binding of organometallic ruthenium ethylenediamine complexes to nucleic acids: Novel recognition mechanism. *J. Am. Chem. Soc.* **2003**, *125*, 173–186.
- (43) In the absence of explicit solvent we decided neither to investigate the binding energies of the chloro species nor of the deprotonated N3-thymine species as both would involve the high energies of unsolvated negatively charged ligands.
- (44) This observation is not in agreement with the interpretation of a pK_a titration experiment carried out on a reaction mixture of $[(\eta^6\text{-biphenyl})\text{Ru}(\text{en})\text{Cl}]^+$ and 5'-CMP in which peaks were assigned to Ru–O(PO₃)CMP and Ru–N3CMP but no one to Ru–O2CMP. Unfortunately, the same experiment with cytidine could not be performed due to the low concentration of the product (ref 42). An experiment with the pure nucleobase cytosine (as in our calculation) was not performed.

CT6003577

Stochastic Search for Isomers of the *sec*-Butyl Cation

Valerije Vrčec,[†] Olga Kronja,^{*,†} and Martin Saunders^{*,‡}

Faculty of Pharmacy and Biochemistry, University of Zagreb, A. Kovačića 1,
10000 Zagreb, Croatia, and Department of Chemistry, Yale University,
New Haven, Connecticut 06520

Received October 18, 2006

Abstract: A stochastic search procedure for locating energy minimum structures was applied to the *sec*-butyl cation. A previously unreported structure **3'** with strong H-hyperconjugative stabilization of the carbocation center was found at several levels of theory (HF, B3LYP, and MP2). The theoretical equilibrium isotope effect (EIE) for the monodeutero isotopomer of **3'** ($K_{\text{eq}} = 1.4$; $t = -130$ °C) indicates that the new structure is likely to be largely responsible for the experimentally observed EIE.

Introduction

Only three simple secondary carbocations have been prepared in stable solution. The isopropyl,¹ *sec*-butyl,² and cyclopentyl³ cations have all yielded valuable and novel information about carbocation rearrangement processes through experimental observations. The isopropyl cation has a basically classical structure with NMR signals for the inside carbon and hydrogen shifted far downfield. These chemical shifts are close to those predicted by current quantum mechanics programs for the bare carbocation. The inside C and H can be shown to exchange with the methyl carbons and hydrogens by the NMR line shape method and also by isotopic labeling, in both cases yielding rates and barriers. Although the first mechanism suggested began with an uphill 1,2 hydride shift to the primary *n*-propyl cation, no minimum has been found on the energy surface near this structure. The experimental data are consistent with a mechanism involving going over a transition state to a protonated-cyclopropane intermediate.¹

The cyclopentyl cation shows a single sharp NMR signal for the carbons and a single line for the protons even at very low temperatures.³ This is evidence for extraordinarily rapid hydrogen shifts over low barriers. However, it can be demonstrated that carbon scrambling in this ion has a high barrier. The 1,2 and 1,3 di-¹³C-labeled cations give distinct CMR signals and do not interconvert up to the stability limit

of the cation. In addition, no conversion to the isomeric methylcyclobutyl cation can be detected even though this cation can be independently prepared and is also stable. It is striking that many attempts to prepare the cyclohexyl cation have failed and have resulted only in the formation of the methylcyclopentyl cation.⁴

The *sec*-butyl cation is probably the most interesting of the three. The *sec*-butyl cation was first examined experimentally in a superacid solution at low temperatures (below -100 °C)^{2,5} and later in the solid state.⁶ ¹³C NMR and ¹H NMR spectra show that the two methyls are very rapidly interconverted. The inside carbons give a single averaged peak as do the three inside hydrogens. This **must** be due to a rapid process since no structure has been suggested which makes the three inside hydrogens equivalent. The barrier must be extremely low since no line-broadening has been seen at very low temperatures in solution. Even studying the ion in the solid state at temperatures close to 0 K has shown no sign of slowing this process.

It can be demonstrated that the inside and outside hydrogens and inside and outside carbons interchange rapidly enough in the stability range for this cation via line shape and isotopic labeling methods. However, even though ¹³C can go back and forth between the inside and outside, not all isotopomers are in equilibrium. Three of the four di-¹³C-labeled ions interconvert, but the fourth one is unchanged over time. This striking result follows directly from the protonated-cyclopropane mechanism which had been proposed for this rearrangement.^{2c}

Examining the NMR chemical shifts (experimental and calculated) and monitoring rearrangements has given us much information about these ions but, fortunately, does not

* Corresponding author phone: +385 1 481 8301 (O.K.); fax: +385 1 485 6201 (O.K.); e-mail: kronja@pharma.hr (O.K.), ms@gaus90.chem.yale.edu (M.S.).

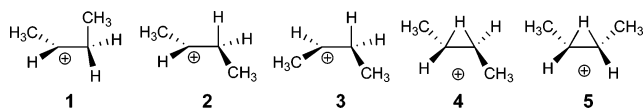
[†] University of Zagreb.

[‡] Yale University.

exhaust our methodology. When there are degenerate and rapid rearrangements, introduction of the isotopes so as to break the degeneracy often produces a substantial splitting in the averaged peaks. This procedure, called the isotopic perturbation method, has been applied to many carbocations (and also to non-carbocation cases).⁷ The 2,3-dimethylbutyl cation yields very large and temperature-dependent splittings as a result of introducing deuterium. This perturbs a rapid rearrangement process involving a degenerate hydride shift.⁸ Quantum mechanical calculation of the Cartesian force constant matrix for an optimized structure for this ion, followed by application of the program QUIVER,⁹ allowed prediction of the equilibrium isotope effects (EIEs) for a large number of deuterated isotopomers for this ion. This enabled an accurate fitting of the splittings in the CMR spectrum. In the norbornyl cation, deuteration induces no observable splitting. This is one of the strongest pieces of evidence for the symmetrically bridged (nonclassical) structure for this ion.

In the *sec*-butyl cation, structures with deuterium on a methyl show substantial splitting in the ¹³C NMR spectrum of the inside carbons. The unusual feature of the splitting is that it becomes larger at higher temperature (10.85 ppm at -134 °C, 10.95 ppm at -130 °C, and 11.02 ppm at -126 °C, respectively). This suggests that at least two different structures exist in solution and that the structure having higher energy induces a larger splitting. The presence of several different minimum-energy structures makes accounting for this splitting both challenging and interesting.

Quantum chemical calculations have been done in the past at the HF/6-31G(d) level on the partially bridged structure **1** with strong C-hyperconjugation and on the open-chain form **2** with H-hyperconjugative stabilization (methyl groups in the trans relation).¹⁰ The open-chain form **3** with methyl groups in the cis relation (C_s symmetry) was located as a transition-state structure. At theoretical levels including electron correlation [MP2(full)/6-31G(d) level, four minima were found: **1**, **2**, and the two symmetrically hydrido-bridged forms **4** and **5** in which methyl groups are in the trans or cis position, respectively. However, isomer **2** refined into a bridged structure **4** when a larger basis set [6-311G(d,p)] was used.^{10a}



Since only structure **1** of all located minimum energy structures undergoes rapid equilibrium interchanging the hydrogen, we calculated the equilibrium isotope effect at -130 °C (experimental temperature) that would produce **1**, using the program QUIVER,⁹ and obtained $K_{eq} = 1.005$. Such a small effect would split the central carbons less than 1 ppm (vs 11 ppm in the experiment). Therefore, it was apparent that a fraction of 2-butyl cations must exist in a form that had not yet been theoretically located on the potential energy surface (PES). At least one additional structure must be responsible for the observed large EIE.

It is highly desirable to locate all of the accessible minimum-energy structures in order to account for experi-

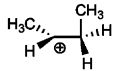
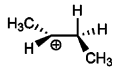
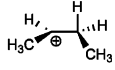
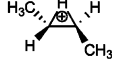
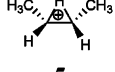


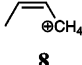
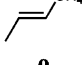
mental results theoretically. Until recently, chemists entered all of the approximate structures that they could think of and then refined each of them using quantum mechanics calculations. Calculations could be done at higher and higher levels in attempting to obtain accurate results. However, if a structure close to one of the minima on the energy surface is not thought of, it will not be found using this procedure. For common molecules with well-defined bonds, it is relatively easy to suggest all of the possible structures. However, carbocations can have fractional bonds of various orders and very unusual geometries. For the *sec*-butyl cation, the known energy surface is so rich that one must be very concerned about the problem of finding all of the important minima. Fortunately, a stochastic search procedure for locating all the isomers on an energy surface defined by quantum chemical calculations has been described recently.^{11,12} The method is analogous to the stochastic random search procedure for finding conformers previously developed and extensively used for molecular mechanics surfaces.¹³ An important feature of these two methods is that intensive enough application is virtually certain to find all of the structures. In applying this method, a starting structure is subjected to a “kick”, which moves each atom in a random direction over a random distance within a sphere of given radius (R), which represent the maximal kick size. Optimization of the kicked structure with a quantum mechanical optimizer could take it back to the initial structure, or it can be refined to give a different isomer. To imagine that there is some minimum which **cannot** be found using this method even with a very large number of kicks, one must conceive of a structure which cannot possibly be produced by a kick. This is hard to imagine. Quantum mechanical calculations can be done at many levels. It is possible that a structure which is a minimum at one level is not a minimum at another level. In principle, stochastic searches could be carried out at all levels, but the computer time required would be very large. A way of improving the likelihood that one has found all minima is to use each of the found minima in turn as the starting point for a new search. If each minimum yields all of the other known minima, that is an encouraging sign.

We applied the stochastic search procedure on the PES of the 2-butyl cation to seek additional structures. We first applied it at the HF level of theory, and then also at B3LYP and MP2 levels.

Results and Discussion

Stochastic Search Procedure at HF Levels. Five different 2-butyl cation isomers were used as initial structures for the stochastic kick procedure at the HF/6-31G(d) level (Table 1): the open-chain forms **1** (C_1 point group, NImag = 0), **2** (C_1 point group, NImag = 0), and **3** (C_s point group, NImag = 1) and the two hydrido-bridged forms **4** (C_2 point group, NImag = 1) and **5** (C_s point group, NImag = 1). The protonated methylcyclopropane **6** (C_1 point group, NImag = 0) was also used as the initial structure in this procedure. Each $C_4H_9^+$ isomer was kicked systematically with kicks ranging from 0.7 to 1.1 Å. It has been found that the convergence failure or fragmentation of the initial structures occurred frequently during optimization if kicks larger than

Table 1. Relative Energies of Structures 1–9 Found by the Stochastic Search Method Performed at the HF, DFT, and MP2 Levels

Structures located by stochastic search method	$\Delta E/\text{kcal mol}^{-1}$ ^a			
	HF/6-31G(d)	B3LYP6-31G(d)	MP2(FU)/6-31G(d)	CCD/6-311G(d,p) ^b
	0	0	0	0
1				
	-0.4	-0.2	2.0	-
2				
	0.1	-0.1	2.3	0.3
3'				
	-	1.0 ^c	1.2	-1.0
4				
	-	1.9 ^d	2.1	-0.03
5				
	14.8	11.7	8.1	8.2
6				
	-14.7	-14.9	-12.9	-14.1
7				
	-	-	48.5	43.3
8				
	-	-	46.6	41.3
9				

^a Relative energies including ZPE corrections. ^b CCD geometry optimization of the corresponding MP2 structures found by stochastic search. ^c First-order saddle point; NImag = 1 (-126; hydride shift). ^d First-order saddle point; NImag = 1 (-180; hydride shift).

1.1 Å were applied. The range of kick sizes between 0.8 and 0.9 Å was found to be optimal for the stochastic search here. Optimizations of kicked structures were easily completed and led to stationary points, and only relatively few fragmentations occurred.

By using the stochastic search method, the additional minimum **3'** (cis isomer) was discovered (Figure 1). The open-chain form **3'** (C_1 point group, NImag = 0) is the CH-hyperconjugative isomer and is similar in geometry to the symmetrical transition structure **3** (C_s point group, NImag = 1) reported previously. The isomer **3'** is stabilized by 2-fold hyperconjugative interaction between C1–H and C3–H bonds and the formally empty 2p orbital at the C2 carbon atom. These C–H bonds are elongated (1.101 and 1.103 Å, respectively).

It has been found that, regardless which of the initial structures **1**–**6** has been used for stochastic search, all other $C_4H_9^+$ isomers could be located, including structure **3'**. In addition to 2-butyl cation isomers (**1**, **2**, and **3'**) and to protonated methylcyclopropane (**6**), the *tert*-butyl cation (**7**)

was also located no matter which starting structure for a search was used. Therefore, every starting structure converged to every other isomer easily, indicating a high probability for the corresponding isomerization. The exception is the *tert*-butyl cation (**7**), which, when used as a starting point for a search, fell back to the initial structure if the optimization converged successfully. The *tert*-butyl cation is much lower in energy and far removed in structure space from all of the *sec*-butyl structures discussed here.

As mentioned above, by applying kicks larger than 1.1 Å, fragmentation of the molecule often occurs. These fragmentation results are interesting since they can be compared with both experimental and theoretical studies of the carbocation rearrangements and carbocation dissociation chemistry.¹⁴ For example, it is shown that metastable $C_4H_9^+$ ions dissociate by the loss of methane or ethene, yielding the fragment 2-propenyl ion $CH_3C^+CH_2$ or the nonclassical $C_2H_5^+$ ion, respectively.¹⁵ These types of dissociation processes observed experimentally in the gas phase were “reproduced” during the geometry optimization of the

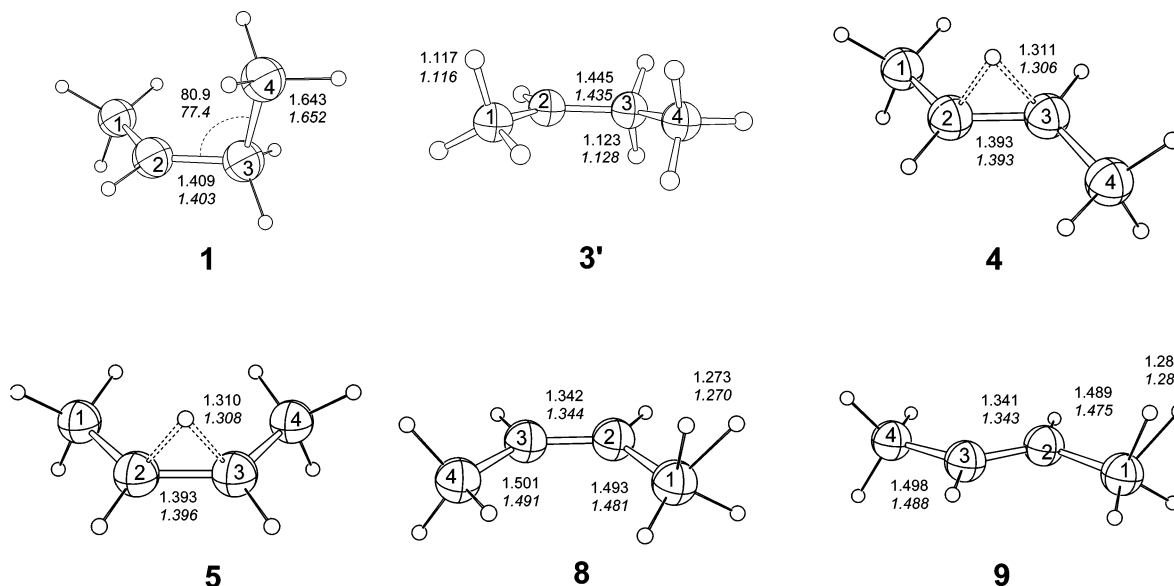


Figure 1. CCD/6-311G(d,p) optimized structures of the 2-butyl cation isomers **1–9** located at the $C_4H_9^+$ PES using the stochastic search method at the MP2(full)/6-31G(d) level (MP2 geometry parameters are in italics). Bond distances are in angstroms; bond angles are in degrees.

corresponding kicked structures. In addition to the elimination of methane and ethene, several geometry optimizations completed with the ethane, carbene CH_2 (yielding the isopropyl cation), or H_2 eliminations.

Stochastic Search Procedure at MP2 and Density Functional Theory (DFT) Levels. The stochastic search procedure for $C_4H_9^+$ isomers was repeated at the MP2(full)/6-31G(d) level of theory, using the same kicked input as for the procedure at the HF/6-31G(d) level. Several new minima, not observed at the HF/6-31G(d) level, were located. Along with structures **1**, **2**, **6**, and **7**, the two hydrido-bridged *trans* (**4**) and *cis* (**5**) forms were found to be minima (Figure 1), which is in agreement with earlier computational studies.^{10a} The open-chain form **3'**, not reported in earlier studies as a minimum at the MP2 level, was located as well. We feel that this structure is likely to be the “missing structure” that is required to account for the experimentally measured equilibrium isotope effect.

Some unusual and unstable (ca. 40 kcal/mol less stable than **1**) $C_4H_9^+$ structures were also discovered this way (Figure 1), such as the methyl-protonated *cis*-butene (**8**) and *trans*-butene (**9**). These two structures are related to studies on the acid-catalyzed isomerization and rearrangements of *n*-butane and 2-butene.¹⁶

Again, it was found that, by using initial structures **1–6** for the stochastic search at the MP2 level, and kicks ranging from 0.7 to 1.1 Å, all other $C_4H_9^+$ isomers (**1–7**) were located. If the *tert*-butyl cation (**7**) was used as an input structure for the stochastic search, the kicking procedure and the subsequent geometry optimization of the corresponding kicked structure always returned to **7**. In comparison with the HF/6-31G(d) level of theory, the number of convergence failures or fragmentations of the initial structures during the geometry optimizations was reduced when the MP2/6-31G(d) level was employed (Table 2). The reason that relatively few structures converged to the *tert*-butyl cation if any of

Table 2. Results of the Stochastic Search Performed by Subjecting the Input Structure **3** to 50 Kicks and Optimizing the Kicked Structures at Different Levels of Theory^{a,b}

HF/6-31G(d) ^{c,d}	B3LYP/6-31G(d) ^{c,d}	MP2(FU)/6-31G(d) ^{c,d}
3' (26)	3' (30)	3' (24)
6 (2)	1 (2)	1 (2)
7 (2)	6 (2)	6 (2)
X (20)	7 (2)	7 (2)
	X (14)	5 (8)
		4 (2)
		8 (2)
		X (8)

^a Initial structure **3** was perturbed by a kick of 0.8 Å. ^b Route section: Opt = Tight, Freq, IOP(5/13 = 1). ^c The bold number represents the energy minimum structure obtained by geometry optimization of the kicked structure; the number in parentheses corresponds to the number of optimization procedures that converged to a given minimum (out of 50 kicks). ^d **X** represents any fragmentation or convergence failure during a geometry optimization procedure.

the $C_4H_9^+$ structure was used as an initial structure is due to the relatively small kick size applied.

Overall, five 2-butyl cation structures (**1**, **2**, **3'**, **4**, and **5**) were located as minima at the MP2(full)/6-31G(d) level, and their relative energies are presented in Table 1. The new minimum **3'**, not reported previously, was found to be the least stable isomer, that is, 4.0 kcal/mol less stable than the partially methyl-bridged structure **1** [0.9 kcal/mol at the HF/6-31G(d) level]. The isomer **3'** is, similarly as on the HF level, characterized by 2-fold hyperconjugative interaction between C1–H and C3–H bonds and the formally empty 2p orbital at the C2 carbon atom.

The results obtained from the stochastic search at the HF/6-31G(d) and MP2(full)/6-31G(d) levels were compared to those obtained with the B3LYP/6-31G(d) method (Tables 1 and 2). Again, three different minima (**1**, **2**, and **3'**) of the 2-butyl cation were discovered using the stochastic method at the DFT level. At the B3LYP/6-31G(d) level, the two

H-bridged *trans* (**4**) and *cis* (**5**) forms, found to be minima at the MP2/6-31G(d) level, were located as transition states for the 1,2-hydride shift in **2** and **3'**, respectively. The stochastic methodology might be also applied in searching for the transition states on an energy surface. However, as was stated before,¹¹ a complete search for transition state structures would take much more computer time (many more kicks needed to find them all).

Once the energy minimum structures were located at the MP2(full)/6-31G(d) level, the results were refined by calculations performed at higher levels of theory. All stationary points located by the stochastic search method at the MP2-(FU)/6-31G(d) level were subjected to optimization and frequency calculation at the CCD/6-311G(d,p) level of theory (Table 1). At this level of theory, structure **2** vanished from the C₄H₉⁺ PES and converged to hydrido-bridged structure **4**. The same was observed at the MP2/6-311G(d,p) and CCD/6-311G(d,p) levels of theory by Schleyer et al.,¹⁷ which suggests that structure **2** cannot be characterized as a minimum. In order to verify that structure **3'** is a real minimum at the PES, its structure was optimized using the larger basis set [6-311G(d,p)] at levels which provide a more sophisticated treatment of electron correlation: MP n , CCD, and QCISD. Similarly as with structure **2**, at the MP2/6-311G(d,p) and MP3/6-311G(d,p) levels, structure **3'** converged to hydrido-bridged structure **5**. However, at the MP4(SDQ)/6-311G(d,p) and CCD/6-311G(d,p) levels of theory, open-chain energy minimum structure **3'** with strong H-hyperconjugation was located. At the former level, it was confirmed that structure **3'** is a minimum; that is, all calculated frequencies were real. The same result was obtained at the CCD level of theory with an extended basis set, 6-311++G(d,p), which includes additional diffusion functions on both carbon and hydrogen atoms. Finally, the QCISD level of theory, which represents a more sophisticated method for the treatment of electron correlation beyond MP4 (and usually providing even greater accuracy), was used for the optimization of structure **3'**. No conversion to the hydrido-bridged structure was observed upon geometry optimization. Therefore, it can be concluded that four different minima (not including structures **8** and **9**) exist on the 2-butyl cation PES: a CC-hyperconjugatively stabilized isomer **1**, a 2-fold CH-hyperconjugatively stabilized isomer **3'**, and two hydrido-bridged structures **4** and **5**. At the CCD/6-311G(d,p) level, hydrido-bridged structure **4** is calculated to be the most stable isomer, but the energies of **1**, **3**, and **5** are in the very narrow range of only 0.3 kcal/mol.

It is important to emphasize again that each of the input structures (**1–6**) converged to all energy minimum structures (**1–7**), which indicates the reliability of the method. The big advantage of the stochastic method is that it is very much less likely to miss structures than the “classical method” in which reasonable guessed starting geometries are used as an input in searching for the structures.

In order to carry out the stochastic search effectively, attention should be focused on the following points:

1. The range of kick size between 0.8 and 0.9 Å is optimal for this stochastic search; that is, most of the optimizations of kicked structures were completed, and only a few

fragmentations occurred. In this kick size range, the fewest kickings are required to discover all the isomers.

2. The efficiency of the optimization of the kicked structures depends on the choice of the coordinate system. Redundant internal coordinates were the best choice for optimizing initial structures.

3. Convergence- and algorithm-related options could be more important to implement when doing stochastic searches on larger molecular systems. It is found that, when the size of the kicked structure is large, the number of convergence failures and fragmentations will increase.

4. Electron-correlated methods, such as MP2, seem to be more effective than HF methods in searching for new isomers.

5. The results of the stochastic search at the DFT level are dependent on the numerical integration grid used in calculations. The number of steps for geometry optimization and the number of imaginary frequencies of isomers located are affected if different grid sizes are applied in DFT calculations.

Equilibrium Isotope Effect of the 2-Butyl Cation. As mentioned above, a new structure **3'** was found to be a minimum at all levels of theory. In order to find out whether the monodeuterated isotopomer of **3'** (one deuterium on the methyl group) can produce splitting of the central carbon in ¹³C NMR that is in accord with the experimental findings, we calculated the EIE with the program QUIVER⁹ using the geometry optimized at the MP2(FU)/6-31G(d) level and obtained $K_{\text{eq}} = 1.396$ (at -130 °C). When the equation $K_{\text{eq}} = (\Delta + \delta)/(\Delta - \delta)$ was used, in which K_{eq} is the equilibrium constant of interchange of the hydrogen between C2 and C3 in the monodeuterated isotopomer, Δ is the chemical shift difference between C2 and C3 carbons in the static carbocation,¹⁸ and δ is the splitting caused by deuterium,¹⁹ it was predicted that the central carbons in the ¹³C NMR spectrum of pure **3'** at -130 °C should be split by 41 ppm. Because of the very flat surface, all four established isomers (**1**, **3'**, **4**, and **5**) interconvert over very low barriers, so the net splitting of the central carbon atoms reflects the weighted average contribution of all structures. Since only **3'** produces considerable splitting of the central carbons, it is expected that the observed splitting will be smaller than that calculated for the pure isomer **3'**. This is in accord with the experimental result (ca. 11 ppm). Experimental observations that the splitting of the central carbons increases at higher temperatures are consistent with theoretical results according to which isomer **3'** is the highest-energy structure of all energy minimum structures of the 2-butyl cation. Therefore, isomer **3'** is indeed likely to be the previously “missing” energy minimum structure on the PES of the 2-butyl cation that is largely responsible for the observed EIE.

Computational Methods

The quantum chemical calculations were performed using the Gaussian 98 program suite.²⁰ All structures were fully optimized using the DFT method (B3LYP) or ab initio methods, (Hartree–Fock, Møller–Plesset perturbation theory, and coupled cluster calculation). The MP2 calculations were performed using the Full option (all electrons included in

the correlation calculation), while coupled cluster calculations were performed using double substitutions from the Hartree–Fock determinant (CCD). The standard split valence and polarized 6-31G(d) basis set was employed in the geometry optimizations and frequency calculations. For comparison, we also carried out calculations with the larger basis set 6-311G(d,p). A vibrational analysis was performed at the same level of theory in order to determine the zero-point vibrational energy (ZPE) and to characterize each stationary point as a minimum (NImag = 0) or transition state structure (NImag = 1). The optimized MP2/6-31G(d) geometries were subjected to geometry optimization and frequency calculations at the CCD/6-311G(d,p) level. Corrections for ZPE (not scaled) are included in the calculated energies. The relative energies are given in kilocalories per mole with respect to the 2-butyl cation isomer **1** and are listed in Table 1.

For comparison, a job completed (geometry optimization successfully converged to one of the isomers) in 70 steps using the HF/6-31G(d) method requires 43 min (RWF = 6 MB), whereas corresponding jobs using the MP2(full)/6-31G(d) or B3LYP/6-31G(d) method require 130 (RWF = 10 MB) or 216 min (RWF = 10 MB), respectively. Frequency calculations at corresponding levels require 4.5 (RWF = 15 MB), 20 (RWF = 299 MB), and 25 (RWF = 15 MB) minutes, respectively. All these calculations were performed as single-processor jobs on a Linux computer with mem = 256 MB and maxdisk = 2000 MB options.

Details of the Stochastic Search at the HF Level. To check whether the results of these isomerizations depend on the coordinates in which structures are optimized (redundant internal coordinates were used as a default), we repeated the geometry optimizations of the kicked structures (with the same input) using Cartesian and internal coordinates (Z matrices). In some cases, the geometry optimization of the kicked structure gave different results when performed in a different coordinate system. For example, the optimization of the initial *cis*-2-butyl cation structure (**3** kicked by 0.8 Å) converged to isomer **1** when using redundant internal coordinates; structure **3'** was obtained when using Cartesian coordinates, and the minimization failed (the CH₂ fragment was “eliminated” and the isopropyl cation formed) when using internal coordinates (Z matrices). In general, the overall results of the stochastic search for C₄H₉⁺ isomers were quite similar regardless to the coordinate system used in the optimization procedure. The same pattern that one isomer gives all others was observed when optimizations of the kicked structures were carried out in the model solvent ($\epsilon = 78.4$ and $a_0 = 4.0$ Å) using the Onsager reaction field model (self-consistent reaction field = dipole) at the HF/6-31G(d) level of theory. As expected,²¹ redundant internal coordinates were the best choice for optimizing these kicked geometries. The number of steps required to fully optimize kicked geometries was the lowest when redundant internal coordinates were used. Cartesian coordinates were shown to be superior to internal coordinates (Z matrices). This is probably because programs (Gaussview, Molden, or NewZMat utility in Gaussian), which can generate a Z matrix automatically from other coordinates, make a poorly constructed Z matrix for atypical (kicked) geometries.²²

The efficiency of the optimization in redundant internal coordinates could also be improved by the Expert option (“OPT = Expert” keyword in the input route section). It is a convergence-related option which relaxes various limits on maximum and minimum force constants and step sizes enforced by the Berny program.²³ It is useful in cases where the forces and force constants are very different from those of typical molecules such as in kicked structures. In our case, this option led to faster convergence and decreased the number of optimization steps. It can be used in conjunction with an option (CalcFC) which specifies that the force constants be computed at the first point.

Algorithm-related options (Steep, GDIIS, and the quadratically convergent SCF procedure) were also tested, but only minor effects were observed. However, these convergence- and algorithm-related options might be more important if implemented in stochastic searches on larger molecular systems. It is likely that if the kick size is larger, the number of convergence failures and fragmentations (which cannot be foreseen from the initial kicked input) will also increase. In the case of simple models reported previously,^{11,12} no elimination of small molecules occurred, whereas in the case of the C₄H₉⁺ system, such fragmentations were quite frequent during the optimization procedure.

If the stochastic search for C₄H₉⁺ isomers was begun with all atoms at the origin, as described for the C₆ cluster,¹¹ no optimization converged at all, even though different convergence- and algorithm-related options were used. In contrast with the case of C₆ clusters, kicking the atoms-at-origin input and subsequent optimization of the kicked structure resulted in either hydrogen elimination or abnormal job termination.

Details of the Stochastic Search at MP2 Level. When the initial kicked structures (isomer **3** kicked by 0.8 Å) were optimized at the MP2 level, only eight optimization procedures failed (out of 50), whereas 20 failures occurred if the same structures were optimized at the HF level. Although more expensive,²⁴ electron-correlated methods, such as MP2, are more effective in searching for new isomers and more useful in describing the C₄H₉⁺ PES via the stochastic search procedure. For example, the geometry optimization of the initial *cis*-2-butyl cation structure (**3** kicked by 0.8 Å) converged to seven different isomers (**1**, **2**, **3'**, **5**, **6**, **7**, and **8**) when using the MP2 method, whereas only three (out of five possible) different isomers (**3'**, **6**, and **7**) were located when the HF method was employed.

Details of the Stochastic Search at the DFT Level. The density functional theory was found to be less effective than the MP2 method in searching for new isomers on the C₄H₉⁺ PES. A much larger number of kicks (with different kick sizes) is necessary to reproduce the results calculated at the MP2 level.

The efficiency of the DFT method is comparable to that of the HF method. However, the number of steps needed to complete the geometry optimization of the initial kicked structure is usually larger in the case of the B3LYP method. For example, the geometry optimization of the initial *cis*-2-butyl cation structure (**3** kicked by 0.8 Å) converged to corresponding isomers (**1**, **2**, **3'**, **5**, **6**, **7**, or **8**) in ca. 50–60

steps when using the HF (or MP2) method, whereas more than 100 steps were needed to complete the optimization procedure when the DFT method was employed. To solve this convergence problem when using the DFT method, we have tested a “loose” option which sets the optimization convergence criteria to a maximum step size of 0.01 au and an RMS force of 0.00017 au. These values are consistent with the SG1Grid grid size [IOP(5/44=1) setting] which is expected to speed up geometry optimizations, especially when still far away from the next stationary point. Although the loose option is intended only for a preliminary work, we found it useful to speed up the DFT convergence. The isomers located with the tight option were reproduced with the loose option but in a much smaller number of steps (ca. 70 steps). Smaller grids [a CoarseGrid grid size with IOP(5/44=2) setting] were also tested, but no improvement was obtained. On the contrary, all geometries obtained with a small grid size are characterized with one or more imaginary frequencies (mostly methyl rotor). This artifact is known for methods which use numerical integration of the functional, such as density functional theory, since the accuracy of this grid size is not high enough for computing low-frequency modes very precisely.

Therefore, the results of the stochastic search at the B3LYP level are dependent on the numerical integration grid used in calculations.²⁵ Both the number of steps for geometry optimization and the number of imaginary frequencies of isomers located are affected if different grid sizes are applied in DFT calculations.

Acknowledgment. We gratefully acknowledge the financial support of this research by the National Science Foundation and the Ministry of Science, Education and Sport of the Republic of Croatia.

Supporting Information Available: Cartesian coordinates of structure **3'** optimized at the HF, MP2, and CCD levels and optimized structures **1**, **4**, **5**, **6**, **8**, and **9** at the CCD/6-311G(d,p) level. Cartesian coordinates of structure **3'** optimized at the MP4(SDQ)/6-311G(d,p), CCD/6-311++G(d,p), and QCISD/6-311G(d,p) levels are enclosed as well.

References

- Olah, G. A.; Baker, E. B.; Evans, J. C.; Tolgyesi, W. S.; McIntyre, J. S.; Basteion, I. J. *J. Am. Chem. Soc.* **1964**, *86*, 1360–1373. (b) Saunders, M.; Hagen, E. L. *J. Am. Chem. Soc.* **1968**, *90*, 6881–6882. (c) Saunders, M.; Hewett, A. P.; Kronja, O. *Croat. Chem. Acta* **1992**, *65*, 673–679.
- (a) Saunders, M.; Hagen, E. L.; Rosenfeld, J. C. *J. Am. Chem. Soc.* **1968**, *90*, 6882–6884. (b) Saunders, M.; Kates, M. R. *J. Am. Chem. Soc.* **1978**, *100*, 7082–7083. (c) Walker, G.; Kronja, O.; Saunders, M. *J. Org. Chem.* **2004**, *69*, 3598–3601.
- Saunders, M.; Kates, M. R. *J. Am. Chem. Soc.* **1978**, *100*, 708–709.
- Saunders, M.; Rosenfeld, J. C. *J. Am. Chem. Soc.* **1970**, *92*, 2548–2549.
- Olah, G. A.; White, A. M. *J. Am. Chem. Soc.* **1969**, *91*, 3954–3956.
- Myhre, P. C.; Yanoni, C. S. *J. Am. Chem. Soc.* **1981**, *103*, 230–232.
- (7) For general treatment of isotope effects see: (a) Biegeleisen, J.; Wolfsberg, M. *Adv. Chem. Phys.* **1958**, *1*, 15–76. (b) Melander, L. In *Isotope Effects on Reaction Rates*; Ronald Press: New York, 1960. (c) Collins, C. I.; Bowman, N. S. In *Isotope Effects in Chemical Reactions*; Van Norstrand Reinhold: New York, 1970; ACS Monograph 167. (d) Wolfsberg, M. *Acc. Chem. Res.* **1972**, *7*, 225–233. (e) Melander, L.; Saunders, W. H., Jr. In *Reaction Rates of Isotopic Molecules*; Wiley: New York, 1980.
- (8) (a) Saunders, M.; Cline, G. W.; Wolfsberg, M. *Z. Naturforsch., A: Phys. Sci.* **1989**, *44*, 480–486. (b) Saunders, M.; Cline, G. W. *J. Am. Chem. Soc.* **1990**, *112*, 3955–3963.
- (9) Saunders, M.; Laidig, K. E.; Wolfsberg, M. *J. Am. Chem. Soc.* **1989**, *111*, 8989–8994.
- (10) (a) Sieber, S.; Buzek, P.; Schleyer, P. v. R.; Koch, W.; Carneiro, J. W. de M. *J. Am. Chem. Soc.* **1993**, *115*, 259–270. (b) Ibrahim, M. R.; Jorgensen, W. L. *J. Am. Chem. Soc.* **1989**, *111*, 819–824. (c) Radom, L.; Pople, J. A.; Schleyer, P. v. R. *J. Am. Chem. Soc.* **1972**, *94*, 5935–5945.
- (11) Saunders, M. *J. Comput. Chem.* **2004**, *25*, 621–626.
- (12) Bera, P. P.; Sattelmeyer, K. W.; Saunders, M.; Schaefer, H. F.; Schleyer, P. v. R. *J. Phys. Chem. A* **2006**, *110*, 4287–4290.
- (13) Saunders, M. *J. Am. Chem. Soc.* **1987**, *109*, 3150–3157.
- (14) (a) Boronat, M.; Viruela, P.; Corma, A. *Appl. Catal., A* **1996**, *146*, 207–223. (b) Hudson, C. E.; Eapen, S.; McAdoo, D. J. *Int. J. Mass Spectrom.* **2003**, *228*, 955–967. (c) Boronat, M.; Viruela, P.; Corma, A. *J. Phys. Chem.* **1996**, *100*, 633–637.
- (15) Aubry, C.; Holmes, J. L. *J. Phys. Chem. A* **1998**, *102*, 6441–6447.
- (16) Esteves, P. M. G.; Alberto, G. P.; Ramirez-Solis, A.; Mota, C. J. A. *J. Phys. Chem. A* **2000**, *104*, 6233–6240.
- (17) Schleyer, P. v. R.; Maerker, C.; Buzek, P.; Sieber, S. In *Stable Carbocation Chemistry*; Prakash G. K. S., Schleyer, P. v. R., Eds.; John Wiley & Sons: New York, 1997; Chapter 2.
- (18) Vrček, V.; Kronja, O.; Siehl, H.-U. *J. Chem. Soc., Perkin Trans.* **1999**, *2*, 1317–1321.
- (19) Anet, F. A. L.; Basus, V. J.; Hewett, A. P. W.; Saunders, M. *J. Am. Chem. Soc.* **1980**, *102*, 3945–3946.
- (20) Frisch, M. J.; Trucks, G. W.; Schlegel, H. B.; Scuseria, G. E.; Robb, M. A.; Cheeseman, J. R.; Zakrzewski, V. G.; Montgomery, J. A., Jr.; Stratmann, R. E.; Burant, J. C.; Dapprich, S.; Millam, J. M.; Daniels, A. D.; Kudin, K. N.; Strain, M. C.; Farkas, O.; Tomasi, J.; Barone, V.; Cossi, M.; Cammi, R.; Mennucci, B.; Pomelli, C.; Adamo, C.; Clifford, S.; Ochterski, J.; Petersson, G. A.; Ayala, P. Y.; Cui, Q.; Morokuma, K.; Malick, D. K.; Rabuck, A. D.; Raghavachari, K.; Foresman, J. B.; Cioslowski, J.; Ortiz, J. V.; Baboul, A. G.; Stefanov, B. B.; Liu, G.; Liashenko, A.; Piskorz, P.; Komaromi, I.; Gomperts, R.; Martin, R. L.; Fox, D. J.; Keith, T.; Al-Laham, M. A.; Peng, C. Y.; Nanayakkara, A.; Gonzalez, C.; Challacombe, M.; Gill, P. M. W.; Johnson, B.; Chen, W.; Wong, M. W.; Andres, J. L.; Gonzalez, C.; Head-Gordon, M.; Replogle, E. S.; Pople, J. A. *Gaussian 98*, revision A.7; Gaussian, Inc.: Pittsburgh, PA, 1998.
- (21) Baker, J. *J. Comput. Chem.* **1993**, *14*, 1085–1100. (b) Pulay, P.; Fogarasi, G.; Pang, F.; Boggs, J. E. *J. Am. Chem. Soc.* **1979**, *101*, 2550–2560.

- (22) Geometry optimizations in internal coordinates (Z matrices) were often aborted with a message that “angle Alpha is outside the valid range”, that is, that the conversion from Z matrix to Cartesian coordinates failed.
- (23) See the Gaussian 98 User’s Reference on the Web. http://www.gaussian.com/g_downloads/g98help.zip (accessed Oct 1, 2006).
- (24) Frequency calculations of $C_4H_9^+$ isomers at the MP2(FU)/6–31G(d) level of theory are about 5 times slower than the corresponding calculations at the HF/6–31G(d) level.
- (25) It is important to use the *same* grid for all calculations where one intends to compare energies (e.g., computing energy differences or heats of formation).
CT600308B